Cable & Connectivity Industry Forum™

by IWCS

2023 PROCEEDINGS

72ND ANNUAL IWCS CABLE & CONNECTIVITY INDUSTRY FORUM

SEPTEMBER 17–20, 2023 | ORLANDO, FLORIDA, USA



TABLE OF CONTENTS

Click on a session below to navigate to that section of the Proceedings.

SESSION 1: EXECUTIVE SESSION

1-1 **Metallic Wire and Cable: Recession Risk vs. Green Energy Transition**

1-2 **Optical Cable: Demand Growth Pared Back as Challenges Mount**

1-3 **Digital Electricity: Leading the Transition to an Energy Efficient World**

1-4 **Global Economic Outlook**

1-5 **Elements of an Industry Business Plan to be Successful in the World of AI and Electrification**

PLENARY LUNCHEON

Keynote Presentation: **Disruptive Opportunities: Building the Ambient Intelligence Backbone;** Scott Klososky, Founding Partner, Future Point of View, LLC.

PANEL DISCUSSIONS

- **Environmental Sustainability and Recycling for the Cable Industry**
- **Fault-Managed Power: A Safe and Disruptive Innovation for Powering the Future**
- **Renewable/Offshore Energy**

SUPPLIER SPOTLIGHT SESSION

SESSION 2: NETWORK RELIABILITY & MEASUREMENTS

2-1 **Power Storage Control Method for Multiple Remote-Operated Optical Fiber Switching Nodes**

2-2 **A Fiber Inspection Microscope Integrated with Cleaning Function**

2-3 **Reliable Prediction of Data Center Interconnect Network Flaps via Distributed Acoustic Sensing (DAS) and Supervised Machine Learning**

2-4 **Artifacts for Measuring Bias and Repeatability of Fiber Inspection Scopes**

SESSION 3: DESIGN, TESTING & APPLICATIONS FOR COPPER ETHERNET, POE AND ENERGY CABLES - PART 1

3-1 **Extracting and Discriminating Spontaneously Recovering Faults, Case Study on Pressurized Cable**

3-2 **Impact of Thermal Aging on Safety Performance of Power-Over-Ethernet Cables**

3-3 **Channel Performance Degradation From Installation Stresses**

3-4 **Topography Scanner for Quality Control of Power Cable Manufacturing**

SESSION 4: POSTER

4-2 **High-Density Optical Cable with Ultra-Low-Loss, Large Effective Area ITU-T G.654.E Optical Fiber**

4-3 **Evaluation of 165μm Reduced Coating Diameter Fibers for High Density Cable Applications**

4-4 **High-Density Micro Cable Family with Next Generation 190 Micron Fibers**

4-5 **Development of a High Fiber Density 432-Fiber Microduct Cable**

SESSION 5: SPECIALTY APPLICATIONS

5-1 **Sea Trail Results of OCC-SC630**

5-2 **Development and Application of an Air-Blown Optical Cable with Bidirectional Construction**

5-3 **35 Years Of Fiberoptic Coastal Installations In Norway**

SESSION 6: FIBER MANUFACTURING

6-1 **Design Process of a 192-Fibre Cable with Fibres Coated to 180μm Diameter**

6-2 **A Novel Modelling Approach for Sintering of Cylindrical Silica Soot Preform**

SESSION 7: CONNECTIVITY

7-1 **Liquid Immersion Multi-Fiber Connector for Data Center Cooling System**

7-2 **Connection Characteristics of Coupled Multicore Fiber Connector**

7-3 **Optical Transceivers and Structured Cabling with Expanded Beam Connectors as an Alternative to Active Optical Cables**

7-4 **A VSFF, Multi-Row, Multi-Fiber Connector with Multi-Vendor Interoperability**

7-5 **A Novel, Low-Loss, Multi-Fiber Connector with Increased Usable Fiber Density**

7-6 **Sustainable Network Design: Plastic Reduction with Ultra High-Density Cabling with Thinner Coating and VSFF Connector in Data Centers**

SESSION 8: MULTI-CORE & SPECIALTY FIBER

8-1 **100G/Lane Enabled Multimode Fiber: A High-Speed Solution for Short-Reach VCSEL Transmission**

8-2 **A Low Crosstalk Weakly Coupled 7-Core Single Mode Fiber**

8-3 **Multicore Fiber for Space-Constrained, High Bandwidth Density Applications**

8-4 **Research of Crosstalk Characteristics Based On Weakly Coupled Seven-Core Fiber**

8-5 **Low-Loss All-Fiber Mode Multiplexer for Weakly-Coupled Few-Mode Fiber**

8-6 **Crosstalk Characteristics of 200mm Coating 4-Core Fibers in 288-Fiber/864-Fiber Freeform Ribbon Cables**

8-7 **Low Attenuation Orbital Angular Momentum Fiber**

SESSION 9: CODES & STANDARDS

9-1 **Clarifying the Changes – Update on Revisions To UL'S Certification Documents**

9-2 **Emissivity - A Relevant Parameter for Burn Testing According to EN 50399**

9-3 **Single Pair – Next Steps**

9-4 **Predictive Modeling of Large-Scale Flame Tests on Cables Using Cone Calorimeter**

9-5 **Cabling for Fault-Managed Power Systems (What Is Class 4?)**

SESSION 10: DESIGN, TESTING & APPLICATIONS FOR COPPER ETHERNET, POE AND ENERGY CABLES - PART 2

10-1 **Extended 10Gbps Data Transmission Over Cat 6A: Facts vs Myths**

10-2 **Intra-Pair Skew: About Wave Propagation in Screened Single Pair**

10-3 **Coupling Attenuation and Burst Test on Balanced Cables and Cabling Systems**

10-4 **Designing of Single-Pair Ethernet Cable**

10-5 **Environmental Resilience of Twisted Pair Ethernet Applications at Lengths Greater than 100 Meters**

10-6 **Relation of Coupling Attenuation and Unbalance Attenuation**

10-7 **Measuring and Simulating TCTL in Unbalanced Cable**

10-8 **Power Over Communication Cables for Extended Distance: Myths and Misconceptions**

SESSION 11: CABLE MATERIALS & PROPERTIES

11-1 **New Advancement in Polyvinylidene Fluoride (PVDF) Materials**

11-2 **Foamed PVDF Jacket for Power-Over-Ethernet Cables to Overcome Thermal Aging Challenges**

11-3 **Materials Considerations for Laser Printed Jacket Solutions**

11-4 **Effects of Filler Surface Modification on Coupling Effects in Halogen Free Flame Retardant Cable Compounds**

11-5 **Polyurethane Resin-based FRP Rods as Embedded Strength Members in Optical Fiber Cables**

11-6 **Tailored Color Packages for Optimizing the Processing and Performance of Crosslinking Polyolefins**

11-7 **Fluoropolymer Processing Aid Replacement in Cable Jacketing Compounds**

11-8 **Research On Influencing Factors Of Smoke Density In Flame Retardant Optical Cable**

SESSION 12: CABLE MODELING & DESIGN

12-1 **Exploration Study of Jacket Shrinkback Test Methods**

12-2 **An Analytical Formula of Microbending Sensitivity for Reduced Diameter Optical Fibers**

12-3 **Indoor-Outdoor Air Blown Optical Cable**

12-4 **Central Tube Cable Design for Easy Access of Embedded Strength Members**

12-5 **Hybrid Cables for 4G/5G Technology Networks**

SESSION 13: OPTICAL FIBER COATING MATERIALS

13-2 **Next Generation Optical Fiber Coatings with Excellent Accelerated Aging Performance, While Maintaining Robust Draw Processing Capability**

13-3 **Impact of Environmental Stresses and Lifetime Aging Simulation on Optical Fiber Coatings**

13-4 **Prediction of Physical Properties of Optical Fiber Coating Resins Based on Chemical Kinetics**

13-5 **Investigation on Application of Biomass Raw Materials to Optical Fiber Coating Agents**

13-6 **UV-Curable High Temperature Resistant Dual Layer Coating System for Specialty Optical Fiber Applications**

SESSION 14: SPECIALTY INSTALLATION

14-1 **Installing a Cable in a Duct Solely by the Flow of Water, Faster than the Flow Itself!**

14-2 **Cable Jetting Velocity Prediction Model**

14-3 **Pre-Connectorized Ultra-High-Density Cable for Easy Installation**

14-4 **Fundamental Study of Planar Closure for Wiring on Road Surface**

14-5 **Study of Easy Thin Optical Fiber Cabling Method**

14-6 **Study on Streamlining Cable Removal Process**

14-7 **Methodology to Maintain Low Breaking Load and High Mechanical Reliability in Optical Fiber Drop Cable for Fttx Network**

SESSION 15: HIGH DENSITY RIBBON

15-1 **Development of Low Loss Central Core Rollable Ribbon Cable**

15-2 **High-Density Cables with 200-Micron Flexible Ribbons**

15-3 **Single Jacket Armored Wrapping Tube Cable with Easy Fiber Access**

15-4 **High Fiber Density 3456F Flexible Ribbon Indoor/Outdoor Cable for Indoor Outdoor Data Center Applications**

15-5 **144F High-Density Ribbon Cable Supporting/Compatible to Legacy Network**

15-6 **Optical Fiber Ribbon Cables with Full Color Spectrum**

POSTER SESSION

- **Development of 22.9Kv Submarine Horizontal Directional Drilling (HDD) Power Cable**
- **Experimental Study on Measuring Method of Residual Torsion of Fiber Ribbon**
- **UV Protection and Lightfastness of Outdoor Cables**
- **A Method for Estimating the Combustion Performance (Smoke Density) of Optical Cables Based on Material Thermal Analysis Techniques**
- **Research on Shrinkage Performance of Central Core Tube Optical Cable**
- **Optical Cable Impact on Environmental Performance of Single-Fiber Patchcord**
- **Print Length Verification System**
- **Temperature Performance Study of Loose Tube Materials**

SESSION 1: EXECUTIVE SESSION

Click on a session or panelist name below to navigate to that section of the Proceedings.

The Executive Session is designed for the general management of the wire and cable producing companies and their suppliers. Important issues facing the industry will be addressed by expert speakers in a provocative session that includes the following topics and presenters.

Chairperson: David B. Kiddoo; IWCS, USA

1-1 **Metallic Wire and Cable: Recession Risk vs. Green Energy Transition**

1-2 **Optical Cable: Demand Growth Pared Back as Challenges Mount**



Chenfei Wang, *CRU*

Chenfei is Head of CRU's Wire and Cable team, and works across the full portfolio of products analysing key trends and developments in both the metallic wire and cable, and optical fibre industries.

Learn about recession trends and how growing demand green energy is impacting the forecast of insulated metallic wire and cable demand around the world. Chenfei will present back-to-back presentations in this session.

1-3 **Digital Electricity: Leading the Transition to an Energy Efficient World**



Stephen Eaves, *VoltServer*

Stephen is the founder and CEO of VoltServer and is the inventor of Digital Electricity. The company has deployed the technology in over 1,000 large venues worldwide. Steve has more than 30 years of experience innovating around electrical energy storage, distribution, and control. Steve has authored or co-authored numerous industry and peer reviewed papers related to the energy industry and is an inventor on 35 patents.



Luis Suau, *Sinclair Digital Services*

Luis is the Chief Business Officer of Sinclair Digital Services and one of the original Pioneers of Power over Ethernet technology as well as a pioneer in the application of Digital Electricity to smart buildings. Luis has 40 + years of experience in IT, 26 years at Cisco in internal Consulting and R&D roles and is an inventor on 4 patents.

Digital Electricity was adopted into the National Electric Code in 2023 under the generic industry term "Fault Managed Power Systems" or FMPS. This talk will introduce the concept of Fault Managed Power Systems, its incorporation into building code, and the potential to fundamentally change the materials, practices and trade skills for electricity distribution.

1-4 **Global Economic Outlook**



Robert Fry, *Chief Economist, Robert Fry Economics*

Robert analyzes and forecasts the global economy to guide business decision-makers. He publishes a monthly newsletter, "Current Economic Conditions", and speaks on the economic outlook to corporate leadership teams, customer events, and trade association meetings. In 2018, Robert was elected a Fellow of the National Association for Business Economics, in recognition of his outstanding service as a professional business economist and his contributions to the field of business economics.

Robert Fry will discuss current conditions in the global economy and the outlook for future growth, with emphasis on U.S. manufacturing and on markets important to the wire and cable industry. In particular, he will discuss high inflation and what it implies about the likelihood of a recession in the near future. Among the topics covered will be growth in GDP and industrial production, including wire & cable production, housing starts, light vehicle sales, inflation, and interest rates.

1-5 **Elements of an Industry Business Plan to be Successful in the World of AI and Electrification**



Scott Klososky, *Future Point of View, LLC.*

Scott lives on the leading edge of technology and innovative thinking. Scott speaks to large audiences worldwide about the intersection of humanity and the Digital Transformation.

Scott will be sharing some of the latest thinking in leadership concepts that can be applied to a world where cabling infrastructure will soon be supporting an AI powered world. High Beam strategic improvements today will pay off well when organizations build an ambient intelligence layer that augments the decision making done by humans today.

Click here to return to the **Table of Contents**

Metallic Wire and Cable: Recession Risk vs. Green Energy Transition



Chenfei Wang
CRU Group
Room 1002, Plaza 336, No.336 Middle Xizang Road, Huangpu District, Shanghai, 200001
+86 21-63793322; chenfei.wang@crugroup.com

Abstract

Interest rates continue to rise in the US and Europe, increasing the likelihood of a recession. Construction-related cable demand struggles, though green energy transition cables are resilient. Chinese GDP growth of over 5% in 2023 will provide significant support for domestic cable consumption. However, production growth will be more modest as exports weaken. CRU forecasts world insulated metallic wire and cable demand will grow by 2.4% y/y this year, healthy growth but not spectacular. However, the emergence new key cable demand driver as energy security has superseded decarbonization as a priority will support global HV and EHV cable demand to grow at a 11.7% CAGR between 2022 and 2029. Subsea cables which are mainly used in offshore wind and interconnector applications will grow at above 25% CAGR over the same time horizon.

Keywords: low-voltage energy cable, HV and EHV, communications cable, winding wire, renewables, e-mobility, energy transition, energy security, macro-economic trends

Bio

Chenfei is Head of CRU's Wire and Cable team, and works across the full portfolio of products analysing key trends and developments in both the metallic wire and cable, and optical fibre industries. He is a Principal Analyst and also the current editors of CRU's Telecom Cables Market Outlook and Optical Fibre and Cable Monitor.

Chenfei joined CRU in early 2019 as an Analyst within the Wire and Cable team. At CRU, Chenfei held various editorship roles including Wire and Cable Market Outlook and HV and EHV Cables Market Outlook. Prior to CRU, Chenfei was working at Rolls-Royce in a variety of engineering leadership roles, with a focus on aeroengine technology development and manufacturing process improvement.

He holds an MSc in Advanced Materials Science and Engineering from Imperial College London, and a BEng (Hons) in Chemical and Materials Engineering from the University of Auckland. Chenfei spent 3.5 years in CRU London office and he is now based in CRU Shanghai office.

Optical Cable: Demand Growth Pared Back as Challenges Mount



Chenfei Wang
CRU Group
Room 1002, Plaza 336, No.336 Middle Xizang Road, Huangpu District, Shanghai, 200001
+86 21-63793322; chenfei.wang@crugroup.com

Abstract

The 2023 outlook for optical cable demand further deteriorated since the beginning of the year. The China Mobile tender announcement has delayed by more than six months. This has taken a toll on Chinese domestic optical cable demand in the first quarter of this year. As a result, CRU further downgraded the country's full year optical cable demand growth. Off the back of weaker domestic demand, top Chinese producers are actively exploring more oversea market opportunities. US cable demand growth for this year has been further tempered. The supply chain still needs to reduce the accumulated fibre and cable inventories after some "panic buying" from last year. Some carriers have reduced their FTTH deployment targets in 2023 due to inflation concerns and labour shortages. Despite the near-term slowdown, we remain optimistic about North America's mid-term demand outlook driven by both private and public funding opportunities.

Keywords: optical fiber, communication cable, FTTH, 5G, data center, telecom infrastructure, broadband networks, fiber prices

Bio

Chenfei is Head of CRU's Wire and Cable team, and works across the full portfolio of products analysing key trends and developments in both the metallic wire and cable, and optical fibre industries. He is a Principal Analyst and also the current editors of CRU's Telecom Cables Market Outlook and Optical Fibre and Cable Monitor.

Chenfei joined CRU in early 2019 as an Analyst within the Wire and Cable team. At CRU, Chenfei held various editorship roles including Wire and Cable Market Outlook and HV and EHV Cables Market Outlook. Prior to CRU, Chenfei was working at Rolls-Royce in a variety of engineering leadership roles, with a focus on aeroengine technology development and manufacturing process improvement.

He holds an MSc in Advanced Materials Science and Engineering from Imperial College London, and a BEng (Hons) in Chemical and Materials Engineering from the University of Auckland. Chenfei spent 3.5 years in CRU London office and he is now based in CRU Shanghai office.

Executive Session

"Digital Electricity - Trends and Opportunities"

Stephen Eaves, *VoltServer, USA*

Luis Suau, *Sinclair Digital Services, USA*





Steve Eaves
CEO
VoltServer Inc
East Greenwich, Rhode Island, USA
T: 401-474-4616
M: stephen.eaves@voltserver.com

Luis Suau
CBO
Sinclair Digital Services, Inc
Fort Worth, Texas, USA
T: 954-579-8737
M: lsuau@sinclair-digital.com

Summary

While communications and computing have evolved exponentially in recent years, there has been little change in how electricity has been distributed since the late 1800's.
In 2014 VoltServer invented the first Fault Managed Power System (FMPS) under the trade name Digital Electricity™. A transmitter unit converts AC or DC electricity to discreet packets of energy and data sent hundreds of times a second over thin communication cables to a receiver - each packet is checked to ensure that not even small amounts of energy are lost to a fault. For the first time, even at hundreds of Volts, shock and fire hazards are managed by converting electricity to a format that is inherently safe from the source, rather than being contained in metal conduit with add-on safety devices and complicated installation practices. Moreover, the two traditionally separate worlds of operational (electrical) and information technology converge with Digital Electricity as it accommodates data and "AC-like" power levels in the same cable or duct, using IT trade skills. Digital Electricity was adopted into the National Electric Code in 2023 under the generic industry term "Fault Managed Power Systems" or FMPS. This talk will introduce the concept of Fault Managed Power Systems, its incorporation into building code, and the potential to fundamentally change the materials, practices and trade skills for electricity distribution. The use case of the Marriott Sinclair will be presented. The Sinclaire is a luxury "smart" hotel in Ft. Worth Texas that employs FMPS and Power Over Ethernet technology to deliver an unprecedented user experience to its customers.

Keywords: Fault Managed Power, Class 4 Power, Digital Electricity, PoE, Power over Ethernet, Smart Buildings

Bio

Stephen Eaves is the founder and CEO of VoltServer and is the inventor of Digital Electricity, a new electricity format adopted into the US National Electric Code in 2023. The company has deployed the technology in over 1,000 large venues worldwide. Steve has more than 30 years of experience innovating around electrical energy storage, distribution, and control. Steve has authored or co-authored numerous industry and peer reviewed papers related to the energy industry and is an inventor on 35 patents.

Luis Suau is the Chief Business Officer of Sinclair Digital Services and one of the original Pioneers of Power over Ethernet technology as well as a pioneer in the application of Digital Electricity to smart buildings. Luis has 40 + years of experience in IT, 26 years at Cisco in internal Consulting and R&D roles and is an inventor on 4 patents.

Executive Session
"Global Economic Outlook"



Robert Fry
Robert Fry Economics LLC
Greenville, DE USA
+1-302-743-8553 · robertfryeconomics@gmail.com

Abstract

Robert Fry will discuss current conditions in the global economy and the outlook for future growth, with emphasis on U.S. manufacturing and on markets important to the wire and cable industry. In particular, he will discuss high inflation and what it implies about the likelihood of a recession in 2023. Among the topics covered will be growth in GDP and industrial production, including wire & cable production, housing starts, light vehicle sales, inflation, and interest rates. A brief Question & Answer period will follow Robert's presentation.

Keywords: Economy, macroeconomics, manufacturing, GDP, industrial production, recession, recovery

Bio

Robert Fry is Chief Economist of Robert Fry Economics LLC, where he analyzes and forecasts the global economy to guide business decision-makers. Robert publishes a monthly newsletter, *Current Economic Conditions*, and speaks on the economic outlook to corporate leadership teams, customer events, and trade association meetings

In 2018, Robert was elected a Fellow of the National Association for Business Economics, in recognition of his outstanding service as a professional business economist and his contributions to the field of business economics. He joins an exclusive group that includes four Nobel laureates and the last four Chairs of the Federal Reserve. He is also a member of the *Consensus Economics*, *Wall Street Journal* and CNBC survey panels and has taught Economics to MBA students at the University of Delaware.

Until retiring in June 2015, Robert was Senior Economist at DuPont, where he analyzed the global economy and its impact on DuPont, published a monthly newsletter sent to thousands of DuPont employees and customers, and made more than 800 speeches on the economic outlook to DuPont senior management, business teams, customers, and trade associations.

While at DuPont, Robert and his colleague Bob Shrouds were named among the top economic forecasters by Bloomberg, USA Today, and the Wall Street Journal. In 2005, they won the prestigious Lawrence R. Klein Award for Blue Chip Forecasting Accuracy, making the DuPont Economist's Office the first three-time winner of the award.

Robert received his Bachelor's degree in Economics from Ohio University and his Master's degree and PhD in Economics from Harvard University.

Robert has served on the boards of seven non-profit organizations, including the National Association for Business Economics, the nationally recognized Charter School of Wilmington, and the Honors Tutorial College at Ohio University. He would welcome the opportunity to use his board experience and knowledge of the global economy by serving on the Board of Directors of a for-profit company.

Executive Session

Elements of an Industry Business Plan to be Successful in the World of AI and Electrification



Scott Klososky
Founding Partner of Future Point of View, LLC.
Edmond, OK
T: +1 405-226-9897; scott@fpov.com

Description

One of the more difficult tasks leaders have today is designing and redesigning their digital strategy roadmaps. Technology evolution is exciting and at the same time problematic when it comes to making decisions on investing time and money! In this executive session Scott will be sharing some of the latest thinking in leadership concepts that can be applied to a world where cabling infrastructure will soon be supporting an AI powered world. High Beam strategic improvements today will pay off well when organizations build an ambient intelligence layer that augments the decision making done by humans today.

Keywords Digital Leadership, High Beam Strategy, Humalogy, Artificial Intelligence, The Ambient Mesh, Digital Strategy Roadmapping

Bio

As a founding partner of digital strategy firm, Future Point of View (FPOV), Scott lives on the leading edge of technology and innovative thinking. Scott speaks to large audiences worldwide about the intersection of humanity and the Digital Transformation. Through FPOV, Scott provides advisory work for clients including Fortune100, SMB's and government entities. This work has driven him to develop unique concepts such as the HUMALOGY® Scale for measuring the amount of human or machine involved in a system or process, and the Rivers of Information® process for building learning eco-systems. He also pioneered a framework for looking accurately into the future of an industry sector in order to set organizational strategy: The High Beam process.

PLENARY SESSION AWARDS AND KEYNOTE

GREETINGS/ANNOUNCEMENTS



David B. Kiddoo
CEO/Director
IWCS, Inc.



Ben Waite
Vice Chair of the Board
Fiber Optic Center



Dr. Bianca Hydutsky
2023 Committee Chair
The Chemours Company

Keynote Presentation



Scott Klososky
Founding Partner
Future Point of View, LLC.

"Disruptive Opportunities: Building the Ambient Intelligence Backbone"

As a founding partner of digital strategy firm, Future Point of View (FPOV), Scott lives on the leading edge of technology and innovative thinking. Scott speaks to large audiences worldwide about the intersection of humanity and the Digital Transformation. Through FPOV, Scott provides advisory work for clients including Fortune100, SMB's and government entities. This work has driven him to develop unique concepts such as the HUMALOGY® Scale for measuring the amount of human or machine involved in a system or process, and the Rivers of Information® process for building learning eco-systems. He also pioneered a framework for looking accurately into the future of an industry sector in order to set organizational strategy: The High Beam process.

Click here to advance to the **Keynote description**

2022 Awards & Recognition

Jack Spergel Memorial Award for Outstanding 2022 Technical Paper

Development of Best Practices and Guidelines for the Use of Expanded Beam Connectors in Data Center Applications
Dr. Tatiana Berdinskikh, Senko Advanced Components, USA

Kitts-Kingsley Award for Best 2022 Presentation

HFFR Cable Compounds: Influence of Flame-Retardant Filler and Coupling Agent on EVA/LLDPE Blend Systems
Dr. Michael Heinz, Corning Optical Communications, Germany

Award for Outstanding 2022 Poster Paper

"Development of Anti-Hacking Optical Cable"
Yongchan Park, GAON Cable, Republic of Korea

Honoring Retiring IWCS Board of Directors & Committee Members



Larry Bleich
CommScope, Inc.



Robert Canny
TE Wire & Cable



Steve Galan
UL Solutions



Mike Patel
Teknor Apex Company

Click here to return to the **Table of Contents**

Plenary Session

Disruptive Opportunities: Building the Ambient Intelligence Backbone



Scott Klososky
Founding Partner of Future Point of View, LLC.
Edmond, OK
T: +1 405-226-9897; scott@fpov.com

Abstract

The digital transformation is not even halfway through its level of impact on humanity. There are many innovations and combinations of digital inventions still to come over the next twenty years. Underneath the new layers of ambient intelligence and computing power will be infrastructure that will need to support vastly different computing needs than today. The more accurate our High Beam vision, the better investments and strategic moves can be made.

Keywords Artificial Intelligence, convergence, IoT, Quantum Computing, Metaverse, Web3, Humalogy, Digital Centaurs, The Ambient Mesh

Bio

As a founding partner of digital strategy firm, Future Point of View (FPOV), Scott lives on the leading edge of technology and innovative thinking. Scott speaks to large audiences worldwide about the intersection of humanity and the Digital Transformation. Through FPOV, Scott provides advisory work for clients including Fortune100, SMB's and government entities. This work has driven him to develop unique concepts such as the HUMALOGY® Scale for measuring the amount of human or machine involved in a system or process, and the Rivers of Information® process for building learning eco-systems. He also pioneered a framework for looking accurately into the future of an industry sector in order to set organizational strategy: The High Beam process.

INDUSTRY SUSTAINABILITY PANEL DISCUSSION

ENVIRONMENTAL SUSTAINABILITY AND RECYCLING FOR THE CABLE & CONNECTIVITY INDUSTRY

Sponsored by: Chemours™

Click on a person below to advance to their biography.



Brian Ensign
Superior Essex Communications



Cy Genna
The Chemours Company



Dr. Bianca Hydutsky
The Chemours Company
MODERATOR



Ralph Marcario
Fluoropolymer Resources USA



Dustin Smith
Copperweld Bimetallics



Jay Thomas
Vinyl Sustainability Council

Click here to return to the **Table of Contents**

Environmental Sustainability and Recycling for the Cable & Connectivity Industry
Special Session Panelist
"Cable Products to Assure a Sustainable Future"



Brian Ensign
VP of Marketing
Superior Essex Communications
Atlanta, GA
T: +1-770-547-0796; brian.ensign@spsx.com

Summary

Sustainable cabling is enabling the next generation of smart buildings to be more adaptive and efficient than ever before. Digital building applications supported by Power over Ethernet (PoE) cabling are delivering a host of sustainable benefits for the built environment – from increased energy efficiency and lower capital and operating costs to improved occupant well-being and productivity. With products and accessories manufactured sustainably and designed to minimize environmental impact, this enables us to contribute to leading green building standards such as: USGBC LEED v4, Living Building Challenge and the International WELL Building Institute.

Brian will bring his experience and the perspectives on the contributions a leading cable manufacturer can bring to assuring a sustainable future.

Bio

Brian Ensign is VP of Marketing for Superior Essex Communications. He has more than three decades of experience in the ICT and market development industry, working in the structured cabling, intelligent spaces, cyber security, and sustainability spaces. Brian is an active member of trade associations throughout his career; he is currently the Chairman of the Board of Continental Automated Buildings Association (CABA), President of Communications Cable and Connectivity Association (CCCA), and a past president of BICSI. Brian holds a degree in Electrical Engineering Technology from the SUNY Polytechnic Institute and has RCDD, NTS, OSP and RTPM designations from BICSI.

Environmental Sustainability and Recycling for the Cable & Connectivity Industry
Special Session Panelist
"Mission Critical and Sustainable Fluoropolymer Solutions"



Cy Genna
Product Stewardship and Regulatory Manager
Chemours Advanced Performance Materials
Wilmington, Delaware, USA
T: +1-302-540-5423; simone.m.genna@chemours.com

Summary

The world needs chemistry. Fluoropolymers and fluorinated gases (f-gases), power the largest industries and value chains, touching nearly every sector of the economy. They are critical solutions that will enable the energy transition, electrify transport, power AI, and battle the next pandemic. Their highly unique combination of properties gives them unmatched levels of performance. There are no alternatives that possess all these unique properties while delivering the same high level of performance.

Proposed regulations in Europe, the U.S. and elsewhere aim to restrict the manufacturing, use, and import of these and other PFAS substances on the market. Such a restriction would have a devastating impact on jobs, supply chains, the economy, and the ability to achieve climate, strategic autonomy, and innovation objectives. Chemours supports and advocates for a coherent regulatory approach that allows for the use of safer, better performing chemistries. We invite companies that produce or use fluoropolymers and f-gases, their customers, and their value chains to join us in this effort.

Bio

After several years focusing on fluoropolymer wire & cable applications and markets Cy was North America Regional Business Manager for PTFE & Melts from 2008-2018 (DuPont/Chemours). Cy played a key role in managing all aspects of a portfolio of fluoropolymer products from manufacturing through sales. Before his current role Cy was Global Quality Manager for Chemours Fluoroproducts, which included fluoropolymers and f-gases.

Since 2021 Cy has been representing the Advanced Performance Materials business of Chemours within industry associations advocating for the continued responsible manufacturing and safe intended uses of fluoropolymers in the face of mounting restrictions and other regulations on "PFAS". Cy works with industry partners to advance sustainable chemistry and encourage industry to be an active stakeholder in regulatory processes. Cy has a B.S. degree in Accounting from Penn State University and an MBA from the Northeastern University.

Environmental Sustainability and Recycling for the Cable & Connectivity Industry
Special Session Moderator



Dr. Bianca Hydutsky
Global Technology Director
Chemours Advanced Performance Materials
Wilmington, Delaware, USA
T: +1- 302-773-6548; bianca.hydutsky@chemours.com

Summary

The world needs chemistry. Fluoropolymers and fluorinated gases (f-gases), power the largest industries and value chains, touching nearly every sector of the economy. They are critical solutions that will enable the energy transition, electrify transport, power AI, and battle the next pandemic. Their highly unique combination of properties gives them unmatched levels of performance. There are no alternatives that possess all these unique properties while delivering the same high level of performance.

Proposed regulations in Europe, the U.S. and elsewhere aim to restrict the manufacturing, use, and import of these and other PFAS substances on the market. Such a restriction would have a devastating impact on jobs, supply chains, the economy, and the ability to achieve climate, strategic autonomy, and innovation objectives. Chemours supports and advocates for a coherent regulatory approach that allows for the use of safer, better performing chemistries. We invite companies that produce or use fluoropolymers and f-gases, their customers, and their value chains to join us in this effort.

Bio

Dr. Bianca Hydutsky received her Bachelor of Science degree in Chemistry from Millersville University and Doctorate in Chemistry from Penn State University. Her career began at DuPont in 2008 and when The Chemours Company was formed as a spinoff of DuPont in 2015, she elected to go with the Chemours team. After several impressive promotions, Dr. Hydutsky is presently the Global Technology Manager for The Chemours Company.

Dr. Hydutsky is the 2023 IWCS Symposium Committee Chair and she is involved in the women's network at Chemours.

Environmental Sustainability and Recycling for the Cable & Connectivity Industry
Special Session Panelist
"Circular Life Cycle and Sustainable Solutions for Fluoropolymer Components"



Ralph Marcario
Executive VP, Sales & Marketing
Fluoropolymer Resources USA
North Windham, Connecticut, USA
T: +1-203-313-0092; rmarcario@friusa.net

Summary

As the industrial world seeks to expand their core competencies to include circular product life cycles, responsible selection of materials and production impact on the environment, it has become increasingly critical for manufacturers to find effective partners to collaboratively manage sustainable end-of-life solutions for their products.

Since its founding in 1991, Fluoropolymer Resources has innovated and successfully implemented multinational end of life solutions for products made with fluoropolymers and a broader portfolio of plastics. Our current mission is to couple and expand our technical and logistical infrastructure to meet the increasing commitment of the global manufacturing base to circularity of their products.

Bio

After beginning his career at GE Silicones, Ralph has held commercial leadership positions in the fluoropolymer industry for the past twenty years. He served as Director of Sales and Marketing at Chromatics Inc. (now part of Avient) for fifteen years, ultimately joining Fluoropolymer Resources in his current role in 2018. He has a BS in Chemical Engineering from Rensselaer Polytechnic Institute.

Environmental Sustainability and Recycling for the Cable & Connectivity Industry
Special Session Panelist
"Sustainable Solutions for the Copper Crisis"



Dustin Smith
Chief Commercial Officer
Copperweld Bimetallics
Brentwood, TN
T: +1-615-440-0064; dsmith@copperweld.com

Summary

A copper crisis is looming!

Mining shortages, supply deficits, skyrocketing copper prices, as well as the "electrification" of many new applications, have combined to create unsustainable demand for copper. Annual demand is projected to increase to 40+ million tons by 2031, with a supply forecast of only 33+ million tons. That creates a 7.1-million-ton copper shortfall by the start of the next decade! Considering the wide-reaching impact of this issue, it's no surprise that the Department of Energy officially listed copper on its "2023 DOE Critical Materials List."

Many industries are beginning to look for safe alternatives to single-metal copper products. Bimetals are metallurgically bonded metals that have the potential to help close the distance between copper demand and supply. Bimetal alternatives to copper not only save copper, they often provide enhanced performance along with other benefits.

Keywords: Copper, Copper Shortage, Critical Materials, Bimetals, CCA, CCS

Bio

As Chief Commercial Officer for Copperweld, Dustin Smith is responsible for sales and marketing ideation and strategic direction. As a market disrupter, Dustin thrives on positioning unique but proven products in markets where they provide a distinctive advantage.

"The impact of diminished availability of copper for the global market is significant. Bringing alternative solutions to the world's requirement for a critical metal frees up copper resources for other products. Solutions create a bigger pie for everyone."

Dustin holds an MBA from Lipscomb University and served in active duty as a U.S. Marine from 2000-2005.

Overall, Dustin has 17 year's experience in the metals industry, with a focus in sales, marketing and distribution. Since joining Copperweld in 2015, the company's annual sales have increased by more than 500%.

Environmental Sustainability and Recycling for the Cable & Connectivity Industry
Special Session Panelist
"Connecting the Value Chain to Advance Sustainability in the Vinyl Industry."



Jay Thomas
Executive Director
Vinyl Sustainability Council
Washington, DC
T: +1-202-256-9531; jthomas@vinylinfo.org

Summary

The Vinyl Sustainability Council (VSC) is a voluntary membership organization that is taking a leadership role in uniting the industry to advance sustainable performance throughout the vinyl value chain.

Through the organization's +Vantage Vinyl sustainability standard, member companies receive 3rd party verification of compliance to five pillars of sustainability and signal to the world that they meet important environmental health and social criteria.

The VIABILTY™ recycling grant program, is providing up to $3 million in grant funding to spur interest and drive innovation in post-consumer vinyl recycling to help the industry reach its recycling goal.

VSC membership includes, and is open to, companies and organization throughout the vinyl/PVC value chain including: resin, compound and additive manufacturers, vinyl product manufacturers, extruders, recyclers, equipment manufacturers, distributors, and retailers.

Bio

Jay serves as the Vice President of Sustainability for the Vinyl Institute and the Executive Director of the Vinyl Sustainability Council. In these roles he is responsible for developing and implementing the strategies and tactics that support the sustainability mission and policies of the Vinyl Institute.

He has more than 25 years of vinyl industry experience in the wire and cable, roofing and flooring industries having worked in various capacities at Tyco International and Sika Corporation.

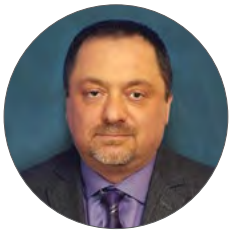
Jay is an emeritus director of the Green Building Initiative and is a certified Green Globes Professional. He holds a Bachelor of Science from Northeastern University and an M.B.A. from University of Massachusetts

EMERGING TECHNOLOGY PANEL DISCUSSION

FAULT-MANAGED POWER:
A SAFE AND DISRUPTIVE INNOVATION FOR POWERING THE FUTURE

Sponsored by: UL Solutions

Click on a person below to advance to their biography.



Dmitriy Bodik
UL Solutions
MODERATOR



Steve Eaves
VoltServer Inc.



Ken McKinney
UL Solutions



Susan Stene
UL Solutions



Michael Bodzay
Belden

Click here to return to the **Table of Contents**

"Digital Electricity: A Safe and Disruptive Innovation for Powering the Future"
Special Session Panelist



Steve Eaves
CEO
VoltServer Inc
East Greenwich, Rhode Island, USA
T: 401-474-4616

M: stephen.eaves@voltserver.com

Summary

While communications and computing have evolved exponentially in recent years, there has been little change in how electricity has been distributed since the late 1800's. Digital Electricity™ is a new electricity format where even at hundreds of Volts, shock and fire hazards are managed by an advanced power source, or transmitter, rather than requiring metal conduit, add-on safety devices and complicated installation practices. "AC-like" power levels and data are both transmitted on structured cable, converging the traditionally separate worlds of operational and information technology. Digital Electricity was adopted into the 2023 National Electrical Code® under the generic industry term "Fault Managed Power Systems" or Class 4 power, in conjunction with the launch of two new UL standards to qualify equipment and cable. So, what will the convergence of the IT and OT worlds mean to the cable and connectivity industry? How difficult is it to build and qualify Class 4 cable, and what are the connectivity aspects? These questions and others will be the subject of discussion in the panel session.

Bio

Stephen Eaves is the founder and CEO of VoltServer and is the inventor of Digital Electricity, a new electricity format adopted into the US National Electric Code® in 2023. The company has deployed the technology in over 1,000 large venues worldwide. Steve has more than 30 years of experience innovating around electrical energy storage, distribution, and control. Steve has authored or co-authored numerous industry and peer reviewed papers related to the energy industry and is an inventor on 35 patents.

“Digital Electricity: A Safe and Disruptive Innovation for Powering the Future”
Special Session Panelist



Ken McKinney

Principal Engineer
UL Solutions
RTP, North Carolina, USA
T: 919-809-3464

M:Kenneth.l.mckinneyjr@ul.com

Summary

Fault-Managed Power Systems or Class 4 Systems is a new intelligent power distribution technology that limits the amount of energy that can go into a fault, without limiting the power of the system. When these systems were introduced into the market, there were no product certification standards available or specific codes requirements to address their installation.

Ken adds his experience as the Chair of the UL Working Group that developed the UL 1400 Series of Standards for Fault-Managed Equipment, as well as a member of NFPA 70 Code Making Panel 3, who was responsible for the new Articles in the NEC for Fault-Managed Equipment and Cables.

BIO

Ken McKinney has been with UL Solutions for 28 years, in various roles. He is currently a Principal Engineer responsible for Transformers, Class 2 Power Supplies and Fault-Managed Equipment. He has been an NFPA 70 Code Panel Member for the last six cycles and is currently a member of Code Making Panel 1, as well as a member of many UL Technical Committees. Ken has a BS in Electrical Engineering from North Carolina State University.

"Fault Managed Power: A Safe and Disruptive Innovation for Powering the Future" Special Session Panelist



Susan Stene
Principal Engineer
UL Solutions
Fremont, CA, USA
T: 510-319-4312

M: susan.l.stene@ul.com

Summary

Fault Managed Power Systems (FMPS), or Class 4 power was adopted into the 2023 National Electrical Code®. In order to provide the listing requirements for these systems, UL solutions, in conjunction with industry members, developed two new certification documents, UL 1400-1 covering the general requirements for the system, and UL 1400-2 covering the requirements for the cables.

At first glance, Class 4 cables look very similar to Class 2 and Class 3 cables. What makes the construction of these cables different? How are the safety concerns associated with FMPS addressed in UL1400-2? What future developments are expected in UL1400-2? These and other questions will be addressed during the panel session.

Bio

Ms. Stene works for UL Solutions as a principal engineer in wire and cable. She brings over 34 years of UL Solutions experience to this role. While most of her time at the company was spent in wire and cable, she has also worked in such diverse areas as fork-lift trucks, flammable liquid tanks and office furnishings. Prior experience includes work as a manufacturing engineer and research chemist at a heat-shrink tubing manufacturer.

In addition to being a member of ULSE technical committees nos. TC83, TC719, TC758, TC814, TC2263 and TC4703, Ms. Stene is a member of IEC TC 20 working groups 17 and 19; the CANENA harmonization committees for building wire, flexible cords, photovoltaic wire and test methods; CSA ICWC01, 02 and 06; NEC code-making panel 6; and an invited guest to the NEMA Section 7 committees on high performance wire, building wire and flexible cords. She was recognized by UL Solutions as a Distinguished Member of Technical Staff, a part of the William Henry Merrill Society.

INDUSTRY SUSTAINABILITY SPECIAL SESSION

RENEWABLE / OFFSHORE ENERGY

Sponsored by: Prysmian Group



Brian Risch
Prysmian Group



Richard Ellis
Cable Materials Inc.

Click here to return to the **Table of Contents**

“Renewable/Offshore Energy”
Special Session Panelist



Brian Risch
Materials Technology Manager
Prysmian Telecome North America
Claremont, North Carolina, USA
T: (1) 828-459-8435

M: Brian.Risch@prysmiangroup.com

Summary

The renewable energy market is experiencing unprecedented growth globally, particularly in US where robust state-level procurement targets, national targets and technological advancements have inaugurated the era of offshore wind. This push for clean energy has spotlighted demand for improved system performance, the development of sustainable and circular cable materials, new installation methods, long-term protection systems, and efficient system design are all part of enabling the energy transition. With the great growth potential in the market, challenges still exist in development of standards, regulatory challenges, and establishment of domestic cable production for all renewable markets.

This Panel Session will focus on current cable transmission system developments which are facilitating the transition to green energy. The Panelists will provide an overview of the current market, various projects, an update on the progress of standards, and key challenges in offshore wind farm applications. It will also cover the cable systems involved in bringing this energy to communities.

Bio

Dr. Risch is the Materials Technology Manager for Prysmian Telecom North America. He holds a B.A. degree in physics from Carleton College and a Ph.D. in Materials Science and Engineering from Virginia Polytechnic Institute and State University. Brian has more than 30 years of experience in the study of structure property relationships in polymeric materials and materials reliability. Brian has over 20 years of experience in the fiber optic cable business. Prior to working for Prysmian, Brian worked for Alcatel and Draka specializing in cable materials and fundamental material reliability. Brian also has 6 years of experience at Hewlett Packard doing failure analysis engineering.

“Renewable/Offshore Energy”
Special Session Panelist



Richard Ellis
Principal
Cable Materials Inc.
Atlanta, GA 30338
T: 678-848-4805

M: rellisga@cablematerialsinc.com

Summary

The renewable energy market is experiencing unprecedented growth globally, particularly in US where robust state-level procurement targets, national targets and technological advancements have inaugurated the era of offshore wind. This push for clean energy has spotlighted demand for improved system performance, the development of sustainable and circular cable materials, new installation methods, long-term protection systems, and efficient system design are all part of enabling the energy transition. With the great growth potential in the market, challenges still exist in development of standards, regulatory challenges, and establishment of domestic cable production for all renewable markets.

This Panel Session will focus on current cable transmission system developments which are facilitating the transition to green energy. The Panelists will provide an overview of the current market, various projects, an update on the progress of standards, and key challenges in offshore wind farm applications. It will also cover the cable systems involved in bringing this energy to communities.

Bio

Richard received his BS Electronics Engineering in 1972 and has worked in the wire and cable market for over 50 years. Cable Materials Inc. is a manufactures representative agency and consultancy business for the W&C market, focusing on compounds and water blocking materials for optical fiber and power cables. Sr. Member of IEEE, IEEE-SA, PES-ICC, AWEA, and CIGRE. Active working group member for several power cable standards including Underground, Submarine, and OWF IAC and EXP cables.

SUPPLIER SPOTLIGHT PRESENTATIONS

Chairperson: Jon Mello, Teknor Apex, USA

Durable and Sustainable Aegis® Nylons for Wire Jacket Applications, AdvanSix

Robust CPE Alloy Jacketing for the Evolving Cable Industry, Aurora Plastics, LLC

Challenges and Options in Cable Shielding, Wardwell Braiding

Elastollan® N – A 50% Biobased TPU for Cable Jacketing and Overmolds, BASF

Supporting Quality Management with Cablebuilder, Cimteq by UL Solutions

Specialty Gels for Wire and Cable and Beyond, Info-Gel

Advanced LED Systems for the Curing of Fiber Coatings, Excelitas Technologies Corp.

From VW1 through FT4 – Learn How Halguard® LS HFFR Compounds Can Meet The Strictest Regulations, Teknor Apex

Fluoropolymer Solutions for the Wire and Cable Industry, Jinhua Yonghe Fluorochemical Co., LTD

Movacolor Products for Dosing and Blending, KN Manufacturing Solutions

Sustainable Products for Wire & Cable, M. Holland Company

Orion Wire and Cable Black Portfolio for Medium and High Voltage Cables, Orion Carbon

The Latest Cable Packaging Innovations, REELEX Packaging Solutions, Inc.

New Solutions for THV Alternatives, AGC Chemicals

Click here to return to the **Table of Contents**

SESSION 2

Click on a session below to navigate to that section of the Proceedings.

SESSION 2: NETWORK RELIABILITY & MEASUREMENTS

Chairperson: Ben Waite, Fiber Optic Center, Inc., USA

2-1 **Power Storage Control Method for Multiple Remote-Operated Optical Fiber Switching Nodes**; Mr. Akihiro Kuroda, NTT Access Network Service Systems Laboratories, NTT Corporation, Japan

2-2 **A Fiber Inspection Microscope Integrated with Cleaning Function**; Dr. Paul Huang, Panduit, USA

2-3 **Reliable Prediction of Data Center Interconnect Network Flaps via Distributed Acoustic Sensing (DAS) and Supervised Machine Learning**; Dr. Badri Gomatam, Sterlite Technologies Limited, India

2-4 **Artifacts for Measuring Bias and Repeatability of Fiber Inspection Scopes**; Doug Wilson, FiberQA, USA

Click here to return to the **Table of Contents**

Power Storage Control Method for Multiple Remote-Operated Optical Fiber Switching Nodes

Akihiro Kuroda, Tomohiro Kawano, Hiroshi Watanabe, Kuniaki Terakawa, Ikutaro Ogushi
NTT Access Network Service Systems Laboratories, NTT Corporation
1-7-1, Hanabatake, Tsukuba, Ibaraki, 305-0805 Japan
+81 29 868 6392, E-mail:akihiro.kuroda@ntt.com

Abstract
We propose a power storage control method for multiple remote optical fiber switching nodes in a new optical access network with loop-type configuration. The multiple nodes are driven by optical power supply from the central office and controlled by optical communication. In order to control multiple nodes connected in series to a single optical fiber, it is necessary to switch the power supply destination node appropriately. Therefore, we introduce a power storage control method for the central office. The operation of the storage control method is verified by connecting four nodes in series.

Keywords: Power-over-fiber; Optical fiber switching; single mode fiber; optical access network.

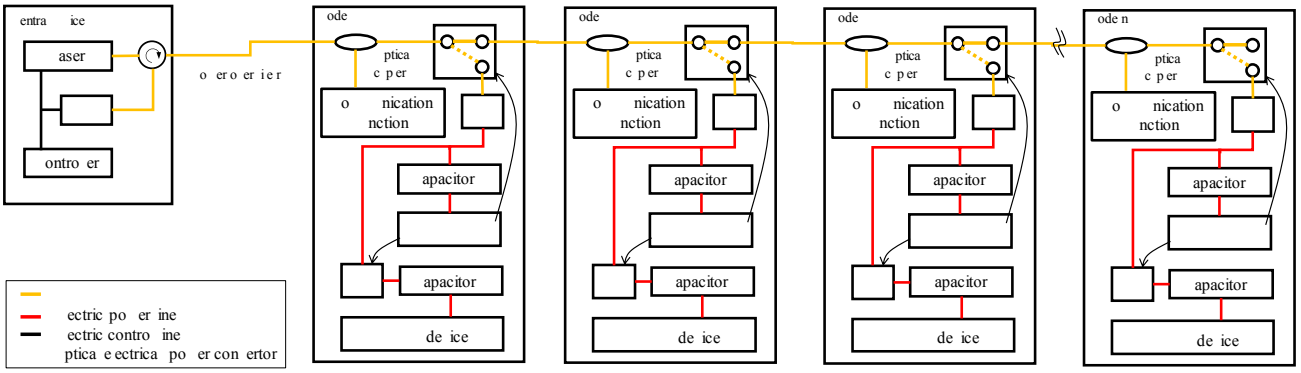
1. Introduction
We propose an optical access network design theory based on the concatenated loop topology [1] as the next generation optical access network. This topology is based on a loop-type configuration that consists of an upper loop connected to a central office and a lower loop connected to the upper loop. By switching between loops, the route to the user can be freely selected. Even if there is a depletion of free fiber in one route, service provision becomes possible without laying additional optical cable by being able to select another route. For this loop-type configuration, we propose a remote-operated optical fiber switching node that can switch optical fibers remotely by installing an optical cross connect at the connection point between the upper loop and the lower loop [2]. This node is intended to be installed in a maintenance hole where commercial power supply is difficult to secure making optical fiber power supply essential. When a number of nodes are installed in the upper loop, the number of optical fibers needed for optical power supply to the nodes is must be minimized. Therefore, a series connection system has been proposed to supply optical power to multiple nodes by a single optical fiber [3]. By mounting a 1x2 switch (SW) on the node, the node that receives the optical power supply supplied from the central office can be switched. By using a 1x2 SW, the loss is lower than using a power branch coupler, and the number of nodes can be increased or decreased as needed, making it superior in scalability. In addition, since it can be driven by optical fiber power supply and fiber switching can be performed by remote control, it can be used not only in loop topologies. For example, we believe that it can be used to flexibly switch the optical fiber networks of schools and companies. Unfortunately, only one control method has been proposed for the serial connection system, a two-unit control method using one 1x2 SW, and it has not been clarified whether it can continuously control three or more nodes by controlling a number of 1x2 SWs. Also, it has not been shown whether control remains possible given the power consumed by the switching devices.

In addition to the previously reported threshold control method, we propose here a power storage control method that includes a selection criterion of a power supply destination for reliably supplying optical power to a number of nodes. In addition, to elucidate the operating range of the power storage control method when the optical cross-connect device is active during power storage control, the response of the system is calculated by replacing the device by a load resistance and conducting bench tests.

2. Proposed Power Storage Control Method
Figure 1(a) shows the serial node connection configuration considered here. Starting from the central office, several nodes, 1~n, are connected in series by a single mode fiber for power supply and control via a 1x2 SW in each node. To implement optical power supply, the central office and the nodes are connected one by one. Nodes closer to the central office than the node being charged can continue to communicate with the office. However, since the optical power supply uses a single optical fiber, control commands are transferred in time division manner. The central office hosts a controller that determines the destination of the optical power supply by giving instructions to the nodes. Each node is equipped with a micro processing unit (MPU), which measures the voltage of the two capacitors charged by photoelectric conversion according to instructions from the central office. Capacitor C1 is used for MPU driving and communication while C2 supports device driving; two capacitors are needed so that MPU operation remains stable during device operation. A load switch (LSW) is used to charge C1 or C2 while the 1x2 SW is used is used to charge the node's capacitors or pass the optical power to downstream nodes.

In order to ensure node operation, it is necessary to be able to continue control in three power storage states (State 1: charge, State 2: standby, State 3: device operation). In order to do so, it is necessary to switch the optical power supply so that the node close to the central office is given priority and the charging state can be maintained. In the state 1, the power held by nodes upstream of the node being charged must not be exhausted. In the state 2, it is necessary for the optical power supply to each node to continue without breaking the order. In the state 3, it is necessary to perform the optical power supply with the same priority as in state 1 when recharging the node on which device operation has been performed. While the device is being operated, C1 of the other nodes can become depleted, but operation of the MPUs of those other nodes must be maintained.

Figure 1(b) shows the proposed power storage control method. The nodes are numerically indexed using X (X = 1, 2, 3, …). In Step 1, the controller sequentially measures the capacitor voltages V1 and V2 from node 1 to node X. In Step 2, C1 from node 1 to node X is sequentially compared with the lower limit threshold. In step 3, node is found to be below the lower limit, Node Y. Step 4(a) entered with the target being node Y-C1. If no such node is found, the process of Step 4(b) is performed. Step 4(a) changes the power supply destination from node X to node Y. First, the LSW of node X is turned OFF, and the 1x2 SW is switched to its own node. Next, node X-1 is similarly switched, and the switching is repeated up to



node Y. In Step 4(b), if node X-C1 voltage is higher than the upper limit threshold, the process proceeds to Step 5, and if the upper limit threshold is not reached, the process returns to Step 1. In Step 5, the capacitor to be charged in node Z is switched from C1 to C2. In Step 6, node X-C2 is compared with the upper limit threshold, and if it is above the upper limit threshold, the process proceeds to Step 7, and if it is below the upper limit threshold, the process returns to the start. In Step 7, if there is a node X+1 downstream of node X, the 1x2 SW of node X is switched and the power supply destination is changed; if there is no node X+1, the power supply destination is returned to node 1. When this storage control method is used, the upper limit threshold is set below the maximum output voltage as a guideline for switching the power supply destination, because the output voltage of the optical/electrical power (O/E) conversion has the characteristic that the change range decreases as voltage is increased. Since the controller needs to grasp the capacitor voltage, voltage information is collected from each node at a regular communication interval, t, and power storage control is performed.

Further, in order to ensure correct operation of the optical cross-connect device at any node Z in the standby state, in which each node is charged by the control method of Figure 1(b), it is necessary to clarify the operating conditions of the device such that C1 of the other nodes do not fall below the lower threshold voltage during the operation of the optical cross-connect device. The discharge time T_1 at C1 of the other nodes is given by equation (1).

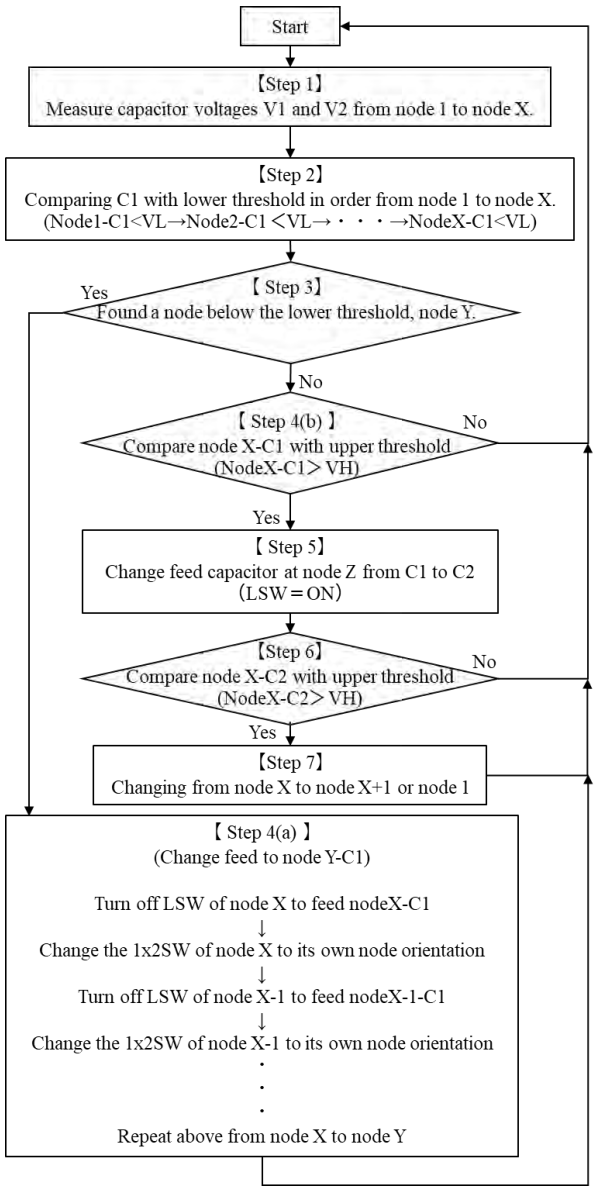
$$T_1 = C_1(V_a - V_b)/I \qquad (1)$$

The capacity of C1 of the other nodes, the C1 voltage before discharge, the C1 voltage after discharge, and the consumption current of the MPU are represented by C_1, V_a, V_b, and I, respectively. When the optical cross-connect device is replaced with a resistive load R, the discharge time T_2 of node Z-C2 under load operation is given by equation (2).

$$T_2 = C_2 R \ln(V_A/V_B) \qquad (2)$$

The capacity of C2 of node Z, the C2 voltage before discharge, and the C2 voltage after discharge are represented by C_2, V_A, and V_B, respectively. Figure 2 shows the circuit configuration during load operation. In this case, when $T_1 > T_2$, the condition R under which the proposed storage control method is valid is given by the following equation.

$$R < C_1(V_a - V_b)/IC_2 \ln(V_A/V_B) \qquad (3)$$



(b) Power storage control method

Figure 1. (a) Proposed serial connection node configuration and (b) power storage control method

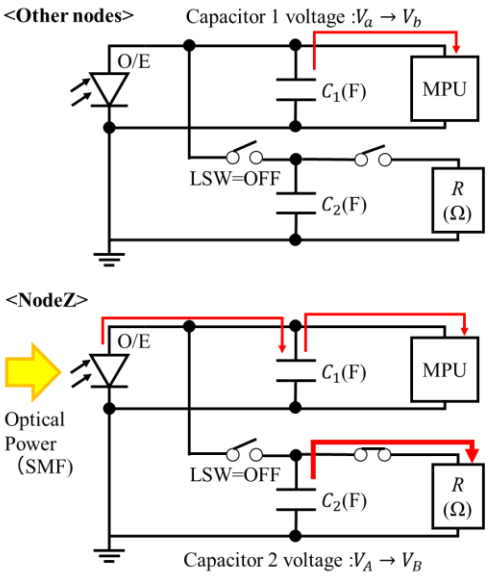


Figure 2. Circuit state during load operation

3. Experiment

3.1 Verification Contents and Methods

Operation of the power storage control method shown in Figure 1(a) was verified by examining system performance in three power storage states (1, 2, 3). In the state 1, assuming that all capacitor voltages are 0 V immediately after installing the nodes in the field, we check whether the nodes could be started sequentially from that state. In the state 2, after charging all capacitors to the upper limit threshold, we check whether the standby state can be continued without disrupting the charging order. In the state 3, we check whether the power storage state of the other nodes can be maintained when the C2 power consumed by the load operation is recharged within $T_1 > T_2$. Further, it was also confirmed that the power storage control method fails when $T_1 < T_2$.

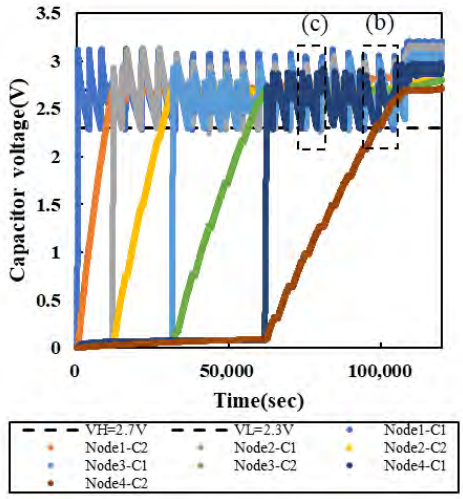
Four prototype nodes were used for the verification system and connected in series using 1x2 SWs as shown in Figure 1(a). The electrical energy yielded by O/E conversion is used to charge C1 and C2. C1 is used to drive the MPU, a micro electro mechanical system on-off SW for upstream communication, and the 1x2 SW. As shown in Figure 2, load resistor R is connected to node 4-C2 to replace the optical cross-connect device. C_1 is 47 mF and C_2 is 2.5 F. The optical powers received by the O/E convertors are as follows. $P_{Node\,1}$ = 7.3 dBm, $P_{Node\,2}$ = 5.5 dBm, $P_{Node\,3}$ = 4.1 dBm, $P_{Node\,4}$ = 3.0 dBm. The wavelength of the laser light source is 1490nm. The lower limit of the threshold voltage is set to 2.3 V while the upper limit to 2.7 V. Communication for confirming the storage voltage of the node and instructing the switching of the power supply destination from the controller is performed at intervals of t = 100 seconds.

During the load operation, the MPU operated stably and directed the optical power supply to C1 of node 4. Therefore, optical power passed straight through nodes 1~3. In this case, T_1 at node 1 is calculated to be 14,100 seconds if V_a = 3.2 V from the output voltage determined by the optical power received, V_b = 2.0 V from the minimum operating voltage of the MPU, and the current cons ed in the stand y state o the is 4 μA. hen V_A = 2.9 V and V_B = 2.0 V in node 4, the load under the condition of $T_1 > T_2$ is $R <$ 5 kΩ. In this eri ication, e set R to 00 Ω and 5 kΩ. The transition in power storage voltage at the establishment and failure of the power storage control method was measured.

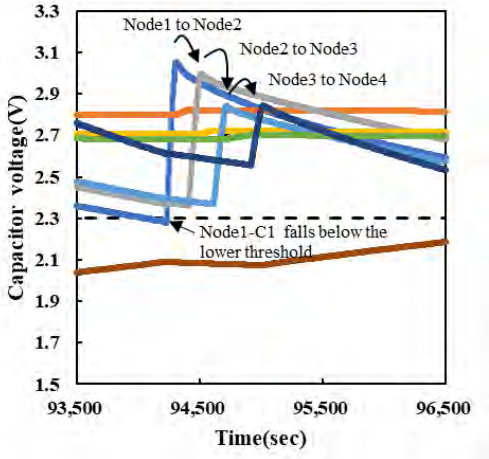
3.2 Verification Results

Figure 3(a) shows the power storage voltage characteristics in the cold start state. It was possible to charge all 8 capacitors of the 4 nodes to the upper threshold voltage in about 33 hours. The enlarged view of Figure 3(b) shows that node 1-C1 fell below the lower limit threshold while supplying power to node 4-C2, and the power supply was successfully switched to node 1-C1 by performing Step 4(a) of Figure 1(b). Thereafter, after charging node 1 to node 4 in order, the power supply to node 4-C2 can be resumed. In Figure 3(c), since node 4-C1 fell below the lower limit threshold, Step 4(a) of Figure 1(b) was performed. Then, as node 3-C1 fell below the lower threshold, the feed destination was switched again. Furthermore, it was confirmed that recharging could be performed in accordance with Figure 3(b) even when node 1-C1 falls below the lower threshold.

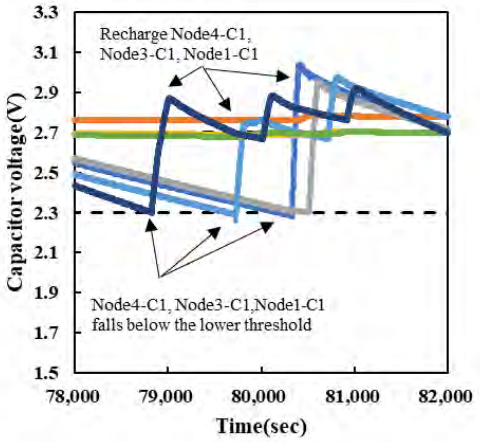
Figure 5 shows the power storage voltage characteristics in the standby state. As shown in the enlarged view, nodes 1 to 4 were sequentially charged, and capacitor voltages were maintained at the threshold value without executing Step 4(a) of the storage control method. Moreover, it was confirmed that the power storage state was maintained without breaking the power supply order.



(a) Power storage voltage characteristic



(b) Enlarged view 1



(c) Enlarged view 2

Figure 3. Measurement result of the state 1: charge

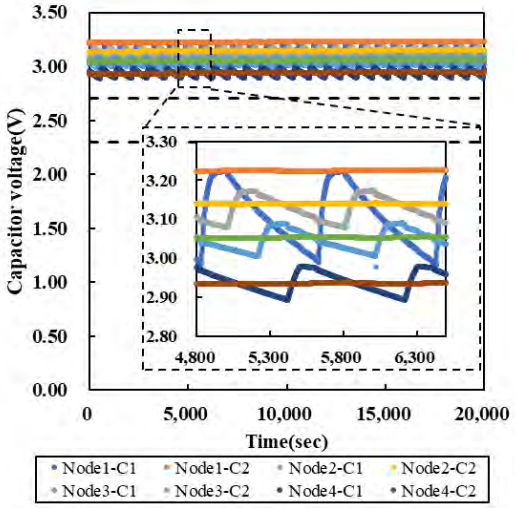
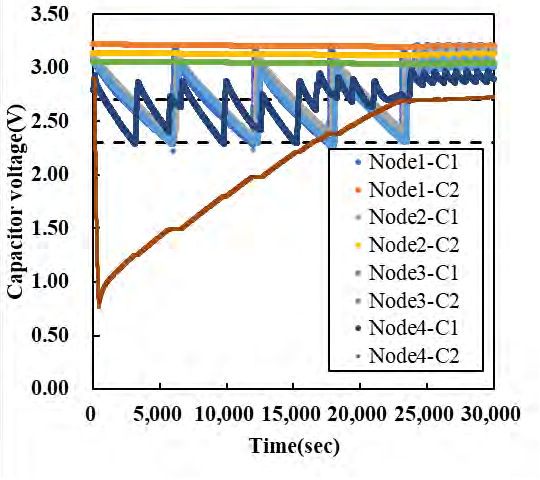
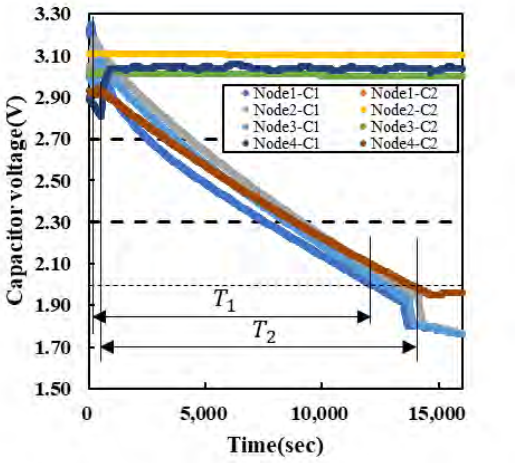


Figure 4. Measurement result of the state 2: standby

Figures 5(a) and 5(b) show the characteristics of the power storage voltage when node 4-C2 became discharged with the two load resistors. In Figure 5(a), discharge commenced from the standby state shown in Figure 4, and after discharge, node 4-C2 was recharged by repeating Step 4(a) as shown in Figure 3(c). In Figure 5(b), because node 1-C1 fell below the MPU operating voltage during the discharge of node 4-C2, the 1x2 SW of the node 1 became inoperable and the power supply destination could not be changed to node 1. It can be seen that the node 1-C1 could not be recharged and the power storage control method failed. Since there was no response to the voltage measurement request from node 1 after the load operation is completed, the controller executes Step 4(a) on node 2~4, but since the C1 voltage of node 2~3 was also below the MPU operation voltage, the power supply destination switching could not be executed, so a mismatch occurred between the power supply destination determined by the controller and the actual power supply destination. Therefore, when this power storage control method is implemented, the requirement for its successful operation is setting R such that $T_1 > T_2$.



(a) $T_1 > T_2$ ($R = 100\ \Omega$)



(b) $T_1 < T_2$ ($R = 15\ \mathrm{k}\Omega$)

Figure 5. Measurement result of the state 3: load resistance operation

4. Conclusions

In this paper, we proposed a power storage management method for achieving control of multiple remote-operated optical fiber switching nodes connected in series. The power storage control method was shown, and the requirement for successful control was calculated from the discharge time relationship of each capacitor in load operation simulating a switch device. It was shown that the switching device must satisfy Equation (3), which was confirmed by verification.

5. Acknowledgement

The support of Kazunori Katayama is acknowledged.

6. References

[1] https://group.ntt/en/newsrelease/2021/06/18/210618a.html. (accessed 2023 July 7th)

[2] H. Watanabe, T. Kawano, C. Fukai, R. Koyama, K. Nakae, T. Fujimoto, Y. Abe and K. Katayama, “Remote Operated Optical Fiber Switching Node and Optical Cross-Connect Function applied to Optical Access Network based on oncatenated oop Topo ogy,” Internationa a e & Connectivity Symposium 2021, ,2021.

[3] T. Kawano, T. Manabe, A. Kuroda, K. Nakae, H. Watanabe and K. Kataya a, “ ontro sing o er-over-Fiber for Remote-perated ptica i er itching odes,” Internationa a e & Connectivity Symposium 2022, 4-3, 2022.

7. Authors



Akihiro Kuroda is an Engineer at NTT Access Network Service Systems Laboratories. He joined NTT in 2015. Recently, he has been engaged in the research and development of optical fiber technologies for remote operated optical fiber switching nodes.



Tomohiro Kawano is an Engineer at NTT Access Network Service Systems Laboratories. He joined NTT in 2010. Recently, he has been engaged in the research & development of optical fiber technology for remote operated optical fiber switching nodes. He is a member of the Institute of Electronics, Information and Communication Engineers (IEICE) of Japan.



Hiroshi Watanabe received B.E., M.E. degrees in applied physics from the University of Tokyo, Japan, in 1996 and 1998, respectively. He received a Ph.D. in engineering from Hokkaido University in 2017. In 1998, he joined NTT Access Network Service Systems Laboratories, Ibaraki, Japan. He is currently engaged in the research of remote operated optical fiber switching nodes. He is a member of the Institute of Electronics, Information and Communication Engineers (IEICE) of Japan.



Kuniaki Terakawa is an Engineer at NTT Access Network Service Systems Laboratories. He joined NTT in 1996. Recently, he has been engaged in the research and development of optical fiber technologies for remote operated optical fiber switching nodes.



Ikutaro Ogushi received a B.E. and M.E. in electrical engineering from Osaka University in 2000 and 2002. In 2002, he joined NTT Access Network Service Systems Laboratories. He is currently engaged in the research of remote operated optical fiber switching nodes. He is a member of the Institute of Electronics, Information and Communication Engineers (IEICE) of Japan.

A fiber inspection microscope integrated with cleaning function

Paul Huang, Jose M. Castro, Thomas Sedor, Rick Pimpinella, Bulent Kose, Brett Lane
Fiber Research Labs, Jack Caveney Innovation Center, Panduit Corp., Tinley Park, Illinois
paul.huang@panduit.com

Abstract

In this paper, we present a novel apparatus that can inspect and clean the end face of the fiber-optic connector without the need to switch the connector from one tool to another.

Keywords: Fiber optics connector inspection, connector end face cleaning

1. Introduction

Fiber optic links are susceptible to dust, oil, and other contaminants on the mating connector face [1]. Therefore, verifying that the connector end face is cleaned before a connection is important during the network installation. The degree of cleanliness can be determined using a fiber inspection microscope. For example, if the dust on the connector's end face is too large to pass the requirement of the standard [2], it needs to be cleaned. A reel-type one-click cleaner is a standard tool for cleaning optical connectors or receptacles, as shown in Fig.1.



Fig.1. reel-type one-click cleaners

The cleaning and inspection operation is performed separately in the visual inspection microscope or cleaner devices described above. However, a device that can do both cleaning and inspecting almost simultaneously without disconnecting the device under test is not available in the market. Therefore, there is a need for such a device, which can enable more reliable installation of optical interconnects while reducing time and saving costs.

2. A new apparatus for fast inspecting and cleaning MPO connector

A fiber inspection microscope typically consists of an illuminator, a lens, and a camera sensor, as shown in Fig.2. These visual inspection systems could either have a manual focus or autofocus functionalities which can automatically center, focus, capture images, and analysis of the contamination of the connector end face.

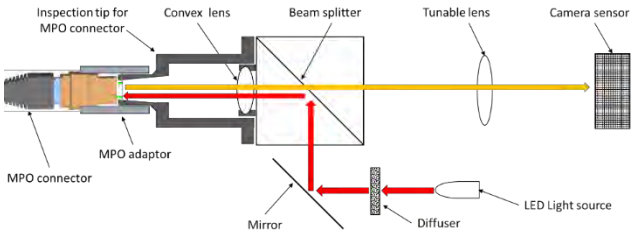


Fig.2 a microscope for connector inspection

As we can see from Fig. 2, there is no space to insert the one-click cleaner to clean the MPO connector under inspection. To clean that MPO connector, usually, we need to remove the MPO connector from the inspection microscope, insert it into an MPO adaptor, and insert the one-click cleaner from the other side to clean its end face. However, if we add a moveable mirror to fold the optical path from the microscope by 90 degrees, the one-click cleaner can enter the MPO adaptor after pushing the moveable mirror away.

Our solution is shown in Fig.3(a), a moveable mirror is attached to a hinge and is pushed to rotate clockwise by the spring inside the hinge. The mirror is limited by a stop so that it forms an angle of 45 degrees with the optic axis of the microscope. When the moveable mirror remains at this angle, the microscope can see the MPO connector's end face, and the system continues to work in inspection mode. If dust is found on the end face of the MPO connector, the user can push the one-click cleaner down along the guiding slot for cleaning access. The cleaner will force the moveable mirror to rotate counter-clockwise so the cleaner can reach the MPO connector end face, as shown in Fig.3(b). When the user releases the one-click cleaner, the moveable mirror retracts, and the user can inspect the end face of the MPO connector once again to see if the dust has been removed.

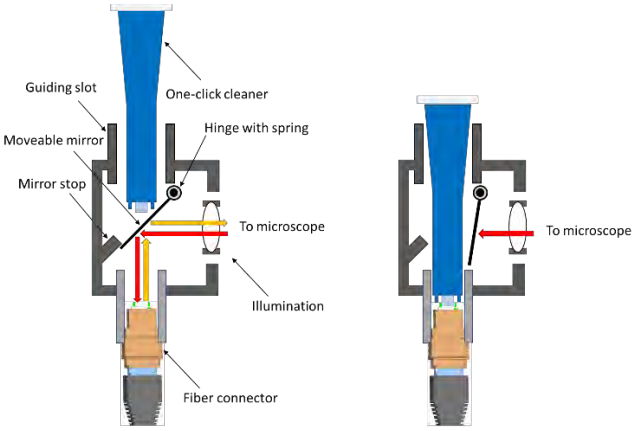


Fig.3. a system that can perform both inspection and cleaning of the MPO connector

To build such a system that can fast inspect and clean a connector, we need to develop an inspection microscope that can check the MPO end face in a short time at first. To overcome the slow speed of most commercial MPO inspection microscopes that need to inspect the fibers one by one due to their narrow field of view, we built a wide-view inspection microscope that can view the whole MPO connector end face in one image in real time. The microscope prototype is shown in Fig.4(a). This microscope has a field of view covering an MPO connector's 12 or 24 fibers. To further extend its field of view, we align the MPO connector in the diagonal direction of the camera sensor so that the microscope can also see the two pinholes of the MPO connector, as shown in Fig.4(b).



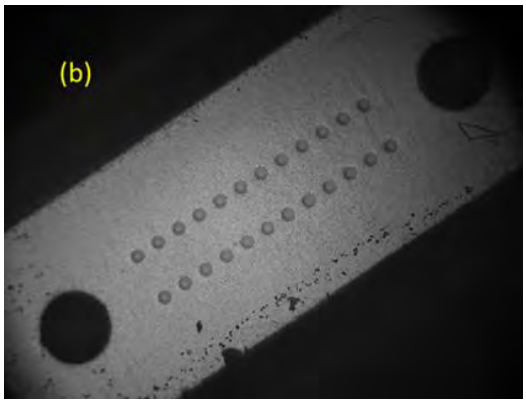


Fig.4(a) microscope prototype, (b) MPO end face image taken by the microscope

Furthermore, we built the prototype of a moveable mirror system that can be attached to the wide-view microscope, as shown in Fig.5. It enables the microscope to inspect and clean an MPO connector without switching the connector from one tool to another.

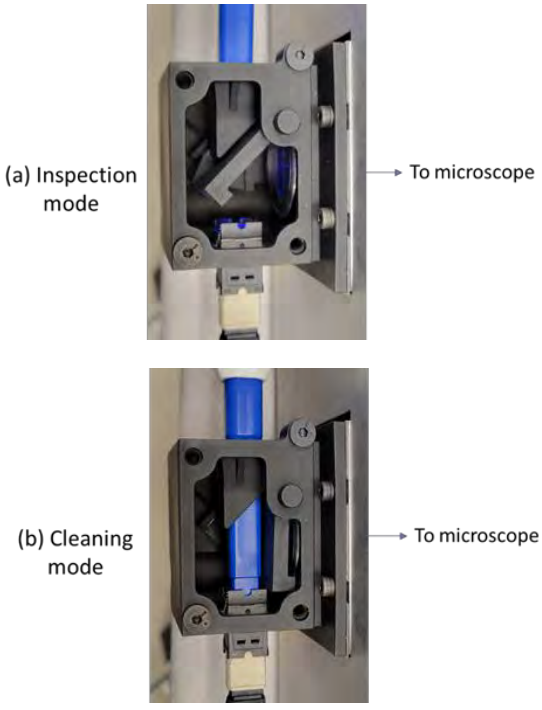


Fig.5 prototype of a moveable mirror system enabling a microscope to both inspect and clean the MPO connector

Fig.6(a) shows the microscope picture when a dirty MPO connector with a fingerprint is inserted into the inspection tool. Fig.6(b) shows the microscope picture when the user pushes the one-click cleaner to access the MPO connector. Fig.6(c) shows the microscope picture of the MPO connector after cleaning. The MPO connector is typically cleaned after one round of inspection with a single cleaner insertion. This saves time and labor costs on inspection and cleaning. Moreover, if one cleaner insertion is insufficient to clean a connector, the user can perform several inspection rounds to certify end face cleanliness. Hence, utilizing this inspection and cleaning system will further reduce the time and labor on these connectors that need multiple cleaning.

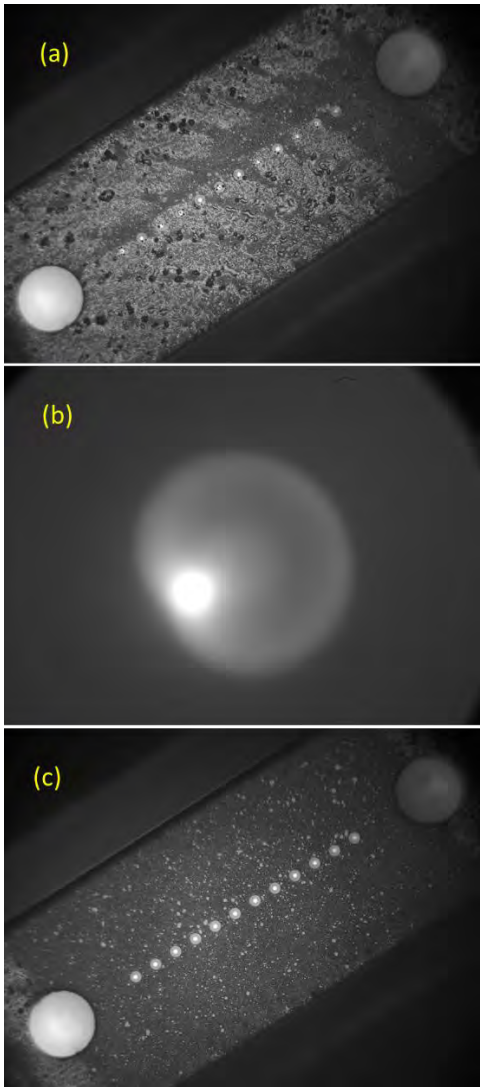


Fig.6(a) microscope picture of the end face of a dirty connector, (b) microscope picture when the apparatus is cleaning the connector end face, and (c) microscope picture of the end face of the cleaned connector

3. Discussion, Summary, and Conclusions

We designed and built a novel apparatus with a moveable mirror attached to an inspection microscope. It allows the user to inspect and clean the MPO end face without switching the MPO connector from the inspection microscope to the cleaning tool, saving time and manufacturing costs. Such a system is not limited to MPO

connectors but should also work for single fiber connectors. It could work manually and as an automatic inspection and cleaning system in mass production.

4. References

[1] T. Berdinskikh, J. Bragg, E. Tse, J. Daniel, P. Arrowsmith, A. Fisenko, S. Mahmoud, "The contamination of fiber optics connectors and their effect on optical performance', in Technical digest series of OFC 2002, Anaheim, California, March 17- March 22, 2002, pp. 617-618.

[2] IEC 61300-3-35:2022, Fibre optic interconnecting devices and passive components - Basic test and measurement procedures - Part 3-35: Examinations and measurements - Visual inspection of fibre optic connectors and fibre-stub transceivers

5. Authors

Paul Huang, Ph.D.



Dr. Paul Huang is a Principal Optical Engineer at Panduit Corp's Fiber Research Department since 2014. His expertise centers on image optics for fiber connector testing and inspection. He earned his Ph.D. in Optical from Shanghai Institute of Optics and Fine Mechanics, Chinese Academy of Science. Prior to Panduit, he contributed to fiber optic, image, and display optics at Lightwaves2020 Inc., Siwave Inc., and Dovi Inc. He has authored more than 30 technical papers and holds 16 US patents.

Jose M. Castro, Ph.D.



Dr. Jose Castro is currently the Manager of the Fiber Research Group in Panduit. He received his PhD. in Electrical Engineering from the University of Arizona, Tucson, in 2006. Jose was the editor for Fibre Channel T11.2 Physical Interfaces standard for 64G transmission. He is currently working on the next fiber interface for 256G. Last year, he was the recipient of the Technical Excellence Award, from the International Committee for Information Technology Standards. Jose authored over 70 technical articles and international conference papers in areas of multimode fibers, optical communication, integrated optics, imaging systems and LAN copper cables. He has multiple contributions to TIA, IEEE and Fibre Channel standards in topics related with fiber and VCSELs. He is also a co-author of a book in Holographic Applications in Solar-Energy-Conversion Processes, and holds over 20 patents.

Thomas Sedor



Thomas Sedor is a Senior Principal Development Engineer in the Data Center Product Engineering Group at Panduit Corp. He has over 22 years of experience in the research and development of fiber optic network infrastructure solutions. Thomas received his B.S. in General Engineering from the University of Illinois at Urbana/Champaign in 1991. Before joining Panduit, he worked at Midway/Atari Games designing interactive arcade games and AT&T designing various central office solutions. Thomas holds 14 US patents and 5 international patents.

Rick Pimpinella, Ph.D.



Dr. Rick Pimpinella received his B.S., M.S., and Ph.D. degrees in Physics from New York University, Tandon School of Engineering in 1976, 1978, and 1981 respectively. From 1981 to 2001 he was employed with Bell Laboratories, where he pioneered the use of silicon processing technology for the fabrication of optical subassemblies for the passive alignment of optical fibers to photodetectors and lasers. In 1994, as a Distinguished Member of Technical Staff, he designed and developed a micro-miniature expanded beam optical backplane connector, which was deployed in the US Air Force F 22 Raptor and F35 Lightning II. In 1998, as Technical Manager, he led the design and development of intelligent remote fiber test systems for monitoring and testing the outside optical fiber cable plant. In 2002, he joined Panduit where he managed for Fiber Business Unit and later, created and managed the Fiber Research Department. Dr. Pimpinella is a Panduit Fellow, a member of the IEEE, and is actively pursuing his research interests in multimode and single-mode optical fiber. He has published over 50 technical papers and articles, and holds more than 60 US Patents.

Bulent Kose



Bulent Kose is a Senior Principal Optical Engineer in the Fiber Research Department at Panduit Laboratories, Panduit Corp. Bulent has over twenty years of experience in fiber optics in areas of LAN cabling research and application testing, on-fiber device development, link simulation and modeling. Bulent is member of TIA TR-42-12 and IEC SC86A USTAG and has several technical contributions to TIA-TR42 on optical fiber measurements and specification developments. Prior to joining Panduit, he worked at Nexans Inc., on advanced LAN application R&D projects, on both fiber and copper. Bulent received his M.S (Electrical Engineering, 1997) from Drexel University and BS (Electrical Engineering, 1993) from Middle East Technical University (Ankara/Turkey.)

Brett Lane, Ph.D.



Dr. Brett Lane has over 25 years of experience in research, development, and management of network and electrical infrastructure solutions. He is the Chief Technology Officer of Panduit Corporation, headquartered in suburban Chicago, where he is responsible for driving sustainable business growth by delivering a continuous flow of innovative solutions through research, advanced development, and corporate entrepreneurship.

Before becoming CTO in early 2018, Brett held a variety of technical and commercial leadership positions within Panduit's R&D and Business organizations. As a research leader, Brett has a passion for technical advantage. His team delivered new-to-the¬world discoveries that enabled differentiated fiber optic products that continue to earn the business of high-value customers. As a commercial leader, Brett emphasizes a customer-focused approach. His team delivered revenue and profit growth through successful new product introductions, efficient volume manufacturing processes, and effective product life cycle management. Prior to joining Panduit, Brett worked at Molex on advanced optical transceiver design and manufacturing processes. In addition to delivering product innovations throughout his career, Brett's contributions to the communications industry through standards development organizations and technical forums have enhanced Panduit's overall brand as an industry leader. Respected widely as an industry expert with a highly collaborative style, Brett has held multiple leadership positions within the domestic and international standards community. He has authored over 40 technical publications and holds 19 US patents.

Brett received his MBA from the University of Chicago Booth School of Business, earned his PhD in Electrical Engineering from Northwestern University, and holds a BS in Mechanical Engineering from the University of Texas at Austin.

Reliable prediction of data center interconnect network flaps via distributed acoustic sensing (DAS) and supervised machine learning

Badri Gomatam, Shubham Jagtap, Arvind Chandel, Abhishek Sati, Ashit Padhi, Sarman Panugothu, Pratik Sakode, Nagaraju Bezawada, Bikram Jyot

Centre of Excellence, Sterlite Technologies Limited

Aurangabad, Maharashtra, India

+91-02030514000 · badri.gomatam@stl.tech

Abstract

We report a highly reliable method for detection and localization of events that cause "physical" network flaps, i.e. short term outages of optical fiber link connectivity. Distributed acoustic sensing coupled with a neural network model is trained to detect and classify physical events in the outside plant that disrupt path connectivity. Our study was performed on an in-service cable over a single (dark) fiber strand multiplexed with a traffic generator and the DAS sensing signal.

Keywords: Network flap; Distributed acoustic sensing; Machine Learning.

1. Introduction

A network flap occurs when the link alternates between "down" (loss of signal or LOS) and "up" states on a time scale of a few milliseconds to a few seconds. This condition is usually attributed to switching/routing equipment malfunctions - but not in every case. For networks with their OSP situated in areas experiencing a high likelihood of network disruption, such as construction, roadwork, utility repairs et cetera, such flaps are extremely hard to detect and geo-locate given their short duration. This adversely affects quality of service (QoS) and is expensive especially for data center operators and requires significant investment in redundant network routes.

Distributed acoustic sensing (DAS) belongs to a family of techniques called distributed fiber optic sensing[1]. It was first proposed in the 1990s[2] and has since been used in a multitude of applications. DAS offers some unique advantages such as high sensitivity, high spatial resolution and long sensing range. Its unique advantages helped DAS play an important role in many fields such as monitoring of oil and gas pipelines, protection of high value perimeters and borders, rail monitoring etc[3-5]. These applications typically use dedicated fiber networks built for the purpose. Recently, there is growing interest in using DAS capabilities to enhance network operation efficiency of telecom and data center networks using deployed fiber network architecture through prevention of fiber cuts, locating deployed cable routes accurately and creating new use cases like traffic monitoring[6].

Application of machine learning and AI algorithms has gained significant attention recently for automatic detection and classification of DAS events in real time [6]. Combined with availability of ever increasing high speed GPUs for processing and computations, it is possible to achieve real-time event detection and classification over long sensing lengths of tens of kilometers.

In this paper, the unique sensing capability of DAS coupled with a machine learning model is reported to detect and classify the events that cause network flaps.

2. DAS Working Principle

DAS works based on the principle of phase optical time domain reflectometer (Phase OTDR). Figure 1 shows the block diagram of direct detection DAS. CW light from a narrow linewidth laser (linewidth ~ few kHz) is converted into pulses using an external modulator. These pulses are amplified using EDFA to high peak power but below the nonlinear limit. These pulses are launched into optical fiber with a repetition frequency of ~ few kHz. As the amplitude of the backscattered signal is small, another EDFA is used to amplify the signal before reaching the receiver. Receiver converts the optical signal into analog voltage signal and electronic gain is applied as required. ADC converts the analog output signal of the receiver into digital data and sends it to the processing unit for further processing. As the coherence length of the narrow linewidth laser is much longer than pulse width, coherent interference takes place between random back scattered electric field components within the pulse. In the absence of any acoustic disturbance near fiber, the backscattered signal from each location remains the same for successive pulses. When there is perturbation at a location of fiber, the backscattered signal reflected back from that particular location changes. By comparing the traces with and without acoustic disturbance, the sensor detects and pinpoints the location of disturbance or vibration. The exact location of the event is obtained from time of flight calculation.

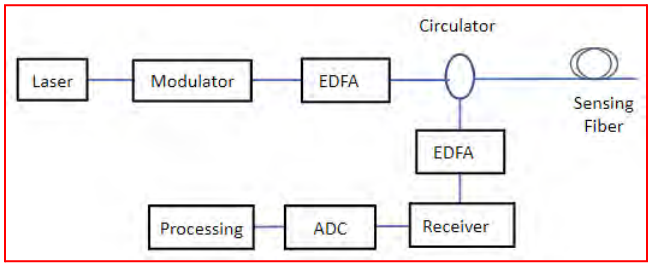


Figure 1. Block diagram of DAS

3. Test Setup

Figure 2 illustrates our field test set-up. Firstly, DAS parameters such as pulse width, peak power and EDFA gain are configured. Pulse width is set to 100 ns which corresponds to a spatial resolution of 10 m. Back scattered signal is sampled at a sample rate of 100 MSPS, which corresponds to a sample spacing of ~ 1

m. Trace averaging is done to filter the noise. Number of averages is chosen such that the Nyquist frequency is larger than the highest event frequency. DAS is connected to a dark fibre in the cable at Site A. A WDM multiplexer (MUX) is used to combine the DAS signal with BERT data channel. On the other end, a demultiplexer (DEMUX) is used to separate BERT data from sensing channels. Sensing channel is terminated at Site B to suppress high reflection from the fiber end.

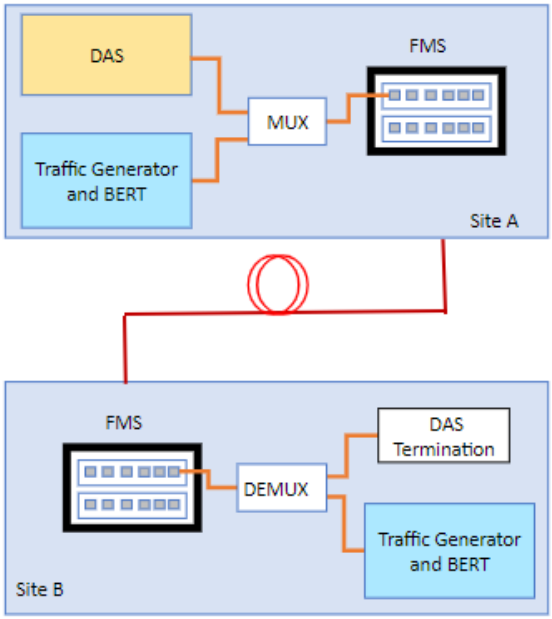


Figure 2. Schematic DAS Setup deployed in the field

Signal wavelength of the BERT channel is chosen such that it does not overlap with the wavelength of the sensing channel. Fiber is characterized using a standard OTDR for attenuation and reflections.

4. Results and Discussion

4.1 Identification of Flap Events

To identify the events that are causing flaps, we started acquiring DAS data for the entire route for a few weeks. Analysis of this data set has shown that the majority of the flaps were caused due to bends or bend-"like" events applied on the fibre. Figure 3 shows the DAS data in a "waterfall" plot where y-axis shows the time and x-axis shows the fiber distance.The waterfall is of 30 sec duration in a section of the 19 km long network. The dark blue portions in the waterfall plot is due to low background noise whereas light blue regions represent high intensity sections due to continuous or intermittent disturbances occurring on or nearby cable due to events such as human movement, vehicle traffic etc or ambient noise. During bend the intensity after the bend reduces significantly as the bend causes a significant drop in the signal level.

Our study also reveals several possible physical causes for intermittent network outages - faulty connectors, intermittent cable bends, unscheduled repair/maintenance, poorly trained field personnel among others specific to the OSP. With several weeks of field observation and sensor data collection, we show that a series of events preceding a network flap can be detected and classified - such as cable movement, hand-hole disassembly, joint-closure disassembly and splice-tray handling, among others. These "precursor" events have a very high degree of correlation to a network flap event that is expected to occur within a short period of time but in the future.

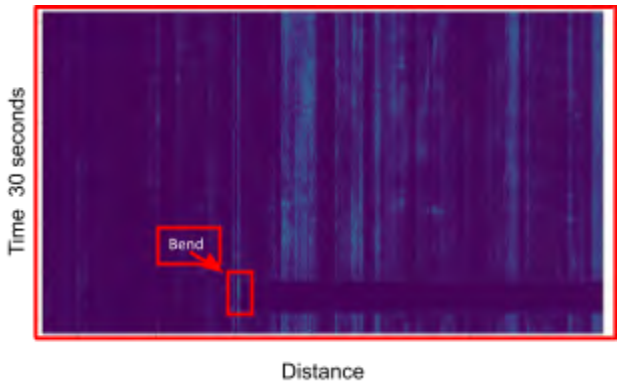


Figure 3. Waterfall plot from the DAS sensor with a bend event. Event location is shown in the inset

4.2 ML Model Development

A machine learning model was developed for detection and classification of bend events. We are using a CNN deep learning model. The various steps involved in the process are data collection, data preprocessing, data representation, collecting training data, CNN architecture design, model training, validation and optimization and testing & deployment. Using CNNs for event classification in fiber optic sensing has several advantages, including their ability to automatically learn and extract relevant features from the data, their robustness to noise, and their capability to handle complex patterns and variations in the signals. This enables accurate and efficient event classification, which is essential for many fiber optic sensing applications.

The ML model is used to correlate field events for training and deployed for inference in a live network setting. Reliability of our predictive model was verified by correlating time-stamps with the multiplexed traffic generator and BERT on the shared fiber path, as well as live events of outage from the network element management systems.

Table 1. Confusion matrix for the predictive model

	Actual Negative	**Actual Positive**	**Precision**
Predicted Negative	654 (TN)	17 (FN)	97.46%
Predicted Positive	8 (FP)	1075 (TP)	99.26%
Recall	98.79%	98.44%	

We collected 5460 samples of simulated fiber bend events at different locations across the network route. A deep learning model was trained with approximately 80% of labeled data from this data set. The remaining 20% of data from this set was used to validate the model. Table 1 shows the results of the model on the validation data set.

The trained model was subsequently tested in real time to monitor flap events. During the monitoring period, 30 flaps were observed and confirmed via the network element management system. For these observed 30 flaps, the model was able to detect and classify 29 fiber bend-"like" events correctly, leading to a detection and classification rate of ~97%. Subsequent investigation led to a confirmation that these events occurred due to unplanned repairs along the route.

5. Conclusions

DAS enabled by CNN model is used to detect and classify physical events that cause intermittent network outages due to disruptions in the outside plant connectivity. Offline analysis of historic waterfall data is performed to identify the field events causing network flaps. Analysis has shown that the majority of flaps are caused by fiber bend events. Next, a machine learning model is developed and trained for detection and classification of bend events. Detection and classification rate of ~ 97% along with low false alarms is achieved with fine tuning of the model.

6. References

[1] X. Bao and L. Chen, "Review recent progress in distributed fiber optic sensors". *Sensors*, 12, 8601–8639 (2012).

[2] H.F. Taylor and C.E. Lee, "Apparatus and Method for Fiber Optic Intrusion Sensing", *U.S. Patent US005194847A* (1993).

[3] J. Tejedor, J. Macias-Guarasa, H. F. Martins, J. Pastor-Graells, P. Corredera, and S. Martin-Lopez, "Machine learning methods for pipeline surveillance systems based on distributed acoustic sensing: A review," *Applied Sciences*, 7(8), 841 (2017).

[4] J.C. Juarez and H.F. Taylor, "Field test of a distributed fiber-optic intrusion sensor system for long perimeters", *Appl. Opt.*, 46, 1968–1971(2007).

[5] F. Peng, N. Duan, Y.-J. Rao, J. Li, "Real-Time Position and Speed Monitoring of Trains Using Phase-Sensitive OTDR", *IEEE Photon-Technol. Lett.*, 26, 2055–2057 (2014).

[6] G. A. Wellbrock et al., "Explore Benefits of Distributed Fiber Optic Sensing for Optical Network Service Providers", *Journal of Lightwave Technology*, 41, no. 12,758-3766, (June, 2023).

7. Pictures of Authors

Badri Gomatam



A photonics expert, Dr. Badri leads core research in optical communications products and network solutions. With a view on emerging network technologies, Badri guides the Company's technology vision. Under his leadership, the Company today has over 650 patents to its credit. He has an MS and Ph.D. from the University of Massachusetts, Amherst, and a BS from the Birla Institute of Technology. He joined STL in 2011.

Shubham Jagtap



Shubham Jagtap is Technology support engineer in R&D department of Sterlite Technologies Limited. He holds a bachelor degree from the Dr.Babasaheb Ambedkar Technology university. Since 2021, he has been working on Fiber optic sensor development.

Arvind Chandel



Arvind Chandel is a Machine Learning Engineer in R&D of Sterlite Technologies Limited. He holds a Master degree in Computer Engineering from SGSITS Indore. His area of expertise includes Deep Learning, Intelligent video analytics and Computer Vision.

Abhishek Sati



Abhishek Sati is Solutions Development Manager in the technology department of Sterlite Technologies Limited. He holds a bachelor degree in Chemical Engineering from MNNIT Allahabad. Since 2012, he has been working with Sterlite Tech. Limited on various new product development projects.

Ashit Padhi



Ashit is a Digital Transformation Leader with over two and half decades of experience working with global IT organizations. He has experience and expertise in designing, implementing and supporting large scale Enterprise IT Programs and Products. He has a unique blend of experience spanning across large corporations and start-ups. He is a Technology Evangelist with focus on cutting edge technologies - AI and Blockchain Technologies. He joined STL in 2022.

Sarman Panugothu



Panugothu Sarman is application engineer in the R&D Department of Sterlite Technologies Limited. He holds a Master Degree in Electronics from JNTU Hyderabad. Since 2019 he is involved in developing and deployment of fiber sensing systems. He has more than 11 years experience in the fiber optics field.

Pratik Sakode



Pratik Sakode is R&D engineer in Sterlite Technologies Limited. He holds a master degree in Electronics Systems from IIT Bombay. He joined Sterlite in 2016 and since then he has been working on fiber sensing, image processing and ML.

Nagaraju Bezawada



Nagaraju Bezawada joined Sterlite Technologies Limited in 2010 and has been involved in development of next generation optical fibers and fiber sensors. He is currently technical manager in R&D. Nagaraju received his Ph.D. in Physics from IIT Delhi in 2010. His research interests include design and characterization of novel optical fibers and distributed fiber sensors.

Bikram Jyot



Bikram Jyot is Deputy Manager in the R&D department at Sterlite Technologies Limited. He joined Sterlite in 2018. He holds a masters degree in software systems from BITS Pilani. Bikram has more than 13 years experience in System Integration, Software Development & Measurement System Analysis.

Measuring Bias and Repeatability of Fiber Inspection Scopes using Artifacts

Douglas H. Wilson, FiberQA
10 Vista Drive, Suite 101, Old Lyme, CT, USA
+1-860-961-8559 : dwilson@fiberqa.com

Vitalina Rudyk, Petro Shegedin, Farhad Towfig, Sumix; Gang He, EXFO; Julien Maille, Data-Pixel
Alexis Bartels-Popelar, Matthew Adams, VIAVI Solutions; Jamie Chivers, DORC
Seymour Goldstein, Fluke; Michael Gurreri, CommScope

Abstract
Inspection, and if required cleaning, of the end face of fiber optic interfaces is an important step to ensure the reliable operation of connectorized fiber optic systems. The IEC, specifically SC86B WG4/6, has created inspection standards to help industry institute quality systems to assure their parts meet the required surface finish.

A Visual Inspection Task Force (VITF) was created by IEC SC86B/Working Group 4 (WG4) to:

1. Study suitability of one or more artifacts to serve as certification devices to quantify the mean error (bias) and repeatability of defect diameter and scratch width measurements by fiber inspection scopes. Further, the artifacts would qualify the scope's ability to detect minimal sized features.
2. Develop recommendations for a future edition of the IEC 61300-3-35 related to performance capabilities of fiber inspection systems.
3. Conduct a multi-phased Round Robin (RR) to compare results across multiple systems from different manufacturers for both artifact candidates and real fiber samples.

In this paper, we report on the findings of the VITF related to the suitability of three types of artifacts and initial assessments of bias and repeatability among several fiber inspection scopes.

Keywords: Fiber optics, fiber optic end face inspection, visual inspection, automated end face inspection, test standards, fiber optics microscope, calibration, defect artifact, repeatability, reproducibility.

1. Introduction
Under this project, the VITF was tasked to investigate a suitable artifact (or set of artifacts) for use in qualifying fiber inspection equipment. The artifacts would allow suppliers to certify that inspection equipment was capable of measuring defects and scratches to meet the inspection criteria of the IEC 61300-3-35[1] standard.

Two types of features are specified in [1], scratches and defects. Scratches are defined as permanent surface features on the fiber end face where the width of the damaged area is smaller than or equal to one fifth of its length. Defects are permanent non-linear surface features on the fiber or ferrule end face within the regions of interest, which includes, but is not limited to, pits, chips, edge chipping, and/or non-removable foreign material. Width is the key parameter for scratches. Diameter, defined as its encompassing circle, is the key parameter for defects in [1].

The VITF decided on a Round Robin method for evaluation using instruments from multiple vendors. In addition to testing three candidate artifacts, real parts were also included in the RR. There were three phases to the Round Robin:

1. **Phase 1**: Artifacts
2. **Phase 2**: Scratch Samples: Artificially Scratched LC and MT
3. **Phase 3**: Scratch Samples: Production Rejects

Phase 2 and Phase 3 are outside the scope of this paper.

The results presented are preliminary and subject to change as the VITF goes through the review process within the IEC.

2. Artifact Description
The VITF participants agreed to investigate artifacts proposed and submitted for this study by members of the VITF. These were Chrome on Glass (CoG) MT ferrule emulations and Focused Ion Beam (FIB) MT ferrule with features etched into the fiber ends. Later in the study, the Nano-Indented (NI) artifact, in the form of an SC ferrule in a custom housing, was added as a third candidate. All three artifact types had the potential to emulate defects and scratches. The CoG and FIB artifacts had both types of features, while the NI artifact was implemented with scratches only for this study. The FIB and NI sample artifacts were designed for this study, while the CoG MT artifact has been in commercial use for several years.

2.1 Chrome on Glass (CoG) Artifact
One of the VITF members developed and employed CoG targets in many form factors including single MT ferrule emulation, D38999 full connector emulation, plates with very large number of MT-12, MT-24, MT-48, and MT-72 emulations. In fact, an MTP artifact (earlier version of the one used in this study) was used for a similar purpose as this study, determining reproducibility among instruments and repeatability within an instrument in Ref [2].

An example of the MT-12 emulation in an MPO connector used in Phase 1, Figure 1. The features, including fibers, defects and scratches, pin/hole and ferrule material were etched in the chrome. The fiber cladding region was chrome, and the defects/scratches were "holes" etched through this chrome. To make the features appear dark (less reflective), the chrome side of the glass was painted with an ultra-flat black paint.

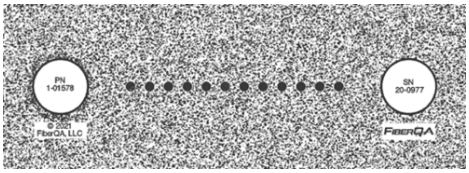


Figure 1: MT-12 Artifact Artwork

The glass target was fixed to a holder inserted into a standard MPO connector body, Figure 2, with the chrome surface at the same focus location as a normal ferrule. In this configuration, the fiber inspection scopes view the target chrome through the glass. An advantage of this construction was that the critical surface of the chrome is protected by the glass. Further, the front surface of the

glass is normally well out of focus, so surface contamination was not critical. If needed, the glass may be cleaned with standard glass cleaning materials and techniques. More details on the construction of the MT CoG Artifact may be found in Ref [3].

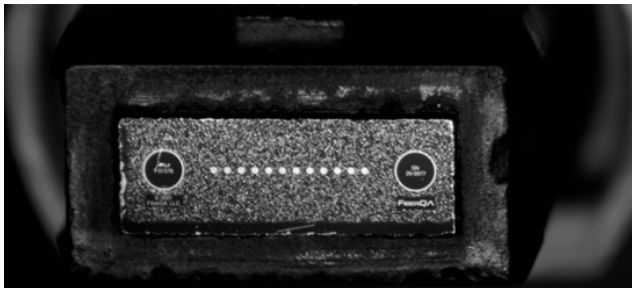


Figure 2: CoG MT-12 Artifact in MPO Connector

Each fiber in the emulated MT had one of three patterns; dots to emulate defects, lines to emulate scratches, or no pattern to emulate a perfect fiber. There were sixteen dots on defect fibers and six lines on scratch fibers. All dots and lines were at the same location relative to the fiber center, Figure 3. The diameter of the dots within a fiber were the same size, with unique diameters of 1.75, 2.0, 2.5, 4.5, 5.0, 5.5 and 10 µm on Fibers 1 through 7. Fiber 8 was a defect free fiber. Fibers 9 through 12 had lines with widths of 2, 3, 4, and 5 µm, respectively.

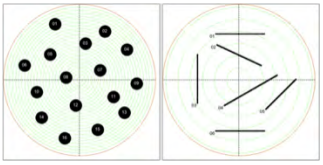


Figure 3: Dot and Line Locations

The CoG was considered a high contrast artifact target, where the emulated features appeared dark black (low reflectance) against the bright (high reflectance) chrome background emulating the fiber cladding.

2.2 Focused Ion Beam (FIB) Artifact

The FIB target was created by patterning dots and lines on fibers in an MT-12 ferrule, Figure 4. For purposes of this study, we used Fibers 01 and 07, which each had unique patterns of dots and lines to emulate defects and scratches, respectively. The MT artifact was mounted in a standard MPO connector.

With the bright features almost twice the reflectance of the cladding of the fiber, the FIB was considered a high contrast artifact target.

2.3 Nano-Indented (NI) Artifact

Nanoindentation techniques offer a valuable approach for generating controlled scratches and defects on fiber optic connectors [4]. These artifacts are proposed to be used for verification of fiber inspection microscope's ability to detect and accurately measure the width of scratches and diameter of defects. The morphology of a scratch formed within a specific depth range depends on several parameters. These include the applied force, type and orientation of the indenter tip, tip wear and tear, and more. Among these parameters, the most influential factor on scratch depth is the applied force. In the case of the Berkovich indenter tip, the width of the scratch is directly linked to the angle/orientation of the indenter tip. Similarly, with conical indenter tips, a correlation exists between the scratch angle and the tip's radius.

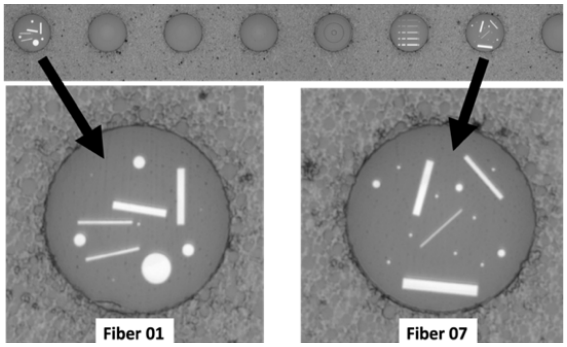


Figure 4: FIB Artifact with Closeup of Fibers 01 and 07

For the RR Phase 1A test, 5 samples with 2 scratches on each, made with the Berkovich indenter tip, were selected. The measured widths of each of the ten scratches are shown in Table 1.

Table 1: NI Artifact Scratch Widths

Sample & Scratch ID	Width (µm)	Sample & Scratch ID	Width (µm)
21-063-1	2.7	21-065-2	2.9
21-063-2	2.5	21-066-1	2.7
21-064-1	2.7	21-066-2	2.7
21-064-2	2.9	21-068-1	2.3
21-065-1	2.9	21-068-2	2.0

The NI samples were created on SC ferrules mounted in a custom housing, Figure 5.



Figure 5: NI Scratch Artifact

The depth of scratches was chosen based on the results of measurements of actual field scratches using atomic force microscopy (AFM). Thus, these data artifacts were designed to replicate real field scratches in terms of their shape and geometric parameters. Also, these ferrules were assembled into housings in such a way that the orientation of scratches was different for each sample, effectively simulating experiments involving connector rotation. An example AFM image and line profile used to measure the scratch depth and width was shown in Figure 6.

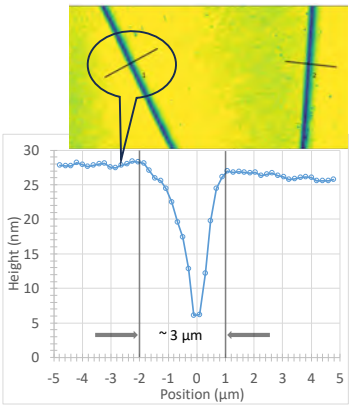


Figure 6: Example AFM Image and Line Profile

Figure 7 was an example of a microscope image of an NI artifact.

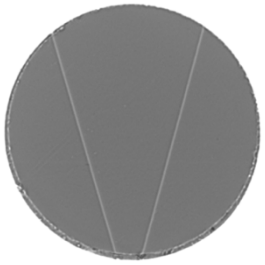


Figure 7: Example NI Scratch Artifact Image

3. Round Robin Test Description

The Phase 1 artifact testing was conducted as a completely open test; that is, all participants knew the location and sizes of the features. The participants reported data only on those features.

Five fiber optic inspection vendors participated in the Round Robin, using one or more instruments each.

Vendors were free to use multiple instruments, either unique instances of the same model or different models. The dataset from each instrument was assigned a unique Instrument ID by the Data Collector. The Data Collector knew which vendor submitted each data set but was not told which product was used. This process preserved anonymity among all the participants in the study and any published reports

While the exact models were not disclosed, it was known that instruments with resolutions differing by at about a factor of 2.5 were included in the study. Based on image scale factor, G and H are low-resolution, while all others were high resolution devices.

The basic process for the RR was:

1. Circulate the samples to each participant for data collection.
2. Each participant used one or more fiber inspection systems to capture and process images of the artifacts or fiber end faces.
3. Data collection was very structured to allow for easy comparison of the data from all instruments:
    a) Three tests, with the sample removed and reinserted in between each test to estimate the part handling reproducibility. In some cases, the part was rotated for each test.
    b) Eight repeat measurements were collected for each test.
    c) Measurement data was stored in a CSV spreadsheet file in an agreed format.
    d) Images were stored with an agreed naming convention, including a single letter code assigned by the Data Collector for each instrument.
4. Detailed data and images were submitted to the Data Collector, who anonymized and compiled the detailed measurements into a single spreadsheet.
5. Data Collector distributed the spreadsheet and anonymized images to the participants for data reduction and analysis.

Throughout the RR, the VITF participants met periodically to discuss any issues which arose with the collection, processing, or distribution of data. This feedback was incorporated directly into the collection and analysis process.

4. Phase 1 Results

4.1 Measurement Scope

The focus of Phase 1 was the study of the three kinds of artifacts described in Section 2: CoG, FIB and NI. Artifacts were supplied by members of the VITF. The sizes of the features of the artifacts were provided by the artifact supplier.

For Phase 1, measurement data was collected from six instruments from five vendors. These were anonymized as instruments B, G, H, M, R, and V.

4.1.1 Chrome on Glass (CoG)

As described in section 2.1, the CoG artifact had 16 defects per size, ranging from a nominal diameter of 1.75 μm to 10 μm. VITF participants collected a data set of 3 tests x 8 repeats x 16 defects for a total of 384 samples for each defect size. A total of seven defect diameters were included, so the total number of individual diameter measurements was 2688 for each instrument.

During the data collection phase, the VITF participants were not able to detect and process the line features as scratches. It was beyond the scope of this study to determine why the systems were not able to process the scratches. Scratch data using the CoG artifact was omitted from this study.

4.1.2 Focused Ion Beam

The participants of the study were not able to reliably detect the features on the FIB, so it was ruled out, at least in this instantiation, as a candidate for an artifact. It was beyond the scope of this study to determine why the systems were not able to process the features on this artifact. However, the FIB process has some potential advantages over the other two techniques, most notably arbitrary 3D features.

4.2 Measurement Data

The participants reported measured diameter, area, and location (XY center relative to the cladding center) for every fiber, defect, test and repeat in a spreadsheet. The diameter data for each valid measurement was plotted in Figure 8. The data was sorted by nominal diameter, then Test Number, and finally Repeat Number.

The X-axis labels show both the nominal diameter and the Test Number, with the X major grid lines showing the dividing line for each test. While we did not do a stationarity calculation, it appeared that there was no significant contribution from removing and reinserting the part between tests. Therefore, we elected to process all the data together. This effectively combined the reproducibility and repeatability estimation, yielding a total of 384 measurements for the statistics of mean and standard deviation.

A small snippet of the spreadsheet was shown in Table 2. For purposes of this paper, only the diameter data was analyzed and reported.

4.3 Example Images

One set of images from each instrument with the smallest diameter defect was shown to allow the reader to visualize the artifact as viewed by the instruments.

The images shared by the participants vary in image size and lighting, Figure 9. This can make them seem more different than was really the case due to visual perception issues. Two corrections were applied to remove these effects to aid the reader in comparing the results, Figure 10:

1. Images were scaled to the same size.
2. Intensity was normalized based on cladding levels.

These adjustments were made to improve comparisons among the images to account for differing lighting and/or scaling of the Field of View (FOV). The scale factor had a high-resolution value of

~0.41 µm/pixel to a low-resolution value of ~1.03 µm/pixel, or about a factor of 2.5. For intensity, the nominal cladding mean value ranged from a low of 108 (42% of camera range) to about 240 (94%). Each inspection system's processing software was designed to work properly with the lighting and image used. The adjustments made for presentation purposes were done solely for cosmetic reasons to improve viewability.

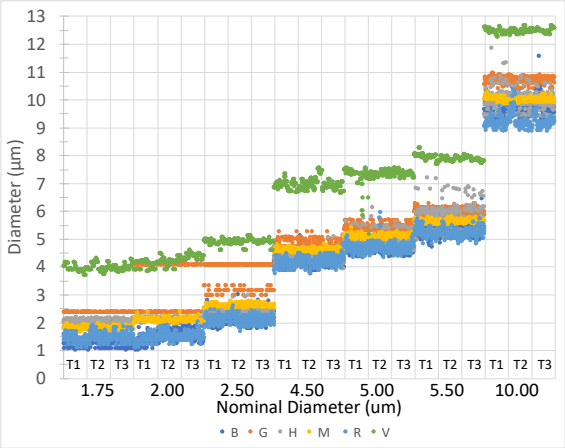


Figure 8: All Measured Diameters

Table 2: Data Spreadsheet Snippet

Fiber	Defect	Test	Repeat	Diameter (um)	Area (um^2)	Center X (um)	Center Y (um)
1	1	1	1	1.57	1.34	-20.11	-47.55
1	1	1	2				
1	1	1	3	1.22	0.87	-20.17	-47.62

Judging by the subjective quality of the intensity normalized and scaled images, all the systems were able to image the artifact features very well. There was slight, but obvious, differences in sharpness, most likely due to optical resolution differences among the instruments. Of course, the objective data provided by the vendors on defect diameters was the real test of the capability of the instrument. The processing software combined with the image acquisition hardware constituted the entire inspection system.

4.4 Results

The intent of using an artifact for calibrating and certifying fiber inspection systems is to achieve more consistent Pass/Fail results among instruments, whether from different manufacturers, different models, or instances of the same type. The VITF determined that three metrics would be measured during this test:

1. Bias or systemic error from the nominal value(s)
2. Random errors: Repeatability and Reproducibility
3. Detectability of the smallest size of interest

While listed last, detection is the first step in grading a fiber end face. Stating the obvious, the system cannot measure something until it first detects it. Reference [1] mandates a detection rate of 98% or greater.

4.4.1 Bias Estimates

For the CoG artifact the defect diameters were accurately known. While the article used for this testing was not calibrated, it is possible to calibrate the defect diameters, and other feature sizes such as cladding and hole/pin diameters, traceable to national laboratory standards (such as NIST) to within ±0.1 µm. The photolithography process used to create the glass target portion of the artifact is very well controlled yielding parts that are within ±0.1 µm of the design feature size.

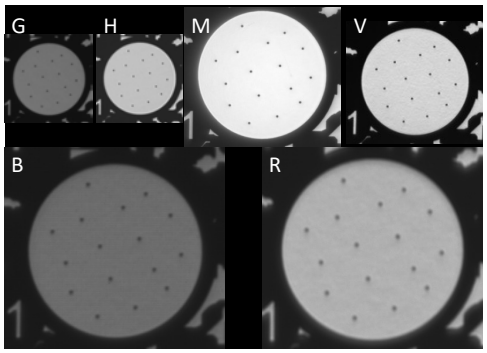


Figure 9: Original Images

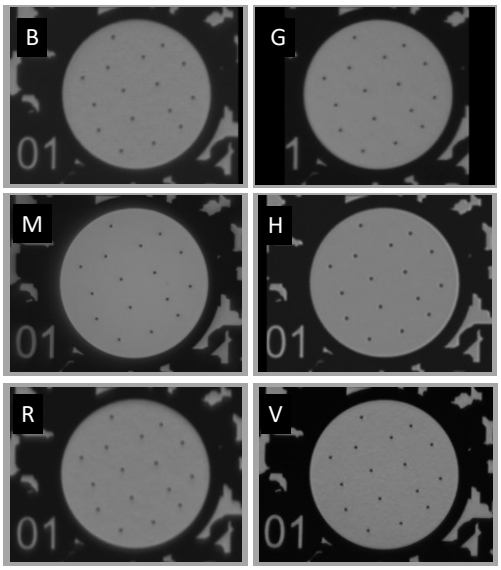


Figure 10: Images Matched in Scale and Intensity

The known and measured defect diameters were processed together to estimate the bias errors in a three-step process, separately for each instrument:

1. For each defect size, the means of all diameter measurements for all tests and repeats were calculated to form a "Mean Diameter", Figure 11.
2. The known diameter was subtracted from the measured means to form a "Mean Diameter Error", Figure 12.
3. The mean value of the errors for each instrument was then calculated and subtracted from the Mean Diameter Errors to form the "Corrected Mean Diameter Error", Figure 13.
4. This simple offset correction appears to be an adequate correction factor to reduce the mean bias error to zero across all sizes, at least for purposes of this report. In practice, each vendor will decide the best method to use the artifact to calibrate their defect diameter measurements. There remains a residual bias error of about ±0.4 µm across all sizes and instruments, excluding one wild point.

It is important to note that the minimum defect diameter that must be reliably detected in [1] is 3 µm. The range of mean diameter errors without artifact-based compensation is about 2.8 µm. This is almost 100% of the Pass/Fail limit value. With correction by means

of an artifact this value should be reduced to below 25% for the fully corrected diameter. This will directly translate to significantly better agreement across the fiber inspection industry.

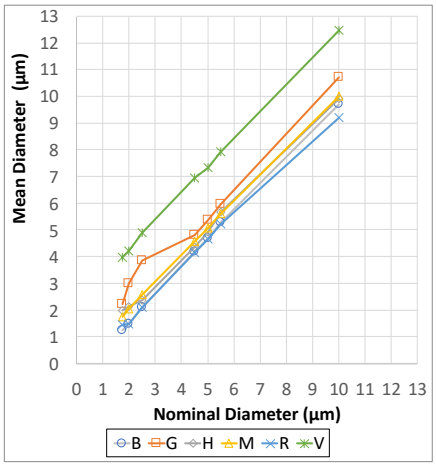


Figure 11: Mean Diameter

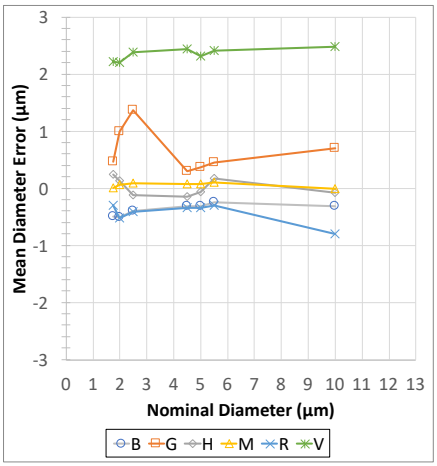


Figure 12: Mean Diameter Error

The mean diameter error for each instrument and each diameter, and the mean value of the errors across all nominal diameters were shown in Table 3. The last row is the standard deviation of the mean error across the nominal defect diameters. The low values are one of the indicators of validity of a simple offset as the final correction factor to lower the bias among instruments.

The final reduction in bias error illustrated in this analysis shows that it is possible for vendors to use an artifact to reduce the bias error significantly. This is the first time there has been a means of quantifying the magnitude of the inter-instrument bias error.

Further evaluation of data from other artifacts may be required for the VITF to recommend one or more artifacts for defects and scratches. The full WG4 will evaluate the data, results, and recommendations of the VITF before deciding which artifacts to specify in a future version of or amendment to Reference [1].

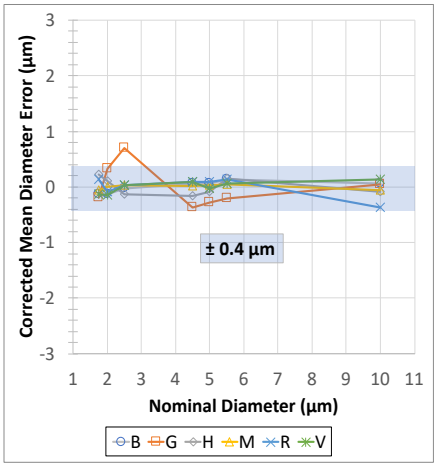


Figure 13: Corrected Mean Diameter

Table 3: Mean Diameter Error

Diameter (µm)	Mean Diameter Error (µm)					
	B	G	H	M	R	V
1.75	-0.500	0.677	0.242	0.005	-0.298	2.212
2.00	-0.518	0.989	0.128	0.061	-0.523	2.203
2.50	-0.393	1.367	-0.094	0.093	-0.402	2.382
4.50	-0.307	0.296	-0.149	0.075	-0.334	2.439
5.00	-0.313	0.376	-0.068	0.082	-0.324	2.319
5.50	-0.237	0.449	0.168	0.105	-0.277	2.405
10.00	-0.313	0.706	-0.084	-0.003	-0.798	2.477
Mean	**-0.387**	**0.694**	**0.020**	**0.060**	**-0.422**	**2.348**
StDev	**0.106**	**0.378**	**0.154**	**0.043**	**0.185**	**0.108**

4.4.2 Repeatability and Reproducibility

As previously discussed, the RR procedure had a limited number of tests (3) and repeats within a test (8). However, for the CoG artifact, with a high number (16) of defects for each of seven diameters being measured in each event, a significant number of independent samples were collected within the experiment. For each test, there were 128 samples of each diameter (8 repeats*16 defect/diameter). In fact, as explained in Section 4.2, data from all tests and repeats were combined, making the total number of samples of each diameter 384.

There were two distinct instrument groupings observed when the standard deviation of the diameters was calculated. Instruments B, M, R, and V (BMRV) had significantly lower values than G and H (GH). For clarity, the data of the BMRV set were plotted in Figure 14. The data for the GH set were plotted in Figure 15.

For the BMRV set, the maximum standard deviation was about 0.28 µm and under 0.2 µm if an apparent outlier could be removed. This was consistent with the measured values reported for a high-resolution scope in Reference [2], where the maximum value was less than 0.25 µm.

Instrument G had a standard deviation peak value of about 0.85 µm or 3-4 times higher than the BMRV set. H had a standard deviation peak value of about 0.45 µm.

Looking more closely at the data from G and H there seem to be significant irregularities, which we did not investigate further. For purposes of this study, it makes sense to ignore those data sets.

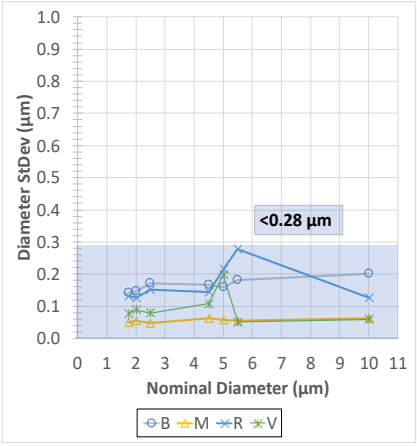


Figure 14: StDev for High Resolution Instruments

4.4.3 Detectability

One of the rules for use of the data submission spreadsheet was to have a cell for every test, repeat, fiber and defect. A way to describe this was that the spreadsheet was a flat database structure, with one row for every item. If an instrument did not detect a given defect, then the data fields were left empty. All the identifier fields***, *Fiber, Defect, Test, and Repeat*** were populated. The second row of data in the spreadsheet snippet shown in Table 2 was an example of a non-detected defect.

For this experiment the total number of physical samples was 112 (seven fibers with 16 defects each). These were each measured 24 times in 3 tests of 8 repeats each. The product of those yielded the total number of 2688 unique, uncorrelated data points.

This version of the CoG target was designed when there were two key diameters, 2 and 5 µm in the previous version of [1]. That is why there were defects at those two diameters, with bracketing defects above and below. As a compromise, we will look at the detection percentage for the 2.5 µm diameter.

The detection counts for all the instruments for each defect diameter were tabulated, as percentages of the total number of samples, in Table 5.

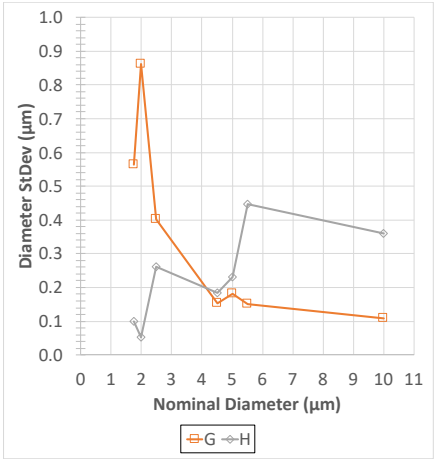


Figure 15: StDev for Low Resolution Instruments

The standard deviation values for each instrument and each diameter, and the maximum value of the standard deviation across all nominal diameters were shown in Table 4. The last row is the maximum of the standard deviation across the nominal defect diameters.

Table 4: Standard Deviation of Diameter

	StDev Diameter (µm)					
Diameter (µm)	B	G	H	M	R	V
1.75	0.140	0.564	0.098	0.051	0.131	0.078
2.00	0.147	0.863	0.051	0.054	0.127	0.088
2.50	0.171	0.401	0.260	0.047	0.150	0.078
4.50	0.167	0.152	0.183	0.062	0.145	0.108
5.00	0.160	0.181	0.230	0.057	0.216	0.197
5.50	0.181	0.150	0.446	0.055	0.277	0.050
10.00	0.202	0.108	0.359	0.063	0.126	0.059
Max	**0.202**	**0.863**	**0.446**	**0.063**	**0.277**	**0.197**

Table 5: Detection Percentages by Defect Diameter

Diameter (µm)	B	G	H	M	R	V
1.75	95.1%	100.0%	93.8%	100.0%	100.0%	100.0%
2.00	96.9%	100.0%	95.8%	100.0%	100.0%	100.0%
2.50	100.0%	100.0%	88.0%	100.0%	99.2%	100.0%
4.50	100.0%	100.0%	95.8%	100.0%	100.0%	100.0%
5.00	100.0%	100.0%	95.8%	100.0%	100.0%	100.0%
5.50	100.0%	100.0%	95.8%	100.0%	100.0%	100.0%
10.00	100.0%	100.0%	95.8%	100.0%	100.0%	100.0%
All	98.8%	100.0%	94.4%	100.0%	99.9%	100.0%

Instruments G, M and V had a perfect 100% detection rate for all defect sizes.

Instrument B detected 100% of all defects with diameter >= 2.5 µm. It missed 31 defects for the two smallest diameters with a minimum rate over 95%.

Instrument R missed only 3 defects at the 2.5 µm diameter for a 99.2% success rate, with a 100% success rate for all other sizes.

Instrument H did not perform well. It missed 46 defects at the 2.5 µm diameter, for an 88% detection rate. It missed another 104 defects for a grand total of 150 non-detects. It was near or below 95% for all diameters.

All instruments, except H, met or exceeded the detection rate of >98% for the smallest defect of interest per [1].

Overall, while not perfect, the detection results were quite good, except for H. From the perspective of the artifact, this test demonstrated that it was a useful tool to measure the detection capability of end face inspection systems.

5. Phase 1A: NI Artifacts

5.1 Measurements Scope

For Phase 1A, measurement data was collected from one instrument from each of five vendors. These were anonymized as instruments G, H, M, T, and V.

The VITF is continuing to analyze the results of Phase 1A. However, we already believe that the data shows similar capability for measuring scratches as was observed with the CoG artifact for measuring defect diameters. These are preliminary results and subject to change as we continue the analysis. However, it seems use of this artifact may reduce the variability reported in [5-6].

The measured mean widths, as a function of known width, were shown in Figure 16. Without any corrections, there was a spread of

about 2 µm across all samples and all instruments. This is a significant error and illustrates one of the major reasons for the search for artifacts for certifying instrument's capability.

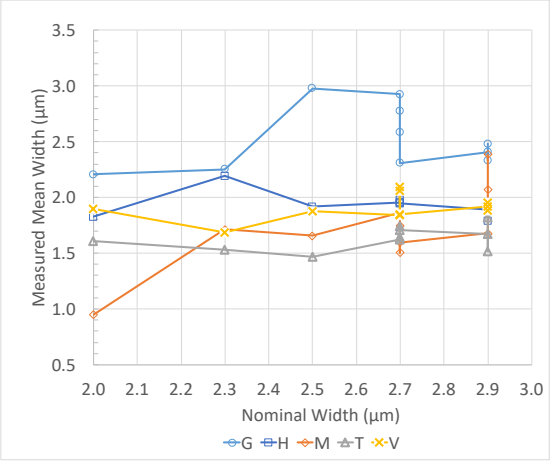


Figure 16: NI Artifact Measured Mean Widths

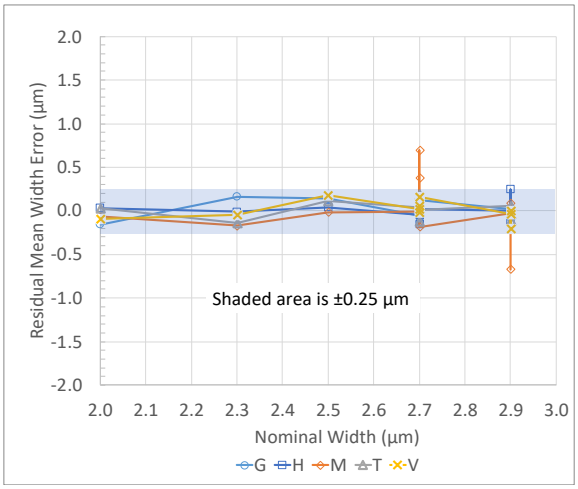


Figure 17: NI Artifact Residual Mean Width Errors

These means were further processed by calibrating using true size from the AFM measurements made by the vendor. The data from all the instruments had a linear trend which was removed by linear regression. The residual mean width errors were shown in Figure 17. This reduced the spread to about ±0.7 µm, about a 3x reduction in bias error. Stating this in standard deviation terms, the standard deviation was 0.11 for instruments G, H, T, and V and 0.36 for instrument M. If instrument M is excluded, the peak bias error was about ±0.25 µm and standard deviation was 0.105 µm.

Subsequently, the manufacturer was able to create samples with well-formed scratches up to 6 µm in width. Combined with the initial samples, that provides NI artifacts with a width range of 2 to 6 µm. All ten samples will be measured during an upcoming Phase 1B RR. Once that is concluded, we will review the results in WG4. We will have a more complete analysis, including both bias (relative to absolute values of the artifact) and reproducibility and repeatability. Where practical, Phase 1B will look at the reproducibility effects of not only insertion of the samples, but rotation. Documenting the degree of variation in detectability and width of scratches including rotation, is of keen interest to the experts of WG4, including the participants in this RR.

6. Conclusions

In this paper we have presented the results from a portion of our mandate from the IEC SC86B/WG4; namely to determine the suitability of one or more artifacts to be used to determine if a given inspection system meets the capability required to test parts to the standard [1].

Three candidate artifacts were evaluated: Chrome on Glass, Focused Ion beam etched fiber and Nano-Indented fibers.

1. We demonstrated that the CoG artifact has the potential to serve as artifact for defects. Unfortunately, systems were not able to process the CoG's emulated scratches.
2. We determined that the current instantiation of the FIB technique was not usable. We ruled out the FIB evaluated during this study.
3. We partially completed evaluation of the NI artifact. Based on the preliminary processing of the data, it appears to have potential to serve as artifact for scratches. In this study the NI artifacts had scratch widths from just above 2 µm to just below 3 µm.

The assessments of the artifacts should be considered preliminary and subject to change as the results are discussed with the experts of WG4. A decision on suitability of any of these artifacts for certification in an updated standard [1] requires the approval of WG4 and the IEC. The VITF will present these findings and other data from the other phases of the RR at an upcoming IEC WG4 meeting in November of 2023.

Consistency among fiber inspection instruments has been an elusive goal of the fiber cable assembly industry for a very long time. Finding artifacts to measure the bias errors and measurement reproducibility and repeatability of features of interest will enable the standard [1] to specify a robust process to certify instruments.

The benefits of attaining a robust certification process that allows for a minimal, quantifiable limit to the measurement uncertainty cannot be overstated. Use of this process and artifacts will create confidence and consistency in inspection results throughout the manufacturing supply chain and during the deployment lifetime of fiber systems, even when different models of inspection systems are used.

This study used a robust engineering approach to collect and analyze detailed feature dimensions from multiple instruments. This was done together with the evaluation of multiple types of artifacts. Detailed data was the key to a proper comparison of results across instruments and evaluation of artifacts to minimize the uncertainty.

Employing artifacts was demonstrated to significantly reduce the systemic errors for defect diameter and scratch width. Using artifacts, the magnitude of random errors, both reproducibility and repeatability, were reliably measured. This was a first critical step along the path to minimizing and documenting the uncertainty in fiber end face inspection measurements.

These tests were conducted in a laboratory environment by engineers. The scratch artifact was tested with a very limited number of samples and narrow range of widths. So, while the artifact results measured during this RR are encouraging, further work needs to be done with both artifacts. For both artifacts, all results must be thoroughly vetted by the IEC WG4.

Being able to use an artifact to measure the residual bias errors and the standard deviation of the random errors may allow the next version of the standard to define Pass/Fail limits that account for these known error sources.

The final step in successfully implementing the certification process using artifacts will be to work with end users for feedback and ultimately acceptance of this new process.

This data presented in this paper demonstrated that the VITF conducted a thorough investigation of certification artifacts that yielded very promising results. We tackled a very tough problem with a systematic and detailed, data-driven approach to improve the state of the art in fiber end face inspection.

We intend to complete the balance of the RR testing and analysis to further validate the improved agreement among fiber end face inspection instruments when artifacts are used to correct their measurements. Phase 2 and Phase 3 will be vitally important to determine if the improved agreement when measuring artifacts carries over to real product samples in a production environment.

A new era of confidence in automated inspection hardware and software is on the horizon!

7. References

[1] IEC 61300-3-35 Ed. 3.0 b:2022, "Fibre Optic Interconnecting Devices And Passive Components - Basic Test And Measurement Procedures - Part 3-35: Examinations And Measurements - Visual Inspection Of Fibre Optic Connectors And Fibre-Stub Transceivers", Sept 2022

[2] C. DiSaverio; C. J. Wilson; D. H. Wilson, "Measuring Fiber End Face Inspection Microscope Reproducibility using Chrome on Glass Artifacts", *2017 IEEE Avionics and Vehicle Fiber-Optics and Photonics Conference (AVFOP)*, Nov 2017.

[3] Douglas H. Wilson, "Measuring Repeatability of Fiber Inspection Systems Using Chrome on Glass Artifacts", *IWCS 2019 Cable & Connectivity Symposium)*, Sept 2019.

[4] S.P. Baker, J. Liu, Nanoindentation Techniques in Reference Module in Materials Science and Materials Engineering, 2016

[5] IEC TR 63367 ED. 1.0 EN:2021, "Fibre optic interconnecting devices and passive components – Summarizing results of end face scratch recognition and verification round robin", Nov 2021

[6] J. Webb, T. Berdinskikh, D. Daems, T. Bolhaar, M. Gurreri, "Review of Connector End Face Scratch Recognition and Verification Study for Automated Microscopes", *IWCS 2021 Cable & Connectivity Symposium)*, Ocy 2021.

8. Pictures of Authors



Douglas H. Wilson
FiberQA, LLC
10 Vista Drive, Suite 101, Old Lyme, CT
1-860-961-8559, dwilson@fiberqa.com

Douglas Wilson received his Bachelor of Science in Electrical Engineering from the U.S. Naval Academy in 1977. He served for five years as a Naval Officer in the US Navy, followed by 14 years as a civil service engineer at the Naval Undersea Warfare Center designing submarine towed arrays. From 1996 to 1999, he was General Manager of Automation Systems at Analysis and Technology. In 1999, he formed PVI Systems, developing custom test systems, including development of fiber end face inspection systems. In 2012, he co-founded FiberQA, where he now serves as Founder and CTO, by spinning out the fiber inspection technology. He has been an active member of IEC (SC86B/WG4&6), iNEMI, SAE (AS-3) and ARINC (FOS) for many years. He holds a total of six patents.



Vitalina Rudyk
Sumix Corp.
3532 Seagate Way, Suite 100, Oceanside, CA, 92056, USA
1-877-233-3385, vitalina.rudyk@sumix.com

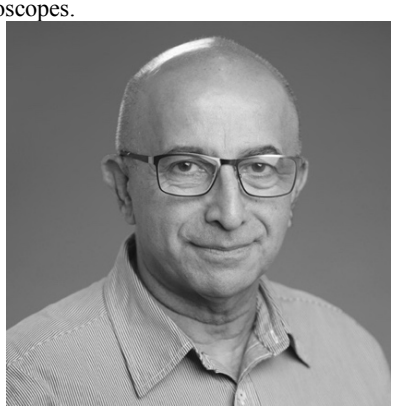
Vitalina Rudyk received her master's degree in Computer Science and Cybernetics from Taras Shevchenko National University of Kyiv. Since joining Sumix Ukraine LLC in 2012 as a Software Engineer, she has excelled in designing and implementing image and signal processing algorithms for fiber optic connector testing devices, specifically for interferometers and microscopes. Her specialization encompasses the development of libraries for detecting scratches and defects and measuring their parameters. She has been a member of IEC, TC 86/SC 86B since 2015.



Petro Shegedin
Sumix Corp.
3532 Seagate Way, Suite 100, Oceanside, CA, 92056, USA
1-877-233-3385, pshegedin@sumix.com

Petro Shegedin holds a Ph.D. degree in Computer Systems and Components and a M.S. degree in Metrology and Information Measurement Systems. Petro has been working in the fiber optic industry for over 10 years, and currently holds the position of Product Development Manager and COO Sumix Ukraine LLC. He uses his accumulated experience to create tools for measuring the

parameters of fiber optic connectors, including interferometers and optical microscopes.



Farhad Towfiq
Sumix Corp.
3532 Seagate Way, Suite 100, Oceanside, CA, 92056, USA
1-760-529-1365, farhad@sumix.com

Farhad Towfiq has been the CEO of Sumix Corporation, since 1999. He received his Ph. D. from UC Irvine in Electrical and Computer Engineering in 1984 with a focus on Digital Signal Processing, Communications, System Identification, Control, and parametric/non-parametric pattern classification. He was employed by Philips ultrasound, Diasonics, and GE ultrasound in product development for various medical ultrasound imaging and measuring systems. He was employed with Northrup Grumman for CAD-based vision in design and manufacturing automation, and with NASA Ames AI lab for compact modeling of fluid dynamic data. He has authored several patents in 3D ultrasound and optical interferometry imaging and measurements. He presently is interested in 4D(3D+time) solid modeling for detection and autopilot.



Gang He
Exfo
400 Avenue Godin, Québec (Québec) G1M 2K2 Canada
1-418-683-0211 x 24064, gang.he@exfo.com

Gang He received his Ph.D. degree in Physics from Laval University, Canada, in 1995. He is currently principal research scientist in EXFO's R&D department. His main research interests include advanced optical design, innovative spectral characterization methods, guided wave behavior and T&M technologies on next generation networks. He has been actively participating in the work of Standard Committees of IEC, TIA, ISO/IEC and ITU-T. He is now the vice chair of Canadian Standards Subcommittee IEC/SC86B and IEC/SC86C. He has 24 patents, 27 published papers in Journals, international conferences, and a book chapter. He is a member of OPTICA and SPIE.



Julien Maille
Data-Pixel
27 rue Saturne, ZAC Altaïs, 74650 Chavanod, France
+33 4 50 67 39 80, julien.maille@data-pixel.com

Julien Maille graduated from CPE Lyon in 2007 with an M.S. degree in Computer Science and Signal Processing. He began his career at Data-Pixel as a software engineer, where he developed algorithms for defect recognition and 3D reconstruction of connectors' end-faces. Currently holding the position of R&D manager, he has over 12 years of experience in the design and development of interferometers, microscopes, and concentricity devices dedicated to the fiber optic industry. As an IEC-recognized expert, he has contributed to documents related to visual inspection and geometry measurement and holds patents in this field.



Alexis Bartels-Popelar
VIAVI Solutions, Inc.
22215 26th Ave SE Ste 120, Bothell WA 98021, USA
1-425-368-2220, Alexis.Bartels-Popelar@viavisolutions.com

Alexis Bartels-Popelar is a Test Engineering Manager at VIAVI Solutions working on innovative fiber inspection and test products. With 5 years of experience in the fiber optic industry, her experience includes verifying and validating new fiber optic test products and maintaining product quality. She leads an engineering team dedicated to testing and compliance for products at VIAVI. Alexis joined the IEC in 2020 and is an active contributor and technical expert for TC 86/SC 86B. Alexis was recently selected by the USNC as a winner of the 2023 IEC Young Professionals Competition and is slated to participate in the Young Professionals Programme. She graduated with a Bachelor of Science in Robotics Engineering from the University of California, Santa Cruz in 2016.



Matthew Adams
VIAVI Solutions, Inc.
61 Bill Leathem Drive, Nepean, ON K2J 0P7, Canada
1-613-843-4300 Matthew.Adams@viavisolutions.com

Matthew Adams is a Senior Product Manager at VIAVI Solutions. For over 25 years, he has held leadership positions spanning R&D, technology planning, and product management. He is currently focused on developing measurement solutions supporting the design and manufacture of next generation fiber optic components, modules, and sub-systems. He is an active contributor to international standards, a co-author of several articles and has several patents in the area. Matthew has a Master's degree in Engineering Physics from McMaster University.



Seymour Goldstein
Fluke Corporation
6920 Seaway Blvd., Everett, WA
1-512-541-8866, seymour.goldstein@flukenetworks.com

Seymour Goldstein received his received a Bachelor of Science degree in Electrical Engineering from Syracuse University in 1978. From 1978 to 1986, he worked for Bunker Ramo and Bendix Oceanics, as the lead analog design engineer for an acoustic counter-measure device. From 1986 to 1992, he worked for Photodyne Inc., commercializing fiber optic test equipment. after Photodyne was acquired by 3M, he served as section leader, continuing to develop fiber optic measurement methods and equipment. In 2000, 3M technology was acquired by Fluke Networks where he opened a design lab for development and commercialization of fiber optic test equipment. He is a Fellow at Fluke Corporation in the technology and innovation group.



Jamie Chivers
DORC
8725 115th Avenue North, Largo, Florida 33773 USA
1-727-319-9000, Jamie@dorc.com

Jamie Chivers grew up in the south of England, United Kingdom and graduated from Southampton Institute of Technology with a degree in Marine Electronics and Radar in 1985. Jamie then worked for York Technology, a manufacturer of preform and fiber test equipment for several years - before transferring to their California office in 1989 and travelling the world as a technical support engineer. After leaving York in 1992, Jamie decided to stay in the USA and founded Direct Optical Research (DORC) in 1992. DORC manufactures fiberoptic connector end face measuring interferometers and inspection equipment. Jamie holds numerous patents on innovations related to this technology.



Michael Gurreri
CommScope
1100 Commscope Pl SE, Hickory, North Carolina 28602 USA
1-717-546-3401, michael.gurreri@commscope.com

Michael Gurreri received his B.S. degree in Mechanical Engineering in 1997 and his M.S. in Engineering Science in 2005 from Pennsylvania State University. He joined CommScope (via divestiture from TE Connectivity and prior AMP) in 1998 as a Product Development Engineer in the Fiber Optics Business Unit, taking on various management and technology development roles throughout his career. Mike is currently a Fellow in the Network Connectivity segment of CommScope and is a delegate to IEC SC 86B, where he received the 1906 award for contributions to multifiber optical interfaces. He holds over 50 US patents in the field of fiber optics and was named a CommScope Master Inventor in 2020.

SESSION 3

Click on a session below to navigate to that section of the Proceedings.

SESSION 3: DESIGN, TESTING & APPLICATIONS FOR COPPER ETHERNET, POE AND ENERGY CABLES - PART 1

Chairperson: Trent Hayes, CommScope, Inc., USA

3-1 **Extracting and Discriminating Spontaneously Recovering Faults, Case Study on Pressurized Cable**; Mr. Kaoru Kawasaki, Nippon Telegraph and Telephone East Corporation, Japan

3-2 **Impact of Thermal Aging on Safety Performance of Power-Over-Ethernet Cables**; Dr. Bo Xu, Product Development Center, Superior Essex Communications, USA

3-3 **Channel Performance Degradation From Installation Stresses**; Mr. Brian Marchant, Leviton, USA

3-4 **Topography Scanner for Quality Control of Power Cable Manufacturing**; Mr. Jussi Hanhirova, Maillefer Extrusion Oy, Finland

Click here to return to the **Table of Contents**

Extracting and discriminating spontaneously recovering faults, A case study on pressurized cable

Kaoru Kawasaki, Keiji Fujihashi, Takeshi Sawa, and Osamu Sasaki

Strategic Network Management Department, NTT East

19-2, Nishi-shinjuku, 3-chome, Shinjuku-ku, Tokyo, 163-8019, Japan

+81 3 5359 4450 ·kaoru.kawasaki.sk@east.ntt.co.jp

Abstract

To visualize the relationship between gas pressure and temperature, we created a linear function for each pressure transmitter. Subsequently, we performed cluster analysis utilizing the "correlation coefficient", "intercept", "R2", and "the difference between the maximum and minimum gas pressure values for one year" as explanatory variables. one cluster demonstrated a significant correlation coefficient, R2, a notable difference, and a small intercept, indicating that it is a "spontaneously recovering faults". Subsequently, a linear discriminant was created to distinguish between "spontaneously recovering faults" and "others." The explanatory variables were the same as those used in cluster analysis. The analytical model demonstrated a correlation ratio of 0.5 or higher and a discriminative accuracy of over 90%. By utilizing this formula, effective maintenance may be realized by identifying "spontaneously recovering faults".

Keywords: reduction in operation, pressurized cable, maintenance, statistical analysis

1. Introduction

In recent years, the declining working population has become a major issue in Japan, and the decreasing number of engineers is a significant problem for NTT. Specifically, NTT faces the issues of maintaining the aging facilities of pressurized cable networks, which are cables that run from a central office to a feeder point and are filled with dry air at high pressure. Therefore, NTT has been conducting research on efficient maintenance methods and maintenance-free systems [1]-[3].

Pressurized cable networks are particularly susceptible to breakdowns in winter due to the shrinkage of the airtight tape used in their closure, caused by temperature changes. This shrinkage can lead to dry air leakage. If the pressure drops below a certain level, water may enter the closure and disrupt communication services. However, among these failures, there are cases of "spontaneously recovering faults" where the faults can be restored by a rise in temperature.

In this study, we propose a method for extracting and distinguishing "spontaneously recovering faults" from other failures using statistical analysis. This method enables the efficient maintenance of pressurized cable networks.

2. Pressurized cable networks

2.1 Architecture

In the context of NTT's pressurized cable networks, the organization has been previously discussed in NTT's research [3]. This paper also discusses this in detail.

Figure 1 presents an overview of the structure of pressurized cable networks. Dry air (gas) is supplied to the pressurized cable from an air compressor located within the NTT building. The gas flows through the copper wires, while at the cable splice point, it diffuses into splice protectors that are filled with the gas. The gas pressure is maintained at 63.7 kPa and monitored using a pressure transmitter.

2.2 Failure of pressurized cable

Figure 2 show the failure state of a pressurized cable. The primary cause of failure is the shrinkage of closure components due to temperature variations, leading to the formation of gaps. Repair criteria may vary among maintenance engineers, but generally, monitoring of the cable is necessary when the pressure falls below

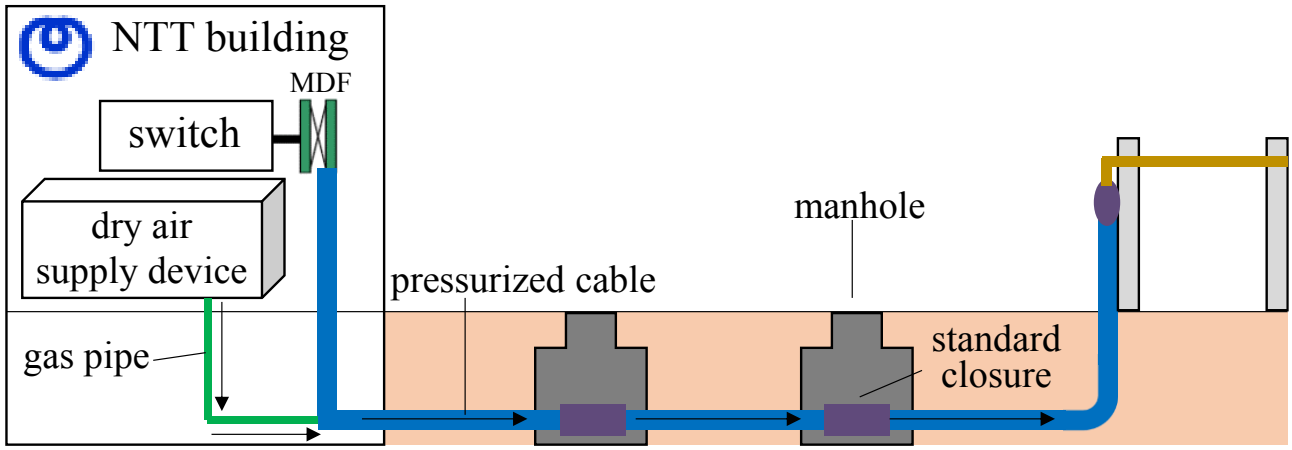


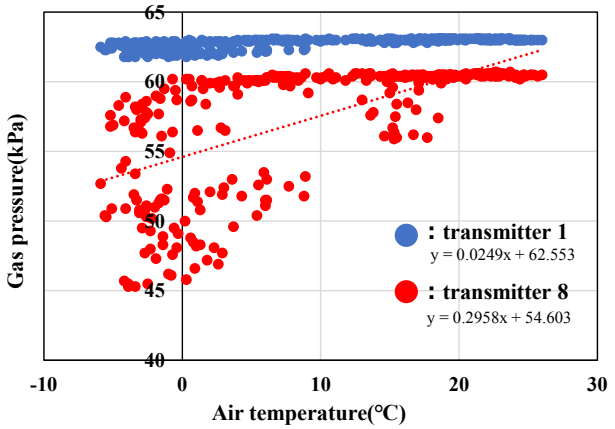
Figure 1. Pressurized cable network

40.0 kPa, followed by repairs when it drops below 30.0 kPa. The "spontaneously recovering faults" that we deal with this time are thought to be those that have a positive correlation between gas pressure data and air temperature, as shown in Figure 3.

Figure 4 demonstrates the process of opening and closing manholes for repair purposes. When dealing with pressurized cable, it is essential to estimate the faulty closure based on gas pressure data. However, these estimates are not conclusive, and in some cases, inspection of five or more manholes becomes necessary. Repairing the failure requires opening and closing the manhole, which poses a physical burden on workers due to the heaviness of the manhole cover. Furthermore, if water accumulates inside the manhole, additional time is needed for drainage. Consequently, minimizing repairs is crucial for operational efficiency. Figure 5 outlines the current cable



Figure 2. Pressurized cable failure



※Transmitter 1 is the transmitter closest to the NTT building
※Transmitter 8 is the transmitter closest to the gas leakage point

Figure 3. Correlation (gas pressure and temperature)



Figure 4. How to open a manhole

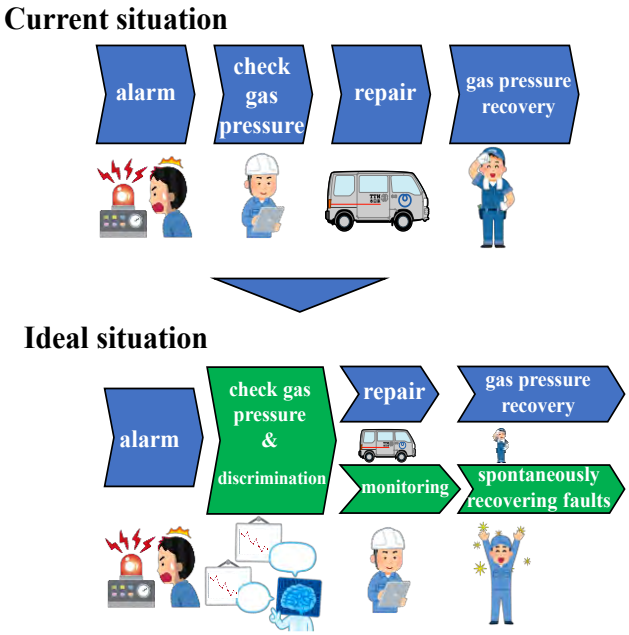


Figure 5. Current situation and ideal situation

maintenance system and presents a system designed for identifying "spontaneously recovering faults" as discovered in this research. To ensure safety, do not immediately search for failure points, instead continuous surveillance is employed to reduce operation. In the event of a sudden drop in gas pressure, a prompt search and repair of the failure point are necessary.

3. Analysis overview

3.1 Data

Table 1 presents an overview of the analytical data. Given the significant influence of temperature variations on the failure of pressurized cables, the analysis focuses on Hokkaido, Japan. We

Table1. Analysis data summary

Analysis target area	Sapporo, Hokkaido
Data collection method (gas pressure)	Automatic measurement once a week
Data collection method (temperature)	Japan Meteorological Agency
Analysis period	2019/01/07～2019/12/30
The number of samples	1,902(Number of pressure transmitters)

used gas pressure data spanning one year from 10 NTT buildings in Sapporo, Hokkaido. Additionally, minimum temperature data from the Japan Meteorological Agency is incorporated by aligning the dates of gas pressure measurements, thus obtaining daily data on minimum temperature and gas pressure in Sapporo city. Explanatory variables include the "correlation coefficient," "intercept," "R2," and the "difference between the maximum and minimum gas pressure in one year" derived from the gas pressure and temperature approximation formula. The decision to not directly employ the numerical value of gas pressure aims to account for the possibility of persistently low gas pressure in certain cables due to unforeseen circumstances.

3.2 Cluster analysis

Cluster analysis is conducted using the K-means method, considering the wide range of scenarios for gas pressure fluctuations. Prior to analysis, numerical values of various variables are standardized to have a mean of 0 and a variance of 1.

3.3 Discriminant analysis

For discriminant analysis, linear discriminant analysis is employed to distinguish between "spontaneously recovering faults" and "others" identified through cluster analysis. The reliability of the discriminant is evaluated based on correlation ratios and discriminant accuracy. Similar to cluster analysis, each variable is standardized to have a mean of 0 and a variance of 1.

4. Results of cluster analysis

The results of the cluster analysis are presented in Table 2, with a total of 8 identified clusters and their corresponding names.

1) Clusters 0, 1, and 3 exhibit high correlation coefficients, large R2 values, and small differences, suggesting some degree of leakage. Among these clusters, Cluster 3 is presumed to have the highest leakage, while Cluster 1 has the lowest.

2) Cluster 2 displays small correlation, R2, and difference values, but a large intercept, indicating a cable with no leakage.

3) Cluster 4 exhibits an abnormal difference value. Upon examining the analysis data, it appears to be an error in the transmitter. To exclude such erroneous values, utilizing K-means for cluster analysis would be more suitable.

4) Cluster 5 demonstrates a moderate correlation coefficient and a large difference, but a small R2. This suggests that the R2 value decreased due to rapid gas pressure recovery after repair, despite the occurrence of failures in winter.

5) Cluster 6 has a significantly negative correlation coefficient, along with moderate R2 and difference values.

6) Cluster 7 displays high correlation coefficients, R2, and difference values, accompanied by a small intercept. This suggests that even when gas pressure drops during winter, it rises as the temperature increases in summer (spontaneously recovering faults).

As a result, we successfully identified cables that can be considered "spontaneously recovering faults" by applying statistical processing. In the following section, we will calculate a linear discriminant to distinguish these cables from others.

5. Results of discriminant analysis

Table 3 presents the linear discriminant calculated through discriminant analysis. The correlation ratio, which indicates the reliability of the analysis model, exceeds 0.5, and the discriminant accuracy rate in the analysis data surpasses 90%. Based on these findings, it can be inferred that, at least in the Hokkaido area, there is a high likelihood of accurately identifying "spontaneously recovering faults". To further validate the accuracy of this model, it will be necessary to examine gas pressure data for cables where engineers cannot conclusively determine whether a failure is self-

Table 2. The mean value of the variable in each cluster

Cluster ID / variable	0	1	2	3	4	5	6	7
correlation coefficient	**0.091**	0.022	**0.009**	**0.083**	**-0.086**	0.067	**-0.160**	**0.214**
intercept	61.106	**62.884**	**63.019**	**58.072**	**64.484**	61.514	**60.909**	**58.880**
R^2	**0.735**	**0.679**	**0.162**	0.576	**0.003**	**0.162**	0.480	**0.669**
difference	**3.393**	**1.054**	**1.912**	3.638	**111.200**	**9.587**	7.542	**8.155**
N	397	517	512	110	1	142	24	199

※1：The top 3 clusters with the highest values for each variable are colored blue, and the bottom 3 clusters with the lowest values are colored red.

※2："Correlation coefficient", "intercept" and "R^2(coefficient of determination)" are all approximate values of temperature and gas pressure

Table 3. Linear discriminant and precision

linear discriminant	η^2	Discriminant accuracy
$z = -1.33a + 0.20b + 0.15R - 0.14d + 1.41$	0.51	93%

z ：discriminant score (If less than 0, spontaneously recovering faults, if 0 or more, otherwise)
a ：correlation coefficient
b ：intercept
R ：R^2
d ：the difference between the maximum and minimum gas pressure values for one year
η^2 ：correlation ratio

recoverable.

It is important to note that this analysis focused on a specific area, limiting the applicability of the linear discriminant to Sapporo, Hokkaido. The selection of Sapporo City, characterized by significant temperature variations, served as a case study. To develop a linear discriminant suitable for various regions, meticulous preparation of temperature data for each area is necessary by aligning weather data observation points with NTT buildings' addresses.

6. Conclusions

In this study, we employed statistical analysis to develop a linear discriminant model for classifying pressurized cable and determining their status as " spontaneously recovering faults". Our results demonstrate that we were able to achieve a categorization level that aligns reasonably well with field observations and recognition. Moreover, we successfully created a linear discriminant model with statistically significant accuracy.

Moving forward, it is essential to leverage the utility of the developed linear discriminant model for maintenance purposes and assess its accuracy and impact on reducing operational activities using data beyond the scope of this study. It is worth noting that the application of cluster analysis for categorizing failure-related data and the utilization of discriminant analysis for constructing a linear discriminant model to identify specific phenomena can find application not only in reducing operational activities related to pressurized cable but also in various other domains, including equipment operation. For that reason, it is necessary to continue to acquire a wide range of data on the equipment you own.

7. References

[1] T. Okamoto, M. Okada, K. Mine, and K. Uehara, Proc. of the 65th IWCS Conference, p. 325-328, Oct. 2016.

[2] T. Okamoto M. Okada, K. Mine, and K. Uehara., IWCS China 2017, 4-6, 2017.

[3] C. Kito, H. Kuwabara, H. Shimabara, and T. Ebine, IWCS China 2019, 6-5, 2019.

8. Pictures of Authors



Kaoru Kawasaki is an Engineer at NIPPON TELEGRAPH AND TELEPHONE EAST CORPORATION. He joined NTT in 2019 and moved to his current position in 2021. Since then, he conducts research on telephone pole and pressurized cable maintenance.



Keiji Fujihashi is an Engineer at NIPPON TELEGRAPH AND TELEPHONE EAST CORPORATION. He joined NTT in 2011 and moved to his current position in 2021. Since then, he conducts research on copper cable and pressurized cable maintenance.



Takeshi Sawa is a Manager at NIPPON TELEGRAPH AND TELEPHONE EAST CORPORATION. He joined NTT in 2006 and moved to his current position in 2022. Since then, he has been actively engaged in developmental research on underground and aerial closure technology.



Osamu Sasaki is a Senior Manager at NIPPON TELEGRAPH AND TELEPHONE EAST CORPORATION. He joined NTT in 2000 and moved to his current position in 2022. Since then, he has been actively engaged in developmental research on access network systems.

Impact of Thermal Aging on Safety Performance of Power-over-Ethernet Cables

Bo Xu, Christopher McNutt, Amir Sekhavat

Superior Essex International LP – Communications

Atlanta, Georgia

+1-770-657-6620 · Bo.Xu@spsx.com

Abstract

Power over Ethernet (PoE) is a technology that enables the transmission of data and electrical power over copper twisted-pair cables to remote devices, eliminating the need for separate power supplies and outlets. This innovation improves flexibility, reduces costs and simplifies installation. However, concerns have been arisen about the temperature rise of PoE cables, which can lead to system failures, safety hazards, reduced cable performance and a shortened lifespan. Our previous work focused on the thermal degradation of the polyolefin insulation and polyvinyl chloride (PVC) jackets of 4-pair PoE (4PPoE) cables. We found that PVC jackets can experience significant weight loss and deterioration in electrical performance due to thermal aging.

In this study, we investigated how thermal degradation of polymeric jackets impacts the safety performance of PoE cables. We selected four 4PPoE cables, three with PVC jackets and one with a polyvinylidene fluoride (PVDF) jacket, based on their temperature ratings and estimated lifespan. Our analysis examined the physical and chemical properties of both unaged and aged jackets to understand heat-induced changes and their effects on UL NFPA 262 burn performance. Heat aging of PVC jackets produced weight loss, shrinkage, and an increase in carbonyl groups and double bonds. Although all aged cables still meet the specifications of UL-defined plenum burn, the heat aging changes their smoke and flame behavior. The burn temperature decreased due to weight loss of PVC jackets. Extensive weight loss facilities combustion, reducing smoke and flame propagation. Conversely, limited weight loss and formed moieties in PVC jackets led to more incomplete combustion, increasing smoke release. The PVDF jacket exhibited excellent thermal stability; however, heat aging or annealing caused phase transformations, leading to an increased presence of α phase and reduced β phase. This change is believed to worsen combustion in the presence of alumina shield tape, resulting in higher smoke release in the PVDF jacketed cable after aging.

In conclusion, our study highlights how thermal degradation of polymeric jackets can impact cable safety performance. The divergent behaviors observed in PVC and PVDF jackets emphasize the importance of selecting appropriate materials for specific PoE cable applications to ensure optimal safety standards.

Keywords: PoE; Thermal Aging; Safety; PVC; PVDF; Thermal Stability; TGA; Weight Loss; NFPA 262; Smoke; Flame Propagation.

1. Introduction

Power over Ethernet (PoE) is a technology standardized by the IEEE 802.3af, 802.3at, and 802.3bt (Types 3 and 4) standards that delivers electric power along with data over copper twisted-pair cables [1-3]. It is commonly used to power devices such as IP cameras, wireless access points, detectors, displays, and VoIP phones, among others [4]. PoE eliminates the need for separate power supplies and outlets, enhancing flexibility and innovation while reducing costs and installation time. While PoE offers significant convenience and cost savings, it is crucial to address various safety considerations. These concerns encompass electrical hazards, device compatibility, heat dissipation, cable quality among others. As the number of PoE devices continues to grow, the power levels for PoE category cables have been steadily increasing and are projected to rise further. Consequently, the issue of cable heating becomes increasingly more important, especially in enclosed spaces with large cable bundles. The potential for overheating poses significant risks, including system failures, safety hazards, reduced cable performance and shortened lifespan [4-7]. Addressing these safety concerns is paramount to ensuring reliable and secure PoE deployments.

In our previous work on 4-pair PoE (4PPoE) cables, we observed that cable heating can result in low power efficiency and high operating cost [8, 9]. Excessive temperatures can cause the polyolefin insulation of PoE cables to degrade [8], while PVC jackets may experience significant weight loss [9]. These issues can result in the decay or failure of electrical performance, leading to reduced lower power efficiency [8], increased Near-End crosstalk (NEXT) [9] and higher insertion loss [4, 10]. Additionally, thermal aging may lead to changes in the fire resistance of the insulating and jacketing materials due to chemical alterations. Therefore, it is essential to investigate how thermal degradation of polymeric jackets could impact the safety performance of PoE cables.

As part of our ongoing research, the current study aims to investigate the influence of thermal degradation of polymeric jackets on the burn behavior of specific PoE cables. We conducted aging experiments on four 4PPoE cables, three with PVC jackets and one with a PVDF jacket. The aging process followed jacket temperature ratings and estimated lifespan. Through a comprehensive analysis of the physical and chemical properties of both unaged and aged jackets, we aimed to identify heat-induced changes and their effects on UL NFPA 262 burn performance. These investigations are of utmost importance as they provide valuable insights into the safety and performance aspects of PoE cables, informing the development of more reliable and robust systems. By understanding the impact of thermal degradation on polymeric jackets, engineers and manufacturers

can make informed decisions to enhance the overall safety and efficiency of PoE technology.

2. Experiment Details

2.1 Cables

Three PoE category cables with four twisted pairs and 22 AWG fluorinated ethylene propylene (FEP) insulated copper wire were selected from the market. In our previous work [9], we labeled their PVC jackets as PVC1, PVC3 and PVC4, as listed at Table 1. Among these cables, C2 is a Cat5e cable rated at 105°C, while C1 (Cat6) and C3(Cat5e) are 90°C rated. C4, a Cat6a cable, features a PVDF jacket and four unshielded twisted FEP insulated copper pairs wrapped in an overall alumina foil shield (F/UTP). Our work indicates that C4 can be rated as high as 150 °C based on aged tensile results [11]. Table 1 summarizes the characteristics of these four cables. Table 1 lists the characteristics of these four cables.

Table 1. Summary of PoE Cable Samples

Cable	Jacket	Jacket Thickness	Jacket Rating	Cable OD	Copper Wire	UL Burn Rating	Insulation	Shielding
		mm	°C	mm	AWG			
C1	PVC1	0.36	90	5.59	22	CMP	FEP	UTP
C2	PVC3	0.43	105	6.10	22	CMP	FEP	F/UTP
C3	PVC4	0.41	90	5.80	22	CMP	FEP	F/UTP
C4	PVDF	0.48	150	7.83	22	CMP	FEP	UTP

2.2 Jacket and Cable Aging

The jackets of all four cables listed in Table 1 were first stripped in 1-foot increments. These jacket specimens were then placed on a piece of rockwool insulation within an environmental chamber.

30 ft lengths of the cables were bundled together and positioned onto a modified steel reel in the same chamber for cable aging, as illustrated in Figure 1(a). For PVC cable bundles, the aging temperature was set at 121 ˚C, with C1 and C3 aged for 10 days, and C2 for 21 days. C4 was subjected to aging at 136 ˚C for 12 days. The jacket specimens experienced the same thermal history as the cable bundles inside the same chamber, and their weights and lengths were monitored after each aging period.

2.3 NFPA 262 UL Steiner Tunnel Burn Tests

As shown in Figure 1b and 1c, unaged and aged cable specimens of 25 feet installed in a single layer across the bottom of the cable tray, which has a width of 11.25 inches, in the south Steiner Tunnel Furnace at UL (Chicago). After the burn test, Figure 1d displays the charred remains of PoE cables on the cable tray. To meet the UL requirements for plenum-rated cables, three critical parameters over a 20-minute burn are typically required: flame propagation of ≤ 5 feet, optical density peak of smoke (≤ 0.5) and optical density average of smoke (≤ 0.15). In addition to these three parameters, we also monitored the temperature of the thermocouple in the chamber air at 23 feet from the burner (labeled as TC #1) and the total smoke release over time. The former indicates the total energy release, while the latter reflects the total smoke release during the burn. Further test details may be found in NFPA 262 2023 Edition "Standard Method of Test for Flame Travel and Smoke of Wires and Cables for Use in Air-Handling Spaces".

2.4 Material Testing

Thermogravimetric Analysis (TGA). TGA was performed on a TA Instruments Discovery TGA under an air atmosphere with a purge rate of 25 ml/min. TGA samples weighing 7- 9 mg were cut from the jackets and placed in 100 µL platinum-HT sample pans. The temperature ramp procedure followed these steps: the samples were equilibrated at 30 °C, and then heat was applied in the temperature range 30 – 720°C at a heating rate of 20°C/min.

Fourier Transform Infrared Spectroscopy (FTIR). FTIR Attenuated Total Reflectance (ATR) spectra were collected using a Perkin Elmer Spectrum Two spectrometer from 4000 cm-1 to 400 cm-1, with a resolution of 4 cm-1. Both the external and internal jacket surfaces were scanned. For a comparison, the spectra of PVDF jackets were normalized by using the peak at 2853 cm-1 from CH2 symmetrical stretching (ν_s CH2).

Differential Scanning Calorimeter (DSC). Thermograms of PVDF jackets were obtained using Thermal Analysis DSC Q100. About 2-3 mg of samples were sealed within aluminum pans and subjected to a heating rate of 10 °C/min across a temperature range from -50 to 200 °C under a nitrogen flow of 50 ml/min.



Figure 1. Cable bundles uploaded onto a modified steel reel placed in an environmental chamber for cable aging (a); unaged (b) and aged (c) cables installed in a single layer across the bottom of the cable tray and burnt cables (d) in the south Steiner Tunnel Furnace at UL (Chicago) for NFPA 262 burn tests.

3. Results and Discussion

3.1 Jacket and Cable Aging

PoE cables with polymeric jackets encounter thermal aging challenges, particularly when carrying a high level of power, which can lead to temperature rise. Our studies on PoE cables and jackets have revealed that thermal aging causes significant weight loss in PVC jackets, resulting in dimensional shrinkage and increased hardening [9]. The resulting tightness on the conductor pairs inside the cable exacerbates crosstalk and may eventually lead to electrical performance failure. In our previous work [9, 11], the estimated lifetime of PVC jackets in C1, C2, and C3 to meet aged-tensile properties for a temperature rating was less than 10 days at 121 ˚C, while the PVDF jacket in C4 was projected to last over 100 years at 150 ˚C. In addition, C2 is rated at 105 ˚C, thus, the jacket specimens were aged within the heat limitation of the chamber used in the cable aging process. Figure 2 illustrates the weight loss and shrinkage of jackets from these cables over time. The PVDF jacket demonstrates very limited weight loss and

shrinkage, while the PVC jackets exhibit divergent changes. PVC1 experienced weight loss more rapidly and had 3.4% loss by the end of aging, whereas PVC3 and PVC4 show similar patterns in weight loss. PVC3 experienced 8.5% shrinkage, while PVC1 and PVC4 display similar patterns in shrinkage.

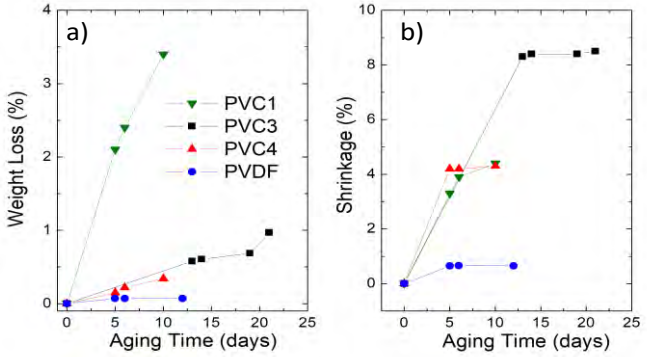


Figure 2. Effects of isothermal aging on jacket specimens from all Cables, C1- C4: (a) weight loss; (b) shrinkage.

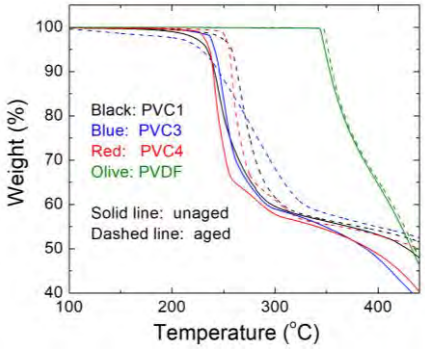


Figure 3. TGA curves of unaged and aged jackets from all cables, C1-C4. The aged jackets were taken from aged cables.

Upon aging, the jacket specimens from the cables experienced weight loss and shrinkage, potentially leading to a decrease in mechanical properties of the jackets and electrical performance of their cables [9, 11]. Below are two technologies applied to investigate the changes that occurred to the jackets after aging. TGA curves, as shown in Figure 3, reveal that aging, to some extent, delays weight loss, while unaged and aged PVDF jackets show almost identical traces. The aged PVC 1 and PVC4 display better stability compared to the unaged counterparts before reaching 250 ˚C. Prior to 245 ˚C, aged PVC3 displays more weight loss compared to unaged PVC3. This result indicates that aging generates more volatile chemicals in PVC3 on the low temperature side. Overall, heat aging shifts the majority of decomposition events of PVC jackets to higher temperatures. Notably, the PVDF jacket exhibits an onsite decomposition temperature around 350 ˚C, while PVC jackets have an onsite decomposition temperature of ~ 250 ˚C. This difference indicates that the PVDF jacket has significantly better thermal stability.

The thermal degradation of PVC compounds involves the loss of HCl, the formation of conjugated double bonds, and the evaporation and degradation of plasticizers and additives [12]. In the FTIR spectra, the peaks in the range of 1400-1800 cm^{-1} originate from stretching vibrations in carbonyl groups (C=O) and double bonds (C=C). Figure 4 (a,b,c) shows FTIR spectra in this range for the PVC jackets. Remarkably, the aged external surface exhibited significant degradation, evident from the presence of extra peaks, while the aged internal surface appears to remain largely intact.

When subjected to thermal aging below 160 ˚C, PVDF often exhibits distinct polymorphs instead of undergoing thermal degradation, with the most common phases being α (TGTG', form II), β (TTT, form I), and γ (TTTGTTTG', form III) [13]. Figure 2a shows that aging resulted in no weight loss for PVDF jackets, while Figure 3a indicates no significant variation in thermal stability. However, thermal annealing leads to phase transformation, as indicated in Figure 4d. In the range of 1250-1440 cm^{-1}, the specific peaks are exclusive to each phase: around 1423 and 1383 cm^{-1} for the α phase, around 1277 cm^{-1} for the β phase, and around 1431 cm^{-1} for the γ phase. Many other exclusive peaks for each of these phases are not presented here [13]. Aging strengthens the α peaks and weakens β and γ peaks, suggesting some interchanges among crystal phases, *e.g.*, β, γ , amorphous phase → α in this grade of PVDF. Both surfaces of the jackets contain these phases, but the external surface exhibits a higher proportion of β and γ phases, while the internal surface displays a greater amount of α phase. DSC curves of PVDF jackets (not depicted here) indicate a melting range of 140 to 170 ˚C. The onset melting points shift to lower temperatures after aging at 136 ˚C for 7 days, remaining consistent over extended annealing periods. An endothermic peak at 144 °C, attributed to the relaxation of conformers, is also observed.

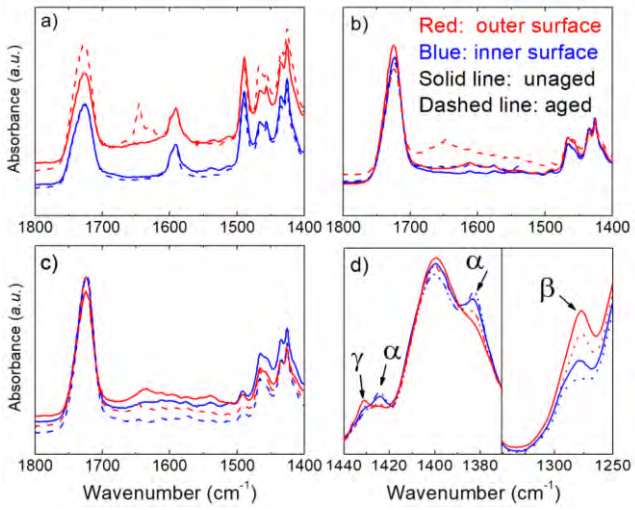


Figure 4. FTIR spectra of both sides of jackets from unaged and aged cables: (a) PVC1, (b) PVC3, (c) PVC4, and (d) PVDF. The external surface is the outer surface of the jacket, and the internal surface is the one adjacent to the cable core.

3.2 NFPA 262 UL Steiner Tunnel Burn

The NFPA 262 UL Steiner Tunnel Burn tests were conducted on both unaged and aged cables, and the burn test results are

summarized in Table 2. To meet the UL plenum rating, both the peak and average of optical density (OD) must be ≤ 0.5 and ≤ 0.15, respectively. Overall, all tested cables fulfill these criteria. However, aging has a notable impact on the burn behavior of the cables. C1 performed better after aging, with lower peaks and a smaller average, while the others displayed slightly worse burn test results, showing higher peaks and larger averages.

Table 2. Summary of NAPA 262 Burn Results

Cable	Unaged or Aged	Cable OD	Number of Lengths	Max. flame Propagation	Peak OD	Average OD	Max. TC #1	Aged – Unaged in Max. TC #1
		mm		ft			˚F	˚F
C1	Unaged	5.59	50	3.5	0.38	0.14	529	-26
	Aged	5.50	50	1.0	0.28	0.12	503	
C2	Unaged	6.10	47	1.0	0.24	0.07	522	-23
	Aged	6.07	47	1.0	0.23	0.09	499	
C3	Unaged	5.80	49	1.5	0.16	0.07	513	-10
	Aged	5.74	49	2.0	0.22	0.09	503	
C4	Unaged	7.83	36	1.5	0.19	0.05	525	7
	Aged	7.83	36	1.5	0.30	0.12	533	

Figure 5 exhibits the OD traces during the 20-minute burns for all unaged and aged cables. Upon heat aging, the OD peaks of C1 significantly weakened, with the second peak completely disappearing. Conversely, C2 and C3 show increased smoke density. Aged C2 exhibits stronger smoke earlier and two smoke peaks compared to the unaged version. Aged C4 displays an earlier and stronger spike of smoke and another broader OD peak around 15 minutes than the unaged counterpart. Notably, C4 with a PVDF jacket demonstrates delayed smoke generation but does not exhibit a reduction in OD peak and average during the late burn, unlike cable with PVC jackets.

In Figure 6, the observed flame propagation distance during the burn is depicted. Significant changes in this flame parameter were observed in C1 and C4. The flame distance in C1 is significantly diminished upon aging, and the flame is propagated earlier for the aged C4. Aging generates slight differences in C2 and C3.

Figure 7 depicts the total smoke traces for unaged and aged cables during the burn. Upon heat aging, C1 releases less smoke, while other cables release more smoke. However, the unaged C1 exhibits the highest smoke generation among all cables. C2 and C3 show comparable smoke levels. The unaged PVDF jacket generates the least smoke, but after aging, it experiences a rapid increase in smoke generation after the first 10 minutes of the burn, while the total smoke of the unaged C4 levels off.

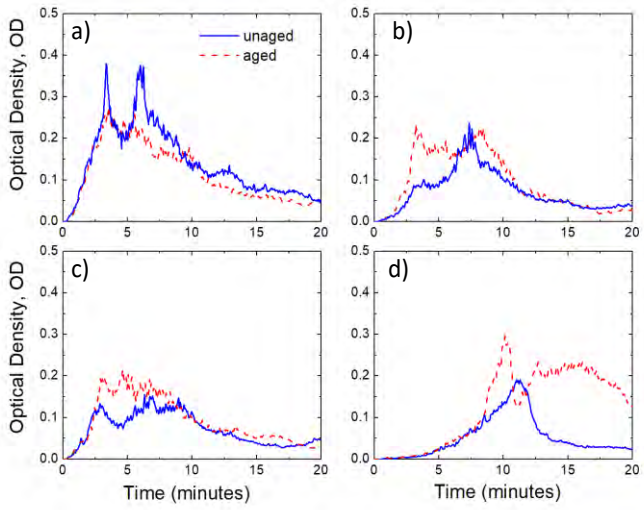


Figure 5. Optical density over burn time for unaged and aged cables: (a) C1, (b) C2, (c) C3, and (d) C4.

Figure 8 presents the temperature of the thermocouple (TC #1) in the chamber air at 23 ft from the burner, reflecting the energy generated by burning the cables on the cable tray. For PVC jackets, aging leads to a reduction in the burn temperature, with the magnitude of reduction observed in the order: C1 > C2 > C3, as listed in Table 2. On the other hand, the temperature trace of aged C4 almost completely overlays with that of the unaged one, except for the last 5 minutes when the temperature of the former become higher than the latter, ending with a 7 ˚F difference.

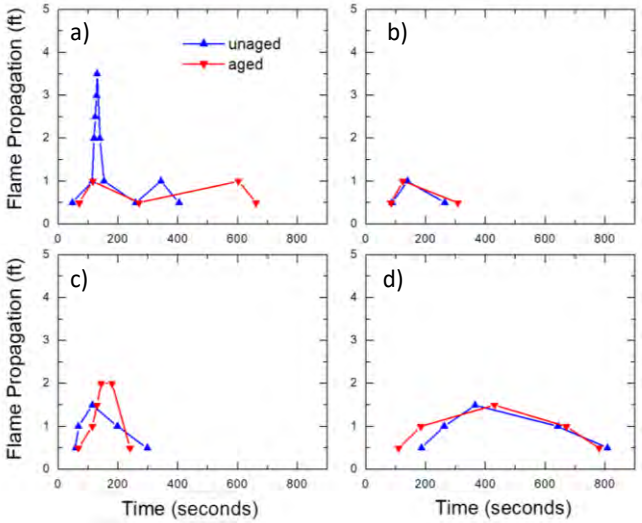


Figure 6. Flame propagation distance as a function of burn time for unaged and aged cables: (a) C1, (b) C2, (c) C3, and (d) C4.

3.3 Discussion

Heat aging affects PoE cables, leading to weight loss and shrinkage of their jackets. The rate of weight loss varies based on the type of jacket compounds and is significantly influenced by the activation energy of the weight loss. For PVC jackets, the activation energy (E_a) of isothermal aging is 103.4, 108.1, 115.3 kJ/mol for PVC1, PVC3, PVC4, respectively [9]. In contrast, the PVDF jacket displays a much higher E_a (185 – 195 kJ/mol) [11]. Thus, the weight loss of the aged jackets follows the order: PVC 1 > PVC3 > PVC4 > PVDF, as shown in Figure 2a. However, the order of shrinkage of aged jackets differs from this sequence. PVC3 experiences over 8% shrinkage, while PVC1 and PVC4 only have around 4% shrinkage. This discrepancy can be attributed to the diverse formulation of these PVC compounds,

implied by different activation energy values of their degradation. The aged PVDF jacket, on the other hand, shows only 0.65% shrinkage with almost zero weight loss due to the α phase generation and phase transformations.

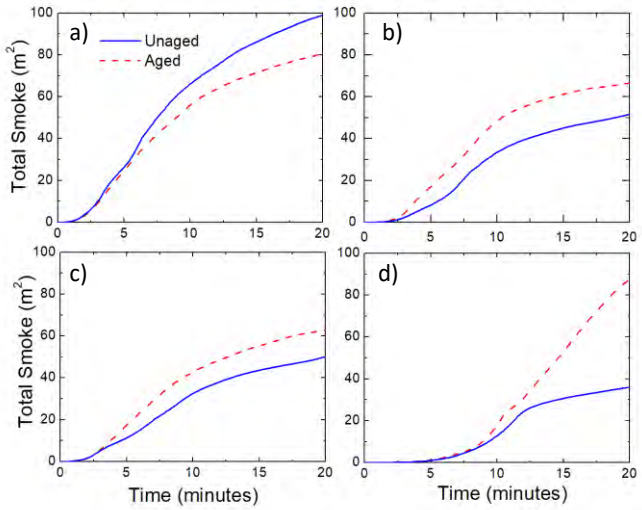


Figure 7. Total smoke over burn time for unaged and aged cables: (a) C1, (b) C2, (c) C3, and (d) C4.

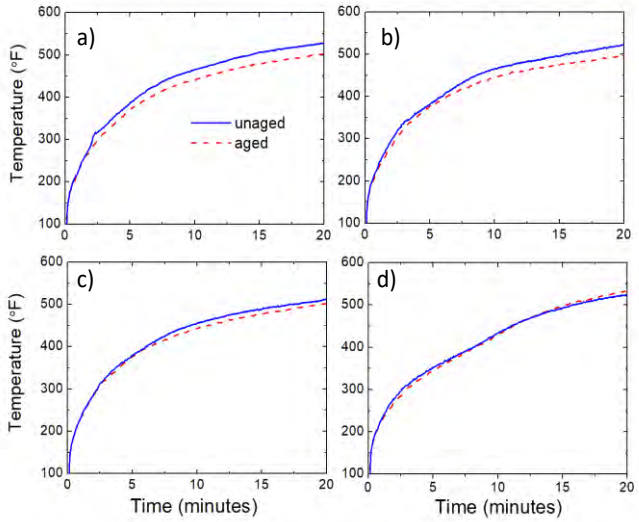


Figure 8. Temperature of the thermocouple in the chamber air at 23 feet from the burner (labeled as TC #1) as a function of burn time for unaged and aged cables: (a) C1, (b) C2, (c) C3, and (d) C4.

Heat aging generates distinct chemical changes on the external surfaces of PVC jackets, while their aged internal surfaces remain intact. The aged external surfaces display an increase in carbonyl groups and/or double bonds, which are believed to originate from diffused-out plasticizers, loss of HCl and oxidation. The aged external surfaces of C1 and C2 show more noticeable changes compared to C3, which aligns with their weight loss levels. When exposed to heat annealing at 136 ˚C for 12 days, the PVDF jacket undergoes the α phase generation and phase interchanges (β, γ, or amorphous phase → α), because the α phase shows a maximum crystallization rate at around 130 ˚C [14].

Although aged PVC jackets show better overall thermal stability compared to unaged ones, these aged cables exhibit diverse burning behavior concerning temperature, smoke density, total smoke production and flame propagation. A larger reduction in burn temperature is observed with increased weight loss, which can be attributed to less materials involved in the burn. Moreover, significant weight loss (*e.g.*, > 3%) facilitates smoke and flame propagation reduction due to improved combustion, as demonstrated by the aged C1. However, extensive weight loss negatively impacts the mechanical properties of the aged jackets and the electrical performance of the aged C1 [9]. Conversely, when the weight loss is relatively smaller (*e.g.*, < 1%), more smoke is generated, likely due to incomplete combustion, resulting from the presence of more carbonyl groups and unsaturated hydrocarbons in the aged jackets. This observation aligns with a widely recognized fact that saturated hydrocarbons produce clean flame, while unsaturated carbon compounds produce yellow flame with black smoke.

Interestingly, despite the heat aging process resulting in zero weight loss and no evident chemical changes in the PVDF jackets, the aged PVDF jacket produced more smoke than the unaged counterpart. The burn temperature remained nearly identical, except for a slightly higher temperature observed during the last 5 minutes of burning. The jacket also displayed limited shrinkage, indicating that the dimension of the cable remains the same. Additionally, no significant changes were detected in other components of C4 upon aging, including polyester-coated alumina tape, FEP insulation and FEP cross filler. The aged PVDF jacket in C4 only experienced an increase in the α phase and a reduction of the amorphous phase, and β and γ phases due to phase transformation. On one hand, these phase shifts may cause easier melting and dripping of PVDF jackets, intensifying the burning process. On the other hand, the study by Zheng, *et al.* [15] reported that the combustion performance of PVDF and alumina nanoparticle composites is influenced by the mass fraction of the β phase. Increased β phase content corresponds to enhanced combustion performance, while little correlation was observed for other two phases. This improvement is attributed to the structural alignment of F atoms along one side of the β-PVDF polymer chain, promoting interaction with Al particles and forming strong Al-F bonds. These robust interactions result in a higher binding energy between PVDF and A, potentially leading to diminished combustion of the PVDF jacket contacting the alumina tape. These two hypotheses align well with the observations of more smoke generated after aging.

Nevertheless, to gain a more comprehensive understanding, further investigation should be conducted to determine if the NFPA 262 burn results of the C4 cable without alumina shield tape show any change in smoke density and total smoke upon aging.

4. Conclusions

In this study, we have demonstrated that heat aging induces significant variations in the combustion and flame behavior of PoE cables during the UL Steiner Tunnel burn. The thermal degradation of the PVC jackets results in weight loss, shrinkage, and an increase in carbonyl groups and double bonds.

The weigh loss of PVC jackets leads to a reduction in the burn temperature. Extensive weight loss facilitates combustion,

reducing smoke, and limiting flame propagation, although it adversely affects the surrounding environment and the physical and electrical performance of the aged cables. Conversely, limited weight loss or degradation leads to the formation of moieties in PVC jackets, with a minor loss of plasticizers and other additives. This is likely responsible to incomplete combustion, increased smoke release, while still maintaining comparable flame propagation during cable burns. On the other hand, the PVDF jacket exhibits better thermal and dimensional stability upon aging; however, it undergoes phase transformations marked by increased α phase and reduced amorphous, β and γ phases. These transformations are likely responsible for potential melting and dripping or less efficient combustion of the PVDF jacket, resulting in a higher smoke release observed in the aged cable.
It is noteworthy that all burn tests meet the criteria for the UL-defined plenum rating. However, these findings underscore the importance of jacket compounds, cable constructions and their combinations in addressing safety challenges caused by cable heating.

5. Acknowledgments

The authors sincerely thank Martina Upton, Rodney Kron, and McIntire Frank for their valuable assistance with the chamber aging setup, oven aging testing and Steiner tunnel burn. Furthermore, we are grateful to Martin Shumate, Robert Bellassai, and Nathan Percival from UL for generously granting us access to the UL facilities and raw data. Without their support, this research would not have been possible.

6. References

[1] G. Mendelson, "All You Need to Know About Power over Ethernet (PoE) and the IEEE 802.3af Standard," White Paper, PowerDsine, 2004.

[2] M. Eisen, "Introduction to PoE and the IEEE 802.3af and 802.3at Standards," 29 10 2009. [Online]. Available: https://www.ieee.li/pdf/viewgraphs/introduction_to_poe_802.3af_802.3at.pdf. [Accessed 8 8 2022].

[3] CISCO, "What Is Power over Ethernet (PoE)?" [Online]. Available: https://www.cisco.com/c/en/us/solutions/enterprise-networks/what-is-power-over-ethernet.html. [Accessed 8 8 2022].

[4] R. Ivans, "Power over LAN Cable - Keeping pace with this Key Powering Strategy," in Proceedings of the 65th International Wire & Cable Symposium, Providence, 2016.

[5] R. Speer, S. Lee, R. Ozisik and C. Glew, "The Future of Materials Selection Criteria for Power over Local Area Networks," in Porceedings of the 65th International Wire & Cable Symposium, Providence, 2016.

[6] B. Marchant, "Impact of Installation Geometry on Temperature Rise due to Power over Ethernet," in Proceedings of the 65th International Wire & Cable Symposium, Providence, 2016.

[7] W. Hopkinson, "Evolving Methods of Evaluating Cable Heating," in Proceedings of the 65th International Wire & Cable Symposium, Providence, 2016.

[8] T. Lanoe, C. McNutt and A. Sekhavat, "Four Pair Power over Ethernet (4PPoE) Depolyment: Standards, Performance, and Challenges," in Proceedings of the 66th International Wire & Cable Symposium, Orlando, 2017.

[9] B. Xu, C. McNutt, B. Gebs and A. Sekhavat, "Investigation of Thermal Aging Challenges for Power-over-Ethernet Cables with Polyvinyl Chloride Jackets," in Proceedings of the 71st International Wire & Cable Symposium, Providence, 2022.

[10] C. M. Glew and C. A. Glew, "The Effects of Electrical Properties in Power over Ethernet Cables as a Result of Thermocycling Materials," in Proceedings of the 68th International Wire & Cable Symposium, Charlotte, 2019.

[11] B. Xu, C. McNutt, A. Sekhavat and J. Henry, "Foamed PVDF Jacket for Power-over-Ethernet Cables to Overcome Thermal Aging Challenges," in Proceedings of the 72nd International Wire & Cable Symposium, Orlando, 2023.

[12] V. V. Krongauz and Y. P. Lee, "Kinetics of Thermal Degradation of Poly(Vinyl Chloride): Thermogravimetry and Spectroscopy," Journal of Thermal Analysis and Calorimetry, vol. 106, no. 1, pp. 139-149, 2011.

[13] X. Cai, T. Lei, D. Sun and L. Lin, "A critical analysis of the alpha, belta and gamma phases in poly(vinylidene fluoride) using FTIR," RSC Adv., vol. 7, pp. 15382-15389, 2017.

[14] N. Vasic, J. Steinmetz, M. Gorke, M. Sinapius and C. Huhne, "Phase Transitions of Polarised PVDF Films in a Standard Curing Process for Composites," Polymers, vol. 13, pp. 3900 - 3911, 2021.

[15] S. Huang, S. Hong, Y. Su, Y. Jiang, S. Fukushima, T. M. Gil, N. Yilmaz, S. Tiwari, K. Nomura, R. K. Kalia, A. Nakano, F. Shimojo, P. Vashishta, M. Chen, and X. Zheng, "Enhancing Combustion Performance of Nano-Al/PVDF Composites with belta-PVDF," Combustion and Flame, vol. 219, pp. 467-477, 2020.

7. Authors

Superior Essex International LP – Communications
Production Development Center
3600 Cobb International Blvd, Suite 400
Kennesaw, Georgia 30152



Bo Xu is a Materials Engineer at Superior Essex International Communications. He earned a Ph.D. in Polymer Engineering from Georgia Institute of Technology in 2010, and a M.S. in Material Science at Zhejiang University in 2004. Bo Xu has an extensive background in polymers, with over 30 scientific and conference papers published, and he holds 6 patents. Prior to joining Superior

Essex in 2017, he worked as a Packaging Analytical Scientist at the Coca-Cola Company.



Christopher McNutt is Director of Product Development for Superior Essex. He is listed as the inventor or co-inventor on numerous industry patents. He holds a B. S. degree in Chemical Engineering from the University of Tennessee.



Amir Sekhavat is Global Director of Product Management and Enterprise Market Development at Superior Essex. Amir has twenty years of experience in the telecommunications industry, specializing in communications cable products. Amir has published numerous articles and is listed as the inventor or co-inventor of several patents related to data cable performance and connectivity. Amir is currently chairman of CCCA datacenter subcommittee.

Channel Performance Degradation from Installation Stresses

Brian Marchant and Matt Schumacher
Leviton Network Solutions
New Holland, PA
+1-717-351-9305 · brian.marchant@leviton.com

Abstract

The Ethernet cabling installation process is as important as the components used. Incorrect techniques or damaging installation can inflict performance degradation on the resultant channels. Category-compliant components may yield incompliant channels from installation damages. Some degree of this can be mitigated with durable products designed for their installation and use.

This study was conducted using a variety of copper twisted pair cabling products and fixtures intended to recreate the stresses that can be found in installations. Enough samples were tested to create populations of performance results in order to observe the trends rather than relying on single sample impacts. By comparing the performance of products before and after stressing, specific damages can be identified and conclusions on materials and designs can be made.

Two main points of installation were focused on for this investigation. The first portion was the cable installation, which is typically exposed to dragging corners, tensions, and hard angles. The second portion of the investigation was the connectors and termination.

The results of the investigation allow for matching between installation verification testing and the types of issues being observed. The investigation also provides information on the range of tensions and other factors that can be used to produce high-performing channels. Options for improving the performance of the channels by cabling component choice are highlighted for the damaging installation scenarios.

Keywords: Cable, Connectors, Twisted Pair, Installation, Damage, Performance

1. Introduction

Cable installation damage and termination effects at connection points can result in changes to the transmission lines within the cabling. Such changes impact specific performance parameters. If stretching compresses the conductor insulation, the impedance and return loss could change. If the overall geometry of the cable is altered (such as squeezing effects), the crosstalk could be impacted. If there is poor mating between the cable conductors and the connectors, then the balance parameters might be affected.

Industry installation standards and manufacturer's recommendations give guidance for high performance installations with minimal damage to the cabling products. Even with an installer's best efforts, it is not difficult to exceed the manufacturer's maximum installation tension for cable products. Tension can greatly increase if, for example, there is a snag, if the cables have to go around too many edges or turns, if the fit in a conduit is improper, or if there were any irregularities in the cable's packaging. Figure 1 shows an example of a cable that was pulled at an elevated tension around an edge – the jacket shows scuff marks that match the lay of the pairs beneath the cable jacket.



Figure 1. Example Cable Damage Marks

If the cable is twisted while installed, there could be a kink or harsh bend that could severely misshape the transmission lines of the pairs. One common case where this could happen is if there was any slack or pause to a cable pull. The cable could form a loop which would become a damaging kink when the tension was reapplied. Figure 2 shows an example of a cable exposed to this kind of installation damage.

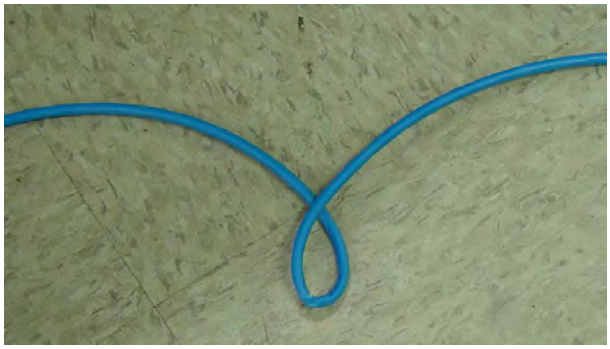


Figure 2. Tightened Loop Causing Cable Damage

Even if the tension isn't excessive, a jacket worked around rough corners could be scraped or broken. As the cables are designed to maintain their jacket for fire safety reasons, broken jacket damages during installation should be avoided.

Considering the sheer variety in installations and the variety in the cable physical traits when considering different manufacturers, it is possible to have a cabling run with stress-impacted segments that are not visible at all. The only indication of damage would be the performance test result or the impact on the channel's capacity to carry data signals.

Just as cable damage can degrade the transmission line, so can connector installation issues. Figure 3 shows examples of connector installations that could cause issues.

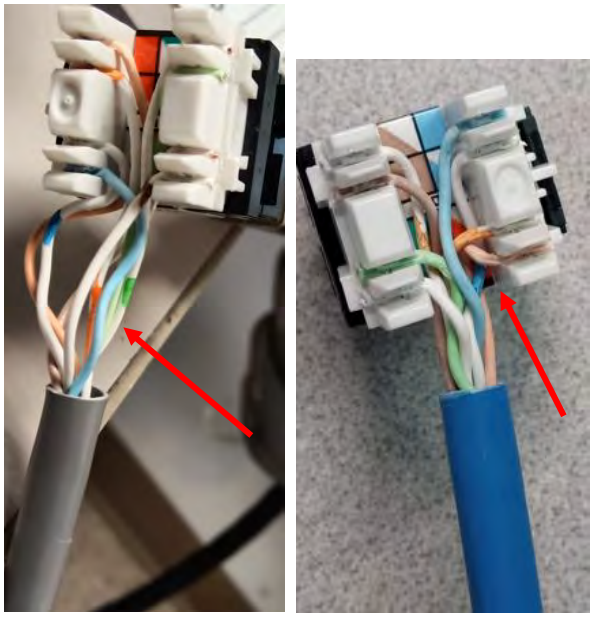


Figure 3. Example Connector Issues: Excessive Untwisted Pairs (Left), Conductor Routing (Right)

The connector and cable region creates an alteration of the transmission line. It is vulnerable because the regular structure of the cable is broken by the physical connection to the connector. The impedance of the pair is impacted by the loss of jacket in the connector region. Pairs untwisted and spread to reach contacts no longer keep the spacing between the conductors. The shape of the conductors and the spacing to nearby metallic surfaces can have capacitive effects. Each of these potential impacts can be handled or exacerbated depending on the components used and the installation process.

As reflections from connection points or from cable damage regions are common, Return Loss (RL, the measure of reflected signal compared to sent signal on a transmission pair) is a parameter that was studied in this investigation. Crosstalk, specifically Near-End Crosstalk (NEXT), is also important as damages can increase the capability of signals transferring between different transmitting pairs.

2. Test Methods and Samples

2.1 Cable Installation

The first test represents some of the most common installation effects. Drag and high tension in an installation are a primary concern. During installation, a cable could be crushed underfoot or rolled over by a cart, reel, or other wheel. Slack during the pull can allow for loops which become harsh kinks when the pull resumes.

These stresses were applied one-at-a-time to cabling samples with the performance measured after each stress. To provide a reference with which to measure the performance impact, a baseline measurement was taken after the cable was installed in as close to ideal conditions as possible. The baseline measurement was performed with a low-tension pull into a fixture that kept the cables suspended in air. Figure 4 shows the accumulator (pulleys and a frame for holding cable) used for the baseline measurement.

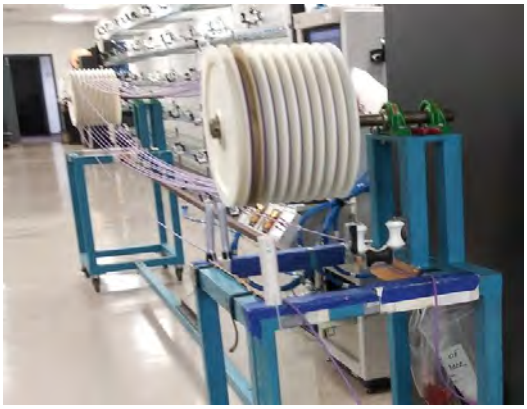


Figure 4. Baseline Measurement Setup

After the baseline measurement, the cable was pulled through a fixture designed to simulate pathway interference, like a corner. The first part of the fixture was a roller setup that increased the tension required. The second part of the fixture was a set of bridle rings set to cause the cable to drag across their edges. This combination within the fixture resulted in a rough pull that could occur in the field which could affect the cable. Figure 5 shows the concept of the hard pull simulating fixture.

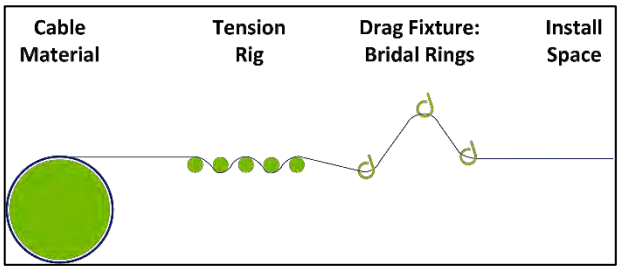


Figure 5. Hard Pull Fixture Concept Drawing

Once the cable was pulled through the first fixture, other damaging stresses were applied. A crushing damage was applied by rolling a weighted wheel over a length of the test sample. Figure 6 shows an image of the kind of damage that this could cause.



Figure 6. Example Crush Damage

After the performance measurement after the crush damage, a loop was formed in the cable and tightened to cause a harsh bend/kinked cable damage. This test looked similar to Figure 2.

A variety of cable types were tested using this method. Different categories, designs, and cable manufacturers were investigated to determine their impact.

One cable design feature that was studied was the presence or lack of any element to separate the pairs of the conductors within the cable. These separators are commonly called "fillers" as they fill a space inside the center of the cable. In the rest of this text, cables with pair separators are referred to as "fillered" and cables without pair separators are referred to as "fillerless."

Multiple samples of each cable type were tested using this method. The measurements were compared to the appropriate category standard – ANSI/TIA 568.2-D Cat 6 and ANSI/TIA 568.2-D Cat 6A. The test results could be reduced to minimum margin performances relative to industry standards and these could be compared as populations rather than single tests. This reduces the inherent variability from these sorts of tests.

2.2 Connector Installation

The connector installation test set is focused on connection points in an installation. A single set of Category 6 cables was used for this testing. The connections on these cables were replaced and adjusted to create conditions similar to what can occur during installations.

As with the cable installation test set, a baseline measurement was used on the samples under test. This baseline measurement for investigating connection issues was a set of link and channel tests performed on samples with "as neat as possible" termination. This should result in as much performance margin as possible for the system. Figure 7 shows the termination that was used as the baseline.



Figure 7. Baseline Connector Termination

Common termination issues arise because of issues with the conductors that are outside of the jacket at the termination area. The jacket of a cable protects the pairs of conductors and maintains a consistent transmission environment. If the conductors outside the jacket near connectors are too long or are straightened out excessively, they could become vulnerable to external noise signals or physical damage. The potential for degraded performance increases with the depth of irregularity in the transmission lines created by the twisted pairs of conductors. This is especially true if the exposed conductors are bent, curved, or damaged.

The first test after the baseline in the connection installation set was to expose the pairs of conductors of the cables for three inches. Figure 8 shows this test configuration. This exposed region would have a different impedance than the rest of the cable, which could affect the Return Loss parameter.

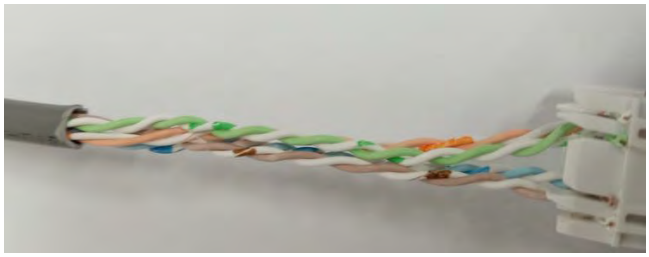


Figure 8. Long Exposed Conductors Termination

The second test after the baseline was to untwist the conductors outside of the jacket. Figure 9 shows the configuration used for this testing. Untwisted conductors do not hold the spacing, which causes a change in the capacitance and impedance. The untwisted pairs also can act as a region where interfering signals can couple into the communication. This test was targeted to see the impacts on Return Loss and Near-End Crosstalk.



Figure 9. Long Untwisted Conductors Termination

The third termination test after the baseline was to press the long untwisted conductors into the jack termination space. This causes loops and bends that are not part of the designed shapes of the conductors. Figure 10 shows this test configuration. Loops can cause inductive effects and irregular transmission line effects near other conductors which are also irregular can cause energy transfer between pairs that will show up as crosstalk at the jack location.

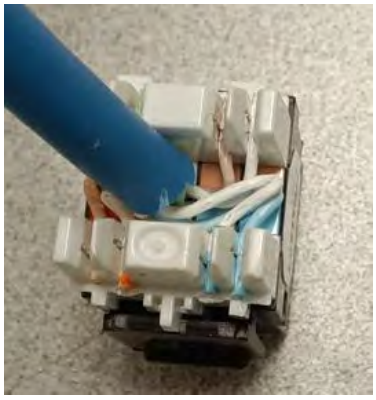


Figure 10. Irregular Loops and Bends Caused by Pushing Straightened Conductors into a Space

The fourth termination test after the baseline was to terminate using a variety of different jacks, specifically targeting different quality levels. The different jacks had different termination instructions. Some jacks required more conductor length to be exposed from the jacket to reach a termination. Other jacks, such as shown in Figure 11, almost forced a neater termination because of the locations of the jacket-gripping pieces and the cable management of the jack.



Figure 11. Jack With Management Components

The expectation was that each type of jack would offer a different performance level, but also that the resulting links and channels should meet the industry standard requirements.

3. Test Results

3.1 Cable Installation

One observation from the high tension pull test was that tensions applied to the cables were not uniform between different designs. Weight, rigidity, and jacket traits related to dragging friction were different between the designs. The tension rig setup and the drag path were kept the same between tests of the same category of cables rather than adjusting everything for each cable design. There were adjustments to the setup between Category 6 and Category 6A cables as these were different enough in design to result in severely different tensions and drag damage.

Figures 8 through 11 show example box plot distributions for the margin measurements of cables that have were tested for harsh installation performance. In these graphics, the dots indicate individual measurements while the boxes and bars indicate the statistical population (mean, quantiles, etc.) Figures 12 and 13 are the RL and NEXT for a set of Category 6 cables that did not include a filler in the center of the design to maintain pair spacing. Figures 14 and 15 are the RL and NEXT for a set of Category 6 cables that did have a filler in the center of the design to maintain pair spacing.



Figure 12. Example Return Loss of a Set of Category 6 Cables without a Filler

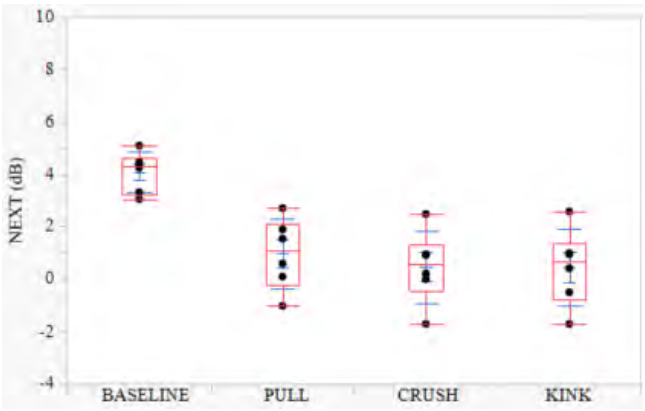


Figure 13. Example Near-End Crosstalk of a Set of Category 6 Cables without a Filler



Figure 14. Example Return Loss of a Set of Category 6 Cables with a Filler

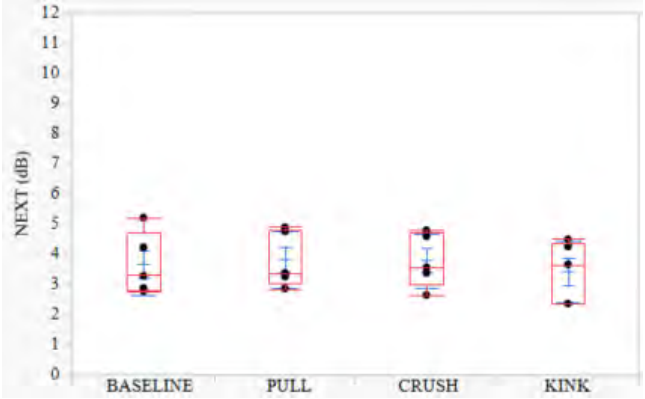


Figure 15. Example Near-End Crosstalk of a Set of Category 6 Cables with a Filler

Figures 16 through 19 show examples of baseline RL and NEXT measurements and the same samples after they have been pulled through the installation setup.

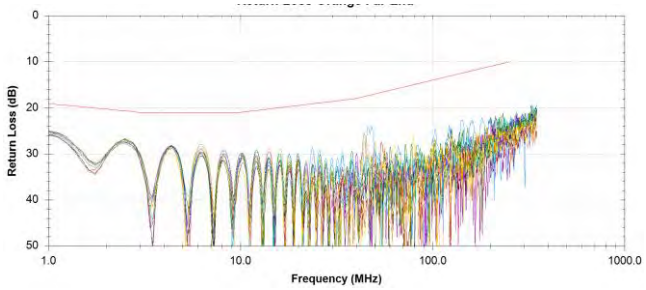


Figure 16. Example Cat 6 Fillerless RL Baseline

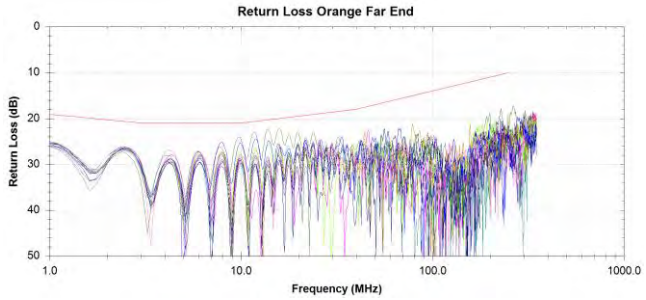


Figure 17. Example Cat 6 Fillerless RL After Pulling

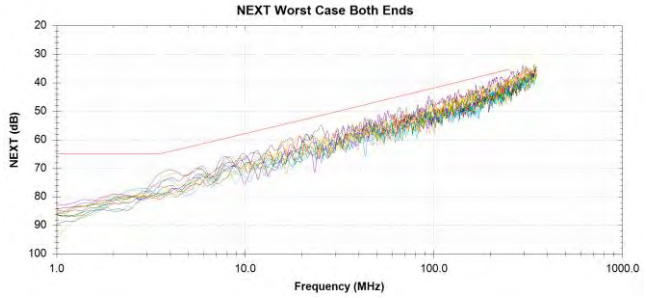


Figure 18. Example Cat 6 Fillerless NEXT Baseline

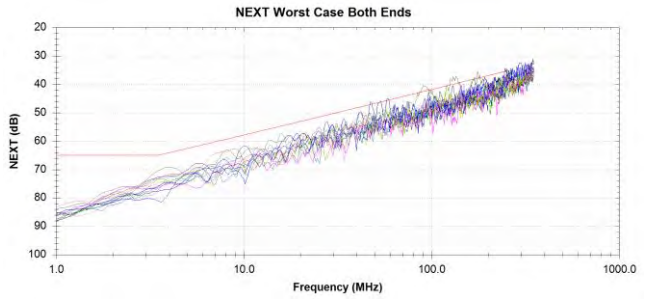


Figure 19. Example Cat 6 Fillerless NEXT After Pulling

Figures 20 and 21 show examples of time domain crosstalk measurements that are produced for diagnostic purposes by the handheld test equipment. These plots can be used to determine the physical location of damages or locations where irregularities in the tested sample are. Indicating Arrows in Figure 21 point to the effects from test activities which can be easily observed when compared to the baseline measurement. The crush and kink events resulted in single peaks in the measurement. The pull effect can be observed over the entire region where the cable was pulled at higher tension through the installation setup.

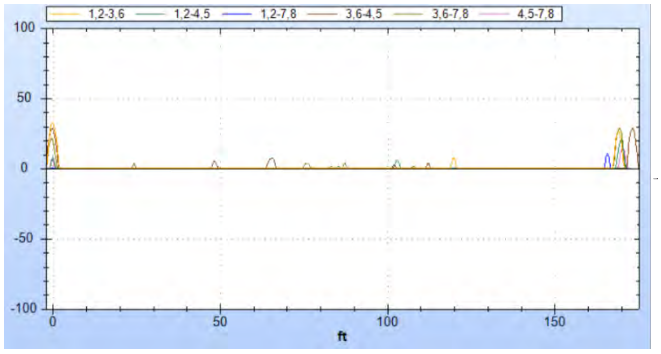


Figure 20. Example Time Domain Measurement: Baseline

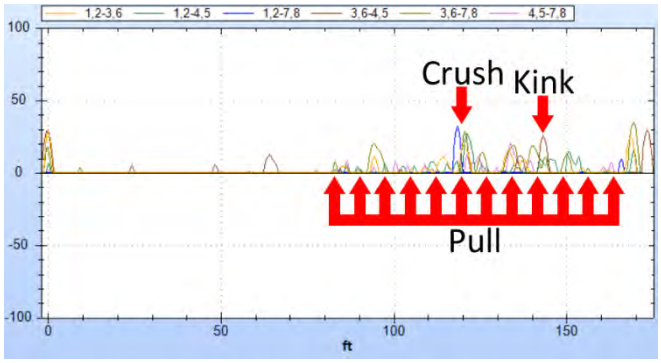


Figure 21. Example Time Domain Measurement after Testing All Installation Stresses

Tables 1 and 2 show the average margins (in dB) to the ANSI/TIA-568.2-D RL and NEXT specifications of cable sets that were tested with this installation procedure. Each Cable ID column is the average result of 5 or more individual cables tested. These populations were tested to reduce the issues caused by the variations in results from damages inflicted on the cables.

The Baseline rows are the sample margins from the test on the accumulator of the undamaged material. The Pull rows are the same samples' margins after the samples were pulled through the tension rig and across the dragging surfaces. The Crush rows are the samples' margins after enduring being crushed at a set point by a set weight. The Kink rows are the samples' margins after being subjected to a kink damage by tightening a loop until the cable is damaged.

The data in these tables is separated by the category of the cables, which results in different specifications (Cat 6 cables are compared to Cat 6 specifications; Cat 6A cables are compared to Cat 6A specifications). The results are further separated by whether or not the cable samples have center filler elements for managing the pair locations within the cables.

Table 1. RL Average Margins (dB) of Populations of Different Cables Sorted by Cable ID and Design

Cable Type	Cat 6 Filered				
Cable Design	A	B	C	D	E
BASELINE	3.3	3.8	4.4	4.2	5.1
PULL	3.0	3.6	4.4	4.2	4.9
CRUSH	3.0	3.7	4.4	4.3	4.9
KINK	3.0	3.7	4.4	4.2	5.0

Cable Type	Cat 6 Fillerless									
Cable Design	F	G	H	I	J	K	L	M	N	O
BASELINE	6.0	5.2	6.2	5.5	5.4	4.7	4.7	2.9	5.0	5.4
PULL	5.5	5.1	5.0	4.5	4.3	4.3	4.8	2.8	4.6	4.7
CRUSH	5.5	5.3	5.0	4.5	4.5	4.2	4.8	2.8	4.7	4.6
KINK	5.3	5.2	5.0	4.7	4.6	4.2	4.8	2.8	4.7	4.5

Cable Type	Cat 6A Filered		
Cable Design	P	Q	R
BASELINE	4.2	4.9	2.0
PULL	4.3	4.8	1.8
CRUSH	4.3	4.7	1.8
KINK	4.2	4.8	1.8

Cable Type	Cat 6A Fillerless			
Cable Design	S	T	U	V
BASELINE	5.4	5.4	4.6	4.4
PULL	5.1	5.1	4.9	4.1
CRUSH	5.1	5.1	4.9	4.1
KINK	5.1	5.1	5.0	4.0

Table 2. NEXT Average Margins (dB) of Populations of Different Cables Sorted by Cable ID and Design

Cable Type	Cat 6 Filered				
Cable Design	A	B	C	D	E
BASELINE	6.0	4.1	9.4	10.1	3.7
PULL	2.0	4.5	7.8	7.1	3.8
CRUSH	1.5	4.3	6.8	6.4	3.8
KINK	1.6	4.1	6.8	6.4	3.4

Cable Type	Cat 6 Fillerless									
Cable Design	F	G	H	I	J	K	L	M	N	O
BASELINE	4.7	4.1	4.3	2.8	2.8	6.6	6.2	5.4	5.1	4.9
PULL	1.2	1.0	0.3	-0.1	0.5	3.2	3.9	3.4	2.6	1.8
CRUSH	0.0	0.5	-0.7	-0.2	-0.4	2.2	2.9	3.0	2.1	1.3
KINK	-0.2	0.5	-0.7	-0.6	-0.5	2.0	2.6	2.2	2.5	1.1

Cable Type	Cat 6A Filered		
Cable Design	P	Q	R
BASELINE	5.0	9.0	5.8
PULL	5.1	10.0	6.1
CRUSH	5.1	10.1	6.1
KINK	5.1	10.0	6.0

NEXT	Cat 6A Fillerless			
Cable Type	S	T	U	V
Cable Design	4.8	4.8	3.3	4.7
PULL	3.7	3.7	2.5	4.8
CRUSH	3.5	3.5	2.3	4.4
KINK	3.4	3.4	2.3	4.5

Tables 3 and 4 shows the final worst margin losses in the populations of cable measurements that were performed in this installation set. This reduces the series of tests to one metric – how much margin was lost from the installation damages (on average for each cable type). This allows for a much simpler comparison between the cable designs.

Table 3. Worst Loss of RL Margins (dB) From Installation Tests Performed on Cable Populations

Cable Type	Cat 6 Filered				
Cable Design	A	B	C	D	E
Worst Loss (dB)	0.2	0.2	0.0	0.0	0.2

Cable Type	Cat 6 Fillerless									
Cable Design	F	G	H	I	J	K	L	M	N	O
Worst Loss (dB)	0.7	0.1	1.2	1.0	1.1	0.5	-0.1	0.1	0.4	0.9

Cable Type	Cat 6A Filered		
Cable Design	P	Q	R
Worst Loss (dB)	0.0	0.1	0.2

Cable Type	Cat 6A Fillerless			
Cable Design	S	T	U	V
Worst Loss (dB)	0.3	0.3	-0.4	0.4

Table 4. Worst Loss of NEXT Margins (dB) From Installation Tests Performed on Cable Populations

Cable Type	Cat 6 Filered				
Cable Design	A	B	C	D	E
Worst Loss (dB)	4.4	0.0	2.6	3.7	0.2

Cable Type	Cat 6 Fillerless									
Cable Design	F	G	H	I	J	K	L	M	N	O
Worst Loss (dB)	4.8	3.6	5.0	3.4	3.3	4.5	3.6	3.2	3.1	3.7

Cable Type	Cat 6A Filered		
Cable Design	P	Q	R
Worst Loss (dB)	0.0	-1.0	-0.2

Cable Type	Cat 6A Fillerless			
Cable Design	S	T	U	V
Worst Loss (dB)	1.4	1.4	1.1	0.3

3.2 Connector Installation

The measurements most affected by the changing terminations and jacks in this test set were the RL and the NEXT. Of those, the crosstalk experienced the greater impact. Table 5 shows the average of the minimum margins of the measurements taken for the parameters for both the links and channels for each test setup.

Table 4. Averages of Minimum Margins for Sets of Tests of Different Connector Installations

Test Set	Channel RL Margin (dB)	Channel NEXT	Permanent Link RL	Permanent Link NEXT
Baseline	9.4	7.0	7.1	3.4
Long Exposed Conductors	8.4	7.1	7.5	4.6
Long Untwisted Conductors	5.6	-7.5	2.2	-10.0
Irregular Loops	10.0	1.6	7.7	-0.7
Different Jack A	8.6	7.2	7.7	4.2
Different Jack B	9.6	7.5	7.6	3.6
Different Jack C	4.4	-7.1	0.9	-10.1

Two of the different jacks used in this set had results very similar to the baseline test. The test results with jack set labeled “C” was from an older jack that was not similar to the other jacks used in this testing. The “C” jacks were not able to produce Category 6 compliant links or channels.

There was very little difference in margin between the baseline and the test set with the long exposed conductors. Despite the jacket being removed from the conductors for several inches, the effect on the channel and link performance was on par with changing the brand of jack used.

Manipulating the conductors outside the jacket in various ways proved to be extremely detrimental to the performance of the links and channels. Untwisting the conductors caused over 10 dB of additional crosstalk loss. This caused failures on both the link and channel tests. Figure 22 shows an example set of traces with the

untwisted pair measurement and the baseline measurement in the same graph.

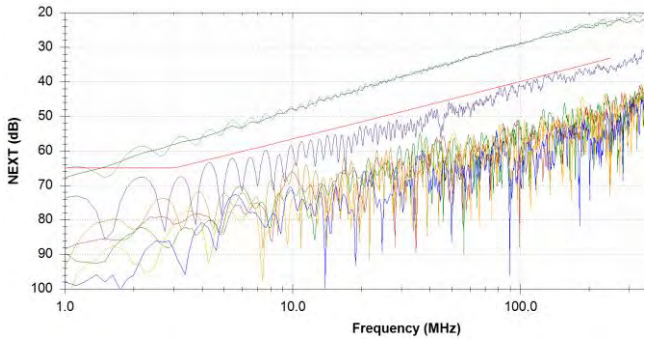


Figure 22. Example NEXT Measurement for Untwisted and Baseline Sets

The test set with irregular loops in the conductors right in the jack region are of especial interest. These loops produced severe results even though they were much smaller and appeared more "normal" for a termination than the other effects tested. When creating these loops, one method was to prepare the termination with the pairs coming in from the side of the jack and then folding the pairs so that they could be managed directly from the rear of the jack. This amount of manipulation was sufficient to cause failures in the channel test.

4. Observations and Conclusions

The testing in this set was designed to be at the harsher end of what can be expected from a typical installation. More harsh conditions would be destructive and not representative. From this testing, the kinds of damages and the ability of products to resist the damages can be reviewed. With the review of multiple products from multiple manufacturers, the conclusions can inform expectations.

The cable installation testing did not cause failures for the Return Loss parameter. Crushing the cable at a point, kinking the cable at a point, and pulling the cable at elevated tension did reduce the Return Loss margin by up to 1 dB on some of the fillerless cable designs. This makes sense as the amount of tension or damage was not enough to cause a break in the transmission lines or to destroy the insulation between the conductors.

The NEXT of most of the cable populations were affected by the installation testing. Notably, the entire set of Category 6 cables without fillers lost between 3 dB and 5 dB of crosstalk margin. The pairs of the conductors within these cables were most likely brought closer together by the installation and this closeness allowed for more energy to transfer between them. Of the other types of cables, the Category 6A cables with fillers showed almost no impact from the installation. As these cables tend to be designed with more material and designed to handle crosstalk more effectively, it is unsurprising that they were not strongly impacted. Some of these measurements showed a gain in margin for the populations. This is more likely caused by the installation "working out" the effects of the packaging on the cable than tester variation. Most of the fillerless Category 6A designs showed around 1 dB of loss of NEXT margin. These designs were more robust than the fillerless Category 6 cables but not as robust as the fillered Category 6A cables. These designs' resilience to the installation could be accounted for by the pair designs or the tape layers that some of the designs have. These features could have absorbed some of the stresses. The different sets of cables used in the fillered Category 6 cables shows an unexpected range of test impact. Some of the populations had negligible loss while others showed several dB of margin loss. Inspecting the cables that were used, further design features like the kind of filling element used to separate the conductors, the tightness of the jacket of the cable, and other features of the products were different enough to potentially account for the difference in resistance to the installation effects.

For the cable populations that were more affected by the installation, the measurement traces looked similar and the handheld tester tools showed similar types of effects. The time domain traces could be used to show which parts of the cable were affected by each test.

For the connection portion of the testing, certain tests showed effectively no impact on the test results while other tests caused margin loss and failure. Of the four jacks tested, three performed very similarly and one caused failures.

Unexpectedly, removing the jacket for several inches did not ruin the Return Loss or performance. However, it should be noted that this testing was in a lab condition so no further manipulation, additional electrical noise, or damage could happen to the exposed conductors. The jacket of the cable protects the transmission pairs from damages and stresses. The rest of the testing showed that it is very easy to cause failures if the pairs of the cable are manipulated.

Untwisting lengths of the pairs or excessively bending the conductors to fit a jack were both able to cause failures for the NEXT parameter. With the amount of margin loss that occurred, it is not feasible to overcome the difference with cable performance. In other words, if the connector installation is done poorly, the rest of the components cannot make up for the damage done. For this reason, good connection is a critical part of installation.

5. Recommendations Based on Findings

The first recommendation is to plan the installation to avoid excessive stresses, pulls, kinks, and crushes. This test shows that some cables can survive harsher installations, but it is possible to have such stresses that any cable would be destroyed.

If the installation is to be on the harsher end, fillered products and higher category products will lose less crosstalk margin. The fillered Category 6A cables and the one fillerless Category 6A cable with the extra tape layer showed almost no impact from the installations. Failing these, we recommend choosing products with enough guaranteed performance margin that the installed systems will still pass industry standards.

For connector installation, the best recommendation is to follow the manufacturer's instructions and keep the conductors neat and regular. Do not untwist inches of length. Do not bend the twisted pairs into loops in the jack region. Plan ahead – if the cable management is straight then install straight rather than installing from the side and bending to fit. If possible, use quality jacks and jacks that have built-in management to ensure that the terminations do not cause loss of margins and failures.

6. Authors



Brian Marchant is a graduate of the Pennsylvania State University with a Master of Science in Electrical Engineering. He has worked for Leviton for fifteen years and is currently a senior test engineer.

Mailing Address: 132 White Oak Rd, New Holland, PA 17557



Matt Schumacher is a graduate of Millersville University with a Bachelor of Science in Mathematics and Physics. He has worked for Leviton for fifteen years and is currently a senior applications engineer.

Mailing Address: 132 White Oak Rd, New Holland, PA 17557

.

Topography Scanner for Quality Control of Power Cable Manufacturing

Jussi Hanhirova
Maillefer Extrusion Oy
Ensimmäinen savu
FIN-01511 Vantaa, Finland
+358 9 88 665 600 jussi.hanhirova@maillefer.net

Janne Harjuhahto
Maillefer Extrusion Oy
Ensimmäinen savu
FIN-01511 Vantaa, Finland
+358 9 88 665 600 janne.harjuhahto@maillefer.net

Mikko Lahti
Maillefer Extrusion Oy
Ensimmäinen savu
FIN-01511 Vantaa, Finland
+358 9 88 665 600 mikko.lahti@maillefer.net

Abstract

Quality control is essential in medium and high voltage power cable manufacturing. In the first production phase the metal conductor is insulated with three layers of plastic. This phase is the most critical and prone to manufacturing defects. Current quality control systems measure the layer thicknesses of the three plastic layers with x-rays from several points around the cable. Power cables are also routinely tested after production in order to find defective products before installation.

In this paper, we present a topography scanner device designed for measuring the surface geometry of power cable products in real-time during production. The topography scanner contains an array of laser sensors, which are placed around the cable to cover the full 360° of the cylindrical cable. The topography scanner provides continuous quality measurements of the cable geometry and a complete three dimensional topographical map of the cable surface. A single measurement produces the cross-sectional shape of the cable, and derived quality metrics, such as, diameter, ovality, roundness, and minimum and maximum radius. Multiple consecutive measurement are used to generate the detailed 3D topographic map of the cable surface. The 3D surface map is used by an automatic defect detection system, which seeks for cable surface defect and geometric anomalies, such as scratches, extrusion residues and scorched raw material, as well as, sink-ins and sudden diameter changes.

The topography scanner system extracts detailed quality information from cable manufacturing process, which can be used to ensure product quality, to improve the process conditions, and to spot maintenance needs in line equipment. It is an invaluable tool for power cable making

Keywords: Extrusion, power cable, quality control, defect detection.

1. Introduction

High and extra high voltage power cables, ranging from 66 to 525 kV, need electrical insulation to confine the flow of current to the conductor wire. Power cable insulation is done in the continuous vulcanization process, where a metal conductor is insulated with three layers of plastic: an inner semi-conductive layer, an insulating layer and an outer semi-conductive layer.

This insulation process is critical and prone to manufacturing defects. Any irregularities at the plastic layer boundaries will cause heightened electrical stress through the field enhancement phenomena. Increased local electrical stress will significantly increase the risk of electrical breakdown.

Rigorous testing is carried out after manufacturing, in order to find any defective products before installation. Routine electrical testing can only be done after all of the production phases for finished cable products. There is significant added value in detecting manufacturing defects as soon as possible, before the produced reel is sent onwards to time consuming subsequent processes.

Return to Table of Contents

Currently most of the produced high voltage or extra high voltage cables are not examined by any surface quality monitoring system. Current measurement systems are typically aimed towards measuring the layer thicknesses of the three plastic layers with x-rays and are not designed for local surface defect detection.

The structure of this paper is as follows. In chapter 2 the topography scanner is presented. Chapter 3 presents the topography scanners inference system, which is used to automatically detect possible defects on the cable surface. Chapter 4 discusses the process optimization possibilities that the topography scanner enables. Chapter 5 concludes this article.

2. Topography Scanner

The topography scanner is a measurement device for quality control of power cable manufacturing. The topography scanner measures the power cable surface geometry in real-time during production. The unit is placed in the end part of the production line, where the cable has cooled down and acquired its final shape. Figure 1 shows a picture of the unit, with the measured cable running through the device.



Figure 1. The topography scanner.

The topography scanner uses an array of laser displacement sensors to measure the cable surface from all directions. Figure 2 represents a unit with an arrangement of six sensors around the cable core. Different number of sensors can be used for different types of production lines.

In high and extra-high voltage power cable manufacturing the cable moves typically at speeds of 0.5 to 2 m/min. The topography scanner measures the moving cable at an adaptive speed between 200 to 800 Hz. The measurement speed is adjusted according to production line speed in order to provide a uniform distance between two consecutive measurements.

In medium voltage applications the cable can move up to 20 m/min. The topography scanner system can be configured to measure at 2000 Hz without reducing the resolution of measurements.

The laser displacement sensor data is used to generate precise 2D cross-sectional shape of the cable and a 3D topographical surface map of the moving cable core.

Quantitative quality metrics are derived both from a single cross-sectional measurement and from the continuous topographical map.

Metrics derived from a two dimensional cable cross-section measurement are: diameter, radius, roundness and ovality.

Ovality is defines as the difference between the maximum and minimum diameters:

$$D_{max} - D_{min}$$

Roundness is the proportion between the minimum and maximum diameters:

$$D_{min} / D_{max}$$

In addition, the quality metrics include the minimum and maximum diameter and radius, together with their position on the cable. Also, from the topographical map of the cable surface metrics for cable lengthwise waviness are calculated.

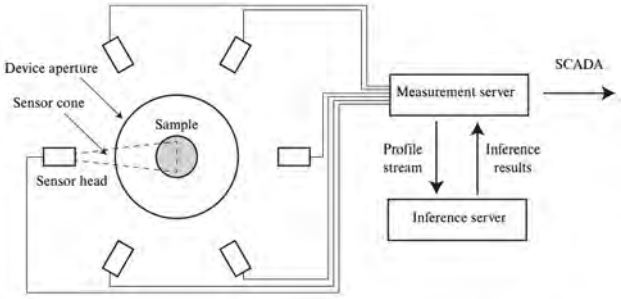


Figure 2. An example of laser sensor arrangement around the cable.

A single measurement from the topography scanner produces the cross-sectional two dimensional shape of the cable. Multiple consecutive cross-sectional measurements are used to generate a three dimensional topographical map of the cable surface.

Figure 3 represents an example of a cable cross-sectional measurement. In this example the ovality is about 1.3mm. Scale of the cross-sectional figures can be adjusted to reveal even the smallest deviations from the perfectly round shape of an ideal cable core.

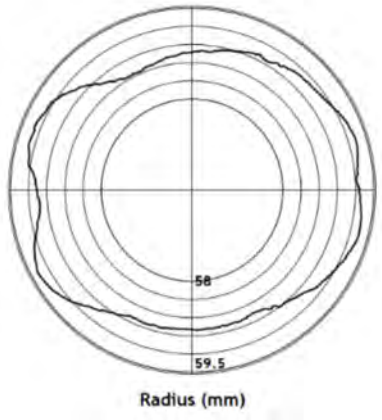


Figure 3. A 2D cross-sectional view of a cable.

Return to Table of Contents

Figure 4 represents examples of 3D topographical maps of cable surfaces. Topmost of the topographical maps represents a cable surface with higher lengthwise waviness as compared to the topographical map on the bottom of the figure.

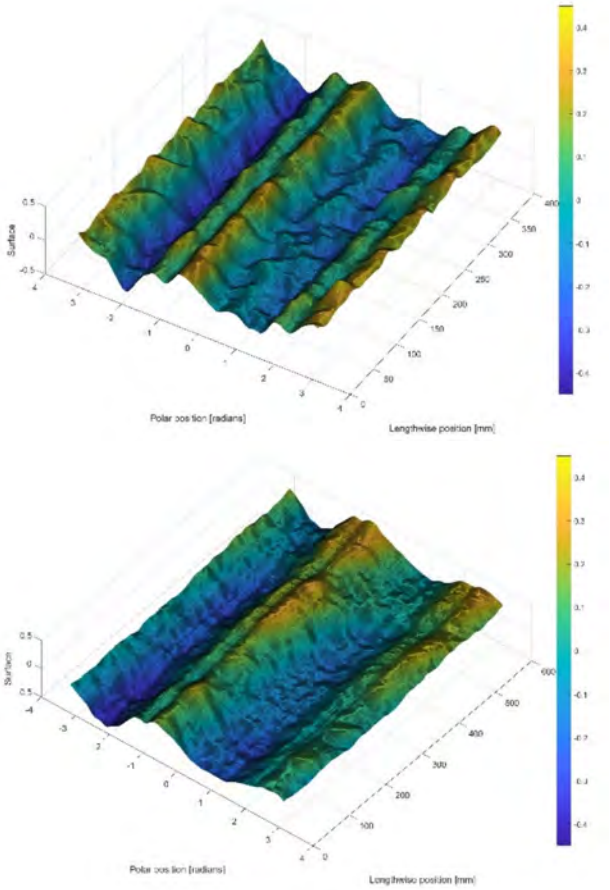


Figure 4. 3D topographical maps of cable surface.

3. Defect Detection

The topography scanner contains an inference system which continuously analyzes the cable surface for possible defects and other surface geometry anomalies. Detected defects and other geometric anomalies are reported immediately for the line operators and are saved to a database.

The topography scanners inference system detects, measures and classifies all found defects. The inference system is based on continuous analysis of the topographical surface map data using custom algorithms and convolutional neural networks trained using deep learning methods. [1, 2]

Figure 5 shows an example of a detected defect. On the right side is a 3D representation of the defect on the cable surface. On the left side of the figure the 3D data is projected onto a 2D grayscale representation, where high areas are represented by more white colors and low areas are represented by darker colors.

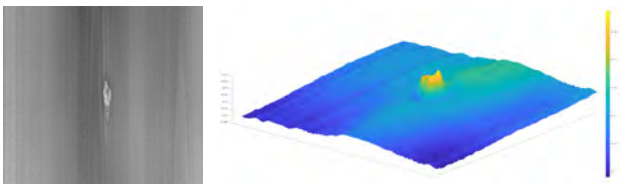


Figure 5. A small defect represented as a grayscale image (left) and as a 3D render (right).

3.1 Defect classification

The surface defects encountered in power cable production can be divided in multiple categories depending on their appearance. The topography scanners inference system gives a classification for each found defect. Classification is based on use the use of custom trained convolutional neural networks.

The convolutional neural network classification gives probabilities for the defect to belong to each of the possible classes. The class that has the highest probability is the most probable class for a defect. Defect classification allows filtering defects based on their type, thus minimizing defect alarms on defects that are considered non-critical.

Defect classes used by the convolutional neural networks in the topography scanners inference system include twelve categories. Potentially critical defect classes are: *Scorch*, *scratch* and *die drool*. Non-critical defect classes are different type of *by-products*, which are separated into six different classes based on their visual appearance: *Bumps*, *dots*, *line*, *small bump*, *splash* and *splash lines*. Other defect classes are: *Die line*, *water* and *cable joint*.

Scorch class includes defects that compose from material that has burned inside into the surface. *Scratch* class represents defects which have been cut inside the surface due to some mechanical contact by production machinery. Not all scratches are critical, but the presence of any mechanical damage is an indication of potentially faulty equipment or a need of maintenance.

Defects belonging to the *die drool* class can be spotted on a production line where a *die line* marking is used to track the rotation of the cable during production. Leftmost image in Figure 8 represents an example of a *die line* marking. *Die drool* is referred to as the buildup of materials on the surface of the extrusion die. When the buildup will break-off it can attach itself to the cable surface, resulting in a *die drool*. An example of a *die drool* is represented in the rightmost image of Figure 6.

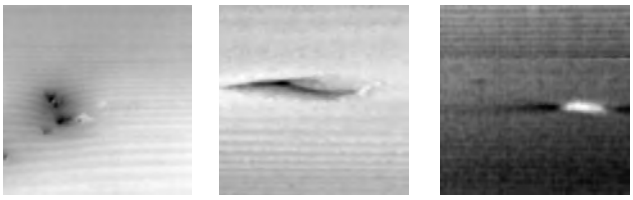


Figure 6. Examples from potentially critical defect classes, from left: Scorch, scratch, and die drool.

Return to Table of Contents

Figure 6 represents grayscale rendered image examples of defects belonging to the *scorch*, *scratch* and *die drool* classes. The grayscale rendered images are projections of the 3D topographical data to 2D image. Black and darker regions in images represent deeper areas, whereas white and lighter regions represent areas that are higher from the overall surface.

By-products are different types of residues left over from the manufacturing process. Depending on the amount of material and the section of the production line where the *by-product* gets in contact with the cable it can acquire different forms.

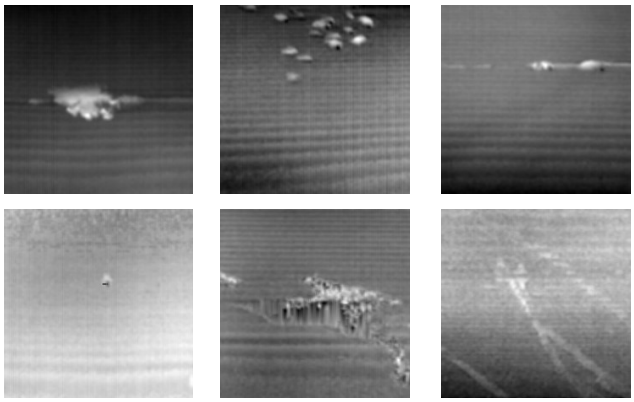


Figure 7. Examples from non-critical by-product classes.

Figure 7 represents grayscale rendered example images of different type of *by-products*. The top row of Figure 7 starting from left shows by-products of type: *bumps*, *dots* and *line*. The bottom row of Figure 7 shows by-products of type: *small bump*, *splash* and *splash lines*.

Defect belonging to the *water* class can occasionally be observed in production lines with water cooling. Water droplets on cable surface are non-critical for the production. But, if water droplets are not classified correctly, they could generate false alarms thus lowering the precision of the defect detection system. Example of a water droplet is represented in the middle image of Figure 8.

Although detections classified as *by-products* or *water* are not critical regarding the quality of the end product, they provide valuable information regarding the condition of the manufacturing line machinery. For example, increase in amount of *by-products* can be an indication to take predictive maintenance actions on the line.

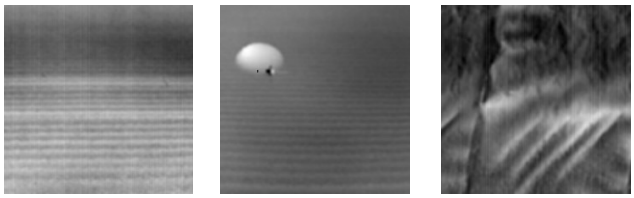


Figure 8. Examples from other defect classes

Cable joint class is used in the defect detection system to identify when the connection between a start cable and the production cable arrives to the topography scanner. Example of a *cable joint* detection is represented in the rightmost image of Figure 8.

The measured data of all defects is saved to a database together with metadata, such as time, production length and orientation of the defect on the cable surface. In addition, stored defect data includes the defect class, as well as, defect height and area on the cable surface. Defect data can be browsed and examined later from the database.

3.2 Geometric anomalies

Geometric anomaly is an unwanted change in cable geometry. Typically they are different types of sink-ins or local changes in cable diameter. The topography scanner detects all different types of geometric anomalies.

Geometric anomalies are reported to the operators immediately and they are saved to a database. Figure 9 represents data saved from a geometric anomaly, in which the diameter of the cable grows suddenly by 0.2mm.

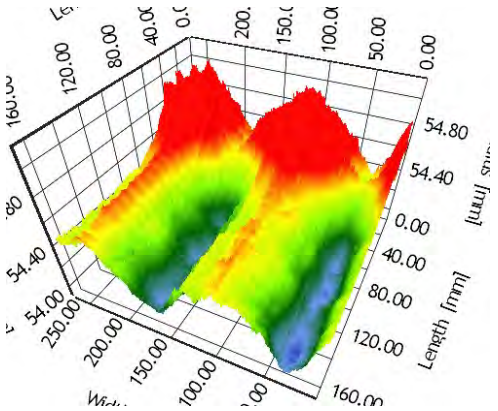


Figure 9. An example of a geometric anomaly on the surface of the cable.

3.3 Detection sensitivity

Industrial quality control scenarios demand automatic detection systems with high detection accuracy and low false alarm rates.

The topography scanner system contains configuration parameters that can be used to adjust its sensitivity for reporting detected defects. The parameters control which defects and geometric anomalies are reported to the operators, which are only saved to the database, and which are omitted from reporting and saving.

Defect detection sensitivity control includes the estimated height and area of the defect and its convolutional neural network classification. Defects have to meet defined minimum size and selected class parameters in order to be saved to a database and to be reported.

Geometric anomaly detection sensitivity is controlled by adjusting how much the cable geometry metric values (radius, diameter, roundness, ovality and lengthwise fluctuation) can vary on a given distance. When one of the values varies over the threshold value, a geometric event is recorded.

Return to Table of Contents

Defect and geometric anomalies saved to the database can be browsed and filtered based on their size and classification parameters.

The topography scanners defect detection system sensitivity can be adjusted to meet customer specific needs.

4. Process optimization

Continuous measurement of the cable surface provides valuable quality data of the end product, the production process and the production line.

Data measured by the topography scanners data can be used to ensure product quality. The continuous measurements guarantee that specifications are met throughout the production run.

Defect detection ensures that no critical defects go unnoticed, and for possible defects the required actions can be taken immediately during or after the production.

By combining process data and quality data measured by the topography scanner the process can be improved towards more optimal conditions.

Topography scanner also enables predictive maintenance functionalities by finding minor anomalies in the process data before they affect the end product quality.

Data from multiple topography scanner units enable optimization and diagnosis across production lines. Comparison of topography and process data from multiple production lines can be used to identify differences in line performance and their root cause.

Data provided by the topography scanner is a key enabler in designing smart process control and future smart manufacturing systems.

5. Conclusions

In this paper, we have presented the topography scanner and its defect detection system.

The topography scanner system can extract detailed quality information from cable manufacturing process and its detection system can automatically find defects and other anomalies on cable surface during production.

The detection sensitivity of the topography scanner can be adjusted, so that only desired defects are reported to the operators.

Linking the detailed quality information to line control data opens up new means for process optimization and predictive maintenance actions.

References

[1] Y. LeCun Y. Bengio and G. Hinton. ”Deep learning,” Nature, Vol. 521, May 2015

[2] J. Hanhirova, J. Harjuhahto, J. Harjuhahto and V. Hirvisalo, "A machine learning based quality control system for power cable manufacturing," *2019 IEEE 17th International Conference on Industrial Informatics (INDIN)*, Helsinki, Finland, 2019, pp. 193-198, doi: 10.1109/INDIN41052.2019.8972281.

Author biographies



Jussi Hanhirova received his M.Sc. degree in Computer Science in 2015 from Aalto University. From 2006 to 2012 he has developed software systems as an entrepreneur and participated to various industrial projects as technology consultant. Prior to joining Maillefer Extrusion Oy in 2019 he worked for 7 years at Aalto University, from which the last four years as a PhD researcher in the School of Science. At Maillefer he works as Data Scientist on R&D pilot projects developing artificial intelligence systems for future cable manufacturing equipment.



Janne Harjuhahto studied chemical engineering and polymer chemisty at Aalto University. He joined Maillefer Extrusion in 2014 as an R&D Engineer working with medium, high and extra high voltage cable machinery and production processes. His work focuses on improving both manufacturing efficiency and the end quality of the product.



Mikko Lahti received the degree of M. Sc. in Chemical Engineering in 1991 and the degree of Dr. Tech. in Polymer Technology in 1996. Before joining Nextrom in 1997 he worked as Research Scientist in European Joint Research Center in Milan. From 1997 to 2006 he held nine years various positions in Nextrom’s product management being actively involved with process development for fiber optic cables. Then he joined Maillefer Extrusion Oy in 2006 as Extrusion Development Manager responsible for the development of the extrusion processes for different cable applications. Currently as R&D director he is responsible for R&D in Maillefer Group. Mikko has 20 years of experience working on cable industry. His work has ranged across R&D, product management, product development, process development and material science.

Return to Table of Contents

SESSION 4

Click on a session below to navigate to that section of the Proceedings.

SESSION 4: HIGH DENSITY LOOSE TUBE

Chairperson: David B. Kiddoo IWCS, Inc.

4-2 **High-Density Optical Cable with Ultra-Low-Loss, Large Effective Area ITU-T G.654.E Optical Fiber**; Mr. Jairo Stoco, Corning, United Kingdom

4-3 **Evaluation of 165µm Reduced Coating Diameter Fibers for High Density Cable Applications**; Yunfeng Gu, Corning Incorporated, USA

4-4 **High-Density Micro Cable Family with Next Generation 190 Micron Fibers**; Mr. Sebastian Olszewski, Corning Optical Communications Polska Sp. z o.o., Poland

4-5 **Development of a High Fiber Density 432-Fiber Microduct Cable**; Mr. Ray Lovie, Prysmian Cables and Systems USA, LLC, USA

Click here to return to the **Table of Contents**

High-density optical cable with ultra-low-loss, large effective area ITU-T G.654.E Optical fiber

Jairo Stoco [(1)], Ian Davis[(2)], Lidia Galdino [(3)], Gianni Maiorani [(4)]

[(1)] Jairo Stoco - Lakeside Business Village, CH5 3XD, UK, Corning, stocoj@corning.com

[(2)] Ian Davis - Lakeside Business Village, CH5 3XD, UK, Corning, davisim@corning.com

[(3)] Lidia Galdino, Lakeside Business Village, CH5 3XD, UK, Corning, GaldinoL@corning.com

[(4)] Gianni Maiorani - Roseto Degli Abruzzi, Teramo, 64026 Italy, gianni.maiorani@ecotelcavi.it

Abstract

This article presents a new terrestrial optical fiber cable using the ITU-T G.654.E Corning TXF® fiber and describes its technical characteristics and applications. The cable features a very compact design, containing ultra-low attenuation G.654.E fiber (typically 0.166 dB/km at 1550 nm) and large effective area (typically 125 μm^2 at 1550 nm), allowing 50% more light to be pumped into the fiber when compared with a ITU-T G.652.D single-mode fiber. The fiber's large effective area helps mitigate undesirable non-linear effects like Cross Phase Modulation, Self-Phase Modulation or Four-Wave Mixing, therefore maintaining a higher SNR for data rates up to 800G, enabling longer transmission distances and higher capacity networks. The high-density cable designed by Ecotel features 96 fibers on a reduced cable diameter and weight compared to existing G.654 cable design, addressing customer needs for use in pre-existing micro-ducts, with limited right of way and space constraints. The high density of the cable required the use of colored and ring-marked fibers inside loose tubes for identification.

Keywords: Terrestrial optical-fiber cable; Ultra-low-attenuation; large effective-area; High density cable; G.654; Loose tubes; G.654.E; Micro-ducts; Space constraint.

1. Introduction

The advent of new technologies and the high level of connectivity necessary to link devices has driven the growth in the telecommunications industry in the last few decades. Most recently, the growth of on-demand video, 5G, Internet of Things (IOT) Artificial Intelligence (AI) and many other applications are increasing the demand for more bandwidth. Ultra-low loss and larger effective area fibers are being identified by cablers and end users as the best solution to deliver more capacity, reduce the cost per bit, and increase system reliability. The amount of flowing information is higher than ever, and it needs to travel faster, further, and without delays.

Ultra-low attenuation pedigree single-mode optical fiber cable is more than ever considered critical on the Application Service Providers (ASPs) mission to grow high bandwidth capacity over terrestrial networks, interconnecting large data-hubs to metropolitan areas and integrating these networks to subsea backhaul.

In developed nations with a crowded sub-terranean infrastructure, space constraint is another growing challenge for operators and installation teams, as well as the right of use for these pathways. In this scenario, smaller, denser cables are more efficient to expand the network, reducing costs and installation time.

To accomplish that new demand, Corning and Ecotel partnered to design and build a cable using an established and reliable design, but with a fiber that delivers the demanding needs for high bandwidth over long distance using an ultra-low loss G.654.E fiber with large effective area. This fiber is deployed in a small form factor 96-fiber micro-cable measuring only 7.6 mm in diameter, generating total cable data carrying capacity of up to 4 Pb/s. The fiber features ultra-low attenuation (typically 0.166 dB/km), and high fiber effective area (typically 125 μm^2), allowing ~50% more optical power to be launched than for conventional G.652.D fiber. These two features combined deliver extended network reach and capacity. The next sections will detail each of these aspects, and how Corning and Ecotel believe this cable is part of the solution to expand the current telecommunications backhaul capacity.

2. Fiber and cable product description

2.1 Cable details

The micro-cable design chosen (Figure 1) contains 96 fibers in 4 loose tubes and are stranded together with 2 extra tubes containing blank elements only, to maintain the cable circularity. The 4 tubes contain 24 Corning® TXF® fibers each (ITU-T G.654.E standard), being 12 fibers colored and 12 fibers colored with 1 ring-mark added for differentiation. The cable cross section diameter measures 7.6 mm. The outer jacket has been selected to assure very low coefficient of friction with micro-ducts, to facilitate fast blowing installation.

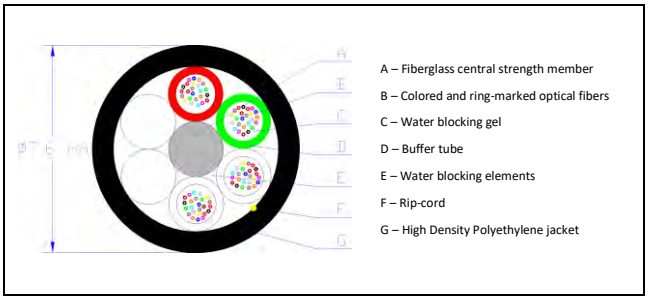


Figure 1. Details of the cable

Manufacturing challenges

The large effective area of G.654.E fiber (Aeff typically 125 µm2 which corresponds to 12.4 µm Mode Field Diameter at 1550 nm), may introduce elevated macrobend and microbend behavior when the fiber is locally stressed and bent if the cable is incorrectly designed. This elevation can be introduced during the various cabling processes (e.g. coloring, possibly with ring-marks, buffering, stranding or sheathing) or installation in a constrained space if the cabling process is sub-optimal. The adoption of special procedures during various production steps has been necessary to ensure that the ultra-low-loss transmission performance of fiber was preserved in the cable.

Coloring process

For the fiber coloring and ring-marking process, focus has been given to selection of proper tools, correct UV power irradiation, coloring and ring-marking speed, and winding of colored fiber on take-up spools.

Buffering process

On the buffering process, the extrusion of the protecting tube, made of techno-polymer, has been reviewed and adapted to preserve the attenuation. This was achieved using a proper set of tools and improved post-extrusion shrinking controls.

Final steps and Production results

The tubes have been stranded using standard S/Z technique but assuring a proper and constant tension on binding yarns. Extrusion of HDPE or Halogen Free jacket completes the production process.

The measurements taken after each cable manufacturing step and the final measurements of the attenuation of the cable, taken at the reference wavelength of 1550 nm, shows very little attenuation increase after each step. It can be seen also that, after the dwell time, there was a small relaxation on the cable, and the attenuation remained stable. Important to notice that results above 0.190 dB/km are outliers that correspond to only 0.06% of the results, with more than 99% of the fibers remaining with attenuation below 0.185 dB/km after cabling:

Bare fiber		After coloring	After buffering	Final cable
Minimum	0.164	0.166	0.166	0.162
Median	0.166	0.169	0.169	0.168
Maximum	0.170	0.174	0.176	0.195

Table 1 – Measured attenuation at 1550nm after each manufacturing step

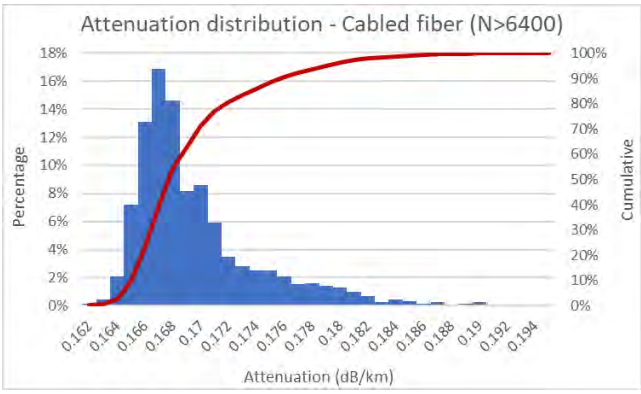


Figure 3 – Attenuation of cabled fiber

Mechanical and environmental performance

Cable qualification testing was carried out to determine compliance with installation environment, customer specification and the requirements of IEC 60794-3-20:

- Tensile test at 1000 N with no attenuation increase at 1550 nm allowed and fiber elongation < 0.15%;
- Crush test at 1000 N/10 cm, without permanent attenuation increase at 1550 nm;
- Impact test with three J/3 impacts, and no permanent attenuation increase at 1550 nm;
- Repeated bending with 30 cycles on 20x diameter and no damage resultant to the fiber or to cable elements;
- Temperature Cycling Test from -30°C to 60°C and attenuation increase < 0.05 dB/km on 3 complete cycles.

2.2 Fiber details

Low attenuation and large effective area are the two properties of optical fiber that are the most important to deliver enhanced capacity, reach, and cost efficiency.

2.2.1 - Attenuation

Attenuation continues to be the most important characteristic of an optical fiber cable, and Corning G.654.E fiber features ultra-low attenuation, typically 0.166 dB/km at 1550 nm. The most significant benefits of ultra-low attenuation are reach and capacity.

Longer Spans

The lower attenuation of Corning G.654.E fiber translates into longer spans with sustained fiber capacity throughout longer distances, even when using more efficient transmission protocols (which are more demanding in terms of required OSNR). Experiments demonstrate an increase of up to 55% on the reach of a 200 Gb/s link compared to conventional G.652.D fiber to over ~4500 km [2]. Another experiment [3] demonstrated unrepeated transmission with 200 Gb/s over a 520 km terrestrial network, using ROPAs and distributed Raman amplifiers. Reduction in the number of amplifier sites in a given route, generates lower initial costs associated with establishing optical amplification sites as well as lower ongoing operational costs.

Capacity increase

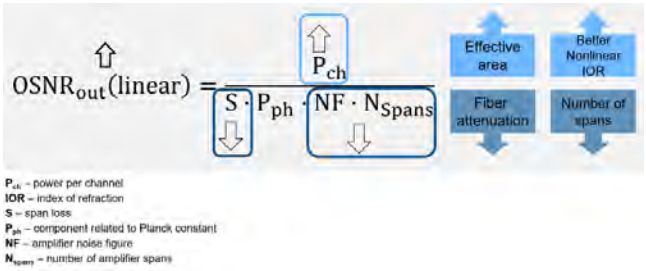
Higher speed protocols rely on the phase, amplitude, and polarization states of the signal to deliver improved data capacity, which will be demonstrated by simulation in section 3. These protocols are spectrally efficient modulation formats, but this improved efficiency comes with a price, as these protocols place much more stringent demands on OSNR [4] to allow the signal to be accurately detected, causing significant impact on the reach of these systems. Ultra-low attenuation ensures that the signal strength decays more gradually, whilst the reduced requirement for amplifiers causes lower noise build-up from amplified spontaneous emission noise (ASE). In this way, the G.654.E fiber is an enabler for maximizing capacity through transmission of the highest speed protocols, allowing upgrades up to ≥ 800G data rates over longer distance links.

2.2.2 - Large Effective Area (A_{eff})

Together with ultra-low attenuation, large effective area (A_{eff}) is another important fiber attribute for long-haul systems, which leads to superior transmission performance [6] through its capability to transmit higher power density and suppress non-linear effects.

Power density and non-linear effects suppressing

Achieving higher bandwidth over longer distances requires improved OSNR and one of the key components to achieve that is increasing in the power per channel as expressed on the Equation:



$$\uparrow OSNR_{out}(linear) = \frac{\uparrow P_{ch}}{\downarrow S \cdot P_{ph} \cdot NF \cdot N_{Spans}}$$

Equation 1. Impact of the higher Effective Area (P_{ch}) over the OSNR.

Wavelength Division Multiplexing (WDM) generates very high optical power in the fiber compared to single wavelength transmission. The optical power that can be launched into the fiber is determined by the size of its effective area. Above a threshold power level, non-linear signal distortions such as four-wave mixing, self-phase modulation and cross-phase modulation impact to compromise the accuracy of signal detection. A large effective area fiber serves to lower the optical power density across the core, extending the threshold for generation of non-linear distortion. Corning G.654.E fiber features a typical 125 µm^2 area, spreading optical power more broadly across the core, [5] which allows 50% more signal power to be launched, compared to a standard G.652.D fiber, further enabling longer links and fewer amplification sites.

3 Transmission System Modelling

A cable capacity study was designed to compare the performance of the cable manufactured by Ecotel and Corning, featuring G.654.E fiber, vs the performance of a similar cable featuring G.65.2D fiber.

Fundamental limits of an optical communication system are imposed by a combination of noise from the transceiver subsystem and optical amplifiers and optical fiber nonlinear distortion. An upper bound on the achievable SNR in coherent optical communication systems is set by the noise introduced by the transceiver subsystems. During transmission, the achievable SNR is further limited by amplified spontaneous emission noise (ASE) from optical amplifiers in the transmission line and by nonlinear signal distortion, inherent to transmission through silica optical fibers. To investigate the transmission system performance, a basic SNR model is used. After coherent detection and electronic dispersion compensation, the received signal-to-noise ratio can be calculated as:

$$SNR_{TOTal} = \frac{P}{kP + NP_{ASE} + NP_{NLI}}$$

Equation 2. Received SNR (after coherent detection and electronic dispersion)

P = Signal launch power;
K = 1/SNR_{TRX}, were SNR_{TRX} is the maximum SNR that can be achieved in a given transceiver sub-system;
N is the number of fiber spans;
$\mathbf{P_{ASE}}$ is the accumulated ASE noise power generated by the inline amplifiers;
$\mathbf{P_{NLI}}$ is the nonlinear coefficient calculated using the GN-model [6]

The transmission system under investigation consists of N_{ch} = 90 WDM 64QAM channels with symbol rate of 95 GBd, Nyquist spaced, and a transceiver noise (SNR_{TRX}) of 18 dB. The transmission link comprises of 1 to 50 spans of 80 km ITU-T G652.D or G654.E fiber with optical characteristics described in Table 2. The link is amplified using discrete optical amplifiers with 5 dB noise figure, and a total gain bandwidth of 4.8 THz at C-band window. To calculate per channel and fiber capacity a 3-dB gap to Shannon was considered.

Fiber type	ITU-I G.652	ITU-I G.654.E
Attenuation [dB/km]	0.19	0.166
Effective Area [µm^2]	82	125
Dispersion [ps/nm/km]	17	21
Non-linear refractive index n2 [m^2/W]	2.3x10^{-20}	2.2x10^{-20}

Table 2 – Details of the fiber used on the transmission system modeling of the cable

As observed in figure 5, due to the accumulation of amplifier spontaneous emission noise and nonlinear interference noise, the channel data rate decreases as transmission distance increases, and the 800 Gb/s rate is achieved across a 1000 km link. 75% of the transponder data rate (600 Gb/s) is still achieved across a link of 4000 km.

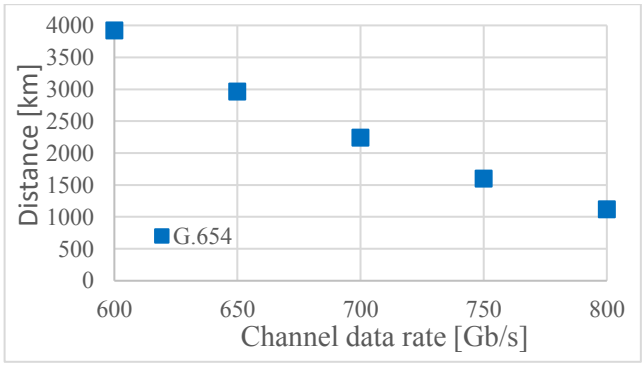


Figure 5. Link distance vs channel data rate

3.1 Cable capacity – G.654.E vs G.652.D fibers bandwidth comparison

As observed in figure 6, the optimum launch power for the G.654.E fiber to reach its maximum SNR is 4 dBm, yielding a SNR_{Total} of 15.3 dB. In comparison, the optimum launch power for a G.652D fiber is around 3 dBm, which yields an SNR_{Total} of 13.8 dB.

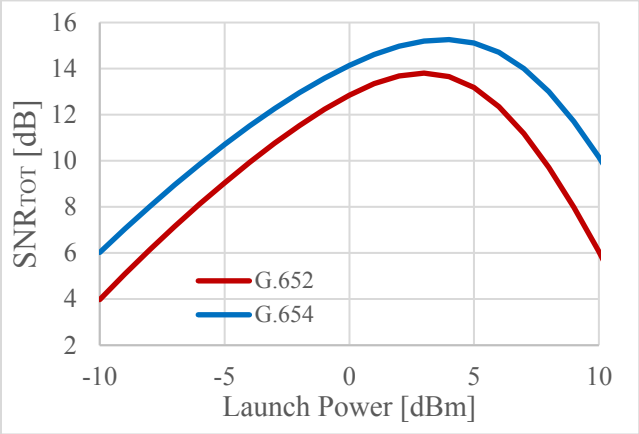


Figure 6. Comparison of optimum launch power to reach the higher OSNR for G.652D and G.657 E fibers

This extra optical budget of the G.654.E fiber compared to the G.652.D fiber allowed by the larger effective area and ultra-low attenuation reflects on the fiber and cable capacities throughout the link, and the advantage increases with distance. Each G.654.E fiber can potentially transmit ~41 Tb/s for an 800 km link. For a 96F cable, 48F will be transmitting each direction, therefore multiplying each fiber capacity per number of fiber transmitting at the same directions it will deliver a 2 Pb/s cable capacity per direction. The same cable using G.652.D fibers instead would reach 1.83 Pb/s, a difference of 170 Tb/s, which is equivalent to 4 extra G.652.D fibers. For a much longer 4000 km link the advantage of the G.654.E fiber over the G.652.D becomes even more visible, increasing to 297 Tb/s, or the equivalent of the capacity of almost 13 extra G.652.D fibers.

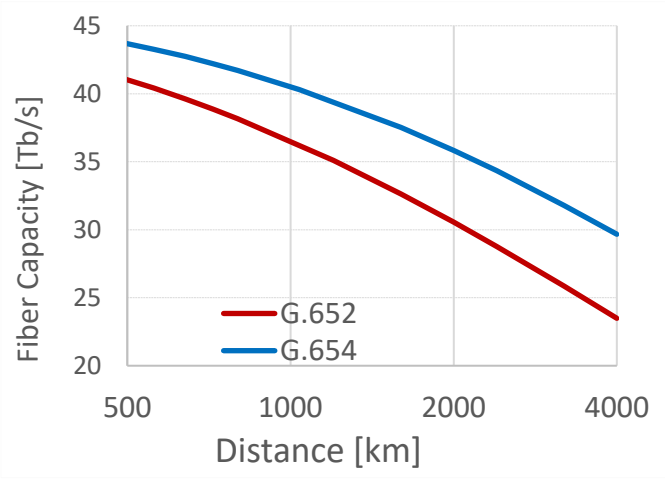


Figure 7. Fiber capacity vs link distance

4. Application environment

This is a terrestrial cable for which the main application is long-haul networks with longer spans. The high capacity, enabled by ultra-low attenuation and large effective area fiber, and the superior, lightweight cable design make it a great choice to interconnect data centers, metropolitan regions and backbones.

5. Conclusions

The strong growth of on-demand video, 5G, IOT, AI and many other virtual applications are increasing the demand for more bandwidth, and high data rate capable cables are identified as critical technology to deliver more capacity and reduce the cost per bit. The high-density micro-cables also address another problem which is the space constraint of the already crowded sub-terranean infrastructure. Corning developed the G.654.E fiber used by Ecotel to produce a 96F cable that can deliver up to 2 Pb/s per direction over twice the distance compared to G.652.D/G.657.A1 fibers. The lower attenuation and large effective area of the fiber allows the use of longer spans and fewer amplification sites, reducing the ASE and consequently improving the link SNR, and delivering enhanced capacity.

6. References

[1] Shargh, R.S., Al-Mansoori, M.H., Anas, S.B.A., Sahbudin, K.Z. and Mahdi, M.A. (2010). OSNR enhancement utilizing large effective area fiber in a multiwavelength Brillouin-Raman fiber laser. Laser Physics Letters, [online] 8(2). doi:https://doi.org/10.1002/lapl.201010110.

[2] Downie, J.D., Makovejs, S., Kaliteevskiy, N., Hurley, J., Wright, S. and Towery, C. (2017). Transmission Performance of Large Aeff Ultra-Low-Loss Terrestrial Fibre in 200 Gb/s EDFA and Raman-Assisted Systems. [online] IEEE Xplore. doi:https://doi.org/10.1109/ECOC.2017.8345898.

[3] Starykh, D.D., Akopov, S.G., Kharasov, D.R., Konyshev, V.A., Sergejs Makovejs, Nanii, O.E., Shikhaliev, I.I. and Treshchikov, V.N. (2019). 200 Gb/s per Channel Unrepeatered Transmission Over 520 km Terrestrial Fibers. IEEE Photonics Technology Letters, [online] 31(22). doi:https://doi.org/10.1109/lpt.2019.2947760.

[4] Corning (2017). Corning TXF Optical Fiber Featuring ultra-low-loss and Large Effective Area for Extended Reach. [online] Corning. Available at: https://www.corning.com/media/worldwide/coc/documents/Fiber/white-paper/WP8105_1.17.pdf [Accessed 12 May 2023].

[5] Zhou, H., Wang, R., Liu, Y., Sun, X., Chen, S., Zhang, L., Zhang, L. and Wang, H. (2017). Research on Fiber Nonlinear Coefficient. 2017 16th International Conference on Optical Communications and Networks (ICOCN). [online] doi:https://doi.org/10.1109/icocn.2017.8121350.

[6] P. Poggiolini, "The GN Model of Non-Linear Propagation in Uncompensated Coherent Optical Systems," in Journal of Lightwave Technology, vol. 30, no. 24, pp. 3857-3879, Dec.15, 2012, doi: 10.1109/JLT.2012.2217729.

7. Pictures of Authors



Gianni Maiorani
Technology Manager - ECOTEL cavi.
Gianni Maiorani is responsible for the development of cable products, process for cable manufacturing and technology upgrades at ECOTEL Cavi. Additionally, he provides support to sales and customers across all ECOTECH Group of companies, which are based in Italy. He holds a Diploma in Mechanical Engineering, and a Certification in Optical Fiber Transmission Technology from the University of Ancona. Gianni's career journey began in 1991, when he joined TELECO Cavi. Subsequently, he worked with SIEMENS and later joined Corning Cable Systems company. Throughout his career, he held various positions in the field of copper and optical fiber cables production technology. His extensive experience in the industry has equipped him with valuable expertise in these domains.



Ian Davis

Applications Engineering Manager, EMEA - Optical Fiber
Corning Optical Communications
Ian Davis is the Applications Engineering Manager for EMEA, responsible for technical support for optical fiber customers and end-users within the region.
Davis joined Corning in 1989 and has held various positions in product engineering, product line management, marketing and pplications engineering. Previously, Davis held the position of World-wide Applications Engineering Manager.

Davis received First Class Honors from Nottingham University, graduating with a Bachelor of Science Degree in Physics. He also received a diploma in Management Studies from St. Helens Technical College in Merseyside, England.



Jairo Stoco
Applications Engineer, EMEA - Optical Fiber
Corning Optical Communications
Jairo Stoco joined Corning in 2018, and since then is responsible for technical support for optical fiber customers and end-users within the EMEA region.
Stoco is graduated with a bachelor of Radio and Television from the Methodist University and also Bachelor of Telecommunications Engineering at the Salesian University, both in Brazil. Currently Stoco is a Global MBA candidate at the Manchester University. Over the years Stoco focused his career on many areas of Telecommunications, working with RFID, Unified Communications and Optical Fibers.



Lidia Galdino
System Engineering Manager
Corning Optical Communications
System Engineering Manager
Corning Optical Communications
Lidia Galdino is a System Engineering Manager at Corning, responsible for defining and driving long-haul terrestrial and submarine optical fiber and cable product strategy. She received a Ph.D. from University of Campinas. She is an Associate Editor for the Journal of Lightwave Technology, and serves on several technical program committees, including OFC and ECOC. She has authored > 100 peer-reviewed papers on optical fiber communication systems

Evaluation of 165 Micrometer Reduced Coating Diameter Fibers for High Density Cable Applications

Yunfeng Gu*, Weijun Niu, Brett Knowlton, Bryan Wakefield, Jeffery Stone, Hector De Pedro, Aditya Kaimal, Darren Stainer, Sebastian Olszewski, Sonya Raney, Scott Bickham, Ming-Jun Li

Corning Incorporated

Corning, New York, USA

+1-607-974-9000 · *guy@corning.com

Abstract

As one of several approaches to increase fiber density in cables, reduced coating diameter fibers (RCDF) are attracting a lot of interest due to their compatibility with the standard 125 μm clad diameter. Through our systematic study on the impact of RCDF coating thickness on mechanical and optical performance, we narrowed down coating diameters to the range of 160-170 μm using current commercial coating materials. We then conducted two loose tube cable trials to further evaluate fiber handleability and cable performance. In this paper, we present our recent progress in fabrication and evaluation of 165 μm RCDF for high density cable applications through fiber tests and loose tube cable trials.

Keywords: Data center; Fiber cable; Fiber coating; Fiber attenuation; Fiber design; Fiber reliability; Microbending; Reduced coating diameter fiber; High density cable; Loose tube cable.

1. Introduction

Growing exponentially in bandwidth demand, hyperscale data centers ask for high density fiber solutions to meet capacity and footprint needs. To increase the bandwidth of optical transmission links, systems with higher data rates [1] and more wavelengths [2] are being developed. Another dimension for increasing the bandwidth is to increase the core density in fiber and cables. Space division multiplexing (SDM) has been proposed using new types of multicores fibers or few modes fibers [3-5]. However, a new ecosystem needs to be developed for deploying these new SDM fibers including low-cost fiber manufacturing, fan-in/out or mode mux/demux devices, splicing and connector technologies.

The fiber density can also be increased by reducing the fiber diameter. Our simple calculation indicates that the relative fiber density in a cable can be increased by a factor of 2, 3, and 4 when the coating diameter is reduced from 250 μm to 175, 145 and 125 μm, respectively [6]. The fiber diameter can be reduced by decreasing the polymeric coating thickness and/or glass diameter. Fibers with the standard 125 μm glass diameter and reduced coating diameters of 190 μm to 200 μm have been commercially available for the past decade. Further reducing the coating diameter to below 190 μm with the standard glass diameter has been proposed [6-9]. In parallel, reduced cladding fibers with a glass diameter of 80 μm and a coating diameter around 165 μm have also been proposed for DCI beyond the specialty applications [10-12].

Reducing coating thickness could face some challenges in fiber mechanical reliability and microbend sensitivity. In the past, we made RCDF in our R&D lab with coating diameters varying from 140 to 175 μm using current commercial coating materials [8]. Fiber optical measurement results showed that thin coatings didn't impose appreciable attenuation penalty on RCDF on shipping spools, however, significant increase in fiber breakage was observed during the proof test at 100 kpsi when the coating diameter was reduced below 160 μm. As a result, we selected fiber coating diameter in the range of 160-170 μm and conducted two cable trials to determine fiber handleability and cable performance. In this paper, we present our recent results in development of next generation RCDF for high density cable applications.

2. RCDF Preparation and Testing results

2.1 Fiber Coating Geometry and Optical Properties

The first cabling trial was designed to study the impact of coating thickness and core profiles on fiber handleability and cable performance. Therefore, we designed and drew four fibers having coating diameters of 160 and 170 μm with two different core profiles as summarized in Table 1. Fig. 1 shows the schematics of the core glass profile designs including a graded-index core with dual clad layers and a step-index core with a low index F (fluorine) trench. The latter profile had better bending insensitivity but more design complexity. All fibers had conventional coatings and diameters within +/- 5 μm of the target. Fig. 2 shows the cross-sectional images of one 160 μm fiber and one 170 μm fiber. Fig. 2(a) is FS160-2 with the primary coating/secondary coating diameters of 140/162 μm. Fig. 2(b) is FS170-2 dual coating layers with the primary coating/ secondary coating diameters of 148/175 μm. They show excellent coating concentricity. The concentricity errors for both the primary and secondary coatings are less than 3 μm as shown in Table 1. FS170-1 fiber had better coating concentricity than FS170-2, and FS160-2 fiber had better coating concentricity than FS160-1.

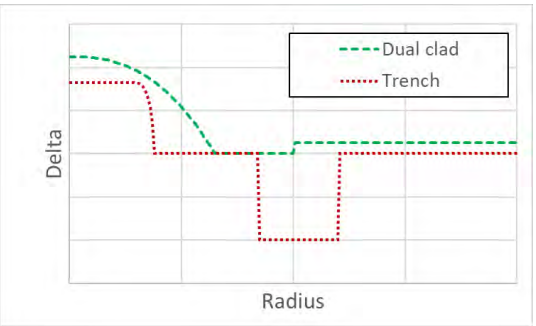


Figure 1. Schematics of core profiles designs used in RCDF

Table 1. Geometry and coating concentricity of the four 160 µm and 170 µm natural fibers tested in the 1st cable trial

Fiber Code	Core profile	Glass diameter, µm	Primary coating diameter, µm	Secondary coating diameter, µm	Concentricity error for Pri. coating, µm	Concentricity error for Sec. coating, µm
FS170-1	Dual clad	125.3	145	174	1.3	1.7
FS170-2	F Trench	125.3	148	175	2.4	2.2
FS160-1	Dual clad	125.0	140	161	0.9	2.6
FS160-2	Dual clad	125.3	140	162	0.3	1.5

Table 2. Comparison of measured cable cutoff wavelengths, MFD and attenuation between RCDF with different coating diameters and the standard 242 µm fiber

Fiber Code	Core profile	Cable Cutoff, nm	1310 nm MFD, µm	1550 nm MFD, µm	1310 nm Attenuation, dB/km	1550 nm Attenuation, dB/km
FS170-1	Dual clad	1212	9.2	10.3	0.337	0.190
FS170-2	F Trench	1261	9.2	10.3	0.332	0.191
FS160-1	Dual clad	1204	9.2	10.2	0.337	0.189
Control	Dual clad	1205	9.2	10.2	0.337	0.190

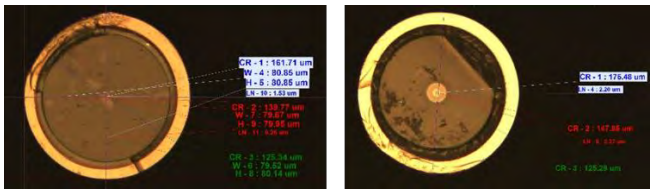


Figure 2. Cross-sectional images of two RCDF with different coating diameters: (a) 140/162 µm dual coating; (b) 148/175 µm dual coating

The fibers were characterized for cable cutoff wavelengths, mode-filed diameter (MFD) and attenuation. Table 2 summarizes the results. The fiber cable cutoff wavelength and MFD were measured using the standard FOTP procedures. The attenuation was measured on fiber wound on a standard shipping spool of 15 cm in diameter with 70 g winding tension. Table I shows that the cable cutoff wavelengths and MFD are within the typical distributions for standard single-mode fibers, i.e., cable cutoff wavelength between 1180 to 1260 nm, and MFD between 8.8 to 9.6 µm. All three RCDF show good attenuation around 0.19 dB/km at 1550 nm wavelength, similar to the attenuation of our control fiber with 242 µm coating diameter, which confirmed that thin coatings have minimal penalty on attenuation on shipping spool.

All fibers passed the proof test at 100 kpsi with fiber break rates close to the 242 µm fiber. The screened fibers were then colored using the standard off-line coloring process. No fiber breaks and other major processing issues were observed. The colored fiber diameters were in the range of 165-166 and 178-180 µm, respectively.

2.2 Fiber Microbending Testing and Results

Fiber microbending sensitivity of colored RCDF were measured along with control fibers using a method of sandpaper on a fixed drum. In this test, the fiber is wound on a drum covered with a sandpaper at varying tensions. The contact force between the fiber and the sandpaper is calculated by F = T/R where T is the winding tension, and R the drum radius. Fig. 3 shows the measured attenuation delta as a function of the external force applied to the fibers with different primary and secondary coating diameters for the dual clad and the trench profile designs. Three control fibers with coating diameters of 190, 200 and 242 μm were uncolored fibers. The mechanical properties of the ink layer are very similar to those of the secondary coating.

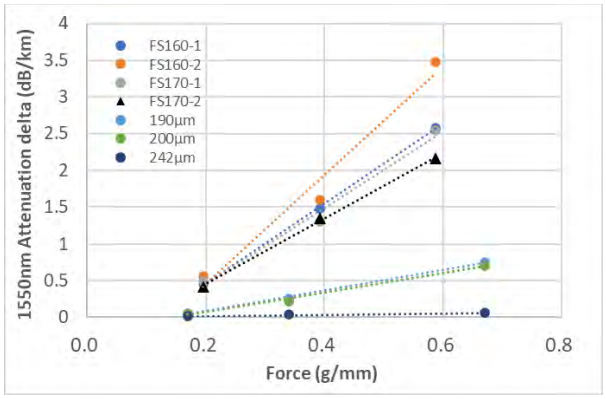


Figure 3. Attenuation increase at 1550 nm as a function of the external force applied to colored RCDF and uncolored control fibers with various primary and secondary coating diameters: FS160-1 (140/166 µm), FS160-2 (140/167 µm), FS170-1 (145/180 µm), FS170-2 (148/180 µm) with trench, 190µm (160/190 µm), 200µm (167/200 µm), and 242µm (190/242 µm)

As shown in Fig. 3, the attenuation delta increases linearly with the winding force, and the linear fits for the fibers with thinner coating or thinner primary coating have higher slopes, indicating that RCDF with smaller coating diameters have higher attenuation

sensitivity to the external force, which is also called higher extrinsic microbending sensitivity [8]. On the other hand, the trench profile has lower extrinsic microbending sensitivity than the dual clad profile with the same 142/178 µm coating diameters.

We analyzed the dependence of the slope on the fiber and coating parameters and found that the slope correlates with the ratio of the primary coating thickness over the MFD as shown in Fig. 4. The attenuation slope can be reduced by increasing the primary coating thickness or using a better primary coating material. The attenuation slope can also be reduced by using fiber designs with smaller MFD or using fiber design with a low index trench [13] as used in bend insensitive fibers.

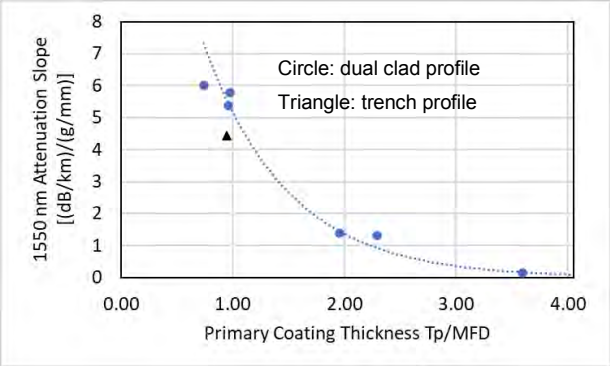


Figure 4. Attenuation change rate with external force as a function of the ratio of the primary coating thickness over the MFD

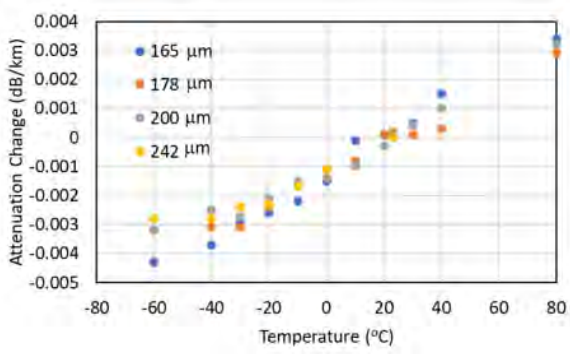


Figure 5. Attenuation change with temperature cycling on loose coiled fibers

This testing results indicate that the microbending performance depends on the force applied to the fiber in real cables. If the external force is less than 0.1 g/mm, the loss increase due to microbending is negligible. To minimize the microbend loss, it is critical to use cable designs that minimize the external force applied to the fiber for high density cables using RCDF.

To confirm the low microbend attenuation with low external force in a wide temperature range, we measured RCDF attenuation changes while the temperature was cycled from -60 to 80 °C with the fibers deployed in a loose coil configuration. Fig. 5 plots the attenuation change with temperature for fibers with four coating diameters. The performance for the 165 and 178 µm fibers are very similar to the 200 and 242 µm fibers in the loose coil configuration. The analysis and experimental results suggest that with optimized fiber designs to reduce microbend loss and optimized cable designs to minimize external perturbations, it is possible to use reduced diameter fibers for high density cables.

3. Loose Tube Cabling Trials and Results

The loose tube cable in the first trial comprises a cable jacket, 8 buffer tubes, and a glass reinforced polymer rod in the center as shown in Fig. 6. The cable had an outside diameter (OD) of 6.1 mm, an inside diameter (ID) of 4.9 mm. The buffer tubes contain 24-26 fibers, yielding a range of fiber free space, which is defined as $F_s = (A_t - A_f)/A_t$, where A_t is the inner area of the buffer tube, and A_f is total cross-sectional area of all the fibers added together. The fibers were handled and processed during cabling using the standard procedures designed for 250 µm coated fibers without any issues. No fiber breaks were detected during the cabling processing including the buffering, stranding, and jacketing steps.



Figure 6. Structure of an optical fiber loose tube cable

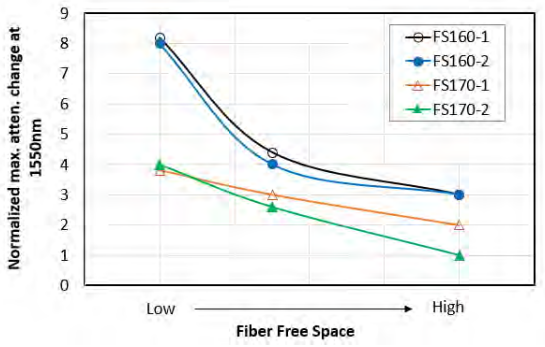


Fig. 7. Maximal attenuation changes as a function of fiber free space for 160 and 170 µm coating diameters with the dual clad and trench profile designs. FS170-2 has trench profile and others have dual clad profile

The cabled attenuation for all the fibers at room temperature in the cable easily met our typical requirement at 1550 nm. A temperature cycling test (TCT) was conducted between -40 °C to 70 °C to determine cable microbending performance. It was found that attenuation response depends on fiber density. Fig. 7 shows the maximal attenuation change between -30 °C to 70 °C at 1550 nm as a function of free space between fibers in the tube. Using a typical limit for the maximal attenuation change, we see that the free space needs to be greater for the 160 µm as compared to the 170 µm coated fibers with the dual clad design, respectively to meet the -30 °C requirement. It is worthwhile to point out that the free space limits are specific to the test cable used and could vary significantly with cable design. For the 160 µm coated fibers FS160-1 and FS160-2 having different coating concentricity, we didn't observe significant difference in fiber handleability and

cable performance. For the 170 µm coated fiber FS170-2 with the trench design, the free fiber space can be reduced further, although the trench profile has not been fully optimized. The results indicate that choosing the right free space is an effective way to ensure the microbend performance for RCDF in a loose tube cable. Cable design must be adapted to these RCDF to get lower response.

The second loose tube cabling trial was conducted to further confirm fiber handleability and evaluate cable performance of RCDF with optimization of trench profile design. Three same coating diameter fibers were designed to have a range of MAC number which is defined as the ratio of the mode field diameter and cutoff wavelength in common units. A total length of 300-400 km was drawn for each fiber, followed by screening at 100 kpsi. The fiber break rates were similar to typical break rates for 242 µm fiber. The attenuation loss on the shipping spools was similar to the standard production fibers with coating diameters of 190 and 200 µm, respectively. The fibers were colored and ring-marked without fiber breaks detected through an off-line coloring process. The post-coloring fiber OD was measured to be 166-167 µm, which is the same as the 160 µm fibers in the first cable trial.

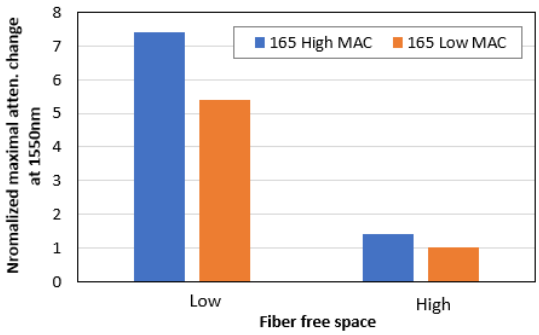


Figure 8. Maximal attenuation changes at -40 ºC for colored 165 µm fibers cabled in buffer tubes of low and high free spaces, respectively

In the second cable trial we used the same 8-tube cable design and similar two tube ID sizes. Two free space values, low and high, were selected from a range of free space similar to that in the first cable trial. The cabled attenuation for all the fibers at room temperature in the cable was good and below 0.20 dB/km at 1550 nm. The TCT results show that all 160 µm fibers with high free space passed -40 ºC test with maximal attenuation increase below our normal requirement. On the other hand, all fibers with low free space didn't pass -40 ºC test with the cabled attenuation higher than our requirement. The low MAC fibers showed slightly lower attenuation increase than the high MAC fibers, as shown in Fig.8. As a comparison, the dual clad 160 µm fibers in the first cable trial with similar free space had doubled maximal attenuation change at -40 ºC compared to the fibers in this trial with the optimized trench profile. Therefore, core glass profile design is another approach to improving the microbend performance for RCDF in a loose tube cable.

It is worthwhile to point out that in both cabling trials, the standard cleavers, strippers, and splicers were used during cable testing for cleaving, stripping, and splicing. No significant issues were detected.

4. Conclusions

All fibers with coating thickness of 160 and 170 µm passed the proof test at 100 kpsi with fiber break rates close or similar to the 242 mm fiber. The attenuation on shipping spools was identical to the 242 µm fiber, indicating that there is no significant attenuation penalty for thin coatings. The sandpaper microbending test showed higher microbending sensitivity for RCDF, depending on the external force. Thermal cycling of these small diameter fibers exhibited comparable attenuation changes to the 242 µm fiber in a loose coil. The screened fibers went through coloring and cabling processes without major issues in both trials, indicating good fiber handleability.

The cable attenuation for all the fibers at room temperature was well below our typical requirement at 1550 nm. In the thermal cycle test, the first loose tube cable trial showed that the maximal attenuation changes at -30 ºC decreased with increasing fiber free space in tubes. It was found that the free space needs to be greater for the 160 µm than the 170 µm coated fibers with the dual clad design to meet the maximum attenuation change limit at low temperatures. In the second trial, the cable with 160 µm fibers passed -40 ºC thermal cycle test with maximum attenuation change smaller than our typical requirement at 1550 nm due to use of optimal trench profile design. Furthermore, no cleaving, stripping and splicing issues were observed during cable testing using the standard processing tools. In conclusion, through optimization of both the fiber design and cable design, the RCDF with coating diameter around 165 µm could be a promising candidate for high density cable applications.

5. References

[1] IEEE P802.3bs 400 Gb/s Ethernet Task Force, 2018. [Online]. Available:www.ieee802.org/3/bs/

[2] IEEE P802.3cw 400 Gb/s over DWDM Systems Task Force, 2022. [Online]. Available: www.ieee802.org/3/cw/

[3] M. Li, "New development trends in optical fibers for data center", in *Proc. Eur. Conf. Opt. Commun.*, 2018, pp. 1–3.

[4] D. L. Butler et al., "Space division multiplexing in short reach optical interconnects," *J. Lightw. Technol.*, 35(4), 677–682 (Feb. 2017).

[5] Y. Sasaki, R. Fukumoto, K. Takenaga, S. Shimizu, and K. Aikawa, "Optical fiber cable employing 200 μm-coated multicore fibers for high density wiring in datacom," in *Proc. Opt. Fiber Commun. Conf. Exhibit.*, 2021, pp. 1–3.

[6] W. Niu et al., "Thin-coated fibers for high-density optical interconnects", in *Proc. Op. Fiber Commun. Conf. Exhibit.*, 2021.

[7] P. Sillard, A. Amezcua-Correa, H. Maerten, and C. Mentzler, and A. Pastouret, "180μm-coated bend-insensitive fiber and micro-duct cable," in *Proc. Eur. Conf. Opt. Commun.*, 2021, pp. 1–4.

[8] M. Li, "Reduced coating diameter fibers for high density cables," in *Proc. Opt. Fiber Commun. Conf. Exhibit.*, 2022, pp. 1–3.

[9] P. Sillard, A.Amezcua-Correa, C.Mentzler, and G. Ferri, "Reduced-coated fibers and micro-duct cables," in *Proc. Opt. Fiber Commun. Conf. Exhibit.*, 2022, pp. 1–3.

[10] S. R. Bickham, M. A. Marro, J. A. Derick, W.-L. Kuang, X. Feng, and Y. Hua, "Reduced cladding diameter fibers for

high-density optical interconnects," *J. Lightw. Technol.*, 38(2) 297–302 (Jan. 2020).

[11] K. Mukasa, T. Mihálffy, and Z. Várallyay, "Optimizations of thin cladding diameter fibers," in *Proc. Opt. Fiber Commun. Conf. Exhibit.*, 2021, Paper M3C.1.

[12] S. Matsuo et al., "1,728-fiber cable with 12-fiber ribbons comprising 160 μm coating fiber with 80-μm cladding," in *Proc. Opt. Fiber Commun. Conf. Exhibit.*, 2021, Paper M3C.3.

[13] P. Sillard, S. Richard, L. -A. de Montmorillon, and M. Bigot-Astruc, "Micro-bend losses of trench-assisted single-mode fibers," in *Proc. 36th Eur. Conf. Exhib. Opt. Commun.*, 2010, pp. 1–3.



Yunfeng Gu, Corning R&D Corporation, SP-FR-03-R3S12V, 1 Riverfront Plaza, Corning, New York 14831. Yunfeng received Ph.D. in Materials Chemistry from University of Science and Technology of China in 1999. After completion of postdoc research in Kyushu University in Japan and Virginia Tech, he joined Corning in 2006. His expertise and contribution to Corning have been focused on research and early-stage development in materials and processing across different fields - ceramic membranes & separation, glass surface treatment & coating, and optical fibers. Currently he is a project lead for early-stage development of next generation optical fibers. He holds 23 U.S. patents and has 32 peer-reviewed Journal papers published.



Weijun Niu, Corning R&D Corporation, SP-FR-06-R6S29E, 1 Riverfront Plaza, Corning, New York 14831. Born in China, Weijun earned a B.S. in chemistry from Hangzhou Normal University, a M.S. in physical chemistry from Hangzhou University, and a Ph.D. in chemistry from University of New Hampshire in 2003. After completing his post-doctoral research in organic chemistry form the North Carolina State University and the University of South Carolina, he joined Corning in 2008 as an organic chemist in the Organic and Biochemical Technologies department, where he has conducted fundamental and applied research related to novel organic materials and coatings. His applied research work includes fiber coatings and designing of different types of reduced coating diameter fibers, different glass coatings such as coatings for pharmaceutical vials and coatings related to foldable glass and display glass, waste glass recycling, and organic materials syntheses. Weijun has obtained 32 granted patents, about 50 patent applications and 16 peer-reviewed publications from his applied research work at Corning.



Brett Knowlton, Corning R&D Corporation, SP-TD-02-T2N15JJ, 1 Riverfront Plaza, Corning, New York 14831. Brett has been working for Corning Incorporated as a Development Draw Technician since 2017. He spent several years running a specialty fiber production draw before recently moving to a research and development focused draw tower. Brett also maintains the departments Hydrofluoric Acid bench and is a Safety Coordinator.



Bryan Wakefield, Corning Research and Development Corporation, SP-TD-02-T2N17Y, 1 Riverfront Plaza, Corning, New York 14831. Bryan received a Bachelor of Science degree in electrical engineering from The Pennsylvania State University and a Master of Science in Engineering Science (major in mechanical engineering) from the Naval Postgraduate School. Bryan served 5 years in the U.S. Navy as a nuclear engineer. Bryan has worked for Corning Incorporated since 2005, spending the entirety of his career in optical fiber. Currently he is the draw supervisor in the Applied Research and Development directorate for Optical Communications.



Jeffery Stone, Scientist and Distinguished Associate of Corning R&D Corporation. He has consistently delivered ground-breaking innovation throughout his 26-year career with Corning. His impact spans research and development for multiple businesses. He has contributed to multiple Journal publications as well as holds 18 patents.



Hector de Pedro, Corning R & D Corporation, 1 Riverfront Plaza, Corning, New York, 14831. He received his Ph.D. in Physics from the University of Texas in Dallas. He is a measurement development supervisor supporting the measurement development activities for Corning Optical Communications.



Aditya Kaimal, Corning Optical Communications, 310 N. College Rd., Wilmington, NC, USA. Aditya attended Georgia Institute of Technology and North Carolina State University, where he studied Mechanical Engineering and received Bachelor and Master of Science degrees. In 2011, he joined the Product and Process Development (PPD) department at Corning Optical Communications as a development engineer. During his career at Corning, he has developed and deployed different optical fiber testing and processing equipment and methods. Currently, he is a sr. development engineer in the PPD group in Wilmington, NC



Darren Stainer, Corning R&D Corporation, WL-STF-1-8, 310 N College Rd, Wilmington, North Carolina 28405. Darren received his bachelor's in chemical engineering from Swinburne University of Technology in Melbourne Australia in 1992. He has worked for Corning Incorporated since graduation and has held many roles across multiple locations in both manufacturing and development. His expertise and interests have been focused on fiber drawing, UV coatings and fiber measurements. He is currently the Product and Process Development Manager for optical fiber.



Sebastian Olszewski, Corning Optical Communications Polska, Smolice 1e,95-010 Strykow, Poland. Sebastian (born in 1979) attended the Technical University of Białystok, where he studied optoelectronics and received Master of Science degree. In 2006, he joined the Cable Development department of Corning Cable Systems Poland as a process engineer. During his career at Corning, he has designed and developed numerous mini cable products. Currently, he is a head of process and product development team in Stryków.



Sonya Raney, Corning R&D Corporation, 310 North College Road, Wilmington, NC 28405. Sonya received a M.S. in Chemical Engineering from North Carolina State University (1996) and B.S in Chemical Engineering from Auburn University (1994). In her 26 years with Corning, she has specialized in the invention, development, and commercialization of new optical fiber products and processes. Currently she is a project lead for development of next generation optical fibers.



Scott Bickham is a Development Fellow in the Corning Research and Development Corp. supporting Corning Optical Communications. He received a B.S. in physics from Purdue University in 1984 and his M.S. and Ph.D. degrees in physics from Cornell University in 1991 and 1995, respectively. Dr. Bickham holds over 100 patents relating to optical fibers and has co-authored over 60 publications.



Ming-Jun Li, Corning R&D Corporation, SP-AR-02-4, 1 Riverfront Plaza, Corning, New York 14831. Ming-Jun joined Corning in 1991 and is currently a Corporate Fellow. He has contributed to many single mode and multimode fiber products for optical communications and specialty fibers for different applications. He is a member of the US National Academy of Engineering, a Fellow of Optica and IEEE. He was inducted into the National Inventors Hall of Fame in 2022. He has served as Associate Editor and Coordinating Committee Member, and currently is Deputy Editor for Journal of Lightwave Technology. He has also served as a guest editor for several special issues and as committee chair or member for many international conferences. He holds 282 U.S. patents and has published 6 book chapters and authored over 350 technical papers.

High density micro cable family with next generation 190 micron fibers

Sebastian Olszewski[1], Snigdharaj K Mishra[2],

[1] Corning Optical Communications Polska Sp. z o.o. Smolice 1e,95-010 Strykow, Poland
[2] Corning Research & Development Corporation, 310 N. College Rd. Wilmington, NC 28405

Abstract

Micro cables were first introduced in the market more than 20 years ago and have evolved over time, becoming smaller and lighter weight. The main features such as low weight, small diameter and high fiber density make them ideal for installation by air blowing into modern duct systems.

Increasing global demand for high-speed network access has caused displacement of some conventional outside plant cables by micro cables which require less space and smaller ducts. The demand for maximum utilization of existing duct systems drives a further increase in fiber density in these cables. It requires development of low diameter fibers that can be used in increasingly more dense cable conditions. So far, 8/10mm (ID/OD) micro duct could accommodate 144f cable, while 10/12mm could 216f cable. With new 190-micron fibers and re-designed cables ducts can accommodate 192f and 288f respectively.

The 190-micron fiber used in these micro cables combines lower attenuation with improved bend performance that is fully compliant with international standards, such as ITU-T G.652.D and G.657.A2 recommendation. This fiber also provides greater MFD compatibility with legacy single mode fibers (9.2 +/- 0.4 µm).



Figure 1. Cross section of 192f micro cable

Keywords: micro cable, 190micron fiber, ITU G.652.D, ITU G.657.A2, high density cables, blowing, thermal cycling.

1. Introduction

Micro cables are designed to be installed by blowing/jetting with support of compressed air. This technique has been well-established and spread to many types of optical networks: long-haul and city-ring networks, as well as for fiber-to-the-home (FTTH) networks and recently in-building networks.

For optimum blowing performance, cable-duct filling ratio (calculated as cable outer diameter divided by duct inner diameter) is advised to be in the range of 50-80%. Lower values can lead to cable buckling while values greater than 80% may not be practical due to increased friction in undulated ducts. Other important parameters are coefficient of friction and cable stiffness, which must be optimized during development of new cables. Despite their very small size, micro cables exhibit all the design attributes of the well-known standard duct cables with the benefit of being tailored for their specific application. The micro cables discussed herein have six (144f) up to twelve (288f) tiny buffer tubes stranded around a glass-reinforced central member, surrounded by a high-density polyethylene jacket. This micro cable design advantageously combines a smaller outer diameter, low weight, outstanding blowing-in performance and easy mid-span access with an excellent operating temperature window from -40°C to 70°C.

This paper describes high density micro cables up to 288 fibers optimized for blowing (jetting) installation utilizing a next generation G.657.A2 bend insensitive fiber having a 7.5 mm minimum bend radius, a 9.2 µm mode field diameter, 0.32 dB/km low loss at 1310 nm and 0.18 dB/km low loss at 1550 nm and a 190 µm low outer diameter.

2. Initial experiment

To compare the performance and select the optimized fiber solution, a cable experiment was performed using targeted 192f 6.2 mm cable. The cable was designed to fit in an 8/10mm duct with approximately 77% filling ratio. The cable consists of eight buffer tubes, with 24 fibers in each tube stranded around glass reinforced plastic rod and jacketed with easy open features. The cable design and manufacturing process were modified to make the cable more susceptible to fiber micro-bending and macro-bending such that fibers of different designs and having different coating diameters can be studied for room temperature and cold temperature performance.

The goal of the experiment was to compare cabled fiber attenuation and cold temperature response of the following fibers:

- G657.A2 fiber with 9.2 µm MFD - newly developed,
- G657.A1 fiber with 9.2 µm MFD - legacy,
- G657.A2 fiber with 8.6 µm MFD - legacy.

Each fiber type was used with both 200 µm and 190 µm outer diameters with similar ratios of secondary coating to primary coating thickness of about 0.8.

For the experiment, series of 192f cables were manufactured, with eight of the buffer tubes having 200 µm fibers and the other eight

tubes having 190 µm fibers. In each buffer tube 12 fibers were simply colored and the remaining 12 fibers were ring marked and colored for identification purposes. Each buffer tube contained a mixture of three fiber types listed above.

Attenuation of experimental cables was measured using an OTDR. Fig. 2 shows the attenuation response of two 192-fiber cables on the reel in ambient temperature. It was observed that the 190 µm diameter fibers showed lower attenuation and smaller spread compared to the 200 µm diameter fibers. The lowest attenuation was measured for the newly developed 9.2 µm MFD G657.A2 fibers with 190 µm OD.

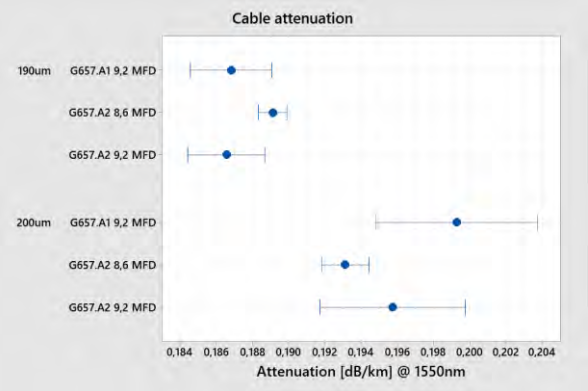


Figure 2 Attenuation behavior at 1550 nm at ambient temperature of different fiber types having different coating thicknesses.

The experimental cables respooled to loose coils were next subjected to temperature cycling tests according to the temperature profile shown in Fig10.

Fig. 5 shows normalized results of the attenuation increase of the different fibers in experimental cables. It was observed that the 9.2 µm MFD G657.A2 fiber demonstrated significantly lower attenuation increase at -40°C for both 200 µm and 190 µm coating diameters compared to the 9.2 µm MFD G657.A1 fiber. The attenuation increase for the 9.2 µm MFD G657.A2 fiber was approximately 75% lower than 200 µm legacy G657.A1 and more than 50% lower compared to 190 µm legacy G657.A1. Furthermore, the loss performance of 9.2 µm MFD G657.A2 fiber during thermal cycling was comparable to the G657.A2 fiber with 8.6 µm MFD, despite having much higher MFD that is matched to legacy single-mode fibers.

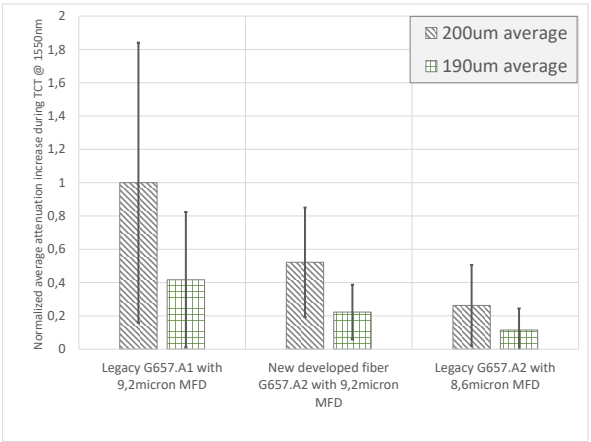


Figure 3 Normalized attenuation increase during thermal cycling test observed in different fibers in cables

3. 190 micron fiber

Typically, most 190-micron fibers in the market have a smaller MFD compared to standard single mode fibers to realize improved bend performance. Corning's G.657A2 fiber is designed to deliver enhanced macrobending and microbending performance while maintaining compatibility with current equipment, practices, and procedures by having a 9.2 µm MFD. Its 190-micron diameter coupled with better bend resilience makes this newly developed fiber ideal for high density cable applications. This full-spectrum fiber is operational in regional, metro, access, mobile, and fiber to the home (FTTH) applications.

This new 190-micron fiber design also offers improved attenuation (Figure 4) to extend the reach of a network and yield greater subscriber coverage from a central office to raise the possibility of central consolidation in access networks as well as the wider application of micro cables in Long Haul networks.

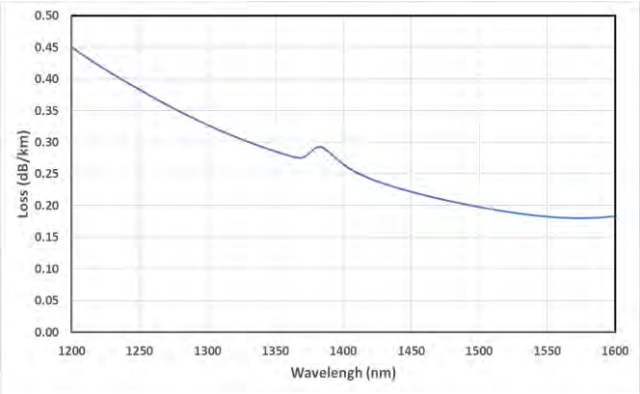


Figure 4 Spectral attenuation of the G.657.A2 190um fiber.

This newly designed 190-micron fiber also exhibits better macrobend and microbend performances. Fig.5 and Fig.6 show the macrobend and microbend loss of this fiber.

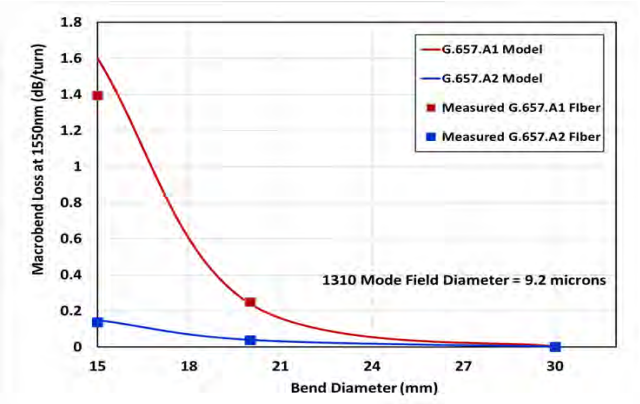


Figure 5 Macrobend loss of the G.657.A2 fiber

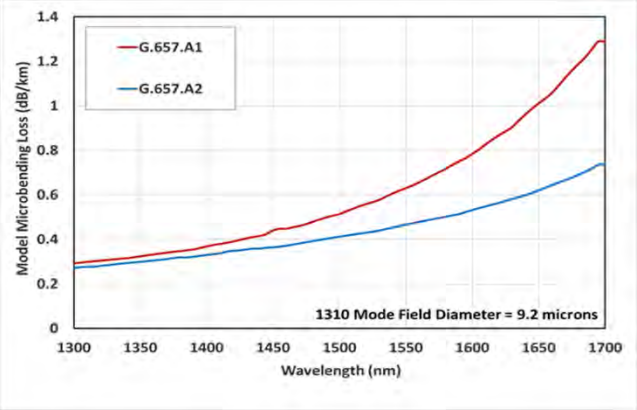


Figure 6 Microbend loss of the G.657.A2 fiber

We tested homogeneous and heterogeneous fusion splice performance of the G657A2 with 9.2MFD fiber as well as splicing performance to other Corning optical fibers. All fiber splices were completed using a commercially available active core alignment fusion splicer, Fujikura 90S, using a standard pre-set factory program (SM-AUTO). Table.1 shows the splice loss of the G.657.A2 fiber with other fibers.

Table 1 The newly developed G657A2 with 9.2MFD Fiber Typical Splice Loss to Other Corning Optical Fiber Products

Fiber A	Fiber B	1310 nm		1550 nm		1625 nm	
		Mean (dB)	Max (dB)	Mean (dB)	Max (dB)	Mean (dB)	Max (dB)
G657A2 with 9.2MFD	G657A2 with 9.2MFD	0.02	0.04	0.02	0.03	0.02	0.03
G657A2 with 9.2MFD	SMF-28 Ultra optical	0.02	0.05	0.02	0.04	0.02	0.04
G657A2 with 9.2MFD	SMF-28e+ optical	0.04	0.09	0.03	0.06	0.04	0.06
G657A2 with 9.2MFD	SMF-28 ULL optical	0.03	0.05	0.04	0.07	0.05	0.08
G657A2 with 9.2MFD	ClearCurve ® LBL optical	0.03	0.07	0.03	0.05	0.03	0.06

4. Cable Design

4.1 Basic Requirements

General market requirements for high fiber count micro cables are:

- wide range of operating temperature typically from -30 to 70^{0}C,
- long installation lengths
- easy fiber identification and handling
- mechanical properties for optimal installation
- optical compatibility with existing networks

Detailed cable design requirements for a next generation family of cables were set to optimize cable outer diameter to common duct sizes therefore 192f cable must fit to 8/10mm duct or 288f cable in 10/12mm duct. Cable modelling shows that those requirements can be achieved with 24 fiber per tube design. Calculation indicates that 36 fiber per tube design allows further reduction of cable OD, but some may prefer to stick with 24 fibers per tube and avoid differences in handling during splicing or fiber distribution in splice trays.

4.2 Cable Design

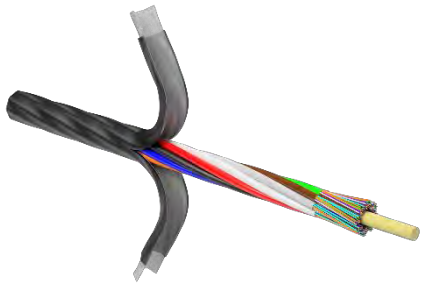


Figure 7 Exemplary 3D render of experimental cable.

A new cable family was modeled and consists of 4 designs. All cables were built over a glass-reinforced (GRP) central strength member with numerous SZ stranded tubes with 24 190micron fibers. The duct size and the maximum cable OD limited the buffer tube OD to a maximum of 1.4 mm, all jacketed with high-density polyethylene (HDPE) with jacket wall thickness of approx. 0.5 mm.

Table 2 below includes basic data about this new micro cable family based on 190 micron fibers:

Table 2 Cable design

Fiber count	144f	192f	216f	288f
Cross section				
Cable OD	5.4mm	6.2mm	7mm	8.1mm
Fiber density	6.29f/mm^2	6.36f/mm^2	5.61f/mm^2	5.59f/mm^2
Dedicated duct	8/10mm	8/10mm	10/12mm	10/12mm
Duct fill ratio	68%	78%	71%	81%

In order to accommodate the extremely small cable diameter, no additional tensile strength elements were included. Nevertheless, the expected maximum short-term fiber strain during installation is well below 0.33% at 1000 N tensile force, which ensures maximum lifetime of the optical fiber.

Materials for the buffer tube were selected to ensure excellent thermal stability especially when un-opened buffer tubes are routed for slack storage at a splice point and to guarantee a mechanically stable tube with maximum inner diameter, resulting in an optimum temperature operating window from -40° to 70°C.

Easy opening features were redesigned from double lobes to double grooves to reduce max cable diameter and further improve blowing performance with similar function of locator of cable opening.

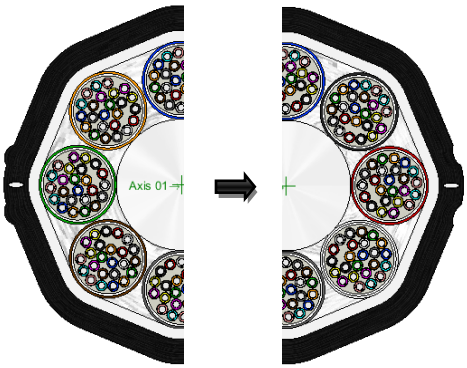


Figure 8 Old (left) and new (right) design of opening features

5. Cable Performance

5.1 Cable Test Results

The newly developed cable family has been tested according to the IEC 60794-1 standard in our internal laboratory. Testing parameters were set to check typical micro cable requirements and real limits of cable performance. Table 3 shows the list of tests performed during qualification.

Table 3 Cable testing plan

Parameter	Specification	Details/ Comments	Specification reference
Water penetration	No Water	1m sample / 1m head / 24hr	IEC60794-1-22
Tensile – Under load	Fiber Strain ≤ 60% proof strain	1000N	IEC60794-1-21
Tensile - Residual load	Fiber Strain ≤ 20% proof strain Attenuation ≤ 0.15dB	30% of rated load above	IEC60794-1-21
Tensile – Removed Load	Attenuation ≤ 0.05dB	Load removed after test above	IEC60794-1-21
Crush	During load: Attenuation ≤ 0.15dB After test: Attenuation reversible	50N/cm 1min	IEC60794-1-21
Impact	During load: Attenuation ≤ 0.15dB Attenuation ≤ 0.1 dB @ 1550nm	1 Impacts min 300mm Rad hammer 1Nm in 3 locations 150mm apart	IEC60794-1-21
Bend	Attenuation reversible after test <=0.05 dB	Bend Diameter: 20 X Cable OD 5 turns 3 cycles	IEC60794-1-21
Repeated Bending (Cycle Flex)	No Cable Damage Max ≤ 0.15dB	Bend Diameter: 10 X Cable OD Load 50N 25 cycles	IEC60794-1-21
Bend (Hot/Cold Bend)	No Cable Damage Max ≤ 0.10dB	50C & -20C Bend Diameter: 20 x Cable OD 4 turns 3 cycles	IEC60794-1-21
Torsion (twist test)	No Cable Damage Attenuation reversible after test <= 0.05dB	2m ±180° and 10 cycles	IEC60794-1-21
Cable Kink	No Cable Damage Kink OD < 40 X Cable OD	Calculation for Loop OD = Circ/π	IEC60794-1-21
Temperature Cycling	@ 1550 ≤ 0.05dB/km @ 1550 ≤ 0.15dB/km	2 full cycles in Pans (-30C to 70C) (-40C to 70C)	IEC60794-1-22
Aging	Avg ≤ 0.10dB/km Max ≤ 0.25dB/km	85C 168 hr + 2 full cycles (-40C to +70C)	IEC60794-1-22

Figure 9 shows cable attenuation in room temperature collected from 10 drums of 6km 192f cables. Average values and standard deviations confirm low attenuation of fibers in cabled form.

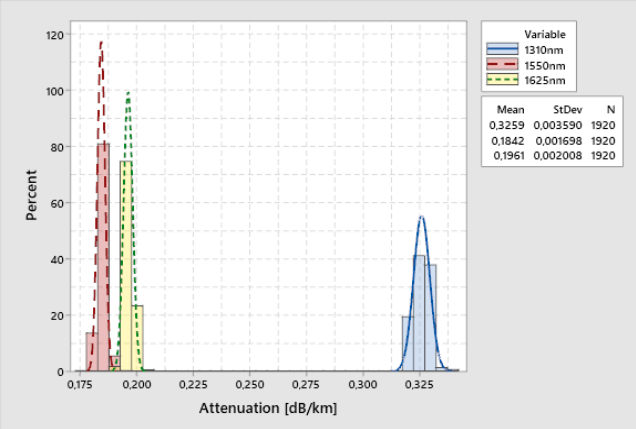


Figure 9 Distribution of cable attenuation coefficients at 1310nm/1550nm/1625nm from 10 cables.

Figure 10 summarizes the attenuation increase during temperature cycling of these cables. Max increases and standard deviations at -30C and -40C are low, as expected, and prove that despite the high fiber density, excellent test results can be reached for newly developed 9.2 µm MFD G657.A2 fiber.

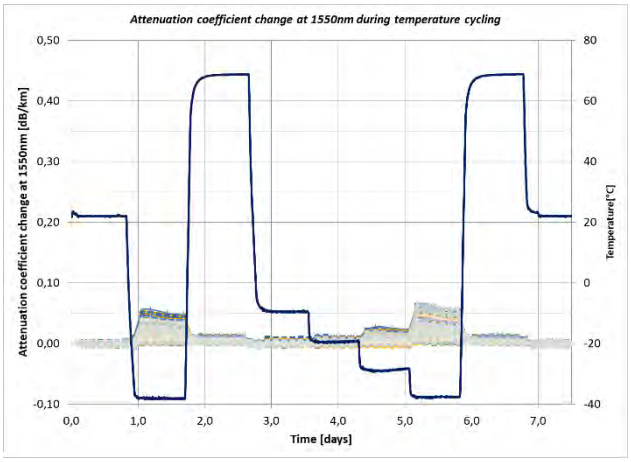


Figure 10 Attenuation changes during temperature cycling.

5.2 Blowing-in performance

Cable installation trials were conducted at Vetter GmbH Kabelverlegetechnik in Germany. For the testing, best in class blowing equipment, MiniJet-System with IntelliJet-P02 (Plumettaz) was used. For each cable, a different duct size was prepared according to table 2 with a length of more than 2000m. Before each trial the duct was calibrated, crash test for setup of maximum pushing force performed and a sponge with standard lubricant was blown through the duct.

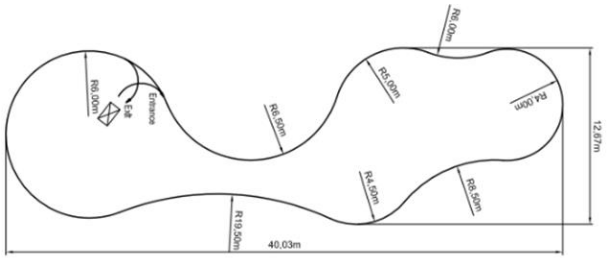


Figure 11 Vetter GmbH Kabelverlegetechnik test track

The results of the blowing-in trial are shown in Figure 12. All cables were blown in similar condition, and each achieved blowing distance exceeding 2000m. After the trial each cable was blown out which means that reinstalling the cables is possible too. This excellent result illustrates the advantages of the optimized design parameters of the micro cable such as a small diameter, low weight, adequate cable stiffness and low friction.

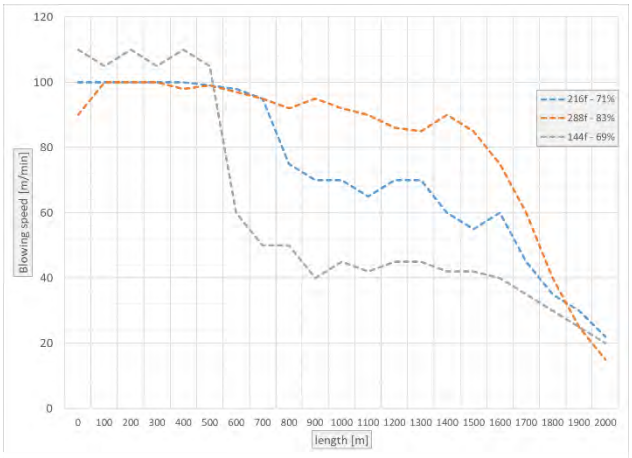


Figure 12 Blowing-in performance of 144f, 216f and 288f micro cables.

6. Conclusions

High density micro cables intended for installation by blowing into micro ducts with newly developed 190 micron fibers were designed, manufactured, and tested.

Even though the dimensions of these cables had to be scaled down to fit into standard duct sizes, these cables easily fulfilled all the requirements. Cable OD and weight reduction of approximately 15%, and plastic components reduction close to 50% led to significant carbon footprint decrease of the new cable family. Their excellent temperature performance between -40° to +70°C is particularly noteworthy because the attenuation change at 1550 nm was less than 0.05 dB/km. The optimization of the design parameters such as OD, weight, stiffness, and friction led to a blowing-in performance of at least 2000m with a high blowing speed. Utilization of a new bend improved, low loss fiber with the same MFD as standard single mode fibers in high density micro cables extends the application of 190 micron fibers for all sections of the fiber optic network.

7. References

[1] A. Weiss, P. Lausch, K. Nothofer, "Optimized 72f Cable for Blown Installation in 10/8 mm Microducts", *Proceedings 52 IWCS/Focus 2003*, p.38 f, (Nov.2003)

[2] Pushkar. Tandon, Snigdharaj Mishra, Roshene McCool (1), Sebastian Olszewski, Mike Ellwanger: "Performance of Large Mode Field Diameter (MFD) Bend Insensitive G.657.A2 Optical Fiber in High Fiber Density Cables" IWCS2022

8. Authors:

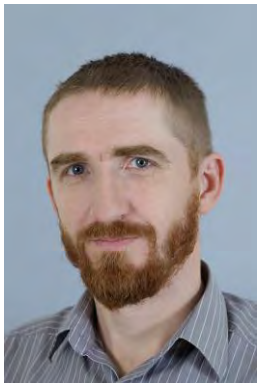
Presenting author:

Sebastian Olszewski

Corning Optical Communications Polska

Smolice 1e,95-010 Strykow,

Poland



Sebastian Olszewski (born in 1979) attended the Technical University of Białystok, where he studied optoelectronics and received Master of Science degree. In 2006, he joined the Cable Development department of Corning Cable Systems Poland as a process engineer. During his career at Corning he has designed and developed numerous mini cable products. Currently, he is a head of process and product development team in Stryków.

Co- author:

Snigdharaj K Mishra

Corning Research & Development Corporation

310 N. College Rd, MS-6

Wilmington, NC 28405



Dr. Snigdharaj (Raj) Mishra is a Development Fellow with Corning Optical Fiber in Wilmington, NC, USA. His work has included modeling and simulation, design, development, and characterization of optical fibers. Dr. Mishra joined Corning in 1999 after completing post-doctoral research works in Physics at Massachusetts Institute of Technology and Max-Planck Institute, Stuttgart, Germany and began working on submarine and terrestrial transmission fiber systems. During his career at Corning he has designed, developed and is the co-inventor of more than 15 new optical fiber products for various applications. He has B.S, M.S, and PhD degree in Physics. Dr. Mishra holds 71 US patents and has co-authored 35 publications. He has also co-authored a chapter in a book. He serves as Editorial Board Member of American Journal of Optics and Photonics.

Development of a High Fiber Density 432-Fiber Microduct Cable

Ray Lovie
Prysmian Cable and Systems USA, LLC
Claremont, North Carolina 28610
+1-828-459-8356 · ray.lovie@prysmiangroup.com

Abstract
This paper describes the design, development, and qualification testing of a next-generation, small-diameter, lightweight optical fiber cable. This cable contains 432 bend-insensitive single-mode fibers and is intended for installation by air-blowing. Fiber density has been maximized and raw material usage has been greatly reduced compared to legacy designs of equal fiber count, with no reduction in environmental or mechanical performance and no compromise in fiber reliability.

Keywords: Optical fiber; microduct; blowing; fiber density; sustainability

1. Introduction
The demand for digital services is increasing at a very high rate. The wide popularity of 5G telecom, social media, entertainment streaming, and internet usage requires the generation, transportation, and storage of massive amounts of digital data. State-of-the-art fiber optic networks are being built, creating a demand for high fiber count optical cables. One popular means of deploying such cables is by using buried multi-path microducts and specially designed microduct cables intended for installation by cable jetting technology (blowing).

Network installers and operators are being challenged to save space, time, and costs. These challenges are passed on to cable manufacturers, who must find ways to reduce material and labor cost without compromising performance and reliability. This can be achieved by using microduct and microduct cable technology to replace the incumbent duct-pull and direct buried installations of traditional outside plant loose tube cables.

2. Cable Design
A next-generation microduct cable has been developed, containing 432 single-mode optical fibers. The main features of this cable include:

Optical fibers complying with G.657.A2 requirements and having a coating diameter of 200 microns. Compared to traditional 250-micron fibers, each optical fiber itself consumes 36% less space

Optical units with a diameter of 1.40mm, each containing 24 fibers. Ring-mark fiber color-coding is used. Each miniature unit forms a tight, color-coded sheath to segregate 24-fiber groups, unlike the traditional loose tube structure where the inside diameter of the tube is greater than the diameter of the fiber bundle.

A thin, rugged overall jacket, having a diameter of 8.0 millimeters. The jacket material has a coefficient of friction ideal for installation by blowing into a 10-millimeter (inside diameter) duct.

The cable has flexibility that allows it to be handled easily, yet it is stiff enough to maximize blowing distance.

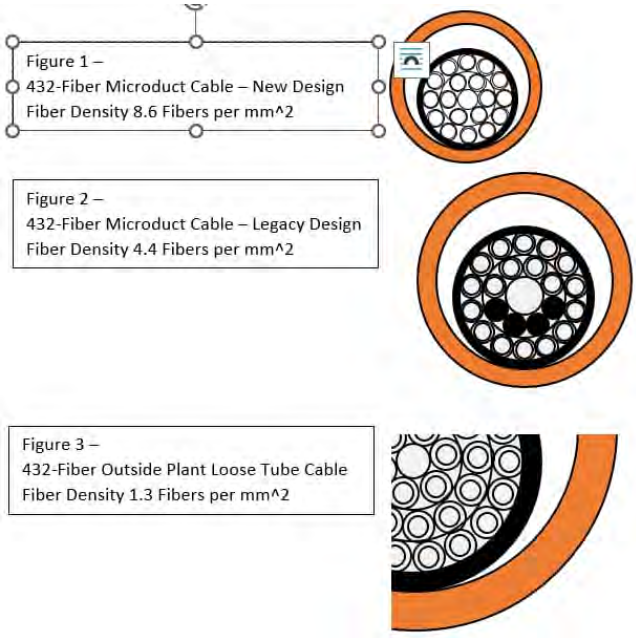
The finished cable has a fiber density of 8.6 fibers per mm^2 of cable cross-section.

To fully appreciate the reduction in cable and duct size, the following figures are presented (all to the same scale):

Figure 1: The next-generation 432-fiber microduct cable, placed in a 14/10 microduct

Figure 2: A legacy 432-fiber microduct cable, placed in a 18/14 microduct

Figure 3: A traditional non-armored 432-fiber outside plant loose tube cable, placed in a 32/26 duct.



3. Manufacturing Processes and Material
Well-known traditional loose-tube manufacturing processes and materials served as the basis for this development, however certain material and process advancements were required to ensure high-speed and high-yield manufacturing.

The use of 200-micron bend-insensitive fiber provided a foundation for the overall reduction in cable size

Densely packed, very small optical units are made from specially formulated thermoplastic compound, color concentrates, and filling gel. These materials are ideal for high-speed, thin-wall extrusion.

Exact extruder output control and precise filling gel application within the unit making process. Automated flaw detection and reporting prevent any defects in the unit from reaching the stranding operation.

Core stranding requires tight control of payoff and take-up tensions. Small, lightweight cross-binders are applied with low tension to avoid indenting or otherwise damaging the units.

Precise tension control at jacketing is required to avoid damaging the core or finished cable. Automated flaw detection and reporting prevent jacket holes or lumps that would ultimately compromise the efficiency of the blowing process.

4. Sustainability

There is a keen awareness of the topic of environmental sustainability and the desire to reduce, re-use, and re-cycle materials. This new cable offers substantial reductions in the volume of fiber coatings, in the amounts of raw materials forming the cable structure, and in the amounts of raw materials forming the microducts themselves. These are shown in Table 1.

Table 1. Material Reduction

	Legacy Microduct Cable	New Microduct Cable	REDUCTION	INCREASE
Coating Cross-Section (mm^2)	14.6	8.3	-43%	
Cable Diameter (mm)	11.2	8.0	-29%	
Cable Cross-Section (mm^2)	98.5	50.3	-49%	
Cable Weight (kg/km)	103	54	-48%	
Duct Inner Diameter (mm)	14	10		
Duct Outer Diameter (mm)	18	14	-22%	
Duct Cross-Section (mm^2)	101	75	-25%	
Fiber Density (f/mm^2)	4.4	8.6		95%

Apart from the finished cables themselves, additional materials and cost saving can be realized in the areas of packaging and transportation. Smaller spools can be used, owing not only to the smaller cable diameter, but also to the smaller allowable bend radius. Consider a fixed length of each of three different finished cables, each coiled to their minimum bend radius. The relative volumes occupied by such cables are shown in Table 2.

Table 2. Volume Reduction

	Standard OSP Cable	Legacy Microduct Cable	New Microduct Cable
Cable Diameter (mm)	20.4	11.2	8.0
Minimum Bend Radius (mm)	204	112	80
Relative Volume Units	100	33	16
Volume occupied by a fixed length of cable			

5. Performance Testing

For this development to be considered successful, installation craft-friendliness and operational reliability must be ensured. As the fibers, fiber units, and finished cables become smaller, there is increased risk of a reduction in thermal and mechanical protection.

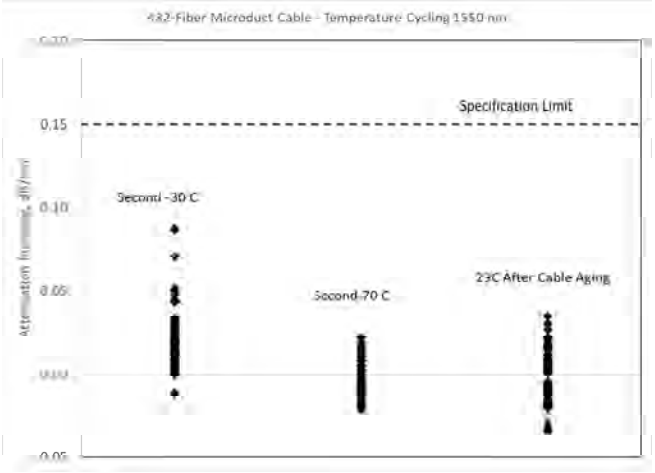
A full battery of Qualification Tests was performed, per Industry standard methods and evaluation/acceptance criteria. A matrix of these cable tests is provided in Table 3.

Table 3. Qualification Test Results

TEST	SPECIFICATION	RESULT
Tensile Rating	IEC 60794-1-21-E1	PASS
Compression (crush)	IEC 60794-1-21-E3	PASS
Impact	IEC 60794-1-21-E4	PASS
Cyclic Flexing (Repeated Bending)	IEC 60794-1-21-E6	PASS
Torsion (Twist)	IEC 60794-1-21-E7	PASS
Bending	IEC 60794-1-21-E11	PASS
Temperature Cycling	IEC 60794-1-22-F1	PASS
Water Penetration	IEC 60794-1-22-F5B	PASS
Midspan Temperature Cycling	ICEA 744	PASS
Low/High Temperature Bending	ICEA 744	PASS
Ripcord Access	ICEA 744	PASS
Jacket Print Adhesion	ICEA 744	PASS
Cable Kinking	ICEA 744	PASS
Cable Material Compatibility	ICEA 744	PASS
Compound Flow	ICEA 744	PASS
Blowing Trial	Internal	PASS

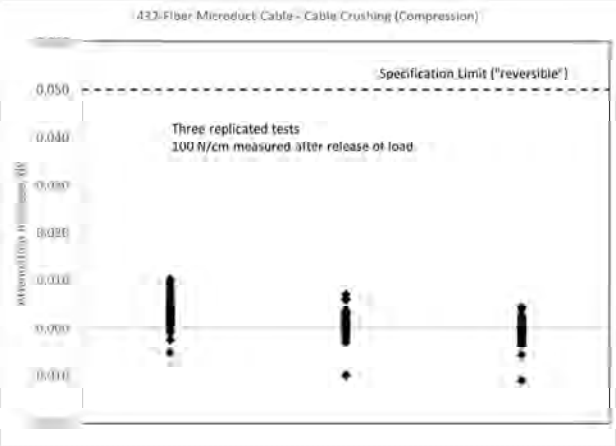
The cable must be capable of performing in operating temperatures between -30C and 70C. Figure 4 shows the result of a temperature cycle test, wherein optical power changes were minimal at temperature extremes and were completely reversible after an aging period.

Figure 4. Temperature Cycling



The potential for cable crushing can be a concern, whether it be damage from accidental mishandling during field preparation or damage caused by the blowing machine itself. Figure 5 shows the results of replicated cable crushing tests, wherein loads of 100 N/cm were applied with no loss of optical power upon release of load.

Figure 5. Cable Crushing (Compression)

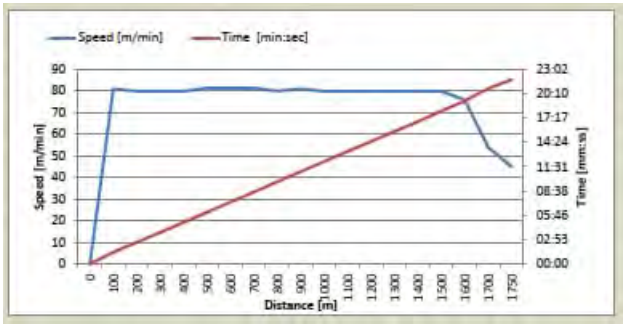


6. Blowing Trial

A small, light, and mechanically robust cable is of little use if it cannot be quickly and efficiently installed as intended by blowing into the microduct.

A blowing trial was conducted, wherein a length of 1,750 meters (over 5,700 ft) was installed into a 14/10 microduct using a MiniJet blowing machine. An average speed of 80 m/min allowed the full length to be installed in just over 20 minutes, with no evidence of damage. See Figure 6

Figure 6. Blowing Trial





7. Conclusions

A next-generation optical fiber cable has been developed and industrialized, incorporating 432 fibers in a small, light-weight structure that is optimized for fiber density, thermal and mechanical performance, and blowing efficiency.

8. Acknowledgments

The author would like to acknowledge colleagues in Prysmian Slatina (Romania) for their initial design and development work, the Claremont Process Engineering Group for their invaluable input, and the Prysmian Claremont Quality Assurance Group for their expertise in conducting numerous tests.

9. Pictures of Authors



Ray Lovie

Prysmian Cables and Systems USA, LLC

Fiber Optic Cable R &D

2512 Penny Rd.

Claremont, NC 28610

Ray Lovie is Product Development Manager at Prysmian located in Claremont, N. Carolina, USA. He holds a B.Sc. (Mechanical Engineering) degree from the University of Manitoba and has over 30 years' experience in the design, development, and manufacture of Outside Plant and Premises optical fiber cables.

SESSION 5

Click on a session below to navigate to that section of the Proceedings.

SESSION 5: SPECIALTY APPLICATIONS

Chairperson: Mike Gimblet, Corning Optical Communications LLC, USA

5-1 **Sea Trail Results of OCC-SC630;** Mr. Hirose Tadafumi, *OCC Corporation, Japan*

5-2 **Development and Application of an Air-Blown Optical Cable with Bidirectional Construction;** Mr. Yuxuan Zhou, *Fiberhome Communication Technology Co., LTD, China*

5-3 **35 Years Of Fiberoptic Coastal Installations In Norway;** Dr. Svend Hopland, *Hopland MarinInstal, Norway*

Click here to return to the **Table of Contents**

Sea Trial Results of OCC-SC630

HIROSE Tadafumi, YASUHARA Keisuke, MASUDA Daishi

Submarine System Plant, OCC Corporation

1-105-2, Hibiki-machi, Wakamatsu-ku, Kitakyushu, 808-0021 Japan

+81-93-751-6500, hirose.occ@nec.com

Abstract

The OCC-SCXYZ series optical submarine cable, well known for its "3 Divided Steel Segment" core design, has a track record supported by more than 400,000km of cable that has been supplied for various projects worldwide since its first manufacturing in the 1980's. This unique core design, providing robust high pressure resistance and low torque generation characteristics, offers the ideal structure to take full benefit of recent high performance optical fibers.

The development towards higher bit rate optical communication systems has been rapidly evolving in recent years and the advances in transmission technologies have increased the level of requirements for each element of the system. Also, with the introduction of Open Submarine Cable System concept, where both wet plant (cable, repeater and branching unit) and dry plant (SLTE) are designed to start operation under a minimum configuration, the system's "cost per bit" has been given more importance than ever.

During IWCS 2019, we presented evaluation results of OCC-SC6YZ series, our advanced small diameter submarine cable.

And, in this paper we present the sea trial results of OCC-SC630 cable. The mini block for sea trial was configurated with various cable types (LWS, SA and DA), joint boxes, dummy repeater and dummy ROADM unit as shown in Figure 1. We conducted the sea trial with previously mentioned mini block, on the sea area around Hachijyo island. Water depth of trial area was 1,600 to 2,400m. We continuously monitored optical attenuation during laying and recovering operations and confirmed stable performance. As result of laying, holding and recovering operations, cable onboard handling ability and laying/recovering performances using conventional drum cable engine were also good.

Through sea trial operations we confirmed suitability of cable design, including joint boxes and couplings (connection) to repeater and ROADM.

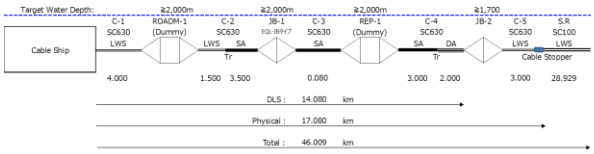


Figure 1. Straight Line Diagram of Mini Block

Keywords: Submarine cable; Sea Trial

1. Introduction

In this paper we describe the development of OCC-SC6YZ cable series, an advanced small diameter submarine optical cable for short and medium range repeatered systems. The cable structure is entirely based on our conventional OCC-SC5YZ cable series copper tube design with its insulating sheath design been optimized to address both electrical and mechanical performance as well as cost effectiveness. This 14mm outer diameter cable core is capable of withstanding the high voltage power feeding regime required in short and medium range repeatered systems with conductor resistance and mechanical performance optimized for this application. Performance of this new reduced size submarine cable design and its various armored variants, including joint box and cable to repeater couplings, have been successfully tested and qualified in accordance with ITU-T Recommendation G.976 and internal programs, demonstrating its high reliability and conformity to the latest open submarine cable system requirements. Qualification and Evaluation test and sea trial results of cable equipped with current high performance low attenuation and large effective area optical fibers are presented.

2. Optical Submarine Cable Design

2.1 Cable Structure

The cable structure was designed following our experience on manufacturing cables characterized by the deployment of a 3-divided steel segment core structure. Figure 2 shows the structure of the core cable. The most notable change from our former design is the size reduction of the polyethylene insulation layer. The 3-divided steel segment and high tension steel stranding wires were designed to allow a maximum of 32 250μm coated fibers and 48 200μm coated fibers to be accommodated in the finished 14mm outer diameter core cable, which can be deployed at depths up to a maximum of 6,000 meters. This new cable was designed with 3 different protection structures as shown in Figure 3, which were also optimized to obtain the same level of performance as current cable designs with a considerable size reduction. Table 1 summarizes some of the key parameters of the Light Weight Screened (LWS) cable, Single Armored (SA) cable and Double Armored (DA) cable.

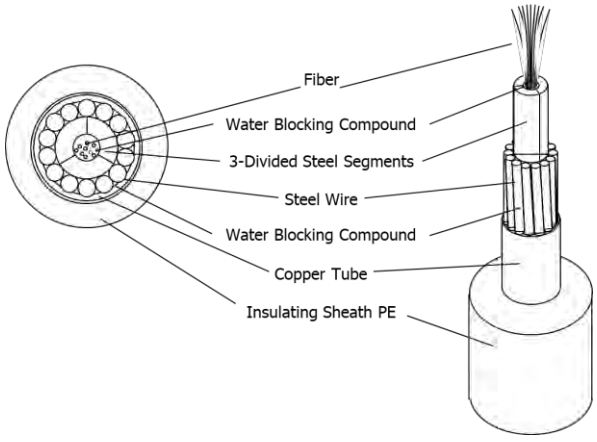


Figure 2. 14mm Outer Diameter Cable Core Structure

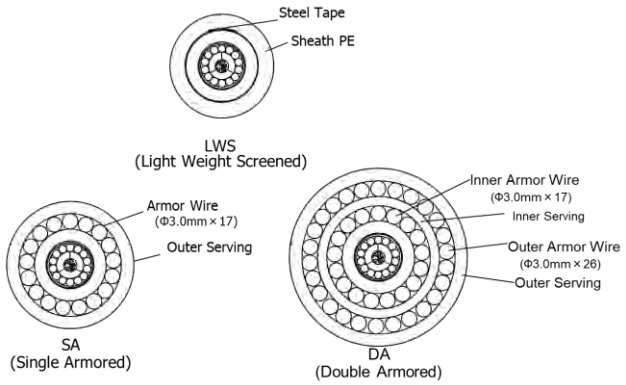


Figure 3. Armored Cable Variations

Table 1. OCC-SC630 Cable's typical characteristics

Item		LWS	SA	DA
Cable nominal diameter		20.4 mm	24.8 mm	34.4 mm
Fiber count	250μm	~32	~32	~32
	200μm	~48	~48	~48
Cable weight in air		7.0 kN/km	15.9 kN/km	32.2 kN/km
Cable weight in water		3.8 kN/km	11.7 kN/km	24.2 kN/km
Minimum breaking load		77 kN	220 kN	420 kN
Minimum bending radius (Without tension, long term storage)		0.9 m		
DC resistance		1.2 Ω /km at 3 deg.C		
Voltage Rating		8 kV		

2.2 Cable Termination and Joint Structure

The cable termination (CPL) and joint box (JB) structures are shown in Figure 4. These designs are based on our conventional CPL and JB designs.

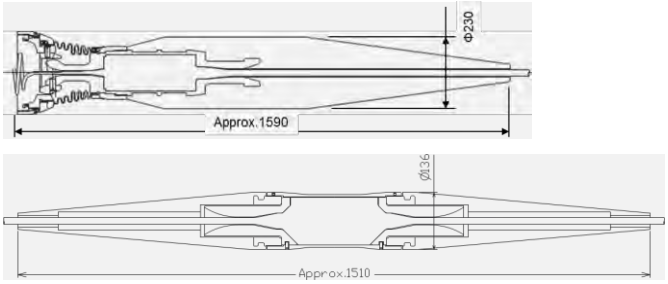


Figure 4. CPL and JB Structure for Armorless Cable

3. Manufacturing Process

Excess fiber length in the cable is managed by a novel mechanical control method, which involves a delicate synchronization for assembling the 3-divided steel segments, tension control and fiber insertion technology. The key manufacturing technology developed for this cable structure can be summarized in the following points;

•A novel technique used to insert the optical fibers into the tube without back tension.

•The establishment of excess fiber length insertion and control technique.

4. Qualification and Evaluation Test

Performance of each cable type was tested and confirmed following the ITU-T Recommendation G.976 and internal standards. Results obtained confirmed that this compact cable design reaches the same level of mechanical performance and reliability in conformance to the latest system requirements. The cable evaluation items are listed in Table 2. These results were presented during the IWCS 2019.

Table 2. Test Items for Submarine Optical Cable

No.	Item
1	Manufactured Cable Loss
2	Temperature Stability
3	Hydraulic Pressure Resistance
4	Tensile Test with Twist Restrained
5	Tensile Test with Torque Minimized
6	Mechanical Fatigue Test
7	Sheave Tests
8	Crush Resistance
9	Impact Resistance
10	Flexure Resistance
11	Water Ingress Tests

5. Manufactured cable loss of sea trial cables

Large core optical fibers were introduced into the OCC-SC630 cable to confirm the cabling effects on the optical attributes of such fibers. Figure 5 shows optical attenuation behavior during cabling process, attenuation values after Copper Tubing, Core, LWS (PE sheath) and Armored process shows small variations from fiber's original optical attenuation, that is consistent with current production cable performance.

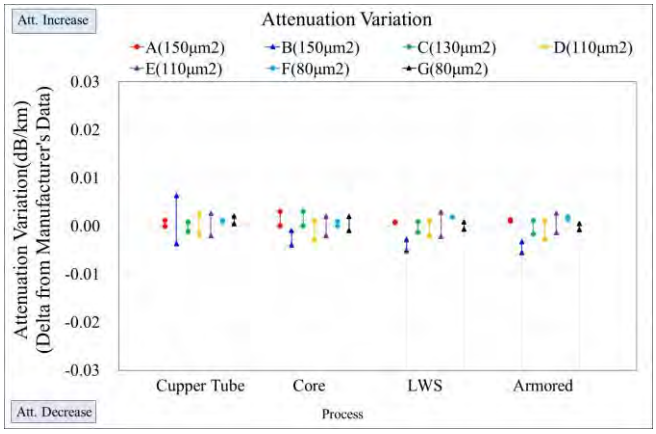


Figure 5. Attenuation Variation During Cabling (Effective area of fibers are 80 to 150 μm², outer diameters are 250 μm)

6. Sea Trial

6.1 Sea Trial Outline

The sea trial was conducted in the sea area around Hachijyo island in October 2020, where the above-described mini block cable configuration was deployed to water depths from approximately 1,600 m to a maximum depth of approximately 2,400 m to confirm the cable characteristics during installation operations as well as cable coordination with cable ship equipment. Figure 6 presents a schematic layout of the sea trial.

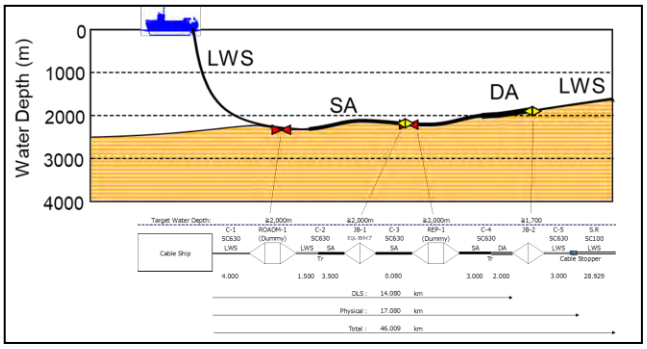


Figure 6. Schematic Layout of Sea Trial

6.2 Optical Performance

The optical measurement paths were configured as described in Figure 7. Optical attenuation variation was continuously measured with loop #1 and #2. Spectral attenuation characteristic and OTDR traces of the optical path were measured with loop #3 to #11.

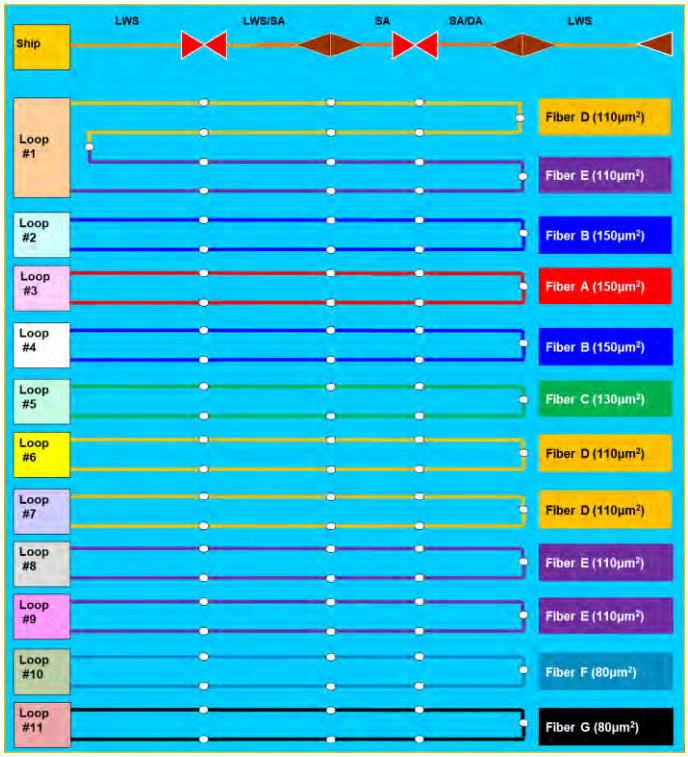


Figure 7. Optical Measurement Path Configurations

Figure 8 shows the optical attenuation change on two different fiber loops as well as the cable tension during the cable lay, hold and recovery operations. Although a very small attenuation change remained just after cable recovery, this variation decreased to negligible levels after a period of time.

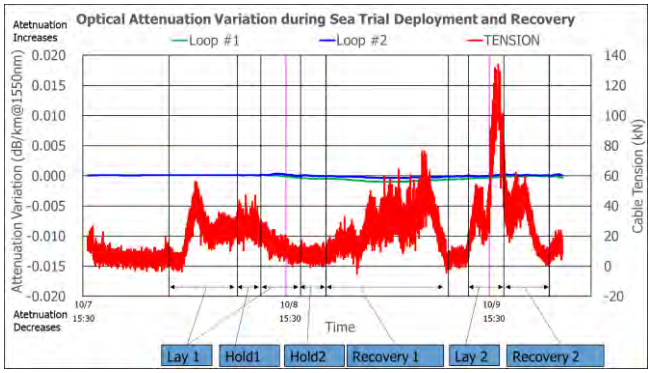


Figure 8. Optical Attenuation during Sea Trial

Other optical fiber's attenuation results are shown in Figure 9. Optical attenuation at Factory, as reference, was measured with the cable coiled. A small variation (attenuation increase) during laying was confirmed, this change is presumed to be caused by laying tension being applied to the submarine cable section between seabed touch down point and cable ship. After laying operation, attenuation values show small variations from measured data at our factory.

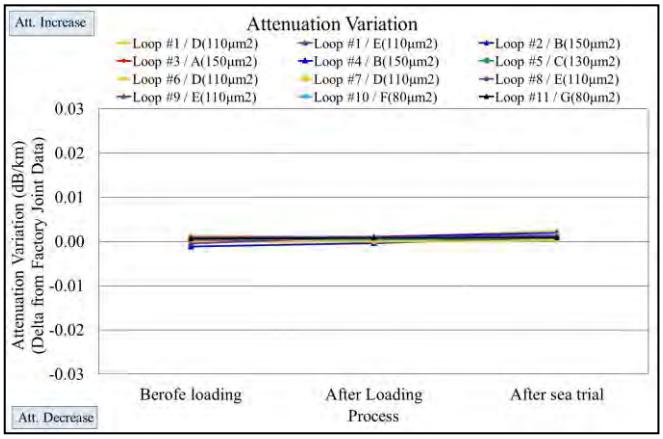


Figure 9. Attenuation Variation During Sea Trial (Effective area of fibers are 80 to 150 μm², outer diameters are 250 μm)

6.3 Mechanical Performance

The cable was completely recovered without any damage or visible anomalies and was naturally coiled on the ship's cable tank at the same time. Figure 10 shows the dummy ROADM unit after recovering. Figure 11 shows the LWS/SA/DA cable while is coiled after recovery.

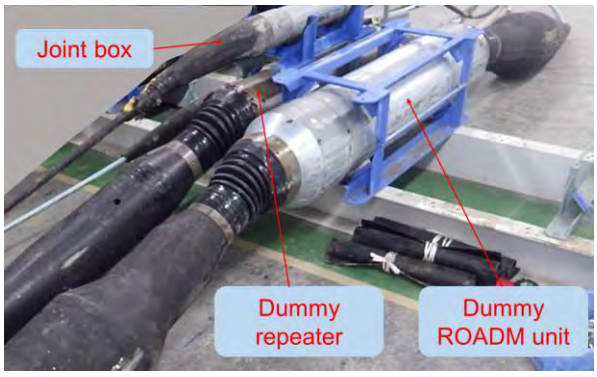


Figure 10. Dummy ROADM Unit after Recovering from 2,300m

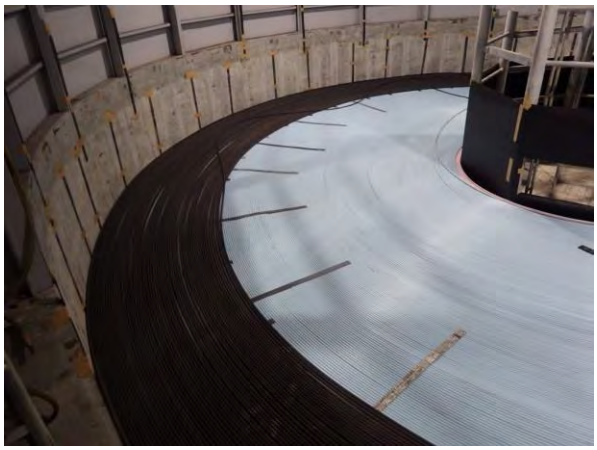


Figure 11. LWS/SA/DA Cable after recovered

7. Conclusions

The OCC-SC63Z series with its compact design was confirmed to fulfill all technical requirements of current systems while satisfying standard operational conditions. Performance during sea trial confirmed not only its easy handling properties but also demonstrated its ability to withstand deployment and recovery operations without optical or mechanical characteristics variations. This new design is a good alternative for optimizing initial cable installation and operational costs, while contributing to realize lower cost-per-bit systems.

8. Acknowledgments

Our special thanks to all the people who worked and collaborated at manufacturing and evaluating the cables.

9. References

[1] T. HIROSE et al., "Development of 14mm outer diameter core series submarine cable", IWCS2019, Section14-3.

[2] D. MASUDA et al., "SDM Submarine cable with 200μm diameter optical fiber", IWCS 2022, 6-1

[3] D. MASUDA et al., "Mass Production Results of High Fiber Count Submarine Cables", SubOptic2023, WT02

10. Pictures of Authors



HIROSE Tadafumi (hirose.occ@nec.com) is an engineer in the OCC's Submarine Systems Division Engineering Department. He joined OCC's Submarine Systems Division in 2013. His responsibility is submarine cable R&D. He received his B.E. from Kyushu University in 2013.



YASUHARA Keisuke (yasuhara.occ@nec.com) is an engineer in the OCC's Submarine Systems Division Engineering Department. He joined OCC's Submarine Systems Division in 2015. His responsibility is submarine cable R&D. He received his B.Sc. from Nagasaki University in 2015.



MASUDA Daishi (masuda.occ@nec.com) is an engineering manager in the OCC's Submarine System Plant Engineering Department. His current roles are management of new cable development, optical fiber evaluation and design of cable connection hardware for submarine cable systems. He joined OCC's Submarine Systems Division in 2000. He received his BSEE degree from Kitakyushu College of Technology in 2000.

Development and application of a bidirectional gas-blown optical cable

Hongguang Sun, Cheng Liu, Yuxuan Zhou, Min Wang, Jiaming Shen, Zhihao Li, Minghao Nie, Lei Zhang

Fiberhome Telecommunication Technologies Co., LTD., Wuhan, China

hgsun@fiberhome.com

Abstract

With the arrival of the 5G era, the development of the communication industry, mobile 5G construction and data have shown explosive growth, urban land resources are increasingly scarce, urban pipeline resources are increasingly strained, and massive data needs to be realized through intensive networking. It is widely used in backbone network, local area network and access network with the advantages of high fiber density, small diameter, light weight, high efficiency of blowing and laying, which can effectively save pipeline resources and meet the needs of network expansion construction. At present, the traditional wind-blown optical cable is mainly through the structure of the wind-blown optical cable smaller size, lighter weight, high fiber density, and reduce the material cost and processing costs. However, with the increase of the weight of the optical cable, the traditional air-blown optical cable is difficult to lay during construction, the efficiency of blowing is reduced, the distance of blowing is shorter, and the difficulty of recycling is increased. To some extent, it occupies the urgently needed and limited pipeline resources. Therefore, increasing the air blowing distance of the cable in the air blowing pipeline, developing recyclable technology, and two-way construction of the air blowing cable technology have become one of the important ways to solve this problem.

In this paper, a bidirectional structure air-blown optical cable is developed and its manufacturing technology is introduced. The cable core of the structure can be a central tube type or a lamination type. The surface of the cable core adopts the outer sheath as a groove structure. Due to the periodic convex formed by the casing grain in the groove, the air blowing force area of the cable is increased, and the convenience of subsequent construction is improved. At the same time, the manufacturing method of the air-blown optical cable is also introduced. Greatly improve the production efficiency. On the other hand, adding longitudinal grooves through the optical cable surface greatly reduces the weight of the optical cable and reduces the product cost.

Key words: Air blowing; Optical cable; A groove; Two-way construction

Return to Table of Contents

1. Introduction

With the construction of the 5G era in full swing and the development of the communications industry, optical fiber communication has been widely used and has become more and more intensive. Not only that, after nearly 30 years of development, air-blown microcable technology as a new optical cable network construction scheme has been fully mature, air-blown equipment, construction units, microcables and auxiliary accessories are provided by manufacturers, and it has been widely developed and popularized worldwide. At the same time, with the increasing maturity of optical cable production technology, as well as the fierce competition in the optical cable market, the high efficiency, refinement and certain cost advantages of the production of optical cable are increasingly becoming an evaluation index of the core competitiveness of an enterprise, coupled with the diversification of optical cable production, a large number of structures and continuous research and development of new products, people are increasingly demanding for the production efficiency and quality of optical cable. Therefore, it is particularly important to develop some new bidirectional air-blown micro-optical cables.

The core of the conventional air-blown microcable can be a central tube or a layer flow, and the air-blown microcable is driven by the power generated by the air compressor and the mechanical thrust generated by the air-blown machine to move in the pipeline for a long distance. This paper mainly develops a bidirectional wind-blown optical cable structure with grooves on the surface, and because the grooves highlight the lines on the surface of the optical cable and form intermittent bumps on the side wall of the grooves, the optical cable can be quickly recycled and reused to increase the air-blown force area, so as to meet the installation and work in special scenarios.

2. Product design

Air blown microcable has the characteristics of small diameter, light weight, moderate hardness, suitable for air blown laying, high fiber density to make full use of pipe hole resources, suitable for construction in crowded metro area pipe, no need to pay high costs for laying; Microcables can be blown out, new varieties of microcables can be replaced in the future in order to maintain the technological lead, and the installation project can be blown into the optical cable in batches with the growth of communication traffic, reducing the initial investment, and can be invested step by step. Without affecting the normal operation of other optical cables, it is not necessary to decide in advance where to place the connection box and optical cable differences, and the external protection and microtubules can be cut off anytime and anywhere to carry out optical cable differences, saving the number of manholes, hand holes and connectors, and reducing costs.

According to IEC 60794-5-10：2014 "Air blown micro Cable and optical fiber Unit for Communication Part 1: General Principles" Air blown micro cable is mainly divided into two structures according to the structure of the center beam tube type and the laminar-stranded type. The laminar air-blown micro-fiber cable has the advantages of large low temperature window, easy identification and divergence of fiber, and easy construction and connection. In this paper, the conventional 96-core microcable is selected as an example, and the specific structure of the air-blown optical cable is shown in Table 1.

Table 1. Structure of air-blown microcable

fiber cores	Tubes mm	loose tube	Reinforcer	Cable core structure	Yarn	Optical cable outer diameter	Sheath wall thickness
96	1.4/1.15 mm	PBT	2.4mm	1+8	2*1000 dtex	6.2mm	0.5mm

Return to Table of Contents

In order to ensure the effect of air blowing, the surface structure of the optical cable is designed as a groove structure, and the quality of the optical cable product is guaranteed without breaking the skin and other quality problems. Intermittent protrusions are formed through the grain of the optical cable surface and the side wall of the groove to increase the area of air blowing force, as shown in Figure1.

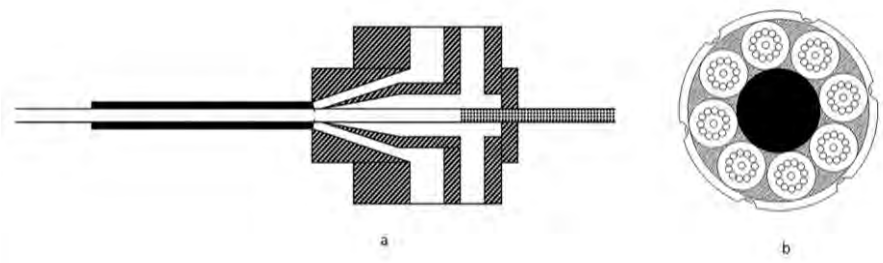


Figure 1. (a) Air blown microcable forming diagram; (b) Schematic diagram of air - blown microcable secondary plastication

3. Test and characterization of optical cable

Combined with the requirements of IEC 60794-1-21-2015 Method E24 Installation test for microduct cabling and IEC 60794-5-10:2014, The performance requirements of air-blown microcables in this paper are shown in Table 2.

Table 2. Air blown microcable standard requirements

Items		index
Tensile strength	Stress situation	Temporary (when laying)
	Allowable strain of fiber in cable	≤0.2%
	Allowable tensile force N	350N-10min 700N-10min
temperature cycle ºC		-25~+70℃, 2cyces, 4h
Air blowing distance m		1500m

4. Performance verification

4.1 Air blowing performance verification

Through the improvement of the sheath mold, as shown in Figure 2, three different types of optical cables are obtained by extrusion, among which there are no grooves, two grooves, and multi-grooves. In order to verify the optical cable structure sizes manufactured under three different conditions, wall thickness tests were carried out for different optical cables according to IEC 60811-1-1：2001 method, and the test results are shown in Table 3. In addition, in order to verify the influence of this groove on the air blowing performance of the optical cable, the air blowing experiment is conducted through route B according to IEC 60794-5-10：2014 standard.

Return to Table of Contents

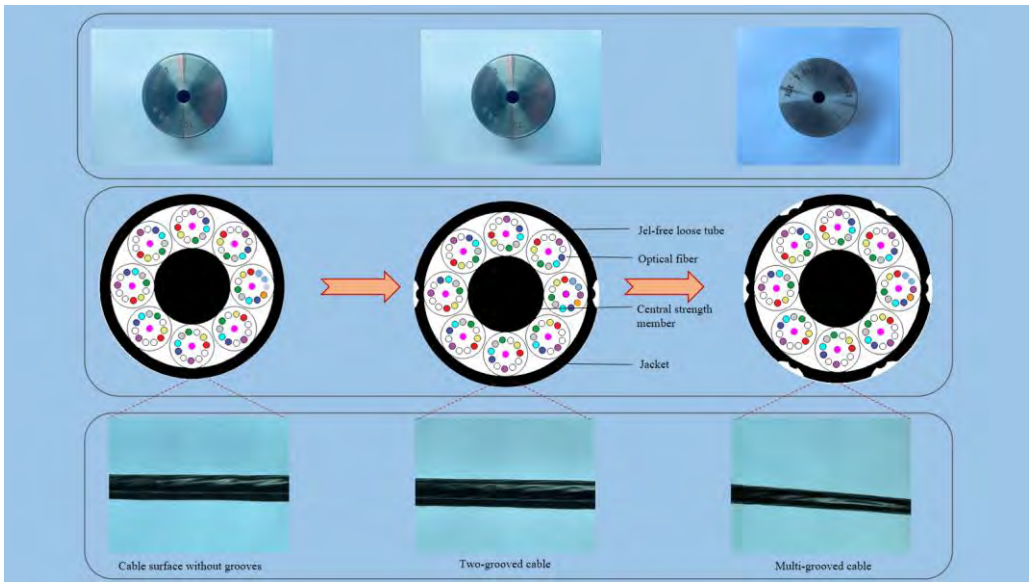
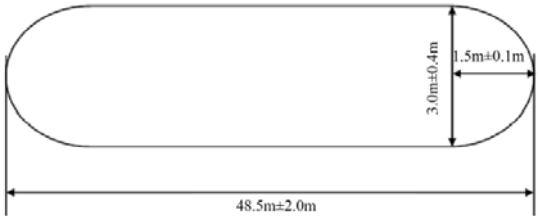


Figure 2. Schematic diagram of different types of air-blown microcables

Table 3 Micro-cable air blowing test data

Testing standard: IEC 60794-5-10：2014			
			
Test items	Type A	Type B	Type C
Cable wall thickness	0.5	0.5/2*0.2	0.5/6*0.2
Air blowing distance(m)	1530	1670	1800
terminal velocity (m/min)	30	30	30
Test results	PASS	PASS	PASS

Return to Table of Contents

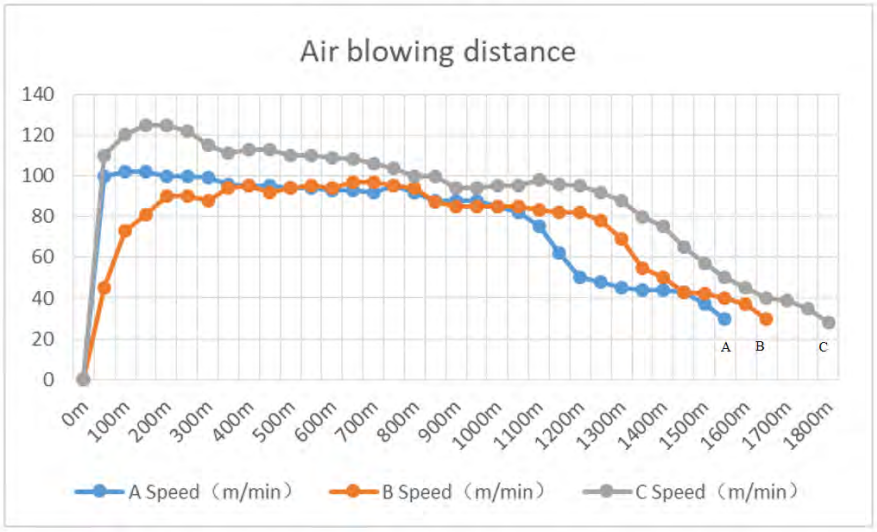


Figure 3. Different types of air blowing microcable air blowing effect

As can be seen from the experimental results in Table 3, the fluted air-blown miniature optical cable was successfully prepared, and the wall thickness of the fluted outlet was 0.2mm, and the wall thickness of the non-fluted outlet was 0.5mm, which reached the expected design of the experiment. In addition, it can be seen from Figure 3 that the cable with more grooves has a longer air blowing distance. Compared with the structure without grooves, the air blowing distance is increased by about 17%, and the average air blowing speed is increased, all of which can meet the standard IEC 60794-5-10：2014, which has practical application value and can be used for two-way construction.

4.2 Tensile and temperature cycle performance verification

In order to ensure the tensile performance of the improved air-blown optical cable, three different types of optical cables were tested under the same IEC 60794-1-22:2017. The tensile force value of the optical cable was limited to 1000N, and 12 optical fibers were sampled evenly for each bushings. The experimental results are shown in Figure 4.

At the same time, in order to ensure the stable operation of the air-blown micro-cable under high and low temperature conditions, we conducted high and low temperature cycle tests on the air-blown micro-cable with different number of grooves at different temperatures. The test conditions are as follows: in accordance with IEC 60794-1-2-2017 standards, and the test results are recorded, as shown in Table 4. The sample length is 2 km, and the temperature range is -30 ℃~ +70℃. The duration of each step :12h, the number of cycles :2 times, the experimental results are as follows.

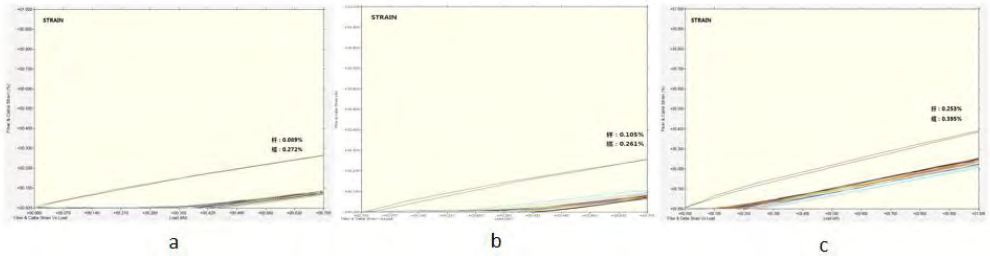


Figure 4. Drawing curves of different types of air-blown microcables

Return to Table of Contents

Table 4. Height temperature results of different types of air-blown microcables

Test items	-30℃, 4h	0℃, 4h	70℃, 4h
1310nm Additional attenuation(dB/km)	-0.02	0	-0.009
1550nm Additional attenuation(dB/km)	-0.012	0	-0.001
1625nm Additional attenuation(dB/km)	-0.012	0	-0.001

According to the experimental results, the tensile properties of the three types of optical cables are at the same level and meet the design expectations of the optical cable structure. The optical fiber strain is less than 0.3% when the optical cable is stretched by 1000N external force, indicating that the groove structure has little influence on the tensile properties of the optical cable.

Through the high and low temperature experiment results of the three types of optical cable, it can be seen that its 6 grooves have little impact on the shrinkage and high and low temperature resistance of the optical cable, and the additional attenuation is less than 0.02dB/km, which can meet the application requirements.

5. Conclusions

As a high-end special optical cable, air blown microcable has higher and higher requirements for its feed, and it is particularly important to construct long distance air blown microcable in both directions. When the air-blown micro-cable is provided with intermittent grooves within the range of the cable wall thickness deviation, it can increase the force area of the air flow of the air-blown micro-cable to a certain extent, increase the air blowing distance, and can be repeated construction, two-way air blowing, and has little impact on the tensile and high and low temperature performance of the cable, which has great practical significance for the air-blown micro-cable.

6. Acknowledgments

Special thanks to all the colleagues during the experiment.

7. References

[1] Sato F, Suzuki Y, Takami M,et al.Ultra-High-Density Microduct Optic Cable with 200μm Freeform Ribbons for Air-Blown Installation[C]//International Wire & Cable Symposium.2019.

[2] IEC 60794-5-10：2014: Optical fibre cables-Part 5-10: Family specification for outdoor microduct optical fibre cables, microducts and protected microducts for installation by blowing.

[3] IEC 60794-1-21-2015: Optical fibre cables. Part 1-21_Generic specification. Basic optical cable test procedures-Mechanical test methods.

[4] IEC 60811-1-1:2001: General test methods for insulation and sheathing materials for cables and optical cables. Part 1-1: General application methods. Measurement of thickness and total dimensions. Mechanical properties test.

[5] IEC 60794-1-22-2017: Optical fibre cables-Part 1-22: General specification optical fibre cable basic test procedures Environmental test methods.

[6] IEC 60794-1-2-2017: Optical fibre cables - Part 1-2: Generic specification - Basic optical cable test procedures - General guidance.

Return to Table of Contents

8. Pictures of Authors



Sun Hongguang

Sun Hongguang, an engineer, is studying for a PhD in Huazhong University of Science and Technology. After graduating with a master's degree in 2019, he joined FiberHome Communications Technology Co., LTD., China Information and Communication Technology Group, and is committed to the position of optical fiber communication process engineer.



Liu Cheng

Cheng Liu joined Wuhan Research Institute of Posts and Telecommunications (WRI, currently CICT Group) in 1989, where he has been engaged in research and development on optical fibre and cable. He has contributed to the activities of ITU-T SG15 since 2013. He is presently a Senior Technical Expert, Chief Engineer of FiberHome Telecommunnication Technologies Co. Ltd.He is the Fellow of China Insititute of Communications (CIC).



Wang Min

Wang Min, an engineer, graduated from Wuhan Institute of Posts and Telecommunications in 2021 and joined FiberHome Communications Technology Co., LTD., China Information and Communications Technology Group, dedicated to the position of network engineer.



Shen Jiaming

Shen Jiaming, Cable Department, Fiberhome Communication Technology Co., LTD., graduated from Wuhan University of Technology in 2006, and has been conducting research on optical cable production and manufacturing technology in Fiberhome Communication Technology Co., LTD.



Li Zhihao

Li Zhihao, graduated from Hubei University with a master's degree in 2021, joined FiberHome Communications Technology Co., LTD., China Information and Communication Technology Group, and is committed to the position of optical fiber communication process engineer.

Return to Table of Contents



Nie Minghao

Nie Minghao (1990-8), male, Assistant process engineer, Cable Department, Fiberhome Communication Technology Co., LTD., graduated from School of Chemistry and Molecular Science, Wuhan University in 2016, and has been conducting research on optical cable production and manufacturing technology in Fiberhome Communication Technology Co., LTD since 2016.



Zhang Lei

Zhang Lei,joined FiberHome Communications Technology Co.,China Information and Communication Technology Group，after graduation from Harbin University of Science and Technology in 2006. He has been working in optical fiber cable technology area.

Return to Table of Contents

35 Years of Fiberoptic Coastal Installations in Norway

Dr. Svend Hopland

Hopland MarinInstal, Prestegardsveien 12B, 0851 Oslo NORWAY
sven-hop@online.no

Abstract

In this paper we outline key experiences with the installation of underwater cables along the Norwegian coast in the period 1985-2022. We review the cable installation story as well as the cable fault story and investigate the distinct types of faults and their origin in a 35-year perspective. We outline the installation method and the importance of carefully controlling the slack during laying. Recently, remote laying control has been introduced and is now used routinely. A ROV survey shows a placement accuracy on the seabed of 5-10 % of the sea depth without any surface compensation.

Keywords: Underwater cables, cable laying, sea bottom terrain

1. Introduction

We have earlier presented several papers describing the challenges of installing optical underwater cables along the Norwegian coastline [1]-[5]. Telenor installed the first underwater optical cable on the west coast of Norway in 1983. Since then, nearly 850 cable routes with a total length of more than 6000 km have been installed along the coastline at depths ranging from zero to 1300 m.

Ten years ago, we outlined the key issues during 25 years of use [6]. In this paper, we give an update and outline new experiences made during the last 10 years.

2. Cable installation history

The sea bottom terrain along the Norwegian coastline is challenging with rugged underwater terrain formations and steep slopes. To secure a safe installation an advanced laying technique was early developed [1] and has been later continuously improved through the years. More details of this laying method are given later in Chapter 4.

Because of the ongoing buildup of the optical network, the number of installed kilometers has varied through the years, as shown in Figure 1.

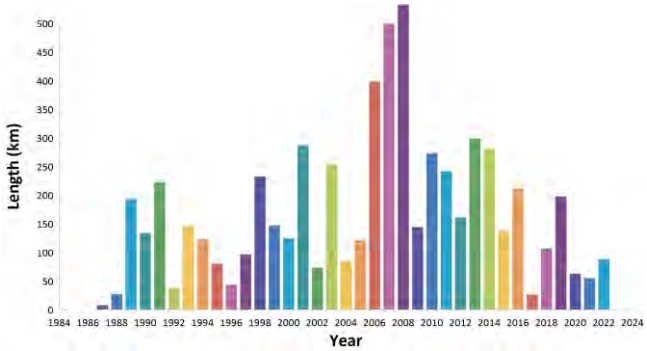


Figure 1: Installed per year in period 1985-2022

At a given time, we can calculate the corresponding total accumulated product (KmDeployed*InstalledTime). This product should in theory be proportional to the running accumulated number of cable faults. In Figure 2 we have shown the value of the product during the years 1985-2022 based on the installation data, indicating the year-by-year trend for the accumulated number of cable faults in the period 1985-2022.

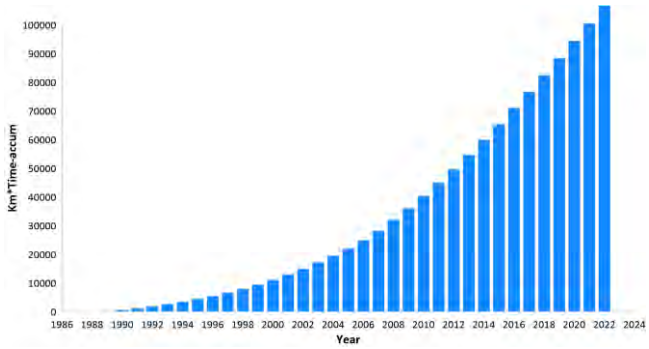


Figure 2: Accumulated failure probability based on installation data 1985-2022

3. Cable faults history

A major issue concerning the coastal installations is the cable fault history. In this respect, the installed underwater cables have showed an inherently low number of fractures or damages in the course of time.

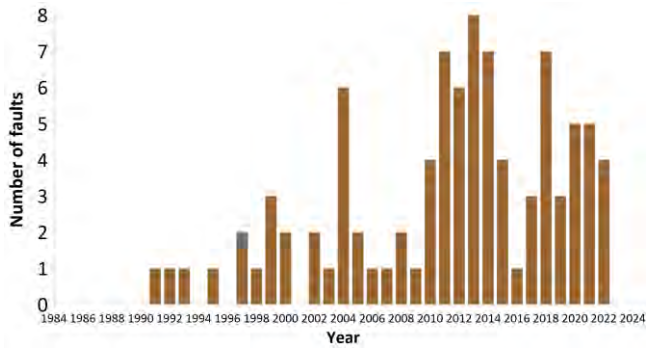


Figure 3: Cable faults per year in period 1985-2022

In Figure 3 are shown the actual number of cable faults per year in the period 1985-2022. After 35 years, a total number of 92 cable faults have occurred, corresponding to an average of 2.6 faults per year.

From the data in Figure 3, we can calculate the cumulative number of real failures during the years 1985 to 2022, which are shown in Figure 4. We note the similarity in the field data compared to the

theoretical data in Figure 2. However, since the actual data contains many different fault categories, with individual time dependencies according to their nature, the field data is expected to show a more varying dependency with time, which is also the case. This will be discussed later in Chapter 3.

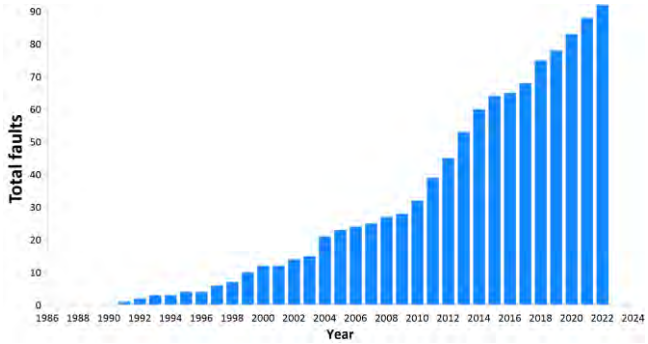


Figure 4: Accumulated number of cable faults 1985 – 2022

3.1 Cable fault types

The total number of cable faults during the years 1985-2022 amounts to 92 and are separated into different categories according to the reason of failure, as shown in Figure 5.

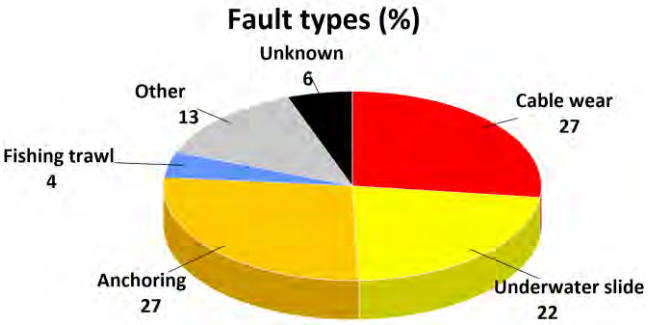


Figure 5: Pie chart of cable faults 1985-2022

The three largest failure types are:

1. Anchoring
2. Underwater slides
3. Cable wear small depths

, each constituting approximately 25 % of the total number of faults.

An accurate and interesting feature of the individual fault types is their dependence on the number of years after installation. In this respect, we have investigated more closely the different failure types to reveal possible time dependent trends.

In Figure 6 is shown the total number of faults versus number of years after installation.

There are some interesting features evident in this diagram. We note that faults due fishing trawls are in fact close to zero in the 30 years perspective. A few faults occurred in the early 1990 'ies, but have decreased to zero since then. This is a successful result of the obligatory pre installation hearing process among fishermen performed by the Fisheries Authorities regarding the final positions of cable routes.

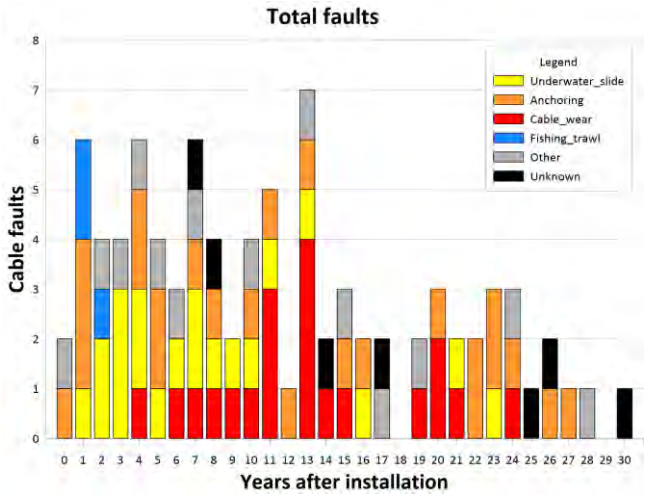


Figure 6: Total number of faults

We also note that fault categories "Other" and "Unknown" are evenly spread in time, which is expected due to their arbitrary nature. The category "Other" includes shipwrecking, lightening and underwater trenching, among others.

3.1.1 Anchoring

Anchoring originates partly from ships and partly from fish farms. Unpredictable ship anchoring may sometimes happen due to adverse situations like severe weather or vessel casualty. In addition, the large fish farm activity along the coast results in numerous anchor settings, pulls and drags. Obviously, the optical cables are not able to withstand anchoring attacks.

In Figure 7 are shown the cable faults due to anchoring. We note that ship anchoring as well as fish farm anchoring are fairly evenly spread in time, as expected due to their arbitrary nature.

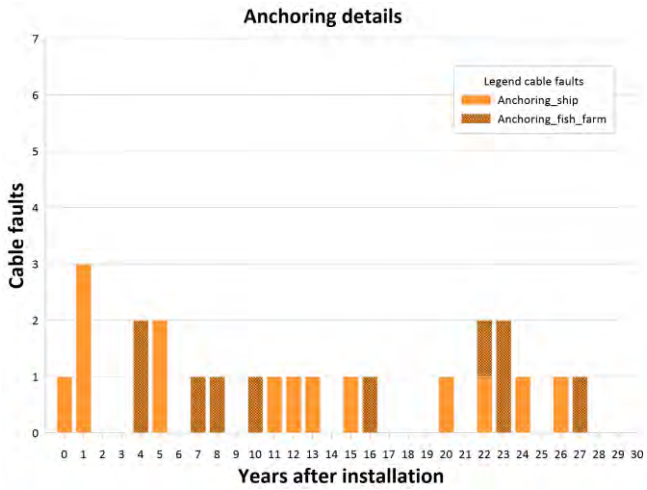


Figure 7: Anchoring faults

3.1.2 Underwater slides

Underwater slides may occur due to long term displacement of sediments near the outlet of some rivers. Furthermore, extreme weather may in some cases unleash nearshore underwater slides. Finally, land works with corresponding dumping of mass into the sea could be the potential origin of "man-made" underwater slides. An underwater slide is impossible to withstand and is ruinous to the cable.

In Figure 8 are shown cable faults due to underwater slides. An amount of three cables have been hit twice with some time separation. We note that slide faults are relatively evenly distributed in time due to their arbitrary nature. However, there seems to be a decaying effect with time since there is a limited number of potential areas where underwater slides are likely to occur. In addition, the learning effect for the installer will obviously have an impact on sub additional faults.

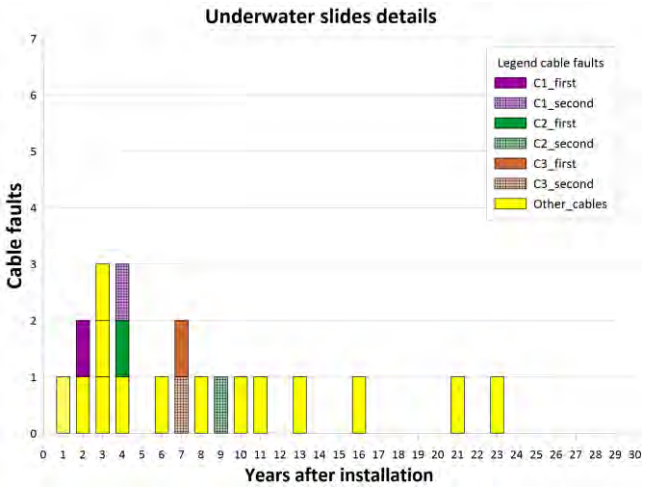


Figure 8: Underwater slides faults

3.1.3 Cable wear small depths

Cable wear resulting in a fault occur in nearly 100 % of the cases at small depths 20-50 m in areas with strong sea currents. We have experienced only one single cable wear fault during 25 years at deeper water greater than 100 m. In Figure 7 are shown all cable faults, including the single fault at deeper waters.

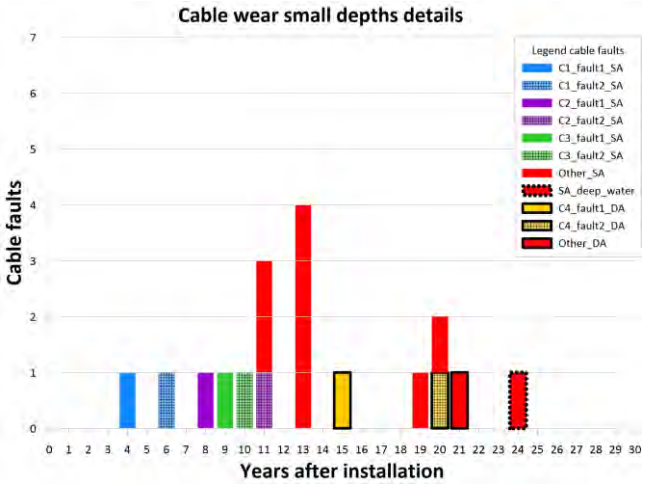


Figure 9: Cable wear small depths faults

There are some features to be noted in Figure 9. All cable wear faults, except two, are Single Armoured (SA) cables. This underline the fact that Double Armoured cables (DA) adds significantly increased steel reinforcement compared to SA cables, and that the heavier cable is more resistant to movements caused by currents on the sea bottom.

3.2 Repairs and route improvements

In the case of a cable fault due to anchoring ship, the whole route, or part of it, is re-layed using a reinforced double armoured (DA) cable. In the case of a cable fault due to anchoring fish farm, one must find a new route away from the fish farm facility. The whole route, or part of it, is then re-layed using a DA cable.

If the cable fault is caused by an underwater slide, it is necessary to find a new and better cable route, and re-lay the whole route, or part of it, using a DA cable.

Since the majority of cable faults due to cable wear takes place on small depths and near landing points, the chosen repair method is to remove the cable length between the land point and the cable fault, then perform a underwater cable splice at the cable ship and re-lay the spliced-in DA length back to the landing point. If the cable wear fault is in the middle of the cable route, one would re-lay the full cable route using a DA cable. Simultaneously one would try move the exposed part of the route to deeper water, if possible.

4. Cable installation method

The cable installation method has been presented earlier [1]-[3]. A key element is the utilization of detailed topography terrain maps of corridors along the cable routes. The maps are studied carefully to find optimal routes regarding slopes and terrain formations. However, steep slopes and rugged formations cannot be avoided.

When laying the cable, the ship follows the surface projection of the desired cable bottom line, except in regions where the bottom line changes its course (turns). Here, the cable ship performs a surface compensation to obtain landing of the cable on the wanted bottom positions. The amount of surface compensation depends on sea depth and magnitude (degrees) of the turn [3].

4.1 Cable payout during laying

Steady state laying is obtained when laying on a perfectly flat bottom with equivalent ship speed and cable payout rate. In this case the angle between the cable and the sea surface (laying angle) is constant and depends on factors as ship speed, cable weight, cable diameter and cable outer surface characteristics [2].

To maintain steady state laying condition during laying, the payout rate relative to the ship speed (slack) must be carefully controlled. Varying bottom slopes (decent and climb) along the route increases or decreases the slack. Also, during turning points along the route, the slack is adjusted as well, since the ship positions deviate from the sea bottom cable positions. Finally, but not at least, the laying angle must adapt to the varying climb angles along the cable route.

An optimal laying angle with corresponding slack profile is selected for each route, and the slack is continuously controlled by the laying computer as the cable ship moves along the laying line. Normally, ship speeds in the region 1.8-2.0 knots are feasible. However, in some cases, lower ship speeds must be used due to occasionally very steep terrain slopes.

4.2 Monitoring during laying

During laying, we monitor continuously surface ship positions in a detailed seabed contour map corridor along the route in a window with a bird's eye view as shown in Figure 10.

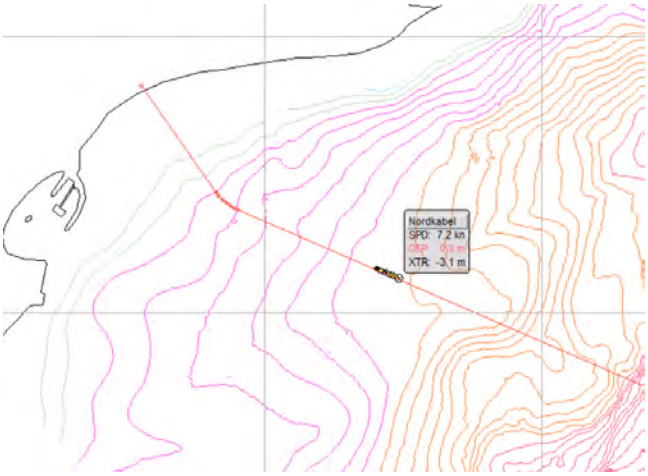


Figure 10: Laying ship in contour map – bird's eye view

Simultaneously, the cable ship and laying angle are put to screen in a window with a side view, as shown in Figure 11.

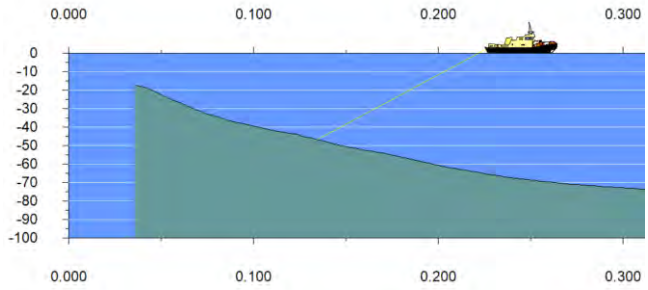


Figure 11: Laying the cable - side view

On the cable laying control screen (not shown here) all cable laying parameters are monitored. Any deviation from the payout profile is visible on the screen and is automatically corrected. In case of major deviations, such as temporarily ship stop, or drifting too far away from the lying line, the control system would be shifted into a manual laying mode, if necessary.

A method for improved overview and control, is 3D visualization of the cable laying. In Figure 12 and Figure 13 are shown examples of 3D visualization of cable laying along a specific route corridor. This technique offers "fingertip" feeling for the experienced laying operator.

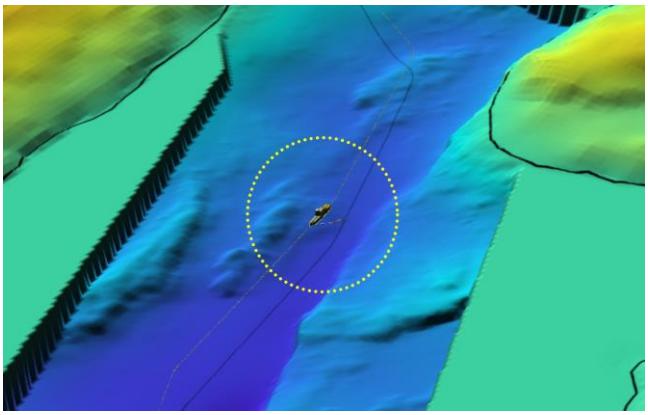


Figure 12: 3D view of cable laying

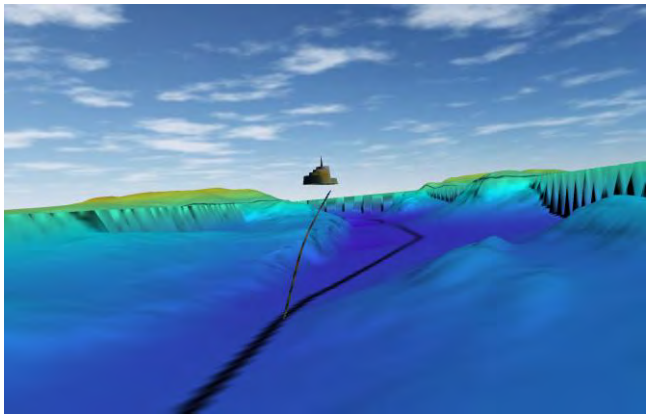


Figure 13: 3D view of cable laying– different view

4.2.1 Remote laying control

Throughout the years, the cable laying operator used to travel back and forth the cable ship, staying onboard during transport, preparation, follow-on and the laying itself.

In November 2021, we tested successfully for the first time remote laying control. In this scenario, live data from the cable ship is transferred via the mobile network to the remote site. Unlike in the past, operator presence is then only needed from start to end of the actual cable laying. This option reduces the extent of work greatly, and the working conditions as well. Since then, remote laying control has been applied on all installations.

4.3 ROV survey of laid cable

Further to have a tight slack control, it is important to achieve high placement accuracy on the sea bottom. I order to investigate this topic further; a Remotely Operated Vehicle (ROV) was launched in order to confirm the installed DA-cable bottom positions of a 38 km long fjord crossing route with depths varying from zero to 500 m. In Figure 14 are shown the calculated cable positions as well as laid cable positions at 320-420 m sea depth in the region around waypoint no 10 of the route, in a bird's eye perspective. We note that the deviations are in the range 25-30 m.

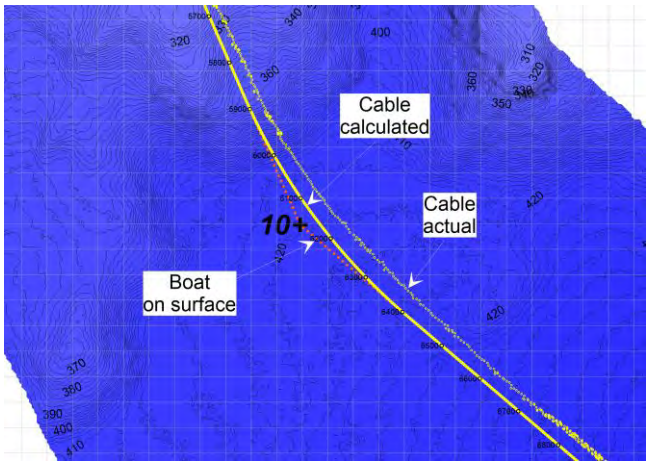


Figure 14: Laid vs precalculated positions of cable

Furthermore, in Figure 15 are shown in more detail the deviations along the full route.

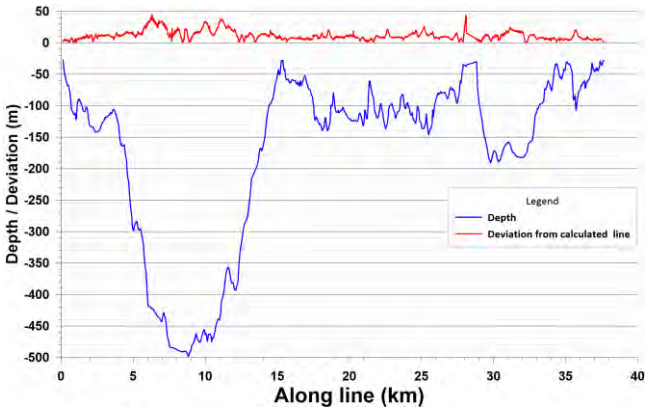


Figure 15: Deviations from calculated positions of laid cable

It should be pointed out that varying crossing sea currents were present along the entire cable route. In this respect, no action is taken to compensate for the crossing currents with some suitable offline ship manoeuvres, assuming that the tight slack control will keep the cable sufficiently close to the precalculated landing positions.

From the data in Figure 15, we can conclude that the offline deviations are within 5-10 % of the sea depth along the entire length, which is fully acceptable.

5. Fiber attenuation

Fibre attenuations in old underwater cables has an historical background due to the hydrogen issue in open cables [4]. Today, the hydrogen induced losses in the old open cables have more or less returned to zero [6]. In general, fibre attenuation in underwater cables has proven to be excellent and stable over decades. In specific, fewer splice points contribute to lower total loss budgets.

6. Summary and conclusion

We have outlined key experiences with the installation of more than 6000 km and nearly 850 fiberoptic underwater cable routes during 35 years along the Norwegian coast.

We have presented the installation history which is in line with the ongoing build-up of the optical network. We have shown that the accumulated cable fault history compares well with what could be expected from the cable installation rate.

Furthermore, we have investigated in detail the fault histories for the most frequent fault types, which have proved to be anchoring, underwater slides and cable wear at small depths. Each type constitutes approximately 25 % of the total number of faults up to now.

Anchoring originates partly from ships and partly from fish farms, and faults are evenly spread in time, as expected due to their arbitrary nature. For underwater slides, there seems to be a decaying effect with time since there is a limited number of potential areas. Finally, cable wear occurs in 100 % of the cases at small depths in areas with strong sea currents, and more than 80 % of faults are on SA cables.

Repairs are performed by solely splicing in lengths of DA cable, and to change the damaged part of the cable route to safer or deeper water, if possible. This will to a large extent reduce the risk for future faults.

We have described the laying procedure in detail, emphasizing the importance and method of controlling the cable slack during laying. We have also described the running control screens used to monitor the cable laying, including a new 3D visualization. Remotely controlled cable laying has been carried out on a regular basis since late 2021.

Finally, we have shown in a ROV mapping survey of a 38 km installed cable, that a bottom placement accuracy of 5-10 % of the sea depth is routinely obtained without performing any ship surface compensation manoeuvres.

Fibre attenuation in underwater cables has proven to be excellent and stable over decades.

7. References

[1] S. Hopland and Albert Klykken: "Installation of submarine fiberoptic cables in rugged coastal terrain" *Proceedings International Wire & Cable Symposium 1992*, Reno, Nevada, U.S.A, pp.492-497

[2] S. Hopland: "Investigation of cable behaviour in water during laying of fiberoptic submarine cables." Proceedings International Wire & Cable Symposium 1993, St. Louis, Missouri, USA, pp. 734-740.

[3] S. Hopland:"Alter course cable behaviour in water during laying of fiberoptic submarine cables" International Wire and Cable Symposium 1995, Philadelphia, Pennsylvania, USA, pp.592-597.

[4] S. Hopland: "Long Term Behaviour of Hydrogen Induced Losses in Installed Fibreoptic Submarine and Underwater Cables". Proceedings International Wire and Cable Symposium 1997, Philadelphia, Pennsylvania, U.S.A, pp. 316-325

[5] S. Hopland: "A New Cost Effective Approach to Coastal Underwater Fibre Cable Installation". Proceedings International Wire & Cable Symposium 2002, Lake Buena Vista, Florida, USA, 18-21 November 2002.

[6] S. Hopland and Magnar Greve:"25 Years of Experience – Using Underwater Cable Installations Along the Norwegian Coastline". Proceedings International Wire & Cable Symposium 2014, Providence, Rhode Island, USA, 9-12 November 2014



Dr Svend Hopland
sven-hop@online.no

Svend is a consultant in Fibre Optics & Marine Installations in his own company Hopland MarinInstal. He was Chief Engineer on optical fibre cables and fibre transmission in Telenor Norway from 1986 to 2017, and he holds a PhD on optical fibres. He is a fibre expert and has extensive experience with field measurements on fibre cable links as well as lab measurements and fibre cable testing. He has since 1987 worked with underwater cable installations along the Norwegian coastline.

SESSION 6

Click on a session below to navigate to that section of the Proceedings.

SESSION 6: FIBER MANUFACTURING

Chairperson: Yoshihiro Arashitani, Furukawa Electric Co., LTD., Japan

6-1 **Design Process of a 192-Fibre Cable with Fibres Coated to 180µm Diameter;** Mr. Onno Bresser, *TKH Group NV, China*

6-2 **A Novel Modelling Approach for Sintering of Cylindrical Silica Soot Preform;** Mr. Debangshu Debnath, *Sterlite Technologies Limited, India*

Click here to return to the **Table of Contents**

Design process of a 192 fibre cable with fibres coated to 180 µm diameter

Onno R. Bresser, Zhang Li, Ning Siping
Twentsche (Nanjing) Fibre Optics Ltd.
Nanjing, Jiangsu, China
+86 1360 517 6848 onno_bresser@tfo.com.cn

Abstract
To increase fibre density in underground ducts, worldwide efforts are undertaken to reduce the diameter of optical fibre cables. That is partly realized by reducing the coated fibre diameter. For many years fibres coated to a diameter of 250 µm were in use. About a decade ago also fibres coated up to 200 µm were introduced. This paper discusses a cable design based upon fibres coated to a diameter 180 µm. For a long time "loose tube" structures were applied where cable length variations were isolated from the fibres by putting them in a helix with flexible diameter. With reducing tube diameters the fibre freedom that can be created with the helix is gradually reduced to impractical low values. In the presented design the radial free space for the fibre is reduced in such a degree that buckling, that normally determines the functional limit of "loose tube" designs, no longer can occur.
To optimize cable design and its process of manufacturing we used a Taguchi L8 design of experiment. With 8 experiments we can check the influence of 7 parameters on 2 levels. To perform the 8 experiments we took a 192 fibre cable built from 8 tubes with 24 fibres each. Each tube had its special settings for fibre properties, tube design and processing parameters. We further looked at the effect of the fibre colour layer on microbending sensitivity. We also saw that master batches used for colouring the tube materials have their influences.
We will present the quantitative influence of a number of fibre and cable design parameters, as well as process settings of cabling.

Keywords:.Optical fibre cable, 180 µm fibre, microbending sensitivity, Taguchi L8, tight tube

1. Introduction
In cable industry there is a strong tendency to reduce cable diameters in order to increase fibre density of cable ducts. Main driver there is a continuous reduction of the diameter of coated fibres. Present stage is the introduction of fibres with an overall diameter of 180 µm.
In reducing the coated fibre diameter we meet two challenges. The first challenge is the fibre's mechanical quality. For basic feasibility of the fibre we have to meet requirements for stripping, tensile strength and stress corrosion susceptibility. Table 1 gives average results of tests on these properties. For comparison data on 242 and 200 µm fibres are given.

Table 1 - Average results on mechanical tests

Parameter	Unit	Requirement	242 µm coating	200 µm coating	180 µm coating
Coating strip force (average)	N	≥ 1.0 (250 µm) ≥ 0.4 (200 µm)	1.25	1.08	0.82
Tensile strength (median)	GPa	≥ 3.8 (0.5 m)	4.92 (10 m)	5.02 (10 m)	4.82 (10 m)
Stress corrosion suceptibility parameter, n_d		≥ 18	24.1	25.3	26.7

From the table it is clear that the fibre coated up to 180 µm passes all tests with flying colours.

The second challenge is the increased microbending sensitivity due to reduced buffering properties of the coating. This paper addresses how we cope with this in cabling 180 µm fibres. In loose tube designs the fibre attenuation at low temperatures is limited by fibre buckling when the design limits are reached. To take full advantage of reduced fibre diameter also tube dimensions need to be adapted. This soon limits the fibre's "free space" in the tube to impractically low values.
This brought us to a new concept where the tube is so tight that fibre buckling simply is not possible anymore, so to a completely new concept to cable optical fibres, to which we further will refer to as "tight tube design".
In this paper we lead you a little bit through the cable development process of 192 fibre cable built from 8 tubes with 24 fibres each and a total diameter of 5.1 mm.

2. First trial experiences
When a trial cable shows acceptable attenuation values after cabling a next step mostly is to look at the temperature behaviour. In figure 1 the behaviour is shown of 48 fibres of a 144 fibre cable in a temperature cycle with several steps between -40ºC and +70ºC. Fibres were systematically taken from the 6 tubes with 24 fibres each.

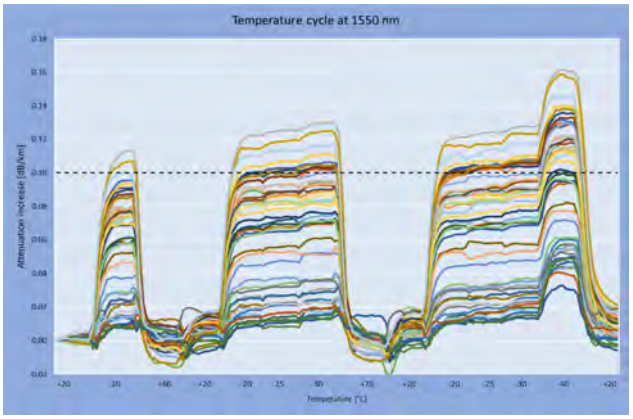


Figure 1 - 1550 nm attenuation during temperature cycling

From the figure it is clear that not all fibres pass the test, a few fibres already fail when the cable is subjected to a temperature of -20°C. For better understanding we zoom in on individual fibres. In figure 2 we see the attenuation increase of the various colours at - 40°C.

Return to Table of Contents

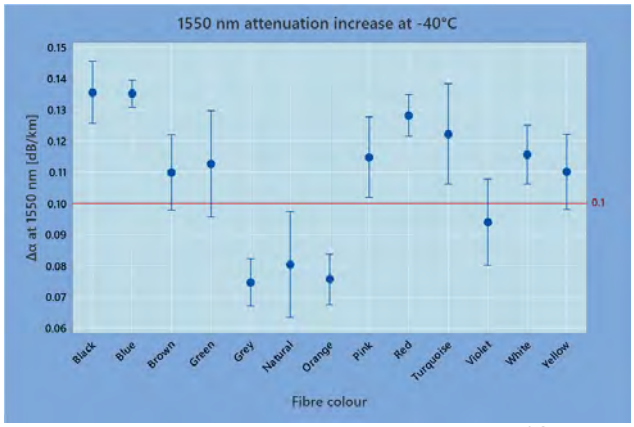


Figure 2 - 1550 nm attenuation increase at -40°C as a function of fibre colour

We see 4 colours passing the test, 9 colours fail. The pattern we see can have 2 causes:

1. The microbending sensitivity of the fibres is colour dependent,
2. The attenuation increase depends on the position of the fibre on the machine.

We will investigate both aspects in more detail.

We also looked at the influence of the various tube colours. The pattern of fibre attenuation increase is given in figure 3.

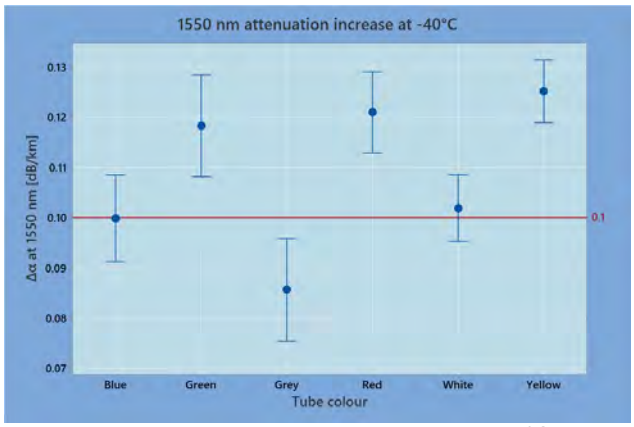


Figure 3 - 1550 nm attenuation increase at -40°C as a function of tube colour

We see 1 tube passes, 3 tubes fail and 2 are at the edge of the specification. Also here it can have 2 causes:

1. Tube material properties such as Young's modulus and coefficient of thermal expansion are influenced by the masterbatch used to colour tubes,
2. The tube pay-offs behave differently.

Also here we need to do further investigations.

3. Analysis of fibre colour dependency of attenuation

In this chapter we try to understand the observed attenuation variation. We will start with the potential influence of the fibre position on the pay-off. Then we look at potential influence of the used colour pigments. Here we will look at 2 aspects:

1. Influence of the colour pigments on the transmission of whispering gallery modes
2. Influence of the colour pigments on increase of the modulus of the primary coating layer due to additional UV cure during the fibre colouring process

2.1 Influence of fibre pay-off position

Figure 4 shows configuration of the fibre the pay-offs in front of the tube extruder.

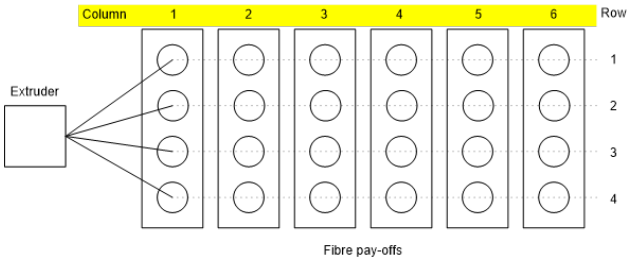


Figure 4 - Pay-off column configuration

The 24 fibres are placed on 6 units (here further referred to as columns) that each contain 4 fibres. Per unit they share the electrical tension control. Individual fine tuning of the 4 fibres can be done using hydraulic devices.

In figure 5 we give the 1550 nm attenuation increase at -40°C for the various columns.

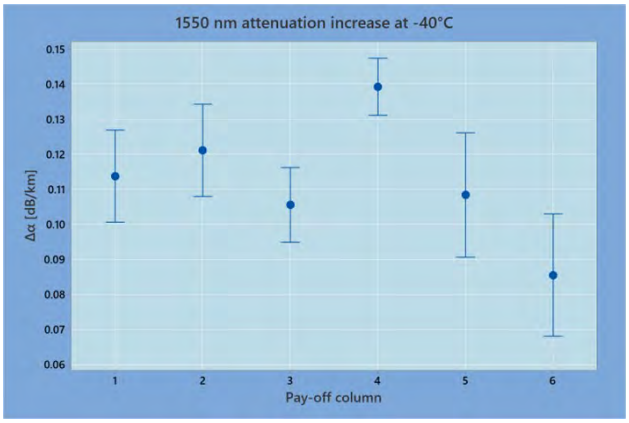


Figure 5 – Pay-off column dependency of attenuation increase

Maybe with exception of column 6 all others need attention.

The same we can do for the row pay-off positions in figure 6.

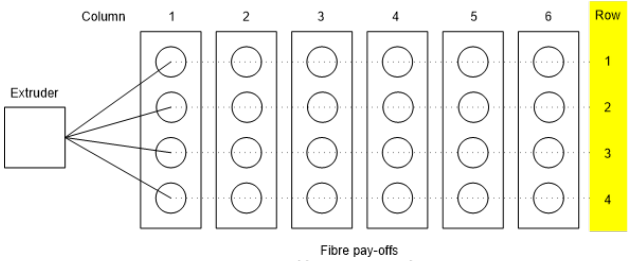


Figure 6 - Pay-off row configuration

Return to Table of Contents

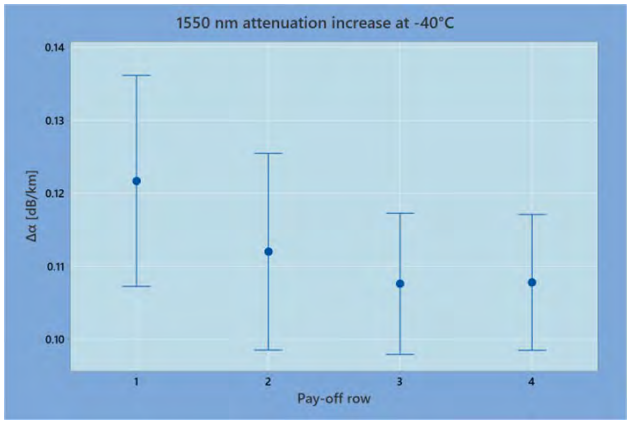


Figure 7 - Pay-off row dependency of attenuation increase

The two top rows show a higher attenuation increase than the two bottom rows. It might be due to the different positioning of the tension controlling dancers.

In preparation for a next trial extreme attention was paid to calibration of fibre tension, proper functioning of pulleys and optimization of the fibre paths.

2.2 Influence of whispering gallery modes on microbending sensitivity

In order to investigate the influence of the various colours on microbending sensitivity of the fibre we took one fibre and subsequently coloured a few hundred metres with all applicable colours. We then measured microbending sensitivity using method B as described in IEC/TR 62221:2012 [1]. The results are given in table 2 where we can see that difference of microbending sensitivity can be as high as 34%.

Table 2 - Fibre colour and microbending sensitivity

Colour	Microbending sensitivity (rel)
Natural	1.00
Yellow	1.01
Green	1.12
Black	1.13
Blue	1.14
Slate	1.16
White	1.19
Red	1.19
Violet	1.20
Orange	1.21
Aqua	1.24
Brown	1.25
Rose	1.34

In a previous IWCS paper [2] we described how we could eliminate the influence of whispering gallery modes on the result of macrobending measurements by choosing a proper curve fitting method. This results in considerably more accurate results of the macrobending measurement.

In a similar way we now compared measured microbending loss values with fitted values. The difference between the two we qualified as influence of whispering gallery modes. Results for the various fibre colours are given in table 2.

Table 3 - Whispering gallery modes and microbending

Microbending loss due to whispering gallery modes [dB/km]					
Colour	1310 nm	1550 nm	1625 nm	Max	Min
Aqua	0.007	0.030	0.007	0.058	-0.070
Black	0.028	0.030	0.056	0.141	-0.129
Blue	0.017	0.005	0.069	0.090	-0.080
Brown	0.019	0.066	-0.004	0.082	-0.096
Green	0.026	0.017	0.048	0.114	-0.088
Natural	0.014	-0.015	0.086	0.167	-0.129
Orange	-0.012	0.018	-0.019	0.097	-0.078
Red	0.014	0.015	0.005	0.072	-0.077
Rose	0.028	0.010	0.060	0.050	-0.060
Slate	0.006	0.013	0.015	0.072	-0.076
Violet	0.025	0.030	-0.013	0.068	-0.081
White	0.005	0.043	-0.001	0.081	-0.067
Yellow	0.036	-0.043	0.099	0.158	-0.130

The contribution of whispering gallery modes showed to be smaller than 2% of the totally measured microbending loss, so we concluded: Noticeable but negligible.

Because of the small effect of whispering gallery modes we extended our research to the modulus of the primary coating layer for the various colours

2.3 Influence of colour pigments on modulus of the primary coating layer

The protective fibre coating normally consists of 2 layers, a soft inner layer, and a hard outer layer. The contribution to the microbending sensitivity depends on the thickness of the 2 layers and their Young's moduli. The influence of coating geometry and mechanical properties on microbending sensitivity can be calculated e.g. with a formula derived by Baldauf and others. It easily can be seen that the most dominant parameter is the modulus of the primary coating.

In the test we did it appeared that during colouring of the fibre an additional cure of the inner coating layer occurred. This results in a slight increase of the modulus and thus an increase of the microbending sensitivity.

The relation between microbending sensitivity and modulus of the primary coating material is given in figure 8. On both axes we use use normalized values.

Return to Table of Contents

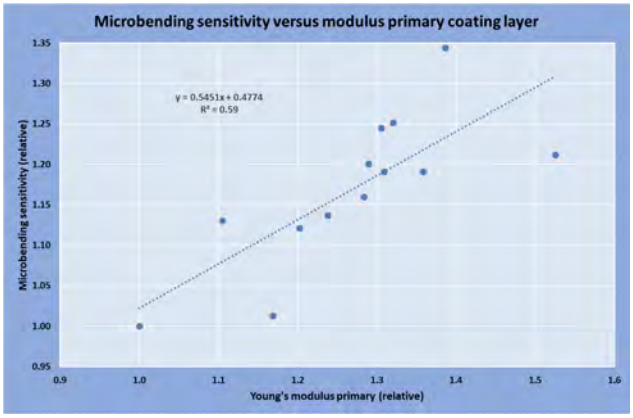


Figure 8 - Microbending and primary modulus

3. Using of a Taguchi method for experimental design of a cable

Starting in 1950 Genichi Taguchi, a Japanese engineer and statistician, developed engineering methods to optimize quality and minimize costs of manufactured goods [3].
One of his methods is the use of orthogonal arrays. When e.g. you want to determine the effect of 7 parameters on 2 levels in a full factorial trial you have to do $2^7 = 128$ tests. Taguchi limited the number of tests by only taking 8 orthogonal combinations. This is known the L8 array and is shown in table 4. Consequence of this efficiency is that you miss interactive relations of parameters in case there are. L8 only gives you a linear dependency. In case you want to look at quadratic terms also you can use the L9 array that gives you the dependency of 4 parameters at 3 levels by doing only 9 tests instead of $3^4 = 81$ in a full factorial trial.

Table 4 - Taguchi L8 schedule

Test run	Factors						
	A	B	C	D	E	F	G
1	1	1	1	1	1	1	1
2	1	1	1	2	2	2	2
3	1	2	2	1	1	2	2
4	1	2	2	2	2	1	1
5	2	1	2	1	2	1	2
6	2	1	2	2	1	2	1
7	2	2	1	1	2	2	1
8	2	2	1	2	1	1	2

By choosing the proper cable designs you can do an L8 or L9 trial in one cable. In table 5 we show how we did set various product and process properties for the various tubes. In a similar way you can set up a 9 tube design for investigating 4 parameters at 3 levels.

Table 5 - Test setting 8 tubes of 192 fibre cable

Test	Tube colour	Fibre pay-off tension	Tube pay-off tension	MAC	CD ratio	Column pay-off configuration	Row pay-off configuration
1	Black	H	H	L	H	A	A
2	Black	H	H	H	L	B	B
3	Black	L	L	L	L	A	B
4	Black	L	L	H	H	B	A
5	Natural	H	L	H	H	A	B
6	Natural	H	L	L	L	B	A
7	Natural	L	H	H	L	A	A
8	Natural	L	H	L	H	B	B

The first parameter is added to get an impression of the influence of the tube colour. We made the cable with black tubes and tubes made from the natural material. By choosing the right tube sequence we are able to identify the various tubes. By using only two tube colours we maximally reduced eventual mechanical influences of the tube pay-offs.



Figure 9 - Structure of 192 fibre test cable

The following two parameters are process parameters, the fibre pay-off tension and the tube pay-off tension.

The 4th parameter is the MAC value, defined as MFD/COW (COW is fibre cut-off wavelength). In theory microbending sensitivity decreases with decreasing MAC.

As 5th parameter we defined the new concept of CD ratio, the quotient of diameter over primary coating and diameter over secondary coating layer. Microbending sensitivity decreases with increasing CD ratio.

The high and low parameter values of MAC and CD ratio we took from produced fibres according to the schedule in table 6

Table 6 - Selection scheme for MAC and CD ratio

		MAC	
		H	L
CD ratio	H	MAC ≥ μ_{MAC} CD ratio ≥ $\mu_{CD\ ratio}$	MAC < μ_{MAC} CD ratio ≥ $\mu_{CD\ ratio}$
	L	MAC ≥ μ_{MAC} CD ratio < $\mu_{CD\ ratio}$	MAC < $_{MAC}$ CD ratio ≥ $\mu_{CD\ ratio}$

We added these last two parameter to get a better quantitative impression of their influence.

Finally we added parameters that should give insight in the effectiveness of our fibre pay-off optimization actions.

4. Test results of Taguchi trial

Results of the trial showed that the modifications made on fibre pay-off configuration was such that influence of the fibre pay-off positions further could be neglected, so we limit ourselves here to the other 5 parameters. Figure 9 gives the influence of exposure to -40°C on the attenuation at 1550 mm

Return to Table of Contents

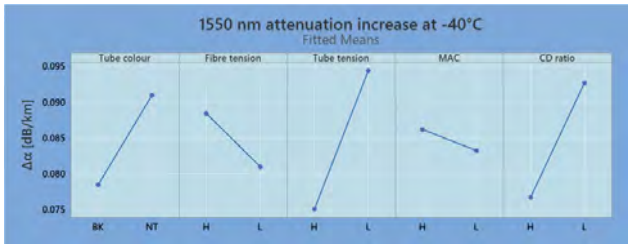


Figure 9 – Regression analysis of attenuation increase at -40°C

It shows:

- The black tube (with masterbatch) performs better than the tube made of natural material;
- lower attenuation increase with lower fibre pay-off tension;
- lower attenuation increase with higher tube pay-off tension;
- lower attenuation increase with lower MAC, a result as expected but quantitively the lowest influence of the 5 monitored parameters;
- lower attenuation increase with increasing CD ratio, quantitatively a little higher than expected.

In figure 10 we see the influence of the 5 parameters on the residual attenuation increase after the temperature cycle.
In comparison with the -40ºC results we see a much smaller influence of tube tension, and a relatively larger influence of the MAC value. It must be noted that the scale in figure 10 is about a factor of 4 smaller than the scale in figure 9.

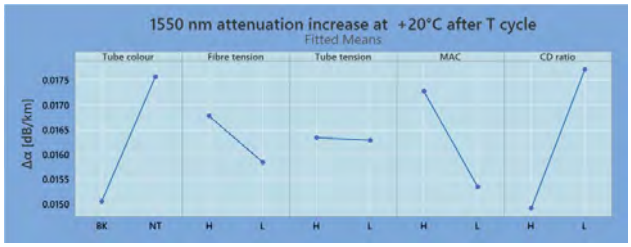


Figure 10 - Regression analysis attenuation increase after temperature cycle

In table 5 the test results are given in a qualitative way, the "positive" points in green, the "negative" in red. Based on that we tried to make a ranking. We estimated tube BK1 to be the champion, followed by tube NT4. The quantitative results in figure 11 show a little deviation view, but the trend is visible. With exception of tube NT3 all tubes passed the -40ºC requirement. By proper selection of parameters considerable quality improvement can be attained.

Table 5 - Qualitative overview of test results

Tube colour	Fibre pay-off tension	Tube pay-off tension	MAC	CD ratio	Column pay-off configuration	Row pay-off configuration	Rank
BK1	H	L	L	H	A	A	1
BK2	H	L	H	L	B	B	3
BK3	L	H	L	L	A	B	4
BK4	L	H	H	H	B	A	4
NT1	H	H	H	H	A	B	3
NT2	H	H	L	L	B	A	3
NT3	L	L	H	L	A	A	4
NT4	L	L	L	H	B	B	2

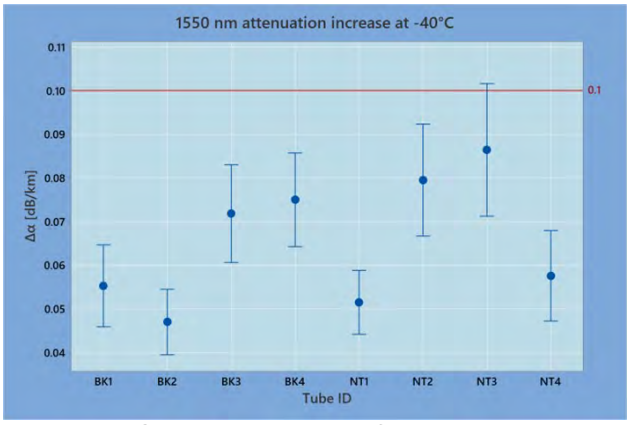


Figure 11 – Quantitative results of the various tubes at -40ºC

5. Multi-parameter regression

For a multi-parameter regression we added two parameters that we did not include in the Taguchi trial. We added:

- Relative microbending sensitivity of the various fibre colours (MBS rel), and
- Coloured fibre diameter.

In our very first analysis we saw an attenuation difference between ring marked fibres and fibres without mark. Further research revealed that due to manufacturing on different machines ring marked fibres had a smaller diameter and thus a higher microbending sensitivity. The difference in average diameter of the two fibre groups was about 2 µm.

Results of the multiparameter regression are laid out in figures 12 - 14.

Figure 12 gives the values after cable manufacturing, just before start of the temperature cycle. The 3 main influencers are: tube tension, MAC-value and diameter of the coloured fibre.

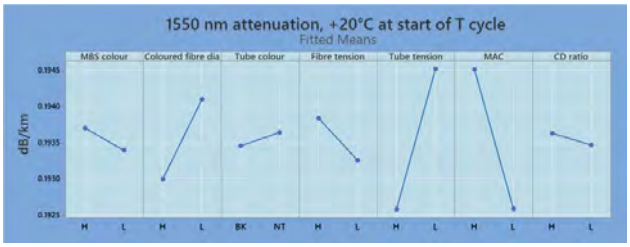


Figure 12 - 1550 nm attenuation on finished cable

The behaviour at -40ºC in figure 13 shows tube tension, CD ratio and tube colour as most important factor.

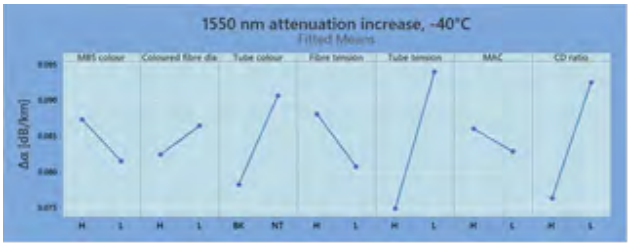


Figure 13 - 1550 nm attenuation increase at -40ºC

After the temperature cycle a permanent attenuation increase has high influence of tube colour, MAC, and CD ratio.

Return to Table of Contents

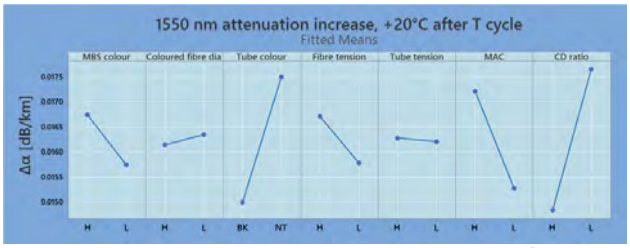


Figure 14 - 1550 nm attenuation increase after temperature cycle

Overall we see important effects of tube colour, tube tension, MAC and CD ratio.

6. Mechanical limits of the cable design

To determine the mechanical abilities of the cable design we performed what we call "limit tests". Where actual values are specified in e.g. bending, kink and torsion specification values are largely exceeded. A potential specification for impact, crush and tensile performance for the cable can be found under point 5, 6 and 7 in table 6.

Table 6 - Results of "limit tests"

1 Cable Bend					
Details	Specification value	Test criteria			Limit result
Bending radius	15D	No damage of sheath, tubes and fibres			**10D, 10 turns**
Number of turns/helix	4	SMF	$\delta\alpha_{1550}$	≤ 0.1 dB	0.048
Number of cycles	3		$\Delta\alpha_{1550}$	≤ 0.05 dB	0.009
2 Repeated Bending					
Details	Specification value	Test criteria			Limit result
Bending radius	20D	No damage of sheath, tubes and fibres			**5D**
Number of cycles	100	SMF	$\delta\alpha_{1550}$	≤ 0.1 dB	0.013
Tensile load	10N		$\Delta\alpha_{1550}$	≤ 0.05 dB	0.009
Cycling rate	±15/min				
3 Kink					
Details	Specification value	Test criteria			Limit result
Loop diameter	30D	No kinking may occur			**15D**
		SMF	$\delta\alpha_{1550}$	≤ 0.1 dB	0.010
			$\Delta\alpha_{1550}$	≤ 0.05 dB	0.003
4 Torsion					
Details	Specification value	Test criteria			Limit result
Rotation	360°/m	No damage of sheath, tubes and fibres			**720 °/m**
Number of cycles	5	SMF	$\delta\alpha_{1550}$	≤ 0.1 dB	0.008
Temperature	Ambient		$\Delta\alpha_{1550}$	≤ 0.05 dB	0.006
Tensile load	100N				
5a Impact (300 mm hammer)					
Details	Specification value	Test criteria			Limit result
Number of locations	3	No damage of sheath, tubes and fibres			**1 J (6 locations)**
Number of impacts/location	1	SMF	$\delta\alpha_{1550}$	≤ 0.1 dB	0.007
Hammer radius	300 mm		$\Delta\alpha_{1550}$	≤ 0.05 dB	0.001
5b Impact (10 mm hammer)					
Details	Specification value	Test criteria			Limit result
Number of locations	3	No damage of sheath, tubes and fibres			**1 J (6 locations)**
Number of impacts/location	1	SMF	$\delta\alpha_{1550}$	≤ 0.1 dB	0.015
Hammer radius	10 mm		$\Delta\alpha_{1550}$	≤ 0.05 dB	0.009
6a Crush (long term)					
Details	Specification value	Test criteria			Limit result
Number of locations	3	No damage of sheath, tubes and fibres			**500 N**
Plate	100*100 mm	SMF	$\delta\alpha_{1550}$	≤ 0.1 dB	0.008
Test time	10 minutes		$\Delta\alpha_{1550}$	≤ 0.05 dB	0.005
6b Crush (short time)					
Details	Specification value	Test criteria			Limit result
Number of locations	3	No damage of sheath, tubes and fibres			**1500 N**
Plate	100*100 mm	SMF	$\delta\alpha_{1550}$	NR	3.420
Test time	1 minute		$\Delta\alpha_{1550}$	≤ 0.05 dB	0.006
7 Tensile performance					
Test criteria	Limit result				
Fiber strain	0.2% (10min)			0.6% (10min)	
Tensile	**500N**			**2000N**	
$\delta\alpha_{1550}$	0.042 dB			0.083 dB	

7. Stripping "tight tubes"

An important aspect for successful introduction of the new concept in the application field is the processability of the cable in the field. We especially paid attention to the strip ability in the field. We tested all stripping tools used in our daily practices and concluded that they performed more than satisfactory, of course with proper knife settings and adequate training of the operators.

8. Conclusions

- We showed a successful new cabling concept which could be described as "tight tube". It overcomes the limits of the "loose tube" concept in enabling further reduction of cable diameters.
- The method to use a Taguchi L8 test schedule to optimize a cable design and its manufacturing processes showed to be very powerful and efficient in developing a new cable concept.
- The influence of fibre properties could be improved by decreasing MAC and increasing CD ratio.
- Tension control in the fibre tubing and stranding process is paramount to maintain product quality.
- It might be worthwhile to reduce the after cure effect in the primary coating due to the colouring process.
- One should strive at reduction of fibre diameter variation in the cable by careful control of intermachine differences in the colouring process.
- The influence of tube colour masterbatches on E-modulus and coefficient of thermal expansion of the tube material needs further investigation. It might well be that e.g. matching tube colour and tension settings could reduce influence on cable quality.
- Normal installation practices apply in processing this new cable concept, of course with proper settings of tooling and training of operators.

9. Acknowledgements

We thank our management, Elling de Lange, CFO of TKH Group NV, and Xia Li, CEO of Twentsche (Nanjing) Fibre Optics Ltd., for giving us the opportunity to present the results of our cable development activity.

We thank Zheng Ming and Xie Shengfu for optimizing the processes and making the trial cable, Fang Hongbing for all the cable tests, Zhou Lijia and Duan Linlin for all fibre measurements.

We further are grateful to our collegues at BV Twentsche Kabelfabriek, Henk Woldhuis, André Steghuis, Olaf Grosskurt and Sido Oevering, for their contributions in the discussions about test results, and John Jongman for doing the tube stripping tests.

10. References

[1] IEC/TR 62221:2012: "Optical Fibres - Measurement methods Microbending sensitivity", Edition 2, 2012-12

[2] Siping Ning, Onno R. Bresser, Linlin Duan, Bin Wang, "Use of Weighted Least Square Fitting Methods in Microbending Loss Tests on Single-mode Fibres", Proceedings of the 63rd IWCS Conference, 2014, pp 92-96

[3] Genichi Taguchi, "System of Experimental Design", Engineering Methods to Optimize Quality and Minimize Costs, Volume One, UNIPUB/Kraus International

Return to Table of Contents

Publications and American Supplier Institute Inc., 1987, pp 165-183

[4] John Baldauf, Naoki Okada, Matsuhiro Miyamoto, “Relationship of Mechanical Characteristics of Dual Coated Single Mode Optical Fibers and Microbending Loss, IEICE Trans. Commun., Vol. E76-B, No. 4 April 1993, pp. 352-357

11. Authors



Onno Bresser received his M.Sc. degree in Electrical Engineering at the University of Technology of Delft (The Netherlands) in 1975. After that he joined NKF Kabel (later Draka) where he founded a group for development of optical fibre cable and associated technologies. From 1990 till 1995 Onno worked as an independent consultant, in which period, amongst other things, he developed optical tow cables for sonar systems for military surface vessels as well as submarines. In 1995 he joined TKH Group where he did build a plant for manufacturing optical fibre and cable in Nanjing (People’s Republic of China). Presently Onno is Director Development of Optical Fibre and Cable at TKH Group as well as Chief Technical Officer at Twentsche (Nanjing) Fibre Optics Ltd.. Onno attended the IWCS for the first time in 1976.



Zhang Li (Lily Zhang) graduated from Xi'an Jiaotong University in year 1993. She has been engaged in fibre optic cable research and development in Beijing Corning from 2000 to 2014. She joined TFO in 2016. Now she is Cable R&D manager of Twentsche (Nanjing) Fibre Optics Ltd..



Siping Ning (Steven Ning) received a B.Sc in Automation from Harbin Engineering University and a MBA from Tianjin University. He has been engaged in optical fibre and optical fibre cable manufacturing and products measurements and tests since 2000. He joined TFO in year 2010, now he is a senior engineer and the director of Quality Management and Test Department for fibre and cable of Twentsche (Nanjing) Fibre Optics Ltd..

Return to Table of Contents

A Modeling Approach for the Sintering of Cylindrical Silica Soot Preform

Debangshu Debnath[1], Arpit Sen Shrivastava, Sandeep Gaikwad & E. Sudhakar Reddy

Research and Innovation, Sterlite Technologies Limited, E1, E2, E3, Waluj MIDC

Aurangabad, Maharashtra: 431136, India

[1]debangshu.debnath@stl.tech

Abstract

This study presents a model for describing the sintering of a porous silica cylindrical preform used for optical fiber manufacturing. Modeling of the process is performed from first principles and an analytical model is developed and solved using numerical methods. The effect of the physical properties of preform and the furnace temperature on the temperature, viscosity, porosity, and radius of the preform with time is discussed in detail. The density profile of a partially sintered preform, at different stages of time-temperature scale, measured using a CT scan, is used to validate the model.

Keywords: Modeling; Porosity: Heat Transfer; CT scan, Optical fiber.

1. Introduction

Industrially, glass optical fibers are drawn from bulk glass cylinders. These glass bodies are manufactured by sintering porous silica soot cylindrical preforms deposited by an OVD process. The sintering process involves closure of the open pores within the body and subsequent closed pores collapsing resulting in the shrinkage of the green body. This bulk shrinkage can be attributed to the coalescence of the silica particles due to reduction in surface energy of the system.

The green body absorbs energy via two mechanisms; wherein the surface of the green body is heated via radiation followed by conduction within the green body which leads to the increase in the temperature of the body. Once the temperature of the green body reaches the sintering temperature, viscous flow starts and the pores begin to collapse to attain a lower surface energy [2].

In the present investigation, we propose an approach for modeling the sintering behavior of the silica green body by combining the heat equation and shrinkage models available in literature [1.2]. Previous studies have highlighted the influence of heat transfer mechanisms on the variation of physical parameters like temperature, porosity, thermal conductivity and shrinkage of the green body [3,4]. Furthermore, the model has been validated using the experimental value pertaining to the density of the green body as obtained from the CT scan data/experiments [10].

2. Background

Previously, work has been done by *McKenzie et. al (1949)* and *W.Scherer (1976)* [1,2] which demonstrated the rate of variation of porosity of an unit cell with respect to time. This concept has been extensively been used for demonstrating the shrinkage behavior of small scale soot bodies by *Doorawar et al (2010)* [4] or the diffusion kinetics of dopant gases inside the porous soot during sintering by *Tandon (1994)* [5]. Also microscale analysis of the conversion of silica particles into large multi-particle aggregates and their fractal behavior is clearly demonstrated in the works of *Rosner and Tandon (1995)* [6]. However all of these studies focused mostly on mathematical simulation and no experimental validations were available. Recent studies involving the effects of the sintering gases in dehydroxylation and the resulting shrinkage of a lab scale sample has been demonstrated by *Ma Qianli et al (2010)* [7] with proper validation of the shrinkage kinetics and gas concentration inside the sample. Although, the size of the specimen used in this case is not explicitly mentioned. Overall, there was a need for the analysis of the unit operations taking place during the sintering of a full scale preform subjected to gravitational and thermal forces. An approach for modeling the dynamic coupling between preform input parameters, furnace input parameters and shrinkage of preform and estimating the optimum completion time for the process has been discussed in this work.

3. Theoretical Analysis

The sintering process takes into account the transfer of thermal energy from the furnace coil surface to the silica soot preform. Along with this heat transfer process, viscous flow takes place along the surface of the soot particles according to Frenkel's theory. This, in turn dictates the kinetics of sintering where the porosity at every point in the system is governed by the local temperature, time elapsed from sintering onset and the initial porosity. Hence, by accurately capturing the temperature and the starting density, the total time of sintering and the final physical properties of the sintered preform can be predicted without the application of any sintering gases.

4. Mathematical Model

In the current setup, thermal energy is transferred from the wall of the furnace onto the outer surface of the cylindrical soot body. Once the outer surface attains an equilibrium temperature with the furnace wall, the heat is assumed to be conducted radially inside the soot body as the axial thermal gradient is very small. Hence we initially apply the Fourier's law of heat conduction in the cylindrical coordinate with no temperature variations in the axial or azimuthal directions. Also the radial domain is discretized in such a way that the mass of each section in between two adjacent nodes remains constant throughout the sintering process.

4.1. Discretized Domain and the Heat Transfer Equations: The radial domain is discretized into a fixed number of sections according to the user as per the following schematic

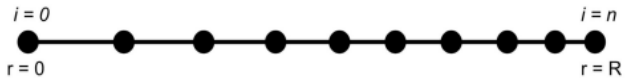


Figure 1. The discretization of the radial domain according to the mass equivalency

The heat transfer inside the preform is modeled using the one dimensional heat conduction equation in the cylindrical coordinates as follows.

$$\frac{1}{\alpha}\frac{\partial T}{\partial t} = \frac{\partial^2 T}{\partial r^2} + \frac{1}{r}\frac{\partial T}{\partial r} \quad (1)$$

Where α is the thermal diffusivity of the material, and T is the temperature, which is a function of radial distance r, and time.

4.2. Temperature Dependence on Viscosity:

The viscosity of silica varies greatly in the range of sintering temperature. This variation is modeled by fitting the experimental data [8] to the VTF equation. [9]

$$ln[\eta(T)] = A_{VTF} + \frac{B_{VTF}}{R(T - T_V)} \quad (2)$$

4.3. Equations of Sintering Kinetics:

The densification of the preform is modeled using the work of Scherer [2] and McKenzie and Shuttleworth [1]. When the solid fraction of glass is less than 0.94, Scherer's model is used,

$$\varphi = 1 - \varepsilon \quad (3)$$

Where φ is the solid fraction and ε is the porosity. A non-dimensional parameter x is calculated from the solid fraction (φ) according to the following equation,

$$\varphi = 3\pi x^2 - 8\sqrt{2}x^3 \quad (4)$$

The change is solid fraction with respect to time is then calculated using the following equation,

$$\frac{dx}{dt} = \frac{1}{2}\left(\frac{\sigma n^{\frac{1}{3}}}{\mu}\right)\left(3\pi - 8\sqrt{2}x\right)^{\frac{1}{3}} x^{\frac{2}{3}} \quad (5)$$

Where σ is the surface-tension coefficient, n is the number of pores per unit volume, and μ is the viscosity of the material. Once x is calculated, the solid fraction can be obtained again using equation (4). For solid fractions higher than 0.94, the Scherer's model is no longer applicable. The model given by McKenzie and Shuttleworth [1] is used for modeling the densification in this case.

$$\frac{d\varepsilon}{dt} = -\frac{3}{2}\left(\frac{4\pi}{3}\right)^{\frac{1}{3}} \frac{\sigma n^{\frac{1}{3}}}{\mu} \varepsilon^{\frac{2}{3}} (1 - \varepsilon)^{\frac{1}{3}} \quad (6)$$

Thus, the combination of these two models allow us to model the porosity change with time and other material properties for the entire range of porosity values.

4.4. Solution of the Model:

The equations from (1) through (6) mentioned above are discretized and solved numerically to obtain the temperature at every node in accordance with the initial and boundary conditions set by the user. The corresponding temperature values are read into equations (2) through (6) and the real time porosity values are computed. Once the updated porosity values for all the shells are known, their radii are calculated and updated with the assumption that the mass remains the same during densification.

5. Model Validation:

To conduct our validation, we employed Computed Tomography (CT) scanning, a non-destructive technique that uses X-ray measurements taken from multiple angles to construct cross-sectional images or 'slices' of an object. These slices offer an intricate view of the internal structure of the object and facilitate accurate estimation of its density through the calculation of the attenuation coefficient.

For validation purposes, the sintering of a preform was interrupted intermittently after a known period of time, and the preform is subjected for scanning. The scanning provides a porosity profile of the preform at that particular interval of time from the start of sintering. Thus the transient change in porosity along the radius may be validated using this method. The data obtained from the CT scans were initially recorded as DICOM files, with pixel values denoted in Hounsfield units (HU).

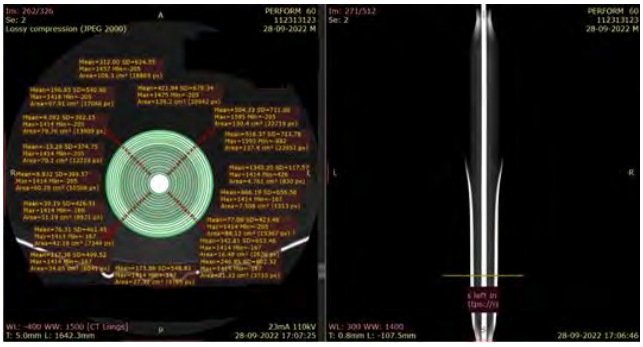


Figure 2. The CT Scanning of the partially sintered preform and the density analysis from the HU Values of the same

To facilitate our analysis, these values were converted into the corresponding values of porosity using CT scan machine calibration data. The porosity profiles at different times thus obtained from the CT scan data are then used to validate the predictions of the model.

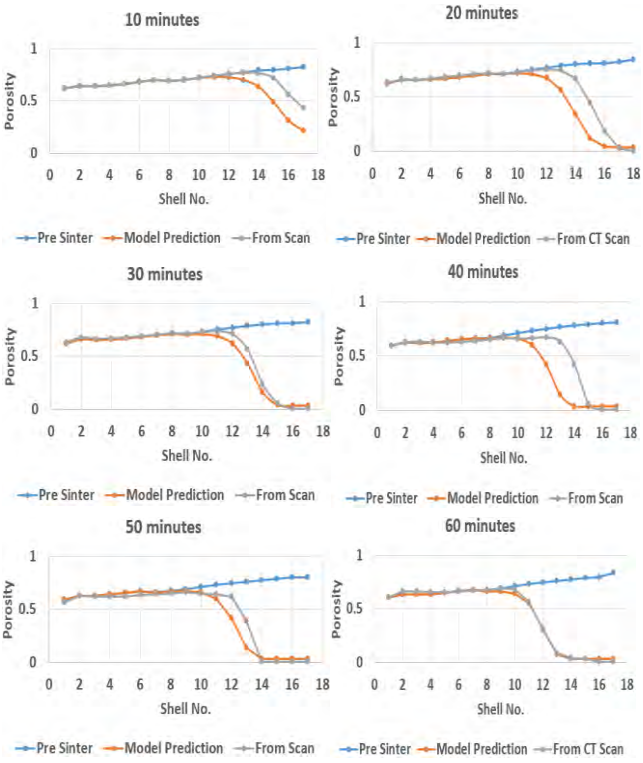


Figure 3. The correlation of the model estimated values of the radial porosity profile of the preform sintered for 10 minutes through 60 minutes at 10 minutes of interval with respect to the actual porosity profile determined through CT scan method

6. Results and discussion:

The simulation results, as depicted in Figure 3, illustrate the porosity profile predicted by our model for varying process times, ranging from 10 minutes to 50 minutes. We observe a slight deviation between the predicted and measured porosity values within this time range, although the overall trend closely followed the model prediction results. However, when the process time is extended to 60 minutes, our model exhibits a remarkably close match with the measured porosity profile.

To validate the overall robustness of the model in the practical industrial implications, we also correlated the other variable parameters during the course of complete sintering of our regular preforms and noted the correlations with our actual process parameters.

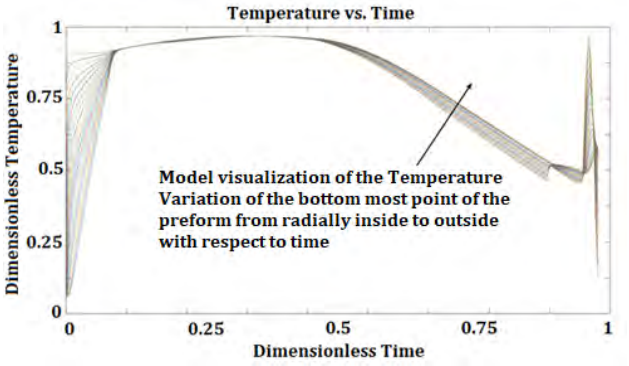


Figure 4a. The estimation of the temperature variation with respect to time across a particular cross section of the preform

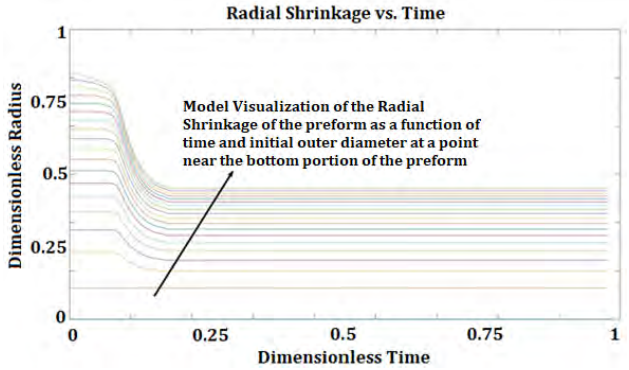


Figure 4b. The estimation of the radial shrinkage with respect to time across a particular cross section of the preform which lies within 10% of the actual shrinkage time in the preform

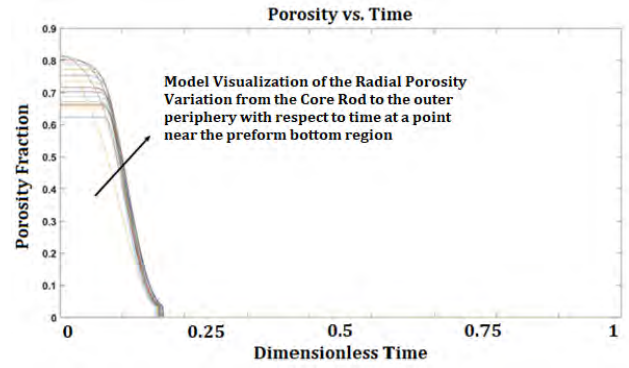


Figure 4c. The estimation of the porosity profile with respect to time across a particular cross section of the preform which almost correlates with the total sintering time

The figures 4a through 4c represents the model estimation of the different parameters of the preform with respect to time. The results successfully demonstrate the applicability of a one-dimensional model for approximating the sintering process. This outcome reinforces our confidence in the validity of the assumption of a one-dimensional representation.

Having successfully validated our model, we can now employ it to determine the optimal sintering time for any specific preform and sintering conditions. As a result, our model holds the potential for optimizing industrial sintering processes, contributing to enhanced efficiency and improved outcomes in such applications.

7. Conclusion:

The study demonstrates a predictive model that can estimate the porosity profile, instantaneous outer diameter and the radial temperature profile of optical fiber preforms during the sintering process. The model's performance was robust. A particularly strong correlation was observed between the model predictions and the actual porosity measurements, obtained through CT scans, for longer sintering times. However, the model exhibited small deviations from the actual values during intermediate sintering times. These discrepancies underline potential areas of further refinement of the model. Nevertheless, even during these periods, the overall trend and nature of the model's predictions closely matched the actual measurements, supporting the validity of the model.

The successful application of CT scanning technology for validation of the model has been a significant aspect of this study. This non-destructive and precise method allows for an accurate determination of the porosity profile across the preform's radius, thereby serving as a reliable real-world check for the model's predictions. The positive correlation between the CT scan results and the model outputs strengthens the model's credibility and provides a robust pathway for future modeling studies in this field.

The research findings underscore the importance and potential of computational modeling as a tool to optimize the sintering process in optical fiber production. This approach could greatly contribute to improved efficiency and cost-effectiveness in the manufacturing process. Future research may further refine this model and validate its applicability across a wider range of sintering conditions and preform materials.

8. Acknowledgement:

We would like to acknowledge Dr. Saurabh Kapoor for the discussions on glass sintering and the properties of glass.

9. Picture of Authors:

Debangshu Debnath is a process simulation and modelling engineer at Sterlite Technologies Limited, India. He holds a master's degree in Chemical Engineering from Indian Institute of Technology,



Kharagpur. He has 4 years of experience in modelling of thermal domain problems related to the manufacturing of Optical Fiber and Optical Fiber Cables.

9. References:

[1] J. Mackenzie and R. Shuttleworth, "A phenomenological theory of sintering," *Proc. Phys. Soc. Sect.* B 62, 833 (1949).

[2] G. W. Scherer, "Sintering of low-density glasses: I, theory," J. *Am. Ceram. Soc.* 60, 236–239 (1977).

[3] "Process for Sintering porous optical fiber preform", *European Patent Application Number 0626351A1* (1994)

[4] S. Doorwar, S. Chakraborty, and S. Neogi, "A multiscale model for quantifying helium diffusion in porous unsintered glass," *The Can. J. Chem. Eng*. 88, 153–160 (2010).

[5] P. Tandon, "Doping of silica during sintering," J. non-crystalline solids, 1466–1472 (2005).

[6] P. Tandon and D. E. Rosner, "Sintering kinetics and transport property evolution of large multi-particle aggregates," *Chem. Eng. Commun.* 151, 147–168 (1996).

[7] Q. Ma, L. Zheng, G. Zhang, C. Shang, and H. Fang, "Numerical modeling of sintering and dehydroxylation of porous silica preform for low-hydroxyl silica glass fabrication," *Ceram. Int.* 46, 23067–23083 (2020).

[8] "4 - physical and chemical properties of silica glasses," in Silica Glass and its Application, vol. 11 of Glass Science and Technology I. Fanderlik, ed. (Elsevier, 1991), pp. 194–270.

[9] M. I. Ojovan et al., "Viscosity and glass transition in amorphous oxides," *Adv. Condens. Matter Phys*. 2008 (2008).

[10] D.H.Philips, Lannutti, "Measuring Physical Density with X-ray Computed Tomography", *NDT&E International Vol.30 No.6*

SESSION 7

Click on a session below to navigate to that section of the Proceedings.

SESSION 7: CONNECTIVITY

Chairperson: Mike Gurreri, CommScope, Inc., USA

7-1 **Liquid Immersion Multi-Fiber Connector for Data Center Cooling System;** Prof. Mitsuru Kihara, *Osaka Electro-Communication University, Japan*

7-2 **Connection Characteristics of Coupled Multicore Fiber Connector;** Mr. Yuki Fujimaki, *Chiba Institute of Technology, Japan*

7-3 **Optical Transceivers and Structured Cabling with Expanded Beam Connectors as an Alternative to Active Optical Cables;** Dr. Earl Parsons, *CommScope, USA*

7-4 **A VSFF, Multi-Row, Multi-Fiber Connector with Multi-Vendor Interoperability;** Mike Hughes, *US Conec Ltd, USA*

7-5 **A Novel, Low-Loss, Multi-Fiber Connector with Increased Usable Fiber Density;** Dr. Scott Bickham, *Corning Optical Communications, USA*

7-6 **Sustainable Network Design: Plastic Reduction with Ultra High-Density Cabling with Thinner Coating and VSFF Connector in Data Centers;** Mr. Takeshi Kasai, *Senko Advanced Components, USA*

Click here to return to the **Table of Contents**

Liquid-immersion Multi-fiber Connector for Data-center Cooling Systems

Mitsuru Kihara*, Yuto Tameoka*, Koichi Arishima**, Tetsuo Miya**, and Motohiro Nakahara**

*Osaka Electro-Communication University and **Nakahara Opto-Electronics Laboratories, Inc.

Neyagawa, Osaka 572-8530, Japan

+81-72-824-1131· kihara@osakac.ac.jp

Abstract

This paper presents a novel liquid-immersion multi-fiber connector for data centers. The optical connector is an expanded beam (EB) connector with a graded-index (GRIN) lens array attached to a mechanically transferable (MT) connector. The insertion loss of the fabricated EB connector had a low insertion loss of 1.0 dB or less in both air and a cooling liquid. We measured the insertion loss by changing the gap of the EB connector and clarified that the insertion loss does not change in both air and cooling liquid compared with a conventional MT connector. We also immersed the EB connector in aqueous solutions with varying amounts of mud powder, measured the insertion loss, and clarified that the tolerance for foreign matter in an aqueous solution is greater than that of a conventional MT connector.

Keywords: Optical fiber. Optical connector, GRIN lens, Data center

1. Introduction

The demand for data centers has increased as the amount of data communication increases. In 2020, data centers around the world consumed about 1% of the world's electricity. A liquid-immersion cooling system that cools servers by immersing them in liquid is gaining attention for data centers to reduce power consumption [1]. Compared with gases used in air conditioning, liquids have a cooling capacity that is up to hundreds of times higher than gases, leading to a significant reduction in power consumption.

In data centers, in addition to electrical equipment such as servers, much optical equipment, such as optical fibers and optical connectors, are also used. Since the optical connector is an optical component intended for use in atmosphere, there has been little research on optical connectors for liquid immersion.

We fabricated a novel liquid-immersion multi-fiber connector for use in data centers. We experimentally investigated the optical characteristics of our connector in cooling liquid to verify its effectiveness.

2. Liquid-immersion multi-fiber connector

Figure 1 shows our liquid-immersion multi-fiber optical connector (hereafter, expanded beam (EB) connector). It has a structure in which a graded index (GRIN) lens array [2] is attached to the end face of a mechanically transferable (MT) connector [3] for connecting a multi-fiber ribbon. With this structure, the beam of light from the connector end face expands to form an EB connector. Conventional beam-enlarging optical connectors have a structure in which a ball lens or convex lens is attached to the end face of an optical fiber [4]. Our EB connector can be used for both air and liquid immersion cooling.

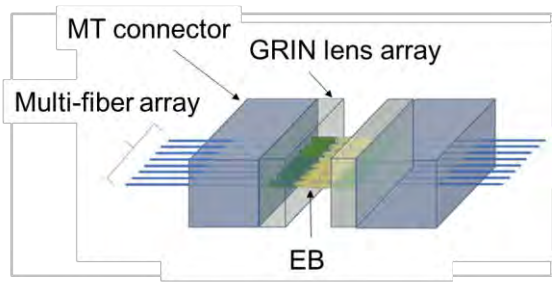


Figure 1. Fabricated liquid-immersion multi-fiber connector with GRIN lens array (EB connector)

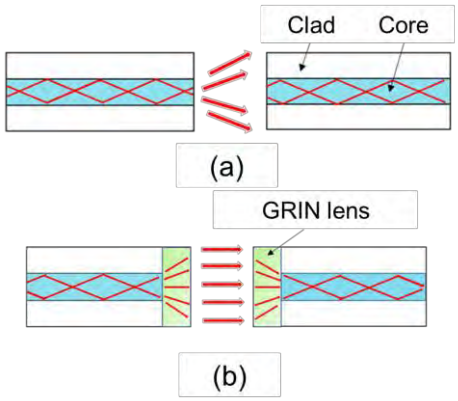


Figure 2. Optical path of fiber connection (a) in MT connector and (b) in EB connector

Compared with the conventional MT connector, our EB connector changes the optical path of light from radiation to parallel due to the refractive index distribution in the GRIN lens. Figure 2(a) shows emitted light from the optical-fiber end face of an MT connector and (b) emitted light from the lens end face of our EB connector. When there is a gap in the MT connector, the light beam radiates from the end face, whereas in our EB connector the light beam emitted from the end face expands and travels straight. A feature of this connector is that the transmission loss does not change in different media such as air and liquid, even if the gap is widened, by adopting a structure through which this GRIN lens is passed.

Figure 3 shows photos of the end faces and top of our EB connector, which is an optical connector consisting of 12 multimode fibers (50 μm GIF). A transparent GRIN lens array is attached to the end face of the MT connector. The GRIN lens array was fabricated using fiber-optic fabrication methods. The attachment of the GRIN lens array to the MT-connector end face is precisely aligned and adhesively fixed using precision image-processing technology.

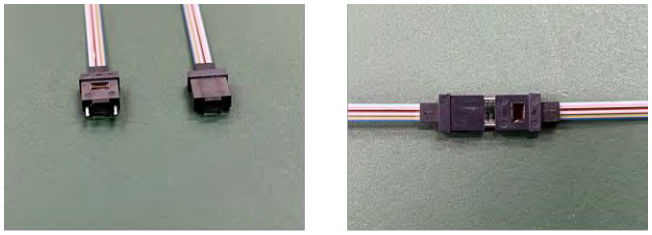


Figure 3. Photos of (a) end faces and (b) top of our EB connector

Table 1. Return losses and refractive indices of various media

	Return loss (dB)	RI (Experiment)	RI (Literature)
Air	14.69	1.001	1.000
Water	26.19	1.318	1.332
Ethnol	28.96	1.354	1.360
Cooling liquid	23.04	1.263	1.260

3. Cooling liquid

There are two main cooling liquids used in data centers. One is a two-phase refrigerant and the other is a single-phase refrigerant. We used a fluorinated liquid equivalent to 3M's Novec 649, a two-phase refrigerant. A major feature of this liquid is that it is a highly volatile liquid with a boiling point of 49ºC. Another feature its low refractive index (RI) of 1.26, measured at a wavelength of 589 nm. The light we used had a wavelength of 1550 nm. Therefore, to confirm whether there is a difference in the RI depending on the wavelength, the RI of the medium was measured from the return-loss measurement with the right-angled end face of a single-mode optical fiber [5]. Table 1 lists the measurement results and those from previous studies [6]. For comparison, the results for air, water, and ethanol are also shown. The return loss of the cooling liquid at 1550 nm was 23 dB, and the RI was 1.26, which is the same as that at the wavelength of 589 nm.

4. Experiments and results

We measured the insertion loss of our EB connector using a distributed feedback (DFB) laser light source (LS) and optical power meter (OPM). Figure 4 shows the experimental setup. The insertion loss was obtained from the difference in transmitted light intensity due to connector insertion using fusion splicing. Figure 5 shows the measured insertion loss for each fiber channel of our EB connector, where the blue squares represent in air and red circles represent in cooling liquid. Although the loss in the cooling liquid was smaller than that in air, we were able to achieve a low insertion loss below 1.0 dB.

We then intentionally created a gap between the end faces of our EB connector and investigated the change in insertion loss. Figure



Figure 4. Experimental setup of connector-insertion-loss measurement

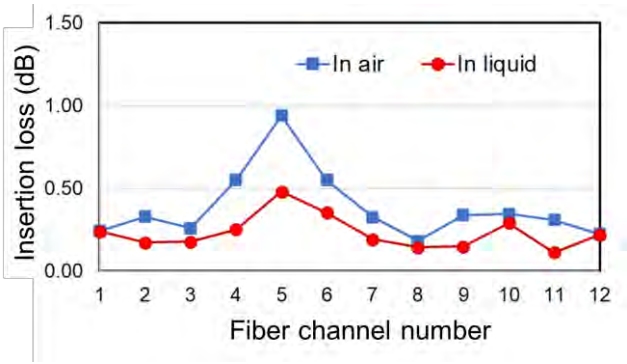


Figure 5. Insertion loss of our EB connector

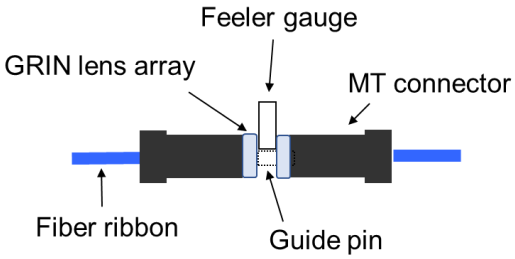


Figure 6. Experimental sample of our EB connector with feeler gauge

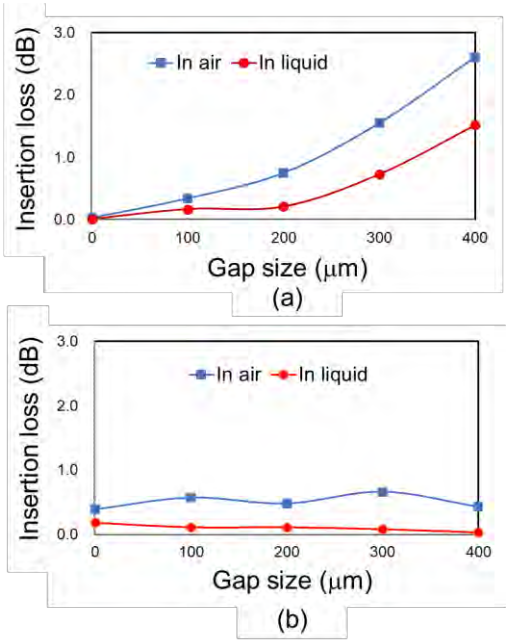


Figure 7. Gap-size dependence of insertion loss with (a) MT connector and with (b) our EB connector

6 shows a schematic of an experimental sample of our EB connector. We investigated 4 samples with feeler gauges (thin metal plates) of differing thicknesses: 100, 200, 300, and 400 μm sandwiched between the EB-connector end faces, and the change in the insertion loss of the EB connector in air and in the cooling liquid was measured. Figures 7(a) and (b) show the measurement results of the change in insertion loss of an MT connector and our EB connector in air and liquid. The insertion loss of the MT connector increased as the gap increased and was greater in air was than in liquid. This is because the insertion loss caused by the gap depends on the refractive index of the media in the gap.

With our EB connector, the change in insertion loss was smaller than that with the MT connector even when the gap was increased and medium changed. This is considered due to the GRIN lens not being affected by the gap or medium.

Finally, we investigated the optical characteristics of our EB connector in turbid water. A muddy-water sample solution was prepared by adding 0.1 g of mud powder to 100 ml of water. Figure 8 shows photographs of muddy water to which (a) 0.5 g and (b) 2.0 g of mud powder were added. We measured the insertion loss of the MT connector and our EB connector with a feeler gauge of 400 μm in muddy water. The results are shown in Fig. 9. The MT connector's insertion loss increased as the amount of mud powder increased, reaching 20 dB at 0.5 g. In contrast, the loss of our EB connector did not change significantly up to 1.2 g of mud powder and increased when the amount of mud powder exceeded 1.2 g. These results indicate that our EB connector is more tolerant of foreign matter in water than the MT connector. We consider this the reason for the beam expansion and straightness in the gap of our EB connector.

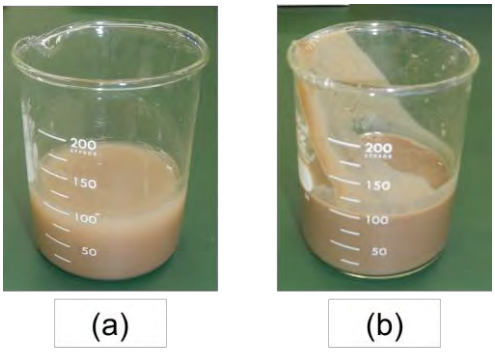


Figure 8. Examples of muddy water with (a) 0.5 g and (b) 2.0 g of mud powder

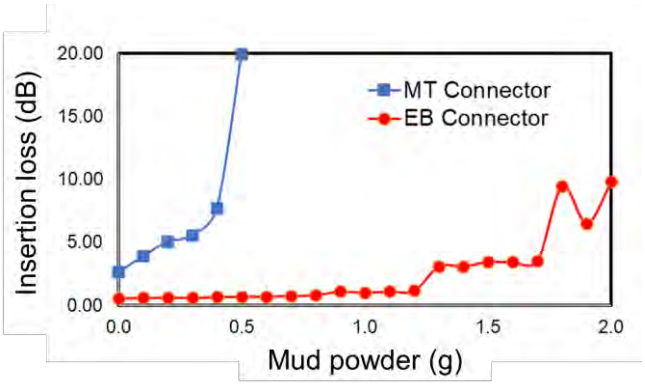


Figure 9. Insertion-loss change of MT and EB connectors in muddy water

5. Conclusions

We presented a novel liquid-immersion multi-fiber connector for data centers. The optical connector is an EB connector with a GRIN lens array attached to an MT connector. The insertion loss of the fabricated EB connector had a low insertion loss of 1.0 dB or less in both air and cooling liquid. As a result of an experiment in which the gap of the EB connector was changed, the insertion loss did not change in both air and liquid, even if the gap was increased by passing a GRIN lens compared with a conventional MT connector. As a result of immersing our EB connector in muddy water with varying amounts of mud powder and measuring the insertion loss, the tolerance for foreign matter in an aqueous solution is greater than that of an MT connector. These results indicate that our EB connector is effective as an optical connector for future immersion cooling.

6. Acknowledgments

This work is supported by the Go-Tech project of the Ministry of Economy, Trade and Industry of Japan.

7. References

[1] I. W. Kuncoro, N. A. Pambudi, M. Biddinika, I. Widiastuti, M. Hijriawan, and K. M. Wibowo, “Immersion cooling as the next technology for data center cooling: A review,” Journal of Physics: Conference Series, vol. 1402 (2019).

[2] i-GRIN: Registered trademark (JP6184912) of Nakahara Optoelectronics Laboratory.

[3] T. Satake, S. Nagasawa, M. Hughes, and S. Lutz, “MPO-type single-mode multi-fiber connector. Low-loss and high-return-loss intermateability of APC-MPO connectors,” Optical Fiber Technol., vol. 17, pp. 17–30 (2011).

[4] A. Nakama, H. Asada, K. Fujiwara, K. Shindo, and K. Takizawa, “Lensed connector for single mode fiber,” Fujikura Technical Reports (Japanese), vol. 131, pp. 40–44 (2018).

[5] M. Kihara, S. Nagasawa, and T. Tanifuji, “Return loss characteristics of optical fiber connectors,” J. Lightwave Technol., vol. 14, pp. 1986–1991 (1996).

[6] Chemical handbook (Japanese), (Maruzen, 2021).

8. Authors



Mitsuru Kihara received a B.E. and M.E. in nuclear engineering and a Dr. Eng. in electronic engineering from Kyushu University, Fukuoka, Japan, in 1988, 1990, and 1997. From 1990 to 2017, he worked on optical fiber interconnecting techniques, future network planning, and optical fiber sensing techniques at NTT Laboratories. Since 2017, he has been a professor at Osaka Electro-Communication University, where he is engaged in the research and education of optical fiber communication and sensing technologies. He is a member of the IEEE, the Optica, and the Institute of Electronics, Information and Communication Engineers (IEICE) of Japan.



Yuto Tameoka received B.E. degree in communication engineering from Osaka Electro-Communication University, Neyagawa, Osaka, Japan, in 2023. He currently works at Nippon Dentsu Co., Ltd, where he is engaged in the construction and maintenance of communication facilities.

Koichi Arishima joined Nippon Telegraph and Telephone Corporation in 1977, where he was engaged in the development of organic photo-functional materials. In 2000, he joined NTT Electronics Corporation, where he was engaged in the development of optical components, including bend-insensitive fibers. In 2017, he joined Nakahara Optoelectronics Laboratory, Inc. and has been working on the development of GRIN lenses.

Tetsuo Miya graduated from Tohoku University in 1975 and joined in Nippon Telegraph and Telephone Corporation, where he has been engaged mainly in research on fabrication of optical single-mode fiber, both MCVD and VAD method. He realized the ultimate-low-of-0.2dB optical single-mode fiber in 1979 and also made clear that minimum optical dispersion can be realized in this ultimate low-loss region by controlling fiber parameters.

After his work in NTT Optoelectronics Laboratories incorporation, he is now working in Nakahara Opto-Electronics Laboratories, inc.

He received his Bachelor and Master degree in physics from Tohoku University in 1971 and 1975, respectively and his doctor degree in engineering also from Tohoku University in 1983.



Motohiro Nakahara, Ph.D joined NTT in 1969 and engaged in research and development of optical fiber fabrication technologies. He worked at NTT Electronics from 1994 to 2003 as the business promotion manager for optical components. In 2003, He established Nakahara Opto-Electronics Labs., Inc. and started the business of precise glass capillaries and integrated GRIN lenses. He is a member of Optica and Japan Society of Applied Physics.

Connection characteristics of coupled multi-core fiber connectors

Yuki Fujimaki Soma Takura Daiyu Nozaki Ryo Nagase

Chiba Institute of Technology

2-17-1 Tsudanuma, Narashino, Chiba 275-0016, Japan

+81-47-478-4303 s18A2110HQ@s.chibakoudai.jp

Abstract

A transmission system using coupled multi-core fiber (C-MCF) has been proposed as a candidate for future long-distance and large-capacity communication. Optical connectors that can be detached and connected are essential if C-MCFs are to be put to practical use. We have developed an SC-type optical connector for connecting uncoupled multi-core fiber (UC-MCF) and confirmed that it performs sufficiently well to be used in practical applications. However, there have been no reports on the connection characteristics of C-MCF. In this study, we measured the attenuation of randomly mated SC-type C-MCF connectors and compared it with electromagnetic field analysis results of the attenuation of C-MCFs.

Keywords: optical connector; SC-type optical connector; multicore fiber, coupled multicore fiber

1. Introduction

Single-mode fiber (SMF) is widely used in current optical communications. The transmission capacity per SMF is limited to 100 Tbit/s, and space division multiplexing (SDM) transmission using multi-core fiber (MCF) is attracting attention to achieve even higher capacity [1]. MCFs currently under study can be broadly classified into two categories: uncoupled multi-core fiber (UC-MCF), which uses each core as an independent transmission path and transmits optical signals in a single mode and coupled multi-core fiber (C-MCF), which couples optical signals between cores in close proximity and transmits them in a multi-mode. C-MCF is more suitable for longer distance optical signal transmission than UC-MCF.

When MCFs are used for transmission paths, optical connectors that can be detached and connected are essential. In UC-MCFs, the optical signals propagating through each core are single-mode, so the relation between the amount of lateral misalignment of each core and attenuation is clear. Therefore, the accuracy of the optical connectors required to achieve low attenuation can be determined and utilized in the design of the MCF connectors. We have developed SC-type optical connectors to connect 4CFs with a standard cladding outer diameter (125 μm), which is considered to be close to practical use as UC-MCFs and have confirmed that it performs at a practical level [2].

Studies have been conducted on the structure and connection characteristics related to UC-MCF connectors [3]-[5]. However, the relation between the amount of lateral misalignment and attenuation has not been clarified for C-MCF connectors, and the accuracy of optical connectors required to achieve low attenuation remains unknown. With C-MCFs, since optical signals propagating through one core are coupled with other cores, the mechanical accuracy required for optical connectors cannot be obtained using the same method as that employed for SMFs, as is the case with UC-MCFs. Therefore, it is necessary to clarify the effect of the lateral misalignment of C-MCFs on attenuation and then clarify the required mechanical accuracy to design C-MCF connectors. In addition, as with UC-MCF connectors, C-MCF connectors require a procedure for measuring their connection characteristics, but the characteristics of each core cannot be measured because the optical signals of each core are combined. Mode MUX/DEMUX is needed to check the connection characteristics of the C-MCF required for transmission paths. However, mode MUX/DEMUX is not suitable for the pre-shipment inspection of optical connectors due to the large scale of the equipment. Since the conventional attenuation measurement procedure is not applicable, a new procedure should be considered. For this purpose, it is necessary to determine accurately the amount of lateral misalignment of each core at connection points before proceeding with the study. However, although for UC-MCFs the amount of lateral misalignment can be calculated from the attenuation of each core, it cannot be calculated for C-MCFs, so it must be estimated by another method.

In this study, the relation between the amount of lateral misalignment and attenuation for the design of 4-12 core C-MCF optical connectors with a standard cladding diameter (125 μm) was analyzed by using electromagnetic field analysis. In addition, we report the results of the actual fabrication of SC-type C-MCF connectors and attenuation measurement.

2. Overview of SC-type MCF connectors

2.1 Structure of SC-type MCF connectors

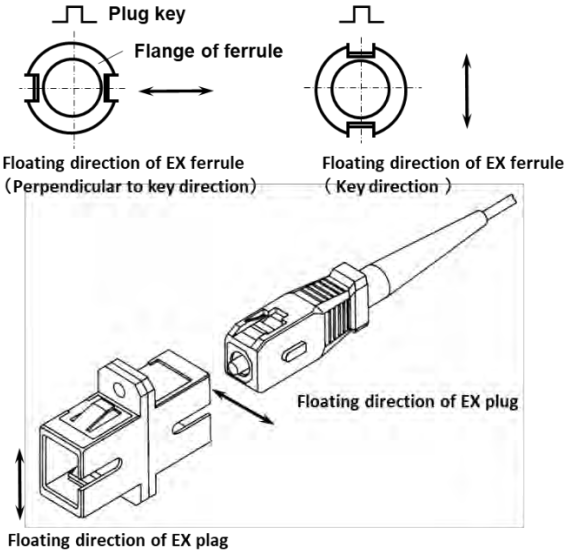
Since optical connectors are usually connected to optical fiber cables, we must consider the possibility of external forces of tens of newtons acting on the cables. When such forces act on optical connectors, plug housings would be deformed by more than 10 μm, much more than the alignment tolerance of SMFs. To solve this problem, a floating mechanism is widely used that offers tolerance between the ferrule and the plug housing.

To connect MCFs, there must be angular accuracy around the ferrule axis, but the floating mechanism and angular accuracy are mutually contradictory requirements. To solve this problem, MU-type MCF connectors with Oldham's coupling mechanism were proposed [6]. MU-type MCF connectors have sufficient mechanical performance for use in communication networks, including test for transmission with applied tensile load (IEC 61300-2-51) [7].

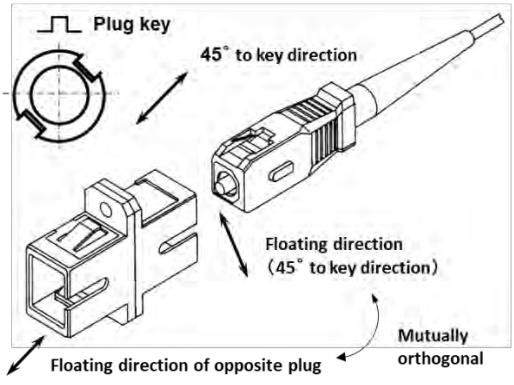
UC-MCF connectors have polarity because each core ID must be connected to the same core ID. Therefore, the two ends are defined as the IN and EX end, respectively. To connect to optical transceivers, etc., it is necessary each plug must be equipped with Oldham's coupling mechanism in, but if the connection is limited to a cable to cable connection, it is considered sufficient to configure Oldham's coupling mechanism in a pair of connectors (IN and EX).

Figure 1 shows the structure of SC-type MCF connectors. The ferrules of SC-type SMF connectors float in all directions in the plug housings and can even rotate. In contrast, the ferrules of SC type MCF connectors float in only one direction, which results from narrowing the keyway. Since UC-MCFs have polarity, as

shown in Fig. 1(a), the floating direction at the IN end is set in the key direction of the plugs and the floating direction at the EX end is set perpendicular to the key direction of the plugs. By combining the IN and EX ends, Oldham's coupling mechanism can be established without having a complicated structure inside each plug. This structure facilitates accuracy when adjusting the angle of rotation of a ferrule to align it so that it is perpendicular/parallel to the reference plane.
On the other hand, C-MCFs cannot identify each core ID as UC-MCFs because the optical signal is coupled between cores. Since there is no polarity and the IN and EX ends cannot be distinguished, C-MCFs are constructed to float in a direction 45° from the key, as shown in Fig. 1(b), to form Oldham's coupling mechanism when same plugs are opposed to it.



(a) SC-type UC-MCF connectors



(b) SC-type C-MCF connectors

Figure 1. SC-type MCF connectors

2.2 Attenuation of SC-type MCF connectors

This section describes the attenuation of SC type MCF connectors. 10 UC-4CFs were fabricated with SC type optical connectors on both ends, and measurements were performed with randomly mated connectors (IEC 61300-3-34) between the same lot.
In the random mated measurement, the characteristics were evaluated for all combinations of 10 optical connectors that served as the master and 9 optical connectors that were connected to the master. Optical signals were injected into each core of an UC-4CF by selecting the core using an optical switch and a fan-in/fan-out device (FIFO), and the outgoing optical power was measured. Next, other UC-4CF connectors were connected to a master UC-4CF connector, an optical switch was selected, and the outgoing optical power was measured. The difference between the two measured values was used as the attenuation. The attenuation fluctuations associated with switching an optical switch were less than 0.05 dB. An ASE light source (1520~1570 nm) was used in this measurement.
Figure 2 shows the distribution of the measured attenuation of UC-4CF connectors. The data numbered 360, with an average attenuation of 0.07 dB and a maximum value of 0.34 dB for all cores. Based on these results, the maximum lateral misalignment of the fabricated SC-type MCF connectors is considered to be about 1.4 μm.

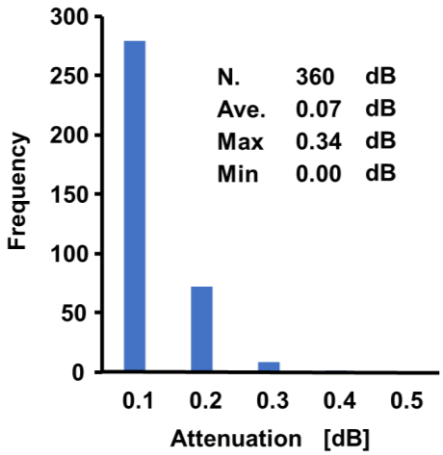


Figure 2. Measurement attenuation results for SC-type UC-4CF connectors

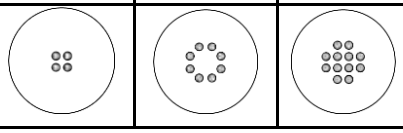
In addition, previous studies have reported on the amount of angular misalignment that occurs during MCF connector fabrication, and the maximum angular misalignment has been measured to be about ±0.5° [8]. From this value, the maximum lateral misalignment due to angular misalignment is estimated to be 0.18 μm in C-12CF (Table 1). Since this value is sufficiently small, the lateral rather than angular misalignment is the dominant factor in the attenuation of MCF connectors. Based on the above, we first considered only lateral misalignment in the design of C-MCF connectors.

3. Simulated attenuation of C-MCFs using electromagnetic field analysis

3.1 C-MCF models and parameters s

We performed finite element electromagnetic field analysis using Synopsys' FemSIM FEM to obtain the C-MCF propagation modes and mode distributions. Table 1 shows the analysis conditions. Parameters were adjusted assuming 4-12 core C-MCFs with a standard cladding diameter (125 μm).

Table 1. Analysis conditions

Parameter	C-4CF	C-8CF	C-12CF
Cross section			
Core material	SiO_2		
Wavelength	1550 nm		
Cladding OD	125 μm		
Core radius	4.8 μm		
Core pitch	14.8 μm	15.5 μm	15.5 μm
Core Δ	−0.35 %		
Mesh size	0.1 μm		

3.2 Attenuation calculation method

If the electromagnetic field (mode distribution of the fiber) on the incident side is $\boldsymbol{E}_{\mathrm{i}}$ and the electromagnetic field (mode distribution of the fiber) on the receiving side is $\boldsymbol{E}_{\mathrm{r}}$, the coupling efficiency η is obtained by overlap integration, as shown in Eq. (1) [9].

$$\eta = \left|\int_S \boldsymbol{E}_{\mathrm{i}} \cdot \boldsymbol{E}_{\mathrm{r}}\, \mathrm{d}S\right|^2 / \left(\int_S \boldsymbol{E}_{\mathrm{i}}{}^2\, \mathrm{d}S \cdot \int_S \boldsymbol{E}_{\mathrm{r}}{}^2\, \mathrm{d}S\right) \quad (1)$$

Attenuation α is expressed by Eq. (2) using the coupling efficiency η.

$$\alpha = -10 \log \eta \ \ [\mathrm{dB}] \quad (2)$$

However, S is the connecting cross section and must be integrated over the entire cross section.

In this study, the amount of lateral misalignment that may occur during optical connector fabrication was taken into account and analyzed assuming a lateral misalignment of 0~2.0 μm. During the analysis, a case with no lateral misalignment (0 μm) was used as the reference, and the difference between the 0~2.0 μm misalignment in the x-axis direction shown in Fig. 4 and the reference was defined as the lateral misalignment [10].

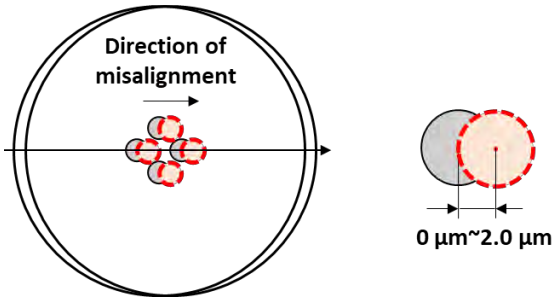


Figure 3. Lateral misalignment of C-MCF

3.3 Attenuation analysis results

Based on the analysis results, the effective modes of propagation for 4-12CF are m01-m08, m01-m16, and m01-m24, respectively. While considering these results, we analyzed the attenuation of each mode with respect to lateral misalignment using Eqs. (1) and (2). The electromagnetic field with no lateral misalignment (0 μm) is $\boldsymbol{E}_{\mathrm{i}}$, and that with lateral misalignment (0~2.0 μm) is $\boldsymbol{E}_{\mathrm{r}}$, calculated using Eqs. (1) and (2). Figure 4-6 show the relation of attenuation to the amount of lateral misalignment for each mode of 4-12CF.

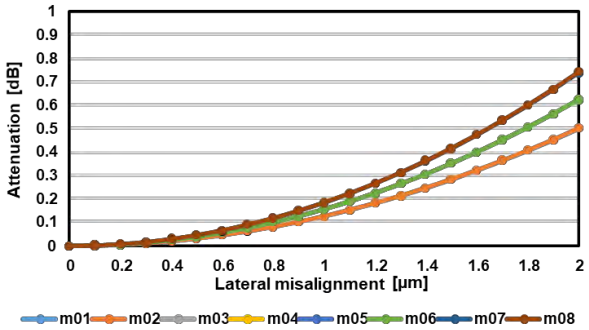


Figure 4. Attenuation of each mode of C-4CF with respect to lateral misalignment

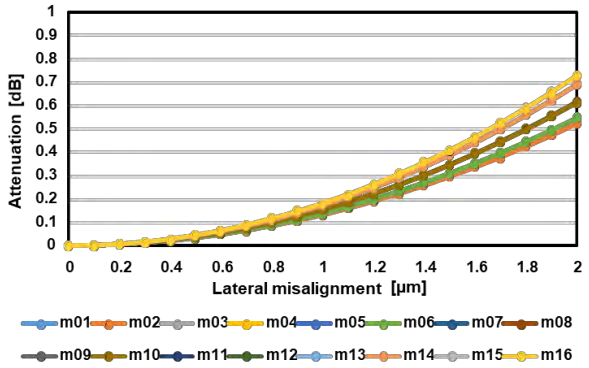


Figure 5. Attenuation of each mode of C-8CF with respect to lateral misalignment

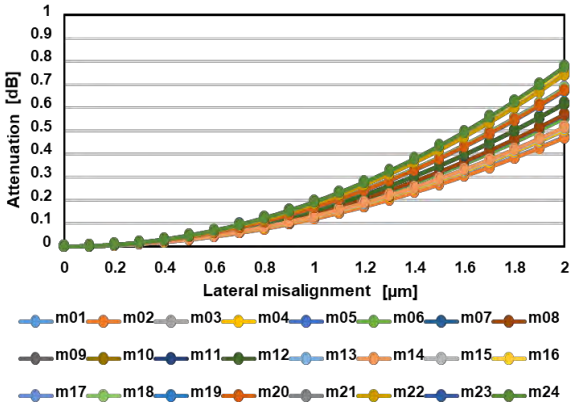


Figure 6. Attenuation of each mode of C-12CF with respect to lateral misalignment

The results show that modes with an attenuation exceeding 0.5 dB appeared at a lateral misalignment of 1.7 µm or more. When optical connectors are applied to a communication system, the attenuation must be less than 0.5 dB. Considering this point, Figs. 4-6 shows that a lateral misalignment of 1.7 µm or less is acceptable for C-MCFs. As mentioned in section 2.2, we consider that the maximum lateral misalignment of the SC-type MCF connectors we developed [3] is 1.4 µm. Therefore, the same optical connectors can be attached to C-MCFs without any problem.

4. Attenuation of SC-type C-MCF connectors

4.1 Measurement procedure

Since optical signals are combined between cores in C-MCFs, it is not possible to measure the attenuation of each core as in UC-MCFs. In this study, we used 4-12CF to measure the attenuation caused by random mated connections. Ten 4-12CFs each with SC-type optical connectors at both ends were fabricated and measured using an ASE light source with a wide wavelength range (1520-1570 nm) to determine the average attenuation of each mode. As shown in Fig. 7, one of the cores of a 2 m long C-MCF was spliced to the core of an SMF, and optical signals were injected from the SMF side to excite all the modes of a C-MCF. As plugs, we used SC-type optical connectors with the structure shown in Fig. 1(b), which were newly developed for use as C-MCFs.

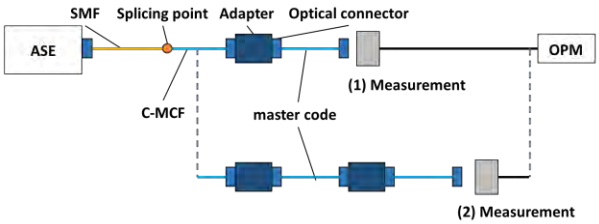


Figure 7. Setup for measuring attenuation of random mated

4.2 Attenuation measurement results

Figures 8-10 show 4-12CF attenuation measurement results. We measured 3 x 90 connection points. The average attenuation values were 0.11, 0.13, and 0.12 dB, respectively. In addition, we obtained values satisfying Grade B (97% less than 0.25 dB) in the optical interface standard for optical connectors (IEC 61755-1). On the other hand, the estimated lateral misalignment from the analysis results shown in Fig. 4-6 was 0.4 to 1.4 µm. Since C-MCFs have a higher bending loss than SMFs [11], changes in fiber formation can cause optical power fluctuations, and changes in modes can cause changes in attenuation as shown in Fig. 4-6. Therefore, further study of the procedure for measuring attenuation is needed if we are to obtain accurate measurements.

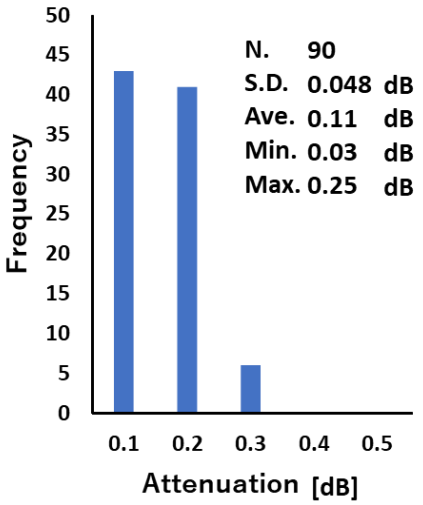


Figure 8. Measurement results of attenuation of C-4CF connectors

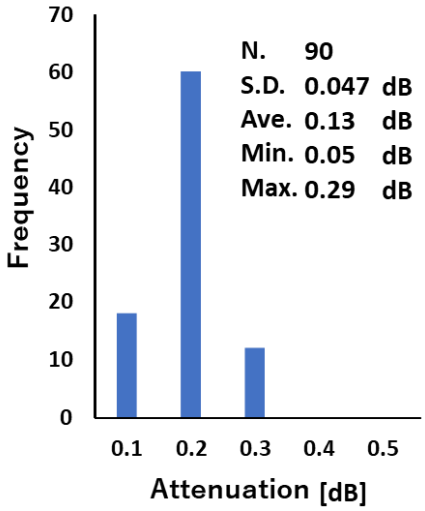


Figure 9. Measurement results of attenuation of C-8CF connectors

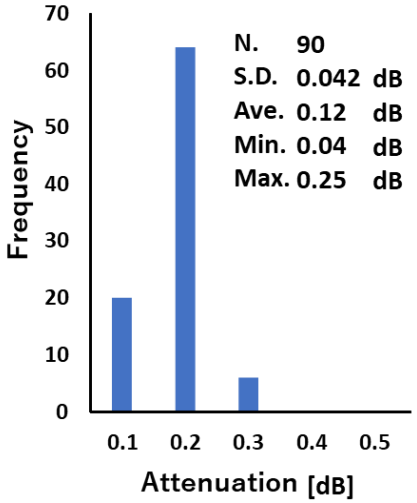


Figure 10. Attenuation measurement results for C-12CF connectors

5. Conclusions

In this study, we employed electromagnetic field analysis to determine the relationship between the amount of lateral misalignment and attenuation required for the design of C-MCF connectors, and we fabricated SC-type C-MCF connectors and measured the attenuation.

The average attenuation of all the cores of the SC-type UC-MCF connectors we have developed was 0.07 dB, and the maximum attenuation was 0.34 dB. Based on these results, we consider the maximum lateral misalignment of fabricated SC-type MCF connectors to be about 1.4 µm. Based on the maximum angular misalignment, which is expected to be ±0.5°, the lateral misalignment of the outermost core is estimated to be 0.18 µm. Since this value is sufficiently smaller than the maximum lateral misalignment of the fiber, angular misalignment was not considered in this study.

Next, we used electromagnetic field analysis to calculate the attenuation for each mode of the C-MCFs with respect to the amount of lateral misalignment. The results show modes with 0.5 dB or more of attenuation for a lateral misalignment exceeding 1.7 µm. Since communication systems require optical connectors to have an attenuation of less than 0.5 dB, we found that a lateral misalignment of less than 1.7 µm was acceptable for each mode. Since the maximum lateral misalignment of the SC-type MCF connectors we developed is 1.4 µm, we consider that the same optical connectors can be used for C-MCFs.

Finally, we fabricated SC-type C-MCF connectors, and the attenuation, one of the important characteristics of optical connectors, was measured by using random mated. The attenuation of 4CF, 8CF and 12CF were measured and found to average 0.11, 0.13, and 0.12 dB, respectively. Attenuation satisfying Grade B in IEC 61755-1 was obtained, which indicates that the optical performance is sufficient for application to optical communication networks. On the other hand, compared with the electromagnetic field analysis results for the attenuation of C-MCF, the lateral misalignment of SC-type C-MCF connectors is considered to be about 0.4 to 1.4 µm. In addition, in measurements using C-MCFs, changes in the arrangement of the measurement setup may cause optical power fluctuations and mode conversion, so a reexamination of the measurement procedure is necessary if we are to measure attenuation accurately.

6. Acknowledgments

Some of the results of this research were obtained through the contract research project (No. 01010) sponsored by the National Institute of Information and Communications Technology (NICT). The authors also thank K. Kamimura, H. Saito and Y. Mori, former students at Nagase Labs.,

7. References

[1] K. Imamura, K. Mukasa and R. Sugizaki, "Trench assisted multi-core fiber with large Aeff over 100 µm^2 and low attenuation loss," in. Proc. ECOC2011, Mo 1. LeCervin, (2011).

[2] K. Kamimura, Y. Fujimaki, H. Hoshikawa and R. Nagase, "Connection performances of standard outer diameter 4-core MCF connector," IEICE Tech. Rep., vol. 121, no. 375, OCS2021-46, pp. 27-31, (in Japanese, 2022).

[3] K. Imaizumi and R. Nagase, "SC-type multicore fiber connector with simplified structure," in Proc. IWCS 2019, 8-1, (2019).

[4] K. Izawa, K. Imaizumi, K. Kamimura and R. Nagase, "Performances of SC-type multicore fiber connector," IEICE Tech. Rep., vol. 120, no. 425, EMD2020-34, pp. 27-31, (in Japanese, 2021).

[5] K. Kamimura, Y. Fujimaki, H. Hoshikawa, K. Imaizumi, K. Izawa and R. Nagase, "Return loss measurement procedure for multicore fiber connectors," IEICE TRANSACTIONS on Electronics, Vol. E105-C, No.12, pp.721-728

[6] R. Nagase, K. Sakaime, K. Watanabe and T. Saito, "MU-type multicore fiber connector," IEICE TRANS. ELECTRON., vol. E96-C, no. 9, pp. 1173-1177, (2013).

[7] K. Sakaime, R. Nagase, K. Watanabe and T. Saito, "Mechanical characteristics of MCF connector," IEEE summer Topical Meeting Series, pp. 172-173, Jul. (2014).

[8] K. Sakaime, K. Arai, R. Nagase, K. Watanabe, T. Saito and R. Sugizaki, "Study on primary attenuation factors of MU-Type MCF connector," IEICE Tech. Rep., vol. 116, no. 455, OCS2016-81, pp. 53-56, (in Japanese, 2017).

[9] J. Sakai, "Transmission Loss Theories of Optical Fibers: Part I," The Review of Laser Engineering, vol. 7, no. 3, pp. 251-263, (1979).

[10] K. Kamimura, Y. Fujimaki, H. Saito, Y. Mori and R. Nagase, "A study on attenuation of coupled 4-core MCF," IEICE Tech. Rep., vol. 122, no. 380, OFT2022-59, pp. 41-44, (in Japanese, 2023).

[11] R. Imada, T. Sakamoto, T. Mori, Y. Yamada and K. Nakajima, "A study on bending loss property of coupled multicore fiber," IEICE Tech. Rep., vol. 122, no. 380, OFT2022-58, pp. 37-40, (in Japanese, 2023).



Yuki Fujimaki received a B.E. degree from Chiba Institute of Technology, Chiba, in 2022. He is a student at the Graduate School of Engineering, Chiba Institute of Technology.
s18A2110HQ@s.chibakoudai.jp



Soma Takura is a student at Chiba Institute of Technology.
s20A2080BS@s.chibakoudai.jp



Daiyu Nozaki is a student at Chiba Institute of Technology.
s20A2103FW@s.chibakoudai.jp



Ryo Nagase received B.E., M.E. and Ph. D. degrees in precision engineering from Tohoku University, Sendai, Japan, in 1983, 1985, and 1998, respectively. From 1985 to 2009, he was engaged in the research and development of optical fiber connectors at NTT Laboratories. Since Oct., 2009, he has been a professor of precision engineering at Chiba Institute of Technology, Chiba, Japan. His current interests are the microscopic deformation of optical components and optical remote-sensing technology.
ryo.nagase@it-chiba.ac.jp

Optical Transceivers and Structured Cabling with Expanded Beam Connectors as an alternative to Active Optical Cables

Rich Baca[a], Earl Parsons[b], Kevin Chaloupka[c], Paul Leblanc[c], Kam Patel[b]

[a]Microsoft Azure, Redmond, Washington

[b]CommScope, Richardson, Texas

+1-972-792-3269 · earl.parsons@commscope.com

[c]3M, Austin, Texas

Abstract

This study will review insertion loss and return loss results of expanded beam connectors as well as transmission testing of expanded beam connectors terminating multimode fiber cable. Experimental results of commercially available AOCs that have been cut and terminated with expanded beam connectors will also be presented. These terminated AOCs will be tested with several OM4 fiber cables to determine the margin with and without expanded beam connectors.

Keywords: AI/ML, multimode fiber, data centers, expanded beam connectors, multi-fiber connectors

1. Introduction

The use of public cloud services continues to grow. Gartner predicts 33% increase in IT spending from 2020 to 2024[1]. This has led hyperscale data center operators to continue to build data center capacity across the globe. Fiber optics can play a part in helping to reduce the power consumption in these data centers by enabling new architectures, but the risks associated with introducing more fiber optic links need to be addressed.

Fig. 1 shows a folded-clos architecture commonly deployed with copper direct attach cable (DAC) connecting servers to top of rack (TOR) switches. The DAC is a very reliable electrical connection. Optical transceivers at the server would allow for bypassing the TOR and connecting directly to the middle of row (MOR) or Tier 1 switches. This would eliminate a tier in the architecture and utilize high-radix network ASICs more efficiently leading to more optimized server architecture. The right side of the figure depicts optical connections from server rack to patch panels on top of the racks. When compared to a TOR-Tier 1 AOC connected data center, the number of optical connectors increases by 18x or additional 100k's connectors in a hyperscale data center. Inspecting, cleaning, and reinspecting these physical contact (PC) parallel connectors in a deployment becomes prohibitively time consuming. The risk of poor link performance due to contaminated connector end faces is high. An RJ45-like plug-n-play optical connector that does not require cleaning or inspecting could enable new data architectures to be deployed with lower operator risk.

Expanded beam optical connectors have shown benefits in terms of dust immunity and consistent insertion loss performance when repeatedly connected without cleaning and inspecting. [2,3] These expanded beam connectors have been deployed in high-volume in HPC and medical applications. Both multimode and single mode fiber (MMF, SMF) expanded beam connectors have been developed to help mitigate deployment risks of connectors contaminated with debris [4]. iNEMI has also kicked off a project to investigate the impact of contamination with expanded beam connectors and to compare to PC connectors [5, 6]. In this paper we will explore a multimode fiber connector for use with VCSEL based high-data rate applications. SMF connectors have also been studied and deployed in data center applications.

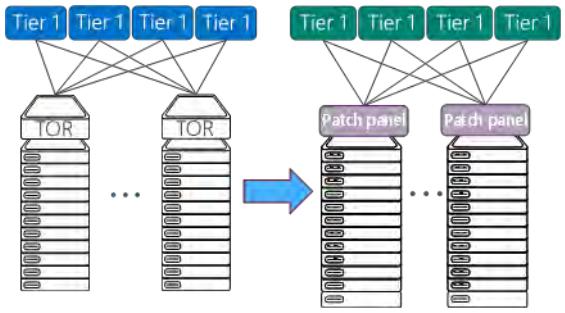


Figure 1. Data center architecture

The wide adoption of Artificial Intelligence (AI) and Machine Learning (ML) clusters in data centers has dramatically increased the presence of short fiber optic links that are both inter-rack and intra-row. Typically, these links are connected with Active Optical Cables (AOCs) that use multimode fiber. These AOCs do not require installation by workers skilled in fiber optic connectivity. Since AOCs present no fiber optic connector to the installer, they do not require cleaning and inspection and there is no risk of link failure due to contaminated connectors. Compared to optical transceivers connected with structured cabling, AOCs have a cost of reduced network flexibility, increased failure rate, and longer outage times. In this work we study AOC replacement with optical transceivers and cabling terminated with expanded beam connectors. Expanded beam connectors are well known for their reduced sensitivity to contaminants and cleaning requirements.

This study reviews insertion loss and return loss results of expanded beam connectors as well as transmission testing of expanded beam connectors terminating multimode fiber cable. Experimental results of commercially available AOCs that have been cut and terminated with expanded beam connectors are also presented. These terminated AOCs are be tested with several OM4 fiber cables to determine the margin with and without expanded beam connectors.

These results demonstrate that expanded beam connectors can achieve performance comparable to MPO connectors and do not impair transmission over multimode fiber. The AOCs terminated with expanded beam connectors provide plenty of margin for AI and ML links. Optical transceivers with expanded beam connectors offer a cost-effective and technically feasible alternative to AOCs.

2. AI Cluster Architecture

The computation for AI is carried out in graphical processing units (GPUs). These specialized chips are best at parallel processing and are well suited to AI. The models used to train and run AI are too large for a single machine. Multiple GPUs, spread over many servers and racks, are required to handle these large models. These GPUs need to be connected to allow them to do the work of AI.

As discussed above, nearly all modern data centers, especially hyperscale data centers, use a Folded Clos architecture, also called leaf-spine. All the leaf switches in a data center connect to all the spine switches. In the data hall, server racks connect to a top-of rack (ToR) switch. The ToR is then connected to a leaf switch at the end of the row or in another room with fiber cable. The servers in the rack are connected to the ToR with short copper cables. These copper cables are one to two meters long and carry 25G or 50G signaling.

This configuration uses few fiber cables in the data hall. For example, Meta data centers that use the F16 architecture [7] will have 16 duplex fiber cables from each of the server racks in a row. These cables run from the ToR to the end of the row, where they connect with modules that combine duplex fibers to 24 fiber cables. The 24 fiber cables then run to another room to connect to leaf switches.

Data centers that implement AI will house AI clusters next to compute clusters with traditional architecture. Traditional compute is sometimes called the front-end network, and the AI clusters are sometimes called the back-end network.

AI clusters require a new data center architecture. The GPU servers require much more connectivity between servers, but there are fewer servers per rack due to power and heat restraints. This leads to situations where we have more inter-rack cabling than traditional data centers. Each GPU server is connected to a switch within the row or room. These links require 100G to 400G at distances that cannot be supported by copper. In addition, each server requires connectivity to the switch fabric, storage, and out-of-band management.

As an example, we can look at the architecture proposed by NVIDIA, a leader in the AI space. NVIDIA's latest GPU server is the DGX H100 and has 4x800G ports to switches (operated as 8x400GE), 4x400GE ports to storage, and 1GE and 10GE ports for management. A DGX SuperPOD (as in Fig. 2 [8]) can contain 32 of these GPU servers connected to 18 switches in a single row. Each row would then have 384x400GE fiber links for switch fabric and storage and 64 copper links for management. This is a remarkable increase in the number of fiber links in the data hall. The F16 architecture mentioned above would have 128 (8x16) duplex fiber cables with the same number of server racks.

In the ideal scenario illustrated by NVIDIA, all the GPU servers in an AI cluster will be close together. AI/machine learning algorithms, like high-performance computing, are extremely sensitive to link latency. One estimate claimed that 30 percent of the time to run a large training model was spent on network latency and 70 percent was spent on compute time. Since training a large model can cost up to $10 million, this networking time represents a significant cost. Even a latency saving of 50 nanoseconds, or 10 m of fiber, is significant. Nearly all the links in AI clusters are limited to 100 m reaches.



Figure 2. Rendering of Nvidia SuperPOD [8]

Unfortunately, not all data centers will be able to locate the GPU server racks in the same row. These racks require ~40 kilowatts to power the GPU servers. This is more power than typical server racks, and data centers built with lower power requirements will need to space out their GPU racks.

3. Expanded Beam Connectors

The expanded beam multimode fiber connector used in this study is based on a new 12 fiber expanded beam ferrule design. (Fig. 3) Light propagating from the end of each fiber expands in the ferrule until it is reflected by a concave mirror using total internal reflection. At the mirror, the beam is nominally collimated and turned approximately 90 degrees. The expanded beam then exits through a recessed window in the flat mating surface of the ferrule. An anti-reflection coating is applied to the window area to minimize insertion loss and reflections. Critical ferrule-to-ferrule alignment is achieved using a pin and socket design in which the nose of the ferrule is aligned by the socket in the back of the mating ferrule. This design allows for reliable mating even with significant initial misalignment of the ferrules.

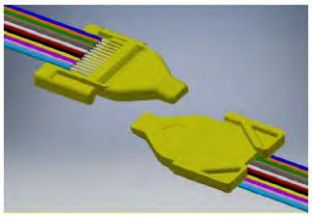


Figure 3. Two 12-fiber ferrules attached to ribbon fiber, unmated.

When mated in connectors (Fig. 4), the ferrules are held together with the spring force provided by their corresponding attached fibers. During mating of the connectors, the fibers supporting the ferrules are bent slightly beyond their unmated resting state and the ferrules rotate slightly relative to the connector body [9]. Each fiber ribbon is permanently attached to a collet several millimeters from the ferrule. The collet is easily seated or removed from a socket which holds it in a fixed location in the connector body. With this rigid attachment of the external ribbon to the connector body, the connector can be made insensitive to movement or tension in the external fiber. This fiber supported ferrule scheme allows for connector designs with densely stacked ferrule assemblies and allows for low mating force: less than 1 N per ferrule.

Unlike traditional multi-fiber physical contact connectors, the new expanded beam ferrule allows connectors to be constructed so that

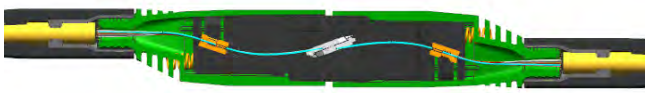


Figure 4. Section view of a connector with a pair of mated ferrules. Each ferrule is supported by its optical fibers. The fibers are permanently attached to a collet, which is held in a fixed position in the connector body.

critical optical surfaces are recessed and not exposed at the connector end; they are thereby protected from being damaged by unintended contact with external objects. Additionally, the orientation of the ferrules in the connector in Fig. 4 is such that the collimated beams are not directed out at the end of the connectors, reducing eye safety concerns. The connectors can be hermaphroditic in design, eliminating the need for separate male and female connector genders, and the expanded beam ferrule design allows the connector to be less sensitive to dust compared to traditional multi-fiber physical contact connectors.

4. Insertion loss and return loss measurements

The insertion loss (IL) and return loss (RL) of the multimode expanded beam connectors were measured at 850 nm as illustrated in Fig. 5. Hybrid cables with 12 fiber MPO connectors on one end and 12 fiber expanded beam connectors on the other end were used to connect to lab measurement equipment. Encircled flux (EF) was measured and controlled at the input to the first hybrid cable. The loss reference value was measured by mating the two hybrid cables together. Before mating, each expanded beam connector was cleaned only with compressed air.

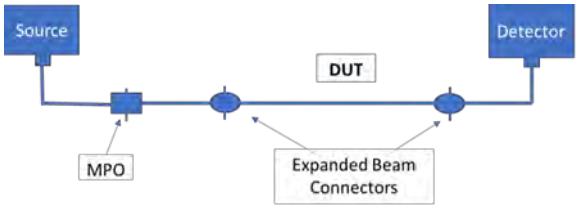


Figure 5. Setup for expanded beam connector insertion loss and return loss at 850 nm

Fig. 6 shows the IL and RL results vs. fiber number for the 20 connectors tested. The average, standard deviation, minimum, maximum, and mean plus three standard deviations are all plotted. For all fibers the mean average value is <0.3 dB. The maximum IL value measured was 0.43 dB on fiber #2. An IL value of 0.53 dB is three standard deviations above the mean. All of the RL values were above 30 dB, and most were above 40 dB. These IL and RL values are good enough to support advanced modulation formats like PAM4 [10] and are compliant with Grade Bm/2m in IEC 61753-1 Edition 2.1 [11].

5. Transmission Testing

Further experiments were conducted to observe the interaction of expanded beam connectors on transmission with AOCs. Tests were carried out with 200G-SR4 AOCs that transmit 4x50G PAM4 signals bidirectionally. The received average power (Prec) reported by the transceiver and BER were recorded for each lane individually. BER was then converted to Q for margin analysis. Transmission testing was conducted with the AOCs as manufactured and with AOCs that were cut and terminated with expanded beam connectors. Different OM4 cable lengths and different number of expanded beam connectors were inserted between the terminated AOC ends.

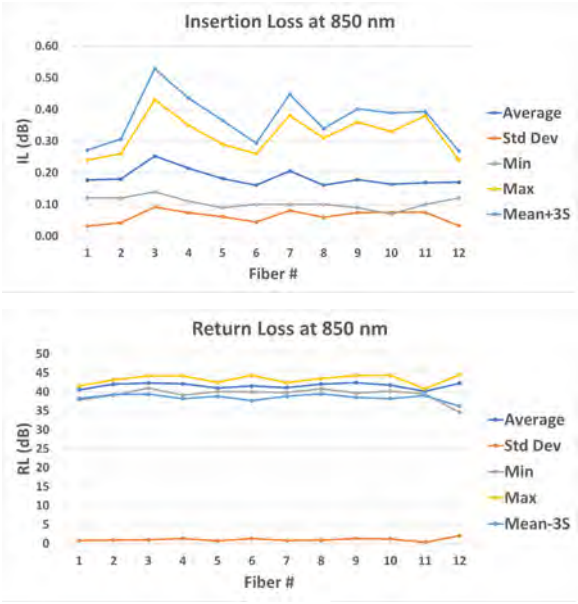


Figure 6. Insertion loss and return loss results per fiber for 12 fiber expanded beam connectors. The average, standard deviation, minimum, maximum, and mean plus three standard deviations are shown from all twenty samples.

Ethernet standards specify two key parameters that are used to analyze link margin. The minimum Prec for transceivers compliant to 200G-SR4 is -8.4 dBm. The FEC limit for 200G-SR4 is a BER < 2.4e-4 which is equivalent to Q < 5.43 dB.

Fig. 7 shows the initial experimental setup. Two Ethernet testers were used, and each had a QSFP port with 4x50G lane capacity. A 3m 200G-SR4 AOC was inserted between the testers. Four lanes were transmitted and measured simultaneously over a two-minute window. Eight AOCs were tested in this manner.

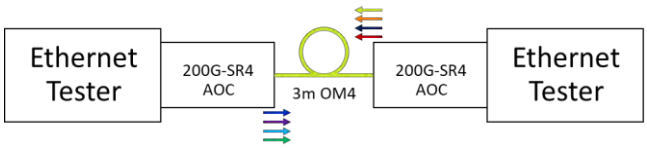


Figure 7. Experimental setup to test AOCs

Fig. 8 plots Q vs. Prec for each lane from the eight AOCs tested. The black line indicates the 200G-SR4 specification of Prec > -8.4 dBm and Q > 5.43 dB. The Q values above 9 dB represent lanes where no errors were reported in the two-minute time window. A BER of 1e-16 (Q = 9.15 dB) was used as a placeholder for those data points. For all lanes there is significant margin both in terms of power and BER.

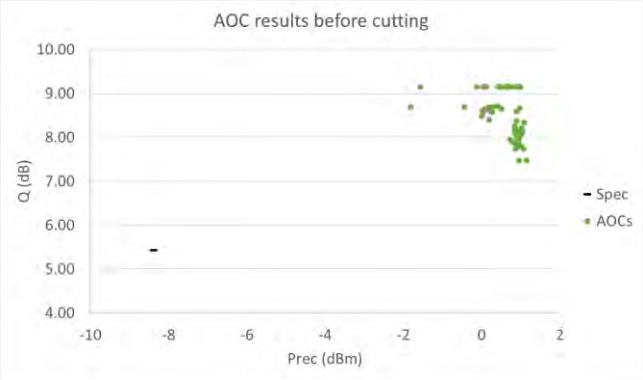


Figure 8. Q vs. Prec power for 200G-SR4 AOCs. Significant Q and power margin were measured.

Next the AOCs were cut in two and each fiber end was terminated with expanded beam connectors. Fig. 9 shows the next round of experiments where eight fiber OM4 cables with lengths of <1 m, 50 m, 100 m, and 150 m were inserted between the two ends of the AOCs. There were two expanded beam connector (EBOs) pairs in the path.

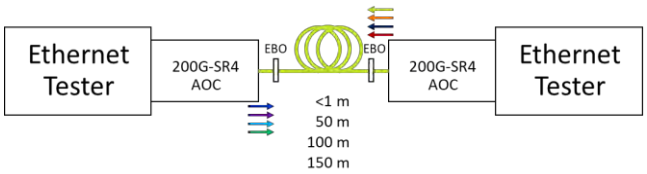
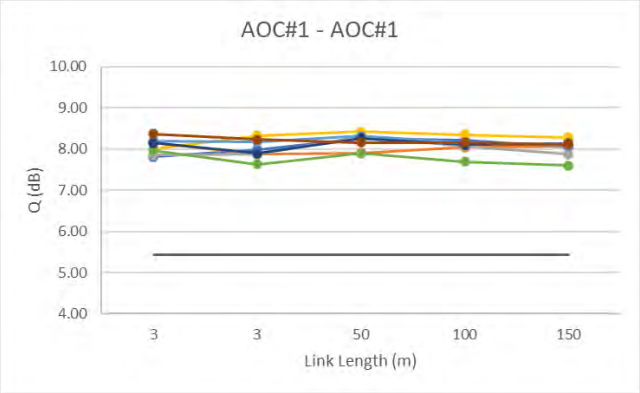
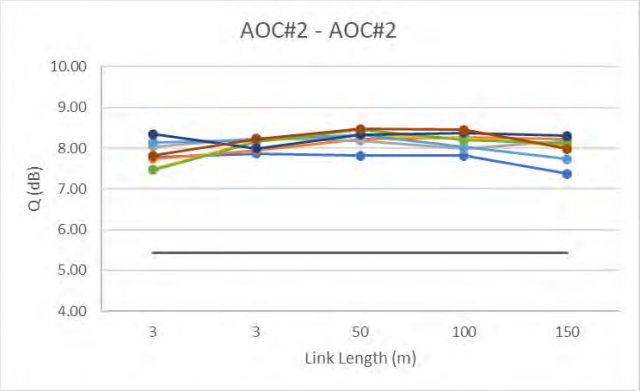
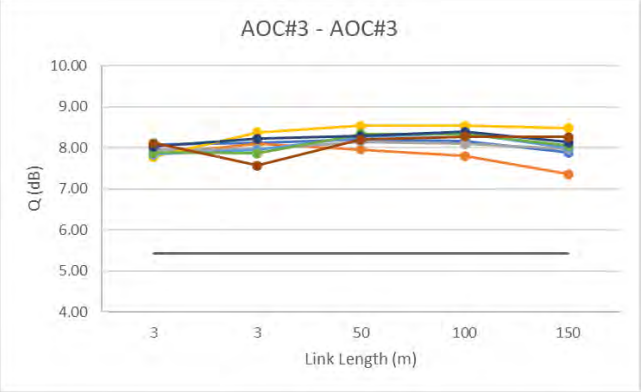


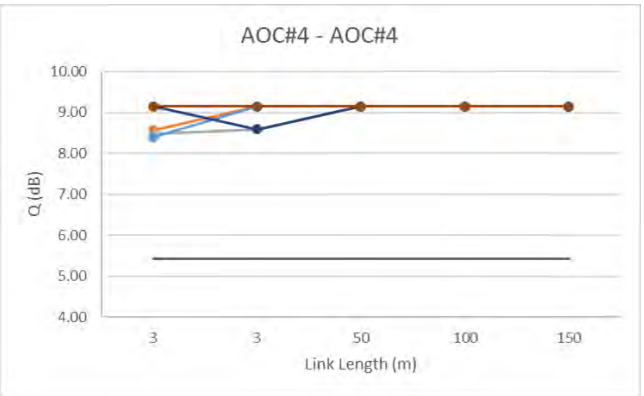
Figure 9. Experimental setup to test cut AOCs with expanded beam connectors

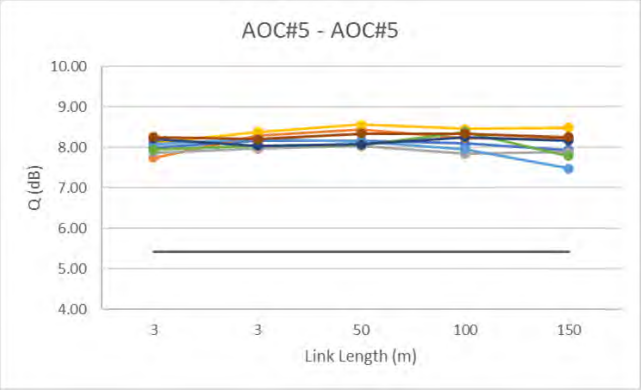
Six AOCs were tested in this manner. In each plot in Fig. 10, Q from eight lanes are plotted vs. link length. In each of the below charts the leftmost data point is the uncut AOC and the other points correspond to <1 m, 50 m, 100 m, and 150 m OM4 cables.











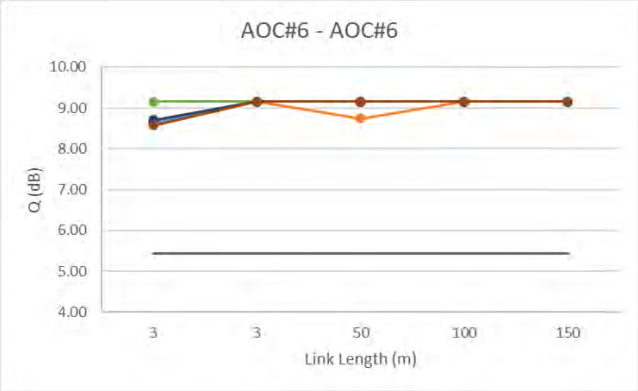
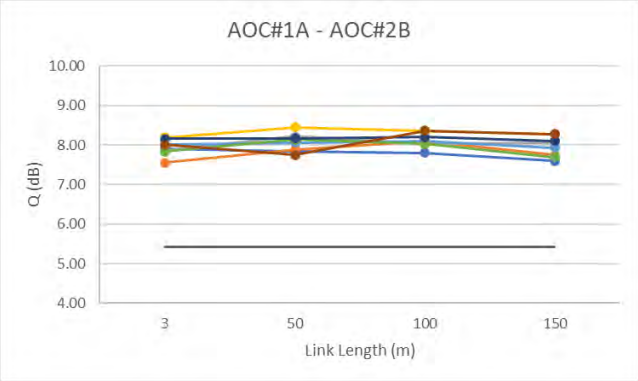
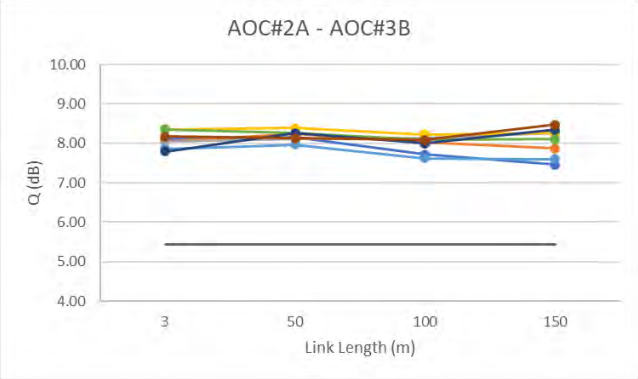
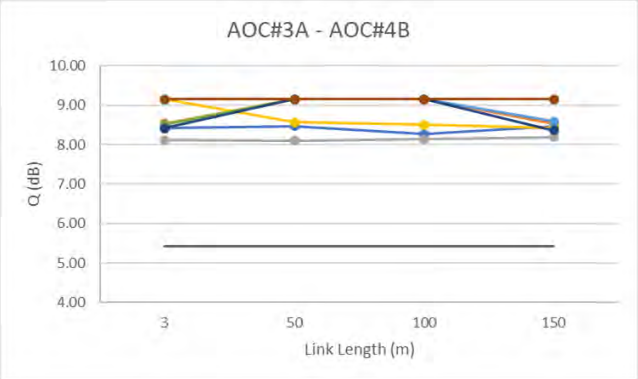


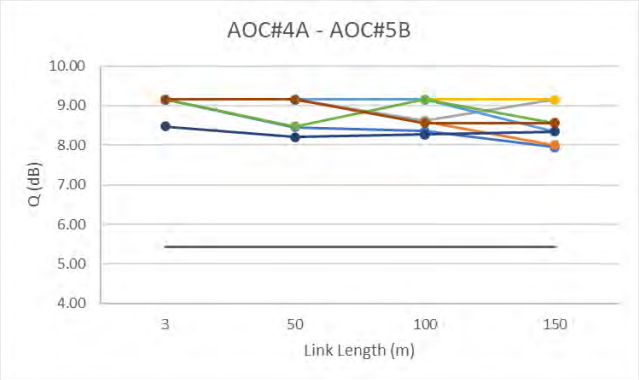
Figure 10. Experimental results for matched AOCs

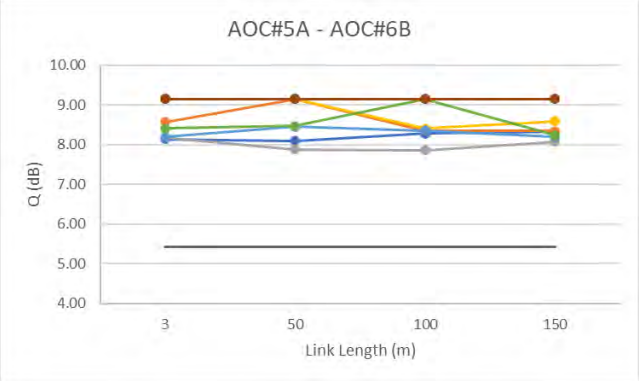
Next, the same AOCs and cables were used with mismatched transceivers. AOCs ends that were not originally paired were tested and graphed in Fig. 11.











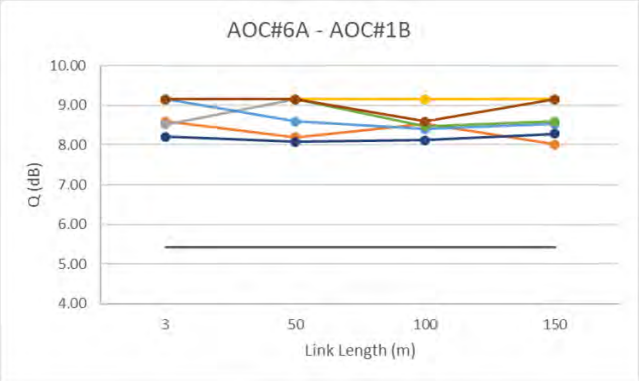


Figure 11. Experimental results for mismatched AOCs

For all lanes for all cases of matched and unmatched AOC ends the Q exceeded 7 dB. Some lanes were error free even with two expanded beam connector pairs and 150 m cable in the path.

Next, cables were combined to simulate extended reach as in Fig. 12. Short (<1 m) cables were used between each longer spool to maintain polarity. This configuration also increases the number of expanded beam connectors used. Total lengths of 200 m (with 4 expanded beam connectors), 250 m (with 4 expanded beam connector pairs), and 300 m (with 6 expanded beam connector pairs) were measured.

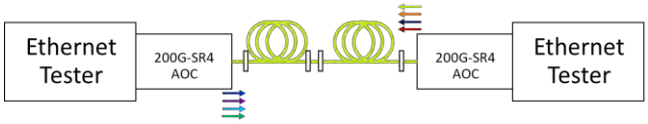
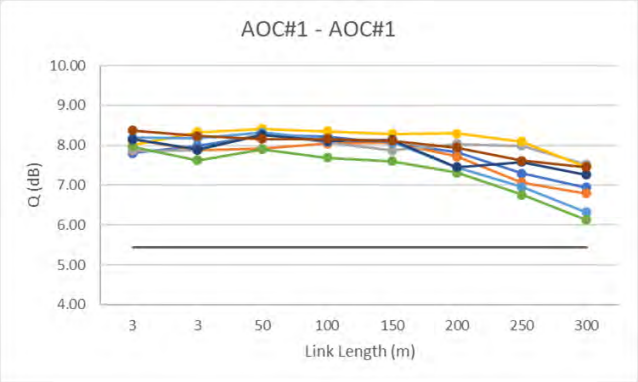
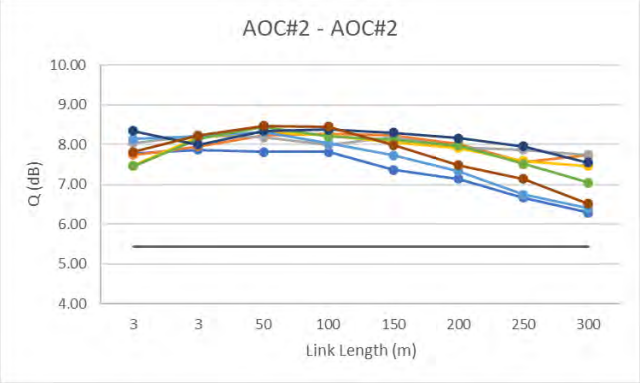
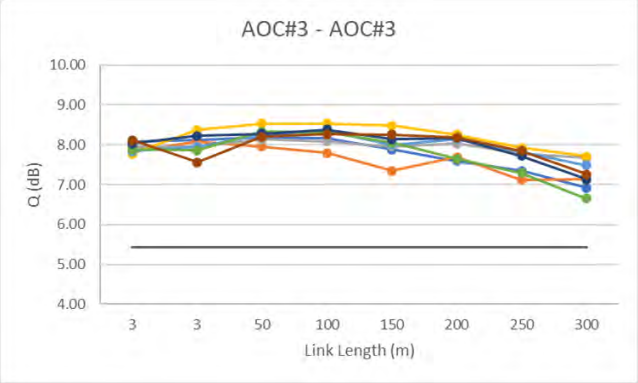
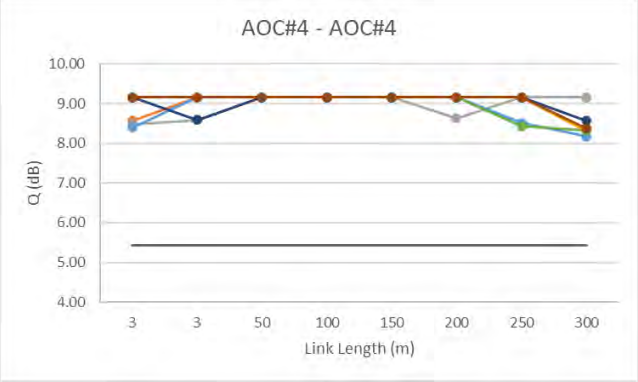


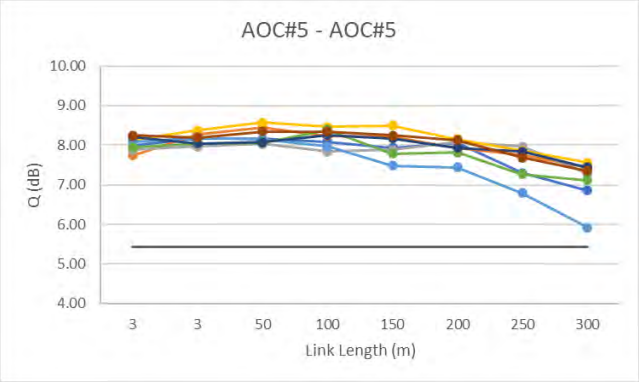
Figure 12. Experimental setup for extended reach











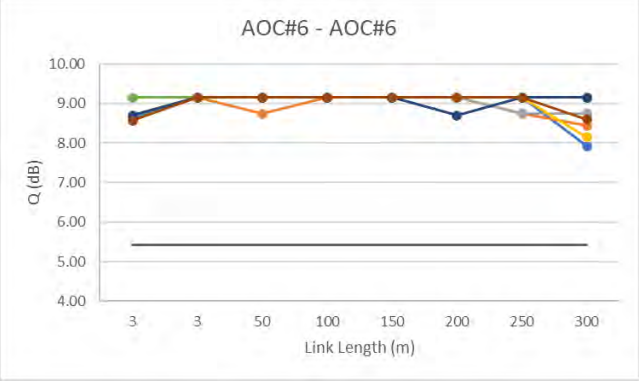


Figure 13. Experimental setup for extended reach

As reach increases to 300 m, there is a drop in Q. Even at these extreme distances the Q is at least 0.5 dB above the FEC limit.

Finally, an extreme number of connectors were inserted together with 150 m cables as in Fig. 14. Either 10 or 20 short cables with expanded beam connectors were inserted for either 12 or 22 total expanded beam connector pairs in the path. Both matched and unmatched cases were tested.

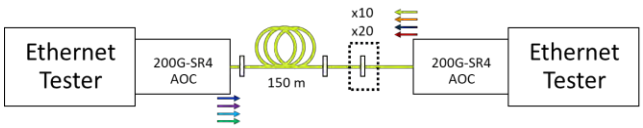
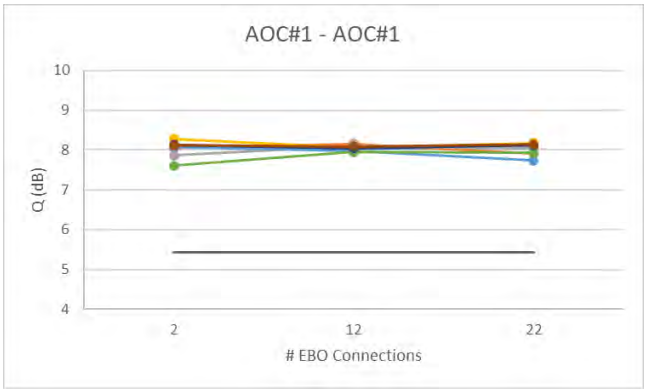
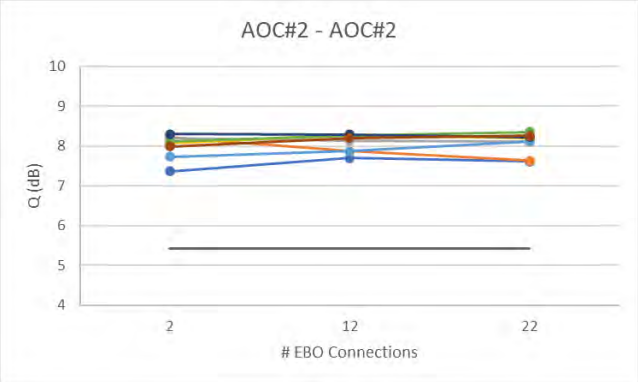
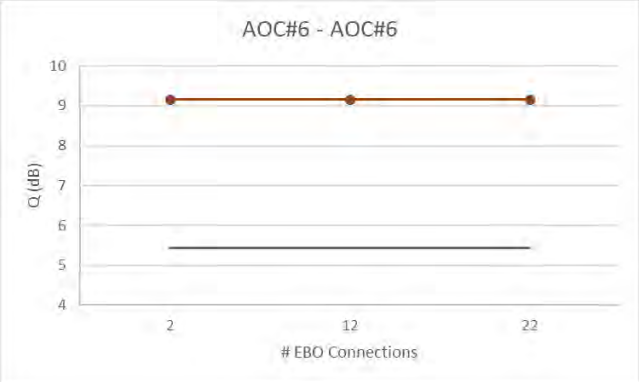
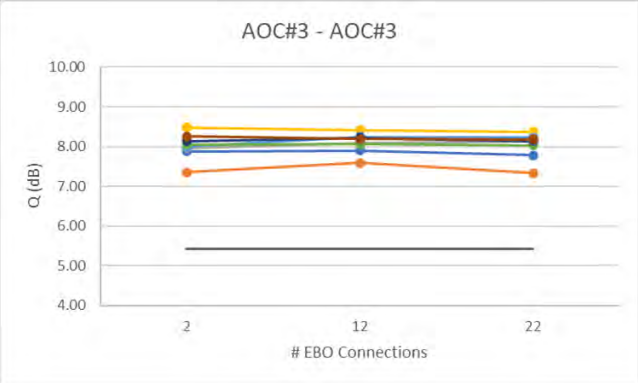


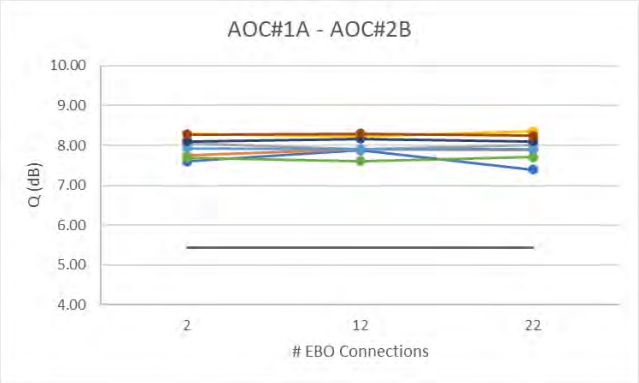
Figure 14. Experimental setup with many connectors

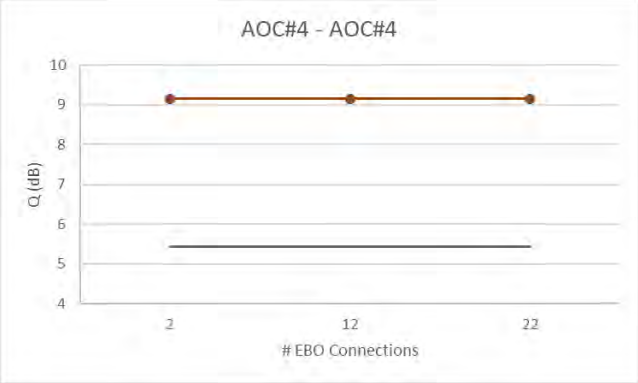


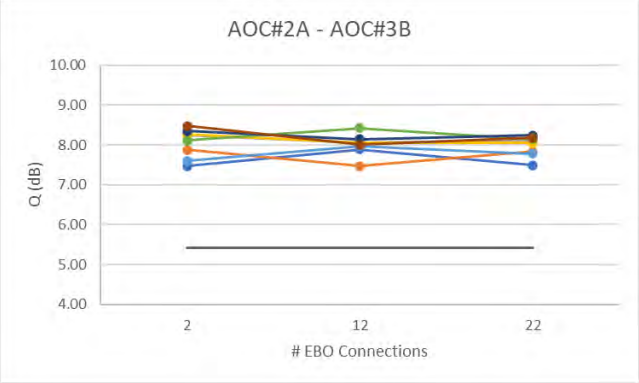

AOC#2 - AOC#2
Q (dB)
EBO Connections

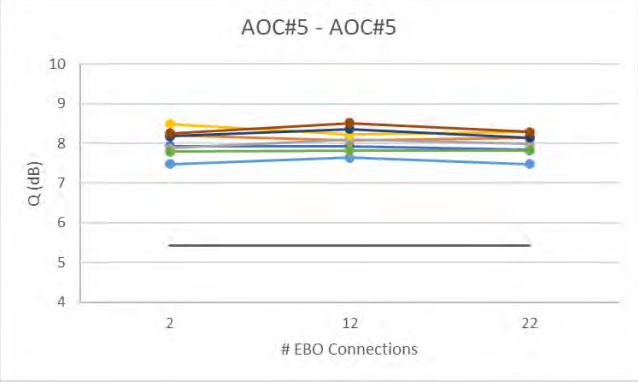

AOC#6 - AOC#6
Q (dB)
EBO Connections

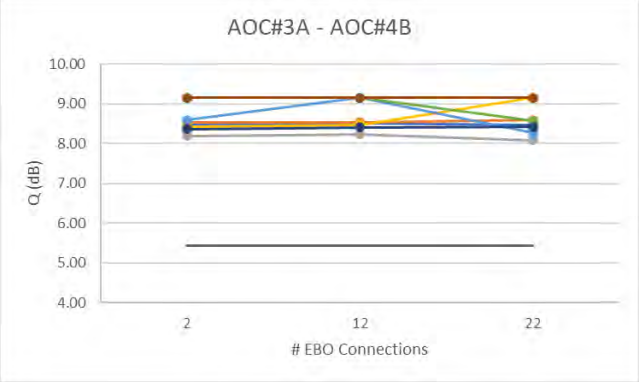

AOC#3 - AOC#3
Q (dB)
EBO Connections

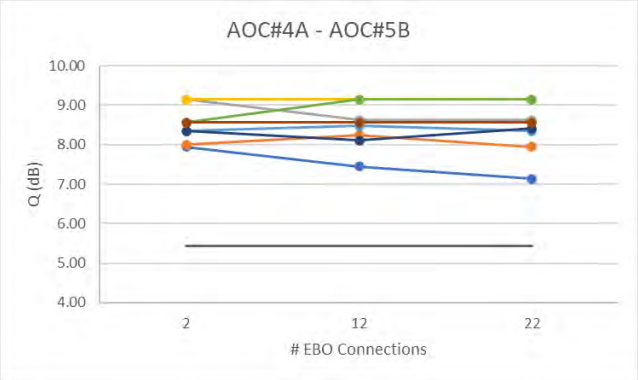

AOC#1A - AOC#2B
Q (dB)
EBO Connections

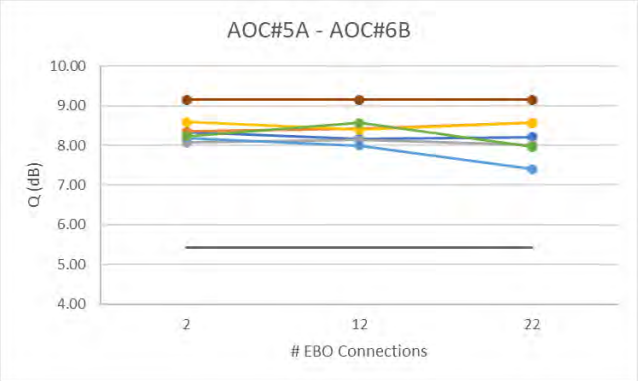

AOC#4 - AOC#4
Q (dB)
EBO Connections


AOC#2A - AOC#3B
Q (dB)
EBO Connections


AOC#5 - AOC#5
Q (dB)
EBO Connections


AOC#3A - AOC#4B
Q (dB)
EBO Connections





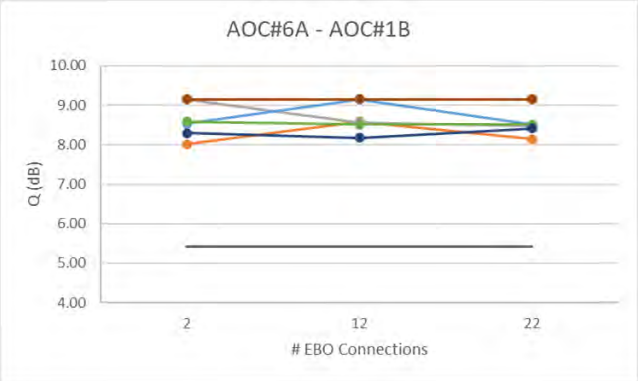
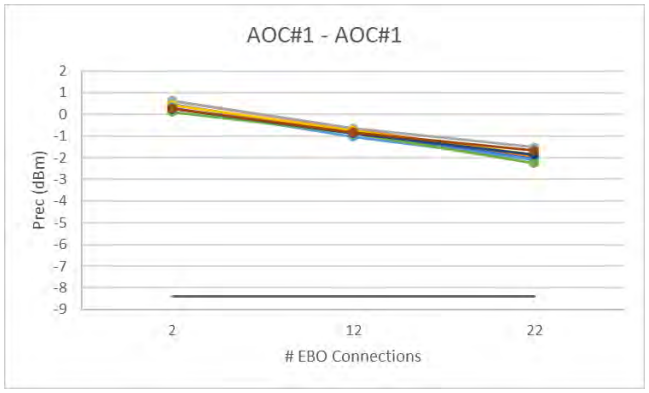
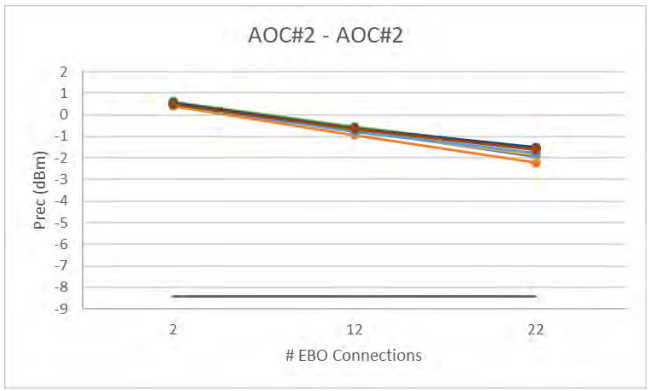


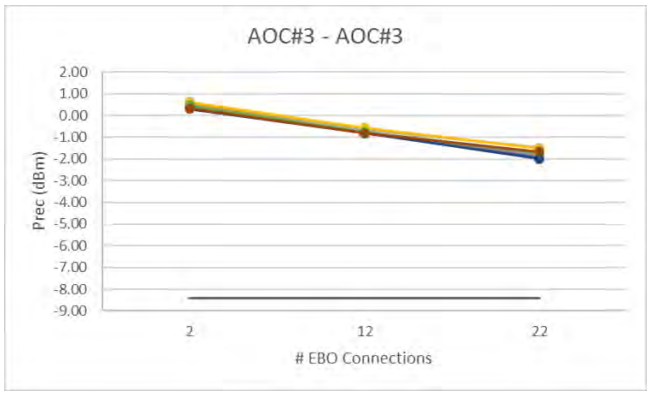
Figure 15. Experimental results with many connectors

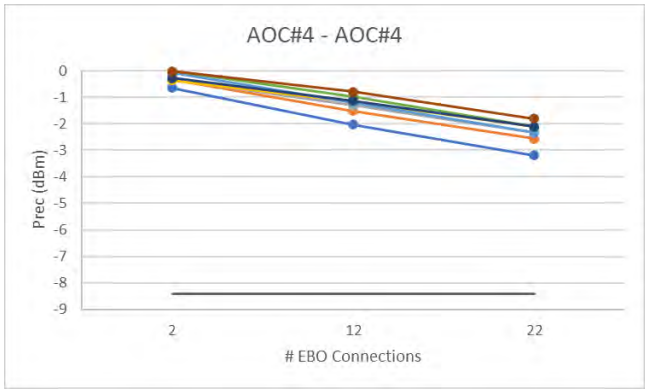
Even with a large number of expanded beam connectors in a 150 m link, (Fig. 15) Q exceeded 7 dB. Some lanes were error free no matter how many connectors were in the path.

Below in Fig. 16 the received power vs. # of connections is plotted. All lanes show a gradual decrease in received power in a well-behaved manner.









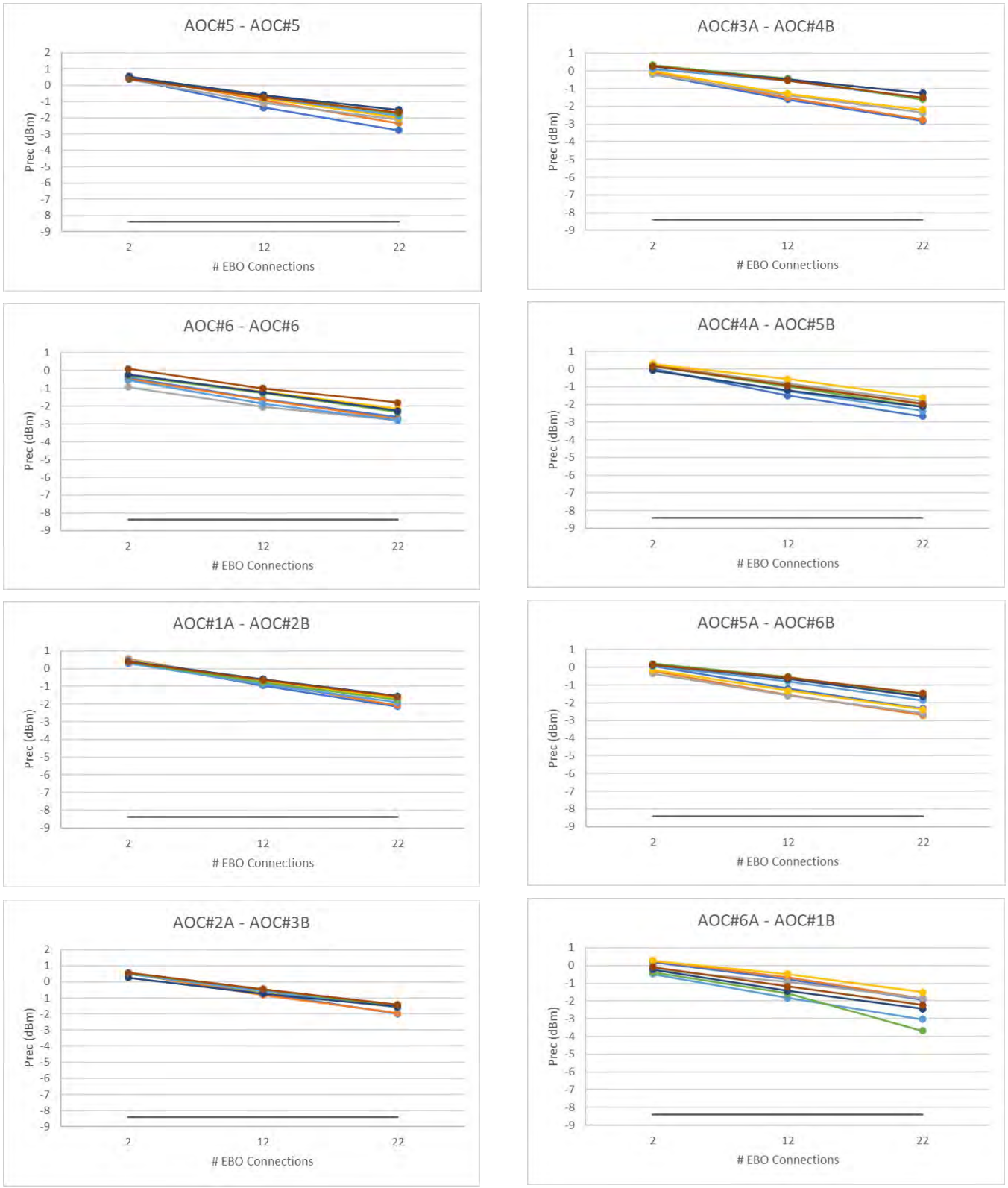


Figure 16. Received power results with many connectors

6. Conclusions

200G-SR4 active optical cables with expanded beam connectors were tested up to 300 m and up to 22 connections. Each test had at least 0.5 dB Q margin. At 150 m OM4 with 2 expanded beam connections there was >7 dB power margin and > 1.5 dB Q margin. Structured cabling with expanded beam connectors presents a path to AOC replacement. AI clusters can use structured cabling and expanded beam connectors to ensure faster deployment, less downtime, and lower cost upgrade paths with optical connectors that are resilient in the face of contamination.

7. References

[1] Gartner report "Cloud Shift Will Shape IT Strategies for Executive Leaders Through 2024" Published 25 January 2021 - ID G00743172.

[2] A. Nakama, et al., "High Density Optical Connector with Unibody Lensed Resin Ferrule", Fujikura Technical Review No. 45 Dec 2015.

[3] Dirk Schoellner, et al., "Performance Methodology and Characterization of a Multi-Fiber Expanded Beam Lensed Optical Interconnect" 2016 IEEE 66th Electronic Components and Technology Conference (ECTC), 2016.

[4] D. Childers, et al., "New, single-mode, multi-fiber, expanded beam, passive optical interconnect", Proceedings of the SPIE, Volume 8991, id. 89910J 14 pp. (2014).

[5] https://www.inemi.org/exp_beam_data_ctrs

[6] A. Cuno, et al., "Development of Best Practices and Guidelines for the Use of Expanded Beam Connectors in Data Center Applications", IWCS 2022.

[7] https://engineering.fb.com/2019/03/14/data-center-engineering/f16-minipack/

[8] https://www.nvidia.com/en-us/data-center/dgx-superpod/

[9] M. Haase, T. Smith, B. Koch, D. Wang, A. Mathews, 'Optical Connector', US Patent 10,139,571, November 2018.

[10] E. Parsons, et al., "Impact of Multimode Connector Return Loss on 400G Cloud Scale Data Center Links", IWCS 2020.

[11] IEC TC 86/SC 86B, "Fibre optic interconnecting devices and passive components - Performance standard – Part 1: General and guidance," IEC 61753-1 Ed 2.1 June 2020.etc.

A Very Small Form Factor, Multi-Row, Multi-Fiber Connector with Multi-Vendor Interoperability

Mike Hughes, Jennifer Cline, Ian Dancel, Michael Kadar-Kallen, William Kettlety, Sharon Lutz

US Conec, Ltd.

Hickory, NC

+1-800-769-0944 · mikehughes@usconec.com

Abstract

The paper describes the design, performance, backwards compatibility, and supply chain maturity of a new, very small form factor (VSFF) multi-fiber interconnect variant of the TMT ferrule. The 24-fiber TMT ferrule is designed with two rows of 12 fibers with the same alignment structure as traditional 24-fiber MT ferrules, enabling the TMT ferrule to be directly mated to legacy MT ferrules. The MMC connector format was used to validate the performance of the 24-fiber TMT design. The connectors were tested in accordance with the requirements of Telcordia GR-1435 [1]. Furthermore, the ferrule was tooled by three different component vendors and a random optical intermate was performed to demonstrate interoperability with ferrules and cable assemblies made from different termination factories.

Keywords: MT; TMT; MPO-24; MMC multi-fiber connector; VSFF; density; co-packaged optics; multi-vendor; interoperability; intermateability.

1. Introduction

Advancements in network switching and artificial intelligence technologies deployed in data center applications are outpacing the bandwidth capabilities of optical transceivers resulting in networks with higher optical fiber density requirements. Subsequently, emerging hyperscale data center architectures are demanding cabling solutions which cannot be managed with legacy connector types. A VSFF multi-fiber connector system has been previously demonstrated to improve usable fiber density when compared to the incumbent MPO connector format [2]. This paper addresses a higher density, multi-row variant of the VSFF connector system.

This new, high density connector technology enables unmatched fiber density for cabling, patch panel, card-edge and on-card applications. A single rack unit (RU) with a 19-inch span, typically supporting 72 LC duplex ports, or 144 fibers, can support up to 6336 fibers with granularity of 24 fibers per connector. This 24-fiber VSFF connector format establishes the lowest loss, highest density and optimal granularity for emerging optical link technologies (see Figure 1).

Emerging transceiver formats are now evolving with two multi-fiber connector port interfaces. For example, 800 Gb/s transceivers for artificial intelligence data center clusters are now being deployed with a 2 x 400 Gb/s configuration utilizing two base-8 MPO connectors. OSFP-XD has now specified 2-port MPO and 2-port VSFF transceiver formats. While two vertically oriented MPOs fit within the transceiver footprints, the size of the MPO format drives the vertical interface of the module to be larger, impeding airflow. The vertical orientation also results in more challenging internal fiber routing. Two MMC connectors can be placed in the transceiver in either a vertical or horizontal orientation, enabling a reduced footprint, improved airflow, and improved internal fiber routing for future transceiver formats [3]. Furthermore, as the industry looks to pluggable transceiver formats at 1.6 Tb/s and 3.2 Tb/s, VSFF connector formats with multiple rows of fibers will be needed.

The density explosion is challenging overall fiber management in data center environments, driving reduced size and multi-row connectivity solutions.

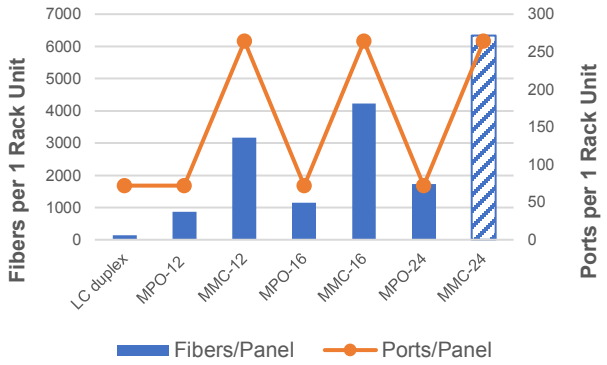


Figure 1. Fiber and Port Density

The 24-fiber TMT ferrule is designed with less than 40% of the material volume used in traditional MT ferrules while supporting two rows of 12 optical fibers on the industry standard pitch of 250 µm. The overall height is reduced by approximately 30%, while the ferrule length is 1/2 of the MT ferrule length. The external MT shoulder is removed, reducing the width of the ferrule to 6.4 mm as shown in Figure 2.

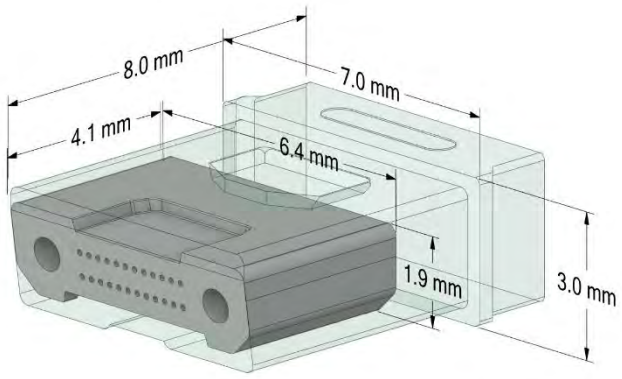


Figure 2. Comparison of the outer dimensions of the MT and TMT ferrules.

This ferrule is designed with the structural integrity required to support industry standard mechanical and durability requirements in push-on/pull-off connector formats. The precision optical and mechanical tolerances are designed to be compliant with the MT optical interface IEC 61755-3-31 for Grade B performance [4]. Nominal optical fiber datum locations and guide hole size and pitch are designed to be compliant with the multi-row MPO as defined in IEC 61754-7-2 [5] (see Figure 3).

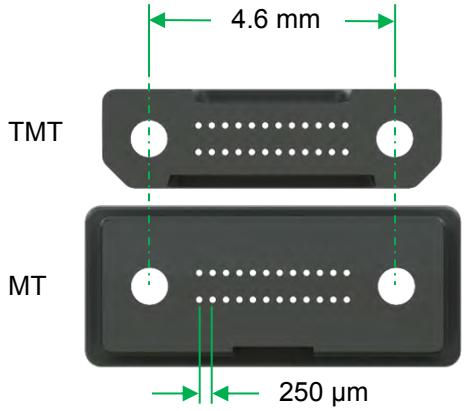


Figure 3. Ferrule structure harmonized to IEC 61754-7-2.

Compliance with MT-based standards allows for the ferrule mating to be compatible with MT ferrules, an important feature for data center infrastructure ecosystems, including cabling, equipment and transceivers.

The TMT ferrule is designed for ease of termination to enable improved yield in cable assembly manufacturing.

The epoxy window in a traditional MT ferrule is eliminated in the TMT ferrule (see Figure 4) which allows for an improved fiber lead-in structure. The chamfered fiber holes of this lead-in design provide 360-degree guidance for each fiber during the termination process. The design offers more forgiveness in the ribbonized fiber-to-fiber pitch tolerance as compared to traditional fiber lead-in designs of MT ferrules.

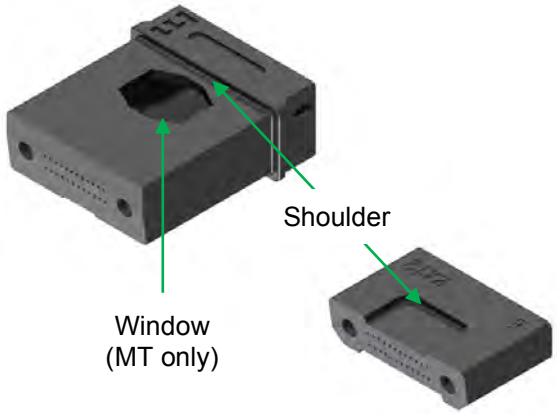


Figure 4. Comparison of external features of TMT and MT ferrules.

The outer profile of the TMT ferrule, including internal shoulders, ensures error-free assembly within the MMC connector due to keying for single-orientation insertion as shown in Figure 5.

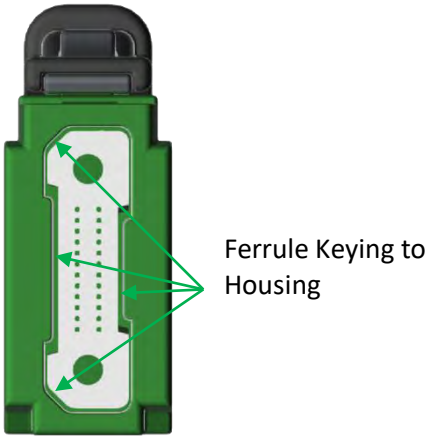


Figure 5. Endface view of a TMT ferrule in an MMC connector.

2. Compatibility with ≤ 250 µm Ecosystems

Designed with a fiber hole pitch of 250 µm, the TMT ferrule is compatible across all existing and future application needs, including environments with 250 µm fiber cabling solutions as well as those leveraging smaller diameter fibers (e.g., 200 µm, 165 µm).

Data center interconnect applications with high fiber count cables that can reach up to 6912 fibers per cable are leveraging small diameter single-mode fibers (e.g., 200 µm) today and likely will migrate to 165 µm diameter optical fibers in the future to meet the requirements for pathway spaces. With growth in other high-density applications such as machine learning, data center back-end networks are driving an increasing number of optical fiber links. Traditional indoor data center pathways can become congested and may not be rated for the loads or space required for the increased volume of cable. In single-mode applications, small diameter fibers, such as 200 µm and future 165 µm or smaller, may be leveraged to reduce the diameter and weight of the cable infrastructure. At the same time, there are short distance machine learning applications driving a resurgence of multimode (250 µm) fiber deployments. With cabling solutions using a mix of fiber diameters including 250 µm single-mode, multimode, and possible future multicore fibers, as well as ongoing decreases in single-mode fiber diameter for some environments, it is critical to have ferrule and connector platforms that do not restrict the ability to terminate optical fiber cables that will be used in current and future applications. While we have previously demonstrated that a fiber hole pitch of 165 µm is achievable in multi-fiber ferrules, maintaining a pitch of 250 µm ensures compatibility with all fiber types and interfaces [6].

To terminate optical fiber cables using small diameter fibers, a method is available to ribbonize fibers on a 250 µm pitch. A tool has been created to enable easy conversion of the small diameter fibers into the correct order and pitch for ribbonization, as demonstrated in Figure 6. The molded plastic tool contains 200 µm (or 165 µm) pitch grooves that fan out to 250 µm pitch on the opposite end. Following application of a quick cure adhesive, the ribbonized fibers can then be removed from the handler, stripped and cleaved for ferrule insertion using industry standard tools.

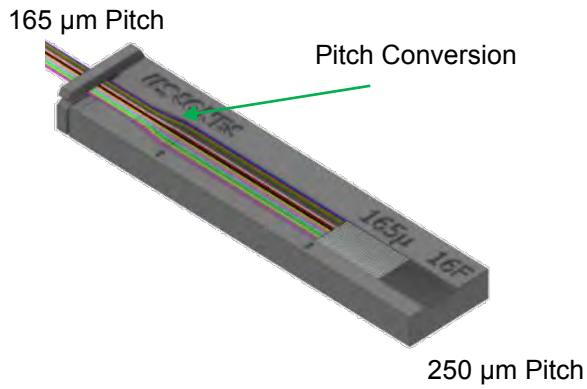


Figure 6. 165 µm Fiber Ribbonization on 250 µm Pitch.

3. Connector Performance

GR-1435 testing of the MMC connector with 24-fiber TMT ferrule has been completed. Figures 7 through 10 show results from tests that are key to optimal performance of connectors in data center applications. The insertion loss results collected for new product measurements (see Figure 7) exceed IEC Grade B requirements.

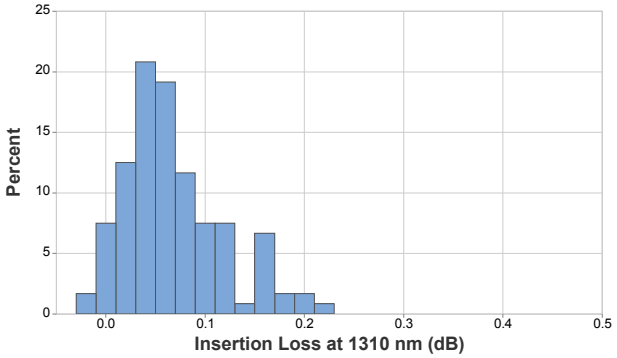


Figure 7. Insertion Loss at 1310 nm prior to environmental exposure.

Physical contact of multi-fiber ferrules is directly correlated to the endface flatness achieved during polishing. The design of the TMT ferrule results in superior endface flatness when the ferrule is polished, illustrated by the minus coplanarity histogram in Figure 8. The IEC minus coplanarity limit for a 12 fiber MT ferrule (400 nm) is shown for reference. There is currently no IEC endface geometry specification for 2x12 MT ferrules.

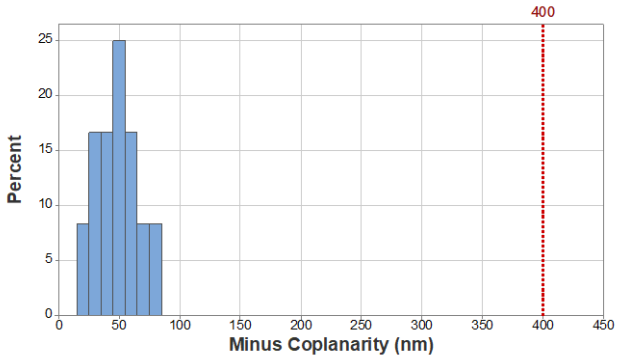


Figure 8. Endface geometry (Minus Coplanarity).

With a reduced size ferrule design that does not utilize an epoxy window, the TMT ferrule has improved symmetry and reduction in epoxy volume needed; subsequently, the insertion loss of the 24-fiber MMC connector is extremely stable during environmental testing. Figure 9 shows the change in loss through GR-1435 controlled environment testing, consisting of thermal aging (60°C, 96 h), humidity aging (40°C, 95% RH, 96 h), thermal cycling (-10°C to 60°C, 40 h), and a dry-out period (60°C, 24 h). The change in loss is < 0.1 dB relative to the start of the test through all environments.

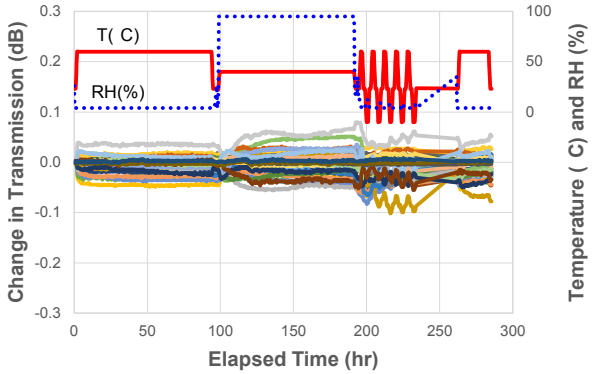


Figure 9. Change in transmission through environments: thermal aging; humidity aging; thermal cycling; dry-out.

Durability testing was completed with MMC connector pairs each mated 50 times per the GR-1435 standard. The durability test results are shown in Table 1. Figure 10 shows images of a female connector end face before and after a male connector was cycled manually 50 times.

Table 1. Durability test results.

Parameter (dB)	1310 nm	1550 nm
Delta IL Max	0.12	0.09
Delta IL Avg	0.03	0.02
IL Max	0.25	0.18
IL Avg	0.07	0.05

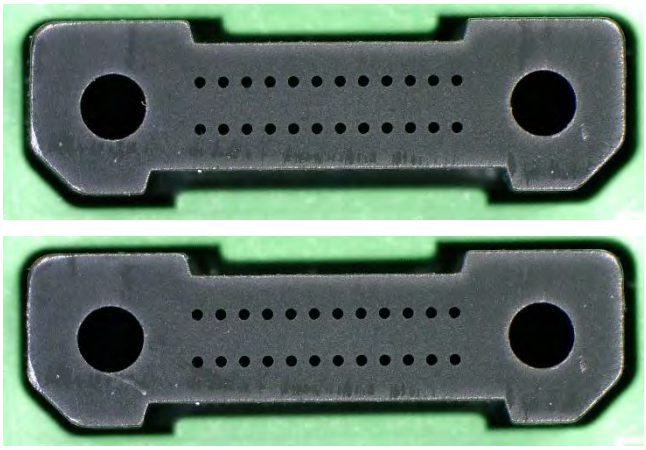


Figure 10. Pre- and Post-durability images of a female connector after manual cycling of a male connector.

4. Compatibility with MT/MPO

While the TMT ferrule structure can support a fiber hole pitch of less than 250 µm to enable 24 fibers in a single row [6], ferrule geometries designed for a reduced fiber hole pitch (e.g., 200 µm) would not be compatible with standard MT ferrules. To maintain backward compatibility and intermateability with standard MT ferrule and MPO connector deployments and ecosystems, the TMT ferrule leverages a 250 µm fiber hole pitch design. In addition to leveraging the advantages of a standardized 250 µm fiber hole pitch, the guide pin bore size and pitch are compliant with the multi-row MPO as defined in IEC 61754-7-2 (Figure 11).

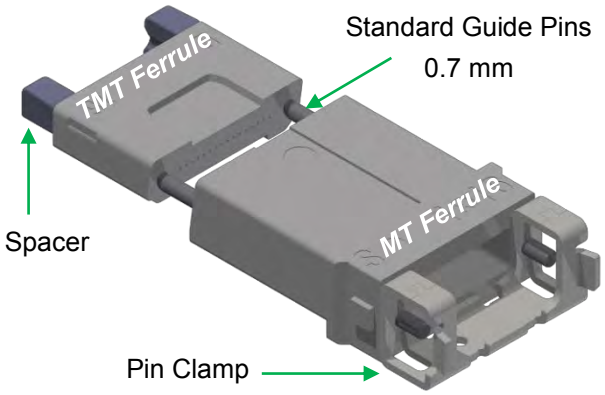


Figure 11. TMT / MT Ferrule Compatibility.

To validate the optical intermateability of the TMT and MT ferrule technologies, testing was completed consisting of 2x12 MT/MPO single-mode connectors mated to 2x12 TMT/MMC single-mode connectors. The MMC and MPO connectors were mated to each other using a hybrid adapter (Figure 12).

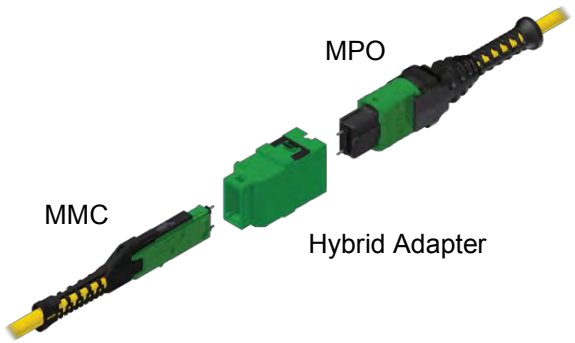


Figure 12. Hybrid adapter for mating MMC (TMT ferrule) to MPO (MT ferrule).

The intermateability results shown in Figure 13 demonstrate loss performance with an average IL of 0.12 dB and a maximum IL of 0.32 dB.

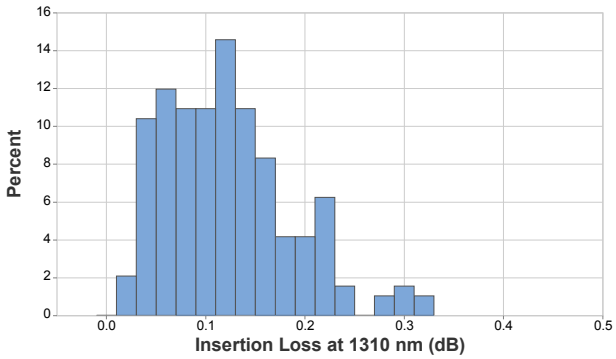


Figure 13. Insertion loss distribution of intermated MPO and MMC connectors.

TMT ferrule to MT ferrule intermateability reduces risk in both legacy and future cabling builds. With demonstrated optical performance when mating MMC connectors to MPO connectors, a migration to the VSFF platform for retrofits in brownfield environments is made easy by enabling backward compatibility with existing structured cabling while still maintaining flexibility for future cabling and technology choices.

5. Multi-Vendor Interoperability

The MMC ecosystem has continued to mature with multi-vendor component supply and termination capabilities. Previously, interoperability testing of 1x16 MMC connectors was completed with TMT ferrules molded independently by both US Conec and Fujikura [7].

US Conec and two additional optical component vendors have independently tooled and molded 2x12 TMT ferrules with a 250 µm fiber hole pitch. An intermateability study was conducted which included ferrules molded by US Conec and the two additional component suppliers, as well as four cable assembly factories, each terminating assemblies at an independent location. The cable assemblies were manufactured with cable using ≤ 200 µm optical fibers. Results from the study demonstrate low insertion losses (see Figure 14) and establish a baseline for optical performance across three ferrule molding vendors and four cable assembly vendors.

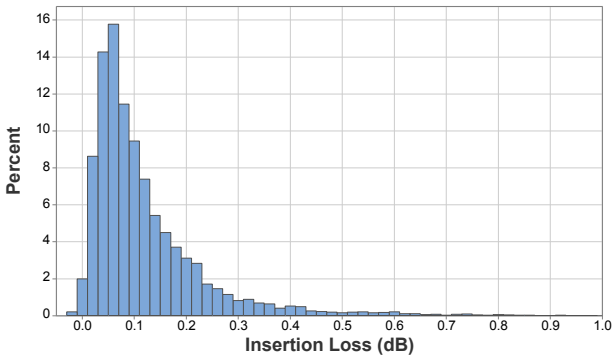


Figure 14. Histogram of the insertion loss measurements at 1310 nm for the multi-vendor interoperability test.

In Figure 15, the insertion loss data is grouped according to whether the mating connectors are from the same vendor (within a vendor) or from different vendors (between vendors). The insertion loss distributions are similar, validating the interoperability performance between suppliers.

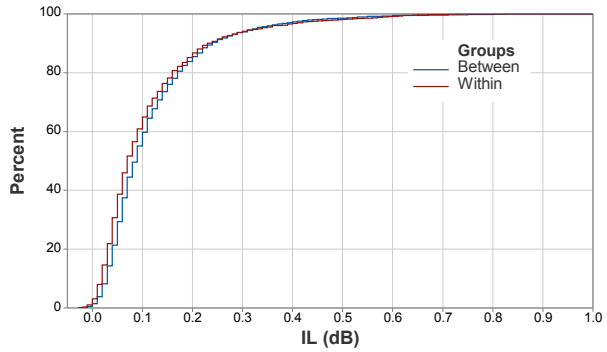


Figure 15. Cumulative distribution functions for the multi-vendor interoperability test, comparing mating between/within vendors.

6. Conclusions

A new, 24-fiber, VSFF TMT ferrule has been developed and tested to the controlled environment requirements of GR-1435. A termination and polishing process was developed in which the endface geometry far exceeds the flatness tolerance requirements defined in the MT optical interface IEC 61755-3-31. US Conec and two additional optical component vendors have tooled the new ferrule design with independent tooling and molding process designs. Ferrules produced from the three component vendors were mated to establish multi-vendor interoperability with cable assemblies produced in four different termination factories. In addition, the new connector format was mated directly to traditional 24-fiber MPO cables establishing backwards compatibility with existing cabling infrastructure. The new, multi-row TMT ferrule format is compatible with existing and emerging small diameter fiber formats and interfaces and enables fiber interconnect densities necessary to support next generation, high fiber-density networks.

7. Acknowledgments

We thank the following companies who participated in the multi-vendor interoperability study: AFL; Corning Optical Communications; Fujikura, Ltd.; Sumitomo Electric Industries, Ltd. [8].

8. References

[1] "Generic Requirements for Multi-Fiber Optical Connectors," GR-1435-CORE, Issue 2, May 2008.

[2] D. Childers, J. Hendrick, J. Higley, M. Hughes, D. Kurtz, S. Lutz, D. Schoellner, "A Novel, Low-loss, Multi-Fiber Connector with Increased Usable Fiber Density," IWCS Cable & Connectivity Industry Forum, (2021).

[3] "OSFP-XD, OCTAL SMALL FORM FACTOR eXtra Dense PLUGGALE MODULE." OSFP-XD, Rev 1.0, March 17, 2023.

[4] "Fibre optic interconnecting devices and passive components – Connector optical interfaces, Part 3-31: Connector parameters of non-dispersion shifted single-mode physically contacting fibres – Angled polyphenylene sulphide rectangular ferrules", IEC 61755-3-31, Edition 1.0, June 2015.

[5] "Fibre optic interconnecting devices and passive components – Fibre optic connector interfaces, Part 7-2: Type MPO connector family, Two fibre rows", IEC 61754-7-2, Edition 1.0, December 2017.

[6] H. Asada, D. Childers, M. Hughes, T. Ishikawa, S. Lutz, D. Schoellner, K. Shindo, Y. Wada, "Next Generation Multi-Fiber Ferrule Using 165 Micron Pitch Optical Fiber," Photonics West Optical Interconnects XXI, SPIE, (2021). http://dx.doi.org/10.1117/12.2578649.

[7] K. Yamanaka, S. Kanno, Y. Sakaguchi, S. Shida, Y. Wada, T. Ishikawa, K. Shindo, "Development of 16F, low-loss, IEC-Grade B, MMC High-Density Optical Connector and Corresponding Cleaning Tool," IWCS Cable & Connectivity Industry Forum, (2022).

[8] https://www.aflglobal.com/

https://www.corning.com/optical-communications/worldwide/en/home.html

https://www.opticalcomponent.fujikura.com/products/mmc-connector-3

https://sumitomoelectriclightwave.com/mmc-connector-high-density-vsff-mpos-for-your-data-center/

9. Biography



Mike Hughes is the Vice President of Product Management at US Conec Ltd. He has over 30 years of experience in copper and fiber optic connectors and cabling products. Mike has held engineering and commercial positions in high density optical interconnect technology for 22 years. Mike holds a Bachelor of Science in Mechanical Engineering from North Carolina State University and Master of Business Administration from Wake Forest University.



Ian Dancel received a Bachelor of Science degree in computer engineering from the United States Military Academy at West Point in 1997. He has been involved in telecommunications and network engineering in field and laboratory environments for 19 years. He joined US Conec in 2016 and is currently focused on fiber optic components as the Process Development Engineering Supervisor.



Jennifer Cline is the Director of Business & Technology Development at US Conec. With nearly 25 years of experience in the fiber optic telecommunications industry, Jennifer has held roles in engineering, commercial and product management, with a predominant focus on data centers throughout her career. Jennifer holds a Bachelor of Science in Mechanical Engineering from North Carolina State University and Master of Business Administration from Purdue University.



Michael Kadar-Kallen received a B.S. in Physics and B.A. in Mathematics from the University of Rochester in 1985, and a Ph.D. in Physics from Princeton University in 1992. Michael has been working in the fiber optics industry since 1994, after completing postdoctoral work in atomic physics at Wake Forest University. He is currently a Senior Principal Engineer at US Conec.



William Kettlety received a Bachelor of Science degree in mechanical engineering from North Carolina State University in 2022. He joined US Conec in 2022 and is currently focused on fiber optic components as a Process Development Engineer.



Sharon Lutz has over 21 years of experience in fiber optic interconnects with US Conec and is currently the Product Manager over precision optical components. Sharon has served as a technical expert for various industry standards including IEC, IEEE, and TIA. She is currently an active member within IEC and serves as convener of the IEC SC 86B WG6 for the development of fiber optic connector standards. Sharon received her Bachelor of Science degree in Mechanical Engineering from the University of North Carolina at Charlotte and her Master of Business Administration from Wake Forest University.

A Novel, Low-loss, Multi-Fiber Connector Compatible with Reduced Coating Diameter Fiber

Sharon Lutz[1], Scott Mendenhall[1], Tom Mitcheltree[1], Lucas Schmidt[1], Dirk Schoellner[1], Scott Bickham[2], Kefeng Li[2], Sonya Raney[2], Pushkar Tandon[2]

[1]US Conec, Hickory, NC [2]Corning Incorporated, Corning, NY

+1 828-323-8883 · sharonlutz@usconec.com

Abstract

This paper examines the advantages of a new 165 µm diameter fiber with a 125 µm cladding diameter, and a new very small form factor multi-fiber connector with a miniature physical contact multi-fiber ferrule. This combination maintains compatibility with existing ferrule geometries and the fiber handling ecosystem. Environmental and mechanical test data is reported using the new ferrule, connector, and 165 µm diameter fiber.

Keywords: TMT ferrule, MMC connector, multi-fiber connector, VSFF, density, co-packaged optics, reduced coating diameter, 165 µm diameter optical fiber, MPO connector.

1. Introduction

The bandwidth demand of data centers continues to increase faster than optical transceiver speeds can support due to applications such as cloud computing, remote working, machine-learning, the Internet of Things (IoT) and artificial intelligence. This trend is encouraging the development and deployment of small diameter cables and high-density fiber optic connectors to compensate for the transceiver speeds [1].

Inside the rack, high-density optical interconnects are becoming a critical component for switches and servers. Fibers with 200 µm and smaller coating diameters are being tested and implemented for these applications, but smaller cladding diameters have been resisted, partially due to the cost and technical challenges required to change the prevalent infrastructure built around 125 µm cladding diameter fibers.

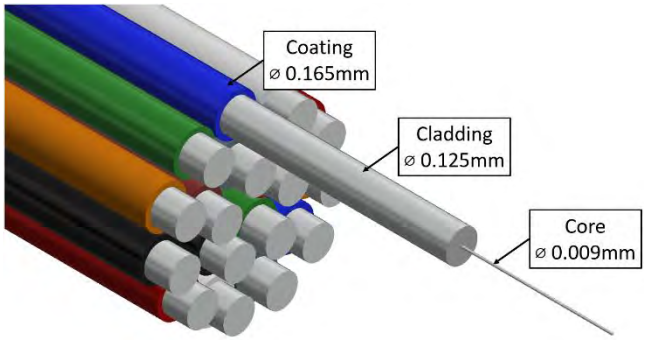


Figure 1. Reduced coating fiber with an overall diameter of 165 µm

Fiber and connector manufacturers have partnered to develop new components that reduce both the fiber coating diameter and the overall cable weight, yet still maintain the existing ecosystem of 125 µm cladding. This paper presents a new very small form factor (VSFF) MMC connector and TMT ferrule that supports a reduced coating fiber with a total diameter of 165 µm. Figure 1 shows the new fiber structure, and Figure 2 shows the accompanying new multi-fiber MMC connector with reduced footprint and support for 165 µm fiber [2]. The new reduced diameter cable and connector are targeted towards several application markets. As will be discussed further below, since the connector maintains a standard 250 µm fiber array spacing, the MMC connector is compatible with existing MPO formats and termination and testing techniques.

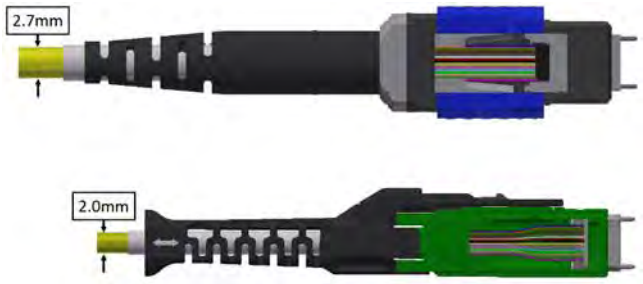


Figure 2. (a) traditional MPO connector with 250 µm coating fiber and (b) new 165 µm diameter fiber and reduced footprint MMC connector

1.1 Structured Cabling

Pluggable transceivers continue to be the primary data center (DC) optical interconnect solution for the foreseeable future. The past few years have seen fiber counts within the transceiver rise to support higher data rates, where schemes such as Dual Duplex LC (four fibers) and Dual MPO8 (sixteen fibers) are popular with hyperscale DCs because they double the module port bandwidth (e.g., 2x400G) [3, 4]. However, Figure 3 (a) shows how little room there is to fit two of these legacy optical connectors into a single pluggable module. Accessing a connector without disturbing its neighbor has proven to be challenging in the field. Often, the entire transceiver module must be unplugged from the panel just to service one optical connector. The smaller footprint of the new MMC connector provides more space for access to the connector body, as shown in Figure 3 (b).

Similarly, optical patch panels are becoming increasingly dense. Hyperscale applications prefer to leverage existing infrastructure and keep their patching within the same rack unit (RU) height. DCs are also concerned with the additional bulk and weight of additional fiber, as next generation patching needs exceed even what MPO connectors can provide.

Table 1 quantifies the additional fiber density the MMC connector provides. Smaller connectors result in smaller pluggable modules, less panel space consumed, and improved air flow. When terminated with 165 µm coating fibers, DCs gain the additional benefit of lower cable weight and size.

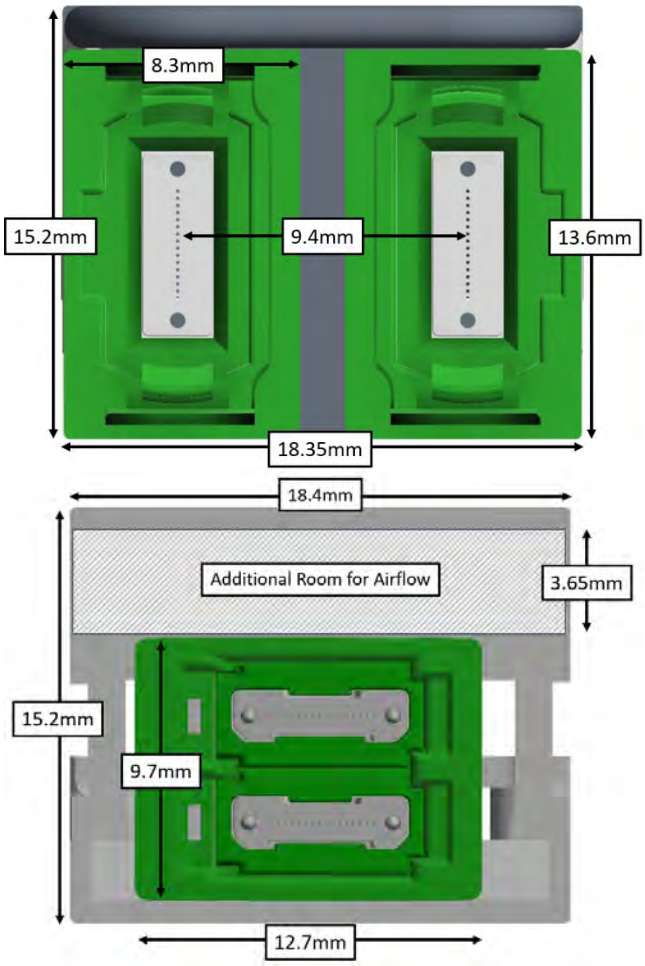


Figure 3. (a) Dual MPO and (b) Dual MMC footprints

Table 1. Number of connectors and fiber a 1RU rack can support by connector type

1RU Panel Max Density			
80 MPO Connectors		264 MMC Connectors	
12f MPO	960	12f MMC	3168
16f MPO	1280	16f MMC	4224
24f MPO	1920	24f MMC	6336
32f MPO	2560	32f MMC	8448

1.2 Co-Packaged Optics

Inside the switch, co-packaged optics (CPO) and silicon photonics use smaller fibers that alleviate the routing and size constraints of conventional 250 µm diameter fibers. Figure 4 illustrates how these optical interconnects were envisioned to eliminate the copper traces to reduce the power consumption latency associated with extracting the clock and data from the electrical signal.

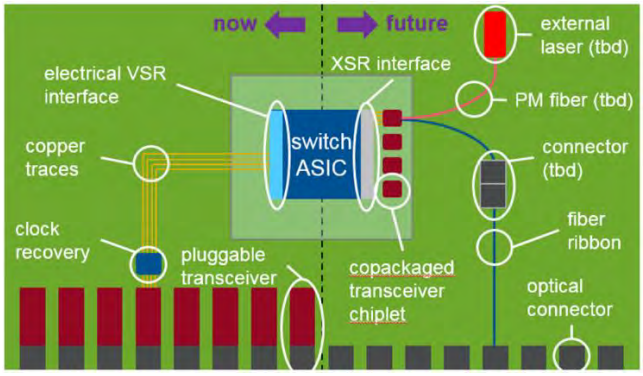


Figure 4. (Left) Traditional copper track layout, and (right) optical interconnects replace the copper for improved latency and power consumption

Optical interconnects are typically accomplished using v-groove arrays to maintain the fiber pitch while providing a bonding surface. Building the v-groove arrays with 165 µm fiber enables the fiber-chip connectivity to have a 33% smaller footprint, as shown in Figure 5. The 125 µm cladding diameter maintains compatibility with the optical connectors currently being integrated into the faceplates of optical switches and transceivers.

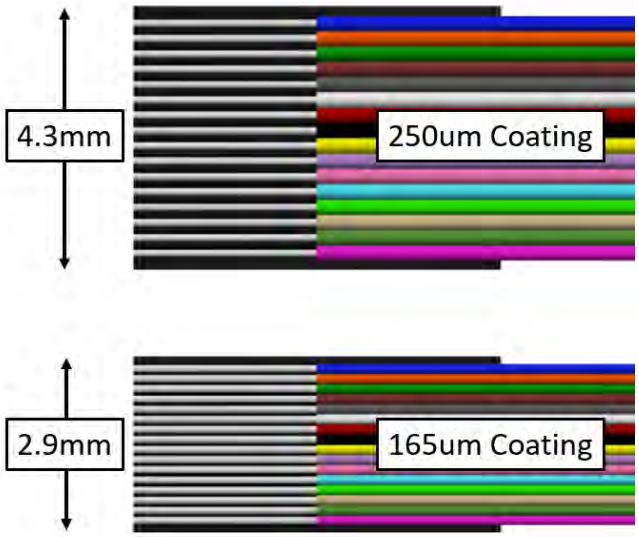


Figure 5. V-groove pitch comparison between the different fiber types

1.3 Artificial Intelligence/Machine Learning

In the past few years, the computing power needed to train the large size artificial intelligence and machine learning (AI/ML) training models has significantly outpaced the performance of the individual Graphics Processing Units (GPUs), resulting in the formation of AI/ML clusters in the hyperscale DCs with 1,000's or 10,000's of GPUs to meet computation demand [5].

It is estimated that the growth of the AI/ML clusters will lead to five to ten times more optical interconnects in AI-centric DCs versus recent hyperscale architectures [6]. Increased connectivity density is becoming a problem for AI/ML system builders that 165 µm diameter fiber cable addresses.

1.4 Data Center Interconnects

Data center interconnects (DCI) use thousands of fibers in small two-to-three inch diameter conduit to connect hyperscale campuses. These links are transitioning from spliced to connectorized solutions to significantly reduce installation time and eliminate the need for special equipment. Reducing the size of the connector and fiber will help maximize fiber counts in these small conduit applications.

2. 165 µm Fiber Design Summary

One of the key concerns in the utilization of smaller diameter optical fibers is microbending sensitivity, which can lead to elevated losses. This limitation was addressed by using a trench-assisted design in which the fiber core is surrounded by a fluorine-doped cladding region which reduces coupling between the optical signal and the cladding modes [7]. A two-layer coating system that includes a low-modulus inner, primary coating helps further suppress the microbend losses that could occur.

A second concern is greater susceptibility to glass damage through perforation of the protective polymer coatings during fiber processing and handling. Puncture of the protective secondary coating is one of the possible failure modes that has been analyzed in detail [8, 9]. While this phenomenon will invariably be higher in small-diameter fibers, an outer, secondary coating with a high modulus provides more damage protection than legacy coatings.

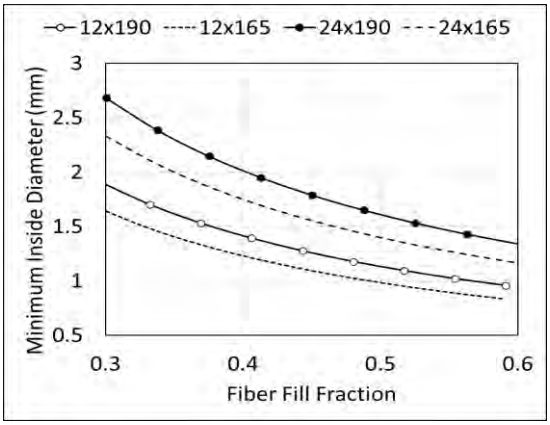


Figure 6. Comparison of fill fractions vs. fiber diameter

The maximum number of fibers that can be incorporated into a buffer tube can be calculated using the mathematical theory of circle packing. For a relatively small number of circles, the maximum bundle (fill) fraction is approximately 75%, but the small amount of free space would result in a very inflexible cable because the fiber positions cannot change when the cable is bent. As a result, fill fractions between 30% and 60% are more typical for the buffer tubes used in optical fiber cables, particularly when aramid yarns are used to enhance the strength. Figure 6 is a plot of the minimum inside diameters of buffer tubes with 12 and 24 fibers as a function of the fiber fill fractions. For both fiber counts, the minimum inside diameter is around 0.2 to 0.3 mm with 165 µm fiber compared to 190 µm fiber. While this difference is small, it is enough to improve the compatibility with the footprints of VSFF multi-fiber connectors.

3. MMC Connector

3.1 TMT Ferrule Design

The TMT ferrule employs the same alignment structure as a traditional MT ferrule. The guide pin bore diameter and guide pin pitch align with MT ferrules defined in IEC 61754-7 series interfaces [10]. This feature allows for the ferrule to be backwards compatible with MT ferrules, an important feature for existing deployed infrastructures. The overall ferrule height is reduced by approximately 30%, while the ferrule length is half of the MT ferrule length. The external MT shoulder is removed, reducing the width of the ferrule to 6.4 mm, as shown in Figure 7. The TMT ferrule has an internal shoulder and an asymmetrical shape, effectively keying the ferrule to the connector for error free assembly. For the testing reported within this paper, a TMT ferrule with two rows of 12 fibers per row was used, but variants with 16 fibers within a row are also available to support Base 8 applications. The TMT ferrule is primarily designed to support existing applications that are using 250 µm fiber pitch, but it can support even higher densities for future applications with tighter fiber to fiber pitch.

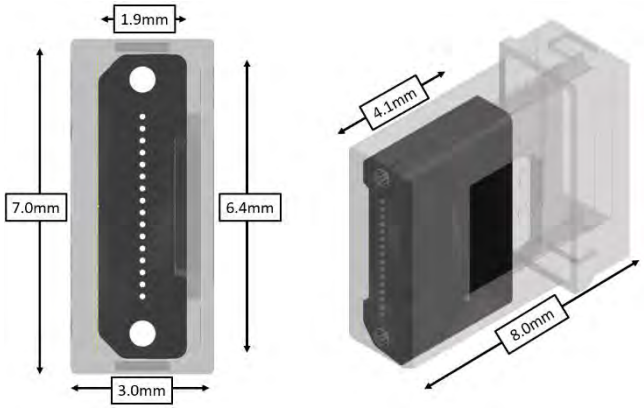


Figure 7. MT (Transparent) and TMT (Solid) comparison

3.2 MMC Connector Format

The MMC connector footprint is also reduced in comparison to the MPO connector footprint. In Figure 8, the footprints of the two connectors are compared. The MMC connector utilizes a rail structure to maintain polarity as shown in Figure 8. This configuration simplifies polarity management within the applications.



Figure 8. MMC and MPO 24 fiber connector formats

The pitch between connectors is limited by cable outer diameters. The MMC connector can accommodate up to 2.5 mm nominal cable sizes with a connector-to-connector pitch of 3.9 mm. Smaller coated fibers allow for increased fiber counts within the cable diameter.

3.3 Qualification Testing

To validate performance over typical operating ranges, qualification testing was performed according to Telcordia GR-1435 controlled environment requirements [11]. For this testing, 24-fiber cable assemblies were built using traditional 250 µm fibers. The assemblies were exposed to the conditions outlined in Table 2.

Table 2. Environmental conditions

Test	Condition	Duration
Thermal Aging	60°C	4 days
Humidity Aging	40°C / 95% RH	4 days
Thermal Cycling	-10 ºC to 60 ºC	5 cycles / 40 hours
Dry Out	60°C	1 day

The environmental performance summary for all tests is shown in Table 3 below. A snapshot of the in-situ insertion loss performance during the thermal cycling testing is shown in Figure 9. The MMC exhibits exceptional stable performance over the entire testing sequence.

Table 3. In-situ insertion loss performance during environmental testing

Specification	Performance	1310nm (dB)	1550nm (dB)
New Product	IL Max	0.32	0.26
	IL Avg	0.11	0.08
Thermal Aging	IL Max	0.38	0.27
	IL Avg	0.11	0.07
Humidity Aging	Delta IL Max	0.16	0.07
	Delta IL Avg	0.04	0.02
	IL Max	0.39	0.27
	IL Avg	0.12	0.08
Thermal Cycling	Delta IL Max	0.15	0.07
	Delta IL Avg	0.05	0.02
	IL Max	0.36	0.26
	IL Avg	0.10	0.07
Dry Out	IL Max	0.36	0.25
	IL Avg	0.10	0.06

Overall, the optical performance for the Telcordia GR-1435 controlled environment conditions is well within the acceptable limits dictated by the industry standard.

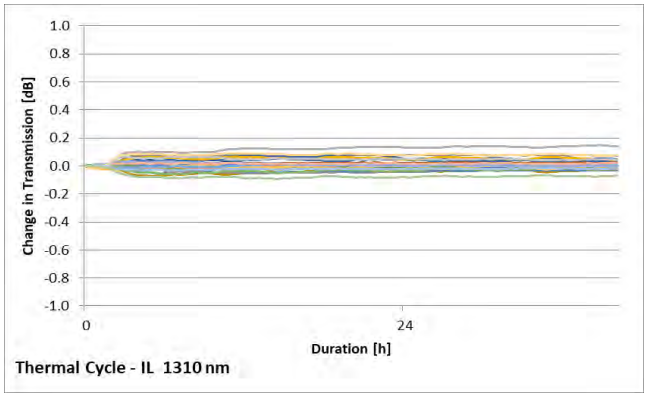


Figure 9. Thermal cycling performance

4. Termination

Multi-fiber connectors are commonly built around a 250 µm fiber pitch to match standard ribbonized fiber. To keep the TMT ferrule backward compatible and intermatable with the MT ferrule and MPO connector, the TMT ferrule is also based around a 250 µm fiber pitch. Therefore, a method is needed to adapt the 165 µm pitch fiber to the 250 µm ferrule pitch. A tool has been created to enable easy sorting of the smaller fibers into the correct order and pitch for ribbonization, as shown in Figure 10. The molded plastic tool contains 165 µm pitch grooves that fan out to 250 µm pitch. The loose fibers can be ordered and placed in the 165 µm end, and by running a finger along the tool, the fibers will seat in the grooves and fan out to the correct ferrule pitch. A ribbonizing cyanoacrylate epoxy, such as Loctite 4861, is then applied and quickly cures to create a temporary ribbon matrix to secure the fibers for handling. The fiber ribbon can then be removed from the handler, stripped, and cleaved for ferrule insertion using industry standard tools [12]. Since the fiber matrix material is smaller than conventional 250 µm fibers, it might be necessary to adjust the blade heights on the tooling to ensure adequate contact with the fiber.

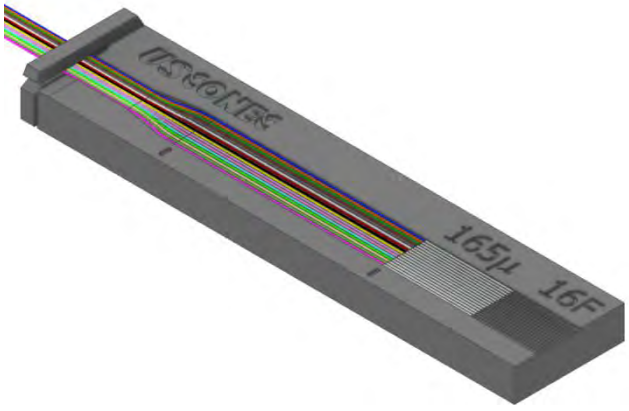


Figure 10. 165µm ribbonization tool for termination

The TMT ferrule is terminated using conventional MT ferrule termination techniques [13]. After the fiber is stripped and cleaved, it is inserted into the ferrule with epoxy and cured. Polishing is also comparable to MT polishing and uses standard MT polishing recipes and films, but since the ferrule surface area is significantly smaller the polishing times need to be reduced by approximately

55%. The TMT ferrule geometry is quantified using standard endface geometry interferometers and the same specifications.

To demonstrate connector performance with the reduced 165 µm fiber, 10 jumpers were built using the 2.0 mm 24-fiber cable described above. Each jumper was terminated on one end with a 24-fiber MPO connector, and with a 24-fiber MMC connector with TMT ferrule on the other end; half of the jumpers were male connectors, and the other half were female. Table 4 shows the endface geometry results for the set of TMT ferrules, along with the current grading range used for acceptable ferrules.

Table 4. Endface geometry results for TMT ferrules

	Average	Std Dev	Min	Max
Minus Coplanarity (nm):	57	27.18	-	150
Ferrule X Angle (deg):	-0.03	0.01	-0.15	0.15
Ferrule Y Angle (deg):	7.91	0.03	7.8	8.2
Fiber Height (nm):	2236	55.86	1000	3500
Adj Fiber Height (nm):	61	38.73	0	300
Fiber Tip Radius (mm):	3.30	0.22	1	-
Ferrule X-Radius (mm):	49251	95720	2,000	-
Ferrule Y-Radius (mm):	204	20	5	-

Connectors were then intermated to measure insertion loss performance at 1310 nm and 1550 nm wavelengths. Each male connector was used as a launch and every female connector intermated to the launch connector, producing 600 mated fiber measurements. The histogram of all the insertion loss measurements is shown below in Figure 11. The average insertion loss was 0.08 dB at 1310 nm, and 0.06 dB at 1550 nm. The 97% insertion loss values were 0.26 dB and 0.20 dB respectively.

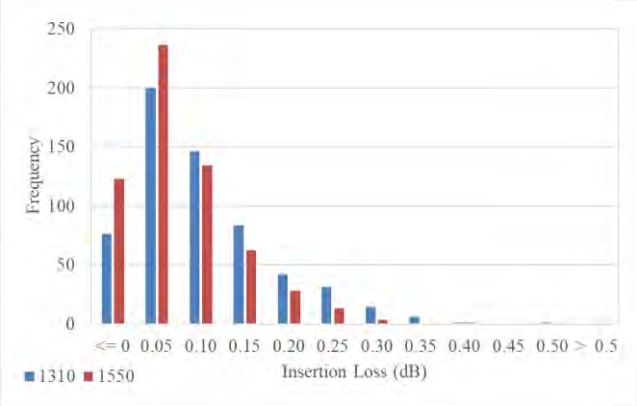


Figure 11. Insertion loss histogram for 600 connections with reduced coating diameter fiber

The above jumpers were then mated into pairs and tested to the Telcordia GR-1435 controlled transmission with applied load (TWAL) media type II 90° standard to ensure that the smaller diameter fiber cable and connector could still perform to required mechanical standards. For each connector pair, insertion loss was measured initially. A 2.2 N force was then applied on the cable perpendicular to the connector directly behind the connector boot, and insertion loss measured again. Finally, the weight was removed, and insertion loss was measured a final time. The GR-1435 specification requires that loss does not change more than 0.50 dB with the applied load. Figure 12 shows the insertion loss histograms of the measurements initially, during load, and after load removal where it is evident that there was no significant change in the performance. The average change with the load applied was 0.003 dB, which is well within the measurement repeatability of the testing, and no measurements changed by more than 0.18 dB, well under the 0.5 dB specification.

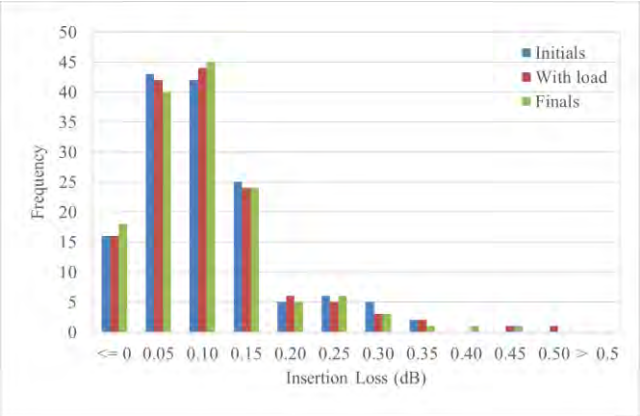


Figure 12 Insertion loss histogram at 1310 nm of GR-1435 TWAL 90° testing.

5. Sustainability

With the reduced connector footprint and smaller cable diameters, there is a significant reduction in raw materials. Lowering the material usage can be correlated to a decrease in the overall weight, as well as in the energy used to produce the raw materials, supporting green initiatives. Table 5 shows the material reductions of MMC connectors.

Table 5. Reduction in raw materials used for the new MMC connector

MPO	MMC	Reduction
Mass (g): 2.37	Mass (g): 0.89	62%

When examining 3,456-fiber DCI cables, reducing the fiber to a 165 µm diameter allows for a different cable structure with a smaller total cable diameter that reduces the total cable mass by 36% per unit length [14, 15].

6. Conclusions

The MMC connector with TMT ferrule is compatible with new 165 µm diameter fiber. The combination of these new developments allows for a decreased overall footprint for high density applications with significant size and weight savings. The new connector is intermatable with existing MPO connectors and the traditional 250 µm pitch ecosystem. Connector test results through GR-1435 environmental and TWAL testing show excellent performance.

7. References

[1] Lightcounting, "AI Creates a New Wave in Demand for Optical Connectivity," https://www.lightcounting.com/newsletter/july-2023-mega-data-center-optics-204 (Accessed August 18, 2023).

[2] D. Childers, *et al*., "A Novel Low-Loss Multi-Fiber Connector With Increased Usable Fiber Density," *Proc. 70th IWCS,* (2021).

[3] QSFP-DD MSA, "QSFP-DD/QSFP-DD800/QSFP112 Hardware Specification," *QSFP-DD/QSFP-DD800/QSFP112 HW Rev 6.3*, http://www.qsfp-dd.com/specification/ (2022).

[4] OSFP MSA, "OSFP-XD, Octal Small Form Factor Extra Dense Pluggable Module," *OSFP-XD Specification Rev 1.0,* https://osfpmsa.org/specification.html (2023).

[5] J. Sevilla, *et al*., "Compute Trends Across Three Eras of Machine Learning", *IEEE 2022 International Joint Conference on Neural Networks*, (2022).

[6] A. Alduino and R. Stone, Optical Interconnects for AI/ML. *Open Computer Summit*, (2022).

[7] Y. Gu *et al*., "Evaluation of 165 Micrometer Reduced Coating Diameter Fibers for High Density Cable Applications," *Proc. 72nd IWCS,* (2023).

[8] G.S. Glaesemann and D.A. Clark, "Quantifying the Puncture Resistance of Optical Fiber Coatings," *Proc. 52nd IWCS*, pp. 237-245 (1993).

[9] S.R. Bickham *et al*, "Microbend Performance and Puncture Load Resistance of Reduced-Clad Fibers," *Proc. 71st IWCS* (2022).

[10] International Electrotechnical Commission, "Fibre optic interconnecting devices and passive components - Fibre optic connector interfaces - Part 7-3: Type MPO connector family," *IEC 61754-7-3:2019*, (2019).

[11] Ericcsson Inc., "Generic Requirements for Multi-Fiber Optical Connectors GR-1435 Issue 02," (2008).

[12] US Conec, Ltd., "US Conec Recommended MTP® Brand Multifiber Connector Production Equipment," *US Conec AEN-1801* (2020).

[13] US Conec, Ltd., "MTP® Brand Connector Installation Onto One Row Jacketed Round Cable with Loose Fibers," *US Conec AEN-1407,* (2023).

[14] A. Sullivan, P. Tandon, R. McCool, A. Diaz and C. Hermann, "A Sustainable Future with Optical Fiber", *Corning Incorporated White Paper WP1000*, March 2023.

[15] A. Sullivan, P. Tandon, M. Srygler, E. Hudson and C. Stroup, "Reducing Costs and Environmental Impact of Data Center Interconnects with Novel Pre-Terminated High-Fiber Density Cable Solutions", Paper #3-8, *Proc. 71st IWCS Conference*, (2022).

8. Authors



Sharon Lutz has over 20 years of experience in fiber optic interconnects with US Conec Ltd. and is currently the Product Manager with responsibility over precision optical components. She received her Bachelors of Science degree in Mechanical Engineering from the University of North Carolina at Charlotte in 2004 and her Master of Business Administration from Wake Forest University in 2019. In June of 2008, Sharon became an active technical expert in multiple industry standards including TIA, IEEE and IEC. Since 2017, Sharon has served as convener of IEC SC 86B Working Group 6 while continuing to contribute to the technical work in both working groups 4 and 6.



Scott Mendenhall is a Connector Development Engineer at US Conec Ltd. He recently started this portion of his career in fiber optic connectors after the completion of his Bachelor of Science in Mechanical Engineering from the University of North Carolina at Charlotte in 2018. Currently, Scott is pursuing a Masters of Engineering in Management from North Carolina State University.



Tom Mitcheltree has over 20 years of experience in fiber optics and is currently the Advanced Technology Manager at US Conec Ltd. He received his Bachelor of Science degrees in Physics and Mathematics from Westminster College in 1995. Tom represents US Conec at IEEE, OIF, and multiple MSA committees.



Lucas Schmidt is a Connector Development Engineer at US Conec Ltd. From 2021-2022 he completed two summer internships with US Conec, during which he helped develop processes to accurately and repeatably measure the endface geometry of TMT ferrules. After receiving his B.S. in Mechanical Engineering from Baylor University in 2022, Lucas joined US Conec in 2023.



Dirk Schoellner received his M.S.E.E. from The Ohio State University in 1999. He has been involved in research and development in fiber optic companies for twenty years. He joined US Conec, Ltd. in 2007 as a Senior Development Engineer in the Research and Development Department. Currently Dirk is the Manager, Connectivity Processes and Testing at US Conec.



Scott Bickham is a Development Fellow in the Corning Research and Development Corp. supporting Corning Optical Communications. He received a B.S. in physics from Purdue University in 1984 and his M.S. and Ph.D. degrees in physics from Cornell University in 1991 and 1995, respectively. Dr. Bickham holds over 100 patents relating to optical fibers and has co-authored over 60 publications.



Kefeng Li has over 15 years of experience in materials science and fiber optics. He is currently the Technology Strategy Manager at Corning. Prior to this role, Kefeng was the Product Line Manager responsible for the P&L, Product Strategy, Sales, and Innovations of Corning High Purity Fused Silica. Kefeng received his PhD degree in Materials Science from the University of Chinese Academy of Sciences (2011) and an MBA in marketing and finance from the University of Connecticut School of Business (2017)



Pushkar Tandon is a Corporate Fellow at Corning Incorporated and Corning Optical Communications. He received a B.Tech. in Chemical Engineering from the Indian Institute of Technology Delhi (India) and Ph.D. also in Chemical Engineering from Yale University in 1995. Dr. Tandon holds over 215 US patents and has co-authored over 60 publications and 45 conference papers.



Sonya Raney is a Senior Program Manager in the Corning Research and Development Corp. supporting Corning Optical Communications. Sonya joined Corning in 1997 after receiving an M.S. in Chemical Engineering from North Carolina State University (1996) and B.S. in Chemical Engineering from Auburn University (1994). She has specialized in the invention, development, and commercialization of new optical fiber products and processes. Her current focus is the development of next generation optical fibers.

Sustainable Network Design: Plastic Reduction with Ultra High-Density Cabling with Thinner Coating and VSFF Connector in Datacenters

Takeshi Kasai[1], Bernard Lee[1], Tatiana Berdinskikh[1], Tiger Ninomiya[1]; John Lu[1]; Michihiko Kato[2]; Hiroshi Nakamura[2]

[1]Senko Advanced Components MA, USA

[2]Furukawa Electric, Japan

Abstract

With the increasing demand for bandwidth globally, data centers are expanding their capacity to support this global demand. This global demand requires more fiber optics components such as cabling, connectors, and adapters, where plastic materials play a significant role. Despite their convenience, plastics are harmful to the environment as they do not degrade and cause carbon emissions during production and incineration. This paper proposes an effective way of minimizing plastic's negative effects with proper network design, including ultra-high density trunk cabling and Very Small Form Factor (VSFF) connectors and adapters.

Very Small Form Factor (VSFF) connectors and ultra-high density trunk cables with reduced coating can significantly reduce the footprint in inter/intra datacenter connectivity compared to the conventional trunk cable and connectors like LC and MPO. With a reduced footprint, plastic consumption can also be reduced. The benefits of adopting new ultra-high-density cabling and VSFF connectors in data centers are discussed.

Keywords: Optical connectivity; Very Small Factor (VSFF) connectors; Ultra-high density cabling, sustainability; plastic reduction; fiber optics, data center.

1. Introduction

More bandwidth is required today as streaming videos on the internet and smartphones become more common. This growth of bandwidth has increased significantly with covid pandemic requiring many people to work from home and have online calls daily. In 2022, even after the pandemic slowed down, the global internet bandwidth rose by 28% [1]. To support this, higher speed and higher density components are required for data centers. According to Lightcounting, more than 3.5 million modules have shipped to cloud datacenters in 2022 [2] and this demand continues to grow as more than 2 million of 800G pluggable transceivers are expected to ship in 2025. With this adoption, data centers can now support higher bandwidths. However, there are concerns about the negative impacts on the environment because more power consumption is required to support higher data rate transceivers. data rate transceivers.

The energy consumption for the Information and Communication Technology (ICT) industry has been increasing every year. In 2019 the ICT was responsible for 3.7% of total greenhouse gas emissions. This was higher than aviation, which generates 2.4% of the total greenhouse gas emission [3]. Connectivity plays a role in increasing the rate of carbon emission as well. Even though connectors and patch cords are passive components, they are mostly made of plastic. Plastic produces greenhouse gas during production and incineration. Furthermore, after disposal, it may take from 20 to 500 years to decompose, depending on the material structure and some environmental factors, such as sunlight exposure [4]. Many countries and governments are working to reduce the consumption of single-use plastic and increase the amount of recyclable plastic through plastic taxes. The United Kingdom has recently introduced regulations that require increased recycled plastic content for packaging [5]. Many other European countries have chosen to impose a plastic packaging tax as well.

However, recyclable plastic is less than 10% of total plastic waste that is discarded each year [6], and it requires the user to separate the plastic, then ship it to a recycling plant after use. This could be impractical, especially for fiber optic patch cords, as they contain aramid yarn, glass fiber, and metal pieces depending on the connector types. Therefore, this paper explores a new approach for sustainable networks by reducing the amount of plastic used for each connection.

Very Small Form Factor (VSFF) connectors and ultra-high density trunk cables with reduced coating can significantly reduce the plastic consumption and carbon footprint in inter/intra datacenter connectivity compared to the conventional trunk cable and legacy connectors like LC and MPO.

This paper summarizes the impact of the VSFF connector and reduced coating of high-density trunk cable on carbon emission on inter/intra datacenter connectivity. This paper is organized to:

1. Highlight the technology of VSFF connector and reduced coating of high-density trunk cable.
2. Introduce the typical connectivity and transceivers for inter/intra data center applications.
3. Clarify the prospects for sustainable network design using VSFF connector and ultra-high density trunk cable.

Several types of VSFF connectors were chosen for comparison, including ceramic ferrule-based SN and CS connectors and multi-fiber plastic ferrule-based SN-MT

connectors. For the fiber optics cabling, 1728 fiber and 3456 fiber trunk cable are typical fiber counts for the data center interconnect. Cabling and connector weight was measured for plastic components only.

In the paper, a comparison of plastic weight was made in several lengths to simulate the actual application of 500m, 2,000m, 10,000m, and 40,000m, which is the maximum transmission length for DR, FR, LR, and ER optics-based transceivers. Case study is presented with 100G-BASE LR4 to illustrate the environmental benefits of the VSFF connectors and new cabling design with thinner coating trunk cable.

2. Comparison of conventional and new sustainable cabling design with VSFF connectors

Currently, the most common types of connectors used inside the data center are the LC and MPO connectors, as they are the most common interfaces to be used with pluggable transceivers. The LC connector was developed by Lucent Technologies in the early 2000s. It is a single fiber connector that uses a 1.25 mm outer diameter ceramic ferrule. For usage with pluggable, it is mostly used in a duplex type where two connectors are joined together at the boot section, as shown in Figure 1.

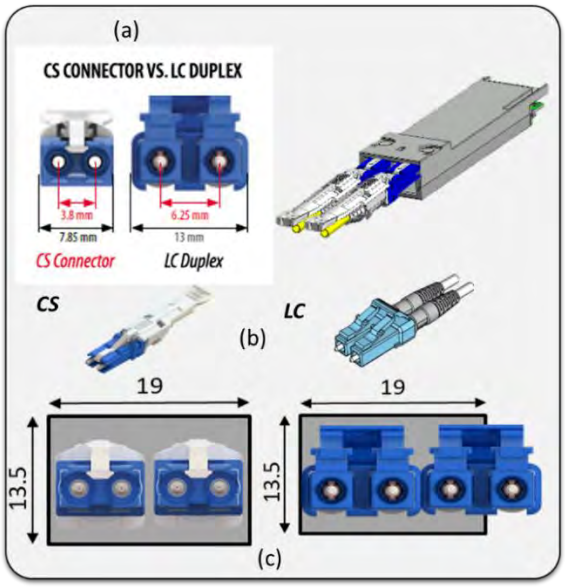


Figure 1. Size comparison of CS and LC Duplex connectors

(a) Width and ferrule pitch comparison of CS (left) and LC duplex (right) connectors

(b) Isometric view of two CS connectors inside transceiver (top right), CS connector (middle left), LC connector (middle right)

(c) Front view diagram showing two CS and two LC duplex inside QSFP module

The Duplex LC has 2 of the 1.25mm ferrules, which are 6.25mm apart. The MPO connector was developed by NTT in 1998 and has a plastic ferrule that can house multiple fibers, as shown in Figure 2. Up to 16 fibers can fit in 1 row where each fiber holes are 250um apart. LC connectors are used most in servers, whereas the MPO are used for leaf and spine switches and the end of the trunk cable.

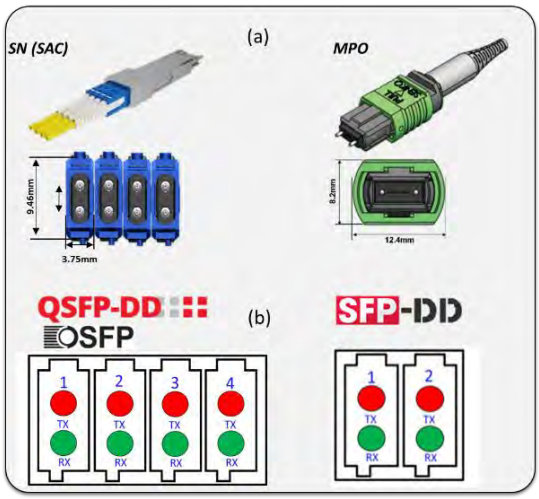


Figure 2. Size comparison of SN (SAC) and MPO connectors

(a) Isometric and front view of four SN (SAC) connectors (top left), and MPO connector (top right)

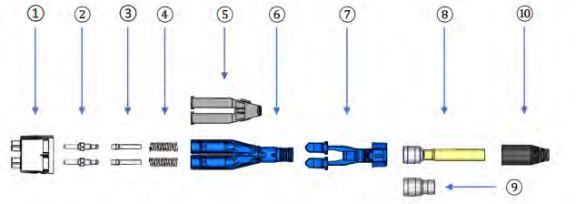
(b) Diagram demonstrating four SN (bottom left) and two SN (bottom right) connectors inside respective transceiver

Very Small Form Factor connectors (VSFFs) are connectors that have a smaller footprint than the LC and MPO connectors. CS connector is a duplex connector with 2 1.25mm ceramic ferrules which are the same as the LC ferrules. It is standardized by TIA/ANSI-604-19 as SEN connector [7]. The CS connector's ferrule pitch is 3.8mm, and the housing body width is 7.85mm, Figure 1. LC duplex connector housing width is 13mm. With this smaller body, the QSFP module can accommodate two CS connectors, delivering four fibers to the module. SN connector has an even smaller footprint than CS or LC. For SN connector, 2x 1.25mm ceramic ferrule are aligned vertically inside a housing with 3.1mm pitch. QSFP and OSFP modules can accommodate 4 SN connectors with eight fibers delivered to the module. SN-MT connector has the same exact size as the SN connector, but it carries a plastic ferrule similar to the MPO connector. Fiber pitch is reduced from 250um to 200um pitch for easier conversion from the ultra high density cables. With the smaller footprint, VSFF connectors can contribute to the material consumption reduction when thousands of connectors deployed inside the data center. Moreover, the smaller footprint contributes to saving rack space. Racks would require their cooling system, and reducing the number of racks would also contribute to reducing carbon footprint.

Fiber optic cables contribute to material consumption inside the data center as well. Especially since emergence of cloud providers, the fiber count that is required for intra-datacenter connectivity has increased. Trunk cables, a type of cable used for intra datacenter connectivity, are critical to material consumption as they usually have thicker jacket material, and their installation distance is longer than the cables that run inside the datacenter. Before the cloud adoption, the most common fiber count for intra-datacenter connectivity was 288 fibers. Inside these 288 fiber cables, the conventional trunk cable would have 250um coated ribbon and 12 fiber ribbons stacked inside the jacket and buffer tubing material inside for each subunit. There is also a stress rod at the center of the outer jacket to give it mechanical strength. This makes the trunk very bulky, especially when trying to upscale the cable to fit 1728 or 3456 fibers. Multiple cabling manufacturers have developed ultra-high-density trunk cables using thinner-coated fiber to solve this issue. This new and sustainable solution for higher fiber count trunks uses 200um or even thinner coating, and instead of stacking the ribbons inside each subunit, the ribbons are glued together in a mesh-like shape and rolled up inside the cable. Unlike the conventional cable, the stress rods are on the outer jacket. This makes the jacket thickness thicker, but the overall weight, outer diameter, and materials used for the manufacturing of the cable are greatly reduced.

3. Experimental methodology

To find the environmental impact of the VSFF connector and ultra high density cable network design, the plastic weight of the connectors and cable was measured. For example, the LC connector is comprised of 9 parts as illustrated in Figure 3.



Label	Name
1	Dust Cap
2	Ferrules
3	PTFE Flange Tubes
4	Springs
5	Housing Cover

Label	Name
6	Bottom Housing
7	Latch
8	Crimp Sleeve for 2.0mm
9	Crimp Ring for 3.0mm
10	Boot

Figure 3. Duplex LC connector sub-components

Each plastic component, except the dust cap, is measured three times using the scale with the 0.001g measurement reliability. The weight of ferrules, springs, and crimp rings are not measured as they are not plastic, and the weight of dust caps is not reported as they will be discarded when in use. This process was repeated for MPO, CS, SN, and SN-MT connector. MPO and SN-MT connectors have plastic ferrules and thus the ferrule was included in the measurement. The average plastic weight of LC duplex, MPO, CS, SN, and SN-MT is summarized in Table 1.

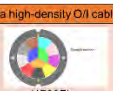
Table 1. The plastic weight difference between VSFF connectors and conventional (duplex LC and MPO) connectors

		Conventional connector	VSFF connector		Weight difference vs the conventional
2F Connector	Connector type	LC Duplex	CS connector	SN connector	
	Footprint				
	Total weight	2.9	1.55	0.86	
	Total plastic weight	2.8g	1.45g	0.76g	CS : 1.35g (52%) SN :2.04g (73%)
Multi-Fiber Connector	Connector type	MPO connector	SN-MT connector		
	Footprint				
	Total weight	3.24	1.94g		1.30g
	Total plastic weight	3.19g	1.76g		1.43g (55% reduction)

The average weight for the LC duplex connector is 2.8g; it is 1.45g for CS and 0.76g for SN connector. Therefore, the plastic weight is reduced by 1.35g or 52% for the CS connector compared to the LC duplex connector. Similarly, the SN connector offers the lowest weight of plastic components (0.76g), which is a 2.04g (73%) plastic reduction compared to the LC duplex connector. SN-MT connector offers a 1.43g (55%) of plastic content reduction compared to the MPO connector, as illustrated in Table 1.

Table 2 summarizes the plastic weight of conventional and new design outside plant (OSP) cables with 1728 fibers and 3456 fibers. The plastic weight is reduced from 315g/m for the conventional design cable to 292 g/m for the new design OSP cable with 1728 fibers providing a plastic reduction of 23 g/m. A more significant plastic reduction in the amount of 197g/m is achieved for a new cable design with 3456 fibers.

Table 2. Comparison of plastic weight of conventional and new OSP cable designs

Fiber count	Item	Conventional OSP cable	Ultra high-density O/I cable	Weight difference
	Schematic	 (1728F)	 (1728F)	
	Rollable ribbon	250 μm fiber RR	200 μm fiber RR	
1728F	Weight (ALL materials)	424 [g/m]]	352 [g/m]	72 [g/m]
	Weight (Plastic only)	315 [g/m]	292 [g/m]	23 [g/m]
	Jacket thickness	1.5 [mm]	3.5 [mm]	
3456F	Weight (ALL materials)	790 [g/m]]	538 [g/m]	252 [g/m]
	Weight (Plastic only)	629 [g/m]	432 [g/m]	197 [g/m]
	Jacket thickness	1.5 [mm]	3.5 [mm]	

4. Results and Data Analysis

Methodology discussed in the previous paragraphs only calculates connector deployed connections between MDIs (Media Dependent Interface), as shown in Figure 4 [8].

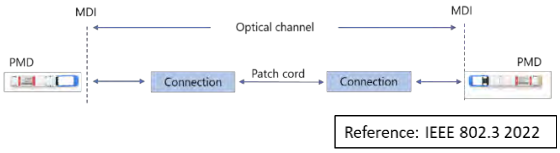


Figure 4. Optical connections in the link between MDI [8]

IEEE Std 802.3™-2022 standard for Ethernet indicates that total connection loss is the maximum connector and splice loss between MDIs, with an average 0.5dB insertion loss per connection and splice. The maximum link loss and connections allowed in total optical channel are shown in Table 3:

Table 3. The IEEE 802.3 specification with connection count based on allowable loss

PMD	Distance	loss	Connection	Interface
100GBASE-DR	500m	2.75 dB	5	LC
100GBASE-FR1	2000m	3 dB	6	LC
100GBASE-LR1	10000m	2 dB	4	LC
100GBASE-LR4	10000m	2 dB	4	LC
100GBASE-ER4	40000m	2 dB	4	LC
200GBASE-DR4	500m	2.75 dB	5	MPO
200GBASE-FR4	2000m	3 dB	6	MPO
200GBASE-LR4	10000m	2 dB	4	MPO
200GBASE-ER4	40000m	2 dB	4	MPO
400GBASE-DR4	500m	2.75 dB	5	MPO
400GBASE-FR4	2000m	3 dB	6	MPO
400GBASE-FR8	2000m	3 dB	6	MPO
400GBASE-LR8	10000m	2 dB	4	MPO
400GBASE-ER8	40000m	2 dB	4	MPO

For example, the maximum link distance is based on a 3dB total connection loss for FR allocation, which supports six connections with an average insertion loss of 0.5 dB per connection or more connections that can meet the total link loss budget [9]. According to Table 1, a replacement of the LC connector with the VSFF SN connector can save 4.08g of plastic per connection, and a change of MPO to SN-MT connector can save 2.86g of plastic per connection. Utilizing the connection count based on IEEE 802.3, the plastic reduction per link is achieved by using VSFF connectors in between MDIs as shown in Table 4. Table 4 summarizes the plastic weight reduction for a link with an average insertion loss of 0.5dB per connection. This plastic reduction was achieved by the replacement of LC and MPO connectors with VSFF connectors.

Table 4. Plastic reduction for a link with an average insertion loss of 0.5dB per connection

Legacy connector type	VSFF connector type	PMD	Plastic reduction per link with VSFF connectors
LC	SN	DR	20.4g
LC	SN	FR1	24.48g
LC	SN	LR1	16.32g
MPO	SN-MT	DR4	14.3g
MPO	SN-MT	FR4	17.16g
MPO	SN-MT	LR4	11.44g
MPO	SN-MT	ER4	11.44g
MPO	SN-MT	DR8	14.3g
MPO	SN-MT	FR8	17.16g
MPO	SN-MT	LR8	11.44g
MPO	SN-MT	ER8	11.44g

However, newly emerged applications such as AI have driven the data center data traffic transformation from NORTH-SOUTH traffic of client-to-server to EAST-WEST traffic of server-to-server.

Over 70% of data stream is inter/intra datacenter of server to server traffic [9]. Therefore, average insertion loss 0.5dB per connection provides insufficient optical link loss budget for high-density patch panels with cross-connection function.

Considering the challenges in network design with 0.5dB loss per connection, IEC grade B connectors, connectors with random mating insertion loss of 0.25dB, offer benefit to hyperscale data centers [10]. As IEC grade B connectors offer lower loss, connection count per link between MDIs can be increased, resulting in further plastic reduction amount as illustrated in Table 5.

Table 5. Plastic reduction for the link with Grade B connectors

Legacy connector	VSFF connector	PMD	plastic reduction per link
LC	SN	DR	40.8g
LC	SN	FR1	48.96g
LC	SN	LR1	32.64g
MPO	SN-MT	DR4	28.6g
MPO	SN-MT	FR4	34.32g
MPO	SN-MT	LR4	22.88g
MPO	SN-MT	ER4	22.88g
MPO	SN-MT	DR8	28.6g
MPO	SN-MT	FR8	34.32g
MPO	SN-MT	LR8	22.88g
MPO	SN-MT	ER8	22.88g

According to Table 2, upgrading from conventional to thinner coating trunk cable reduces 252g/m of plastic

material. Combined with the maximum allowable transmission length from Table 3, the material reduction for each type of PMD using 3456 fiber trunk cable are calculated. The results are summarized in Table 6:

Table 6. Calculation of the plastic material reduction of cable based on max allowable distance.

PMD	distance (m)	plastic reduction with reduced coating trunk cable(kg)
50GBASE-FR	2000	504
50GBASE-LR	10000	2,520
50GBASE-ER	40000	10,080
100GBASE-DR	500	126
100GBASE-FR1	2000	504
100GBASE-LR1	10000	2,520
100GBASE-LR4	10000	2,520
100GBASE-ER4	40000	10,080
200GBASE-DR4	500	126
200GBASE-FR4	2000	504
200GBASE-LR4	10000	2,520
200GBASE-ER4	40000	10,080
400GBASE-DR4	500	126
400GBASE-FR4	2000	504
400GBASE-FR8	2000	504
400GBASE-LR8	10000	2,520
400GBASE-ER8	40000	10,080

5. Case Study Using 100GBASE-LR4

Utilizing the reduction data from Tables 5 and 6, calculation of material reduction for both the cable and connectors can be measured for intra datacenter connection. This case study will compare network design using 3456 fiber trunk cable for intra datacenter connection with 100GBASE-LR4. For legacy network design, conventional outside plant cable with 250um coating will be deployed for 8km leaving 1km for each side. 24 fiber MPO connector is terminated on the end of the trunk cable, which connects to a 24 Fiber MPO to 3x 8 fiber MPO connectors. Each 8 fiber MPO connector will then connect to a patch panel that has 8 fiber MPO – 8 LC connector fanout cable inside a cassette as LR4 is a LC based transceiver. LC duplex – LC duplex cable will be plugged in to the LC side of the cassette with the other side plugging into the connector as the figure below shows.

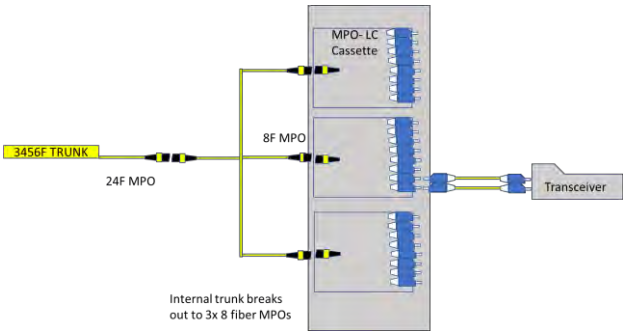


Figure 5. Example of Legacy network design with MPO and LC connectors for 100G-LR4 applications

The sustainable network design uses a thinner coating 3456 fiber trunk with SN-MT 24 fiber connector terminated on each end. Each 24 fiber SN-MT connector fans out to 3x 8 fiber subsections. Each of these subsections is terminated to 4x SN connectors clipped together inside a patch panel. As SN connector is a two fiber connector, it can breakout to LC duplex connectors without using cassettes as shown in Figure 5.

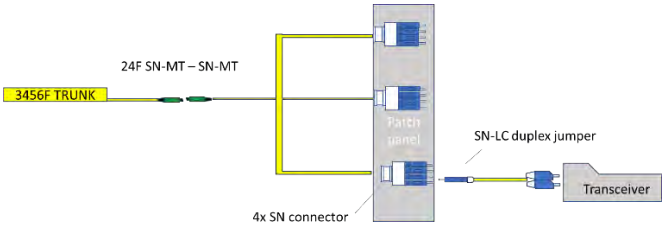


Figure 6. Example of sustainable network design with VSFFs for 100G-LR4 applications

There are several considerations to calculate the connector quantities. First, the total fiber count of 3456 is divided by respective fiber count for each connector type. For example, the quantity of SN-MT connector is identified by dividing 3,456 fibers in a trunk cable by 24 fibers in SN-MT connector. Second, the number of connectors is doubled for mated pairs. Finally, the number of connectors is doubled again to include the opposite site of the trunk cable. After the connector count for the entire topology is identified, the total plastic weight is calculated by multiplying the individual connector weight listed in Table 1 to corresponding connector quantity.

Connector count and weight for each network is summarized in Table 7.

Table 7. Connector count and total plastic weight for legacy and sustainable LR4 network designs.

Connector type	Legacy (pcs)	Sustainable (pcs)
LC Duplex qty	10,368pcs	3,456pcs
LC Duplex weight	29.03kg	9.68kg
MPO qty	2,184pcs	-
MPO weight	6.97kg	-
SN qty	-	6,912pcs
SN weight	-	5.25kg
SN-MT qty	-	576pcs
SN-MT weight	-	1.01kg
Total connector qty	**12,552pcs**	**10,944pcs**
Total plastic weight(kg)	**36.03kg**	**15.94kg**

With the sustainable network designs 1,608 connectors can be eliminated. This is equivalent to 20.36kg or 57% of material reduction in the entire network. Furthermore, sustainable designs eliminate the need for cassettes as well with SN-LC patch cord. Changing network designs for 100GBASE-LR4 from conventional to sustainable can provide 2,520kg of plastic material reduction according to Table 6. Therefore, in total, the implementation of sustainable design saves 2540.36kg of plastic material. In addition, SN-MT fiber pitch being 200um will not require any upribboning process when termination connector onto the thinner coating high density trunk cable.

6. Case Study of environmental impact of 100GBASE-LR4 optical connection

This paragraph elaborates on the prior case study of plastic reduction, comparing duplex LC and VSFF SN connector environmental impact by calculation CO_2eq emissions from plastic consumption. The plastic reduction discussed in this paper can be used as guidance for higher tier data centers design, but also an evaluation of the environmental impact of data centers using legacy interconnect and cabling and VSFF interconnects. On the other hand, optical connectors require high precision and stable optical performance at the same time, the material consisting of the connector must be robust and inherit thermal and environmental performance. Therefore, vendors of connectors often choose high grade amorphous plastic such as Polyetherimide (PEI) to be the main body of the connector.

PEI subcomponents in typical LC duplex connector and SN components are illustrated in Figure 5:

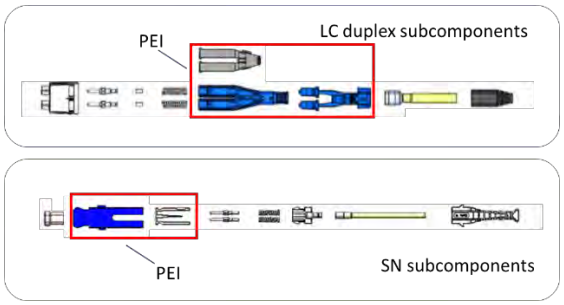


Figure 5. Illustration of the PEI parts in LC duplex and SN subcomponents

PEI weights for LC duplex and SN connectors are summarized in Table 8. Changing LC duplex connector to SN connector in a link results in 0.72g of PEI material reduction per connector.

Table 8 PEI weight comparison of LC Duplex and SN connector

Connector type	PEI weight(grams)*
LC Duplex	1.23
SN	0.51
PEI reduced per connector	0.72

*Note: each component is weighted 3 times with an electronic scaler of 0.01gram accuracy, and other components have been removed including zirconia ferrule, sleeve, spring, crimp ring illustrated in Figure 3

Furthermore, PEI has higher environmental impact against most other plastics. According to Sabic's research, to produce 1kg PEI resin would generate 18.24kg of CO_2 equivalent (CO_2eq) [11]. This data is generated using IPCC 2013 GWP 100A V1.03 method [13]. As discussed in Paragraph 4, IEEE802.3 100GBASE-LR4 can allow total of 8 connections with 16 connectors within the total optical link (Figure 4) if each connector performs under 0.25dB insertion loss. Using the reduced amount shown in Table 8, a total of 0.21kg of CO_2eq (0.00072kg/connector*18.24kg*16connectors=0.21kg) can be saved within total optical link per pair of 100GBASE-LR4 transceivers.

According to Lightcounting report [2], there are 1,706,219 pcs of 100GBASE-LR4 QSFP28 transceivers that were sold equipped with legacy LC duplex connectors, in 2020 estimated 100GBASE-LR4 links are 853,109 pairs (Figure 4). From this data, the reduced amount of CO_2eq within the link can be calculated, Table 9.

Table 9. Estimated CO2 eq reduction for 100GBASE-LR4 links with QSFP transceivers and SN connectors

CO_2eq reduced per pair of 100GBASE-LR4 by using SN	Pairs of 100GBASE-LR4 equipped with legacy LC	Estimated CO_2eq reduction
0.21kg	853,109 pairs	179,152.89

Using EPA calculator [14], the amount of reduction in CO_2eq can be converted to 20,159 gallons of gasoline consumed.

7. Conclusions

The paper introduces the new VSFF connectors technology and ultra-high-density trunk cables with reduced coating. Then, a comparison of plastic consumption against the conventional connection is made when deployed in various lengths often suited.

The total plastic weight for VSFF connectors is significantly lower than the duplex LC connector. The plastic weight of the CS connector is only 48% of the plastic weight of the LC connector resulting in a 52% plastic weight reduction. This plastic weight reduction is even more significant for the SN connector consuming only 27 % of the plastic weight of the LC duplex connector. Similarly, the SN-MT connector saves 55% of plastic weight compared to conventional MPO connectors.

The plastic weight of conventional and new design outside plant (OSP) cables with 1728 fibers and 3456 fibers are compared. A new OSP cable design with 1728 fibers provides a plastic reduction of 23g/m (23kg/km). The most significant plastic reduction in the amount of 197g/m (197kg/km) is achieved for the new cable design with 3456 fibers.

The data is used to investigate the impact of VSFF connectors and new cable design on plastic weight savings for DR, FR, LR, and ER links. Detailed calculations are provided for the 100GBASE-LR4 link. Based on the findings, changing network designs for 100GBASE-LR4 from conventional to sustainable can save ~ 2540kg of plastic material. Finally, carbon emission reduction is calculated based on the difference in plastic consumption of LC duplex and SN connectors for 100GBASE LR-4 link using LCA methodology based on ISO 14040.

VSFF connectors and ultra-high density trunk cables with reduced coating offer important environmental benefits by significantly reducing the plastic consumption and carbon footprint in inter/intra datacenter connectivity compared to the conventional trunk cable and legacy connectors like LC and MPO.

8. Acknowledgement

The authors wish to thank Tyler Royer at SENKO Advanced Components for providing advice and feedback as well as paper review.

9. References

[1] IEEE Communications Society technology blog, https://techblog.comsoc.org/2022/09/19/telegeography-global-internet-bandwidth-rose-by-28-in-2022/#:~:text=According%20to%20Telegeography%2C%20Global%20internet,of%20growth%20has%20been%20slowing.Source

[2] High-speed Ethernet optics, Lightcounting report, Mar 2023

[3] https://www.climatiq.io/blog/measure-greenhouse-gas-emissions-carbon-data-centres-cloud-computing

[4] How long does plastic take to decompose? The waste management and recycling blog, https://www.forgerecycling.co.uk/blog/how-long-it-takes-everyday-items-to-decompose/#:~:text=While%20some%20plastics%20are%20reusable,factors%20such%20as%20sunlight%20exposure

[5] https://www.gov.uk/guidance/check-if-you-need-to-register-for-plastic-packaging-tax#:~:text=You%20will%20need%20to%20pay,regulations%20and%20food%20safety%20standards.

[6] https://repurpose.global/blog/post/why-is-most-plastic-not-recycled#:~:text=About%2075%25%20of%20global%20plastics,them%20near%2Dimpossible%20to%20recycle

[7] ANSI/TIA-604-19 FOCIS 19 Fiber Optic Connector Intermateability Standard - Type SEN Connector, 2021 Edition, July 30 2021

[8] IEEE Std 802.3-2022, IEEE Standard for Ethernet PDF: ISBN 978-1-5044-8725-2 STD25431

[9] Cisco Global Cloud Index 2016-2021

[10] IEC 61753-1: 2018 Fibre optic interconnecting devices and passive components - Performance standard - Part 1: General and guidance

[11] SABIC ULTEM resin LCA data only available per request https://www.sabic.com/en/products/specialties/ultem-resin-family-of-high-heat-solutions/ultem-resin

[12] Global Warming Potentials (IPCC Second Assessment Report)| UNFCCC https://unfccc.int/process/transparency-and-reporting/greenhouse-gas-data/greenhouse-gas-data-unfccc/global-warming-potentials

[13] CO2e Definition https://www3.epa.gov/carbon-footprint-calculator/tool/definitions/co2e.html

[14] Greenhouse Gas Equivalencies Calculator | US EPA website:

https://www.epa.gov/energy/greenhouse-gas-equivalencies-calculator

10. Biography



Bernard Lee is a senior telecommunications and business strategy professional with more than 20 years of global experience in telecommunication & data communications arena especially in the field of optical fibre communications. He currently the Director of Technology & Innovation at SENKO Advanced Components. He started his career in 2003 with Telekom Malaysia R&D as the Head of Photonic Network Research and then as the Head of Innovation and Communications. Bernard then joined the parent company, Telekom Malaysia (TM) in 2010 as the Assistant General Manager at the Group Business Strategy Division. Bernard is currently an Expert at the International Electrotechnical Commission (IEC), a Chartered Engineer (CEng) accredited by the Engineering Council of UK, and is also a Registered Communications Distribution Designer (RCDD).



Tatiana Berdinskikh is the founder of Novophotonics. She has 25+ years of experience in fiber optics, telecommunications, optoelectronics, and photonics. Tatiana is the Canadian Technical Expert for standards activities of IEC SC 86B, SC 86C, and a Chair of the Canadian Mirror Committee of SC 86B. In 2016, she received the IEC 1906 Award for her contribution to the development of cleanliness specifications of fiber optic connectors. Tatiana chairs the iNEMI (International Electronics Manufacturing Initiatives) project "Development of the best practices for expanded beam connectors in the data center applications" and has contributed to the development of the iNEMI Optical Technology Roadmaps. She has co-authored over 50 journal publications and conference papers in the field of optoelectronics and photonics, and the book "Degradation of Semiconductor Light-Emitting Diodes and Lasers". Tatiana is a member of the Professional Engineers of Ontario.



John Lu graduated from Shanghai International Studies University; he is currently the Product Manager at Senko advanced Components (Shenzhen). He joined Senko in 2018 as a connector expert at Senko Shenzhen. John Lu started his career in passive components especially connectivity product in 2014 as a sales manager in Northern America. He is participating in IPEC on behalf of SENKO and within IPEC he is currently the deputy of the Marketing work group.



Takeshi Kasai is a Technical Specialist at SENKO advanced Components in the Technology and Innovation Group. He is supporting sustainability programs as well as other testing and publications. He graduated Sophia University in 2019.



Tiger Ninomiya is currently Senior Technologist at SENKO Advanced Components. He is participating in the MSA and Consortiums. Within COBO, he is currently a chairman of Co-Packaged Optics working group and Associate Director of Board of Director.



Michihiko Kato is an Assistant Manager of Optical Fiber & Cable Engineering for Furukawa Electric. He has more than 20 years of experience in the optical fiber cable, connectivity and fusion splicer engineering since he joined Furukawa Electric in 1998. He holds a BE degree in Mechanical Engineering from the Waseda University.



Hiroshi Nakamura is a Senior Manager of Optical Fiber & Cable Engineering for Furukawa Electric. He has more than 20 years of experience in the optical fiber and cable sales engineering. Prior to this period, he worked 5 years as an optical fiber measurement expert after 4-year R&D activities about optical fibers and amplifiers since he joined Furukawa Electric in 1992. He participates in IEC standards activities since 2005. He holds a BE degree in Electrical Engineering from the University of Tokyo.

SESSION 8

Click on a session below to navigate to that section of the Proceedings.

SESSION 8: MULTI-CORE & SPECIALTY FIBER

Chairperson: Eric Whitham, OFS, a Furukawa Company, USA

8-1 **100G/Lane Enabled Multimode Fiber: A High-Speed Solution for Short-Reach VCSEL Transmission;** Dr. Hao Dong, *Corning Optical Communications, USA*

8-2 **A Low Crosstalk Weakly Coupled 7-Core Single Mode Fiber;** Mr. Imtiaz Majid, *Yangtze Optical Fibre and Cable Joint Stock Limited Company (YOFC), China*

8-3 **Multicore Fiber for Space-Constrained, High Bandwidth Density Applications;** Dan Neugroschl, *Chiral Photonics, USA*

8-4 **Research of Crosstalk Characteristics Based On Weakly Coupled Seven-Core Fiber;** Imtiaz Majid, *Yangtze Optical Fibre and Cable Joint Stock Limited Company (YOFC), China*

8-5 **Low-Loss All-Fiber Mode Multiplexer for Weakly-Coupled Few-Mode Fiber;** Imtiaz Majid, *Yangtze Optical Fibre and Cable Joint Stock Limited Company (YOFC), China*

8-6 **Crosstalk Characteristics of 200mm Coating 4-Core Fibers in 288-Fiber/864-Fiber Freeform Ribbon Cables;** Takuji Nagashima, *Sumitomo Electric Industries, Ltd., Japan*

8-7 **Low Attenuation Orbital Angular Momentum Fiber;** Mr. Imtiaz Majid, *Yangtze Optical Fibre and Cable Joint Stock Limited Company (YOFC), China*

Click here to return to the **Table of Contents**

100G/lane Enabled Multimode Fiber: A High-Speed Solution for Short-Reach VCSEL Transmission

Hao Dong[1], Xin Chen[1], Zoren Bullock[1], Hao Chen[1], Ming-Jun Li[1], Jianwei Mu[2]

1. Coring Optical Communications

Corning, NY 14845

2. Hisense Broadband Inc.

2580 North First St, San Jose, CA 95131, USA

+1-607-974-4084 · dongh3@corning.com

Abstract

In this paper, we introduce a novel solution of high data-rate multimode fiber ("HDR MMF") specifically designed to overcome the fiber bandwidth limitation issue in multimode applications operating at 100G/lane. By using 100G BiDi as a specific example, we found that the "HDR MMF" could transmit over 150 m, equivalent to the performance of an OM5 fiber.Furthermore, we found that "HDR MMF" can transmit over 100 m in 800G BiDi applications, aligning with our expectations for 100G/lane transmissions.

Keywords: Multimode Fiber, BiDi application, data center.

1. Introduction

The exponential growth of global internet traffic in cloud and enterprise data centers has fueled rapid advancements in optical transmission technology. Data center operators strive to build faster, denser, more cost-effective, and power-efficient data centers that are sustainable and resilient. Multimode fibers (MMFs) have emerged as a widely deployed solution for short-distance data center communications, particularly with VCSEL-based transceivers, forming a cost-effective ecosystem [1-2]. Driven by the explosive increase in data traffic and demand for cloud computing in data centers, optical transmission technology has evolved to meet the increasing capacity demands, utilizing multiple fibers, higher data rates, and additional wavelengths. One notable advancement is the Bidirectional (BiDi) transceiver [3], enabling bidirectional transmission at ~850 nm and ~910 nm. With the development of 100G BiDi and 400G SR4.2 transceivers standardized by IEEE 802.cm, BiDi technology has expanded to higher data rates. Another competing technology is short wavelength division multiplexing (SWDM) [4,5], utilizing four wavelengths, including a new grade of MMF called OM5 standardized in 2016 [6].

Recent advancements in VCSEL technology standardized at 100 Gbps per lane at 850 nm have led to the availability of 400G SR4 and 800G SR8 transceivers. BiDi technology using 850 nm and 910 nm is also progressing towards 100 Gbps per lane, with the Terabit BiDi multi-source alliance aiming for data rates up to 1.6 Tbps [7]. However, reach capability becomes a limitation.

In this paper, we introduce the concept of 100G/lane and BiDi optimized MMFs based on using a subset of OM3 and OM4 fibers among the whole distribution. In Section 2, we show the system reach capability of existing transceivers and the limitation at 100G/lane VCSEL transceivers. We also studied the wavelength dependence of modal bandwidth for MMF and present the new MMF concept optimized for BiDi transmission in this section. In Section 3 we demonstrate the results of using such fiber with comparison to OM5 fiber in 100G BiDi transmission and 800G BiDi transmission results using a BiDi optimized OM4 fiber over 100 m.

2. MMF Transmission Capability

2.1 BiDi Technology

For short distance data center communications, multimode fibers (MMFs) have been widely deployed. Existing 50-micron core MMFs are categorized in IEC 60793-2-10 standards as Type A1 OM2, OM3, OM4, and OM5. For 25 Gbaud based transmission (i.e. 25G NRZ or 50G PAM-4), OM3 and OM4 are two primary MMF types covering 70 m to 100 m links. The details of various types of 25 GBaud based VCSEL transceivers are listed in Table 1.

Table 1. System reach for 25 Gbaud-based VCSEL transceivers

Protocol	MSA/Std.	OM3 Reach	OM4 Reach	Fiber Count
25G SR		70	100	2
100G SR4	IEEE 802.3bm	70	100	8
100G BiDi	-	70	100	2
100G SWDM4	MSA	75	100	2
400G SR8	IEEE 802.3cm	70	100	16
400G SR4.2	MSA/IEEE 802.3cm	70	100	8

One type of VCSEL transceiver of interest is a BiDi transceiver in which signals are carried through bidirectional transmission in two wavelengths, nominally 850 nm and 910 nm. The first generation 40G BiDi transceivers for MMF transmission were commercially deployed around 2014 and offered 40 Gb/s traffic over duplex multimode fibers using two 20 Gb/s NRZ wavelength channels. Both Corning and Cisco were among the first vendors that developed the transmission reach specification and supported the eco-system. Building upon the successful 40G BiDi pathway, 100G BiDi transceivers debuted in 2018. Essentially, 100G BiDi utilizes 50G PAM-4 signals at the same wavelengths and over the same duplex fiber that 40G BiDi does. In 2019, IEEE Ethernet standards were updated to include BiDi technology with the 400G-SR4.2 transceiver, which uses

50G PAM-4 signals over eight fibers for 400G total transmission.

BiDi transceivers deliver the benefits of high data rate (and high capacity) with minimal changes on structured fiber cabling. The data center industry has expressed interest in this technology for even higher data rates. In late 2021, the Terabit BiDi Multi-Source Agreement (MSA) group announced its formation as an industry consortium to develop interoperable 800 Gb/s and 1.6 Tb/s optical interface specifications for parallel multimode fiber (MMF) [7]. Terabit BiDi is based on 100G PAM4 transmission at both 850 nm and 910 nm. Leveraging a large installed base of 4-pair parallel MMF links, the new MSA defined specification enables an upgrade pathway for the parallel MMF based 400 Gb/s BiDi to 800 Gb/s and 1.6 Tb/s data rate.

2.2 System Reach Limitation at 100G/lane

The industry is accustomed to 70 m OM3 and 100 m OM4 transmission reaches for several generations. As is illustrated in Figure 1, 70 m OM3 or 100m OM4 are sufficient to cover the interconnect needed in Leaf-and-Spine architectures.

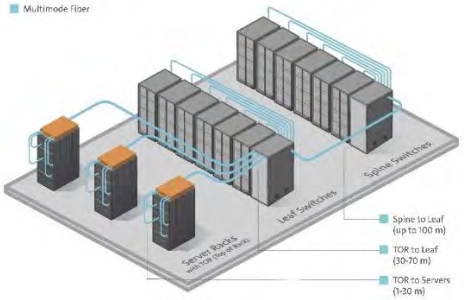


Figure 1. Standard OM3 and OM4 deployed for up to 70 m or 100 m data center links.

Figure 2 illustrates a variety of 25 GBaud based multimode transceivers that can support up to 70 m over OM3 or 100 m over OM4. Some customers and some regions prefer 70 m reach using OM3 as it is more cost-effective and meets the requirements in specific applications, while other customers use both OM3 and OM4 to address their needs.

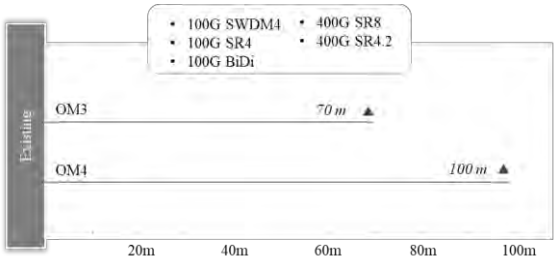


Figure 2. Reach capabilities of legacy multimode OM3 and OM4 fibers for typical IEEE standards or MSAs.

However, when 100G/lane is introduced, the system reach is dramatically reduced in some cases due to bandwidth limitation at 850 nm and/or 910 nm. For Terabit BiDi MSA, the specifications for OM3 and OM4 transmission reach are reduced to 45 m and 70 m respectively [7].

The transmission capability reduction is not only limited to Terabit BiDi; similar reductions also happened to other 100G/lane based applications such as IEEE Std.802.3db [8]. Figure 3 shows the system reach information for 100G/lane based transceivers. Specifically, IEEE Std.802.3db defined that 850 nm only transceivers (100G SR, 200G SR2, and 400G SR4) can only transmit up to 60 m over OM3, due to its modal bandwidth limitation around 850 nm.



Figure 3. System reach for 100G/lane based VCSEL transceivers

2.3 Bandwidth capability of MMFs

The modal bandwidth of an MMF is wavelength dependent and is generally peaked at a certain wavelength λ_p, and falls off on either side [9]. As is the nature of MMF making, each individual MMF can have its peak bandwidth different from others and the λ_p can spread out over a range.

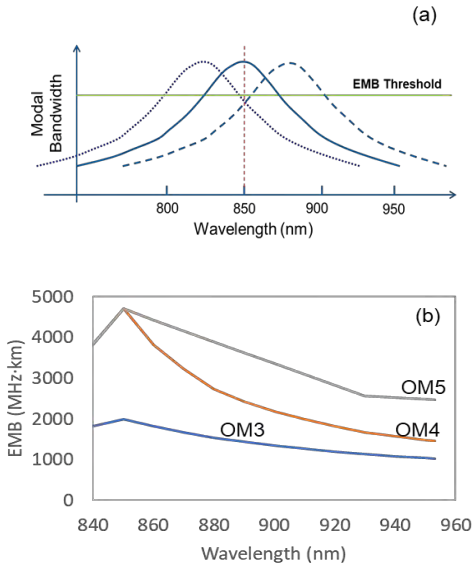


Figure 4 (a) The schematic illustration of MMF with different peak wavelengths; (b) The EMB values over 840-953 nm wavelength range for OM3, OM4 and OM5 following IEC 60793-2-10 guidance.

In Figure 4(a), it's evident that OM3 and OM4 fibers need to meet the specified EMB values at 850nm. However, these values can vary depending on the wavelength λ_p, and the peak bandwidth may also differ among different fibers. The wavelength dependence and detailed analysis of this phenomenon have been extensively studied and documented in Ref. [10]. Recently, the IEC standard also issued the EMB guidance for OM3, OM4 and OM5 over the wavelengths from 840 nm to 953 nm as shown in Figure 4 (b) [11]. The EMB values are defined as the worst-case scenario for each type of MMFs, from which the system reach capability can be defined.

Interestingly, within the population of OM3 and OM4 fibers, a significant portion exhibits superior performance beyond the worst-case scenario, enabling longer system reaches. Ref. [10] highlighted the advantages of these fibers in extended reach applications, surpassing the reach specifications set for OM3 and OM4 fibers in general. This observation served as the foundation for the development of BiDi-optimized multimode fiber.

3. HDR Multimode Fiber Solution

3.1 Concept of "HDR MMF"

In response to the reach reduction challenge discussed in section 2.2, the Terabit BiDi MSA has included OM5 as a solution to achieve 100 m reach for 800G-SR4.2 and 1.6T-SR8.2 [7].

OM5 is a sub-category of OM4 fiber, sharing the same effective modal bandwidth (EMB) values at 850 nm. Additionally, OM5 fiber has its EMB value also specified at 953 nm , allowing it to support mulitmode transmission at wavelength up to 953 nm. In principle, OM5 fiber is specifically optimized for SWDM transceivers when operating at the long wavelengths including 953 nm. However, it's important to note that currently, commercially available SWDM transceivers only support data rates of up to 40G (based on 10Gb/s NRZ signals) and 100G data rate (based on 25Gb/s NRZ signals) over four wavelengths between 850 nm and 953 nm [5], there are no SWDM products available for data rates of 400G or higher. Consequently, the advantages of OM5 are believed to be limited [12]. For BiDi transmission, where the highest operational wavelength is 915 nm, OM5 is not the only option to meet the 915 nm EMB requirements.

To address the needs of high data rate transmission for Terabit BiDi applications, we proposed a high data rate optimized multimode fiber ("HDR MMF") concept for future-ready 100G/lane multimode applications [13,14]. Essentially, "HDR MMF" is defined based on re-categorizing a subset of OM3 and OM4 fibers. Such fibers are more cost-effective than OM5 and are available in scalable volumes. Under the current 800G BiDi specifications, fiber must meet certain link bandwidth requirements including the modal bandwidth and chromatic dispersion contributions at 850 nm and 910 nm operating windows. We meet such requirements by defining the HDR MMFs with the EMB values specified in Table 2.

Table 2. Fiber ("HDR MMF") definition for 100 m and 80 m applications.

MMF Solution	EMB at 850nm	EMB at 910nm	Reach for 800G BiDi	Reach for IEEE 802.3db
"HDR OM3"	**2,890 MHz·km**	**2,220 MHz·km**	**80 m**	**80 m**
"HDR OM4"	**4,700 MHz·km**	**3,100 MHz·km**	**100 m**	**100 m**
Standard OM3	2,000 MHz·km	1,260 MHz·km	45 m	60 m
Standard OM4	4,700 MHz·km	1,980 MHz·km	70 m	100 m

The proposed EMB values for "HDR MMF" align with the link bandwidth requirements derived from Terabit BiDi and the IEEE 802.3db specifications. At 100 m reach, the EMB values for 850 nm and 910 nm wavelengths are 4700 MHz·km and 3100 MHz·km, respectively, which are essentially the same values for OM5 for these two wavelengths following IEC 60793-2-10 guidance. This means that "HDR OM4" meets the link bandwidth requirements for both 850nm and 910nm operating window, making it a viable option for high data rate applications such as 100G/lane BiDi transmission.

We also define an 80 m grade "HDR OM3" to address broader market needs for some customers using 70-80 m distances to cover a majority of their links. At 80 m reach, the EMB values for 850 nm and 910 nm wavelengths are 2890 MHz·km and 2220 MHz·km, respectively. These EMB values are lower than 100 m grade "HDR MMF", but are still sufficient to cover link bandwidth requirements for many data center applications. "HDR OM3" can offer customers an additional option to achieve the most cost-effective solution suitable for their distance and bandwidth requirements.

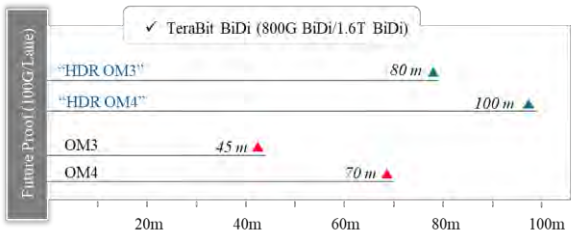


Figure 5. Defined HDR MMF for 80 m and 100 m for 800G BiDi applications.

The reach capabilities of "HDR MMF" are illustrated in Figure 5 and Figure 6 for Terabit BiDi and IEEE 802.3db defined applications. "HDR MMF" offers the clear benefits of legacy standard OM3 and OM4 multimode fibers, such as availability and compatibility with existing infrastructure, while providing the improved reach and performance needed for high data rate applications. This makes it an attractive option for 800G BiDi and 1.6T BiDi transmission, as well as 400G SR4 and 800G SR8 defined in IEEE Std.802.3db.

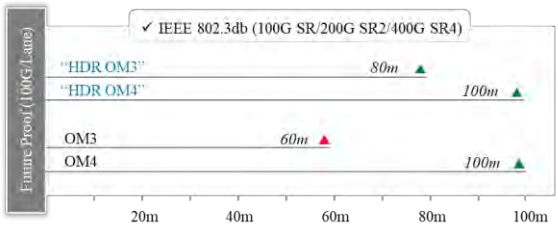


Figure 6. Defined "HDR MMF" will be applicable for IEEE 802.3db applications.

3.2 100G BiDi Experiment Results

In order to validate the performance advantage of "HDR MMF," we conducted a evaluation of transmission performance over a "HDR OM4" fiber using both 100G BiDi and 800G BiDi transceivers, as referenced in [16, 17]. The definition of "HDR OM4" fiber, as outlined in Table 2, has been identified. It meets the EMB requirements for an OM4 fiber at 850 nm. However, at 910 nm, its EMB is approximately 4 GHz·km, exceeding the 3100 MHz.km requirement, but falling short of the EMB requirement for OM5 fiber at 953 nm. For this experiment, we prepared a 150-meter length of "HDR OM4" fiber out of the same fiber along with 150 meters of OM5 fiber, both terminated with LC connectors to match the connector interface for the 100G BiDi transceiver..

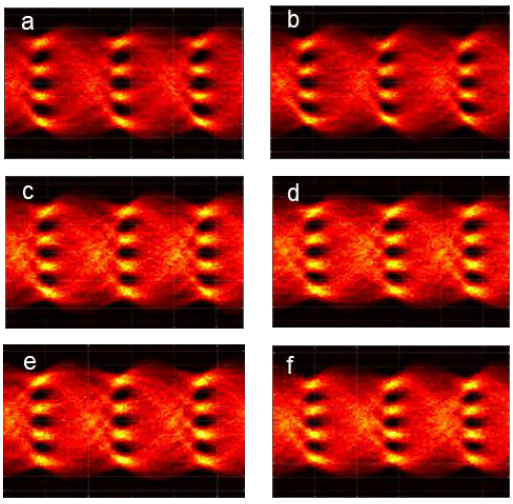


Figure 7(a) 850 nm eye diagram in BtB condition; (b) 910 nm eye diagram in BtB condition; (c) 850 nm eye diagram with 150 m "HDR OM4"; (d) 910 nm eye diagram with 150 m "HDR OM4"; (e) 850 nm eye diagram with 150 m OM5; (f) 910 nm eye diagram with 150 m OM5

For this experiment, we utilized a 100G BiDi transceiver (AFBR-89BDDZ) provided by FIT. To access the transmission performance, we employed a Viavi 100G optical network tester (ONT) (model number: ONT-603) with network traffic involved for testing. Both "HDR OM4" and OM5 fibers, were subjected to transmission testing for a duration of 18 hours.

Figure 7 shows the obtained eye diagrams, including back-to-back (BtB) condition, as well as over 150 m "HDR OM4" and 150 m of OM5. As is shown in Figure 7, both "HDR OM4" and OM5 fibers exhibit similar, high-quality eye diagrams, with no significant degradation observed compared to the BtB condition.

3.3 800G BiDi Tranmission Results

Furthermore, we performed an analysis using an 800G BiDi transceiver incorporating Broadcom chip sets (DSP BCM87800, VCSEL AFCD-V84LP (850nm), AFCD-V84LQ (908nm) & PIN BPD3058-4). Considering the EMB value of the "HDR OM4" fiber is 3100 MHz·km at 910 nm, which is the same as OM5, we anticipate that the fiber will exhibit the same transmission reach for 800G BiDi applications. To validate this assumption, we conducted transmission tests using the aforementioned 800G BiDi transceiver [15], and the results are presented in Figure 8.

In BtB conditions, the transmission can reach BER below 1.5×10^{-8} and 7.0×10^{-9} at 850 nm and 910 nm respectively. With the 100 m BiDi optimized OM4, the transceiver can still achieve BER better than 6.4×10^{-8} and 3.2×10^{-8} at 850 nm and 910 nm respectively. Notably, the performances in both wavelengths remains close to BtB condition after 100 m "HDR OM4", which aligns with expectation based on the EMB of the fibers. By employing forward error correction (FEC), the BER was effectively reduced to error free.

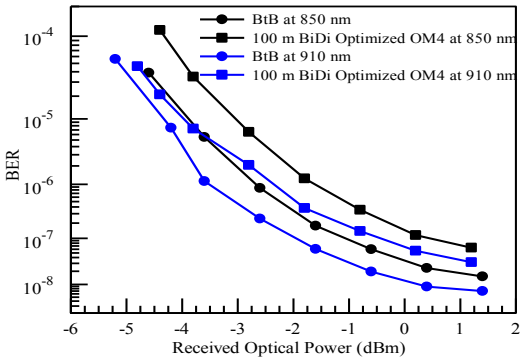


Figure 8. BER vs. received optical power measured at two fiber configurations at 850 nm and 910 nm wavelengths.

4. Conclusion

The emergence of 100G/lane VCSEL-based multimode applications, including both 850 nm only and BiDi transceivers, has posed challenges to the system reach capability due to the worst-case modal bandwidth limitations of the multimode fibers. To address this challenge, we have proposed the concept of "HDR MMF" to have the same EMB as OM5 at 910 nm to include a much large portion of fibers from the OM4 population. Additionally, we have proposed "HDR OM3" that enables transmission over 80 meters using

100G/lane VCSEL transceivers, catering to customers with link distance requirements ranging up to 70 to 80 meters.

Using 100G BiDi transmission as an example, we have demonstrated that "HDR OM4" fiber can achieve transmission distances of up to 150 meters, equivalent to OM5 fiber. Furthermore, by using the newest developed 800G BiDi SR4.2 transceiver, we have observed that the 100 m “HDR OM4” fiber exibits excellent BER better than 6.4×10^{-8} and 3.2×10^{-8} at 850 nm and 910 nm respectively , leaving sufficient margin for FEC to further enhance the transmission performance, ultimately reducing the BER to virtually error free.

5. Acknowledgments

We thank Ramana Murty, I Hsing Tan, and Tzu Hao Chow from Broadcom Inc. for fruitful discussions which helped us understand the VCSEL technology and Terabit BiDi requirements.

6. References

[1] Xin Chen, Scott R. Bickham, John S. Abbott, J. Doug Coleman, Ming-Jun Li, “Multimode Fibers for Data Centers (book chapter)”, in Handbook of Optical Fibers, pp. 1-57. Singapore: Springer, 2018. DOI:10.1007/978-981-10-1477-2_68-1.

[2] M. -J. Li, "MMF for high data rate and short length applications," OFC 2014, San Francisco, CA, USA, 2014, pp. 1-3, doi: 10.1364/OFC.2014.M3F.1.

[3] https://www.cisco.com/c/en/us/products/collateral/interfaces-modules/transceiver-modules/data_sheet_c78-660083.html.

[4] Jim A. Tatum et al, “VCSEL-Based Interconnects for Current and Future Data Centers”, J. Lightwave Technol., 33 (4), pp.727-732, (2015).

[5] https://www.swdm.org/.

[6] TIA Standard, TIA-492AAAE , “Detail Specification for 50-µm Core Diameter/125-µm Cladding Diameter Class 1a Graded-IndexMultimode Optical Fibers with Laser-Optimized Bandwidth Characteristics Specified for Wavelength Division Multiplexing,” (2016).

[7] Terabit BiDi MSA specifications.

[8] https://standards.ieee.org/ieee/802.3db/10283/.

[9] Xin Chen, Jason E. Hurley, Scott Bickham, John Abbott, Bruce Chow, Doug Coleman, and Ming-Jun Li. "Evaluation of extended reach capability of 40G BiDi VCSEL-based WDM transmission over OM4 multimode fibers." In Broadband Access Communication Technologies X, vol. 9772, pp. 29-33. SPIE, 2016.

[10] Xin Chen, Hao Dong, Hao Chen, Jianwei Mu, Long Zheng, Sigeng Yang, Jason E. Hurley, William A. Wood, Zoren Bullock, and Ming-Jun Li, “Concept of BiDi Optimized OM4 Multimode Fiber for High Date Rate Short Reach VCSELTransmission,” OptoElectronics and Communications Conference (OECC) 2023.

[11] IEC 60793-2-10, Optical fibres–Part 2-10: Product specifications – Sectional specification for category A1 multimode fibres, Edition 7.0 2019-05.

[12] Understanding the Differences Between OM4 and OM5 Multimode Fiber. https://www.cisco.com/c/en/us/products/collateral/interfaces-modules/transceiver-modules/diff-om4-om5-multimode-fiber-wp.html.

[13] Hao Dong and Xin Chen, “The Road to 800G with Multimode Fiber,” https://www.corning.com/catalog/coc/documents/articles/CO8000_Article_Road%20to%20800G%20multimode%20fiber.pdf.

[14] Xin Chen and Hao Dong, “High Data Rate Optimized Multimode Fiber for 100G/Lane based VCSEL Transmission.” https://www.cisco.com/c/en/us/products/interfaces-modules/transceiver-modules/white-paper-listing.html.

[15] Xin Chen, Hao Dong, Hao Chen, Jianwei Mu, Long Zheng, Sigeng Yang, Jason E. Hurley, William A. Wood, Zoren Bullock, and Ming-Jun Li, “Concept of BiDi Optimized OM4 Multimode Fiber for High Date Rate Short Reach VCSELTransmission,” OptoElectronics and Communications Conference (OECC) 2023

[16] https://ii-vi.com/swdm4-transceivers/.

[17] https://www.hisensebroadband.com/html/company/news_events/20230306_369.html.

A Low Crosstalk Weakly Coupled 7-core Single Mode Fiber

Liubo Yang[1,2], Lei Zhang[1,2,3], Lei Shen[1,2,3], Jie Luo[1,2,3], Zhuang Xiong[1,2], R. Matai[1,2]

1. State Key Laboratory of Optical Fiber and Cable Manufacture Technology, 430073, China

2. Yangtze Optical Fiber and Cable Joint Stock Limited Company, 430073, China

3. Optics Valley Laboratory, 430074, China

Email address for corresponding author:yangliubo01@yofc.com

Abstract

This paper report the design, measurement and application performance of a weakly-coupled 7-core single mode fiber used in long haul network communication. Through the special profile design and the optimization of the preform and drawing process, the 7-core fiber has good mechanical properties, excellent bending performance, low crosstalk and splicing loss. Fiber cabling and cable environmental performance meet long haul communication scenarios, it can multiply the core density of channel, and the fiber shows great advantages and application prospects as an optimal scheme to replace the traditional single-mode long-haul transmission fiber.

Keywords: multi core; weakly coupled; splice; crosstalk; Long-haul transmission cable

1. Introduction

With the development of the Internet, optical communication technology has been advancing rapidly, supporting our increasingly information-driven society and economy, over the past 40 years, a series of technological breakthroughs have allowed the transmission capacity of fibers to increase ~10-fold every four years. Transmission technology has thus far been able to keep up with the steady exponential growth in the Internet protocol traffic [1-2]. However, the demand for higher transmission capacity will further increase, with the growth of the information demand at 30%–40% per year. Optical fibre communication system based on single mode fibres (SMF) is rapidly approaching the capacity limits imposed by the combination of Shannon's information theory and nonlinear fibre effects.

The space division multiplexing technology based on multi-core optical fiber can greatly increase the communication capacity because of the large expansion potential in the spatial dimension [3-6]. At present, due to the influence of bending performance, crosstalk and splice performance, the multi-core fiber is mainly used in data center interconnection networks and other short-distance scenarios [7-8]. Therefore, it is necessary to develop a kind of multi-core fiber which can be used in long-haul communication and has the similar application performance as the traditional single-mode fiber.

In order to meet the above requirements, we have designed a weakly coupled 7-core single-mode fiber. The cladding diameter of the fiber is 150μm, and the fiber diameter is 245μm. The fiber consist of hexagonal arrangements of trench-assistant single mode cores, the pitch between cores is 43 μm, the main optical parameters, such as the MFD, attenuation, cut-off wavelength, bending performance and mechanical properties of the fiber are similar to the G.652.D fiber. To guarantee the application reliability of the 7-core fiber, we also did the splice and crosstalk test, and in addition, we prepared a GYTA cable and a series of special environment tests were carried out, the additional attenuation of seven-core fiber fully meets the IEC environmental test standard for outdoor cable.

2. Fiber design and key parameters

2.1 Fiber design

The MCFs discussed in this work consist of hexagonal arrangements of single mode cores. As illustrated in Fig.1, the pitch between cores is 43 μm, enabling the positioning of seven single mode cores in a fiber with a cladding diameter of 150 μm. As is known, with the appropriate core arrangement and dimensions, the crosstalk between MCF cores can be drastically reduced, therefore the fabrication of a MCF requires a strict control of the fiber structure, in addition, to further reduce the XT, with the proper selection of the core refractive index, i.e. surrounding the core with a trench for better mode confinement, the core-to core separation can be significantly reduced and maintaining low crosstalk values. At the same time, the macro bending loss can be optimized due to trench assistant structure [9-12]. The end face and core profile of the seven-core fiber glass are shown in Fig.1.

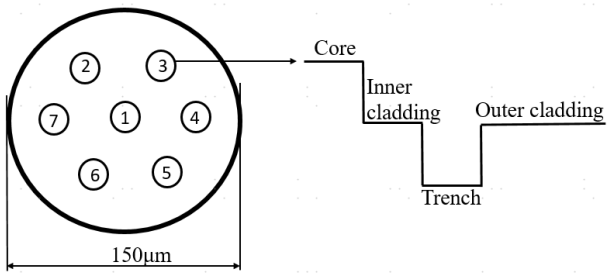


Figure 1. Cross-sectional and fiber core profile

2.2 Fiber key parameters

Table 1. Key parameters of 7-core fiber

Key parameters	Typical value	Unit
Cladding diameter	150	[μm]
Coating diameter	245	[μm]
Core pitch	43	[μm]
MFD@1550nm	8.9	[μm]
22m Cutoff wavelength	1220	[nm]
Attenuation (1550nm)	0.21	[dB/km]
Crosstalk	-46	[dB]
Microbending loss(1550nm)	0.17	[dB]
Screening strength	100	kpsi

Table 1 shows the main parameters of weakly coupled 7-core single mode fiber. The fiber diameter is the same as traditional single-mode fiber. There are seven cores in a fiber, and the transmission capacity is 7 times that of the traditional single-core fiber, which is benefit to the miniaturization of the cable and optical device.

2.3 Fiber bending performance

The 1550nm macrobending performance of 7-core fibres at different bending radius were tested, the bending induced loss are shown in Table2. It can be seen that under each bending radius condition, the macrobending induced loss of the middle core is larger than the edge cores. According to the research of R. Ulrich [13], this phenomenon is related to the elastic-optical effect, and the birefringence phenomenon causes the difference of macrobending loss of 7 cores.

Table 2. Macrobending loss of 7-core fiber

Conditions	R30mm 100turns	R15mm 10 turns	R10 mm 1turn	R7.5mm 1turn	R5mm 1turn
Center core	0.061	0.035	0.034	0.060	0.151
Edge core	0.013	0.003	0.013	0.037	0.111

The test data of the microbending loss at 1550nm of the 7-core fiber are shown in Table3. There is no significant difference in the microbending performance between the middle core and the edge core, both of which are less than 0.2dB /km, which is similar to the microbending performance of G.657.B3.

Table 3. Microbending loss of 7-core fiber

Microbending loss	#1Center core	#2	#3	#4	#5	#6	#7
dB/km	0.13	0.20	0.16	0.17	0.19	0.17	0.15

3. Application performance test

In order to verify whether 7-core fiber can meet the practical application of long-distance communication, a series of application performance tests were carried out. The test results show that the 7-core fiber described in this paper can replace the traditional single mode for long-distance transmission.

3.1 Temperature cycling test

Temperature cycling test was carried out in the range of -60°C to +85°C. In the whole test process, the maximum additional loss at 1550 nm does not exceed 0.005 dB/km, and the attenuation does not increase after returning to room temperature (Table4), which is in accordance with IEC 60793-2-50 standard for single-core fiber. This shows that the 7-core fiber can withstand the harsh environment and has good reliability.

Table 4. TCT Induced loss of 7-core fiber

Induced loss (dB/km)	#1 Center core	#2	#3	#4	#5	#6	#7
Maximum	0.001	0.004	0.002	0.003	0.005	0.004	0.004
Ending value	-0.004	-0.001	0.000	-0.003	-0.001	-0.002	0.000

3.2 Splice performance

The splicing performance is very important in the actual deployment of communication network. In order to reduce the splicing losses, the fiber is designed as a homogeneous seven-core fiber with a symmetrical center structure, each core has the same profile, through the optimization of the preform and drawing conditions, the fluctuation of the core pitch can be controlled to within 0.6μm, combined with the customized multi-core fiber welding equipment and splice program, the splicing loss between seven core fibers can be reduced effectively. According to the statistics of 260 groups of splicing loss data under laboratory conditions (Figure 2), the typical splicing loss is 0.2dB and the maximum splicing loss is 0.6dB, which fully meets the application requirements.

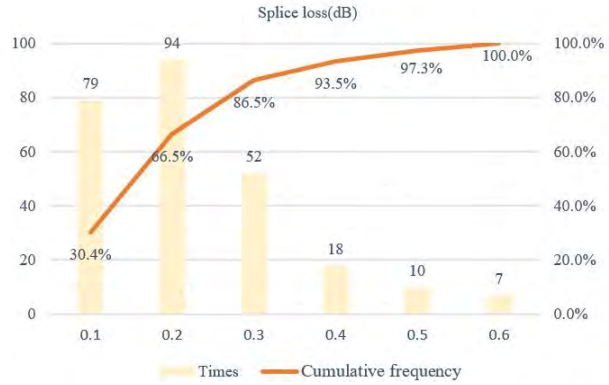


Figure 2. Splice loss of 7-core fiber

3.3 Crosstalk

In order to reduce crosstalk between adjacent fiber cores, this paper has optimized from two aspects. First, as shown in Figure3, annular low-refractive index regions are added outside the inner cladding of each fiber core to restrict the signal leakage from the inner cladding. Second, the distance between fiber cores is 43um, which is conducive to reducing crosstalk between cores. As can be seen from Figure 3, our 7-core fiber crosstalk, with a typical value of -46dB, fully meets the requirement of long-distance communication.

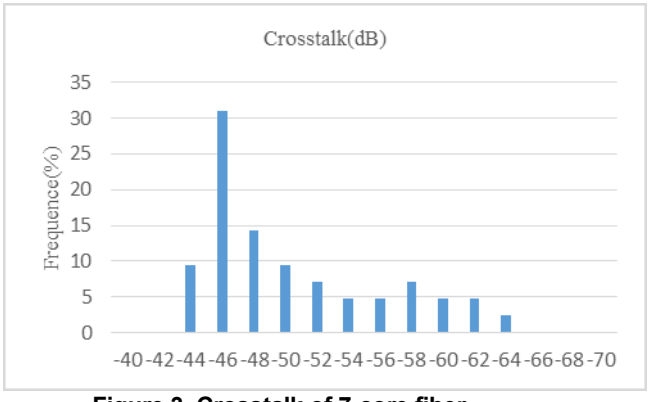


Figure 3. Crosstalk of 7-core fiber

3.4 Cable test

To realize much higher-density in a cable, it is an effective way to apply the SDM fibers to the high-density optical fiber cable. In order to investigate applicability of the MCF high-density cable,

we fabricated a 4km GYTA test cable containing six loose tubes, each of which contained 12 core fibers, including 10 7-core fibers and 2 std-G.652.D as reference. The diameter of the loose tubes was 2.4mm, the final outer diameter of the cable is 11mm.

Taken the attenuation of nature fiber as initial value, the environmental test of the cable is carried out as follow steps: First, two temperature cycle tests were carried out in the range of -40℃~ +70℃, and then ageing at 85℃ for 7 days, then two temperature cycle tests were carried out in the range of -40℃~ +70℃, and finally returned to room temperature. The typical additional attenuation of the two optical fibers is shown in Figure 4. In the whole process of cabling and environmental testing, the additional loss of 7-core fibers in each step were less than 0.01dB/km at 1550nm, which fully meets the IEC 60794-5-10 standard for outdoor cable.

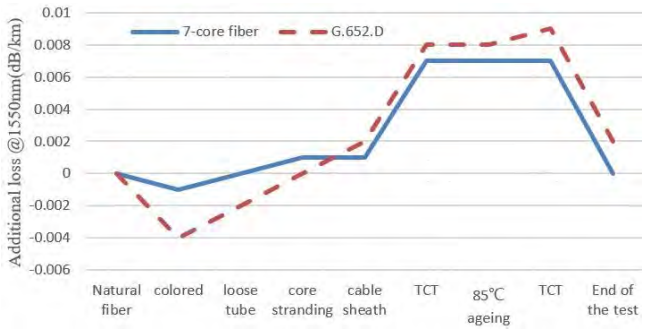


Figure 4. Cabling and cable environmental performance of 7-core fiber

4. Conclusions

In this paper, the design, fabrication and measurement of a low crosstalk weakly-coupled 7-core fiber was reported, the crosstalk of the cores are less than -46dB/km and the typical splicing loss is 0.2dB, this paper evaluate the cabling and temperature variation to attenuation, with low splicing loss and low crosstalk, this MCF can be used in long-haul weakly-coupled SDM systems that allows to multiply the capacity.

5. Acknowledgments

This work was supported by National key research and development projects 2021YFB2800902.

6. References

[1] Richardson D J, Fini J M, Nelson L E. Space-division multiplexing in optical fibres. Nature Photonics, 2013, 7(5): 354–362.

[2] Desurvire E B. Capacity Demand and Technology Challenges for Lightwave Systems in the Next Two Decades [J]. Journal of Lightwave Technology, 2006, 24(12): 4697-4710.

[3] Lei Shen, Zhaohui Li, et al. Design, fabrication, and characterization of a low-index center and trench-assisted 7-ring-core 5-mode-group fiber for dense space-division multiplexing, Optics express 2022 Vol.30 No.1 P650-663.

[4] Li Shen, Lei Shen, Rui Zhang, Songnian Fu, et al. Distributed curvature sensing based on a bending loss-resistant ring-core fiber, Photonics Research 2020 Vol.8 No.2 P165-174.

[5] Lei Shen, Jun Chu, Yin Li, Zhao Yao, Peng Li, Liubo Yang, Lei Zhang, Jie Luo, Xiaobo Lan, et al. Design, Fabrication and Measurement of a Novel Ultra Low Crosstalk 7-core-10-mode Fiber, 2021 Asia Communications and Photonics Conference (ACP) Shanghai, China 2021.

[6] Lei Shen, Lei Zhang, Changkun Yan, Liubo Yang, Ruichun Wang, Jun Chu, et al. Experimental Demonstration of Chaotic Secure Transmission with Mutual Injection of Semiconductor Lasers over 130-km Multi-Core Fiber, 2023 Optical Fiber Communications Conference and Exhibition (OFC).

[7] Y. Kang et al., Broadband Low-Loss Fan-In/Fan-Out Devices for Multicore Fibers [C]//2019 Asia Communications and Photonics Conference (ACP), 2019, pp. 1-3.

[8] J. E. Antonio-Lopez, J. C. Alvarado-Zacarias, S. Wittek, D. , et al, SDM Fibers and Devices: Design, Manufacturing, and Applications [C]//2021 Optical Fiber Communications Conference and Exhibition (OFC), 2021, pp. 1-3.

[9] L Zhang, et al. The Influence of Trench Design on Single-Trench-Assisted Bending-Insensitive and Ultra-Bending-Insensitive Fiber [C]//IWCS2013, 111-115 (2013).

[10] She Sheng fei, Liu Bo, et al. Characterization and properties of large-core fluorine-doped fibers based on depressed inner cladding design [J]. Acta Photonica Sinica, 2019, 48(11): 1148013.

[11] ZH.Xelin, Lu.Yuangang, et al. Trench assisted multimode fiber used in Brillouin optical time domain sensors [J]. Opt Express, 2019, 27(8):11396-11405.

[12] L.Zenghui, L.Shuguang, et al. Double-trench assisted thirteen-core five-mode fibers with low crosstalk and low non-linearity [J]. Acta Phys. Sin., 2021, 70(10): 104208.

[13] R. Ulrich, S. C. Rashleigh, W. Eickhoff. Bending-induced birefringence in single-mode fibers [J]. Optic Letters, 1980, 5(6):273-275.

Multicore Fiber Cable Link for Space-Constrained, High Bandwidth Density Applications

Dan Neugroschl, Victor I. Kopp, Jongchul Park, Jing Zhang, Jonathan Singer, Norman Chao

Chiral Photonics, Inc.
Pine Brook, New Jersey
+1-973-732-0030 · dann@chiralphotonics.com

Abstract

Here we review the design, deployment and testing of the world's first ultra-dense, space division-multiplexing multicore fiber cable link in a metro network and the insights that it provides regarding the maturity of the multicore fiber ecosystem. This deployment features three primary advancements: (a) multicore fiber within a collapsible ribbon cable, (b) low loss, multicore fiber fanouts, and (c) automated multicore fiber splicing. The cable integrates 288 4-core multicore fibers within 24 200-µm collapsible ribbons within a 10 mm outer diameter cable. Using commercial fusion splicers the multicore fibers are fusion-spliced at both ends of the cable to 576 multicore fanout devices, which provide conventional single-core interfaces at patch panels at both ends of the link. This unprecedented bandwidth density can serve space- and/or weight-constrained applications with a smaller bend radius-capable solution that is transparent to the customer and seamlessly integrates into the ubiquitous, conventional singlemode fiber network.

Keywords: Multicore fiber (MCF); multicore fiber fanouts; high bandwidth density; space division multiplexing (SDM); multicore fiber cable; multicore fiber splicers; collapsible ribbon.

1. Introduction

The global internet bandwidth rose by 28% in 2022, in line with the 4-year compound annual growth rate of 29% [1]. This bandwidth growth, occurring across all elements of the ubiquitous fiber optic network, including submarine cables, terrestrial long haul, metro and enterprise networks and data centers of all sizes, increasingly runs into space and weight constraints. For example, conduit congestion, especially in urban areas, can limit the distance a cable can be drawn or blown, how much fiber a cell tower can carry or lead to unexpected, time-consuming, costly permitting and disruptive construction. Although advances such as collapsible ribbons [2] and reduced coating fibers [3] have helped to shrink cable outer diameters (ODs), reduce minimum bend radii and weight, additional measures are required to reduce the number of cables needed to keep up with bandwidth demands.

Multicore fiber (MCF) cables, which can be further future-proofed via wavelength division multiplexing (WDM), greatly increase bandwidth density, reducing the need for additional cables. The first submarine cable employing MCF to enhance space division multiplexing (SDM) and increase cable bandwidth [4], has recently been announced [5]. Here we review the deployed 800-m-long, 1152-core SDM MCF link in a metro network [6, 7], shown schematically in Figure 1. This link incorporates three primary elements: (1) a 10 mm OD 288 4-core fiber MCF cable, (2) MCF fanouts, enabling seamless integration with the single core network, and (3) automated MCF-MCF splicing, enabling automated, low loss and fast installation.

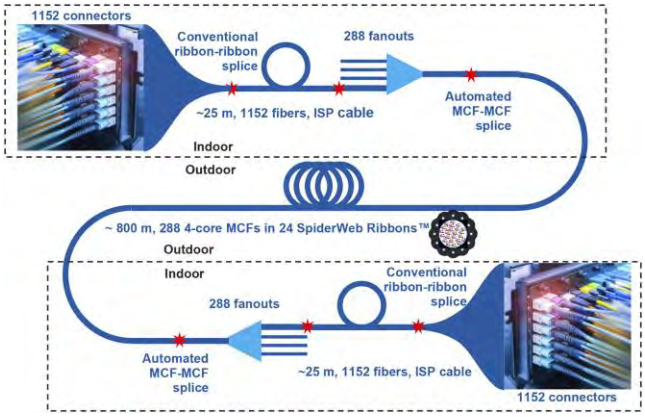


Figure 1. Schematic of the deployed MCF link.

2. MCF Cable and Deployment

The MCF cable, whose cross-section is shown in the center of Figure 1, was designed and fabricated by Fujikura. It features an ITU-T C.657.A1 compliant 4-core MCF with 125 µm OD and a 200 µm OD acrylate coating. The fiber's cores have a step refractive index profile, which is easier to manufacture than trench-assisted designs. Step index designs typically exhibit higher crosstalk but this fiber's is still low enough for short links. Inter-core crosstalk for these cores, arranged in a square grid with 40 +/-0.2 µm spacing, is less than -50 dB/km at 1310 nm and -36 dB/km at 1550 nm. The 288 MCF fibers, 1152 cores, are incorporated into 24 12-fiber SpiderWeb Ribbons (SWRs) whose collapsible design enables the cable's minimal OD of 10 mm with a minimum bend radius of 19 cm, as compared to a conventional

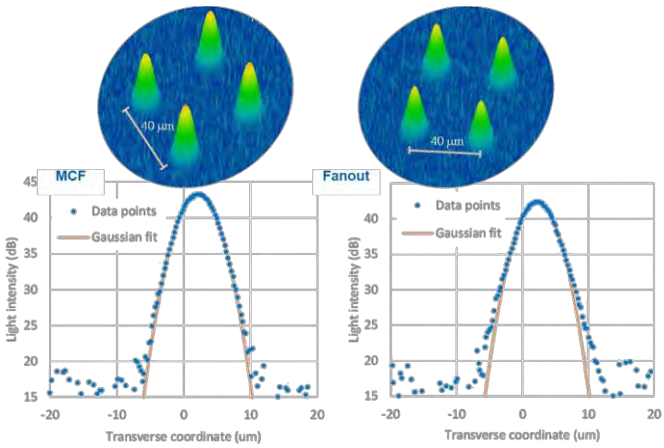


Figure 2. Near field imaging used to optimize matching of the fanout and MCF.

1152-core cable's typical OD of 26.6 mm OD and minimal bend radius of 28 cm [8]. The cables jacket incorporates strength members designed for blowing and the cable was deployed between two buildings within a 13 mm ID / 15 mm OD conduit that featured four 90-degree bends over its 800-m span which also

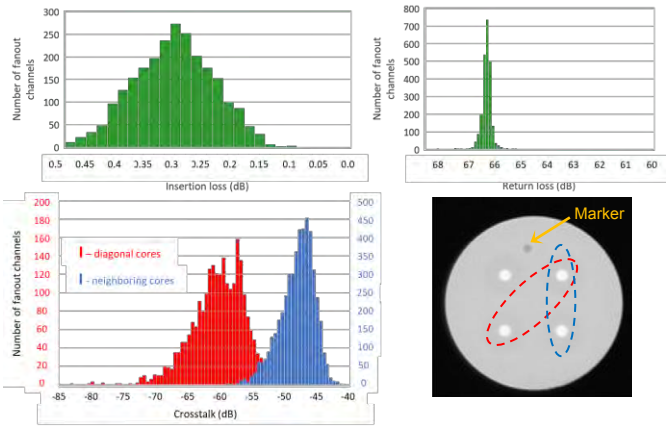


Figure 3. Insertion loss, return loss and crosstalk distributions at 1550 nm of 2448 channels of 612 fanouts. Horizontal axis ranges cover all the measured fanouts. MCF endface view shown right bottom indicating diagonal (red) and nearest neighbor (blue) cores.

ran through a mid-span outside manhole. During deployment, the average site temperature was 10°C.

3. MCF Fanouts

MCF fanouts, as shown in Figure 5, are 60 mm long passive optical components that provide a low loss breakout from the MCF, shown to the right, to conventional single core fibers, shown to the left. These fanouts are based on Chiral's vanishing core approach [9]. Near field imaging, as shown in Figure 2, was used to optimize matching of the mode field size and shape of the fanout to the 200-4CF MCF [10] and this resulted in the 0.3 dB average insertion loss at 1550 nm shown in Figure 3, which also shows the fanout performance distributions across all 612 fanouts fabricated for this link, which included 36 backup devices beyond the 576 fanouts used in the link, one for each end of the 288 MCFs. Return loss averaged below -66 dB at 1550 nm and crosstalk, measured with an amplified spontaneous emission light source averaged over a 2-nm band centered at 1550 nm, averaged below -47 dB for nearest-neighbor cross-propagating cores and below -60 dB for co-propagating diagonal cores. Typical spectral performance is shown in Figure 4 across the O- and C-bands.

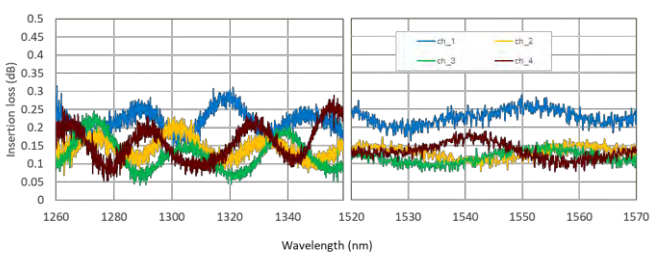


Figure 4. Typical fanout insertion loss across the O- and C-bands.

4. MCF Splicing and Handedness

Both ends of the 800-m cable were individually MCF-MCF spliced to 288 fanout devices using a Fujikura FSM-100P fusion splicer. A splicing mode, based on the IPA method [11] and tailored to this 200-4CF fiber, was developed to enable automated alignment based on the fiber's marker, splicing, and loss estimation that took approximately 3 minutes per splice. The single-core fanout pigtails were ribbon-spliced to 25-m ISP cables, which, were spliced to the patch panels.

The fiber exhibits a handedness, or polarity, as shown in Figure 5, which is important to note in order to maintain and mate the same cores at all splice or connection points. Two ends of the same spool will have opposite handedness and, similarly, the MCF pigtail of the fanout will mate, or be spliced to, an MCF end of opposite handedness, similar to opposite poles of a magnet attracting. We typically mark the right-handed end of the spool in red and the left-handed end of the spool in blue. Similarly, fanouts will have handed MCF pigtails. 'Red' fanouts are spliced to the 'blue' end of the MCF and vice versa.

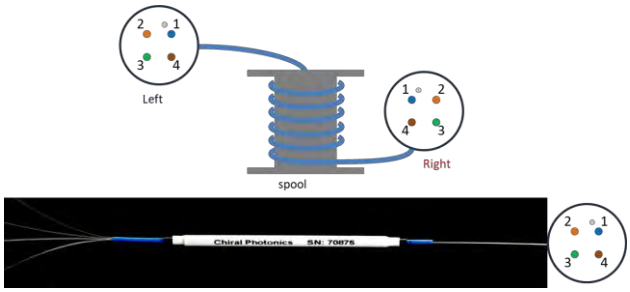


Figure 5. MCF handedness of two ends of the spool. To maintain integrity of cores, shown schematically for a 4-core MCF with a marker next to channel 1, the MCF pigtails with opposite handedness must be mated. A 'blue' left-handed fanout will properly mate with the right-handed 'red' end of the spool. However, it will not properly mate with the similarly handed left end of the spool, which would require a 'red' fanout.

5. Characterization of Deployed MCF Link

After installation, optical losses were measured from patch panel to patch panel using an optical loss test set at both 1310 and 1550 nm. 1102 of the 1152 channels had losses below the 3 dB link loss budget with average losses of 1.2 and 1.5 dB at 1550 and 1310 nm, respectively. Channels were also analyzed with a Luna 6415 optical frequency domain reflectometer (OFDR), which provides a high-resolution profile of the first 100 meters of the channel length. Within this length, one can identify and attribute most of the loss- and backscatter-contributing elements of the MCF link. Figure 6 shows an OFDR trace of the first 50 meters of an

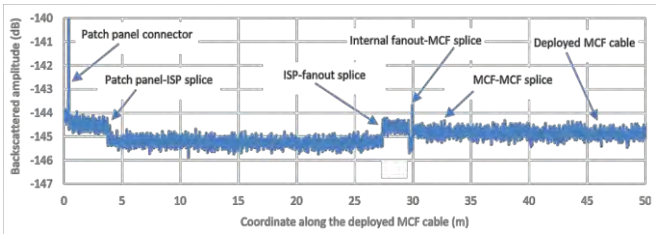


Figure 6. First 50 meters, from the patch panel, of one of the 1152 channels in the MCF cable.

exemplary MCF link channel. One can see all the junctions in this trace, starting with (a) the patch panel connector at approximately 1 meter with its characteristic reflection peak, moving to (b) the patch panel pigtail splice to the ISP single core cable at about 4 meters. This ISP cable is then (c) spliced to the single core pigtails of the fanout at about 27.5 meters and one can then see (d) the backscattering peak from the fanout's internal splice to the MCF at about 30 meters and (e) the low back-reflection MCF-MCF splice at 33 meters. Beyond that 'event,' the trace does not indicate any significant backscattering events. The distribution in the losses over the first 90 meters for 1152 channels is shown in Figure 7. The average insertion loss is 0.56 dB. There are 20 channels with insertion loss greater than half the link loss budget, 1.5 dB. All of these 20 channels did not suffer from losses attributable to the MCF or fanout interfaces but rather due to poor patch panel splices or connectors.

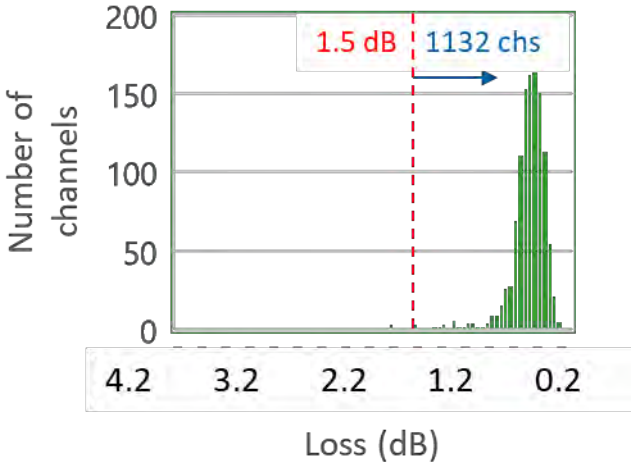


Figure 7. Distribution of losses in first 90 meters of 1152 channels in MCF link.

6. Conclusions and Maturation of MCF Ecosystem

The world's first metro link deployed an 800-m 1152 channel, 10 mm OD cable MCF link between two buildings. The deployment demonstrated the commercial readiness of the co-developed 4-core 200-µm SWR, low-loss MCF fanouts and automated MCF splicing. The link averaged less than 1.5 dB losses across all channels.

Since this MCF link deployment, the MCF ecosystem commercial readiness has continued to advance with more companies supplying MCF and high bandwidth density cables thereof, as well as fanouts and other related optical components, to meet communications needs, from submarine to data centers, as well as for other specialty applications, such as 3D shape sensing for commercialized biomedical equipment.

Another automated MCF splicer, the Fitel S185PM-ROF, has been released, featuring a field-friendly design and a triad electrode design that enables lower loss splicing [12]. More companies are developing and producing and utilizing MCFs, which is increasing the pool of personnel with MCF experience.

Submarine landings of MCF cables now in production within the next two years are expected to further spur MCF adoption as pricing benefits from scaling and technology migration continues to accelerate from the increasing integration of submarine cable landing sites and data centers, further blurring the delineation between terrestrial and subsea networks [13].

7. References

[1] https://blog.telegeography.com/internet-traffic-and-capacity-remain-brisk

[2] K. Toge, Y. Yamada and K. Hogari, "Ultra-high-density optical fiber cable with rollable optical fiber ribbons," OECC/ACOFT 2008 - Joint Conference of the Opto-Electronics and Communications Conference and the Australian Conference on Optical Fibre Technology, Sydney, NSW, Australia, 2008, pp. 1-2.

[3] S. Matsuo, K. Yamashiro, Y. Tsujimoto, M. Miyata, A. Murata, T. Ishikawa, T. Nakajima, and K. Osato, "1,728-Fiber Cable With 12-Fiber Ribbons Comprising 160-µm-Coating Fiber With 80-µm Cladding," J. Lightwave Technol. 40, 1552-1559 (2022).

[4] https://dgtlinfra.com/tpu-subsea-cable/

[5] https://www.datacenterdynamics.com/en/news/google-announces-us-taiwan-philippines-cable-with-chunghwa-globe-and-att/

[6] V. I. Kopp, J. Park, J. Zhang, J. Singer, D. Neugroschl, T. Oda, O. Mukai, and U. Nasir, "Ultra-dense, 1152-core, broadband multicore fiber link deployed in a metro network," Opt. Express 31, 5794-5800 (2023).

[7] T. Oda, S. Kajikawa, K. Takenaga, O. Mukai, D. Takeda, N. Angra, U. Nasir, J. Park, J. Zhang, V.I. Kopp, D. Neugroschl, and K. Ichii, "Loss performance of field-deployed high-density 1152-channel link constructed with 4-core multicore fiber cable," in Optical Fiber Communication Conference (OFC) 2023, Technical Digest Series (Optica Publishing Group, 2023), paper Tu2C.4.

[8] https://na.prysmiangroup.com/sites/default/files/product_center/north-america/files/TLS-DS-B-205-0321_576-1728F%20MassLink%E2%84%A2%20FlexRibbon%C2%AE%20I%26IO%20Multi-Tube%20NA%20250um.pdf

[9] V.I. Kopp, J. Park, M. Wlodawski, J. Singer, D. Neugroschl, and A.Z. Genack, "Pitch reducing optical fiber array and multicore fiber for space-division multiplexing," 2013 IEEE Photonics Society Summer Topical Meeting Series, pp. 99–100 (2013).

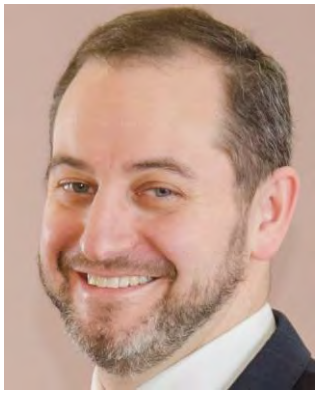
[10] V.I. Kopp, J.Park, J.Singer, D.Neugroschl, K.Takenaga, and U.Nasir, "Low-Loss, O- and C-Band, 4-core MCF Fanouts for Datacom SDM Applications," Optica Open, https://doi.org/10.1364/opticaopen.22179329.v1

[11] W. Zheng, "Automated alignment and splicing for multicore fibers," in Optical Fiber Communication Conference (OFC), paper OM3I.4 (2013).

[12] T. Kremp, Y. Liang and A. H. McCurdy, "Less Than 0.03 dB Multicore Fiber Passive Fusion Splicing Using New Azimuthal Alignment Algorithm and 3-Electrode Arc-Discharging System," 2022 European Conference on Optical Communication (ECOC), Basel, Switzerland, 2022, pp. 1-4.

[13] Clark, K. (2022, November 21). Data center markets: Drivers and influencers, 127, 8-13. https://issuu.com/subtelforum/docs/subtel_forum_127

8. Authors



Dan Neugroschl is the President of Chiral Photonics, which he co-founded in 1999. Prior to Chiral Photonics, he was VP of Operations and Advanced Development and a founder and director of Schick Technologies (currently Sirona, Nasdaq: XRAY), which designs develops and manufactures digital radiographic imaging systems for the dental and medical markets, from its inception in 1991 until 1998. Dan received an MS in Materials Science from Columbia University and was a researcher at IBM Research from 1989-1991.



Victor I. Kopp is Director of Research and Development at Chiral Photonics Inc., which he co-founded in 1999. Results of his research on wave propagation through periodic media, nonlinear optics, photonic devices, and fiber optics are presented in more than 60 publications. Dr. Kopp was awarded the Hewlett-Packard Best Paper Award of the SPIE 1999 Photonics West Conference. He has over 40 US and international patents on photonic devices and fiber optics.



Jongchul Park is a Research and Development Scientist at Chiral Photonics Inc. He received his Ph.D. degree in Physics from the Graduate Center of the City University of New York and MS and BS degrees in Physics from Dankook University in South Korea. His research interests include wave propagation through periodic and random media, statistical optics and fiber optic communication devices.



Jing Zhang is a Fiber Optic Engineer at Chiral Photonics, leading splicing and characterization efforts in support of research and development as well as production. Jing has contributed to several publications and patents. She received a BS in Computer Engineering from the New Jersey Institute of Technology in 2017.



Jonathan Singer is the Director of Engineering of Chiral Photonics since 2000. Prior to joining Chiral, Jonathan was the VP of Engineering and a founder of Schick Technologies (currently Sirona, Nasdaq: XRAY). There, he was responsible for the development of several products including the CDR system, a digital intra-oral x-ray sensor, CDR-CAM, an intra-oral video camera, accuDEXA, a bone mineral density testing device and CDR-Pan, a digital x-ray sensor retrofit for use in Panoramic x-ray systems. He supervised over forty mechanical, electrical and software engineers. Prior to Schick Technologies, Mr. Singer was a project engineer at Cox and Company. Mr. Singer has several patents in digital x-ray imaging and dual energy x-ray analysis. He also has several publications regarding the control of chaotic systems in addition to his fiber optic publications and patents. Jonathan has an MS degree in Mechanical Engineering and Applied Science from the University of Pennsylvania. He received his BS in Mechanical Engineering from the Massachusetts Institute of Technology.



Norman Chao is the Director of Production at Chiral Photonics since 2000 in addition to contributing to publications and patents. Prior to joining Chiral, Norman was Director of Manufacturing at Schick Technologies (currently Sirona, Nasdaq: XRAY) from inception through $35 million in revenues, 400 employees and successful release of numerous product lines and a successful MRP implementation. Prior to Schick Technologies, he was a Manufacturing Engineer at Cox and Company. Norman has an MS in Electrical Engineering from Polytechnic University.

Research of Crosstalk Characteristics Based on Weakly Coupled Seven-core Fiber

Li Zhang, Shuo Xu, Jie Luo, Liubo Yang, Lei Zhang, Lei Shen, Zhuang Xiong, Liyan Zhang, R. Matai

State Key Laboratory of Optical Fiber and Cable Manufacture Technology, Wuhan, 430073, China
Yangtze Optical Fiber and Cable Joint Stock Limited Company, Wuhan, 430073, China
Optical valley laboratory, Wuhan, 430073, China
+86-027-6788-7602 ·zhangli_5000490@yofc.com

Abstract

In this paper, the crosstalk measurement method of multicore fiber is studied based on the weakly coupled seven-core fiber, and an accurate and convenient crosstalk measurement method is established by using the self-developed fan-in/fan-out device and splicing procedure. This paper simulates the actual engineering application scenario, and evaluates the influence of five important factors of fiber length, splicing, bending, temperature and cabling on the crosstalk of the seven-core fiber. The results show that this seven-core single-mode fiber has stable and low crosstalk performance, and is the preferred solution for the next generation of large-capacity fiber transmission, providing a technical reserve for the realization of single-fiber long-distance core-division multiplexing transmission in the future.

Keywords: Multicore fiber; space division multiplexing; crosstalk; fiber splicing; bending loss

1. Introduction

With the revolution of new Internet technologies and applications such as ultra-high definition video, virtual reality and 5G mobile communication rising in the world, network traffic has shown explosive growth, and the capacity of single-mode optical fiber in large capacity transmission systems is rapidly approaching the limit of Shannon's theory[1]. The space division multiplexing technology can break through this limitation and provide a new solution for the continuous growth of optical fiber capacity in the future[2].

Multicore fiber (MCF) based space division multiplexing technology is one of the candidate technologies to cope with the growing traffic. Multicore fiber is a new transmission technology with multiple single-mode fiber cores in a single fiber to realize multiplexing. Each fiber core in the multicore fiber can be regarded as an independent transmission channel, which greatly increases the communication capacity of the fiber transmission system. However, compared with traditional single core optical fiber, the unique inter core crosstalk in multicore fiber will seriously affect the quality of optical signal transmission system and reduce the communication capacity[3]. In recent years, researchers have done a lot of work in the design of low crosstalk multicore fiber. In order to reduce crosstalk between cores, low refractive index grooves can be used to reduce mode field overlap between two cores; The phase mismatch between fiber cores can also be introduced through heterocore design to suppress crosstalk, thus improving the transmission performance of the system. [4-5]

In order to analyze the performance of multicore fiber transmission system, it is very important to evaluate and study the inter core crosstalk. In the linear propagation region, the coupled mode theory and the power coupling theory provide a strong theoretical basis for the study of inter core crosstalk characteristics[6]. In the weak coupling multicore fiber, the existing crosstalk characteristics are mostly based on theoretical research, such as the analysis of the average power evolution of the inter core crosstalk, the characteristics that change with time and frequency, and other characteristics caused by the fiber structure and external conditions[7]. However, for practical engineering application scenarios, there is little research work on the crosstalk characteristics of multicore fiber under different deployment conditions. Crosstalk is very sensitive to deployment conditions and environmental changes. Research shows that crosstalk follows chi square statistical distribution[8], and a single measurement of crosstalk cannot reflect its distribution, so it can not be used as a basis for transmission system engineering. Therefore, it is necessary to characterize the crosstalk distribution of multicore fiber under different deployment conditions in transmission system engineering.

In this paper, an accurate and convenient crosstalk test method is established; Then, the actual engineering application scenario is simulated, and the impact of five important factors, fiber length, splicing, bending, cabling, high and low temperature, on the crosstalk of the seven core fiber is evaluated. The results show that the seven core fiber has stable and low crosstalk performance, which provides technical reserves for the future realization of single fiber long distance core division multiplexing transmission.

2. Crosstalk of Multicore Fiber

Inter core crosstalk is the core index of multicore fiber[9]. The optical power injected into a fiber core will be coupled to the adjacent fiber cores during the propagation, and the crosstalk reflects the coupling. Crosstalk is defined as

$$XT = 10\log10(P'/P)\ [dB]. \quad (1)$$

where P and P 'are the output power of a certain core and the output power of adjacent cores after a certain core is specified. The theoretical value of inter core crosstalk can be obtained based on mode coupling theory (CMT) and power coupling theory (CPT) respectively[10]. The power coupling coefficient method of exponential autocorrelation function is usually adopted, and its crosstalk calculation formula is

$$XT = \tanh(\bar{h}_{mn}L). \quad (2)$$

where $\bar{h}_{mn}$ is the average power coupling coefficient of m and n cores, and L is the transmission distance. When the core is homogeneous:

$$\bar{h}_{mn} = \frac{2\kappa_{mn}{}^2 R}{\beta_m \Lambda}. \quad (3)$$

where R is the bending radius, λ is the core spacing, κ_mn is the coupling constant of two cores, β_m is the transmission constant of the mode in the core. According to Formula (3), in order to reduce the crosstalk between cores, the coupling coefficient can be reduced

by increasing the core spacing and the refractive index difference between core and cladding. It can be seen from Formula (2) and (3) that inter core crosstalk is directly related to transmission length, bending radius and mode coupling coefficient. Combined with the theory and practical engineering application scenarios, this paper evaluates the impact of multiple factors on the crosstalk of multicore fiber, which provides an important basis for realizing long-distance transmission.

The multicore fiber evaluated in this paper is a self-developed homogeneous seven core optical fiber[11], which uses a low refractive index groove aided design to reduce inter core crosstalk, and its core spacing is 42 μm, cladding diameter is 150 μm, coating diameter is 250 μm. The end face and optical characteristics of the fiber are shown in Figure 1 and Table 1 respectively. This type of optical fiber is used without special description in the article, and the test wavelength is 1550nm.

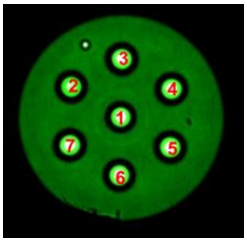


Figure 1. Sectional view of 7-core fiber

Table 1. Optical properties of the each core of the 7-core fiber

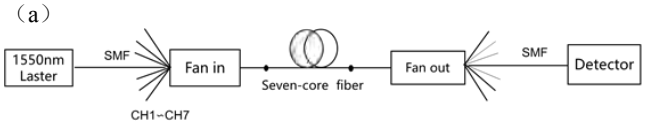
core	Attenuation (dB/km)	MFD (1550 nm, μm)	Dispersion (1550nm, ps/nm/km)	Macro-bending, R=15mm, 10turns (dB)	Micro-bending(1550nm, dB)
1	0.199	8.85	20.922	0.002	0.132
2	0.206	8.88	20.797	0.004	0.201
3	0.201	8.98	20.824	0.006	0.159
4	0.204	8.82	21.002	0.005	0.167
5	0.199	8.87	20.966	0.003	0.173
6	0.207	9.01	20.890	0.003	0.192
7	0.200	9.00	20.716	0.001	0.171

3. Analysis of Crosstalk Test Methods

For the crosstalk of multicore fiber, no standard test method has been established in the world at present. According to the reported literature[12], this paper compares the accuracy of the fan-in/fan-out device method and the spatial light method. The test system is shown in Figure 2.

Figure 2(a) is the schematic diagram of the device method. The self-developed fan-in/fan-out (FIFO) device[13]is used to realize the conversion from SMF to MCF, so as to test the crosstalk between one core and the other six cores, and thus obtain the crosstalk matrix; Figure 2(b) shows the optical path diagram of the spatial light method, that is, the crosstalk test is carried out by means of spatial alignment without FIFO devices.

（a）



（b）

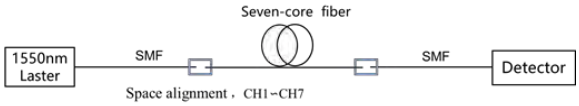


Figure 2. Schematic diagram of crosstalk test system (a) FIFO device method (b) Spatial light method

In this paper, the crosstalk of FIFO devices is measured and the crosstalk matrix shown in Table 2 is obtained. It can be seen that the device crosstalk is mainly distributed between -45 dB and -70 dB, and its maximum and typical values (here refers to the average value of all crosstalk data) are -47 dB and -59 dB respectively, In order to facilitate data statistics and analysis, the crosstalk matrix is characterized by the maximum and typical values of crosstalk later. The device has low crosstalk and excellent performance.

Table 2 FIFO device crosstalk matrix

Fan in / Fan out	CH1	CH2	CH3	CH4	CH5	CH6	CH7
CH1		-50.1	-55.1	-63.1	-57.1	-63.1	-56.1
CH2	-60.2		-59.2	-67.2	-63.2	-62.2	-50.2
CH3	-61.3	-53.3		-56.3	-65.3	-68.3	-61.3
CH4	-58.5	-58.5	-47.5		-55.5	-57.5	-62.5
CH5	-60.6	-55.6	-58.6	-55.6		-53.6	-62.6
CH6	-57.4	-60.4	-62.4	-69.4	-59.4		-56.4
CH7	-55.7	-59.7	-64.7	-67.7	-69.7	-55.7	

In order to investigate whether the FIFO device interferes with the optical fiber crosstalk test, this paper selects two discs of fiber to carry out the crosstalk contrast test using the device method and the spatial light method, and the test results are shown in Table 3.

Table 3 The crosstalk test results were compared between the device method and spatial light method

Crosstalk /dB	FIFO B2B	Fiber 1(32km)		Fiber 2(19km)	
		Method 1*1	Method 2*2	Method 1	Method 2
Max	-47.5	-44.3	-44.9	-47.0	-50.0.
Typ	-59.0	-53.0	-52.0	--57.7	-57.9

*1 Method 1 represents the FIFO device method.

*2 Method 2 represents the spatial light method.

Table 3 shows that the crosstalk data obtained by the two test methods for fiber 1 under test are consistent, while the maximum crosstalk value of fiber 2 has a certain deviation; In theory, the spatial light method is a more accurate method for fiber crosstalk test, and no additional device crosstalk will be introduced. Based on the crosstalk measured by the spatial light method, the following conclusions can be obtained by analyzing the data in Table 3: when the crosstalk of the FIFO device is greater than the crosstalk of the fiber, the crosstalk of the device dominates the test results, and at this time, the crosstalk of the device on the fiber is affected; When the device crosstalk is less than the fiber crosstalk, the test result is dominated by the fiber crosstalk. At this time, the crosstalk measured by the FIFO device method is consistent with the spatial light method. Therefore, to ensure the accuracy of fiber crosstalk

test, device crosstalk needs to be better than fiber crosstalk. In the following experiments, in order to facilitate the test, FIFO devices with excellent performance are used for fiber crosstalk test.

4. Study on Crosstalk Characteristics of Optical Fiber

Inter core crosstalk is an important standard for detecting whether optical fiber can be used for long-distance transmission[14]. It is of great significance to evaluate the crosstalk distribution of multicore fiber in actual deployment. In this paper, fiber crosstalk is systematically evaluated from five aspects: fiber length, fiber fusion, bending radius, temperature and cabling.

4.1 Influence of Fiber Length on Crosstalk

Theoretical research shows that the inter-core crosstalk is directly related to the transmission length of optical fiber[15]. Considering the application of multicore fiber in long-distance transmission system, this paper studies the trend of multicore fiber crosstalk with length. In this chapter, we selected five kinds of seven-core fibers with different lengths from the same disk for crosstalk test, and the test results are shown in Figure 3.

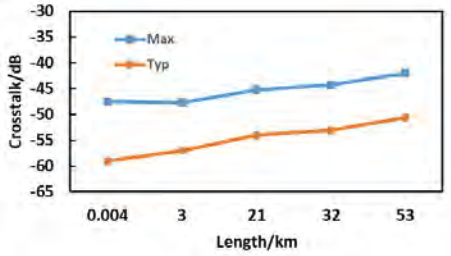


Figure 3. Schematic diagram of variation of fiber crosstalk with length

Figure 3 shows that the maximum crosstalk of the fiber to be tested increases from - 47.7 dB (3 km) to - 42 dB (53 km), and the typical value increases from - 59 dB to - 51 dB, indicating that the crosstalk of the seven-core fiber is related to the length of the optical fiber. The longer the length of the optical fiber, the greater the crosstalk (the greater the crosstalk, the worse the crosstalk); The crosstalk of seven-core fiber will deteriorate with the length, which is consistent with the previously reported crosstalk rule[16]. The seven-core fiber used in this paper can ensure that the crosstalk of the 60km optical fiber does not exceed - 40dB under the worst conditions, meeting the application scenario of long-distance communication.

4.2 Influence of Splicing on Crosstalk

In practical engineering applications, a single section of 2-3km long optical fiber is usually selected for section laying, and the splicing between each section of optical fiber is essential, while the off-core splicing may affect the crosstalk of multicore fiber, thus affecting the application of multicore fiber in actual deployment. So we designed experiments to study the influence of optical fiber splicing on crosstalk, cut the 60km optical fiber into different lengths, and use the customized splicing machine to splice it, and evaluate the crosstalk changes under the splicing points of 2, 3, 5, 9, and 21.

The splicing loss distribution of 21 splicing points (cut into 20 plates for 3km) is shown in Figure 4, and 147 (7 cores × 21) splicing data. According to the calculation in Figure 4, the average splicing loss of 21 splicing joints is 0.30dB, and the probability of splicing loss less than 0.30dB is 67% (in order to simulate the actual splicing scenario, the splicing conditions are not optimal, and the current laboratory splicing level is 0.2dB). The splicing loss and link loss of each core of the 60km and 20km optical fiber after splicing are summarized in Table 4.

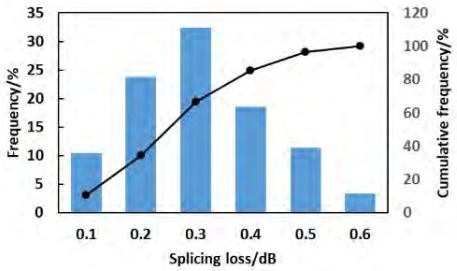


Figure 4. Histogram of fusion loss of all cores

Table 4 Summary of link losses and splicing losses

Core	Link loss/dB		Splicing loss/dB (3km*20)	
	60km	3km*20	Avg	Max
1	-15.3	-17.7	0.16	0.35
2	-17.4	-22.0	0.33	0.33
3	-17.1	-20.2	0.28	0.48
4	-16.3	-21.5	0.30	0.50
5	-15.9	-21.0	0.29	0.58
6	-17.0	-22.3	0.34	0.55
7	-16.7	-22.6	0.36	0.60

Crosstalk tests were carried out on optical fibers with different splicing points, and the test results are shown in Figure 5. The figure shows that the optical fiber crosstalk has almost no change under different splicing points, and its typical value and maximum value are consistent. This shows that in this splicing case, the optical fiber splicing will not interfere with the crosstalk basically, which is of important guiding significance for the future laying of long-distance trunk optical cables.

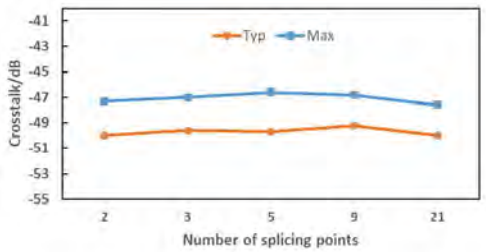


Figure 5. Schematic diagram of crosstalk variation under different number of splicing points

4.3 Influence of Different Bending Radius on Crosstalk

In the actual optical cable laying, for the construction and maintenance of the optical cable, a certain length of optical fiber will be reserved at the specific construction site to store it in a circle; In addition, the optical fiber will also be placed in the optical cable junction box in a circle at the optical fiber splicing joint. Theoretical research shows that optical fiber bending will make light energy leak to the cladding, and the optical energy loss will increase while the crosstalk between adjacent fiber cores will also increase[17]. So this paper focuses on the influence of fiber bending on crosstalk. Four bending radii are set in this chapter: (1) 10mm radius, one circle; (2) 15mm radius, one circle; (3) 15mm radius, 10 circles; (4) 30mm radius, 100 circles. The crosstalk under these four bending

conditions is tested respectively, and the test results are shown in Figure 6. The maximum and typical values of fiber crosstalk are almost unchanged, and the crosstalk between fiber cores remains stable under different bending conditions. This bending condition has no effect on the crosstalk test of seven-core fiber. The seven-core fiber not only has excellent macro-bending performance, but also has stable and low inter-core crosstalk, which can be used for long-distance system transmission.

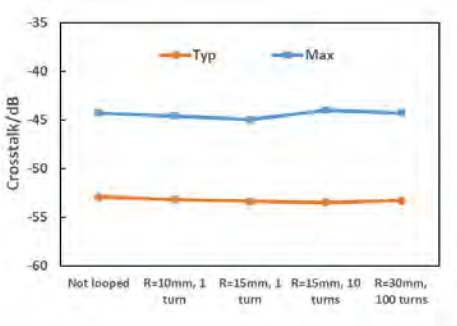


Figure 6. Schematic diagram of crosstalk variation under different bending conditions

4.4 Influence of high and low temperature on crosstalk

Considering the actual optical fiber laying scenario, this paper further evaluates the impact of different temperature scenarios on the crosstalk of seven-core fiber. Take a section of seven-core fiber and place it in the high and low temperature cycling test chamber, with the temperature range of -40℃~85℃. Fig. 7(a) shows the temperature profile. Fig. 7(b) shows the variation of crosstalk over time. The fiber crosstalk is distributed between -57.8 and -59.3dB, which indicates that crosstalk fluctuates less in the environment of -40 to 85℃. The seven-core fiber can withstand extreme temperature environment, and has good stability and reliability.

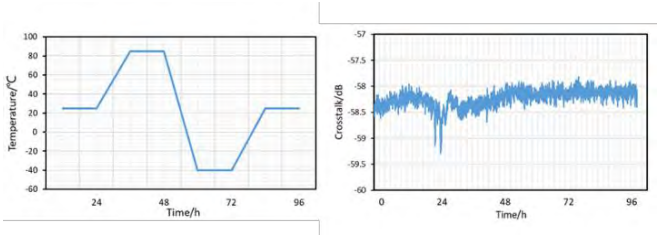


Figure 7. (a) Temperature profile (b) Crosstalk variation over time

4.5 Influence of cabling on crosstalk

The optical fiber cabling goes through several processes, including coloring, two sets, cabling, protective layer, etc. Fiber crosstalk may vary before and after cabling. In order to evaluate whether the cabling will affect the fiber crosstalk, the inter-core crosstalk of the bare fiber and the fiber after cabling are tested respectively. The test results are shown in Figure 8. Crosstalk before and after fiber cabling is not different. Multiple processes of fiber cabling will not affect fiber crosstalk. The seven-core fiber has stable inter-core crosstalk.

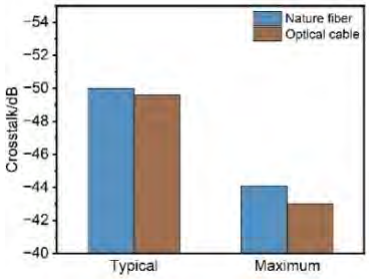


Figure 8. Schematic diagram of fiber crosstalk before and after cabling

5. Conclusion

This paper first probes into the test method of multicore fiber crosstalk. For the test of multicore fiber, the self-developed fan-in/fan-out device is used. Before testing the crosstalk of the fanin/fan-out device, it is necessary to test the crosstalk of the fan-in/fan-out device first. After ensuring that the crosstalk of the device is better than the crosstalk of the optical fiber, the method of using the device method to test the crosstalk of the optical fiber is accurate and reliable. In addition, we simulated the actual engineering application scenario in the laboratory, evaluated the impact of five important factors on crosstalk, such as fiber length, splicing, bending, high and low temperature, cabling, and got the following conclusions: (1) The crosstalk of seven-core fiber is related to the length. The longer the fiber length, the worse the crosstalk will be. At present, the self-developed seven-core fiber can ensure that the crosstalk of 60km fiber does not exceed - 40dB under the worst conditions, meeting the long-distance communication application scenario. (2) Splicing, bending, temperature and cabling will not have a statistically significant impact on crosstalk. The seven-core fiber has stable and low crosstalk performance, providing technical reserves for realizing single-fiber long-haul core division multiplexing transmission in the future.

6. Acknowledgments

This work was supported by National key research and development projects 2021YFB2800902

7. References

[1] Writer M L S T . “Records Broken for Optical Fiber Capacity and Distance”. Engineering, 139-140(2021).

[2] S. Penet, et al. “A Thousand Seven Hundred and Twenty Eight Fiber Cable for Installation in a 32 mm Sub-Duct”. IWCS 2014, 730-733(2014)

[3] Hayashi T , Taru T , Shimakawa O , et al. “Design and fabrication of ultra-low crosstalk and low-loss multi-core fiber”. Optics Express, 2011, 19(17), 16576-16592(2011).

[4] Abouseif A , Othman R B , Jaoun Y. “Channel model and optimal core scrambling for multi-core fiber transmission system”. Optics Communications, 2020, 454, 124396(2020).

[5] L Zhang,et al. “The Influence of Trench Design on Single-Trench-Assisted Bending-Insensitive and Ultra-Bending-Insensitive Fibre”.IWCS2013,111-115 (2013)

[6] Hayashi T, “Multi-core Fibers for Space Division Multiplexing Handbook of Optical Fibers”. Singapore: Springer Singapore, 2019, 1-47(2019).

[7] W. Wang, L. Xiang, W. Shao and G. Shen, “Stochastic Crosstalk Analyses for Real Weakly Coupled Multicore Fibers Using a Universal Semi-Analytical Mode”. Journal of Lightwave Technology, 2021, 39(13), 4503-4510(2021).

[8] Hayashi T, Taru T, Shimakawa O, et al. “Characterization of Crosstalk in Ultra-Low-Crosstalk Multi-Core Fiber”. Journal of Lightwave Technology, 2012, 30(4), 583-589(2021).

[9] Awaji Y, Sakaguchi J, Puttnam B J, et al. “High-capacity transmission over multi-core fibers”. Optical Fiber Technology, 2016, 35(FEB.), 100-107(2016).

[10] Li M J, Li S, Modavis R A. “Coupled Mode Analysis of Crosstalk in Multicore Fiber with Random Perturbations”. OFC2015.W2A.35(2015).

[11] Lei S , Su C , Sun X , et al. “Design, Fabrication, Measurement and Splicing evaluation of a Novel Ultra Low Crosstalk 7-core Fiber”. OFC2018, paper W1A.3(2018).

[12] Nazarov V, Kuchinsky S A, Zakharian A R, et al. “Crosstalk Statistical Distributions in Multicore Fibers Under Different Deployment Conditions”. OFC2021, 1-3(2021).

[13] J. Chu et al. “Low-Loss Fan-In/Fan-Out Device for 8-Core Fiber”. ICOCN2021, 1-3(2021).

[14] H. Zhou, et al. “A Bend-insensitive Ultra Low Loss and Large Effective Area Fibre for Long Haul Transmission”. OFC2016, Paper Tu3G.2 (2016)

[15] Alves T M F, Soeiro R O J, Cartaxo A V T. “Probability Distribution of Intercore Crosstalk in Weakly Coupled MCFs With Multiple Interferers”. IEEE Photonics Technology Letters, 2019, 31(8), 654-654(2019).

[16] Ricardo O J, Alves T M F, Cartaxo A V T. “Inter-Core Crosstalk in Weakly Coupled MCFs with Arbitrary Core Layout and the Effect of Bending and Twisting on the Coupling Coefficien”. Optics Express, 2019, 27(1), 74-91(2019).

[17] Hayashi T, Sasaki T, Sasaoka E. “Microbending-induced crosstalk increase in heterogeneous multi-core fiber”. ECOC 2011, 1-3(2011).

Low-Loss All-Fiber Mode Multiplexers for Weakly-Coupled Few-Mode Fiber

Ying Li, Tingting Dong, Ruichun Wang, Lei Zhang, Lu Dai, Lei Shen, Zhuang Xiong, Raadjkoemar Matai

Key Laboratory of Optical Fiber and Cable Manufacture Technology, Wuhan 430073, China

Yangtze Optical Fiber and Cable Joint Stock Limited Company, Wuhan 430073, China

Yanshan University, Qinhuangdao, 066000, China

Zhejiang University, Hangzhou, 310058, China

+86-027-6788-7602 · liying_5000344@yofc.com

Abstract

The multiplexers/demultiplexers are crucial components in mode-division multiplexing fiber transmission systems. An all-fiber mode multiplexer/demultiplexer for weakly-coupled 4 mode fiber and its measurement are reported in this paper, this device is cascaded by different mode-selective coupler , which uses a fused tapering method to achieve it. The insertion loss of a single mode-selective coupler is less than 0.8dB, the insertion loss of LP01, LP11, LP21 and LP02 is less than 2 dB after cascading, and the modal crosstalk is lower than −15dB. The few-mode multiplexer has great stability, and after 168 hours of high-temperature testing, the insertion loss changes in each mode are less than 0.8dB.

Keywords: All-fiber mode multiplexers, mode-selective coupler, mode-division multiplexing

1. Introduction

With the increasing demand for channel capacity, optical fiber communication technology is continuously advancing. Over several decades, the system capacity of single-mode fibers (SMF) has experienced significant growth, and a traditional SMF has already achieved high-capacity transmission of up to 100Tb/s, approaching its physical limit. To further increase the dimension of channel, the mode-division multiplexing (MDM) technology of few-mode fiber (FMF) has gradually become a hot research topic[1].

In mode-division multiplexing systems, mode-selective coupler (MSC) and mode multiplexers are crucial components that enable the implementation of the MDM system. Mode-selective coupler are used to achieve the conversion between the fundamental mode and higher-order modes. When MSCs are cascaded, they act as multiplexers, allowing multiple modes to be coupled into the few-mode fiber. Therefore, the FMF multiplexers/demultiplexers (MUX/DEMUX) and its preparation method are extremely important and have become one of the key technologies for promoting the practical application and cost reduction of FMF. At present, there are three main technical methods for mode multiplexing devices: free space optics[2], 3D waveguide type[3], and all-fiber type[4].

Free-space optics require high-precision coupling alignment, have large physical dimensions, and are challenging to integrate. 3D waveguide-type devices cannot be directly connected to optical fibers, and the fabrication difficulty increases sharply with the increase in mode numbers. In optical fiber communication systems, all-fiber mode multiplexers demonstrate excellent compatibility, easy connectivity, and are more suitable for engineering applications[5].

In this paper, a high-performance tapered few-mode fiber multiplexers for supporting all-fiber mode-division multiplexing was prepared and tested.

2. Design of FMF and MUX/DEMUX device

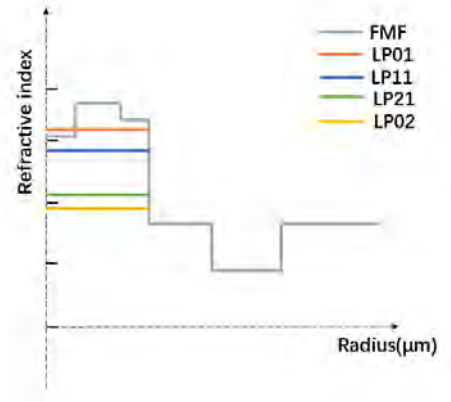


Figure 1. Refractive index profile of proposed TRC-FMF and neff of all 4 modes

Table 1. Key parameters of 4-mode fiber

Key parameters	Typical value			
	LP01	*LP11*	*LP21*	*LP02*
Cladding diameter (μm)	125±0.7			
Coating diameter (μm)	250±1			
Refractive index (n_{eff})	1.452215	1.450277	1.477285	1.445394
Macrobending@1550nm, R=30mm,100 Turns	0.004	0.003	0.007	0.046
Dispersion@1550nm (Ps/nm/km)	20.2	18.57	22.69	23.46
Attenuation@1550 nm (dB/km)	0.204	0.207	0.212	0.211

The FMF used in this paper is a weakly coupled triple-ring-core (TRC) 4-mode fiber (4MF) produced by YOFC. Figure 1 shows the refractive index profile of the 4MF, and Table 1 shows the basic

performance parameters. It can be seen that the fiber core has 3 layers of rings to help distrbute the effective refractive index(neff) of all 4 LP modes as evenly as possible between the refractive indices of fiber core and cladding. In this FMF, each mode is transmitted with a different effective refractive index, forming independent channels.The effective refractive index differences between different modes are deliberately increased to effectively separate all LP modes and suppress mode crosstalk. Meanwhile, this fiber has excellent long haul transmission performance, the attenuation of all four modes is less than 0.22 dB/km at 1550nm.

When the mode propagation constant of the SMF matches the propagation constant of a certain high-order mode in the 4MF, the energy in the SMF can be coupled to the 4MF and continue to propagate in that mode, completing the excitation and conversion of the high-order mode[6]. Figure 2 shows the schematic of the MSC structure.

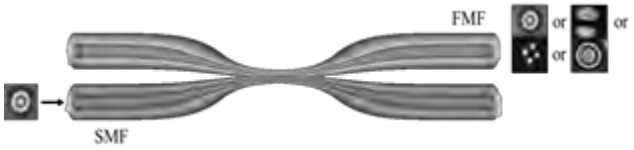


Figure 2. Refractive index profile of proposed TRC-FMF and neff of all 4 modes

3. Fabrication of MUX/DEMUX DEVICE

In order to obtain the low-loss mode multiplexers, the SMF and the FMF are tapered simultaneously, and the fire temperature and stretching speed are controlled in the process, so that the refractive index of the SMF match the high-order mode of the FMF. By using this method to obtain a specific mode-selective coupler (MSC), four kinds of MSCs can be cascaded to obtain the 4-mode MUX/DEMUX. Figure 3 shows the schematic of the coupling region of the MSC after fused tapering. Figure 4 shows the finished product of a single MSC after packaging. The coupling region is fixed with a high stability UV glue, and then multilayer glass tubes are used for nested packaging to maintain a constant inert environment inside. Finally, a metal tube is used for outer packaging to ensure the overall strength after packaging. Figure 5 shows schematic of the cascading structure, the required target mode MSCs are cascaded to obtain MUX/DEMUX.



Figure 3. The coupling region of the mode-selective coupler after tapering

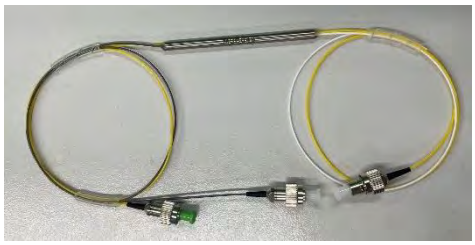


Figure 4. The mode-selective coupler after packaging

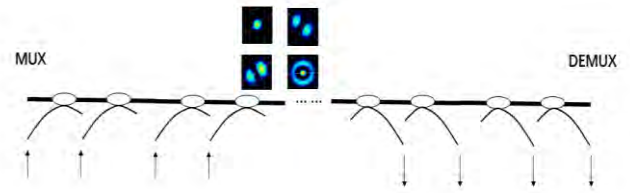


Figure 5. The schematic of the mode MUX/DEMUX

4. Measurement and results

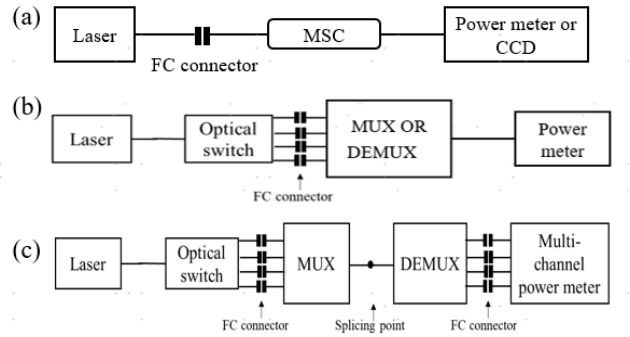


Figure 6. (a) The insertion loss test schematic diagram of MSC, (b) the insertion loss test schematic diagram of MUX/DEMUX, (c) the modal crosstalk test schematic diagram of MUX and DEMUX

Figure 6 shows the test schematic of the insertion loss and crosstalk. Firstly, the insertion loss of the single MSC is tested in the 1550nm band, with typical values of insertion loss ⩽ 0.3dB for LP_{01} and LP_{02}, and ⩽ 0.8dB for LP_{21} and LP_{02} as Table 2 shows. Table 3 shows the insertion loss of LP_{01}, LP_{11}, LP_{21} and LP_{02} after cascading, the insertion loss is less than 2dB. In general, mode MUX and DEMUX are used in pairs. Table 4 shows the crosstalk of a pair of 4-mode MUX and DEMUX obtained by cascading 8 MSCs, and the modal crosstalk is lower than −15dB.

Table 2. The insertion loss of single MSC

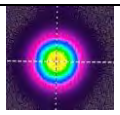
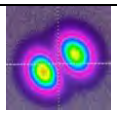
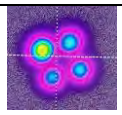
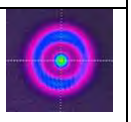
Unit: dB				
	LP_{01}	LP_{11}	LP_{21}	LP_{02}
IL	-0.21	-0.32	-0.70	-0.75
Mode				

Table 3. The insertion loss of LP01, LP11, LP21 and LP02 after cascading at 1550 nm

Unit: dB				
	LP_{01}	LP_{11}	LP_{21}	LP_{02}
MUX/IL	-0.64	-0.56	-2.00	-0.77
DEMUX/IL	-0.69	-0.78	-1.89	-0.75

Table 4. The modal crosstalk matrix of a pair of 4-mode MUXs/DEMUXs at 1550nm

Unit: dB

Input / Output	LP_{01}	LP_{11}	LP_{21}	LP_{02}
LP_{01}	0	-15.75	-23.12	-24.67
LP_{11}	-16.30	0	-22.95	-18.54
LP_{21}	-31.72	-20.54	0	-17.47
LP_{02}	-36.51	-28.34	-16.98	0

In the cascaded MUX/DEMUX, the insertion loss of each mode significantly compared to a single MSC. This is because in this cascaded structure of mode MUX/DEMUX, some higher-order modes need to pass through multiple fiber tapering regions, and the fiber core structure will undergoes some changes resulting in some modes of light losing when passing through these regions. The more modes there are, the greater the cascading loss it brings. Designing new SMF as bridging fibers ,reduce the tapering ratio o f few-mode fibers to solve this problem.

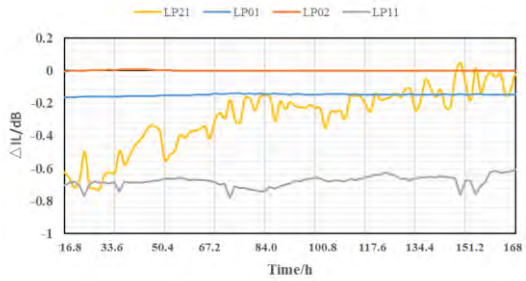


Figure 7. Additional losses in high-temperature environments

To validate the stability of the device, this paper further evaluated the high-temperature aging performance of the multiplexer. 4-mode multiplexers are placed inside a high-temperature test chamber for 168 hours at a temperature of 85°C. Figure 7 shows the variation of additional insertion loss of the multiplexer over time. The insertion loss changes for LP_{01} mode and LP_{02} mode are less than 0.1 dB, while for LP_{11} mode and LP_{21} mode, the insertion loss changes are less than 0.8 dB. This confirms that the few-mode multiplexer exhibits excellent high-temperature stability.

5. Conclusions

This paper provides a detailed explanation of the technical method, fabrication process, and testing methods for fused tapering few-mode fiber multiplexer. And it also proposes solutions to further enhance its performance. The insertion loss of a single mode-selective is less than 0.8dB, the insertion loss of LP_{01}, LP_{11}, LP_{21} and LP_{02} is less than 2 dB after cascading, and the modal crosstalk is lower than −15dB. The few-mode multiplexer has great stability, and after 168 hours of high-temperature testing, the insertion loss changes in each mode are less than 0.8dB.The single MSC has a small volume, high mode coupling efficiency, excellent stability, and can achieve any combination of target modes, which can be flexibly applied to mode division multiplexing transmission systems.

6. Acknowledgments

This work was supported by National key research and development projects: 2021YFB2800902.

7. References

[1] T Morioka, “Recent progress in space-division multiplexed transmission technologies”, OFC2013.

[2] Inan, B Beril, et al. “Low computational complexity mode division multiplexed OFDM transmission over 130 km of few mode fiber”, OFC2013.

[3] Driscoll, Jeffrey B. et al. “Asymmetric Y junctions in silicon waveguides for on-chip mode-division multiplexing”, Optics Letters 38.11(2013):1854-1856.

[4] Igarashi, Koji, et al. “All-fiber-based selective mode multiplexer and demultiplexer for weakly-coupled mode-division multiplexed systems”, Optics Communications (2018):S003040181730737X.

[5] Dawei Ge, Juhao Li, Jinglong zhu, et al. “Design of a Weakly-Coupled Ring-Core FMF and Demonstration of 6-mode 10-km IM/DD Transmission”, Optical Fiber Communications Conference(2018).

[6] Song, Kwang Yong, and B. Y. Kim. “Broad-band LP02 mode excitation using a fused-type mode-selective coupler”, Photonics Technology Letters IEEE 15.12(2003):1734-1736.

8. Pictures of Authors



Ying Li is an engineer of R&D center of YOFC. He received her M.S degree in materials from Wuhan University of University of Technology, China. She joined YOFC in 2020. Her current research interests r is mode division multiplexing optical devices. Her mailing address:liying_5000344@yofc.com



Tingting Dong is a professional degree of optical engineering of Yanshan university in 2021. The current reseach field is space division multiplexing optical devices. Her mailing address: dongtingting0639@163.com



Lei Zhang is of manager of R&D center of YOFC. He received his M.S degree in functional materials from Dalian University of Technology, China. He joined Yangtze Optical Fiber and Cable Co. Ltd. (YOFC) in 2010. His current research interests are bending insensitive, low loss, ultra low loss and large effective area fiber. His mailing address: zhanglei@yofc.com



Ruichun Wang is the Vice-president of R&D center of YOFC. He specializes in preform making and drawing process, and has led many R&D projects for improvement of optical fiber products. He received his M.S. degree in Material Science from Zhejiang University, China. His mailing address: wangruichun@yofc.com

Crosstalk Characteristics of 200-µm-Coating 4-Core Fibers in 288-Fiber/864-Fiber Freeform Ribbon Cables

Tetsuya Hayashi, Ayumi Inoue, Yohei Suzuki, Takuji Nagashima, Yuki Shimoda, and Fumiaki Sato

Sumitomo Electric Industries, Ltd.

Yokohama, Kanagawa, Japan

t-hayashi@sei.co.jp

Abstract

Multicore fiber can significantly increase the spatial density of optical fiber cables, and would realize light-weight ultra-high-density cable suitable for low-cost cable installation. To realize MCF cables with better optical performance, the crosstalk change due to cabling is nonnegligible. In this study, we fabricated 288-fiber and 864-fiber partially-bonded-ribbon cables with 200-µm-coating MCFs, which can suppress the XT increase due to cabling.

Keywords: multi-core fiber; partially-bonded ribbon; freeform ribbon; optical fiber; microduct cable

1. Introduction

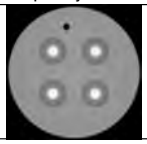
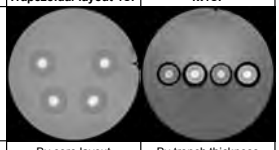
In recent years, with the dramatic increase of data capacity among all over the world due to expanding of crowd computing, the demand for high-fiber-count and high-density optical cable increases. To construct optical networks more economically, it is necessary to make effective use of existing ducts and spaces for the installation of optical fiber cables. Several studies on ultra-high-density optical fiber cable with partially-bonded ribbons have been reported. Recently, the multi-core fiber (MCF) has been actively studied for further improvement of spatial channel density and an MCF cable with partially-bonded ribbons was also reported. A 200-fiber partially-bonded-ribbon cable with 250-µm-coating MCFs (100f/250µm-MCF cable) [1], and a 288-fiber partially-bonded-ribbon cable with 200-µm-coating MCFs (288f/200µm-MCF cable) have been reported [2]. The crosstalk (XT) increase due to cabling was well suppressed in the 100f/250µm-MCF cable, but was somewhat higher in the 288f/200µm-MCF cable.

In this paper, we present 288-fiber and 864-fiber partially-bonded-ribbon cables with 200-µm-coating MCFs, which can suppress the XT increase due to cabling.

2. 125-µm-cladding 4-core fibers and related MCF technologies

In this section, we review the 125-µm-cladding 4-core fibers and related MCF technologies. For practical use of MCFs, 4-core fibers with the standard 125-um cladding have been proposed [3], [4]. Table 1 shows the examples of the 125-µm-cladding 4-core fibers. The square- and trapezoidal-layout 4CFs were fabricated using simple G.652/G.657.A1 compatible cores. The square 4CF has XT for counter-propagating signals (XT_{bidir}) ≤−40 dB/10km at 1550 nm, which provides future compatibility to wavelength band migration from O-band to C-band. In fact, Soma *et al.* demonstrated the transoceanic distance bidirectional transmission over step-index 4-core fibers with the standard cladding diameter [5]. The other short-reach MCFs are optimized for O-band transmissions and have XT_{bidir} << −40 dB/10km at 1310 nm. The trapezoidal 4CF realizes core identification without additional marker and easier rotational alignment. The 1x4CF can pack 8.6-µm MFD cores on a linear array in the 125-µm cladding and can be coupled to PLC-based fan-in/fan-out (FIFO) (i.e., simple waveguide pitch converter) and edge couplers of photonic integrated circuits. Heterogeneous index trench thickness also realizes core identification without additional marker. All of these 125-µm-cladding 4-core fibers are compatible to either of 250-µm coating or 200-µm coating.

Table 1. 125-µm-cladding 4-core fibers [4].

Applications	Short-/medium-reach		Short-reach	
Fiber ID	Square-layout 4CF		Trapezoidal-layout 4CF	1x4CF
Cross section				
Core identification	By marker		By core layout	By trench thickness
Core pitch Λ	40 µm		37 µm	25 µm
Cable cutoff λ	1239–1244 nm		1129–1159 nm	1060–1186 nm
Operation λ (λ_{op})	1310 nm	1550 nm	1310 nm	1310 nm
MFD at λ_{op}	MFD 9.0 µm	-	MFD 8.6–8.9 µm	MFD 8.4–8.7 µm
Loss at λ_{op}	0.327–0.329 dB/km	0.194–0.197 dB/km	0.321–0.325 dB/km	0.317–0.359 dB/km
XT_{dir}[a] at λ_{op}	−68 dB at 1km	−36 dB at 1km	−52 to −51 dB at 1km	−50 to −45 dB at 1km
Total XT_{bidir}[b] at λ_{op}	−84 dB at 10km	−47 dB at 10km	−68 to −65 dB at 10km	−66 to −59 dB at 10km

a) XT_{dir}: Core-to-core XT between co-propagating lights in nearest neighboring cores
b) XT_{bidir}: XT in bidirectional transmission where signals propagate in counter directions between every pair of nearest neighboring cores.

Various MCF technologies necessary to realize MCF links have also been developed. Single-MCF connector (Fig. 1) was demonstrated with the simple structure without additional high-precision components, thus suitable for volume manufacturing [6]. The fabricated MCF LC connectors realized ultralow insertion loss (IL) and high return loss (RL) connections [IL histogram shown in Fig. 1(right)], and passed Telcordia GR-326-CORE mechanical and environmental tests. For the square-layout 4-core fibers, the compact FIFO based on etched fiber bundle technology (Fig. 2) has been well developed with low IL and high RL, and IL variation during temperature cycle was well suppressed [7].

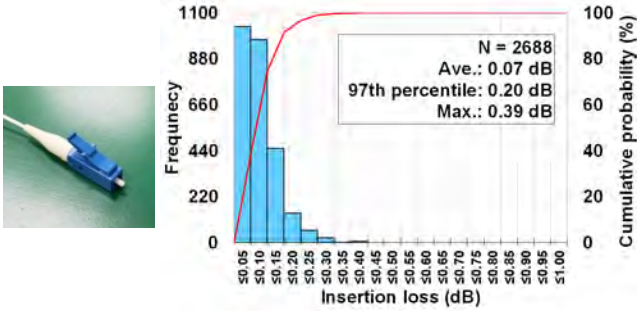


Figure 1. (left) Appearance of the single-MCF LC connector, and (right) the IL histogram for random mating test [6].

The FIFO technologies for these 4-core fibers have also been proposed and developed. For the square-layout 4-core fibers, the compact FIFO based on etched fiber bundle technology (Fig. 2) has been well developed with low IL and high RL, and IL variation during temperature cycle was well suppressed [7]. For the trapezoidal-layout 4-core fibers, the laser-inscribed 3-dimensional waveguide [8] can be a good choice. As already mentioned, the 1x4CF can be coupled to PLC-based FIFO and edge couplers of photonic integrated circuits, which can be easily realized with commercial volume-manufacturable technology.

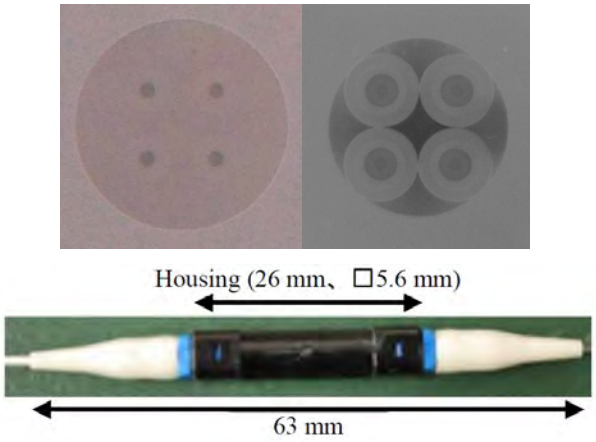


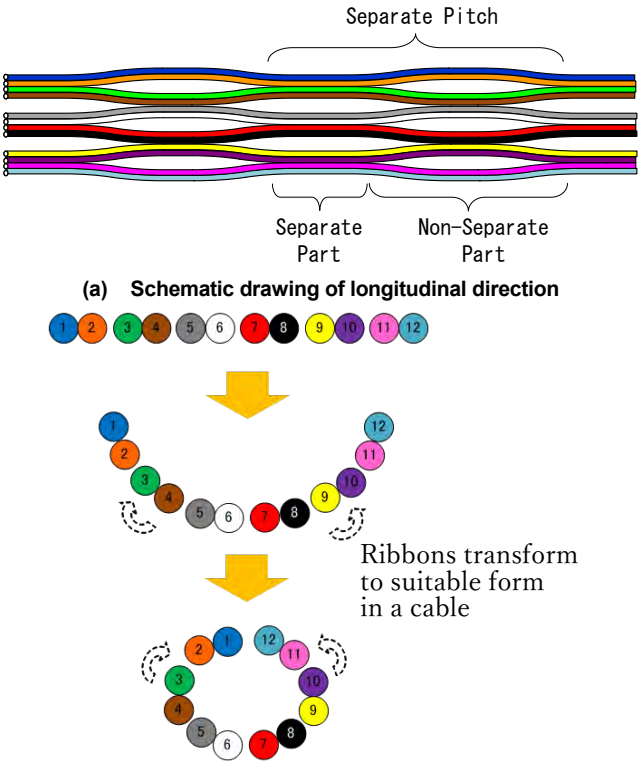
Figure 2. Compact MCF fanout with etched fiber bundle. (top left) End face of MCF, (top right) end face of bundle, and (bottom) appearance of the fanout [7].

3. Freeform Ribbon Cables with 200-μm-coating step-index 4-core fibers

We fabricated 200-μm-coating step-index square-layout 4-core fibers [square-layout 4CF, Table 1(left)] and Freeform Ribbon (partially-bonded ribbon, see Fig. 3) cables with 288 fibers in the cable outer diameter of ~9.5 mm [Fig. 4(left)] and 864 fibers in the cable outer diameter of ~12.8 mm [Fig. 4(right)] using the 4CFs. Table 2 summarizes the properties of the 4-core fibers used for the cable fabrication.

Table 2. Properties of the 4-core fiber spools used for Freeform Ribbon cable fabrication.

MCF samples		4CF-1	4CF-2
Fabricated cables		288f cable	864f cable
Core layout		Square	
Core pitch [μm]		39.5-39.8	39.6-39.8
Cladding diameter [μm]		125 ± 1	
Coating diameter [μm]		205 ± 10	
MFD [μm]	1310nm	8.7-8.8	8.4
λ_{cc} [nm]		1328-1359	1219-1251
Loss [dB/km]	1310nm	0.333	0.332-0.334
	1550nm	0.192-0.193	0.187-0.191
XT [dB at 1km]	1310nm	n/a	-78
	1550nm	-38	-41
Average bend radius [m] in fiber spools		~0.15	~0.09



(a) Schematic drawing of longitudinal direction

(b) Schematic diagram of cross-sectional deformation

Figure 3. Schematics of 12-fiber Freeform Ribbon [9].

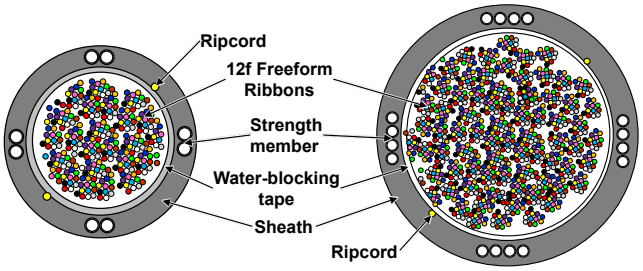


Figure 4. Schematics of (left) 288-fiber and (right) 864-fiber cables using Freeform Ribbons.

Figure 5 shows the dependence of the core-to-core XT in the 4-core fibers in the fabricated 288-fiber and 864-fiber Freeform Ribbon cables during temperature cycling tests. The XT slightly decreased with temperature decreased. Since the XT of homogeneous MCFs is approximately linear proportional to the fiber bend radius [10], [11], the XT variation with temperature change can be considered due to the fiber bending radius change in cables. We can consider that the cable sheath shrinked and the fiber bending radius in the cables became slightly tighter when temperature decreased. The estimated XT at fiber bending radius (R) is 0.15 m and 0.09 m are also plotted in Fig. 5.

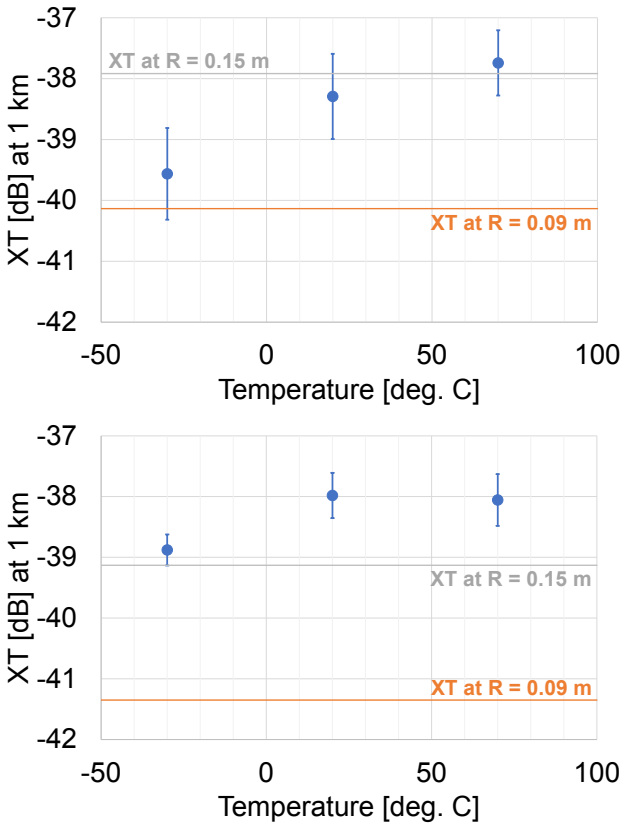


Figure 5. XT at 1550 nm vs temperature of the 4-core fibers in (top) 288-fiber and (bottom) 864-fiber Freeform Ribbon cables.

Using the linear proportionality of the XT to the fiber bending radius, the average fiber bend radius of the MCFs in a cable can be estimated from the XT difference of the MCF between the fiber spool and the cable drum when the drum diameter is much larger than the fiber spool diameter. Using this estimation method, we estimated the average fiber bend radius of the MCFs in the fabricated 288-fiber cable and 864-fiber cable, as shown in Fig. 6. The estimated average fiber bend radius was 0.1-0.15 m in the 288-fiber cable and ~0.2 m in the 864-fiber cable, which realized low XT compared to earlier studies with the estimated average fiber bend radius of ~0.3 m with the 288-fiber partially-ponded-ribbon cables with 200-µm-coating fibers.

Figure 7 shows the XT increase due to cabling, depending on the fiber spool radius before cabling and the fiber bending radius in cables, which clearly shows the proper control of the fiber bending radius in cables is important to realize low XT MCF cables. The fabricated cables demonstrate that partially-bonded-ribbon cables with 200-µm-coating MCFs can also suppress the XT increase due to cabling and can relax the MCF XT requirements.

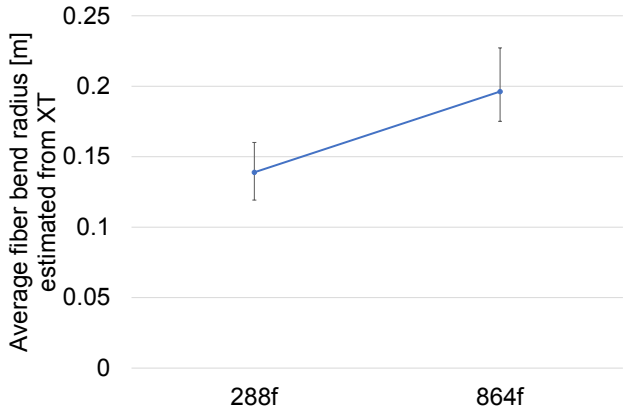


Figure 6. Fiber bending radius in the fabricated Freeform Ribbon cables, estimated from the XT change in the 4-core fibers before/after cabling.

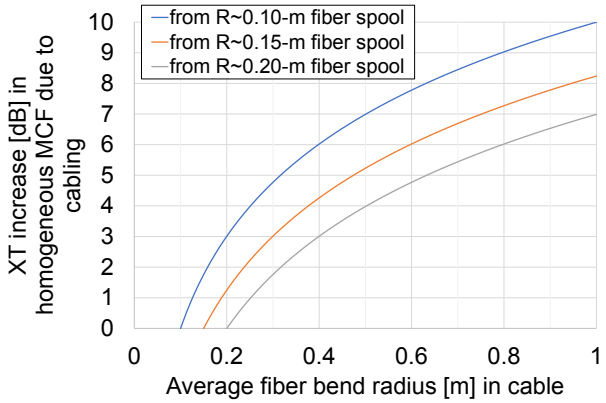


Figure 7. XT increase in homogeneous MCFs due to cabling

4. Conclusions

We reviewed the recent progress of the MCF technologies for practical realization, and presented newly fabricated 288-fiber and 864-fiber partially-bonded-ribbon cables with 200-µm-coating MCFs, which can suppress the XT increase due to cabling, thanks to the proper control of average fiber bending radius in the cables. Our cabling technology will enable low XT MCF cables and help the practical realization of optical communication networks with thin and lightweight high-density MCF cables.

5. References

[1] T. Hayashi *et al.*, "Crosstalk Characteristics of Multi-Core Fibers with Different Cladding Diameters in High-Density Optical Cable with Freeform Ribbons," in *Int. Wire Cable Symp. (IWCS)*, Providence, 2018, p. P-6.

[2] Y. Sasaki *et al.*, "Optical-Fiber Cable Employing 200-µm-Coated Four-Core Multicore Fibers," *J. Lightwave Technol.*, vol. 40, no. 5, pp. 1560–1566, Mar. 2022.

[3] T. Matsui *et al.*, "Step-index profile multi-core fibre with standard 125-µm cladding to full-band application," in *Eur. Conf. Opt. Commun. (ECOC)*, 2019, p. M.1.D.3.

[4] T. Hayashi *et al.*, "Uncoupled Multi-core Fiber Design for Practical Bidirectional Optical Communications," in *Opt. Fiber Commun. Conf. (OFC)*, San Diego, 2022, p. M1E.1.
[5] D. Soma *et al.*, "Transoceanic-Class Transmission over Step-Index Profile Standard Cladding 4-Core Fibre with Bidirectional Transmission Technology," in *Eur. Conf. Opt. Commun. (ECOC)*, Basel, 2022, p. Th1D.2.
[6] T. Morishima *et al.*, "Simple-structure low-loss multi-core fiber LC connector using an align-by-contact method," *Opt. Express*, vol. 29, no. 6, pp. 9157–9164, Mar. 2021.
[7] T. Kikuchi *et al.*, "Low insertion loss and high return loss fiber bundle fan-in/fan-out for four-core multi-core fiber," in *OptoElectron. Commun. Conf./Photonics in Switching and Computing (OECC/PSC)*, 2022, p. TuC4-2.
[8] S. Gross and M. J. Withford, "Ultrafast-laser-inscribed 3D integrated photonics: challenges and emerging applications," *Nanophotonics*, vol. 4, no. 3, pp. 332–352, Nov. 2015.
[9] F. Sato *et al.*, "Characteristics of Ultra-High-Fiber-Count and High-Density Optical Cables with Pliable Ribbons," in *Int. Wire Cable Symp. (IWCS)*, Orlando, Florida, 2017, pp. 304–311.
[10] T. Hayashi, "Multi-Core Fiber Technology from Design to Deployment," in *Eur. Conf. Opt. Commun. (ECOC)*, Basel, 2022, p. Mo4D.1.
[11] T. Hayashi *et al.*, "Design and fabrication of ultra-low crosstalk and low-loss multi-core fiber," *Opt. Express*, vol. 19, no. 17, pp. 16576–16592, Aug. 2011.

6. Pictures of Authors



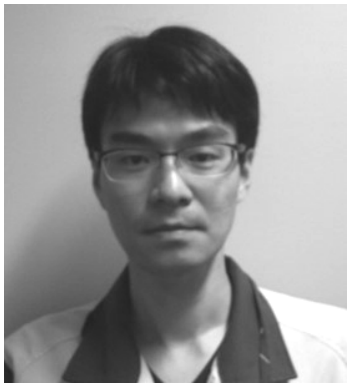
Tetsuya Hayashi received the B.E. and M.E. degrees in electronic engineering from the University of Tokyo, Japan, in 2004 and 2006, respectively, and the Ph.D. in engineering from Hokkaido University, Sapporo, Japan, in 2013.

In 2006, he joined Optical Communications Laboratory, Sumitomo Electric Industries, Ltd., Yokohama, Japan. He has been engaged in research and development on optical fibers and fiber optics. He is currently a Group Manager for advanced optical fiber R&D. He has authored and coauthored more than 120 publications in international journals and conference proceedings, and four book chapters.

Dr. Hayashi is a Senior Member of the Institute of Electronics, Information and Communication Engineers (IEICE) of Japan, the Institute of Electrical and Electronics Engineers (IEEE), and Optica (formerly OSA). He received various awards and prizes including the Tingye Li Innovation Prize from OSA at Optical Fiber Communication Conference (OFC) 2017.

Ayumi Inoue received the B.E and M.E. degrees in Applied Chemistry from Keio University, Kanagawa, Japan, in 2017 and 2019, respectively.

In 2019, she joined Optical Communications Laboratory, Sumitomo Electric Industries, Ltd., Yokohama, Japan, and since then has been engaged in research and development of optical fibers.



Yohei Suzuki received his M.S. degree from Tokyo University of science in 2006. He joined Sumitomo Electric Industries, Ltd. in 2006 and he has been engaged in plant and process engineering of optical cables and in development of optical fibers and cables since then.

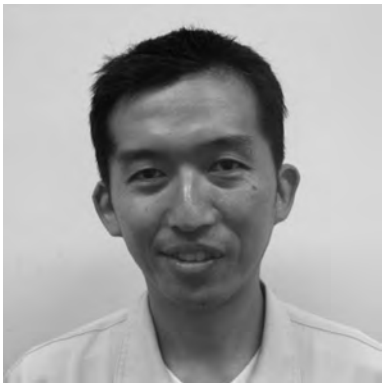


Takuji Nagashima received the B.E. and the M.E. degrees in electronic engineering from Kyoto University, Kyoto, Japan, in 2005 and 2007, respectively.

In 2007, he joined Optical Communications Laboratory, Sumitomo Electric Industries, Ltd., Yokohama, Japan, and since then has been engaged in research and development of optical fibers.



Yuki Shimoda received his M.S. degrees from Osaka University in 2001. He joined Sumitomo Electric Industries, Ltd. in 2001 and has been engaged in engineering and development of optical fibers and cables since then. He is a Project Manager of Data Center Optical Cable Engineering Group in Optical Fiber and Cable Division.



Fumiaki Sato received his M.E. degrees from Tohoku University in 2000. He joined Sumitomo Electric Industries, Ltd. in 2000 and he has been engaged in design and development of optical fibers and cables since then. He is a Group Manager of Data Center Optical Cable Engineering Group in Optical Fiber and Cable Division.

Low attenuation orbital angular momentum fiber

Shuo Xu*[a,b], Li Zhang [a,b], Lei Shen [a,b,c], Lei Zhang [a,b,c], Jie Luo [a,b,c], Liubo Yang [a,b]

[a]State Key Laboratory of Optical Fiber and Cable Manufacture Technology, Wuhan 430073, China

[b]Yangtze Optical Fiber and Cable Joint Stock Limited Company, Wuhan 430073, China

[c]Optics Valley Laboratory, Wuhan 430073, China

+86-027-6788-7509 · xushuo@yofc.com

Abstract

In order to realize the possibility of OAM fiber for long-distance trunk transmission, we have developed a new type of OAM fiber, which supports four modes of transmission simultaneously. The test results show that the fiber has good mechanical properties and hydrogen aging performance, the attenuation of the four modes before and after cabling lower than 0.215dB/km, and the maximum additional loss of the fiber temperature cycle test lower than 0.013dB/km. The orbital angular momentum optical fiber designed and developed in this paper can meet the actual needs of cabling engineering. Orbital angular momentum fiber is the preferred solution for next-generation long-distance high-capacity fiber-optic transmission.

Keywords: OAM fiber; attenuation; hydrogen aging performance; optical cable environmental performance

1. Introduction

In recent years, with the explosive growth of various communication traffic caused by cloud computing, streaming media, etc., single-mode optical fiber communication capacity is facing the limit of approaching the Shannon–Hartley theorem, and the development of optical fiber communication ushered in unprecedented opportunities and challenges. Researchers have made varying degrees of breakthroughs in the transmission rate and capacity of communication networks from multiple physical dimensions [1].

Since 2012, the space division multiplexing technology based on multi-core fiber and few mode fiber has become one of the hot spots of high-capacity optical fiber communication. The orbital angular momentum (OAM) multiplexing method in space division multiplexing is one of the best physical dimensions to break through communication challenges [2-4]. The OAM mode only requires 4*4 MIMO signal processing at the receiving end to simultaneously carry more data capacity.

OAM fiber is mainly used for various transmission experiments in laboratory scenarios [5-8] due to its complex doping system and preparation difficulty compared to ordinary single-mode fiber, and there is almost no research in long-distance communication fields such as cabling. Therefore, it is necessary to develop an OAM fiber with optical performance comparable to traditional single-mode fibers, low attenuation, excellent hydrogen aging performance and environmental testing performance, and can be applied in long-distance communication fields.

In order to meet the above requirements, this article designs and develops an OAM fiber, with the fiber diameter and coating layer diameter consistent with traditional single-mode fibers. Using the above OAM optical fibers for cabling, successfully passed environmental testing.This article validates the design, key parameters, and performance of the OAM fiber mentioned above, and analyzes and discusses its application prospects in long-distance trunk communication.

2. Design, preparation, and testing platform construction of optical fibers

2.1 Design of optical fibers

OAM fiber adopts a groove assisted structure in the design of refractive index fiber structure, which can improve the bending performance of the fiber [9]. The core layer adopts a circular core structure to achieve transmission of multiple OAM modes. Figure 1 is a schematic diagram of the OAM fiber optic profile.

In order to ensure the reliability of optical fibers during installation and transmission in the final application scenario, this article strictly controls the core rod preparation process, optimizes the drawing tension and speed, and achieves small-scale mass production and stable output of optical fibers, which can withstand a screening strength of 100kpi.

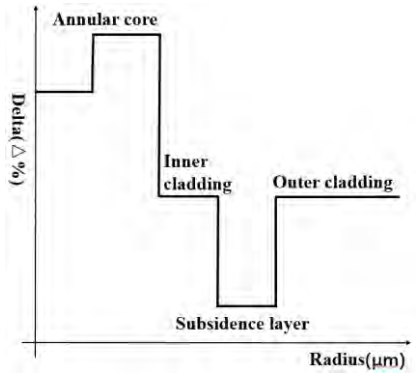


Figure 1. Fiber glass profile schematic of OAM fiber

2.2 Construction of testing platform

The OAM testing platform can modulate high-order modes through spatial light and couple them into a few mode fiber for transmission, thus achieving optical performance testing of various modes.Figure 2 is a schematic diagram of the excitation light path. The single wavelength excitation light emitted by a laser source is amplified by EDFA and connected to a polarization controller, which is then coupled into a fiber collimator to form a parallel excitation light beam.The excitation light is modulated into various higher-order modes through a phase plate, and coupled into the OAM fiber by an objective lens. The mode patterns transmitted in the OAM fiber are ultimately captured and displayed by a CCD camera, and the attenuation of each mode can be tested through this optical path.Figure 3 shows the 0-3 mode light spot excited by the excitation optical path using the testing platform shown in Figure 2,

as well as the light spot transmitted through a 4km fiber. It can be seen from the figure that the OAM fiber can support transmission of four modes.

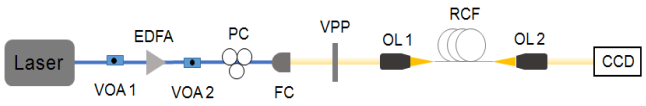


Figure 2. Schematic diagram of excitation light path

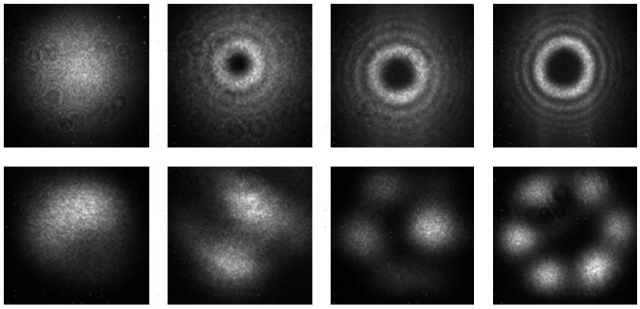


Figure 3. Mode spot before and after fiber transmission

2.3 Main parameters of optical fiber

Based on the testing platform shown in Figure 2, this article tested the attenuation of OAM optical fiber before and after cabling. Table 1 shows the main parameter indicators of OAM optical fiber. The attenuation of each mode is relatively low, and the optical fiber can withstand a screening tension of 100kpi, which is in line with the application scenario of long-distance trunk lines. Compared to traditional single-mode optical fibers, the same outer diameter of the optical fiber has four times the number of transmission channels, which is conducive to the miniaturization of optical cables and optical components.

Table 1. Key parameters of OAM fiber

The key parameters	Typical value	Unit
Cladding diameter	125±0.7	[um]
Fiber diameter	245±10	[um]
Attenuation of natural fiber at 1550nm	0.207 (0 mode)	[dB/km]
	0.207 (1 mode)	[dB/km]
	0.207 (2 mode)	[dB/km]
	0.207 (3 mode)	[dB/km]
Fiber attenuation at 1550nm after cabling	0.208 (0 mode)	[dB/km]
	0.208 (1 mode)	[dB/km]
	0.209 (2 mode)	[dB/km]
	0.213 (3 mode)	[dB/km]
Screening tension	100	kpsi

3. Performance testing of optical fibers

3.1 Mechanical properties

In order to ensure the stability of optical fiber transmission, we conducted tests on the tensile strength, dynamic fatigue (n_d value), and peeling force of OAM optical fibers. The experimental results are shown in Table 2, and the test results indicate that the mechanical properties such as dynamic fatigue and tensile strength of the optical fiber comply with the IEC 60793-2-50-2018 standard for single core optical fibers.

Table 2. Mechanical performance of OAM fiber

Test items	Test Results	#1	#2	#3
Tensile strength (GPa)	$F_{15\%}$	4.98	5.10	5.28
	$F_{50\%}$	5.26	5.17	5.33
n_d Value	/	27.8	28.4	26.8
Strip force (N)	avg.	1.7	1.7	1.8
	peak	1.8	1.8	1.9

3.2 Registered Names and Trademarks

To further verify the bending performance of OAM fiber, we conducted macro bending and micro bending tests on it. The macro bending test conditions were as follows: the radius of 15mm was wound 10 times, and the additional loss at 1550nm was only 0.002dB, which is similar to the system error. Therefore, the macro bending data is not listed in this article.

Then, a micro bending test was conducted on the OAM fiber, and the micro bending test method met the IEC TR 62221-B specification. The micro bending losses of the four modes of OAM fiber at the wavelength of 1550 nm are shown in Table 3. The micro bending losses of the fiber are similar to G.657.B3 and smaller than those of the single mode G.654 fiber. The micro bending loss of all modes is very small, and there is no significant difference between modes. This indicates that OAM optical fiber can withstand harsh environments and has good operational reliability.

Table 3. Microbending loss of OAM fibers

Mode	0 mode	1 mode	2 mode	3 mode
Additional Att.(dB/km)	0.109	0.136	0.212	0.155

3.3 Hydrogen aging performance

Hydrogen gas diffuses into the optical fiber and reacts with defects in the glass, leading to increased attenuation of the optical fiber, which may cause irreversible damage to the optical fiber. In order to test the hydrogen aging resistance of OAM optical fibers, we conducted multiple hydrogen aging tests on OAM optical fibers to detect the attenuation changes of the fibers. The experimental results of hydrogen aging are shown in Figure 4, where it can be seen that the additional attenuation of the third order mode is relatively high. The reason for the high additional attenuation of the third order mode is that it is closer to the outside of the mode field and more susceptible to the influence of hydrogen. After baking, the additional attenuation of the optical fiber is lower than that of the hydrogen aging process. Throughout the entire test process, the maximum hydrogen loss of OAM optical fiber was 0.015dB/km, and the hydrogen aging performance of the optical fiber can meet the requirements of long-distance trunk communication.

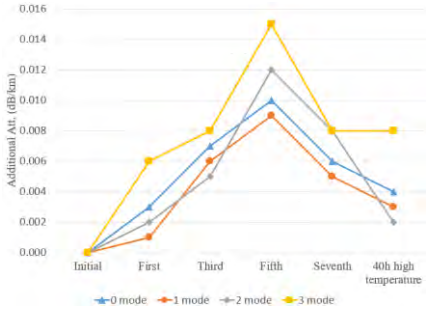


Figure 4. Hydrogen aging performance of OAM fiber

4. Environmental testing performance before and after cable formation

The OAM optical fiber designed in this article supports four modes of transmission. Without increasing the number of links, higher transmission capacity can be achieved per unit volume, greatly improving the channel density of the optical cable. Compared to optical cables made of single core fibers, OAM optical cables with the same diameter have larger transmission capacity. Table 4 lists the differences in the number of optical cable channels of the same size formed by different types of optical fibers, demonstrating the enormous application potential of OAM optical fibers in cabling.

Table 4. Comparison between OAM fiber and std-G.654.E fiber cable

Fiber Type	Fiber OD (μm)	Loose Tube OD (mm)	Sheath Thickness (mm)	Cable OD (mm)	Number of Channels
G.654.E	125/245	2.4(12F)	1.8	17	144
OAM	125/245	2.4(12F)	1.8	17	576

4.1 Environmental testing performance of OAM optical fibers

In order to further verify the practical application performance of OAM fiber, the Temperature cycling test of OAM fiber is conducted. The initial fiber attenuation was measured at room temperature as a reference value. The high and low temperature cycling test was conducted within the range of -60 ℃ to 85 ℃. Due to the stable 0-order fundamental mode of OAM fiber, the additional attenuation of the fundamental mode must be smaller than that of the high-order mode. Therefore, the 0-order additional attenuation was not tested in this fiber TCT test. Figure 5 shows the additional attenuation diagram of TCT in each mode of the fiber. Since the third-order is more sensitive to the first-order and second-order attenuation changes, the third-order Temperature cycling test added two more cycles.

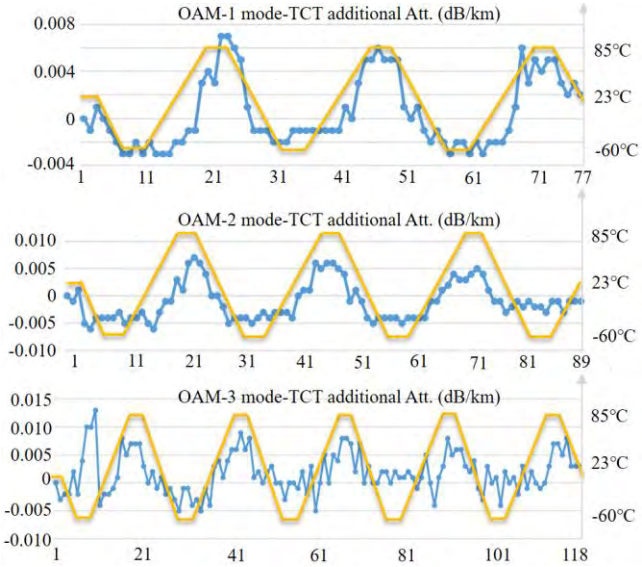


Figure 5. TCT additional attenuation of OAM fiber.

It can be seen that the OAM fiber has a higher additional attenuation in the third-order mode, which is because the third-order mode is closer to the outside of the mode field and has a higher possibility of light leakage. The maximum additional loss at 1550 nm wavelength is 0.013 dB/km, and after TCT testing, the additional loss recovered to room temperature is less than 0.005 dB/km. This result indicates that OAM fiber can withstand harsh environments and has good reliability.

4.2 Environmental testing performance of optical cables

In order to further verify the application performance of OAM fiber coloring, during and after the cable formation process, a 4km loose sleeve layer twisted non armored test optical cable was prepared, which consists of six loose sleeves. Each loose sleeve contains 12 core OAM fiber, with a diameter of 2.4mm and a thickness of 0.325mm. The thickness of one side of the cable skin is 1.8mm, and the middle steel wire is 1.6-1.8mm. The final outer diameter of the optical cable is 11mm. Taking the attenuation value of the uncolored optical fiber as the initial value, the optical cable was subjected to environmental testing: first, two Temperature cycling were conducted within the range of -40 ℃~70 ℃, then it was aged at 85 ℃ for 7 days, then two Temperature cycling were continued within the range of -40 ℃~70 ℃, and finally it was restored to room temperature. The test results are shown in Figure 6.

During the entire process of cable formation and environmental testing, due to the third order mode being closer to the outside of the mode field, the probability of light leakage is higher. It can be seen that the additional attenuation of the third order mode is higher than that of the first and second order modes. The maximum additional attenuation of OAM fiber at 1550nm wavelength is ⩽ 0.03dB/km (Figure 6), which complies with the IEC 60794-5-10-2014 specification (additional attenuation ⩽ 0.05 dB/km) and meets the requirements of long-distance communication applications.



Figure 6. Cabling and cable environmental performance of OAM fiber

5. Conclusions

We designed and prepared an OAM fiber for long-distance communication, introduced the testing optical path diagram of the fiber, tested the mechanical, hydrogen aging, and environmental performance of the fiber, and also conducted special environmental tests for coloring, cabling, and optical cables. The test results show that the optical parameters of this OAM optical cable are equivalent to traditional G.654. E optical cables. The special environmental testing of the optical cable shows that the OAM fiber optic cable can meet long-term application requirements. OAM fiber optic cabling can significantly improve the channel density of optical cables, and has great application prospects in the field of high-density long-distance trunk communication.

6. Acknowledgments

This work was supported by National key research and development projects 2021YFB2800902.

7. References

[1] Y. Awaji, J. Sakaguchi, B. J. Puttnam, et al. "High-capacity transmission over multi-core fibers." Optical Fiber Technology 35(2):100-107 (2016).

[2] Z. Wang, G. Tu, S. Gao. "Transmission and Generation of Orbital ANGULAR Momentum Modes in Optical Fibers." Photonics 8.7:246 (2021).

[3] C. Brunet and L. A. Rusch. "Optical fibers for the transmission of orbital angular momentum modes." Academic Press 35 (2017).

[5] R. Zhang, H. Tan, J. Zhang, et al. "A novel ring-core fiber supporting MIMO-free 50km transmission over high-order OAM modes." Optical Fiber Communication Conference (2019).

[6] X. D. He,J. Tu, X. Xu, et al. "All-fiber third-order orbital angular momentum mode generation employ an asymmetric long-period fiber grating." Optics Letters 45.13 (2020).

[7] L. Shen , C. Su, X Sun, et al. "Design and Fabrication of 6-LP-mode fiber with low DGD and low loss." Asia Communications and Photonics Conference (2016).

[8] W. Zhou, L. Wang, L. Shen, et al. "First demonstration of ultra-long-distance mode-division multiplexing transmission using orbital angular momentum (OAM) modes over 150-km low-loss ring-core fiber without amplifiers." European Conference on Optical Communication (2019).

[9] J. W. Zhang, J. Liu, L. Shen, et al. "Mode division multiplexed transmission of WDM signals over 100-km single-span OAM fiber." Photonics Research 8.7(2020).

SESSION 9

Click on a session below to navigate to that section of the Proceedings.

SESSION 9: CODES & STANDARDS

Chairperson: Dmitriy Bodik, UL Solutions, USA

9-1 **Clarifying the Changes – Update on Revisions To UL'S Certification Documents;** Ms. Susan Stene, *UL Solutions, USA*

9-2 **Emissivity - A Relevant Parameter for Burn Testing According to EN 50399;** Dr. Waldemar Stoecklein, *Corning Optical Communications, Germany*

9-3 **Single Pair – Next Steps;** Mr. Dave Hess, *Cord Data, USA*

9-4 **Predictive Modeling of Large-Scale Flame Tests on Cables Using Cone Calorimeter;** Dr. Jiyuan Kang, *UL Solutions, USA*

9-5 **Cabling for Fault-Managed Power Systems (What Is Class 4?);** Ronald Tellas, *Belden, USA*

Click here to return to the **Table of Contents**

Clarifying the Changes – Update on Revisions to UL Certification Documents

© 2023 UL LLC. All rights reserved

Susan Stene
UL Solutions
Fremont, Calif.
+1-510-319-4312 · Susan.L.Stene@ul.com

Abstract
UL Solutions is an independent organization that has been evaluating products in the interest of public safety for over 125 years. UL Solutions staff are involved in many aspects of the wire and cable industry, working with code authorities, manufacturers, and various technical committees to develop safety standards for wire and cable.

This paper covers new proposals and recent revisions to UL Standards for wire and cable, and to standards covered under Consejo de Armonizacion de Normas Electrotecnicas de Las Naciones de Las Americas (CANENA) harmonization activities. CANENA covers both binational harmonization with the Canadian Standards Association (CSA) and tri-national harmonization with CSA Group and Asociación de Normalización y Certificación (ANCE).

Keywords: wire; cable; standards; harmonization; ANCE; CSA; CSDS; NEC; Underwriters Laboratories; UL Standards & Engagement. ULSE; UL 13; UL 44; UL 62; UL 66; UL 83; UL 444; UL 493; UL 719; UL 758; UL 854; UL 1072; UL 1277; UL 1581; UL 1651; UL 2250; UL 2263; UL 2276; UL 4127; UL 1400-2, UL 6288, Class 4

1. Introduction
A review of upcoming standards proposals and recently published revisions is important, so that both manufacturers and users are aware of the changes, understand the ramifications of the changes, and may take the appropriate steps to ensure that the wire and cable manufactured to these standards continue to comply with the requirements.

2. Standards writing and development
UL Standards & Engagement uses its technical committees (TCs) for consensus standards development. TCs are a central part of the process by which ULSE develops and maintains its Standards. A TC is a group of individuals representing a variety of interest groups related to the UL Standard. UL Solutions has membership on the TCs related to all wire and cable standards. The TC is responsible for reviewing, commenting, and voting on proposals for new UL Standards or revisions to existing UL Standards.

The UL Solutions Collaborative Standards Development System (CSDS) provides online access to the UL Standards development process.

UL Solutions is also involved in the development of standards harmonized under the CANENA process. This process involves manufacturers and standards development organizations (SDOs) from at least two of the three North American countries. UL Solutions also participates in the standards writing committees of other organizations such as CSA Group, IEC, TIA, SAE and ASTM.

The updates and revisions described are current as of July 1, 2023.

3. Revisions to UL Standards or Outlines of Investigation

3.1 UL 66, the Standard for Fixture Wire

3.1.1 Requirements for Types HF, HFF and RFH-1 were added Jan. 18, 2023. Types HF and HFF are ECTFE insulated fixture wires and Type RFH-1 is a 300V version of RFH-2, a XL or rubber insulated fixture wire.

3.2 UL 493, the Standard for Thermoplastic-Insulated Underground Feeder and Branch-Circuit Cables

3.2.1 A revision for the push-in terminal markings was published Jan. 9, 2023. The revisions align the tag markings for 12 – 10 AWG copper-clad aluminum with UL 20, the Standard for General-Use Snap Switches, and UL 498.

3.2.2 Further revisions to the tag markings were proposed March 10, 2023. This proposal deletes specific requirements for the types of devices that copper-clad conductors can be terminated to. This would align the requirements for copper-clad aluminum conductors with those of copper and aluminum conductors. The comment period for this proposal closed on April 25, 2023. Although this ballot received consensus, similar proposals to UL 719 and UL 854 did not achieve consensus. Therefore, a technical committee meeting was held on May 24, 2023, to discuss the comments for all three standards. Comments are being resolved and a recirculation area will be available soon.

3.3 UL 719, the Standard for Nonmetallic-Sheathed Cables

3.3.1 The same proposal for the push-in terminal marking as noted under UL 493 was published January 9, 2023. Similarly, a revised proposal and TC meeting as discussed for UL 493 occurred. Comments are being resolved and a recirculation area will be available soon.

3.4 UL 758, the Standard for Appliance Wiring Material

3.4.1 Table 5.3 covering the conductor materials was revised Nov. 11, 2022. These revisions added requirements for high strength annealed copper alloy conductors. The revisions also changed the conductor diameter requirements from AWG size to diameter for ASTM B3 and B33 conductors.

3.5 UL 854, the Standard for Service-Entrance Cables

3.5.1 A revision for the push-in terminal marking, the same as noted under UL 493 was published Jan. 4, 2023. Similarly, a revised proposal and TC meeting as discussed for UL 493 occurred. Comments are being resolved and a recirculation area will be available soon.

3.6 UL 1072, the Standard for Medium-Voltage Power Cable

3.6.1 A proposal to align the thickness requirements in UL 1072 with those in the ICEA and CSA standards for similar products published March 16, 2023.

3.6.2 An ad-hoc industry meeting was held to discuss the required samples for the vertical tray flame test. The proposal under discussion indicated that a single conductor cable, when subjected to the vertical tray flame test(s) would only qualify the manufacturer to mark single conductor constructions. A similar revision would apply to multi-conductor cables. Following the meeting a new proposal was drafted and will be proposed.

3.7 UL 1277, the Standard for Power and Control Cable

3.7.1 The revision to clarify the test program for jackets thinner than prescribed and to permit laser printing of the surface markings was published Oct. 27, 2022.

3.8 UL 1400-2, the Standard for Fault-Managed Power Systems – Part 2: Requirements for Cables

3.8.1 A new type – CL4Z – has been added. Type CL4Z is intended for outdoor use only and is not to be attached to or used within a building structure. Requirements for jacket materials that are different than those described in Section 50 of UL 1581 have also been added. These published July 13, 2023.

3.9 UL 1581, the Reference Standard for Electrical Wires, Cables and Flexible Cords

3.9.1 The addition of the requirements for copper-clad aluminum that meet the requirements in article 310.3 of the NEC and the revisions to include a new table for flexible polyvinylidene fluoride (PVDF) were published November 15, 2022.

3.10 UL 1651, the Standard for Optical Fiber Cable

3.10.1 A revision to delete the carbon-arc exposure from the sunlight resistance test was published April 13, 2023.

3.11 UL 2250, the Standard for Instrumentation Tray Cable

3.11.1 Instrumentation tray cables was relocated in the NEC from Article 727 to Article 335. A proposal to reflect this change will be made to the scope of UL 2250.

3.12 UL 2882, the Standard for Radio Head Cable

3.12.1 Revisions to the outline include correction of the oil resistance marking from PR2 to PRII. The requirements for a jacket rated 105C were removed as the maximum rating of these cables is 90C. The marking for the temperature rating of the jacket was made optional. Reference was made to UL 1569 for constructions employing an armor.

3.13 UL 6288, the Standard for Decorative Lighting Cords

3.13.1 The proposed first edition of UL 6288 was presented to the technical panel for their preliminary review on May 9, 2023, for a 2-week comment period. This Standard will contain all of the decorative cord types that are currently in UL 62 for US installations. For Canada, the requirements will be relocated to CSA C22.2 no. 127. In Mexico, the requirements are located in NMX-J-588. Once the requirements are published in the US and Canada, the requirements will be withdrawn from UL 62 and CSA C 22.2 no 49.

The comments received during the preliminary review are being reviewed. It is expected that the draft will be available for the technical committee ballot in late August.

4. Revisions to harmonized standards

4.1 UL 44, the Standard for Thermoset-Insulated Wires and Cables

4.2.1 The current edition of UL 44 was published Jan. 9, 2018, with revisions dated May 14, 2021. The CANENA harmonization committee is currently reviewing proposal to UL 44. Significant proposals include:

- Adding additional acceptance criteria for the glancing impact test to look for splitting of the insulation
- Adding requirements for jacketed XHHW wire types
- Revision to the criteria for the dropping particles test
- Proposal to require the burning particles test for those cables that are marked FT2
- Clarification of test procedure to be applied to composite constructions

- Adding construction and test requirements for types XHWN and XHHN
- Adding halogen free requirements

4.2 UL 62, the Standard for Flexible Cords and Cables

4.2.1 The 20th edition of the tri-national standard is dated July 6, 2018. The draft for the 21st edition is nearing completion. Once completed, it will be sent to the respective standards development organizations for their review processes. The last significant item still pending a decision involves the need to perform a repeated flexing test on elevator cables using 21 – 24 AWG communication and signal circuits.

4.3 UL 83, the Standard for Thermoplastic-Insulated Wires and Cables

4.3.1 The current edition of UL 83 was published July 28, 2017, with revisions dated April 10, 2020. The CANENA harmonization committee is currently reviewing proposals to UL 83. Those proposals include:

- Clarifying when the RP1 test is required in Mexico
- Including the method for evaluating print that is under a nylon jacket
- Correcting the method of determining compliance in the dry insulation resistance method
- Adding the test temperature for the cold bend test performed on submersible pump cables
- Revising the markings for conductors similar to those discussed for UL 719, UL 493 and UL 854
- Referencing the requirements in UL 1581 for copper-clad aluminum conductors

4.4 UL 444, the Standard for Communications Cables

4.4.1 A proposal dated April 7, 2023, was submitted to add a new type CMX outdoor-plenum cable, to remove the carbon arc from the method for performing the sunlight resistance test, and to add laser printing as an option for surface marking the cable. A clarification of the compliance criteria on the VW-1 flame test was also proposed. The ballot closed on May 8, 2023. Consensus was achieved and there were no comments to resolve. The revisions published on June 30, 2023.

4.5 UL 1569, the Standard for Metal Clad Cables

4.5.1 The current edition of UL 1569 was published May 4, 2018. The CANENA harmonization committee is currently reviewing proposals. Those proposals include:

- Adding 1000V to the scope
- Review of the requirements for the overload test

4.6 UL 1426, the Standard for Boat Cables

4.6.1 The CANENA committee is drafting the first harmonized edition of the standard for boat cables. The standard will be based on the US requirements, as Canada and Mexico do not currently have standards covering the product. In addition to reformatting the standard to meet the style for harmonized standards, the following new criteria are proposed to be added:

- Requirements for copper conductors
- Requirement that all conductors be tinned
- Requirement that all conductors be flexible stranded (ASTM Class K or M)
- Addition of FT1 and FT2 flame tests
- Optional FT4 flame test rating
- Optional 1000 hr sunlight resistance
- Mandatory -40C rating

4.7 UL 2263, the Standard for Electric Vehicle Cables

4.7.1 The first edition was published May 9, 2022. A new revision cycle is starting. The standards development organizations made a call for proposals, and there was no input from the respective national technical committees. Items under consideration for the next edition include:

- Addition of requirements for electric vehicle cables containing fluid filled tubes used for cooling
- Increase in scope to include a 1500Vdc rating
- Clarification of crush test method

4.8 UL 2556, the Standard for Wire and Cable Test Methods

4.8.1 The current edition of UL 2556 was published April 30, 2021, with revisions dated June 3, 2021. The CANENA harmonization committee is currently reviewing proposals to UL 2556. Those proposals include:

- Adding a method for measuring the percent overlap of a spirally or longitudinally applied tape,
- Defining tolerances on the kraft paper used in small-scale flame tests
- Incorporating the best of UL 1685 into the vertical tray flame test methods
- Clarifying how to proceed when particles drip on the lower clamp in the small-scale flame tests

- Clarifying where tensile and elongation samples shall be selected if laser printing is used to mark a cable
- Clarifying which procedures apply to which cable types when performing a detailed exam/construction review.
- Defining the position of the inner blue cone when performing the FT5 flame test

5. Conclusion

UL Standards are used to assess products, test components, materials, systems, and evaluate environmentally sustainable products, renewable energies, food and water products, recycling systems and other innovative technologies. Evolving technology and advancements in how to address safety and sustainability issues require new standards or the revision of existing standards. Manufacturers, consumers, government officials, industrial and commercial users, inspection authorities and others must be mindful of the revision process and be aware of the proposed changes and provide relevant input by using the standards development process.

6. Acknowledgments

Special thanks to Anthony Tassone, Jeff Lutke and Paul Knapp, all of UL Solutions, for their contributions of the content and review of the final document.

7. Author



Susan Stene
UL Solutions
47173 Benicia Street
Fremont, CA 94538

Ms. Stene works for UL Solutions as a principal engineer in wire and cable. She brings over 34 years of UL Solutions experience to this role. While most of her time at the company was spent in wire and cable, she has also worked in such diverse areas as fork-lift trucks, flammable liquid tanks and office furnishings. Prior experience includes work as a manufacturing engineer and research chemist at a heat-shrink tubing manufacturer.

In addition to being a member of ULSE technical committees nos. TC83, TC719, TC758, TC814, TC2263 and TC4703, Ms. Stene is a member of IEC TC 20 working groups 17 and 19; the CANENA harmonization committees for building wire, flexible cords, photovoltaic wire and test methods; CSA ICWC01, 02 and 06; NEC code-making panel 6; and an invited guest to the NEMA Section 7 committees on high performance wire, building wire and flexible cords. She was recognized by UL Solutions as a Distinguished Member of Technical Staff, a part of the William Henry Merrill Society.

Emissivity – a relevant parameter for burn testing according to EN 50399

Thomas Meyer, Dr. Waldemar Stoecklein, Anish Gunjal, Hariom Bhargava
Corning Optical Communications GmbH & Co. KG, 12489 Berlin, Germany
+49 (0)30 297 720 4015 · thomas.meyer@corning.com
+49 (0)30 297 720 4004 waldemar.stoecklein@corning.com
+91 (20)69101601 gunjalaa@corning.com, +91 (20)69101601 bhargavah@corning.com
+

Abstract
In June 2017 a new European regulation (Construction Product Regulation) became effective Subsequently, it became mandatory in Europe for all cables to be rated for their ability to resist fire before they can be used permanently in buildings. The test procedures are described in the European (Cenelec) standards EN 50399 (CPR tests) and the classification of the cables is defined in the standard EN 13501-6. The corresponding CPR classes of cables are mainly determined by measuring their vertical flame spread (FS), heat, and smoke release parameter. The tests will be performed by certified independent test laboratories (Notified Bodies).

To be able to characterize the newly developed Flame Retardant cables, a brand new burn chamber was installed in the Corning cable development facility at the Corning Technology Center Berlin (CTCB). Intensive burn testing started in 2015. From the beginning a reference cable was used for the characterization of the burn chamber conditions. Especially, the vertical flame spread (FS) was monitored since it is very sensitive against any changes in the operating as well as environmental conditions. Comparative round robin tests in European test labs were performed which showed a systematically lower average flame spread in the order of 0.4 m, measured on the reference cable. However, test results achieved in other newly installed chambers confirmed a higher flame spread comparable to that measured at the beginning in our chamber. Long term monitoring (2015 – 2022) of the FS in our chamber revealed a gradual decrease of the flame spread by approx. 0.2 m. The following paper will prove that the observations mentioned above can be explained by a gradual change of the emissivity of the inner walls of the burn chamber by "aging." The most prominent aging effect is the coverage of the originally shiny metall surfaces by a black soot.

Keywords: Construction Products Regulation, CPR, EN 50399, emissivity, aging, coating, CTCB (Corning Technology Center Berlin),

1. Introduction
The European Construction Products Regulation (CPR) came into force on 1 July 2017. All concerned cable products must be tested and certified according to the CPR by accredited test laboratories before they can be placed on the European market. The testing effort is considerable. It has also been shown that the new test method for investigating the cable burn performances according to the EN 50399 standard imposes very high requirements on the test laboratories in order to obtain comparable and consistent results. As shown before in IWCS contributions by Corning [1], [2], deviations may occur between the test results for an identical cable in different test laboratories, and often the causes are very difficult for the test laboratories to identify.

To improve the situation, Corning developed a reference cable which excludes any effects of varying results caused by the cable (see [3]).

Cable testing has been performed since 2015 on a brand new burn chamber which fulfilled all requirements listed in the standard CLC EN 50399. All parameters, e.g., gas flow rates for the burner supply, the gas analysis system, the smoke detection, heat transfer through the chamber walls were carefully monitored and measuring devices were calibrated. The impact of the air flow was investigated and adjusted so it did not impact the burn results significantly (see [4]). The flame shape was monitored and verified to be in the boundaries as defined in CLC EN 50399 Annex K (see [5]). Environmental conditions (temperature, and humidity) were kept almost constant since tests were performed indoors in a controlled environment. Cable mounting was always done exactly the same way. Cable tension, cable spacing, total width of the mounted cables were monitored and kept constant.

It was believed that all parameters which could impact the burn test results did not varied to achieve the repeatability in experiments.

Nevertheless, the results achieved in our burn lab at CTCB showed a flame spread higher than 0.4 m than the average flame spread observed during EU wide Round Robbin tests (see figure 2).

2. Observations
2.1 Round Robbin testing
As mentioned in the introduction Round Robbin tests were performed within certified test laboratories as well as industrial labs within the European Union. To ensure that the test results are comparable, all tests were performed on the reference cable [see Figure 1 and [3]). Test conditions were adjusted according to the settings defined in the standard EN 50399.

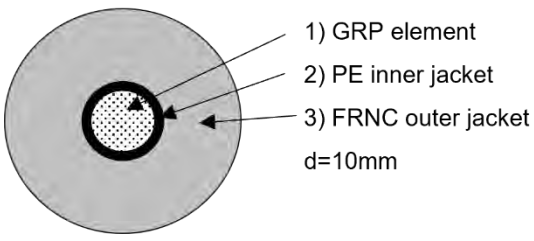


Figure 1. Cross section of the reference cable

Figure 2 shows the statistical spread of FS results for the experiments conducted in European labs (red: certified labs, blue: industrial labs) compared to the results achieved in our burn test lab at CTCB (green).

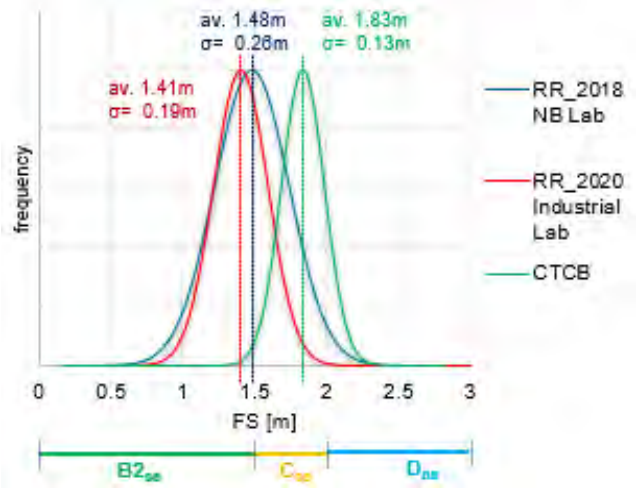


Figure 2. Flame spread (FS) measured in different European Burn test laboratories and industrial labs in comparison to results achieved at CTCB.

It became obvious that the flame spread (FS) results differ remarkably even when the variation of the data is taken into account. The average values are 1.48 m for the Certified Test Labs and 1.41 m for the industrial labs. The average FS determined in our Berlin facility was around 1.83 m. The variation of the results (characterized by σ) is smaller when fewer labs are involved. Even though most of the parameters are "fixed" some unpredicted variation might occur which leads to more variation when more laboratories are involved.

The difference of approx. 0.4 m **cannot** be explained by statistical variations of the settings **within** the specified limits.

2.2 Burn testing in newly installed chambers

Another interesting observation was made, when FS results achieved in other newly installed burn chambers of the same brand were compared.

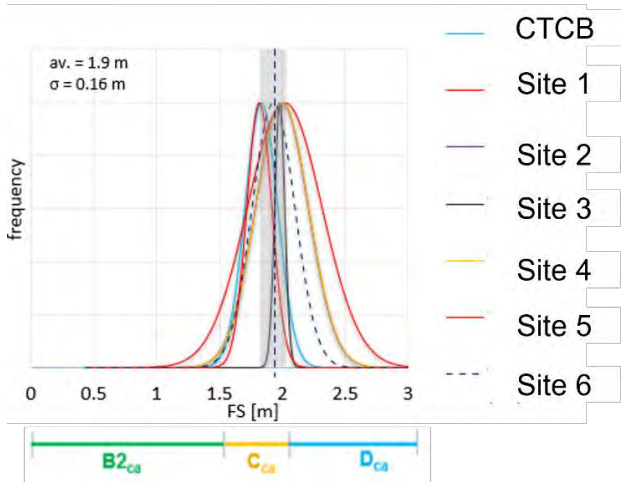


Figure 3. FS values achieved when the reference cable was tested in other "new" chambers of the same brand.

The distribution of the FS-data received from the different sites 1 to 6 and the distribution of the FS data from CTCB overlap (see Figure 3). The averages are 1,83 m (CTCB) vs 1.9 m (sites 1 to 6). That means that all new chambers (same brand) seem to show results which are remarkably higher than the FS-data from the other older laboratories.

2.3 Evolution of the flame spread with time

Our burn chamber was installed in 2015. Since then, we started to check the burn performance of the system with the help of a reference cable (see [3]). The graph shown in Figure 4 contains all FS data which were deduced from burn tests always performed with identical parameter settings. Even though a spread of the FS data is obvious the statistical analysis over the years shows a decrease of the FS from approx. 2.0 m in 2015 down to 1.8 m in 2021.

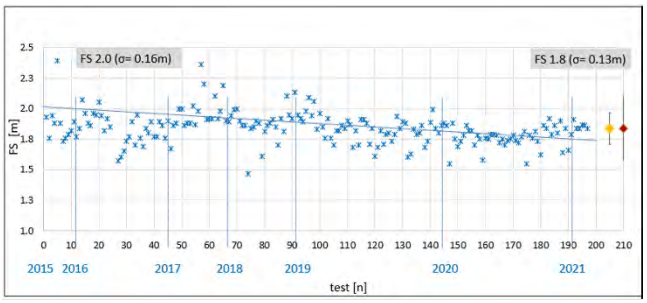


Figure 4. Flame spread measured on the reference cable under identical conditions between 2015 and 2021 at CTCB.

In the following paragraph a hypothesis which will explain these observations will be discussed.

3. Hypothesis

3.1 Qualitative explanation

After a careful investigation of the impact of variation of parameter settings it became obvious, that changes in the flame spread in the order of 40 cm can only be achieved when the allowed variation ranges for the different parameters, e.g. propane and air feed rates, flame shape, asymmetries in the air flow… were remarkably exceeded ([1], [2], (3], [4], [5]). Thus, most likely a parameter has to be taken into account which has not been addressed yet. It seems that the emissivity of the walls of the chamber might have the impact to explain all of the observations made so far. The following hypothesis was applied: The parameter emissivity of the surface of the inner walls of the burn chamber is not same in the chambers of the test laboratories. The parameter emissivity e can vary (theoretically) between 0 and 1. Chamber inner walls which are ideally black (e = 1) - absorbs all incident radiation. A surface which is shiny (typical for virgin polished metal surfaces) can approach e = 0 which means that most of the radiation is reflected. Chambers which have been in use for many years are approaching the state to be ideally black and thus have emissivity values e >0.9. "Young" chambers which have not been in operation for a long time still show a relatively shiny surface with emissivity values much lower than 0.9 (e.g. e between 0.4 and 0.7). In the case of high emissivity, thermal radiation is taken away from the interior of the chamber and thus less heat is present to support the burn of the cables. When however, the emissivity is low radiation is reflected from the walls and thus more heat is present at the cable surface to support the burn. Thus, a higher flame spread is expected

when wall emissivity is lower. For the situation of high emissivity (e > 0.9) a lower flame spread will occur.

Note: Other effects like loss of energy through the walls by heat flow are not taken into account. The impact on the flame spread is under evaluation.

4. Experiments to prove the hypothesis

To prove the hypothesis a series of experiments was performed:

1. Burn tests in a chamber with virgin / shiny metal surfaces (low emissivity),
2. Burn test in a chamber with a surface with high emissivity.
3. Burn test in a chamber "as it is" after 7 years of operation.

All experiments described below were performed in our CTCB burn chamber. For all burns the reference cable [3] was used. The emissivity of the surfaces was determined experimentally as described in the Annex A.

4.1 Burn tests in virgin chamber

To be able to perform experiments in a chamber with virgin/shiny metal surfaces the existing chamber had to be modified. Metal plates as used originally were ordered from the supplier of the chamber and installed on top of the existing plates (see Figure 5a).



a) „shiny" wall b) „aged" wall (as it is) c) „coated" wall

Figure 5. Burn chamber equipped with a) virgin metal plates, "shiny" e < 0.4, b) "aged" as it is, e = 0.6 to 0.8, c) "coated", e > 0.9

The emissivity was e < 0.4 (this Figure was taken from literature and can be seen as an upper limit. Normally the e values are smaller. Direct measurement on shiny metal surfaces is faulty when the method described in the Annex A is used).

Ten burns were performed in the modified chamber which simulated the state as it was when we started in 2015. The average flame spread was: 1.96 m ± 0.17 m. This has to be compared with the old data from 2015 which showed a flame spread of 2.00 m ± 0.16 m

4.2 Burn tests in chamber with coated walls

The other extreme which should be tested is a chamber with walls having emissivity of 0.9 and more. There are several methods which can be used to increase the emissivity of a metallic surface: make the surface rough, either mechanically or chemically; cover the surface with a coating which has an emissivity as high as e > 0.95; or apply a thick layer of black soot. This can be automatically achieved when e.g., cables with a PVC jacket are burned. However, when cables jacketed with LSZH materials are burned even after 7 years the coverage with soot is not sufficiently strong. For our chamber, the option of coating the walls with high emissivity paint was used. Commercially available paint (Aremco HiE-Coat 840-Series) was bought and applied manually with the help of a roller. Approx. 180 g / m^2 were applied.. Figure 5c) shows the interior of the chamber with a homogenously distributed black paint. e > 0.9.

The average flame spread resulted in: 1.58 m ± 0.08 m

4.3 Burn tests in the chamber "as it is"

The burn test data achieved in the experiments above (shiny and coated walls) have to be compared with burn results achieved in the chamber with aged surfaces due to continuous operation. The average flame spread for the aged chamber is 1.78 m ± 0.11 m. The average emissivity is e = 0.6 to 0.95 (see Figure A1)

5. Analysis of the results

A summary of the flame spread results generated under the different conditions described in 4.1 to 4.3 is presented in Figure 6.

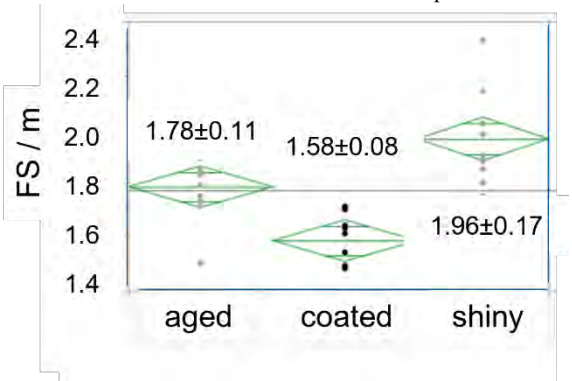


Figure 6. Comparison of the flame spread results

Even though some spread of the data can be seen, the statistical analysis shows that the results are significant.

Figure 7 shows the correlation between FS and the resulting emissivity values for the different wall conditions (coated, aged, and shiny) as determined in the Annex.

As expected, the flame spread decreases when the emissivity increases. The wall coated with paint results in an emissivity of approx. 0.95 which is close to the maximum achievable value 1. On the other hand the wall which consists of virgin metal plates has a much lower emissivity and thus reflects most of the radiation which leads to a more favorable burn conditions which is evident from higher flame spread values. The vertical bars attached to each data point in Figure 7 show the range of the emissivity values which might be present. As mentioned in the Annex the emissivity of a metal surface cannot be determined accurately with the method/procedure described. Thus, literature values are represented by the vertical bar. The current status of aging by continuous use of the chamber leads to emissivity values between e = 0.7 to 0.8. As indicated in Figure A1 the emissivity of the inner walls varies. Based on these measurements we assumed that e values in the order of 0.7 to 0.8 might be suitable.

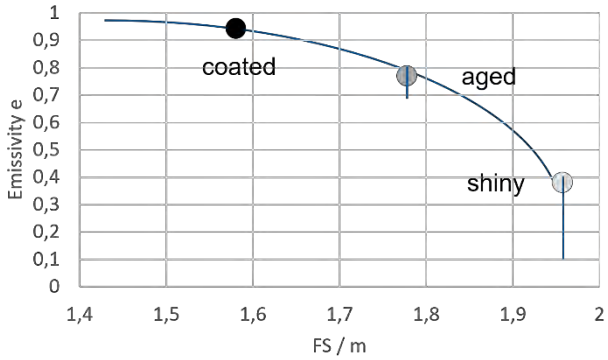


Figure 7. Correlation of the flame spread and emissivity for the coated, aged and shiny wall conditions.

According to the results shown in Figure 7, the flame spread approaches approx. 1.4 m when the emissivity runs towards 1. This is in agreement with the observations made during the round robin testing within European laboratories. Data from the past showed that the average flame spread measured on the reference cable was 1.48 m. This would correspond to an emissivity e > 0.95. This seems to support the assumption that "old, incumbent" laboratories are using chambers which are in use for many years are well covered with soot which leads to a high emissivity.

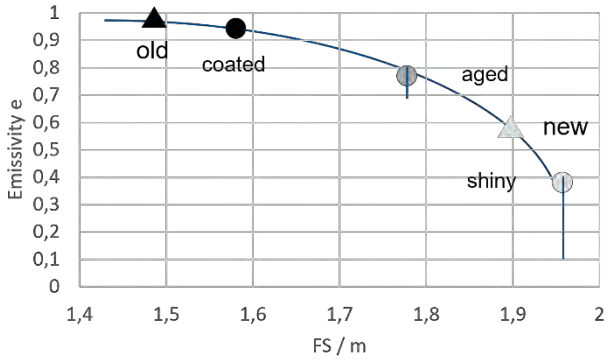


Figure 8. As Figure 7 however results from "old, incumbent" labs and results from new chambers are included

It needs to be mentioned, that the emissivity values for the "old" and "new" data points are not confirmed by measurements. The flame spread data were known. Under the assumption that they follow the correlation curve defined in Figure 7, the emissivity values can be estimated, which aligns perfectly with the hypothesis.

6. Theoretical considerations

To understand the effect of wall emissivity on cable-burn, a Computational Fluid Dynamics (CFD) based model was developed in Ansys Fluent. As discussed in previous publications [4-5], a half-symmetry computational domain was used. The computational domain and associated boundary conditions are shown in Figure 8.

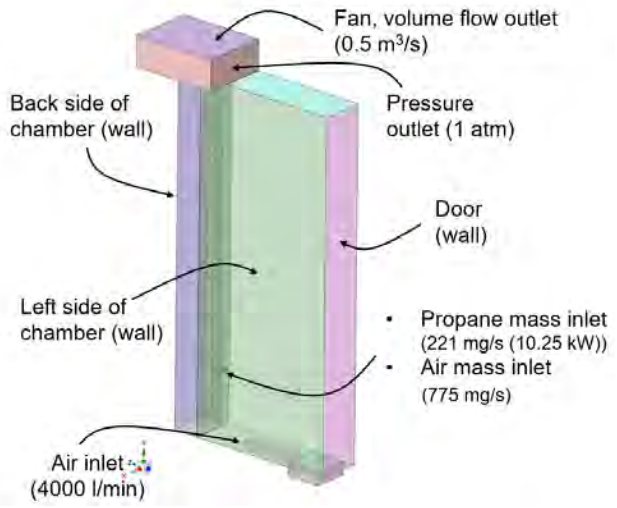


Figure 8. Computational domain with boundary conditions

Due to the complex nature of the cable arrangement on ladder, the cable geometry is not modeled explicitly. Instead, a simplified approach was adopted wherein cables are replaced by an equivalent rectangular slab. The model was augmented with pyrolysis behavior of the cable material, obtained through lab-testing on small samples of cable material. This allows studying transient heat release from the cable and flame spread during the test, using the model. The kinetics of cable pyrolysis was modeled as first order rate as given by eq (1).

$$\frac{dX}{dt} = -A \exp\left(-\frac{E_a}{RT}\right) X \qquad (1)$$

where, X is the un-pyrolyzed fraction of the material, T is material temperature, A and E_a, respectively are the pre-exponential factor and activation energy of the pyrolysis reaction, R is the universal gas constant.

The cable undergoes pyrolysis due to heat gain from surrounding hot gases, and releases combustible products into the chamber. These gases further combust in the chamber leading to enhanced heat release. The hot gases radiatively interact with chamber walls.

The effect of wall emissivity was investigated using the model. For the analysis purpose two cases were considered: one with low emissivity of chamber wall (emissivity = 0.05) which represents shiny chamber walls, and another with higher emissivity (emissivity = 1) which represents the walls covered with soot. Figure 9 shows the transient heat release rate from the cable during the burn-test for these two cases.

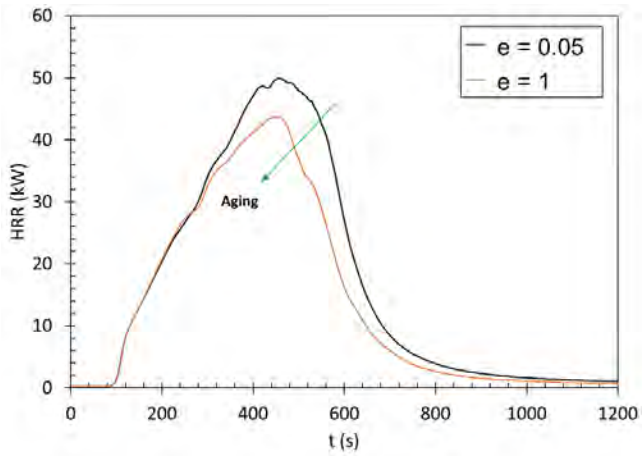


Figure 9. Effect of wall emissivity on heat release rate from cable

The burner is ignited at t = 0 s, and the cable starts pyrolyzing post t = 100 seconds. The peak heat release rate and total heat release from the cable are lower for higher emissivity. This is because, for the case with higher emissivity, the chamber walls absorb more heat, resulting in higher chamber wall temperatures, see Figure 10.

To evaluate the impact of emissivity on vertical flame spread, we defined a parameter called "Burn Fraction" which is defined as the ratio of pyrolyzed material with total available material. A burn fraction value of unity indicates complete pyrolysis. Figure 11 shows the spatial distribution of burn fraction for cables for Shiny (e = 0.05) and Aged (e = 1) chamber at the end of the test. The model predicts lower burn fraction and hence lower vertical flame spread for higher emissivity case. These observations are consistent with experimental results discussed in the earlier sections and align well with the proposed hypothesis.

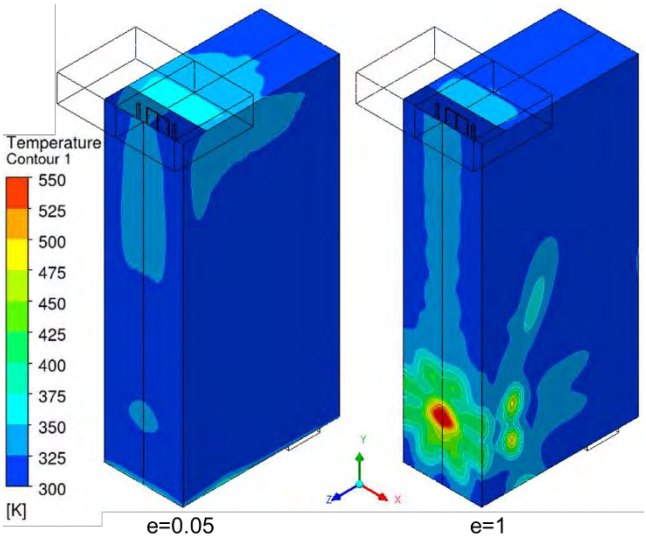


Figure 10. Effect of wall emissivity on chamber temperature at the end of the test.

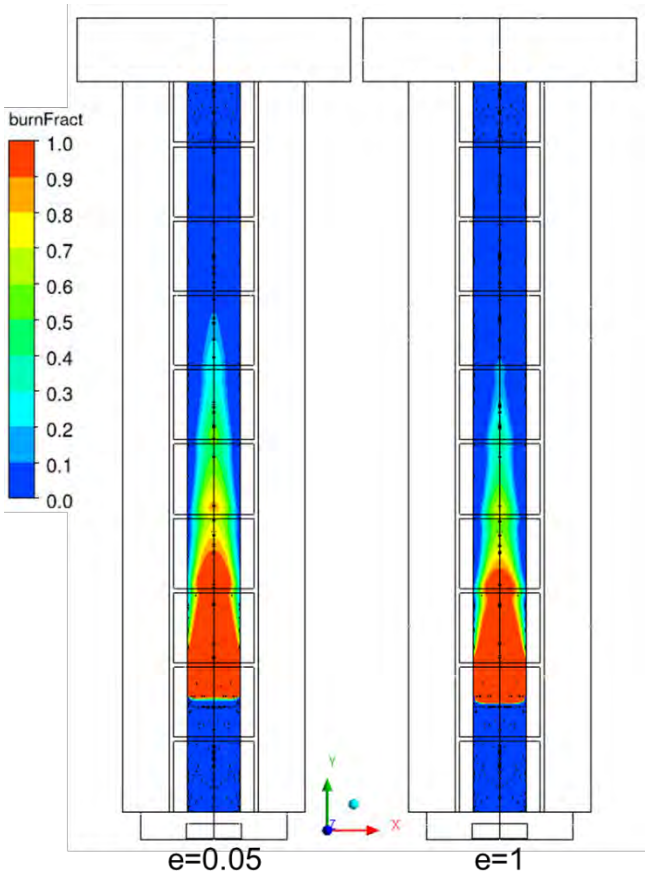


Figure 11. Effect of wall emissivity on cable burn profile at the end of the test.

7. Conclusion

Historical experimental evidence was indicating gradual and systematic reduction of flame spread for standard cable. Based on the outcome of round Robbin test and the clear distinction in Corning's burn chamber outcome over a period, we hypothesized that the chamber wall emissivity must be playing a critical role. Experimental and numerical work was undertaken to understand the effect of chamber aging on the outcome of EN 50399 burn test. Three conditions were tested in the CTCB test facility viz. Shiny, Coated, and Aged. Simulations were performed considering low and high chamber wall emissivity. Both experimental and numerical investigations show similar outcomes on the effect of chamber wall emissivity. Experiments with high emissivity coat on chamber walls show reduction in the flame spread compared to the case with the virgin shiny walls. Modeling also predicted lower vertical flame spread and heat release inside the chamber as the chamber wall emissivity increases. Due to gradual soot deposition, i.e., chamber aging, the wall emissivity increases, which leads to higher heat loss to the ambient and thus low retention of heat inside the chamber.

8. Annex

8.1 Determination of the emissivity

The emissivity can be determined with special test equipment e.g., so called pyrometers (FLIR TG167, Sovarcate HS960D, BTmeter BT-1500). Alternatively also a thermographic camera can be used.

In our lab the thermographic camera Testo88 (Testo) was used. The temperature of a surface can be determined as follows: 1. Install a thermocouple on the surface and measure the temperature. 2. Take a thermographic picture of the surface. Ensure that any radiation from the sides is avoided. 3. Adjust the parameter "emissivity" in the camera settings until the temperature displayed by the camera is the same as the one measured with the thermocouple. The emissivity input is the wanted measure. For highly reflective metal surfaces the method does not give accurate results. In that case literature data have to be taken.

The method as described before was applied to determine the e – values in the case of the "aged" chamber and the "coated" chamber. The e-values for the coated walls was very homogeneous and as stated by the supplier of the coat e = 0.95. The aged walls show different emissivity values depending on the structure / condition of the wall. Picture A1 shows the distribution of the emissivity e on the inside of the chamber.

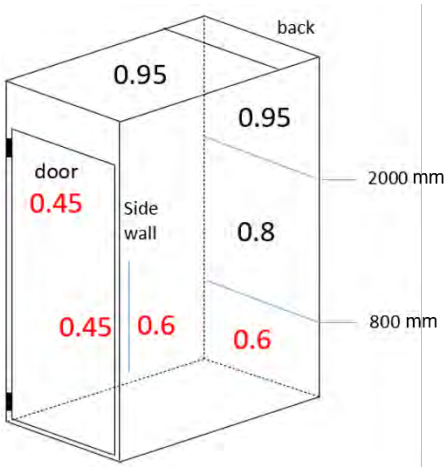


Figure A1. Sketch of the chamber. Different areas on the wall show different emissivity values.

For a simplified approach the emissivity values on the backside of the chamber wall which is close to the cables were averaged and assigned to the flame spread data (aged) which are shown in Figure 7.

9. References

[1] „Round robin cable burn tests on a single fiber cable", R. Kinnera, E. Gallo, Proceedings 63nd IWCS (2014), Charlotte, pp 485-489

[2] „Investigation of reliability of the test for assessing reaction to fire of cables according to CPR," K. Langfeld, Th. Meyer, Proceedings 66th IWCS (2017), Orlando, pp 562-568

[3] "Reference cable for CPR burn testing", Th. Meyer, W. Stöcklein, Proceedings 69th IWCS (2019), Charlotte, 10-2

[4] „Impact of air flow distribution on flame propagation during the EN 50399 bunched cable test (CPR)", W. Stoecklein, Th. Meyer, P. Rajeshirke, Proceedings 69th IWCS (2019), Charlotte, 10-1

[5] „Impact of the burner flame shape on cable performance testing according to EN 50399",Th. Meyer, W. Stoecklein, Proceedings 70th IWCS (2021), virtual, 12-3

9. Acknowledgement

Special thanks to Gani Thiele, Fred Guenzius and Wolfgang Schulz for their experimental support.

7. Authors

Thomas Meyer (meyert@corning.com) received his degree in mechanical engineering from University of Applied Sciences Dresden in 1987.



He has more than 25 years' experience in the field of fiber optics in varying engineering roles such as application engineer manager and RD&E process engineer. In 2016 he joined Corning's materials group of the technology department as manager of the fire performance lab.

Dr. Waldemar Stoecklein (Waldemar.stoecklein@corning.com) is director of Material Science, responsible for global materials development within Corning Optical Communications and representative in cable related international and national standards bodies.



He joined Siemens in 1988 as a physicist and worked as a development engineer in Cable Development located in Neustadt b. Coburg in Germany. In 1992 he took over the lead of the cable evaluation laboratory in Neustadt. In 2000 Corning took over all Siemens cable activities. Since then Stoecklein was responsible for the cable development in EMEA. After internal restructuring in 2009 he was transferred into the position of Technology Integration. Herein he was responsible for information exchange within the EMEA technology organization, coordination of training and innovation, support of cable development. In 2012 he took over responsibility of his current position. Waldemar Stoecklein holds the degree of Dr. rer. nat. in solid state physics from University of Bayreuth. Stoecklein is an active contributor in IEC, CENELEC and DKE. In addition he is an active member in the German Cable association ZVEI as well as the European Cable Association ECBL (EuropaCable).

Anish Gunjal (gunjalaa@corning.com) did his graduation in Mechanical engineering from University of Mumbai, Masters in thermal system design from Sardar Vallabhbhai National Institute of Technology, Surat and PhD from Indian Institute of technology Bombay, Mumbai. Anish is presently working as Scientist in Corning Research Center India and supporting modeling work in Cable Process Modeling team.



Hariom Bhargava (bhargavah@corning.com) received his master's degree in mechanical engineering from Indian Institute of Technology (IIT), Bombay in 2017. He joined Mahindra & Mahindra Limited as Senior Engineer in 2017. Since 2019, he works at Corning Research Center India as Scientist and models flow and thermal processes for various Corning businesses.



Single Pair - Next Steps

Peter Fischer
BKS Kabel-Service AG
Derendingen, Solothurn, Switzerland
+41-32-681-5456 · p.fischer@bks.ch

Dave Hess
Cord Data
Wyomissing, Pennsylvania, USA
+1-610-698-4790 · dave.hess@corddata.org

Abstract
Single Pair Ethernet (SPE) is evolving. New speeds are under discussion at IEEE and cabling standards are stepping ahead to voting at ISO/IEC. A final standard can be expected in one to two years; therefore, it is a good time to dig a bit deeper to see what we can expect from the new single pair cabling.

After the 2 A discussion seems to be resolved in the main document, the topic how to manage it is discussed in many other standardisation projects, the installation standard and a document describing cable heating and bundling, which might have impact back to the main document. This is currently a real 'hot' topic as a standard with channel and link definitions alone does not mean a lot if there are no installation guidelines attached to it. This paper explains the status of these documents too.

Additionally, guidelines for cable sharing, the parallel operation of several single pair channels running on the same 4-pair cable, and multidrop, a kind of daisy-chain network, where many devices are on a bus-like structure, are both discussed.

The cable sharing document is still at working draft level; however, it is building the bridge between the well-known 4-pair cabling and the new upcoming single pair cabling. ISO/IEC TR 11801-9911 describes how the existing 4-pair cabling can be used to run single pair cabling applications.

Keywords: Single Pair Ethernet; SPE; Single Pair Ethernet applications; IEEE 802.3da; Multidrop; IEEE 802.3dg; 100 Mbit/s long reach Point-to-Point; Single Pair cabling; Single Pair cables; Single Pair connectors; Single Pair testing in the field and laboratory; Cable sharing.

1. Introduction
Even if standardisation is often not as fast as expected, there are still plenty of news from the emerging technology of SPE, if all committees and levels are considered as sources, like application level, system level, and component level.

This paper is based on current developments in standards related to cable sharing and multidrop in ISO/IEC, single pair cabling requirements and application requirements from IEEE.

As cabling standards are stepping ahead it gets clearer on what we will get from the different committees and how it will change the way network installations are done today in respect to the use of single pair cabling.

The new technology 'Single Pair' will have impact on how buildings and industrial areas are connected to the Information Technology (IT) network, especially the newly added sensors and actuators which deliver data to edge devices. These devices again take direct action to change the environment in case the temperature is too high or too low or any other parameter which must be changed according to the system settings of the user.

The new technology will need much more interaction between the user and its network, how it is configured and maintained. This is called individualisation or personalisation. This leads to a multiplication of sensors and requires a new kind of network, which has one key requirement: efficiency.

2. Overview
This paper is structured in such a way to give an overview on the different projects running under the topic of SPE and related work:

Single Pair Ethernet applications:

- IEEE P802.3da Multidrop
- IEEE P802.3dg 100Mbit/s long reach point-to-point

Single Pair cabling:

- ISO/IEC 11801-1 AMD1
- ISO/IEC 11801-6 AMD1
- ISO/IEC TS 11801-9903
- ISO/IEC TR 11801-9906
- ISO/IEC TR 11801-9911
- ISO/IEC 14763-2
- ISO/IEC 14763-5
- ISO/IEC TS 29125 AMD2

Single Pair cables:

- IEC 61156-11/-12/-13/-14
- IEC TS 61156-1-2

Single Pair connectors:

- IEC 63171
- IEC 63171-X series
- IEC 60512-99-003
- IEC 60512-28-100

Single Pair testing in the field:

- IEC 61935-4

The below information is given by the best knowledge of the editor. As standardisation is an ongoing process some information might be outdated when reviewed months or years after publication of this paper. Therefor it is only a view on the current status at a specific point of time, as predictions on future progress and developments are difficult to make, it will be a reference for why development choices were made.

3. Single Pair Ethernet applications

3.1 Prior IEEE single pair ethernet projects

The current projects are all somehow related to former work done and are a direct extension of this base project. This project is called IEEE 802.3cg and consist of 3 different 10Mbit/s applications:

- Long reach: 1000m point-to-point
- Short reach: 15m point to-point
- Bus structure: 25m with up to 8 devices (multidrop)

3.2 IEEE P802.3da Multidrop

The IEEE P802.3da project is an extension of the bus structure project part of IEEE 802.3cg. The new project focus on the same data rate but for a longer distance of at least 50m, up to 16 devices and adding power to the link segment.

At the beginning it sounded like a straightforward project, but it developed into many difficult unsolved but interrelated issues. The result was a huge delay and many revisions of the project timeline. Recently some progress was made, and the definition of a link segment seems reachable in a reasonable time.

As there are at least 16 devices connected, the power available for each will be approximately 2 W only. However, as at least a part of the trunk will carry the full load, the requirements for components will be nevertheless demanding.

As simulations have shown, the T-connector will consist of some compensation components to correct the impact of the capacitive load of the devices and the drop cables.

If the project will move forward as expected, it might be possible to have a standard by late 2025. As further issues may arise it is possible to get it done even later.

More detailed and up to date information can be found on the specific project homepage:

https://www.ieee802.org/3/da/index.html

3.3 IEEE P802.3dg 100 Mbit/s long reach point-to-point

The IEEE P802.3dg (100Base-T1L) project is also a follow up project of IEEE 802.3cg but related to the long reach point-to-point project at a 10 times higher data rate of 100 Mbit/s mainly on cost of a length reduction to increase the signal, a 3 times larger bandwidth to account for the higher speed and tighter requirements to reduce the impact of noise.

Even if there is faster progress as for the IEEE P802.3da project, also here the first aggressive timeline could not be met and publication will be earliest in 2025, under the condition of no additional delay caused by new unknown issues which may arise during the further development of the project.

Now most of the transmission parameters are defined, however the PHY specialists must figure out if the active interface to such a link segment is feasible at reasonable cost. When this is done further details can be fixed.

More detailed and up to date information can be found on the specific project homepage:

https://www.ieee802.org/3/dg/index.html

3.4 Future IEEE SPE projects related to generic horizontal cabling

For the time being there are no other SPE projects running. However, already during the study group phase, which led to the 100Mbit/s project also a higher speed in parallel development was discussed. At that time, many experts had the impression such a parallel development could slow down the progress of the 100 Mbit/s project.

On the other hand, there was also interest for 1 Gbit/s over a longer distance than the currently available 40 m application IEEE 802.3 bp. Studies have shown that 100 m is feasible with a bandwidth of approximately 600 MHz on a single pair with AWG 23 wires.

As the IEEE P802.3dg project is progressing, people will start thinking about the next higher speed on long reach again.

4. Single Pair cabling

4.1 ISO/IEC 11801-1 AMD1

ISO/IEC 11801-1 AMD1 is the main document related to single pair cabling. Herein we can find all channel definitions and specific requirements. JTC 1/SC 25/WG 3 has adopted the applications relevant for cabling installations from IEEE.

For 10Base-T1L a respective channel of 1000 m (T1-A-1000) was defined. For shorter lengths additional channels are available, for 400 m (T1-A-400), for 250 m (T1-A-250) and for 100 m (T1-A-100). As IEEE 802.3dg is not stable yet, the committee has prepared additional channels for higher speeds with a bandwidth of 600 MHz (T1-B) and 1250 MHz (T1-C), which are capable of 1 Gbit/s or more.

The upcoming IEEE P802.3dg specification is projected into a second amendment of ISO/IEC 11801-1 which should be started as soon as the 100Base-T1L project is stable, which might be end of this year or beginning of the next year.

4.2 ISO/IEC 11801-6 AMD1

The ISO/IEC 11801 series is structured in several parts, designed to fit in different areas, like offices (ISO/IEC 11801-2), industry (ISO/IEC 11801-3), homes (ISO/IEC 11801-4) data centres (ISO/IEC 11801-5), and smart building (ISO/IEC 11801-6).

To define the structure for single pair networks, serving the emerging IoT/IIoT (Internet of Things/ Industrial Internet of Things) networks, the respective latest amended parts ISO/IEC 11801-3 (published) and ISO/IEC 11801-6 (committee draft) are defined. These parts now get amendments similar to ISO/IEC 11801-1 to include all information needed to build such networks.

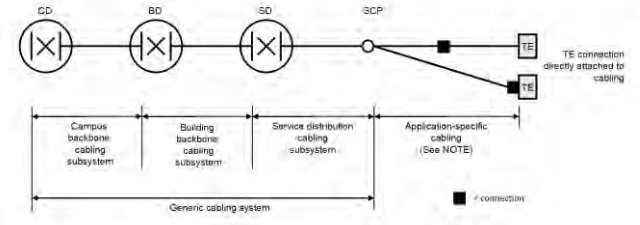


Figure 1. Structure of Type B generic cabling

Beside the so called traditional ‘Type A’ cabling a new ‘Type B’ cabling is used to connect a broad variety of sensors and actuators to the network. The new type can consist of a fibre optic connection to an active service concentration point (SCP) or a 4-pair cable to a passive SCP.

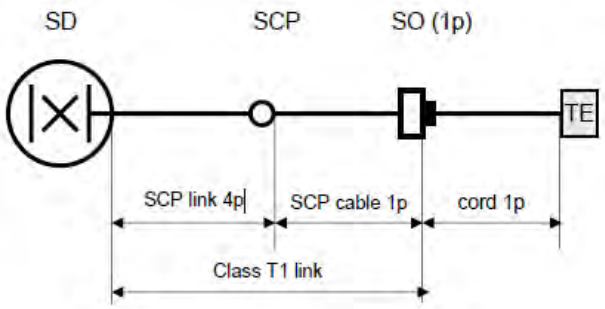


Figure 2. Example of single pair extension

The SCP is meant to be in the ceiling and arranged in zones, like wireless access points (WAPs), to connect to a huge number of nearby devices.

4.3 ISO/IEC TS 11801-9903

The technical specification ISO/IEC TS 11801-9903 is currently running; however, it is not related to single pair cabling.

The main topic of the document is modelling of 4-pair channels and links but can also be used to model single pair channels and links. For all interested in additional background information, it is explained how different components, like cables and connectors can be combined to get to a link or channel model.

The modelling can be utilised to estimate SNR based on signal theory to calculate the maximum data rate of a channel. It is also of great interest if in case the data rate is marginal to figure out which of the parameters must be improved and by which amount to achieve a higher bandwidth or additional margin for the extended reach.

4.4 ISO/IEC TR 11801-9906

The ISO/IEC TR 11801-9906 is a technical report focussed on the specifications related to single pair cabling and components. Such a document can be used together with the above-mentioned ISO/IEC TS 11801-9903 to calculate the resulting channel capacity from single components.

The document consists of helpful information as a collection of requirements from different committees. It is referenced by the published ISO/IEC 11801-3 AMD1 standard as a base for the channels and links for the industrial area.

4.5 ISO/IEC TR 11801-9911

This document is still at working draft level; however, it is building the bridge between the well-known 4-pair cabling and the new upcoming single pair cabling. ISO/IEC TR 11801-9911 describes how the existing 4-pair cabling can be used to run single pair cabling applications.

The popular name of this document is ‘cable sharing’. Additional details on what should be considered is given further below in clause 9.

4.6 ISO/IEC TS 29125 AMD2

This document is currently in the focus as it is the base for the further below described installation standard ISO/IEC 14763-2 in clause 4.7.

Over the last decades power transmission became increasingly important. What started with 15 W on 2 pairs was expanded to a full 4-pair application allowing 90 W power transmission from the power source equipment (PSE) to the powered device (PD).

For SPE a wide range of power levels is available, many related to automotive applications. For cabling 6 levels are mostly relevant from the milliwatt level up to 52 W.

As for 4-pair cabling, lower power levels are not critical, for connectors in the case of unmating under electrical load but also for cables related to heating and related bundling restrictions. It becomes obvious, the higher the power level is, the lower is the number of cables in a bundle. As single pair connectors are specially designed to carry power, the connectors are much less critical even when currents are up to 2 A per contact. Further details are described below in clause 6.3 related to IEC 60512-99-003.

Cable heating on the other hand is related to the current and therefore much more critical especially if higher power levels are transmitted over lower diameter wires. That brings the number of bundled cables down to just a few for the highest currents.

The highest current of the available applications of 1.579 A is applicable only for large wire diameter cables like AWG 18 or larger as defined for the T1-A-1000 channel. However, such a current reduces the maximum length to approximately 140 m due to voltage drop.

Cables based on wire diameters known from 4-pair cabling like AWG 23 are not capable to carry such high currents and must be somehow restricted in the amount of transmitted power. Calculations from 4-pair cabling show a current carrying capacity of 0.75 A, which covers 5 out of 6 power classes.

This restriction is valid for all AWG 23 wire diameter-based cables and leads as an additional parameter for cable sharing based on 4-pair cables.

4.7 ISO/IEC 14763-2

The ISO/IEC 14763-2 standard is the connection between the channel specification in ISO/IEC 11801-1 AMD1 and the cable heating document of ISO/IEC TS 29125 AMD2 resulting in installation guidelines. Only the complete framework of standards allows network designers to define a network, which can be used for most of the use cases.

In the installation guidelines we find a lot of useful information related to bundling of powered cables and predefined installation environments. These environments have a major impact on cable heating, beside the current, as they define how the produced heat can be dissipated to the surrounding material. This can go from air to isolation material.

4.8 ISO/IEC 14763-5

In ISO/IEC 14763-5 another emerging topic is covered: Sustainability. On one side the impact of cabling networks is described from mining till recycling or deposition.

In the middle we have operation which gets more into the focus. Beside the power consumption of IT equipment also the power loss in cables is a factor which has to be considered.

It becomes obvious that huge power losses due to cable heating must be avoided as much as possible. As the document is still a draft the requirements might change again but it is certain that sustainability will be a topic for future installations.

4.9 Multidrop in cabling specifications

As the related IEEE P802.3da project is delayed, also the project in ISO/IEC is delayed. As the IEEE project will progress in draft levels, also JTC 1/SC 25/WG 3 will follow.

5. Single Pair cables

5.1 IEC 61156-11/-12/-13/-14

As cable standards are usually much less political and controversial as connector and cabling standards the projects progressed well in the past and the remaining work seems unproblematic.

The horizontal cable standards IEC 61156-11 and IEC 61156-13 were published as respectively second and first editions earlier this year. There were small adjustments needed for IEC 61156-11, mainly to add a higher level of performance up to 1250 MHz to cover the requirements of the highest cabling class T1-C.

When the horizontal cables are close to publication, the standards for flexible wires are written with mainly similar requirements beside wire related parameters like resistance and attenuation. This guarantees a fast progress of these projects.

While IEC 61156-12 has reached committee draft (CD) level and IEC 61156-14 is an agreed new work item proposal (NP) with the CD in preparation, publication of both documents can be expected in late 2024 or early 2025.

5.2 IEC TS 61156-1-2

The former amendment of the technical report (TR) related to balunless testing was merged with the base document. During this process, the format was increased to a technical specification to reduce the needed amount of work for adjustments.

This TS consists of cable theory, requirements for cable testing and the respective equipment which should be used to evaluate the performance of a cable.

The document was adapted to be useful for single pair cable testing. The TS should be published still in September 2023.

6. Single Pair connectors

6.1 IEC 63171

On the connector side the structure is different, as there are several designs available for the 2 main areas of single pair cabling. One is the industrial area with ingress and particle (IP) requirements, which describes the level of IP protection.

For building automation, the IP20 level is usually used, and for industrial areas it can go up to level IP69. However, not all industrial areas require such high levels of IP protection levels, often IP44, IP55 and IP67 are used.

The IEC 63171 standard consists of all single pair connector requirements beside the mechanical dimensions. Depending on the category the requirements are defined up to the needed frequency for the channel:

- T1-A: 0.1 MHz to 20 MHz
- T1-B: 0.1 MHz to 600 MHz
- T1-C: 0.1 MHz to 1250 MHz

These transmission requirements are combined with a long list of environmental tests to assure the durability of the connectors.

6.2 IEC 63171-X series

Table 1. Types of single pair connectors

IEC number/ Style name	MICE	Number of pairs/ Power contact	Transmission category
IEC 63171-1 LC copper	M1I1C1E1 Shielded and unshielded	1 pair No extra power contacts	B
IEC 63171-2 MSP	M1I1C1E1 Shielded and unshielded	1 pair No extra power contacts	B
IEC 63171-4 MMC	M1I1C1E1 unshielded M1I1C1E3 shielded	1 pair, 2 pairs, 4 pairs Multipair connectors may be used for data and separate power transmission	B (unshielded C (shielded))
IEC 63171-5 MSP	M1I1C1E1 to M3I3C3E3	1 pair No extra power contacts	B
IEC 63171-6 T1 Industrial style	M1I1C1E1 to M3I3C3E3	1 pair, M8 hybrid with 2 extra power contacts	B
IEC 63171-7 Hybrid	M1I1C1E1 to M3I3C3E3	1 pair + up to 5 additional power contacts	B

The mechanical dimensions are given in this series of standards. All connectors must comply with the electrical specification in the parent document IEC 63171.

The look and feel of each connector differ from type to type.

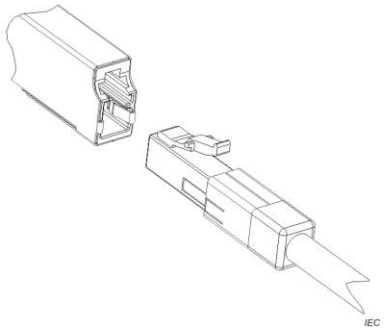


Figure 3. Picture of an IEC 63171-1 LC copper connector

The LC copper connector shown above is meant for building automation.

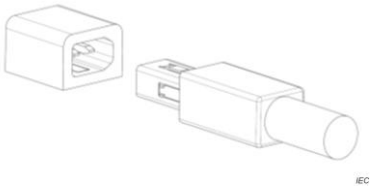


Figure 4. Picture of an IEC 63171-2 MSP connector

The MSP connector according to IEC 63171-2 is meant for building automation and is intermatable with the IEC 63171-5 connector.

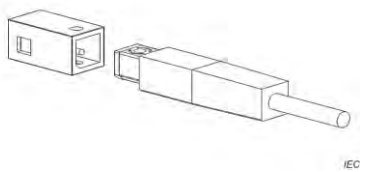


Figure 5. Picture of an IEC 63171-4 MMC connector

The MMC connector shown above is meant for building automation. The multipair versions can be used for cable sharing.

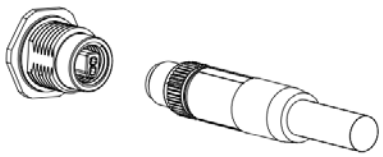


Figure 6. Picture of an IEC 63171-5 MSP connector

The MSP connector above is meant to be used for industrial automation and is intermatable with the IEC 63171-2 connector.

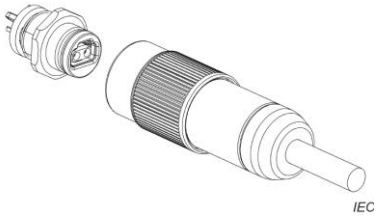


Figure 7. Picture of an IEC 63171-6 T1 Industrial style connector

The T1 Industrial style connector is meant to be used for industrial automation.

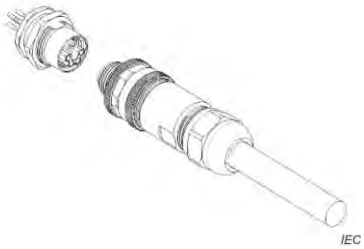


Figure 6. Picture of an IEC 63171-7 Hybrid connector

The IEC 63171-7 connector is meant for industrial automation where much more power is used as it allows to transmit up to 10 kW of AC or DC power on additional contacts.

6.3 IEC 60512-99-003

For single pair connectors new test methods are needed. As using power became incredibly famous for data transmission connectors with 4 pairs, it is expected that power transmission will be a key factor for single pair connectors too.

Therefore, a similar method as before for 4 pairs described in IEC 60512-99-001 and IEC 60512-99-002 was started to cover single pair connector unmating under electrical load.

The current per contact for single pair connectors is much higher than for 4-pair connectors and the components for simulating the electronics have been also changed. This is compensated by much better contacts separating the contact and the sparking area.

6.4 IEC 60512-28-100

The standard IEC 60512-28-100 describes the testing of all transmission parameters. The procedures had to be adjusted to fit for single pair connectors. Reducing the number of pairs is a simple adjustment but also a frequency extension down to 0.1 MHz was needed.

7. Single Pair testing in the field

7.1 IEC 61935-4

All the above standards are all needed but for the end user a test standard must be available too, which describes the requirements a test equipment must fulfil to be used for testing of a specific category of cabling.

The most difficult part is to go to lower frequencies, while keeping the high frequencies. In fact, spanning four decades is a significant challenge, as the hardware and software must be adjusted for such low frequencies.

This project is currently a bit behind the schedule as specific parameters have to be defined at frequencies new to the tester companies which were used before to measurements from 1 MHz and upwards.

It might seem to the reader that lower frequencies might be easier but in electronics it can be also the exact opposite.

8. Single Pair: Next steps

8.1 Application level

As already mentioned, there are no new projects in planning for now. However, if the current projects progress one might start to think about the next speed for extended reach.

The 1000Base-T1L application seems to be the next obvious step to go but till now no one has called for interest of such a project yet. The technical feasibility was already shown during the study group phase prior to the IEEE P802.3 dg project.

8.2 Single Pair cabling

Single pair cabling seems ahead of time related to the available applications. However, it is good to have some extra margin represented in a channel with higher requirements, to show to end users that also in the future, new speeds can be expected.

For the 100Base-T1L project, which is IEEE P802.3dg, a second amendment to ISO/EC 11801-1 is planned which will cover up to at least 60 MHz. This will be started soon but depends on the progress of the IEEE project.

Simulations show that more than 100 m can be reached for a future 1000Base-T1L application with reasonable requirements, which can be reached with screened single pair components.

8.3 Single Pair cables

As the cable development depends heavily on the cabling progress and therefore on the progress of IEEE P802.3dg, a new cable specification to cover the 100Base-T1L application can be expected to be started soon after JTC 1/SC 25/WG 3 has started the project.

In principle there are two options: A revision of IEC 61156-13/-14 or a new project, where the next available number would be -16/ and -17. To have two more standards to check is the downside of this direction and therefore it is more feasible to integrate the 60 MHz specification into the existing standards.

8.4 Single Pair connectors

For connectors no new projects were announced yet, new connector standards cannot be expected at this time. However, if a manufacturer finds a specific need for a connector, which is not yet covered by existing connectors, this might lead to additional connectors in the IEC 63171 series.

9. Further exploration on cable sharing

As explained in clause 4.5 and 4.6, cable sharing is an efficient way for single pair cabling as discussed on several levels. Beside represented in the IEC 63171-4 connector standard, it is the preferred option of cable manufacturers as they can produce the

same cables they have already in their assortment. The cabling is explained in ISO/IEC TR 11801-9911.

The topic of high density is important for device manufacturers too as less space leads to lower cost. Finally, PHY manufacturers are thinking on how they can connect relatively low speed single pair outlets to the high-speed bus in their devises. Further discussions will show how that can be realised.

9.1 Principal and structure

The principle of cable sharing is based on a 4-pair horizontal cabling section from the service distributer (SD) to the service concentration point (SCP). A CP cable may be used to connect the SCP with a single pair service outlet (SO 1P).

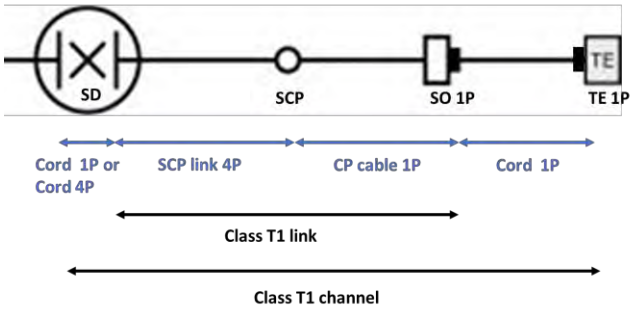


Figure 7. Channel structure

In the case of connectors which provide a multipole interface with separated single pair outlets for cable sharing, like IEC 63171-4, the CP cable and a separate single pair outlet is not needed.

At the single pair terminal equipment (TE 1P) side of the permanent link (Class T1 link) a single pair patchcord (Cord 1P) must be connected. At the SD side a cord 1P or a 4-pair cord can be connected. The 4-pair cord would be the best option if the outlet inside the active equipment, e.g., a switch, would present a 4-pair interface which allows to serve 4 single pair applications. This would lead to a 4-pair to 4-pair cord on the SD side and 4 times a single pair to single pair cord on the TE side. Alternatively, on the SD side a fan-out from 4-pair to 4 single pair connectors would be also possible.

9.2 Detailed analyses

If single pair and 4-pair components are combined, an analysis is provided to guide users thru the different parameters in the document. It is easily visible for which parameter some additional examinations must be considered.

For each parameter it is indicated if these parameters are met by design (D), met when passing a qualification test (Q), met when mitigation action is taken (M), not applicable (NA) and not possible (N).

The below parameters and criteria must be checked:

- Frequency range
- Return loss
- Insertion loss
- Direct current (DC) loop resistance
- Direct current (DC) resistance unbalance
- Current carrying capacity
- Dielectric withstand
- Propagation delay
- TCL (unscreened only)
- ELTCTL (unscreened only)
- Coupling attenuation (screened only)
- PS ANEXT
- PS AACR-F
- Different disturbers
- Cables
- Connectors
- Installation
- Bonding
- Administration
- Supported applications: Data + Power according to IEEE Std 802.3, Clause 104
- Segregation of maximum 0.75A cabling components from higher power applications

The technical report explains which parameters are met by passing the 4-pair requirements of a respective class or some additional testing is recommended.

9.2.1 Extension lengths for T1-A-1000

If a 4-pair link will be extended to a T1-A-1000 channel, the maximum extension length depends on the power class which want the user to be run over this link. The reason for this is the DC loop resistance limit.

Table 2. Maximum extension length for T1-A-1000

Class	Reference length (m)	Powering Class 11, 14 of T1-A-1000 (m)	Powering Class 10, 13 of T1-A-1000 (m)
D	100	0	468
E	100	0	468
E_A	100	0	468
F	100	0	468
F_A	100	0	468

As the DC loop resistance for any 4-pair class is 25 Ω, which is the same as for the powering classes 11 and 14, no extension is possible. Only for the powering classes 10 and 13 an extension is possible, as the allowed DC loop resistance is 65 Ω.

9.2.2 Extension lengths for T1-A-250 and T1-A-400

In case someone wants to extend a 4-pair link, as above, the DC loop resistance is the parameter which restricts the length of the channel.

Table 3. Maximum extension length for T1-A-250 and T1-A-400

Class	Reference length (m)	Powering Class 11, 14 of T1-A-400 (m)	Powering Class 10, 13 of T1-A-400 (m)	Powering Class 11, 14 of T1-A-250 (m)	Powering Class 10, 13 of T1-A-250 (m)
D	100	0	300	0	150
E	100	0	300	0	150
E_A	100	0	300	0	150
F	100	0	300	0	150
F_A	100	0	300	0	150

The extension is related to the powering classes. For class 11 and 14 no extension is possible. In case of powering classes 10 and 13 an extension to the maximum channel length is possible, results in a maximum extension length of 150m for a T1-A.250 channel and 300m for a T1-A-400 channel.

9.3 Most critical parameters and criteria

As listed under clause 9.2 not all parameters are critical for an existing 4-pair class link to pass the single pair channel requirements. However, there are some parameters for which testing is recommended.

9.3.1 Frequency range

As the frequency range for 4-pair classes is starting at 1 MHz, in principle the performance from 0.1 MHz to 1 MHz is unknown. From physical properties most of them behave predictable if extended to lower frequencies.

On the other hand, the upper frequency is for some single pair classes above the upper frequency of the 4-par class and has therefore to be evaluated.

9.3.2 Return loss

As generally noted above, the performance between 0.1 MHz and 1 MHz is not covered by the 4-pair classes. For the applications under consideration the return loss limit is much lower than the 4-pair class return loss in the overlapping frequency range. Therefore, it can be expected that lower frequencies do not cause any problems. This is related to the fact that an additional relaxation is specified for this frequency range.

Even if the currently application under development 100Base-T1L is not stable yet, it is foreseeable that the return loss requirements will be similar to 10Base-T1L and therefore no issue for 4-pair classes.

For higher classes, as T1-B and T1-C, the requirements of the single pair channels are slightly higher than the requirements of the 4-pair classes. Therefore, testing is recommended.

9.3.3 Insertion loss

The insertion loss for 10Base-T1L for 1000 m is much higher than all single pair 100 m classes and 4-pair classes and therefore uncritical. The only critical channel is T1-A-400 as it is close to the link defined for the 1V peak-to-peak requirement. The cabling committee has taken this into consideration and set the requirement always slightly below the link requirement of 10Base-T1L and is uncritical as additionally covered by low insertion loss plateaus.

9.3.4 Current carrying capacity

It is clearly stated several times in this TR that single pair channels build with 4-pair components in it are restricted to the current carrying capacity of the 4-pair components which is 0.75 A. All currents provided by IEEE or other application standardisation committees above this limit are out of scope.

Table 4. Support of single pair cabling classes by 4-pair cabling classes based on IEEE Std 802.3, Clause 104 powering classes

Powering Classes	D	E	E_A	F	F_A
10, 11, 13, 14	M	M	D	D	D
0-8, 12	M	M	M	M	M
9, 15	N	N	N	N	N

That results in full support of powering classes 10, 11, 13 and 14. For powering classes 0-8 and 12 mitigation is needed, which means a length reduction according to the DC loop resistance to approximately 40 m.

The high current powering classes 9 and 15 are not possible and therefore out of scope of ISO/IEC TR 11801-9911.

9.3.5 Unbalance attenuation (unscreened only)

As a screen is absent in unscreened channels the mode conversion, one of the most important parameters for single pair cabling, is reduced from coupling attenuation to TCL and EL TCTL only, as the screening attenuation is zero.

The requirements were set higher to allow unscreened channels, however technically such levels are difficult to reach. Even if components can be made passing such levels, installation practices have a huge impact on the performance of TCL and EL TCTL. Testing is recommended as the requirements for 4-pair classes are 10dB below the single pair requirements.

9.3.6 Coupling attenuation (screened only)

The requirements for coupling attenuation are only applicable for screened cabling in accordance with the requirements of ISO/IEC 11801-1.

9.3.7 Alien crosstalk (PS ANEXT and PS AACR-F)

Alien crosstalk for unscreened systems is known as a parameter leading to a lot of additional work after installation, as many combinations must be assessed, summed up and finally compared to a tight limit. In case of cable sharing first the overall construction of the 4-pair cabling must be considered. All U/UTP constructions are for further studies and therefore not discussed in the TR.

All evaluations of screened cabling can be simplified as all pairs or cables around a specific screened 4-pair channel can be neglected. Only the other pairs of the 4-pair cabling, which are under the same sheet and therefore under the same screen must be considered. This reduces the Alien crosstalk measurement to the well-known crosstalk measurement of the 4-pair channel or link. Therefore, the limits can be compared easily between 4-pair and single pair classes.

9.3.7.1 Correction factors

In principle a 3 dB factor is applicable as 4-pair cabling alien crosstalk is based on 6-around-1 measurements and single pair cabling is based on 3-around-1 configurations, which reflects the cable sharing case. Additional correction can be applied if not all of the 3 possible disturbers are used for data transmission inside the 4-pair link. For 2 disturbers a correction of 4.8 dB applies, for one disturber even 7.8 dB. In the case of no disturber the cabling meets the requirement by design.

9.3.7.2 PS ANEXT evaluation

For broadband evaluation, the linear frequency scale is easier to read if the higher end of the frequency band is evaluated, however, the logarithmic scale is better to evaluate low frequencies compliance.

All classes meet the T1-A requirements with a different amount of margin. For class D the margin is low, and a screen is necessary to avoid additional noise coupling into the pair. Class E and E_A show a good margin in case they are at least overall screened. For the single pair class T1-B at least the 4-pair class F is required, testing is recommended.

For the single pair class T1-C at least the 4-pair class F_A or better is required, testing is recommended. To achieve the tight requirements better connectors, as they are the weak point, must be considered. This is often named as category 7_B or class F_B cabling up to at least 1250 MHz to cover 25GBase-T and 4 independent T1-C single pair channels with a capacity of at least 2.5Gbit/s.

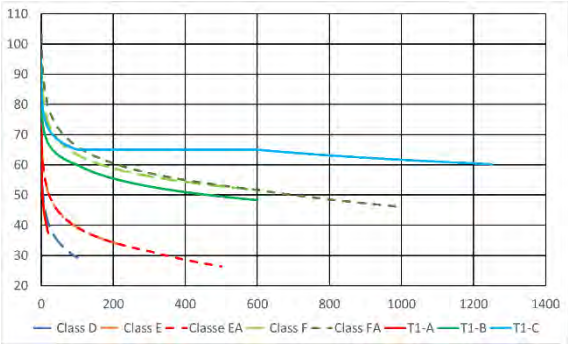


Figure 8. PS ANEXT linear frequency scale

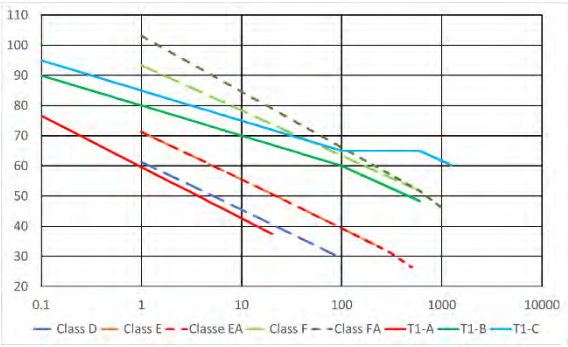


Figure 9. PS ANEXT logarithmic frequency scale

9.3.7.3 PS AACR-F evaluation

The PS AACR-F evaluation reveals the weakness of class D and E channels, which are below the T1-A requirements or marginal.

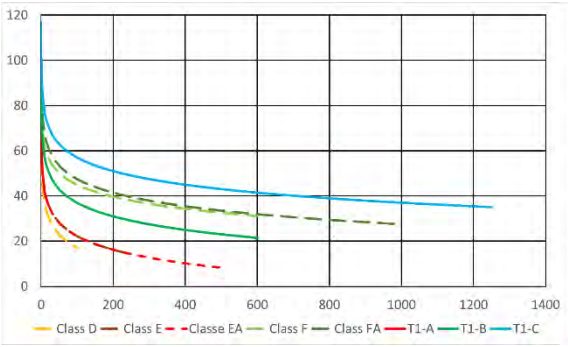


Figure 10. PS AACR-F linear frequency scale

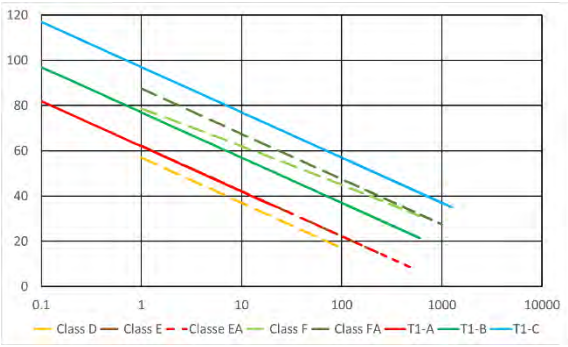


Figure 11. PS AACR-F logarithmic frequency scale

Therefore, it is not recommended to use such cabling classes for cable sharing.

For the single pair class T1-B also in the case of PS AACR-F at least class F is needed to pass the single pair requirements.

Like PS ANEXT for single pair class T1-C the 4-pair class F_A or better is required. To achieve the tight requirements better connectors, as they are the weak point, must be considered. This is often named as category 7_B or class F_B cabling up to at least 1250 MHz to cover 25GBase-T and 4 independent T1-C single pair channels with a capacity of at least 2.5Gbit/s.

9.3.8 Installations

How to install single pair cabling in general is one of the big open points in the framework of the standards for single pair cabling. Whereas data transmission is well defined, the power transmission and the impact and restrictions arising from cable heating.

As the revision of the standard has just been started it is difficult to predict what the finale document will require. However, the impact of power on cables is available in ISO/IEC TS 29125, also respective cable bundling and the wire diameter.

The second parameter to be considered is the installation environment. Cabling can be installed in air or in closed conduits which has a huge impact on heat dissipation.

By studying ISO/IEC TS 29125 it becomes clear that AWG23 wires carrying a current of 2 A must be installed in air as single pairs and never in a bundle. Such a restriction is theoretically possible, but practically useless for installations.

9.3.9 Supported applications

The range of applications running on channels consisting of single pair and 4-pair components are all applications for T1-A, T1-B and T1-C up to 100m with a maximum current of 0.75 A. The list of the available applications can be found in ISO/IEC 11801-1 AMD 1.

If further restrictions do need to be taken into considerations, for installations ISO/IEC 14763-2 must be consulted, for power and cable heating ISO/IEC TS 29125.

For powering class 12 length reduction is required to respect the DC loop resistance limitation of 9.5 Ω, which leads to a maximum length of approximately 40 m. An overview on all power classes is given in table 4 in clause 9.3.4.

9.3.10 Segregation of maximum 0.75 A cabling components from higher power applications

Due to the issues described above, mainly cable heating and bundling, cabling systems which can carry only up to 0.75 A have to be separated from systems and devices which are able to deliver higher currents to end devices.

There are different options proposed to secure connection of high-power sources to lower power cabling. These options are:

- Connectors, which are not intermatable with connectors used for high-power sources. This may be achieved by different connector interfaces, housings or keying features.
- When the same connectors are used which allow interconnection to high power equipment, the connector should be visibly and permanently labelled as having a lower current carrying capacity.
- Additionally different colours of cables may be used. Labelling is still recommended.

- The building owner should document within the installation plan how to segregate low and high-power circuits.

10. Conclusions

Standardisation is work in progress. Therefore, prediction of the outcome of the process is difficult to predict.

This paper gives an overview on the current status of standardisation projects related to single pair cabling, from the application level over the system level to the component level. This shows the amount of work which is needed to build and standardise a new technology like single pair ethernet.

As an efficient way of connecting future IIoT/IoT devices to the IT network this paper explores deeper into cable sharing and its boundary conditions.

It is important to understand how the structure of cable sharing is looking and how cable sharing is building a bridge between the existing 4-pair cabling and the emerging single pair cabling. A list of parameters has to be considered to make sure single pair ethernet applications run over 4-pair cabling channels and links.

The current carrying capacity of a single pair channel using 4-pair components is restricted to the limit set by the 4-pair component, which is 0.75 A.

Alien Crosstalk parameters of screened cable sharing systems reduce the formerly huge amount of measurement time used to a simple crosstalk measurement in the same link. Figures can be drawn, and a comparison can be made. It becomes obvious that class D and E 4-pair cabling classes shall not be used for cable sharing. For the single pair class T1-A at least the 4-pair class E_A is recommended. For T1-B at least class F cabling is required and for class T1-C better than class F_A cabling has to be used.

The largest open point is the installation standard and the related cable heating technical specification. The ISO/IEC 14763-2 standard use the cable heating concept of ISO/IEC TS 29125 AMD 2. Depending on the current and the environment a different size of cable bundles is allowed. Smaller wire diameters like AWG 23 are restricted to 1 pair in air with a maximum current of 2 A. Therefore, such a cabling system is theoretical possible but practically useless for installation practice.

With cable sharing 5 out of 6 power classes according to the IEEE Std 802.3, Clause 104 powering classes are possible to be used and power levels up to 20 W can be covered. This allows a broad range of applications to be served by cable sharing.

With a good class F or F_A cabling system an efficient cable sharing system can be built, which allows to run 4 independent single pair ethernet applications over a 4-pair cabling system with a data rate of 10/100/1000Mbit/s per pair over 100m.

11. Acknowledgments

Special thanks go to the IWCS staff for making the most important industry event possible to highlight the progress on current and future cabling systems. Special thanks go to Dave Hess, as Co-Editor, for the great support and for holding the presentation.

12. References

The references are given directly in the document.

13. Authors



Peter Fischer studied Electrical Engineering at the University of Applied Science in Winterthur and has concretised his past managerial experiences and business administration knowhow by obtaining a double degree EMBA/MBA at HWZ in Zurich and USQ, University of Southern Queensland, Australia. He joined BKS Kabel-Service AG in 2020 as Head Business Solution & Innovation after formerly working 6 years at AESA Cortaillod in Colombier, Switzerland as R&D Project Manager/ Product line Manager and 6 years in the RF lab at Reichle & De-Massari AG in Wetzikon, Switzerland.

Peter Fischer is member of the IEEE 802.3 working group, experts of ISO/IEC JTC 1/SC 25/WG 3, IEC TC46 and SC48B standardisation committees and its working groups. He is the editor of the following international standardisation projects:

- WD ISO/IEC TR 11801-9911
- IEC 63171 Ed2.0
- IEC 63171-4 (published)
- IEC 60512-28-100 Ed3.0
- IEC 60512-99-003 Ed1.0 (to be published)
- IEC TS 61156-1-2 Ed1.0 (to be published)

In 2015 Peter Fischer has received the 'Urban J. H. Malo Memorial Medal Award in the Electrical division' of the Wire Association International. In 2023 IEC TC 46 announced him to get the IEC 1906 award for his contributions to data cable and the respective test standards.



Dave Hess. dba CORD DATA. currently works as a subject matter expert facilitating international standards development for connectivity technology. particularly in the area of shielded pair differential cabling. He has worked for more than 40 years in both fields of electronic and photonic wired data communication connectivity and participates on the standards committees for physical interface and cabling standards: ISO. IEC. IEEE. INCITS. EIA. TIA. CTA. and ANSI. He has been project leader for over 20 international standards. He received IEC 1906 awards for technical contributions in 2011 and 2014. He holds a B.S. degree in Mathematics from Pennsylvania State University and is a life member of IEEE.

Predictive Modeling of Large-Scale Flame Tests on Cables Using Cone Calorimeter

Dr. Jiyuan Kang
Engineered Materials, UL Solutions
Northbrook, IL
+1-847-664-8381 · Jiyuan.Kang@ul.com

Abstract
Cables in buildings are commonly installed through open or concealed vertical and horizontal passages, which can facilitate flame and/or smoke movement in the event of fire. To establish the fire safety of wire and cable products, UL Solutions conducts large-scale flame tests in accordance with safety standards, including NFPA 262 (plenum), UL 1666 (riser), and EN 50399. These tests require the use of large fire flame test chambers (with precise environment control) and a great deal of cable length (hundreds or even thousands of feet, depending on cable size). To supplement the large-scale fire tests and to address the above challenges, UL Solutions has developed predictive models that estimate the large-scale test performance of cables based on small-scale fire tests conducted using A cone calorimeter.

Keywords: Wire and Cable, Fire Testing, Machine Learning, Predictive Modeling.

1. Introduction
UL Solutions is a global leader in applied safety science that was founded 1894. It delivers testing, inspection and certification services, together with software products and advisory offerings, that support the customers' product innovation and business growth. Wire and Cable is one of the first industries UL Solutions started serving more than a century ago. Its laboratory staff conducted its first test on wire in 1896. The company played an important role in the early development of wire and cable testing, and fire safety has always been a major field of interest.

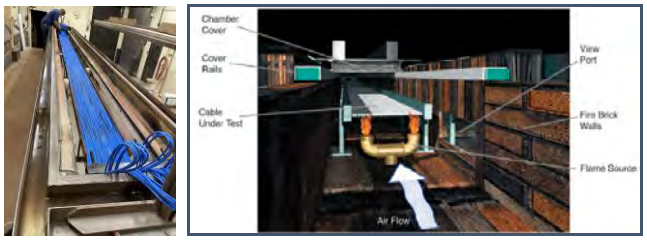
In modern buildings, there is always a large number of wires and cables installed in passages that connect rooms and floors to power electronics and facility devices. These structures can easily assist flame and smoke travel in the event of fire. To increase the fire safety of people's living and workspaces, UL Solutions has been conducting both large-scale and small-scale fire tests on wire and cable products for decades. With this long history of experience and understanding, UL Solutions determined the potential of creating predictive models by training computer algorithms to learn the correlation between large-scale fire performance from selected samples and their flammability characteristics measured from small-scale analyses. Then the algorithm uses that data to predict the new sample's large-scale fire performance based on input from small-scale analyses only.

To better represent the use of wire and cable products in modern buildings, the large-scale fire test standards NFPA 262, UL 1666 and EN 50399 were selected to be studied in this work. Samples were subjected to these tests in the corresponding large-scale apparatus first, then short lengths of the same cable from the large-scale tests were subjected to the cone calorimeter test in accordance with the test method specified in ASTM E1354. Cable samples obtained from NFPA 262 tests were examined using the sample holder specified by the standard, while samples obtained from UL 1666 and EN 50399 tests were tested using a vertical sample holder designed by UL Solutions. The large-scale test results were compared to the small-scale data using machine learning methods within a robust data science framework.

This paper will discuss three machine learning models that were created with respect to NFPA 262, UL 1666, and EN 50399 tests. The models were validated using data excluded from their training sets and examined during UL Solutions' surveillance programs.

2. Large-scale fire tests
2.1 NFPA 262 – plenum cable tests
NFPA 262, Standard Method of Test for Flame Travel and Smoke of Wires and Cables for Use in Air-Handling Spaces, was designed to evaluate cables intended to be installed through open or concealed, horizontal passages, which are used for environmental air-handling. Cables need to be designed to meet these rigorous requirements for fire resistance and limited smoke production.

The test is conducted in the test apparatus, also known as the Steiner Tunnel, described in NFPA 262. The test requires 24 ft ± 6 in lengths of cables to be installed in a single layer across a cable tray (see Figure 1a). The cable is ignited by a burner positioned close to the inlet of the tunnel (see Figure 1b). The flame propagation distance and smoke release data are recorded from the test.



(a) (b)



(c)

Figure 1. (a) Cable mounting in Steiner Tunnel, (b) Illustration of tunnel inlet, (c) View of Steiner Tunnel

The pass/fail requirements of this standard are that the cable under test shall achieve a maximum peak optical density (POD) of 0.50 or less, an average optical density (AOD) of 0.15 or less and a maximum flame spread distance of five feet or less.

2.2 UL 1666 riser cable test

UL 1666, the Standard Test for Flame Propagation Height of Electrical and Optical-Fiber Cables Installed Vertically in Shafts, was designed to evaluate riser cables installed in vertical runs in a shaft and penetrate one or more floors.

The cable specimen is installed vertically in the riser test chamber, with the burner positioned at the bottom of the first floor. Eight 28 AWG Type K thermocouples with an Inconel sheath are to be located in the slot on the second floor. During the test, ignition is initiated at the bottom end of the cable sample, and then the flame propagation in the vertical direction and temperatures in the second-floor slot are measured.

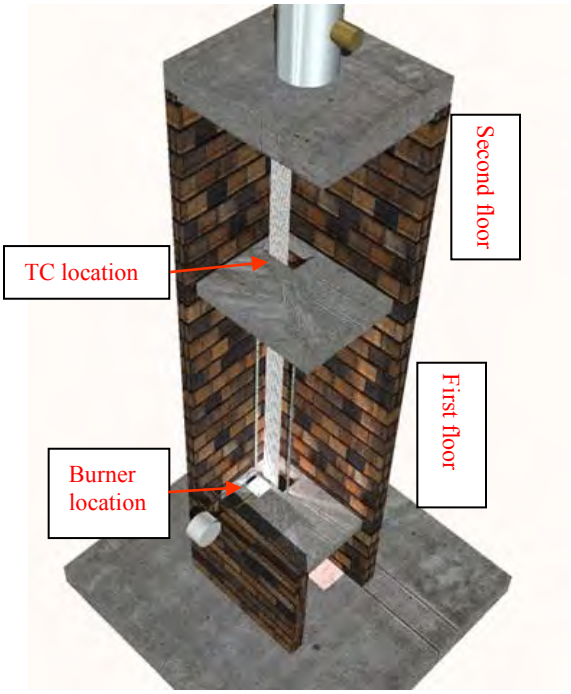


Figure 2. Illustration of the riser chamber

The pass/fail criteria states that the flame propagation height of each set of cables shall not equal or exceed 12 feet (3 m, 66 cm) and that the temperature of any thermocouple on the second floor shall not exceed 850 degrees F (454.4 degrees C).

2.3 EN 50399 CPR cable test

EN 50399, common test methods for cables under fire conditions, is used to evaluate wire and cable products under EU Regulation 305/2011 — harmonized conditions for the marketing of construction products, which is also called Construction Products Regulation (CPR). The requirements cover all types of cables used in construction works irrespective of type, size, shape, material, or end-use application (does not regulate cable installation location).

The test sample is mounted on the front of the standard ladder while the individual cable length or bundle is spaced in accordance with the standard. The mounting rule is described in section 6.4 of EN 50399.

The cable ladder is installed vertically in the EN test chamber (see Figure 3), and the burner is positioned above the lower edge of test pieces. During the test, the combustion gas generated from the burning sample will be directed through a smoke measurement system and then fed into a gas analyzer. As an outcome of this test, the flame spread distance, heat release rate, peak heat release, smoke production rate, peak smoke production, fire growth rate index (FIGRA) and occurrence of flaming droplets/particles are recorded.



(a) (b)

Figure 3. (a) Overview of the EN 50399 test chamber, (b) Cable installation before (upper) and during (lower) the test

As opposed to the plenum and riser flame tests noted above, the EN 50399 test does not have pass/fail test results. Instead, based on the results, the cables are placed into different classes based on a classification system that also references other standard tests. Detailed requirements are specified in EN 13501-6.

3. Cone calorimetry tests

The cone calorimeter is a fire testing tool based on the principle that the amount of heat released from a burning sample is directly related to the amount of oxygen consumed during combustion [4].

UL Solutions uses cone calorimetry to analyze short lengths of cables to determine their fire characteristics using the test method specified in ASTM E 1354 standard [5].

For plenum cable samples, the short lengths of cables are installed in the standard horizontal sample holder, and a spark igniter is used to trigger the sample ignition (see Figure 5).



Figure 5. Plenum cable sample loading and testing using cone calorimeter

In order to analyze riser and CPR cable samples, the special fire dynamic caused by vertical flame propagation in the large-scale test had to be taken into consideration. While conducting large-scale tests, it was determined that the cable sample at the upper location in the chamber is receiving heat from both the burner and the burning of the cable at the lower position. The standard sample holder specified in ASTM E 1345 standard was determined not suitable to replicate this fire dynamic, and as a result, UL Solutions has developed a small-scale ladder holder, which holds longer cable lengths in a vertical direction. In addition, an additional ignition burner is used at the bottom of the sample to test riser and CPR cables under the cone (see Figure 6).



Figure 6. Riser and CPR cable loading and testing using cone calorimeter

In order to develop a reasonable testing process for riser and CPR samples, UL Solutions used the riser chamber as a reference and conducted a set of thermal analyses on multiple tests. During the tests, thermocouples were used to measure temperature distribution on large-scale cable samples during the test (see Figure 7). Based on data analyses, a burner and cone heater output combination was created, which simulates the thermal environment that cable samples can experience between 4ft to 6ft inside the riser chamber.

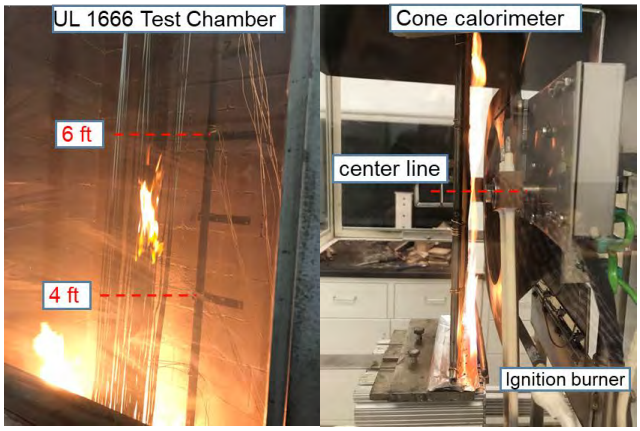


Figure 7. Riser chamber thermal analyses

4. Model development

The general principles for developing the machine learning predictive model are:

1. Collect large-scale flame data.
2. Collect data using cone calorimeter.
3. Develop computer algorithms to use the data to determine the correlation between cable fire properties and its large-scale fire performance.
4. Use computer algorithms to predict the large-scale fire performance of an unknown cable based on small-scale test data only.

In this stage, cone calorimetry was used to collect heat release history, smoke generation data and mass consumption from cable samples, then compile the data together with corresponding large-scale test results to form a training data set for model training (see Figure 8).

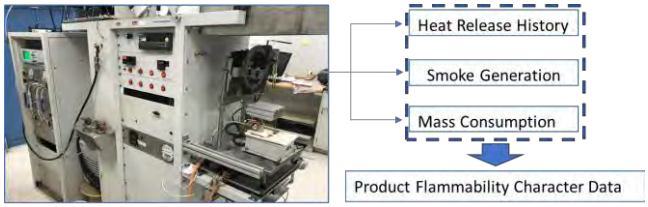


Figure 8. Data arrangement of cone calorimetry

4.1 Plenum model

The predictive model to predict NFPA 262 test was updated in early 2021. The formal UL Solutions' cone datasheet was revised to reflect model prediction for the large-scale test performance criteria.

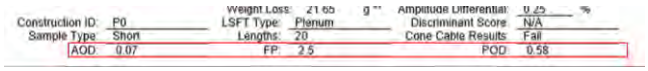


Figure 9. Cone datasheet with plenum prediction

The model output includes three parameters: predicted average optical density (AOD), predicted flame propagation (FP) and peak optical density (POD), which directly relate to the large-scale test results (see Figure 9).

The model was validated using 17 cables purchased in the U.S. market that were self-declared as being plenum cables. These cables were subjected to both large-scale and small-scale tests. The model showed a perfect performance on predicting the LSFT pass/fails, the predictions were confirmed by the actual large-scale tests.

4.2 Riser model

The development of a predictive model to predict a UL 1666 test was also updated in early 2021 and was deployed in a similar structure as the plenum model.

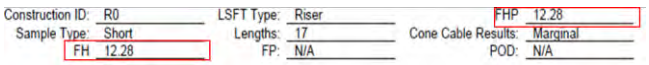


Figure 10. Cone datasheet with riser prediction

The riser model output includes two parameters: predicted flame height (FH) and flame height prediction (FHP), the thermocouple readings of riser chamber are not included in model prediction. The FH parameter is the direct prediction of the UL 1666 test result. Its maximum output is 12.5 ft, which is the testing section

height of the riser chamber. While making the FHP output, the model is assuming that the sample height is unlimited. When predicted flame height is less than 12.5 ft, the FHP value will be equal to the FH value. For a very flammable cable that can have a flame propagation reaching the second floor slot of the riser chamber, the FH value will be 12.5 ft, which is the maximum result a UL 1666 test can generate, while the FHP value will be the predicted flame height of the same cable with unlimited flame height.

The FHP output was determined to be a very useful reference to help determining the level of non-conformances. The riser model was hence particularly accurate in predicting significant nonconformances (SNCs).

The riser model was validated using seven cables purchased in the U.S. market that were self-declared as being riser cables. After subjecting the cables to both large-scale and small-scale tests, the model was proven to be accurate in determining pass/fail results.

4.3 EN 50399 model

The development of EN 50399 model was completed during Q1 of 2023. The model is currently under internal validation/review.

The model was developed with the combined use of both classification and regression modeling techniques, focusing on Class B2ca, Cca, and Dca predictions. The model was designed to be capable of classifying the sample as well as predicting the THR, Peak HRR, FIGRA, and fire spread. Smoke production and droplets were not included in the model prediction.

5. Conclusions

Using small-scale testing as a supplementary piece in the large-scale cable flame evaluation system can provide many advantages.

In comparison to the large-scale flame test, conducting a small-scale cone test is more time and cost-efficient and requires only 20 ft of cable (in comparison to hundreds or thousands of feet of cable required for one large-scale fire test). Although the models were proven to yield high accuracy during validation, they are not yet 100% perfect for a variety of reasons. UL Solutions continues to collect data points to improve model accuracy and actively invests in developing new predictive models.

6. Acknowledgments

Special thanks to Anthony Tassone and Dmitriy Bodik for their contributions to the content and review of the final document.

7. References

[1]. NFPA 262. *Standard Method of Test for Flame Travel and Smoke of Wires and Cables for Use in Air-Handling Spaces.* 2023 Edition. Quincy. MA. NFPA Standards. 2023.

[2]. UL 1666. *UL Standard for Safety for Test for Flame Propagation Height of Electrical and Optical-Fiber Cables Installed Vertically in Shafts.* 5th ed. 2021.

[3]. EN 50399. *Common test methods for cables under fire conditions - Heat release and smoke production measurement on cables during flame spread test.* 2022 Edition. Brussels, Belgium. CENELEC. 2022.

[4]. "Cone Calorimeter." TOOLS & INSTRUMENTS, 5 June 2014, www.nist.gov/laboratories/tools-instruments/cone-calorimeter.

[5]. ASTM E1354. *Standard Test Method for Heat and Visible Smoke Release Rates for Materials and Products Using an Oxygen Consumption Calorimeter*. ASTM International. West Conshohocken. PA. 2023. DOI: 10.1520/E1354-22A.

8. Pictures of authors



Jiyuan Kang

UL Solutions

333 Pfingsten Rd

Northbrook, IL, 60062

Dr. Jiyuan Kang is a fire scientist working in the field of fire protection for wire and cable products. He earned his Ph.D. in mechanical engineering at Case Western Reserve University, with his research interests focused on combustion and fire science. He is a senior staff engineer in the Engineered Materials Operating Unit at UL Solutions. He has published articles in Fire Technology and Journal of Fire Science. He is based out of the UL Solutions headquarters in Northbrook, IL, USA.

Cabling for Fault-Managed Power Systems (What is Class 4?)

Ronald Tellas
Belden
St. Augustine, FL
+1-219-218-5699 · ronald.tellas@belden.com

Abstract

Remote powering enables you to place end devices where they're needed—instead of worrying about their proximity to a power source. There are several options when it comes to remote powering: direct current (DC), Power over Ethernet (PoE) and now fault-managed power systems (FMPS). Each one has its own benefits and is defined in the NFPA 70® National Electrical Code® (NEC) as a different class.

Class 2 remote power delivery (DC power supplies and PoE) carries a 100W power limitation and has a "practical" reach of only a few hundred meters. Network connectivity to end devices that require more than 100W or are installed several hundreds of meters from a switch or patch panel can lead to costly solutions. FMPS is a new technology, now defined as Class 4, that goes beyond the limitations of Class 2 while maintaining the benefits and flexibility of remote powering.

To be properly listed, Class 4 cables require UL 1400-2 certification. Belden is the first cable manufacturer to receive certification to Class 4 requirements for copper-only and hybrid cables. Within this paper, definitions of NEC Classes 1, 2, 3 and 4 are discussed, along with cable requirements for each class and the types of cables available for each class (Category cabling, copper-only cables and hybrid cables). An explanation of UL 1400-2 certification requirements is discussed as well.

From this paper, you'll better understand what Class 4 is, what cabling is required to support it and how it fits into the NFPA 70 NEC. Empowered with this information, you'll be able to make the right decision about remote power options and know how to properly connect end devices to optimize your network for today and tomorrow.

Keywords: fault-managed power; cable; class 4; hybrid cable; NEC; remote power; NFPA 70

1. Introduction

Remote powering enables the ability to easily place end devices where they are needed instead of based on proximity to a power source. Class 2 remote power delivery (DC power supplies and Power over Ethernet) carries a 100W power limitation and has a "practical" reach of only a few hundred meters. Network connectivity to end devices requiring more than 100W or spanning several hundreds of meters can lead to costly solutions. A fault-managed power system (FMPS) is new technology, defined as Class 4, that can go beyond the limitations of Class 2 and maintain the benefits and flexibility of remote powering. Understanding remote powering options will help you make the right decision to optimize your network for today and tomorrow.

2. Remote Powering

2.1 Capabilities of DC, PoE and FMPS

End devices on the network need data and power connections. A centralized remote power delivery system delivers both data and power from one location. Data rate, delivered power and distance determine which method of centralized remote power delivery can be used (DC, PoE or FMPS).

2.1.1 Class 2, DC Power

The limit of a Class 2 power supply is 100W. The delivered power depends on the voltage drop limit of the cable, which is determined by the designer of the power delivery system; the gauge size of the conductors used; and the voltage drop requirement. The overall reach is determined using an online calculator, as shown in Table 1, using a 57 VDC power supply. Conductors for power delivery are generally located within a separate cable or combined with singlemode fiber to form a hybrid cable, making this power delivery system independent of data speed.

Table 1. Class 2 DC Maximum Power Delivery and Reach

Power, Source	Voltage Drop	Power, Delivered	Wire Size	Reach	Maximum Data Speed
100W	10%	90W	16 AWG	405 ft (123 m)	Not Dependent on Reach
	20%	80W		809 ft (247 m)	
	10%	90W	18 AWG	254 ft (78 m)	
	20%	80W		509 ft (155 m)	

2.1.2 Class 2, Power over Ethernet

As stated previously, the limit of a Class 2 power supply is 100W. The requirement for power over direct lines in IEEE 802.3 (commercially known as PoE) states that the DC loop resistance of the conductors cannot exceed 25 Ω. The physical limitation of PoE is due to the resistance of the wires within the cable, suggesting that the maximum reach can be extended by increasing the gauge of the wires.

Because the cabling supplies data and power, the actual limit must take into consideration the desired data speed of the application, along with the DC loop resistance. The traditional 100 m channel reach associated with balanced twisted-pair cables is no longer the limit for Category cables made with exceptional headroom or balanced twisted-pair cables that are designed for specific application support, as shown in Table 2.

Table 2. Class 2 PoE Maximum Power Delivery and Reach

Power, Source	Power, Delivered	Cable Type, Wire Size	Reach	Maximum Data Speed
90W	71W	Category 6A 23 AWG	328 ft (100 m)	10 Gb/s
			361 ft (110 m)	1 Gb/s
			394 ft (120 m)	100 Mb/s
			394 ft (120 m)	10 Mb/s
		Application Cabling 22 AWG	Not Specified	10 Gb/s
			426 ft (130 m)	1 Gb/s
			656 ft (200 m)	100 Mb/s
			705 ft (215 m)	10 Mb/s

2.1.3 Class 4, Fault-Managed Power

Class 4 systems, like the limited-power classes, are designed with safety at the forefront. Instead of limiting power source output, they limit the energy and power available during a fault event. If a line-to-line or line-to-ground fault does occur, then the system immediately and automatically shuts off before causing harm.

To limit fault energy, a transmitter and receiver continuously monitor for faults and control power delivery. This technology makes Class 4 systems just as safe as—if not safer than—Class 2 and Class 3 systems. The reach and power of an FMPS are dependent on the manufacturer of the system. Typical lengths and power delivery using a commercially available Class 4 FMPS are given in Table 3. Conductors for power delivery are generally located within a separate cable or combined with singlemode fiber to form a hybrid cable, making this power delivery system independent of data speed.

Table 3. Typical Power and Reach for a Commercially Available FMPS

Power, Source	Power, Delivered	Wire Size	# of pairs	Reach	Maximum Data Speed
Undefined	100W	16 AWG	1	6,500 ft (1,982 m)	Not Dependent on Reach
	600W		1	4,000 ft (1,220 m)	
	1,200W		2	1,900 ft (579 m)	
	2,400W		4	500 ft (152 m)	
	100W	18 AWG	1	6,500 ft (1,982 m)	
	600W		1	2,500 ft (762 m)	
	1,200W		2	1,200 ft (366 m)	
	2,400W		4	400	

2.2 NEC Definition of Class Circuits

Adopted in all 50 states, NFPA 70, National Electrical Code (NEC) is the benchmark for safe electrical design, installation and inspection to protect people and property from electrical hazards. Communication systems no longer use cabling to only deliver data to end devices, but also deliver power for certain classes of power delivery systems, provided that the cables are properly listed.

Cabling that delivers power is considered a circuit, and definitions of these circuit classes as given in the 2023 NEC are presented in Table 4.

Table 4. NEC Definitions of Class Circuits

Type	2023 NEC Definition
Class 1 Circuit	The portion of the wiring system between the load side of the Class 1 power source and the connected equipment.
Class 2 Circuit	The portion of the wiring system between the load side of a Class 2 power source and the connected equipment. Due to its power limitations, a Class 2 circuit considers safety from a fire initiation standpoint and provides acceptable protection from electric shock.
Class 3 Circuit	The portion of the wiring system between the load side of a Class 3 power source and the connected equipment. Due to its power limitations, a Class 3 circuit considers safety from a fire initiation standpoint. Since higher levels of voltage and current than for Class 2 are permitted, additional safeguards are specified to provide protection from an electric shock hazard that could be encountered.
Class 4 Circuit	The portion of the wiring system between the load side of a Class 4 transmitter and the Class 4 receiver or Class 4 utilization equipment, as appropriate. Due to the active monitoring and control of the voltage and current provided, a Class 4 circuit considers safety from a fire initiation standpoint and provides acceptable protection from electric shock.

2.2.1 Class 1 Circuits

There are two categories of Class 1 circuits: remote-control and signaling circuits, which shall not exceed 600V, and power-limited circuits, which operate at no more than 30V and 1,000VA, with limited source output. Power-limited circuits also restrict the amount of supply current on the circuit in the event of a ground fault, short circuit or overload. Typically, Class 1 circuits are found in environments where motors and compressors are used.

2.2.2 Class 2 Circuits

Class 2 circuits can support power up to 100VA, consider safety from a fire initiation standpoint and provide acceptable protections from electric shock. Applications include audio systems, low-voltage lighting systems, security systems, thermostats and PLCs. Class 2 power is often delivered using PoE, which combines power and data in a listed balanced twisted-pair cable.

2.2.3 Class 3 Circuits

Class 3 circuits function similarly to Class 2 circuits, but with higher voltage and power limitations, and usually aren't as common as Class 2 circuits. Class 3 power is used for equipment that requires more than what Class 2 can provide, such as nurse call systems, commercial public address systems and commercial intercom systems. Similar to Class 2, Class 3 power is often delivered using a listed balanced twisted-pair cable.

2.2.4 Class 4 Circuits

Class 4 circuits utilize systems with sophisticated monitoring and controls that monitor the circuit for faults and limit the power transmitted to ensure that the energy delivered into a fault is limited. Class 4 fault-managed power systems are not power limited at the source but between the output of the Class 4 transmitter and input of the Class 4 receiver with respect to risk of electric shock and fire hazards. To obtain higher power or reach possibilities needed for distributed antenna systems (DAS) or POLAN applications, Class 4 is delivered with larger-diameter conductors than what are used in a typical Category cable.

A summary of key parameters of each circuit class is given in Table 5. Note that the Cable Listing classification is only a partial list, many others exist for Class 1 circuits made of insulated conductors. The key parameters of safety from a fire initiation standpoint and provision of acceptable protection from electric shock are only met by Class 2 and Class 4 systems, making them equally as safe. The ability to distinguish the occurrence of a line-to-line or line-to-ground fault is only possible with FMPS, which fuels the argument that Class 4 systems are the safest.

Table 5. Key Parameters of Class Circuits

Key Parameter	Class 1	Class 2	Class 3	Class 4
Safety from fire initiation standpoint	No	Yes	Yes	Yes
Provides acceptable protection from electric shock	No	Yes	No	Yes
Cable Listing	TC TC-ER	CL2 CL2R CL2P CL2X	CL3 CL3R CL3P CL3X	CL4 CL4R CL4P
Minimum voltage cable rating	600V	150V	300V	450V

3. Class 4 Cables

3.1 Certification Requirements

To substantiate the need for a new NEC article for Class 4, and to certify cables and systems, a research and development project was created. Members of this project, led by Underwriters Laboratories (UL), included manufacturers of equipment, cable and materials, as well as members of the Alliance for Telecommunications Industry Solutions (ATIS). After much collaboration and testing, two documents were produced.

UL 1400-1, *Outline of Investigation for Fault-Managed Power Systems - Part 1: Safety Requirements*

UL 1400-2, *Outline of Investigation for Fault-Managed Power Systems – Part 2: Requirements for Cables*

An outline of investigation is a published document suitable for certifications and can be edited to add additional content prior to becoming an ANSI-certified standard. This is a common path of standards development to make changes and adjustments more quickly than in the traditional change process for ANSI standards.

Cable requirements in UL 1400-2 closely follow UL 13, Standard for Safety Power-Limited Circuit Cables. The Class 4 FMPS voltages require a cable with a voltage rating of 450V. This rating is required to cover the actual line-to-line potential difference with allowance for a safety margin. The voltage requirement, along with limiting the conductors to a range between 24 AWG and 6 AWG copper, mandated a new certification document. When compared to UL 13, the UL 1400-2 document has greater insulation thickness and greater voltage to spark test the cable after jacketing and to test the dielectric-withstand.

3.2 Class 4 Cable Examples

In roughly eight years, tens of thousands of FMPS systems have been deployed. These systems supply power to DAS, small cells, passive optical LAN, agricultural lighting and power distribution infrastructure. Millions of linear feet of cabling have been deployed to support these systems. The cables are similar in appearance to Figure 1, with the following characteristics.

- 16 or 18 AWG
- Copper or Hybrid
- Plenum or Riser
- Shielded or Unshielded
- Indoor or Outdoor

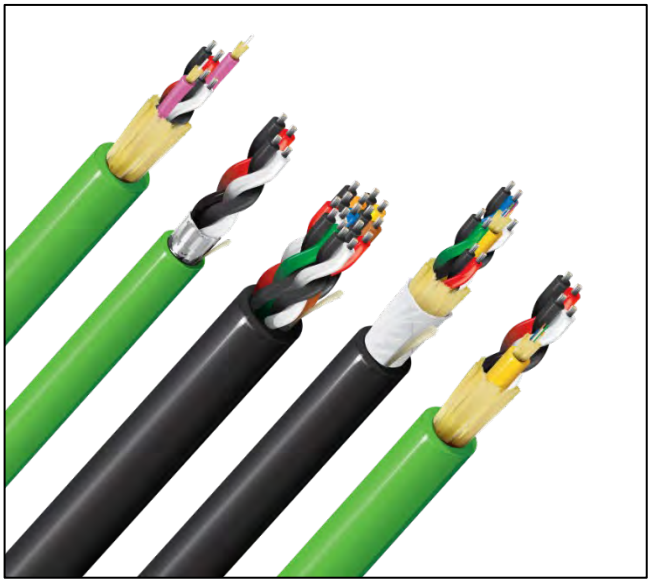


Figure 1. Cabling Optimized for FMPS

For jurisdictions adopting the 2023 NEC and later, it will be important to verify that the cabling is Class 4 certified. Cables

certified to UL 1400-2 are found under product category DLPY in the UL Product iQ database (https://iq.ulprospector.com/).

3.3 Installation Use Cases

The code-making panel that created the new Article 726 in the 2023 NEC was very mindful to ensure that the code supported the technology benefits of Class 4 FMPS to connecting edge devices to the network. The excerpt of 726.139(C) is shown in Figure 2.

726.139(C) Class 4 Cables With Other Circuit Cables.

Jacketed cables of Class 4 circuits shall be permitted in the same enclosure, cable tray, raceway, or cable routing assembly with jacketed cables of any of the following:

(1) Power-limited fire alarm systems in compliance with Parts I and III of Article 760
(2) Nonconductive and conductive optical fiber cables in compliance with Parts I and IV of Article 770
(3) Communications circuits in compliance with Parts I and IV of Article 805
(4) Community antenna television and radio distribution systems in compliance with Parts I and IV of Article 820
(5) Low-power, network-powered broadband communications in compliance with Parts I and IV of Article 830

Figure 2. Class 4 Permissions from 2023 NEC

In short, the article states that Class 4 cabling can use the same pathways and spaces as communication systems cabling and follow the same separation rules. The ultimate benefit of the Class 4 technology is the cost savings from the use of trays. Figure 3 shows how a Class 4 cable can be installed in a tray alongside fiber optic cabling.

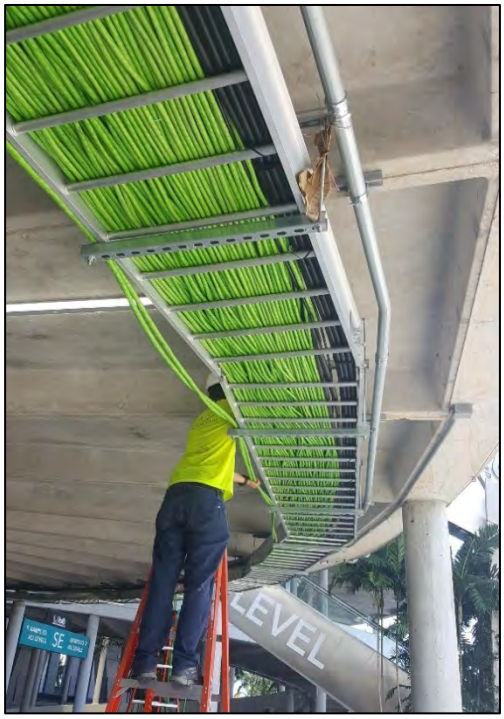


Figure 3. FMPS Cabling Installed per 726.139(C)

4. Conclusion

Class 4 circuits provide the convenience and safety of Class 2, just like PoE; however, Class 4 also offers close to 20 times the power of PoE across hundreds of meters, presenting a safe alternative to remote powering. Unlike Class 2 and Class 3 power-limited circuits, Class 4 circuits don't limit power source output. Instead, they constantly monitor for faults and control the delivery of power current available during an abnormal condition. This mitigates the risk of shock or fire by limiting the amount of energy that can go into a fault.

To verify compliance with NEC requirements, Class 4 circuits must be certified. UL recently published UL 1400-2 as an Outline of Investigation (the first step toward a standard) to define safety considerations and criteria for evaluating Class 4 circuit cabling. Cables for Class 4 circuits are certified to the published document.

5. References

[1] CCCA New Technology and Trends Committee, "Going the distance: What you need to know about breaking the 100-meter distance limitation" *Cabling Installation & Maintenance Mag.*, vol. 30, no. 4, 16-25 (September/October, 2022).

[2] National Fire Protection Association, NFPA 70 ®, "*National Electrical Code ® (NEC)*", 2023 Edition.

[3] UL, "*UL 1400-2, Outline of Investigation for Fault-Managed Power Systems – Part 2: Requirements for Cables",* Issue Number: 2, July 2023.

[4] Betsy Conroy, "FAULT MANAGED POWER—A Safe and Disruptive Innovation for Powering the Future*", ICT Today Mag.,* Volume 44, Number 2, 6-11, (Apr/May/Jun 2023).

6. Acknowledgments

Special thanks to the Belden R&D and Product Line Management teams for valuable input into the content and to Leah B. Grout-Garris for assistance in the writing and editing this paper.

7. Author



Ronald Tellas
Technology and Applications Manager
Smart Buildings and Data Centers
Belden

Ronald Tellas is a subject-matter expert in RF design and Electromagnetic Propagation and joined Belden in 2016 to help define the roadmap of technology and applications in the Smart Building and Data Center. He represents Belden in the ISO WG3 committee, TIA TR42 Premises Cabling Standards and IEEE 802.3 Ethernet Working Group and is a committee member of NFPA 70 Code-Making Panel 3 and 16. Ron is the inventor of 16 US patents. He has a Bachelor of Science degree in Electrical Engineering from Purdue University, a Master of Science degree in Electrical Engineering from Illinois Institute of Technology, and a Master of Business Administration from Purdue University.

.

SESSION 10

Click on a session below to navigate to that section of the Proceedings.

SESSION 10: DESIGN, TESTING & APPLICATIONS FOR COPPER ETHERNET, POE AND ENERGY CABLES - PART 2

Chairperson: Ed Fenton, Daikin America, USA

10-1 **Extended 10Gbps Data Transmission Over Cat 6A: Facts vs Myths;** Solomon Girma, *Superior Essex Communications, USA*

10-2 **Intra-Pair Skew: About Wave Propagation in Screened Single Pair;** Dr. Boris Dardel, *AESA SA, Switzerland*

10-3 **Coupling Attenuation and Burst Test on Balanced Cables and Cabling Systems;** Dave Hess, *Cord Data, Germany*

10-4 **Designing of Single-Pair Ethernet Cable;** Dr. Juliusz Poltz, *OptEM Engineering Inc., Canada*

10-5 (10:05) **Environmental Resilience of Twisted Pair Ethernet Applications at Lengths Greater than 100 Meters;** Mr. Michael Dodds, *Leviton Manufacturing Co., Inc., USA*

10-6 **Relation of Coupling Attenuation and Unbalance Attenuation;** Mr. Dave Hess, *CORD DATA, USA*

10-7 **Measuring and Simulating TCTL in Unbalanced Cable;** Dr. Juliusz Poltz, *OptEM Engineering Inc., Canada*

10-8 **Power Over Communication Cables for Extended Distance: Myths and Misconceptions;** Mr. Amir Sekhavat, *Superior Essex, USA*

Click here to return to the **Table of Contents**

Extended 10Gbps Data Transmission over CAT 6A: Facts Vs. Myths

Solomon Girma, Christopher McNutt, Amir Sekhavat

Superior Essex International LP- Communications

3600 Cobb International Blvd, Suite 400

Kennesaw, Georgia 30152

5712303110 Solomon.girma@spsx.com

Abstract

This paper investigates the feasibility of using extended distance applications to achieve data rates of 10 Gbps over distances greater than one hundred meters. The primary goal is to determine whether using such applications would be practical and cost-effective by eliminating the need for additional telecom rooms. To evaluate the quality of the communication channel, several performance parameters were measured, including insertion loss, PSNEXT, PSFEXT, PSANEXT, and PSAFEXT. These parameters help determine how much signal is lost or distorted as it passes through a communication channel. The measured data was analyzed to determine the overall performance, and one such parameter is Signal to Noise Ratio (SNR), SNR is as ratio of the signal to Crosstalk Noise. Shannon-Hartley Maximum Data Rate and Bit Error Rate (BER) were calculated based on the SNR and modulation index. The IEEE standard for Ethernet communication systems specifies a maximum BER of 10^-12, which was achieved when the length of the cable was 110 meters or less. Finally, the theoretical calculated results were validated by separate measurements performed at a third-party lab. The results showed that data rates of 10 Gbps could be achieved over distances of up to 110 meters using extended distance applications.

Keywords: Shannon-Hartley, Bit Error Rate, Signal to Noise Ratio.

1. Introduction

The Telecommunications Industry Association (TIA) TR-42 plays a crucial role in establishing and upholding standards for telecommunications cabling. Among these standards, ANSI/TIA-568.B [1] outlines the cabling and link requirements for achieving 10 Gbps operation at one hundred meters. This standard incorporates a specific modulation type to meet the data rate requirements.

However, there is a growing demand to extend the reach of 10Gbps data transmission while minimizing the need for additional telecom rooms. This research aims to determine the practicality of using extended distance applications.

To evaluate the feasibility of such applications, we conducted theoretical calculations on electrical parameters to assess their suitability for achieving 10 Gbps data rates at longer distance. The calculations conducted in this research highlighted the significance of not extending the 10 Gbps application beyond the recommended distance of one hundred meters. To validate the accuracy of the theoretical calculations, we conducted separate measurements in a third-party laboratory. Through these calculations and third-party validation, it became evident that exceeding this distance can have adverse effects on the performance and reliability of the application.

2. Methodology

We conducted two separate studies in different labs for this investigation. In our lab, we measured the electrical parameters and used Bit error rate model for 128-DSQ modulation and check a requirement of at least 10^-12 has been achieved [5][6].

In the third-party lab, The BER calculation involves comparing the received data with the transmitted data and determining the number of bit errors that occur. By analyzing the ratio of bit errors to the total number of transmitted bits, the BER can be calculated. If the calculated BER is equal to or lower than the IEEE standard of 10^-12[5][6], it indicates that the system is performing within the expected range.

2.1 Measured Parameters in our Laboratory

To evaluate the quality of the communication channel, several performance parameters were measured at a temperature of 21.0°C, including insertion loss (IL), PSNEXT, PSFEXT, PSANEXT, and PSAFEXT at the distances of 140m, 130m, 120m, 110m, and 100m.

The IL represents the loss of signal power in the communication channel, and Noise refers to the combined power of the noise sources affecting the signal. In a cabling system, the main sources of noise or interference are typically associated with crosstalk between different wire pairs or cables [1][2][3].

$$Noise = \sum (PSNext + PSFEXT + PSANEXT + PSAFEXT) \quad (1)$$

Where:

PSNEXT: Power Sum Near End Crosstalk

PSFEXT: Power Sum Far End Crosstalk

PSANEXT: Power Sum Alien Near End Crosstalk

PSAFEXT: Power Sum Alien Far End Crosstalk

2.1.1 Signal-to-Noise Ratio (SNR). SNR is a measure of the signal strength compared to the background noise level. It is typically expressed in decibels (dB) and indicates the quality of the received signal. Signal to noise ratio can be represented in [2][3]. as follows:

$$SNR = IL - Noise \quad (2)$$

Where:

SNR: Signal-to-Noise Ratio

IL: Insertion Loss (in dB)

Noise: Power Sum of the Noise Contributors (in dB)

***2.1.2* Shannon-Hartley Theorem.** The Shannon-Hartley theorem provides an upper bound on the achievable data rate for a given channel bandwidth and SNR. It calculates the maximum data rate (in bits per second) that can be reliably transmitted over the channel.

The formula for calculating the theoretical maximum data rate is [2][3]:

$$C = \int_0^B log_2(1 + SNR)df \quad (3)$$

Where:

C: Channel capacity (maximum data rate)

B: Bandwidth of the channel (in hertz)

SNR: Signal-to-Noise Ratio

2.1.3 Bit Error Rate (BER) for Different Modulation Types. BER represents the probability of an error occurring in a received bit of data. It is influenced by factors such as modulation type, channel conditions, and SNR [2].

The mathematical relationship between BER, SNR, and modulation index can vary depending on the modulation scheme and the system design [2][3].

In the case 10Gbps, the 128-DSQ (128-Dimensional Square Constellation) are adopted to achieve higher data rates while maintaining the desired BER requirements [3]. 128-DSQ constellation is the natural in-between 8-PAM and 16-PAM modulation [4].

The relationship between BER, SNR, and modulation index in PAM modulation can be approximated by the equation (4) as in [2]:

$$Bit\ Error\ Rate = \frac{2(M-1)}{Mlog^2M} Q\left(\sqrt{\frac{6*log_2M*SNR}{M^2-1}}\right) \quad (4)$$

Where:

BER: Bit Error Rate

SNR: Signal-to-Noise Ratio

M: the number of levels or modulation index

In IEEE standards, a Bit Error Rate (BER) requirement of at least 10^-12 is expected for reliable data transmission. This means that the probability of an error occurring in the received data should be less than or equal to 10^-12[5][6].

The main study on the research is to find Signal-to-Noise Ratio (SNR) required to achieve a Bit Error Rate (BER) of 10^-12 for a 10 Gbps system using 128-DSQ modulation and validate that using the third-party lab measurement.

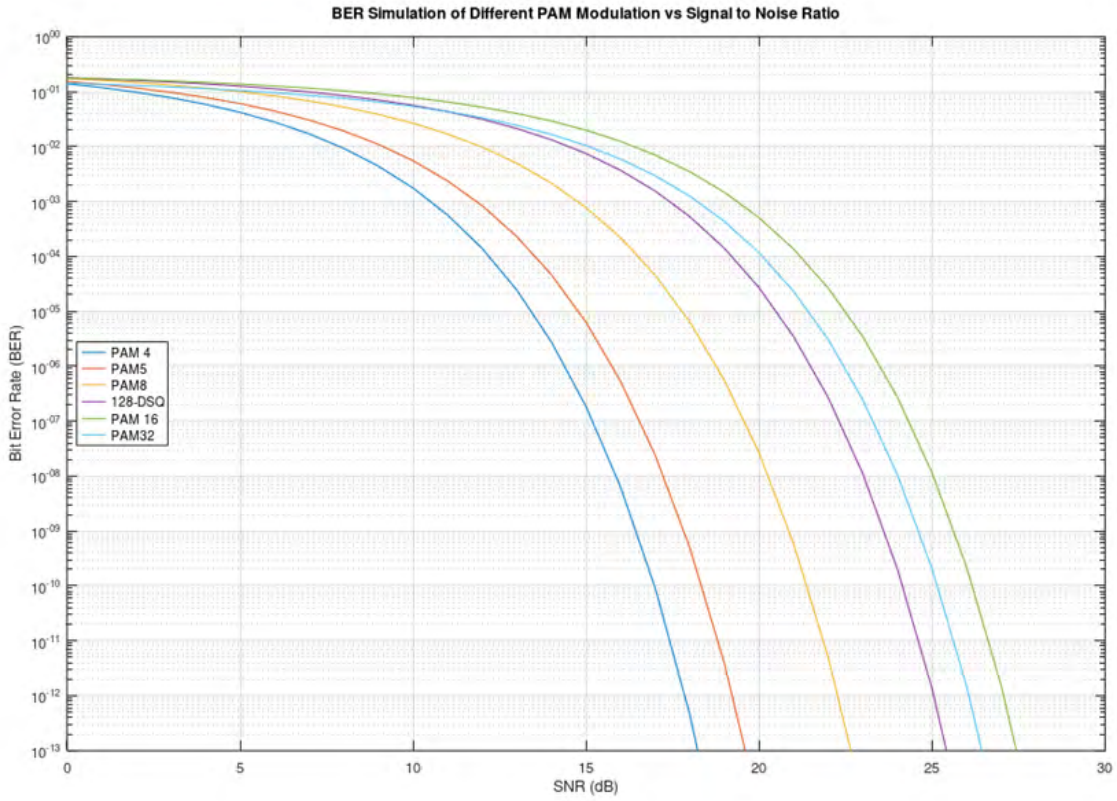


Figure 1:BER Simulation of Different PAM Modulation Vs Signal to Noise Ratio

To determine whether the required SNR has been achieved for the desired bit error rate (BER), we calculate the SNR at various cable lengths: 140m, 130m, 120m, and 110m. This analysis helps us assess if the BER requirement for 10Gbps application has been met.

2.2 Third party Test

In the third-party test, CAT 6A cable performance was measured at a temperature of 21.0°C using both solid and stranded patch cords. The test was initiated at a length of 160 meters, and in cases where the data transmission failed to achieve 10 Gbps, a 5-meter cable cut back was performed before retesting.

This testing approach was used to determine the maximum achievable distance for dependable 10 Gbps data transmission over CAT 6A cable, considering the specific patch cord types (solid and stranded) and the environmental conditions (temperature).

Configuration #1: Patch Cord on One Side

In the configuration where a patch cord was connected on one side of the system, and the data rate is 10 Gbps, the transmission is conducted over CAT 6A cable at different lengths until the system passes the test.

Configuration #2: Patch Cord on Both Sides

In the configuration where patch cords are connected on both sides of the system, the additional patch cord can indeed have an impact on the overall system performance, including parameters such as insertion loss, crosstalk, and signal integrity. The Test is repeated until 10Gbps are received without error.

3. Experimental Result

The figure 1 shows the BER rate performance of PAM modulation at different modulation index. The simulation results show the IEEE standards, a Bit Error Rate (BER) requirement of at least 10^-12 is achieved at different SNR values for different modulation index.

According to the simulation results, for the 128-DSQ modulation scheme, it is determined that to meet the IEEE standards' Bit Error Rate (BER) requirement of at least 10^-12 or higher, the system Signal-to-Noise Ratio (SNR) needs to be 25 dB or better.

This finding suggests that to achieve a BER of 10^-12, the SNR should be at least 25 dB higher than the noise power in the system. This indicates the need for a strong and reliable signal relative to the noise level to ensure accurate data transmission for the 128-DSQ modulation scheme and 10Gbps application**.**

3.1 Validation Results

Based on the adopted modulation type for 10Gbps applications, it has been determined that to achieve a Signal-to-Noise Ratio (SNR) of 25 dB or higher for reliable communication without errors. Table 1 indicates SNR calculations performed from the insertion loss and crosstalk measurements; the corresponding length of the cable is slightly over 110 meters.

This finding helps establish the maximum cable length for achieving the specified performance criteria in terms of SNR. It indicates that 10Gbps application, cables exceeding 110 meters in length resulted in lower SNR values and degradation in communication performance.

Table 1: Signal to Noise Ratio Calculation at Different Length of cable

Distance (m)	SNR (dB)	Pass/Fail
100	28.32	Pass
110	25.65	Pass
120	23.9	Fail
130	21.28	Fail
140	18.92	Fail

Table 2 shows the test measurement results conducted by the third party on CAT 6A cable performance. According to the results, it has been determined that the CAT 6A cable can support 10 Gbps applications over a little over 110 meters in two different configurations.

Table 2: **Results from the third-Party Laboratory**

Test	Configuration	Horizontal Cable (m)	Patch Cord(m)	Total Length (m)	Pass/Fail
Solid Patch	I	110	2	112	Pass
Stranded Patch	I	115	1	116	Pass
Solid Patch	II	110	2	114	Pass
Stranded Patch	II	105	4.5	114	Pass

4. Conclusions

The findings from the tests conducted in our lab and the third-party lab showed strong similarities between the theoretical expectations and the actual test results obtained in both labs. This consistency indicates the reliability and accuracy of the conducted tests.

The study shows that the 10 Gbps application can reach up to 110 meters. However, it is important to note that the industry standard for this application typically specifies a maximum distance of one hundred meters for reliable transmission [1]. The standard is based on many factors such as signal degradation, insertion loss, crosstalk, and overall performance considerations.

While the tested setup was able to sustain 10 Gbps transmission up to a slightly longer distance, it is possible that the performance may start to degrade or fall outside the specified tolerances beyond the industry standard distance.

Considering the industry standards and guidelines is important to ensure reliable and consistent performance in real-world deployments. While the test results show the potential for a slightly longer distance, it is advisable to adhere to the industry standard of one hundred meters for 10 Gbps applications to maintain optimal performance and compatibility across different network infrastructures.

5. References

1. ANSI/TIA/EIA 568-B,' Commercial Building Telecommunications Cabling Standard,' Quang Dung Technology Distribution Company,
2. Andrea Goldsmith,' Wireless communications,' Cambridge University Press, New York, 2005
3. T. Rappaport, 'Wireless Communications: Principles and Practice (second ed.),' Prentice Hall PTR, Upper Saddle River', NJ, USA (2001)
4. IEEE P802.3an Task Force,' 10GBASE-T Coding and Modulation: T Coding and Modulation:128-DSQ + LDPC DSQ + LDP,' Broadcom, Ottawa, September 29 – October 1, 2004.
5. Newcome-Acorn Joint Workshop,'10GBASE 10GBASE-T: 10Gbit/s Ethernet over copper,' Vienna, 20-22 September 2006
6. Shimon M, Jeff W, Geoff T, Bruce T and Brad B,'IEEE 802 10GBASE IEEE 802 10GBASE-T Tutorial,' November 2003.

6. Authors

Solomon Girma is a R &D Engineer at Superior Essex International LP - Communications for the premises copper cables.

He has background in RF system, EMC/EMI, Transmission Line Theory, and POE. He holds a Ph.D. Degree in Telecommunication

Engineering from Jomo Kenyatta University of Agriculture and Technology.



Christopher McNutt is Director of Product Development for Superior Essex. He is listed as the inventor or co-inventor on numerous industry patents. He holds a B. S. degree in Chemical Engineering from the University of Tennessee.



Amir Sekhavat is Global Director of Product Management and Enterprise Market Development at Superior Essex. Amir has twenty years of experience in the telecommunications industry, specializing in communications cable products. Amir has published numerous articles and is listed as the inventor or co-inventor of several patents related to data cable performance and connectivity. Amir is currently chairman of CCCA datacenter subcommittee.



Intra-Pair skew: About wave propagation in screened single pair

Boris Dardel, Fabrice Pfefferli, Laurent van Rysselberghe, Wolfgang Klein, Denis Milz, Vincent Arbet-Engels

AESA S.A.

CH-2022 Bevaix - Switzerland

+41 32 841 5177 – aesa@aesa-cortaillod.com

Abstract

We show that intra-pair skew cannot be properly defined on a single screened pair, as the signal launched in a single wire does not propagate as such along the pair due to inter-wire coupling.

This coupling and propagation behaviour is illustrated using an analogy with the coupled pendulum system.

The measurement results can be described using a combination of the common and differential propagation modes. This is confirmed by TDR results of signal propagation.

Keywords: Wire; Cable; Single-Pair; Skew

1. Introduction

In-Pair skew is defined as the difference of the propagation time between the signal travelling in one wire and the other wire of a pair (cf. IEC 62783-1-1:2022). This time difference is expected to affect the differential signal and hence perturb the integrity of the communication.

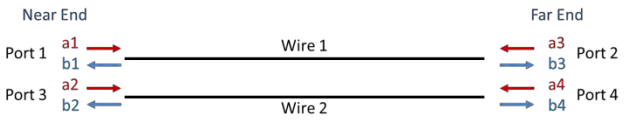
However, literature is not clear about this topic and different publications highlight the difficulty in interpreting the measurement results [3].

This paper gives a more thorough physical understanding of the signal propagation and clarifies the fact that Intra-Pair skew cannot be defined as such.

2. Ports definition for single pair

Measurements performed for this paper are done using a four port vector network analyser (VNA).

The cable is connected according to the scheme here below. As usually defined, “a” and “b” are the incoming and reflected waves, respectively.



- S_{mn} represents the response at port “m” of a signal send on port “n”

Hence:

- S_{21} represents the response at the far end of the first wire of a signal sent from its near end
- S_{43} represents the response at the far end of the second wire of a signal sent from its near end

As per IEC 62783-1-1:2022, Intra-pair skew is defined as propagation time (phase) difference between S_{21} and S_{43}.

3. Single wire measurements on pair

As S_{21} represents the signal propagation in one wire of the pair, it is expected to be a smoothly decreasing curve. However, measurement does not show the expected behaviour (cf. Figure 1). Measured S_{21} is a “bumped” curve with dips falling to zero (or close to) at regular frequency intervals.

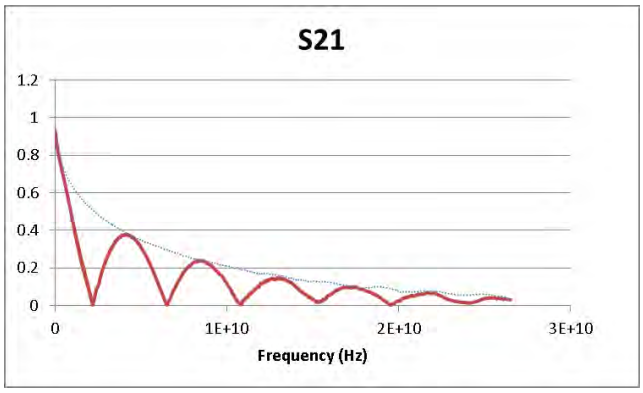


Figure 1: Measured S_{21} on a single pair (red curve) and its expected behaviour (blue dotted line)

Owing to the noise disturbance, phase computation at frequencies where the amplitude is close to zero is difficult. Moreover, closely looking at the dips where the signal amplitude falls close to zero (cf. Figure 2), the phase curve shows jumps of π. These jumps lead to a non-linear curve when unwrapping the phase (cf. Figure3)

This observation is not compatible with the common understanding of single wire signal propagation.

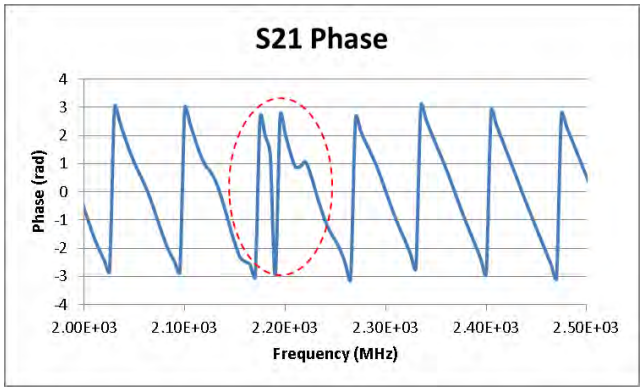


Figure 2: Phase of S_{21} around a point where the module of S_{21} is close to zero. One can see a phase distortion and a jump of π in the absolute value of the phase

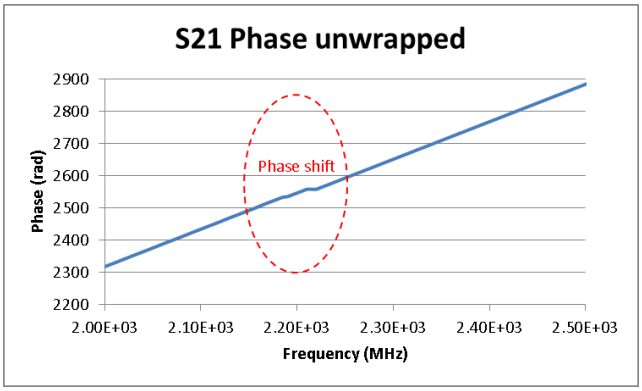


Figure 3: The phase distortion of figure 2 shown in the unwrapped phase representation. A phase jump of π is clearly visible

S_{41} (signal sent on the same wire but measured on the other wire) measurements are also surprising (cf. Figure 4). Instead of being close to zero, the signal shows similar amplitude behavior, but with dips at frequencies where S_{21} is maximal. This confirms the presence of inter-wire coupling i.e. signal is present on the wire where no signal was launched. It suggests that the signal does not propagate solely on a single wire.

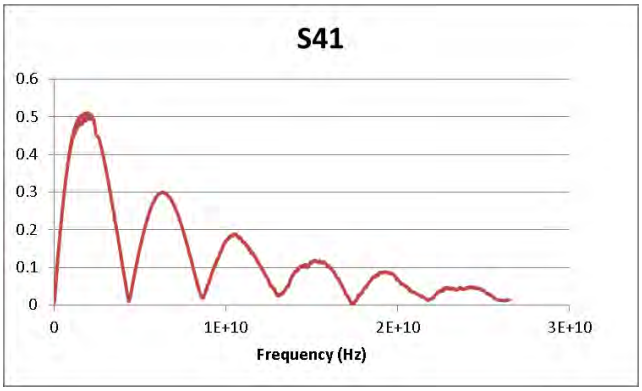


Figure 4: Measured S_{41} on a single pair

Note: S_{43} and S_{23} are similar to S_{21} and S_{41} respectively.

4. Data interpretation – the coupled pendulum

In order to get a tangible picture of coupled modes propagation in a screen pair, a direct analogy with the behaviour of a coupled pendulum is used.

The model: Two equivalent pendulums are coupled with a spring.

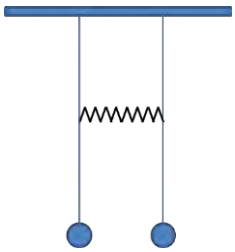


Figure 5: The coupled pendulum model

In this mechanical example, a stable oscillation corresponds to the situations where both pendulum are excited (oscillate) in phase or 180° out of phase. These modes are called “eigenstates”.

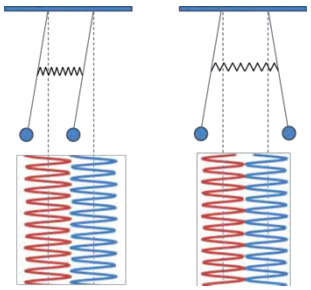


Figure 6: In phase and 180° out of phase modes

In our screened pair system, this can be related to the common and differential modes of propagation, which represent the eigenstate of the pair excitation. The displacement amplitudes of the pendulum correspond to the voltage amplitude on the wires.

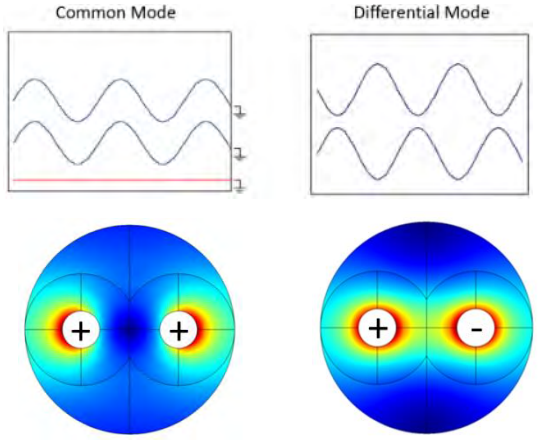


Figure 7: The common and differential propagation modes in a screened pair and associated electrical field distributions

When exciting only one pendulum, it is well known and understood that the energy of the system is periodically transferred over time from one pendulum to the other.

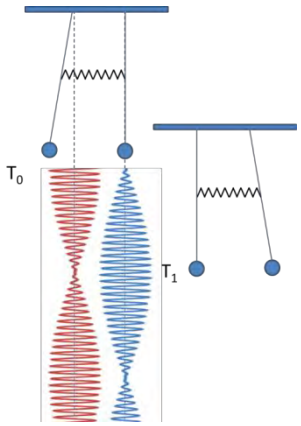


Figure 8: The coupled pendulum when one single pendulum is excited at time T_0. After a while (T_1) all the energy is transferred to the other pendulum

The periodic movement of the pendulums over time is shown in the following figure.

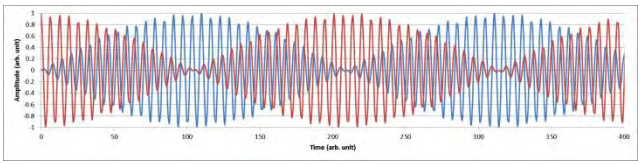


Figure 9: Oscillations of both pendulums over the time

5. Interpretation in the case of the screened pair

As both wires are electromagnetically coupled to each other, launching a signal in a wire of a screened pair is exactly like exciting one pendulum in the state described above.

The signal will propagate along the pair length and its energy will be transferred back and forth between both wires.

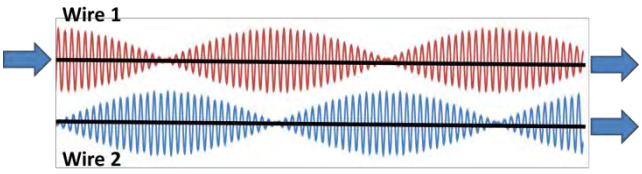


Figure 10: Signal propagation in a screened single pair when only one wire is excited

Any excitation mode can be described as a linear combination of the eigenmodes of the system.

Assuming a perfect cable, a single wire excitation can be constructed by the linear superposition of the common and differential modes with identical amplitudes.

Hence, assuming a perfect connector, by injecting a signal into a single wire, both propagation mode occur with equal amplitudes.

These 2 modes will then propagate through the pair. Measuring a single wire at some place along the pair will reveal the superposition of the state of these 2 modes at that position.

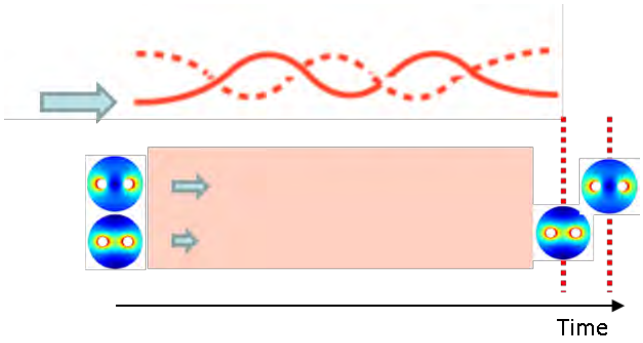


Figure 11: Decomposition of a single wire excitation into common and differential mode signals and their propagation. The propagation speed of both modes is different, so they will not reach the cable end simultaneously

This can be easily simulated by the sum of 2 sine waves with different propagation speeds and attenuation, as it is the case for common and differential modes.

Doing so, one can perfectly fit the measured curves.

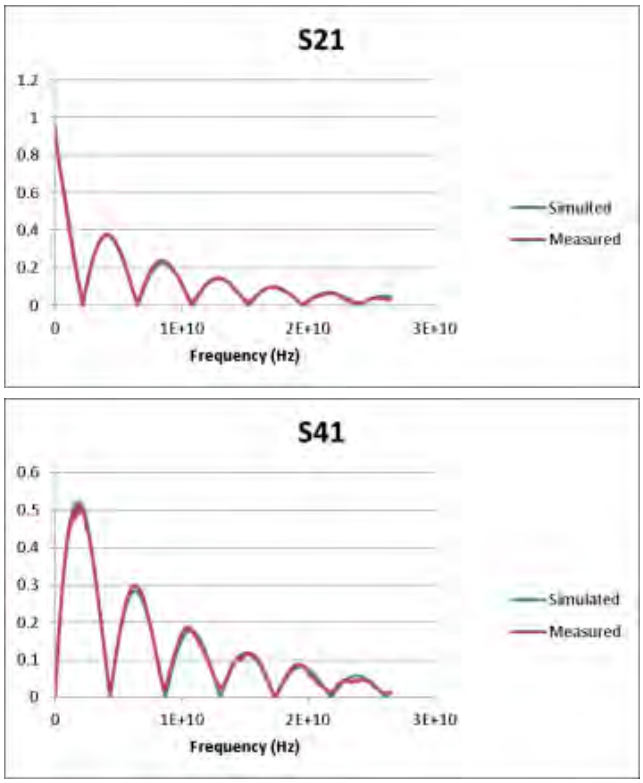


Figure 12: Comparison between measured S parameters and calculated ones using Common and Differential mode propagation with different speeds and attenuations

Note: Using mixed mode theory, S_{dd21} and S_{cc21} (the differential and common mode signals respectively) can be calculated from the single wire measurements. These two signals show the expected monotonic power decrease with frequency.

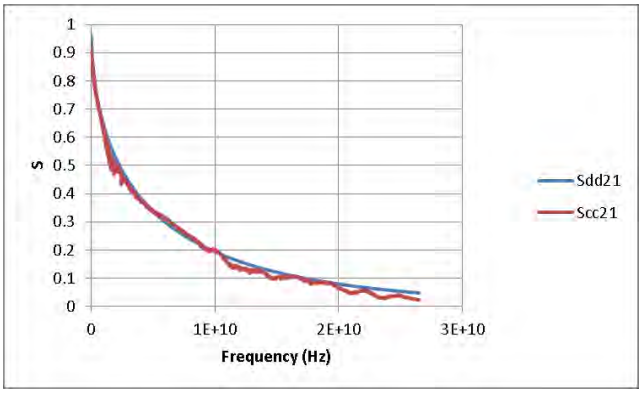


Figure 13: S_{dd21} and S_{cc21}

6. Time domain curves – propagation speeds

When looking at the calculated TDR of S_{21}, one gets 2 distinct reflection peaks (cf. Figure 14). The propagation speeds of differential and common mode can be computed from measured S_{cc21} and S_{dd21} respectively. The product of propagation speed and cable length result in the exact time where both peaks appear.

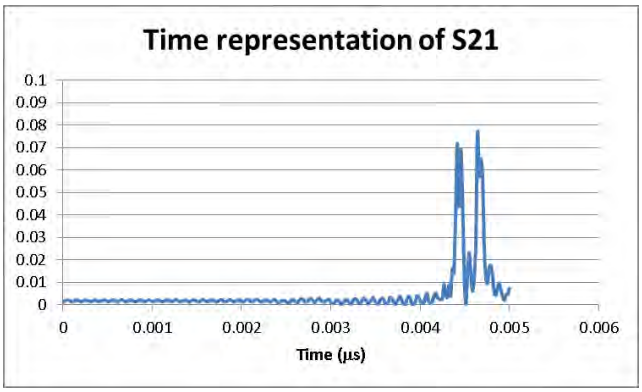


Figure 14: Time domain representation of S_{21} showing dual propagation times of the signal corresponding to common and differential modes

This corroborates our interpretation of wave propagation based on the superposition of common and differential modes.

7. Notes

The theoretical description given above corresponds to a situation using perfect connectors and cable.

In the real world, the transfer of the signal from the connector to the wire may not be perfect and may thus result in different amplitudes of the differential and common modes. This will lead to S21 and S_{43} parameter that do not completely reach "zero" amplitude at dips. If the cable is perfect, this property might be used to characterize the connector.

In the real world also, the cable is not ideal and the eigenmodes may deviate slightly from the differential and common modes shown in Figure 7. These new eigenmodes are called "quasi-differential" and "quasi-common modes" by J.Poltz "[4]. This will not significantly affect our analysis, except that both modes will not be populated with equal amplitude using a perfect connector.

Eigenmodes are by definition orthogonal and hence propagate without interaction through the cable.

Irregularities along the cable length will however lead to alteration of the quasi-eigenmodes and hence to mode coupling.

For short cable length or low frequencies, when the transfer of power on the second wire remains low, the "usual" description of in-pair skew may still be appropriate.

8. Conclusion

Single wire wave propagation in screened single pair is not possible due to existing coupling between both wires. Energy is hence continuously transferred from one wire to the other.

This can be interpreted in terms of common/differential modes (which represent the eigenmodes) excitation and propagation. Modelling this behaviour perfectly reflects the measured curves.

Intra-pair skew as defined in the standards is hence not a relevant parameter. It is moreover obvious that the measured signals will strongly depend on the position of the measurement i.e. the length of the cable.

Perturbing effects like mode coupling must then rather be looked at using differential to common mode conversion parameters.

9. Annex

9.1 Modified mixed mode representation of Intra-Pair skew

Another description of intra-Pair skew has been proposed in [1] using modified mixed mode S-parameters.

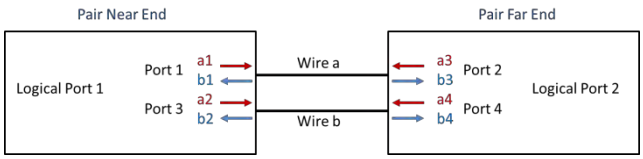
In this representation, intra-pair skew is defined as the difference in the propagation time (phase difference) of a differential signal sent at differential Port 1 and received respectively at single wire ports 2 (S_{2d1}) and 4 (S_{4d1}).

One can show that

$$S_{2d1} = \frac{1}{\sqrt{2}}(S_{21} - S_{23}) \qquad (1)$$

$$S_{4d1} = \frac{1}{\sqrt{2}}(S_{41} - S_{43}) \qquad (2)$$

Where d1 stand for "differential mode at logical port 1"



One can however also show (using mixed mode parameters description) that

$$S_{2d1} = \frac{1}{\sqrt{2}}(S_{dd21} + S_{cd21}) \qquad (3)$$

$$S_{4d1} = \frac{1}{\sqrt{2}}(-S_{dd21} + S_{cd21}) \qquad (4)$$

Considering for ease of interpretation that

$$S_{dd21} \gg S_{cd21} \qquad (5)$$

(which is the case for the measured cable), the phase difference between these 2 new S parameters will be π (minus sign of S_{dd21}) plus some oscillations which amplitude is related to the ratio between TCTL (S_{cd21}) and differential IL (S_{dd21}) and phase related to the difference in propagation speed of both differential and common modes.

Exchanging the sign of S_{4d1} as suggested in [1] to take into account the 180° phase difference between both "signals" of the differential mode will only move the curve by π down to around 0.

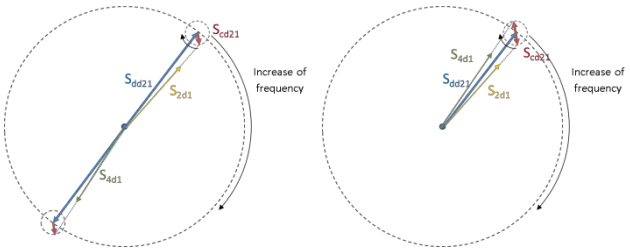


Figure 15: Graphical representation of S_{2d1} and S_{4d1} calculated from S_{dd21} and S_{cd21}

This is what is observed in the measurement.

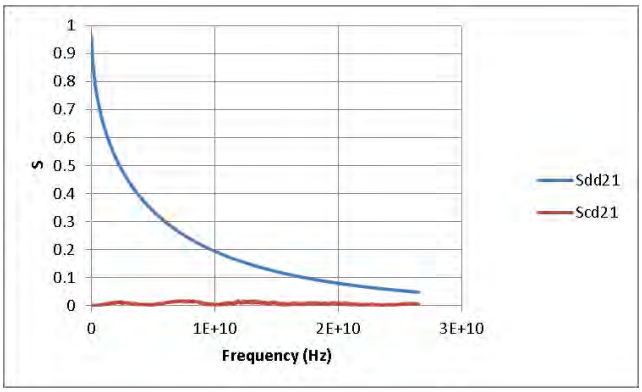


Figure 16: S_{dd21} and S_{cd21}

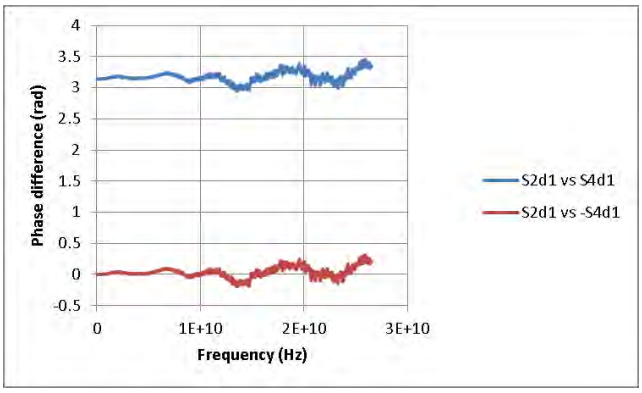


Figure 17: Phase difference between S_{2d1} and $\pm S_{4d1}$

This is then obviously not related to some propagation speed difference between both wires, but the envelope of the curve reflects the relative importance of TCL as compared to IL.

10. References

[1] S. Baek, E. Lee and B. Sung, "Computation of Intra-pair Skew for Imbalance Differential Line using Modified Mixed-mode S-parameter," 2007 IEEE Electrical Performance of Electronic Packaging, 2007, pp. 179-182, doi: 10.1109/EPEP.2007.4387154.

[2] Ron Olisar , HDMI, DVI and DisplayPort jitter from unbalanced twisted pair and differential cables, EDN October 31, 2008, https://www.edn.com/hdmi-dvi-and-displayport-jitter-from-unbalanced-twisted-pair-and-differential-cables/

[3] E. Mayevskiy, J. Huffaker, Limitations of intra-pairs skew measurements in Gigabit range interconnects, DesignCon 2016, TE Connectivity

[4] J. Poltz, J. Beckett, M. Josefson, Measurement and simulation of differential skew in twisted pair cables, Proceedings of 55th International Wire & Cable Symposium

11. Authors



Boris Dardel obtained his PhD in physics in 1994 at the University of Neuchatel (Switzerland) in Condensed Matter Physics. He then joined the cable manufacture of Nexans Suisse SA in Cortaillod (Switzerland) where he managed different technical departments linked with materials, cable designs, testing and R&D. In 2016, Dr. Dardel came to AESA SA in Colombier (Switzerland) as R&D Manager, responsible for designing and leading R&D processes, specifically linked to the measurement of electrical resistance for energy cables.



Fabrice Pfefferli owns an MSc in in biomedical engineering from the University of Bern. He joined AESA in 2020 as electronics and software engineer. He is in charge of the development of AESA new measuring software for automated test equipment (ATE).



Laurent Van Rysselberghe joined AESA in March 2019 as R&D project manager in the field of automatic test equipment. He owns a Bachelor of Science in Electrical Engineering from the Ecole d'Ingénieurs de l'Etat de Vaud in Yverdon HEIG-VD). He had previously worked for 20 years within the cable manufacturing group Nexans. At Nexans, he occupied various positions in high voltage, optical fibres or CATV/radiating cable families as R&D engineer, operational quality manager and production manager of the Cortaillod production plant. He then evolved into the technical expert ladder in electrical performances and testing.



Wolfgang Klein holds a degree of Dipl.-Ing. (TH) Information Technology from RWTH Aachen University (Germany). During and after his university education he worked in the testing department of the German cable manufacturer Kerpenwerk.

His responsibilities connected with central IT were related to networking and automating test equipment. In 1994, he joined M.E.A. (Mauf und Rudow) where he used his practical experience to design the Quality Management System CIQ 3.0. He also developed the foundation of some modern telecom automatic test equipment such as the balunless data cable measurement systems “Cobalt”. Since the merger of M.E.A. and AESA, he continues his role as head of the System Development Department.



Denis Milz is the Area Sales Manager at AESA. He joined the company in June 1997. Owner of a Bachelor of Science in Electronics and electrical engineering from the Ecole d’Ingénieurs du Locle, Neuchâtel, he began his career at AESA as a software developer. He was then put in charge of the after-sales service department for a few years before moving to a more commercial position.

Denis Milz is in parallel responsible for the product line of automated test equipment (ATE) for Copper communication cables.

Vincent Arbet-Engels is the CEO/Managing Director of AESA, a leading manufacturer of test equipment for the cable industry. Prior to AESA, he held various scientific and management positions at CERN, IBM, and Abilis Systems, in both the USA and Europe.



Dr Arbet-Engels graduated from the University of California, Los Angeles (UCLA) in 1992, with a Ph.D. in Electrical Engineering. He also earned a M.S. from UCLA, as well as a M.S. and B.S. from the Swiss Federal Institute of Technology in Lausanne (EPFL) in Microengineering.

Coupling attenuation & Burst test on balanced cables and cabling systems

Ralf Damm
bda connectivity GmbH
35614 Asslar, Germany
ralf.damm@bda-c.com

Dave Hess
CORD DATA
Wyomissing, Pennsylvania, USA
dave.hess@corddata.org

Bernhard Mund
bda connectivity GmbH
35614 Asslar, Germany
bernhard.mund@bda-c.com

Ralf Tillmanns
Weidmüller Interface GmbH & Co. KG
83413 Detmold, Germany
ralf.tillmanns@weidmueller.com

Abstract

The term SPE describes the new Single Pair Ethernet technology based on transmission standards according to IEEE 802.3cg. In addition to good transmission properties, high electromagnetic compatibility (EMC) from 100 kHz upwards is required for SPE cables, SPE connectors and SPE cabling systems.

Evidence of a correspondingly high EMC (emission and ingress) of balanced cables and components can be provided by measuring the coupling attenuation (CA) and the low frequency coupling attenuation (LFCA) according to IEC 62153-4-7 or IEC 62153-4-9. Alternatively, the interference immunity of SPE components can be determined by using the burst test according to IEC 61000-4-4 and evaluated according to IEC 61000-4-6.

The following report describes the measurement of coupling attenuation and burst test on SPE cables, components and systems. Measurement results and the correlation between both procedures are considered and discussed.

A mathematical description of the relationship between both test procedures is given.

Keywords: EMC, Coupling attenuation, Single pair ethernet, SPE, Burst test, Unbalance attenuation, Cable assembly, SPE connector, Correlation, Mode conversion, MICE table

1. Screening Parameters

1.1 General

The physical principles for measuring transfer impedance and screening or coupling attenuation on cables, connectors and other components using the triaxial method are described in detail in the literature, see [1, 2, 3, 4, 21] among others.

For coaxial cables, connectors and components, the transfer impedance Z_T applies at frequencies up to approx. 30 MHz. From 30 MHz the screening attenuation a_S is the measure of the shielding effect.

For screened balanced cables, connectors and components, the coupling attenuation a_C is the measure of their shielding effectiveness and is largely responsible for the EMC of the systems implemented with it. The coupling attenuation of balanced pairs is proportional to the unbalance attenuation of the balanced pair and the screening attenuation of the screen.

1.2 Unbalance Attenuation

The unbalance attenuation a_U of a balanced cable describes in a logarithmic ratio how much power is coupled over from the differential mode to the common mode system (or vice versa). It is the logarithmic ratio of the power fed in the differential mode P_{diff} to the power coupled over into common-mode P_{com}. [1, 2, 3, 4].

$$a_u = 10 \cdot \log\left(P_{diff}/P_{com}\right) \quad (1)$$

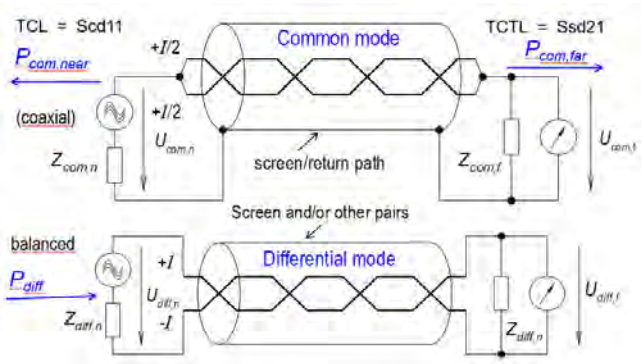


Figure 1 - Common and differential mode of a screened twisted pair (STP)

For low frequencies, the unbalance attenuation decreases with increasing length. With increasing frequency and/or length, the unbalance attenuation - similar to the screening attenuation - asymptotically approaches a limit value (assuming systematic coupling). The unbalance can be determined for both the near end and the far end of a cable, see Figures 2a and 2b [5, 6, 8]

Different conductor resistances, insulation diameters, core capacities, uneven stranding and changing distances between the inner conductor and the shield e.g. can be causes of the asymmetry.

The unbalance attenuation can be measured according to IEC 61156-1 with a multi-port VNA and "virtual balun" function. The unbalance attenuation at the near end is described as Scd11 (TCL) and the unbalance attenuation at the far end is described as Scd21 (TCTL), [3].

The transfer function of the unbalance attenuation of balanced (symmetrical) pairs and the coupling transfer function of screened balanced pairs is described more detailed in [6].

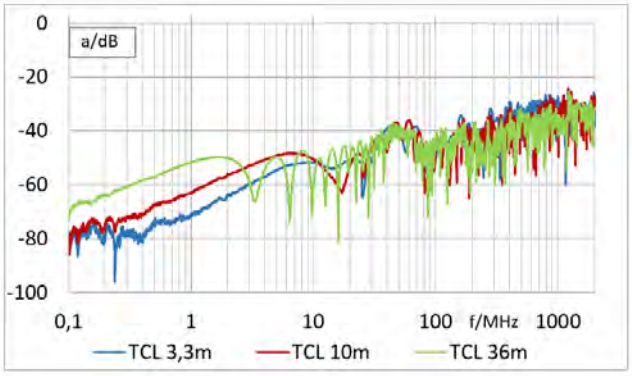


Figure 2a: Unbalance attenuation of a shielded SPE cable at the near end (TCL), different lengths

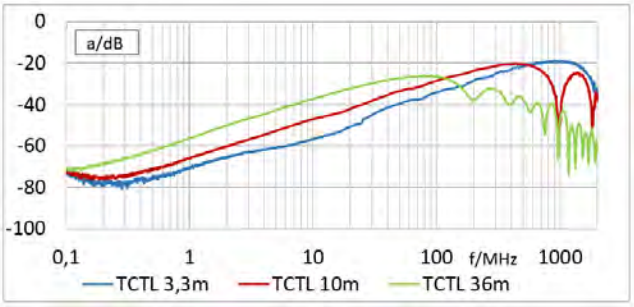


Figure 2b: Unbalance attenuation of a shielded SPE cable at the far end, (TCTL), different lengths

1.3 Screening Attenuation

The screening attenuation a_S of a cable screen is defined as the logarithmic ratio of the power P_1 fed into the matched cable and the maximum peak power $P_{2,max}$ in the matched outer circuit, in a frequency range where the cable is electrical long.

$$a_s = 10\log_{10}\left|\frac{P_1}{P_{2,\max}}\right| \qquad (2)$$

Details of the screening attenuation measurement of cable screens are described in IEC 62153-4-4 [1, 2, 3, 21]. Below the cut off frequency according to IEC 62153-4-4, where the cables are electrical short, length dependence of a_S shall be considered.

2. Measuring the Coupling Attenuation with the Triaxial Method

2.1 General

The coupling attenuation a_C of shielded balanced pairs describes the overall effect against electromagnetic interference (EMI) and takes into account both, the screening effect of the screen and the mode conversion or the unbalance attenuation a_U of the pair.

At a first approach (and at low frequencies) the coupling attenuation a_C of a single screened balanced pair (SPE) can be considered as the addition of the near end unbalance attenuation of the balanced pair and the screening effectiveness of the screen.

The coupling attenuation of screened balanced SPE cables can be measured according to IEC 62153-4-9 using the triaxial method, see Figure 3.

The balanced cable to be tested forms a three-wire system together with the measuring tube, consisting of the balanced pair, the cable shield and the measuring tube.

The balanced pair of the cable under test is fed with a differential 100 Ω signal via two 180° phase-shifted generators. Energy first couples from the differential-mode into the common-mode circuit and then from the common-mode circuit into the measuring tube (the outer circuit). Due to the total reflection at the short circuit at the end close to the generator (the near end), all of the energy coupled into the outer circuit runs to the receiver, [5]. Measurement results of a SPE cable are shown in Figure 4, (raw values).

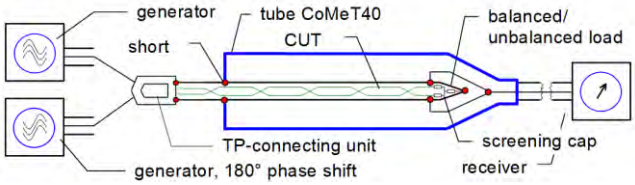


Figure 3: Measurement of the coupling attenuation a_C of a screened balanced SPE cable with multi-port VNA and with virtual balun according to IEC 62153-4-9

The measurement results of balanced cables changes at low frequencies depending on the measurement length. In order to achieve comparable results, a measuring length of 3m for LFCA is required in the IEC standards for SPE cables [25].

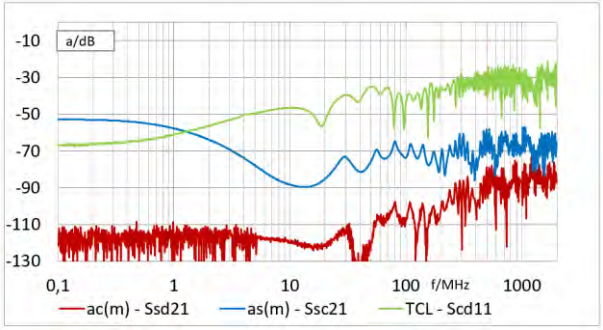


Figure 4: Unbalance attenuation a_U (Scd11, TCL), screening attenuation a_S(m) (Ssc21) and coupling attenuation a_C(m) CA/LFCA (Ssd21) 5m SPE cable, raw values

2.2 Coupling Attenuation at Low Frequencies, LFCA

The lower cut-off frequency to measure coupling attenuation according to IEC 62153-4-9Ed2 is given by:

$$f > \frac{c_0}{2*l*\left|\sqrt{\varepsilon_{r1}}-\sqrt{\varepsilon_{r2}}\right|} \qquad (3)$$

where:

c_0 = velocity of light, l = test length
ε_{r1}, ε_{r2} = dielectric constant of inner and outer circuit

That means, coupling attenuation on screened balanced pairs with manageable length can be measured only from about 30 MHz upwards. A test procedure for the EMC behavior of screened balanced cables at lower frequencies is needed.

The extension of IEC 62153-4-9Amd1 describes the measurement of the coupling attenuation at low frequencies (LFCA) on symmetrical cables from 100 kHz upwards. The measurement set-up is the same as the set-up for measuring the coupling attenuation at higher frequencies, [5]. The LFCA can also be measured analogously for SPE connectors and SPE cable assemblies.

LFCA varies with length. In order to get comparable test results between different test laboratories respectively between different test samples, the same test length shall be applied. For LFCA measurements on balanced cables and connectors, a test length of 3m is recommended.

2.3 SPE connectors

The IEC 62153-4-7Ed3 standard, describes various methods for measuring the coupling attenuation of connectors and ready-made cable asemblies, based on IEC 62153-4-9.

Figures 5a and 5b shows the basic measurement set-up for measuring the coupling attenuation of a screened balanced connector using the tube-in-tube method. An RF-tight tube is inserted into the measuring tube. The inner tube forms a 50 Ω system with the outer tube.

The shielded balanced connection cable is located in the inner tube. For mechanical reasons, the contact between the shield of the connection cable and the inner tube is approx. 3 cm in front of the connector to be tested.

This measures both the connector to be tested and the quality of the connection between the connector and the connection cable. The selected distance between tube-in-tube and the test object should be documented in the test report for comparison measurements.

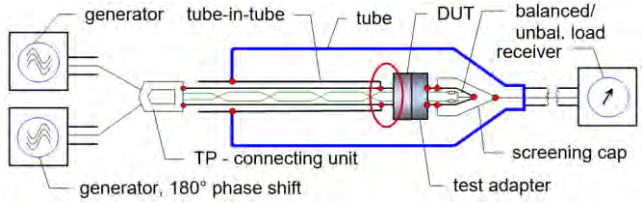


Figure 5a: Measuring CA/LFCA of a connector with tube-in-tube with short piece of connecting cable

Figure 5a shows the measurement CA/LFCA with tube-in-tube and a short piece of connecting cable. In this way the influence of assembling of cable and connector is measured

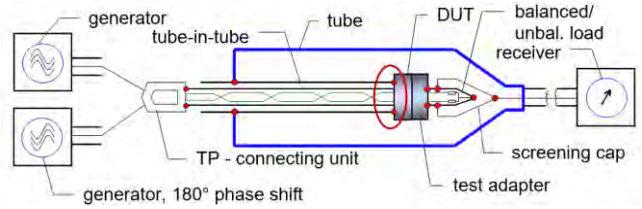


Figure 5b: Measuring CA/LFCA of a connector with tube-in-tube with direct connection

Appropriate test adapters are required for both procedures. As they will influence the test result, they shall be as good as possible.

2.4 Coupling Attenuation of Cable Assemblies

Measuring of coupling attenuation of cable assemblies with tube in tube procedure is shown in Figure 6.

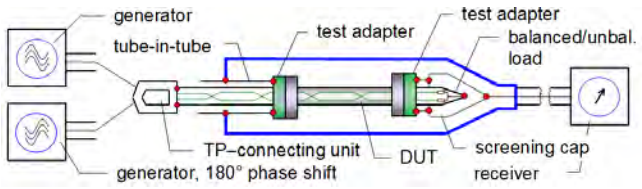


Figure 6: Measuring the coupling attenuation $a_{C_}$ of a balanced assembly with tube-in-tube method according to IEC 62153-4-7 with test adapter

Another option for measuring of paired connectors arrangement is shown in Figure 7. The pair of connectors is placed in the middle of the measuring tube. In contrast to the measurement set-up shown in Figure 6, the contribution of the feed and termination lines is not eliminated by the tube-in-tube application, but is superimposed on the coupling through the connectors.

This arrangement enables the measurement of long SPE cable assemblies (> 3m), splitting them in the middle and plugging them in at the ends.

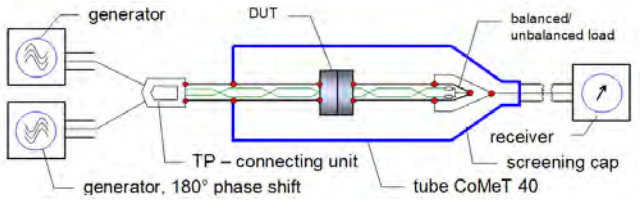


Figure 7: Measuring of CA/LFCA (Scd21) of a pair of SPE connectors in the middle of the tube

2.5 Unscreened Balanced Cables & Connectors

In case of unshielded balanced pairs, the inner system consists of the unshielded DUT fed in differential mode. The outer system is formed by the the common mode of the test object and the measuring tube. Because there is no shield at the unshielded pair, there is no near-end short circuit. The wave towards the near end is not reflected in the tube and travels back to the generators.

Therefore, coupling attenuation of unshielded pairs can be measured at both ends as near end and far end coupling attenuation.

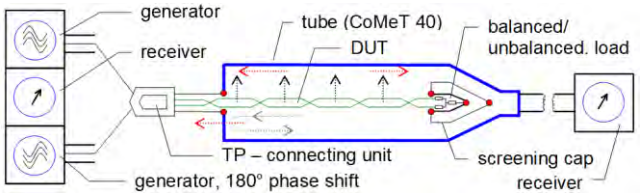


Figure 8: Coupling attenuation of unscreened balanced cables

The wave running back towards the near end in Figure 8 can be measured as S-parameter Scd11; it can be viewed as the near-end coupling attenuation. In the field of cable standardization, the parameter Scd11 is also defined as the near end unbalance attenuation (TCL) of the unshielded pair, [3, 4, 5]. That means, in case of unshielded balanced pairs, the near end coupling attenuation is in principle the same as the near end unbalance attenuation TCL.

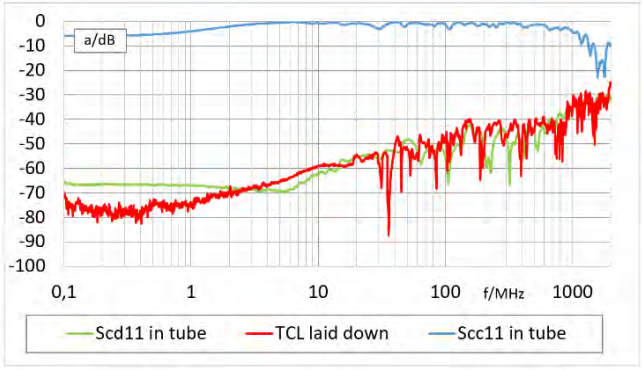


Figure 9: LFCA/CA of an unscreened balanced cable

3. Burst test

3.1 General

Alternatively to the measurement of coupling attenuation, the interference immunity of SPE cables, connectors and components can be measured using the burst test according to IEC 61000-4-4 and evaluated according to IEC 61000-6-1 or /-6-2. IEC 61000-6-2 describes requirements for SPE applications in harsh environments.

Electrical Fast Transient/Burst (EFT/B) are short, repeated pulses of high voltage that typically occur e.g. when motors start or equipment changes state. The pulses can interfere in the frequency range used by Ethernet, which is 1 MHz to 500 MHz. Ethernet cables usually have well-balanced twisted pairs and high levels of screening attenuation to protect from this sort of interference.

3.2 Test Procedure

The repetitive fast transient test according to IEC 61000-4-4 is a test with bursts consisting of a number of fast transients which are coupled into power, control, signal and earth ports of the DUT, see Figure 10. Significant for the test are the high amplitude, the short rise time, the high repetition frequency, and the low energy of the transients [27].

The test is intended to demonstrate the immunity of electrical and electronic equipment when subjected to types of transient disturbances such as those originating from switching transients (interruption of inductive loads, relay contact bounce, etc.) [27].

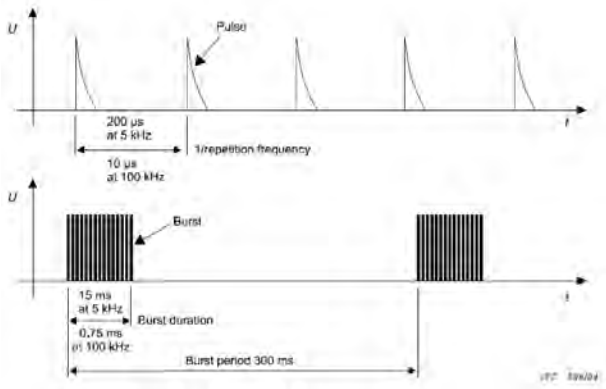


Figure 10 – Burst signal (source: IEC 61000-4-4)

The shape of the burst signal is generated using a burst generator and capacitively coupled into the cabling system with a coupling clamp. At the same time, data packets are transmitted via the cabling system. The IEC 61000-6-2 standard entitled "Electromagnetic compatibility (EMC) Part 6-2: Generic Standards for Immunity for Industrial Areas" describes various performance criteria with defined limit values.

For the fast transient (burst), the limit value for data signal transmission is ± 1 kV with test criterion B. This means that the amplitude of the burst signal is ± 1 kV and data packets may have errors, but operation of the data transmission is still functional, [7].

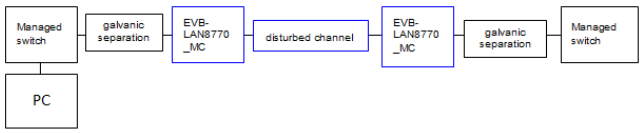


Figure 11: Cabling system for burst test

The test is intended to simulate the effect of a nearby disturbance (e.g., inverter, brush fire, etc.).

The test setup required for the burst test is shown schematically in Figure 11. First, a communication-capable Ethernet network is required for the test. This consists of three network devices, a PC and two Ethernet switches. Data transmission is initiated between these network devices so that data packets pass through the disturbed cabling system.

Since a single-pair Ethernet 100Base-T1 application is being tested, a conversion to the SPE system is required first. This conversion from 100Base-Tx to 100Base-T1 is performed by two evaluation boards.

3.3 Modified Burst Procedure

IEC 61000-4-4, Electrical fast transient/burst immunity test describe the burst test with fixed voltages, depending on the level of tests.

During the modified burst tests in this paper, the burst voltage was increased gradually. The level of the interference signal amplitude, at which the first errors occur in the transmitted data packets, was recorded. The test was carried out in the same setup with shielded and unshielded SPE components.



Figure 12a: Test set-up for burst test



Figure 12b: Test set-up for burst test

4. MICE table

The MICE table according to ISO/IEC 11801-1, subclause 6.2.2 classifies the environment for generic cabling, see Table 1.

The letters in MICE each represent one type of environmental impact – Mechanical, Ingress, Climatic/Chemical and Electromagnetic.

Table 1 – Channel environments

	1	2	3
Mechanical rating	M_1	M_2	M_3
Ingress rating	I_1	I_2	I_3
Climatic rating	C_1	C_2	C_3
Electromagnetic rating	E_1	E_2	E_3

For each of these environmental impacts, there are three classes – 1, 2, and 3 – that represent levels of severity. Class 1 stands for lower impact as for office applications, class 2 for light industry and class 3 for heavy industry environments.

In this paper the electromagnetic rating respectively the MICE requirements for burst test are of interest.

Table 2 – MICE requirements for burst test

Electromagnetic rating	E_1	E_2	E_3
EFT/B (comms)	500V	500V	1000
	IEC 61000-6-1		IEC 61000-6-2

Table 2 (extract of table 2 of ISO/IEC 11801-1 and of table 6 of ISO/IEC TR 29106) describes the respective electro-magnetic environment and burst test requirements. (EFT = electromagnetic fast transient).

Channel environments may be classified by using any combination of the MICE scheme, e.g. $M_1I_2C_3E_1$.

5. Test Results

Compilation of coupling attenuation of different SPE cables are shown in Figure 13.

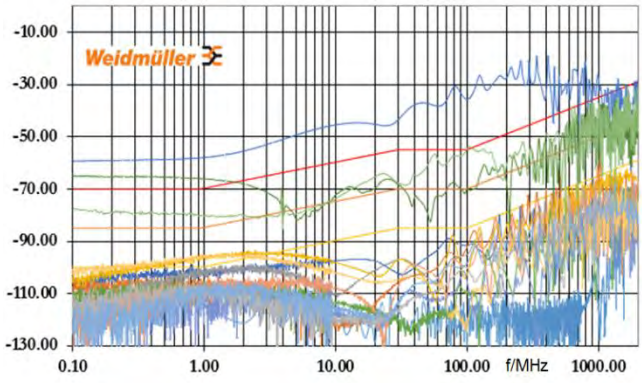


Figure 13: Coupling attenuation of different SPE cables

Coupling Attenuation CA and Low Frequency Coupling Attenuation LFCA of different SPE cables was measured with the triaxial test procedure according to IEC 62153-4-9, see Figure 13.

Cables with foil/braid constructions and good unbalance attenuation fulfills Coupling attenuation Type I requirements,

Cables with foil only or with poor unbalance attenuation are in the range of coupling attenuation Type Ib

Unscreened single pairs did not fulfill Coupling attenuation Type II requirements of IEC 61156 series.

Correlation between coupling attenuation measurement and Burst test is shown in Figure 14.

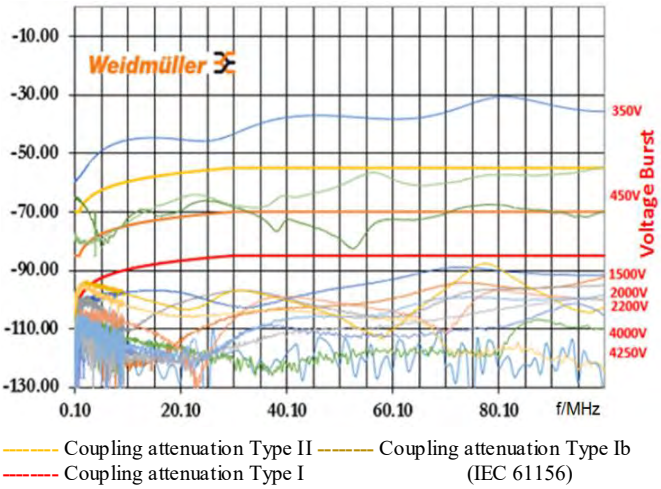


Figure 14: Correlation between Coupling attenuation and Burst test

Figure 14 shows the coupling attenuation of different SPE cables according to IEC 62153-4-9 up to 100 MHz versus burst test.

The Y-axis on the right shows the burst voltages above which transmission according to IEC 61000-6-2 is no longer possible. The maximum burst voltage is correspondingly higher for cables with high coupling attenuation.

6. Conclusion and Outlook

The coupling attenuation of balanced cables can be measured according to IEC 62153-4-9, connectors, assemblies and components can be measured according to IEC 62153-4-7 using the tube-in-tube method. Based on the supplement to IEC 62153-4-9 Amd1, the coupling attenuation of balanced connectors and assemblies can also be measured at low frequencies from 100 kHz upwards as low frequency coupling attenuation, LFCA.

Alternatively to the measurement of coupling attenuation, the interference immunity of SPE cables, connectors and components can be determined by using the burst test according to IEC 61000-4-4 and evaluated according to IEC 61000-6-1 or /-6-2. This is e.g. a requirement for SPE applications in harsh environments according to the MICE table of ISO/IEC 11801-1.

Although there is no linear relationship between coupling attenuation and burst test, it is shown, that systems with SPE cables with high coupling attenuation can also withstand higher burst voltages.

- only shielded SPE cables meet E_3 requirements,
- unscreened or poor screened SPE cables meet E_1 & E_2 requirements,
- further measurements are necessary,
- a mathematical description of the relationships between coupling attenuation and burst test is in preparation,
- repeated tests with 10 Base-T1 application are in progress.

7. Literature

[1] Thomas Hähner, Bernhard Mund: Test methods for screening and balance of communication cables; Proceedings of EMC Zurich, 1999, pp. 533-538

[2] Lauri Halme & Bernhard Mund: EMC of Cables, Connectors and Components with Triaxial Test set-up, IWCS, 62th International Wire & Cable Symposium, Charlotte, Nov. 2013

[3] B. Mund & C. Pfeiler: Balunless measurement of coupling attenuation of screened balanced cables up to 2 GHz, Proceedings of the 64th IWCS Conference, Atlanta, USA, October 2015

[4] T. Hähner, B. Mund, & T. Schmid: History and recent trends of Triaxial test procedure, Proceedings of the 67th IWCS Conference, Providence, RI, USA, October 2018

[5] T. Hähner, B. Mund, T. Schmid: Screening effectiveness of unscreened balanced pairs, EMC Barcelona 2019

[6] T. Hähner, C. Pfeiler, B. Mund & T. Schmid: EMC Parameter of single pair Ethernet cables, Wire & Cable Technology International, May 2022

[7] Helmut Reiter & Ralf Tillmanns: Untersuchungen zur geschirmten und ungeschirmten Verkabelung für 10BASE-T1, Anwenderkongress Steckverbinder, Vogel Verlag Würzburg, 04. - 06. July 2022

[8] Ralf Damm, Bernhard Mund et. al., EMC of SPE cables, connectors and assemblies, Proceedings of the 71th IWCS Conference, Providence, RI, USA, October 2022

[9] Dave Hess, Shielded Pair Differential Cabling Phase Matters, Proceedings of the 71th IWCS Conference, Providence, RI, USA, October 2022

[10] Ralf Damm, Bernhard Mund & Ralf Tillmanns, EMV von SPE Steckern und Anschlusskabeln, Anwenderkongress Steckverbinder, Vogel Verlag Würzburg, 12. - 14. Juni 2023

[11] Dave Hess, Relation of Coupling Attenuation and Unbalance Attenuation, Proceedings of the 72th IWCS Conference, Orlando, FL, USA, September 2023

8. Standards

[21] IEC TR 62153-4-1, Introduction to electromagnetic (EMC) screening measurements

[22] IEC 62153-4-7Ed3, Test method for measuring of transfer impedance Z_T and screening attenuation a_S or coupling attenuation a_C of connectors and assemblies up to and above 3 GHz - Triaxial tube in tube method

[23] IEC 62153-4-9Ed2, Coupling attenuation of screened balanced cables, triaxial method

[24] IEC 62153-4-9Ed2Amd1, Measuring the screening effectiveness of unscreened single or multiple balanced pairs & LFCA

[25] IEC 61156-13, Symmetrical single pair cables with transmission characteristics up to 20 MHz - Horizontal floor wiring - Sectional specification

[26] EN 50289-1-9, Electrical test methods – Unbalance attenuation, (longitudinal conversion loss, longitudinal conversion transfer loss)

[27] IEC 61000-4-4, - Electromagnetic compatibility (EMC) – Part 4-4: Testing and measurement techniques – Electrical fast transient/burst immunity test Electrical fast transient/burst immunity test

[28] IEC 61000-6-1, Electromagnetic compatibility (EMC) – Part 6-1: Generic standards – Immunity standard for residential, commercial and light-industrial environments

[29] IEC 61000-6-2, Electromagnetic compatibility (EMC) – Part 6-2: Generic standards – Immunity standard for industrial environment

[30] ISO/IEC 11801-1, Information technology - Generic cabling for customer premises

9. Authors



After having successfully completed his apprenticeship as Radio- and TV Technician in 1979, **Ralf Damm** received his diploma in Telecommunications and Microprocessor-Technologies at FH Giessen-Friedberg. In 1987 he joined bda connectivity GmbH (former Berkenhoff & Drebes GmbH), working with electronic development of fibre optic components. In 2018 the bedea cable division has changed to bda connectivity GmbH.Later he was responsible for sales and supports for data communication networks and structured cabling. He is now member of the bda cable R&D department and responsible for sales & technical support of the CoMeT product line.



Dave Hess, dba CORD DATA, currently works as a subject matter expert facilitating international standards development for connectivity technology, particularly in the area of shielded pair differential cabling.

He has worked for more than 40 years in both fields of electronic and photonic wired data communication connectivity and participates on the standards committees for physical interface and cabling standards: ISO, IEC, IEEE, INCITS, EIA, TIA, CTA, and ANSI,. He has been project leader for over 20 international standards. He received IEC 1906 awards for technical contributions in 2011 and 2014. He holds a B.S. degree in Mathematics from Pennsylvania State University and is a life member of IEEE.



Bernhard Mund received his apprenticeship diploma as Broadcast- and TV Technician in 1971 in Marburg, Germany and his diploma in Telecommunications- and Micro processor-Technologies 1984 from FH Giessen-Friedberg, Germany.

Bernhard Mund has been in the cable business since 1985 when he joined the cable manufacturer bda connectivity GmbH (former bedea Berkenhoff & Drebes GmbH) in Asslar, Germany. Formerly being R&D Manager of communication cables, he is now member of the RF- and EMC test engineering department responsible for R&D of the CoMeT system. Besides his work for bda, Bernhard Mund has been contributing for more than 38 years in national and international standardi-zation organizations.

He has srved as Chairman of the German committee UK 412.3, Koaxialkbel as well as of Secretary of IEC SC 46A, Coaxial cables and of CLC SC 46XA, Coaxial cables. Among further standardization activities in different committees and working groups he is member of IEC TC 46/WG5, Test methods for electromagnetic compatibility (EMC).



Dipl.-Ing. (TH) **Ralf Tillmanns** studied communication technology at the Technical University of Duisburg.

He has more than 20 years of experience in network technology. Since 2000, his focus has been on the areas of development and measurement technology for data connectors and IT cabling infrastructure.

In addition, Ralf Tillmanns is active in various national and international standardization committees. Among others in the following committees: German speaker IEC TC46; IEC TC 46/ WG9; IEC TC 46/SC46C WG7; IEC SC48B WG3;WG5; SC65C.

Designing of Single-Pair Ethernet Cable

Juliusz Poltz
OptEM Engineering Inc.
Calgary, Alberta, Canada
+1-403-289-0499, jpoltz@optem.com

Dave Hess
CORD DATA
Wyomissing, Pennsylvania, USA
+1-610-698-4790 · dave.hess@corddata.org

Abstract
Single-pair Ethernet (SPE) is already used by the automotive industry, replacing traditional bus systems with Ethernet based integrated controls, communication, and safety functions. These advantages can also serve robotics, industrial automation and connecting smart offices and homes. These efforts concentrate around the selection of the correct design and a suitable manufacturing process which will reduce manufacturing cost. In the paper it is demonstrated how initial selection of conductor size leads to necessity of scaling insulation diameter in order to keep the desired 100 Ohm characteristic impedance. Although the Unscreened Twisted Pair (UTP) configuration is the smallest and most inexpensive solution available, its unpredictability due to exposure to external noise, makes the Screened Twisted Pair (STP) configuration an obvious choice for GHz SPE cables. It is also demonstrated that designers must rely on insulation materials with the lowest possible dielectric constant and loss tangent to lower insertion loss of SPE cables that are expected to operate in GHz range. Using foaming to achieve the desired characteristic of insulation material can be cost effective. It is envisaged that multiple various applications of SPE cables with different frequency range and reach will have to be individually optimized using design software equipped with electromagnetic solver and bill of materials module to select an initial design for prototyping.

Keywords: single-pair; Ethernet; SPE; STP; UTP; Type-B; single-pair; twisted-pair; balanced; cable; cabling; channel; link; Class T1-B; Category T1-B; Class T1-C; Category T1-C; Class-E_A; Category 6_A; Class-F_A; Category 7_A; model; data; rate; reach; signal-to-noise-ratio; SNR; margin; capacity; screen; shield; insulation; foaming, bill of materials; BOM;

1. Introduction
The current related international standards, published and under development, for SPE data cabling systems, including standards from IEEE 802.3, ISO/IEC SC 25, IEC SC 46C, and IEC SC 48B, are covered in a brief overview. The range of standard SPE physical layer link segment data rate and reach extend from 10 Mb/s over 1000 m of unshielded single-pair cabling, to 25 Gb/s over 15 m of shielded single-pair cabling. The possibilities for extended reach are already being explored by considering larger conductor sizes, lower loss dielectric materials, and more effective shielding.

Considering the very diverse applications of SPE, we decided to design, optimize, and investigate 100 Ohm SPE cables with 22 to 26 AWG copper wires (Fig. 1). We included 26 AWG UTP configurations in the study to demonstrate the necessary size correction needed for screened cables. Designers should be aware that a 22 AWG STP cable is twice the size of a 26 AWG UTP cable and related costs of manufacturing are even greater. However, this is the price of noise immunity and reliability that is expected from various applications of SPE cables. Attenuation requirements are forcing engineers to increase diameters of copper wires of the SPE cables, and the presence of the screen significantly increases the overall size of the cable, as seen in Figure 1.

To test the impact of insulation material on the performance of 100 m, 100 Ohm STP cables, we used the STP 26_{AWG} as our sample design with insulation materials of various electrical properties. Then we investigated the impact of insulation material on cable speed of propagation and attenuation.

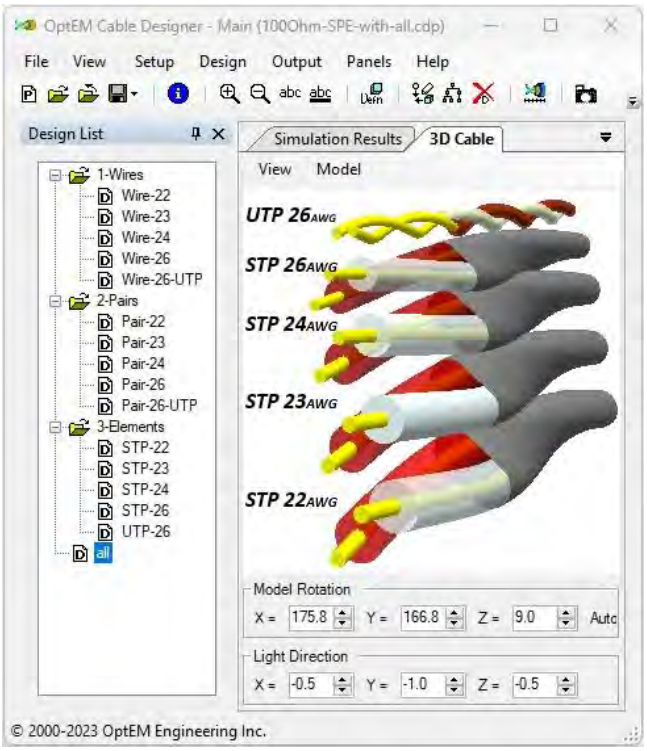


Figure 1. Optimized models of 100 Ohm UTP and STP cables in their proportional dimensions

At the end of the paper, we discuss the necessity of relying on insulation materials with the lowest possible dielectric constant and loss tangent for cables operating in GHz range. We also use foaming to achieve the desired characteristic of insulation material.

2. Single-pair Cabling Standards

2.1 Standards Organizations

Single-pair cabling standards support data communication physical interface standards from international standards development organizations (SDO), such as IEEE, ISO/IEC, IEC, and TIA.

2.2 IEEE SA (Institute of Electrical and Electronics Engineers, Standards Association)

IEEE-SA 802 LAN/MAN Standards Committee is the international group responsible for developing the Ethernet® wired, and WiFi® wireless, and related internet data communications standards, for local area networks and metropolitan area networks (LAN/MAN); 802.3 working group publishes Ethernet standards, for wired internet data transport used between practically all microprocessor-controlled equipment.

Physical-layer interface (PHY) specifications for Single-Pair Ethernet (SPE) are the new focus for copper links; originally intended for automotive applications, these PHYs support mechanical robustness, environmental endurance, and electrical efficiency, by full-duplex operation over a single-pair while using fewer modulation levels, e.g., PAM-3 & PAM-4.

The current version of ISO/IEC/IEEE 8802-3:2021 Standard for Ethernet [1] and its amendments covering SPE PHYs are listed in Table 1.

Table 1. SPE link segment characteristics

SPE link segment	Data rate	Reach	Frequency range	IEEE physical layer
PHY	Mb/s	m	MHz	Standard
25GBASE-T1 (cy)	25,000	15	$10 \le f \le 9{,}000$	ISO/IEC/IEEE 8802-3:2021 amendment (clause 165)
10GBASE-T1 (ch)	10,000	15	$1 \le f \le 4{,}000$	ISO/IEC/IEEE 8802-3:2021 amendment (clause 149)
5GBASE-T1 (ch)	5,000	15	$1 \le f \le 2{,}000$	ISO/IEC/IEEE 8802-3:2021 amendment (clause 149)
2.5GBASE-T1 (ch)	2,500	15	$1 \le f \le 1{,}000$	ISO/IEC/IEEE 8802-3:2021 amendment (clause 149)
1000BASE-T1 Type B (bp)	1,000	40	$1 \le f \le 600$	ISO/IEC/IEEE 8802-3:2021 (clause 97)
1000BASE-T1 Type A (bp)	1,000	15	$1 \le f \le 600$	ISO/IEC/IEEE 8802-3:2021 (clause 97)
100BASE-T1L (dg)	100	500	$0.1 \le f \le 60$	ISO/IEC/IEEE 8802-3:2021 amendment (clause tbd)
100BASE-T1 (bw)	100	15	$0.3 \le f \le 66$	ISO/IEC/IEEE 8802-3:2021 (clause 96)
10BASE-T1L (cg)	10	1000	$0.1 \le f \le 20$	ISO/IEC/IEEE 8802-3:2021 (clause 147)
10BASE-T1S (cg)	10	15	$0.1 \le f \le 20$	ISO/IEC/IEEE 8802-3:2021 (clause 147)

2.3 ISO/IEC (International Standards Organization / International Electrotechnical Commission)

ISO/IEC JTC1 SC25 covers interconnection of microprocessor-based IT equipment.

2.3.1 Generic Cabling Specifications. Wired network cabling systems for LAN applications in buildings are covered in ISO/IEC 11801-1 [2] for all media-types, which are referenced by the other 11801-x series standards covering implementations for various application spaces, e.g., 2-Enterprise, 3-Industrial, 4-Homes, 5-Datacenter, and 6-Smart-building.

The cabling requirements cited in this paper are covered in ISO/IEC 11801-1 [2] which covers, among various media types, the standard balanced cabling channel specifications, and respective component category specification: e.g., Class-E_A/CAT6_A, and Class-F_A/CAT7_A. Amendments are underway for 11801-x series, which add the new media type, balanced single-pair cabling.

ISO/IEC 11801-1 [2], Information technology -- Generic cabling for customer premises -- Part 1: General requirements; standard covering the generic cabling channel requirements for LAN applications, is currently being amended to include new single-pair cabling channel classes for some SPE PHYs, which are listed in Table 2.

Table 2. Balanced single-pair cabling channels

Cabling Type	Frequency range
Type name	MHz
T1-C	$0.1 \le f \le 1{,}250$
T1-B	$0.1 \le f \le 600$
T1-A-1000	$0.1 \le f \le 20$
T1-A-400	$0.1 \le f \le 20$

2.3.2 Application Specific Cabling Guidelines and Specifications. New technical reports and technical specifications precede the amendments and revisions to the ISO/IEC 11801-x cabling standards to support new applications, e.g., Single-pair Ethernet (SPE). ISO/IEC/TR 11801-9906 [3], Information technology – Generic cabling for customer premises – Part 9906 - Technical report: single-pair cabling channels up to 1,250 MHz, includes Table 3 below, covering the SPE link segment specifications currently supported by the ISO/IEC 11801-1 single-pair cabling channels and components.

Table 3. SPE link segments supported in ISO/IEC/TR 11801-9906

SPE link segment	Data rate	Reach	Frequency range
PHY	Mb/s	m	MHz
1000BASE-T1 Type B (bp)	1,000	40	$1 \le f \le 600$
1000BASE-T1 Type A (bp)	1,000	15	$1 \le f \le 600$
100BASE-T1L (dg)	100	500	$0.1 \le f \le 60$
100BASE-T1 (bw)	100	15	$0.3 \le f \le 66$
10BASE-T1L (cg)	10	1,000	$0.1 \le f \le 20$
10BASE-T1S (cg)	10	15	$0.1 \le f \le 20$

2.4 IEC (International Electrotechnical Commission)

IEC TC 46, for Cables, wires, waveguides, RF connectors, RF and microwave passive components and accessories, is the standards committee covering basic measurement and test procedures for data communications cables and cable assemblies, used with related standard connectors for data communications cable and assemblies.

Cable Component subcommittee IEC SC46C, Wires and symmetric cables, committee covers balanced cables for data communications. IEC 61156-x series covering balanced cables.

IEC 61156-11 ED2 (draft) [4], Multicore and symmetrical pair/quad cables for digital communications - Part 11: Symmetrical single pair cables with transmission characteristics [from 0.1 MHz] up to 1250 MHz – horizontal floor wiring – Sectional specification; covers single-pair component cable, new media-type for data communication applications, e.g., Single-pair Ethernet (SPE) and Fieldbus. Related standards 61156-12, -13, -14 cover related single-pair cable standards, see Table 4.

Table 4. Balanced single-pair cable types

Cabling Type	Frequency range	Conductor type	Balanced single-pair cable standard	Cable use case
Type name	MHz			
T1-C	$0.1 \le f \le 1{,}250$	Solid	IEC 61156-11	Horizontal
T1-C	$0.1 \le f \le 1{,}250$	Stranded or solid	IEC 61156-12	Work area
T1-B	$0.1 \le f \le 600$	Solid	IEC 61156-11	Horizontal
T1-B	$0.1 \le f \le 600$	Stranded or solid	IEC 61156-12	Work area
T1-A-1000	$0.1 \le f \le 20$	Solid	IEC 61156-13	Horizontal
T1-A-1000	$0.1 \le f \le 20$	Stranded or solid	IEC 61156-14	Work area
T1-A-400	$0.1 \le f \le 20$	Solid	IEC 61156-13	Horizontal
T1-A-400	$0.1 \le f \le 20$	Stranded or solid	IEC 61156-14	Work area

The respective single-pair cable insertion loss specifications are summarized in ISO/IEC/TR 11801-9906, see Table 5. The legacy IL specifications, such as from Class-E_A/CAT6$_A$, formed the basis for the single-pair cable insertion loss specifications, see Table 5.

Table 5. Balanced single-pair cable IL

Cable type Upper frequency	Frequency range	Cable IL
MHz	MHz	dB/100m
Horizontal 1,250	$0.1 \le f \le 1{,}250$	$1.8\sqrt{f} + 0.0050f + 0.25/\sqrt{f}$
Work area 1,250	$0.1 \le f \le 1{,}250$	$2.7\sqrt{f} + 0.0075f + 0.36/\sqrt{f}$
Horizontal 600	$0.1 \le f \le 600$	$1.8\sqrt{f} + 0.0050f + 0.25/\sqrt{f}$
Work area 600	$0.1 \le f \le 600$	$2.7\sqrt{f} + 0.0075f + 0.36/\sqrt{f}$
Horizontal 20	$0.1 \le f \le 20$	$1.23\sqrt{f} + 0.01f + 0.2/\sqrt{f}$
Work area 20	$0.1 \le f \le 20$	$1.84\sqrt{f} + 0.01f + 0.2/\sqrt{f}$

2.5 TIA (Telecommunications Industry Association)

TIA Standards committee TR42, TIA-568 cabling media-type standards, for IT network cabling systems, for building application spaces: Enterprise, Datacenter, Industrial, Residential, and Intelligent buildings; supporting US telecommunications standards.

TIA-568.5, [5] Balanced single twisted-pair telecommunications cabling and components standard covering the single-pair media-type channels and components, also conform to ISO/IEC 11801-1 requirements.

3. Designing 100 Ohm Single-Pair Cable

Various frequency range and IL requirements (Table 5) make SPE cable prototyping very slow and expensive. Since computer modeling has proven its ability to predict cable performance with high accuracy [7] we used OptEM Cable Designer v.10 software to design optimal SPE cables, report on bill of materials, simulate, plot and document results.

Despite its simple geometrical structure, twisted pair cable design offers challenges for numerical modeling and electromagnetic simulation. Although cable length may exceed 50,000 times its cross-sectional dimensions, its cross-sectional details must be modeled with micro-meter precision. With the increase in operating frequencies beyond 10 GHz it is necessary to include insulation material frequency dependent characteristics, twisting of wires and pairs, stranding and plating when building cable models.



Figure 2. After specifying details of SPE designs in Excel, the user can model and simulate them in OptEM Cable Designer which automatically displays performance plots.

Since results of numerical simulations cannot be more accurate than the geometrical models representing the cable, it is essential to specify the cable geometry as accurately as possible. Rather than modeling one cable prototype at a time, the user can specify entire families of nearly identical designs using an Excel spreadsheet, open it with the software (Fig.2), then simulate them all and select the optimal design. This optimal design can be further investigated in the software where exact manufacturing instructions can be prepared.

OptEM Cable Designer uses a built-in Maxwell-equations solver which calculates current and charge distribution using a combination of Finite Element Method (FEM) and Boundary Element Method (BEM). Bulky conductors are divided into finite elements, whereas ground and power planes are modeled as multilayer boundaries. The simulation of electromagnetic performance of SPE cable includes skin and proximity effects in wires, eddy currents in cable shields, and dielectric losses in the insulation layers. The skin effect causes reduction of the

interconnect inductance and a rapid increase of the interconnect equivalent resistance.

The solver maps the changes of the inductance, resistance, capacitance, and conductance matrices along cable length. After building a circuit model of the entire cable, the software uses chain and S-parameters to report on cable propagation parameters.

The first objective of the design process was to select wire insulation diameter. To ensure optimal performance, the cable should match the desired characteristic impedance of 100 Ohms. All models used solid polyethylene (PE) with dielectric constant (Dk) of 2.3 and electric loss tangent (Lt) of 0.0001. STP designs were enclosed in a uniform 20 µm Al screen and used lay length of 40 mm. The small cross-section UTP cable had 8 mm lay. Table 6 presents the insulation diameter and its mass for cables with growing copper diameter represented by its gauge.

Table 6. 100 Ohm SPE with PE insulation

Cable type	Copper diameter	Insulation diameter	Insulation mass (relative)
	mm	mm	
UTP 26AWG	0.404	0.676	1
STP 26AWG	0.404	1.291	4.97
STP 24AWG	0.511	1.637	8.02
STP 23AWG	0.574	1.843	10.19
STP 22AWG	0.643	2.067	12.86

The relative dimensions of Cable type listed in Table 6 are visible in Figure 1. Attenuation / IL requirements at higher frequencies will force engineers to increase diameters of copper wires. In addition, the presence of the screen significantly increases unit capacitance of the cable and triggers a dramatic increase in size of the 100 Ohm STP configuration (Figure 1). As seen in Table 6, the diameter of the insulated wire in STP 26AWG (1.291 mm) is almost twice the size of UTP 26AWG insulated wire (0.676 mm).

4. Insertion Loss of 100 Ohm SPE Cable

IL for 100 m length cables listed in Table 6 were simulated and compared with CAT6A standard (Figure 3). UTP 26AWG is showing IL by about ~1dB smaller than STP 26AWG. Nonetheless, we believe that when installed, the STP will certainly show a lower IL, since the UTP link will have to struggle with different ground configurations and resulting imbalances, reflections, radiation, and transmission losses. Of course, UTP and STP (with identical conductors) will exhibit the same Rdc and losses. However, when transmitting HF signals, STP have additional eddy-current losses in conductive screen - so theoretically UTP should have visibly smaller IL. However, lots of tests show UTP performing worse. This is mostly due to the proximity effect that causes UTP currents to accumulate at the segments of the conductors facing each other. STP cable have balanced "return" eddy currents in the screen allowing the conductors to distribute their currents more uniformly. This reduction of losses in STP conductors is countered by eddy-current losses in the screen. Theoretical results demonstrate a very close performance of UTP and STP cables. Practically, for the reasons listed above, STP will outperform UTP.

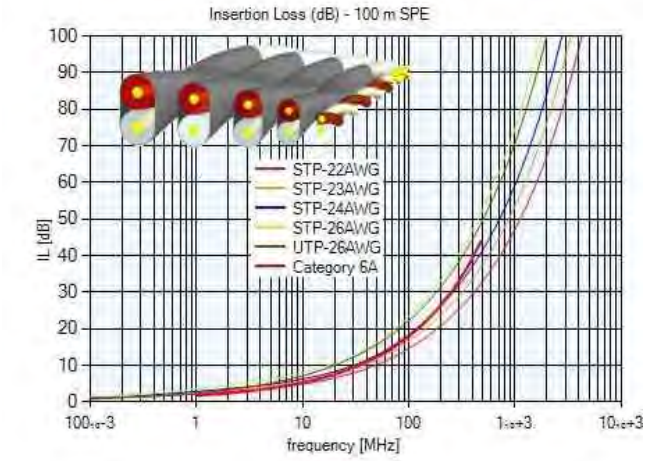


Figure 3. Simulated IL for designed SPE cables listed in Table 6.

Both UTP 26AWG and STP 26AWG do not pass the CAT6A standard and cannot operate with 100 m reach demonstrated by the lower gauge STP designs from Table 6. However, they can successfully operate within shorter segments of 15 m and 40 m, as discussed earlier in Tables 1 and 3.

5. Impact of Insulation Material

To test the impact of insulation material on the performance of 100 m, 100 Ohm STP cables, we used the STP 26AWG cable as our design with insulation Dk from 1.4 to 3.2 and identical loss tangent of 0.0001.

Once the cables are designed and only need tuning for different Dk, the Graphical User Interface (GUI) of OptEM Cable Designer can be successfully employed. The software can quickly adjust the material properties of insulation for recurring simulations (Fig. 4).

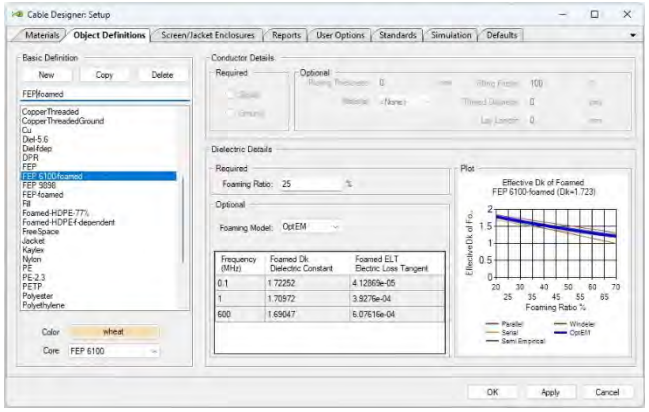


Figure 4. Setting up properties of frequency dependent materials

As expected, lowering Dk allows one to design the 100 Ohm cable from smaller insulated wires. Material-related lowering of capacitance must be matched by geometrical reduction of inductance (to keep the ratio L/C, which controls characteristic impedance, unchanged). Proportionally scaled insulation diameters for cables with Dk=1.4, 2.0, 2.6 and 3.2 are visible above the plot area in Figure 5.

The speed of propagation (plotted as a fraction of c) behaves as expected. Since STP cable is partially filled with air, the gain on

speed is slightly smaller than the square root reduction of Dk. However, the attenuation (which is equivalent to IL for characteristic loading conditions) for better dielectrics (smaller Dk) is deteriorating. This is not what we would like to see but it can be explained. Lower dielectric constant makes the insulation OD smaller. A thinner insulation layer puts the screen closer to signal wires which induce stronger eddy-currents in the screen. The screen losses are powered from the signals and hence the attenuation of cables designed with higher Dk insulation is smaller. Designers will have to choose between faster but more lossy smaller-cables and slower but less lossy bigger-cables. Fortunately, the difference in attenuation is not so significant and can be considered a small price to pay for a faster transmission.

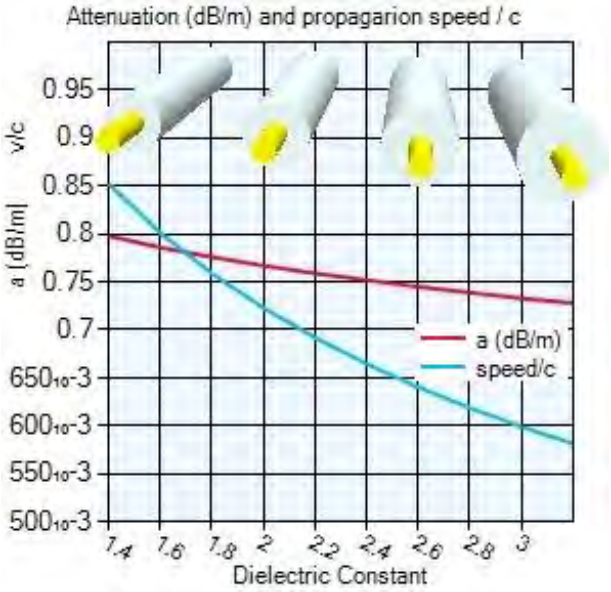


Figure 5. Impact of dielectric constant on attenuation and propagation speed of 100 Ohm STP 26AWG cable simulated at 1 GHz. Relative insulation diameters for cables with Dk=1.4, 2.0, 2.6 and 3.2 are visible above the plot area.

Figure 5 can be used to estimate the dimensional and propagation speed gain for reducing Dk when designing 100 Ohm STP. However, practical insulation materials not only differ by their Dk value, but they also have different electric loss tangent (Lt).

To demonstrate the impact of Dk and Lt on IL of the 100 Ohm STP, we designed it with two commonly used insulation materials: solid polyethylene (PE) that we used in section 3 and 4 above (Dk=2.3, Lt=0.0001) and polyvinyl chloride (PVC) with Dk=4, Lt=0.01. Figure 6 presents the IL of the 100m long 100 Ohm STPs with PE and PVC insulation with CAT6A requirements in the background. As pointed out earlier, the 26 AWG cables fail to reach the 100m requirement. At frequencies below 10 MHz, both cables show the same losses since they have identical conductors and screens (although different insulation thickness) and the dielectric losses are negligible. However, the cable with PE insulation shows far better performance in higher frequencies. At frequency 100 MHz (marker with Label 4 in Figure 6) the IL of the cable with PVC insulation is 13.7 dB higher, and at 1 GHz the PVC cable attenuates the signal 145 dB (~10^7 times) more than the cable with PE insulation. This staggering rise of attenuation in PVC cable is due to the rapid growth of dielectric loss (Figure 7).

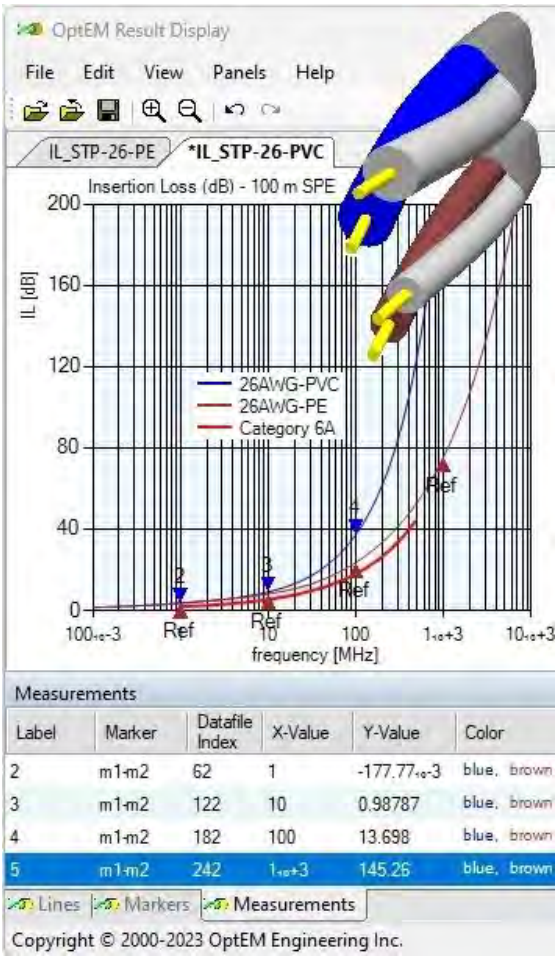


Figure 6. Comparison of IL performance of 100 Ohm SPE cables with PE and PVC insulation

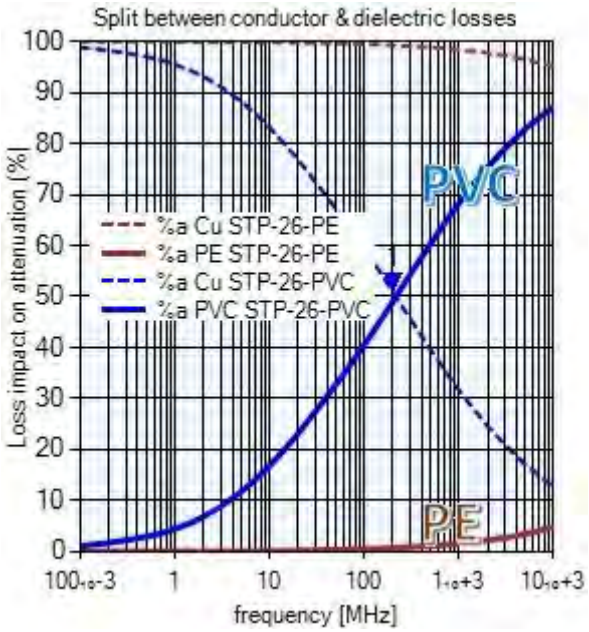


Figure 7. Impact of conductor and dielectric losses on attenuation of 100 Ohm STP cable with PVC and PE insulation

At 200 MHz (marker 1 in Figure 7) PVC losses contribute to attenuation as much as conductor losses. For frequencies higher than 200 MHz, PVC losses (due to high Lt) dominate as they are proportional to frequency. Conductor losses, on the other hand, rise proportionally to the reduction of skin depth (which is proportional to the square root of frequency). In higher frequency ranges the designer must choose insulation materials with as low as possible Lt.

6. Impact of Foaming

An alternative and very effective way of reducing Dk of material used as insulation of STP 26AWG is to use foaming. OptEM Cable Designer software can adjust the Dk based on foaming ratio. For example, if we use data from section 5 above, foaming ratios required for reducing Dk=3.2 to 2.6, 2.0 and 1.4 are respectively: 19.2%, 39.4% and 66.7% (see Figure 8).

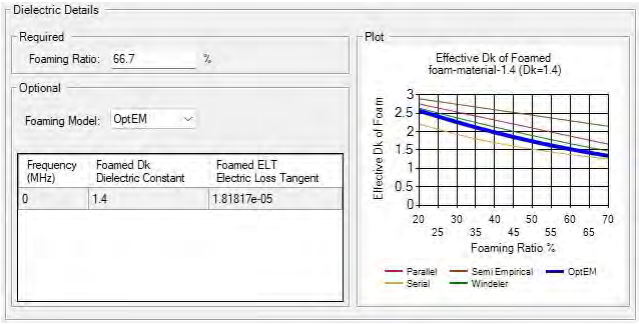


Figure 8. The software automatically adjusts dielectric constant and loss tangent based on foaming ratio.

Since smaller Dk material also requires insulation diameter to be scaled down (see models in the top section of Figure 5), saving on insulation material usage is really significant. Volume, mass and cost can be directly extracted from the Bill of Materials (BOM) report available in the software (Figure 9).

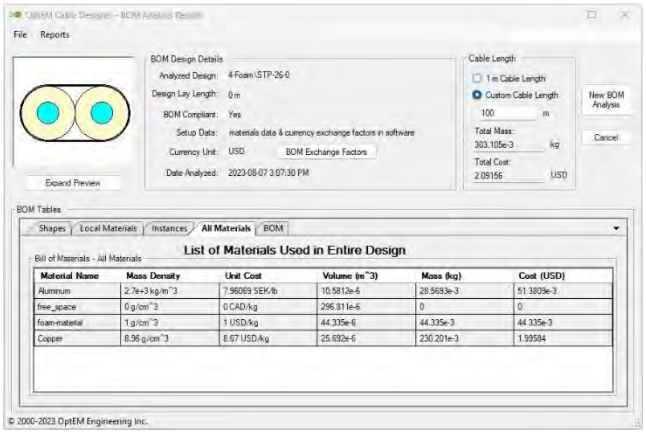


Figure 9. BOM report on foaming material usage

Table 7 summarizes results showing percentage of insulation material used for manufacturing 100 m, 100 Ohm STP 26AWG cables when a foaming process is used during extrusion.

Table 7. 100 Ohm STP 26AWG with foamed insulation

Insulation Dk	Insulation diameter	Foaming ratio	Insulation mass (relative)
	mm	%	%
3.2	1.583	0	100
2.6	1.387	19.2	60.6
2.0	1.195	39.4	32.6
1.4	1.004	66.7	12.0

7. Conclusions

Design and optimization of a 100 Ohm SPE cable leads to the following conclusions:

- 100 m UTP and STP cables with identical conductors show very similar IL performance.
- However, we believe that when installed, the STP will show a lower IL, since UTP link will have to struggle with different ground configurations and resulting imbalances, reflections, radiation, and transmission losses.
- Both UTP 26AWG and STP 26AWG do not pass CAT6A standard for 100 m reach, however both pass for standard 40 m reach.
- Reducing insulation Dk increases propagation speed in the 100 Ohm STP cable, but the rate of increase is slower than expected from the material properties.
- However, IL of STP 26AWG cables with better (smaller Dk) dielectrics is slowly deteriorating.
- Practical designs of 100 Ohm STP cables with PVC and PE insulation show superiority of insulation materials with low loss tangent for constructing cables operating above 100 MHz.
- Significant savings of insulation materials can result from using foaming during the manufacturing process.

8. Acknowledgments

Special thanks to IWCS organization and sponsors for continuing this forum for more than 30 years, contributing to the development of 7 generations of balanced cabling.

Special thanks to IEC TC46 and ISO/IEC JTC1 SC25 for their collaboration and dedication to advancing the cabling standards.

Special thanks to Ms. Joan Beckett for helping with the manuscript and simulation.

9. References

[1] ISO/IEC/IEEE 8802-3:2021 Standard for Ethernet

[2] ISO/IEC 11801-1, Information technology -- Generic cabling for customer premises -- Part 1: General requirements

[3] ISO/IEC TR 11801-9906, Information technology – Generic cabling for customer premises – Part 9906 - Technical report: Balanced single-pair cabling channels up to 600 MHz

[4] IEC 61156-11, Multicore and symmetrical pair/quad cables for digital communications - Part 11: Symmetrical single pair cables with transmission characteristics up to 1 250 MHz – horizontal floor wiring – Sectional specification

[5] TIA-568.5 (2022) Commercial Building Telecommunications Cabling Standard Part 5: Single-Pair Cabling Components, Telecommunications Industry Association (TIA)

[6] Dave Hess, "Shielded Pair Differential Cabling Phase Matters", Proceedings of the 71st IWCS Cable & Connectivity Symposium, 2022

[7] J. Poltz, "Design Optimization of Screened Twisted Pairs," Paper 6-6 presented at the 68th International Cable and Connectivity Symposium, Charlotte, North Carolina, USA, 30 September – 2 October 2019

10. Authors



Juliusz Poltz holds M.Sc. and Ph.D. degrees in both mathematics and electrical engineering from Universities in Poznan, Poland. He works in Canada since 1989, where he has published over 80 technical papers related to EM field analysis and numerical simulation of copper cables. In 1992, Dr. Poltz co-founded OptEM Engineering Inc. in Calgary, Alberta. OptEM is a software company specializing in EM analysis and circuit simulation.



Dave Hess, dba CORD DATA, currently works as a subject matter expert facilitating international standards development for connectivity technology, particularly in the area of shielded pair differential cabling. He has worked for more than 40 years in both fields of electronic and photonic wired data communication connectivity and participates on the standards committees for physical interface and cabling standards: ISO, IEC, IEEE, INCITS, EIA, TIA, CTA, and ANSI,. He has been project leader for over 20 international standards. He received IEC 1906 awards for technical contributions in 2011 and 2014. He holds a B.S. degree in Mathematics from Pennsylvania State University and is a life member of IEEE.

Relation of Coupling Attenuation and Unbalance Attenuation

Dave Hess
CORD DATA
Wyomissing, Pennsylvania, USA
+1-610-698-4790 · dave.hess@corddata.org

Abstract

New single-pair copper cabling channel specifications cover both unshielded twisted-pair and shielded pair differential cabling. Whereas the transmission parameter characterization of twisted-pair cabling has been primarily based on crosstalk loss, the new single-pair cabling characterization is primarily based on mode-conversion loss parameters, such as unbalance attenuation and coupling attenuation. Over the past 20 years, verification of installed twisted pair cabling, particularly crosstalk performance verification, has become normal practice using standard portable instruments. Adapting this industry standard practice to single-pair cabling requires practical mode-conversion loss verification. Ideally this will be accomplished using adaptations of available standard instruments. This paper covers an adaptation approach using shielded reference cords.

Keywords: single-pair; Ethernet; SPE; Type-B; single-pair; twisted-pair; balanced; cable; cabling; channel; link; Class T1-B; Category T1-B; Class T1-C; Category T1-C; Class-E_A; Category 6_A; Class-F_A; Category 7_A; Class-I; Category 8.1; Class-II; Category 8.2; common-mode; coupling; coupling-attenuation; mode-conversion; conversion-loss; electromagnetic; EMC; model; data; rate; reach; signal-to-noise-ratio; SNR; margin; capacity; screen; shield;

1. Introduction

Differential-to-common-mode-conversion-loss is defined using mixed-mode S-parameters, which are amplitude plus phase characterizations using balunless 4-port vector S-parameter measurements. Current state-of-the-art field testing of installed Category 6A cabling, particularly for modular plug terminated links (MPTL), uses precision reference cords for de-embedding from vector network analyzer (VNA) measurements of the full complex parameter matrix, including insertion loss, return loss, near-end & far-end unbalance attenuation, and near-end & far-end crosstalk loss. The recent solution for unbalance attenuation measurements implies the possibility for measuring coupling attenuation by substituting shielded reference cords. However, near-end & far-end coupling attenuation must be defined, so that unbalance attenuation and coupling attenuation can be modeled and measured interchangeably.

The basic concept of this approach to shielded cable testing has already been validated by demonstrating that a simple common-mode return loss measurement of a shielded cable, transformed to time-domain, has sufficient resolution to detect the location of open shield segments (Harshang Pandya, "Measuring shield integrity for twisted pair cabling systems" 2020 IWCS [17]). This paper covers scaling up to a de-embedded common-mode double-ended insertion loss measurement of a shielded cable assembly.

The various shielded cable test procedure standards, e.g., IEC TS 61156-1-2, are undergoing amendments and revisions to include balunless 4-port vector S parameter measurements, to extend frequency range, and to specify accuracy for verifying mode-conversion loss parameters. This paper includes a proposal for defining near-end & far-end coupling attenuation, and for defining the common-mode circuit measurement points for detecting the signal in the shield outer-loop circuit (see Figure 3-4).

2. Single-Pair Cabling Standards

2.1 Standards Organizations

Single-pair cabling standards support data communication physical interface standards from international standards development organizations (SDO), such as IEEE, ISO/IEC, IEC, and TIA.

2.2 IEEE SA (Institute of Electrical and Electronics Engineers, Standards Association)

IEEE-SA 802 LAN/MAN Standards Committee develops the Ethernet® wired, and WiFi® wireless, internet data communications standards, for local area networks and metropolitan area networks (LAN/MAN); 802.3 working group publishes Ethernet standards, for wired internet data transport supporting between practically all microprocessor-controlled equipment connectivity.

2.2.1 Ethernet PHYs

Physical-layer interface (PHY) specifications for Single-Pair Ethernet (SPE) are the new focus for copper links; originally intended for automotive applications, these PHYs support mechanical robustness, environmental endurance, and electrical efficiency, by full-duplex operation over a single-pair while using fewer modulation levels, e.g., PAM-3 & PAM-4.

The ISO/IEC/IEEE 8802-3:2021 Ethernet Standard [1] and its amendments cover several SPE PHYs ranging from 10 Mb/s to 25 Gb/s. For illustration, this paper uses the original SPE PHY:

- 1000BASE-T1 [2] IEEE 802.3 (bp) 2016, Type-A short reach PHY, clause 97, runs up to 15 m over single-pair at about 375 MHz, and 1000BASE-T1 Type-B medium reach PHY, clause 97, runs up to 40 m over single-pair at about 375 MHz.

2.2.2 Ethernet PHYs' Coupling Attenuation Requirements

Prior to SPE, BASE-T PHYs relied on a form of coupling attenuation for unshielded cabling to assure common-mode noise rejection; the original injection clamp method of 1000BASE-T [1] was updated for 25G/40GBASE-T [1].

SPE PHYs adopted IEC coupling attenuation requirements:

- 1000BASE-T1 Type-B [2], references coupling attenuation measurement from IEC 62153-4-14 [15].
- 10BASE-T1L [1], includes low-frequency coupling attenuation requirements.
- MultiGBASE-T1 [1], references coupling attenuation measurements using triaxial method IEC 62153-4-7 [12].

2.3 ISO/IEC (International Standards Organization / International Electrotechnical Commission)

ISO/IEC JTC1 SC25 covers interconnection of microprocessor-based IT equipment.

2.3.1 Generic Cabling Specifications

Wired network cabling systems for all media-types for LAN applications in buildings are covered in ISO/IEC 11801-1 [3], which is referenced by the other 11801-x series standards covering implementations for: 2-Enterprise, 3-Industrial, 4-Homes, 5-Datacenter, and 6-Smart-building.

The cabling requirements cited in this paper are covered in ISO/IEC 11801-1 [3] which covers standard balanced cabling channel specifications: e.g., Class-E_A/CAT6$_A$ & Class-F_A/CAT7$_A$. Amendments are underway for 11801-x series, which add the new media type, balanced single-pair cabling.

2.3.2 Application Specific Cabling Guidelines and Specifications

New technical reports and technical specifications precede the ISO/IEC 11801-1 series cabling standards to extend support to new applications, e.g., Single-pair Ethernet (SPE):

- ISO/IEC/TS 11801-9903 [6], Information technology - Generic cabling for customer premises - Part 9903: Matrix modelling of channels and links, covers 4-port network matrix model for links and channels; mixed-mode S-parameters have been added to support shielded single-pair cabling.
- ISO/IEC/TR 11801-9906 [7], Information technology – Generic cabling for customer premises – Part 9906 - Technical report: single-pair cabling channels up to 600 MHz; covers the SPE link segment specifications supported by single-pair cabling channels and components.

2.4 IEC (International Electrotechnical Commission)

IEC TC 46, for Cables, wires, waveguides, RF connectors, RF and microwave passive components and accessories, is the standards committee covering basic measurement and test procedures for data communications cables and cable assemblies, used with related standard connectors for data communications cable and assemblies.

2.4.1 Cable Component Specifications

IEC SC46C, Wires and symmetric cables, subcommittee covers balanced cables for data communications. IEC 61156-x series covering balanced cables.

- IEC 61156-11 ED2 (draft) [8], Multicore and symmetrical pair/quad cables for digital communications - Part 11: Symmetrical single pair cables with transmission characteristics [from 0.1 MHz] up to 1250 MHz – horizontal floor wiring – Sectional specification; covers single-pair component cable, new media-type for data communication applications, e.g., Single-pair Ethernet (SPE) and Fieldbus. The standard specifies two cable types, T1-C type cables up to 600 MHz, and T1-D type cables up to 1250 MHz. Related standards IEC 61156-12, -13, -14 cover other related single-pair cable standards.
- IEC TS 61156-1-2/ Ed 1.0: Multicore and symmetrical pair/ quad cables for digital communications - Part 1-2: Electrical transmission characteristics and test methods of symmetrical pair/ quad cables; this technical specification describes the 4-port network, S-parameters, mixed-mode cable model supporting balunless measurements.

2.4.2 Connector Component Specifications

SC48B, Electrical connectors, subcommittee covers multiconductor connectors for data communications. IEC 63171-x series covers single-pair connectors; mixed-mode and coupling attenuation requirements are included among the connector transmission requirements.

- IEC 63171 ED1 [10], Connectors for Electrical and Electronic Equipment – Shielded or unshielded free and fixed connectors for single-pair data transmission with current carrying capacity; transmission requirements and tests. Related standard series IEC 63171-1, -2, (-3), -4, -5, -6, & -7 cover the single-pair connector series variants' mechanical detail standards.

2.4.3 Cable Assembly Specifications

IEC TC 46 standards also cover balanced cable assemblies, which are standardized within the IEC 61935-x series; mixed-mode and coupling attenuation requirements are included.

- IEC 61935-2 ED4 [12], Specification for the testing of balanced and coaxial information technology cabling - Part 2: Cords as specified in ISO/IEC 11801 and related standards; single-pair cord specifications will soon be included and added by an amendment.
- IEC 61935-4 ED1 [13], Draft specification for the testing of single-pair information technology cabling - Part 4: Installed single-pair cabling as specified in ISO/IEC 11801-1 and related standards.

2.4.4 Cable EMC Related Specifications

IEC TC46 standards include EMC related tests for communication cables and assemblies, which are standardized within the IEC 62153-4-x series. This test procedure series includes coupling attenuation measurements, which are being amended or revised to include 4-port mixed-mode measurements improvements resulting from applying S-parameters to coupling attenuation, see [17].

- IEC 62153-4-7 ED3 [14], Metallic cables and other passive components test methods - Part 4-7: Electromagnetic compatibility (EMC) -Test method for measuring of transfer impedance Z_T and screening attenuation a_S or coupling attenuation a_C of connectors and assemblies – Triaxial tube in tube method
- IEC 62153-4-14:2012 ED1 [15], Metallic communication cable test methods - Part 4-14: Electromagnetic compatibility (EMC) - Coupling attenuation of cable assemblies (Field conditions) absorbing clamp method

2.5 TIA (Telecommunications Industry Association)

TIA Standards committee TR42, TIA-568 series cabling standards, for IT network cabling systems, for building application spaces: Enterprise, Datacenter, Industrial, Residential, and Intelligent buildings; covering US building standards includes:

- TIA-568.5, [16] Balanced single twisted-pair telecommunications cabling and components standard; single-pair media-type, channels, and components.

The TIA-568 series cabling standards conform to the ISO/IEC 11801-1 [3] cabling standard and reference IEC 62153-4-x series coupling attenuation measurement standards.

3. Single-pair Cabling Channels

3.1 Extended Reach

The application space for SPE PHYs spans a very wide range of rate-over-reach, from 10 Mb/s-over-1000 m to 25 Gb/s-over-10 m. The latest project objective is for 100 Mb/s over 500 m.

Increasing SNR and reach can be accomplished by increasing the signal, by increasing cable size, but this has practical limits. Increasing SNR and reach can also be accomplished by reducing noise, by increasing differential-mode to common-mode conversion loss, i.e., by increasing unbalance attenuation or coupling attenuation.

3.2 Differential-Mode to Common-Mode Conversion-Loss, Model and Measurements

The various mixed-mode cabling transmission parameters comprising common-mode conversion loss that combine to form the cabling channel noise factor are identified in Table 3-1.

Table 3-1, Interrelation of Mixed-Mode, Common-Mode Conversion, and Related Parameters

		Launch near-end		Launch far-end	
		CM	**DM**	**CM**	**DM**
Detect near-end	**CM**	RL NEXT	TCL NEXT	IL FEXT	TCTL FEXT
	DM	LCL NEXT	RL NEXT	LCTL FEXT	IL FEXT
Detect far-end	**CM**	IL FEXT	TCTL FEXT	RL NEXT	TCL NEXT
	DM	LCTL FEXT	IL FEXT	LCL NEXT	RL NEXT

NOTE: "CM" is common-mode; "DM" is differential-mode
NOTE: Intra-pair parameters are "IL", "RL" , "TCL", "TCTL" , "LCL", "LCTL"; Inter-pair parameters are "NEXT", "FEXT"
NOTE: coupling attenuation a_{CN} & a_{CF} are Intra-pair parameters, variants of "TCL" , "LCL", "TCTL", "LCTL"; see [18]
NOTE: see Table 6-1 for definitions: "IL", "RL", "TCL", "LCL", "NEXT", "FEXT"

Single-pair channel SNR is essentially determined by four parameters; IL determines the signal level and RL, TCL, & TCTL determine the noise level. These four parameters are made up of power-sums of combinations of four basic S-parameters; see equations (1), (2), (3), and (4); see [17] for S-parameters.

$$IL_{dd} = -20\log(S_{DD21}) = -20\log\left(\frac{1}{2}(S_{31} - S_{41} - S_{32} + S_{42})\right) \quad (3\text{-}1)$$

$$RL_{dd} = -20\log(S_{DD11}) = -20\log\left(\frac{1}{2}(S_{11} - S_{21} - S_{12} + S_{22})\right) \quad (3\text{-}2)$$

$$TCL_{cd} = -20\log(S_{CD11}) = -20\log\left(\frac{1}{2}(S_{11} + S_{21} - S_{12} - S_{22})\right) \quad (3\text{-}3)$$

$$TCTL_{cd} = -20\log(S_{CD21}) = -20\log\left(\frac{1}{2}(S_{31} + S_{41} - S_{32} - S_{42})\right) \quad (3\text{-}4)$$

3.3 Relation of Coupling Attenuation and Unbalance Attenuation

Mixed-mode parameters are used to specify Common-mode noise rejection. Unbalance-attenuation and Coupling-attenuation, respectively for Unscreened and Screened cabling components and assemblies, are mixed-mode parameters typically expressed as a frequency response in dB, for the differential-mode-to-common-mode-conversion-loss of a pair.

It is generally understood, for Unscreened and Screened cabling, by definition:

unbalance-attenuation + screening-attenuation = coupling-attenuation

Thus, for Unscreened cabling, having:

screening-attenuation = 0
then
unbalance-attenuation = coupling-attenuation

UTP unbalance attenuation and UTP coupling attenuation are one and the same!

Results of applying this identity to coupling attenuation:

Harmonization of various mixed-mode parameter measurement methods enables quantitative comparison of cabling EMC related performance.

- Harmonized models for radiated and conducted RF immunity (E_1, E_2, & E_3, see [3]) and coupling attenuation (a_{CN} & a_{CF}).

A harmonized mixed-mode parameters model for Unscreened and Screened cabling supports:

- Interoperability and harmonization of Unscreened and Screened cabling component and assembly specifications;

3.4 Mixed-mode, Near-End & Far-End Coupling Attenuation Model: The Shield is the Balun

The mixed-mode parameters for unbalance attenuation, defined in IEC TS 61156-1-2 AMD1 ED1 [9], have been applied to coupling attenuation, according to IEC 62153-4-7 [14]. All of the cabling mixed-mode, common-mode conversion, and related parameters are defined using the same four-port S-parameter network model, according to ISO/IEC TS 11801-9903 [6], also see [17].

The new shielded differential pair cable network model, which has been updated and illustrated in IEC TS 61156-1-2-ED1 [9], uses the shield in a real common-mode signal path; see Figure 3-1.

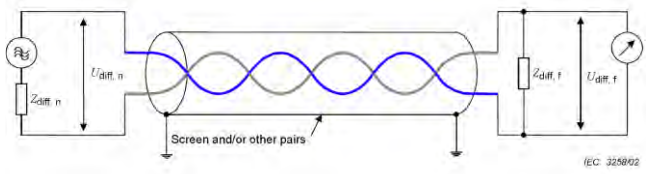


Figure 3-1, Shielded Mixed-Mode Network Model, Differential Mode, Reference IEC TS 61156-1-2-ED1 [9]

The common-mode signal is launched and detected directly through single-ended transmission ports for measurement and comparison; see Figure 3-2.

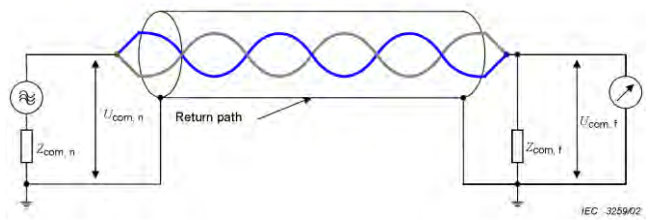


Figure 3-2, Shielded Mixed-Mode Network Model, Common Mode, Reference IEC TS 61156-1-2-ED1 [9]

3.5 Mixed-Mode, Near-End & Far-End Coupling Attenuation Measurement: Triaxial Method

For several decades, the triaxial fixture has been used as the preferred method for cable screening attenuation measurements.

Results of applying balanced cabling 4-port measurement techniques to the triaxial fixture method used for coupling attenuation:

- Harmonized balun and balunless measurement approaches; whereby balun approach provides scalar DM detection of a_{UN}, a_{UF}, a_{CN}, & a_{CF}.
- Cable assemblies coupling attenuation measurements can use de-embedded reference assemblies.

The Triaxial fixture, illustrated in IEC 62153-4-7 [14], provides a significant reduction of coupling attenuation measurement uncertainty, see Figure 3-3.

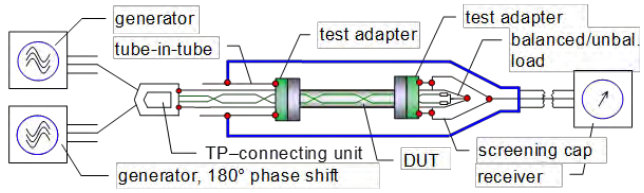


Figure 3-3, Single-Ended Measurement Setup for Coupling Attenuation (a_C) of a Balanced Assembly According to IEC 62153-4-7 Tube-in-Tube Method

The triaxial method can be adapted to be equivalent to current signal integrity methodology, wherein a cable-assembly-under-test is closely and uniformly suspended over a ground-plane, so the common mode circuit approaches a uniform transmission line. This is the current setup specified in IEEE 802.3 1000BASE-T1 [1]; see Figure 3-4.

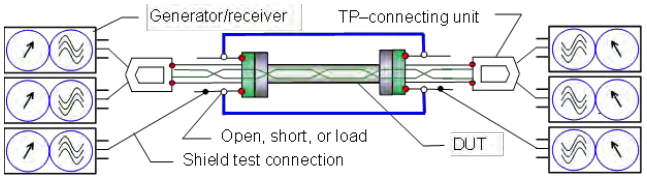


Figure 3-4, Adapted Double-Ended Measurement Setup for Coupling Attenuation (a_C) of a Balanced Assembly Using Elements of IEC 62153-4-7 Tube-in-Tube Method

TCL/TCTL are suitable for adaptation to near-end and far-end coupling attenuation parameters measurements, thus providing equivalent unbalance attenuation, common-mode coupling loss, measurements for shielded differential pair cable. The TCL/TCTL approach to coupling attenuation measurement launches the differential-mode signal directly through the matched differential transmission ports for measurement and comparison, while the common-mode signal is detected directly from the outer surface of the shield. This arrangement provides sufficient measurement sensitivity needed to detect coupling attenuation common-mode conversion loss signals conducted through the shield [17].

Coupling attenuation measurement of installed cabling is possible using de-embedding of a reference cord: a) by balunless method using a direct measurement through a reference triaxial cord, or b) by balun method using an indirect measurement through a reference cord together with an absorbing clamp (balun: common-mode current probe [15]) which is calibrated against the reference cord, which is measured using the triaxial-method.

4. Channel Margin Simulation

4.1 Example Single-Pair Cabling Channel Specifications

4.1.1 Example IEEE 802.3 Bp 1000BASE-T1 Type-B SPE Link Segment Over ISO/IEC 11801-1 Class T1-B Single-Pair Cabling Channel

The example channel margin simulation is based on IEEE 802.3 bp 1000BASE-T1 Type-B SPE, which is supported by ISO/IEC 11801-1 [3] single-pair cabling Class T1-B channel (600 MHz).

The 1000BASE-T1 Type-B physical layer interface (PHY) standard is designed to operate up to 40 m over screened single-pair cabling. It is the first IEEE 802.3 PHY standards to make a normative reference to the ISO/IEC 11801-1 E_1, E_2, & E_3 electromagnetic classifications [3].

For the purpose of illustration, some parameter specifications are simplified, extended, or truncated. The simulated frequency range upper bound is 3000 MHz; however, for simplification the results only show up to 1000 MHz. The ISO/IEC 11801-1 Class T1-B channel standard frequency range lower bound is 0.1 MHz; however, for simplification this simulation uses 1.0 MHz, because the lowest frequency band has an insignificant effect on channel margin.

4.1.2 Example 1000BASE-T1 Type-B Physical Layer Interface (PHY)

1000BASE-T1 Type-B physical layer interface (PHY) standard basic specifications are 1000 Mb/s, full-duplex transmission over single-pair at about 375 MHz.

The 1000BASE-T PHY covers two reach objectives: Type-A up to 15 m, for automotive applications; Type-B up to 40 m, for industrial applications.

This simulation uses 1000 Mb/s rate and 100 m reach for margin comparisons up to 1000 MHz for the purpose of convenient comparison to common cabling specifications.

4.1.3 Model Channel Specifications and Implementation

Single-pair Ethernet (SPE) physical-layer interface standards are intended to run over a range of single-pair cable sizes and types. SPE cabling channel specifications and standards were originally based on $CAT6_A$/Class-E_A unshielded twisted-pair cabling model, and the comparable $CAT7_A$/Class-F_A shielded twisted-pair cabling model, which are used in this simulation.

NOTE: this simulation uses IL values based on single-pair cable using 22 AWG conductor and 100 ohm differential mode characteristic impedance.

For this simulation, all channels use the same implementation topology, i.e., 2-connector channel, with 2 m total length of 1.0X de-rated patch cord.

4.2 Example Cabling Channel SNR Parameters

4.2.1 Simulated Cabling Channel SNR Parameters

See 6.1 below for the SNR formulas used for this simulation.

The signal term is composed of the insertion loss (IL).

The noise term is composed of the power sum of the noise components (RL, Crosstalk Loss, & CMCL), which is dominated by the RL component in this simulated performance comparison. The SNR in this simulation practically equates to IL/RL.

4.2.2 Insertion Loss (IL)

Channel IL is dominated by the cable attenuation. The channel IL formula used for this simulation is taken from standard shielded twisted-pair cabling.

Equation (5) giving the formula for channel IL, given in dB, is similar to Class-F_A/CAT7$_A$, see [19].

$$\mathbf{1.00}\left(\mathbf{1,8}\sqrt{f}+\mathbf{0,0050}f+\frac{\mathbf{0,25}}{\sqrt{f}}\right)+\mathbf{4}\times\mathbf{0,02}\sqrt{f} \qquad \textbf{(4-1)}$$

where f is frequency in MHz

As this simulation uses IL values based on single-pair cable using 22 AWG conductor, the IL formula conductor term "a" coefficient, "1.8", is reduced by a factor of 0.793036, see 6.2 below.

4.2.3 Return Loss (RL)

All parameters used are specification limits except for RL, which uses typical RL values for a S/FTP cable from good shielding and low common-mode impedance are about 10dB better than the T1-C RL limits; see IEC TR 61156-1-3 , see Figure 4-1, see [10].

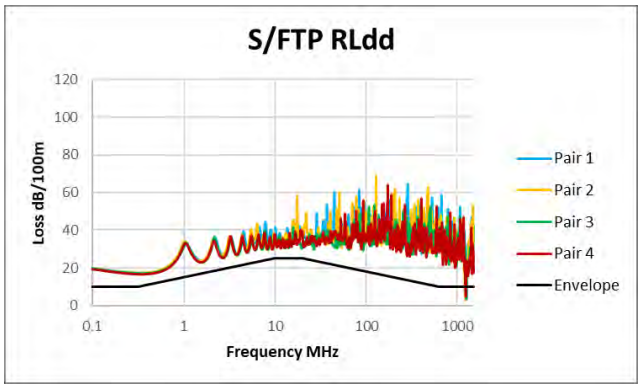


Figure 4-1, Typical S/FTP RLdd

Table 4-1, Balanced 1-Pair Shielded Cable Model RL

Upper Frequency	Frequency Range	RL
MHz	MHz	dB
1250	$1 \le f \le 10$	$20 + 10 \log(f)$
	$10 < f \le 100$	30,0
	$100 < f \le 1250$	$50 - 10 \log(f)$

4.2.4 Crosstalk Loss (NEXT, FEXT, ANEXT, AFEXT)

For the purpose of including component crosstalk figures, Class T1-B channel minimal crosstalk limits are simulated in the single-pair cabling channel model by using the noise-floor figure for the crosstalk model and power-summing the total crosstalk figure including near-end & far-end and internal & external crosstalk parameters.

4.2.5 Simulation Variable: Common-Mode-Coupling Loss (CMCL) Parameter (TCL, TCTL, a_{CN}, a_{CF})

The common-mode-coupling-loss (CMCL) parameters include unbalance attenuation or coupling attenuation, which are used to simulate the common-mode conversion loss.

CMCL is the variable parameter used in this modeled performance comparison. A range of coupling attenuation figures is used for this simulation and sensitivity analysis:

For this simulation, the CMCL is varied over four values:

Table 4-2, CMCL, Simulation Variable

CMCL, f = Frequency MHz
dB
60-10log(f) dB
80-10log(f) dB
100-10log(f) dB
120-10log(f) dB

4.2.6 PHY Implementation Margin

Cancelation, or PHY "implementation margin", is included and used in this simulation for RL only, using moderate values:

- 24 dB RL cancellation
- 0 dB PSNEXT and 0 dB PSFEXT cancellation
- 140-10log(f) dB crosstalk and noise-floor figure

4.3 Simulation Results

4.3.1 Channel SNR

Channel SNR is the difference between signal IL and the noise figure, PS Noise (PSN). The standard SNR component parameters frequency responses, example 100 m channel, 60-20log(f) dB PSCMCL, are shown in Figure 4-2.

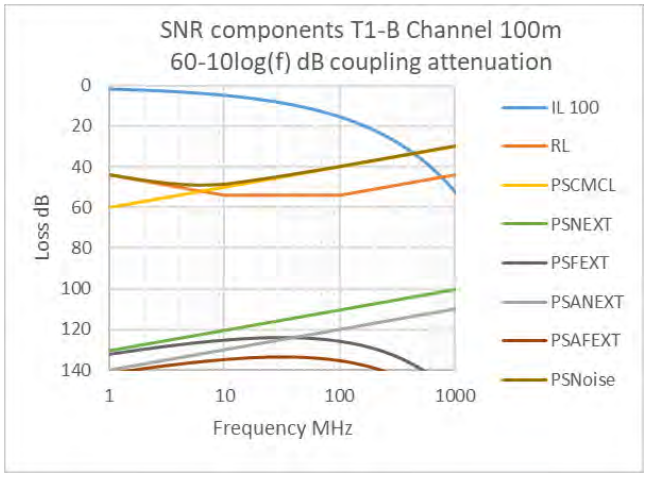


Figure 4-2, Channel SNR Components, Class T1-B, 100 M, RL Cancellation Included; Example 60-10log(F) dB PSCMCL

The effect of improved PS noise is simulated by varying the PSCMCL, see Figure 4-3.

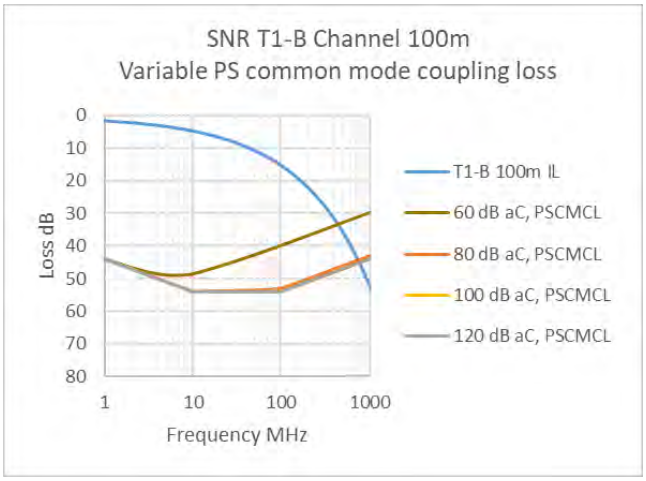


Figure 4-3, Channel SNR, Class T1-B, 100 M, Variable PSCMCL Range 60-10log(*F*) to 120-10log(*F*) dB

NOTE: CMCL values 100 & 120-10log(*f*) provide insignificant improvement in SNR due to the RL level of 80-10log(*f*); this simulation amounts to a comparison between CMCL values 60 & 80-10log(*f*).

4.3.2 Channel Capacity and Margin

Channel SNR is used to calculate Channel Capacity, Margin-to-capacity, Margin versus reach, and Reach versus bandwidth.

Channel SNR margin is an expression for the average difference in decibels (dB) between the channel maximum (Shannon) capacity in bits per second (bit/s) and a specific application data rate in bits per second (b/s), see 6.3 below.

More margin provides more capacity above the required minimum capacity for the application data-rate, thus margin-to-capacity. Similarly, more margin provides: more throughput (higher data rate, bits-per-second, b/s), more reach (longer length, meters, m), and less error (improved bit-error-ratio, BER), see [17].

4.3.3 Channel Capacity

In Figure 4-4, Channel capacity exceeds 1.0 Gb/s at 375 MHz for standard Class T1-B 100 m channel with 60-10log(*f*) dB PSCMCL. Channel capacity exceeds 3.0 Gb/s with 80-10log(*f*) dB PSCMCL, but it approaches the maximum for higher capacity from higher PSCMCL, due to the RL limit.

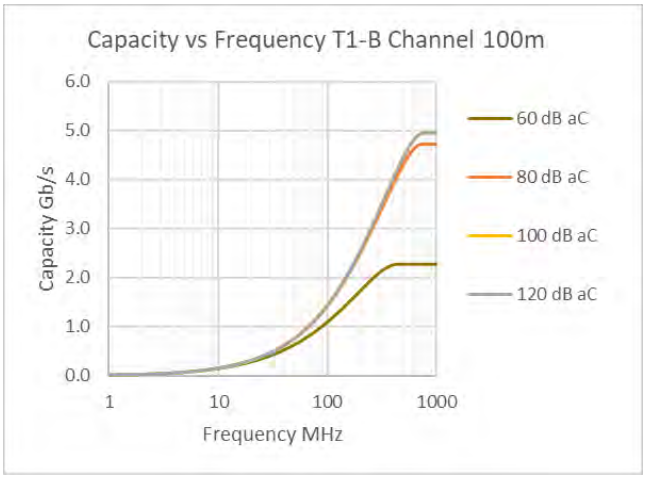


Figure 4-4, Channel Capacity, Class T1-B, 100 M, Variable PSCMCL Range 60-10log(*F*) to 120-10log(*F*) dB

4.3.4 Margin-to-Capacity

A common expression for evaluating cabling implementations is margin-to-capacity, dB versus bandwidth frequency Hz, i.e., the margin between channel capacity and data rate for a fixed reach, versus variable frequency.

FigureFigure 4-5 shows 60-10log(*f*) dB PSCMCL results in nominal margin of 6 dB for 1.0 Gb/s over a 100 m, Class T1-B channel, at about 375 MHz. PSCMCL of 80-10log(*f*) dB results in additional margin of about 12 dB.

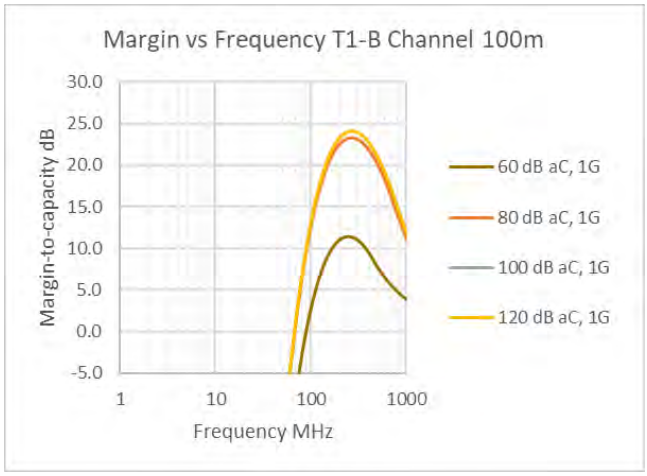


Figure 4-5, Channel Margin vs Frequency, Class T1-B, 100 M, Variable PSCMCL Range 60-10log(*F*) to 120-10log(*F*) dB

4.3.5 Margin versus Reach

A more practical expression for evaluating cabling implementations is margin-to-capacity dB versus reach m, i.e., the margin between channel capacity for a specific application data rate at a fixed frequency, versus variable reach.

Figure 4-6, as expected, shows 60-10log(*f*) dB PSCMCL results in nominal margin, about 6 dB, for a reach of 100 m, at 375 MHz for 1.0 Gb/s operation over a Class T1-B channel. Moreover, 80-20log(*f*) dB PSCMCL, provides sufficient additional margin to reliably reach 150m.

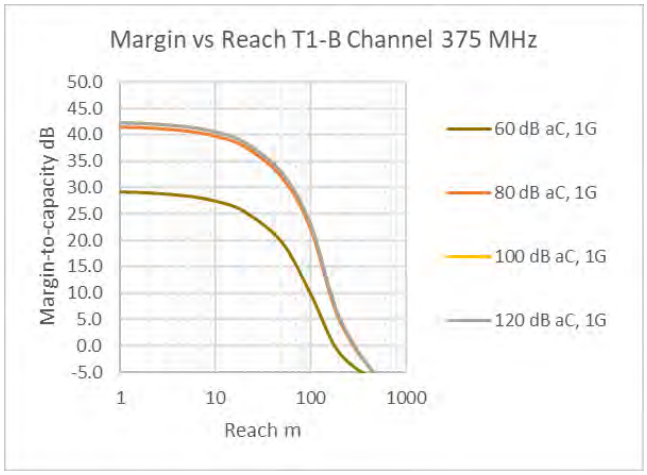


Figure 4-6, Channel Margin vs Reach, Class T1-B, 375 Mhz, Variable PSCMCL Range 60-10log(*F*) to 120-10log(*F*) dB

4.3.6 Reach versus Bandwidth

By holding margin to a single value, a reach versus bandwidth (BW) frequency curve can be generated.

Figure 4-7 shows 60-10log(*f*) PSCMCL, for a minimum 3dB margin, provides greater than 1000 MHz bandwidth at 100 m, more than sufficient for operation of 1.0 Gb/s up to 100 m. Moreover, it shows 80-10log(*f*) PSCMCL provides greater than 2500 MHz bandwidth at 100 m,

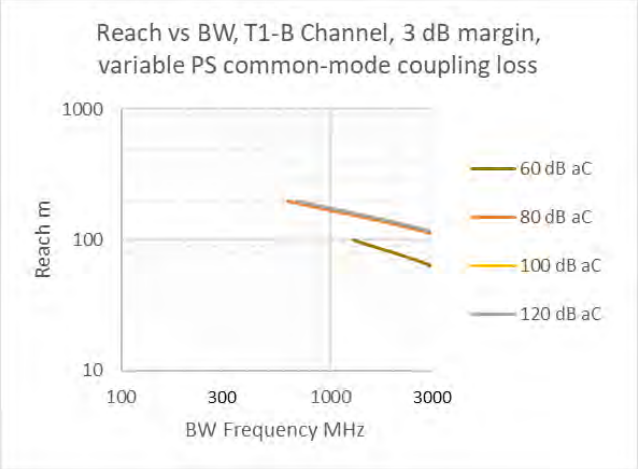


Figure 4-7, Channel Reach vs BW Frequency, Class T1-B, 3 Db Margin, Variable PSCMCL Range 60-10log(*F*) to 120-10log(*F*) dB

NOTE: The calculation method limits the plots for these curves; reach is calculated for discrete points (1, 2, 5, 10, 20, 50, 100, 200, 500, 1000 meters); the curve fitting is limited by the sparse data, e.g., the 60-10log(*f*) curve is truncated at 100 m. Nevertheless, the simulation software used is an ordinary spreadsheet, so you can try this at home.

See 6.3 below for capacity and margin calculations details.

5. Conclusions

- 22 AWG Unshielded Class T1-B channel running 1000 Mb/s can reach 100 meters with 60-10log(*f*) differential-mode to common-mode conversion loss.
- 22 AWG Shielded Class T1-B channel running 1000 Mb/s can reach 150 meters with 80-10log(*f*) differential-mode to common-mode conversion loss.
- 22 AWG Shielded Class T1-B channels running 1000 Mb/s are return loss limited, thus reaching a point of diminishing returns for greater than 80-10log(*f*) differential-mode to common-mode-conversion loss;
- Practical measurement of coupling attenuation up to 80 dB is sufficient for verification of practical shielded cabling implementations.

6. NOTES

6.1 Standard balanced cabling channel SNR model.

6.1.1 Overview

For the purposes of this cabling channel study, only the passive channel signal-to-noise ratio (SNR) over frequency is determined by the ratio of the channel signal level to the channel noise figure. The passive channel's relative signal level is determined by the Insertion-Loss (IL). The passive channel's relative PS-noise figure is dominated by the Return-Loss (RL) value. The coupling attenuation and alien crosstalk are out of the picture.

6.1.2 Signal Level

The total IL over frequency for the single-pair channel determines the signal level frequency response, which is the power sum of the cascaded channel components' attenuation and reflection losses.

6.1.3 Noise Figure

The total noise figure frequency response is the power-sum of the components' noise contributors:

- Return-loss (RL) ("echo"): is treated as a noise parameter.
- Crosstalk loss: includes near-end PSNEXT & far-end PSFEXT, and PSANEXT & PSAFEXT).
- Power-sum-common-mode-coupling-loss PSCMCL, includes near-end TCL & far-end TCTL, LCL & LCTL, or a_{CN}, & a_{CF}.

Table 6-1, Standard Channel SNR Parameter Definitions

Acronym	Parameter
IL	Insertion Loss
RL	Return Loss
PSNEXT	Power-Sum Near-End Crosstalk loss
PSACRF PSFEXT-IL	Power-Sum Attenuation to Crosstalk Ratio, Far-end; Far-end crosstalk minus insertion loss
PSANEXT	Power-Sum Alien Near End Crosstalk loss
PSAACRF PSAFEXT-IL	Power-Sum Alien Attenuation to Crosstalk Ratio, Far-end
TCL	Transverse Conversion Loss (near-end, unbalance attenuation)
TCTL	Transverse Conversion Transfer Loss (far-end, unbalance attenuation)
a_{CN}	Coupling attenuation, near-end
a_{CF}	Coupling attenuation, far-end

Table 6-2, Class T1-B, Cabling Channel Parameters Coefficients

Parameter	Formula Coefficients
Acronym	T1-B
f= MHz	1250
IL	1.8, 0.005, 0.25, 0.02; 100, 1.0, 2
RL	20, -10, 10; 30, 0, 100; 50, 10, 1250
PSNEXT	100, 10, 140, 10, 2, 1250
PSACRF PSFEXT-IL	100, 10, 140, 10, 2, 1250
PSANEXT	100, 10, 1250
PSAACRF = PSFEXT-IL	100, 10, 1250
TCL	(60, 80, 100, 120), 10, 1250
TCTL	(60, 80, 100, 120), 10, 1250
a_{CN}	(60, 80, 100, 120), 10, 1250
a_{CF}	(60, 80, 100, 120), 10, 1250
PSCMCL	(60, 80, 100, 120), 10, 1250

NOTE: The normal figures are given with positive values for loss.
NOTE: Upper and lower measurement bounds are not applied to SNR calculations.
NOTE: Parameters are extended beyond their standard upper frequency specification for SNR calculations, using straight-line extrapolation.

Table 6-3, Standard Cabling Channel Parameters Formulas

Acronym	Formula
IL	(L/100(K(M/L)+(L-M)/L))(a√f+bf+c/√f)+2d√f
RL	A1-B1(log(f)), 1≤f<C1; A2-B2(log(f)), C1≤f<C2; An-Bn(log(f)), C_{n-1}≤f<Cn
PSNEXT	-20log((10^(A1-B1(log(f)))/-20)+E1(10^(C1-D1(log(f/F1)))/-20)), 1≤f<F1; … -20log((10^(An-Bn(log(f)))/-20)+En(10^(Cn-Dn(log(f/F_{n-1})))/-20)), F_{n-1}≤f<Fn; …
PSACRF PSFEXT – IL	-20log((10^(A1-B1(log(f)))/-20)+E1(10^(C1-D1(log(f/F1)))/-20)), 1≤f<F1; … -20log((10^(An-Bn(log(f)))/-20)+En(10^(Cn-Dn(log(f/F_{n-1})))/-20)), F_{n-1}≤f<Fn; …
PSANEXT	A1-B1(log(f)), 1≤f<C1; A2-B2(log(f)), C1≤f<C2
PSAACRF PSFEXT – IL	A1-B1(log(f)), 1≤f<C1; A2-B2(log(f)), C1≤f<C2
TCL	A1-B1(log(f)), 1≤f<C1; A2-B2(log(f)), C1≤f<C2
TCTL	A-B(log(f))
LCL	A1-B1(log(f)), 1≤f<C1; A2-B2(log(f)), C1≤f<C2
LCTL	A-B(log(f))
a_{CN}	A-B(log(f))
a_{CF}	A-B(log(f))
PSCMCL	A-B(log(f))

NOTE: while PSACRF is used for channel limits, PSFEXT is used in the channel power sum noise model, likewise for PSAACRF & PSAFEXT.
NOTE: PSCMCL ≈ PSa_{CN} , PSa_{CF} ,
NOTE: Propagation delay and delay skew are not used in the SNR calculations

6.2 Channel Parameters Affecting IL

Cabling channel insertion loss is reduced by reducing cable attenuation to achieve longer reach, by using cables with enhanced performance; e.g., larger conductor size, higher NVP, or lower dissipation factor; see [19]. The cable Attenuation (A) formula is given by equation (6-1)

$$A = a\sqrt{f} + bf + c/\sqrt{f} \qquad \textbf{(6-1)}$$

6.2.1 IL Relation of Conductor Size and DC Resistance; Reduced Attenuation Relation to Extended Reach

Insertion loss (IL) is essentially proportional to attenuation, which is essentially proportional to the conductor diameter; this is due to the skin effect.

Note, conductor DCR, not signal attenuation, is proportional to the square of the conductor diameter.

Cable attenuation is reduced, by using cables with larger conductor size. For example, CAT7A 24 AWG cable , IL formula conductor term “a” coefficient is “1.8”, which is reduced by a factor of 0.793036 for cable using 22 AWG conductor. Table 6-4 provides conductor diameter related IL factors.

Note, for IL and resistance scaling, additional factors are needed to simulate conductor stranding and conductor alloys with increased resistivity.

Relation of IL to conductor diameter: attenuation, dB, is roughly proportional to the wire size, diameter, according to the following:

- Attenuation, gamma = alpha + *j*(beta), in nepers (see IEC TR 61156-1-3, [10]).
- Nepers are linearly proportional to decibels (1 Np = 8.685 89 dB).
- Gamma is dominated by alpha, while alpha is dominated by resistance (*R*), so gamma is approximately linearly proportional to *R*.
- *R* (at high frequency, > 1 MHz) is halved (not quartered), when diameter (*D*) is doubled (due to skin effect).
- Therefore, attenuation in decibels is approximately halved when *D* is doubled, i.e., for +6 AWG steps.

Table 6-4, Conductor Diameter IL Factors vs Cable Conductor AWG

Metric size	AWG	Diameter Inches	Diameter Mm	IL factor
0.4 mm			0.400 000	1.276 398
	26	0.015 940 6	0.404 892	1.260 977
	25	0.017 900 2	0.454 666	1.122 932
0.5 mm			0.500 000	1.021 118
	24	0.020 100 8	0.510 559	1.000 000
	23	0.022 571 8	0.573 323	0.890 526
0.6 mm			0.600 000	0.850 932
	22	0.025 346 6	0.643 803	0.793 036
	21	0.028 462 5	0.722 947	0.706 219
0.8 mm			0.800 000	0.638 199
	20	0.031 961 5	0.811 821	0.628 906
	19	0.035 890 5	0.911 620	0.560 057
1 mm			1.000 000	0.510 559
	18	0.040 302 7	1.023 687	0.498 745
	17	0.045 257 1	1.149 531	0.444 145
1.2 mm			1.200 000	0.425 466
	16	0.050 820 7	1.290 846	0.395 523

American wire gauge (AWG) conductor diameter (D) is defined by formula in equation (6-2).

$$\boldsymbol{D = 0.005 \times 92^{\frac{(36-\mathrm{AWG})}{39}}} \qquad (6\text{-}2)$$

where *D* is the diameter in inches.
AWG revolves around the set-point: 36 AWG = 0.005 inches;
6 AWG steps equates to approximately doubling the diameter.
EXAMPLE: Diameter for 24 AWG = 0.005 x 92^((36-24)/39)
= 0.0201008

6.2.2 IL Relation of Nominal Velocity of Propagation (NVP), to Relative Permittivity, and to Attenuation; Reduced Delay Relation to Extended Reach

NOTE: In current standards. for clarity. "dielectric constant" has been deprecated and replaced by "relative permittivity".

An engineered channel using cable with higher nominal velocity of propagation (NVP). thus having lower propagation delay. can support more physical length. e.g.. more than 40m. while conforming to 1000BASE-T1-B link segment specifications. including maximum delay specifications.

The implicit maximum relative permittivity used for standard cable types T1-B. 600 MHz and T1-C. 1250 MHz balanced single-pair cable is 2.75. for 4 MHz. which is derived from the standard phase delay limit per using the formula (see IEC 61156-11, [8]):

$$\tau = 534 + 36/\sqrt{f} \qquad \textbf{(6-3)}$$

$$\varepsilon_r = (\tau/\tau_0)^2 \qquad \textbf{(6-4)}$$

where

τ is the delay time (ns/100 m);
τ_0 is the delay time for $\varepsilon r = 1$ i.e.. 333 ns/100 m;
ε_r is the relative permittivity.
f is the frequency (MHz).

For cable types T1-B. 600 MHz and T1-C. 1250 MHz cable. in accordance with the standard phase delay. $\varepsilon r = 2.75$ is used as the standard "BASE" relative permittivity. which is factored into the attenuation formula "*a*" coefficient (a = 1.8. see 4.2.2. see [19]). The "*a*BASE" coefficient is changed to an "*a*calc" coefficient using Formula:

$$a_{\text{calc}} = a_{\text{BASE}}\sqrt{\varepsilon_{\text{r calc}}/\varepsilon_{\text{r BASE}}} \qquad \textbf{(6-5)}$$

NOTE 2.75 (NVP = 60 %) is a practical value corresponding to a medium quality dielectric material. It applies to all standard categories of balanced cables. which also use the same phase delay limit formula.

6.2.3 IL Relation of Dissipation Factor to Attenuation; Reduced Attenuation Relation to Extended Reach:

For frequencies above 1000 MHz. the relation of dissipation factor (tanδ) and the attenuation formula "*b*" coefficient is quite significant. Further significant reduction of attenuation is possible from using superior dielectric materials; see [19].

The explicit dissipation factor (tanδ) used for cable types T1-B. 600 MHz and T1-C. 1250 MHz balanced cable is 0.005. The relation of dissipation factor (tanδ) and the attenuation formula "*b*" coefficient is given by Formulas:

$$b(f) = \pi f \tan\delta(C)(Z_0) \qquad \textbf{(6-6)}$$

$$b \approx \tan\delta \qquad \textbf{(6-7)}$$

where

tanδ is the dissipation factor;
f is the frequency (Hz);
C is the capacitance (F/100 m);
$Z0$ is the characteristic impedance.

NOTE Very conveniently. $\pi fCZ0 \approx 1$ for typical category cable. which is specified at 1 MHz. as 100 Ω. for 100 m. so the attenuation formula's coefficient *b* practically equals tanδ.

For T1-B and T1-C cable. in accordance with the standard phase delay. tanδ = 0.005 is used as the standard "BASE" dissipation factor. which is factored into the attenuation formula "*b*" coefficient (b = 0.005. see 4.2.2. see [19]). The "*b*BASE" coefficient can be changed to a "*b*calc" coefficient using Formula:

$$b_{\text{calc}} = b_{\text{BASE}}(\tan\delta_{\text{calc}}/\tan\delta_{\text{BASE}}) \qquad \textbf{(6-8)}$$

6.3 Legacy Common-mode Conversion S-Parameters. Model and Measurements

The unbalance attenuation transmission parameters. TCL and TCTL. are used to characterize common-mode conversion loss in single-pair cabling channels. links. and components. TCL and TCTL are defined using S-parameters and same approach as crosstalk parameters NEXT and FEXT; see [9].

The common-mode network model and S-parameters are defined according to the network illustrated in IEC TS 61156-1-2 AMD1 ED1 **Error! Reference source not found.**. see Figure 6-1. Originally intended for unshielded twisted-pair cable. using an imaginary circuit with earth as the return path. the common-mode signal is launched and detected through baluns. which transform the common-mode signal ports into equivalent balanced transmission ports for measurement and comparison.

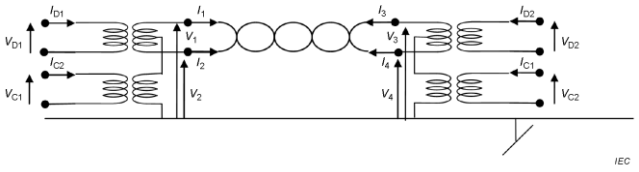


Figure 6-1. Unshielded Mixed-Mode Network Model. IEC TS 61156-1-2-ED1 [9].

The main advantage of S-parameters is their convenient use for both modelling and measurements. Modern vector network analyzers (VNA) use S-parameters for direct measurements and calibration. Moreover. S-parameters are easily transformed to T-parameters. which are used as chain parameters for de-embedding and cascading components. e.g.. connector to cable. per ISO/IEC TS 11801-9903 [6].

6.4 Channel Capacity and Margin

6.4.1 Cabling Channel Signal-to-Noise-Ratio (SNR) [17]

Information capacity of a channel equates to the maximum value. in bits-per-second (b/s). for transmitting data through the channel.

Channel capacity is determined according to the Shannon-Hartley capacity theorem; capacity is proportional to the integrated SNR power over BW.

$$C_{SH} = \int_0^{BW} log_2\left(\left(\frac{S(f)}{N(f)}\right) + 1\right) df \qquad \textbf{(6-9)}$$

where.

***C_{SH}* = channel Shannon capacity**
S(f) is the IL scaled by the TX launch power. and
N(f) is the band-limited white self-noise
BW is the signal bandwidth in Hz.
For Passive Channel. *using flat (white) TX power spectrum*

6.4.2 Margin to Capacity vs Frequency: Channel Figure-of-Merit:

Margin to capacity is the difference in dB between the maximum channel (Shannon) capacity and the link objective capacity. e.g.. 1 Gb/s.

SNR Margin to Capacity:

From Shannon capacity. min SNR in dB is given by

$$SNR_C = 10log_{10}\left(2^{C'/BW} - 1\right) \qquad \text{(6-10)}$$

where.

$$C' = \int_0^{BW} log_2\left((S(f)/N(f)) \times 10^{(SNRmgn(BW)/10)}\right) df \qquad \text{(6-11)}$$

$$SNR_{margin}(BW) = \frac{(C - C') \times 10log_{10}(2)}{BW} \qquad \textbf{(6-12)}$$

where.

C = channel Shannon capacity
C' = *XX* Gb/s minimum required capacity

7. Acknowledgments

Special thanks to IWCS organization and sponsors for continuing this forum for more than 30 years. contributing to the development of 7 generations of balanced cabling. Special thanks to IEC TC46 WG5 & WG9 and ISO/IEC JTC1 SC25 WG3 for their collaboration and dedication to advancing the cabling standards.

8. References

[1] ISO/IEC/IEEE 8802-3:2021 Ethernet Standard and its amendments

[2] IEEE Std 802.3bp™-2016. 1000BASE-T1. Clause 97 of IEEE Std 802.3™-2018: Physical Layer Specifications and Management Parameters for 1000 Mb/s Automotive and Industrial Ethernet. for operation over a Single Twisted-Pair Copper Cable

[3] ISO/IEC 11801-1. Information technology -- Generic cabling for customer premises -- Part 1: General requirements

[4] ISO/IEC 11801-3. Information technology - Generic cabling for customer premises - Part 3: Industrial premises

[5] ISO/IEC 11801-6. Information technology - Generic cabling for customer premises - Part 3: Distributed building services

[6] ISO/IEC TS 11801-9903. Information technology - Generic cabling for customer premises - Part 9903: Matrix modelling of channels and links

[7] ISO/IEC TR 11801-9906. Information technology – Generic cabling for customer premises – Part 9906 - Technical report: Balanced single-pair cabling channels up to 600 MHz

[8] IEC 61156-11. Multicore and symmetrical pair/quad cables for digital communications - Part 11: Symmetrical single pair cables with transmission characteristics up to 1 250 MHz – horizontal floor wiring – Sectional specification

[9] IEC/ TS 61156-1-2/ Ed 1.0: Multicore and symmetrical pair/ quad cables for digital communications - Part 1-2: Electrical transmission characteristics and test methods of symmetrical pair/ quad cables

[10] IEC TR 61156-1-3. Multicore and symmetrical pair/quad cables for digital communications - Part 1-3: Electrical transmission parameters for modelling cable assemblies using symmetrical pair/quad cables

[11] IEC 63171 ED1. Connectors for Electrical and Electronic Equipment – Shielded or unshielded free and fixed connectors for balanced single-pair data transmission with current carrying capacity; General requirements and tests

[12] IEC 61935-2 ED4. Specification for the testing of balanced and coaxial information technology cabling - Part 2: Cords as specified in ISO/IEC 11801 and related standards

[13] IEC 61935-4 ED1. Specification for the testing of balanced and coaxial information technology cabling - Part 1: Installed balanced single pair cabling as specified in ISO/IEC 11801-1 and related standards

[14] IEC 62153-4-7 ED3. Metallic cables and other passive components test methods - Part 4-7: Electromagnetic compatibility (EMC) -Test method for measuring of transfer impedance ZT and screening attenuation a_S or coupling attenuation a_C of connectors and assemblies – Triaxial tube in tube method

[15] IEC 62153-4-14:2012 ED1. Metallic communication cable test methods - Part 4-14: Electromagnetic compatibility (EMC) - Coupling attenuation of cable assemblies (Field conditions) absorbing clamp method

[16] TIA-568.5 (2022) Commercial Building Telecommunications Cabling Standard Part 5: Single-Pair Cabling Components. Telecommunications Industry Association (TIA)

[17] Harshang Pandya. "Measuring shield integrity for twisted pair cabling systems" Proceedings of the 69th IWCS Cable & Connectivity Symposium. 2020

[18] Dave Hess. "The Shield is the Balun" Proceedings of the 70th IWCS Cable & Connectivity Symposium. 2021

[19] Dave Hess. "Shielded Pair Differential Cabling Phase Matters" Proceedings of the 71st IWCS Cable & Connectivity Symposium. 2022

9. Author



Dave Hess. dba CORD DATA. currently works as a subject matter expert facilitating international standards development for connectivity technology. particularly in the area of shielded pair differential cabling. He has worked for more than 40 years in both fields of electronic and photonic wired data communication connectivity and participates on the standards committees for physical interface and cabling standards: ISO. IEC. IEEE. INCITS. EIA. TIA. CTA. and ANSI.. He has been project leader for over 20 international standards. He received IEC 1906 awards for technical contributions in 2011 and 2014. He holds a B.S. degree in Mathematics from Pennsylvania State University and is a life member of IEEE.

.

Measuring and Simulating TCTL in Unbalanced Cable

Juliusz Poltz
OptEM Engineering Inc.
Calgary, Alberta, Canada
+1-403-289-0499, jpoltz@optem.com

Jonathan Silvano de Sousa
GG Group (Gebauer & Griller Kabelwerke GesmbH)
Muthgasse 36, 1190 Vienna, Austria
+43-1-360-20, j.silvanodesousa@gg-group.com

Abstract

Transverse Conversion Transmission Loss (TCTL) is defined as differential mode to common mode insertion loss measured at opposite ends of a cable. Since it is impossible to couple common and differential modes in an ideal symmetrical Shielded Twisted-Pair (STP) cable, TCTL represents a clear measure of cable unbalance. Asymmetry of the wire insulation, caused by different coloring of the two twisted wires, was frequently suspected as a cause for unbalance and related source of TCTL. However, individual testing of the wires did not demonstrate measurable differences. A commercial software tool was used to insert a small amount of uniformly distributed dielectric asymmetry (0.001% to 1% difference between the wires) in 100 Ohm STP cable. Then modes of propagation in the cable were investigated and it was demonstrated that even a very small uniform asymmetry deforms differential and common modes into quasi-differential and quasi-common propagation. Since cables with non-uniform dielectrics propagate modes with different speeds, the existence of TCTL and its known periodic behavior is explained using the asymmetrical modes. Subsequently, 10 m and 100 m sections of the unbalanced STP cables were simulated and TCTL was plotted. It is demonstrated that even 0.001% difference in the dielectric constant causes measurable levels of TCTL. The paper ends with results of a study of 10 m STP cable prototype in which only skins of the wires had small alterations. Simulation and measurements of TCTL produce similar results up to 4 GHz.

Keywords: SPE; STP; single-pair; twisted-pair; unbalance; differential mode; common mode; mode transfer; TCTL; LTCL; cable; cabling; model; screen; shield; insulation; electromagnetic analysis; simulation; software.

1. Introduction

Proper signal balancing is crucial in STP cables to maintain data integrity and minimize interference. Imbalances in the cable may cause conversion of common mode external noise into differential mode signals and become part of the Ethernet signals travelling along the cable. This can be detrimental to the signal transmission speed leading to latent bit errors and retransmissions. The measurement of Longitudinal Conversion Loss (LCL), Longitudinal Conversion Transmission Loss (LCTL), and their respective reciprocals Transverse Conversion Loss (TCL) and Transverse Conversion Transmission Loss (TCTL) play an important role in detecting cable asymmetry and unbalance [1].

Low levels of mode conversion are required in automotive applications to ensure high-speed communication systems such as Internet Protocol (IP) based Ethernet. Noise from engine components and electrical systems may cause data transmission distortions. A properly balanced cable with a minimized TCTL insertion loss, for example, provides enhanced noise immunity, reducing the risk of transmission errors and improving overall system performance [2]. This is particularly important in advanced driver-assistance systems (ADAS) and in-vehicle networks, where reliable data transfer is critical for safety and functionality.

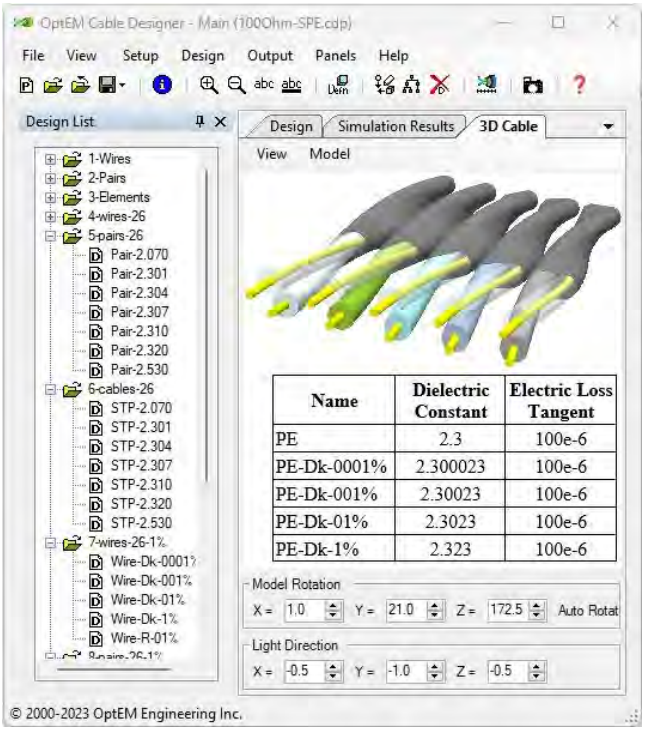


Figure 1. 100 Ohm 26 AWG STP symmetrical cable and its asymmetrical modifications caused by different Dk used in one of the wires (investigated Dk differences include: 0.001%, 0.01%, 0.1%, and 1%)

In fully automated driving designs, where all the decisions are made by artificial intelligence (AI) in all situations (and even at high speeds), data transmission must be in real time, i.e., nanoseconds latency, with the available sensors and actuators using communication signals in high frequencies (in gigahertz range). An automotive high-speed communication system must transfer the data safely and reliably [3-5].

Transverse Conversion Transmission Loss (TCTL) is defined as differential mode to common mode insertion loss measured at opposite ends of a cable. Since perfectly balanced screened twisted-pairs and parallel-pairs isolate differential and common mode propagation, TCTL represents a clear measure of cable unbalance. Even a small difference in capacitance of the signal wires (capacitive unbalance) leads to a rise of common mode propagation. The loss of energy of the differential signal to common mode not only reduces the immunity of the link but also its propagation quality, as the modes lose their symmetry and travel with different speed producing unpredictable frequency characteristics. Mode conversion can be measured using mixed mode S-parameters SCD12/SCD21. Since common mode currents increase almost linearly with intra pair delay skew there is strong motivation to correlate capacitive unbalance, intra pair skew and TCTL with dielectric asymmetry of the pair caused by impurities injected into wire insulation during the manufacturing process.

Automotive grade STP cables with small TCL and TCTL ratios ensure robust and interference-free communication between various electronic modules and sensors in the car. This, in turn, enhances the overall vehicle performance, safety, and passenger experience. Moreover, the geometrical symmetry of the cable is also very important for yielding low TCL and TCTL levels. In state-of-the-art high-data-rate cables, subtle differences on material properties and shielding may also result in data transmission distortions.

This paper uses state of the art simulation algorithms compared with measurements to open ways for the better understanding of the root cause of these effects and to propose solutions.

2. Impact of Cable Asymmetry on Unbalance

Although non-uniformities of the cable can vary along its length, only a uniform unbalance is investigated in this paper. There are some earlier publications comparing numerical simulation with measurement data [6,7]. Typically, they consider three main types of asymmetries, which may lead to unbalance of a pair:

1) geometrical asymmetry - represented by deformation or shift of conductor surface; we believe that pure geometrical asymmetry affects wire inductance (L) and capacitance (C) in an opposite way (when L is rising C is falling and vice versa),

2) conductance asymmetry – represented by a difference in conductivity of wires and parts of the screen, and affecting only cable resistance (R) and L,

3) dielectric asymmetry – represented by variations in dielectric constant, loss-tangent or asymmetry of wire insulation, affecting only cable C and conductance (G).

It is most likely that in practical applications a combination of the three cases influences the measurement results. However, we will concentrate on the impact of dielectric constant (Dk) on mode transfer. We will first illustrate the influence of Dk asymmetry on capacitance of wires and pairs of the investigated cables. We define capacitance Unbalance as the difference of capacitance of individual wires divided by average capacitance of both:

$$Unbalance = 2\frac{C_{11} - C_{22}}{C_{11} + C_{22}} \quad (1)$$

In Table 1 the asymmetry of Dk in the 100 Ohm 26 AWG STP cables (Fig.1) is mapped to Unbalance of capacitance calculated in (1). We can see that capacitance Unbalance is slightly smaller than dielectric asymmetry, which is justified by the fact that insulation material is only a portion of the dielectric filling the space under the screen (the other is air – that we model as free space).

Table 1. Capacitance simulated for the 100 Ohm 26 AWG cables with insulation Dk asymmetry.

Wires Dk Difference	Wire 1	Wire 2	Pair	Unbalance (capacitance)
	pF/m	pF/m	pF/m	%
0	91.553	91.553	49.185	0.0000%
0.001%	91.553	91.553	49.185	0.0009%
0.01%	91.561	91.553	49.187	0.0087%
0.1%	91.619	91.554	49.204	0.0710%
1%	92.329	91.576	49.403	0.8189%

Capacitance of individual wires in the investigated STP is almost 80% higher than pair capacitance (Table 1), indicating the crucial role played by the screen in pair capacitance.

From early measurement reports it was observed that extremely small changes of Dk may cause substantial TCTL levels. To investigate variations of C due to 6th-digit variation of Dk, it was important to make sure that the Boundary Element Method (BEM) solver used to calculate C generates exactly the same pattern of boundary elements in all the investigated cases. In the simulation, the 0.001% asymmetry of Dk generates the same values of C as the balance cable (unbalance 0) when viewed with the standard (5 digits of accuracy visible in Table 1) output report from the software. It is also clear that very small Dk variations may be difficult to detect even with the most precise measurement techniques.

3. Quasi-Common and Quasi-Differential Modes

A two-conductor symmetrical transmission line can propagate two independent TEM modes. These modes do not exchange energy along the cable length and can be considered as perfectly insulated from each other. However, if the line is non-symmetrical, these modes become non-symmetrically differential and common. To demonstrate the impact of capacitance Unbalance (1) we manually modified capacitance of the 100 Ohm 26 AWG STP from 0 (symmetrical line) to 0.3 (30% unbalance would be unacceptable for HF transmission – later we limit the investigation of TCTL to injecting no more than 1% Dk asymmetry ~1% Unbalance).

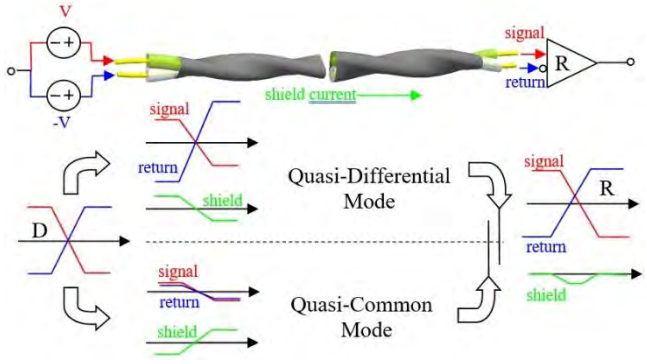


Figure 2. Quasi-Differential and Quasi-Common Modes which propagate with different speed in the unbalanced cable are responsible for TCTL.

Figure 2 shows symbolically the propagation of Quasi-Common and Quasi-Differential Modes. Unlike the ideal differential mode, the Quasi-Differential mode also relies on the current in the screen (marked green). Although we inject in our cable only a differential signal (left on Fig. 2), the transmission line propagates it as a combination of Quasi-Common and Quasi-Differential Modes. Because these modes have different attenuation and phase shift, the common mode shows up at the end of the line, although it was not injected at the start. The existence of Quasi-Common and Quasi-Differential Modes in uniformly asymmetrical STP cables is the real source of TCTL.

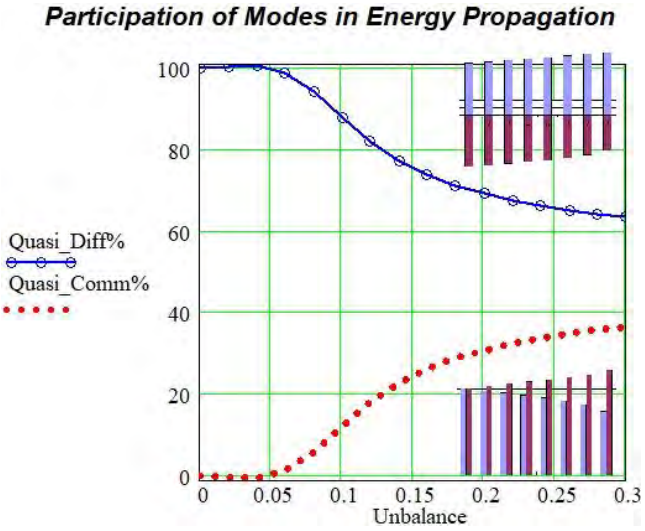


Figure 3. Participation of Quasi-Differential and Quasi-Common Modes in energy propagation along cable with injected capacitance Unbalance (1) at 1 GHz.

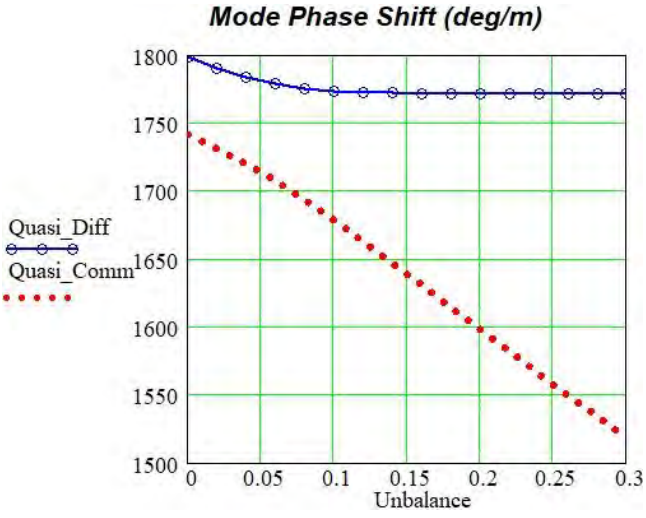


Figure 4. Phase shift [deg/m] for Quasi-Common and Quasi-Differential Modes at 1 GHz as a function of injected capacitance Unbalance (1).

The higher the non-symmetry of the cable, the more difficult it is to recognize the modes as Quasi-Common and Quasi-Differential. The right-top corner of Figure 3 demonstrates symbolic changes of Quasi-Differential Mode and the right-bottom corner of Figure 3 shows changes of Quasi-Common Mode as a function of rising unbalance. Figure 3 shows the split between energy transmitted by Quasi-Differential and Quasi-Common Modes on unbalanced transmission line powered by a pure differential signal. Only the symmetrical line (Unbalance=0) propagates a clean differential signal from the driver to the receiver.

Quasi-Common and Quasi-Differential Modes in an unbalanced transmission line are decoupled (orthogonal) and propagate without exchanging energy with each other. This can be achieved only if there is a balance between magnetic and electric energy in the line and this requires (in a non-symmetrical line) a non-symmetrical set of voltages and currents. The two natural Quasi-Common and Quasi-Differential Modes propagate with different speeds and are differently attenuated. It is very symptomatic that the dielectric asymmetry that is causing capacitance unbalance very quickly changes the phase shift difference between the Quasi-Common and Quasi-Differential Modes (Figure 4), contributing strongly to TCTL.

4. Modeling Unbalanced Pairs

OptEM Cable Designer software was used to design a 100 Ohm 26 AWG STP symmetrical cable and its asymmetrical modifications caused by different Dk in one of its wires. The model with characteristic impedance matching 100 Ohm at 1 GHz was optimized for the TCTL simulation, since the initial concern was about the impact of termination reflections on TCTL results.

Once the geometry of the 100 Ohm 26 AWG STP symmetrical cable was verified, a set of wires with Dk modifications was specified using an Excel spreadsheet (A in Figure 5). The spreadsheet was then imported to software (B) which was used to set 3d models of unbalanced cables (C). The cables were then simulated with a built-in Maxwell-equations solver which calculates current and charge distribution using a combination of Finite Element Method (FEM) and Boundary Element Method (BEM), and subsequently the mixed mode S-parameters were generated and TCTL plotted (D).

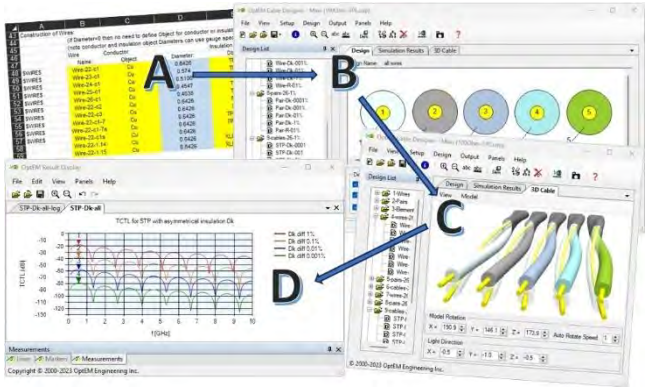


Figure 5. Cable simulation software reads spreadsheet (A), interprets the designs and wires (B), creates models of unbalanced cables (C) and simulates them to plot TCTL results (D).

The software model of the 100 Ohm 26 AWG STP symmetrical cable used solid polyethylene (PE) insulation with dielectric constant (Dk) of 2.3 and electric loss tangent (Lt) of 0.0001. Insulation OD of 1.291mm was optimized to ensure 100 Ohm performance at 1 GHz. The balanced and unbalanced pairs had lay length of 40 mm and were then enclosed in uniform 20 μm Al screens. This section will report only on the designs of the 100 Ohm 26 AWG STP symmetrical cable seen in Figure 1.

The software divides bulky conductors into finite elements, whereas ground and power planes are modeled as multilayer boundaries. The simulation of electromagnetic performance of the cables includes skin and proximity effects in wires, eddy currents in cable shields, and dielectric losses in the insulation layers. Since the unbalance was introduced by extremely small deviations of insulation Dk (0.001% to 1%) it was vitally important to force the solver to use the same finite and boundary element distribution for modeling all samples.

Modifications to the software allowed direct output of the complex eigenvalues and eigenvectors responsible for generation of quasi-differential and quasi-common modes of propagation.

5. Simulation of TCTL in Unbalanced Pairs

The software provides an option to simulate TCTL parameters defined as a measure of mode conversion within a pair at the opposite end of the cable. TCTL is simulated by injecting a differential mode signal into the pair and measuring any common mode signal at the other end of the link. As discussed in sections 2 and 3 above, cable asymmetry (in our case caused by difference of insulation Dk between wire 1 and wire 2) is causing capacitance unbalance, which prevents ideal differential and common mode to propagate. Instead, the cable propagates quasi-differential and quasi-common modes. Since these modes have different attenuation and phase shift characteristics, the received signal contains a common-mode component even if only differential signal was sent. It is generally accepted that TCTL is a measure of cable net unbalance which is caused by geometrical or material asymmetry of the cable. When simulating the symmetrical (balanced) model of the cable, TCTL shows levels of -200 dB, which is equivalent to receiving a signal that represents numerical error of the simulation. The simulation error is caused by numerical precision of the model building and simulation accuracy.

The usual cause of cable asymmetry is insulation skin coloring. To experiment with the model of the 100 Ohm 26 AWG STP we changed the Dk of the entire insulation of one of the wires from original 2.3 by 0.001% to 1% (see Figure 1 for details).

The results of the simulation of TCTL are shown in Figures 6 and 7. Initially, we simulated a 100m section of the cable from 1 MHz to 1 GHz. The results show TCTL rise by 20 dB each time the asymmetry of skin Dk grows by a factor of 10. Even the very small unbalance produced by 0.001% asymmetry of Dk (2.300000 vs. 2.300023) generates visible TCTL of -91 dB (Fig.6. marker 4). The relationship between Dk asymmetry and TCTL levels may be very useful for designers who should be aware that an increase of Dk by 0.1% may already violate standardized TCTL level limits. The remaining issue would be to link the variation of the TCTL levels with the allowable amounts of the die, which should be considered mixed uniformly with the insulation by a certain ratio and affecting the Dk of the mixture by its own Dk. It should be remembered that Dk of conductive material should be considered as infinity. Of course, the smaller the TCTL is, the smaller the transfer of energy from the differential to common mode signal and resulting interference to/from our cable. The simulation results demonstrate that the better the symmetry of the cable, the better is the balance and smaller TCTL of the cable. Because the influence of common mode signal transfer is dependent on the value of attenuated differential signal due to insertion loss, equalization should be applied to take it into account. Although equalization is not shown in this report, the software can apply the IL results to TCTL to plot ELTCTL (Equal Level TCTL).

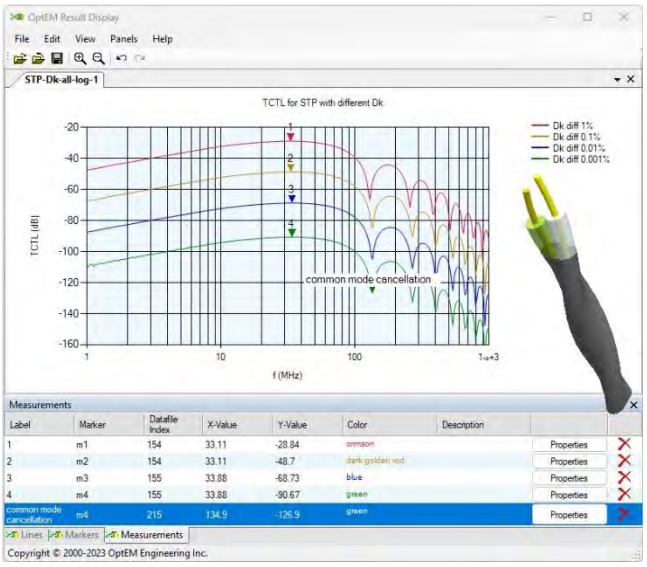


Figure 6. TCTL simulation results for 100 m cable with injected asymmetry.

The frequency of the first dip in TCTL level, marked as "common mode cancellation" in Figure 6 (135 MHz), is inversely proportional to the value of cable length and the difference in propagation speed of the natural modes propagating on the cable (neither of which is purely differential nor common). One can estimate the "mode cancellation" frequency by considering the quasi-modes phase shift difference and the cable length. At the point of "mode cancellation" phases of the quasi-modes differ by 360 deg repeating the modal balance from the start of the line (where they cancel each other's common parts). The values of unbalance and modal propagation speeds, as well as modes configuration in currents and voltages, are all provided by the software in a special report.

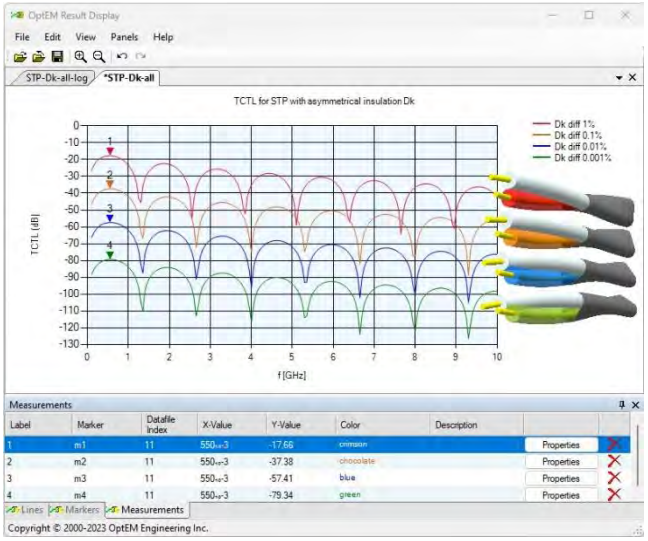


Figure 7. Same Dk asymmetry (as in Figure 6) produces much stronger TCTL in shorter cables, seen here in 10m sample simulated up to 10 GHz.

In linear scale of frequency (Fig.7), the distance between the bumps in frequency domain marks the repetitive nature of the modal cancellation. The existence of these bumps cannot be contributed

to reflections from 100 Ohm terminations, since the cable was designed to match them above 100 MHz. Also observed was that up to 15% termination mismatch has very little effect on simulated levels of TCTL. We believe that the repetitive nature of TCTL plots is sufficient proof of the existence of quasi-differential and quasi-common modes both of which deliver quantities of common mode energy with different speed and attenuation to the receiver.

The damaging effect of the common mode transfer is especially visible in higher frequencies and smaller links of the cable (as seen in Figure 7). Although the bumps on the TCTL plots are shrinking for plots in log scale (Figure 6), they are very regular when viewed in linear scale of frequency (see Figure 7). By reducing cable length (100 m in Figure 6 to 10 m in Figure 7) one proportionally increases the frequency span between subsequent bumps. Subsequent dips in TCTL plots are separated by frequency intervals equal to the "common mode cancellation" frequency, which is marked as 135 MHz in Figure 6, and is equal to 1.35 GHz in Figure 7.

6. Measuring TCTL

The investigation of the TCTL plot features was motivated by experiments conducted on Single-pair Ethernet (SPE) cable samples designed for use in future automotive applications. Ten-meter-long cable samples were investigated using a Vector Network Analyzer (VNA) as depicted in Figure 8. The cable measurement was set up according to the IEC TR 61156-1-2 [8]. The transfer of push-pull signal fed in at the beginning of the line to the common-mode signal at both ends of the line was measured in the frequency domain. The differential pair of the cable was connected to the VNA ports (1) and (2). Test fixtures to connect the cables and the measurement equipment were specifically designed to smooth transition between the SPE cable and VNA coax cables. We measured the reflected common-mode component of the differential signal which is the Transverse Conversion Loss (TCL) (in mixed mode S-parameters: SCD11) and the transmitted common-mode component of the differential signal which is the TCTL. Then we selected a screened parallel pair to be modeled. The measured (dark blue) mixed mode S-parameters SCD12 (TCTL) were compared to simulation results in Figure 10.

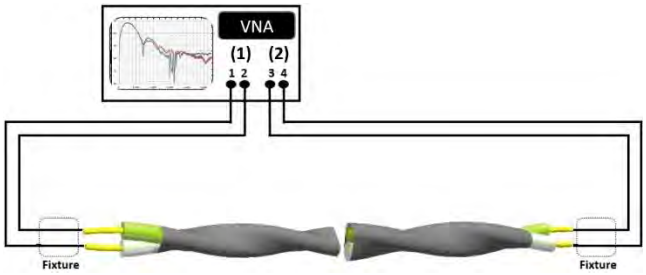


Figure 8. Parallel and twisted pairs were tested. The cable measurement was set up according to the LV213-2 [1].

A model of the cable foam/skin insulation was set up in the simulation software. Only the skin of the wire insulation was modeled with asymmetric Dk. Since results of numerical simulations cannot be more accurate than the geometrical models representing the cable, it is essential to adjust the elasticity of the screen to resemble the measured sample of the cable as accurately as possible (see oval shape of the screen in Figure 9).

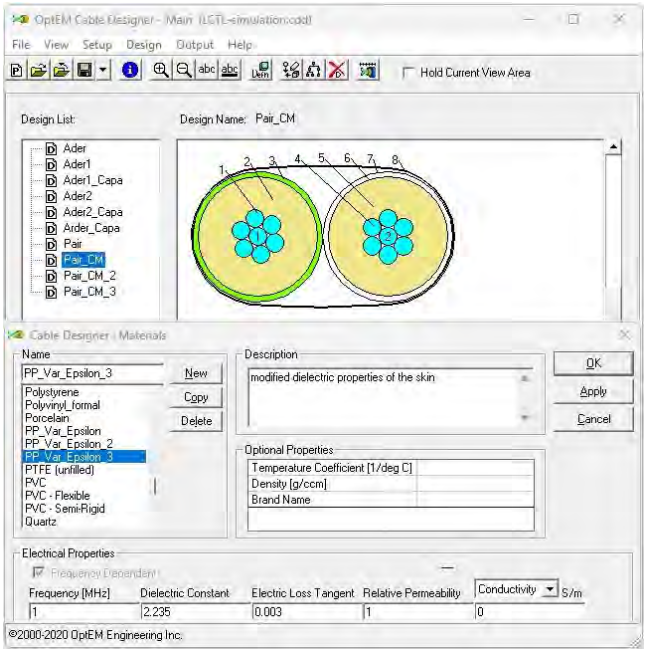


Figure 9. Screened parallel pair with intentional dielectric unbalance modeled in the simulation software for calculating and plotting mixed mode S-parameters SCD12/SCD21 (TCTL).

Similar to the numerical example described in points 4 and 5 above, the asymmetry of wires due to their skin Dk differences caused degradation of natural differential and common modes of TEM propagation on the pair into quasi-differential and quasi-common modes. This effect was investigated using the simulation software and was reported in earlier work [6], although without reference to TCTL. Using a circuit definition module differential and common mode conditions can be defined at cable ends simulating, in effect, mixed mode S-parameters SCD12/SCD21.

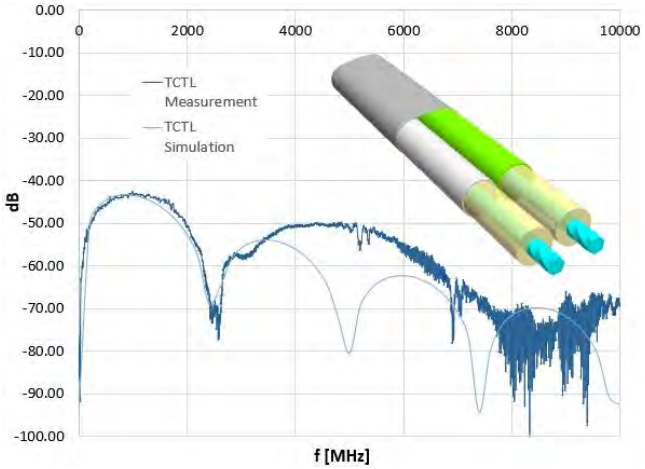


Figure 10. Comparison of TCTL simulation (light blue curve) with measured (dark blue) mixed mode S-parameters SCD12/SCD21 (TCTL) for investigated unbalanced pair.

The simulation results are presented in Figure 10 (light blue curve) together with the measured results (dark blue). The simulation results were confirmed in a frequency range up to 4 GHz by measurements (Figure 10). Above this frequency some additional

tolerances of the cable sample, which are not included in the simulation, play a significant role in shaping the TCTL measurement curve. From simulation we observed that the termination mismatch could not be considered a source of the discrepancy. Most likely, other non-uniformities in the cable along its length are the reason for the measurement data lacking the periodic nature of the simulated TCTL plot.

7. Ethernet Standardization

As industrial Single Pair Ethernet (SPE) and automotive Shielded Twisted Pairs (STP) Ethernet applications move to higher data rates, signal integrity in the link has an increased relevance. The IEEE defines Gigabit Ethernet over a single twisted pair for automotive and industrial applications named 1000BASE-T1 in the in the IEEE802.3bp-2016 release. This standard includes cable specifications for 15 meters (type A) or 40 meters (type B) reach in automotive and industrial applications. The transmission is done using PAM-3 at 750 MBd [10, 11]. Higher speed grades of Ethernet over twisted pair, 2.5 up to 10 GB/s, 2.5GBASE-T1, 5GBASE-T1 and 10GBASE-T1, respectively, have been defined subsequently within the IEEE 802.3ch-2020. Such a system is designed to run over a single twisted pair up to 15 meters in length and use PAM8 modulation (compared to PAM3 modulation in 1000BASE-T1 or PAM-16 + 128DSQ in 2.5GBASE-T/5GBASE-T) [12, 13].

Open Alliance's [14] Technical Committee (TC)9 has the goal to specify electrical requirements and test procedures for channel and components in conformance to the link segment requirements of IEEE 802.3 automotive Ethernet standards at various speed grades [15]. The scope of the document includes specifications on the communication channel; connectors, cables, cable assemblies and wiring harnesses, measurement setup and procedures; electrical requirements and EMC environment. The current Open Alliance TC9 documentation aims to provide electrical requirements and measurement specifications on fully shielded 1000BASE-T1, 2.5GBASE-T1, 5GBASE-T1 and 10GBASE-T1 channels and components. It shall be used as a standardized common scale for the evaluation of the RF properties for physical layer communication channels to enable Multi-Gigabit Ethernet technology in automotive ethernet data transmission. Common mode limits for signal integrity are also included in this document with direct specifications for cables. The TC9 Multigigabit Document specifies max levels of TCTL as low as -20dB for frequencies up to 4GHz in all state-of-the-art speed grades cables.

8. Conclusions

Simulating and measuring TCTL in cables lead us to the following conclusions:

- Any conductor asymmetry in SPE cable results in unbalance of unit circuit parameters (LRCG) of the cable,
- Unbalanced transmission lines propagate two natural modes which are not exactly differential and common but mixed: one with a dominant differential component (Quasi-Differential) and the other with a dominant common mode (Quasi-Common),
- Pure differential signal of the source is forced to propagate along unbalanced cable as a combination of the natural (skewed) modes in the pair,
- Dielectric asymmetry causes substantial phase-shift difference between Quasi-Differential and Quasi-Common Modes which leads to the rise of TCTL,
- The repetitive nature of TCTL plots confirm the existence of quasi-differential and quasi-common modes both of which deliver quantities of common mode energy with different speed and attenuation to the receiver,
- One can estimate the frequency intervals which separate bumps on TCTL plots by considering quasi-modes phase shift difference and cable length,
- By reducing cable length, one proportionally increases the frequency intervals between subsequent bumps of TCTL plots,
- The damaging effect of the common mode transfer is especially visible in higher frequencies and smaller links of the cable,
- The small difference in Dk may be introduced through a coloring agent used in the pair.
- Although the amount of the die may be so small that the Dk difference cannot be measured through capacitance check, its effect is clearly visible in TCTL.
- Theoretical observations were confirmed by measurement,
- In practice, the material and geometrical parameters change along the length of the cable and cause additional secondary effects. Some of them are visible in measured characteristics and manifest themselves in the vague and unpredictable nature of the plot above 3 GHz.
- Moreover, subtle deviations in the cable's properties that can be related to essential steps in the manufacture process can be quantized using simulation methods. This work provides a better understanding of the mechanisms causing unbalance phenomena in data cables beyond geometrical asymmetries. This allows mode conversion engineering and control during cable design, development, and manufacture, which will result in the development of strategies to address future industry mode conversion requirements. More on this topic will be presented in future publications.

9. Acknowledgments

Special thanks to Ms. Joan Beckett for helping with the manuscript and simulation.

10. References

[1] DiBiaso, E., Bergner, B., Wuelfing, J., Wuerker, R. et al., "Designing a Connection System for Gigabit Automotive Ethernet," SAE Int. J. Passeng. Cars – Electron. Electr. Syst. 9(1):134-146, 2016, https://doi.org/10.4271/2016-01-0078,

[2] M. Maki, S. Hamada, M. Tokuda, Y. Shimoshio and H. Koga, "Immunity of communications systems using a balanced cable," 2001 IEEE EMC International Symposium. Symposium Record. International Symposium on Electromagnetic Compatibility (Cat. No.01CH37161), Montreal, QC, Canada, 2001, pp. 37-42 vol.1,

[3] S. Mortazavi, D. Schleicher, A. Stieler, A. Sinai, F. Gerfers and M. Hampe, "EMC Analysis of Shielded Twisted Pair and Shielded Parallel Pair Transmission Lines for Automotive Multi-Gig Ethernet," 2019 IEEE International Symposium on Electromagnetic Compatibility, Signal & Power Integrity (EMC+SIPI), New Orleans, LA, USA, 2019, pp. 193-198,

[4] Lo Bello, Lucia & Patti, Gaetano & Leonardi, Luca. (2023). A Perspective on Ethernet in Automotive Communications—

Current Status and Future Trends. Applied Sciences. 13. 1278. 10.3390/app13031278,

[5] Matheus, Kirsten & Königseder, Thomas. (2017). Automotive Ethernet. 10.1017/9781316869543,

[6] J. Poltz, J. Beckett and M. Josefsson, "Measurement and Simulation of Differential Skew in Twisted Pair Cables," Proceedings of the 55th International Wire and Cable Symposium, Providence, RI, Nov. 12-15, 2006, pp. 141-146 (2006),

[7] Y. Li, F. He, O. Gassab and W.-Y. Yin, "High-Speed Transmission Cable Performance-Simulations and Measurements," Proceedings of the International Conference on Numerical Electromagnetic and Multiphysics Modeling and Optimization, IEEE MTT-S (2020),

[8] IEC TR 61156-1-2: Multicore and symmetrical pair/quad cables for digital communications – Part 1-2: Electrical transmission characteristics and test methods of Symmetrical pair/quad cables.

[9] Rhode & Schwarz ZNB8 and ZNB20.

[10] https://en.wikipedia.org/wiki/Gigabit_Ethernet. (2023,08,18)

[11] https://www.ieee802.org/3/bp/

[12] https://www.ieee802.org/3/ch/

[13] https://en.wikipedia.org/wiki/2.5GBASE-T_and_5GBASE-T. (2023, 08)

[14] https://opensig.org/

[15] https://www.opensig.org/tech-committees/tc9/

11. Authors



Juliusz Poltz holds M.Sc. and Ph.D. degrees in both mathematics and electrical engineering from Universities in Poznan, Poland. He works in Canada since 1989, where he has published over 80 technical papers related to EM field analysis and numerical simulation of copper cables. In 1992, Dr. Poltz co-founded OptEM Engineering Inc. in Calgary, Alberta. OptEM is a software company specializing in EM analysis and circuit simulation.



Jonathan Silvano de Sousa holds a PhD in Physics by the Vienna University of Technology. He currently works as Senior Cable Technology Specialist at GG-Group. He has experiences in the microelectronics industry in fields such as semiconductors, MEMS, and PCBs. During his career he participated in many conferences and published several science and industry related papers. He holds over 70 published patents. Since 2019 he is active by GG in the automotive harness and cable industry supporting product and technology development.

Power over Communication Cables for extended distance: myths and misconceptions

Amir Sekhavat[1], Jason Finnegan[2]

[1]Superior Essex International LP – Communications
Atlanta, Georgia
+1-770-657-6692 · amir.sekhavat@spsx.com
[2]Legrand, North America
New London, Connecticut
+1- 203-910-2600 · Jason.Finnegan@legrand.com

Abstract

Power over Ethernet (PoE) is a technique that delivers electric power along with data over copper twisted-pair cables to remote devices in an Ethernet network, eliminating the need for separate power supplies and outlets, while enhancing flexibility and innovation, reducing costs, and cutting installation time. However, concerns have emerged about the temperature rise of PoE cables causing system failures, safety hazards, reduced cable performance, and shortened lifespans. As we witness the emergence of cable runs for applications beyond TIA's 100m limit, these concerns become amplified.

For these reasons, it has been a controversial topic of discussion over the years. But is the controversy founded and justified? Or is it based on myths and misconceptions, especially with extended distance applications beyond 100m and field testing?

This presentation will review the common myths and misconceptions of high power PoE systems and extended distances. In addition, Superior Essex and Legrand put in place test methodologies to assess the parameters, and to test the real impact on channel distance by understanding different factors such as heat, power transmission, quality of data transmission, and channel configurations on the overall performance of the system. These tests were then performed by independent third party Nationally Recognized Test Labs (NRTL) and internal laboratories to collect data.

Our results will show the real impact and what should be considered as fact and not myths.

Keywords: Power Over ethernet, PoE, Power Efficiency, Category Cables, Ageing, Standards, Data transmission, Power transmission, Powered Device, PSE, Bit Error Rate, channel length, extended distance.

1. Introduction

Power over Ethernet (PoE) is a technology that passes electric power over twisted-pair Ethernet cable to powered devices (PD), such as wireless access points, IP cameras, and VoIP phones, in addition to the data that cable usually carries. It enables one RJ45 cable to provide both data connection and electric power to PDs instead of having a separate cable for each.

This technology has been standardized for decades under the IEEE 802.3 standards as shown in Table 1. From the first version published in 2003, to the latest published in 2018, the power transmission from the source has increased to up to 100W to allow more applications and devices to utilize PoE. We can currently power and control not only IP phones, but also lights, shades, security cameras, monitors, laptops, refrigerators, and countless other devices … Besides IEEE, other standards like ANSI/TIA-568 D defined the requirements for data transmission and component characteristics. Meanwhile, Category 6A cabling and new protocols like 2.5, 5 or 10GBASE-T were also introduced and available.

Table 1. **Summary of IEEE 802.3 evolution**

PoE Standard	PoE Common Name	Power Output	Year
IEEE 802.3af	PoE Common Name	15.40 W	2003
IEEE 802.3at	PoE+, PoE Type 2	30 W	2009
IEEE 802.3bt Type 3	4PPoE, UPoE	60 W	2018
IEEE 802.3bt Type 4	4 PPoE, PoE++	100 W	2018

In 2017, PoE was fully ratified into the NFPA /NEC code. Finally, the emergence of smart building and extended distance applications confirm the increased interest and use of PoE devices, especially for Type 3 and Type 4.

Up to 100m, the above-mentioned standards and codes covered all existing configurations and use cases of PoE for its applications.

With the rise of IEEE Type 3 and 4 PoE, new concerns were raised like power efficiency, impact of heat increase on data transmission, bundling, material ageing or supported distance. Some of these have been addressed by different studies. Connected lighting systems efficiency study part 1 & 2 reports from the U.S. Department of Energy [1] measured the PoE cable

energy losses and showed mainly the impact of the gauge size and category cable design. Technical report “four pair power over ethernet deployment: standards, performance and challenges” [2] covered other concerns like operating costs and lifetime expectations. Another report: “investigation of thermal aging challenges for power-over-ethernet cables with polyvinyl chloride jackets” [3] covers the safety aspect and the impact of heat on the materials and the electrical performances. Limited Power listing from UL (with the study and the burn tests which based on) [4], NEC NFPA Ampacity Table 725.144 [5] or ANSI/TIA offers tables covering the bundling challenges.

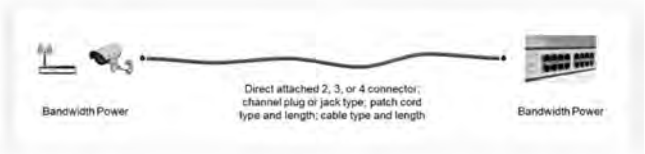
2. Myths and misconceptions over extended distance applications

To support extended distance applications (beyond 100m), there are different methods available on the market, for example: introduction of a local power source combined with communication cables, a local power source combined with WIFI, hybrid cables (FO and Copper conductors under same jacket) with electronic transceiver and receivers, extender switches, FO cables with media converters, and POE over twisted pair copper cable. Each of these have their pros and cons regarding the total cost of implementation of the design, the material, the power, the labor, and the maintenance as shown by CCCA article [6].

Each of these technologies will also support different distances of deployments, limited by the power and/or data transmission.

Per the article, PoE, the most cost-effective solution, has a proven track record of success and presents a growing market. However, current standards only address systems up to 100m in length. With the growing number of applications being introduced to the market, the need to extend the cabling system beyond 100m has become prevalent. Without any standards, each installation (as shown in figure 1) is unique and should be considered as such unique.

Figure 1. typical PoE installation

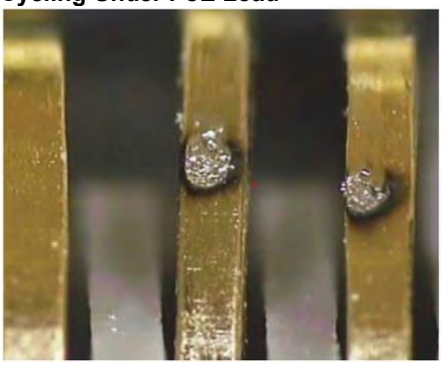


Each component will have its impact on the supported distance. Each powered device (PD) will have specific requirements for bandwidth and power. A device requiring less bandwidth and/or lower power may work perfectly at even longer distances, for example, we defined distances at 1GBase-T, but many cameras require less than 100Mbps. Also, the source will also have its own requirements for providing power, an IP address, and data for each port. A common misconception is to focus only on the network topology to determine if an application will work or not, when in fact any one of the components in the system may be the culprit. For example, a low quality chipset in certain cameras may not register the link, while another camera model drawing even more power and data will work just fine – even at longer distances.

Finally, the passive structured cabling network topology used has the most impact on the supported distance, and the specific loss introduced is highly dependent on the system configuration (permanent link with 2 plugs, modular plug terminated link (MPTL) or channel with one or 2 connectors) and on the quality of each component used. Every passive component in a system will contribute to the overall loss of the system. In other words, the structured cabling system is only as strong as its weakest link. The more components that are added, the more impact each of them will have on the data and power transmission.

- Patch cord considerations include wire gauge (AWG), length, and whether its built using stranded or solid copper.
- Cable design considerations include wire gauge (AWG), length, pulling / install, and design).
-RJ45 jack and plug consideration includes: the quality/shape of the contacts (as shown on Figure 2) and handling of electrical arcing, PCB design [7], and the termination. The level of workmanship will also have its own impact on the data transmission.

Figure 2. Arcing Damage to RJ45 Jack Contacts After Cycling Under PoE Load



Any changes to the future of any components could result in a failure of the PoE application.

The impact of temperature increase due to usage of higher PoE types in extended distance systems will be more important on data transmission due to heat’s impact on attenuation, but there are no studies so far that prove and measure this.

Another common myth is the linkage of distance with the category type. In fact, what is true under 100m is not valid at distances beyond. A category 6A cable with very tight twist lays will not support longer distance over 100m compared to lower category cable design. Over 100m, the eligibility of the signal at the end point is critical, and the tightness of the twist lay determinates the real distance that a signal has to travel through the cable. If you add the impact of heat on data transmission which increased the insertion loss of your cable, you’ll find an environment where its not possible to provide any general distance claim based solely on the category of cabling used.

Another myth is that a system can be validated solely with a field test device, especially as most field testers are not capable of testing data with permanent power load and are based on proprietary data limit extrapolation where there is no standard. Laboratory devices are still the most accurate way to measure the quality of a signal.

In fact, delay skew (which measures the difference in propagation delay between the fastest and slowest pair in a cable) and propagation delay (which measures the amount of time required for a signal to be received after it has been sent) become the most critical electrical characteristics beyond 100m.

Concerning the power efficiency, as stated in the introduction, lots of studies showed that the distance is linked to the gauge of the horizontal cable used. A 22AWG cable will provide better efficiency and longer distances than 23 or 24 gauge. Other studies show that the higher the gauge, the lower the temperature increase inside the cable or inside the bundle will be. The same studies show that a shield used in some cable designs will also help with heat mitigation.

Knowing all that, providing general future proof claims without giving specific details will only create confusion.
The purpose of the test methodologies put in place in this study by Superior Essex and Legrand is to assess the real test parameters and the real impact on the extended distance caused by different factors, such as: heat, power transmission, quality of data transmission, and channel configurations. We decided to perform these tests in a third-party laboratory (UL solutions at Melville) in order to test the signal with permanent power transmission to simulate real world installations.

3. Methodology

To support extended distance applications, beyond all methods available, Superior Essex and Legrand decided to use Bit Error Rate models for 128-DSQ modulation to measure the electrical parameters. The requirement at least 10^-12 must be achieved to check if a signal was considered as pass or fail when read by the receiver. The equipment used by UL laboratory was Spirent SPT N4U as shown in figure 3.

Figure 3. BER laboratory device



We tested different network topologies using bit-error rate (BER) equipment to cover the most common field installations:

Permanent link with plugs (direct connect)



One connector channel or MPTL



Two connector channel



For the last 2 configurations, solid conductor 22AWG versus stranded conductor 24AWG cords were tested to determine the impact of the type of cord on the total channel distance. Max cord length tested was 25ft (7.62m).

Based on all previous studies available, we focused our tests on a 22AWG unshielded cable with optimized twist lay for 1 to 5 GBASE-T applications, which covers today's primary market applications.

For each configuration, the tests began at 160m under ambient temperature to simulate a Type 2 PoE application, and 140m to simulate a Type 4 PoE application. Patch cords ranging from 3ft to 25ft were used during testing. In the event that the channel didn't adequately transmit the data packets in full, the horizontal cable was shortened and re-tested to comply with the target BER limit until we had a complete pass.

For heat concerns, the test was performed in a heat chamber at LP temperature of the cable used to simulate Type 4 PoE along with the data transmission. The cable was disposed on a reel to simulate a field installation following best practices, and to ensure heat was applied consistently along the cable as shown in figure 4.

Figure 4. cable installation in the chamber



With this methodology, we could cover main field installation approaches and market needs.

Our goal was to test how far a pure 1, 2.5 or 5 GBase-T signals provided by a legitimate laboratory source according IEEE requirements under simulated power transmission can be delivered. This approach provides the confidence that systems will adequately perform any device using the afore mentioned data rates at the designated distance.

4. Tests results

The results for permanent link with plugs (direct connect) measured at UL Melville third party laboratory are presented in Table 2

Table 2. Summary of Permanent link with plugs

		PowerWise® 1G	
PL Application	Transmission/ Standard	BER @ Ambient[1] (Type 1 & 2)	BER @ LP[2] (Type 3 & 4)
Data & Power (Bandwidth & Speed)	Max Distance @ 1 Gb/s	160 m	140 m
Data & Power (Bandwidth & Speed)	Max Distance @ 2.5 Gb/s	160 m	140 m
Data & Power (Bandwidth & Speed)	Max Distance @ 5 Gb/s	160 m	135 m

The results for one connector channel (or MPTL) measured at UL Melville third party laboratory are presented in Table 3

Table 3. Summary of one connector channel

	PowerWise® 1G BER @ Ambient[1] (Type 1 & 2)			
Transmission / Standard	One Connector Channel	Horizontal Cable	Stranded Patch Cord[3,6]	Solid Patch Cord[5,6]
Max Distance @ 1 Gbps	160 m	152 m	8 m	8 m
Max Distance @ 2.5 Gbps	160 m	152 m	8 m	8 m
Max Distance @ 5 Gbps	160 m	152 m	8 m	8 m

	PowerWise® 1G BER @ LP[2] (Type 3 & 4)			
Transmission / Standard	One Connector Channel	Horizontal Cable	Stranded Patch Cord[3,6]	Solid Patch Cord[5,6]
Max Distance @ 1 Gbps	140 m	132 m	8 m	8 m
Max Distance @ 2.5 Gbps	140 m	132 m	8 m	8 m
Max Distance @ 5 Gbps	135 m	127 m	8 m	8 m

The results for two connectors channel measured at UL Melville third party laboratory are presented in Table 4

Table 4. Summary of two connectors channel

	PowerWise® 1G BER @ Ambient[1] (Type 1 & 2)			
Transmission / Standard	Two Connector Channel[6]	Horizontal Cable	Stranded Patch Cord[3,6]	Solid Patch Cord[5,6]
Max Distance @ 1 Gbps	160 m	154 m	6 m (qty 2 x 3 m)	6 m (qty 2 x 3 m)
Max Distance @ 2.5 Gbps	156 m	150 m	6 m (qty 2 x 3 m)	6 m (qty 2 x 3 m)
Max Distance @ 5 Gbps	135 m with stranded patch cords	129 m	6 m (qty 2 x 3 m)	–
	145 m with solid patch cords	135 m	–	10 m (qty 2 x 5 m)

	PowerWise® 1G BER @ LP[2] (Type 3 & 4)			
Transmission / Standard	Two Connector Channel[6]	Horizontal Cable	Stranded Patch Cord[3,6]	Solid Patch Cord[5,6]
Max Distance @ 1 Gbps	140 m with stranded patch cords	128 m	12 m (qty 2 x 6 m)	–
	140 m with solid patch cords	124 m	–	16 m (qty 2 x 8 m)
Max Distance @ 2.5 Gbps	140 m with stranded patch cords	128 m	12 m (qty 2 x 6 m)	–
	140 m with solid patch cords	124 m	–	16 m (qty 2 x 8 m)
Max Distance @ 5 Gbps	130 m with stranded patch cords	124 m	6 m (qty 2 x 3 m)	–
	130 m with solid patch cords	120 m	–	10 m (qty 2 x 5 m)

5. Conclusions

The test results at UL laboratories based on our methodology proved that the heat generated by the different types of PoE signal will significantly impact the extended distance supported up to 20m less. We also determined that there was no difference in distance between 1Gbps and 2.5Gbps protocols at ambient temperature - only 5 Gpbs showed reduced distances. As soon as you introduce 2 connectors channel, you notice more significant differences in the maximum allowance of horizontal cable and patch cords between different protocols.

Through this study we were able to define the distances that the passive network topology will support, with the assumption that the power source equipment (PSE) is fully compliant to IEEE PoE requirements, and the powered devices (PDs) comply too.

22AWG unshielded (UTP) cable was chosen for these studies per the results of different published studies. We were able to define and prove longer distances than previously documented. For this reason, we determined any claims with tighter twist lays' in the cable design or lower gauge size will show shorter distances in same environment.

This study proves that each install from PD to source is unique, and any future change to any components could fail the PoE application.

We were able to prove that all the myths used in the market create confusion. Making general claims about PoE extended distance without giving details on the components used will create negative field experiences and add to the confusion of not having standards. Especially because none of the field test devices currently on the market can confirm a pass with power transmission. This study is a beginning to understand all the variables of extended distance, and an attempt to find the characteristics and methods to use to work to establish a standard.

We are considering adding to the study other variables that could impact the signal, like usage of surge arrestor boxes, or the quality of the electronics used in the powered devices, allowing them to work correctly at distances longer than 100m.

6. Acknowledgments

The authors would like to thank Rodney Kron, Solomon Girma, Martina Upton, Ken Cupples, Rob Aekins and Dylan Petruskevicius for their help at Superior Essex and Legrand. We would like also to thank Robert Bellassai, Anthony Tassone, Jerry Matiatos and Michael Askin for all the BER tests perform by UL solutions at their Melville laboratory.

7. References

[1] U.S. Department of Energy, "Connected Lighting Systems Efficiency Study – PoE Cable Energy Losses part 1 & 2", 2017 & 2018.

[2] T. Lanoe, C. McNutt and A. Sekhavat, "Four Pair Power over Ethernet (4PPoE) Deployment: Standards, Performance, and Challenges," in Proceedings of the 66th International Wire & Cable Symposium, Orlando, 2017

[3] B. Xu, C. McNutt, B. Gebs and A. Sekhavat, "Investigation of Thermal Aging Challenges for Power-over-Ethernet Cables with Polyvinyl Chloride Jackets," in Proceedings of the 71st International Wire & Cable Symposium, Providence, 2022.

[4] Antony Tassone, "Fact-finding study on Powering Over Data Cables", UL Solutions, 2016

[5] NFPA NEC 2017 code

[6] CCCA's New Technology & Trends Committee, "Going the distance: what you need to know about breaking the 100-meter distance limitation", article CCCA, 2022

[7] Aekins, Robert CE/BSc., RCDD, "PoE Cabling Loss: An Overview of Connectivity Contribution to POE and Cabling Losses", Legrand, 2022

8. Authors

Superior Essex International LP – Communications

5770 Powers Ferry Rd NW, Suite 400
Atlanta, Georgia 30327



Amir Sekhavat is Global Director of Product Management and Enterprise Market Development at Superior Essex. Amir has twenty years of experience in the telecommunications industry, specializing in communications cable products. Amir has published numerous articles and is listed as the inventor or co-inventor of several patents related to data cable performance and connectivity. Amir is currently chairman of CCCA sustainability and new technology trends subcommittees. He is also board member at Poe Consortium

Legrand North America

125 Eugene O'Neil Drive
New London, Connecticut 06320



Jason Finnegan is the Senior Product Manager for Copper Connectivity and Physical Support products at Legrand. He's been at Legrand for 13 years, holding various roles in Product Strategy, Product Development, and Marketing. He's been the Connectivity Product Manager for the past 5 Years, where he focuses on research and development, strategic market development and thought leadership. Jason has spoken about the emerging smart building and edge infrastructure at numerous industry events, and published articles about the Internet of Things and structured cabling network considerations in publications including Cabling Installation & Maintenance magazine and Mission Critical magazine.

SESSION 11

Sponsored by:



Click on a session below to navigate to that section of the Proceedings.

SESSION11: CABLE MATERIALS & PROPERTIES

Chairperson: Thomas Schelling, J.M. Huber Corporation, USA

11-1 **New Advancement in Polyvinylidene Fluoride (PVDF) Materials;** Azaz Vahora, *Arkema Inc., USA*

11-2 **Foamed PVDF Jacket for Power-Over-Ethernet Cables to Overcome Thermal Aging Challenges;** Dr. Bo Xu, *Product Development Center, Superior Essex Communications, USA*

11-3 **Materials Considerations for Laser Printed Jacket Solutions;** Dr. Brian Risch, *Prysmian, USA*

11-4 **Effects of Filler Surface Modification on Coupling Effects in Halogen Free Flame Retardant Cable Compounds;** Dr. Michael Heinz, *Corning Optical Communications, Germany*

11-5 **Polyurethane Resin-based FRP Rods as Embedded Strength Members in Optical Fiber Cables;** Ms. Aparna Nath, *Sterlite Technologies Limited, India*

11-6 **Tailored Color Packages for Optimizing the Processing and Performance of Crosslinking Polyolefins;** Dr. Eric Laird, *Chroma Color Corporation, USA*

11-7 **Fluoropolymer Processing Aid Replacement in Cable Jacketing Compounds;** Dr. Karl Seven, *Dow, USA*

11-8 **Research On Influencing Factors Of Smoke Density In Flame Retardant Optical Cable;** Ms. Elizabeth Pan, *Hengtong Optic-Electric Co., Ltd., China*

Click here to return to the **Table of Contents**

New Advancement in the Polyvinylidene Fluoride (PVDF) Materials

Azaz A. Vahora, James J. Henry, Luigi Puglia

High Performance Polymer Division, Arkema Inc.

King of Prussia, PA

+1-484-868-6475 · azaz.vahora@arkema.com

Abstract

The continued growth of the Wire & Cable industry in renewables, electric mobility, data centers, fiber optics, and telecommunication is driving demand for higher-performing polymers in the wire and cable industry. Improved polymer durability in higher and lower-temperature environments has become more critical as technology advances and infrastructure demands increase. To address such concerns, new PVDF polymers have been developed to keep up with changes in service conditions and corresponding demands. The following paper will present new developments in PVDF polymer technologies and standards related to performance cable applications. A new PVDF copolymer that can withstand a -60°C impact (35°C to 50°C improvement compared to typical PVDF copolymers) will be discussed to advance low-temperature properties. A new PVDF copolymer that can potentially achieve a temperature rating of 200°C after crosslinking will also be presented. Notably, the changes to UL1581 will be discussed, which now permits using these new flexible PVDF copolymers in communication cables. Finally, to help address the Oil and Gas industry needs, the new ASTM D 8436 entitled "Fluoropolymer-based Materials for Use for Encapsulation of Downhole Cables" will be summarized, including performance data for PVDF polymers relevant to the new specification.

Keywords: PVDF, Kynar®, Homopolymer, Copolymer, Homogeneous, Heterogeneous, Impact, Modifier, Crosslinking, ASTM D8436, UL 1581, low-temperature.

1. Introduction

For many years, PVDF polymers have been used in high-performance cable applications including plenum communication cables, automotive cables, aviation and military cables, and appliance wiring. The selection of PVDF polymers is largely due to a unique combination of properties, including flame and smoke resistance, abrasion resistance, high flexibility, chemical resistance, outdoor weathering resistance, and the ability to be e-beam crosslinked. The wide range of useful properties provided by PVDF polymers helps make them a valuable tool for resolving unique problems under challenging applications. PVDF polymers available include both homopolymers and copolymers. PVDF homopolymers are stiffer and offer higher tensile strength and flexural modulus. In contrast, PVDF copolymers are more flexible with a lower flexural modulus to improve cable flexibility. The PVDF copolymers have superior low-temperature impact properties down to -25°C. Both PVDF homopolymers and copolymers offer higher temperature rating up to 150°C. PVDF polymers have excellent fire resistance and are available with smoke and flame suppressants to be used in plenum spaces which require the highest level of flame and smoke spread resistance. Table 1 summarizes a general property range for the PVDF polymers.

Table 1: Typical Properties for PVDF Polymer

Typical Properties of PVDF Polymer	*Homopolymer*	*Copolymer*
Tensile Strength (Mpa)	30-55	13-48
Flexural Modulus (Mpa)	1380-2310	190-1240
Melting Point, DSC (°C)	155 – 172	117 - 168
Temperature Rating (°C)	150	100 – 150
Ductile-Brittle Temperature, Impact (°C)	- 10 to 10	-25 to 0
Plenum Grades	Yes	Yes

This paper intends to cover new advancements that push the limits of where PVDF polymers can be used in wire and cable products. This paper will cover a few different topics. The first one is the development of the PVDF polymers for extreme low-temperature applications down to -60°C impact resistance. The second one will address high temperature uses. PVDF polymers' high temperature uses are limited to 150°C due to their melting point. We will discuss using PVDF polymers in applications needing up to 200°C temperature rating, which will be achieved via crosslinking. Furthermore, a new standard introduced for selecting the Fluoropolymer for the Downhole cables, ASTM D8436, specifies "Fluoropolymer-based Materials for Use for Encapsulation of Downhole cable". Finally, the paper will talk about a recent addition to UL 1581, a standard for "Electrical Wires, Cables, and Flexible Cords," to allow newer PVDF copolymers with improved flexibility and shrinkage property.

2. PVDF for Extreme Low-Temperature

2.1 Background

PVDF copolymers are commonly used in low-temperature cable applications over PVDF homopolymers. Generally, PVDF copolymers pass the -40°C mandrel wrap. However, their uses are limited to -15°C for cable needing impact resistance for most homogeneous PVDF copolymers. In contrast, heterogeneous PVDF copolymers have a unique morphology that provide low-temperature impact resistance down to -25°C (with better flexibility) and a higher temperature rating of 150°C. In general, a new technology was needed to achieve low temperature impact performance below -40°C (and down to -60°C) while maintaining flexibility for easy wrapping, and a higher temperature rating of 150°C for the heating cable (see Figure 1).

2.2 Experimental Detail

2.2.1 Material: For the study, several PVDF polymers were selected having varied comonomer ratios and morphology to provide a range of flexibility and low/high temperature property, re-

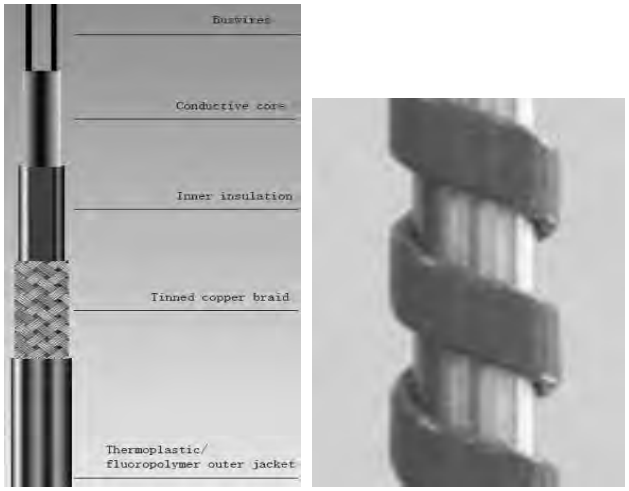


Figure 1: Heating Cable Construction and the Wrapping of the Cable Around the Annular Structure[1][2]

spectively (see Table 2 below). The results presented herein are limited to only heterogeneous copolymers that were found to provide the best performance characteristics. To further improve low temperature impact performance, the addition of impact modifier was studied. Impact modifier selection was limited to those that could improve low temperature performance while not adversely affecting other important properties.

Table 2: Material Composition

Heterogeneous PVDF Copolymer	*Comonomer ratio*
CP 1	High
CP 2	Medium

2.2.2 Sample Preparation and Testing: Tensile properties were tested following ASTM D638, Standard Test Method for Tensile Properties of Plastics. Type I specimens were injection molded and were conditioned at 23°C and 50%RH greater than 48 hours before the test. The tensile test used a grip separation of 4.5 inches (114.3 mm) and a crosshead speed of 2 in/min (50.8 mm/min). Elongation was measured using a high-resolution digital extensometer with a gage length set at 2 inches (50.8 mm). Each sample set consisted of five tensile specimens.

Flexural properties were tested following ASTM D 790-02, Standard Test Method for Flexural Properties of Unreinforced and Reinforced Plastics and Electrical Insulating Materials. Specimens measuring 0.25 inches (6.35 mm) thick x 0.50 inches (12.7 mm) wide x 5.00 inches (127 mm) long were injection molded. All specimens were conditioned at 23°C and 50%RH greater than 48 hours before the test. The specimens of these dimensions call for a support span of 4 inches (101.6 mm) and a crosshead speed of 0.1 in/min (2.54 mm/min) according to the ASTM D790-02 test method. Each sample set consisted of five flexural bars.

All Tensile and Flexural testing was performed using an Instron Universal Test stand.

Low-temperature Impact properties were tested by adapting the ASTM D256-02, the Standard Test Method for Determining the Izod Pendulum Impact Resistance of Plastics. Specimens measuring 0.25 inches (6.35 mm) thick x 0.50 inches (12.7 mm) wide x 2.50 inches (63.5 mm) in length were injection molded. All specimens were notched at a distance of 0.40 inches (10.16 mm) behind the notch using the TMI Notching Cutter, model TMI 22-05. Unlike ASTM D256-02, the specimens were conditioned at test temperatures in the freezer for a minimum of 4 hours before testing. Specimens were tested using a CEAST Resil Impactor with a 7.5 J hammer, a hammer speed of 3.46 m/s, and a drop angle of 150°. The tester's sample holder was covered with dry ice to low the temperature. Each sample set consisted of ten impact bars. The temperature at which a 50% drop in impact energy was calculated was reported as ductile-brittle transition temperature (DBTT) (see Figure 2).

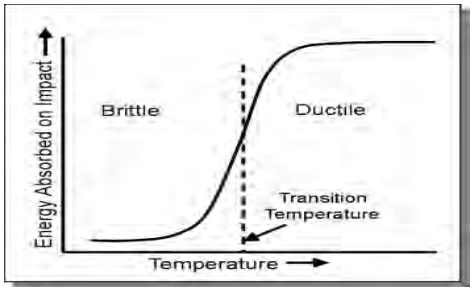


Figure 2: Ductile Brittle Transition[3]

Low-temperature cable impact tests were performed following the ICEA.S.104-696 Indoor Outdoor Optical Fiber Cable standard method. The PVDF material was tube-on jacketed using a 1.25 inches (31.75 mm) single screw extruder on a four-twisted pair core with a wall of 20±2 mil (0.508±0.051 mm). The temperature profile used was 200-235°C on the four zones of the extruder, and the head and die were around 235°C. The cable was cut into 12 in (304.8 mm) long sections and conditioned in the freezer at test temperature for a minimum of 4 hours before the test. The impact fixture (see Figure 3) was also placed in a separate freezer set at a temperature five degrees below the test temperature for a minimum of 4 hours. The impact weight was 1 kg with a rounded top (see Figure 3). The impact height was 6 in (152.4 mm). The cable was taken from the conditioning chamber one at a time for impact testing. Each cable was impacted twice per location, with 9+ impact locations at each condition. Impact testing was stopped after 3 minutes of testing, followed by half an hour of gap to allow the test fixture to cool back down. The cable was visually checked for break or crack after impact. The DBTT was reported as having 50% or more impact resulting in a break in the cable at the lowest temperature.



Figure 3: Cable Impact Tester Fixture with a 1 kg Dome Shaped Impact Weight

2.3 Results and Discussion

Impact modifiers are commonly used to toughen polymers and improve their low-temperature impact resistance. This modifier has

good compatibility with the PVDF resin and has shown improvement in all grades of emulsion PVDF polymer.

As expected, the addition of an impact modifier (IM) reduced the flexural modulus, improved resin flexibility and significantly improved low temperature performance. Properties such as stress and strain at break remained relatively unchanged from the addition of the impact modifier. A summary of these results can be found in Table 3.

Table 3: Effect of Impact Modified on Heterogeneous PVDF Copolymers

Material	*Break Stress (Mpa)*	*Break Strain (%)*	*Flex. Mod. (Mpa)*	*Izod Impact DBTT (°C)*	*ICEA Cable Impact DBTT (°C)*
CP 1	20.6	886	283	-15	-25
CP1+IM	23.3	688	255	-30	~< -50
CP 2	24.4	193	690	-5	-15
CP 2 + IM	24.4	236	552	~< -20	-45

Along with material type, the cable design (cable core) and the geometry influence the DBTT for the cable. Hence, it is essential to perform impact testing on each cable type. In this case, a more complex cable core was used: the four twisted pair, which resulted in uneven wall thickness and a non-uniform jacket. Even with this type of core, the cable with CP – 2 + IM jacket (see Figure 4) was able to pass the -40°C impact test and meet the UL1581 requirement. As mentioned before, the cable design influences DBTT, and for the heating cable (see Figure 1), the CP-2 with IM composition passed -60°C on a cable impact. The CP-1 with IM composition has even better low-temperature properties

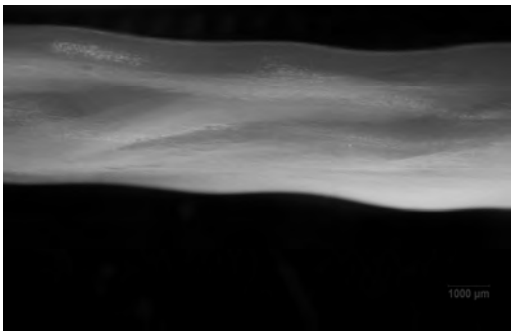


Figure 4: -40°C Impact Tested Cable with CP-2 + MI

Ultimately, the impact modifier makes the composite flexible and lowers the DBTT. The CP-2 with IM composition meets the heating cable requirement and the UL 1581 requirement for a -40°C cable. The CP-1 with IM has much better flexibility, break strength, elongation, and the best DBTT.

3. PVDF for 200°C Rating Cable by Crosslinking

3.1 Background

PVDF polymers are used in high temperature applications such as those found in automotive cables but are often limited to 150°C applications due to the polymers melting point. To increase the upper use temperature of PVDF polymers, ebeam crosslinking is often performed. Crosslinking primarily raises the polymer's upper use temperature. High-performance crosslinked cables take advantage of PVDF polymer's ability to be efficiently crosslinked using ebeam radiation. With sufficient ebeam radiation doses, the cable with PVDF jacket can be rated up to 175°C and allows short-term thermal exposures up to of 200°C (for 240 hours per the ISO 6722 a standard for Road Vehicles- 60V to 600V Single Core Cable). To achieve higher temperature ratings up to and above 200°C, higher levels of ebeam doses are needed. These higher ebeam doses must be carefully considered, as they can lead to issues with thermal color stability and can potentially result in property loss (especially major effect can be seen in low temperature impact resistance due to embrittlement) making it difficult for conventional PVDF grades to achieve a robust Class F 200°C rated cable for automotive (see Figure 5).

Class	Temperature
A	–40 °C to 85 °C
B	–40 °C to 100 °C
C	–40 °C to 125 °C
D	–40 °C to 150 °C
E	–40 °C to 175 °C
F	–40 °C to 200 °C
G	–40 °C to 225 °C
H	–40 °C to 250 °C

Figure 5: Automotive Cable Class Per ISO 6722 for Various Temperature Rating [4]

3.2 Experimental Plan

3.2.1 Material: PVDF polymer grades selected were those known to have most favorable crosslinking characteristics. It is understood that crosslinking efficiency improves as the PVDF polymer viscosity is increased. In addition, higher comonomer ratio improves crosslinking efficiency and provides additional flexibility. The third variable was the morphology; as mentioned before, the morphology drives the low and high-temperature properties like low-temperature impact and melting point, respectively. The material selected based on the above critical are summarized in the Table 4 below.

Table 4: Materials Composition

PVDF Copolymers	*Morphology*	*Comonomer Ratio*	*Viscosity*
CP-3	Heterogeneous	High	High
CP-4	Heterogeneous	High	Low
CP-5	Heterogeneous	Medium	High
CP-6	Homogeneous	High	High

3.2.2 Sample Preparation: All the PVDF copolymers were compounded with the 3% TAIC crosslinking promotor on a 30 mm twin screw machine. Those compounds were used for cable jacketing. The cable was prepared by tube-on jacketing the PVDF compounds on the four twisted pair core using a 1.25 in (31.75 mm) single screw extruder. The jacket wall was 20±2 mil (0.508±0.051mm). The temperature profile used was 200-235°C

on the four zones of the extruder, and the head and die were around 235°C.

The cables were then irradiated to 10 mrads of radiation (crosslinking), a typical dose. The 1 ft (304.8 mm) long pieces of cable were used for thermal aging (see Figure 5). One set was exposed to 200°C for 3000 hours and the other to 225°C for 240 hours per the ISO 6722 for Class F cable.



Figure 6: Crosslinked Cable Hanging in the Convection oven for Thermal Aging at 225°C

Table 5: Thermal Aging of the Automotive Cable by Class Per ISO 6722[4]

Rating Class	*Long Term Aging*	*Short Term Aging*
A to H	3000 hr. @ T=Tr	240 hr. @ T=Tr +25°C

3.2.3 Material Testing: The low-temperature cable impact tests were performed following the ICEA.S.104-696 Indoor Outdoor Optical Fiber Cable standard method at -25°C. The PVDF material was tube-on jacketed using a 1.25 inches (31.75 mm) single screw extruder on a four-twisted pair core with a wall of 20±2 mil (0.508±0.051 mm). The temperature profile used was 200-235°C on the four zones of the extruder, and the head and die were around 235°C. The cables were cut into 12 in (304.8 mm) long sections and conditioned in the freezer at test temperature for a minimum of 4 hours before the test. The impact fixture (see Figure 3) was also placed in a separate freezer set at a temperature of -30°C for a minimum of 4 hours. The impact weight was 1 kg with a rounded top see Figure 3. The impact height was 6 in (152.4 mm). The cable was taken from the conditioning chamber one at a time for impact testing. Each cable was impacted twice per location, with 9+ impact locations at each condition. Impact testing was stopped after 3 minutes of testing, followed by a cool down period of 30 minutes. The cables were visually checked for any breaks or cracks after impact. A "Break" was reported as ≥50% impact exhibiting break or crack.

3.3 Results and Discussion

To better differentiate performance, low temperature impact testing was performed instead of low temperature mandrel wrap testing mentioned in ISO 6722. It is understood that impact testing is much more difficult to pass and is often a better indicator of low temperature performance in dynamic applications. The results from this study found that select PVDF copolymers can meet the low temperature requirements for a 200°C rated cable if crosslinked in the presence of a crosslink promoter. CP-3 with promotor passed the impact testing, which suggests retention of mechanical properties after radiation. All other samples break on impact either due to long-term and/or short-term thermal exposure (see Table 6 below). It is interesting to note that the short term accelerated test defined in ISO 6722 was determined to be more difficult to pass than the long-term test.

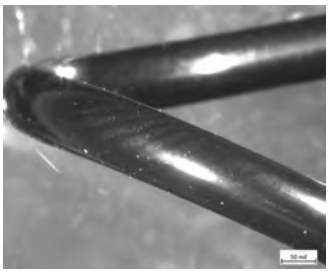


Figure 7: CP-6 Crosslinked Cable after Thermal Aging at 225°C

Table 6: ICEA -25°C Low-Temperature Cable Impact Testing on Crosslinked Cable Aged Per ISO 6722

Crosslinked-PVDF copolymers composition	*TAIC*	*Short Term (240 hrs @ 225°C)*	*Long Term (3000 hrs @ 200°C)*
CP 3	3%	No Break	No Break
CP 4	3%	Break	No Break
CP 5	3%	Break	No Break
CP 6	3%	Break	Break
CP 3	--	Break	Break

4. ASTM D8436 Standard for Encapsulation of Downhole Cable

4.1 Background

PVDF polymer are commonly used as encapsulants in the production of downhole cables such as Tube Encapsulated Cables (TEC cables) (see Figure 8 below). The petroleum and natural gas industries use these cable types during well completion. The function of the encapsulation is to protect the internal components of the down cable, and to ensure alignment and orientation of components. The encapsulation material is exposed to severe mechanical stress, aggressive chemicals, and extreme weather conditions, and improper material selection could lead to premature cable failures. Hence the ASTM D8436, a Standard Specification for Fluoropolymer-based Materials for Use for the Encapsulation of Downhole Cable, was created for material selection guidelines. This standard covers properties needed for the fluoropolymers (see Table 7 below) to be used for cable encapsulation, and retention of properties after exposure and aging in chemicals, thermal, and weathering (see Table 8).

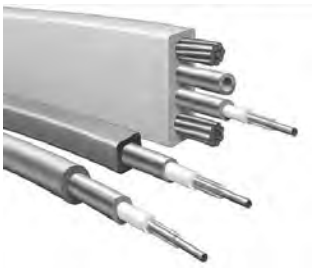


Figure 8: Downhole Cable Examples [5]

Table 7: Unaged Fluoropolymer Property Requirements for the Downhole Encapsulation Materials Per ASTM D8436[6]

*Properties**	*ASTM Standard*	*Min. Unaged Requirement*	*Kynar® PVDF grades*
Melting Point, second heat, °C	4561	125	≥125
Tensile Strength @ break, (MPa)	D638 or D1708	13.8	≥13.8
Elongation @ Rupture (%)	D638 or D1708	30	≥30
Flammability @ thickness of 3 mm	D3801 or UL 94	V-0	V-0
Oxygen Index (OI) @ thickness of 3 mm	D2863	30	≥43
Relative thermal Index (°C)	UL 746B	--	≥140

Table 8: Aging Requirements for the Downhole Encapsulating Materials Per ASTM D8436[6]

Aging Conditions		*Min. aged Requirement*
Diesel B20	14 days @ 70°C	85% retention of Tensile strength and elongation at break of unaged
		Less than 5% weight gain of unaged
Fuel C	14 days @ 70°C	85% retention of Tensile strength and elongation at break of unaged
		Less than 5% weight gain of unaged
90% Sulfuric Acid	14 days @ 70°C	85% retention of Tensile strength and elongation at break of unaged
		Less than 5% weight gain of unaged
Weathering using Xenon arc	Per ASTM D7869 80 cycles of 24 hrs	70% retention of Tensile strength and elongation at break of unaged
		Free of visible cracks or crazing
Thermal	150 days @ T (°C)*	70% retention of Tensile strength and elongation at break of unaged

* Thermal aging per Section 7.6.2: T (°C) =(1.02 (Tr*+273) – 273, whereas Tr is rating temperature in °C.

4.2 Experimental Plan

4.2.1 Material: Benchmark testing against this standard was performed on commercial PVDF grades commonly used in this application. The grades selected included Kynar Flex® 2850-00, KynarFlex® 3120-50, and KynarFlex® 3030-50.

4.2.2 Sample Preparation and Testing: The tensile bars of type I were injection molded per ASTM D638, a Standard Test Method for Tensile Properties of Plastics. The tensile bars were annealed at 90°C ± 2°C for 2 hours for chemical and weather exposure and 159°C ± 2°C (per Section 7.6.2) for 2 hours for thermal aging, followed by slow cooling overnight in an oven. All specimens were then conditioned for a minimum of 40 hours at 23°C ± 2°C and relative humidity of 50 ± 10% per ASTM D8436.

These conditioned specimens were used as controls and were exposed to the aging test mentioned in Table 8 above, following the procedure in ASTM D8436. The thermal exposure was performed at 159°C ± 2°C per Section 7.6.2 in ASTM D8436.

Tensile test on all specimens (aged or unaged) was conducted using a grip separation of 4.5 inches (114.3 mm) and a crosshead speed of 2 in/min (50.8 mm/min). Elongation was measured using a high-resolution digital extensometer with a gage length set at 2 inches (50.8 mm). Each sample set consisted of five tensile specimens.

4.3 Results and Discussion

As mentioned in Table 7 above, the Kynar® PVDF grades selected for the study meet the minimum property requirement set by the standard for unaged Fluoropolymer-based materials.

***4.3.1 Fuel and Chemical Aging*:** The exposure of the B20 Diesel, Fuel C, and 90% Sulfuric acid has no significant effect on the mechanical properties of the PVDF grades, as seen in Figure 9. Additional, weight gain was much below 1% in these chemicals.

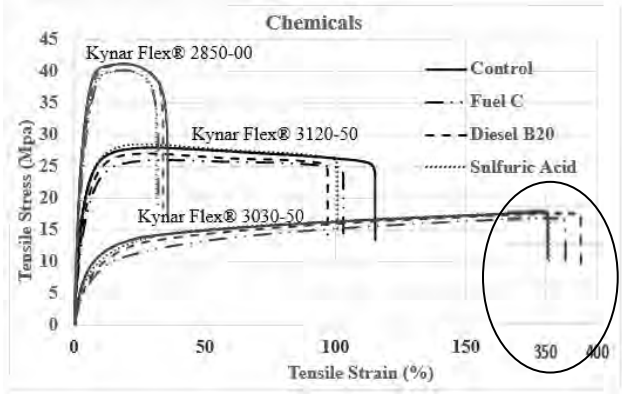


Figure 9: Tensile Plot for Chemically Aged PVDF Against Control Per ASTM D8436

4.3.2 Weathering: The weather also had no significant effect on the mechanical properties (see Figure 10), and no visual cracks or crazing were observed.

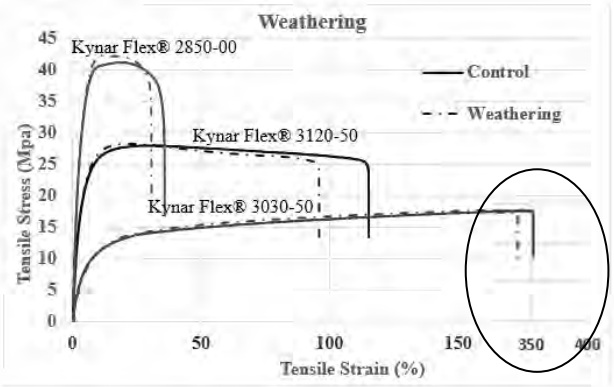


Figure 10: Tensile Plot of Weathered PVDF Against Control Per ASTM D8436

4.3.3 Thermal Aging: Even with thermal aging, PVDF retains mechanical properties minimum 70% of unaged PVDF grades (see Figure 11).

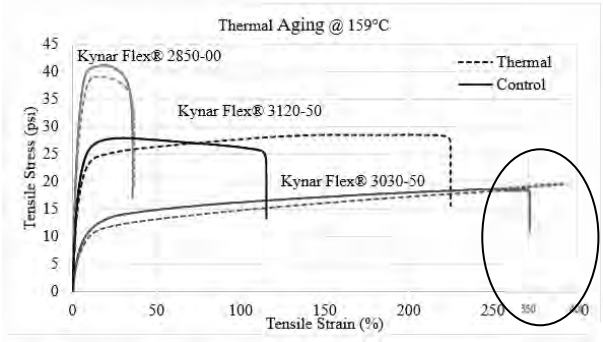


Figure 11: Tensile Plot of Thermal Aged PVDF Against Control Per ASTM D8436

5. UL1581

The UL 1581, a Reference Standard for Electrical Wires, Cables, and Flexible Cords, contains details on the conductor, insulation, jackets, and other coverings. It specifically mentions the requirement of each component by material family. Until recent changes it limited the use of newly developed flexible PVDF copolymer grades. This is because the standard limited the PVDF grades by tensile strength and did not enable the improved flexibility (lower modulus) grades that can have lower tensile strength. The enhanced flexibility, also associated with desirable low shrinkage and shrink back, is essential for fiber optic cables. The lower modulus grades also offer better impact resistance at room temperature and low temperature. Hence a new material category was added to the UL 1581 for the Flexible PVDF copolymer jackets to overcome this constraint (see Figure 12).

Table 50.186
Physical properties of 150°C and 125°C Flexible PVDF jackets[a]

Condition of specimens at time of measurement	Minimum ultimate elongation (1-inch or 25-mm bench marks)[b]	Minimum tensile strength[b]
Unaged	100 percent (1 inch or 25 mm)	2500 lbf/in^2 or 17.2 MPa 24.1 MPa
Specimens of 150°C material:		
Aged in a full-draft circulating-air oven for 60 d at 158° ±1.0°C (316.4 ±1.8°F)	50 percent of the result with unaged specimens	50 percent of the result with unaged specimens
Specimens of 125°C material:		
Aged in a full-draft circulating-air oven for 168 h at 158.0 ±1.0°C (316.4 ±1.8°F)	See note[c]	See note[c]
or		
Aged in a full-draft circulating-air oven for 30 d at 136 ±1.0°C (276.8 ±1.8°F)	See note[c]	See note[c]

[a] Flexible PVDF copolymer designates a thermoplastic material whose characteristic constituent is a copolymer of polyvinylidene fluoride and hexafluoropropylene having a flexural modulus below 60,000 psi when tested per ASTM D790. The material is the uncompounded polymer to which it is appropriate to add a small amount of pigment, lubricant, or both.

[b] Flexible PVDF copolymer is to be tested at a speed of 2.0 ±0.2 in/min or 50 ±5 mm/min.

[c] Aged specimens of the jacket, of the foamed insulation in place on the conductor, or the solid insulation in place on the conductor are to be wound onto a mandrel as described under "Flexibility" in the applicable wire Standard. Unaged specimens of the jacket and of the solid insulation are to be tested for tensile strength and elongation. Jacket damage after aging caused by outgassing of lower-temperature insulated conductors within the cable does not constitute noncomplying performance.

Figure 12: Table 50.186 Added to the UL 1581 for Flexible PVDF Jackets [7]

6. Conclusion

This paper shares two case studies that involve the development of PVDF polymers to be used in applications outside the range of conventional PVDF grades. The impact modified PVDF compositions can resist cable impact below -40°C, which is also influenced by cable design. In the case study, the CP-1 with impact modifier passed the cable impact at -45°C on the four twisted pair. In comparison, the same material passes the impact up to -60°C on a flatter heating cable (see Figure 1). The second case study utilizes crosslinking to use PVDF polymers beyond their normal high use temperature. A specific PVDF polymer with heterogeneous morphology, higher HFP comonomer, and higher viscosity was developed to be highly efficient for crosslinking, which increased the crosslinking in the PVDF polymer with limited radiation doses. This technology minimized the loss in mechanical performance, specifically the low-temperature cable impact in this case, and enabled a high temperature rating up to 200°C. In addition to developing PVDF polymers for extreme applications, there are extreme applications in which PVDF is already used. However, there was a lack of standards for selecting suitable materials, such as downhole cable encapsulation. These cables are exposed to aggressive chemicals, temperature, and weathering conditions. The new ASTM D8436 is the only standard for resin selection for downhole cables, and PVDF resins pass all the requirements per the standard. Finally, latest advancements in cable applications require new flexible PVDF polymer. However, their uses have been limited by older specifications like tensile strength in UL 1581. Hence a new material category has been added to the UL 1581 Table 50.186 for flexible PVDF jackets.

7. Acknowledgments

Special thanks to all the co-authors of this paper.

8. References

[1] https://thermal-resources.com/products/self-regulating-heating-cables/

[2] https://www.valin.com/sites/default/files/asset/document/Industrial-Heavy-Insulated-Non-Hazardous-Heat-Tape-Specification-Sheet.pdf

[3] https://punchlistzero.com/dbtt-ductile-brittle-transition-temperature/

[4] ISO 6722, "Road Vehicles 60V and 600 V Single Core Cables"

[5] https://www.espcablesolution.com/products_info/TEC-Cable--Downhole-Sensor-Cable-331444.html

[6] ASTM D8436, "A Standard Specification for Fluoropolymer-based Materials for Use for the Encapsulation of Downhole Cable"

[7] UL1581, "A Reference Standard for Electrical Wires, Cables, and Flexible Cords"

9. Pictures of Authors



Azaz Vahora
900 Frist Avenue,
King of Prussia PA 19406

Azaz Vahora currently works as a Staff Engineer in the High Performance Polymers Division of Arkema Inc. He holds an M.Sc. (2021) in Material Engineering and B.Sc. (2012) in Chemical Engineering, both from Drexel University. Azaz has 11 years of experience with fluoropolymers, particularly with PVDF, for use in various fields, including the chemical processing industry, wire and cables, water filtration, 3D printing, energy storage and fuel cell. He is based at Arkema Inc.'s North American Headquarters in King of Prussia, PA.



James Henry
900 First Avenue,
King of Prussia PA 19406

James Henry joined Arkema located at the Research Center in King of Prussia, PA in January 2001 and is currently R&D Engineering Operations Manager in the High Performance Polymers NA Division. James received a Bachelor's Degree in Chemical Engineering from the University of Lowell, and a Master's Degree in Plastics Engineering from the University of Massachusetts.



Luigi Puglia
900 First Avenue,
King of Prussia PA 19406

Luigi Puglia has been with Arkema for over 40 years. He is currently a market manager for the wire and cable market in North America**.**

Foamed PVDF Jacket for Power-over-Ethernet Cables to Overcome Thermal Aging Challenges

Bo Xu[1], Christopher McNutt[1], Amir Sekhavat[1], James Henry[2]

[1]Superior Essex International LP – Communications

Atlanta, Georgia

+1-770-657-6620 · Bo.Xu@spsx.com

[2]Arkema Inc.

King of Prussia, PA

+1-610-878-6023 · James.Henry@arkema.com

Abstract

Power-over-Ethernet (PoE) technology is gaining popularity as a means of transmitting electrical power and data to remote devices due to its simplicity and cost-effectiveness. However, with the growing demand for higher power transmission levels, PoE cables can pose significant thermal challenges such melting and degradation of the cable components, resulting in system failures, safety hazards, reduced cable performance and a shortened lifespan. Previous studies have shown that polyolefin insulation and polyvinyl chloride (PVC) jackets exposed to heat may exhibit these issues. Some PVC jackets have shown significant degradation after aging at 136°C for 17 days, causing decay in the electrical performance of their 4-pair PoE (4PPoE) cables, and their lifespan was predicted to be less than 10 years at continuous use temperatures of 75°C or higher. Hence, there is a crucial need to develop thermally stable, durable, and cost-effective jackets for PoE cables with temperature ratings of 90°C or higher.

In this study, we introduced chemically foamed polyvinylidene fluoride (PVDF) jackets for 4PPoE cables and investigated their impact on the cables' thermal stability. We compared the physical properties, thermal aging, flame performance of the foamed PVDF jackets to those of solid PVDF. Using an Arrhenius-type model, we evaluated the lifetimes of both types of jackets. Our findings revealed that foaming PVDF up to 35% had a minimal effect on its thermal stability but significantly limited flame spread. The foamed PVDF jackets can be rated up to 150°C, as they demonstrated almost unchanged heat-aged tensile properties. Moreover, they have an estimated lifespan over 100 years when continuously used at 150°C, which is much longer than some PVC jackets that have a shorter lifespan, even at lower temperatures like 75°C. Furthermore, the electrical performance of the 4PPoE cables with foamed PVDF jackets remains stable over 22 days at 136°C, similar to the cables with solid PVDF jackets and significantly better than those with PVC jackets. Our results suggest that foamed PVDF jackets hold great promise as a material for PoE cables with high-temperature requirements.

Keywords: PoE; Aging; Foam; PVDF; Lifetime; Fire Resistance; Thermal Stability; Degradation Kinetics; Crosstalk.

1. Introduction

Power over Ethernet (PoE) is a technique that allows electric power to be delivered alongside data over standard category cables in an Ethernet network. This eliminates the need for separate power supplies and outlets, saving time and costs while also proving more opportunities for innovations and flexibility [1-3]. PoE has found diverse applications, including lighting, access control, security cameras, sensors, access points, detectors, displays, and more [4]. Additionally, PoE technology facilitates the integration of the Internet of Things (IoT), making all powered and connected devices more intelligent, effective, and cooperative.

As the number of PoE devices grows, the power levels for PoE category cables have been steadily increasing and are expected to continue to rise. For example, the original PoE standard (IEEE 802.3af) in 2003 specified 15.4 watts, while the IEEE 802.3bt in 2018 specified 90 watts, and future standards may specify even higher wattage up to 200 watts or more [5]. However, as power levels increase to 100 watts or greater, cable heating generated by the current transmission through conductors becomes inevitable [6,7], especially when PoE cables are installed in bundles. This can cause temperature rise and create safety and performance issues that must be addressed [5-8].

Standard groups, testing organizations, and industry experts have been researching the impacts of elevated heat on the safety and performance of PoE cables. Their investigations encompass various aspects such as industry standards, cable performance, installation safety and the lifetime of cable insulation for PoE deployment. The objective is to develop effective solutions that address the safety and performance concerns arising from cable heating, ensuring that PoE cables can meet the growing power demands of modern network devices.

In our previous work on 4-pair PoE (4PPoE) cables, we assessed cable performance in terms of cable heating, power efficiency, and thermal aging of insulations and jackets [9, 10]. Our finding showed that cable heating can result in low power efficiency and high operating cost. When exposed to excessive temperatures, the polyolefin insulation of PoE cables can melt or degrade [9], while the Polyvinyl Chloride (PVC) jackets can experience significant weight loss [10]. These issues can cause decay or failure of electrical performance of the cables, resulting in lower power efficiency [9], increased Near-End crosstalk (NEXT) [10] and

higher insertion loss [5, 11]. Thermal aging may also result in downgrading fire resistance levels and temperature ratings as the insulations and jacketing materials lose some ingredients through degradation, sublimation, or even evaporation, thereby significantly shortening the expected lifespan of PoE cables. According to our predictions [10], the lifespan of those PoE cables with PVC jackets is less than 20 years at continuous use temperatures of 90°C or above. Therefore, it is highly desirable to develop thermally stable, durable, and cost-effective jackets for PoE cables with temperature ratings of 90°C or above.

In this paper, we demonstrated chemically foamed polyvinylidene fluoride (PVDF) jacket for 4PPoE cables to address thermal challenges and investigated the effect of foaming on PVDF jackets and how this affected the thermal stability of the 4PPoE cables. We examined physical properties, thermal aging, FT-2 horizontal burn performance on foamed PVDF jackets as compared to the pristine PVDF. Using thermogravimetric analysis (TGA), we determined degradation kinetics parameters for the PVDF jackets as compared to some PVC jackets and estimated their lifespan at possible operating temperatures based on the Arrhenius model. Electrical performance of these PoE cables was also monitored during long-term isothermal aging in a chamber.

2. Experiment Details

2.1 Materials

Two grades of PVDF resin (Arkema, Kynar Flex® 3030-15, Kynar Flex® 3120-50) were selected for jackets. Kynar Flex® 3120-50 resin was used for foamed jackets of the Cat5e and Cat6A cables, while Kynar Flex® 3030-15 resin was for the solid jacket of the Cat6A cable. Foam agent is Kyflex® EZ-foam from Arkema (LDR = 0.9% for the Cat5e cable; LDR = 1.1% for the Cat6A cable). The black color concentrate was purchased from Avient (LDR = 2%). The Kynar Flex® 3120-50 sheets, with a thickness of 30 mils, were molded using a hot press at 210°C.

Two cable cores were built with fluorinated ethylene propylene (FEP) insulated copper wire at Superior Essex (Kansas): one for Cable 1 and the other for Cable 2. Table 1 lists the characteristics of these cables. 2% black concentrates were added for black jackets, while the white jacket of Cable 2 is natural.

Two PoE cables with PVC jackets and FEP insulation reported in our previous work [10], Items 3 and 5, were selected to compare the cables with PVDF jackets. Item 3 is a Cat5e cable with the temperature rating of 105°C, while Item 5 is a Cat6A cable with the 90°C rating.

2.2 Foam Extrusion

PVDF and foam agent with black color added as necessary were extruded in a single-screw SAMP extruder (D = 45 mm and L/D = 32) with a barrier screw and a screw speed of 40 rpm. Figure 1a shows the foam extrusion to make Cable 2 shown in Figure 1c. Figure 1b shows Cable 1 with black foamed PVDF. For a solid PVDF jacket, no foam agent was added (Figure 1d). The line speed was adjusted from 70 - 100 feet per minute to achieve the desired wall thickness of jackets, and the extrusion barrel temperature profile was set as 300 - 420 ˚F in 9 zones. The 40/80/40 mesh screen pack was used, and the trough water temperature was set as 60°C at the first stage and then 20°C for the rest.

2.3 Material Testing

Density and Foaming Level. The density of jackets was measured by following ASTM D 792 – specific gravity by displacement, and then the foaming level (%) was calculated based on the density, 1.775 g/cm3 of unfoamed PVDF: % = 100 – (100 × density of foamed jacket / density of unfoamed jacket). Foamed PVDF jackets of Cables 1 and 2 show 25% and 35% foam, respectively.

Optical Microscopy. Foamed jackets and burned samples were examined by using ZEISS Smartzoom 5. The jackets were cut with a sharp blade, resulting in a clear cross-section.

Mechanical Testing. Tensile properties on 250mm long jacket tubes were measured on a Zwick/Roell Universal Testing Machine equipped with an extensometer by using a crosshead speed of 50 mm/min, a grip gauge of 150 mm and an extensometer gauge length of 50 mm. This tensile test method was customized, since dumbbell specimens cut from foamed jackets by using ASTM D412-D die cutter generated a large variation on the tensile results due to the defects in their edges. An air-circulating oven was utilized for the purpose of conducting aging experiments on PVDF jackets under varying conditions, as outlined in Table 2. Following the aging stage, the cables were also coiled around a mandrel for a flexible testing procedure.

Table 1. Summary of PoE cable samples

Cable	Cable Category	Jacket	Foaming Level	PVDF Grade	Jacket Thickness	Cable OD	Copper Wire	Shielding
			%		mm	mm	AWG	
Cable 1	Cat5e	PVDF	25	3120-50	0.40	5.44	22	UTP
Cable 2	Cat6A	PVDF	33	3120-50	0.60	8.18	22	F/UTP
Cable 3	Cat6A	PVDF	0	3030-15	0.48	7.83	22	F/UTP
Item 3	Cat5e	PVC	0	na	0.43	6.10	22	UTP
Item 5	Cat6A	PVC	0	na	0.51	7.80	22	F/UTP

Thermogravimetric analysis (TGA). TGA was performed on a TA Instruments Discovery TGA under an air atmosphere at a purge rate of 25 ml/min. TGA samples of 7- 9 mg were cut from jackets or 0.50 mm thick PVDF sheets made by cold press from resin pellets (labeled as Pellet 3120-50) and were held in 100 µL platinum-HT sample pans. Following is the temperature ramp procedure (non-isothermal): samples stayed at a thermal equilibrium at 30 °C, then heat was applied in the temperature range 30 – 550°C at the heating rate of 1, 2.5, 5, 10, 15, 20°C/min. The second procedure was used for isothermal studies as follows: samples were initially heated at 50°C/min up to a chosen isothermal temperature and then were maintained at this temperature for a period until the weight loss reached at least 10%. All TGA tests of PVDF degradation were conducted in air flow of 25 mL/min. Based on reasonable instrument time constraints, the isothermal temperatures for the PVDF 3030-15 jacket were selected within the range of 255-310°C, while those for the foamed jackets and Pellet 3120-50 were chosen between 290-325°C. For reliable fitting analysis, we collected no less than 6 data points.

Customized CSA FT2 Flame Test. The flame resistance of PVDF 3120-50 sheets and PVDF jackets was tested using a horizontal configuration. The specimens or jackets were supported by a twisted pair of FEP insulated copper wire and exposed to a flame from a Bunsen burner for 30 seconds. After the tests, the length of the charred portion of the specimen was measured and the photographs were taken to observe the extent of burning.

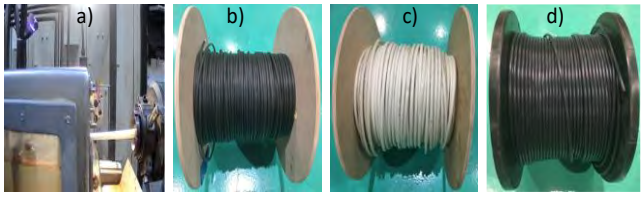


Figure 1. (a) Foam extrusion on Cable 2; (b) Cable 1: PoE Cat5e with foamed black PVDF 3210-50; (c) Cable 2: PoE CAT6A with foamed natural PVDF 3210-50; (d) Cable 3: PoE Cat6A with solid black PVDF 3030-15.

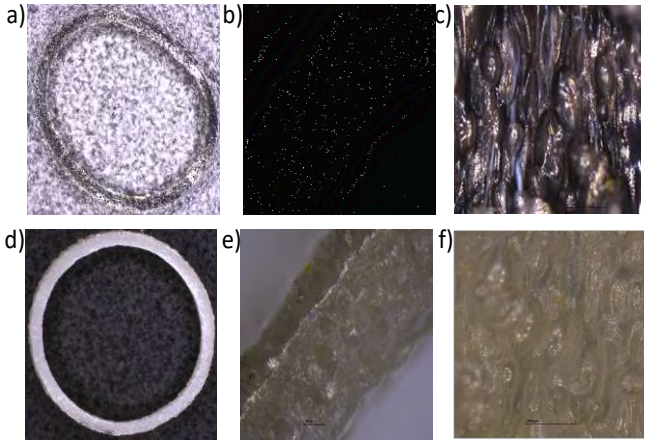


Figure 2. Optical microscope images of foamed PVDF Jackets from Cable 1 (a, b, c) and Cable 2 (d, e, f): (a, b, d, e) for sectional area; (c, f) for outer surface.

2.4 Jacket and Cable Aging

The jackets were first stripped from the cables in 1-foot increments, and then placed on a piece of rockwool insulation within a chamber. The PoE cables of 100 meters were wrapped around a steel reel of which the drum surface was covered with 1-inch thick rockwool insulation to avoid any influence of steel on electrical performance. The cable wires were well separated around the drum when uploaded to avoid their tight contact. The cable aging setup was placed in the center of a chamber (ESPEC). More details refer to our previous work [10]. The cables were threaded through the side of the chamber and connected to the DSX-5000 Fluke Network Analyzer. The cables experienced the thermal cycling as follows: cables were heated from 20°C up to a chosen isothermal temperature, 136°C for 4 hours, and held at that temperature for 2 days, and then cooled down to 20°C for 4 hours and held at 20°C for 12 hours before electrical testing. Jacket samples experienced the same thermal history as the cables did inside the same chamber, and their weight and length were measured at the same time intervals when the electrical testing on the cables was performed in accordance with TIA 568C. The aging time was the total time that the cables have been held at 136°C.

3. Results and Discussion

3.1 Foamed PVDF Jackets and Mechanical Properties

Polymer foam has many advantages such as light weight, cost effectiveness, improved burn performance, etc. It is commonly classified into three types: closed-cell foam, partially open-cell foam, and open-cell foam. The cellular structures and outer surface of foamed PVDF jackets are shown in Figure 2. Both jackets were made of closed-cell foam with the average cell size of around 50 μm. Apparently, their outer surface is bumpy but closed.

Table 2 presents a summary of the tensile properties of unaged and aged jackets, with aging conditions including 7 and 30 days at 136°C, and 7 and 60 days at 158°C. The jacket containing 33% foam in Cable 2 exhibits the tensile strength at break of 2360 psi, while the jacket with 25% foam in Cable 1 has a tensile strength at break of 2818 psi. As expected, the jacket with a higher foam content displays a lower tensile strength. The elongation at break of these two foamed jackets shows no difference, measuring over 200%.

To meet the minimum tensile strength requirement of 2500 psi for foamed PVDF jackets, it is important to determine the ideal foam level for PVDF 3120-50, ensuring that it does not exceed a certain percentage. Notably, the PVDF jackets have demonstrated excellent resistance at 158°C, as they retained their flexibility and tensile properties even after being subjected to various conditions, remaining almost unaged.

According to UL444 and UL1581, the 150°C-rated solid or foamed PVDF jackets must retain 50% tensile properties after aging at 158°C for 60 days. Based on these results, these PVDF jackets can be rated for a service temperature of 150°C.

Table 2. Summary of tensile properties and their retentions after aging

Aging Condition		Tensile Strength Retention (%)			Elongation Retention (%)		
		Cable 1	Cable 2	Cable 3	Cable 1	Cable 2	Cable 3
Unaged [a]		2818 ± 168	2360 ± 174	2924 ± 105	247 ± 27	268 ± 32	424 ± 7
days /136°C	7	100	103	109	105	122	95
	30	95	101	111	95	99	97
days /158°C	7	110	116	117	100	102	94
	60	112	122	114	95	107	99

[a] unaged values are properties including tensile strength (psi) and elongation at break (%).

3.2 Thermal Stability and Fire Resistance

As aforementioned, the thermal stability of PoE cables is especially important in high-power PoE applications. Higher current levels generate more heat, which can increase the risk of cable failure if the cable is not designed to handle it [5]. Thermal stability of jackets from cables listed at Table 1 and pristine PVDF 3120-50 resin was evaluated by TGA and the first-order derivative of weight loss (DTG). These thermograms as a function of temperature are shown in Figure 3. Figure 3a shows that the PVC jackets start to significantly degrade at about 250°C, while PVDF jackets shows higher thermal stability up to 350°C for the PVDF 3030-15 jacket, 420°C for Pellet 3120-50 and 435°C for foamed PVDF 3120-50 jackets. The slight degradation before 420°C for the foamed PVDF jackets, as compared to the pristine PVDF resin, could be due to the presence of residues of the foam agent after jacketing.

The primary degradation was also monitored by onset temperatures (T_{onset}), at which the samples effectively started to

lose their weight. As listed at Table 3, the T_{onset} of foamed PVDF 3120-50 jackets is 20°C higher than that of Pellet PVDF 3120-50. Relatively, the PVDF 3030-15 jacket shows a lower thermal stability with the T_{onset} of 356°C. The onset temperatures (< 300°C) of those two PVC jackets are much lower than those of the PVDF jackets. The jacket of Cable 2, which has 33% foaming, exhibits a slightly higher T_{onset} than the jacket on Cable 1, which has 25% foaming. This suggests that the increased foaming may help to delay the degradation process.

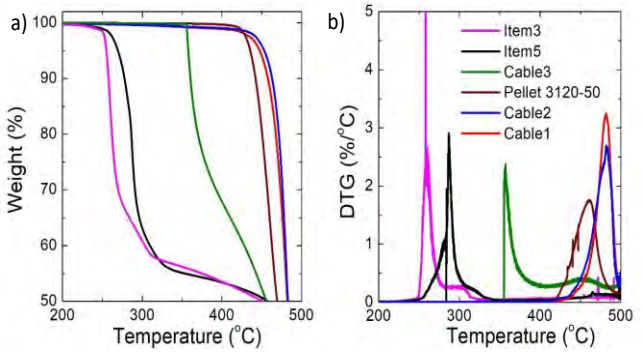


Figure 3. TGA (a) and DTG (b) curves for all jackets listed at Table 1 and cold-pressed sheets of pristine PVDF 3120-50 resin (labeled as Pellet 3120-50) at the heating rate of 15°C/min.

Table 3. Summary of onset temperatures from TGA and peak temperatures from DTG

Sample	Jacket	PVDF Grade	T_{onset} °C	T_{peak} °C
PVDF pellet	Pristine resin	3120-50	440	457
Cable 1	Foamed PVDF	3120-50	463	482
Cable 2	Foamed PVDF	3120-50	467	483
Cable 3	Solid PVDF	3030-15	356	357
Item 3	PVC	na	255	258
Item 5	PVC	na	279	288

The maximum peaks of DTG thermograms can provide valuable information about the thermal stability and degradation of a sample. As shown in Figure 3b and Table 3, the T_{peak} of the PVC jackets is under 300°C, while that of the PVDF 3030-15 jacket is located at 357°C, and that of Pellet 3120-50 reaches 457°C. Once foamed, the PVDF 3120-50 jackets show the peak temperatures of up to 482 °C. Clearly, the presence of foam enhances the thermal stability of the PVDF jackets.

To explore how foam affects the thermal stability of PVDF jackets, the samples in TGA pans were heated up to 465°C at a heating rate of 20°C/min under air flow, and subsequently rapidly cooled down before being analyzed using optical microscopy. As seen in Figure 4a, which exhibits similar TGA curves to those in Figure 3a, Pellet 3120-50 lost about 40 wt%, while the jacket of Cable 2 lost 6 wt% and that of Cable 1 lost 10%. It is evident that the thermal stability of the foamed PVDF jackets in Cables 1 and 2 has been significantly enhanced. The imagines depicted in Figure 4 demonstrate the development of black char on the sample surface, while the foam inside the two jackets creates an irregular surface, as evidenced in Figure 4c and 4d. It is believed that the foam can help prevent the weight loss by forming a physical barrier around or inside the sample, which limits the amount of air that can reach it or go into it. It can also reduce the release of gases (*e.g.*, hydrogen fluoride, HF) and ash that are produced. The jacket of 33% foam in Cable 2 shows higher thermal stability than that of 25% foam in Cable 1. This indicates that increasing the amount of foam enhances barrier effects, leading to greater thermal stability.

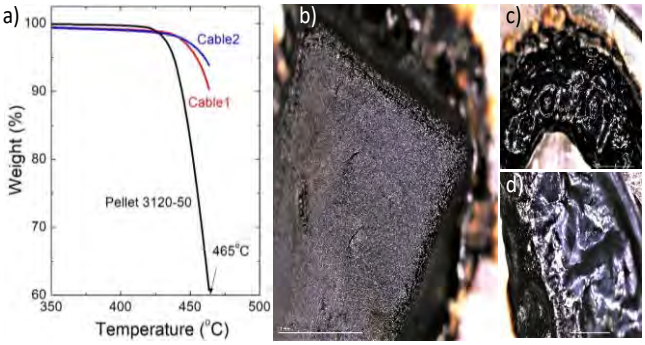


Figure 4. Thermal degradation of Pellet 3120-50 (b) and jackets from Cable 1 (c) and Cable 2 (d): (a) TGA curves at a heating rate of 20°C/min up to 465°C under air flow; (b, c, d) optical microscope images on TGA samples after TGA scans.

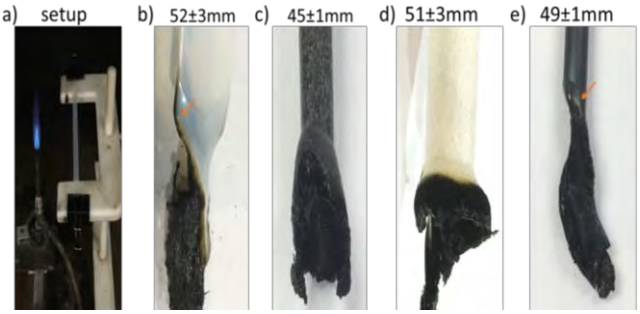


Figure 5. Photos from customized FT-2 burn tests: (a) setup; (b) PVDF 3120-50 sheet, c) foamed PVDF 3120-50 jacket from Cable 1, d) foamed PVDF 3120-50 jacket from Cable 2 and e) solid PVDF 3030-15 jacket from Cable 3. The numbers on the top are the maximum distance of flame spread. The arrows point at the melt flow traces.

Figure 5 depicts photos of a modified FT-2 burn test setup (Figure 5a) and burned ends of PVDF 3120-50 sheet and jackets for Cables 1, 2 and 3. All samples were extinguished after 15 seconds of being set on fire. Figure 5e shows that the PVDF 3030-15 jacket from Cable 3 produces a large chunk of dense char due to the presence of charring agents, while the PVDF 3120-50 samples show less char. At the edges of the burned frontlines, both the PVDF 3030-15 jacket and the PVDF 3120-50 sheet exhibit melt traces due to the heat from the burner and sample burning. In contrast, foamed PVDF 3120-50 jackets expand significantly and show no melt traces. These observations suggest that foamed jackets are more resistant to melting or possibly dripping, which can help contain the fire and prevent it from spreading. The expanded frontlines effectively increase the surface area of the foam, facilitating heat dissipation, and the expanded air pockets

within the foam act as insulators, slowing down heat transfer and limiting flame spread. This is evident from the reduced distance of flame spreads.

3.3 Non-isothermal Degradation Kinetics

In general, thermal degradation of polymeric jackets refers to the complex physiochemical processes occurred due to heat, including oxidation, hydrolysis, the loss of some additives via migration like plasticizers [10], the release of molecules decomposed like hydrochloride [12], etc. Activation energy associated with these degradation processes is often used to evaluate the thermal stability of jacket compounds. The higher the activation energy, the slower these degradation processes will proceed, since it will require a larger input of energy to overcome the energy barrier. With assumptions that these degradation processes obey the first-order Arrhenius kinetics, the activation energy can be determined by using the Ozawa-Flynn-Wall (OFW) method that may be written as follows:

$$\frac{d[\ln(\beta)]}{d(1/T)} = -\frac{1.052E_a}{R} \quad (1)$$

where β is the heating rate, E_a is the activation energy, R is the gas constant (= 8.314 J/(mol·K)) and T is the Kelvin temperature at a certain weight loss (conversion). By using a series of non-isothermal experiments on TGA at a fixed weight loss, the plot of $\ln\beta$ against $1/T$ gives a straight line with a slope of $1.052E_a/R$.

The overall kinetics of the degradation based on weight loss was investigated by TGA experiments at six hearing rates from 1 to 20°C/min, as shown in Figure 6. Figure 6a demonstrates that increases in the heating rate shift the curves to the higher temperature side before 40 wt%. Figure 6b illustrates that the plots of $\ln\beta$ as a function of 1/T form straight lines for a fixed weight loss, suggesting that the OFW method can be used to describe the observed thermal degradation. The activation energies were calculated for all jackets listed in Table 1 and Pellet 3120-50 at different weight losses in the rage of 5 to 30 wt%, as shown in Figure 7. The activation energy varies with the weight loss, indicating of the occurrence of complex mechanisms during the thermal degradation. The activation energy values for the 3030-15 jacket (180-200 kJ/mol) are consistent with previous reports [13], whereas the 3120-50 resin and foamed jackets exhibit higher Ea values (220-250 kJ/mol). In comparison to PVDF jackets, the PVC jackets demonstrate lower E_a values. This result can be attributed to the higher energy required for dehydrofluorination, which leads to the unzipping of H-F molecules along the PVDF chain, as compared to dehydrochlorination in PVC or the release of plasticizers. Note the bond dissociation energy of C-F is 514 kJ/mol, whereas that of C-Cl is 395 kJ/mol [14].

Regardless of calculation errors, it is notable that the activation energy values for two foamed PVDF jackets are comparable within the 5 to 30 wt% weight loss range, whereas Pellet 3120-50 shows higher E_a values. This variation suggests that different and simultaneous weight loss mechanisms may occur after the foaming process. Figure 4a shows that to achieve a weight loss of ≥ 5 wt%, the temperature of the foamed jackets needs to be 10 - 30°C higher than that of the pristine resin. This higher temperature facilitates the H-transfer that generates hydrogen fluoride (HF) and promotes release of HF and other volatile compounds, making these processes occur more readily. The presence of foam agent residues may also contribute to the lower E_a values observed for the foamed jackets.

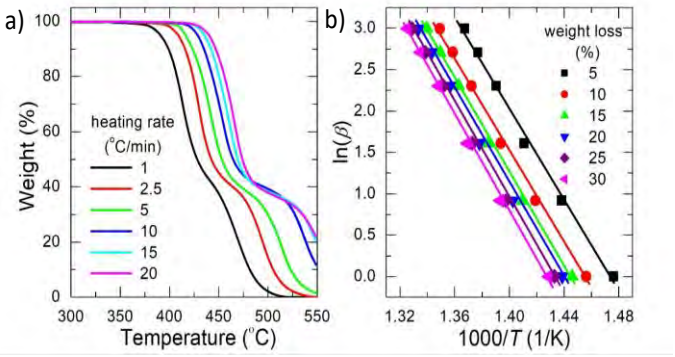


Figure 6. Pellet 3120-50: (a) TGA curves at 6 different heating rates; (b) Plots of $\ln\beta$ verse 1000/T at various fixed weight losses based on Eq.1. The R^2 values for the linear regression analysis here are greater than 0.99.

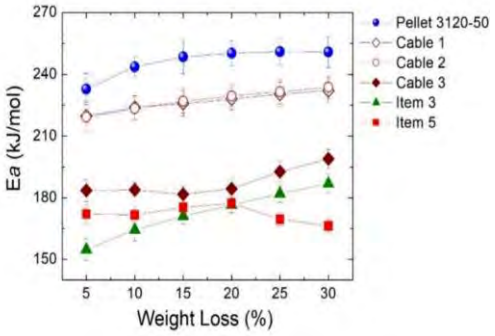


Figure 7. Activation Energy, E_a as a function of weight loss for all jackets and Pellet 3120-50.

The difference in E_a values observed between PVDF 3030-15 and 3120-50 could be primarily linked to their unique chemical composition, which can result in differing pyrolysis processes. This is supported by their respective mechanical properties, which highlight the contrast between the two materials. For instance, PVDF 3030-15 exhibits a tensile strength at break of about 2900 psi and a flexural modulus of around 44 Kpsi, whereas PVDF 3210-50 displays a tensile strength at break of approximately 4000 psi and flexural modulus of about 95 Kpsi.

3.4 Lifetime Estimation from Accelerated Isothermal Aging

In a previous study [10], we employed the Arrhenius-type model to estimate the lifetimes of five PVC jackets from PoE cables. The time needed to reach a fixed weight loss can be estimated through a simplified relation asserting that the natural log of the time, t is linearly proportional to the inverse of the isothermal temperature, T_{iso} in Kelvin [15], *i.e.*,

$$\ln(t) \propto 1/T_{iso} \quad (2)$$

By conducting a set of accelerated isothermal aging experiments and plotting $\ln(t)$ versus $1/T_{iso}$ for a fixed weight loss, a straight line with a slope of E_a/R can be obtained. With this information, it is possible to deduce the lifetime associated with the given weight loss at a lower temperature.

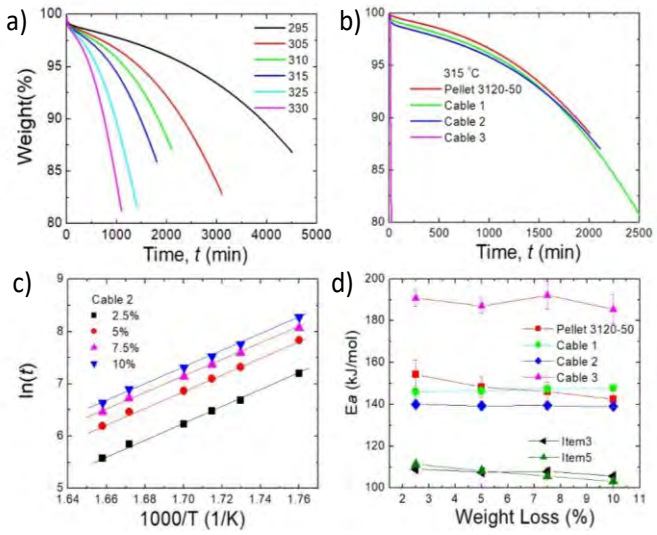


Figure 8. (a) Isothermal TGA curves for the foamed PVDF jacket in Cable 2 at temperature from 295 to 330°C; (b) Comparison of TGA curves form PVDF samples at isothermal 315°C; (c) plots of natural logarithm of isothermal time collected in (a) vs reciprocal Kelvin temperature at the weight loss from 2.5% to 10%; (d) activation Energy, E_a as a function of weight loss from 2.5% to 10% for all jackets listed in Table 1 and Pellet 3120-50.

Figure 8(a) demonstrates the TGA curves of the foamed PVDF jacket in Cable 2 under isothermal conditions. Figure 8(b) compares the TGA curves of PVDF samples at isothermal 315°C. All curves, including their derivative traces (not shown here), exhibits a single stage of weight loss during the observed period. The foamed Kynar 3120-50 jackets present slightly faster weight loss at the beginning of isothermal periods, potentially due to the presence of foam agent residues. After this initial weight loss, both jackets exhibit relatively slower weight loss as compared to the pristine resin, and the weight loss of the jacket with a higher foam level in Cable 2 is even slower than that of the one in Cable 1. The Kynar 3030-15 jacket shows the fastest weight rate at 315 °C.

Figure 8(c) shows the linear plots of ln(t) versus $1/T_{iso}$ using eq.2, based on the data presented in Figure 8(a). The slopes of these plots were used to calculate the apparent activation energies for four weight losses, as shown in in Figure 8(d). The PVDF 3030-15 jacket exhibits the highest E_a values at an isothermal temperature of 255 to 270°C, while the PVC jackets from Items 3 and 5 display the lowest E_a values in the temperature range of 144 to 191 °C [10]. Pellet 3120-50 and foamed jackets have E_a values (140–155 kJ/mol) between these ranges. These E_a values obtained from isothermal experiments were significantly higher than those (220-250 kJ/mol) from non-isothermal experiments. This difference is likely due to the variation in the temperature ranges for a fixed weight loss in these two distinct decomposition tests.

Figure 9 displays the relationship between isothermal temperatures and the duration necessary to achieve a 5% weight loss for the jackets listed in Table 1 and Pellet 3120-50. The data clearly illustrate that thermal stability of PVC jackets is considerably lower than that of PVDF samples. The PVDF 3030-15 jacket requires much less time than the PVDF 3120-50 samples to achieve a 5% weight loss at the same temperature. Notably, the data points for all of the PVDF 3120-50 samples are almost identical. However, as shown in Figure 9b, the data point at 330°C for Pellet PVDF 3120-50 deviates from the linear trend observed between 295 to 325°C, whereas the foamed jackets exhibit a consistent trend. Similarly, for the PVDF 3030-15 jacket, data points at or above 272.5°C deviate from the linear trend observed between 255 to 270°C. These deviations within specific temperature ranges may be attributed to temperature-dependent degradation processes [16]. At higher temperatures, multiple degradation pathways, such as chain unzipping, dehydrofluorination, and pyrolysis, can occur simultaneously, each with a different activation energy requirement. The combined effect of these processes can result in complex temperature-dependent behavior.

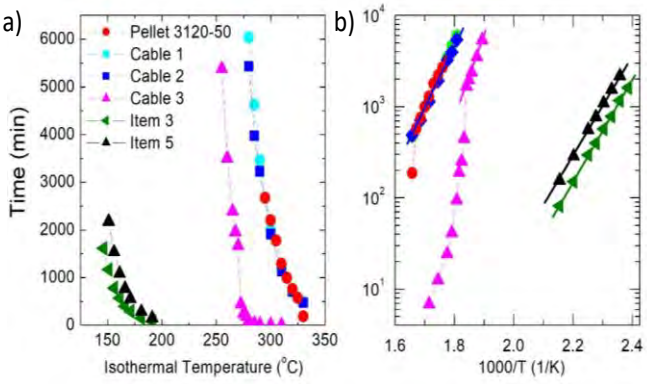


Figure 9. Time needed for a 5% weight loss at isothermal temperatures for the jackets listed in Table 1 and Pellet PVDF 3120-50: time against temperature (a) and log(time) versus $1/T_{iso}$ (b).

The ASTM E1877 guidelines allow for the use of data collected from non-isothermal experiments, as shown in Figure 6, to estimate the lifetime of polymers under different failure temperatures [17]. However, it was observed in Figures 3, 4 and 6 that the temperatures at ≥ 5 wt% are greater than 390°C for Pellet PVDF and 400°C for foamed PVDF jackets. Figure 8 suggests that complex chemical reactions could occur in the PVDF samples, making such an estimation difficult. Therefore, this study utilized accelerated isothermal experiments at relatively much lower temperatures to estimate lifetime of PVDF samples.

Figure 10 shows the predicated lifetime for the foamed jacket from Cable 1 with varying weight losses (Figure 10a), as well as for the jackets listed in Table 1 and Pellet 3120-50 at a 5% weight loss (Figure 10b). The results indicate that the predicted lifetime increases with the increase of weight loss, while increasing aging temperature has the opposite effect. Notably, all PVDF samples exhibit a predicted lifetime of over 100 years at 150°C, which is the maximum continuous operating temperature rating as defined by UL444. The lifetime of the foamed jacket in Cable 1 is almost identical to that of the PVDF 3210-50, whereas their lifetime is 2-4 times that of the foamed jacket in Cable 2. The PVDF 3030-15 jacket in Cable 3 exhibits the highest predicted lifetime for 5% weight loss. In contrast, the PVC jackets in Items 3 and 5 are predicted to last for less than 1 year at 90°C, indicating their inferior thermal stability as compared to the PVDF jackets.

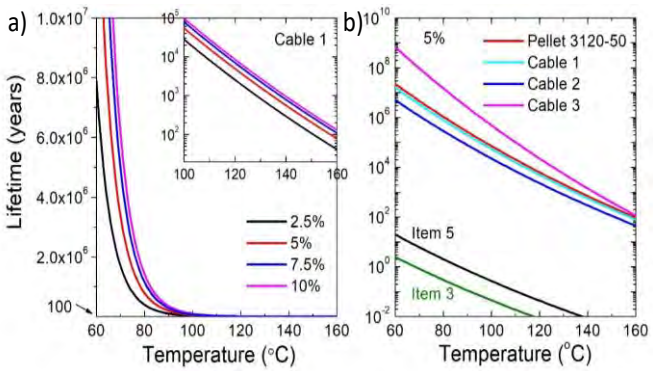


Figure 10. Predicated lifetime in years as a function of aging temperature (a) for the foamed jacket from Cable 1 at weight loss from 2.5% to 10%, and (B) for the jackets listed in Table 1 and Pellet 3120-50 resin at 5% weight loss.

The use of this accelerated isothermal aging methodology to predict polymer lifetime can raise some concerns. One major concern is that degradation processes may involve multiple chemistries with differing kinetics or activation energies across a wide range of aging temperatures, resulting in a plot of eq.2 that displays multiple stages [18]. To address this, it is recommended to select the range of elevated temperatures as close as possible to the predicted temperature, and a single chemistry may be empirically justified if the plot shows a single slope. Another concern is that the elevated isothermal temperatures may be chosen to be higher than their melting point of semi-crystalline polymers, which can cause significant changes in their physical status compared to that at lower application temperatures. The crystalline regions of a semi-crystalline polymer promote improved chain packing, resulting in fewer defects and voids and reduced chain mobility, making the polymer less susceptible to thermal degradation. Moreover, the crystalline lamellar structure in the polymer serves as a physical barrier against oxygen or other chemic intrusions, providing further protection against thermal decomposition. When the isothermal temperature exceeds the polymer's melting point (T_m), only amorphous phases are present, which have higher chain mobility and are more prone to thermal degradation. This can result in increased chain scission and degradation rates, potentially resulting in an underestimation of the polymer's lifetime when calculated using this method at temperatures lower than T_m. In the case of these PVDF samples, which display a melting point of 162-164°C and a crystallinity of about 30%, the isothermal temperatures employed during testing were significantly higher than T_m, suggesting that their lifespan at 160°C or below may have been underestimated.

3.5 Electrical Performance of Cables upon Aging

In our previous study [10], we developed a method to investigate effects of thermal aging on performance of PoE cables and found a good association of the decay of electrical properties of these cables, i.e., crosstalk, with weight losses of their PVC jackets. In the current work, we followed the same method and conducted aging tests on Cables 1,2, and 3 at 136°C compared to Items 3 and 5 we reported in 2022 [10].

Figures 11a and 11b illustrate the changes in the worst-case margin of Near-end Crosstalk (NEXT) from the original electrical measurement taken at time zero. It should be noted that the worst cases may occur between different pairs over time. The results indicate that after a period of aging, the margin of NEXT for Item 3 (Cat5e) and Item 5 (Cat6A) significantly decreased. This trend implies that the near-end crosstalk increased with aging since a smaller NEXT loss value corresponded to higher crosstalk. Figure 10c demonstrates a similar trend in the weight loss of the PVC jackets from these two cables, while Figure 10d shows that the shrinkage of their PVC jackets increases, especially during the first period of aging. In contrast, the PVDF jackets displayed negligible weight loss and only 1-2% shrinkage in their length due to their thermal stability. Consequently, their cables demonstrated much smaller changes in NEXT margin, indicating more stable electrical performance.

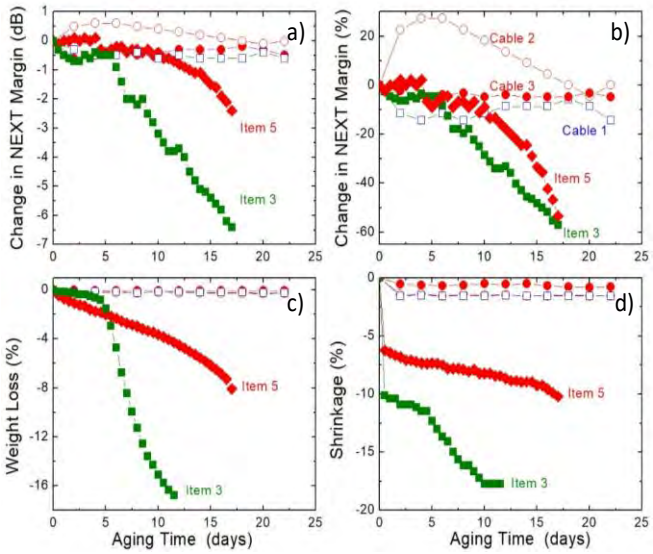


Figure 11. Effects of isothermal aging on Cables and jackets at 136°C: the change (a) and the percent change (b) in the worst-case margin of NEXT for cables, and weight loss (c) and length shrinkage (d) for jackets.

3.6 Discussion

In our previous study [10], we discovered that even PVC jackets rated 75°C or higher temperature, such as Items 3 (105°C-rated), had lifetimes of less than 10 years when exposed to 75°C. Despite meeting the standards for temperature ration of 75°C, 90°C or even 105°C UL 444 (Table 10), these cables were estimated to only last for a maximum of 6 years at 75°C and less than half of a year at 100°C. This falls well short of the expected service time of 20 years in the industry. Therefore, it is important to be cautious about temperature ratings for PVC jackets in PoE cables, as overrating the temperature could pose a real risk for cable design, selection, installation, and application.

In response to concerns about negative impact of thermal aging on PVC jackets in PoE cables that require high power transfer, we have introduced foamed PVDF jackets. Our findings on kinetics of non-isothermal degradation have shown that PVDF exhibited superior thermal stability compared to PVC, and the foam helped shift the degradation to higher temperature by facilitating barrier and char formation. Based on our analysis of the kinetics of isothermal degradation, we estimated that PVDF jackets has a lifetime of over 100 years at 150°C. While the foam showed no

effects on the lifetime, the residue of the foam agent may slightly decrease the lifetime of the foamed jackets.

The deterioration of electrical properties in PoE cables, specifically near-end crosstalk (NEXT), ws believed to be caused by the weight loss of PVC jackets due to heat aging [10]. This process can lead to loss of HCl, formation of conjugated double bonds, and the evaporation and degradation of plasticizers and additives, causing the jackets to shrink and harden. Consequently, the jackets can constrict around the conductor pairs, exacerbating crosstalk issues. PVDF jackets are more thermally stable and exhibit significantly smaller changes in NEXT margin, indicating more consistent electrical performance over time. Moreover, using foamed PVDF could effectively limit flame spread during burning, which may enhance the fire safety of PoE cables. Ongoing investigations are being conducted.

4. Conclusions

In summary, this study highlights the advantage of using chemically foamed PVDF jackets for their 4PPoE cables to address aging challenges caused by cable heating. The results demonstrate that foamed PVDF jackets exhibited excellent thermal stability, mechanical properties, and electrical performance, while also improving fire safety and reducing jacket weight. The foam effectively increased flexibility and raised the degradation temperature by forming a physical barrier to delay the release of volatile compound, and limit flame spread by expanding foam cells to reduce melting and dripping during combustion. Additionally, the study found that the lifespan of foamed PVDF jackets was estimated to be over 100 years when used continuously at 150°C, compared to some PVC jackets with a shorter lifespan of less than 10 years even at a lower temperature of 75°C. The electrical performance of the 4PPoE cables with foamed PVDF jackets was found to be stable over at least 22 days at 136°C, while those with PVC jackets exhibited a significant increase in near-end crosstalk by over 50% upon aging for 17 days at the sample temperature.

Overall, foamed PVDF jackets are ideal for 4PPoE cables that are required to carry high levels of power, with temperature rating up to 150°C and a lifespan of over 100 years. They offer improved flexibility, reduced weight, enhanced fire safety, and stable electrical performance.

5. Acknowledgments

The authors would like to thank Rodney Kron and McIntire Frank for their help with chamber aging setup, and Walters Scott for TGA measurements and Debra Pirritano for electrical performance testing, dimension measurements and oven aging testing.

6. References

[1] G. Mendelson, "All You Need to Know About Power over Ethernet (PoE) and the IEEE 802.3af Standard," White Paper, PowerDsine, 2004.

[2] M. Eisen, "Introduction to PoE and the IEEE 802.3af and 802.3at Standards," 29 10 2009. [Online]. Available: https://www.ieee.li/pdf/viewgraphs/introduction_to_poe_802.3af_802.3at.pdf. [Accessed 8 8 2022].

[3] CISCO, "What Is Power over Ethernet (PoE)?" [Online]. Available: https://www.cisco.com/c/en/us/solutions/enterprise-networks/what-is-power-over-ethernet.html. [Accessed 8 8 2022].

[4] A. V. Sakthivel, "Power over Ethernet Technology to Power a 5W Standard LED," www.researchgate.net, 2017.

[5] R. Ivans, "Power over LAN Cable - Keeping pace with this Key Powering Strategy," in Proceedings of the 65th International Wire & Cable Symposium, Providence, 2016.

[6] R. Speer, S. Lee, R. Ozisik and C. Glew, "The Future of Materials Selection Criteria for Power over Local Area Networks," in Proceedings of the 65th International Wire & Cable Symposium, Providence, 2016.

[7] B. Marchant, "Impact of Installation Geometry on Temperature Rise due to Power over Ethernet," in Proceedings of the 65th International Wire & Cable Symposium, Providence, 2016.

[8] W. Hopkinson, "Evolving Methods of Evaluating Cable Heating," in Proceedings of the 65th International Wire & Cable Symposium, Providence, 2016.

[9] T. Lanoe, C. McNutt and A. Sekhavat, "Four Pair Power over Ethernet (4PPoE) Deployment: Standards, Performance, and Challenges," in Proceedings of the 66th International Wire & Cable Symposium, Orlando, 2017.

[10] B. Xu, C. McNutt, B. Gebs and A. Sekhavat, "Investigation of Thermal Aging Challenges for Power-over-Ethernet Cables with Polyvinyl Chloride Jackets," in Proceedings of the 71st International Wire & Cable Symposium, Providence, 2022.

[11] C. M. Glew and C. A. Glew, "The Effects of Electrical Properties in Power over Ethernet Cables as a Result of Thermocycling Materials," in Proceedings of the 68th International Wire & Cable Symposium, Charlotte, 2019.

[12] V. V. Krongauz and Y. P. Lee, "Kinetics of Thermal Degradation of Poly(Vinyl Chloride): Thermogravimetry and Spectroscopy," Journal of Thermal Analysis and Calorimetry, vol. 106, no. 1, pp. 139-149, 2011.

[13] A. Silva, M. Contreras, C. Nascimento and M. Costa, "Kinetics of thermal degradation and lifetime study of poly(vinylidene fluoride) (PVDF) subjected to bioethanol fuel accelerated aging," Heliyon, vol. 6, pp. e04573, 2020.

[14] Y. Luo, Handbook of Bond Dissociation Energies in Organic Compounds, Boca Raton: CRC Press, 2002.

[15] L. Abate, I. Blanco, O. Motta, A. Pollicino and A. Recca, "The Isothermal Degradation of Some Polyetherketones: a Comparative Kinetic Study Between Long-term and Short-term Experiments," Polymer Degradation and Stability, vol. 75, no. 3, pp. 465-471, 2002.

[16] C. L. Beyler and M. M. Hirschler, "Thermal Decomposition of Polymer," in Polymer Green Flame Retardants, Springer, 2014, pp. 110-131.

[17] "ASTM E1877, Standard practice for calculating thermal endurance of materials from thermogravimetric decomposition data," in Annu. Book ASTM Stand. 2009, pp. 1-6.

[18] I. Blanco, "Lifetime Prediction of Polymers: to Bet, or Not to Bet - Is This the Question?" Materials, vol. 11, no. 8, pp. 1383-1396, 2018.

7. Authors

Superior Essex International LP – Communications
Production Development Center
3600 Cobb International Blvd, Suite 400
Kennesaw, Georgia 30152

Arkema Inc.
900 First Avenue
King of Prussia, PA 19406



Bo Xu is a Materials Engineer at Superior Essex International Communications. He earned a Ph.D. in Polymer Engineering from Georgia Institute of Technology in 2010, and a M.S. in Material Science at Zhejiang University in 2004. Bo Xu has an extensive background in polymers, with over 30 scientific and conference papers published, and he holds 6 patents. Prior to joining Superior Essex in 2017, he worked as a Packaging Analytical Scientist at the Coca-Cola Company.



Christopher McNutt is Director of Product Development for Superior Essex. He is listed as the inventor or co-inventor on numerous industry patents. He holds a B. S. degree in Chemical Engineering from the University of Tennessee.



Amir Sekhavat is Global Director of Product Management and Enterprise Market Development at Superior Essex. Amir has twenty years of experience in the telecommunications industry, specializing in communications cable products. Amir has published numerous articles and is listed as the inventor or co-inventor of several patents related to data cable performance and connectivity. Amir is currently chairman of CCCA datacenter subcommittee.



James Henry joined Arkema located at the Research Center in King of Prussia, PA in January 2001 and is a Principal Engineer focusing on R&D in industrial markets including Wire & Cable. Currently, Jim is the R&D Engineering Operations Manager in the High Performance Polymers NA Division of Arkema. James received a Bachelor's Degree in Chemical Engineering and a Master's Degree in Plastics Engineering from the University of Massachusetts.

Materials Considerations for Laser Printed Jacket Solutions

Brian G. Risch and Chase Erford
*Prysmian Cables and Systems
Telecommunications Americas
P.O. Box 39
Claremont, NC 28610-0039

1-828-459-8435 · brian.risch@prysmiangroup.com

Abstract

Laser marking of materials is already a widely adopted global technology. Application of laser marking for outside plant cable jackets provides some added and unique challenges for this technology requiring proper engineering of both jacket materials as well as laser printing technology. The typical carbon black UV stabilization package contained in polyethylene jackets for telecom cables can create difficulties in achieving good laser print quality, and a reduction of carbon black in cable jackets requires specially formulated, alternative UV stabilization packages. As the carbon black UV stabilization is a proven solution with decades of proven service life, alternative solutions must be well tested. Material and process solutions for laser marking of jackets are evaluated with results presented on long term reliability of materials, print quality, print durability, and overall impact on product capabilities.

Keywords: fiber optic cable, laser marking, jacket, polyethylene, ICEA-640, weathering, reliability, UV.

1. Introduction

Laser marking of materials is already a widely adapted global technology. Until recently the economics and available technology have limited widespread adoption for cable applications. Improvements in raw materials and process technology as well as evolution of cable standards have recently made laser marking of jackets for cable jackets more attractive.

A number of factors make laser making of cables attractive. These include the ability to make very fine and high-resolution print on small cables, reduced compressive forces on sensitive cable designs relative to hot-foil indent printing, elimination of solvents used in inkjet printing, improvements in print durability, and reduction in overall operational costs due to reduced consumable and maintenance costs. Some material limitations, however, can be present when moving towards a laser markable solution. A limitation for cables deployed in environments where exposure to UV radiation is likely is a potential sacrifice of UV weathering performance.[1] Typically, materials with the minimum 2.35% level of carbon black loading previously required by ICEA-640[2] can be difficult to print without the addition of relatively high loading of special additives in the cable jacket. Additionally, the optical energy absorption of cables with high loading of carbon black can result in limitations for linespeeds where print is clearly legible.

New developments in jacket materials involving both UV stabilization and jacket print quality have resulted in solutions that can provide jackets that have a high level of UV stability combined with the ability for high quality laser marking at high speed. Laser marking also allows much greater flexibility in jacket print than conventional printing technologies allowing for easier implementation of more complicated ID codes on cables. Relevant cable standards are also being updated to cover the added considerations required to implement this class of jacketing materials.

2. Experimental

2.1 Updated ICEA 640 Standard

A new revision of ICEA-640 was issued on May 5, 2023.[3] With this new revision of the specification, allowances were made for the use of polyethylene cable jackets with a carbon black level below the previously required loading of 2.35%. Added long-term UV weathering test requirements according to either ASTM G 155, cycle 1 or ASTM G 154 cycle 1 with an exposure time of 4000h are now specified for jacket compounds containing less than 2.35% carbon black. After the UV weathering, the requirements for both jacket tensile strength retention and elongation retention are a minimum of 80%.[3] Details of the two allowable weathering test variants are outlined in Table 1. Comparative spectral irradiance distributions and that for natural sunlight are shown in Figure 1.

Table 1. Details of Weathering Test Variants.

Test Variant	ASTM G 155, Cycle 1	ASTM G 154 Cycle 1
Irradiation Source	Xenon Arc with Daylight Filter	Fluorescent UVA-340 Lamp
Irradiance	0.35 W/(m^2· nm) @ 340 nm	0.89 W/m^2/nm @ 340 nm
Exposure Cycle	102 min light at 63°C black panel temperature 18 min light and water spray	8 h UV at 60°C Black Panel temperature; 4 h Condensation at 50°C Black Panel Temperature
Spectral Distribution	Broad spectrum simulating solar radiation distribution	Narrower radiation spectrum with enhanced UV in the 340nm region

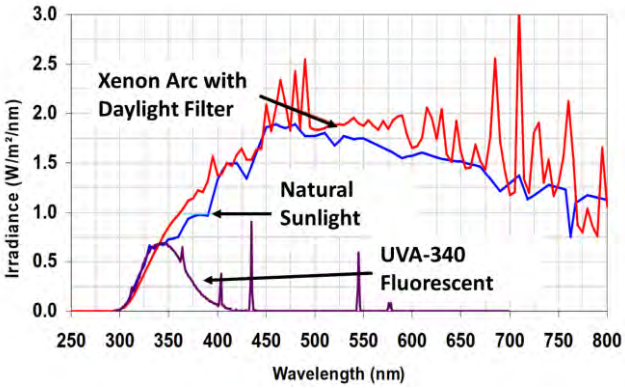


Figure 1: Comparison of Natural Sunlight Spectral Distribution, Filtered Xenon Arc Spectral Distribution, and UVA-340 Spectral Distribution from a Fluorescent Source.

Correlation of accelerated UV weathering tests to natural sunlight exposure is difficult due to many factors. These factors include variability of relative response with different compounds due to formulation differences, variability in the actual UV exposure profile due to geographical and climatological differences[4], other differences in rainfall or heat exposure, and variability in cable deployment. Of the two options for UV weathering, ASTM G 155, Cycle 1 is the easiest to develop correlations to natural UV exposure as the test is designed to simulate the spectral distribution of natural sunlight. Calculations can be made based on total UV radiation dose during testing vs. natural UV exposure. The dose is the radiation energy incident over a specific area for a given period of time. It is expressed either in W*s /m2, Joule/m2 or very often in Langley (Ly).

1 Ly = 1 cal/cm2 = 4.184 E4 Joule/m2 (1)

Standard Xenon Arc weathering according to ASTM G155 Cycle 1 produces 2800 KJ/m^2/hour or about 66 KiloLangleys per 1000h of testing. Natural sunlight annual UV dose is constantly monitored across the globe and representative data is summarized in Table 2[4,5,6].

Table 2. Typical Annual UV Dose by Country/Region.

Country	UV Dose KLy	Country	UV Dose KLy
Australia	180	Northern Europe	80
Brazil	120	Saudi Arabia	200
Canada	100	South Africa	160
China	140	South Europe	140
North Africa	200	Scandinavia	70
India	180	USA	
Italy	120	North	100
Japan	100	Arizona	180
		Florida	140
		Central US	120

Acceleration factors relative to deployment environment can be calculated based on UV dose, but actual acceleration factors can vary as a function of material formulation and other factors. An illustration of the variability in correlation between natural weathering and xenon arc weathering is illustrated in Figure 2. In this figure correlations of multiple materials with different stabilization schemes from multiple studies[7,8,9] are combined into a common graph. Results are based on time to failure. An average acceleration factor of about 4 is observed for the average of this data relative to natural South Florida sunlight exposure which agrees well with the acceleration factor based on UV dose. It is quite evident, however, that each compound may have a different response.

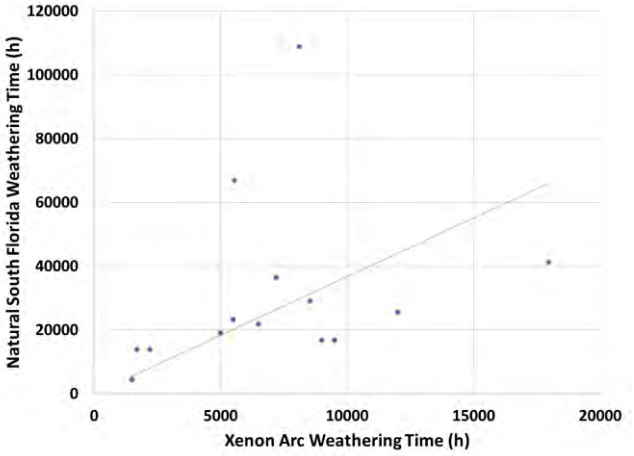


Figure 2: Correlation Between Natural South Florida Sunlight Exposure and Xenon Arc Weathering According to ASTM G155 Cycle 1.

2.2 Print Durability

Print durability was tested according to IEC 60794-1-21, Method E2B with dry and wet felt and a 450g weight for 5 cycles. An added test where the felt was replaced with a Scotch Brite® scouring pad was added as a more severe test.

2.3 Jacket Materials

Two grades of laser printable HDPE compounds with reduced carbon black content were evaluated in this study and compared to a low shrinkage HDPE compound that is in commonly used in the industry. Details of key physical properties are summarized in Table 3.

Table 3. Summary of Jacket Material Properties.

Material Property	Control Low Shrinkage HDPE	Laser HDPE Compound 1	Laser HDPE Compound 2
Density	0.954 g/cc Compound 0.942 g/cc Base Material	0.942 g/cc	0.947 g/cc
Melt Flow Index (190 °C/2,16 kg)	1.7 g/10min	1.7 g/10min	1.2 g/10min

2.4 Jacket Material Testing

The cable jacket materials were tested for jacket shrinkage, tensile and elongation, as well as environmental stress crack resistance according to methods described in ICEA-640. Jacket tensile testing was completed on an Instron Model 5567 with a long length extensometer and a crosshead speed of 2 inches per minute according to FOTP-89.

2.5 Laser Marking Equipment

Laser marking systems from multiple vendors were used for initial evaluation of the compounds used in this study. For cable trials a 50W fiber laser marking system was used. Typical laser parameters for the cable trials were 40 kHz pulse frequency, 10-20 µs pulse length, and a marking scan speed of 5-10 m/s. The right combination of these three parameters is essential for controlling contrast and image quality. An image of a laser marking system and the fume extraction system on the line is shown in Figure 3. An image of actual laser printing while manufacturing a cable is shown in Figure 4.



Figure 3: Fiber laser unit and fume extraction device.

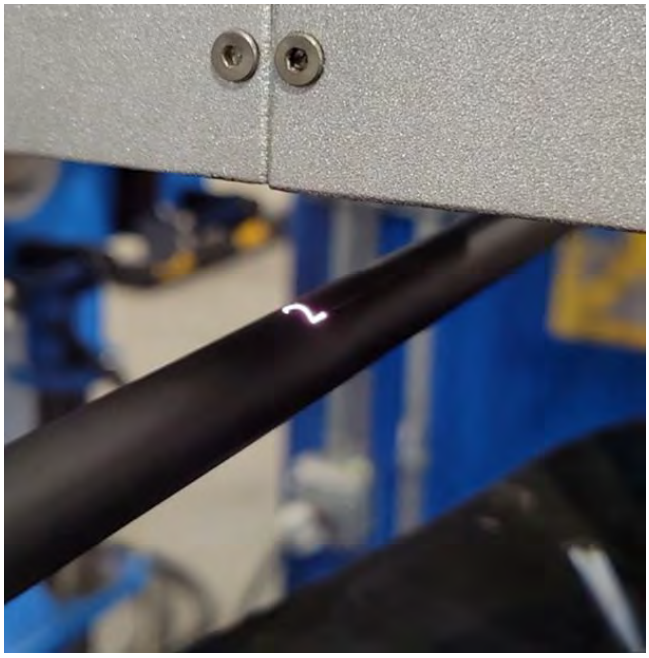


Figure 4: Laser marking on a sample cable during cabling trial.

3. Results and Discussion

Both laser printable materials tested could be easily marked at linespeeds of up to 100m/minute. Figure 5 illustrates representative print quality with increasing linespeed. Figure 6 illustrates a summary of print durability testing. Marking quality was good and showed high clarity and durability.



Figure 5: Laser Print Examples as a Function of Linespeed.



Figure 6: Print Durability Testing as Prescribed in GR-20 Using Felt (Left) and a more aggressive Test Using a Scotch Brite® Abrasive Pad.



Figure 7: An Added Example of Laser Marked Jacket Print on a Small Diameter Cable.

Environmental stress crack resistance of both jacket compounds was excellent. Materials were tested according to ASTM D1693 with 3mm thick tabs in a 10% Igepal solution at 50°C with results surpassing 1000h with no cracks. Similar thermal stress crack resistance testing was also completed at temperatures of 70°C, 85°C, and 100°C to 1000h also with no cracks. An image of both compounds after testing is shown in Figure 8 and results are summarized in Table 4. With these test results under such aggressive test conditions, the excellent stress crack resistance of both compounds is clear.



Figure 8: An Image of Test Specimens of Both Compounds After Successfully Completing Stress Crack Testing.

Table 4. Summary of Stress Crack Resistance.

	Pass/Fail	1000 hr.			
		50°C # failures	70°C # failures	85°C # failures	100°C # failures
HDPE Compound 1	PASS	0/10	0/10	0/10	0/10
HDPE Compound 2	PASS	0/10	0/10	0/10	0/10

Aged and unaged tensile strength and elongation of both jacket materials were conformant to ICEA-640 requirements. Aging was at 110°C for 7 days. Results are summarized in Table 5, and stress-strain curves are shown in Figure 9.

Table 5. Cable Jacket Tensile and Elongation Test Results.

Compound Desingation	Aged/ unaged	Average Yield Strength (psi)	Yield Strength Retention %	Average Elongation (%)	Elongation Retention %	Pass/Fail
Low Shrinkage HDPE Control 30MPM	unaged	2815		677		PASS
	aged	2781	99%	717	106%	
Laser HDPE Compound 1 60MPM	unaged	2870		646		PASS
	aged	2682	93%	539	83%	
Laser HDPE Compound 2 50MPM	unaged	2905		734		PASS
	aged	2919	100%	843	115%	
Laser HDPE Compound 2 100MPM	unaged	2813		734		PASS
	aged	2919	104%	729	99%	
ICEA 640 Requirement: The jacket shall retain a minimum of 75% of its unaged tensile strength and elongation values.						

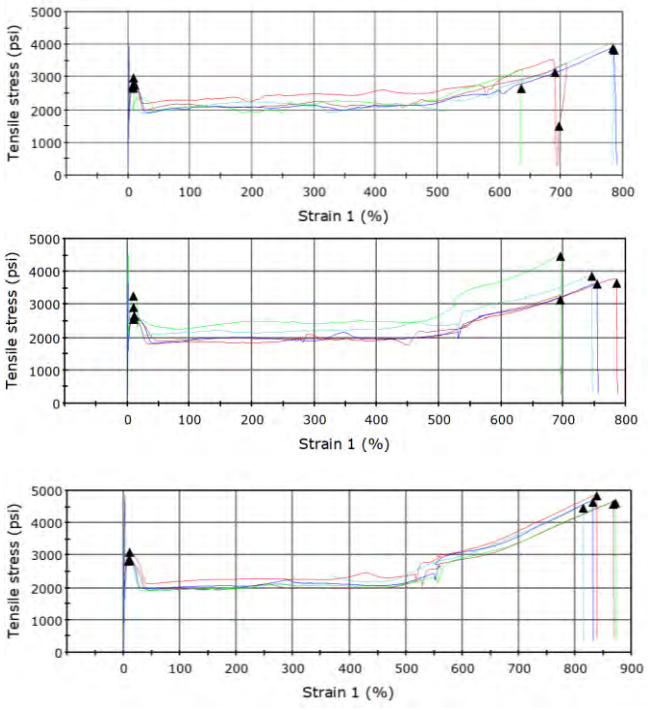


Figure 9: Representative Stress-Strain Curves from Tensile Testing of Control Low Shrinkage Fully Compounded HDPE, Laser HDPE Compound #1 (Middle), and Laser HDPE Compound #2 (Bottom).

Jacket shrinkage test results are summarized in Table 7. Results were easily conformant to ICEA-640 requirements and with little impact evident from increasing linespeed. Results were also very similar to those measured on a fully compounded low shrinkage HDPE compound commonly used in the industry.

Table 6. Cable Jacket Shrinkage Test Results.

Cable ID	With Core* Avg % Shrinkage	Without Core Avg % Shrinkage	Pass/Fail
Low Shrinkage HDPE Control 30mpm	1.6	2.7	PASS
Laser HDPE Compound 1 Shrinkage 60mpm	2.2	2.8	PASS
Laser HDPE Compound 2 Shrinkage 40mpm	2.0	2.8	PASS
Laser HDPE Compound 2 Shrinkage 60mpm	1.5	2.6	PASS
Laser HDPE Compound 2 Shrinkage 80mpm	2.0	2.2	PASS
Laser HDPE Compound 2 Shrinkage 100mpm	1.9	2.1	PASS
Requirement: GR-20 / ICEA 640	5max	5max	
* With Core is not required but provided for additional information.			

Long term UV weathering data is provided in Table 7 and Figure 10. The test results demonstrate that properly stabilized laser markable jacket compounds can meet the new ICEA-640 UV weathering requirements. Laser compound 1 showed conformance to the new ICEA-640 requirements and results nearly more simillar to those for the low shrinkage compound with fully compounded carbon black at 2.5%. Laser compound 2 showed conformance but more marginal performance which was closer to the acceptance limits for the specification. The reduction in properties seen in Laser compound 2 may be partially due to other changes in the materials observed during some heat aging experiments and sample preparation. Further long-term aging tests are ongoing to further understand if reductions in mechanical properties stabilize with time or continue.

Table 7. Long Term UV Weathering Test Results.

	Control HDPE Compound	Laser HDPE Compound 1	Laser HDPE Compound 2
Weather (Sunlight) Resistance -720 hours			
Tensile Strength Retention (%)	100%	100%	100%
Elongation Retention (%)	100%	100%	100%
Weather (Sunlight) Resistance -720 hours			
Tensile Strength Retention (%)	101%	97%	90%
Elongation Retention (%)	101%	88%	89%
Weather (Sunlight) Resistance -1000 hours			
Tensile Strength Retention (%)		91%	85%
Elongation Retention (%)		101%	94%
Weather (Sunlight) Resistance -2000 hours			
Tensile Strength Retention (%)		94%	78%
Elongation Retention (%)		100%	87%
Weather (Sunlight) Resistance -4000 hours			
Tensile Strength Retention (%)	88%	85%	82%
Elongation Retention (%)	101%	87%	84%

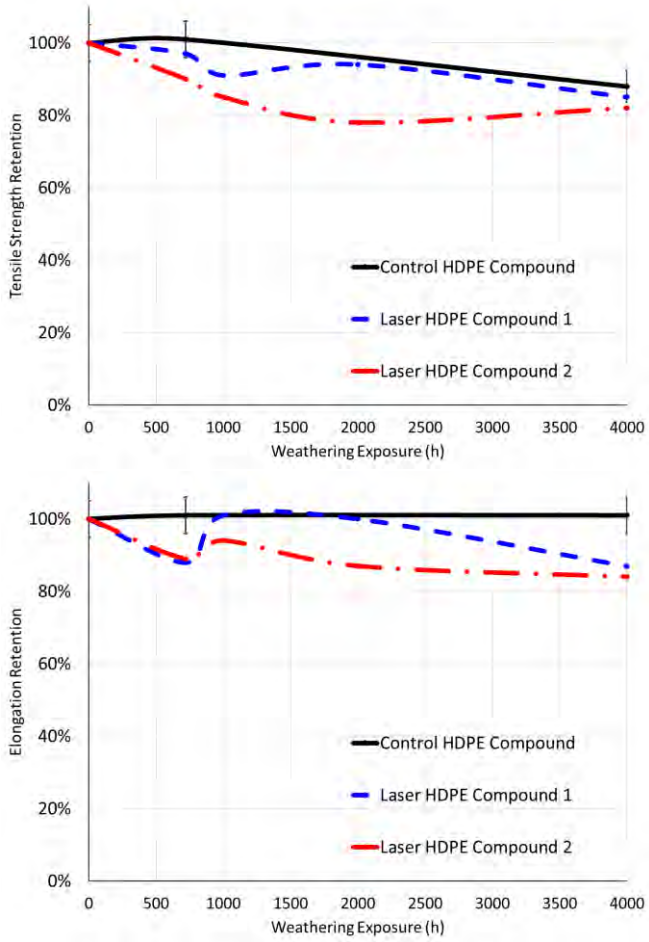


Figure 10: Graphs of Tensile Strength Retention (Top) and Elongation Retention (Bottom) as a function of Long-term UV Weathering.

4. Conclusions

Two laser markable HDPE jacket compounds were evaluated for Laser marking performance and against new ICEA-640 standards for jacket compounds with reduced carbon black including long-term UV weathering. Print marking and durability were shown to be excellent for both compounds. Additionally, environmental stress crack resistance of the new compounds was shown to be excellent. Mechanical properties and shrinkage of extruded jackets were shown to be essentially identical to currently used, low-shrinkage jacket compounds already in use in the market. Shrinkage test results of both laser markable compounds were also shown to easily pass requirements and show little sensitivity to linespeed in the range of linespeeds investigated. It was shown that conformance to new, long-term UV weathering requirements in ICEA-640 is possible with properly formulated and stabilized laser markable jacket compounds. Additionally, longer-term aging beyond the required 4000h testing is ongoing to better understand the weathering performance of these new compounds.

5. Acknowledgements

I would like to acknowledge the assistance of Tina Filip in performing physical testing of the jacket samples. I would also like to thank Brian Hollar for his assistance in running cable trials with the laser markable jacket compounds. I would also like the help of the Prysmian Willimantic test labs in obtaining UV weatherometer data.

6. References

[1] T. Geussens, D_C Lee, and M. Esseghir, "Development of a New Jacket Material for Fiber Optic Mini and Microcables", Proceedings of the 66th International Wire and Cable Symposium, October 2017.

[2] ANSI/ICEA S-87-640-2011 STANDARD FOR OPTICAL FIBER OUTSIDE PLANT COMMUNICATIONS CABLE-5th Ed., (ICEA) Jan. 17, 2012.

[3] ANSI/ICEA S-87-640-2023 STANDARD FOR OPTICAL FIBER OUTSIDE PLANT COMMUNICATIONS CABLE-5th Ed., (ICEA) May 5, 2023.

[4] W. DeWitt, S. Neogi, B. G. Risch, G. Karady, J. Madrid, P. Coat, and D. Ammons "High Voltage ADSS Reliability Modeling: Environmental and Climatological Effects on Advanced Jacket Material Selection", Proceedings of the 49th International Wire and Cable Symposium, November 2000, pp.337-346.

[5] De Jong, B., *Net Radiation Received by a Horizontal Surface at the Earth*, Delft University Press, 1973.

[6] FAO-Environmental and Natural Resources Service (SRDN) Agrometerology Group.

[7] A. R. George, "A New Spectroscopic Method for the Non-Destructive Characterization of Weathering Damage in Plastics", M.S. Dissertation, Brigham Young University, 2006.

[8] Gijsman, P., J. Hennekens, and K. Janssen. "Comparison of UV Degradation of Polyethylene in Accelerated Test and Sunlight." In Polymer Durability: Degradation, Stabilization and Lifetime Prediction: Advances in Chemistry Series No. 249, edited by R. L. Clough, N. C. Billingham, and K. T. Gillen, Washington DC: American Chemical Society, 1996, pp. 621-636.

[9] M. Frigione A. Rodríguez-Prieto, "Can Accelerated Aging Procedures Predict the Long Term Behavior of Polymers Exposed to Different Environments?" *Polymers* 2021, 13, p. 2688.



Chase Erford

Prysmian Group

Optical Cable Process Engineering

2512 Penny Rd.

P.O. Box 39

Claremont, NC 28610

Chase Erford holds a B.S. degree in Engineering with a Mechanical concentration from Campbell University. He joined Prysmian Group in 2022 as an engineer in a functional rotation program. He spent time in fiber optic cable R&D, Process Engineering, and now is a Product Specialist for telecom cables in Claremont, North Carolina.



Brian G. Risch

Prysmian Group

Fiber Optic Cable R &D

2512 Penny Rd.

P.O. Box 39

Claremont, NC 28610

Brian G. Risch is the Materials Technology Manager for Prysmian Telecom North America. He holds a B.A. degree in physics from Carleton College and a Ph.D. in Materials Science and Engineering from Virginia Polytechnic Institute and State University. Brian has more than 30 years of experience in the study of structure property relationships in polymeric materials and materials reliability. Brian has over 20 years of experience in the fiber optic cable business. Prior to working for Prysmian, Brian worked for Alcatel and Draka specializing in cable materials and fundamental material reliability. Brian also has 6 years of experience at Hewlett Packard doing failure analysis engineering.

Effects of filler surface modification on coupling effects in halogen-free flame-retardant cable compounds

Dr. Michael Heinz
Corning Optical Communications GmbH & Co. KG, 12489 Berlin, Germany
+49 (0)30 297 720 4013 · michael.heinz@corning.com

Abstract
This paper publishes the work which was performed following up on IWCS 2022 published results, investigating the influence of flame-retardant filler and grafted coupling agent on EVA/LLDPE blend systems. Therefore, in comparison to uncoated magnesium-di-hydroxide, filler versions with vinyl-silane and amino-silane coating were investigated. They represent different methods of bonding ability and have shown interactions with EVA and LLDPE in the past. The same EVA/LLDPE blends and pure polymers were filled with 30 % and 60 % of coated flame-retardant fillers and then investigated in the established analysis methods. Throughout all tests, differences in compatibility were observable. While uncoated MDH and aminosilane coated MDH performed very comparable, the vinylsilane coated filler showed reduced interaction with the polymer matrix. The addition of MAA-g-LLDPE coupling agent improved the mechanical performance of all filler types, but for vinylsilane coated not so much to overcome the signs of incompatibility. This was also visible in SEM analysis of the cryo-fractured samples, where vinylsilane coated filler did not show interaction with or without coupling agent. Uncoated and aminosilane coated MDH have shown good interaction in the presence of coupling agent and even with pure EVA. The ability to form hydrogen bonds to EVA was the reason both fillers performed very comparable throughout all investigations. While uncoated MDH in presence of coupling agent moved from the EVA phase into the interphase, aminosilane coated filler has shown stronger interaction with EVA. This led to a majority of MDH (around 2/3) staying in the EVA and the interphase and the rest (1/3) moving into the LLDPE phase where it fully coupled with the MAA-g-LLDPE. Vinylsilane coated filler was located in the interphase due to incompatibility and was partially (1/6) incorporated into LLDPE in presence of MAA-g-LLDPE. This might be caused by uncovered areas in the filler coating. The filler location could be clearly identified in SEM, EDX and TGA analysis. As a final investigation, the burn performance of the different compounds was compared and the influence of the polymer base identified.

Keywords: flame retardant cable, cable compound, halogen free, polymer blend, filler, coupling

1. Introduction
In the past, fiber optic data cables where mainly used in the network backbone, while the last portion close to the access points was covered by copper cables. Lately, the continuous increasing demand for more bandwidth drives fiber optic cables more into buildings. The most critical factor for cables in indoor application is the resistance against fire as this is directly related to people's safety. In 2011, the European Union released the construction product regulation (CPR) which resulted in mandatory testing and CE marking of all products which are permanently installed in buildings beginning in June 2016. This regulation produced more stringent burn test procedures which increases the requirements for flame-retardant materials to be used in cable sheathing application. Increased flame retardancy is achieved by incorporating high amounts of mineral filler into a polymeric matrix which results in tradeoffs in regard of mechanical performance. To maintain a certain mechanical strength and to fulfill cable requirements, the fillers need to interact with the polymers. The usage of coupling agents allows to gain influence at the interface and increase polymer-particle interaction. [1] [2]

More recent investigations in the field of grafted coupling agents, focusing particularly on cable compounds and the resulting blend morphology were published at IWCS in 2022. In “HFFR cable compounds: Influence of flame-retardant filler and coupling agent on EVA/LLDPE blend systems”, Michael Heinz published results showing the influence of different filler loadings with and without maleic acid anhydrite grafted coupling agent. [3]

The usage of grafting co-polymers as coupling agents in particulate filled compounds is one of the two most applied approaches. The second common alternative is the usage of surface modifying silanes. The typical structure of a silane is X3Si-R-Y, where Y is an organofunctional group (to bond with the polymer) and X is a hydrolysable group. X either reacts in water to Si-OH or with mineral hydroxide groups (M-OH) to form an oxane bond M-O-Si. R represents an organic structure with various chain length and functionality. Typical organic groups (Y) used in thermoplastic polymer systems are vinyl, allyl, amino, methacryloxy and epoxy. Due to its chemical nature, silane is very famous in the modification of the interface between polymer and glass [6]. The reaction of a silane in the interface between polymer and magnesium-di-hydroxide filler is shown in Figure 1. The silane creates a functional structure on the inorganic filler by hydrolysis which allows the polymer to interact with. Based on the type of organofunctional group, the silane can be coupled by hydrogen bonds or Van der Waals forces. Additional coupling can be achieved by combination with functional peroxides to create covalent bonding to the polymer phase. This step of reactive extrusion can be performed during compounding but requires a very controlled processing and dosing ability. The amount and type of peroxide, as well as processing temperature and shear force show an effect on the resulting coupling functionality. Suppliers of flame-retardant fillers have developed grades which are pre-coated with different silane types. This enables a more even dispersion of the coupling agent throughout the filler and reduces the number of processing steps before compounding. This also solved a common issue with limited shelf life of compounds due to hydrolysis of the silane caused by humidity during storage. [4-7]

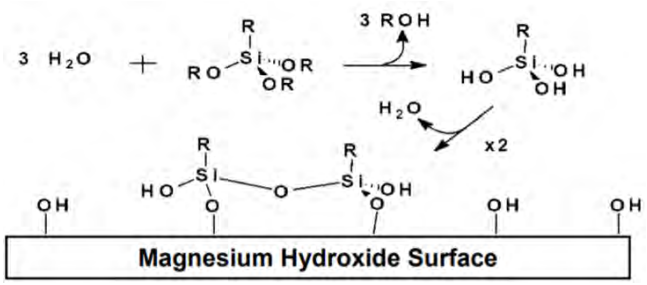


Figure 1 Schematic view of interfacial bonding by a silane coupling agent [8]

The used fillers are commercially available, and pre-coated with vinylsilane (recommended for reactive extrusion) or aminosilane (recommended for EVA based systems). The two coatings are chosen to represent different types of filler-polymer interaction: the ability to form covalent bonds in the presence of radicals (vinylsilane) and the ability to form hydrogen bridges (aminosilane). A question to be answered is, if the vinylsilane can still form a covalent bond in the presence of an activated maleic-acid-anhydrite coupling agent.

Therefore, in this work investigations were performed using a blend of ethylene-vinyl-acetate (EVA) and linear-low-density polyethylene (LLDPE). Comparable to former investigations, blends consisting of 0 %, 45 %, 50 %, 67 % and 100 % EVA were compounded to cover the pure polymers, the regions before and after phase inversion and a typical cable recipe. [3], [9] For most of the shown results, a ratio of 50:50 % was chosen to investigate the instable range in the phase morphology close to the expected phase inversion point. Subsequently, different amounts of Magnesium-di-hydroxide (MDH), with and without surface modifications, were added to investigate the system's response. In some samples, part of the LLDPE was substituted with maleic-acid-anhydrite grafted LLDPE as a function of a coupling agent.

2. Materials

Ethylene-vinyl-acetate (EVA) with VA content of 24 % and linear-low-density polyethylene (LLDPE) were blended in a ratio of 1:1. Parts of the LLDPE (4-5 %) were substituted with maleic-acid-anhydrite grafted LLDPE (MAA-g-LLDPE) as a coupling agent for the mineral filler. For more fundamental investigations on systems with a pure EVA polymer matrix, MAA-g-EVA with a VA content of 24% was also used as a coupling agent. Properties of the polymeric raw materials are listed in Table 1, the values were taken from the supplier datasheets. The polymers were chosen as they represent typical grades used in wire and cable compounds and were used as received.

Table 1. Polymeric ingredients

	T_m	MFR (190 °C/2.16 kg)	Density
EVA (24% VA)	80 °C	3.0 g/10 min	0.94 g/cm³
LLDPE	119 °C	1.0 g/10 min	0.92 g/cm³
MAA-g-EVA	80 °C	7.5 g/10 min	0.94 g/cm³
MAA-g-LLDPE	122 °C	1.6 g/10 min	0.94 g/cm³

To improve the flame retardancy, Magnesium-di-hydroxide (MDH) was added. The chosen grades have a specific surface (BET) of 4-6 m²/g. The particle size is given with d50: 1.6 – 2.0 µm in the technical datasheet. To investigate the influence of the silane surface modification, different coatings (uncoated, vinylsilane and aminosilane) were investigated.

Table 2. Properties of the used MDH types [10]

Property	Magnifin H-5	Magnifin H-5A	Magnifin H5-IV
Formula	$Mg(OH)_2$		
Spec. surface area (BET)	4.0 – 6.0 m2/g		
Particle Size D50	1.6 – 2.0 µm		
Density	2.4 g/cm³		
Physical form	Powder		
Particle morphology	Hexagonal platelet		
Surface coating	none	vinylsilane	aminosilane
Sample name	MDH	MDH VS	MDH AS

The prepared formulations are shown in Table 2. The amount of MAA-g-LLDPE coupling agent (CA) was chosen based on supplier recommendations and then adjusted for the different filler amounts to achieve a ratio of 2 phr coupling agent per 10 wt% of mineral filler. For the reference samples made of pure EVA, the same amount of MAA-g-EVA was used.

Table 2. Compound formulations

	EVA	LLDPE	MAA-g-LLDPE	MDH
0% MDH	50.0 %	50.0 %		
0% MDH + CA	50.0 %	45.0 %	5.0 %	
30% MDH	35.0 %	35.0 %		30.0 %
30% MDH + CA	35.0 %	30.8 %	4.2 %	30.0 %
60% MDH	20.0 %	20.0 %		60.0 %
60% MDH + CA	20.0 %	15.2 %	4.8 %	60.0 %

With the MDH filler further differentiated by MDH, MDH VS (vinylsilane) and MDH AS (aminosilane) in the sample description.

3. Results and Discussion

3.1 Rheology

To understand the blend mixing dynamic in the presence of filler and to calculate potential new phase inversion points, the pure blend components and the blends were characterized in parallel plate rheometry. It is expected that the viscosity and the filler location in the melt are affected by the filler coating.

A comparative overview of the rheological analysis in a frequency sweep for EVA (a), LLDPE (b) and 50/50 % – EVA/LLDPE (c) with different amount of filler is shown in Figure 2. The unfilled version of each polymer composition is shown as a reference in yellow. The samples without coupling agent are drawn in dotted lines, the samples containing coupling agent in solid lines. In pure EVA (a), the general behavior does not show any difference caused by the filler coating. Comparable to former published results, the coupling agent does not show any effect in EVA for the silane coated filler versions [3], [9]. The samples containing uncoated and aminosilane (AS) coated filler show similar results. The sample using vinylsilane (VS) shows comparable behavior with a shift to lower viscosity values which can be a sign for reduced filler-polymer interaction. The viscosity curves of the pure LLDPE compounds (b) also show the lowest viscosity for the vinylsilane coated filler version. In absence of coupling agent, a significant increase in viscosity at low frequency is observed. This "yield stress effect" was also reported by Laun et. al. [11] after observing a viscosity increase to infinite values towards lower shear rates of dispersed latex particles in emulsion. It is described to be caused by

filler particle-interlocking and is a sign of insufficient coupling or polymer coverage. This effect can also be observed for the aminosilane and the vinylsilane coated filler. The three dotted curves proceed parallel throughout the whole measurement with the uncoated sample showing the highest viscosity. This is a sign that both filler coatings show particle-particle interaction at low frequencies. By using the MAA-g-LLDPE coupling agent, these effects are significantly reduced with the uncoated filler showing the strongest difference, followed by the aminosilane sample. The 50/50 % – EVA/LLDPE blend (c) also shows a reduced viscosity of the vinylsilane sample without coupling agent. All other samples are in a very comparable range, uncoated and aminosilane filler show no differences whether coupling agent is present or not.

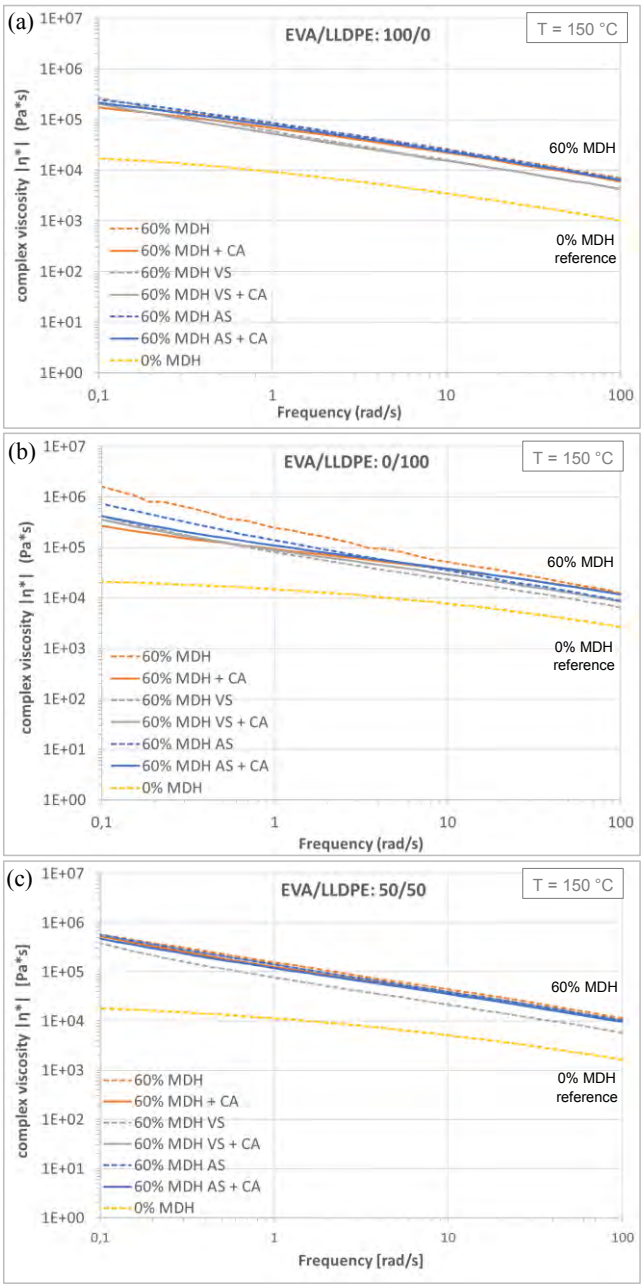


Figure 2. Rheology of filled EVA (a), LLDPE (b) and 50/50 EVA/LLDPE (c), with and without coupling agent (CA)

3.2 Mechanical characterization

The compounds using different filler coatings were extruded as strands and then evaluated in a tensile test. As the 60 % filled versions are of highest interest for the cable application, their results in EVA, LLDPE and 50/50 % - EVA/LLDPE are shown in Figure 3. Comparable results were also observed for the 30 % filled samples. The pure EVA matrix (a) shows the strongest interaction with the aminosilane coated filler resulting in the highest tensile strength, followed by the uncoated filler. Vinylsilane does not show any signs of polymer-filler interaction resulting a high elongation at break values with strong necking of the samples, but low tensile strength. Only minor improvement by the applied coupling agent is visible for all filler types.

The higher stiffness of the neat LLDPE systems (b) can be seen in the higher yield stress and lower elongation values. The vinylsilane coated filler shows the same signs of missing interaction as observed in neat EVA. This changes by the addition of coupling agent resulting in a slight increased yield strength and significant reduction in elongation at break. Also, both other coatings show improvement in polymer-filler interaction by combination with the coupling agent. The combination of the MAA-g-LLDPE coupling agent with uncoated MDH leads to highest improvements in tensile strength and elongation at break.

Beneficial effects of the coupling agent can also be seen in the 50/50 % - EVA/LLDPE blend (c). The addition results in increased strength of all samples. Very comparable properties of the aminosilane coated and uncoated MDH can be seen. The samples using vinylsilane coated filler show signs of coupling by increased tensile strength, but still weaker than the other two filler types. This leads to the assumption that either the vinylsilane filler coating shows low coupling reactivity or the MAA-g-LLDPE coupling agent reacts with sections on the filler surface that are not fully covered with coating.

As material elasticity is important for the application as cable jacket, hysteresis measurements were performed to identify the mechanical retention. The test is performed on all 50/50 blend systems filled with 60 % MDH. The setup is using tensile bars, set to a maximum elongation of 50 % from which the stress is then released. The just described influence of the filler coating and coupling agent on the tensile stress can be also identified in hysteresis measurements (Figure 4). While the tensile stress level of the samples is clearly dominated by the strength of polymer-filler coupling, the residual tensile set is very comparable for all samples at around 33 %. The only significant exception is the sample with uncoated filler without coupling agent (MDH) that did not reach 50 % elongation.

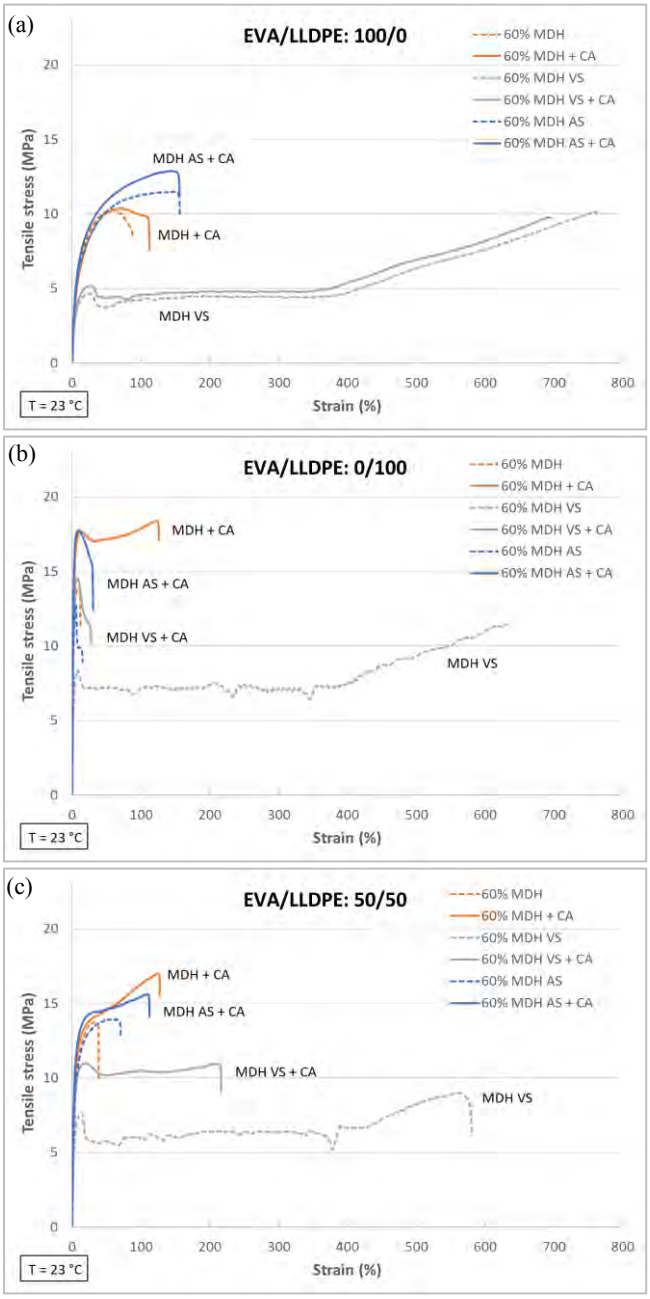


Figure 3. Stress/strain curves of EVA (a), LLDPE (b) and 50/50 EVA/LLDPE (c) filled with 60 % of uncoated, vinylsilane (VS) and aminosilane (AS) coated magnesium-di-hydroxide (MDH), with and without coupling agent (CA)

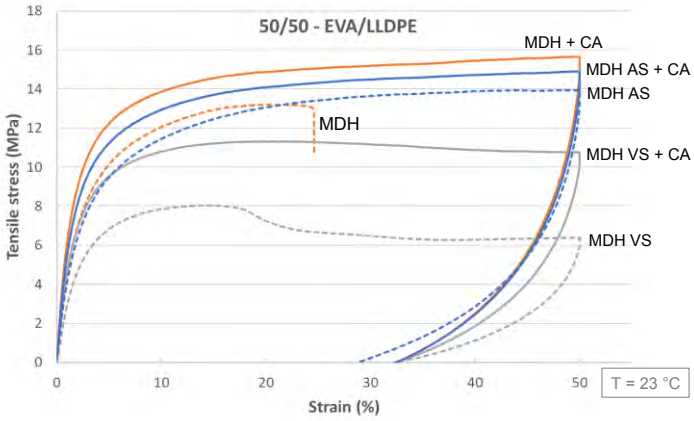


Figure 4. Hysteresis measurement of EVA/LLDPE blends filled with 60 % of uncoated, vinylsilane (VS) and aminosilane (AS) coated magnesium-di-hydroxide (MDH), with and without coupling agent (CA)

3.3 Dynamic mechanical analysis (DMA)

To further investigate the thermo-mechanical stability, DMA tests were conducted. Filled samples made of pure EVA (a), pure LLDPE (b) and exemplary the 50/50 blend (c) are shown in Figure 5. The modulus of the pure EVA (a) sample is not significantly affected by the coating of the filler. Only the vinylsilane samples show a decrease in modulus above 20 °C which underlines the theory of reduced interaction. As seen in previous mechanical results, no influence of the MAA-g-EVA coupling agent can be observed. The LLDPE (b) samples show a clear improvement by the usage of a coupling agent for all filler surface variants. The thermo-mechanical stability of the sample using uncoated filler is the highest, followed by the aminosilane sample and vinylsilane as the weakest. This order of performance is valid for the samples with and without coupling agent. This means that the aminosilane coating still interacts more with LLDPE than vinylsilane. Nevertheless, the interaction is reduced in comparison to uncoated MDH. Looking at the 50/50 blend (c), the same order of performance can be observed. The usage of coupling agent improves the modulus at higher temperatures where the EVA performance shows weakness. This works for both filler coatings, as it was already seen for the uncoated MDH in the previous publication [3]. It is observable, that the mechanic stability at higher temperatures is defined by the filler-LLDPE interaction.

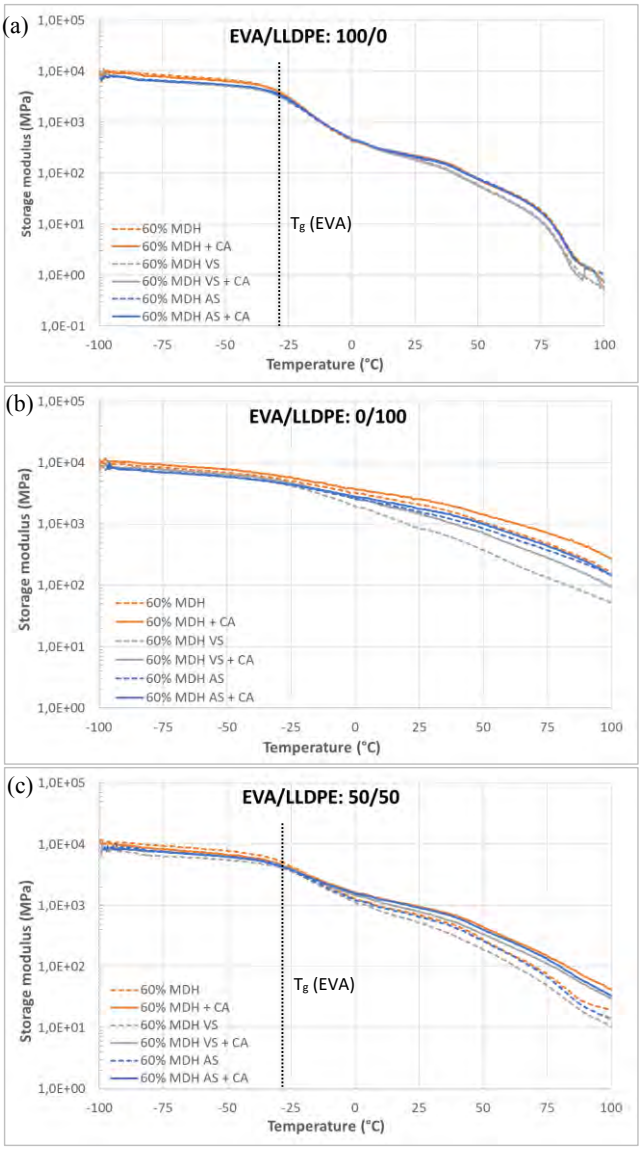


Figure 5. DMA testing of EVA (a), LLDPE (b) and 50/50 - EVA/LLDPE (c) filled with 60 % of uncoated, vinylsilane (VS) and aminosilane (AS) coated magnesium-di-hydroxide (MDH), with and without coupling agent (CA)

3.4 Scanning electron microscopy (SEM)

Before investigating the morphology of the blends, the interaction of the filler using different surface modifications with each polymer needs to be understood. Therefore, samples of pure EVA and LLDPE filled with 60 % of the three flame-retardant filler types were analyzed using SEM microscopy on cryo-fractured specimen (Figure 6).

The uncoated filler shows adhesion to the EVA polymer matrix. The same is visible for the sample using aminosilane coating, the fillers are surrounded by polymer and seem to be even more incorporated. This adhesion can be seen especially on the corners of the large filler particle. The free uncovered area on the filler particle is the result of exfoliation effects where adhered layers of MDH were separated during cryo fracture. This is a sign, that the polymer-filler interaction is strong. Looking at the vinylsilane sample, no interaction of the filler with the EVA can be identified. The sample shows filler particles with gaps in the polymer around and holes where filler particles were pulled out without signs of resistance or adhesion. Looking at the samples with coupling agent, the uncoated and the aminosilane coated fillers show good adhesion while the vinylsilane coated filler still shows no signs of interaction with the EVA. For all samples, no difference between the presence and absence of coupling agent is visible.

Fractured surfaces of the samples of pure LLDPE with 60 % magnesium-di-hydroxide with uncoated, vinylsilane coated and aminosilane coated surface, with and without coupling agent are shown in Figure 7. In the absence of coupling agent, no filler variant (uncoated, vinylsilane, aminosilane) shows signs of interaction with the LLDPE. This can be identified by the polymer-pullout effects between the filler particles. This deformation effect during cryo fracture can be seen for LLDPE due to the lower glass transition temperature of LLDPE (Tg - 110 °C), but not for the EVA samples (Tg -28 °C). Furthermore, no adhesive effects at the filler corners were observed. This changes with the addition of MAA-g-LLDPE coupling agent. The sample using uncoated MDH shows incorporation of the filler into the polymer. An improvement can also be seen for the silane coating surface modified fillers as the pullout effects are reduced. While the vinylsilane sample shows only minor improvement and still barely polymer coverage at the filler surface, the aminosilane coated filler is incorporated into the polymer much better and shows stronger wetting by the polymer.

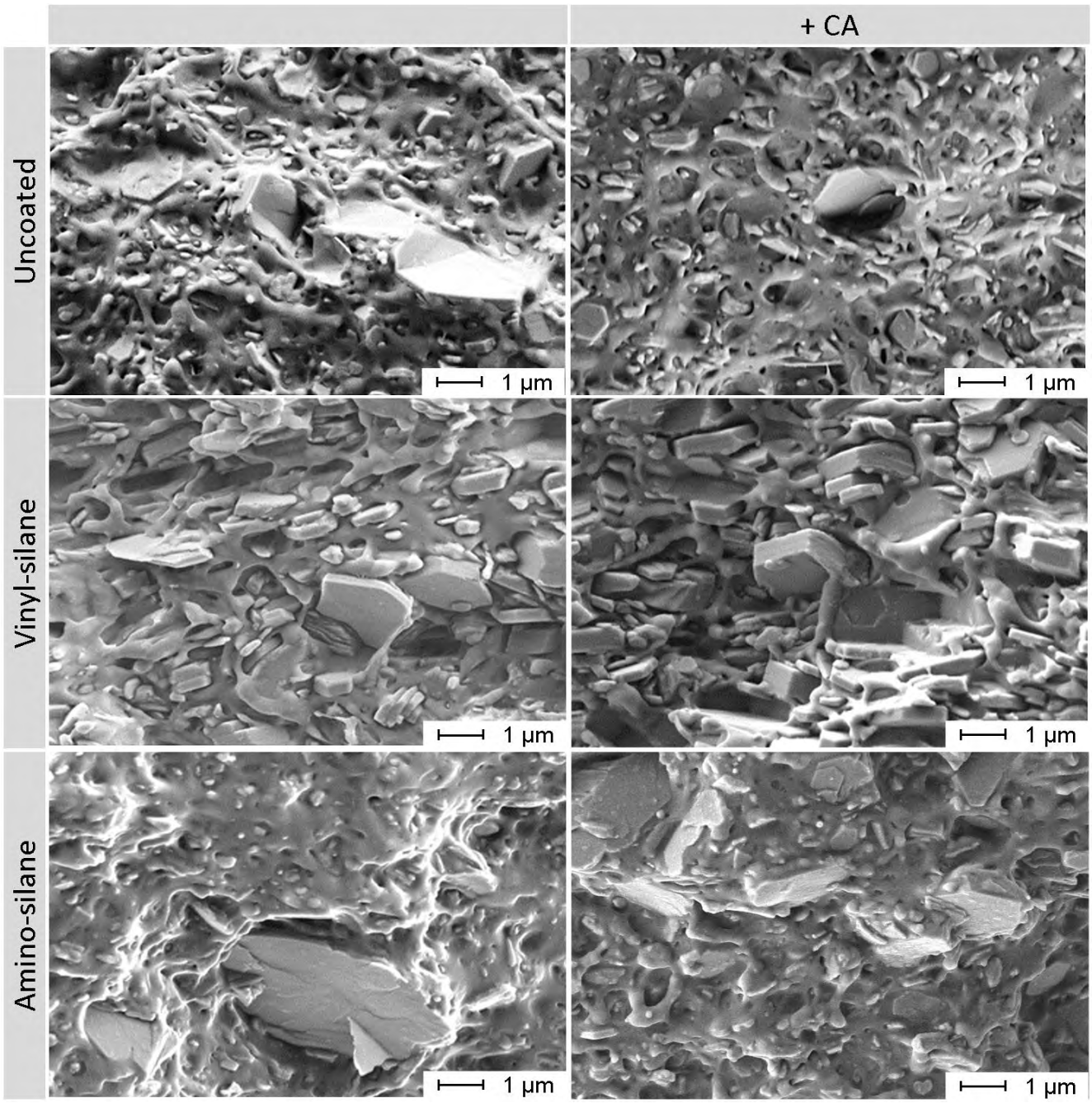


Figure 6. Scanning electron microscopy of cryo fractured EVA filled with 60 % MDH with different surface modifications, with and without MAA-g-EVA coupling agent (CA) – magnification 10,000x

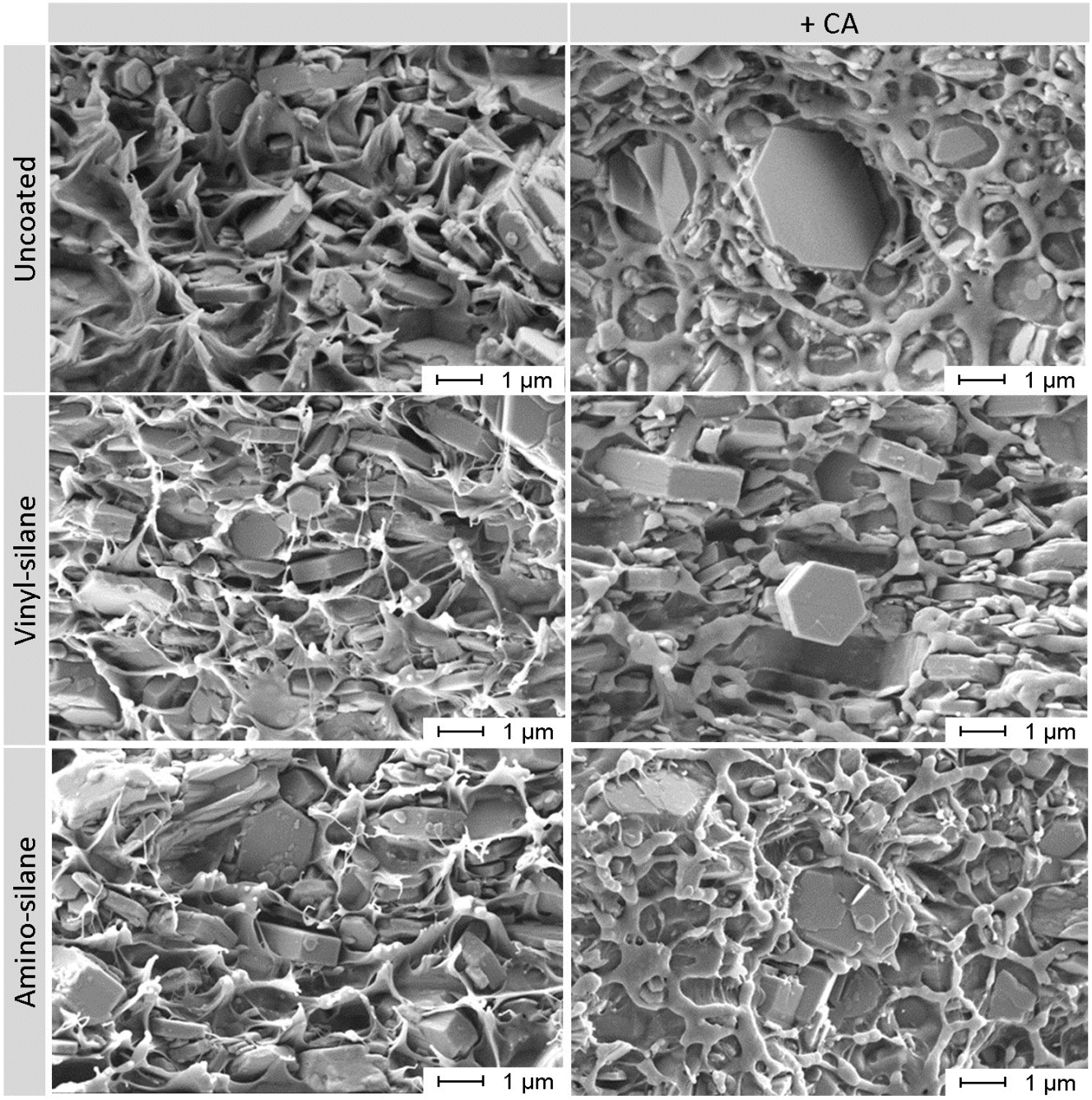


Figure 7. Scanning electron microscopy of cryo fractured LLDPE filled with 60 % MDH with different surface modifications, with and without MAA-g-LLDPE coupling agent (CA) – magnification 10,000x

Based on a visual judgement of the SEM images, the filler-polymer interaction in pure EVA and LLDPE in presence of the coupling agent can be rated as the strongest for the uncoated and the aminosilane coated filler. Vinylsilane shows the weakest interaction in both polymer and coupling agent scenarios.

These observations give a good overview about the polymer-filler interactions to be expected in the blend systems. To understand these, cryo-fractured blends filled with 30 % and 60 % of both silane coated MDH types were etched and the EVA fraction was removed.

To investigate the resulting blend morphology and phase behavior, the scanning electron microscopy results of 30 % MDH filled 50/50 - EVA/LLDPE blend system with and without MAA-g-LLDPE coupling agent are shown in Figure 8. The observed effects using uncoated filler are already described in the former publication [3]. The LLDPE residue of the sample without coupling agent shows a smooth surface and no signs of flame-retardant filler. The addition of coupling agent reduces the LLDPE phase size and moves the filler from the EVA phase into the interphase where it can be seen covering the LLDPE phase. The LLDPE residue of the sample using vinylsilane coated filler without coupling agent (middle left)

shows a more irregular surface in comparison to the residue of the uncoated filled sample (top left). This can be caused by the irregular shape of incorporated filler but will be further discussed in the next paragraph. Looking at the aminosilane samples without coupling agent, the morphology looks very similar to the uncoated filler. The LLDPE residue shows a smooth surface. Due to incomplete etching, parts of the EVA fraction containing all MDH filler are still visible between the LLDPE structures. This observation further proves the theory of complete MDH incorporation in the EVA.

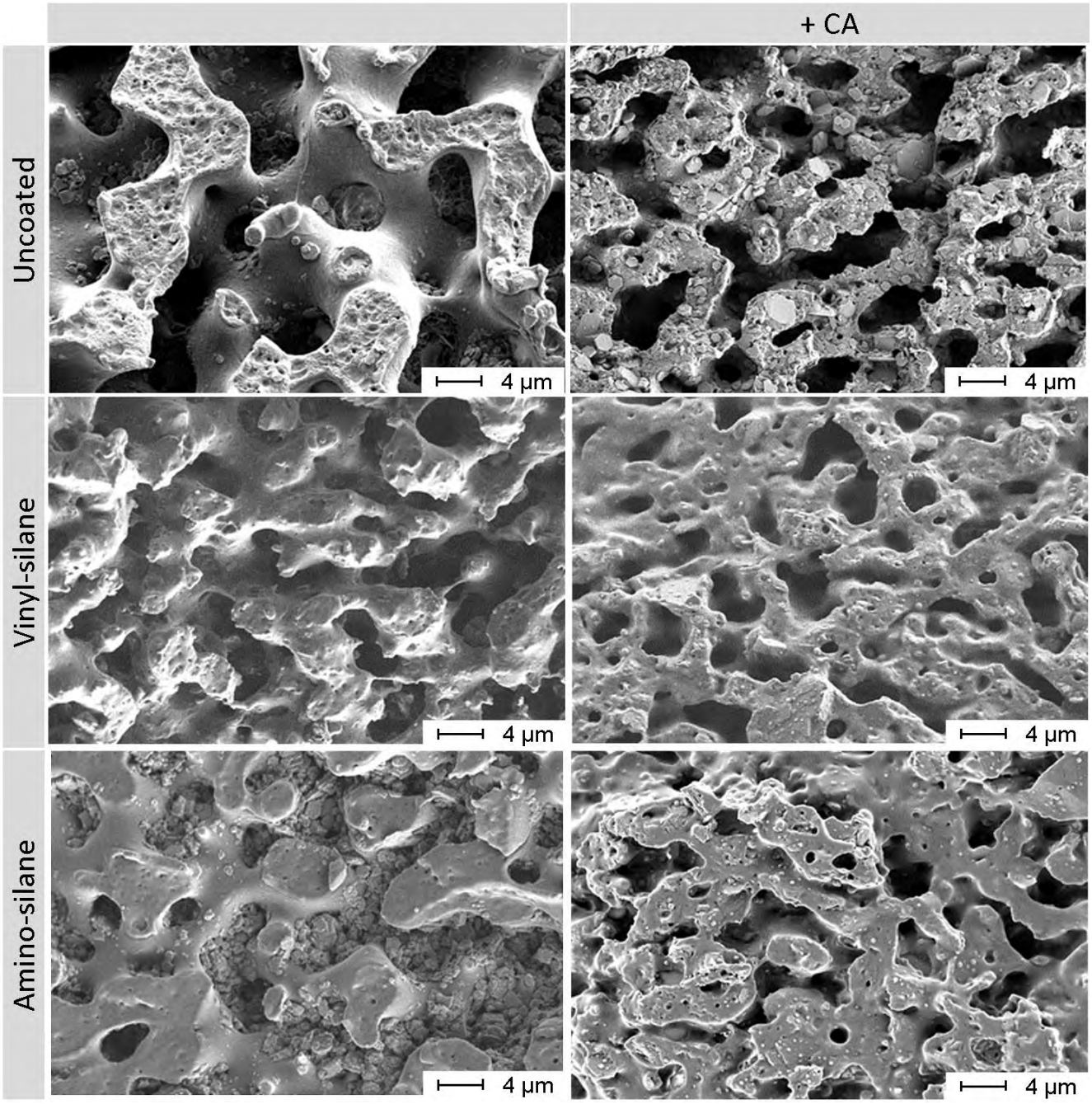


Figure 7. Scanning electron microscopy of cryo fractured and EVA etched 50/50 % – EVA/LLDPE blends filled with 30 % MDH with different surface modifications, with and without MAA-g-LLDPE coupling agent (CA) – magnification 2,500x

To identify the filler locations in the 30 % MDH filled 50/50 % - EVA/LLDPE blend systems, more detailed SEM images are shown in Figure 8. The already described effects of the samples containing uncoated filler (first row) can be clearly identified. The sample without coupling agent (top left) shows only small amount of MDH residue from etching on the surface but no filler in the LLDPE phase. In presence of coupling agent (top right), the filler was found covering the LLDPE surface and not being extracted.

The samples using vinyl silane filler (middle left) shows no signs of filler incorporation, although the phase shape looks more irregular than the uncoated sample. Also TGA and EDX analysis have shown that the LLDPE structures without coupling agent do not contain MDH. This result leads to the hypothesis that this structure is still caused by irregular filler shape, but from the interphase side, where the MDH is located. Contrary to the uncoated filler with coupling agent, the vinylsilane filler does not interact with any of the polymers and therefore moves into the interphase. This also results in a smaller LLDPE phase size because the filler does not contribute to any of the polymer volumes. After addition of coupling agent, parts of the filler were identified in the LLDPE showing surface coupling - marked in the SEM image (middle right). This fits to the observation of slightly improved filler-LLDPE interaction seen in Figure 7. In comparison to the uncoated sample (top right), it is visible that only parts were moved from the interphase to the LLDPE. Further analysis to quantify this effect was performed using TGA, the results will be described in the next section.

The aminosilane sample (bottom left) shows residual EVA containing all MDH filler in the background and the LLDPE phase in the front being free of filler. By adding coupling agent (bottom right), the LLDPE phase becomes finer and shows few filler particles coupled in the LLDPE (highlighted in image). To further understand this effect, TGA analysis was also performed (see Table 3).

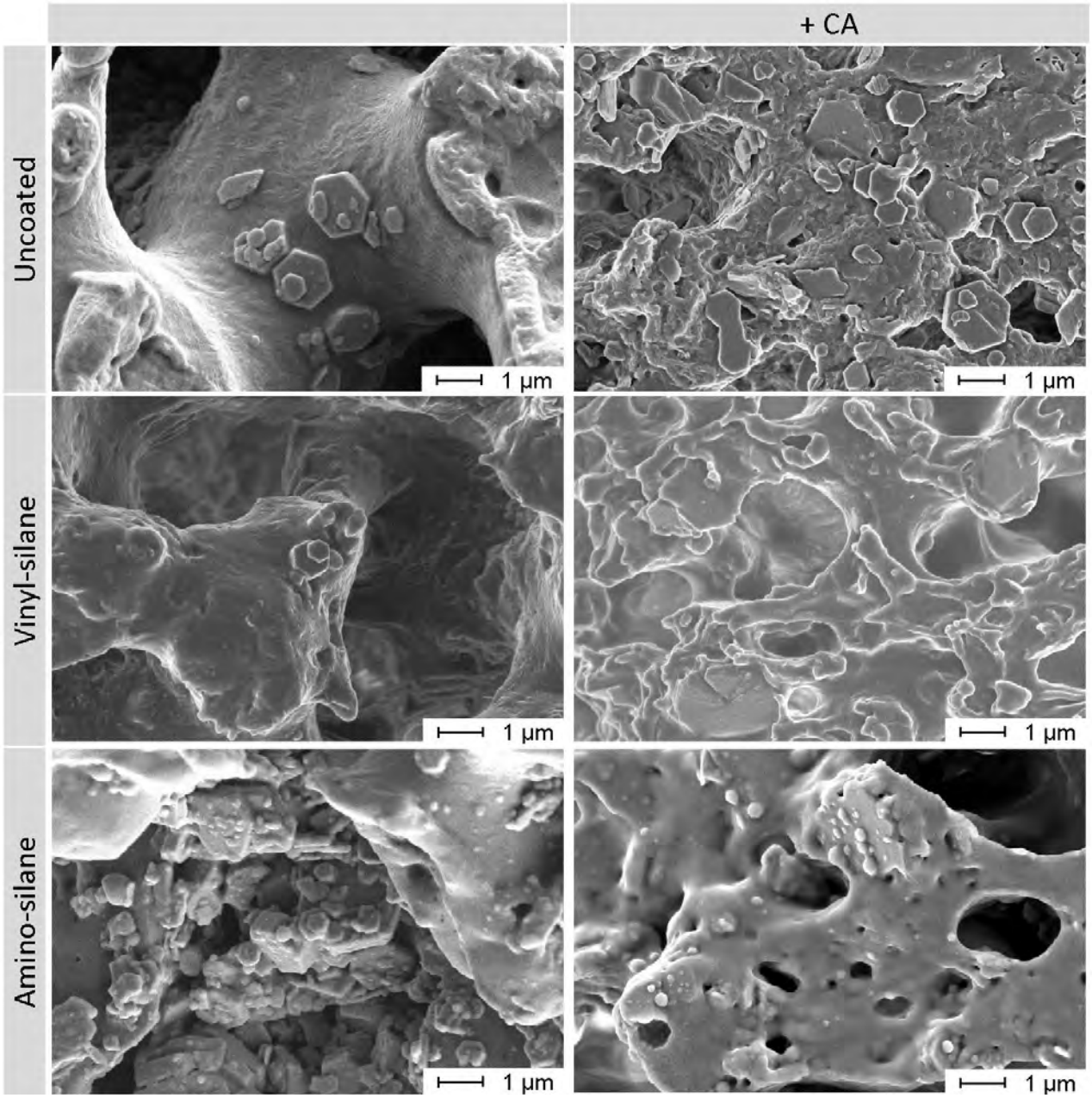


Figure 8. Scanning electron microscopy of cryo fractured and EVA etched 50/50 % – EVA/LLDPE blends filled with 30 % MDH with different surface modifications, with and without MAA-g-LLDPE coupling agent (CA) – magnification 10,000x

The just shown etched samples were cut in thin slices and analyzed using TGA to measure the amount of filler content. The amount of MDH in the sample was calculated based on the inorganic residue after thermal decomposition. For etched samples, the values were referenced to the whole compound formulation to also include the EVA and represent the whole compound.

The TGA results of the etched samples are shown in Table 3. In comparison, the blends without etching were also tested in TGA. The analysis of these "original samples" show that the MDH content is very stable around 30 %. The samples without coupling agent show a very low amount of filler which proves the observations in Figure 7. The values higher than 0 % are caused by contamination which was already seen in the etched aminosilane SEM picture. A significant difference is introduced by the coupling agent. While most of the uncoated filler sticks to the LLDPE, the vinylsilane and aminosilane samples show a lower MDH content. The values fit very well to the observations from SEM analysis of the 50/50 blends but also of the pure LLDPE samples. This is a sign for partial interaction of the coated fillers with the MAA-g-LLDPE coupling agent. The improved interaction of the aminosilane coating with the coupling agent in comparison to the vinylsilane can be quantified by an increase of the filler content from 4.5 % to 9.5 %.

Table 3. Content of magnesium-di-hydroxide filler calculated based on TGA analysis

Filler	Original sample	Sample after etching	
		-	+CA
uncoated	29.9 %	0.7 %	25.7 %
vinylsilane	30.1 %	0.6 %	4.5 %
aminosilane	30.2 %	1.9 %	9.5 %

3.5 Burning behavior

As flame-retardancy is the main reason to incorporate the magnesium-di-hydroxide filler, the burning behavior of the investigated compounds was evaluated in cone calorimetry. Samples with 0 %, 10 %, 30 % and 60 % filler were tested, but strong fluctuations with low amount of flame-retardants were observed. Especially parameters like peak heat release rate show strong scattering for low dosages of flame-retardants. Cable compounds usually contain 60 % and more MDH. The results for the peak heat release rate and total heat release are shown in Figure 9 and 10. The peak heat release rate (figure 9) is increasing with increased EVA content. The curves are very close, especially in the samples up to 50 % EVA. The values above increase and show a stronger difference in between the coatings. The values show strong scatter and no clear picture. For pure EVA, uncoated MDH shows the lowest and vinylsilane the highest values in presence of coupling agent. This order is different for the 67/33 blend where aminosilane shows the best performance. The total heat release rate (figure 10) is clearly decreasing with increasing EVA ratio. The y-axis is not starting from 0 to increase the resolution and display the curves that normally would not be distinguishable. The values are lying all within other's standard deviation and show very comparable values.

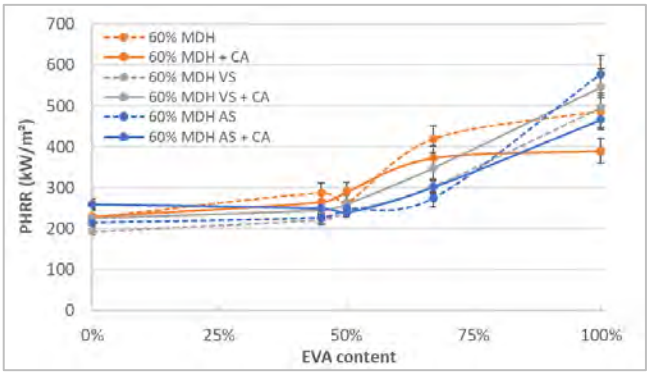


Figure 9. Peak heat release rate (a) of EVA/LLDPE blends filled with 60 % of uncoated, vinylsilane (VS) and aminosilane (AS) coated magnesium-di-hydroxide (MDH), with and without coupling agent (CA)

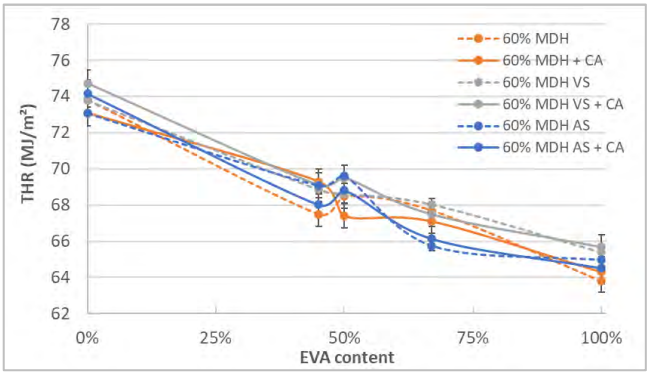


Figure 10. Total heat release (b) of EVA/LLDPE blends filled with 60 % of uncoated, vinylsilane (VS) and aminosilane (AS) coated magnesium-di-hydroxide (MDH), with and without coupling agent (CA)

It was seen that no significant influence of the filler surface modification on the burning behavior was identified. This is different for the polymer composition as the peak heat release rate increases and the total heat release rate decreases with increasing EVA content. This is a sign for an EVA related decomposition effect which was already reported by El Hage et. al. [12]. Around 370 °C deacetylation of the EVA occurs, in addition to the thermal decomposition of the polyethylene backbone around 485 °C. This effect can also be observed on the residue after burning, as it is shown in Figure 11. The deacetylation creates a black incombustible residue that does not contribute to the total heat release rate.

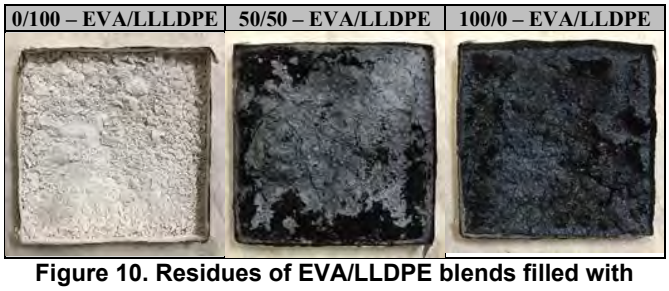


Figure 10. Residues of EVA/LLDPE blends filled with 60 % MDH from cone calorimeter testing

4. Conclusions

After the interaction between both polymers and the uncoated filler has shown such influence in the former publications ([3], [9]), fillers with different surface modifications were investigated. Vinylsilane and aminosilane coated MDH with the same particle size and particle size distribution were used. They represent different methods of bonding ability and have shown interactions with EVA and LLDPE in the past. The same EVA/LLDPE blends and pure polymers were filled with 30 % and 60 % of coated flame-retardant fillers and then investigated in the established analysis methods. Throughout all tests, differences in compatibility were observable. While uncoated MDH and aminosilane coated MDH performed very comparable, the vinylsilane coated filler showed reduced interaction with the polymer matrix. The addition of MAA-g-LLDPE coupling agent improved the performance of all filler types, but for vinylsilane coated not so much to overcome the signs of incompatibility. This was also visible in SEM analysis of the cryo-fractured samples, where vinylsilane coated filler did not show interaction with or without coupling agent. Uncoated and aminosilane coated MDH have shown good interaction in the presence of coupling agent and even with pure EVA. The ability to form hydrogen bonds to EVA was the reason both fillers performed very comparable throughout all investigations. While uncoated MDH in presence of coupling agent moved from the EVA phase into the interphase, aminosilane coated filler has shown stronger interaction with EVA. This led to a majority of MDH (around 2/3) staying in the EVA and the interphase and the rest (1/3) moving into the LLDPE phase where it fully coupled with the MAA-g-LLDPE. Vinylsilane coated filler was located in the interphase due to incompatibility and was partially (1/6) incorporated into LLDPE in presence of MAA-g-LLDPE. This might be caused by uncovered areas in the filler coating. The filler location could be clearly identified in SEM, EDX and TGA analysis. This location was then transferred to the rheological measurements and it was possible to correlate the observed morphology with the calculated theoretical phase inversion points.

5. Acknowledgement

The author is thankful for the support from the Bavarian Polymer Institute (BPI) for using the SEM capabilities and the companies Huber, Silon, DOW and Arkema for providing the sample materials and further technical information. Finally, the author is deeply thankful to Mr. Christoph Callsen and Mr. Alexander Kiel for compounding and testing, Mrs. Ute Kuhn for thermal and rheological analysis and Mrs. Annika Pfaffenberger for the scanning electron micrographs.

6. References

[1] ZVEI e.V., *White Paper: Brandschutzkabel erhöhen die Sicherheit*. https://www.zvei.org/presse-medien/publikationen/white-paper-brandschutzkabel-erhoehen-die-sicherheit/, **2017** (accessed: July 2022).

[2] G. Pritchard, *Plastics Additives*, Springer Science, **1998**.

[3] M. Heinz, *HFFR cable compounds: Influence of flame-retardant filler and coupling agent on EVA/LLDPE blend systems* at IWCS, Rhode Island, **2022**

[4] C. Kumudinie, *Polymer–Ceramic Nanocomposites: Interfacial Bonding Agents* in Encyclopedia of Materials: Science and Technology, Pergamon, **2001**, p. 7574.

[5] C. Dearmitt, R. Rothon, Surface Modifiers for Use with Particulate Fillers. in *Fillers for Polymer Applications*, Springer, **2017**, p. 30.

[6] E. P. Plueddemann, *Adhesion through silane coupling agents* in Fundamentals of Ahesion, Springer, **1991**, pp. 279-90.

[7] B. Borup, K. Weissenbach, *Silane Coupling Agents in Functional Fillers for Plastics*, Wiley-VCH, **2008**, pp. 62 - 90.

[8] T. Chen, A. Isarow, *Use of Surface - Modified Magnesium Hydroxide for Low - Smoke Flame Retardant Thermoplastics Applications* in Functional Fillers for Plastics, Toronto, **2005**.

[9] M. Heinz, C. Callsen,W. Stöcklein, V. Altstädt, H. Ruckdäschel, Polym. Eng. Sci. **2022**, 62(2), 461. https://doi.org/10.1002/pen.25858

[10] Huber Martinswerk, *Technical datasheet: Magnifin grades H-5, H-5A, H-5IV*, **2020**.

[11] H. M. Laun, *Angew. Makromol. Chem.* **1984**, 123, 335. https://doi.org/10.1002/apmc.1984.051230115

[12] R. El Hage, A. Viretto, R. Sonnier, L. Ferry, J. Lopez-Cuesta, „Flame retardancy of ethylene vinyl acetate (EVA) using new aluminium-based fillers," *Polymer Degradation and Stability,* pp. 56-67, 2014

7. Authors

Dr.-Ing. Michael Heinz (michael.heinz@corning.com) is leading the Process Development Team of the Global Materials Group at the Corning Technology Center Berlin.



After working as a development engineer for copper cables for 3 years, he joined Corning in 2014 as a development engineer with focus on materials science. The major scope of his work was the development of fiber optic cables, materials, and processing methodology. Special focus lies on flame retardant cables, halogen free compound development and testing.

Dr. Michael Heinz earned a degree in Materials Science & Engineering at the University of Bayreuth in 2011, where he also received his PhD in 2022. He has over 15 years of experience in polymer materials development, processing, and testing, including 12 years in wire and cable industry.

Polyurethane resin based FRP rods as embedded strength members in Optical Fiber Cables

Pramod Marru, Aparna Nath, Surbhit Awasthi, Jivesh Krishna

Dept. Material Science and New Product Development, Sterlite Technologies Limited

Silvassa, Dadra Nagar Haveli, INDIA

+91-9957803463 · aparna.nath@stl.tech

Abstract

Fiber reinforced plastic rods are widely used in optical fiber cable applications as a central or peripheral or embedded strength member. FRP rods provide anti-buckling strength to the fiber unit and provide tensile strength to the optical fiber cable. These peripheral strength rods should be easily accessible during cable installation.

In this paper we will discuss a type of FRP rod and the resin used in its manufacturing that will provide an optimum bonding with the cable jacket material, thus providing easy accessibility during installation.

Keywords: Fiber reinforced plastic, Polyurethane resin, embedded strength members

1. Introduction

Fiber reinforced plastic rods are manufactured by impregnating the fiberglass with a resin matrix, such as polyester, epoxy, or vinyl ester. The impregnated fibers are then pulled through a heated die (pultrusion process) to shape and cure the resin and create a rod with a consistent cross-section. Finally, the pultruded rods are cooled down to solidify the resin and maintain the desired shape. Depending on the application of these rods, some rods may undergo additional surface treatments or coatings to enhance specific properties such as adhesion. These FRP rods are used as strength members in optical fiber cables. They enhance the cable's mechanical strength and durability and make the cable more resistant to bending, crushing and other physical stresses.

FRP rods are developed for a wide variety of applications based on the optical fiber cable family they are to be used in. In some optical fiber cables, FRPs are used as the central strength member, while in some they are used as peripheral strength members and in some as embedded strength members. When used as a central strength member, the FRP rod is uncoated as no adhesion is required between the FRP and the cable elements. In designs where FRPs are used as a peripheral strength member, uncoated flat FRPs are used to completely cover the cable elements and act as an armor to the elements. Embedded strength members are usually coated as they require bonding between FRP and the cable sheath. Depending on the end use and customer requirements, these coatings or bonding also need to be customized. Conventionally, Ethylene Acrylic Acid (EAA) coatings are done on the FRP rods to promote adhesion between dissimilar materials, such as FRP and polyethylene, creating a strong bond between them.

This paper describes the type of bonding desirable between the FRP and the cable jacket and how that has been achieved to facilitate cable installation.

2. Embedded FRPs in optical fiber cables

The two important factors that govern the bonding between the FRP and the polymer are - a) chemical adhesion, and b) friction due to surface roughness of FRP. Chemical adhesion is often achieved by coating the FRP rods with Ethylene Acrylic Acid (EAA). These coatings are applied with co-extrusion technology and give high adhesion properties to jacket material. Due to this strong adhesion, it becomes difficult to access these FRPs at the time of cable installation. In order to overcome this, often mechanical bonding of FRP with polymer is preferred. Uncoated rough FRPs increase the mechanical interlocking and at the same time are easily accessible during the cable installation.

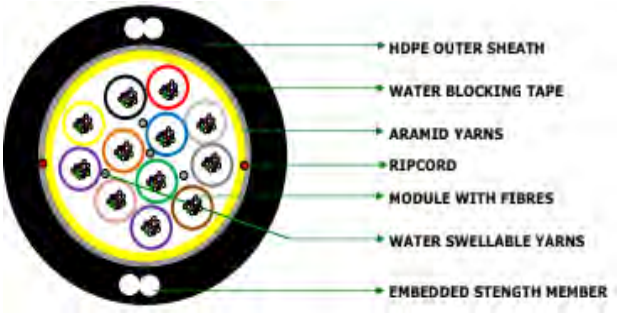


Fig 1: Typical cross-section of optical fiber cable with embedded strength members

2.1. Mechanically bonded FRPs as embedded strength members

In an attempt to develop FRPs that can bond mechanically with the polymer, polyurethane acrylate-based resin was selected for the FRP manufacturing. Polyurethane acrylate oligomers are a class of polyurethane produced by the reaction of polyols with diisocyanate and capped by acrylate. As compared to the traditional epoxy-based resins, these polyurethane acrylate resins do not have aromatic rings in the chemical structure, thus making the FRP rods more flexible. FRPs made with this resin will have a rough surface finish, thus helping in the mechanical bonding or interlocking of FRP to the polymer. Further, no coating was used over the FRP for bonding with the cable jacket.

3. Cable properties, performance and Qualification

3.1 Cable Description

72F micromodule cable was fabricated in order to test the performance of the new FRP rods. Micromodule cables are high

density optical fiber cables with several individual micromodules. The micromodules typically are made of easy peelable polymer (e.g., Low Smoke Zero Halogen) and include optical fibers inside it. Micromodules are thinner by about 55% than conventional loose tubes and provide a reduced space for fiber accommodation. These micromodules are arranged in a sheath for transmitting optical data and are housed in a cable jacket. FRP rods are embedded on the cable jacket laterally (two on each side) along the length.

3.2 Qualification

A series of qualification tests were conducted on the 72F micromodule cable such as tensile, crush, impact, torsion as per XPC standard and environmental testing, along with end preparation, kink and coil tests in order to simulate the field conditions.

In order to simulate stringent field conditions, the cable was first tested for its aging (70 ^{0}C for 14 days) performance followed by mechanical qualification.

Table 1 - Summary of Cable Ageing test

Cable Aging Report		
Test Description	**Acceptance Criteria**	**Result**
Thermal ageing for 14 days at 70°C	The variation in the attenuation factor shall remain ≤ 0.2 dB/km throughout the test duration and shall be reversible. The appearance and characteristics of the cable and cable elements (module) shall be unaffected at the end of the test and after 24 h recovery at 20°C.	Pass

Table 2 - Summary of Cable Mechanical tests

Mechanical Test Results Summary		
S.No.	**Parameter & Acceptance Criteria**	**Result**
1	Tensile Test 1550N @ 0.5% fiber strain Change in attenuation ≤0.1dB/km	Pass
2	Crush Test Load 2000N, change in attenuation ≤0.1dB/km	Pass
3	Impact Test Impact Energy 5Nm, change in attenuation ≤0.1dB/km	Pass
4	Torsion Test Pulling force 100N, change in attenuation ≤0.1dB/km	Pass
5	Cable Kink Test Kink diameter 100mm, change in attenuation ≤0.1dB/km	Pass
6	Cable Bend Test Bending radius 150mm, change in attenuation ≤0.1dB/km	Pass

The cable qualified all the aging and mechanical criteria, thus implying that the strength member can fulfill the basic cable strength requirements. In addition to these tests, the cable was also tested for its application requirements, wherein lies the basic idea for developing this kind of FRP.

The cable was subjected to end preparation and the FRPs were checked for easy accessibility. The sheath was first stripped and the FRPs were easily accessed; unlike the coated FRPs which completely stick to the cable jacket. The **"Banana Peel"** method was then used and the two FRPs on each side were pulled apart without any damage. This easy and clean separation of the FRPs plays a very important role during the cable installation and termination inside joint enclosures.

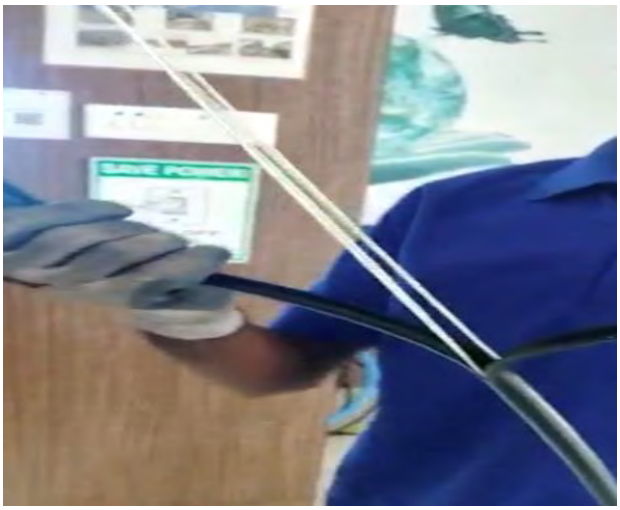


Fig 2: Cable stripping and Banana peeling

Table 3 - Summary of Cable Application tests

Application Assurance Report			
S.No.	**Cable Parameters**	**Observation**	**Result**
1	End Preparation	End preparation of the cable is passed with ring cut tool & banana peel method without any difficulties.	Pass
2	Kink performance	Kinked below 70 mm bend diameter (6 D bend dia).	Pass
3	Coil test	Cable was coiled with 20 D bend diameter in the mid portion. No cable damage was observed within 1 day of observation.	Pass

In addition to the above mentioned tests, another parameter for which the cable was tested was the "**Pistoning Effect**"; an undesirable phenomenon that is observed mostly in cables with embedded FRPs. The FRPs tend to move in and out of the jacket during the cable temperature cycling at low & high temperature (-40 ^{0}C to +70 ^{0}C). The polyurethane resin based FRPs with rough surface had good interlocking with the cable jacket that inhibits any such displacement of the FRP rods.

4. Conclusion

FRP rods were made with Polyurethane based resins to help provide improved bonding of FRP with the cable jacket through interlocking as a result of friction due to the rough surface of the FRP. This paper also discussed how limited bonding of the FRP with the cable jacket can help in the easy installation of cables.

5. Acknowledgements

We thank Mr. Shubham Sachan, Maneesh Kumar and Saji Sahadevan for their support in FRP samples manufacturing, cable manufacturing, testing and validation.

6. References

[1] Juan Pablo et al, "Use of sand coating to improve bonding between GFRP bars and concrete", Journal of Composite Materials 46(18): 2271-2278.

[2] Premamoy Ghosh et al, "FRP composites based on different types of glass fibers and matrix resins: A comparative study", Journal of Applied Polymer Science, Vol 58, 2177-2184.

7. Authors



Pramod Marru received his Ph.D. in Chemical Engineering from IIT Kharagpur in 2015. He joined Sterlite Technologies Limited in 2019 and has been leading the Material Science (R&D) department.



Jivesh Krishna received his Bachelor of Technology Degree in Polymer Science and Engineering from CIPET Raipur in 2021. He joined Sterlite Technologies Limited in 2021 and has been working in the New Product Development (R&D) department since then.



Aparna Nath received her M.Tech. degree in Chemical Engineering from IIT Kharagpur in 2019. She joined Sterlite Technologies Limited in 2019 and has been working in the Material Science (R&D) department since then.



Surbhit Awasthi received his M.Tech. degree in Polymer Science and Engineering from IIT Delhi in 2021. He joined Sterlite Technologies Limited in 2022 and has been working in the Material Science (R&D) department since then.

Fluoropolymer Processing Aid Replacement in Cable Jacketing Compounds

Karl Seven[1], Paul Brigandi[1], Mohamed Esseghir[1], Jingwei Fan[2]
Dow Inc. Wire & Cable R&D
[1] 400 Arcola Rd, Collegeville, PA 19426
[2] Abner Jackson Parkway, Lake Jackson, TX 77566
+1-610-244-7181 · kseven@dow.com

Abstract

Wire and cable jacketing compounds are used across the industry in telecom as well as power cable applications. Many of these jacketing compounds include a fluoropolymer-based processing aid which is classified as a poly/perfluoroalkyl substance, (PFAS). Perfluoralkyl and polyfluoroalkyl substances (PFAS) include over 4000 synthetic chemicals and are mostly based on carbon-fluorine bonds rather than carbon-hydrogen bonds. PFAS, including the fluoropolymer based-processing aids may not readily break down in the environment. PFAS containing products have been a topic of increasing concern from a regulatory perspective. Despite limited data on the environmental hazards of PFAS, there is growing environmentally driven focus worldwide to increase restrictions and bans on all types of PFAS. Restrictions and regulations in Europe for PFA based processing aids used in cables are expected to begin in 2025, with regulations likely to follow in North America. The Wire and Cable value chain is inquiring more frequently about non-PFAS based products. Therefore, there is a need to identify and implement alternative solutions without intentionally added PFAS. This paper reports on development studies to modify MDPE, HDPE and LLDPE jacket compounds by replacing the fluoropolymer-based polymer process aids (PPAs) with equivalent performing PPAs. The extrusion performance of PPAs with different chemical structures are compared and results presented show that equivalent processing aid performance can be achieved with appropriate selection of a non-PFAS based PPA. Replacing PFAS-based PPAs with additives without intentionally added PFAS will lead to more sustainable and environmentally friendly products.

Keywords: Wire; cable; Jacket; die build-up, medium density polyethylene; rheology; viscosity; die swell

1. Introduction

Black polyethylene jacket compounds are widely used in the wire and cable industry for telecommunication and power cable applications. However, these filled polyethylene compounds are susceptible to die build-up during the extrusion process [1]. Die build-up (DBU) refers to the unwanted accumulation of material on the open face of the extrusion die, which can lead to die streaking on the surface of the extruded product as well as additional time and cost to shut down the line and clean the tooling. Excessive die build-up negatively impacts the aesthetic quality and properties of the final product, posing a challenge for the wire and cable as well as the plastic industry. In addition, DBU can be a complex problem to address with many variable factors that can affect it such as tooling, additives, and processing conditions [2, 3]. Although the DBU process that occurs in extrusion is complex, studies reported in the literature show the compositional analysis of DBU material usually consists of low molecular weight species from the polymer. These low molecular weight species may be promoted by shear forces to the die surface [8].

Fluoroelastomer processing aids have proven effective in mitigating die build-up [4, 5]. However, these processing aids are typically based on fluoropolymers and fall under the category of poly/perfluoroalkyl substances (PFAS). PFAS are a group of over 4000 synthetic chemicals characterized by carbon-fluorine bonds rather than carbon-hydrogen bonds. Concerns have been raised about the environmental persistence of PFAS, as they may not readily break down in the environment. Consequently, despite limited data on the environmental hazards, PFAS-containing products have become a subject of increasing regulatory scrutiny [6, 7].

In response to the environmental concerns associated with PFAS, there is potential global impact of increasing restrictions and bans on various types of PFAS. In Europe, restrictions on PFAS-based processing aids used in cables are anticipated to commence in 2025, with similar regulations expected to follow in North America. As a result, the Wire and Cable value chain has raised the need for alternative solutions. Thus, there is a need to identify and implement alternative solutions for polyethylene based jacket compounds that do not rely on intentionally-added PFAS [8].

This paper aims to present fundamental studies by modifying medium density polyethylene (MDPE), high density polyethylene (HDPE), and linear low-density polyethylene (LLDPE) jacket compounds. The objective was to compare fluoropolymer-based polymer process aids (PPAs) with functionally equivalent alternatives that are not considered under the PFAS definition. The performance of these non-PFAS PPAs will be evaluated and compared to the fluoropolymer-based counterparts.

By exploring alternative solutions without intentionally added PFAS, this research contributes to the ongoing efforts to develop environmentally friendly and compliant materials for the wire and cable industry. The findings of this study will provide valuable insights for manufacturers, regulatory authorities, and other stakeholders in their pursuit of sustainable and PFAS-free wire and cable products.

2. Experimental

2.1 Materials

Polymer processing aids with differing chemical structure were melt compounded into LLDPE, MDPE and HDPE jacket compounds and evaluated using a specific DBU test method. The PPA additives used in this study are described in Table 1. The alternative additives listed in Table 1 are not based on fluoropolymer with exception of FP1 and FP2 which are fluoropolymer based and serve as controls. Each PPA will be referred to by the label described in Table 1. The DBU of the jacketing compounds with alternative processing aids were

compared to the DBU of the typical PFA (fluoropolymer) based processing aids. Both FP1 and FP2 are commonly used PFA based PPAs used in MDPE, LLDPE and HDPE jacketing compounds. FP1 has a long history of proven effectiveness for reducing or eliminating DBU in jacketing compounds.

Table 1: Description of Polymer Processing Aids

PPA/ Label	Description
FP1	Fluoropolymer based PA (CAS 25190-89-0)
FP2	Fluoropolymer based PA (CAS 9011-17-0)
Si1	Silicone oil PA
FSi1	Functionalized Silicone oil (high Mw)
FSi2	Functionalized Silicone oil (low Mw)
FPE1	Polar Polymer Additive
FSi1/FPE1	Blend of Functionalized Si oil/polar polymer

The base LLDPE, MDPE, and HDPE resins and final compounds with and without processing aids are described in Table 1. Samples other than base resins were melt mixed in a pilot plant scale Banbury. Each resin or compound will be referred to by the label described in Table 1. All samples with similar labels of the form MDPE 1 BK (No PA) are fully formulated jacketing compounds with all processing aids removed. The BK symbol indicates that the sample contains carbon black.

Table 2: Description of Base Resins and Jacketing Compounds

Resin Label	Description Resin - Compound /PPA	Density (g/cc)
LLDPE	LLDPE jacket base resin	0.920
LLDPE BK(No PA)	LLDPE black compound, No PA	0.932
LLDPE BK/FP1	LLDPE black compound/FP1	0.932
LLDPE BK/FPE1	LLDPE black compound/FPE1	0.932
MDPE 1	MDPE jacket base resin	0.935
MDPE 1 BK(No PA)	MDPE black compound, No PA	0.946
MDPE 2 BK	MDPE Alternate black compound	0.948
MDPE 1 BK/FP1	MDPE black compound/FP1	0.946
MDPE 1 BK FP2	MDPE black compound/FP2	0.946
MDPE 1 BK/FPE1	MDPE black compound/FPE1	0.946
MDPE 1 BK/FSi1	MDPE black compound/FSi1	0.946
MDPE 1 BK/FSi2	MDPE black compound/FSi2	0.946
HDPE 1	HDPE jacket base resin	0.945
HDPE 1 BK (No PA)	HDPE black compound, No PA	0.954
HDPE 1 BK/FP1	HDPE black compound/FP1	0.954
HDPE 1 BK/FPE1	HDPE black compound/FPE1	0.954
HDPE 2	HDPE jacket base resin	0.950
HDPE 2 BK (No PA)	HDPE black compound, No PA	0.960
HDPE 2 BK/FP1	HDPE black compound/FP1	0.960
HDPE 2 BK/FPE1	HDPE black compound/FPE1	0.960

2.2 Test procedures

2.2.1 Die Lip Build-Up (DBU) Evaluation

Figure 1 shows the equipment used to evaluate DBU. Strands are produced by feeding polymer pellets of each sample through a conventional Brabender ¾ in single-screw extruder with standard PE type screw with L/D of 25:1. The die tip size was 0.064 inch diameter. The four heat zones of the extruder were set to 170, 175, 180, 180 °C with a typical melt temperature of 180 °C and extruder rpm of 60. The extruder pressures and melt temperature were captured by a computer and saved (upper right inset of Figure 1). The DBU was captured at equal time intervals up to and including 3 hours. The DBU of selected samples were also captured on video. An example of DBU is shown in the lower left inset of Figure 1. The DBU performance of each sample was evaluated qualitatively at the respective extrusion times typically at 1, 5, 15, 30, 60, 120, 180 minutes using a scale of 1-5 described in Table 3. The target level for achieving low DBU was set at a rating of ≤ 2. Whenever possible the DBU was scraped off the die and weighed with approximate weights for each performance level shown in Table 3. Weighing the DBU was not always possible due to the difficulty in removing trace amounts of DBU from the die face. An intensive cleaning process of all the extruder parts in contact with the melt was carried out between samples to remove any PPA build-up on the metal surfaces and avoid a false reading of the DBU performance.

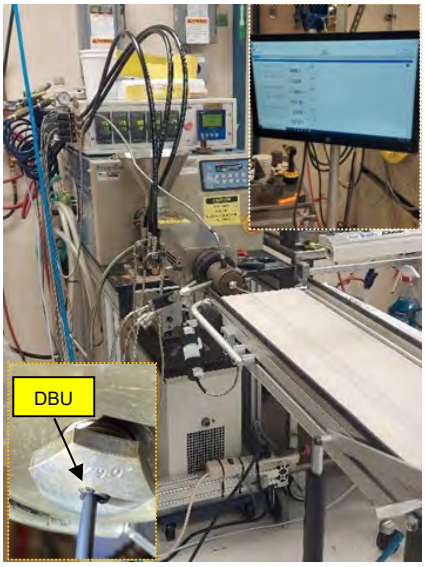


Figure 1: DBU Test Setup

Table 3: Qualitative DBU Performance Scale

Rating	Performance Description
[1]	No DBU observed (≤1mg)
[2]	Slight DBU (>1,≤3mg)
[3]	Moderate DBU (>3,≤6mg)
[4]	Significant DBU (>6,≤9mg)
[5]	Severe DBU observed (>9 mg)

The capillary Rheology curves were obtained with a RH7 floor standing version of a Rosand Precision Rheometer made by Malvern Instruments at 190 °C.

Oscillatory shear measurements were carried out on the samples using 25 mm diameter parallel plates in an Ares Dynamic Mechanical Spectrometer manufactured by TA Instruments. Measurements were conducted at 190 °C and at 0.1 to 100 s-1.

Melt index testing of formulated compounds and resins was carried out on a Tinius Olsen MP-993 unit. Melt index was measured at 190 °C with 2.16 kg and followed the ASTM D 1238 test procedure. The melt flow was also measured in a separate test using a 21.6 kg weight at 190 °C. For each melt property test, the cylinder was charged with 6 grams of material and preheated for 6 minutes.

Tensile strength and elongation were measured according to ASTM D638. Type IV tensile specimens were die-cut from 1.9 mm compression molded plaques. Measurements were made on an Instron 4201 using a 100 lbs load cell with a 2 in/min displacement rate.

Molecular weight and molecular weight distribution were characterized with high temperature gel permeation chromatography (HT-GPC), which consisted of a PolymerChar GPC-IR (Valencia, Spain) equipped with an internal IR5 infra-red detector (IR5). The columns used were four Agilent "Mixed A" columns with 1,2,4-trichlorobenzene (contained 200 ppm butylated hydroxytoluene (BHT) at 150 °Celsius. More details about the measurement method can be found in the reference [9].

3. Results and Discussion

3.1 DBU Results in MDPE

Figure 2 shows images of the DBU over time and performance rating [indicated in brackets] for the MDPE 1 resin control, MDPE 1 BK (No PA), and the MDPE 1 jacket compound containing a commonly used PFA PPA (FP1).

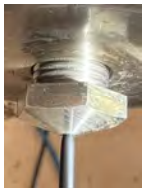
Test time	MDPE 1	MDPE 1 BK (No PA)	MDPE 1 BK/FP1
1 min	 [1]	 [1]	 [1]
15 min	 [3]	 [3]	 [1]
120 min	 [5]	 [5]	 [1]
DBU Onset time (min)	5	5	-

Figure 2: DBU for MDPE 1 Control Samples

The MDPE 1 BK (No PA) is a formulated MDPE black jacket compound with the processing aid removed. The results in Figure 2 indicate that both the MDPE 1 base resin and MDPE 1 BK samples show significant DBU after only 15 minutes run time. Results presented later will show that this lab scale DBU test produces more severe DBU for a given polymer sample when compared to DBU for a wire extrusion line.

Both MDPE 1 and MDPE 1 BK show about equivalent DBU over time although the DBU is slightly worse for the MDPE 1 BK sample. These results suggest that the main contributor to the DBU is the base resin and the other components such as carbon black in the compound may only slightly increase the overall DBU.

The MDPE 1 BK/FP1 containing a typical fluoropolymer PPA has a DBU rating of 1 and shows no DBU over the 3 hrs run time. This result highlights the effectiveness of the FP1 for DBU reduction. Therefore, the target performance rating for achieving about equivalent DBU reduction to the FP1 was a 1 or 2.

Test time	MDPE 1 BK/FP2	MDPE 1 BK/FSi2	MDPE 1 BK/FSi1	MDPE 1 BK/FPE1
1 min	 [1]	 [1]	 [1]	 [1]
15 min	 [3]	 [3]	 [3]	 [1]
120 min	 [5]	 [5]	 [3]	 [2]
DBU Onset time (min)	5	5	15	120

Figure 3: DBU for Selected MDPE 1 Samples

Figure 3 shows images of the DBU as a function of time and performance rating [indicated in brackets] for the MDPE 1 BK/FP2, MDPE BK/FSi1, MDPE BK/FSi2 and MDPE 1 BK/FPE1 samples. Results for the MDPE 1 BK/FP2 showed significant DBU compared to the DBU for the FP1 sample (Figure 2) indicating that not all PFA based PPAs are equally effective for reducing DBU. Results for the samples containing FSi1 and FSi2 at 120 minutes showed that the higher molecular weight silicone oil was somewhat effective in reducing DBU whereas the lower molecular weight silicone oil (FSi2) was not effective. The onset time of DBU for the FSi1 samples was delayed in comparison to the sample with FSi2. Finally, the MDPE 1 BK/FPE1 had very low DBU over the test time and was about equivalent to the results for the sample with FP1. This result confirms that equivalent DBU reduction can be achieved with proper selection of PPA compared to the traditional PFA based processing aid.

Figure 4 summarizes the results of the DBU for selected samples as a function of time. The DBU over time for the MDPE 1 BK sample is slightly worse than the pure MDPE 1 sample which may be due to additives in the MDPE BK sample such as carbon black which may increase the severity of the DBU.

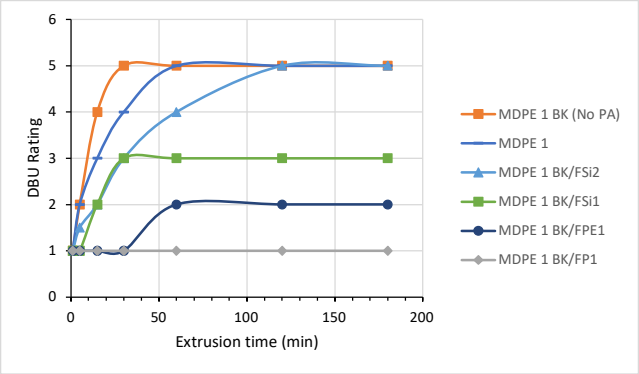


Figure 4: DBU Ratings for MDPE versus time

Figure 5 shows a summary of the DBU performance for the MDPE samples studied. The red dotted line indicates the target performance of ≤ 2. The best performance for the non-PFA based PPAs is achieved with the FPE1 and FSi1/FPE1 PPAs.

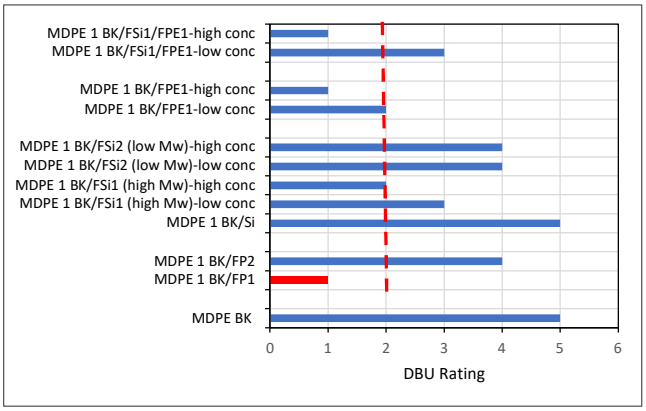


Figure 5: DBU Ratings Summary for MDPE Samples

Figure 6 shows the pressures versus time for selected MDPE samples. The pressure at the die was digitally recorded during the DBU extrusion test. Although there is some scatter in the data, overall trends were observed. The MDPE 1 resin sample without PA (no additives) had the highest overall pressure followed by the MDPE 2 BK sample. The slightly higher pressure of the MDPE 2 BK is likely due to a higher viscosity MDPE resin compared to MDPE 1 BK. It is not known whether the MDPE 2 BK sample contained any PPA. The pressures of the MDPE BK/FP1 and MDPE 1 BK are very similar indicating that the FP1 processing aid did not reduce extrusion pressures. The MDPE 1 BK/FPE1 had the lowest pressure which was slightly lower than the MDPE BK/FP1. This result suggests that the FPE1 PPA will not increase extrusion pressures and pressures will be comparable to compounds containing the traditional FP1 PPA.

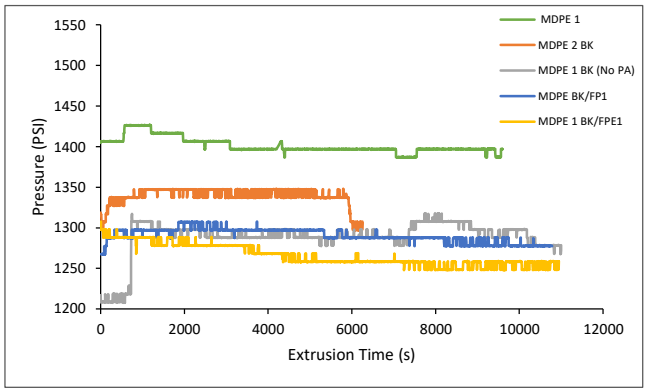


Figure 6: Extruder pressure versus time

3.1.1 Extrusion Scale-up

Selected MDPE samples were evaluated for DBU on a 2.5 inch Davis Standard extrusion wire coating line at 30.5 m/min line speed. The samples were extruded over a period of 2 hours and a subsequent DBU rating determined. A comparison of the DBU ratings for the lab versus scaled up wire extrusion line for the MDPE samples are shown in Table 4. Wire smoothness and breaker plate pressures were also captured during wire extrusion. The DBU overall was much less in the scaled-up wire extrusion compared to the results from the lab DBU method. The lab method provided better differentiation of DBU performance between samples with different PPAs. It should be noted that this was expected since the lab scale DBU test set up exaggerates DBU and provides a worst-case scenario. Results for the MDPE 1 BK/FPE1 showed about equivalent performance to the MDPE 1 BK/FP1 sample in terms of DBU performance as well as wire roughness and breaker plate pressures.

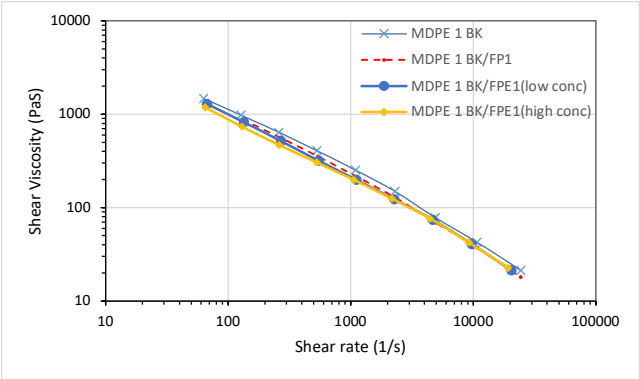
Table 4: DBU Evaluation in Wire Extrusion

Sample / Description	MPDE 1	MDPE 1 BK	MDPE 1 BK/FP1	MDPE 1 BK/FSi1/FPE1 (low conc)	MDPE 1 BK/FSi1	MDPE 1 BK/FPE1
DBU Rating (lab)	**5**	5	1	3	3	2
DBU Rating (wire extrusion)	3	2	2	1	1	1
Wire Roughness (µin) (30.5 m/min)	32.9	15.4	20.7	13.3	13.1	14
Wire Roughness (µin) (115.8m/min)	27.0	27.0	28.6	27.5	26.1	27.8
Breaker plate Pressures (psi) (30.5 m/min), 1hr	3175	3000	2950	2900	2950	3000
Melt temperature (°C)	193.9	193.3	195.0	193.9	195.0	188.9

3.2 Rheology Results

Figure 7a shows that there are no significant differences at the high shear rates as measured by capillary rheometer of the MDPE 1/FPE system compared to the MDPE 1 BK/FP1. These results indicate that the new compounds with non-PFA based PPAs should process equally well as the MDPE 1 BK/FP1 sample. Since it is difficult to see sample differences in Figure 7a, Figure 7b shows an expanded view of the samples in the shear rate range of 100 to about 3000 1/sec. This result shows that the MDPE 1 BK/FPE 1(high conc) sample with higher concentration of the FPE1 additive has slightly lower viscosity compared to the sample with the FP1 PFA based PPA. The lower viscosity of the FPE1 sample is consistent with lower extrusion pressure noted in Figure 6. The blended samples with FSi1/FPE1 are also shown in Figure 7b and have slightly higher viscosities.

(a)



(b)

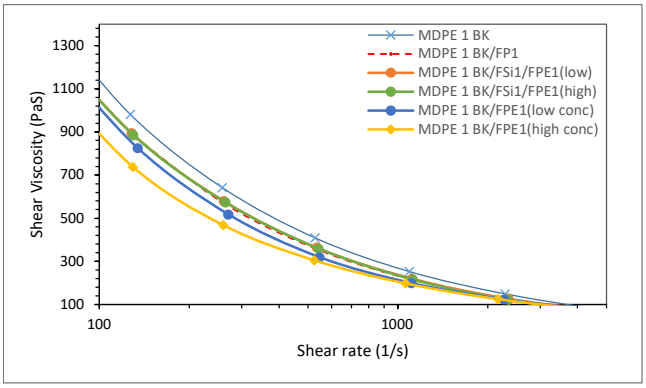


Figure 7: [a] Low to high shear capillary rheology results for selected MDPE samples [b] Expanded view

Strands from the capillary rheometer for selected MDPE samples were captured at different shear rates and examined for flow instabilities such as melt fracture or sharkskin. The lowest shear rates at which flow instabilities first occur were recorded for comparison. Images of the strands at 4 different shear rates are captured in Figure 8. The MDPE 1 resin sample with no PPAs showed flow instability, which appears to be shark skin, at a comparatively low shear rate of 1076 1/s. The MDPE 1 BK sample having no PPA but formulated with carbon black and other additives showed flow instability at 2232 1/s and thus some improvement compared to the MDPE 1 sample. The MDPE 1 BK/FPE(low) with the FPE1 PPA at the lower concentration still shows some flow instability at 2232 1/s but much less pronounced compared to the MDPE 1 BK sample. The MDPE 1 BK/FPE1(high) sample shows no flow instability at 2232 1/s and only some flow defects at a much higher shear rate of 4680 1/s. The results for MDPE 1 BK/FPE(high) is also better than the sample with the PFA based PPA (MDPE 1 BK/FP1), where flow instability occurs at 2232 1/s. It should be noted that these results and method are only valid for making relative comparisons between samples since melt flow stability is highly dependent on many factors including die geometry, temperature profiles and extruder speeds for example. Therefore, these results may not necessarily correspond directly to a full-scale wire extrusion production line. Figure 9 shows low shear oscillating disc rheology results for the

selected MDPE samples. There were no significant differences in viscosity at these low shear rates between samples.

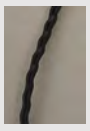
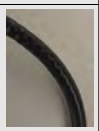
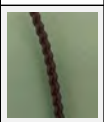
Shear rate (1/s)→ Sample ↓	525.6	1076.5	2232.2	4680.0	Flow instability Onset Shear rate (1/s)
MDPE 1					1076
MDPE 1 BK					2232.2
MDPE 1 BK/FPE(low)					2232.2
MDPE 1 BK/FPE(high)					4680
MDPE 1 BK/FP1					2232.2

Figure 8: Capillary flow versus Shear Rate

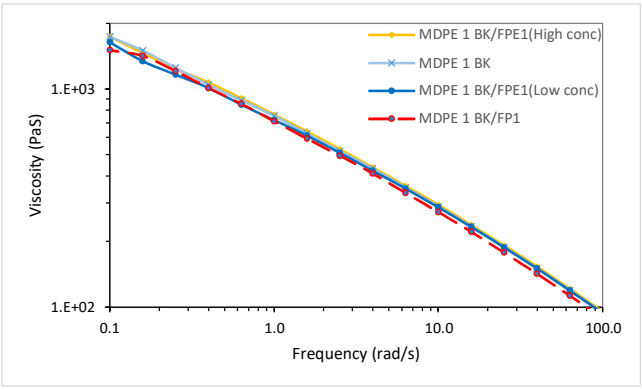


Figure 9: Oscillating Disk Rheology flow

3.3 DBU Analysis

A sample of the DBU from the MDPE 1 sample was captured and analyzed by GPC to gain a deeper understanding of the origin of the build-up. An overlay of the GPC molecular weight distributions (MWD) along with comonomer distributions for the DBU, MDPE 1 and MDPE 1 BK samples are shown in Figure 10. The DBU sample is relatively heavy in low Mw species with Mw at 50,000 and a narrow PDI of 6.3 when comparing to the MDPE compound. Also, the comonomer distributions of the MDPE 1 sample were similar to the related DBU sample. These results are consistent with analysis of DBU samples reported in the literature [10]. Any degradation of the DBU sample while sitting on the die face was minimized by removing the DBU. This hypothesis was consistent with no significant increase at the low molecular weight side in the MWD of MDPE 1 DBU, as shown in Figure 10. More investigation needs to be completed to fully understand the mechanism that leads to the DBU.

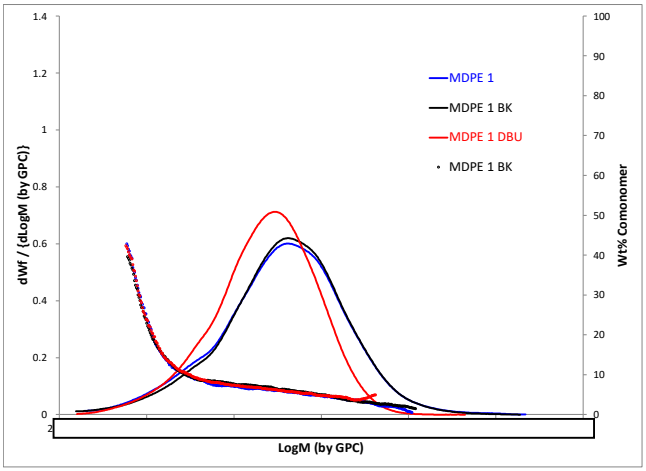


Figure 10: DBU Analysis for MDPE

3.4 MDPE Jacket Properties

The FPE1 additive in MDPE 1 BK/FPE1 was identified as the preferred replacement for the PFA based PPA (FP1). Physical properties of the formulated new compound MDPE 1 BK/FPE1 were compared to the MDPE 1 BK/FP1 to confirm equivalent performance of selected key physical properties. The comparison is shown in Figure 11. These results indicate that the MDPE 1 BK/FPE1 has improved ESCR whereas other measured properties were similar.

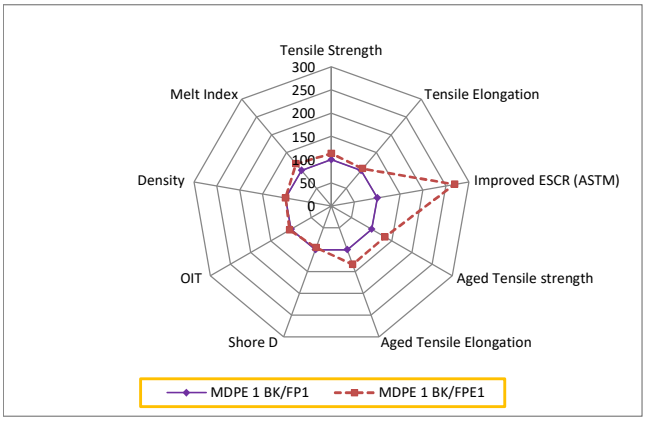


Figure 11: Summary of DBU results comparing the FP1 and FPE1 in the MPDE black jacket compound

3.5 DBU in LLDPE and HDPE

Due to the effectiveness of the FPE1 additive for reducing DBU in MDPE 1, the same additive and concentration was used to replace

the FP PPA in LLDPE and two HDPE jacketing compounds for DBU testing. Results of DBU testing for the LLDPE samples are summarized in Figure 12.

Test time	LLDPE BK (No PA)	LLDPE BK/FP1	LLDPE BK/FPE1
1 min	 [1]	 [1]	 [1]
15 min	 [2]	 [1]	 [1]
60 min	 [3]	 [1]	
180 min	 [4]	 [2]	 [1]
DBU Onset time (min)	10	15	0

Figure 12: DBU Results for LLDPE Jackets

Test/time	HDPE 1 BK (No PA)	HDPE 1 BK/FP1	HDPE 1 BK/FPE1
HDPE 1 at 180 min	 [2]	 [2]	 [1]

Figure 13: DBU Results for HDPE 1Jackets

HDPE 2 BK (No PA)	HDPE 2 BK/FP1	HDPE 2 BK/FPE1 (low conc.)	HDPE 2 BK/FPE1 (high conc.)
 [3]	 [2]	 [2]	 [1]

Figure 14: DBU Results for HDPE 2 Jackets at 3 hrs.

Figure 12 shows the progression of the DBU ratings and images for the LLDPE samples over time up to 180 minutes. The LLDPE BK/FPE1 shows equivalent good performance with little to no DBU over the entire test time. Similar good performance was obtained for both HDPE 1 and 2 and those results at 180 min. are shown in Figure 13 and 14 respectively. The DBU results for HDPE 2 BK/FPE1 were tested at a low and a higher concentration. Results indicated a slight improvement in DBU performance for the sample at the higher concentration of FPE1.

4. Conclusions

The studies presented in this paper confirmed that select non-PFA based PPAs can achieve equivalent performance reduction in DBU in jacketing compounds similar to PFA based PPAs. In addition, this study showed that not all PPAs were effective at reducing DBU, including both PFA (e.g., FP2) and non-PFA (e.g. Si1) based PPAs.

Two non-PFA based additives were effective for reducing DBU, FSi1(high) and FPE1. A lower molecular weight FSi2(low) was not nearly as effective as the higher molecular weight version. Both the FSi1 and FPE1 were able to reduce DBU to the amount roughly equivalent to the FP1 processing aid. The combination of these two additives was also effective as expected. The MDPE 1 BK/FPE1 had slightly lower extrusion pressure compared to the MDPE 1 BK/FP1 in the DBU test. Therefore, the FPE1 was also tested for effectiveness in an LLDPE and two HDPE jacketing compounds. Similar to DBU results for the MDPE jacketing compound, the LLDPE and HDPE results confirmed that the FPE1 additive was equally effective in those jacketing compounds.

More investigation will be considered to determine the cause of DBU however some initial findings by GPC indicate that the DBU mostly originates from the base polymer in the jacketing compound and not significantly affected by other additives. In addition, more experimental work is needed to fully understand how other factors such as shear rates, die geometry and temperature effect the propensity for DBU in these systems.

5. Acknowledgments

Special thanks to Buu-dang Nguyen and the many other contributors from Dow in the Collegeville R&D labs that conducted the testing in this work.

6. References

[1] C.D. Lee, "Die Lip Build-up in the Filled Low Density Polyethylene Wire and Cable Extrusion", *50th IWCS, Proceedings of the International Wire & Cable Symposium (IWCS), Inc* (2001).

[2] F. Ding, L. Zhao, A.J. Giacomin, and J.D. Gander, "Flaring dies to suppress die drool", *Polymer Engineering & Science* 40(10) (2000) 2113-2123.

[3] J.D. Gander and A.J. Giacomin, "Review of die lip buildup in plastics extrusion", *Polymer Engineering & Science* 37(7) (1997) 1113-1126.

[4] S.W. Hotwatt and G.A. Hattrlch, Die Drool in Chemically Crosslinkable Polyolefin Compounds, 46th IWCS, Proceedings of the International Wire & Cable Symposium (IWCS), Inc IWCS, 1997, Philadelphia, PA USA, 1997.

[5] C. Lavallée, "Advances in Polymer Processing Additives (PPA)", *Polyethylene 2005, Maack Conference,* (2005).

[6] O. US EPA, Per- and Polyfluoroalkyl Substances (PFAS), 2024. https://www.epa.gov/pfas.

[7] B. Améduri, Perfluoroalkyl Substances: Synthesis, Applications, Challenges and Regulations, Royal Society of Chemistry2022.

[8] ECHA, Per- and polyfluoroalkyl substances (PFAS) - ECHA, 2023. https://echa.europa.eu/hot-topics/perfluoroalkyl-chemicals-pfas.

[9] T.P. Karjala, L.L. Kardos, H.A. Brown, D.T. Gillespie, Z.L. Polk, and J. Ortega, "*Ethylene-based polymers and processes to make the same*", (2020).

[10] T.A. Hogan, P. Walia, and B.C. Dems, "Investigation of the relationships between die build up and die swell", *Polymer Engineering & Science* 49(2) (2009) 333-343.

7. Pictures of Authors

Karl Seven
400 Arcola Rd. Collegeville, PA 19426, USA



Dr. Karl Seven joined Dow Chemical Company in 2011 and is an Associate Research Scientist within Dow Wire and Cable. He holds M.S. and Ph.D. degrees in Polymer Science & Engineering from Lehigh University. Before joining Dow, he held various technical positions related to polymer product R&D. His present research areas in addition to processing aids include both flame retardant and track resistant polyolefin compounds for wire and cable applications.

Paul Brigandi
400 Arcola Rd. Collegeville, PA 19426, USA



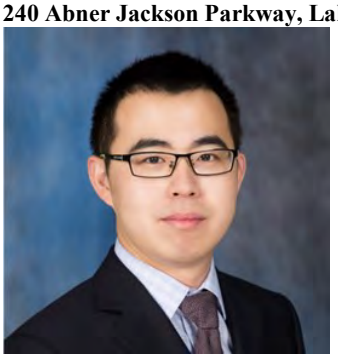
Dr. Paul Brigandi is Application Technology Leader for Dow Packaging & Specialty Plastics Wire & Cable business in North America based in Collegeville, PA. Paul has experience in the power transmission and distribution as well as telecommunication markets focused on research and development of new insulation, jacket, conductive composites, and polymer modifier material developments. His technical expertise includes formulation and processing of polyolefins, elastomers, and polymer composites. Paul is active in several industry organizations including Insulated Conductors Committee, Communications Cable and Connectivity Association, and Fiber Broadband Association technical committees. He also serves as on the Board of Directors of the Society of Plastics Engineers Palisades-MidAtlantic Section. Paul earned a Ph.D. in Polymer Science and Engineering from Lehigh University and a B.S. in Chemical Engineering from the University of Delaware. He is also an active Adjunct Professor at Lehigh University in the Material Science & Engineering department.

Mohamed Esseghir
400 Arcola Rd. Collegeville, PA 19426, USA



Dr. Mohamed Esseghir is a Principal Research Scientist in Elastomers, Electrical & Telecommunications R&D, The Dow Chemical Company. Mohamed holds a B.Sc. in Chemical Engineering from the Algerian Petroleum Institute and M.Sc. and Ph.D. in Mechanical & Aerospace -Engineering from Rutgers University. Following post-doctoral work at Stevens Institute of Technology, Mohamed joined Union Carbides' Polyolefin Research in 1997 then Dow Wire & Cable R&D in 2007. He is currently responsible for new material research for the Telecommunications segment. Mohamed holds over 50 granted patents, he is on the Committee of IWCS, and a past Board member of the Polymer Processing Institute at New Jersey Institute of Technology.

Jingwei Fan
240 Abner Jackson Parkway, Lake Jackson, TX 77566, USA



Dr. Jingwei Fan joined the Down Chemical Company in 2016 and is a Research Scientist within Dow Packaging & Specialty Plastics business. Jingwei earned a Ph.D. in Chemistry from Texas A&M University and a B.S. in Material Chemistry from Nankai University. His current research area includes development and implementation of innovative characterization technologies for polyolefin materials.

Research on Smoke Density Performance of Flame retardant Optical Cables

Yufeng Han, Hao Du, Zhenfu Zhou, Bin Luo, Jianfeng Zhang,Zhuang Hua, Elizabeth Pan,Xuelei Wang

Jiangsu Hengtong Optic-electronic Co., Ltd. Wujiang District, Suzhou City, Jiangsu Province,China

Abstract

With the development of science and technology, modern society pays more and more attention to the flame retardant performance of optical cables. Smoke density and bunching combustion are key indicators for flame-retardant optical cables. In this paper, through the investigation of smoke generation and bundle combustion test of all-medium flame retardant optical cable, it is found that during the combustion test, the polymer content inside the cable core is inversely proportional to the smoke density and bundle index of the optical cable, and the number of molten polymer overflow cable tables inside the optical cable during the combustion process is the key factor affecting the smoke density and bundle combustion index of the flame retardant optical cable. Whether the flame retardant optical cable can pass the bundle combustion test depends on whether the flame center temperature of the optical cable can be continuously reduced after the fire supply is stopped, and the structure of the optical cable and the composition of the sheath material will also affect the bundle test results of the optical cable. On this basis, the structural design and sheath material selection of the optical cable can improve the bundle combustion performance and smoke density of the optical cable.

Keywords: Flame retardant optical cable, Smoke density, Smoke mechanism

1. Preface

With the development of science and technology, people pay more and more attention to the fire safety of living and working environments. Optical cable as an important information transmittance medium, its flame retardant performance is also concerned, in the fire environment due to the combustion of oxygen consumption in the confined space, while releasing a large number of heat, toxic gases and dust, will cause personnel burns and suffocation, fire combustion produced a large amount of smoke will also affect the safe evacuation of personnel. The minimum visibility for people in a smoke environment to correctly determine the direction out of danger is 5 meters, and when the visibility drops below 3 meters, it is very difficult to escape the fire scene. People are extremely unstable in the smoke, which will produce a sense of fear, which causes great difficulties to evacuation and rescue operations, and at the same time the smoke has a shading effect, causing great obstacles to evacuation and rescue operations. According to the statistics of the emergency fire department in 2022, fires caused by electrical reasons accounted for 31.1%, ranking first in the list of fire causes. Compared with flame-retardant cables, flame-retardant optical cables have more flammable substances inside, and it is more difficult to achieve the same flame retardant performance under the same conditions, so the smoke density and bundle combustion of flame-retardant optical cables are the pain points of the current industry.

The current general standards for the test methods of smoke density and bundle combustion of flame retardant optical cables in the industry are IEC61034-2005《Measurement of smoke density of cables burning under defined conditions》 and IEC60332-2-24-2018《Tests on electric and optical fibre cables under fire conditions –Part 3-24: Test for vertical flame spread of vertically-mounted bunched wires or cables – Category C》.

2. Optical cable product structure and performance

In order to better study the flame retardant performance of optical cables, the all-dielectric double-layer flame retardant optical cables commonly used in the rail transit field are selected. In view of the characteristics of the closed and harsh environment of such optical cables, customers have strict requirements for the smoke density and bundle test of optical cables. Its structure is shown in Figure 1, and the structure from outside to inside is: outer protection LSZH, glass fiber armor layer, inner sheath layer LSZH, loose tube, center reinforcement. Figure 2 shows the curve of light transmittance with time during the smoke density test of an all-dielectric double-layer flame retardant optical cable (light transmittance is the specific index of the smoke density of the optical cable). According to the detection technology, there are different opinions on the reasons for the decrease in light transmittance of flame retardant optical cables during smoke density test, which is due to the lack of in-depth exploration of the principle of smoke formation in the smoke density test of optical cables.



Figure 1. Schematic diagram of the structure of the optical cable and the finished product

Return to Table of Contents

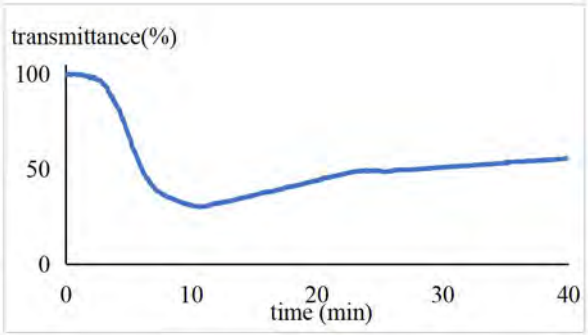


Figure 2.light transmittance change curve of flame retardant optical cable with time during smoke density test

3. Flame retardant optical cable smoke generation principle

3.1 Smoke mechanism

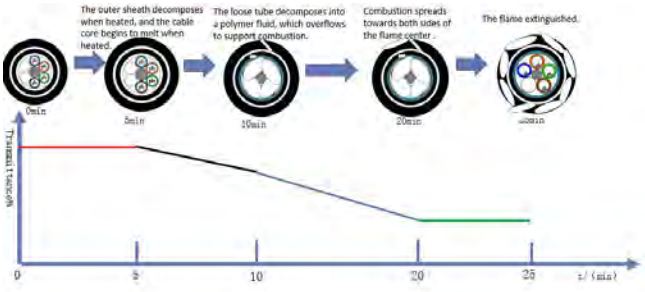


Figure 3.light transmittance curve of all-media double-layer flame retardant optical cable in smoke density test

According to IEC61034-2005 《Measurement of smoke density of cables burning under defined conditions》 the fuel flame temperature used in smoke density testing can reach a maximum of 840°C or more [1].。At this temperature, all materials in the optical cable except metal materials and glass fibers show a carbonized decomposition state.

Within 5min from the beginning of the smoke density test, the low-smoke halogen-free outer sheath of the flame-retardant optical cable is first decomposed by heat, and the smoke component is mainly small molecules produced by the decomposition of the low-smoke halogen-free sheath. Flame retardant substances such as metal hydroxides in the low-smoke halogen-free sheath material are decomposed into water and metal oxides by heat, and the water produced by decomposition will further evaporate and absorb the heat of the cable surface, and the metal oxides produced by decomposition will attach to the surface of the optical cable to form a crusting material, further preventing the outside high temperature from invading the inside of the optical cable. As shown in Figure 4, the decomposition of the LSZH sheath material will produce a honeycomb structure attached to the surface of the steel strip, which will further block the penetration of the external flame and high temperature.



Figure 4.Cable table and fiber optic cable section diagram after 5min heating of flame retardant optical cable

When the smoke density test is carried out to 6-10min, the high temperature generated by the flame passes through the low-smoke halogen-free outer sheath, the glass fiber armor layer, and inner sheath from the outside to the inside to reach the optical cable core, and the polymer material of the cable core is first endothermic melting. The melting temperature range is 200°C-300°C, and the decomposition temperature range are 350°C-500°C. The fiber paste and cable paste in the optical cable will enter the boiling state from the molten state, at this time the internal pressure of the cable core gradually increases, and some polymer materials reach the decomposition state from the molten state, as the temperature of the cable core continues to rise, the molten polymer material will form a polymer fluid under a certain pressure. Under the condition that the outside world continues to provide heat, the polymer fluid will overflow from the lap joint of the glass fiber yarn armor layer, and will be directly ignited by the external flame, and some of the polymer fluid that fails to overflow the cable surface will be carbonized and decomposed inside the optical cable. At this time, the reason for the decrease in light transmittance is that some small molecule polymers are not completely burned. Some optical cables will also enter the next combustion stage in advance due to unreasonable design.



Figure 5.Polymer fluid spillage and cable sheath section view during combustion

When the smoke density test continues to 11-20min, the polymer fluid in the molten state continuously overflows from the cable core to the surface of the optical cable, and the polymer fluid on the cable surface will be directly ignited by the flame. When the overflowing polymer fluid is all burned by the external flame, the amount of smoke produced in this process will be reduced; When the polymer fluid overflows too fast to be completely ignited, the unignited molten substance will directly form small molecular substances under the action of external flames due to the decomposition temperature, and form black smoke visible to the naked eye after exposure to the air. As shown in Figure 6, the polymer fluid that overflows the cable surface

Return to Table of Contents

will form a combustion flame after being ignited, increase the flame temperature, accelerate the overflow of the polymer fluid, and form a deflagration phenomenon, resulting in a cliff-like decline in light transmittance at this time.



Figure 6.Deflagration during smoke density test

When the smoke density test progresses to 20-25min, due to the fuel consumption, it is impossible to continuously provide heat to the optical cable, the polymer fluid inside the optical cable will stop overflowing, and the optical cable will be cooled from the outside to the inside. The smoke accumulated in the smoke density solid chamber has formed a stable aerosol, and when the temperature of the smoke density combustion chamber decreases, the light transmittance value will not change with the decrease of temperature.



Figure 7. Laboratory diagram of fiber optic cable status and transmittance at the end of combustion

After the smoke density test, the optical cable was dissected, the low-smoke halogen-free material inside and outside the optical cable was all decomposed, the sheath material showed a damaged state, except for the glass fiber, the rest of the materials were all carbonized and decomposed, and the optical cable structure was damaged.

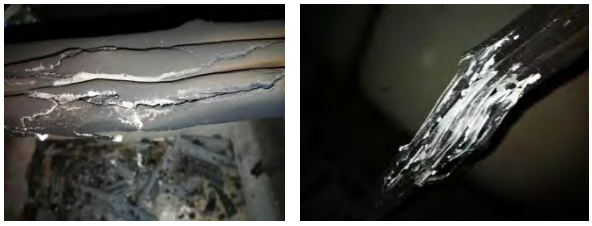


Figure 8. The status of fiber optic cable after burning

4. Material selection and structural design

4.1 Optical cable material selection

4.1.1 Physical property analysis of optical cable materials.

After characterizing some materials of this optical cable by thermogravimetric analyzer (TGA), it was found that the anaerobic decomposition temperature of the polymer material under the protection of N2 atmosphere was concentrated in the range of 250-550°C.

Table 1.The main polymer decomposition temperature and melting interval of optical cable

Fiber optic cable material name	The main components of the material	Melting temperature(°C)	Decomposition temperature(°C)
Fiber paste/cable paste	Unsaturated hydrocarbons	/	250-350
Loose tubing	PBT	225-235	285-325
Tying yarn	PET	257-267	315-425
Low-smoke halogen-free sheath material	PE	180-255	403-581
	Aluminum hydroxide	/	220-320
	magnesium hydroxide	/	355-402
	calcium carbonate	/	583-805

4.1.2 Smoke generation mechanism of materials

4.1.2.1 Calcium carbonate.Calcium carbonate mainly plays a filling role in low-smoke halogen-free materials, and the combination of calcium carbonate and silane coupling agent can improve the oxygen index of the material within a certain range. In the process of smoke density test, because the combustion temperature cannot reach the calcium carbonate decomposition temperature, resulting in the low smoke halogen-free sheath material after heating, the nano-level calcium carbonate distributed in the sheath material directly volatilizes into the air, and the water vapor, dust and particles formed by dispersed combustion form aerosols in a closed environment, which has a Tyndall effect on the light source, so that the light transmittance of the optical cable is reduced. When the calcium carbonate exceeds a certain content, it will directly destroy the shelling performance of the sheath material, so that the structure of the optical cable is damaged during the burning process of the bundle. Figure 9 shows the results of the C test of flame retardant optical cable bundle C with calcium carbonate added more than 15% in the low-smoke halogen-free sheath.

Return to Table of Contents



Figure 9. The test diagram of flame retardant optical cable bundle C with calcium carbonate added more than 15% in low-smoke halogen-free sheath material.

4.1.2.2 Aluminium hydroxide, magnesium hydroxide.

Aluminum hydroxide and magnesium hydroxide materials are flame retardant components widely used in low-smoke halogen-free flame retardant sheaths, both of which are inorganic filler flame retardants. Both types of flame retardants achieve flame retardant effects by decomposing and absorbing heat during combustion to produce water and metal oxide protective shells.

The thermal decomposition temperature and shelling property of magnesium hydroxide are higher than those of aluminum hydroxide[2]. In the all-dielectric double-layer flame retardant optical cable type under the same specification, two aluminum hydroxide and magnesium hydroxide sheath materials with the same filling ratio were used for smoke density test, and the results showed that the sheath material containing only magnesium hydroxide was about 10% higher than the sheath material containing only aluminum hydroxide, and the carbonization height was 15% lower in the bundle test. The reason is: in the combustion process, compared with the decomposition and heat absorption of magnesium hydroxide itself, the thermal conductivity of magnesium oxide generated by the decomposition of magnesium hydroxide is lower, which can block more flames from damaging the structure of the optical cable and prevent the deflagration of the cable core.

Figure 10 ,11 and 12below shows the shelling effect of aluminum hydroxide and magnesium hydroxide sheath material added in the same proportion after the combustion test. It is obvious from the picture that magnesium hydroxide has better catalytic shelling of the resin during combustion, and the shell wall thickness is denser and harder.

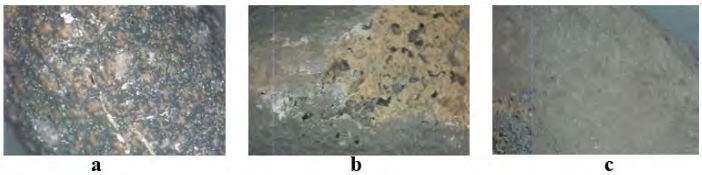


Figure 10. Shelling capacity of magnesium hydroxide and aluminum hydroxide in different proportions.

a magnesium hydroxide shelling surface;b, magnesium hydroxide: aluminum hydroxide 1:1 shelling profile; c, aluminum hydroxide shelling surface

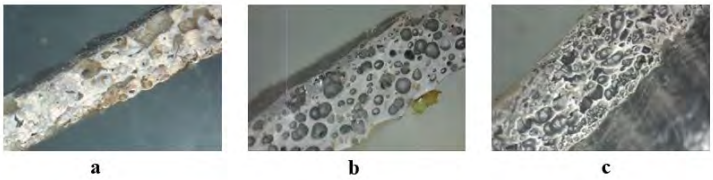


Figure 11. Shelling cross-sectional view of magnesium hydroxide and aluminum hydroxide in different proportions.

a magnesium hydroxide shelling profile; b, magnesium hydroxide: aluminum hydroxide 1:1 shelling profile.;c, aluminum hydroxide shelling profile.

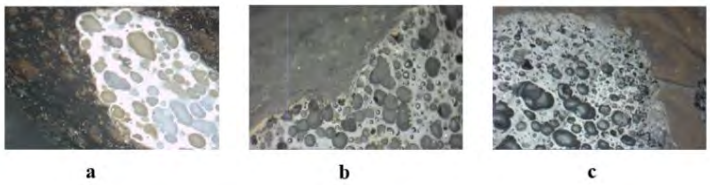


Figure 12. Different proportions of magnesium hydroxide and aluminum hydroxide shell bevel section.

a, magnesium hydroxide shell bevel section; b, magnesium hydroxide: aluminum hydroxide 1:1 shell bevel section; c, aluminum hydroxide shell bevel section

4.1.2.3 Polyethylene resins.Polyethylene resin is the base material of low-smoke halogen-free material and one of the main materials for filling rope. Under normal conditions, whether the polyethylene resin is fully burned is positively relation with the light transmittance in flame-retardant optical cables. The high carbon content of polyethylene resin which decomposition temperature of polyethylene resin is in the range of 400-581 °C, will produce some black smoke even if it is fully burned.

4.1.2.4 LSZH ceramicized materials.LSZH ceramic materials are mainly composed of polyolefin resin, compatibilizer, low-temperature porcelain additives, medium-temperature porcelain additives, high-temperature porcelain additives, inorganic mineral powders, antioxidants and lubricants. The independent use of ceramized materials will cause cracking and breakage during combustion, and the role of shelling and flame isolation cannot be achieved. Therefore, ceramic compounds have limited effect on the light transmittance and bundle combustion of flame retardant optical cables.

4.2 Optical cable structure design

4.2.1 Burn-through scheme

According to the smoke production mechanism of all-media double-layer flame retardant optical cable in the process of smoke density test, the amount of polymer fluid overflow inside the optical cable is inversely proportional to the light transmittance. Therefore, it

Return to Table of Contents

is necessary to control the overflow amount of polymer fluid that the spilled polymer fluid can be fully and completely burned by the flame.

Methods to improve the light transmittance of the optical cable:

- Optimizing the construction of the optical cable.
- Controling the thickness of the LSZH sheath material.
- Reducing the amount of polymer used inside the optical cable to control spillage of the polymer fluid.

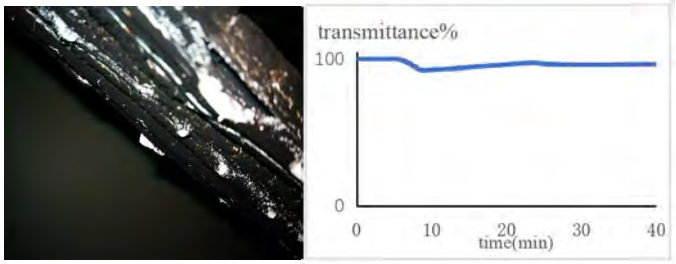


Figure 13.Smoke densitytransmittance of burn-through cable scheme

4.2.2 Controlling Overflow Schemes

Since the burn-through scheme is suitable for the small size direction of the optical cable, it is necessary to strictly control the matching degree of the cable core size and sheath material during the design process. When customers have requirements for the sheath thickness, number of cores and size of flame-retardant optical cables, the optical cables under this idea cannot meet customer requirements. In order to better solve such problems, the comprehensive burn-through scheme and the fully enclosed scheme propose a control overflow scheme for the large core number flame retardant optical cable, and the following improvements are made to the optical cable structure.

The addition of calcium carbonate powder materials to the LSZH sheath material is eliminated, and the use of inorganic phosphorus-based flame retardants with high smoke is eliminated. The flame retardant components in the LSZH sheath material are strictly controlled within a certain range, and the barrier fuel based on magnesium hydroxide flame retardant is used to improve the shelling performance of the flame retardant material. The inner and outer sheaths of flame-retardant optical cables can effectively block the intrusion of more heat from the outside, thereby reducing the temperature inside the cable core to a certain extent and delaying the spillage rate of polymer fluids.

In the structural design of the cable core structure, the filling rope and cushion are made of flame retardant materials to aviod the flame-retardant optical cable structural damaged during the combustion process. And Controling the spillage speed of molten polymers during the combustion process of flame-retardant optical cables to avoid uncontrolled deflagration of molten polymers inside optical cables in a short period of time.

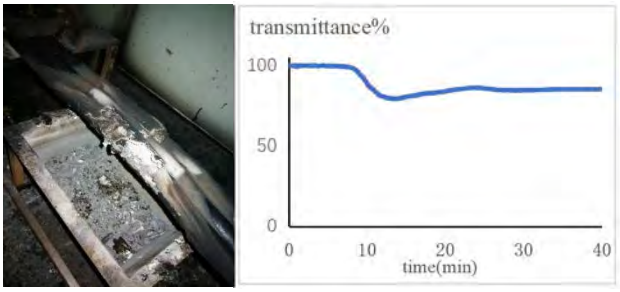


Figure 14.Control overflow scheme smoke density test

5. Category C combustion test

According to the use scenarios of flame retardant optical cables, all-media double-layer flame retardant optical cables are usually required to pass the category C combustion test. Due to the protection of two layers of fuel resistance and glass fiber yarn, the overall structure of the optical cable has little damage during the bunching process, and the internal impact of the flame on the inside of the optical cable is small, and it's easy to pass the category C test.

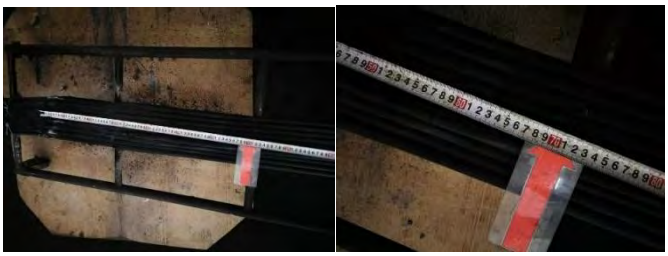


Figure 15.Test results of the category C test

6. Summary

According to the smoke generation mechanism of all-media double-layer flame retardant optical cable, there are currently two ways to improve the high light transmittance of the fuel resistance: the first scheme is to reduce the proportion of polymer materials of optical cables and reasonably control the ratio of cable core and sheath material; Another scheme is to reasonably control the proportion of resistant fuel in the optical cable in the structural design, increase the content of magnesium hydroxide flame retardant in the retardant fuel, so that the structure of the flame-retardant optical cable is not destroyed during the combustion process, so as to better control the amount of polymer fluid overflow inside the cable core during the combustion process and prevent the deflagration of the optical cable during the test.

In the LSZH sheath, due to the use of inorganic phosphorus and calcium carbonate, the light transmittance data of flame retardant optical cable will drop sharply as the outer diameter of the optical cable increases. Therefore, when selecting sheath material for flame retardant optical cables with smoke density requirements, the proportion of this smoke material must be strictly controlled.

The higher the flame retardant composition of the flame retardant material, the better the carbon shelling in the combustion process, the less heat the external flame reaches the inside of the optical cable

Return to Table of Contents

through the sheath material, so that the polymer material in the optical cable is not sufficiently heated, the degree of decomposition and overflow is limited, and the failure to fully burn, the phenomenon of "stewing" occurs, resulting in a cliff-like decline process in the light transmittance before the flame is extinguished [3].

7. References

[1] Hao Jinsheng et al. Measurement of flame temperature of fuel lamps. Experimentation and innovative thinking[J]. Issue 6, 2004.

[2] ZHANG Jun et al. Polymer Combustion and Flame Retardant Technology, April 2005, First Edition, P132-133.

[3] Shi Jiaqian et al. Discussion on smoke density performance of flame retardant optical cable.Proceedings of the 2022 Communication Line Annual Conference of the Chinese Society of Communications.

8. Authors



Yufeng Han received his Bachelor's Degree in 2009. Since then, he has been working in optical fiber cable technology area for more than 14 years. Now he is a R&D director of R&D Department of Jiangsu Hengtong Optic-electric Co., Ltd, engaged in new products, new processes, new materials development and research.



Hao Du , Master of Materials Science and Engineering, used to work for Prysmian as a process engineer, and joined Hengtong Optic-electric Co., Ltd as a R&D engineer in 2021, mainly engaged in the development and research of optical cable materials.



Zhenfu Zhou graduated from Harbin University of Science and Technology majoring in electrical and insulation materials, engaged in optical fiber and cable manufacturing for more than 20 years, and consistently engaged in process research.



Bin Luo, Intermediate engineer, works in Jiangsu Hengtong Optic-electric Co., LTD., has been engaged in the research and development of optical fiber and cable testing, participated in the preparation of national and industry standards of optical fiber and cable and its raw materials for many times and published related papers, won a number of invention patents, and participated in the preparation of professional works.



Jianfeng Zhang, Senior Engineer, the current Hengtong Optic-electric Co., LTD. General manager, Hengtong Industrial design center director, used to be engaged in optical fiber and cable testing technology research and product sales.



Zhuang Hua obtained his B.S. degree in Optical Information Science & Technology from Wuhan University in 2022. He has been working at Jiangsu Hengtong Optic-electric Co., Ltd since then, engaged in the development of flame retardant optical cable.



Elizabeth Pan has over15 years of experie nce working in the telecommunication indu stry. She has worked in a number of public companies including ZTE, SUNSEA TEL ECOMMUNICATIONS, and the HENGT ONG GROUP. In addition to working in th e United States,she has experience working in the Middle East, Europe and North Afri ca. Ms. Pan has worked as a product engine er, sales director, chief representative of overseas , and now serves as G eneral Manager of GIGAWAVE INC, the North American Subsidary o f the Hengtong Group.



Xuelei Wang graduated with a master's degree in Materials Engineering from Hohai University and worked at Jiangsu Hengtong Optic-electronic Co., Ltd. in 2023. Currently, he serves as a research and development engineer for optical cables, ,focusing on the field of high flame retardant refractory materials.

Return to Table of Contents

SESSION 12

Click on a session below to navigate to that section of the Proceedings.

SESSION 12: CABLE MODELING & DESIGN

Chairperson: Ken Cornelison, Wire & Cable Technology Resources, USA

12-1 **Exploration Study of Jacket Shrinkback Test Methods;** Massimo Carboni, *Belden, Canada*

12-2 **An Analytical Formula of Microbending Sensitivity for Reduced Diameter Optical Fibers;** Mr. Takahiro Nomura, *Sumitomo Electric Industries, Ltd., Japan*

12-3 **Indoor-Outdoor Air Blown Optical Cable;** Mr. Naoya Maehara, *Fujikura Ltd., Japan*

12-4 **Central Tube Cable Design for Easy Access of Embedded Strength Members;** Mr. Sravan Kumar Peraka, *Sterlite Technologies Limited, India*

12-5 **Hybrid Cables for 4G/5G Technology Networks;** Mr. Kleber Caliani, *Prysmian Systems S.A., Brazil*

Click here to return to the **Table of Contents**

Exploration Study of Jacket Shrinkback Test Methods

Massimo Carboni, Tahereh (Tara) Ahmadi Tameh, Annabelle Scarpaci*, Joseph W. Koeing*

R&D Fiber Optic Connectivity Dept., Belden Canada ULC.
Montreal, Qc, Canada
*Optical Fiber Cable Engineering Group, Belden,
Richmond, IN, USA

+1-514-822-7507 · massimo.carboni@belden.com

Abstract

In this paper, we present the results of shrinkback study on furcation tubes with outer diameters of 1.6mm/2mm/3mm with different constructions. We used cable and connectivity shrinkback test methods and their variations to find and propose uncomplicated and faster shrinkback test methods for a production environment where rapid cable prototype testing is necessary.

Keywords: Shrinkback; Polyvinyl Chloride (PVC); Fiber Optic Subunit Cabling; Temperature Cycling; Temperature Aging; Rapid Aging; Furcation Tubing; Phase Diagram; Shrinkage.

1. Introduction

Fiber optic cable shrinkback is a controlled variable in the construction and qualification of jacketed cable. Jacketed cable shrinkback can influence the optical performance of an optical cable assembly in terms of deteriorating the attenuation of the assembly. Currently, many fiber optic cable manufacturers use existing standards [1] to measure and evaluate cable shrinkback, however new proposals [2] are putting into question which test method is more appropriate for which specific cable construction and is creating urgency in understanding how environmental testing affects cable shrinkback and why.

The shrinkback effect on the jacketed cable and the rationale behind each behavior was a goal focus of this evaluation. The samples chosen for testing focused solely on Polyvinyl Chloride (PVC) and a PVC + Polyurethane blend (PVC/PU) fiber optic jacketed furcation tubing of various dimensional construction.

For the comparative analysis on shrinkback behavior, different cable and connectivity test methods are evaluated in this study on whole furcation tube or jacket-only. The three cable shrinkback test methods used in this study are as follows: 1) +85°C / 4 hours as per GR-409, 2) 110°C / 2 hours as per GR-409, and 3) 5 cycles between -10°C to +70°C as per IEC TR 62959. Also, we included the connectivity shrinkback test of 1 cycle of -40°C to +75°C as per GR-326. Some other tests were added to verify some aspects of the similar tests.

As commentary to the new IEC 67094-1-211 Method F11A, this paper will propose an alternate test procedure for measuring fiber optic cable shrinkback. Considerations for this alternative method will be the ease of testing (i.e., not requiring sophisticated environmental chambers nor the need for programable chambers which are necessary for thermal cycling). Furthermore, this new test procedure will have considerations for a production environment where rapid cable prototype testing is necessary. The new test procedure must be faster than 2 hours at 110°C and 4 hours at 85°C while still correlating to these methods and their requirements. To quantify the effect of temperature on cable and to determine a justifiable alternate test procedure for measuring fiber optic cable shrinkback, the following test methods were investigated. Samples were tested against the full IEC Method F11A proposed 5 cycles, GR-409 85°C for 4 hours and GR-409 110°C for 2 hours. Furthermore, samples were then tested at 85°C at hourly intervals between 1 to 4 hours to see how cable shrinkback is affected during testing. Finally, samples were tested in temperature cycling for 1 cycle of -40°C to 75°C compared to holding steady state 1 hour of 75°C to quantify the affect low temperature cycling has on cable shrinkback performance.

2. Fiber Optic Cable and Connectivity Shrinkback

2.1. Materials and Manufacturing

Understanding the material characteristics and the manufacturing process of fiber optic cable jackets is essential in defining specifications and the standards in which we will hold the performance of the finished product to. To limit the scope of this study, the focus was specified to cable jackets derived from Polyvinyl Chloride (PVC) and PVC/PU blends, which make up the majority of fiber optic sub-assembly cabling for indoor use sold in North America. PVC is a thermoplastic polymer produced by polymerization of vinyl chloride monomer (VCM) which in turn is the product formed by the pyrolysis of chlorinated ethylene. PVC is an excellent material for cabling jackets as it is lightweight, durable and is resistant to weathering or chemical rotting. PVC blends are also extremely popular, the most common being PVC & Polyurethan blends (PVC/PU) which offer a better chemical and abrasion resistance. PVC and its blends have a high chlorine content making it self-extinguishing at the cost of releasing toxic gases when burned.

Fiber optic cable shrinkback is a consequence of the method of manufacturing cable jackets, which is done through the process of plastic extrusion. During jacket construction, plastic can move through the extrusion die at very high speeds, several hundred meters per minute. As the plastic

gets drawn through the die, it is subjected to extremely high shear stresses; while outside of the die, further stresses are applied to the polymer melt as it is pulled through a tip and a die. The final stage of the extrusion process is a quenching of the melt in water trough before final spooling. Plastic temperature profile, draw-down ration (DDR) defined by tip and die size, and final quenching conditions, all have a significant impact on the resultant cable jackets mechanical performance including its shrinkback. In addition, any variation of the raw compound of the melt can influence shrinkback. PVC is an amorphous polymer made up of long, randomly orientated molecular chains. These chains are randomly entangled and are filled with voids located in the free space between chains or at the ends of the chains. During the die extrusion and the drawing of the polymer melt, a specific orientation is imposed in these chains and the melt is drawn out of the die and following the quench, these imposed molecular orientations are frozen. These molecular chains tend to relax over time when under environmental conditions and re-align themselves back in their amorphous random nature. This movement of the polymer chains results in the shrinkback phenomenon that is the focus of this paper.

The shrinkback effect can be minimized by controlling the processing conditions, specifically around the drawing of the melt as any stretching of the cable jacket during the extrusion process between the extrusion head and the final take-up will affect shrinkage values. Some examples of process controls to reduce shrinkback is lowering the DDR to limit the alignment of the polymer's molecular chains. Additionally, stress in the die can be reduced by selecting appropriate tooling that limits the amount of shear stress and in turn chain alignment. Process temperature can also mitigate cable shrinkback. Running a hotter extrusion process reduces the melts viscosity, therefore, relaxing molecular alignment. Moreover, keeping the melt hotter for longer allows for more relaxation of the polymers chains before being frozen in place.

Knowing why and how cable shrinkback occurs is essential to fiber optic jacket design and manufacturing, however it is equally important to understand the performance target set by standards bodies and the testing procedures put in place to validate these cables. Once the cable is manufactured and the initial shrinkback is experienced, further post-manufacturing shrinkage can be observed which is the main driver for performance standards and the necessity to limit cable shrinkback percentage outside of the manufacturing process.

2.2. Fiber Optic Cable and Connectivity Shrinkback Standards

Current cable shrinkback standards are guided by Telcordia GR-409 generic requirements of indoor fiber optic cable and set the pass/ fail target of cable jacket shrinkage to less than 5% [1]. While Telcordia specifies the target limit for cable shrinkback, the test method is driven by TIA-455-86 (FOTP-86) [3]. The test method calls for samples to be cut at lengths of 150mm and thermally aged at 110°C for 2 hours. It is further specified that for materials with undefined melting point (Tm) which is the case of jacket materials studied in this paper or with a Tm below 110°C, the samples can then be aged at 85°C for 4 hours.

Currently the International Electrotechnical commission (IEC) is proposing a new test procedure along with performance targets for fiber optic cable shrinkback. The new proposal, denoted as method F11 from IEC 60794-1-22:2017 [4] (to be referred to as Method F11), separates from the existing FOTP-86 method in many ways. The first major way that the IEC Method F11 is to subject the test samples to temperature cycling as opposed to holding for a steady state temperature. IEC states that the samples must be thermally aged for 5 cycles of -10°C to +70°C (see figure 1).

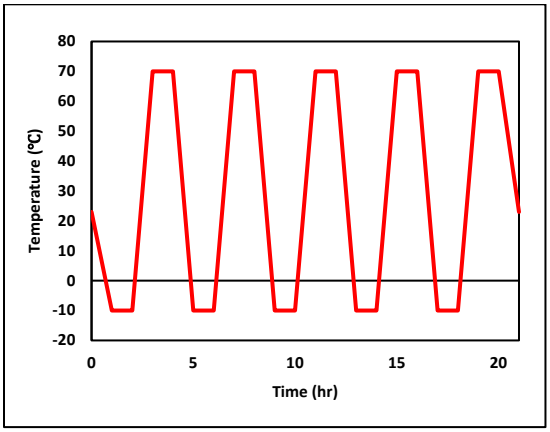


Figure 1: Temperature Plot for IEC Method F11A for C^{HD} Performance Category

Method F11 demands a much long test time compared the FOTP-86, taking over 20 hours to complete all 5 cycles. Additionally, the performance requirement is more severe, stating a maximum allowable shrinkback of 20mm on a 1m sample (2% shrinkback) compared to the 5% allowable limit set by GR-409.

The proposal of method F11 put into question the test procedure for measuring fiber optic cable shrinkback along with the rationale behind current test methods. GR-409 calls for temperatures of 110°C for 2 hours or 85°C for 4 hours for material with a Tm below 110°C or if the material has no well-defined melting point. However, with very low crystallin amorphous materials, such as PVC, the Glass Transition temperature (Tg) is most often lower than room temperature and their melting point (Tm) are usually not well defined. Consequently, it is prudent to run thermal analysis methods, such as thermogravimetric analysis (TGA) to measure the materials physical change over time. In the case of the PVC and PVC blends studied in this paper, Figure 2 shows that around 100°C, there was a sharp drop of weight (%) measured through TGA.

Explanation for this sharp drop of weight is explained by the evaporation of water moisture from the polymer itself. At temperatures near the boiling point of water, moisture is evaporated from within the polymer leading to shrinkage due to drying. The additions of voids in the amorphous structure due to water evaporation allows greater potential for polymer chain movement and stress relaxation.

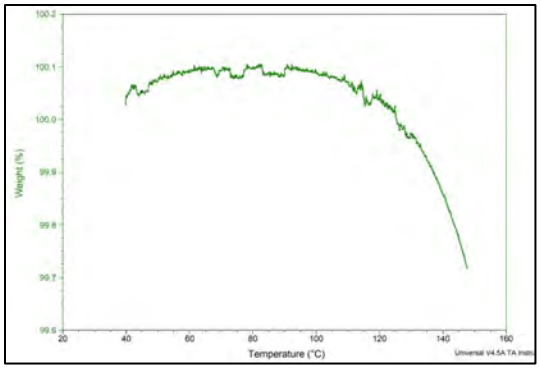


Figure 2 TGA Analysis for Sample # AC-01

Additionally, Method F11 which calls for cycling between -10°C and +70°C (for C^{HD} performance) begins thermal cycling at the low temperature extremes. Thermodynamically, larger movement of molecular chains are expected to occur when commencing a thermal cycling procedure on the high temperature plateau as chains are given more energy to relocate and then are re-frozen in at the low temperature cycle. Furthermore, the thermal exposure duration is also a factor in measuring shrinkback percentage. As the majority of cable jacket shrinkback occurs during the extrusion process where 1 cycle of heating and quenching is experienced by the polymer, the rational for IEC Method F11 having 5 cycles is to be determined.

Telcordia standards separate the thermal loads experienced by fiber optic cable depending on if the cable is terminated with connectors or for general purpose. For connectorized cable assemblies, Telcordia described the temperature, humidity, and condensation tests in GR-326-CORE [5]. Focusing on testing that can affect cable shrinkback on connectorized assemblies, GR-326 demands thermal aging test at steady state 85°C for 168 hours and for thermal cycling test between 70°C and -40°C+ for 21 cycles. As most bulk cable being tested for shrinkback against GR-409 and Method F11, samples will be further tested against GR-326 thermal cycling as it bears investigation how starting cyclic aging at high temperatures and going to low temperatures affect cable shrinkback.

it bears investigation how the low temperatures and high temperatures in the beginning of the cycling affect cable shrinkback.

3. Test Methods

3.1. Cable Type and Materials under investigation

Samples used in this investigation were comprised of plasticized PVC and plasticized PVC/PU blends. All jacketed cable in this study shared the same construction. The jacketed cable evaluated in this study comprise of an inner tube surrounded by aramid yarn strength members under an overall jacket. These type of cable constructions, called furcation tubing, are generally used as fanouts for cable assemblies. Figure 2 shows the general construction of the cable used in this study.

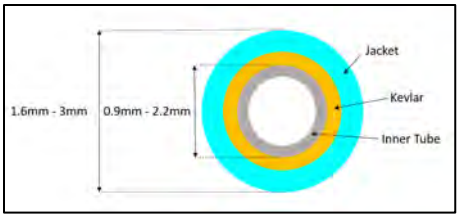


Figure 3 Generic Fiber Optic Furcation Tube Cable Construction

Samples were separated into groups based on outside cable jacket diameters and by manufacturing supplier. Table 1 classifies the varying jacket and construction that were evaluated in study. The first letter of the part number represents the outside diameter (OD) of the jacketed cable. The second letter represents the capacity of inner tube for fiber 250um or 900um.

Table 1: Samples naming.

First Lett.			Second Lett.		
	A	2.0mm		A	1 x 250um
	B	3.0mm		B	2 x 250um
	C	1.6mm		C	1 x 900um
				D	12 x 250um
				E	24 x 250um

Table 2 shows samples and their characteristics used in this study. The numbering after two letters represents three different manufacturers.

Table 2: Samples Dimensions and Construction

Part Number	Jacket OD (mm)	Inner Tube OD (mm)	Denier / Area (Den/m m2)	Inner Tube Material	Jacket Material
AA-01	2	0.9	5608.66	Polypro	PU/PVC
AA-02	2	0.9	4387.33	Polypro	PVC
AA-03	2	0.9	5059.47	Polypro	PVC
AB-01	2	1.1	4415.03	Hytrel	PU/PVC
AB-02	2	1.1	6810.99	Hytrel	PVC
AB-03	2	1.1	4191.50	Hytrel	PVC
AC-01	2	1.5	3455.67	Polypro	PU/PVC
AC-02	2	1.5	14717.32	Polypro	PVC
AC-03	2	1.5	7899.56	Polypro	PVC
BD-01	3	2.2	5519.09	Hytrel	PU/PVC
BD-02	3	2.2	6060.07	Hytrel	PVC
BD-03	3	2.2	3832.79	Hytrel	PVC
BE-01	3	2.2	2612.89	Hytrel	PU/PVC
BE-02	3	2.2	4299.18	Hytrel	PVC
BE-03	3	2.2	3540.58	Hytrel	PVC
CA-01	1.6	0.9	4992.65	Hytrel	PU/PVC
CA-02	1.6	0.9	5477.14	Hytrel	PVC
CA-03	1.6	0.9	5330.24	Hytrel	PVC

We tested the samples as a whole system; with jacket, Kevlar, inner tube and as an isolated system; with jacket-only to determine the effect of filling ratio on the shrinkback. To present the filling ratio, Denier/Area has been calculated where Denier represents the mass of Kevlar and area is the zone between inner diameter of jacket and outer diameter of inner tube.

Note that the jacket material for supplier 01 is PU/PVC, the rest are just in PVC.

3.2. Experimental Results Analysis

Multiple thermal aging tests were conducted on all samples listed in Table 1. The goal of the thermal aging tests was to determine the correlation between current GR-409 test method compared to the IEC proposed test method F11A. Furthermore, more testing was at varying steady state and cyclic temperature as well as at variable exposure times to quantify the effects temperature and time have on the material's shrinkback.

First tests were done on all samples against both test methods described in GR-409; first two sample groups were thermal aged at 110°C for 2 hours and 85°C for 4 hours. Third sample group was aged according to IEC proposed method F11A; samples were exposed to -10°C to 70°C for 5 cycles as per figure 1. These first three test methods were done for baseline comparative analysis for the rest of the experimental testing.

Figure 4 shows the comparison of 3 methods, 4h/85°C, 2h/110°C, and 5 cycles /-10°C to 70°C. IEC cycling shows to have the same pattern as 4hr/85°C even though the test duration is much longer. The impact of cycling on shrinkback was further tested and shown in Figure 5 as it became apparent that the effect of cycling to below 0°C temperatures had negligible effect on jacked shrinkage. The 2h/110°C is observed to be the most sever test method. The severity of shrinkback at 100°C correlates to the TGA analysis shown in Figure 2, where it was determined that moisture evaporation at these temperatures is a source of excessive PVC shrinkage.

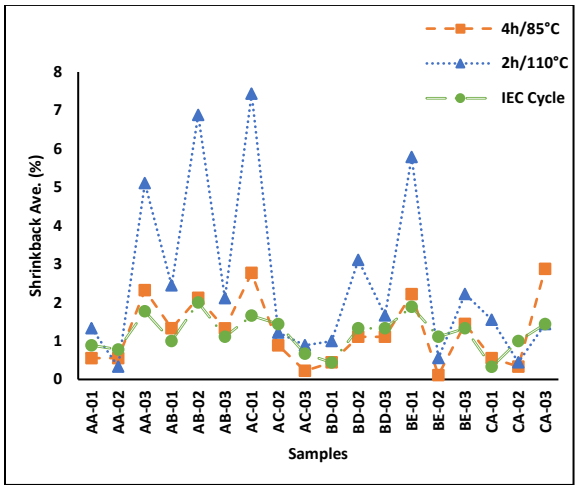


Figure 4 Shrinkage percentage: 4h/85°C, 2h/110°C, and 5 cycles /-10°C to 70°C

The shrinkback results of steady state 75°C/1hr vs cycling of -40C to 75°C for one cycle (for jacket only and full filler) is shown in Figure 5. Despite that the cycling taking a total of 5 hours, the graph shows that these two tests result in comparable amount of shrinkback. This infers with the results of Figure 4 in that cycling does not cause more shrinkback than the holding at a constant elevated temperature. This figure also depicts that the whole furcation tube assembly (with filler) shrinks less compared to the empty jacket as the filling material helps preventing shrinkback.

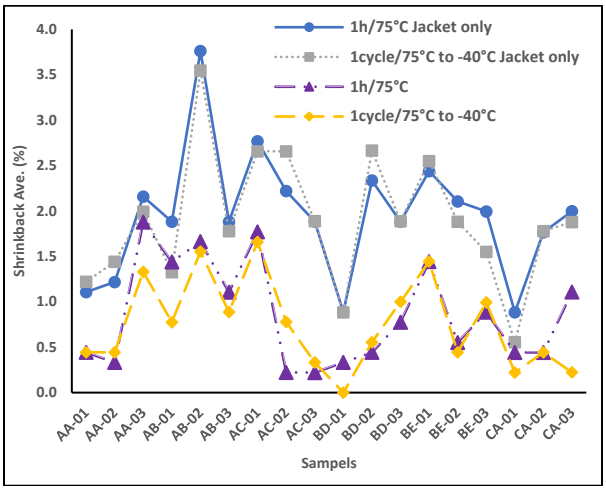


Figure 5 Shrinkage percentage: Cycling vs constant temperature.

Figure 6 shows the shrinkage of the cable jacket only (without any filler) at constant 85°C over time. This curve depicts that the largest % of jacket shrinkage occurs within the first hour of testing, with minimal shrinkage occurring over the rest of the test duration. These results infer a possibility of rapid testing during cable jacket development as an alternative and accurate way to quickly screen against GR-409 and IEC Method F11A standards.

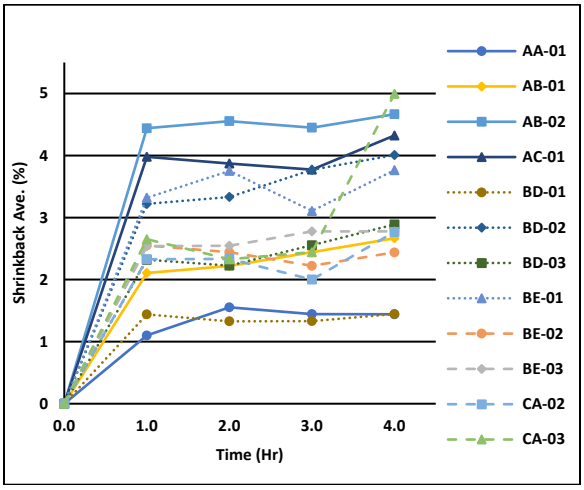


Figure 6 Shrinkage percentage (jacket only) at 85°C from 1h, 2h. 3h, and 4h.

Please note each test has been done independently and is not a continuation of previous test. Additionally, for low shrinkage rates (~1%), there is a higher contribution of measurement error due to the difficulty to accurately measure cable length at those significant figures.

4. Conclusions

These are the conclusions and suggestions:

- 110°C held at 2 hours is not an equivalent test method to 85°C held for 4 hours.
- Cycling test of 5 cycles between -10°C to +70°C has very similar results to +85°C for 4 hours.
- Cycling does not increase the shrinkback compared to the constant temperature.
- Filling the area between jacket and inner tube reduces the shrinkback. In all cases, jacket-only shrunk more than furcation tube (jacket, Kevlar, inner tube).
- The test 85°C/4hrs can be modified as 85°C/1hrs as testing showed there is minimal shrinkback occurring after the first hour.
- The test 85°C/4hrs is comparable to IEC cyclic testing and has the potential to be used as a screening for IEC Method F11A which takes a total of 24 hours over 5 cycles.
- We have not observed any direct relation between den/area and shrinkback as the shrinkback is dependant on many factors and filling ratio is only one of them.

5. Acknowledgments

We are grateful to Belden Fiber Laboratories in Montreal (Canada) and Richmond (USA) for their valuable assistance.

Special thanks to Ana Cruz, Anh-Khoi Vo, Moses Levy, and Luc Milette from Montreal for their work done in the fiber laboratory, and support in allocating resources and standards contributions.

We also appreciate Ken Nardone's support in test planning, result analysis and supporting the fiber laboratory in Richmond.

6. References

[1] "GR-409-CORE Issue 2 Generic Requirements for Indoor Fiber Optic Cable," Telcordia Technologies Generic Requirements, 2008.

[2] "IEC TR 62959 Edition 1.0, Optical fiber cables - Shirnkage effects on cable and cable element end termination - Guidance," International Electrotechnical Commission, Geneva, Feb. 2021.

[3] "TIA-455-86 (FOTP-86), Fiber Optic Cable Jacket Shrinkage", Telecommunication Industry Association, Jan. 1983.

[4] "IEC 60794-1-22, Optical fibre cables – Part 1-22: Generic specification – Basic optical cable test procedures – Environmental test method", 2017.

[5] "GR-326-CORE, Generic Requirements for Single-mode, Optical Connectors and Jumper Assemblies," Feb. 2010.

7. Authors



Massimo Carboni graduated as a Master of Applied Science in Mechanical Engineering (MASc) from Concordia University (CA) in 2020. He previously completed his BEng in Mechanical Engineering at the same University. He joined Belden in 2021 and is currently working as a Product Development Engineer in the R&D Fiber Connectivity team based out of Montreal Qc, Canada.

(massimo.carboni@belden.com)



Tahereh (Tara) Ahmadi Tameh completed her doctoral studies in Electrical Engineering at Polytechnique Montréal in 2017. Building upon her academic achievements, she amassed four years of professional experience at Acuity Brands before embarking on a new chapter with Belden Canada in 2021. Her career journey also includes a noteworthy tenure at the Telecommunication Company of Iran from 2008 to 2012. Notably, she holds a Bachelor of Science (B.Sc.) degree and a Master of Science (M.Sc.) degree from K. N. Toosi University of Technology, earned in 2005 and 2008, respectively.

(tara.tameh@belden.com)



Annabelle Scarpaci is Engineer Manager for the Fiber Cable group at Belden. She has 7 years of experience qualifying materials and developing new designs for optical fiber cable products. Previously, she had 7 years of experience developing materials for nonlinear optical applications. She has a PhD. in Chemistry from the University of Nantes, France. She received the 2018 Platinum-level award in the Cabling Installation & Maintenance Magazine Innovators' Awards. She is the author of 14 publications in peer-reviewed journals, 2 book chapters, 6 patents and multiple white papers.

(annabelle.scarpaci@belden.com)



Joseph W. Koeing is currently studying Materials Engineering and Chemistry at Iowa State University with an expected graduation date of December 2025. He recently joined the Belden Fiber Cable group in Richmond as an R&D Cable Intern.

(joseph.koeing@belden.com)

An Analytical Formula of Microbending Sensitivity for Reduced Diameter Optical Fibers

Takahiro Nomura, Manabu Shiozaki and Kazuyuki Sohma
Sumitomo Electric Industries, Ltd.
1, Taya-cho, Sakae-ku, Yokohama, 244-8588 Japan
+81-45-853-7168 · nomura-takahiro@sei.co.jp

Abstract
In this study, a newly developed analytical formula of microbending sensitivity will be proposed for the reduced diameter optical fibers structure optimization. The new formula shows a different trend when compared to the conventional one for cladding diameters below 110μm. The calculated results for a cladding diameter 80μm exhibit a trend curve similar to the experimental data, indicating its usefulness in optimizing optical fiber structures within the smaller cladding diameters.

Keywords: reduced diameter optical fibers, microbending attenuation

1. Introduction
The advancement of technologies such as cloud computing and 5G has led to a significant increase in communication traffic in recent years. Data centers play an important role for technology, and more cost-effective and space-efficient techniques for network installation have been demanded for data centers. For example, outside plant (OSP) cables are deployed in underground conduits, and the ability to accommodate an increase in the number of cables and/or optical fibers within is highly demanded. Thinner and higher fiber count OSP cables utilizing Reduced Diameter optical Fibers (abbreviated as RDF, hereafter) with an outer diameter of less than 165μm were proposed to meet the demand in a previous study [1]. The study pointed out that lateral force induced attenuation, which is called "microbending attenuation (MB loss)", increased by 17.5 % when optical fiber diameter become from 200μm to 165μm. The MB loss is an important index related to attenuation change of the optical fiber between before and after cabling.

There are two directions to consider when planning to make changes to the structure of RDF. One is to decrease resin layer thickness, while maintaining the standard cladding diameter of 125μm. The other is to reduce the cladding and coating diameters, as shown in figure 1. There are five parameters to be considered for the structural design of RDF coated with two layers. The parameters include the diameters of glass, the primary (inner) coating and the secondary (outer) coating; Young's moduli of primary and secondary coatings. When the structure is decided, an analytical method to estimate MB loss is useful. A few studies [2] have been reported to optimize RDF structure based on the analytical formula developed by Cocchini [3]. The formula was derived based on the structures of standard optical fibers having an outer diameter of 250μm, and they are largely different from RDF as shown in table 1.

In this study, a newly developed analytical formula for MB loss is proposed for RDF structure optimization. The formula is based on the method developed by Cocchini [3]. A new parameter of microbending sensitivity (abbreviated as "MBS" hereafter) is also introduced, which is a normalized value of MB loss by a standard of one. The prediction results calculated by this MBS analytical formula are compared with those of Cocchini's formula, and experimental data. The differences between them are then discussed.

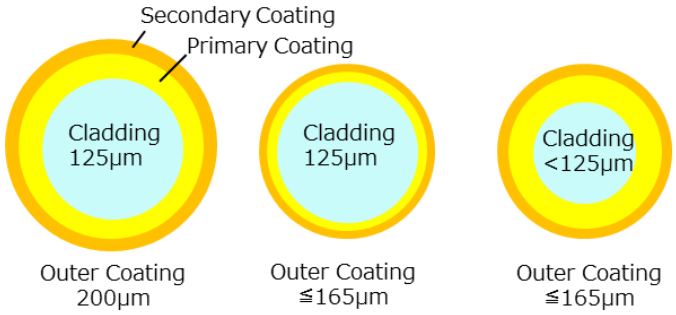


Figure 1. Examples of RDF Structure

Table 1. Comparison of conventional optical fiber and RDF

	Cocchini[3]	RDF
Cladding Diameter (μm)	125	80-125
Secondary Coating Diameter (μm)	250	125-175
Primary Young's Modulus (MPa)	10-20	1.0 or less

2. Analytical Formula
2.1 Cocchini's formula [3]
MB loss α_{MB} can be expressed as Formula (1) [4].

$$\alpha_{MB} \sim A \times (D/H^2) \qquad (1)$$

Here, A is a parameter dependent on optical properties, H and D show the flexural rigidity and lateral rigidity of an optical fiber, respectively. H can be written as,

$$H \propto \pi {R_0}^4 E_0 + \pi({R_2}^4 - {R_1}^4) E_2 .$$

Cocchini [3] derived an expression for D shown as Formula (2).

$$D = E_1 + (E_2 - E_1)\left(\frac{E_1}{E_2}\right)^{\frac{2}{3}}\left(2\frac{R_2 - R_1}{R_2 - R_0}\right)^{\frac{3}{2}} \qquad (2)$$

Here, E is Young's modulus, R is the radius. The subfixes of 0, 1, and 2 represent the cladding, primary layer, and secondary layer, respectively (Figure 2a).

The method to obtain Formula (2) has three steps as explained below.

(i) Optical fiber deformation calculations are conducted by the two-dimensional finite element method (FEM) for several tens of optical fibers with an outer diameter of 250μm, each having different values of R_i and E_i.

(ii) Using the values obtained from the FEM calculations, D for each optical fiber is calculated using the following Formula (3).

$$D = 2F\theta R_2/u_y^* \quad (3)$$

Here, F, θ, and u_y^* are lateral force (1MPa), stress application angle (0-9 degrees), and displacement due to coating deformation (Figure 2b).

(iii) Cocchini defined normalized rigidity as $(D - D_1) / (D_2 - D_1)$ and normalized radius as $(R_2 - R_1) / (R_2 - R_0)$. The analytical formula (2) is obtained by fitting with D as the objective variable and R_i, and E_i as explanatory variables under the approximation expressed as Formula (4).

$$\frac{D - D_1}{D_2 - D_1} \approx \frac{D - E_1}{E_2 - E_1} \quad (4)$$

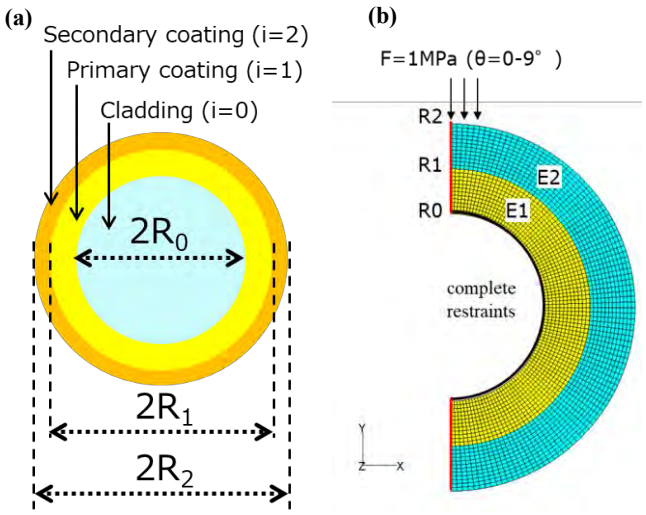


Figure 2. (a) Optical Fiber Structure
(b) An example of the analysis model.

2.2 Newly Developed Formula in this study

There are differences in step (ii) described in section 2.1 compared with our newly developed method, and conditions. They are summarized in Table 2.

Table 2. Comparison of optical fiber structure parameters to obtain the analytical formulas

	This Study	Cocchini[3]
Software	MSC.Nastran 2020sp1	PDE/PROTRAN
Cladding Diameter (μm)	75-130	125
Secondary Coating Diameter (μm)	110-210	250
Primary Young's Modulus (MPa)	0.05-1.0	10-20
Secondary Young's Modulus (MPa)	1000-3000	500-1000
Number of Samples Analyzed	378	30

A polynomial regression is conducted with the obtained D values for 378 structures. The objective variable is the stiffness ratio $(D - D_1) / (D_2 - D_1)$, and the explanatory variables are the radius ratio $(R_2 - R_1) / (R_2 - R_0)$, (E_1 / E_2) and (R_0 / R_2). The fitting parameters are c_{ijk} expressed as Formula (5).

$$log_{10}\frac{D - D_1}{D_2 - D_1} \sim \sum_{i,j,k} c_{ijk}\left(log_{10}\frac{R_2 - R_1}{R_2 - R_0}\right)^i\left(log_{10}\frac{E_1}{E_2}\right)^j\left(log_{10}\frac{R_0}{R_2}\right)^k \quad (5)$$

Here, c_{ijk} and c_l are constants, i, j, k and l are integers from 1 to 3.

It is found that the approximation given by Formula (4) do not hold within the range of calculations in this study. A new approximation formula is determined as

$$\frac{D_1}{E_1} = \frac{D_2}{E_2} = \frac{c_1}{\left(1 - \frac{R_0}{R_2}\right)^{c_2}} + c_3$$

The fitted results of c_{ijk} and c_l are summarized in Table 3.

Table 3. The fitted results of c_{ijk} and c_l

c000	-0.611554	c1	0.209367
c100	3.615414	c2	1.206659
c010	0.253128	c3	0.401169
c001	-7.130445		
c200	0.787599		
c110	0.329243		
c101	2.320080		
c020	-0.062024		
c011	-0.985974		
c002	-8.696048		

The value of D for arbitrary optical fiber structure is calculated using Formula (5), which allows obtaining the value of D / H^2. The value is normalized by that of a conventional optical fiber having a cladding diameter of 125μm and an outer diameter of 200μm.

3. Experimental

3.1 Optical Fiber Fabrication

An optical fiber preform was heated at a furnace, and drawn into a glass fiber having a diameter between 80 and 125μm. After cooling the glass fiber, two layers of ultraviolet curable resins were applied and cured by ultraviolet light sources. The coated optical fiber was wound onto a bobbin. Optical fibers tested in this study were compliant with G. 657. A2. The details of the fabricated optical fibers are summarized in Table 4.

Table 4. Structure of fabricated optical fibers

Cladding Diameter (μm)	80			100			125		
Primary Coating Diameter (μm)	135								
Secondary Coating Diameter (μm)	165								
Primary Young's Modulus (MPa)	0.2	0.4	0.9	0.2	0.4	0.9	0.2	0.4	0.9
Secondary Young's Modulus (MPa)	1500								
Fiber	A2								

3.2 MB Loss Measurement

MB loss was measured in accordance with IEC-TR62221 Method-B. Spectral losses were measured for the optical fiber before and after winding onto a drum wrapped with #240 sandpaper at a tension of 80 N. The loss difference at a wavelength of 1550 nm, expressed as Δα, was defined as MB loss. The length of the optical fiber was 600 m. The drum had a diameter of 280 mm.

4. Analytical Results

4.1 Comparison between formulas of Cocchini [3] and this study

Cocchini's Formula (2) was derived from the FEM results for optical fibers of $2R_0$ = 125μm and $E_1 \geq$ 10MPa. In this study, the structural range of optical fibers upon which the FEM calculations are conducted to obtain Formula (5) are extended. The lower limit of $2R_0$ is 75μm, E_1 is also changed to a lower range of 0.05 to 1.0 MPa. The difference between Cocchini's formula and ours is investigated from the $2R_0$ or E_1 dependence on MBS.

4.2 Cladding diameter ($2R_0$) dependence

Figure 3 shows the analysis results of $2R_0$ dependence on MBS. The red line represents the values calculated from Formula (2) developed by Cocchini [3], while the blue line represents that estimated from Formula (5). MBS decreases when $2R_0$ increases for both of the results. Furthermore, MBS calculated with our formula tends to be lower than that using Cocchini's formula [3] at $2R_0$ of about 110μm or less. When $2R_0$ is reduced from 125μm to 80μm, the MBS or MB loss is expected to be about 6 times higher for our formula.

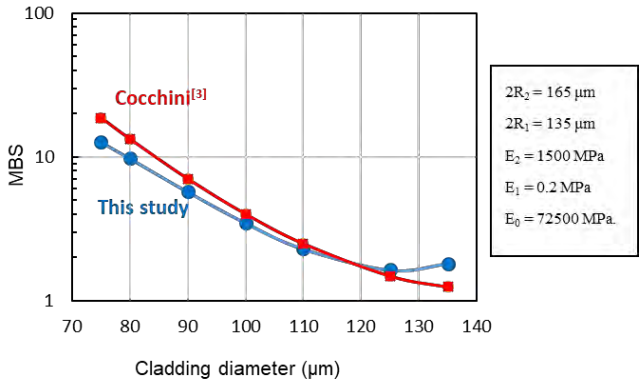


Figure 3. Cladding diameter dependence of MBS

4.3 Primary diameter ($2R_1$) dependence

The dependence of $2R_1$ on MBS calculated from Formula (2) derived by Cocchini and Formula (5) in this study is shown in Fig 4 for $2R_0$ = 125μm and 80μm. The larger $2R_1$ show a lower MBS, and there is no significant difference between the two formulas for $2R_0$ = 125μm. On the other hand, large differences could be found for $2R_0$ = 80μm. For Cocchini's formula, the MBS monotonically decreases with an increase in $2R_1$. In contrast, in our proposed formula, MBS has a similar trend up to $2R_1$ = 150μm, but higher MBS at $2R_1$ = 160μm.

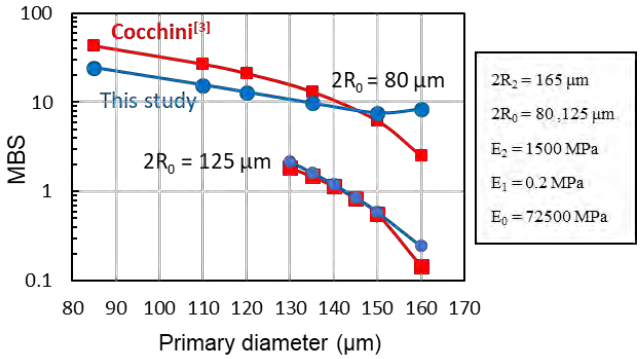


Figure 4. Primary diameter dependence of MBS

4.4 Primary Young's modulus (E_1) dependence

The dependence of E_1 on MBS is shown in Figure 5. MBS decreases when E_1 is decreased for both of the formulas. It can be observed that MBS is influenced more by E_1 when $2R_0$ = 80μm compared with when $2R_0$ = 125μm, indicating that E_1 has a larger effect on MBS when $2R_0$ becomes smaller.

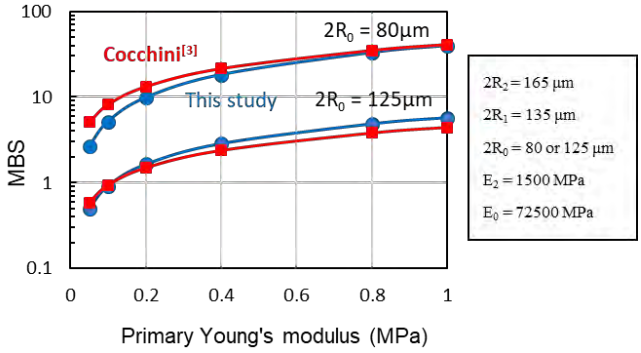


Figure 5. Primary Young's modulus dependence of MBS

5. Discussion

5.1 Comparison between calculated and experimental results

5.1.1 Primary Young's modulus (E_1) dependence on MBS

According to the calculated results shown in chapter 4, MBS has the highest dependence on E_1. Three kinds of uncolored optical fibers having a different E_1 were fabricated. Those MB losses or MBSs are measured and shown in Figure 6 for comparison.

The experimental MBSs at $2R_0$ = 125μm are 5.5 and 6.2 for an E_1 of 0.2 and 0.9 MPa, respectively. The MBS of E_1 = 0.9 MPa is only about 1.1 times higher than that of E_1 = 0.2 MPa, even 3 times for calculated with the new formula in this study. The experimental data seems to show that a small primary thickness of 10 μm makes it difficult for the optical fibers to have enough buffering effect against lateral force from the sandpaper applied at the MB loss measurement.

On the other hand, calculated results for $2R_0$ = 80μm show the same tendency curve as the experimental data. The experimental MBSs are 3.9, 15 and 24 at E_1 of 0.2, 0.4 and 0.9, respectively. The values calculated with our formula are 9.8, 17 and 33. The experimental

results show higher E_1 dependence on MBS than the calculated results.

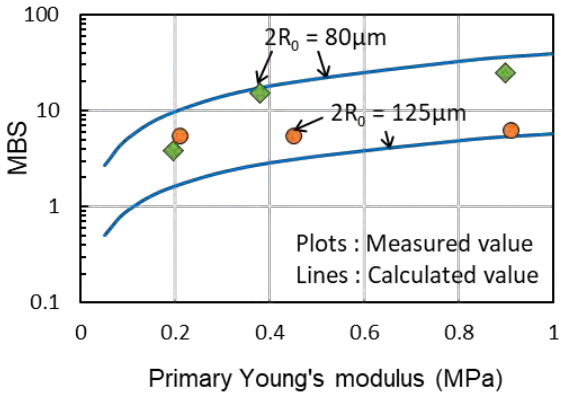


Figure 6. Comparison of measured and experimental values in Young's modulus dependence

When the glass diameter (= $2R_0$) becomes smaller maintaining the same secondary coating thickness (= R_2 - R_1), the thickness of the primary coating (= R_1 - R_0) is larger. It can be thought that the thinner glass diameter resulted in having a higher buffering effect from the primary coating.

Based on the calculation with the new formula proposed in this study, MBSs of $2R_0$ = 80μm are higher than those for $2R_0$ = 125μm for all ranges of E_1. The experimental data show that MBSs of $2R_0$ = 80μm become smaller than those for $2R_0$ = 125μm when E_1 = 0.2 MPa. Further study is needed to explain the phenomenon.

According to the above observations, it is challenging to use the predictions for $2R_0$ = 125μm due to the discrepancies between the calculated and measured values. On the other hand, it can be said that the MBS prediction at a condition of $2R_0$ = 80μm is useful.

5.1.2 Glass diameter ($2R_0$) dependence on MBS

The dependence of the glass diameter ($2R_0$) on the calculated and experimental MBSs are shown in Figure 7 for E_1 = 0.2 MPa, 0.9 MPa. In the calculation with the proposed formula, MBS shows a tendency to be equal or higher when the glass diameter of $2R_0$ becomes smaller.

For E_1 = 0.9MPa, the trend of the calculated values matches with the experimental results.

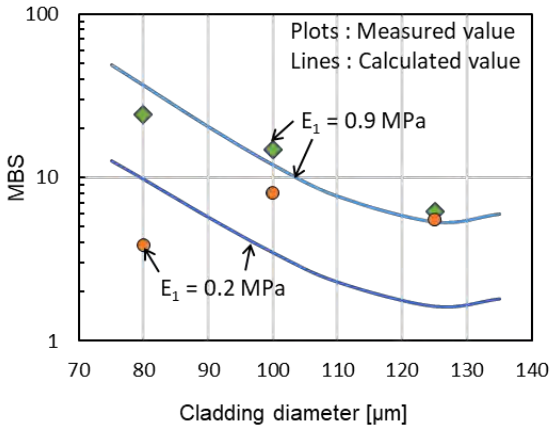


Figure 7. Comparison of measured and experimental values in cladding diameter dependence

On the other hand, for E_1 = 0.2 MPa, the experimental tendency is largely different from the results and the best or lowest MBS data is measured at $2R_0$ = 80μm, and the worst or highest MBS is at $2R_0$ = 100μm. However, we are currently conducting MBS for colored optical fibers, and preliminary results show that $2R_0$ = 100μm exhibits the best MBS after coloring (Figure 8). Further investigations are required to explain the differences between colored and uncolored optical fibers.

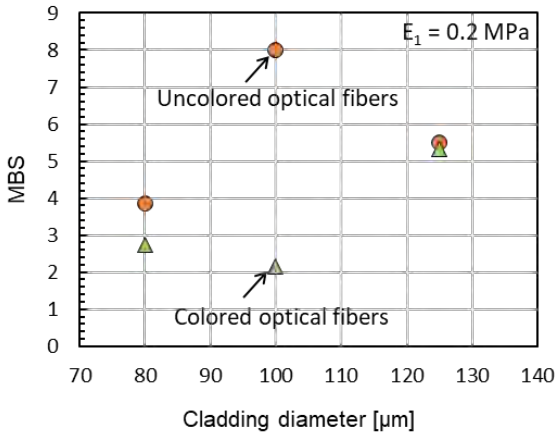


Figure 8. MBS of uncolored optical fibers and colored optical fibers

5.2 Structural Design of RDF

Based on the newly proposed formula in this study, from the perspective of suppressing MBS, it is preferable to have $2R_0$ = 125μm with the lowest possible E_1. However, considering the results as explained above, MBS is lowest at R_0 = 125μm in the range of E_1 is greater than 0.2 MPa, and at R_0 < 125μm in the range of E_1 is less than or equal to 0.2 MPa for uncolored optical fibers. However, as mentioned earlier, colored optical fibers have shown difference in MBS trends compared to uncolored optical fibers, indicating the need for further investigation.

The newly proposed calculation formula in this study shows good agreement with the experimental results and trends under the

condition of $2R_0$ = 80μm, making it highly valuable for MBS prediction in structures with this condition.

In order to decide the structure of thinner optical fiber having a diameter less than 165μm, other properties including puncture-resistance, for example, have to be considered.

6. Conclusions

In this study, a newly developed analytical formula for MBS has been proposed for structure optimization of RDFs. The new formula shows a different trend compared to the formula proposed by Cocchini. In the dependence on $2R_0$, MBS calculated with our formula tends to be lower than that is calculated from Cocchini's formula at $2R_0$ of about 110μm or less.

The calculated results of E_1 dependence on MBS based on our formula for $2R_0$ = 80μm demonstrate trend curves similar to the experimental data compared, indicating its utility in optimizing optical fiber structures within smaller cladding diameters compared to Cocchini's formula.

Considering the experimental results, MBS becomes the lowest at R_0 = 125μm in the range of E_1 is greater than 0.2 MPa, and at R_0 < 125μm in the range of E_1 is less than or equal to 0.2 MPa for uncolored optical fibers. However, in the case of colored optical fibers, the trend of MBS changes, indicating the need for further investigation.

7. References

[1] M-J. Li et al., "Reduced Coating Diameter Fibers for High Density Optical Interconnects," J. of Lightwave Technol., vol. 41, pp. 999–1009 (2023).

Y. Tsujimoto, et al., "6,912 Fiber Cable using 160μm Coating Optical fiber with 80μm Cladding," Proc. of the 71st IWCS, (2022).

[2] P. Sillard et al., "Reduced-Coated Fibers and Micro-Duct Cables," OFC 2022, M4E.2.

P. Sillard et al., "Single-Mode Fibers with Reduced Cladding and/or Coating Diameters," ECOC 2022, Tu3A.1

[3] F. Cocchini, "The lateral rigidity of double-coated optical fibers," J. of Lightwave Technol., vol.13, pp1706-1710 (1995).

[4] M. Wandel & P. Kristensen, J. of Opt. Fiber Commun., No.3, pp.25-60 (2005). G. E. Anderson and B. R. Smith, "Multicarrier Modulation for Data Transmission: An Idea Whose Time Has Come," *Intell. Commun. Mag.*, 28(5), 5-14 (May, 1990).

8. Authors

Takahiro Nomura received a M. S. degree in Chemistry from Saitama University in 2017. He has been in charge of research and development of optical fibers, since joining Sumitomo Electric Industries, Ltd. in 2018.

Manabu Shiozaki is a Senior Specialist in optical design analysis for optical fibers and devices at Sumitomo Electric Industries, Ltd. He has been engaged in research and development using computer simulation since joining the company in 1992.

Kazuyuki Sohma is a manager of the Optical Communications Laboratory at Sumitomo Electric Industries, Ltd. He received his M. S. in 2001, and M. B. A in 2010. He has been involved in optical fiber development since joining the company in 2001.

Indoor-Outdoor Air Blown Optical Cable

Naoya Maehara, Okimi Mukai, Yusuke Yamaki, Akira Namazue and Akira Kori
Optical Cable Research and Development Department, Optical Cable Systems Division, Fujikura Ltd.
1440, Mutsuzaki, Sakura, Chiba, Japan
+81-43-484-3945 · naoya.maehara@jp.fujikura.com

Abstract

We have successfully developed the Air Blown cable with smaller diameter, high-density and superior flame-retardant characteristic. Use of this cables will reduce the person-hour required to connect flame-retardant cables when entering the data center. This cable will contribute to the construction of more efficient network installation between data centers.

Keywords: Optical fiber cable, Air Blown, Flame-retardant

1. Introduction

With the increase in the volume of network traffic and the expansion of data storage services, optical fiber cables are becoming inevitable to efficiently connect data centers. Air Blown cables that can be blown with compressed air into the existing ducts are used as one of the construction methods to satisfy these demands [1].

Another feature of this construction method is that once several ducts are laid below the road, additional cables can be installed in each of the ducts without additional road construction.

On the other hand, since high fiber count Air Blown cables are typically designed for outdoor use, they must be connected to flame-retardant cables when entering the data center, as shown in Figure 1. There are several kinds of cables on the cable trays and/or installation spaces [2].

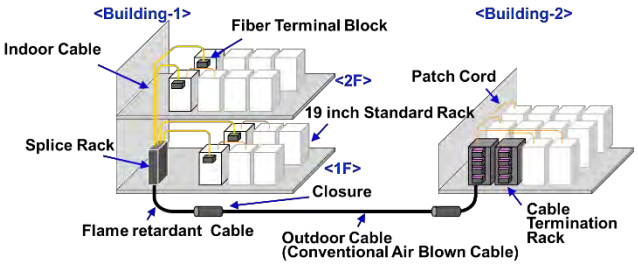


Figure 1. Wiring diagram in data center

This time, we have developed an Indoor-Outdoor Air Blown WTC that satisfies flame-retardant characteristics, with the aim of making it possible for the cable to be pulled directly into the data center from outside as well.

We have been expanding lineup of Air Blown cables with smaller diameter and higher density by applying Spider Web Ribbon® (SWR®) and Wrapping Tube Cable® (WTC®) technologies. Now, our SWR/WTC Air Blown cables are commercially available.

2. Cable Design

2.1 Features of SWR and WTC

The structure of SWR is shown as Figure 2. SWR has single fiber part and bonding part where the adjacent fibers are fixed together intermittently. Thus, it is possible to flexibly change its shape like bundled fiber units. And, it is possible to add SWRs into the cable to achieve high density without increasing the attenuation or subjecting large fiber strain. In the case of rigid ribbons, more skills, working time and special tools are required to separate ribbonized fibers into single fibers. On the other hand, SWR can be separated into single fibers easily without special tools [3]. Therefore, SWR can be connected to existing loose tube cables by splicing single fibers.

The structure of WTC is shown as Figure 3. WTC is central tube cable without slotted core and consists of SWR which is wrapped in a tube made by overlapping tape. Moreover, strength members are embedded side place in the sheath. Therefore, WTC structure achieves reduction in outer diameter and weight dramatically, in addition, it offers quick installation with its full dry structure.

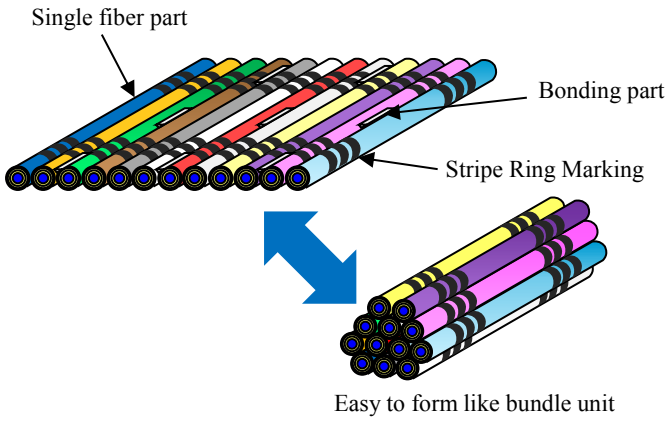


Figure 2. Schematic of SWR

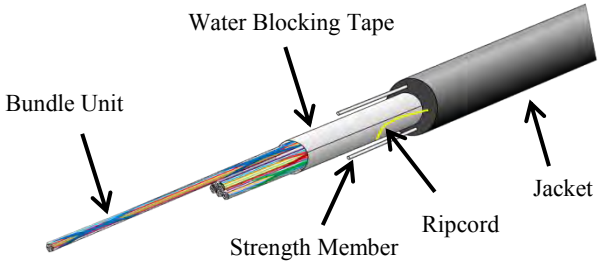
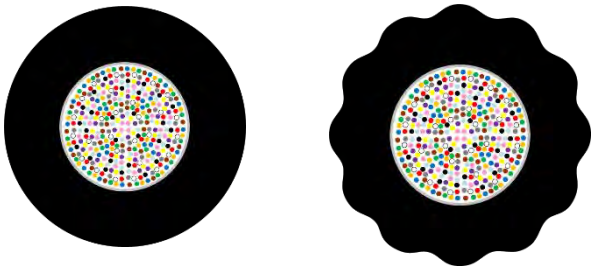


Figure 3. Schematic of WTC

2.2 Features of Air Blown WTC

Unlike conventional round shape cables, Air Blown WTC has concavity and convexity designed outer jacket, as shown in Figure 4. This structure reduces frictional force with the duct and provides excellent push-out characteristics [1].



Conventional Cable　　Air Blown WTC

Figure 4. Structure of Conventional Cable and Air Blown WTC

2.3 Features of new Air Blown WTC

The design concept of new Air Blown WTC is to meet ICEA 744 in mechanical characteristics, to comply with ICEA 696 in environmental characteristics and to have flame-retardant characteristics with sheath as thin as possible. In order to achieve these characteristics, the fibers are mounted in densely to reduce the core area of the cable.

Based on our experience, the cable outer diameter was designed as calculated from the fill ratio for the applicable duct diameter. A fill ratio of 60% to 70% is considered good for Air Blown WTC. The outer diameter was designed to be 9.8 mm because 12 mm and/or 13 mm inner diameter duct is commonly used.

From the viewpoint of flame-retardant characteristics, the developed Air Blown WTC has different structure of strength members from the previous Air Blown WTC.

The outer jacket material of the developed Air Blown WTC was selected by considering mechanical characteristics. It is also easy to strip the cable sheath and pick up the target bundle unit and SWR.

Moreover, this cable has the following three key technologies mainly:

1) Dielectric FRP is used as strength member. Therefore, grounding work is unnecessary because of non-metallic material and the lighter cable weight leads more Air Blown distance.

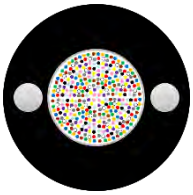
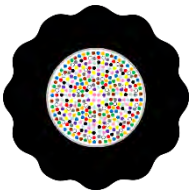
2) In the longitudinal direction, multiple SWRs are stranded by SZ method. This facilitates picking up the target bundle unit and SWR. This structure contributes to excellent mid-span access workability.

3) Talc powder or jelly material are not used. Therefore, the operation time of removing the water blocking tape and picking up the target SWR is much shorter.

3. Comparison of Cable Design

The comparison of the cable design of 288-fiber cable having flame-retardant characteristics is shown in Table 1 [2]. Outer diameter is reduced approximately 22 % and cable weight is reduced approximately 41 % compared with conventional indoor-outdoor cable.

Table 1. Cable Design of 288-fiber Cable

Item	Conventional Indoor-Outdoor Cable	Indoor-Outdoor Air Blown WTC
Cross Section		
Fiber Count	288	288
Outer Diameter	12.5 mm	9.8 mm
Weight	160 kg/km	95 kg/km

4. Cable Characteristics

4.1 Mechanical Characteristics

The mechanical test results of 288-fiber indoor-outdoor Air Blown WTC are shown in Table 2. Test methods were in accordance with standard ICEA S-122-744-2022 for Optical Fiber Outside Plant Microduct Cables [4]. A measurement wavelength for mechanical test was 1550 nm. This cable showed adequate mechanical characteristics.

Table 2. Mechanical test results ICEA 744

Item	Condition	Test result
Cable low and high temperature bend test	ICEA S-122-744 7.17 Diameter of mandrel: 40 ×d (d: cable diameter) Temperature: -30 ℃, +60 ℃ Number of turns: 4	< 0.15 dB/fiber No damage to the cable jacket
Cyclic flexing test	ICEA S-122-744 7.21 Diameter of mandrel: 40 ×d Angle: ±90° Number of cycles: 25	< 0.15 dB/fiber No damage to the cable jacket
Cable impact test	ICEA S-122-744 7.23 Impact energy: 1.0 N・m striking surface radius: 12.5 mm	< 0.15 dB/fiber No damage to the cable jacket
Cable tensile loading and fiber strain test	ICEA S-122-744 7.24 Tensile load: 1×W, 60 min. (W: cable weight (kg/km)) Residual load: 0.3×W, 10min. Remove the load: relax for 5min.	Fiber strain < 0.9% at Tensile load Fiber strain < 0.266% at Residual load <0.15 dB/fiber at Residual load and after relax
Cable compressive test	ICEA S-122-744 7.25 Tensile load: 50 N/cm, 1 min hold Rate 2.5 mm/min	< 0.15 dB/fiber
Cable twist test	ICEA S-122-744 7.26 Sample length: 2 m	< 0.15 dB/fiber

	Test angle: ±180 deg. Number of cycles: 10	No damage to the cable jacket
Cable kink test	ICEA S-122-744 7.29 IEC 60794-1-21 Method E10 IEC 60794-5-10 Loop diameter: < 40 ×d	No kink

4.2 Environmental Characteristics

The environmental test results of 288-fiber indoor-outdoor Air Blown WTC are shown in Table 3. Test methods were in accordance with standard ICEA S-104-696-2019 for Indoor-Outdoor Optical Fiber Cable [5]. A measurement wavelength for mechanical test was 1550 nm. The result of environmental stress crack resistance test showed good results without kink and sheath cracking. The measurement of temperature cycling test was carried out between -40 degree C and +70 degree C for 2 cycle as shown in Figure 5. Within this specified temperature range, maximum variation of attenuation was less than 0.05 dB/km at 1550 nm. This cable achieved satisfactory environmental characteristics.

Table 3. Environmental test results ICEA 696

Item	Condition	Test result
Environmental stress crack resistance	ICEA S-104-696 7.6 Bend diameter : <10 D Test angle: 180 deg. Temperature: 50°C Soak time: 48 hours	No damage to the cable jacket
Cable external freezing test	ICEA S-104-696 7.18 Submerge cables and freeze at -10°C or -40°C Raise temperature to -2°C	< 0.40 dB/km No damage to the cable jacket
Cable temperature cycling test	ICEA S-104-696 7.20 High temperature: 70°C Low temperature: -40°C Number of cycles: 2	< 0.40 dB/km
Cable Water penetration test	ICEA S-104-696 7.28 IEC 60794-1-22 Height of water: 1 m Sample length: 3 m An orifice diameter: 1.50 mm ± 0.25 mm An orifice length: < 30 mm	No fluid leaking from the exposed end of the cable

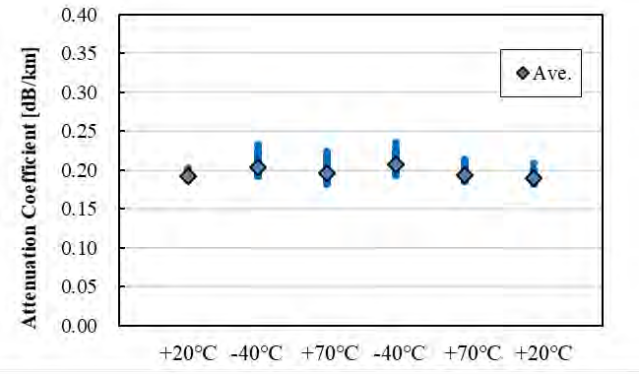


Figure 5. Result of Cable temperature cycling test

4.3 Blowing Performance

Cable installation trials for Indoor-Outdoor Air Blown WTC were conducted at the Dura-line test track in Clinton Tennessee. The test condition at the site is shown in Table 4. The test results are described in Table 5 and Figure 6. Since duct diameters are varied by region and country, two patterns of duct diameters (12 mm and/or 13 mm) were used for testing. We succeeded in blowing about 2000ft, which makes it possible to connect between data centers.

Table 4. Test Conditions of Cable Installation Trials

Item	Condition
Route (per lap)	2700 ft (823 m) 5 sweeping 90-degree angles

Table 5. Test results of blowing performance

Duct size (OD/ID)	16/12 mm	16/13 mm
Fill ratio	67 %	57 %
Blowing distance	1922 ft	2508 ft

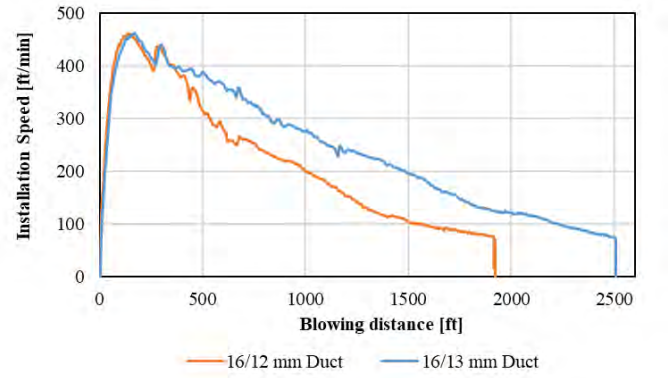


Figure 6. Blowing Performance

4.4 Flame-Retardant Characteristics

Flame-retardant requirements and tests are different by each country or region. The test in accordance with UL 1666 was applied to this cable, and it passed the test as shown in Table 6 [6].

Table 6. Test result of flame-retardant characteristic

Item	Condition	Test result
Vertical flame height	< 3.66 m	Pass
Maximum temperature reading	< 454.4 ℃	Pass

5. Conclusions

We have succeeded in developing the Indoor-Outdoor Air Blown cable with smaller diameter, high-density and superior flame-retardant characteristic. The cable satisfies the mechanical and environmental characteristics and achieves blowing performance about 2000 ft. We can expand further the scope of Air Blown WTC installation, applying SWR & WTC technology. We believe that this cable will contribute to the construction of more efficient network installation between data centers.

6. References

[1] S. Shimizu, et al. "Air-blown Fiber Optic Cable with SWR and WTC Technologies", Proceedings of 67th IWCS (2018).

[2] S. Kaneko, et al. "Development of Indoor/Outdoor cables with high-flame retardant", Proceedings of 70th IWCS (2021).

[3] T. Kaji, et al. "Development of Wrapping Tube Cable with Spider Web Ribbon using fiber based on ITU-T G652 D", Proceedings of 65th IWCS (2016).

[4] ICEA S-122-744-2022, "Standard for Optical Fiber Outside Plant Microduct Cables", (2022).

[5] ICEA S-104-696-2019, "Standard for Indoor-Outdoor Optical Fiber Cable", (2019).

[6] UL 1666, "Standard for Safety: Test for Flame Propagation Height of Electrical and Optical-Fiber Cables Insulated Vertically in Shafts (Ed.5)", (2007).

7. Pictures of Authors



Naoya Maehara
Mr. Naoya Maehara joined Fujikura Ltd. in 2019 after graduation from Keio University with M.E. degree, and has been engaged in research and development of optical fiber cables. He is now an engineer in optical cable research and development.



Okimi Mukai
Mr. Okimi Mukai joined Fujikura Ltd. in 2018 after graduation from Keio University with M.E. degree, and has been engaged in research and development of optical fiber cables. He is now an engineer in optical cable research and development.



Yusuke Yamaki
Mr. Yamaki Yusuke joined Fujikura Ltd. in 2014 after graduation from Tsukuba University with M.E. degree, and has been engaged in research and development of optical fiber cables. He is now an engineer in optical cable research and development.



Akira Namazue
Mr. Akira Namazue joined Fujikura Ltd. in 1997 after graduation from Keio University with M.E. degree, and has been engaged in development of a drawing process of optical fiber, and research and development of optical fiber cables. He is now a group manager in optical cable research and development department.



Akira Kori
Mr. Akira Kori joined Fujikura Ltd. In 1989 after graduation from Yamagata University with B.E. degree, and has been engaged in optical fiber cable production engineering. He is now a general manager in optical cable research and development department.

Central tube cables with easy access of embedded strength members

Sravan Kumar peraka, Atul Mishra, Prasanna Pardesi, Sarin Kumar
Dept. Design and Development, Sterlite Technologies Limited
Silvassa, Dadra Nagar Haveli, INDIA
+91-9016688121 · sravan.kumar@stl.tech

Abstract
With the advancements in technology, optical fiber cables are playing a vital role in building a backbone for high speed internet. There are a wide variety of optical fiber cable designs which are designed based on the type of deployment, regions, ease of installation, low cost etc. The central tube/core designs offer faster deployment due to easy access of fiber units compared to a SZ stranded designs.

Keywords: Central tube cables, FTTx, Ribbon cables.

1. Introduction
Optical fiber outdoor cables are mainly categorized into SZ stranded and Central tube/core designs. The central tube/core designs offer faster installations due to easy access of fibers compared to SZ stranded cable designs.However, central tube/core designs pose challenges in accessing the strength members for termination in a joint closure due to embedding in the jacket .Thus, there is a need to access embedding strength members in cental tube/core designs..

2. Cable design

The central tube/core design employs rigid tensile strength members like FRP/ARP/Steel wire which helps in providing tensile strength to the cable and provides anti-buckling property to provide good bend performance of cable. The typical construction of a central tube/core designs has a buffer tube or multiple buffer tubes in the center of the cable covered with a water blocking tape .The multiple buffer tubes combination is called core. The core is surrounded with a jacket material with embedded strength members.

2.1 Challenges of central tube/core cables

The central tube/core designs helps in reducing the cable termination process due to easy access of fibers compared to SZ cable designs. However, as mentioned above, there are some challenges posed by central tube/core designs. However, there are some challenges in central tube design .Below are key challenges of central tube designs.

1. Preferential bending.

2. Waviness of cable

3.Challenge in accessing strength members for termination in joint closure.

The above mentioned challenges can be addressed by right selection of design, materials,tools and process settings.

Preferential bending is an inherent challenge in central tube cables with rigid strength members embedded 180 degree apart. However, due to faster installation makes it choice of design inspite of preferential bending.

The waviness in cable makes it very challenging to install the cable due to handling challenge. The waviness is caused generally due to improper selection of tensions of individual elements in cable, strength member uneven bonding and improper cooling of cable.

The access to embedded strength members is important as it helps in better termination of cable in joint closure. The conventional central tube cables employ embedded strength members with EAA(Ethylene Acrylic Acid) to have good bonding with jacket and have a good integrity with cable to avoid pistoling of embedded strength members .

Thus, there is a need for a central tube cable design which can address above stated challenges.

2.2 Central tube cable design with easy access of embedded strength members

In an attempt to overcome above challenges, we have come up with a design which has partial embedding of FRPs to facilitate easy access of FRPs for termination in joint closure.

The central tube consist of fiber ribbons, typically 144 fibers with a12Ribbonx12 No.of ribbons configuration. The buffer tube is surrounded by strength yarns (Aramid/Glass yarns) . The strength members are surrounded by a water blocking tape. The entire core is surrounded by a polyethylene jacket with partial embedding of FRPs .The FRPs are embedded in such a way that it has a good balance of access to FRPs, balanced bonding with jacket and no waviness in the cable .

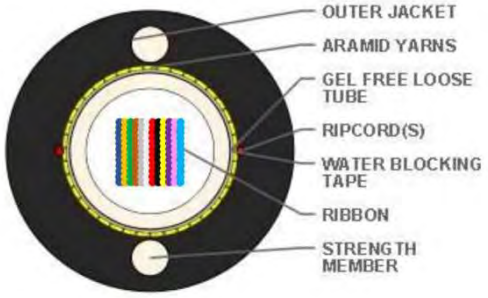


Figure 1.Typical cross section of easy access central tube design

3. Cable properties, performance and Qualification

3.1 Cable design

Conventionally, central tube cables with embedding strength members have FRPs as strength members with a minimum thickness around the FRPs. However, in case of situations where FRPs needs to be accessed during the termination of cable inside a joint closure, it is very difficult to access the FRPs due to high bonding with the jacket. Thus, the FRPs get damaged when separated from the jacket.

A novel cable design with partial embedding of FRPs is designed with a minimal polymer < 50 microns at the inner side of the cable to have a good balance of bonding and FRP separation.

3.2 FRP selection for central tube cables

There are mainly two kinds of FRPs are available for optial fiber cables, a bare FRP and a coated FRP.

The coated FRPs are generally used for embedding designs to provide good adhesion with the jacket material. The coating on the FRP is ethylene acrylic acid (EAA).This coating helps in chemical bonding with the jacket material.

3.3 Cable Performance

The cable is tested as per GR -20 requirements. Additionally, cable is tested for FRP separation test, waviness in the cable and termination in joint closure to ensure the cable meets all the requirements which are essential for field deployments.

Table 1 - Summary of test results of various tests

Product Compliance				
S No	**Requirement**	**Method**	**Actual Result**	**Test Result**
1	Tensile Strength : 2700 N @ 0.6% fiber strain Change in attenuation : ≤ 0.05 db/km	IEC 60794-1-2-E1	Strain : 0.374 % @ 2700 N Change in attenuation : 0.024 dB/km.	PASS
2	Temp. Cycling Test : TA1:-40 °C;TA2:-40 °C;TB1:+ 70 °C;TB2:+ 70 °C Avg. Change in attenuation : ≤ 0.05 db/km @1550nm Max. Change in attenuation : ≤ 0.15 db/km@1550nm	IEC 60794-1-2-F1	**Average Change in attenuation@** 1550nm : 0.025 dB/km, **Max Change in attenuation@** 1550nm : 0.050 dB/km,	PASS
3	FRP seperation from jacket	Customer requirement	FRPs are seperable from jacket wihtout damage.	PASS
4	Wavniess in cable Requirement -There shall be no waviness in the cable when laid on the ground.	Product requirement	No waviness was observed after laying the cable on the floor	PASS
5	Torsion : ± 180 degree Change in attenuation : < 0.05 db/km	IEC 60794-1-2-E7	Change in attenuation : 0.043 dB	PASS
3	Crush : 700 N/100mm Change in attenuation : < 0.05 db/km	IEC 60794-1-2-E3	Change in attenuation : 0.01 dB/km	PASS
4	Impact : 5 Nm Change in attenuation : < 0.05 db/km	IEC 60794-1-2-E4	Change in attenuation : 0.008 dB/km	PASS
5	Torsion : ± 180 degree Change in attenuation : < 0.05 db/km	IEC 60794-1-2-E7	Change in attenuation : 0.043 dB	PASS
6	Bend Test : 10 Cycles Change in attenuation : < 0.05 db/km	IEC 60794-1-2-E6	Change in attenuation : 0.009 dB/km	PASS
7	Water Penetration Test : 1 meter water head, 3 meter sample, 24 hours	IEC 60794-1-2-F5	Water Penetration Test : 1 meter water head, 3 meter sample, 24 hours	PASS

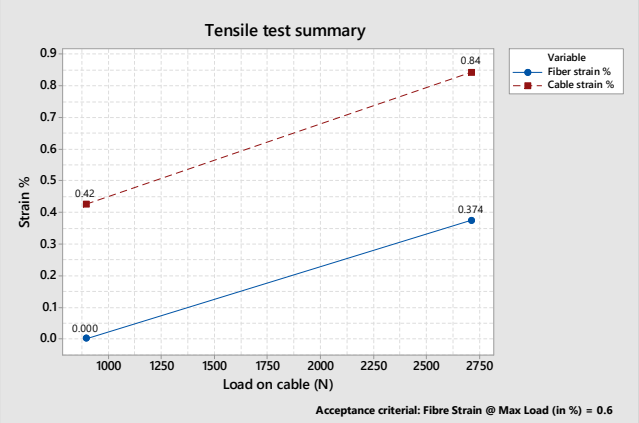


Figure 2 – Tensile test graph

Apart from the GR 20 requirements, FRP separation/access, cable waviness test and FRP termination in joint closure test were performed on multiple cables produced and observed consistent results.

3.2.1 FRP access test

As mentioned above, FRP/rigid strength member's access is required to clamp the cable inside the joint closure.

It is little challenging the produce cable with easy access of embedded strength members due to higher bonding with jacket. The glass fibers of FRP tends to break if bonding of FRP with jacket in beyond a threshold limit. A novel jacketing tooling was developed after several iterations to get a consistent result. More than 10 cables were tested from the bottom and top ends of the cables and found a consistent FRP access results.



Figure 3- Separation of FRP from jacket without damage

3.2.2 Cable waviness test

The cable designs with embedded strength member and aramid yarns exhibit waviness phenomena when laid on the ground due to poor bonding or uneven back-tensions on embedded strength members or peripheral strength members like aramid or glass yarns. Since the strength members are embedded partially, it is important to check the waviness in the cable. The cable is tested for waviness

using in-house developed testing procedure and found no waviness in the cable.



Figure 4- Waviness test on cable

3.2.3 FRP clamp test

The FRP clamping test was performed by preparing the end of the cable. FRPs were separated from the jacket for around 2 meters with ease. The jacket strips were cut after stripping the cable for the final termination of cable in the joint closure. For demonstration purpose, the FRPs were clamped without adding any heat shrink sleeve. It is always important to clamp both the FPRs as clamping on only one FRP with break the FRP due to torsion effect of the cable.



Figure 5 FRP clamping inside the joint closure

4. Conclusion

A novel central tube cable is designed and developed with easy access of embedding strength member which meets all the requirements as per GR 20. Below are the unique features of this cable design.

- FRP separation from jacket without damage/debris of glass.
- Balanced bonding of FRP with the jacket
- Easy clamping of FRPs inside joint closures.
- Faster deployment of the cable due to unitive design .

5. Acknowledgements

I would like to the people who have worked on this project directly and indirectly and contributing for the successful development. Mahesh Deshpande, Gahininath Shinde, Kishore Sahoo, Jyotiprakash, Shubham Sachen, Sumit Dubey, Abishsekh Saha, Bikram Nayak, Raj Gangwar, David Kumar, Raghav Parashar, Shivangi , Surya narayan Bhanja deo,Amitesh Dubey, Pradeep Kumar, Adbul Khalik Manoj Garg., Abasahed Waghmare, Vinayak Pillamari,

6. References

[1] Richard H. Norris, Peter A. Weimann and Howard M. Kemp Performance Aspects of a Novel Two-Rod, Dielectric Sheath Design for Central Tube Cables *International Wire and Cable 2002*

[2] Patrick Van Vickle, Donald Gross, Victor Knight, Steve Stokes Robust High-Count Dry Central Tube Ribbon Cables. *International Wire and Cable Symposium 2002*

Authors



Sravan Kumar Peraka

Sterlite Technologies Limited

Survery no 68/1,Rakholi, Silvassa, India 396230

Sravan Kumar Peraka is the Head of Process Development for cables business, responsible for both optical fiber cables and LAN cables. He holds a chemical engineering degree from IIT Roorkee. He has over 14 year of experience in optical fiber and cables. He worked in operations and lean manufacturing departments before

moving to research and development in 2012. He holds several patent grants in the field of optical fiber cables.



Atul Mishra is the New Product Development Lead of Optical Fiber Cables. He holds a Mechanical engineering degree from Rashtrasant Tukadoji Maharaj Nagpur University .He has an experience of over 13 years from various industries. He jointed sterlite technologies in 2016. He has worked extensively in operations before moving into new product development in 2017. His major contributions include development of high density micro cables, intermittent bonding ribbons and cables.



Prasanna Pardeshi the head of New Product Development and Application Assurance. HE holds a B.Sc degree in physics. He has over 27 years of experience in Optical fiber cable operations, testing, application engineering and customer support. He is an expert in optical fiber cable installation, termination and trouble shooting.



Dr.Sarin Kumar is the Head: R&D for Cables business at Sterlite Technologies Ltd He is responsible for both Optical fiber cables as well as LAN cables. Sarin has ~22 years of both academic and industrial research experience that includes working at University of Geneva, Norwegian University of Science & Technology, Honeywell and Eaton. Sarin has served as a member of the Industry Advisory Board at the Dept. of Metallurgy & Materials Science, College of Engineering Pune. He also served as technical program committee member for IEEE International Frequency Control Symposium in 2009, 2010 and 2011. Sarin Kumar has a Ph.D. in Materials Science & Engineering from Tokyo Institute of Technology, Japan.

Hybrid Cables for 4G/5G technology networks

Felipe Rosa Antunes, Fabio Gouveia Corcini, Kleber Beloni Caliani, Tiago Rafael Cirezola, Edson Jansen Pissini

Prysmian Cabos e Sistemas do Brasil S.A, Sorocaba, Brasil

+55-15-3235-9000• kleber.caliani@prysmiangroup.com

Abstract

This paper presents the development of a hybrid cable made up of optical fibers, twisted metal pairs and electrical power conductors. The need for this development arose from a project to install mobile telephone transmission equipment in the city of São Paulo, carried out by one of Brazil's largest cellular network operators.

The aim was to connect a telephone exchange to points distributed through small cells, carrying an optical signal, electricity to power equipment and metal pairs for monitoring and alarms to the transmission points, covering the Avenida Paulista region in São Paulo, the largest financial center in the country, with a significant demand for access to the mobile network and a high density of constructions and buildings that make it difficult to operate with macrocells.

Keywords: Optical fiber; hybrid cable; 4G; 5G; small cell

1. Introduction

The demand for mobile connectivity and ever faster data speeds has driven a revolution in communication networks. Small cell networks are emerging as a promising solution for improving coverage, capacity and quality of service in dense urban areas and places with high data traffic. This paper presents the development of a hybrid optical cable to serve small cell networks, which involved surveying field needs, designing the cable, developing product prototypes and the production process, qualifying the product and monitoring installation in the field.

Small cell networks refer to small communication devices that operate on cellular frequencies, covering a limited geographical area (tens or hundreds of meters). They are used to improve the capacity and coverage of mobile networks, especially in places where macrocell infrastructure (traditional cell towers) is insufficient.

By implementing small cell networks, it is possible to obtain benefits such as improved coverage, as they fill gaps in signal coverage, ensuring that indoor areas, dense urban spaces and popular tourist spots have robust connectivity, increased capacity due to reduced load on macrocells, as they improve network capacity and avoid congestion, resulting in a more fluid user experience.

Another aspect is the improvement in the quality of service, bringing the network closer to the user, as it reduces interference and improves the quality of voice calls and data speeds. Finally, it is possible to obtain support for future technologies, considering that they will play a crucial role in the 4G/5G transition and beyond, since these technologies require a higher density of access points to work effectively.

The development of the cable to meet the small cells application was especially challenging due to the need to group together different elements in the cable core, fibers and metallic conductors, which have mechanical characteristics and different dimensions, which requires specific adjustments during the process so that the optical fiber doesn't experience too much strain that could compromise its performance.

The structure of the cable developed is shown in figure 1

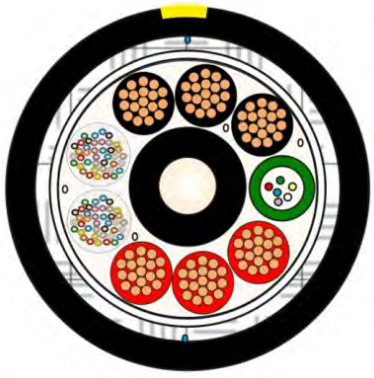


Figure 1. Section view of hybrid cable

The development of this type of product was an important step in the implementation of mobile networks in Brazil, simplifying the cable installation process, compacting the application and saving space in already saturated ducts.

2. Requirements

Due to the innovative nature of this product for the Brazilian market, there were no normative requirements established by the government regulatory agency (Anatel - *Agência Nacional de Telecomunicações*) for the new product developed. In this way, it was used references from customer specifications and the following specific products specifications: ABNT/NBR - *Agência Brasileira de Normas Técnicas / Normas Brasileiras* (Brazilian Technical Standards Agency / Brazilian Standards) ABNT/NBR14566 07/2020 - *Cabo óptico dielétrico para aplicação subterrânea em duto e aérea espinado — Especificação (Dielectric optical cable for underground duct and aerial spinning applications – Specification)*, ABNT/ NBR9124 12/1999 *Cabo telefônico isolado com termoplástico e núcleo protegido por capa APL – Especificação* (Thermoplastic insulated telephone cable with Al jacketed core – Specification), ABNT/NBR5410 09/2004 *Instalações elétricas de baixa tensão* (Low-voltage electrical installations). As international references, the following specifications were adopted: ANSI ICEA.S-87-640:2016 – Standard for Optical Fiber Outside Plant Communications Cable, Telcordia GR 20:2013 – Generic Requirements for Optical Fiber and Optical Fiber Cable and IEC 60794-1-21 / Ed1 Optical fiber cables - Part 1-21: Generic specification - Basic optical cable test procedures - Mechanical tests methods.

Return to Table of Contents

The parameters considered in the product design are shown in table 1

Table 1: Initial requirements of hybrid cable

Cabe Component	Parameter	Unity	Specification
Loose tube	Fiber count		24
	Maximum fiber attenuation	dB/km	0.25
Power conductor	Conductor section	mm^2	2.5
	Electrical resistance DC (20 ºC)	Ω/km	7.98
	Electrical resistance AC (70 ºC)	Ω/km	9.54
	Current capacity	A	24
	Voltage drop (PF=0.92)	V/A.km	6.31
	Electrical resistance DC (20 ºC)	Ω/km	147.2
Twisted pair	Maximum average resistance unbalance (20 ºC)	%	2
	Individual maximum resistance (20 ºC)	%	5
	Mutual capacitance	nF/km	51 ± 5
	Minimum insulation resistance	MΩ.km	15,000

3. Development of 1st prototype

Once the main requirements had been established, work began on evaluating the design of the new product and defining the elements to be used in its construction.

A cable was designed consisting of 24 single-mode optical fibers, in accordance with ITU-T specification G.652D, protected by a polypropylene tube. To protect against the ingress of moisture, a water-absorbing wire was used, which has the property of being hydro-expandable.

After adjusting the extrusion machine and tooling, a 24-fiber SM G.652D tube was obtained in accordance with the maximum attenuation specification of 0.25 dB/km @ 1550 nm

Flexible class 5 copper cables with a metal section of 2.5 mm2 were used as the electrical power conductor. Twenty copper twisted pairs with 0.40 mm conductors were also added to the cable core, divided into two groups of 10 pairs each and shielded by aluminized polyester tape.

All these elements were grouped together in an optical core assembler, applied around an FRP element, and applied in the shape of an SZ. The critical point in this process was to equalize the unwinding tensions of each of the elements to maintain their mechanical stability.

The appearance of the assembled hybrid cable core is shown in figure 2



Figure 2. Stranded hybrid cable core

Considering the access that the cable would make inside the plant, a protective layer of LSZH compound was applied over an aluminum tape, forming the mechanical protection and electromagnetic shielding assembly. In order for the tape to have adequate flexibility to overcome the curvatures involved in the installation without damaging the aluminum shielding, a corrugation process was applied to the tape.

4. Laboratory tests of 1st prototype

After extruding the layer, the prototype's dimensional and optical parameters were evaluated, and a significant increase in the value of the transmission attenuation coefficient at a wavelength of 1550 nm was verified, where the specification provided for a maximum of 0.25 dB/km.

The attenuation coefficient results are shown in figure 3 below:

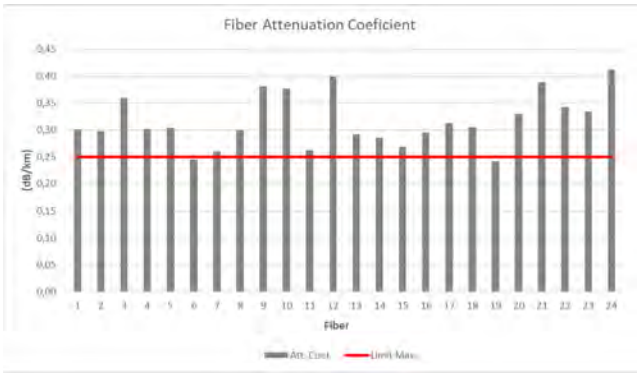


Figure 3. Fiber attenuation coeficient (1st propotype)

Evaluating the dimensions of the fiber optic protection tube, points were found with deformation of up to 30% in diameter, indicating that it suffered compression stresses during the assembly stage of the elements that make up the hybrid cable. Only two of the total of 24 optical fibers in the cable showed a value within the specification of 0.25 dB/km, while the others reached values of up to 0.40 dB/km.

Based on the preliminary results obtained with the first prototype, the cable was considered failed and a new project was started, looking for elements that would reinforce the protection of the optical fibers so that they would not suffer increased attenuation and that would allow the assembled tubes to be more robust during the production process.

The alternative chosen was to use PBT (polybutylene terephthalate) instead of PP (polypropylene), to make the tube more rigid and better able to withstand compressive stress.

A change in the type of optical fiber used was also considered, switching to BLI (bend loss insensitive). These fibers are able to withstand stricter bend radii without suffering significant increases in attenuation. With this modification, the fiber's operating condition went from a bend radius of 30 mm with the ITU-T G.652D fiber to 7.5 mm with the ITU-T G.657 A2/B2 fiber (BLI), as shown in graph 2 :

Return to Table of Contents

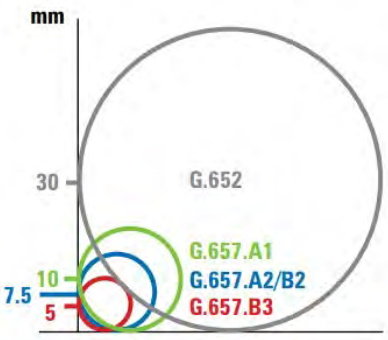


Figure 4. Relevant specified bending radio for ITU-T G.652 and ITU-T G.657 fibers

5. Development of 2nd prototype

Once the design changes had been made, we proceeded to manufacture the loose tube made of PBT, with gel-based moisture protection. This stage was completed without significant changes in optical attenuation when compared to the values at the start of the process.

Next came the process of assembling the elements of the hybrid cable, a 24-fiber loose tube of the BLI type, power conductors and twisted pair groups, all on an FRP (fiber reinforced plastic) pole insulated in polyethylene, in such a way as to hold all the components within its perimeter. At this stage, an additional check of tube deformation and attenuation variation was applied, and no significant changes were observed after the process, indicating the effectiveness of the design revision with the use of PBT in the protection tube and the use of fibers with low sensitivity to bending, translating into greater mechanical robustness for the set that makes up the core of the hybrid cable.

The application of the elements during the assembly of the optical core is shown in figure 5 below:



Figure 5. Stranding of elements of hybrid cable

The external protection was maintained with the same material used in the first prototype, LSZH, together with corrugated aluminum tape. In addition, a longitudinal yellow strip was added to the cable sheath using a coextrusion process. The purpose of this strip was to distinguish the hybrid cable from other dielectric cables installed in shared ducts, and thus provide additional identification in order to prevent accidents with the electrical conductors in the event of intervention on the cable, since the power conductors will be energized with a voltage of over 300 V and the use of tools to access the cable core could come into contact with the energized conductor.

The final visual appearance of the cover made of LSZH material and the longitudinal yellow identification strip is shown in figure 6 below:

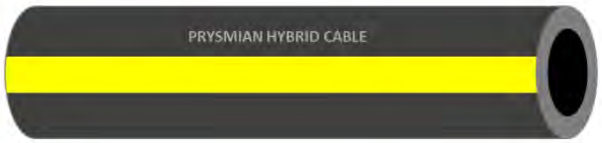


Figure 6. Hybrid cable jacket with coextruded stripe

6. Laboratory tests of 2nd prototype

Once the second prototype was finished, laboratory tests began, with the aim of validating the changes made to the design and checking compliance with the other parameters specified for the product developed.

Initially, attenuation measurements were taken at 1550 nm for all 24 BLI-type optical fibers. The values found are listed in figure 7 below:

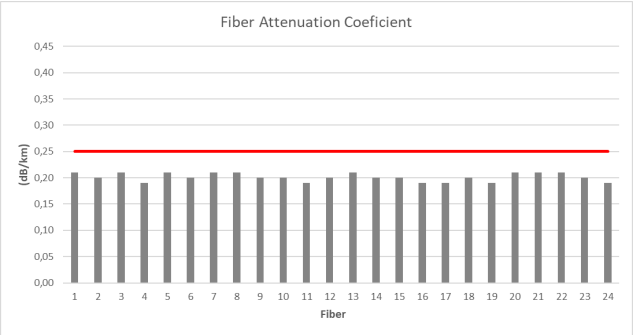


Figure 7. Fiber attenuation coefficient (2nd prototype)

Based on the dimensional evaluation of the tubes, there was a significant reduction in the deformations that occurred after the cable core was assembled, confirming that the replacement of the PP polymer with PBT was successful, giving this element greater resistance to compression and consequently transferring less intense stress to the optical fibers, which also became less mechanically sensitive due to the adoption of BLI technology, resulting in attenuation coefficient values within specification.

Return to Table of Contents

Continuing the process of qualifying the new product, a sequence of tests were carried out, including mechanical and environmental tests, which were determined on the basis of the application for which the product was intended and also by adding references to national and international standards.

The results obtained during the tests are shown in table 2 below:

Table 2: Requirements and results.

Test	Requirements	Results
Optical Attenuation Coefficient	Maximum 0.25 dB/km @1550 nm	0.21 dB/km **Approved**
Optical attenuation uniformity	Maximum 0.05 dB/km @1550 nm	0.02 dB/km **Approved**
Flexing	ΔAt. Max ≤ 0.15 dB	ΔAt. Max = 0.02 dB **Approved**
Torsion	ΔAt. Max ≤ 0.15 dB	ΔAt. Max = 0.01 dB **Approved**
Curvature	ΔAt. Max ≤ 0.15 dB	ΔAt. Max = 0.03 dB **Approved**
Compression	ΔAt. Max ≤ 0.15 dB	ΔAt. Max = 0.07 dB **Approved**
Impact	ΔAt. Max ≤ 0.15 dB	ΔAt. Max = 0.06 dB **Approved**
Repeated bending	ΔAt. Max ≤ 0.15 dB	ΔAt. Max = 0.02 dB **Approved**
Water Penetration	No leak detected	**Approved**
Cable tensile loading and fiber strain test	Def. Load Max.≤ 0.6% Def. Residual.≤ 0.2% ΔAtt. Max ≤ 0.15 dB	Def. Load Max.≤ 0.03% Def. Residual.≤ 0,00% ΔAt. Max = 0.05 dB **Approved**
Cable temperature cycling test	ΔAtt. Max ≤ 0.15 dB/km	ΔAt. Max = 0.09dB/km **Approved**
Electrical resistance DC (20 ºC)	7,98 Ω/km max	7.21 Ω/km **Approved**
Electrical resistance AC (70 ºC)	9.54 Ω/km max	9.07 Ω/km **Approved**
Electrical resistance DC (20 ºC)	147.2 Ω/km max	144.1 Ω/km **Approved**
Maximum average resistance unbalance (20 ºC)	2 %	0.5 % **Approved**
Individual maximum resistance (20 ºC)	5 %	1.9 % **Approved**
Mutual capacitance	51 ± 5 nF/km	52 **Approved**
Minimum insulation resistance	15,000 MΩ.km	200,000 MΩ.km **Approved**
Electrical continuity of conductors	-	**Approved**

Based on the results obtained in the laboratory, the hybrid cable was considered approved and ready to go into the field. As this was a joint development with the client, the technical product development team had access to the installation site to monitor performance during the application.

The details of the installation are described below.

7. Installation

The cable was installed in the city of São Paulo, in the Avenida Paulista area, an important Brazilian financial center with an intense flow of people and consequent high demand for access to the 4G and 5G mobile networks.

The cable was laid between a central office and transceivers installed 2 km away. In the initial stage, five small cells were activated. The cable application map can be seen in figure 8 below:

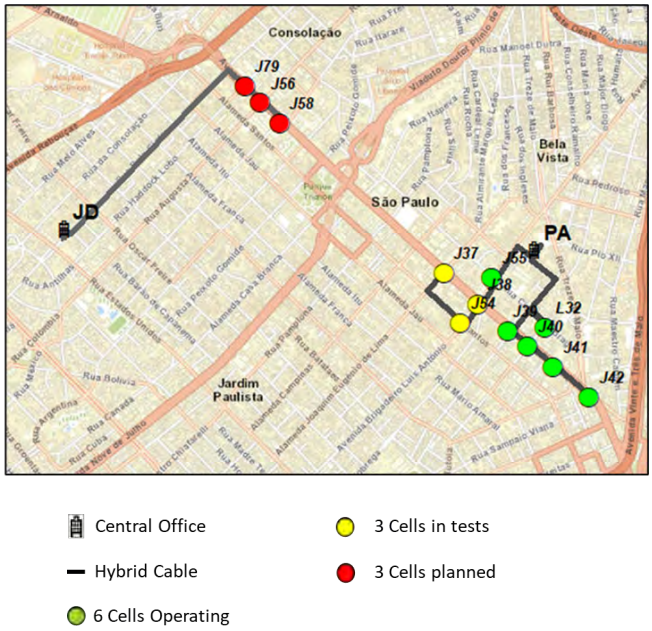


Figure 8. Map of installation of hybrid cable

The cable was laid continuously, without splices, between the central office and the small cell transceiver installation points. A critical aspect of this operation was pulling the cable without damaging the optical fibers and other cable components, since the duct structure was already used by other cables, which made installation difficult and required severe pulling.

The transceiver for the small cells was installed on top of the pre-existing public telephone structure at the site, which simplified the implementation of the system, taking advantage of both the duct network that served the old pay phones and the structure of the pay phone itself, to install the electronic equipment as well as the system's antenna, as can be seen in figure 9:



Figure 9. Small cell installation

Return to Table of Contents

After installing the cable, measurements were taken of the optical continuity of the fibers, the attenuation coefficient, the electrical continuity of the conductors and the insulation resistance of the conductors, in order to check whether the cable's constituent elements had suffered any damage during the installation process. All these parameters showed satisfactory results, in accordance with the product specification.

8. Conclusions

The development of the hybrid cable containing optical fibers, power conductors and twisted pairs proved to be totally feasible during the work on this project.

Initially, challenges were encountered with regard to adding attenuation to the optical fibers, resulting in values out of specification and the first prototype being rejected. This difficulty was overcome by using fibers with low sensitivity to bending and using PBT to form the protection tube.

The technology developed during the project allows for expansion to a variety of cable constructions, with different numbers of fibers and conductors and is of great importance for serving the entire Latin American market.

The development using different elements (optical and electrical) brought great learning and knowledge to the technical team, making it necessary to apply design concepts to both optical fiber cables and metallic conductor cables, two technologies that normally use very different processes, with different machine configurations.

The partnership with the client was fundamental for a correct understanding of the needs in the field, which made it possible to identify specific requirements, such as the need for exclusive identification for the hybrid cable, consisting of a yellow stripe applied by coextrusion to the jacket, to alert operators in the field to the electrical risk involved.

In this way, the product presented proved to be an excellent option for expansion and access to new technologies such as 5G via small cells, in areas where tower structures are not very efficient.

9. References

[1] ANSI ICEA.S-87-640:2016 – Standard for Optical Fiber Outside Plant Communications Cable.

[2] Telcordia GR 20:2013 – Generic Requirements for Optical Fiber and Optical Fiber Cable.

[3] IEC 60794-1-21 / Ed1 Optical fiber cables - Part 1-21: Generic specification - Basic optical cable test procedures - Mechanical tests methods.

[4] Anatel - ATO Nº 948, DE 08 DE FEVEREIRO DE

[5] Anatel - ATO Nº 949, DE 08 DE FEVEREIRO DE

10. Pictures of Authors



Felipe Rosa Antunes graduated in Electrical Engineering in 2012 from Unip- *Universidade Paulista*. He joined Prysmian Cabos e Sistemas do Brasil S.A. in 2011 and is currently responsible for Telecom Technical Sales Solution department.

E-mail: felipe.rosa@prysmiangroup.com



Fabio Gouveia Corcini received his degree in Electrical Engineering from *Faculdade de Engenharia de Sorocaba* - Facens in 2005. He joined Prysmian Cabos e Sistemas do Brasil S.A in 1996. Currently he is the manager of R&D Telecom Department for Latim America.

E-mail: fabio.corcini@prysmiangroup.com

Return to Table of Contents



Kleber Beloni Caliani received his degree in Electrical Engineering from *Faculdade de Engenharia de Sorocaba* - Facens in 2007. He joined Prysmian Cabos e Sistemas do Brasil S.A in 2000. Currently he is the Chief Engineer in Prysmian Brazil

E-mail: kleber.caliani@prysmiangroup.com



Tiago Rafael Cirezola graduated in Electrical Engineering at Unopar – *Universidade Norte do Paraná* in 2006 and he joined Prysmian Cabos e Sistemas do Brasil S.A in 2008. Since 2018 he has been working at R&D department as a Specialist Product Engineer.

E-mail: tiago.cirezola@prysmiangroup.com



Edson Jansen Pissini graduated in Production Process Technology from *Faculdade de Tecnologia de Sorocaba*. He joined Prysmian Cabos e Sistemas do Brasil S.A. in 2006 and he is currently Telecom Process Technologist.

E-mail: edson.pissini@@prysmiangroup.com

Return to Table of Contents

SESSION 13

Click on a session below to navigate to that section of the Proceedings.

SESSION 13: OPTICAL FIBER COATING MATERIALS

Chairperson: Eric Bulington, UL Solutions, USA

13-2 **Next Generation Optical Fiber Coatings with Excellent Accelerated Aging Performance, While Maintaining Robust Draw Processing Capability;**
Dr. Xiaosong Wu, *Covestro LLC, USA*

13-3 **Impact of Environmental Stresses and Lifetime Aging Simulation on Optical Fiber Coatings;** Dr. Brian Risch, *Prysmian, USA*

13-4 **Prediction of Physical Properties of Optical Fiber Coating Resins Based on Chemical Kinetics;** Yudai Watanabe, *Sumitomo Electric Industries, Ltd, Japan*

13-5 **Investigation on Application of Biomass Raw Materials to Optical Fiber Coating Agents;** Mr. Natsuki Hamada, *Japan Fine Coatings Co., Ltd., Japan*

13-6 **UV-Curable High Temperature Resistant Dual Layer Coating System for Specialty Optical Fiber Applications;** Dr. Huimin Cao, *Covestro LLC, USA*

Click here to return to the **Table of Contents**

Next Generation Optical Fiber Coatings with Excellent Accelerated Aging Performance, While Maintaining Robust Draw Processing Capability

Xiaosong Wu, Todd Anderson, Katherine Roberts, Brett Register, Meng He, Eric Urruti
Covestro LLC, Elgin, IL, USA
+1-224-402-0953 xiaosong.wu@covestro.com

Abstract
Next generation, microbending resistant, optical fiber primary coatings have been developed to maintain excellent optical and mechanical properties, after subject to environmental test (accelerated aging) conditions. Such coating system is also fit-for-use for modern fiber draw processes, including super fast draw speed, optimized Helium consumption rate, as well as UVLED curing.

Keywords: Optical and mechanical properties after accelerated aging, microbending resistance, robust draw process operation window, super fast draw speed, optimized Helium consumption rate, UVLED curable

1. Introduction
It's well known [1] that reduced microbending loss is beneficial to overall performance of optical network. With the ongoing 5G network deployment, such requirement is becoming even more crucial for modern high speed, and high bandwidth network.

It's been reported in IWCS of last year, about the development of microbending resistant, next generation primary coatings [2]. Particularly, such coatings demonstrated superior microbending resistance, when tested with IEC 62221 TR Method D (basket weave), at temperature of -40 °C and at wavelength of 1625 nm.

It was also reported [2], that, *in-situ* modulus was reduced by about 70%, from 0.49 MPa of Current Coating, to about 0.15 MPa of Next Generation Coating, as shown in Figure 1. Concerns have been raised, *w.r.t.* how such low modulus primary coatings would perform under severe accelerated aging conditions, such as 85°C/85% Relative Humidity.

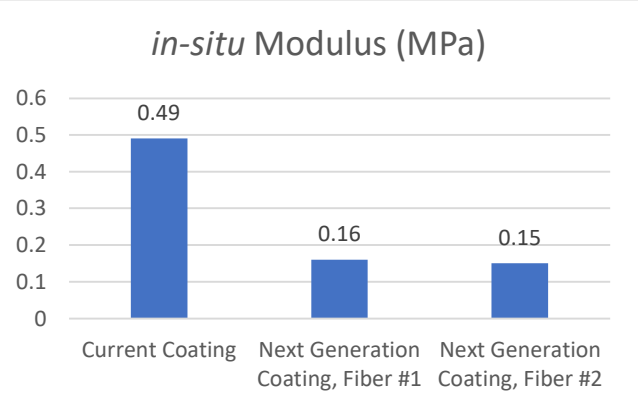


Figure 1. On-fiber *in-situ* Modulus [2]

In this report, optical and mechanical properties, after accelerated aging, are evaluated for fibers coated with Next Generation Coating.

At the same time, Next Generation Primary Coating maintains its fit-for-use for modern fiber drawing processing conditions, such as fast draw speed, optimized Helium consumption rate, as well as UVLED curing [3][4].

2. Experiments
2.1 Damp Heat Environmental Test
Damp Heat Environmental Test was conducted under 85°C/85 Relative Humidity condition, for 30 days, according to IEC 60793-1-50, "Measurement methods and test procedures – Damp heat (steady state)", (Figure 2). De-ionized water was used in the test.



Figure 2. Damp Heat Test Setup

2.2 Change in Attenuation
Change in attenuation was measured according to IEC 60793-1-40 and IEC 60793-1-46. Precise measurement of attenuation was performed at 1310, 1550 and 1625 nm for every 5 minutes in initial 16 h, and then every 30 minutes for the remainder of the test duration, with Photon Kinetics 8000 OTDR.

2.3 Coating Strip Force
Strip force was measured, according to FOTP 178, "Measurements of Strip Force for Mechanically Removing Coatings from Optical Fibers".

2.4 Fiber Tensile Strength
Fiber tensile strength was measured, according to IEC 60793-1-31, "Measurement methods and test procedures – Tensile strength". A detailed description of the test setup is included in the following "Results and Discussion" section.

2.5 Stress Corrosion Susceptibility
Stress Corrosion Susceptibility Constant (a.k.a. Dynamic Fatigue, n_d) was measured, according to IEC 60793-1-33, "Measurement methods and test procedures – Stress corrosion susceptibility". Two-point bending method was used to generate results in this report.

3. Results and Discussion

3.1. Attributes and Requirements, after Damp Heat Environmental Test

In 2002, a Technical Report [5] was published by International Electrotechincal Commission (IEC), to estimate the reliability of fiber under a constant service stress, based on the power law of crack growth. Since then, such accelerated aging methodology has been widely adopted by the community. The most common accelerated aging condition is 85°C/85% Relative Humidity (R.H.) for 30 days, as described in IEC 60793-1-50.

In a recent report [6], 60°C/85% R.H. was suggested to be a more realistic aging condition, as harsher conditions could introduce unrealistic aging mechanisms and give rise to misleading results under prolonged testing periods.

In this report, 85°C/85% R.H. was still employed as the accelerated aging condition, since no official IEC revision of aging condition has been published.

Table 1 summarizes the attributes and requirements, dictated by IEC 60793-2-50, after optical fiber specimen have been subjected to accelerated aging.

Table 1. Summary of IEC Standards, upon Damp Heat Environmental Test (Accelerated Aging)

Attribute	Descriptor	Requirement
Change in attenuation	1550nm wavelength	<= 0.05 dB/km
Coating strip force	Average	1.0 N <= F_{avg} <= 5.0 N
	Peak	F_{peak} <= 8.9 N
Fiber tensile strength	Median	>= 3.03 GPa
	15 percentile of the tensile strength distribution	>= 2.76 GPa
Stress corrosion susceptibility constant, n_d		>= 18

3.2. Change in Attenuation

Change in attenuation upon accelerated aging is of great interest, to monitor the change in optical transmission, therefore to ensure the optical fibers are still fit-for-use for decades, based on the power law prediction of reliability.

Shown in Figure 3, is the change of attenuation, measured at 1550 nm wavelength, after the fibers were subject to 85°C/85 R.H. for 30 days. Change in attenuation of Current Coating was 0.004 dB/km, while the change in attenuation of Next Generation Coating was essentially zero. It's encouraging that the change in attenuation for both Current Coating and Next Generation Coating was well within the IEC standards of <= 0.05 dB/km, indicating excellent retention of optical transmission under accelerated aging conditions, predicting reliable optical transmission performance over the fiber's expected lifetime.



Figure 3. Loose Coil Change in Attenuation (dB/km LSA), Measured at 1550 nm

3.3. Coating Strip Force

Coating strip force is of interest in field operations, and is one of the recommended attribute to monitor, upon accelerated aging.

The test results are summarized in Table 2.

Table 2. Coating Strip Force, Upon Accelerated Aging

	Initial		After Accelerated Aging	
Strip Force (N)	Current Coating	Next Generation Coating	Current Coating	Next Generation Coating
Average	1.6	1.3	4.5	4.1
Peak	2.9	2.2	5.9	4.9

It's apparent that both Average and Peak Strip Forces increased substantially upon Accelerated Aging, by roughly 3 times in Average Strip Force, and by roughly 2 times in Peak Strip Force, when comparing to their initial values (unaged fiber). It's worth noting that, despite of such increases, both Average and Peak Strip Forces are still within the IEC Requirements (Table 1).

It was reported [7] that strip force test is mainly affected by secondary coating viscoelasticity, and is actually not correlated to primary coating *in-situ* modulus. Therefore, the substantial increase in strip force in this report, was likely caused by secondary coating property changes upon accelerated aging (secondary coating was not tested in this study).

3.4. Fiber Tensile Strength

It's utmost important to ensure that optical fiber retains sufficient tensile strength in the duration of application (decades in cable).

One of the challenges with soft (low modulus) primary coating is the difficulty in measuring fiber tensile strength, due to the coated fiber tends to slip on the capstan, as well as random breaking at capstan location (not in the middle of fiber specimen). As a result, the tensile strength data are often scattered, and therefore misleading.

It was reported [8] that a "sandwich tape method" could be applied in most challenging case, to effectively reduce the data scattering.

The fiber tensile strength data in this report was measured, using a custom made setup, as shown in Figure 4. Larger capstan size of 20 cm in diameter is used (vs. previously capstan size of 10 cm in diameter), coupled with a pre-winding 6 cm OD capstan, to greatly

improve the stability of fiber on the main capstan. Another improvement is to use low friction tape, to further reduce the friction between fiber and capstan, therefore reducing the likelihood of fiber breaking at capstan.

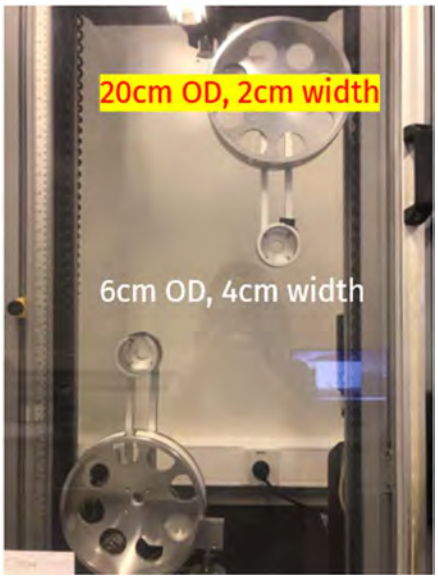


Figure 4. Fiber Tensile Strength Test Setup

The actual fiber tensile strength test results, before and after accelerated aging, are illustrated in Figure 5. For each fiber/condition, 15 fiber specimen were tested. The gauge length was 0.5 m, and the strain rate was 50mm/min (*i.e.* 10%/min).

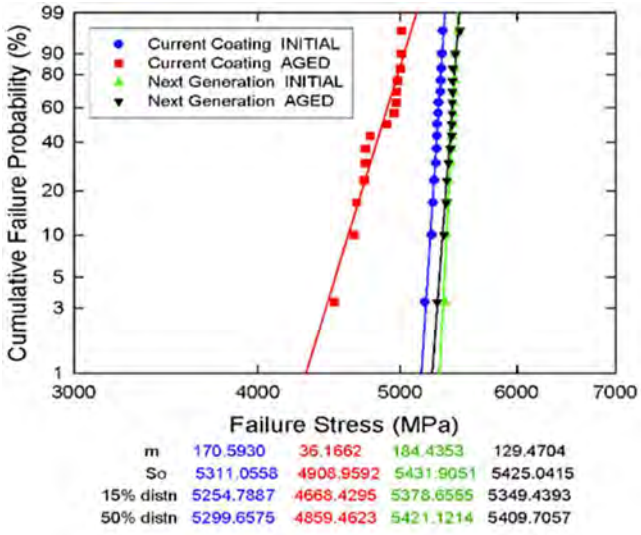


Figure 5. Weibull Plot, Fiber Tensile Strength

In the case of Current Coating, fiber tensile strength reduced from 5.3 GPa (Initial, blue round dots) to 4.9 GPa (Aged, red square). In addition, the data points of aged fiber is more scattered, indicated by reduction in m value (from 171 of Initial to 36 of Aged). Despite of the reduction, fiber tensile strength after aging is still well within IEC Standard (Table 1).

In the case of Next Generation Coating, fiber tensile strength was little changed at 5.4 GPa of both Initial (green triangle) and Aged (black triangle). In addition, data scattering was also better maintained, as measured by m value (from 184 of Initial to 129 of Aged).

Overall, Next Generation Coating system retained fiber tensile strength better than Current Coating system, upon accelerated aging. This is quite remarkable, considering Next Generation primary coating is much softer than Current Coating (Figure 1).

3.5. Stress Corrosion Susceptibility / Dynamic Fatigue

To predict long term reliability of fiber tensile strength, stress corrosion susceptibility (n_d) is measured.

It was reported [9], with improved tensile test method, excellent correlation between tensile method and two-point bending method has been obtained, in testing n_d.

In this report, n_d was measured with two-point bending test method. The Fatigue Plots are included in Figure 6 and Figure 7.

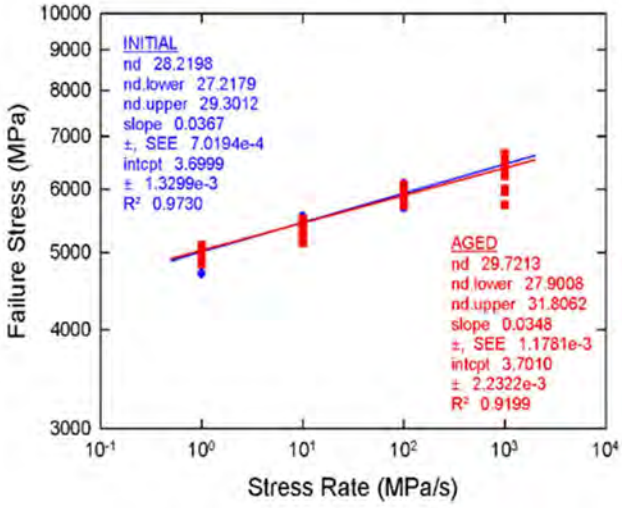


Figure 6. Fatigue Plot of Fiber Coated with Current Coatings

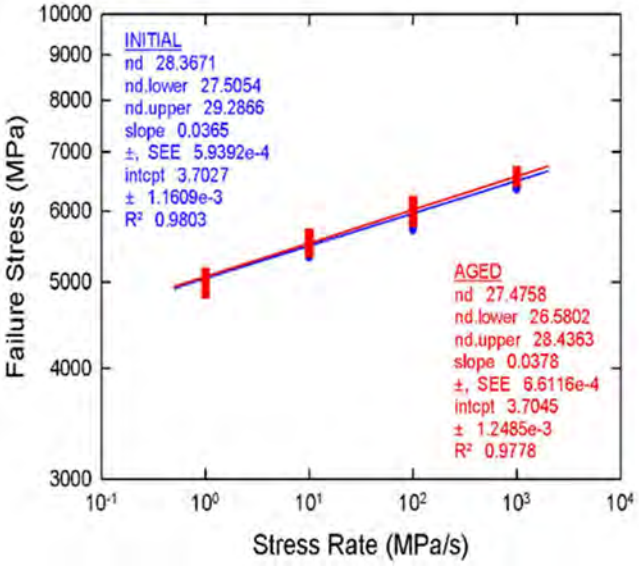


Figure 7. Fatigue Plot of Fiber Coated with Next Generation Coatings

In case of current coating, n_d value increased slightly from 28.2 (Initial) to 29.7 (Aged); while in case of Next Generation Coating, n_d value decreased slightly from 28.4 (Initial) to 27.5 (Aged).

All of these n_d values are well above the IEC Standards of 18.

4. Conclusions

In this paper, Next Generation Coating's long term reliability was evaluated, by monitoring both optical and mechanical properties, after accelerated aging.

Specifically, Next Generation Coating has essentially no attenuation change, during the 30 days of under 85°C/85 R.H. aging condition. Both Average and Peak Strip Force increased, and were still within IEC requirement. Next Generation Coating had excellent retention in fiber tensile strength, as well as n_d being well above IEC requirement, before and after accelerated aging.

At the same time, Next Generation Coating maintains robust processing capability, particularly, its fit-for-use for super high draw speed (>= 3000 m/min), as verified by in-house Draw Tower Simulator trials [4].

In addition, viscosity of Next Generation Coating is designed to be less sensitivity to temperature increase [3], making it more suitable for demanding draw process, in terms of maintaining proper geometry, as well as reducing Helium flow rate/consumption.

And, Next Generation Coating is formulated to be UVLED curable.

5. Acknowledgments

The authors would like to thank Covestro Technical Service Group for performing the tests.

6. References

[1] I. Davis, S. Schmid "Bend Matters, Part 2: Microbending in Optical Fibers", *www.lightwaveonline.com*

[2] X. Wu, *et. al.* "Next Generation Optical Fiber Coatings with Both Improved Tear Strength, and Superior Microbending Resistance, While Maintaining Robust Draw Processing Capability", *IWCS*, 2022.

[3] X. Wu, *et. al.* "Optical Fiber Coatings Capable of Super High Speed Draw Process", *IWCS*, 2019.

[4] X. Wu, *et. al.* "Next Generation Optical Fiber Coatings with Both Robust Draw Process Capability, and Enhanced Optical Performance with Reduced Microbending Sensitivity", *IWCS*, 2020.

[5] IEC TR 62048, "Optical Fibers Reliability - Power law theory"

[6] P. Shah, *et. al.* "Effect of aging conditions on performance properties of selected commercial fibers", *60th IWCS*, 2011.

[7] K. Gan, *et. al.* "Optical Fiber Strip Force Measurement Techniques and Their Implications." *57th IWCS*, 2008.

[8] L. Han, *et. al.* "Characterization of Tensile Properties of Optical Fibers Coated with a New Generation Coating System and the Comparison of Fatigue Behavior by Tensile Test and Two Point Bending Technique", *59th IWCS*, 2010.

[9] H. Cao, *et. al.* "Optical Fiber Coating Systems Designed for Enhanced Fiber Fatigue Performance Measured by the Improved Dynamic Fatigue Tensile Method", *63rd IWCS*, 2014.

7. Authors



Dr. Xiaosong Wu, currently Senior Scientist II, Fiber Optical Materials at Covestro . He holds a Ph.D. degree in Photochemical Sciences, and has been in various Research and Development positions.



Todd Anderson is a Laboratory Technical Expert at Covestro, LLC. He has been working in the application process and testing of optical fiber coatings for over 20 years. Todd graduated with a B.S. degree in biology from Northern Illinois University.



Kate Roberts is a Laboratory Technical Expert for Covestro Energy Curable Solutions. She specializes in customer related issues and assists with application development projects (FTIR, microscopy, fiber fatigue etc.). She received a B.S. in Zoology from Eastern Illinois University. Kate has been with DSM/Covestro in various positions in Research and Development since 1997.



Brett Register, currently Covestro Fiber Optic Materials Technical Service Manager. Worked for R&D since 2000 in various groups including Analytical and physical testing group, New Business

Development of display coatings, Additive Manufacturing, and Fiber Optic Materials.



Dr. Meng He is R&D manager of Fiber Optics Material Development Group at Covestro Energy Curing Solutions, with the role of leading the team on material development for optical fiber applications. His expertise area is on organic chemistry and polymer chemistry.



Dr. Eric Urruti is currently Head of R&D, North America, at Covestro. He has a diverse background encompassing, research, development, manufacturing, and business management with a substantial record of successful new product introductions.

Impact of Environmental Stresses and Lifetime Aging Simulation on Optical Fiber Coatings

Brian G. Risch*, Ryan Truong*, Tina Filip*, Cyril Mentzler*, Corey Palmore**, Isabel Sue**, Michael Oliver**, Yulia Kirina**, and Gary Pickrell**.

*Prysmian Group
P.O. Box 39
Claremont, NC 28610-0039

**Virginia Polytechnic Institute and State University
Department of Materials Science and Engineering
109A Surge Building 0237
Blacksburg, Virginia 24061

1-828-459-8435 · brian.risch@prysmiangroup.com

Abstract

The impact of lifetime aging simulations and other environmental stresses on various coating properties such as coating mass loss, in-situ modulus, coating durability, fiber strip force, stress corrosion parameter, and attenuation are examined for three coating systems. Test data on these fiber coating systems investigated demonstrate a fiber lifetime in excess of 50 years at a service temperature of 50°C.

Keywords: Optical fiber, lifetime modeling, optical fiber coatings, acrylate coatings, reliability.

1. Introduction

Optical fibers have now been deployed for decades with fiber coating technology continually evolving. Telecom networks are expected to be robust to environmental stresses over a lifetime of many decades. At the heart of the network reliability is the protection that the fiber coating systems provide to the optical fibers. Besides providing mechanical protection, the optical coatings must have stable properties over the lifetime of the fiber while exposed to various environmental stresses.

The failure mode of fibers in any elevated temperature environment is typically related to failure in the polymer coating system[1]. Degradation of optical fiber coatings may follow a very complex path, possibly including multiple mechanisms which include loss of low molecular weight species, thermo-oxidative degradation, degradation due to hydrolysis, and changes in crosslink density due to added exposure to UV radiation[2,3]. Physical changes in coatings can manifest themselves in various optical fiber properties including fiber strip force[4], in-situ modulus[5], fiber durability[6], attenuation, and fiber strength. To properly evaluate coating systems against various environmental stresses and modes of failure a variety of aging conditions combined with measurement of changes in a variety of fiber and coating properties is required.

In this study the impact of various environmental stresses is examined on changes in different coating systems through measurements of strip force, in-situ modulus, fiber durability, attenuation, and optical fiber dynamic fatigue parameter. The suitability of each coating system is evaluated based on lifetime expectations calculated based on Arrhenius type modeling with considerations for different aging mechanisms.

2. Experimental

2.1 Optical Fiber and Coating Systems

Single mode optical fibers with a nominal diameter of 242 microns were used in this study with two variants in refractive index profile. One refractive index profile included a trench resulting in a highly bend insensitive fiber.[7,8] The other refractive index profile was a standard, step-index refractive index profile.

Three coating systems were evaluated. Coating system A included a standard temperature acrylate primary and secondary coating system with a pre-colored secondary coating. Coating system B included a modified primary coating system designed to have improvements in primary coating durability as well as improved primary coating cure response. Coating system B included the same pre-colored secondary coating as coating system A. Coating system C was used as a performance benchmark. This coating system was used for selective testing of properties after long-term aging and consists of standard temperature acrylate coating system with uncolored primary and secondary coating layers with an added UV ink layer for fiber identification. A summary of fibers tested in this study is included in Table 1.

Two different cure variants were examined for Coatings A & B. One cure variant was a standard cure that resulted in essentially a full cure of the primary and secondary coatings. A second cure variant which resulted in an intentional undercure of the primary and secondary coatings was also investigated to examine the impact of overall properties and long-term aging performance.

Table 1. Fiber and Coating Systems Investigated in this Study.

Coating Designation	Refractive Index Profile	Cure Level	Color Identification
Coating A	Trenched	Full	Colored Secondary
Coating A	Step Index	Full	Colored Secondary
Coating A	Trenched	Reduced Cure	Colored Secondary
Coating A	Step Index	Reduced Cure	Colored Secondary
Coating B	Trenched	Full	Colored Secondary
Coating B	Step Index	Full	Colored Secondary
Coating B	Trenched	Reduced Cure	Colored Secondary
Coating B	Step Index	Reduced Cure	Colored Secondary
Coating C	Step Index	Full	UV Ink

2.2 Optical Fiber Aging

Loose coils of optical fiber were aged under various environmental conditions for various periods of time to evaluate the impact of aging on optical fibers. Aging conditions included water soak testing at 65°C, dry heat aging at 85°C, humidity aging at 85°C and 85% relative humidity, dry heat aging at 85°C, and long term-dry heat aging at 100°C. During the aging tests fiber attenuation was monitored at wavelengths of 1310nm, 1550nm, and 1625nm by OTDR. After long-term aging sections of aged fiber were set aside for other testing. Aging tests were done for durations of up to 120 days with data being collected on aged samples at various times.

2.3 Temperature Cycling and Low Temperature Attenuation Testing

Optical fiber temperature cycling and low temperature attenuation testing was performed on fibers before and after long term aging. The temperature cycling on unaged fibers was performed on fibers on collapsible spools under no tension. For long-term aging at 100°C the fiber spools were carefully loaded into aluminum pans before aging and measurements.

During unaged temperature cycle measurements fiber measurements are obtained by OTDR at 23°C and then the fibers are cycled to -60°C and to 85°C where measurements are taken at each temperature. A second cycle of -60°C to 85°C is repeated with additional measurements followed by a final measurement at 23°C. Measurements are taken at 1310nm, 1550nm, and 1625nm. For the fibers subjected to long-term aging the reference attenuation data point used to calculate low temperature attenuation differences is the unaged 23°C attenuation value.

2.4 Fiber Pullout Testing

Primary coating durability and primary coating adhesion to glass can be measured with a fiber pullout test described by Overton, *et. al*.[6] Fibers were affixed to a cardboard tab with cyanoacrylate coating and coating was separated from the fiber so that the glass could be pulled from the primary coating over a fixed length of 1.0cm. A rate of 5mm/s. was used for the pullout testing.

2.5 Optical Fiber Coating Strip Force

Optical fiber coating strip force measurements were performed according to IEC 60793-1-32[9] and using a Micro Strip MS-1 stripping tool mounted in a machined aluminum jig. The fiber was stripped using a controlled rate of 500 mm/minute.

2.6 In-Situ Modulus

In-situ modulus was determined using the pullout technique described by Steeman, *et. al.*[5]

2.7 Two-Point Bend Testing

Two-point bend testing was performed according to IEC 60793-1-33 in order to determine the optical fiber stress corrosion parameter, n_d. Fibers were cut down to 5-7 centimeters in length and loaded into the two-point bend test machine. A total of 15 fiber samples were tested at each condition and strain rate. Four strain rates were tested varying by an order of magnitude between different strain rates. An acoustic sensor tuned to the appropriate frequency was utilized to detect the break of each of the 15 fibers to record the associated data.

2.8 FTIR analysis

Fourier transform infrared (FTIR) spectroscopy was performed using a Nicolet Nexus 6700 FTIR with a one bounce diamond crystal HATR accessory. FTIR was used to monitor cure through changes in unreacted acrylate peak in the 1410cm^{-1} region relative to the peak in the uncured acrylate coatings. Other changes in the coatings during long term aging were also monitored by FTIR.

2.9 Optical Fiber Color Identification

Color identification was performed before and after aging of the fibers. Also, color coordinates and color change were quantified using colorimeter measurements. Color coordinates were measured with a Minolta CR-241 colorimeter and with visual standards. For visual color matching fluorescent lighting at 45° illumination and 90° viewing was used. For the colorimeter measurements the light source was a pulsed Xenon Arc lamp, CIE Illuminant C or D65 and measurements were performed against a white background. The effective viewing angle for the colorimeter was normal.

3. Results and Discussion

Two dominant mechanisms of degradation exist for optical fiber coatings. In hot and wet environments optical fibers can undergo hydrolysis. In hot and dry environments optical fibers can undergo thermal degradation. Both degradation mechanisms must be considered when evaluating the lifetime of optical fibers.

Another possible mechanism of coating failure for optical fiber coatings is the failure of the adhesive bond between the glass and primary coating. This mode of degradation may be especially important in wet environments or when the fiber is soaked in water.[10,11] In some cases a failure of the bond between the primary coating and the glass can result in increased optical fiber attenuation due to microbending forces. Primary coatings are typically engineered to have strong adhesion to glass, but the strength of the glass to primary coating bond may degrade with time. Changes of fiber strip force and fiber pullout force can indicate changes in the strength of the glass to primary coating bond.[4]

Thermal degradation of optical fiber coatings can be modeled with the well-known Arrhenius equation. The Arrhenius relationship links absolute temperature (T), activation energy (E_A) and the Specific Rate Constant (K).

$$K = A*EXP -[E_A/kT]. \quad (1)$$

where
K = Specific Rate Constant at a given temperature
A = A constant
E_A= Activation Energy
T = Absolute Temperature
k = Boltzmann's Constant
Or

$$\log K = \log A -[E_A/kT].]. \quad (2)$$

Several studies have been conducted to determine the Arrhenius activation energy for optical fiber coating degradation with measurement of changes in different properties as a function of time at varying temperatures.[1,2,3,12,13] A common methodology is to measure mass loss or volume change of coatings. The extraction of an Arrhenius activation energy from such data must be done with care as multiple mechanisms driving this mass loss are at play. The initial mass loss of water and other low molecular weight species does not correlate to the long-term degradation mechanism and should be avoided in calculations of Arrhenius activation energies. Additionally, error in determination of activation energy can result from too high an acceleration factor. An activation energy of about 130KJ/mol has been determined for multiple UV curable acrylate coatings using a mass loss criterion in the range of 5% - 25%[3,12,13]. This amount of mass loss corresponds to the range where substantial and measurable changes in coating physical properties can be observed.

Numerous studies exist on the hydrolysis of acrylate optical fiber coatings.[14,15,16] Hydrolytic degradation of the urethane linkages in optical fiber polymer coatings can be represented by the chemical equation and rate constant below where A is the concentration of urethane linkages and [H_2O] is the concentration of water molecules which is proportional to the partial pressure of water vapor. The rate constant, K, also follows the Arrhenius equation, but can be substantially different for that determined for thermal decomposition.[10,11,14]

$$\ldots COR^1CONH\ R^2\ldots + H2O \rightarrow \ldots COR^1COOH + NH2R^2\ldots \quad (3)$$

$$\text{rate} = K\,[A]\,[H2O] \sim 1/(\text{Time to Failure}) \quad (4)$$

The evolution of volumetric change of the coatings during aging at 100°C is summarized in Figure 1A. Both colored secondary coating systems performed very well in this study showing below 5% change at 60 days. The inked coating system showed an increased change as a function of time relative to the colored secondary fiber systems which seemed more pronounced in the first hours of thermal exposure. Coating B showed the lowest change as a function of time when fully cured but showed results almost identical to coating A when manufactured with a reduced cure. Determination of cure by FTIR of both primary and secondary coatings also indicated that an increased overall cure of the primary coating was obtained for coating system B at optimal cure conditions and equivalent secondary coating cure. Figure 1B shows added detail of volumetric change during the first 100h of aging at 100°C. During the first few hours, an initial loss of about 1% occurs very rapidly due to loss of water and other low molecular weight species. After this initial phase, the loss continues at a lower rate.

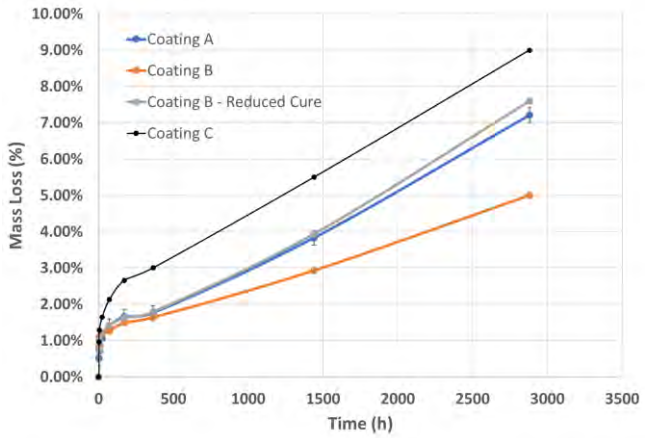


Figure 1A: Coating Volumetric Change vs. Time at 100°C for Various Coating Systems.

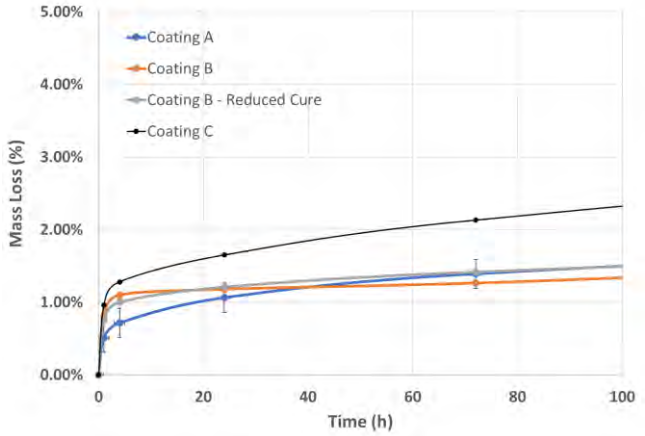


Figure 1B: Detail of Coating Volumetric Change at 100°C for the First 100h of Testing.

Attenuation during water soak testing at 65°C was conducted on all fiber variants with Coating A and Coating B. Results are summarized in Figure 2 for all fiber variants and measurement wavelengths. Attenuation results during the 120-day duration of the test showed no attenuation change outside of the measurement uncertainty at any wavelength.

Figures 3 and 4 show attenuation changes during dry heat aging at 85°C and humidity aging at 85°C and 85% R. H. In both cases the attenuation change observed during the testing was on the order of measurement resolution.

Table 2 shows a summary of low temperature attenuation measurements performed after heat aging at 100°C for 60 days. The attenuation change was minimal at both room temperature and down to -60°C. Where any measurable changes were evident, bend insensitive fibers tended to perform better. Both positive and negative attenuation changes in this test may have been slightly impacted as compared to other loose coil samples tested because these fibers were tested in trays while the fibers for other aging conditions were tested on collapsible spools which resulted in reduced lateral forces on the fibers.

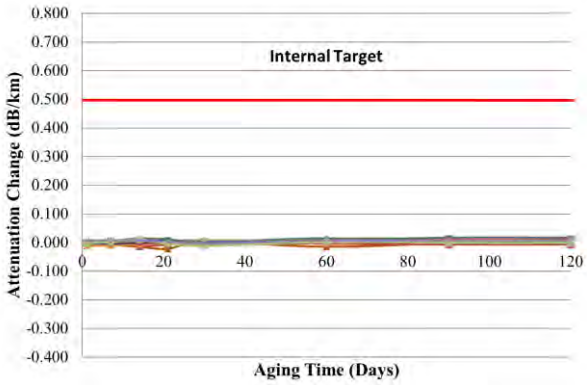


Figure 2: Attenuation Change During Water Soak Testing at 65°C.

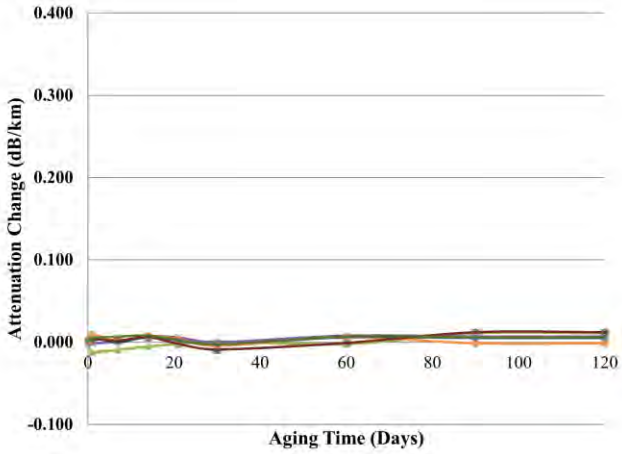


Figure 3: Attenuation Change During Dry Heat Aging at 85°C.

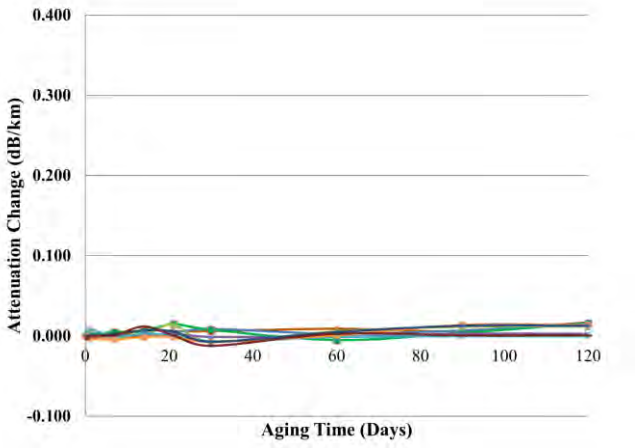


Figure 4: Attenuation Change During Humidity Heat Aging at 85°C/85% RH.

Table 2. Summary of Temperature Cycle Data after Long Term Heat Aging at 100°C for 60 days.

		RT Delta		
Coating Type	Fiber Core Design	Delta_1310	Delta_1550	Delta_1625
Coating A	Standard	0	0.01	0.019
Coating A	Bend Insensitive	0.002	-0.002	0.015
Coating B	Standard	0.005	0.003	0.008
Coating B	Bend Insensitive	-0.001	0.005	0.007
Coating C	Standard	-0.003	-0.001	-0.009
		Delta -50°C		
Coating Type	Fiber Core Design	Delta_1310	Delta_1550	Delta_1625
Coating A	Standard	0.01	0.033	0.055
Coating A	Bend Insensitive	0.025	0.012	0.028
Coating B	Standard	-0.008	0.01	0.033
Coating B	Bend Insensitive	-0.011	-0.003	-0.004
Coating C	Standard	0.001	0.01	-0.001
		Delta -60°C		
Coating Type	Fiber Core Design	Delta_1310	Delta_1550	Delta_1625
Coating A	Standard	0.044	0.022	0.068
Coating A	Bend Insensitive	0.026	0.015	0.026
Coating B	Standard	-0.001	0.012	-0.002
Coating B	Bend Insensitive	-0.005	-0.005	-0.008
Coating C	Standard	-0.001	0.007	0.007

Table 3 shows a summary of pullout force testing which is a measure of fiber durability and adhesion of the primary coating to glass. Dry heat aging seemed to show a higher impact on fiber pullout force than humidity aging, and a more substantial change was observed with the 100°C testing for 60 days. Coating B showed a higher initial fiber pullout force and less change after environmental exposure.

Table 3. Impact of Humidity and Heat Aging on Fiber Coating Pullout Performance.

	Pullout Force (N)			
Coating System	unaged	85°C	85°C/85%RH	100°C
Coating A	4.6	6.8	5.2	9.3
Coating A Delta (%)		47%	12%	102%
Coating B	6.4	9.5	5.4	7.4
Coating B Delta (%)		49%	-15%	16%
Coating C	4.25			8.64
Coating C Delta (%)				103%

Table 4 shows the impact of environmental exposure on strip force testing. For the coatings measured results were conformant to all industry standards after all aging conditions. No substantial change was observed in the strip force testing or the quality of stripping with respect to aging condition.

Table 4. Impact of Humidity and Heat Aging on Fiber Strip Force.

	Fiber strip force (N)			
Coating System	unaged	85°C	85°C/85%RH	100°C
Coating A	1.6	1.8	1.7	1.7
Coating B	1.9	1.95	1.75	1.7

Table 5. Impact of Humidity and Heat Aging on Fiber Coating Stress Corrosion Parameter.

	2-point bend (n_d-Value)			
Coating System	unaged	85°C	85°C/85%RH	100°C
Coating A	24.7	24.7	27.2	29.0
Coating B	24.2	24.3	26.0	25.8
Coating C	24.0			26.5

Table 5 shows the impact of environmental exposure on stress corrosion parameter (n_d). For all fibers and aging conditions, a stress corrosion parameter surpassing IEC 60793-2-50 and GR-20 requirements was measured with little impact of environmental exposure.

FTIR analysis of the outer coating layers showed minor evidence of oxidation for coating C at 60 days of aging at 100°C and minor evidence of the onset of oxidation of the colored secondary coating used in coating systems A&B after 120 days of aging at 100°C. Figure 5 shows the fingerprint region of outer coating C and Figure 6 shows the fingerprint region of the colored secondary coating used for coating systems A & B. The changes were minor but detectable after long aging times at high temperatures. The colored secondary coating showed a slightly higher shoulder in the 1780 cm^{-1} region of the carbonyl peak for the sample that was deliberately undercured while the fully cured samples showed almost no change. Evidence of some residual acrylate in the undercured sample were also still evident through a residual peak in the 1410 cm^{-1} region.

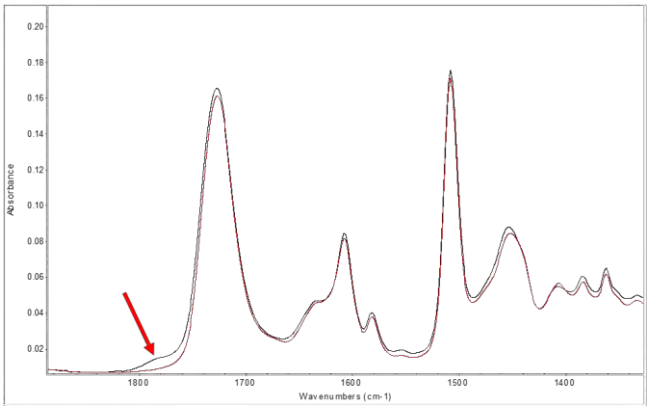


Figure 5: FTIR Data Showing Evidence of Oxidation in Coating C After 60 Days of Aging at 100°C.

The numerous absorption bands in the 1700-1800 cm-1 region can be associated with C=O stretching associated with a number of carbonyl containing oxidation byproducts including aldehydes, esters, ketones, and carboxylic acid groups[17,18]. The exact peak height and location depends on the population levels of specific groups as well as other factors such as conjugation within the degraded coating.

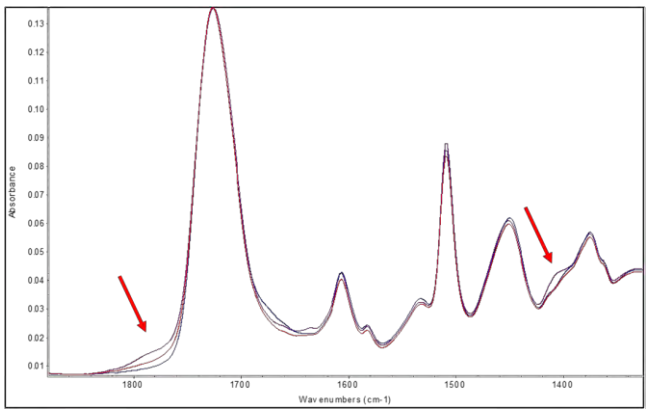


Figure 6: FTIR Data Showing Evidence of Oxidation in Colored Secondary Coating (B&C) After 120 Days of Aging at 100°C

FTIR analysis was also performed on the three primary coatings. No evidence of oxidation was observable by FTIR analysis for any of the coating systems. All three coating systems also showed no evidence of any other substantial changes in the FITR spectrum after long term aging at 100°C. The lack of evidence of oxidation can be explained by the crosslinked secondary coating acting as an effective oxygen diffusion barrier. The secondary coating is designed to inhibit diffusion of species such as water vapor and oxygen, to this data indicates all coating systems are performing as designed. The FTIR results suggest that the changes observed in primary coating properties during long term aging are dominated by mechanisms other than thermo-oxidative degradation. The FTIR fingerprint regions of the primary coatings before and after long term aging are shown in figures 7-9.

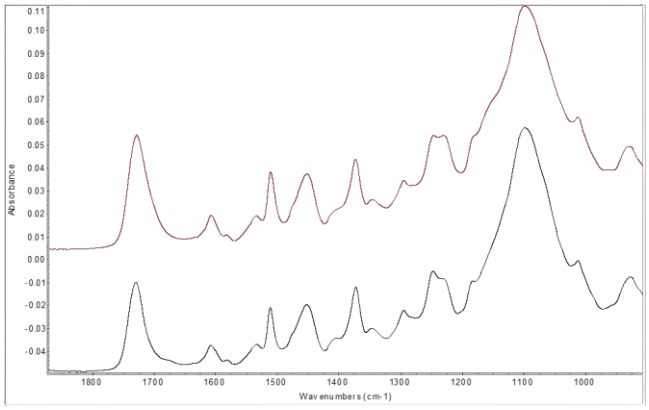


Figure 7: FTIR Fingerprint of Primary Coating A: Top- Fully Cured after 120 Days at 100°C. Bottom- Unaged Baseline for Fully Cured Sample.

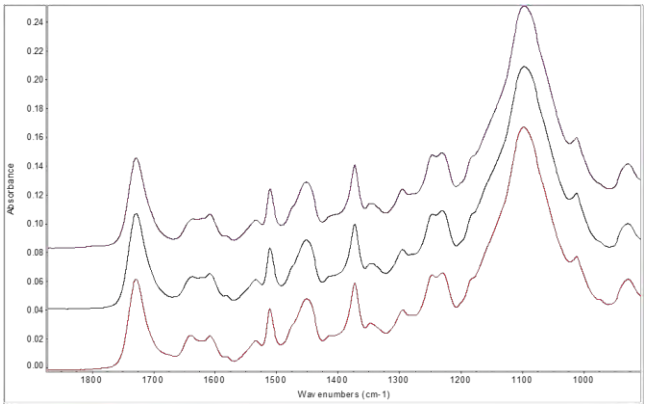


Figure 8: FTIR Fingerprint of Primary Coating B: Top- Reduced Cure After 120 Days at 100°C. Middle- Fully Cured after 120 Days at 100°C. Bottom- Unaged Baseline for Fully Cured Sample.

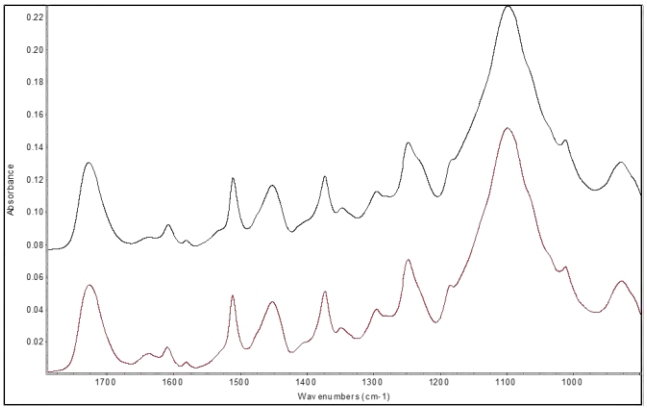


Figure 9: FTIR Fingerprint of Primary Coating C: Top- After 60 Days at 100°C. Bottom- Unaged Baseline.

Fibers could be identified by color after all aging conditions. Tables 6A & B show the impact of aging on color conformance of fibers after aging for 45 days at 85°C and 85%RH. Color conformance was verified against TIA 589D color limits. Although the colors could still be identified after aging, a slight but measurable color shift to yellow was observed on most colors which tended to be more pronounced on lighter colors.

Table 6A. Color Coordinate Mapping of Fibers for Determination of Color Conformance of Unaged Fibers.

Color	Initial (un-aged) - L*a*b*			Initial (un-aged) - Munsell		
	L*	a*	b*	H	V	C
Red	46.56	+62.82	+37.06	5.7R	4.6	15.1
Blue	42.27	-1.56	-46.63	2.8PB	4.1	11.3
Green	55.60	-53.14	+11.66	7.1G	5.5	9.8
Yellow	85.38	-18.56	+68.70	1.9GY	8.4	9.6
Violet	36.18	+44.98	-45.20	3.5P	3.5	14.1
White	89.85	-0.32	1.22	7.5Y	8.9	0.1
Orange	64.44	33.21	55.69	3.1YR	6.3	11.3
Gray	51.69	0.36	6.51	2.5Y	5.1	0.9
Brown	42.21	15.39	19.97	2.9RY	4.1	4.4
Black	27.08	1.81	-1.77	4.7P	2.6	0.5
Aqua	68.72	-30.52	-13.08	9.9BG	6.8	7
Pink	66.39	38.76	11.49	1.0R	6.5	9.4

Table 6B. Color Coordinate Mapping of Fibers for Determination of Color Conformance of Unaged Fibers.

Color	Aged – L*a*b*			Aged – Munsell		
	L*	a*	b*	H	V	C
Red	51.58	+53.49	+47.26	8.7R	5.1	13.9
Blue	40.22	-10.98	-36.85	9.6B	3.9	9.6
Green	57.09	-50.54	+7.88	8.5G	5.6	9.4
Yellow	82.01	-13.32	+69.00	8.5Y	8.1	9.6
Violet	36.15	+34.18	-31.21	4.8P	3.5	10.2
White	86.9	-3.31	20.08	6.0Y	8.6	2.8
Orange	68.69	36.99	58.4	2.2YR	6.8	12.3
Gray	54.94	0.55	0.64	2.2YR	5.4	0.1
Brown	43.58	13.63	15.62	2.0YR	4.3	3.7
Black	27.97	0.67	3.15	0.4Y	2.7	0.4
Aqua	64.25	-33.68	1.1	2.3BG	6.3	6.4
Pink	64.83	34.04	18.47	4.8R	6.4	8.2

4. Conclusions

Multiple coating systems were investigated for reliability after exposure to lifetime simulation aging including dry heat, humidity, and direct water exposure. Under all the environmental conditions examined fiber attenuation increases were negligible. On selected

fibers attenuation increases at -60°C were also verified to be minimal even after an aging lifetime simulation that would exceed 50 years at a continuous fiber use temperature of 50°C.

Numerous other coating properties were also monitored including coating strip force, coating durability, and coating mass loss. Although all the coating properties measured still met functional requirements after all the lifetime simulation aging conditions, coating system B showed the most stable performance with regard to mechanical properties as well as mass loss. By varying coating cure in a controlled manner, it was shown that enhanced initial primary coating cure of coating system B was the primary reason this coating system showed the most stable properties after exposure to environmental stresses.

5. References

[1] B. Overton and L. White, "Aging Studies of High Temperature Coatings," *Proceedings of the 59th IWCS/Focus*, *2010*, 250-255.

[2] A.A. Stolov, D.A. Simoff, and J. Li, "Thermal Stability of Specialty Optical Fibers", *Journal of Lightwave Technology, **26**, 2008, 3443-3551.*

[3] E. Murphy and J. Kelly, "Thermal Characterization of Heat Resistant UV Cure Compositions by Estimated Arrhenius Parameters" *Proceedings of the 59th IWCS/Focus*, 2006, 484-489.

[4] Gan, *et. al*., "Optical Fiber Strip Force Measurement Techniques and Their Implications" *Proceedings of the 57th IWCS/Focus*, 2008, 246-251.

[5] Steeman, *et. al*., "Mechanical Analysis of the In-Situ Primary Coating Modulus Test for Optical Fibers", *Proceedings of the 52nd IWCS/Focus*, 2003, 246-251.

[6] B.J. Overton, *et. al*., "Time Temperature Dependence of Dual Coated Lightguide Pullout Measurements, *Pol. Eng. Sci, **29**, 1989, 1169-71*.

[7] L.A. de Montmorillon, et. al., "Bend-Optimized G.652D Compatible Trench-Assisted Single Mode Fibers", *Proceedings of the 55th International Wire and Cable Symposium*, 2006, 342-347.

[8] L.A. de Montmorillon, et. al., "Different Implementations of G.657B Bend-Insensitive Single-Mode Fibers with Ultra-Low Bend Losses, Still Compatible to G.652D", *Proceedings of the 57th International Wire and Cable Symposium*, 2008, 283-288.

[9] K. Gan, L. Han, K. M. Roberts, B. J. Overton, N. Montaigne, "Optical Fiber Strip Force Measurement Techniques and Their Implications", *Proceedings of the 57th IWCS*, 2008, 214-221.

[10] D. Cuomo & L.Terruzzi, "Coating Ageing and Impact on Fibre Performances", *Proceedings of the 58th IWCS*, 2009, 68-71.

[11] D. Cuomo & L.Terruzzi, "New studies on accelerated ageing of fibre coatings", *Proceedings of the 60th IWCS*, 2011, 30-34.

[12] A. A. Stolov, D. A. Simoff, and J. Li, "Thermal Stability of Specialty Optical Fibers", *Journal of Lightwave Technology*, **26**, 20, 2008, 3443-3451.

[13] A. A. Stolov, D. A. Simoff, and J. Li, "Thermal stability of optical fiber coatings: comparison of experimental thermogravimetric approaches", *Journal of Thermal Analysis and Calorimetry*, 2020.

[14] K. Sohma, N. Iwaguchi, T. Kawano, T. Fujii, and Y. Koyano, "Estimation of Long-Term Change in Physical Property of Optical Fiber Coating Considering Effect of Humidity", *SEI Technical Review*, 81, 2015, 16-21.

[15] H. Okuyama, K. Sohma and T. Fujii, "Design of Coating Properties of Optical Fibers to Maintain Strip Force and Strippability Considering the Aging Effects", *Proceedings of the 67th International Wire and Cable Symposium*, 2018.

[16] C.-K. Chien, "Improved method for characterization of long term fiber coating stability", *Proceedings of the 65th International Wire and Cable Symposium*, 2016, 118-123.

[17] J. V. Gulmine, P. R. Janissek, H. M. Heise and L. Akcelrud, "Degradation profile of polyethylene after artificial accelerated weathering", *Polymer Degradation and Stability*, 2003, **79**, 385-397.

[18] F. Khabbaz, A.-C. Albertsson and S. Karlsson, "Chemical and morphological changes of environmentally degradable polyethylene films exposed to thermo-oxidation", *Polymer Degradation and Stability,* 1999, **63**, pp. 127-138.



Brian G. Risch

Prysmian Group

Fiber Optic Cable R &D

2512 Penny Rd.

P.O. Box 39

Claremont, NC 28610

Brian G. Risch is the Materials Technology Manager for Prysmian Telecom North America. He holds a B.A. degree in physics from Carleton College and a Ph.D. in Materials Science and Engineering from Virginia Polytechnic Institute and State University. Brian has more than 30 years of experience in the study of structure property relationships in polymeric materials and materials reliability. Brian has over 20 years of experience in the fiber optic cable business. Prior to working for Prysmian, Brian worked for Alcatel and Draka specializing in cable materials and fundamental material reliability. Brian also has 6 years of experience at Hewlett Packard doing failure analysis engineering.

Prediction of Physical Properties of Optical Fiber Coating Resins Based on Chemical Kinetics

Yudai Watanabe, Tatsuya Konishi and Kazuyuki Sohma
Optical Communications Laboratory, Sumitomo Electric Industries, Ltd.
Yokohama, Kanagawa, Japan
+8170-7811-1297 · watanabe-yudai@sei.co.jp

Abstract
We have developed a method for predicting physical properties of the optical fiber coatings such as the Young's modulus of primary coating and gel fraction, under arbitrary curing conditions. This method is based on a newly developed chemical kinetics model of photoinitiator.

Keywords: UV Curing; optical fiber; Chemical Kinetics;

1. Introduction
Optical fiber plays an important role in global communication networks. Long-term reliability is required for optical fibers, and production control of optical fiber coating physical properties, such as the Young's modulus of primary coating (E_p) and gel fraction (R_{gel}) is crucial. Ultraviolet (UV) curable resins are normally used for coating, and their properties are largely influenced by curing conditions during the optical fiber drawing process including line speed, UV irradiation power and length. The prediction of resin properties has been sought in order to estimate the production window for curing conditions much easier and faster, without time-consuming optical fiber fabrications. The complicated curing mechanism of resins makes the prediction very difficult, and fewer studies are found in optical fiber related areas. This study reports on a newly developed photoinitiator (PI) concentration formula based on chemical kinetics. Rate constants used in these formulas are determined experimentally, the concentration can be estimated at arbitrary curing conditions. Furthermore, the prediction of physical properties is realized using calibration curbs between PI concentration and the coating properties.

2. Chemical Kinetics Model
2.1 Chemical Reaction of PI
The elementary reactions of PI are described as follows, in this study.

Initiation reaction : $PI + h\nu \rightarrow 2R\cdot$ [$\mathbf{k}$]

Dark reaction : $PI + h\nu' \rightarrow 2R\cdot$ [$\mathbf{k_D}$]

Recombination reaction : $2R\cdot \rightarrow PI$ [$\mathbf{k_R}$]

Here, square brackets show the reaction rate constants for each reaction. R· and hν represent active radical and UV photon, respectively. hν′ is a "virtual" UV photon, which is newly introduced in this study to explain dark reaction. The reaction rate equation for each reaction is solved, and the prediction equation of the photoinitiator concentration after the curing reaction is derived. The details are explained in section 2.2 to 2.4.

2.2 Initiation Reaction
The first step of the radical reactions of UV curable resin is "initiation reaction" [1]. A PI molecule absorbs a UV photon, and generates two radical molecules. Its chemical reaction equation can be written as Eq. (1), and the kinetic equation as Eq. (2).

$$PI + h\nu \rightarrow 2R\cdot \ [\ \mathbf{k}\ ] \quad (1)$$

$$dC_I(t)/dt = -kC_I(t)B \quad (2)$$

Here, C_I, B and t represent PI concentration after initiation reaction, UV dose (the total amount of UV light radiation), and UV irradiation time per UV light source, respectively. B can be expressed as a product of the rated power of a UV light source (M), and the set power of the UV light source (φ). M is included in rate constant **k**, because M can be assumed as a constant by using only one kind of UV light source in this study. When "N" number of the same UV light sources are set during the resin curing process, the solution of Eq. (2) can be written as follows.

$$C_I = C_0 \exp(-t\varphi N \times \mathbf{k}) \quad (3)$$

The reaction rate is thought to be changed with the progress of the curing reaction. The averaged rate constant of "**k**" for all of the curing process is adopted.

2.3 Dark Reaction
The reaction speed of curing can be improved when non-irradiated areas are added in curing process of UV curable resins [2]. This phenomenon is known as "dark reaction". The radical molecules generated from PI by UV light irradiation are gradually consumed even during a subsequent non-irradiated area, and curing of UV curable resin proceeds. For the modeling of this phenomenon, virtual UV light sources were assumed in the non-irradiated section, as shown in **Fig. 1**.

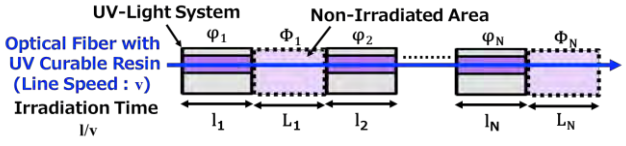


Fig. 1. Model image of Dark Reaction

The chemical reaction can be described as Eq. (4) and this is very similar to Eq. (1).

$$PI + h\nu' \rightarrow 2R\cdot \quad [\ \mathbf{k_D}\ ] \quad (4)$$

In order to solve the kinetic equation, we assumed that the virtual UV light power is proportional to pre-UV light power. The solution can be written as Eq. (5).

$$E_D = \exp(-T\varphi N \times \mathbf{k_D}) \quad (5)$$

Here, T represents the non-irradiated time.

2.4 Recombination Reaction

Some of the radical molecules generated by UV irradiation are deactivated through recombination reaction [3]. The high rate of this reaction sometimes results in an uncured state of the resin. The phenomenon tends to occur especially for resins having a low Young's modulus, such as primary coating resin for optical fiber of less than 1.0MPa, which is much lower than that of a secondary coating about 1000 MPa. The higher concentration of radical molecules generated at conditions of higher irradiation power means a higher possibility of collisions between radical molecules. The collided radicals are deactivated and generates a stable molecule, which is known as "recombination"). The chemical reaction equation and kinetic rate equation for the recombination reaction can be described as Eqs. (6) and (7).

$$2R\cdot \rightarrow PI \quad [\,\mathbf{k_R}\,] \quad (6)$$

$$dR(t)/dt = -\mathbf{k_R}(R(t))^2 \quad (7)$$

The solution of Eq. (7) is described as follows.

$$R = R_0/(1+2\mathbf{k_R}R_0t_R) \quad (8)$$

Here, R, R_0 and t_R represent radical concentration after the recombination reaction, radical concentration before recombination reaction and recombination reaction time respectively. In order to rewrite the equation in practical form, three assumptions were considered.

(i) Recombined PI concentration is half as much as radical consumption.

$$C_R = (R_0 - R)/2$$

Here, C_R represents the concentration of recombined PI.

(ii) R_0 is twice the concentration of consumed PI when the optical fiber passed the first UV light and non-irradiated area.

$$R_0 = 2(C_0 - C_0 \exp(-(t\mathbf{k}+T\mathbf{k_D})\varphi)$$

Here, v represents line speed.

(iii) Recombination reaction time is equal to irradiation time.

$$t_R = Nt$$

Eq. (8) can be written as Eq. (9) under these assumptions.

$$C_R = C_0(1-\exp(-(t\mathbf{k}+T\mathbf{k_D})\varphi))$$
$$\times(1-1/(1+4\mathbf{k_R}NtC_0(1-\exp(-(t\mathbf{k}+T\mathbf{k_D})\varphi)))) \quad (9)$$

2.5 Expression of net PI concentration and rate constants determination

Net PI concentration can be written as

$$C_{Net} = C_I \times E_D + C_R \quad (10).$$

"C_R", which is the concentration of PI molecules generated by the recombination reaction, has the effect of increasing PI concentration, as opposed to "$C_I \times E_D$".

The reaction rate constants of $\mathbf{k}$, $\mathbf{k_D}$ and $\mathbf{k_R}$ are determined by fitting to minimize the squared difference between measured and calculated values of PI reaction rate ($\boldsymbol{R_{PI}}$). $\boldsymbol{R_{PI}}$ is defined as the ratio of remaining versus initial PI concentrations, which is explained in section 3.2.

3. Experiment

3.1 Optical fiber fabrication

Dual coated optical fiber samples were fabricated at a drawing tower, as shown in **Fig.2**. An optical fiber preform was heated in a furnace, and drawn into glass fiber having a diameter of 125 μm. After cooling the glass fiber, two layers of UV curable resins were coated, and cured by UV-LED lamps. The primary resin coated fiber had a diameter of 195 um, and the secondary resin coated fiber had a diameter of 250 μm. After that, the fiber was wound onto a bobbin. Optical fiber samples were fabricated under various irradiation conditions, such as the number of UV-LED, the length of non-irradiated areas, power and dose of UV light, irradiation time and line speed.

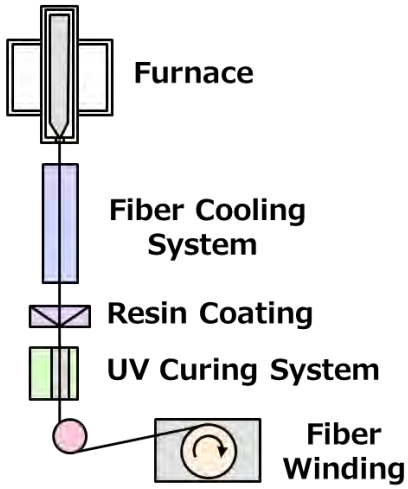


Fig. 2. Optical Fiber Drawing Tower

3.2 PI Reaction Rate (R_{PI}) measurement

ICP atomic emission spectrometry was used to measure the $\boldsymbol{R_{PI}}$ of the optical fiber samples. $\boldsymbol{R_{PI}}$ can be used as a substitute indicator for $C_{Net.}$ The relationship can be described as below.

$$100 \times (1-C_{Net}/C_0) = \boldsymbol{R_{PI}} \quad (11)$$

The measured values of $\boldsymbol{R_{PI}}$ were obtained by comparing the maximum signal values of specific elements in the resins. And here, C_0 is an arbitrary value.

3.3 E_P and R_{Gel} measurements

$\boldsymbol{E_P}$, $\boldsymbol{R_{Gel}}$ were measured in the fabricated optical fiber samples. The measurement method for $\boldsymbol{E_P}$ was referred from a paper [4]. $\boldsymbol{R_{Gel}}$ values were obtained by measuring the difference in the weights of the cured coating resin between before and after immersion in organic solvents.

4. Experimental results

4.1 UV dose dependence R_{PI}, R_{Gel} and E_P

The experimental results for UV dose dependence on $\boldsymbol{R_{PI}}$ are shown in **Fig. 3**. The graph is classified with the setting for the percentage of UV-LED power.

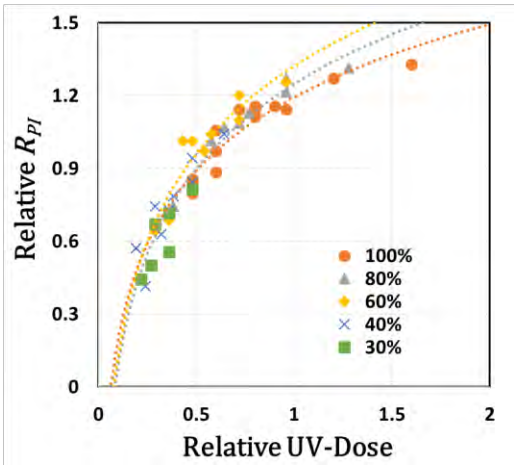


Fig. 3. UV dose dependence on R_{PI}

RPI is strongly dependent on UV-Dose, and R_{PI} increases monotonously when the UV dose increased. It can also be found that higher UV intensity tends to have lower R_{PI}, or higher PI concentration remains in the coating.

The experimental results for UV dose dependence on E_P and R_{Gel} are shown in **Figs. 4** and **5,** respectively.

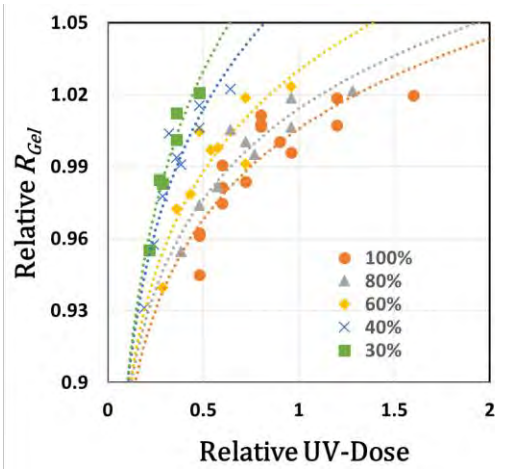


Fig. 4. UV dose Dependence on R_{Gel}, classified with UV-LED power setting percentage

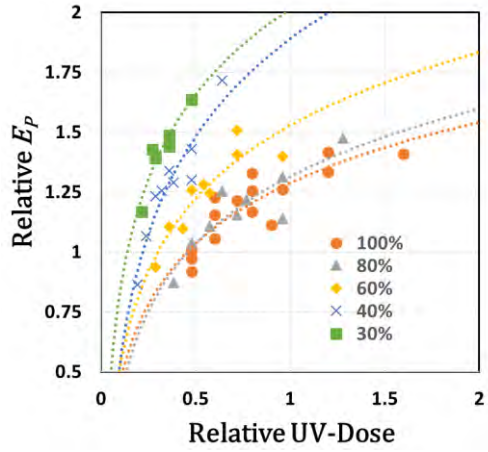


Fig. 5. Dependence for UV irradiation conditions of E_P

Higher UV doses shows higher E_P and R_{Gel}. It is found that lower UV intensities shows higher E_P and R_{Gel} at the same UV-Dose. These trends are more remarkable than that of R_{PI}.

4.2 Calibration Curbs for Calculated Value of R_{PI}

The correlation between R_{PI} and R_{Gel} is shown in **Fig. 6,** and that between R_{PI} and E_P is shown in **Fig. 7**.

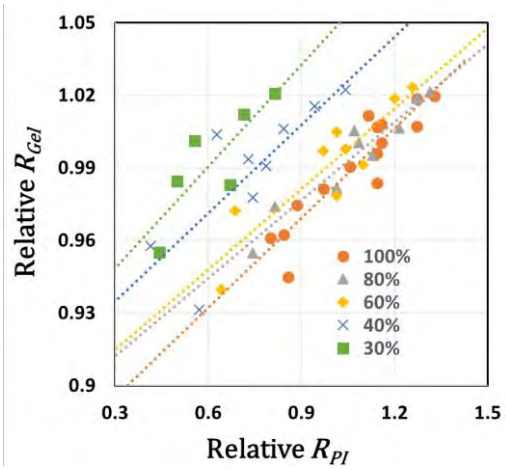


Fig. 6. Relationship between R_{PI} and R_{Gel}

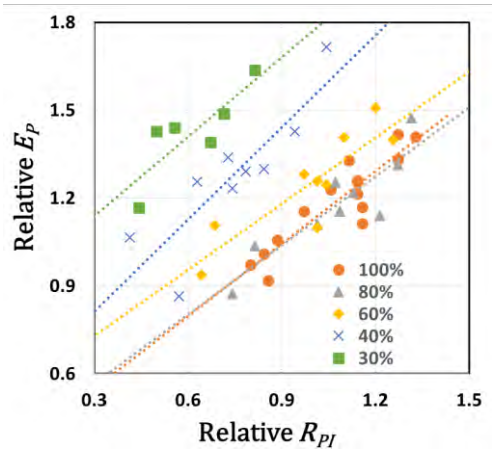


Fig. 7. Relationship between R_{PI} and E_P

These data are classified with UV intensity, and higher intensities tends to have lower R_{PI} and E_P. The results indicate that physical properties can be predicted when RPI is calculated under arbitrary conditions.

5. Discussion

5.1 Derivation of Reaction Rate Constants

The reaction rate constants of **k**, $\mathbf{k_D}$ and $\mathbf{k_R}$ are determined by the fitting to minimize the squared difference between measured and calculated values of RPI, and summarized in **Table1.** The relationship between calculated and measured RPI are shown in **Fig. 8**.

Table.1. The converged values of reaction rate constants

	Initiation	Dark	Recombination
Reaction Rate Constant	k	k_D	k_R
	66	0	0

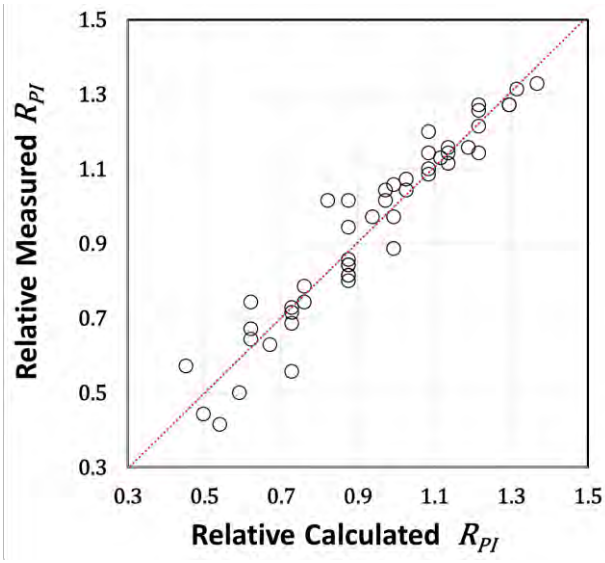


Fig. 8. Correlation between measured and calculated R_{PI}

In this figure, the regression line has a slope of about 1.0, and the coefficient of determination (R^2) has a very high value of about 0.9. Interestingly, the fitting results show that k_D and k_R converged to 0. According to the results of Fig.3, smaller R_{PI} can be observed at higher UV intensity and larger R_{PI} at lower UV intensity. This is expected to be $k_R > 0$, at least. The contradiction can be explained by the fitting method, and further studies have to be conducted.

5.2 Prediction of E_P and R_{Gel}

The predicted R_{Gel} and E_P are derived by using the obtained reaction rate constants of **k**, k_D and k_R, based on our formulas and calibration curbs. The results are shown in **Figs. 9** and **10** respectively.

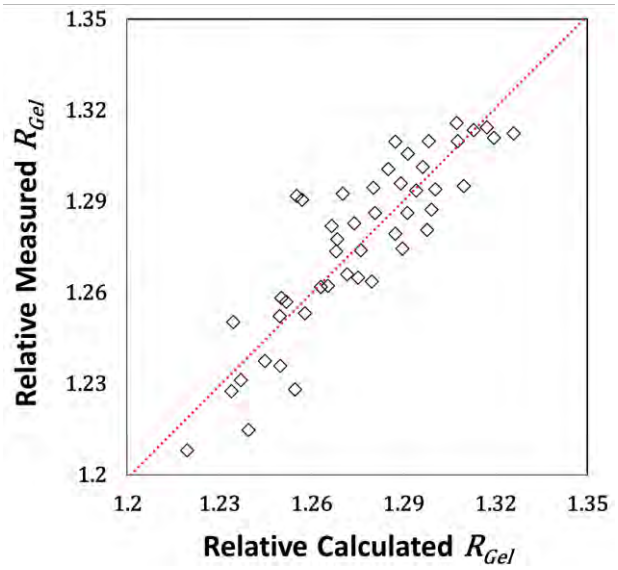


Fig. 9. Correlation between calculated and measured R_{Gel}

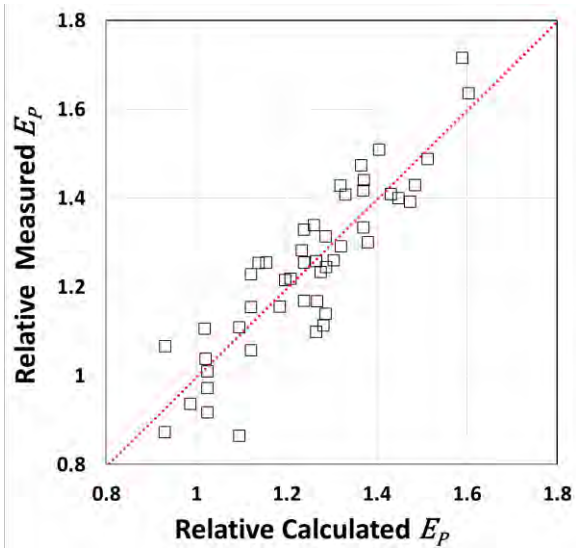


Fig. 10. Correlation between calculated and measured E_P

They show very high correlations and the regression lines' coefficient of determinations are 0.8 for both of the properties.

6. Conclusion

Our novel UV curing reaction model based on chemical kinetics is succeeded in the precise prediction of the physical properties of an optical fibers coating. This model and method enable more rapid determination of the most suitable UV irradiation conditions for optical fiber production.

7. References

[1] H. Cao et al., "Kinetic Study on Cure Speed of Optical Fiber Coatings by Draw Tower Simulator", *Proc. of the 69th IWCS*, Session 16-8, 2020.

[2] J. Pavlinec, et al., "Dark Reactions of Free Radicals Trapped in Densely Crosslinked Polymer Networks After Photopolymerization", *JAPS*, Vol. 89, 579-583, 2003.

[3] Igor V. Khudryakov et al., "Cage Effect Dynamics under Photolysis of Photoinitiators", Designed Monomers and Polymers, 487-496 , 2010.

[4] K. Sohma et al., "Estimation of Long-Term Change in Physical Property of Optical Fiber Coating Considering Effect of Humidity", *the 64th IWCS*, pp. 45-49, 2015.

8. Authors

Yudai Watanabe is an engineer of the Optical Communications Laboratory at Sumitomo Electric Industries, Ltd. He received his Master's degree in chemistry from Tohoku University in 2021. He has been involved in developing optical fibers, since joining the company in 2021

Tatsuya Konishi is a researcher of the Analysis Technology Research Center at Sumitomo Electric Industries, Ltd. He received his doctorate degree in science. He has been involved in the analysis of optical fiber, since 2016.

Kazuyuki Sohma is a manager of the Optical Communications Laboratory at Sumitomo Electric Industries, Ltd. He received his M.

S. in 2001, and M. B. A in 2010. He has been involved in optical fiber development since joining the company in 2001.

Investigation on application of biomass raw materials to optical fiber coating agents

Natsuki Hamada, Hirofumi Uchida, Noriyasu Shinohara
Japan Fine Coatings Co., Ltd, Kanagawa Research & Development Center (KRDC)
Kawasaki, Kanagawa, Japan
+81-44-328-5210 · natsuki.hamada@covestro.com

Abstract
We conducted a feasibility study to clarify whether biomass raw materials can be used for optical fiber coatings. In this study, we blended a composition using biomass as part of the raw material and investigated its characteristics. The characteristics are viscosity and Young's modulus, which are the minimum required performance for an optical fiber coatings. Regarding Young's modulus, we set targets for two types of fiber optic coating applications with different hardness: flexible primary applications and high-hardness secondary applications.

As a result of the investigation, the secondary composition using a specific biomass raw material achieved the target viscosity and Young's modulus. For this composition, we calculated the Biobased content indicating the usage ratio of biomass raw materials, compared the mechanical properties and curing rate with existing petrochemicals, and investigated whether there was any difference in performance due to biomass.

Keywords: UV curable coatings; Optical fiber coatings; Biomass

1. Introduction
Most standard tele-communication fibers have a 125 µm cladding diameter and polymer coating that increases the outside diameter to 250 µm. Structure of optical fiber is shown in Figure 1. For this standard size fiber, 75% of the fiber's three-dimensional volume is the polymer coating. The core and cladding glass account for the remaining 25% of the coated fiber's total volume. The polymer coating layer has a two-layer structure, a softer inner coating called the primary and a harder outer coating called the secondary. In order to achieve high fiber productivity, UV curable coatings are used these layers. Because glass is fragile, the coating must protect it. The bending stresses of the fiber lead to intensity losses for the light transmitted through the fiber. Function of mechanical protection to glass is important. Optical fibers are laid everywhere in the world, including deserts, ocean, underground, country and urban areas. Therefore, performance that is not affected by various environments is required. Coatings play a key role in helping the fiber meet environmental and mechanical specifications as well as some optical performance requirements.

On the other hand, in recent years, with the goal of reducing the carbon footprint, efforts related to biomass have been made in various fields. Our goal is to promote the use of biomass and renewable raw materials across our industry, making chemical production fit for the future. We believe bio-based products are one important step in permanently reducing our emissions and making the chemical industry a more sustainable place. Therefore, it can be said that verifying whether biomass raw materials can be used for our UV curable optical fiber coating is an important theme from the perspective of the SDGs. In this paper, the applicability of biomass raw materials to our UV curable optical fiber coating is studied.

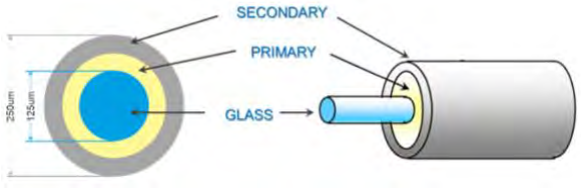


Figure 1. Structure of optical fiber

2. Experiment
2.1 Materials
All samples of primary and secondary coatings consisting of urethane acrylates were prepared in our laboratories. Primary and secondary coatings were designed to perform the high inner cure degree and the high surface cure degree, respectively. Both coatings were optimized for metal-halide lamp.

2.2 Measurement of Viscosity
The viscosity at 25°C. was measured using a BH8 rotator.

2.3 Preparation of Test Specimens
Liquid UV curable coatings were applied on a glass plate with a certain thickness using an applicator bar.

These liquid coatings were cured by UV lamps at a dose of 1 J/cm2 in the air. The cured coatings were allowed to stand for 12 hours or more at a temperature of 23°C.and a relative humidity of 50%, and subjected to the following tests.

2.4 Measurement of Young's Modulus
Young's modulus at 23°C was measured by using a tensile machine at tensile speed of 1mm/min. Young's modulus was defined by the secant modulus at 2.5 % elongation. This property was also measured at -40°C and 60°C.

2.5 Measurement of Cure Speed
For the cure speed test, cured films with a thickness of about 250 µm were prepared by irradiating coatings with UV light at a dose of 0.1J/cm^2 or 1J/cm^2. The cure speed was determined as a ratio of the Young's modulus of the film cured at 1J/cm^2 to the Young's modulus of the film cured at 0.1J/cm^2

2.6 Calculation of Biobased content
The Biobased content[1] of the prototype coating agent was calculated by equation (1).

$$BC_{all} = \Sigma W_i \times BC_i \quad (1)$$

BC_{all} : Biobased content of coating

W_i : Weight fraction of raw material i

BC_i : Biobased content of raw material i

3. Result and Discussion

3.1 Investigation of oligomers using biomass raw materials

Oligomers for fiber coating should be designed with the optimal molecular structure depending on the application and required properties. Therefore, it is important to verify that oligomers can be synthesized using biomass raw materials in the same way as conventional petrochemical raw materials. First, the synthesis of oligomers using biomass raw materials was investigated.

The results of oligomer synthesis are shown in Table.1. Oligomer A and B were designed for primary, a soft material, and for secondary, a hard material respectively.

Table.1 Oligomers using biomass raw materials

	Usage	Handling of Oligomer
Oligomer A	Primary	N.G. *1
Oligomer B	Secondary	Good*2

*1 : Difficult handling

*2 : Easy handling

In the results of this study, it was predicted that the viscosity of oligomer A is very high in its synthesis, and that it is difficult to design the coatings. On the other hand, it was determined that the oligomer B for the secondary has a viscosity suitable for the coating design, and that subsequent resin liquefaction is possible. From the above, the secondary oligomer proceeded with the following test.

3.2 Viscosity and Young's modulus adjustment

Next, the formulation of coatings using oligomers and monomers from biomass raw materials was investigated. In this study, the formulation was adjusted so that the basic properties viscosity and Young's modulus were the target characteristic values among the properties required for fiber coatings.

The reason why viscosity was chosen as the target value is to be able to apply to evaluate the physical properties of the cured films. The target value of viscosity is based on the experience of developing optical fiber coatings conducted so far.

Further, the reason for selecting Young's modulus is to determine whether the composition can be adjusted to the modulus required for the coatings. A standard telecommunications optical fiber has a two-layer structure, a softer inner coating called the primary and a harder outer coating called the secondary. When a pressure is locally applied to an optical fiber side surface, the core of the glass fiber at the portion to which the pressure is applied bends with a small curvature, and as a result, light loss may occur. The primary coating layer is desirably sufficiently flexible from such viewpoints that suppress light loss. On the other hand, the secondary coating layer preferably has a modulus sufficiently high to protect the primary layer. Young's modulus targets for primary and secondary coatings are set based on our know-how to date. In this study, oligomers for secondary coating using biomass raw materials were synthesized as reported in Chapter 3-1, so we tried to adjust the Young's modulus suitable for secondary coating.

Sample A of the bio-based secondary coating composition was prepared using synthesized biomass oligomers and various biomass raw materials. The viscosity and Young's modulus are shown in Table 2. The upper and lower limits of the target values of this study are normalized based on the value of conventional secondary coatings consisting of petrochemical raw materials..

Table.2 Viscosity and Young's Modulus of Sample A

	Target	Sample A
Viscosity	0.7 - 1.3	0.9
Young's Modulus	0.9 – 1.1	0.9

As a result of the examination, sample A having viscosity of 0.9 and Young's modulus of 0.9 which is satisfying the target values was obtained.

3.3 Comparison of Biomass Secondary coating with Conventional Petrochemical coating

In Chapter 3-2, sample A was adjusted for viscosity and Young's modulus for secondary. However, to determine whether sample A is suitable for secondary coating, it is necessary to understand the properties in more detail compared to conventional coatings from petrochemical raw materials. Therefore, characterization was added to understand the performance of sample A. There are three items to be evaluated: mechanical properties, UV curing speed, and Biobased content calculations. Details of mechanical properties were Young's modulus at room temperature, -40 °C, and 60°C. to understand behavior in various temperature environments, tensile strength and elongation at break to understand material strength.

Sample B composed of petrochemicals was used as a comparison target for sample A in this study. It is a composition characterized in that it is close to the 23 °C. Young's modulus of sample A.

The results are shown in Table 3. The characteristic value s of sample A are expressed as relative values with the characteristic value of sample B as 1.0.

Table.3 Properties of Biobased Secondary Coating Sample A

Properties	Condition	Sample A	Sample B
Biobased content (%)		40	0
Young's Modulus	-40°C	1.1	1.0
	23°C	0.8	1.0
	60°C	0.5	1.0
Tensile Strength	23°C	0.8	1.0
Tensile Elongation	60°C	0.8	1.0
Cure Speed	Young's Modulus ratio @ 0.1J/1J	1.0	1.0

Mechanical properties will be described. Compared to Sample B derived from petrochemical raw materials, it was found that Sample A shows Young's modulus at 60°C. was as low as 0.5. From this result, it was indicated that the biomass coating sample A in this study may have lower mechanical properties at high temperatures than sample B of petrochemical products. On the other hand, with respect to the curing rate, the composition had the same level of curing speed as the petrochemical to be compared.

It is necessary to confirm whether the decrease in Young's modulus at high temperatures is a problem. In addition, this study has not sufficiently examined whether mechanical properties including Young's modulus of 60°C. can be adjusted by coating design. Study of coatings using biomass raw materials will continue in the future.

4. Conclusion

In this study, the possibility of utilizing biomass raw materials for optical fiber coating was conducted. This coatings was formulated with some biomass materials and designed for secondary use.

The biomass coating was designed to nearly equal to the target viscosity and Young's modulus for conventional petrochemical secondary coating. The biobased content of the biomass secondary coating was 40%.

Biomass Secondary Coating was examined for property comparison with petrochemical coating which has similar characteristic of young's modulus to 23°C. As a result, characteristic difference was observed at 60°C Young's modulus. But other mechanical properties and curing rates were approximately the same level.

In this study, it has not sufficiently examined whether mechanical properties including Young's modulus of 60°C can be adjusted by coating design. And also it is necessary to confirm whether the decrease in Young's modulus at high temperatures is a problem. Study of coatings using biomass raw materials will continue in the future. Furthermore, it is an urgent subject to search for biomass raw materials for primary coatings. In the presentation, we will also report on the status of consideration of primary coatings.

5. Reference

[1] ISO 16620-1, 4

6. Pictures of Authors



Natsuki Hamada

Kanagawa Research & Development Center (KRDC)

Japan Fine Coatings Co.,Ltd.

Kanagawa Science Park(KSP) Unit C-1225

3-2-1 , Sakado, Takatsu-ku, Kawasaki 213-0012 Japan

Natsuki Hamada received his M.E. degree in organometalic chemistry from Tohoku University of Science and joined Japan Fine Coatings Corp. in 2021. He has been engaged in research and development of polymeric materials including radiation curable materials for optical fiber coating.



Noriyasu Shinohara

Kanagawa Research & Development Center (KRDC)

Japan Fine Coatings Co.,Ltd.

Kanagawa Science Park(KSP) Unit C-1225

3-2-1 , Sakado, Takatsu-ku, Kawasaki 213-0012 Japan

Noriyasu Shinohara received his Ph.D. in organic chemistry from Tokyo Institute of Technology and joined JSR Corp. in 1996. In 2021, he moved to Japan Fine Coatings Corp. He has been engaged in research and development of polymeric materials including radiation curable materials for optical fiber coating.



Hirofumi Uchida

Kanagawa Research & Development Center (KRDC)

Japan Fine Coatings Co.,Ltd.

Kanagawa Science Park(KSP) Unit C-1225

3-2-1 , Sakado, Takatsu-ku, Kawasaki 213-0012 Japan

Hirofumi Uchida received his B.E. degree in material science from Hokkaido University and joined Japan Fine Coatings Corp. in 2021. He has been engaged in research and development of polymeric materials including radiation curable materials for optical fiber coating.

UV-curable High Temperature Resistant Dual Layer Coating System for Specialty Optical Fiber Applications

Huimin Cao, Keegan Orendorff, Todd Anderson, Eric Urruti
Covestro LLC, Elgin, IL, 60120, USA
+1-224-4020950 · huimin.cao@covestro.com

Abstract
Fiber optics technology has been applied into more and more varieties of specialty applications, where the optical fibers/cables are routinely used under harsh environments of high temperatures. The development of a reliable high temperature resistant coating system that can also meet the requirement of fast draw speed of fiber drawing process is highly desirable. In this work, a UV-curable dual layer acrylate coating system has been developed closely matching high temperature thermal stability of a commonly used UV-curable high temperature resistant single coat demonstrated with excellent field performance in the past 10 years. The high temperature thermal stability of the dual layer coating system was evaluated using weight loss by Thermogravimetric Analysis (TGA), as well as mechanical property characterization by Dynamic Mechanical Analysis (DMA) of film samples, in comparison with a standard telecom grade dual layer coating system and the high temperature resistant single coat. The film study from the newly developed dual layer coating system has shown optimized balance between high temperature thermal stability similar to the single coat and improved mechanical properties over single coat as a soft/hard dual layer coating system.

Keywords: optical fiber coating; high temperature resistance; Arrhenius study; lifetime prediction; specialty fiber applications.

1. Introduction
The demand of optical fibers in specialty applications such as automotive, aerospace, optical power composite cable, sensors, oil & gas rigs, high power lasers…has been growing in recent years. These applications require long term durability at mid-high temperature range, or mid-term durability at high temperature range. Conventional high temperature resistant polymers such as silicones or polyimides as thermal curable materials involve complex processing such as solvent removal requiring slow draw speed of optical fiber, which becomes a limiting factor for actual application. Extensive efforts have been reported developing acrylate-based UV-curable high temperature resistant coatings supporting the high drawing speed of optical fiber manufacturing process [1-5].

A high temperature resistant single coat product DF-0009 was introduced to the industry in 2009, based on the work reported by Murphy *et al* [1,2]. From the mechanism of polymer degradation, the weakest link to thermal oxidation and thermal pyrolysis in the commonly used UV curable urethane acrylate compositions for optical fiber coating was identified to be urethane linkage of carbamate moiety, as well as the poly(propylene glycol) moiety in the typical urethane acrylate structure [1]. DF-0009 successfully adopted a non-urethane acrylate composition with significantly improved high temperature resistance. This coating with modulus designed in the medium level ~700MPa as a single coat material has been proven supporting optical fiber applications in long term use at high temperature range 100-150ºC, or short term use at extreme temperature range 150-200ºC. Compared with overall optical and mechanical performance of a standard optical fiber dual layer coating system, intrinsic gap remains with DF-0009 as a single coat system. Single coat is much more difficult to strip, due to the critical bucking force of a 60μm thick single coat is much higher than a 30μm secondary coating in a dual layer coated fiber (soft primary coating modulus contribution negligible, only adhesion to glass having influence to strip force). Another important property is microbending performance: single coat is much worse microbending protection than standard dual layer coating system which provides the combined cushioning and shielding effects against external stress perturbation from the soft inner primary coating + hard outer secondary coating design.

High temperature resistant dual layer UV-curable acrylate coatings have been reported in the past [3-5]. While the high temperature thermal stability has shown greatly improved over conventional coatings with continuous use temperature predicted for 20yrs lifetime improved from ~80°C to ~110°C [4], the gap to DF-0009 single coat reported at 130°C [5] is still significant.

In this paper, a newly developed high temperature resistant dual layer UV-curable coating system is introduced, consisting of primary coating HT-P and secondary coating HT-S. The film study showed close match of high temperature thermal stability of HT-P/HT-S dual layer coating system to DF-0009 single coat, while providing improved mechanical properties as soft/hard dual layer coating system.

2. Experimental
2.1 Coating Film Sample Preparation
Each coating sample was drawn down by Bird bar applicator at a nominal 25μm (1mil) film thickness on glass plate for TGA tests, or 75μm (3mil) film thickness for DMA or tensile tests. Dual layer coating samples for TGA were prepared by first draw down and cure a 1mil layer of primary coating and then use 2mil drawdown bar applying 1mil thickness of secondary coating layer on top of primary coating and cure again. The TGA samples were cut into 0.5cm squares and a single piece was placed into the platinum sample pan for each TGA test.

The sample curing was conducted on Fusion Light Hammer10 conveyor system of Heraeus Noblelight with 10 inch 600 W/in D lamp, purged with 15 ft^3/min N_2. The standard curing dose measured by radiometer ILT800 was 1J/cm^2. The film samples were then conditioned in a temperature/humidity controlled room at 23°C/50%RH.

2.2 Thermal Aging
The aging of 3mil cured coating samples was conducted in Blue M mechanical oven with horizontal air flow which assures uniform thermal condition. The samples after aging were reconditioned in the temperature/humidity controlled room at 23°C/50%RH for >16hrs before conducting weight measurements or DMA testing.

2.3 Thermogravimetric Analysis (TGA)
Thermogravimetric analysis of film samples was conducted using TA Instruments Hi-Res TGA 2950 Thermogravimetric Analyzer.

2.3.1 Dynamic TGA. Dynamic TGA of temperature sweep was set with standard condition of 10°C/min heat rate and 50L/min dry air flow, except for special conditions of different flow rates of air or in N_2 as specified.

2.3.2 Isothermal TGA. For isothermal TGA test, the program sequence was set to first equilibrium at 25°C for 1 min; then ramp up temperature with rapid heating rate of 200°C/min to the target temperature, in order to minimize the weight loss during this ramping period; finally isotherm at the target temperature for a specified time period. This entire process was under the condition of 50L/min dry air flow.

2.4 Dynamic Mechanical Analysis (DMA)

Dynamic mechanical analysis was conducted using RSA-G2 Solids Analyzer from TA Instruments.

2.4.1 DMA Temperature Sweep of Film Samples. Before conducting the temperature sweep, moisture was removed from the test sample by subjecting the test samples to a temperature of 80ºC in a N_2 atmosphere for 5 minutes. The sample was then cooled under liquid N_2 condition to -60ºC and the temperature sweep from -60ºC to 160°C was conducted. The oscillation frequency was set at 1.0 radian/s. The results of storage modulus E′, loss modulus E″ and Tanδ (=E″/ E′) were plotted. The temperature of tanδ peak position was reported as Tanδ T_g, as the glass transition temperature from polymer glassy state to rubbery state. The minimum value at the rubber plateau E′ was reported as equilibrium modulus E_0.

2.4.2 Primary In-Situ Modulus of Glass Fibers. A detailed description of the test method and data processing methodology for primary in-situ modulus on glass fiber was introduced in previous paper [6], using DMA machine shear sandwich mode to measure shear modulus G_p of primary coating under 1 radian/s frequency, and converting to tensile modulus E_p as the primary in-situ modulus.

2.4.3 Secondary In-Situ Modulus of Glass Fiber. The coating tube samples for secondary in-situ modulus were prepared by stripping ~2-5cm length of the dual layer coating tube out of the glass fiber when the coating became stiff after dipping in liquid N_2. DMA machine was used to measure the storage tensile modulus E′ of the coating tube sample. With secondary coating >1000 times higher modulus than primary coating, the contribution from primary coating modulus in tensile mode testing of the coating tube is negligible. The measured tensile storage modulus E′, with geometry entered as a rod with cross section area equivalent to the secondary coating hollow cylinder, is reported as the secondary in-situ modulus.

3. Results and Discussion

3.1 Thermal Degradation of Polymers

Harsh environmental factors such as solar radiation, temperature, and humidity could act interactively in the polymer degradation process. In the high temperature specialty fiber applications, thermal degradation of polymer coatings at high temperature in air environment is the main culprit. Direct thermal decomposition (or thermolysis) of breaking chemical bonds by heat only occurs at the decomposition temperatures, which are typically very high (>300°C), when the thermal energy exceeds the bond association energy of various chemical bonds of the substance. The dominant degradation mechanism for polymers in air environment at a temperature lower than decomposition temperature is thermal oxidation.

Figure 1 illustrates a general free radical thermo-oxidative degradation mechanism for polymers [7]. The role of O_2 in this degradation process is critical: 1) free radical propagation through forming peroxide radical $RO_2\bullet$ 2) auto-acceleration by chain-branching through hydroperoxide decomposes to form more radicals, leading to an increase in the oxidation rate. As the end results of these free radical chain reactions, two major effects are directly responsible for the polymer chemical structure breakdown resulting in physical property degradation such as material weakening and material embrittlement (the loss of tensile strength, elongation, toughness), cracking, chalking, color changing, etc. The two major effects are 1) chain scission: breaking long polymer chains into short chain fragments causing weakening of the material. The polymeric oxy radical $RO\cdot$ is very reactive and readily lead to β-chain scission reaction. 2) crosslinking: the termination by recombination of two radicals results in an increase of crosslinking density. Because the polymer structure already broke down into short chain fragments, the crosslinking of these short chain fragments leads to brittle structure, prone to fracture failure such as cracking and chalking.

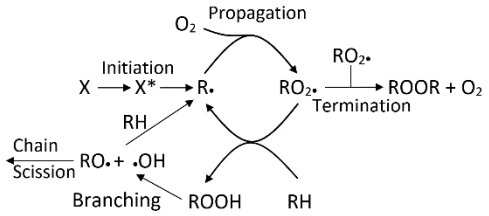


Figure 1. General thermo-oxidative degradation mechanism for polymers

3.2 Failure Mode Analysis on a Standard Coating Coated Fiber after High Temperature Aging

In order to demonstrate different failure modes of conventional telecom grade optical fiber after high temperature degradation, a fiber with a commonly used standard dual layer coating system Std-P/Std-S was placed in 180ºC or 200°C oven and the property changes being monitored for 5 days.

The first change observed was the primary coating turned much softer into a gel-like material after just 1 day of 180°C aging. Figure 2a is the fiber after 1 day 180°C aging, with light pressure manually pressing on the fiber, already created many big cavity/delamination sites in the primary coating. The fiber can also easily tube off by hands, leaving sticky gel-like coating residue on glass. This failure mode represents a chain scission dominated stage in soft primary coating, breaking down crosslinking structure depolymerizing into a gel-like material. Figure 2b is the fiber sample winded in small coil of ~8cm diameter during aging. When sample taken out after 5 days of 180°C, the glass was seen shifted position significantly inside of the primary coating that all primary coatings flowed to inner side of the fiber coil. This again is an indication that primary coating lost elasticity due to chain scission and the glass easily creeped inside of the disintegrated primary coating under the low level winding stress.

Interestingly, this fiber after 5 days of 180°C aging, despite the color turning much darker than earlier days, the coating was no longer easily tubing off, but became very difficult to strip off the glass, indicating at this point the primary coating is no longer a gel-like material. This as explained in the last section, is when the degradation process progressed from early chain scission dominated stage to finally crosslinking dominated termination stage. The direct proof can be found in Figure 3. In-situ modulus of the primary coating (measured at room temperature) with 180ºC aging quickly decreased from the initial value of 0.5MPa to 0.3MPa after just 3hrs, then

dropped to 0.01MPa after 1 day, consistent with modulus level from a very weakly crosslinked gel, then slightly increased to 0.02MPa after 2 days, followed by significant increase to 0.3MPa after 3 days and 3.4MPa after 5 days. This trend of primary coating first softened and disintegrated into a gel then hardened to a much higher modulus brittle material is expected to also apply to lower temperature aging conditions, just taking longer time to go through these different stages. The first stage of chain scission is most risky with regard to fiber performance issues, due to easy formation of delamination and cavitation in primary coating after losing integrity, plus more severe weight loss of primary coating than secondary coating creating high tri-axial tensile stress in primary coating adding more risk for defect formation.

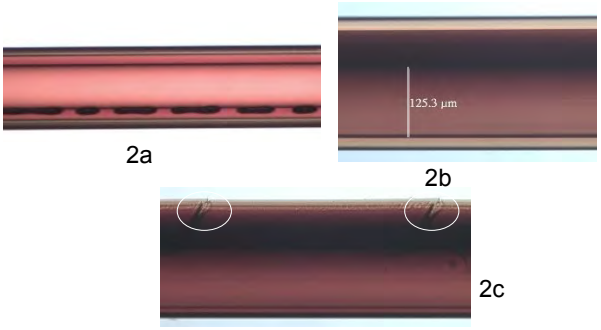


Figure 2. Failure modes of a standard dual layer coating coated fiber after high temperature aging: (2a) 1 day 180°C aged fiber after manual handling. (2b) fiber sample in ~8cm diameter coil after 5 days 180ºC. (2c) 5 days 200°C aged fiber after manual handling

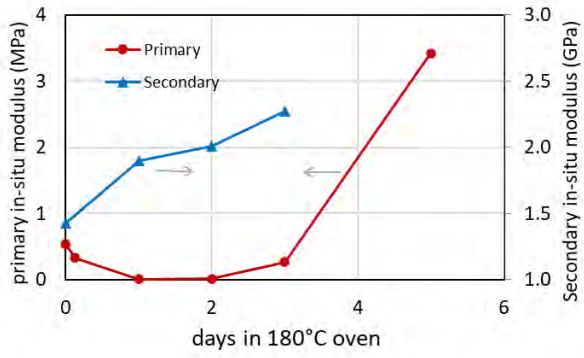


Figure 3. Change of primary and secondary in-situ modulus vs. time of 180°C oven aging for a standard dual layer coating coated fiber

Secondary coating as a harder material with much higher crosslink density than primary coating, although undergoes the same failure mechanism including both chain scission and crosslinking, no clear softening stage was observed as in primary coating, crosslinking dominated and caused embrittlement of the secondary coating. Figure 2c shows cracking started from the secondary layer with 5 days of 200°C aged fiber after manual bending. From Figure 3, the measured secondary in-situ modulus was confirmed to continuously increase with aging time. Modulus increase from initial 1.3GPa to 2.3GPa after 3 days 180°C is still within acceptable range, however, the elongation at break is expected significantly reduced after high temperature aging, causing severe brittleness easy to crack. No secondary in-situ data for the 5 days 180ºC fiber was obtained, because the coating was so brittle that it could not hold integrity when being stripped under liquid N_2.

3.3 Design of UV-Curable High Temperature Resistant Dual Layer Coating System

Based on the failure mode analysis of the standard coating coated fiber which is representative of general failure modes in all conventional urethane acrylate coating coated fibers, the design target of the new dual layer high temperature resistant UV-curable coating system was set to be 1) primary coating: prevent severe chain scission to avoid disintegration into a gel-like material under high temperature applications. 2) secondary coating: prevent severe crosslinking to avoid detrimental embrittlement under high temperature applications. Among these two objectives, primary coating is much more challenging due to low crosslink soft coating intrinsically much more vulnerable to lose network integrity than high crosslink coating after thermal degradation.

The chemistry of both coatings is designed to be non-urethane acrylate based UV-curable material, as proven by the superior thermal stability of DF-0009, successfully used as a high temperature single coat product for specialty applications at 100-200°C mid to high temperature ranges with different durations.

As a dual layer soft/hard coating system design, as shown in Table 1 (tensile modulus from tensile tester, Tanδ T_g from DMA), the primary coating HT-P is designed at medium low modulus level of 5MPa for optimizing both thermal stability at high temperature and mechanical properties. Even though the modulus level is above the standard telecom grade primary coating such as Std-P at 1.2MPa, the improvement on microbending performance over single coat DF-0009 should still be significant; furthermore, the strip force of this dual layer coating is expected to be much lower than single coat due to secondary coating layer thickness as a controlling factor for strip force is only half of single coat coated fiber. The secondary coating HT-S is designed with a high modulus matching standard coating Std-S, for achieving much improved microbending performance than single coat, while T_g is designed to be much lower than Std-S, similar to DF-0009 level in order to reduce brittleness after high temperature aging.

Table 1. Main mechanical property comparison of the newly developed coatings vs. controls

	Tensile Modulus (MPa)	Tanδ T_g (°C)
DF-0009	700	48
HT-P	5	6
HT-S	1200	54
Std-P	1.2	-26
Std-S	1200	90

3.4 Dynamic TGA Results

TGA weight loss is a common characterization method for monitoring the progression of polymer degradation under high temperature conditions. The degree of polymer degradation directly associates with the formation and release of small molecule volatile gases as the depolymerization products from the degradation process. TGA is an accelerated method to monitor this process through precisely measuring weight loss under precisely controlled preset conditions. For Dynamic TGA temperature sweep test, the conditions of heat rate and air flow rate were set arbitrarily, which is for the purpose of relative comparison of different materials under the same condition. Dynamic TGA conducted at different heat rates through Arrhenius equation with failure criteria set, such as 25% weight loss, was commonly applied as a methodology for lifetime prediction [3-5]. Another variable that can influence the TGA weight loss rate is the gas flow rate. Figure 4 shows an example from DF-0009. While it is easily understandable the onset temperature under 50L/min of air is much lower than under 50L/min of N_2, another proof thermal

oxidation dominates the degradation when O_2 is present, it is also clear that the flow rate of air strongly influences the onset temperature. Slower the air flow rate, more closer the curve shifted to the curve in N_2. The likely cause is high-temperature oxidation of these thin small specimens is so rapid, i.e. the O_2 consumption is so rapid, that the local O_2 surrounding the sample could be depleted if the air flow rate is too slow, not able to maintain equilibrium concentration in the coating during the reaction. It is unclear what level of air flow rate setting can better represent the field environment of optical fiber cable in the specialty applications.

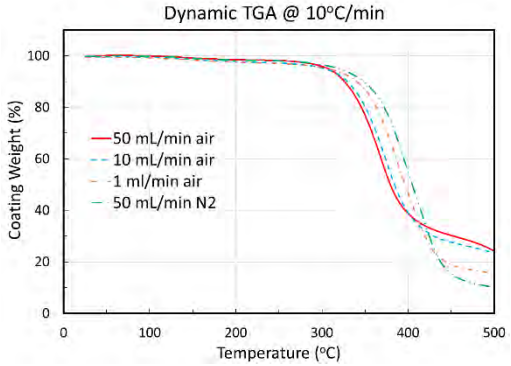


Figure 4. Dynamic TGA of DF-0009 in N_2 or air with different flow rates

Regardless of the uncertainty related to predicting absolute lifetime based on TGA results influenced by the condition setting, the relative trend between different materials in terms of thermal stability and long term durability using TGA comparison is expected to be valid. Figure 5 compares the temperature ramp TGA curves of the 5 coatings, with onset temperature listed in Table 2. It is clear that HT-S matches the thermal stability of DF-0009 with slight increase on onset temperature, or known as oxidation induction temperature (OIT). Primary coating HT-P showed the %weight loss occurred at lower temperature range more than Std-S, but only for the initial 10% weight loss. The onset temperature to sharp drop region is much higher than Std-S and actually similar to DF-0009. This is not trivial considering HT-P is designed with modulus 240 times lower than a regular secondary coating such as Std-S as well as having a much lower T_g.

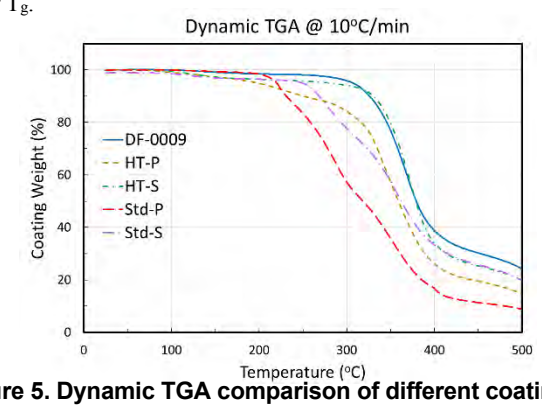


Figure 5. Dynamic TGA comparison of different coatings

3.5 Isothermal TGA Results and Lifetime Prediction

Both dynamic TGA at different heat rates and isothermal TGA at different temperatures can be used for Arrhenius lifetime prediction. In this work, isothermal TGA was used at high temperature range up to 300ºC for prediction of coating lifetime into lower temperature range ≤200°C.

As an example, Figure 6 compares the residual coating %weight vs. time for the 5 coatings at 260°C. The trend of thermal stability from isothermal TGA is in good agreement with dynamic TGA, HT-S slightly better stability than DF-0009; HT-P confirmed to be longer lasting than Std-S due to the much slower rate of weight loss despite the initial lower weight possibly from fast losing of some volatile components in HT-P. The long term thermal stability of HT-P at application temperature is expected to be better than Std-S, and of course significantly better than Std-P.

Isothermal TGA curves at a set temperature can also provide some information on the complex material thermal degradation reaction kinetics. A general mathematical expression of the rate equation is often described as in in Equation 1,

$$\frac{dc}{dt} = k\Pi_i c_i^{\,m_i} \qquad (1)$$

where k is the reaction rate constant, c_i is the molar concentration of reactant i and m_i is the partial order of reaction for this reactant. The exact reaction kinetics can be very complex and understandably very different for coatings designed with different chemistries and different network structures. From Figure 6, DF-0009 and HT-S both are close to a linear decreasing function with time, which indicates a pseudo zero order kinetics. This linear weight drop was tested valid till ~60% residue weight then curved to a much slower rate. This pseudo zero order kinetics of DF-0009 and HT-S indicates the oxidation reaction in these coatings are sufficiently slow that the molar concentrations of the reactive groups are not significantly changing with time until later stage. In contrast, the other three coatings showed faster non-linear weight loss, especially Std-P dramatically faster due to the severe chain scission dominated reactions. These curves, although do not fit perfectly into 1st order kinetics of exponential decay or 2nd order kinetics of reciprocal decay curves, it is for certain strongly dependent on the fast depletion of the reactive moieties.

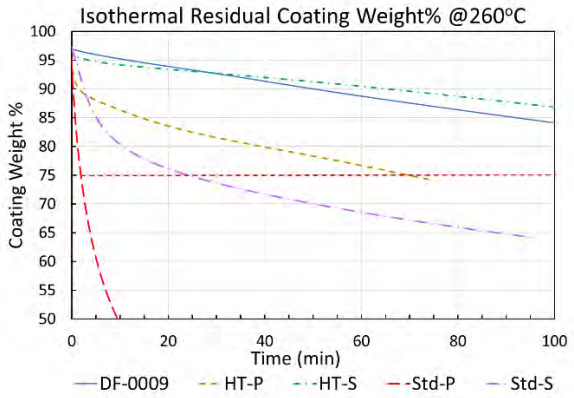


Figure 6. Isothermal TGA comparison of high T and standard coatings at 260°C

Arrhenius equation as in Equation 2 is the commonly used methodology for lifetime prediction of a material at a specified application temperature, or the upper use temperature for a specified lifetime, through conducting accelerated experiments at higher temperature range. Any method using a short term test plotting a property change vs. time under certain accelerated aging condition in attempt to fit degradation reaction constant k, and use the calculated k for the Arrhenius prediction is risky, due to the complex kinetics of different materials not possible to reliably capture k in a short term test. The proper approach as demonstrated in the previous work [1-5] is through measuring time duration reaching a set failure criteria,

lifetime τ. The failure criteria as arbitrarily set [3-5] for TGA weight loss is 25%, where the volume shrinkage and material property change at this level of weight loss are considered significant enough to cause performance failure. Since τ is directly proportional to 1/k, the Arrhenius equation can be rewritten to Equation 3, where the activation energy E_a can be derived from multiplying the slope of the Lnτ vs 1/T Arrhenius linear plot with gas constant R. The intercept combines the Ln(frequency factor A) and other kinetic parameters.

$$k = Ae^{-E_a/RT} \quad (2)$$

$$Ln\tau = intercept + E_a/RT \quad (3)$$

The Arrhenius plots at 25% weight loss of the 5 coatings as shown in Figure 7 clearly illustrates the much superior high temperature stability of HT-P and HT-S, compared to the corresponding conventional coating Std-P and Std-S, with HT-P actually reaching longer lifetime than Std-S which is very impressive as a much softer coating. HT-S is slightly more durable than DF-0009 due to the higher crosslink density design. It should be noted that for Std-P and Std-S, the Arrhenius curves were found not linear at the temperature range of 230°C to 300°C, not valid for lifetime prediction into lower temperatures. Further tests at lower temperature down to 160ºC for Std-P and 180°C for Std-S were able to obtain better linear relationship and used for lifetime prediction. This is an indication for urethane acrylate based conventional chemistry, multiple reactions of different moieties such as urethane linkage, PPG linkage, acrylate linkage, likely have different rate constant k, and their contributions in the overall degradation reaction varying at different temperature ranges. Closer the testing temperature range to the application temperature range, more reliable the lifetime prediction will be.

Figure 8 is the plot of predicted lifetime comparison of the 5 coatings based on the 1mil film isothermal TGA test. The activation energy E_a, intercepts, and the predicted upper temperatures for 20yrs or for 1yr continuous use for the coatings are summarized in Table 2. It should be noted that these absolute values of the lifetime or upper temperature should not be directly taken as for coated fibers. Even based on the same TGA conditions, the film samples are known to have faster weight loss than coating layer on fiber likely because the coating on fiber only having outer surface exposed to air, while the film sample having all surfaces exposed to air (bottom surface not sealed to the pan). A reference data point is DF-0009, with single coating coated fiber TGA Arrhenius test, the upper temperature for 20yrs continuous use was reported to be 130°C [5], while the prediction based this film study is 118°C. All the lifetime or upper temperature prediction based on the film study are expected to be lower than actual coated fibers. The relevant trend from film sample study should still reliably represent the trend from coated fibers. The activation energy of conventional urethane acrylate based primary coating such as Std-P found to be significantly lower than other coatings once again demonstrates conventional primary coating is the weakest link most vulnerable to severe degradation. HT-P activation energy raised to simar level to secondary coatings or single coat is a strong evidence HT-P is a radically improved primary coating with regard to high temperature stability than Std-P, with upper temperature for 20yrs raised ~40°C higher.

In order to more closely simulate the coating behavior on fiber, dual layer coating samples of 1mil+1mil were tested in comparison with 2mil sample of DF-0009. Figure 9 gives an example of the dual layer coating weight loss behavior vs. single layer. The dual layer curve of residue weight% is higher than the average of 1mil individual layer of HT-P and HT-S. The simple reason is dual layer only having secondary top surface and primary bottom surface exposed to air,

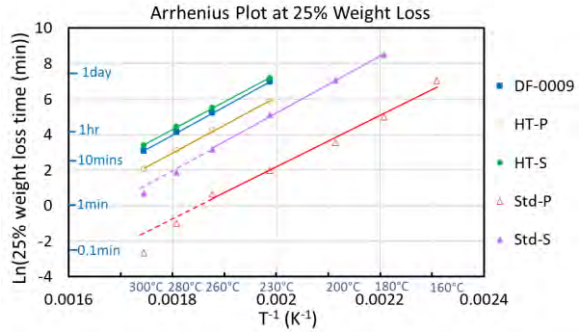


Figure 7. Arrhenius plots of high T and standard coatings from 1mil film samples

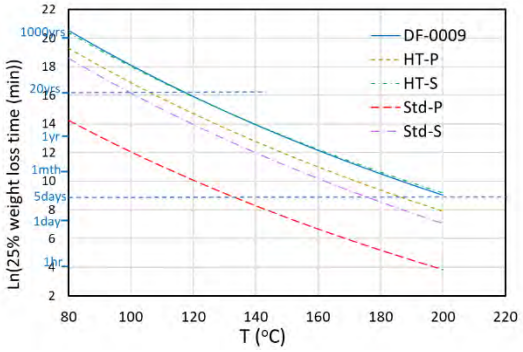


Figure 8. Predicted lifetime (based on 25% weight loss) of high T and standard coatings from 1mil film samples

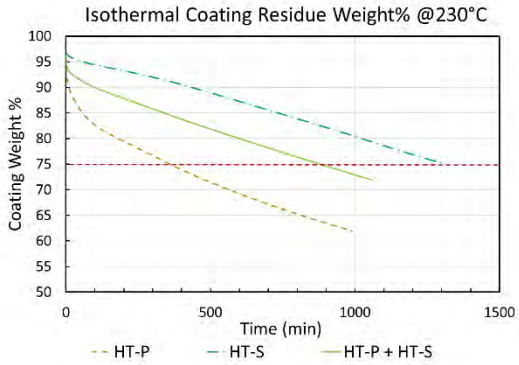


Figure 9. Isothermal TGA comparison of 1mil single layer vs. 1mil+1mil dual layer coatings at 230°C

while single layer film sample having all surfaces exposed to air. This causes the dual layer results to align more with the secondary coating.

Figure 10 and 11 are the Arrhenius plot and the predicted lifetime from the dual layer system in comparison with 2mil DF-0009. Attributed from the slightly longer durability of HT-S than DF-0009 and strong thermal performance of HT-P, the HT-P/HT-S dual layer coating system was tested to match DF-0009 single coat high temperature durability very closely, with lifetime and upper temperature prediction virtually the same level. In contrast, the dual layer conventional urethane acrylate coating system Std-P/Std-S despite the durability being much longer than Std-P alone, the fitted E_a somehow is even lower than primary coating alone, causing the dual layer prediction similar to the primary Std-P. This is not expected to be real as dual layer is supposed to be slower weight loss than single primary layer alone as the total weight loss% is based on the combined two layers. Much longer test run into lower temperature

region is needed to get a more realistic E_a for the Std-P/Std-S dual layer system for predicting into the application temperatures. There is indication the curve might be getting into a higher slope from 160ºC and below. Regardless the uncertainty of the lifetime prediction of the standard coating system, primary coating being the weakest link in the conventional dual layer coating system, as the key factor responsible for the poor thermal stability of the coated fiber at high temperatures is generally true, as demonstrated in section 3.2.

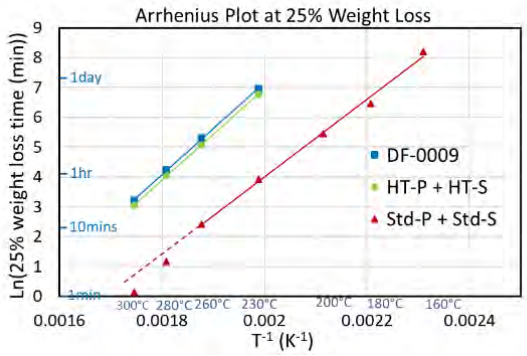


Figure 10. Arrhenius plots of high T and standard coatings from dual layer or DF-0009 2mil film samples

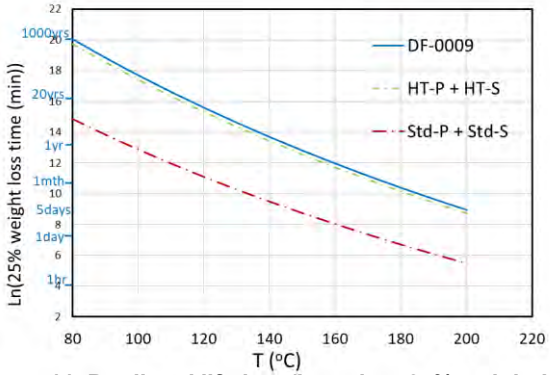


Figure 11. Predicted lifetime (based on 25% weight loss) from dual layer or DF-0009 2mil film samples

Table 2. Dynamic TGA onset temperature and Isothermal TGA Arrhenius fit and prediction

Coatings (1mil sample)	Dyna-mic TGA	Isothermal TGA Arrhenius Prediction			
	Onset T (°C)	Ea (kJ/mol)	Intercept	Upper T for 20yrs (°C)	Upper T for 1yr (°C)
DF-0009	328	133	-24.9	118	148
HT-P	320	132	-25.5	107	136
HT-S	334	130	-23.8	117	149
Std-P	214	120	-26.8	64	90
Std-S	255	134	-26.9	100	128

Coatings (2mil single or 1mil+1mil dual layer)	Isothermal TGA Arrhenius Prediction			
	Ea (kJ/mol)	Intercept	Upper T for 20yrs (°C)	Upper T for 1yr (°C)
DF-0009	128	-23.7	114	146
HT-P+HT-S	127	-25.5	112	143
Std-P+Std-S	108	-23.8	68	91

3.6 Film Test Results from Oven Aging

In order to confirm the coating thermal performance in the targeted application temperatures 100-200°C, 5 days aging was conducted in oven at 125°C, 150°C, 180° and 200°C.

3.6.1 Weight Loss from Oven Aging %Weight loss of the 5 coating samples after 5 days aging at different temperatures were plotted in Figure 12. Compared with the lifetime prediction from Figure 8 based on TGA Arrhenius study, the behavior of DF-0009, HT-P and HT-S from film oven aging weight loss matches the prediction reasonably well considering the effect of arbitrarily set condition of TGA as discussed in section 3.4. DF-0009 and HT-S performed better than prediction only losing ~13% after 5 days of 200°C while prediction for 25% weight loss is ~5 days at 200°C for both coatings. HT-P and Std-S are close to the prediction losing ~20% after 5 days at 180°C while prediction for 25% weight loss is close to 180°C for these two coatings. The biggest discrepancy is Std-P and Std-S at the lower temperature range of 125°C and 150°C. At first look, the weight loss of these conventional coatings at lower temperature range are surprising much lower than prediction, equal or even lower than the high temperature resistant coatings. However from the next section showing property changes, it is clear that these conventional coatings suffered much more severe property deterioration than the high temperature resistant coatings at the whole temperature range including the low temperature data at 125°C and 150°C even with this short term 5 day testing.

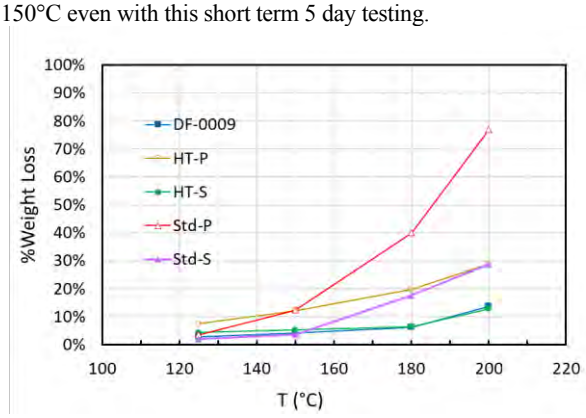


Figure 12. %Weight loss of coating film samples after 5 days in oven at different temperatures

This indicates weight loss from oven test is not a proper failure mode parameter that can represent the actual degree of polymer degradation at these lower temperatures. The cause of this discrepancy needs further investigation. From additional test of TGA at 150°C, 5 days TGA under 50L/min dry air environment resulted in 12% weight loss for HT-P which is similar to oven results, however 28% for Std-P which is much higher than oven. It is assumed moisture could be present at this lower temperature range in oven air flow environment, and different coatings could behave differently on moisture absorption. Measuring property change is more important to monitor the true progression of the coating degradation process at these relatively lower temperature ranges for the oven aged samples.

3.6.2 Change of Mechanical Properties Characterized by DMA Both chain scission and crosslinking are directly associated with mechanical property changes of the polymeric materials after aging degradation. Chain scission causes reduction of crosslink density and it should be reflected in the equilibrium modulus E_0 (rubbery state modulus, directly proportional to crosslink density) drop from DMA. Crosslinking on the other hand causes crosslink density increase and it should result in increase of both T_g and E_0. Figure 13 gives an example of DF-0009 DMA curves showing Tanδ

peak shifting to higher temperature and the equilibrium modulus E_0 shifting higher after 5 days of 180°C aging, in agreement with crosslinking dominated degradation process.

The comparison of T_g increase is given in Figure 14. HT-S shows less T_g shift than DF-0009, which confirms the slightly better thermal stability of HT-S from Figure 7 TGA Arrhenius plot, both much more stable than Std-S at high temperature level. Interestingly, T_g increase in Std-P is even less than HT-P, which may first appear not in agreement with its thermal stability being the worst, however, if considering Std-P is the only coating among these 5 coatings with chain scission being the dominant degradation mechanism, crosslinking being the minor one, this behavior of T_g shift not being so severe in Std-P can be easily understood. The true representation of the severe degradation occurred in Std-P is disclosed in Figure 15. After 5 days, Std-P lost equilibrium modulus E_0 ~50% after 125°C aging, ~80% after 150°C aging, until the reverse trend was seen modulus increased to be even higher than initial at 180°C. The temperature dependent behavior at a fixed time is equivalent to the time dependent behavior at a fixed temperature, which is in complete agreement with the observation in Figure 3 from Std-P/Std-S coated fiber at 180ºC aging primary in-situ modulus first dropped to very low modulus gel state then increased to even much higher value than initial modulus. This confirms once again for conventional primary coating the degradation process progressed from early chain scission dominated stage to later crosslinking dominated stage. The softening and weakening of the material in the first chain scission dominated stage is most risky causing field failure such as attenuation increase and difficulty on handling due to easy tube off. It should be noted that even though the modulus increased to much higher level in the later crosslinking stage, the material is already severely embrittled with much lower elongation and toughness. For example, for Std-P film after 5 days 180°C with modulus appeared to be in similar level as initial film, the elongation at break dropped from initial 120% to 15%, a severely degraded material well passed any failure criteria.

HT-P although also showed minor decrease of E_0 from 4.2 to 3.4MPa after 5 days 125°C, it stayed far from getting into a gel-like stage. This confirms the 1st objective of the dual layer coating design, prevent the primary coating from undergoing severe chain scission to avoid disintegration into a gel-like material under high temperature applications, has been achieved. HT-S by showing the least T_g

increase and negligible E_0 change after 5 days of the tested temperatures, similar behavior to DF-0009 and much better than Std-S, confirms the 2nd objective of the dual layer coating design, prevent the secondary coating from undergoing severe crosslinking to avoid detrimental embrittlement under high temperature applications, has also been achieved.

4. Conclusions

In this paper, the failure mechanism of the conventional urethane acrylate based dual layer coating for optical fiber under high temperature aging is proposed to be chain scission dominated primary coating disintegration and crosslinking dominated secondary coating embrittlement. A non-urethane acrylate based dual layer UV-curable coating system HT-P/HT-S with high temperature resistance has been developed. The evaluation of this new coating system based on the film properties characterized by TGA weight loss and DMA mechanical testing showed superior thermal stability at high temperatures, much better than a standard coating system Std-P/Std-S, matching closely to the single coat high temperature coating DF-0009; furthermore, with the design of soft/hard dual layer coating system, this new generation dual layer high temperature resistant coating system is expected to provide much improved fiber performance such as strip force and microbending protection than the current single coat product for specialty optical fiber applications under high temperature harsh environments.

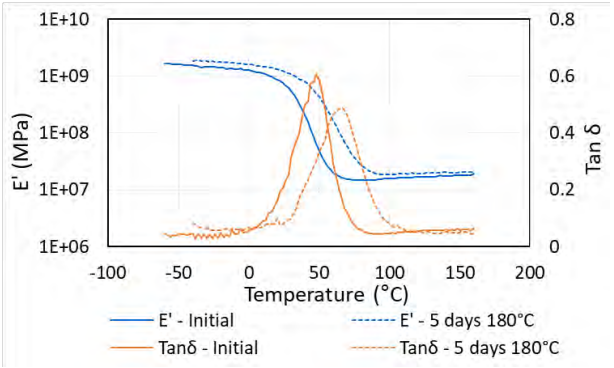


Figure 13. DMA loss modulus E' and Tanδ shift after 5 days in 180° oven for DF-0009 film samples

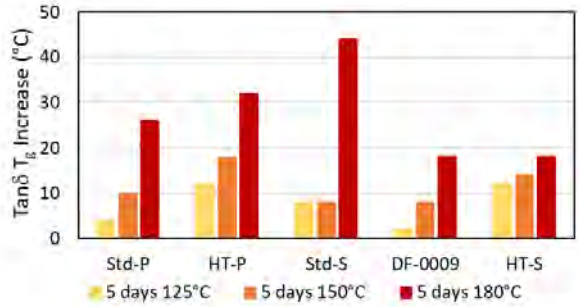


Figure 14. DMA Tanδ T_g increase after 5 days in oven at different temperatures

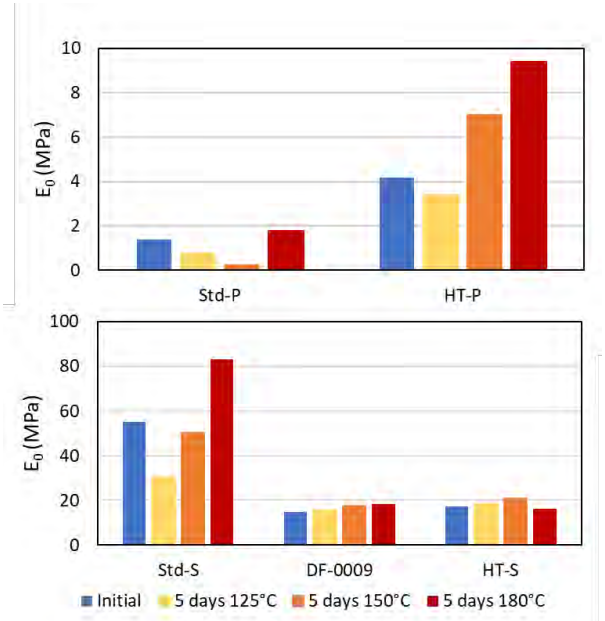


Figure 15. DMA equilibrium modulus E_0 of primary (top) and secondary/single coat (bottom) before and after 5 days in oven at different temperatures

5. References

[1] E. Murphy, W. W. Catton, J. J. Kelly, "Improved Heat Resistant UV Cure Compositions for Optical Fiber Applications", *Proc.* 57th *IWCS*, 197-201 (2008).

[2] E. Murphy, P. Shah, J. J. Kelly, T. Anderson "New Heat Resistant UV Cure Coatings as Protective Overcoats for Optical Fiber Applications", *Proc.* 58th *IWCS*, 90-94 (2009).

[3] A. A. Stolov, D. A. Simoff, J. Li, "Thermal Stability of Specialty Optical Fibers", *J. Lightwave Technology,* 26(20), 3443-3450 (2008).

[4] D. A. Simoff, A. A. Stolov, C. R. Ciardiello, "New Optical Fiber Coating Designed for High-Temperature Applications", *Proc.* 58th *IWCS*, 83-89 (2009).

[5] A. A. Stolov, J. A. Wrubel, D. A. Simoff, R. J. Lago, "Acrylate-Based Specialty Optical Fiber Coatings for Harsh Environments", *Proc.* 65th *IWCS*, 27-34 (2016).

[6] P. A. M. Steeman, J. J. M. Slot, H. G. H. van Melick, A. A. F. v.d. Ven, H. Cao and R. Johnson, "Mechanical Analysis of the In-situ Primary Coating Modulus Test for Optical Fibers", *Proc. 52*nd *IWCS,* 246-251 (2003).

[7] P. Gijsman, *Handbook of Environmental Degradation of materials*, 2nd ed., p. 676 (2012).

6. Pictures of Authors



Dr. Huimin Cao is a Science Fellow at Science and Technology Group at Covestro. Her expertise is material science, with the focus on material properties and structure-property relationships.



Keegan Orendorff is a Chemist at Covestro Fiber Optic Materials Group. He specializes in the production and analysis of UV materials with a focus on fiber optic coatings.



Todd Anderson is a Laboratory Technical Expert at Covestro Fiber Optic Materials Group. He has been working in the application process and testing of optical fiber coatings for over 20 years.



Dr. Eric Urruti is currently Head of R&D, North America, at Covestro. He has a diverse background encompassing research & development, manufacturing, and business management with a substantial record of successful new product introductions.

SESSION 14

Click on a session below to navigate to that section of the Proceedings.

SESSION 14: SPECIALTY INSTALLATION

Chairperson: Mike Gurreri, CommScope, Inc., USA

14-1 **Installing a Cable in a Duct Solely by the Flow of Water, Faster than the Flow Itself!;** Dr. Willem Griffioen, *Plumettaz SA, Switzerland*

14-2 **Cable Jetting Velocity Prediction Model;** Mr. Akshay Parmar, *Corning Technologies India Pvt. Ltd., India*

14-3 **Pre-Connectorized Ultra-High-Density Cable for Easy Installation;** Mr. Fumiaki Sato, *Sumitomo Electric Industries, Ltd., Japan*

14-4 **Fundamental Study of Planar Closure for Wiring on Road Surface;** Mr. Shun Kobayashi, *NTT Access Network Service Systems Laboratories, NTT Corporation, Japan*

14-5 **Study of Easy Thin Optical Fiber Cabling Method;** Mr. Keitarou Yoshida, *Nippon Telegraph and Telephone East Corporation, Japan*

14-6 **Study on Streamlining Cable Removal Process;** Keiji Fujihashi, *Nippon Telegraph and Telephone East Corporation, Japan*

14-7 **Methodology to Maintain Low Breaking Load and High Mechanical Reliability in Optical Fiber Drop Cable for Fttx Network;** Ms. Darshana Bhatt, *Sterlite Technologies Limited, India,*

Click here to return to the **Table of Contents**

Installing a Cable in a Duct Solely by the Flow of Water, Faster than the Flow Itself!

W. Griffioen[1], M. van Moppes[2], J.P. Hegdal[3], J.R. Olsen[3], V. Lilleløkken[3], M. Mockel[3], N. Tito[4], J.B. Laudet[4]

[1]Plumettaz, Bex, Switzerland, +31-620209745 · willem.griffioen@plumettaz.com

[2]HMS machines, Gouda, Netherlands, +31-630203648 · michael.vanmoppes@plumettaz.com

[3]Shawcor, Orkanger, Norway, +47-90219913 · janpeder.hegdal@shawcor.com

[4]Total Energies, Pau, France, +33-618147059 · jean-benoit.laudet@totalenergies.com

Abstract

Installation of cables by floating (water) combines benefits of blowing (distributed propelling forces avoiding capstan effect) and buoyancy (reduction effective cable weight). 12.4 km in one shot was already reached. In this paper tests were done in a 2.54 km dummy track to evaluate feasibility of a 30 km project. Multiple loops were placed to eliminate all other effects than water flow. With 1.5 bar the cable would still move, extrapolated 30 km with 18 bar. A remarkable phenomenon was found: the cable moved faster than the water! This was already forecasted and is further explained in this paper.

Keywords: Cable; duct; installation; blowing; floating.

1. Introduction

Installation of cables in ducts assisted by fluid drag is a well-known practice. When the fluid is air the method is called blowing or jetting and is the most common technique to install optical cables. When the fluid is water it is called floating, besides for optical cables also used for metallic cables. With blowing the common advantage is that the distributed fluid propelling forces can locally compensate gravity friction, minimizing built-up axial forces, hence strongly reducing the capstan effect, and enabling long lengths per single shot. Floating has an additional benefit of reducing the effective cable weight because of buoyancy. This makes it possible to even install longer distances per single shot, the world record now being 12.4 km. That's not yet the theoretical limit. In the present study tests were done in a 2.54 km dummy track (same construction as in the targeted project) in Norway to evaluate a project where the length will be 30 km (rather straight and smooth) and where the cable density is tuned to (sea) water density.

To make sure that extrapolation from the 2.54 km test to the 30 km target is based on pure floating, care had been taken to eliminate all side effects that could influence the test. The flow of water, and nothing else, shall propel the cable.

In the tests the cable was floating with a speed close to that of the water flow propelling it (as only source), even faster. The "old" blowing formulas already forecasted that this is possible. In this paper it is explained how.

2. Blowing and Floating Theory

In order to understand installation of cables into ducts by floating it is needed to dive a bit into the existing theory. A formula for the fluid propelling forces was first introduced in 1982 by British Telecom for Blowing flexible and lightweight fiber members (blown fiber) [1]. Here two kinds of forces propelling the cable were defined, hydrostatic and hydrodynamic propelling force.

2.1 Hydrostatic Propelling Force

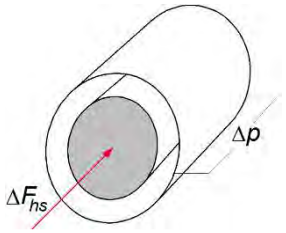


Figure 1. Schematic view hydrostatic propelling force

The hydrostatic force dF_{hs}/dx finds its origin in the pressure drop $|dp/dx|$ of the fluid over the cable volume and is simply given by the cross-sectional area of the cable times this pressure drop [1]:

$$\frac{dF_{hs}}{dx} = \tfrac{1}{4}\pi D_c^2 \left|\frac{dp}{dx}\right| \tag{1}$$

Here D_c is the cable diameter. It seems a bit strange that forces perpendicular to the cable surface contribute to propelling the cable. But, they virtually distribute along the cable the force already given by the machine when pushing the cable into the zone with pressure p, the so-called backpressure force F_{back} [1,2]:

$$F_{back} = \tfrac{1}{4}\pi D_c^2 \cdot p \tag{2}$$

This phenomenon was called the "spaghetti paradox" in [2] and was independently found for pipes under internal or external pressure, called the "Bridgman's paradox" [3].

2.2 Hydrodynamic Propelling Force

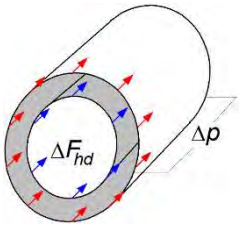


Figure 2. Schematic view hydrodynamic propelling force, on cable (blue) and on duct wall (red)

The hydrodynamic force dF_{hd}/dx is the drag force exerted by the fluid on the cable. A formula for this force is obtained by considering the total force dF_{an}/dx as a result from the pressure drop over the cross-sectional area of the annulus between cable and duct [1,2]:

$$\frac{dF_{an}}{dx} = \tfrac{1}{4}\pi\left(D_d^2 - D_c^2\right)\left|\frac{dp}{dx}\right| \quad (3)$$

Here D_d is the internal duct diameter. In most installations the flow is turbulent. For a non-moving cable (or cable speed much lower than fluid speed, which is the case when cables are blown in) it is assumed that the forces are equally distributed over the surfaces of the cable and of the inner wall of the duct. In that case the cable takes the fraction $D_c/(D_d+D_c)$ of the force over the annulus, resulting in [1,2]:

$$\frac{dF_{hd}}{dx} = \tfrac{1}{4}\pi D_c\left(D_d - D_c\right)\left|\frac{dp}{dx}\right| \quad (4)$$

2.3 Total Propelling Force

The total fluid propelling force dF_{prop}/dx on the cable is equal to the sum of the hydrostatic and hydrodynamic propelling force [1,2]:

$$\frac{dF_{prop}}{dx} = \tfrac{1}{4}\pi D_c D_d\left|\frac{dp}{dx}\right| \quad (5)$$

The trick of blowing is that the distribution of this force along the cable is limiting the capstan effect when compensating gravity friction locally. It was found in 1987 by PTT Netherlands that also cables with quite some stiffness could be blown in and that the pressure gradient was non-linear (air is a compressible fluid), even resulting in doubling of the installation length by synergy of blowing and pushing those stiff cables [2].

2.4 Common Misunderstandings

There are quite a few misunderstandings around cable blowing (and floating). It is good to understand them before treating the remarkable floating phenomena presented in this paper.

1. *Flow is the primary factor and shall be measured*. Yes, the flow plays a role, but is only a secondary factor, directly related to the pressure gradient and geometry. That's why you do not see the flow in the formulas. As long as the pressure is measured there is all information you need. For constant inlet pressure the flow decreases during cable installation, because of the increased pneumatic resistance of the cable filled part of the duct. The effect on the pressure gradient along the cable can be calculated.
2. *During blowing the cable is flying*. This is not true. The flow-lines along a cable in a duct (constant diameters) are parallel, so unlike with airplane wings no Bernouilli lift force is present. The cable just drags over the bottom of the duct (you can hear this when blowing a cable in an above ground duct). Also, if the cables were flying the blowing lengths reached would be far away from the calculated lengths.
3. *The fluid propelling force decreases for large cable filling factor because of limited airflow*. Not true, see Fig. 3, where the static, dynamic and total propelling force are given dimensionless as a function of filling factor D_c/D_d, following directly from the formulas. Only the hydrodynamic force decreases for $D_c/D_d>½$. If for very high filling factor the speed of the fluid is no longer much higher than that of the cable the hydrodynamic force is smaller than shown in Fig. 3. But, still then the static propelling force and the total force increase to the max for 100% filling! In practice, the blowing length in the same duct decreases for larger cable diameter, simply because the weight of the cable grows with the square of it (while the total propelling force only increases linearly). Increased (stiffness) friction due to micro-undulations of cable and/or duct even cause more abrupt decrease in blowing distance for a filling factor above 80%.

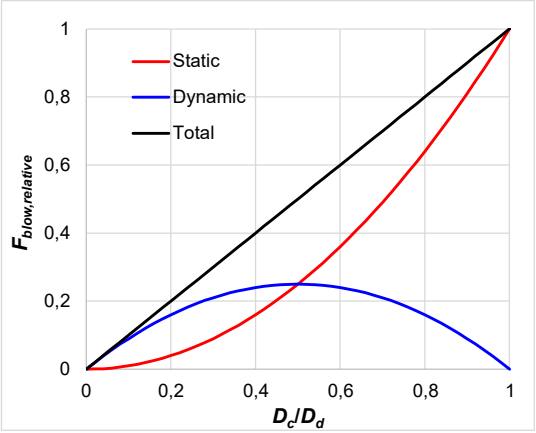


Figure 3. Cable propelling forces dimensionless

2.5 Cable Speed Comparable to Fluid Speed

As already mentioned, the formulas for the propelling forces of blowing can also be used for floating. Here not only the effective weight of the cable is reduced, also now the pressure gradient is linear (water is a non-compressible fluid) so linear extrapolations in floating length can be made (for pure floating). Furthermore, the fluid speed is not always much higher than that of the cable, so the cable speed has to be taken into account too. According to theory, it is possible to float cables with a water speed equal to that of the cable, already forecasted in [6]. Indeed, in floating installations of 5.5 km [4] and 12.4 km [5] it was observed that the cable came almost immediately when the first water poured out of the duct. The cable could not come earlier because the installations started with an empty duct, where the cable would run dry when moving faster than the water flow.

In the tests described in this paper (duct pre-filled with water) the cable speed was even higher than that of the water flow propelling it, the only remaining propelling force (all other possible forces were eliminated). This is indeed possible according to the formulas. The hydrodynamic propelling force equation (4) was derived for a cable speed zero. This cable's fraction of the force over the annulus gets lower when the cable speed becomes close to that of the water. The hydrodynamic propelling force even becomes negative (counter-acting) when the cable moves with a higher speed than that of the water. But, even then the flow can still move the cable forward when the hydrostatic propelling force dF_{hs} compensates the sum of the counter-acting hydrodynamic propelling dF_{hd} and friction force dF_f:

$$\frac{dF_{hs}}{dx} \geq \frac{dF_{hd}}{dx} + \frac{dF_f}{dx} \quad (6)$$

3. Setup and Tests

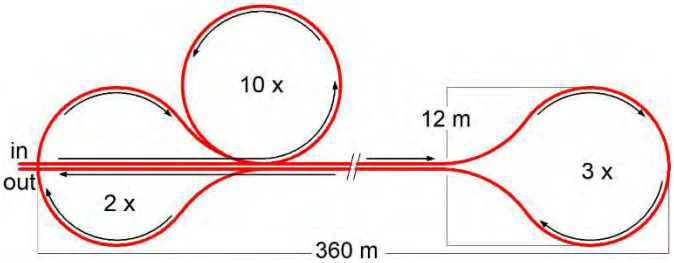


Figure 4. Schematic view of looped duct track (minimum bend radius 6 m)

Floating test were done in a 2.54 km dummy track (same construction as in the targeted project) in Norway to evaluate a project where the length will be 30 km (rather straight and smooth) and where the cable density is tuned to (sea) water density. An 18 mm, 2.47 N/m "buoyancy tuned" (for the local seawater, some margin for compression of the cable under water pressure) cable was installed into 6 parallel 40/30 mm PP ducts in a special configuration, connected by 6 m radius loops and with 10 of those loops immediately at the start of the track, see Fig. 4 and 5.

For pure floating the installation length increases proportionally with the water pressure. In order to extrapolate to a 30 km project from a relatively short test track of 2.54 km it is important to eliminate all edge effects disturbing the test and leading to false information. That is why 10 loops of duct were placed immediately at the entrance of the track. The capstan effect will then kill excess pushing forces, pushing forces which are needed where the cable is injected into the pressure zone, to overcome the so-called backpressure force. If this is not done sufficiently, floating is not effective.

The floating equipment used was a SuperJet (with flow meter) and a 120 l/min water pump, pushing the cable and supplying the water pressure. Lubricant (Jetting Lube) was added to the duct (under pressure) using a lubricant dosing pump. The pressure was measured with a class 0.2 (0.2%) digital manometer.

3.1 Tests



Figure 5. Installation of 18 mm cable in 40/30 mm PP duct, in total 2.54 km long, by floating

First the duct was filled with water (only wall lubricated by first blowing a foam pig with lubricant through). After the duct was filled with water the flow was measured as a function of applied water pressure. This showed that Blasius' law [2] is followed, see Fig. 6.

Then lubricant was added to the water. This was done by continuously feeding lubricant with the lubricant dosing pump. The whole process (until lubricant "reached the end") took about 70 min. Then the flow as a function of applied water pressure was measured again. The expected effect of the lubricant on the flow (increased flow, the "fireman effect") could not be seen during filling with lubricant. No difference was found with the situation before lubrication, see Fig. 6.

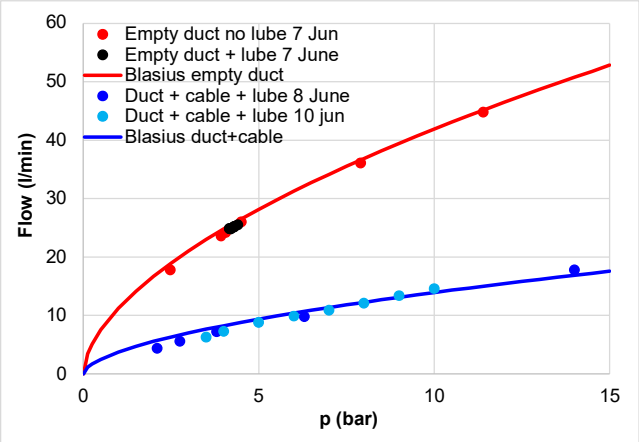


Figure 6. Measured water flow as a function of applied pressure over 2.54 km of 40/30 mm PP duct, with and without 18 mm cable, compared with Blasius' law. Further details in text.

The first cable installation (6 June 2022) was done most of the time with a water pressure of 5 bar, with the speed adjusted to 30 m/min. It was found at the end that the speed (then about 23 m/min) was limited by the settings of the SuperJet, because at the end the water pressure could be reduced to 2.33 bar before the speed started to drop. When reducing the water pressure further to 1.95 bar (could not set lower, pump motor running idle and bypass fully open) the cable speed dropped to 18 m/min.

Also when the duct was filled with cable Blasius' law was followed, when for the annulus between cable and duct the standard hydraulic diameter D_h is taken, defined as "4 times cross-sectional area divided by wetted surface", resulting in $D_h = D_d - D_c$.

After Floating the cable back a second Floating installation (7 June 2022) was done, most of the time with a water pressure of 6.4 bar and with the speed adjusted to 55 m/min most of the time. At the end again measurements were done of pressure, speed and flow, both for moving and non-moving cable. Again Blasius' law was followed for the non-moving cable. For the moving cable the measured water speed took a value between that of Blasius' law for an empty and for a cable-filled duct, see Fig. 8 (note: here speed given instead of flow).

In 2023 two more tests were done, now even 73 m/min reached (most of the time) with a water pressure of 10.2 bar.

The cable speeds for different water pressures with data taken at the end (cable out) from 2022 and 2023 are summarized in Fig. 7.

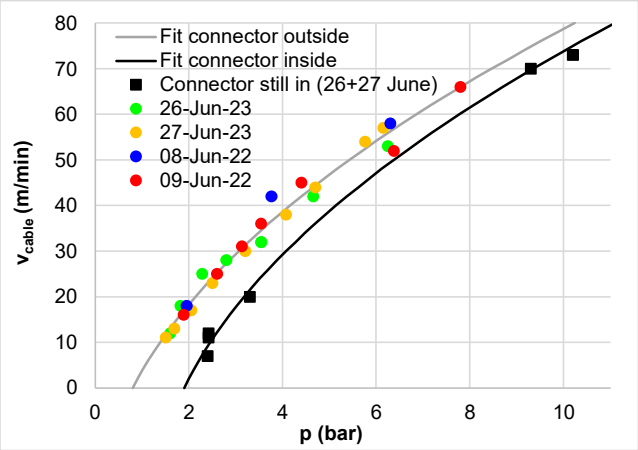


Figure 7. Measured cable speed from tests and data fit

Besides measurements of pressure, speed and flow after the cable came out also a few measurements were done with the cable just did not come out (there was not much time for such measurements because the cable is only for a short time in that region, certainly at the higher speeds). It was found that the cable speed is a bit lower then, see Fig. 7, indicating that the cable end (stiff, with connector) adds a bit to the friction and needs extra fluid drag to overcome this.

According to Fig. 7, installation would even be possible with a cable speed of 10 m/min and a water pressure as low as 1.5 bar (we could not yet get sufficiently low water flow with the equipment we used to reach lower pressures). With the cable end still inside we would need about 2.4 bar for this speed of 10 m/min (if we do not do something to reduce this friction).

A very interesting phenomenon is the fact that the cable speed was higher than that of the water around the cable in all measurements, see Fig. 8. They become about equal in the lowest pressure and speed settings.

Another interesting observation is that the cable can reach higher speeds (for the same pressure) than water flow in the empty duct. In other words: "the cable slides more easily through the duct than water".

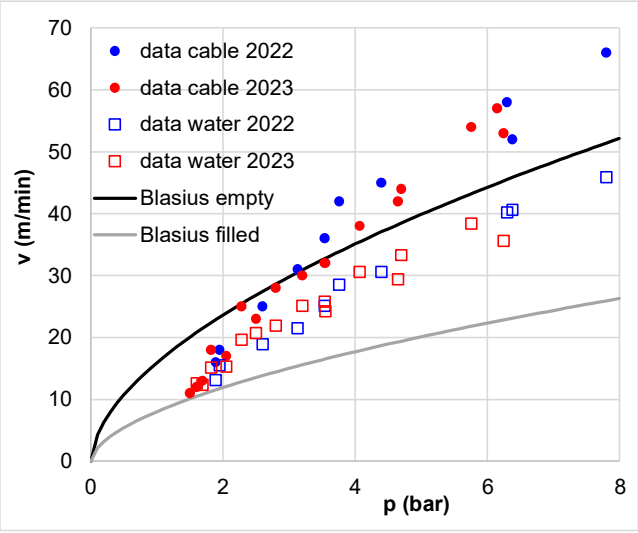


Figure 8. Measured cable and water speeds from tests

3.2 Analysis (for zero cable speed)

The test was done such that the flow of water, and nothing else, propels the cable. For that reason 10 loops of duct were placed immediately at the start of the test track in order to kill by the capstan effect all excessive pushing forces remaining after compensation of the backpressure force. The importance of this is shown in Fig. 9 where a calculation (JetPlanner 4.0 software [7]) was done for the minimum pressure needed to install the cable (diameter 18 mm, linear weight density 2.47 N/m, cable stiffness 8 Nm^2) into a 2.54 km straight duct (coefficient of friction with cable 0.19, "standard" undulations with 4 cm amplitude and 8 m period), no loops programmed yet. The same was done with 10 loops of duct with 6 m radius placed at the entry of the duct (same total length). Here the result is about the same with and without undulations. Note that the calculation still assumed a cable speed much lower than that of the propelling water.

Without the loops the pushing force still has such a large effect that with 400 N almost no water pressure is needed, while with the lowest force 0.65 bar is required, see Fig. 9. With the loops the pushing force hardly influences the minimum pressure needed to install the cable, which is remarkably higher (1.95 bar) than without the loops. But, even a large bend radius of the loops of 6 m still has an effect (due to cable stiffness friction in bends) as can be seen in Fig. 9 with larger bend radii. At 12 m bend radius the cable stiffness effect is close to saturation (not much changes anymore with 40 m loops, about the limit for loops-only on a 2.54 km track). So, the test with 6 m bend radius is worst case and could be closer to reality when selecting larger bend radii. However, this is true for the undulations assumed (which also give cable stiffness friction). And the latter is what we investigate. So, the 6 m loops give a worst case estimate, but we do not exactly know "how worse" it is.

The almost horizontal straight lines in Fig. 9 suggest the situation of pure floating, with the effect of cable stiffness in undulations of the duct and in the loops the only relevant friction contributors. The effect of the loops is clearly shown. Furthermore, to the left of the round points no installation is possible (pushing force not enough to compensate backpressure force).

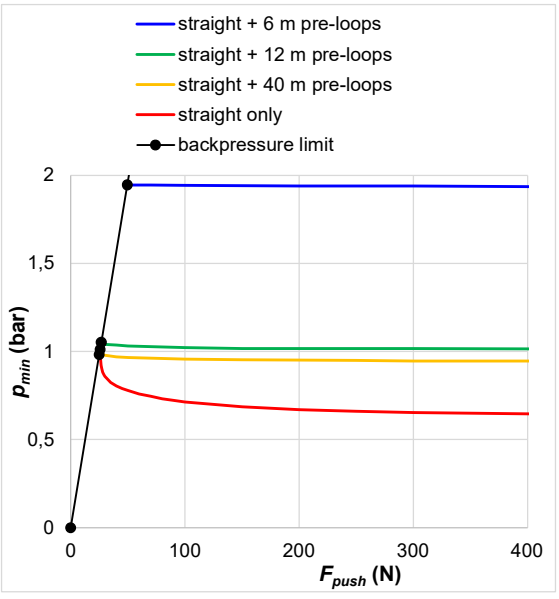


Figure 9. Calculated minimum pressure to install cable in full length of 2.54 km duct when straight and when straight with pre-loops

More loops were placed (programmed) in the track to make the looped 2.54 km length with 6 parallel ducts. All loops have a minimum bend radius of 6 m to limit friction in those loops arising from cable stiffness (last friction contributor). The extra loops have no effect, in fact they "restore" faster from the bending stiffness friction than the initial 10 loops. This can be seen in the JetPlanner 4.0 software [7] simulation, again for a water pressure of 1.95 bar, see Fig. 10.

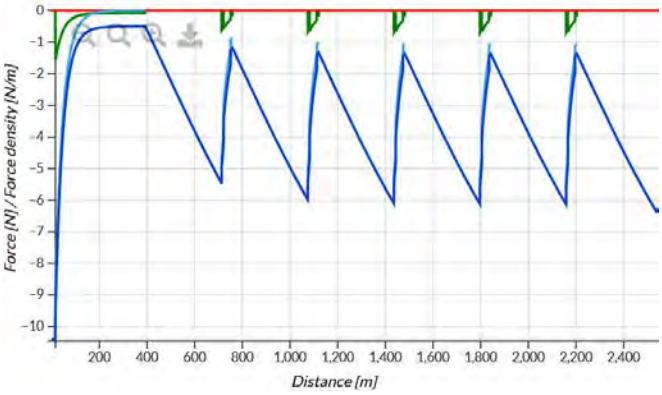


Figure 10. Software simulation of axial force (blue) and radial force density (green) in the cable during floating

3.3 Extrapolation to longer length

It was found that the cable could be floated through the test track with a water pressure of only 1.5 bar and a speed of 10 m/min. Extrapolation (this can be done linear proportionally) to 30 km says that this could be done with a pressure of 18 bar, no problem for an installation time of a few days for a 40/30 mm PP duct. In case the loops in the test track were indeed the dominant factor for the required water pressure, even longer installation length would be possible.

4. Conclusions

It was found that the cable could be floated through the test track of 2.54 km of 40/30 mm PP duct with a water pressure of only 1.5 bar and a cable speed of 10 m/min. Extrapolation, to 30 km, says that this could be done with a pressure of 18 bar, no problem for an installation time of a few days for this PP duct. A higher pressure resulted in a higher speed. This is because of the relatively low water speed. So low that the cable was running faster than the water flow, the only source propelling the cable! This can be explained by the fact that the "hydrostatic" propelling forces from the pressure gradient over the volume of the cable compensate the sum of gravity and cable stiffness friction and even the then counter-acting "hydrodynamic" drag forces. Also it was found that the cable could move faster through the duct than water in the empty duct under the same pressure! The measured water flow in an empty and cable (non-moving) filled duct match with Blasius' law. When the cable moves the water gets a speed between the empty and filled Blasius' speed.

5. Acknowledgments

I wish to express my thanks to Vitor Goncalves, Alexandre Uhl, Nicolas Fournier (Plumettaz), Ronald Gomersbach (HMS machines), Marianne Asbøll (Shawcor), Florent Boumare, Denis Melot, Clement Boireau and Ivo Conradi (TotalEnergies) for their role in this project, the latter as the initiator of this project.

6. References

[1] S.A. Cassidy, M.H. Reeve, "A radically new approach to the installation of optical fibre using the viscous flow of air", *Proc. 32nd IWCS* (1983) 250-253.

[2] W. Griffioen, "*Installation of optical cables in ducts*", Plumettaz SA, Bex (CH) 1993 (ISBN: 90 72125 37 1).

[3] N. Arnfinn, "Effective force; friction or reality?", SPE 174785-MS, *Society of Petroleum Engineers conference*, Houston, Texas, USA, 28-30 September 2015.

[4] W. Griffioen, C. van 't Hul, I. Eijpe, W. Greven, F.R. Bakker, B. Wegbrans, "5.5 km optical cables installed in small underwater tubes using waterflow", *Proc. 50th IWCS* (2001) 736-741.

[5] Nexans Suisse SA, "*Record Mondial, Installation de 13 km de câble à fibres optiques en une seule longueur grâce au portage à l'eau*", Press release 2019.

[6] H. Nobach, "*Effect of cable speed on installation length when installing with water*", KPN Internal report, April 2006.

[7] W. Griffioen, D. Plumettaz. "Cable pulling force in pipes with 3-dimensional bends for different installation methods", *ASCE's Journal of Pipeline Systems - Engineering and Practice*, Vol. 12, Issue 4: 04021060, November 2021.

7. Pictures of Authors



Willem Griffioen received his M.Sc. degree in Physics and Mathematics at Leiden University (NL) 1980, worked there until 1984. Then employed at KPN Research, Leidschendam (NL), on Outside-Plant Installation Techniques. In 1995 he received his Ph.D. (Optical Fiber Reliability) at Eindhoven Techn. University (NL). From 1998 to 2009, he worked at Draka Comteq, Gouda (NL), on Connectivity of FttH. Currently he works at Plumettaz SA, Route de la Gribannaz 7, CH1880 Bex (CH), willem.griffioen@plumettaz.com and is responsible for R&D of cable installation techniques.



Michael van Moppes received a M.Sc. degree in Material Science and Engineering from Delft University of Technology in 1988. After various function's within the aerospace, aluminium and offshore industry he joined Plumettaz b.v. (NL) in 1998 as Area Sales Manager responsible for Northern and Western Europe. From 2005 he has been responsible for APAC region and in 2009 became Vice-General Manager at Plumettaz Project Equipment (Shanghai) Co., Ltd. In 2011 he became General Manager at Plumettaz Singapore Pte. Ltd., and December 2020 he joined H.M.S. Machines, Gouda, The Netherlands as Application Manager Plumettaz Group.



Jan Peder Hegdal received his M.Sc. in Physics and Mathematics from the Norwegian University of Technology and Science (NTNU) in 2007 and has since worked at Shawcor and NTNU with research and development in wet thermal insulation. He is leading Shawcor's R&D department in Norway and was instrumental in the development of several new insulation systems, including the Thermotite® ULTRA™ product line. His department works with lab scale to full scale testing, thermal and structural numerical models, and collaborate extensively with customers and research institutions.



Jim Ronny Olsen is a senior research and development Supervisor/Lead technician at Shawcor Norway AS. He is a certified coating inspector IMPP/Nace Level 2. Has certificates of apprenticeship and skilled workmanship in chemistry and process technology, chemical technical Industry and in polymer process technology and has worked with Shawcor and in the pipe coating industry for 28 years. He joined Shawcor's R&D department in Norway in 2009. He has worked in quality control, lab technician, foreman in thermal coating plant. He has extensive experience in leading teams of foremen working on development in Research and development, anti-corrosion coating, injection moulding, reactive injection moulding and thermal insulation techniques.



Vegard Lilleløkken is a senior research and development technician at Shawcor Norway AS. He holds certificates of apprenticeship and skilled workmanship in chemistry and process technology and in polymer process technology and has worked in the pipe coating industry for 17 years. He joined Shawcor's R&D department in Norway in 2014. Vegard Lilleløkken has studied geography and IT at the Norwegian University of Science and Technology. He has worked in quality control and as a lab technician with measurements of material properties. He has extensive experience in leading teams of technicians working on development in anti-corrosion coating, injection moulding, reactive injection moulding and thermal insulation techniques.



Marcos Mockel received his B.Sc. degree in Chemical Engineering from the Universidad Tecnologica Nacional (AR) in 2002. He was employed by Socotherm Group in 2002 where he held several technology, business, and executive roles. In 2015 he joined Shawcor (US) and is currently the Vice President Marketing & Technology and responsible for the R&D function.



Jean Benoit Laudet holds a M.Sc from ENSTA Bretagne on "Offshore Structure Engineering" and a M.Sc from IFP School on "O&G Development Engineering". He joined TotalEnergies in 2002 in the Drilling & Wells division and held various positions around the globe until 2015 when he was Drilling Manager in Uruguay for the then world deepest water depth exploration well. He then moved to field development engineering group in various positions, the current one being "R&D Deep Offshore Development Manager" based out of Pau, France.



Nicolas Tito is a senior subsea engineer with 30 years' experience in the oil and gas industry. He started his career in COMEX in 1991 in the subsea robotic area. In 1997, after 6 years working offshore all over the world, he decided to join DSND Consub in Brazil as ROV operations Lead. Nicolas joined TOTAL in 2001 as subsea engineer on the Girassol Project. Then he held different positions on major subsea developments. In 2018 he is project manager for the CLOV MPP project in Angola. In 2021 he joined the R&D division as SURF/SPS R&D project manager. Since 2022 he is acting as senior subsea consultant on the Libra Deepwater project in Brazil.

Cable Jetting Velocity Prediction Model

Akshay Parmar [a], Waldemar Stoecklein [b], William C Hurley [c], Steffen Krieger [b], Sunil M Alexander [d]

[a] Corning Technologies India Pvt Ltd, Pune, Maharashtra, India
[b] Corning Optical Communications GmbH & Co. KG, Berlin, Germany
[c] Corning Optical Communications, Hickory, NC, USA
[d] Corning Incorporated, Wilmington, NC, USA

Abstract

Cable jetting is a process of installing cable in a duct by pushing it through a capstan/caterpillar and by blowing the compressed air in the duct. Attaining the minimum jetting distance is a critical customer requirement for any cable to pass. Fundamental understanding of jetting process is important and is desirable by both cable designers and cable installers. The jetting experiment is a time and resource consuming activity. Thus, an analytical dynamic time-marching framework to predict cable jetting velocity as cable head moves inside duct is presented in current work. The model can be used to develop better cables (in terms of jetting), and to optimize jetting process parameters.

Keywords: Cable; Jetting; Blowing; Model; Theory; Installation.

1. Introduction

Cable jetting is a process of installing cable in a duct by pushing it through a capstan/caterpillar and by blowing the compressed air in the duct. Initially, a capstan pushes the cable inside duct by overcoming resistive forces. Once the cable has reached a sufficient length inside duct, air drag dominates over capstan force to jet the cable. Attaining the minimum jetting distance is a critical requirement for any cable to pass. To meet this requirement, fundamental understanding of jetting process is important and is desirable by both cable designers and cable installers. Figure 1 shows the schematic of cable jetting process.

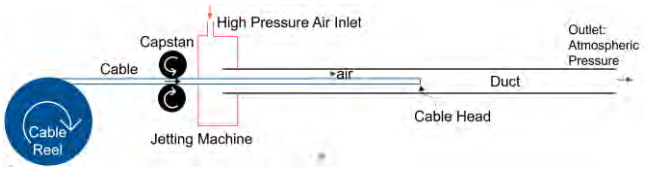


Figure 1: Schematic of cable jetting process.

Jetting velocity depends on the net external force acting on the cable at each cable head location. When the net forward force is positive (in the initial part of jetting process), the cable accelerates. Similarly, the cable decelerates when the net force is in backward direction (resistive). We have developed a model that estimates the net force acting on the cable at any time. The net force can be directly equated to rate of change of momentum of the cable and reel. The net force is calculated by estimating forces acting on cable inside and outside of the duct. The force inside duct includes air drag because of pressurized air as well as resistance inside duct because of weight, bends, buckling and undulations. The forces acting on the outside of duct includes capstan force and resistance in the jetting machine (O-ring).

2. Air Blowing/Drag Force

2.1 Pressure Drop in Empty Duct

The air drag force can be estimated by finding pressure drop in the duct. The pressure drop in an empty duct can be found using Darcy-Weisbach equation. Although, the equation is developed for an incompressible flow, the air flow in jetting can be assumed as locally incompressible and Darcy equation can be applied for compressible air flow during cable jetting.

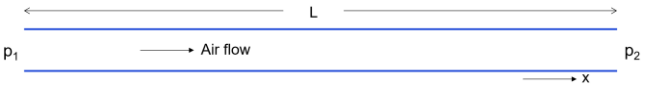


Figure 2: Schematic of an empty duct.

Figure 2 shows the schematic of an empty duct having p_1 and p_2 as inlet and outlet pressure respectively. L is duct length; x is axial length in the duct. The Darcy-Weisbach equation of pressure drop in empty duct is given by Equation 1.

$$\frac{dp}{dx} = \frac{f\rho v^2}{2D} \tag{1}$$

where, p is pressure, f is friction factor (=$0.041/\mathrm{Re}^{0.052}$, provided in Snippe [1.]), ρ is density, v is velocity, D is duct diameter, Re is Reynolds number.

The density and velocity are a function of x because of incompressible flow (iso-thermal flow). Density can be written in terms of pressure using the ideal gas equation and v can be written in terms of density using mass conservation.

$$p = \rho RT \tag{2}$$

$$\rho_1 v_1 = \rho v \tag{3}$$

Substituting (2) and (3) in (1) and by solving the ODE (Ordinary Differential Equation) in pressure, pressure variation in the empty duct can be found using (4).

$$p(x) = \sqrt{{p_1}^2 - ({p_1}^2 - {p_2}^2)\frac{x}{L}} \tag{4}$$

2.2 Pressure Drop in Cable Filled Duct

During cable jetting process, the cable moves inside duct and the location of cable head changes continuously. Thus, pressure formulation inside an empty duct is not valid. In this section, obtaining pressure inside a cable filled duct is discussed. The Darcy-Weisbach equation can be individually applied to part of the duct in which cable is present having hydraulic diameter as D_1 and to part of the duct which is empty having hydraulic diameter as D_2 (equal to duct diameter). Mass conservation at inlet and outlet will be the third equation. p_1 and p_2 are the inlet and outlet pressure respectively. p_h is

the pressure at the location of cable head. Figure 3 shows the schematic of setup.

Solving the two Darcy-Weisbach in both zones and one mass conservation equation, p_h can be obtained as per given by Snippe [1.]. The equation to find p_h is given in (5).

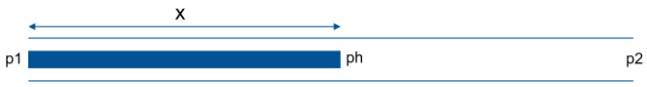


Figure 3: Schematic of duct filled with cable till length X.

$$p_h(X) = \sqrt{\frac{(L-X)p_1{}^2 D_1{}^{4.948} + X p_2{}^2 D_2{}^{4.948}}{(L-X)D_1{}^{4.948} + X D_2{}^{4.948}}} \quad (5)$$

where X is the cable head location inside duct, D_1 is the hydraulic diameter of duct filled with cable, D_2 is the duct diameter. The D_1 can be found using (6) as provided by Griffioen [3.].

$$D_1 = \frac{2(D_d - D_c)}{1+\sqrt{\frac{D_d - D_c}{D_d + D_c}}} \quad (6)$$

where, D_d and D_c are duct and cable diameter respectively.

Once pressure at cable head is obtained from p_1 and p_2, (7) and (8) can be used to calculate pressure inside the duct. (7) estimates the pressure inside the duct part filled with cable. (8) is used to calculate pressure in the remaining duct (empty part).

$$p_f(x) = \sqrt{p_1{}^2 - (p_1{}^2 - p_h{}^2)\frac{x}{X}} \quad (7)$$

$$p_e(x) = \sqrt{p_h{}^2 - (p_h{}^2 - p_2{}^2)\frac{x-X}{L-X}} \quad (8)$$

where, p_f and p_e are pressure inside cable filled part of duct, and empty parr of duct respectively.

$$\frac{dF_{blow}}{dx} = -\frac{\pi}{4} D_c D_d \frac{dp}{dx} \quad (9)$$

The obtained pressure inside the cable filled duct can be used to calculate pressure gradient inside duct which then can be used to obtain air drag or blowing force on the cable based on duct and cable surface area ratio. The blowing force can be calculated from (9) as provided by Snippe [1.]. The blowing force in (9) accounts for both hydrostatic and hydrodynamic force because of presence of pressurized air in the duct.

3. Resistive Forces Inside Duct

The compressed air blows the cable inside duct. Simultaneously, the resistive force inside the duct resists the jetting of cable inside duct. These resistances include resistance because of cable weight, resistance because of bends in the duct trajectory, resistance because of cable buckling and resistance because of duct undulations. The schematic of these resistances is shown in Figure 4. The analytical formulations to estimate these resistances are discussed in this section. Griffioen [2.] has discussed these models in detail.

3.1 Resistance because of Cable Weight

The resistance per unit length because of cable weight can be estimated using normal force of cable per unit length multiplied by coefficient of friction. In case of inclined surface, component of weight can be used to estimate the weight resistance. The equation to estimate resistance because of weight is given in (10).

$$\frac{dF_w}{dx} = \mu W \cos\theta + W \sin\theta \quad (10)$$

where, F_w is the resistance because of cable weight, μ is coefficient of friction, W is normal cable weight per unit length and θ is the surface inclination from horizontal.

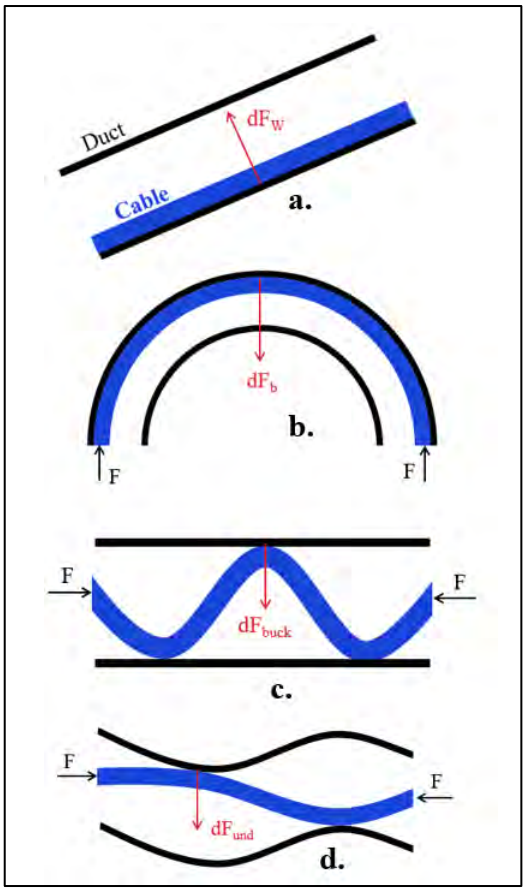


Figure 4: Schematic of resistances experienced by cable having compressive force F inside a small duct element dx. a.) resistance because of cable weight; b.) resistance in the bend; c.) resistance because of cable buckling; d.) resistance because of duct undulations.

3.2 Resistance because of Bends in Duct

The cable experiences resistance when it passes through a bend. The resistance depends on tension/compression in the cable at the bend. Thus, force buildup in cable is required to estimate resistance to cable inside a bend. This can be estimate through (11).

$$\frac{dF_b}{d\varphi} = \mu F \quad (11)$$

where, φ is the angle of bend, F is the force buildup in the cable at the bend location. R is the radius of bend ($R.d\varphi = dx$).

3.3 Resistance because of Cable Buckling Under Compressive Load

During cable jetting, the cable is pushed inside duct through a capstan which causes the compressive force buildup in the cable. This can lead to buckling of cable if bending stiffness of cable is less. The buckling creates extra resistance for the cable to move inside duct. The normal force because of buckling can be estimated by (12) as

given in Griffioen [2.]. The buckling does not happen during tension in the cable.

$$\frac{dF_{buck}}{dx} = \beta F^2 \quad (12)$$

$$\beta = \frac{(D_d - D_c)}{\pi^2 B} \quad (13)$$

where, β is buckling constant, B is bending stiffness of cable, F is compressive force buildup in the cable.

3.4 Resistance because of Duct Undulations

The undulations in the duct can be characterized by amplitude, A and period, P. A stiff cable will experience resistance in passing through a non-straight duct. Griffioen [2.] has provided an analytical formulation to calculate resistance experienced by a cable inside the duct undulations. (14) can be used to estimate this resistance.

$$\frac{dF_{und}}{dx} = \mu(W_B \mp TF) \quad (14)$$

where, W_B is normal force per unit length in undulations because of stiffness, negative and positive signs are used when F is compressive and tensile respectively (in Equation 14).

$$W_B = \frac{384 A_{eff} B}{P^4} \quad (15)$$

$$T = \frac{8\pi A_{eff}}{P^2} \quad (16)$$

$$A_{eff} = A \pm 0.5(D_d - D_c) \quad (17)$$

where, positive and negative signs are used when F is compressive and tensile respectively (in Equation 17).

3.5 Net Cable Resistance Inside Duct

The direction of all above normal/resistances are unknown. Thus, they are assumed to be perpendicular in nature and equivalent resistance is obtained. Since many of these resistances depend on force buildup in the cable, calculation is started from the cable head where tension/compression is taken as zero. Calculation is done backwards and force buildup in cable is calculated based on blowing and resistance force at each cable location till cable entry position in the duct.

The force buildup in the cable is then used to estimate cable jetting velocity which will be discussed in the next section.

4. Cable Jetting Velocity Prediction

In addition to blowing and resistive forces inside duct, the cable also experiences pushing force by capstan motor and resistance inside the jetting machine.

The capstan force is a function of motor speed, and resistance inside jetting machine is typically constant and tuned through experiments for the model. The capstan motor force is highest at zero motor speed and lowest at highest motor speed. Linear negative correlation is assumed between maximum capstan force and maximum capstan speed. The maximum force and speed are obtained from specification sheet of jetting machine.

Figure 5 shows the schematic of major forces acting on the cable during cable jetting process.

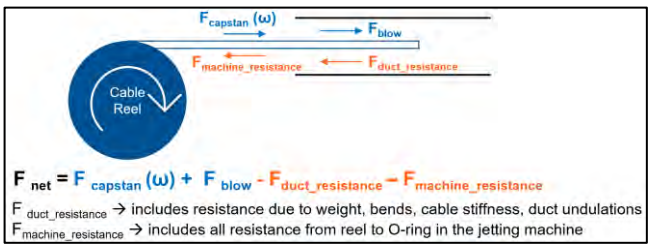


Figure 5: Force acting on cable during cable jetting process.

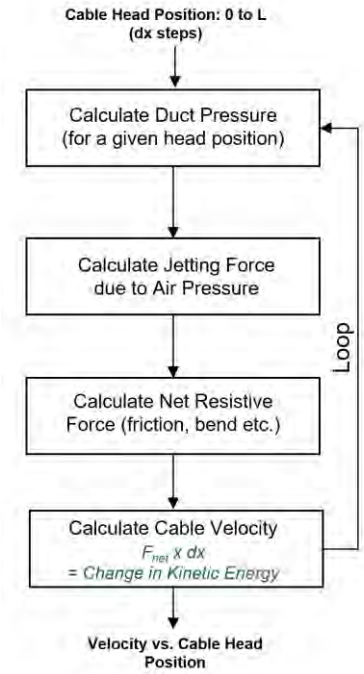


Figure 6: Flow diagram of cable jetting velocity prediction model

The steps involved in estimating cable jetting velocity from estimated forces on cable are as follows. Figure 6 shows the high-level schematic of cable jetting velocity prediction model algorithm.

1. Cable enters the duct. The only force acting currently is capstan motor force and resistance inside jetting machine. No air drag, or resistance inside duct is present.
2. Net force is calculated on cable and momentum of the (cable + cable reel) is changed based on the net external force. This gives us the initial acceleration of cable during jetting.
3. As the cable head moves inside duct, air drag and resistance inside duct is also calculated for each cable head position (along with capstan and jetting machine resistance) and net external force on cable is calculated for each cable head position.
4. The net external force at each head position is used to estimate momentum change of cable and reel at each cable position. This outputs the cable jetting velocity variation as cable moves inside duct.
5. Initially, the net force is positive which accelerates the cable. In the final part of jetting, resistance inside duct dominates and net force is negative which decelerates the cable and ultimately stops the jetting process.

5. Results, Discussion & Experimental Validation

5.1 Modeling Results and Parametric Study

Figure 7 shows the typical output of the cable jetting velocity prediction model. The prediction is shown for a 7.8 mm outer diameter cable inside a 10 mm inner diameter duct. The duct is 1500 m straight track without any bends or undulations. The coefficient of friction between cable and duct is 0.1. The cable weight and stiffness are 40 kg/km and 1 N.m^2 respectively.

Duct is not pressurized in Figure 7 whereas it is pressurized to a constant 10 bar inlet in Figure 8. The capstan motor force and jetting machine resistance is as per Plumettaz Minijet machine.

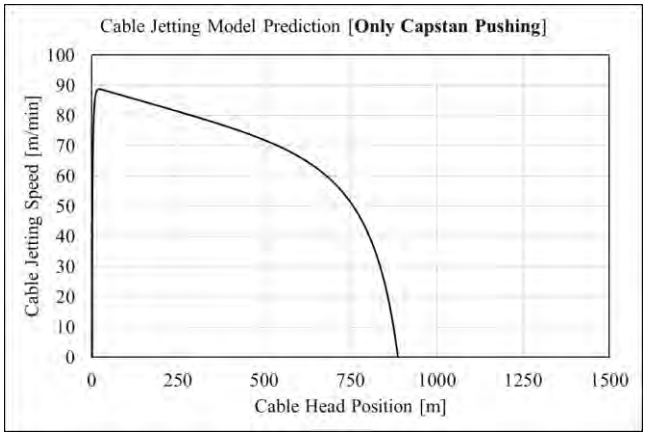


Figure 7: Cable jetting velocity prediction – only capstan pushing, without pressurizing duct

It can be seen from Figure 7 and Figure 8 that the benefit of pressurizing the duct is significant. The capstan only can push cable up to 890 m whereas, along with 10 bar pressurized air, the cable can be installed up to 1480 m. Thus, using a combination of capstan pushing and pressurized air can help in achieving larger installation lengths in cable jetting process. The developed tool can also be used to optimize the duct pressurization timing to achieve maximum jetting distance and minimize back-pressure from pressurized air.

Figure 9 shows the effect of cable stiffness on cable jetting process (duct pressurized to 10 bar). For a straight track, lesser stiff cable buckles and thus, lead to lesser jetting distance in cable jetting process. The cable with higher stiffness (of 1 N.m^2) can jet to a longer distance. If the duct has too many small bends or undulations, the cable will get stuck above a critical stiffness value.

The effect of coefficient of friction between cable and duct is shown in Figure 10. As expected, the setup with the least coefficient of friction is best for cable jetting process. A lower friction coefficient leads to better jetting distance and faster jetting process (higher jetting speeds).

Similarly, the effect of other parameters such as duct inner diameter, cable outer diameter, cable weight, cable reel weight, capstan motor curve can be studied using the presented model. The use of jetting velocity as model output allows easy comparison with experimental jetting data and better understanding of the process.

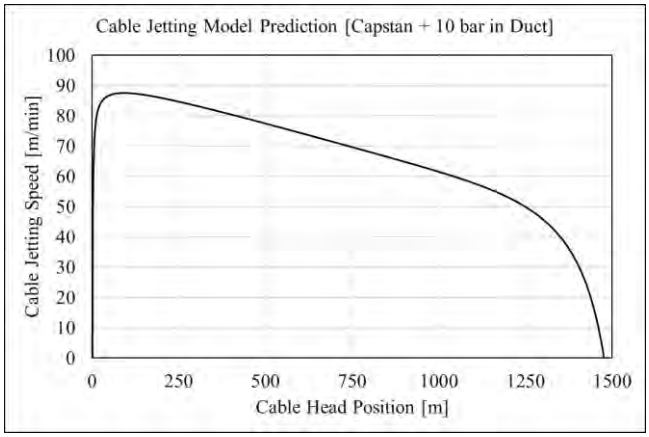


Figure 8: Cable jetting velocity prediction – capstan pushing + 10 bar inlet pressurized duct

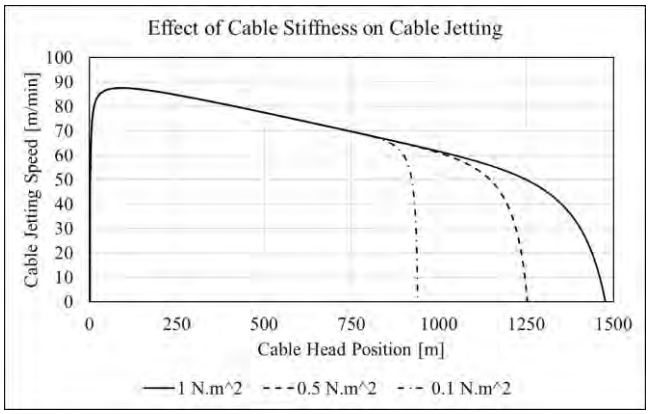


Figure 9: Effect of cable stiffness on cable jetting process

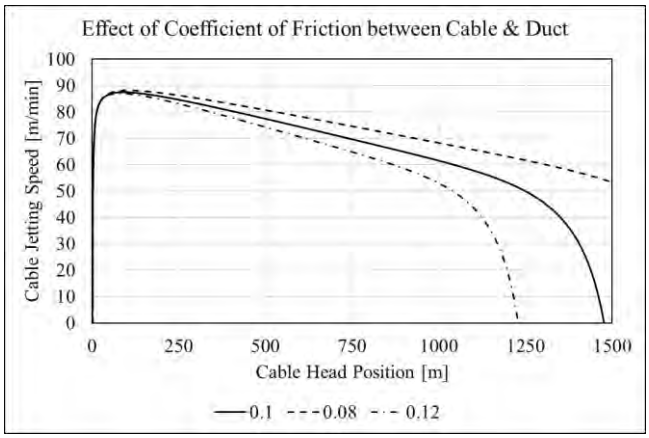


Figure 10: Effect of coefficient of friction on cable jetting process

5.2 Model Validation with Experimental Jetting Data

The cable jetting model prediction is validated with outdoor and indoor cable jetting experiments. Telcordia track with 1524 m length having four loops each having 3 bends are taken for outdoor cable experiments.

For indoor cable, a 160 m long track is chosen with several bends. The experimental jetting data was compared with modeling prediction on the same setup and jetting conditions.

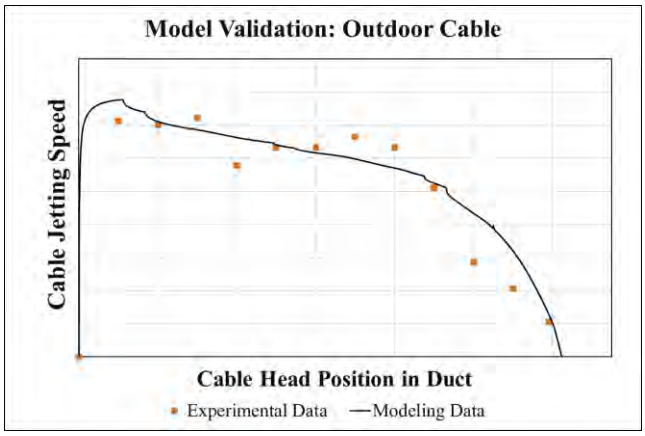


Figure 11: Model validation with outdoor cable jetting experiments

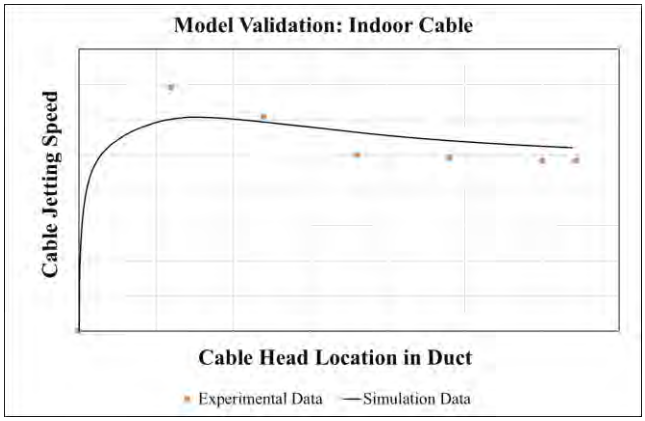


Figure 12: Model validation with indoor cable jetting experiments

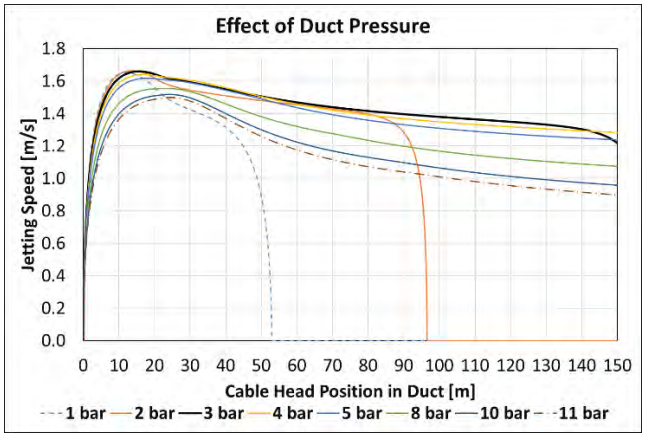


Figure 13: Effect of Duct Pressure on Cable Jetting Process

Figure 11 shows the validation of model prediction with experimental jetting data for outdoor cable. The x and y axis are the same for both experimental and simulation data for even comparison.

Similarly, the comparison of model prediction for indoor cable jetting experiments in Figure 12.

The model is found to match in good agreement with experiments and, thus, can be used to optimize cable design for achieving maximum jetting distance as well as optimizing cable jetting process parameters. An example of process optimization is shown in Figure 13. The results are for an indoor track having bends and vertical sections. The results show that the optimum duct pressure for jetting is about 3 bar. Pressure less than 3 bar is unable to jet the cable to full duct length and pressure above 3 bar is slowing the cable movement because of high back pressure force (since duct is constantly pressurized).

6. Conclusions

Cable jetting is a process of installing cable in a duct by pushing it through a capstan/caterpillar and by blowing the compressed air in the duct. Attaining a minimum jetting distance is a critical customer requirement for any cable to pass. Cable jetting is a time and resource intensive process and thus, a model to predict cable jetting performance is desirable by both cable designers and installers.

We presented a cable jetting velocity prediction model that predicts cable jetting speed as cable head moves inside duct. The model uses traditional force buildup calculation in the cable inside duct. The model estimates net external force on (cable + reel) as cable moves inside duct and predicts change in cable momentum based on that. The model also accounts for varying capstan force in the jetting machine.

The model prediction is validated with experimental jetting data and comparison is found to be in good agreement. The model can be used to optimize cable design for improved jetting performance as well as optimize cable jetting process parameters to achieve maximum cable jetting performance.

7. Acknowledgments

We thank Pushkar Tandon for sharing the learnings from his earlier cable jetting modeling work. We also thank Nikhil Vasudeo, Alan Parsons, Girish Saigaonkar for providing us with the resources to accomplish this work. We thank Zhiye Zhang for improving our cable buckling understanding. We thank Oliver Guy, Anderson Bordim, Yuxuan Zhang, Ilea Nikulin, Ting Xie, and Darwyn Cook for helping us on coding and GUI aspects of the tool.

8. References

[1.] Snippe, A., Bresser, O.R., Hoekstra, S. and Griffioen, W., 2013, November. Modelling the Pressure Profile for Optical Cables in Ducts. In 62nd International Wire & Cable Symposium, IWCS 2013.

[2.] Griffioen, W., Plumettaz, G. and Nobach, H.G., 2006. Theory, software, testing and practice of cable in duct installation. Proc. 55th IWCS, pp.357-365.

[3.] Griffioen, W. and Jonker, J., 2021, December. Guidelines for Conducting Cable Blowing Tests. In Communication Cable Networks; 28th ITG Symposium (pp. 1-7). VDE.

9. Authors



Akshay Parmar [parmara@corning.com] is a Senior Scientist at Corning Technologies India Pvt Ltd, Pune, India (Corning Research Center India). He is currently working in Corning Optical Communication (COC) department to solve flow and thermal related problems for COC products and processes through modeling.

He received dual degree (Bachelors + Masters) in Mechanical Engineering Department with specialization in Thermals and Fluids Engineering from Indian Institute of Technology Bombay (IIT Bombay) in 2017. He joined Corning in 2019.

Prior to Corning, he worked in General Motors Technical Center India where he was involved in developing system level electro-thermal models (motor-inverter-battery) for electric vehicles.

Dr. Waldemar Stoecklein [stoecklew@corning.com] is director of Material Science, responsible for global materials development within Corning Optical Communications and representative in cable related international and national standards bodies.



He joined Siemens in 1988 as a physicist and worked as a development engineer in Cable Development located in Neustadt b. Coburg in Germany. In 1992 he took over the lead of the cable evaluation laboratory in Neustadt. In 2000 Corning took over all Siemens cable activities. Since then, Stoecklein was responsible for the cable development in EMEA. After internal restructuring in 2009 he was transferred into the position of Technology Integration. Herein he was responsible for information exchange within the EMEA technology organization, coordination of training and innovation, support of cable development.

In 2012 he took over responsibility of his current position. Waldemar Stoecklein holds the degree of Dr. rer. nat. in solid state physics from University of Bayreuth. Stoecklein is an active contributor in IEC, CENELEC and DKE.

William C. Hurley [wchurley@corning.com] is a Sr. Development Associate in optical cable design at Corning Optical Communications in Hickory, N.C. His responsibilities include the design, development, and testing of both outside plant and premises cables. He received a B.S. in 1974 and M.S. in 1980 in Chemical Engineering from North Carolina State University. He joined Corning in 1996, after retiring from the United States Air Force as Director of Rocket Systems Engineering at the Air Force Ballistic Missile Office. He holds 71 patents for fiber optic cables and assemblies.



Steffen Krieger [kriegers3@corning.com] works as a development engineer in the global materials group of the Corning technology center Berlin. He is responsible for the developmental activities related to indoor jetting and the installation of micro cables. Steffen received a B.Sc. in mechanical engineering from HTW Berlin and graduated as M.Sc. in production engineering at TU Berlin in 2019. He worked as a quality engineer at BOSCH, before he joined Corning Cable Technology. Steffen has 3 years of experience in wire and cable industry, with focus on process development.



Sunil Alexander [alexandersm@corning.com] is a Program Manager for Corning Optical Communications in Wilmington, NC. His responsibilities include leading technology programs relating to optical connectivity advancements. He received a B.S. and M.Eng in chemical engineering from Cornell University in 2000 and 2001, respectively. He joined Corning in 2001 and has had a variety of roles in operations, engineering, and development.



Pre-connectorized Ultra-High-Density Cable for Easy Installation

Fumiaki Sato[1], Yutaka Hashimoto[1], Yuuki Shimoda[1], Takayuki Shimazu[1], Kenichiro Ohtsuka[1]

[1]Sumitomo Electric Industries, Ltd. 1, Taya-cho, Sakae-ku, Yokohama, 244-8588 Japan
Phone #: +81 45 853 7142, satou-fumiaki@sei.co.jp

Abstract

This paper describes a new pre-connectorized ultra-high-density optical fiber cable that has been developed to reduce installation time in data centers. The cables are made of a thin 3456-fiber optical cable and 288-fiber microduct cable consisting of 200 µm Freeform Ribbon*1 fibers. At both ends of the cable, 24-fiber connectors are assembled and precisely sealed with a protection sleeve. The result of a cable pulling test simulating actual installation confirmed that the developed 3456-fiber cable achieves the same number of optical fibers accommodated in the duct as conventional non-connectorized cables. This cable enables a reduction of connection time by using the MPO connectors instead of mass fusion splicing, and is expected to reduce installation time by about 40% compared to conventional cables. In addition, it was confirmed that the blowing test result of pre-connectorized 288-fiber microduct cable was comparable with non-connectorized 288-fiber cable, the blowing distance was achieved over 2.2km. This cable also enables a reduction of installation time by about 63% compared to conventional OSP cable by using blowing method and MMC connectors.

1. Introduction

Recently, a growing number of data centers (DCs) have been constructed around the world, mainly due to the advancement of cloud computing. In order to cope with the increase in transmission capacity, there is a growing demand for higher-density optical fiber cables connecting DCs and lower installation costs.

Cables that connect DCs are usually installed in underground ducts and the duct space is often limited. Therefore, the technology to accommodate optical fibers in a cable at high density is quite important.

Sumitomo Electric Industries, Ltd. developed and commercialized a 6912-fiber-count optical cable in 2017. This optical fiber cable comprised the highest number of fibers in any cable in the world at that time. The company also developed wiring solutions, as shown in Fig. 1, and contributed to increasing wiring density, and improving workability at entire DCs.

To reduce installation time at DCs, we have developed and commercialized a pre-connectorized 3456-fiber-count optical cable and pre-connectorized 288-fiber-count microduct cable at both ends of which multi-fiber connectors are preassembled at plants.

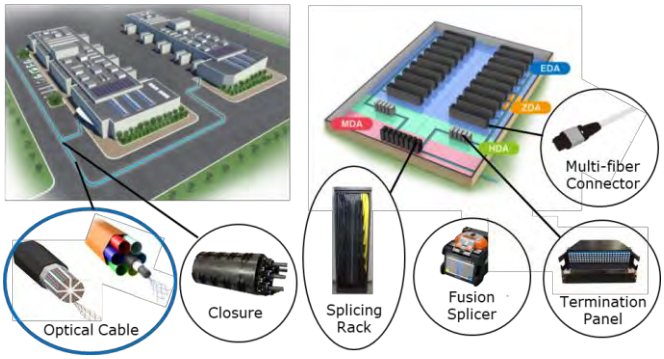


Fig. 1 Schematic diagram of DC wiring solution

2. Structure and Characteristics of Optical Fiber Cable

2.1 Structure of pre-connectorized 3456-fiber-count cable

The slotted core cable structure design has been used this time same with the conventional 250 µm 3456-fiber-count cable, which has no preference in bending direction and high flexibility because of the design that a fiber-reinforced plastic (FRP) strength member is placed at the center of the cable. The optical fibers used in the cable are 200 µm bend-insensitive single-mode fibers (SMFs) (compatible with ITU-T G.657A1 and G.652D specifications) to downsize the 3456-fiber-count cable. Fig. 2 shows a schematic cross-section of the 3456-fiber-count cable. Significant downsizing has been achieved, reducing the cable cross-sectional area by approximately 32% compared to the conventional 250µm 3456-core cable.

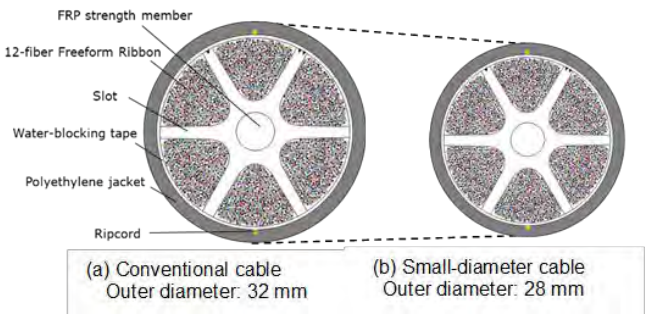


Fig. 2 Schematic cross-section of 3456-fiber-count cables

Fig. 3 shows an overview of the terminals of a pre-connectorized 3456-fiber-count cable, a connector protection sleeve, and an enclosure for connector patching (OPE). The cable is terminated by 144 pcs of 24-fiber MPO connectors and sealed with a protection sleeve with a diameter of 60 mm. To accommodate MPO connectors in the protection sleeve, MPO connectors are assembled in longitudinally shifted positions for every 12 connectors. For ease of installation, the protection sleeve is made of a spiral metal tube with resin coating as they are required to have the same level of mechanical performance as the cable, such as tensile strength, compressive strength, and waterproofing. This provides both high flexibility and tensile strength. For the connection between the protection tube and cable, a part for connecting the protection tube is crimp-fixed to the cable tension member for ease of removal after installation, and the protection tube is attached to this part. This configuration facilitates the removal of the protective tube after installation. The terminals are plugged into the MPO connectors of indoor cables at an OPE.

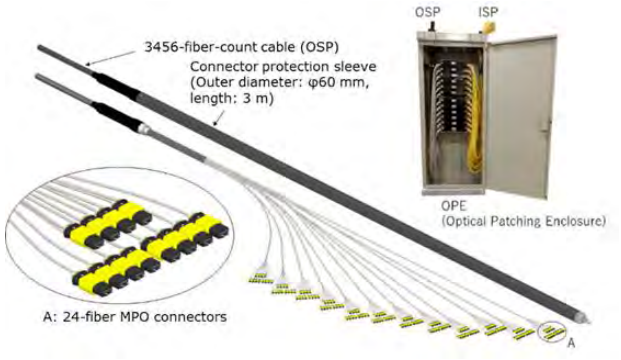


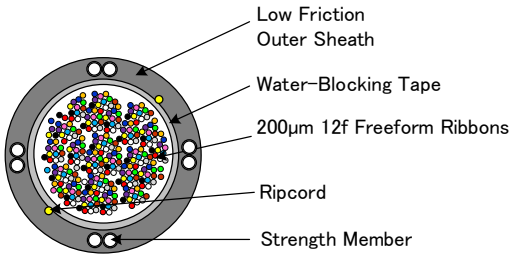
Fig. 3 Overview of pre-connectorized cable terminals and protection sleeve

2.2 Structure of pre-connectorized 288-fiber-count micro cable

In the development of microduct cables, a monotube structure was used to prioritize meeting the thin and lightweight requirements for air-blowing performance, it is shown in Fig.4. Thin strength members were distributed in the jacket to ensure adequate rigidity. This rigidity is required to prevent the cable from meandering inside the duct when the cable is pushed. Regarding the jacket material, a low-friction material was used to improve the air-blowing performance. The friction coefficient of the low-friction jacket material is about one-fourth of that of a conventional general-purpose jacket material.

Fig.5 shows the 288 micro cable terminal configurations. 12 pieces of 24F-MMC is used for the cable terminal configuration to make the diameter as thin as possible. The first connector is mounted at a position about 1.5m from the stripped cable. From the second to 12th, by mounting at a position with a step of 100 mm pitch from the position of prior connector, it is possible to store in protective sleeve with an inner diameter/outer diameter of 14/16 mm.

During installation, fiber/connector stored inside the protective tube. The protective tube is made lighter by using a resin corrugated tube. Tube and cable are assembled with a connecting part. In the case of 288 fibers, the length from the part where the cable coating is removed to the tip of the protective tube is about 3m. After installing(blowing) the cable, remove the protective tube and connect the MMC to ISP side connector at OPE.



(a) Schematic cross section of 288-fiber microduct optical cable



(b) Schematic illustration of microduct

Fig. 4 Schematic cross-section of 288-fiber-count microduct cable

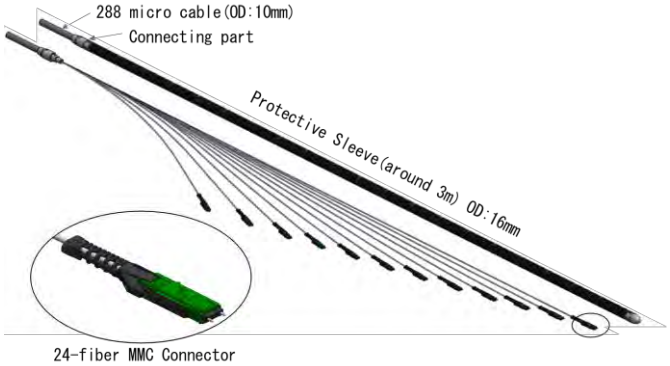


Fig. 5 Overview of pre-connectorized 288f microduct cable terminal, MMC connectors and protection sleeve

2.3 Cable characteristics

Table 1 shows the transmission characteristics and mechanical test evaluation results of the pre-connectorized 3456-fiber-count cable and the connector characteristics. Table 2 shows the evaluation results of the transmission characteristics, mechanical characteristics, and environmental characteristics of the pre-connectorized 288-fiber-count microduct cables.

As shown in Table 1 and Table 2, good characteristics were confirmed in the evaluation of various cable tests.

Table 1 Results of characteristics evaluation of pre-connectorized 3456-fiber-count OSP cable

Item	Test method	Evaluation Results
Attenuation Coefficient	IEC60793-1-40	<0.4dB/km (λ=1310nm) <0.3dB/km (λ=1550nm)
Temperature Cycling	EIA/TIA-455-4 −40/+70°C × 3 cycles, λ=1550nm	Maximum Change in Fiber Attenuation Coefficient ＜0.10dB/km
Crush Performance	EIA/TIA-455-41 2200N/100mm λ=1550nm	Maximum Change in Fiber Attenuation ＜0.1dB No visible cracks, splits, tears on the sheath
Impact Performance	EIA/TIA-455-25 4.4 N, 2 drop impacts λ=1550nm	
Repeated Bending	EIA/TIA-455-104 Bend radius: 10 × D, 25 cycles (D: cable outer diameter) λ=1550nm	
Torsion	EIA/TIA-455-85 ± 180° /2m,λ=1550nm	
Tensile Strength	EIA/TIA-455-33 During installation: 2,670 N, after installation: 800 N	Fiber strain with 2,670 N: less than 0.2% Fiber strain with 800 N: 0.1% or less
Connection loss of 24f MPO	λ=1310nm	＜0.35dB
Return loss of 24f MPO	λ=1310nm	＞55dB

Table 2 Results of characteristics evaluation of pre-connectorized 288-fiber-count microduct cable

Item	Test Method	Evaluation Result
Attenuation Coefficient	IEC60793-1-40 λ=1550nm	<0.30dB/km
Temperature cycling	IEC60794-1-22-F1 -30～+70℃, 2cyc. λ=1550nm	Loss variation <0.3dB/km
Compresive Loading	IEC60794-1-21-E3 1000N/100mm λ=1550nmm	Loss variation <0.1dB No faulty condition in cable appearance
Impact Test	IEC60794-1-21-E4 2.5N·m, 2drop impacts λ=1550nm	
Cyclic Flexing	IEC60794-1-21-E6 Bending radius 20D, 25 cycles ("D" denotes the outer diameter of the cable.) λ=1550nm	
Cable Twist Test	IEC60794-1-21-E7 ±180°, Tension 100N λ=1550nm	
Long Tensile Loading and Fiber Strain Test	EIA/TIA-455-33 Tension : 1334N	≤ 60% of fiber proof level

3. Installation Workability of pre-connectorized 3456 fiber-count cable

3.1 Experiments of pulling into a duct

Using the developed pre-connectorized 3456-fiber-count cable, we conducted experiments of pulling the cable into a duct to check the installation workability. Photo 1 shows the route for the experiments. The duct used in the experiments had an inner diameter of 4 inches. The route had an overall length of 100 m, three 90° curves, and a 180° turn.

The results of the pulling experiments using a conventional 3456-fiber-count cable and a newly developed pre-connectorized 3456-fiber-count cable are shown in Table 3.



Photo 1. Overview of the route for experiments of pulling a 3456-fiber-count cable into a duct (Map data ©2022 Google)

We used the developed pre-connectorized 3456-fiber-count cable as the third cable under Condition A, and confirmed that the cable could be installed with a pulling tension equivalent to that required for installing a conventional cable under Condition B.

Table 3 Results of experiments of pulling a 3456-fiber-count cable into a duct

Experiment conditions	Installation cable	Installation result
Condition A: Two conventional 3456-fiber-count cables + One pre-connectorized 3456-fiber-count cable	First cable (Conventional)	Pass (Pulling tension: 9 kg)
	Second cable (Conventional)	Pass (Pulling tension: 12 kg)
	Third cable (Pre-connectorized)	Pass (Pulling tension: 16 kg)
Condition B: Three conventional 3456-fiber-count cables (Reference)	First cable (Conventional)	Pass (Pulling tension: 12 kg)
	Second cable (Conventional)	Pass (Pulling tension: 14 kg)
	Third cable (Conventional)	Pass (Pulling tension: 15 kg)

3.2 Durability evaluation of terminated protection sleeve

To evaluate the durability of the protection sleeve for a pre-connectorized 3456-fiber-count cable, we repeatedly installed a cable into a 4-inch duct and checked the damage to the protection sleeve.

Photo 2 shows the appearance of the protection sleeve after 30 times installations along a 100 m route.

It was confirmed that there was no problem with the durability of the protective tube even under the severe conditions of 30 repeated installations.



Photo 2. Appearance of the protection sleeve for a pre-connectorized 3456-fiber-count cable after a durability test

3.3 Comparison of installation days

We estimated the efficiency in the reduction of installation work time when using pre-connectorized 3456-fiber-count cables. Fig.6 shows the results of a comparison of the number of installation days required to complete the connection of three 3456-conductor cables through a 4-inch pipe.

As shown in Fig. 6, the use of pre-connectorized 3456-fiber-count cables is expected to drastically reduce the termination time by replacing the fusion splicing with connector plugging. As a result, approx.40% reduction in installation time compared to conventional 3456-fiber-count cables can be expected.

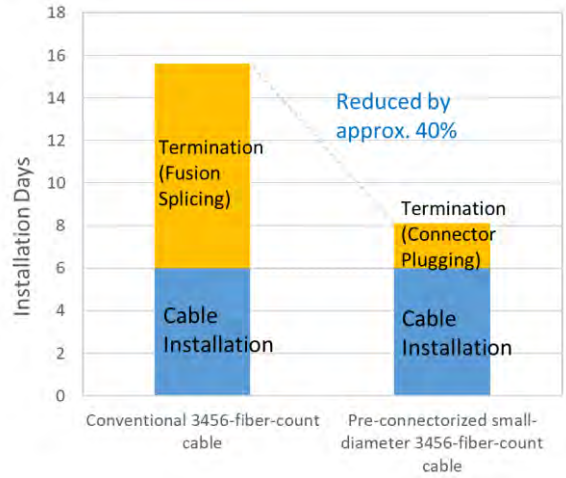


Fig. 6 Comparison of the number of days required for installation of 3456-fiber-count cables

4. Installation Workability of pre-connectorized 288 fiber-count micro cable

4.1 Cable blowing test

Using blowing equipment "MiniJet" manufactured by the Swiss cable blower manufacturer Plumettaz S.A., the blowing performance of the newly developed pre-connectorized 288-fiber-count microduct cable was evaluated. Photo 3 shows the cable blower used in the blowing test. The duct used in the experiments had an inner diameter of 18mm. The test route had an overall length of 2,200 m, the circuit length was 500m that has eight 90° curves, and two 180° turns in Fig.7.

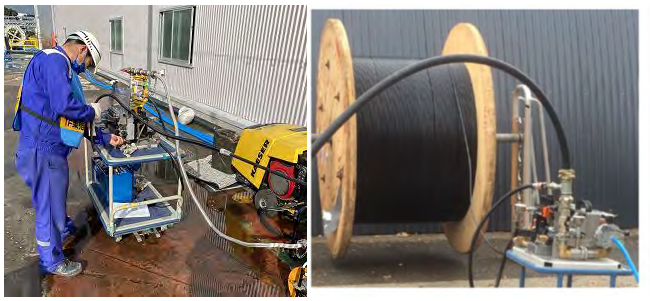


Photo 3. Cable blower used in blowing test

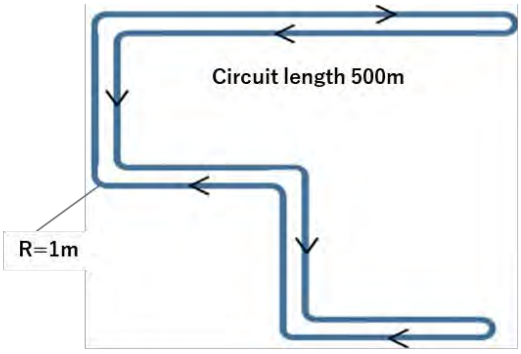


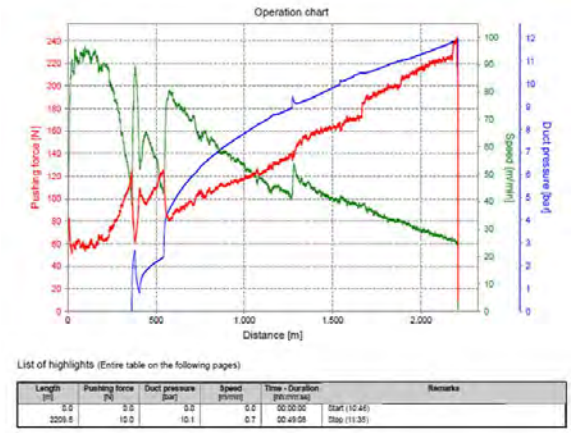
Fig. 7 Air-blowing test circuit

The results of the blowing tests using a newly developed pre-connectorized 288-fiber-count microduct cable and non-connectorized 288-fiber-count microduct cable are shown in Table 4 and Fig.8.

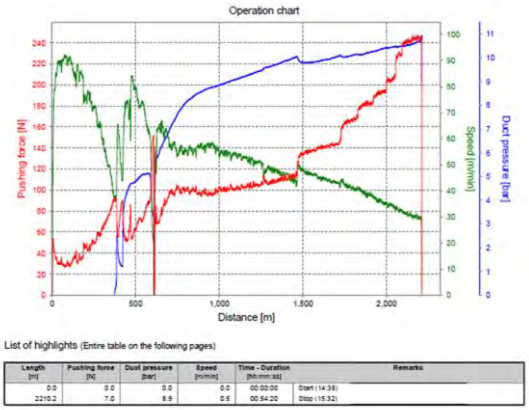
We confirmed that the blowing performance of the developed pre-connectorized 288-fiber-count cable was equivalent to that of non-connectorized 288-fiber-count cable, both cables show excellent blowing property.

Table 4 Blowing test results

Cable sample	Blowing Distance (Blowing time)
Pre-connectorized 288-fiber-count microduct cable	2,210m (49 min.)
Non-connectorized 288-fiber-count microduct cable (Reference)	2,210m (54 min.)



(a) Pre-connectorized 288-fiber-count microduct cable



(b) Non-connectorized 288-fiber-count microduct cable

Fig. 8 Jetting Report of the blowing test

4.2 Comparison of installation days

We estimated the efficiency in the reduction of installation work time when using pre-connectorized 288-fiber-count microduct cables. It was compared that the number of installation days were required to complete the connection of ten 288-fiber-count cables through a 4-inch that is shown in Fig.9.

As shown in Fig. 10, the use of pre-connectorized 288-fiber-count cables is expected to drastically reduce the cable installation time by blowing method and to reduce the termination time by replacing the fusion splicing with connector plugging. As a result, approx.63% reduction in installation time compared to conventional 288-fiber-count cables can be expected.

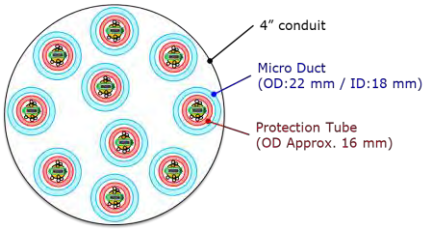


Fig. 9 Schematic diagram of ten 288-fiber-count microduct cable in a 4-inch duct.

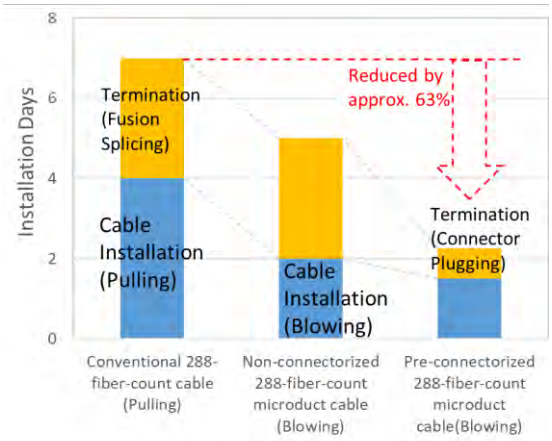


Fig. 10 Comparison of the number of days required for installation of 288-fiber-count cables

5. Conclusions

We have developed and commercialized a pre-connectorized 3456-fiber-count optical cable with MPO connectors on both ends for DC applications. This cable can save connection time by using connectors instead of time-consuming mass-fusion splicing, and is expected to reduce cable installation time by approximately 40% compared to the use of conventional cables.

We also have developed a pre-connectorized 288-fiber-count optical cable with MMC connectors on both ends for DC applications. This cable can save installation time by blowing method and save connection time by using connectors instead of time-consuming mass-fusion splicing, and is expected to reduce cable installation time by approximately 63% compared to the use of conventional cables.

6. Acknowledgments

The authors will express gratitude to all the people who cooperated in the completion of this paper.

7. References

[1] F. Sato, et al., “Ultra-High-Fiber-Count and High-Density Slotted Core Cable with Pliable 12-Fiber Ribbons,”, Proceedings of the 65th IWCS Conference, 2016 (14-5).

[2] F. Sato, et al., “Designs and Characteristics of New UHFC Cables with Freeform Ribbons,”, Proceedings of the 67th IWCS Conference, 2018 (10-3).

[3] F. Sato, et al., “New HFFC cable solution with free form ribbons for easy installation,”, Proceedings of the 69th IWCS Conference, 2020 (6-2).

[4] F. Sato, et al., “Ultra-High-Fiber-Count and High-Density Slotted Core Cable with Pliable 12-Fiber Ribbons,”, SEI Technical Review, No. 83, 2016.

[5] F. Sato, et al., “Ultra-High-Fiber-Count Optical Cable for Data Center Applications,”, SEI Technical Review, No. 86, pp. 45-50, 2018.

[6] E. Fallahmohammadi, et. al., “Ultra-High Fiber Count Cable with 6912f FlexRibbon™ in RILT Design”, Proceedings of the 68th IWCS Conference, 2019.

[7] E. A. Stupca, et al., “Innovative Solutions for High Density Cables Incorporating Conventional Ribbons”, Proceedings of the 68th IWCS Conference, 2019 (11-2).

[8] L.A. Dixon, et al., “Crush and Bending Resistance in Next-Generation Cable Designs”, Proceedings of the 50th IWCS Conference, 2001.

[9] H.P. Debban, Jr., et al., “Development of Central Core Cables Optimized for Small Coil Diameter Incorporating Rollable Ribbon Units”, Proceedings of the 68th IWCS Conference, 2019.

[10] T. Yasutomi, et al., “Development of 6912F Ultra-high Density Optical Cable with 200 micron Fiber Rollable Ribbon”, Proceedings of the 67th IWCS Conference, 2018.

[11] M. Ono, et al, “Development of Ultra-High Density and Fiber-Count WTC with SWRInnovative Solution Using SWR/WTC for Data Centers”, Proceedings of the 66th IWCS Conference, 2017.

[12] S. Kaneko, et al, “Innovative Solution Using SWR/WTC for Data Centers”, Proceedings of the 67th IWCS Conference, 2018.

8. Pictures of Authors

Fumiaki Sato

Sumitomo Electric Industries, Ltd.
1, Taya-cho, Sakae-ku,
Yokohama, 244-8588
Japan

E-mail:
satou-fumiaki@sei.co.jp



Fumiaki Sato received his M.E. degrees from Tohoku University in 2000. He joined Sumitomo Electric Industries, Ltd. in 2000 and he has been engaged in design and development of optical fibers and cables since then. He is a group manager of data center optical cable engineering group in optical fiber and cable division.

Yutaka Hashimoto

Sumitomo Electric Industries, Ltd.
1, Taya-cho, Sakae-ku,
Yokohama, 244-8588 Japan

E-mail:
hashimoto-yutaka@sei.co.jp



Yutaka Hashimoto received his M.E. degrees from Yokohama National University in 2003. He joined Sumitomo Electric Industries, Ltd. in 2003 and he has been engaged in design and development of optical fibers and cables since then. He is an assistant generall manager of data center optical cable engineering group in optical fiber and cable division.

Yuuki Shimoda

Sumitomo Electric Industries, Ltd.
1, Taya-cho, Sakae-ku,
Yokohama, 244-8588
Japan

E-mail:
yuuki-shimoda@sei.co.jp



Yuuki Shimoda received his M.S. degrees from Osaka University in 2001. He joined Sumitomo Electric Industries, Ltd. in 2001 and has been engaged in engineering and development of optical fibers and cables since then. He is a project manager of data center optical cable engineering group in optical fiber and cable division.

Takayuki Shimazu



Sumitomo Electric
Industries, Ltd.
1, Taya-cho, Sakae-ku,
Yokohama, 244-8588
Japan

E-mail:
takayuki-shimazu@sei.co.jp

Takayuki Shimazu received his M.E. degrees from Kansai University in 1998. He joined Sumitomo Electric Industries, Ltd. in 1998, and has been engaged in development of optcal fibers and fiber optic devices since then. He is a senior assistant general manager of DC products marketing & engineering department.

Kenichiro Ohtsuka



Sumitomo Electric
Industries, Ltd.
1, Taya-cho, Sakae-ku,
Yokohama, 244-8588
Japan

E-mail:
ohtsuka-kenichiro@sei.co.jp

Kenichiro Ohtsuka received his M.E. degree from Tohoku University in 1994. He joined Sumitomo Electric Industries, Ltd. in 1994, and has been engaged in the development of optical connectors. He is a general manager of DC products marketing & engineering department.

Fundamental Study of Planar Closure for Wiring on-road Surface

Shun Kobayashi, Takashi Matsuo, Yasuhiro Maehara

and Yusuke Yamada

NTT Access Network Service Systems Laboratories, NTT Corporation,
1-7-1 Hanabatake, Tsukuba, Ibaraki, 305-0805 Japan
+81 20 868 6331, E-mail: zh.kobayashi@ntt.com

Abstract

We have developed a planar closure to be placed on the road surface for the branch and connection of cables utilized in on-road surface wiring.

The results of evaluations using the fabricated closure showed that it meets the requirements for fiber storage, clash, impact, and water jets.

Keywords: Planar closure, optical fiber cable, on-road, cable wiring

1. Introduction

As the demands for optical fiber continue to diversify, including those for applications to IoT, it has also become necessary to meet the demand for 5G base stations. Therefore, optical fiber cables need to be laid more quickly and at a lower cost in urban areas without utility poles where cables are laid underground and in rural areas without civil engineering or utility poles. For this purpose, there is a method for laying cables on road surfaces utilizing optical fiber cables with a small diameter and high strength [1]. However, to provide effective communication services, not only cables but also a closure for the cable branch and connection point is required, as shown in Fig. 1. To meet this need, we developed a planar closure to be placed on-road surface and performed evaluations to determine whether it satisfies the requirements.

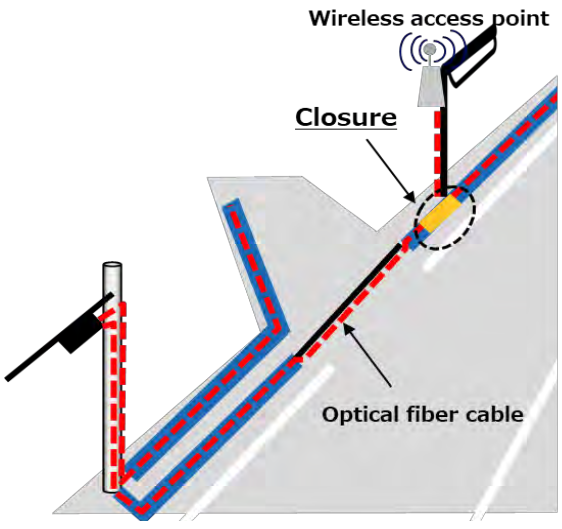


Figure 1. Image of closure placed on- road surface

2. Requirements of closure

The requirements of the closure for wiring on-road surface are listed in Table 1. We assume that the closure is set by digging into the surface of the road. First, the most essential function of the closure is that it be able to store connected or unused fibers. The number of fibers is set to 40, taking into account optical fiber cables for wiring on-road surface [1]. In addition, the closure must be as planar as possible so that the minimum road damage and stable grip of cables in trench can be done. Therefore, a thickness of about 10 mm is required for the closure. In terms of mechanical strength, the requirement for clash is set to 1.0 N/mm2 in order to withstand external forces by vehicles, assuming load on one wheel of a vehicle with a weight of 25 tons. It is also necessary to withstand impact from falling objects such as luggage, so the requirement for impact is set to 15 J , assuming 15 kgf falling from 1 meter. Finally, IPX5 was chosen for water protection to prevent water jets during rainfall from leaking into the closure.

Table 1. Requirements of planar closure for wiring on-road surface

Item	Requirement	Reason
Fiber storage capability	40 fibers (Storage splice sleeve and excess length of fibers)	Maximum number of fibers of the cable [1]
Thickness	less than about 10 mm	For minimum road damage and stable grip of cables in trench
Clash	1.0 N/mm^2 (Load on one wheel of a vehicle with a weight of 25 tons)	Assuming heavy vehicle traffic
Impact	15 J (15 kgf falling from 1 meter)	Assuming impact of falling luggage
Water jets	IPX5, IEC 60529	Expect water jets during rainfall on-road surface

3. Structure

The structure of the closure is based on the requirements shown in Fig. 2. It has a metallic frame and a two-layer fiber storage tray, where the upper tray is used for storing retained fibers and the lower tray for storing connected fibers. There is a two-column structure inside the frame to improve its strength against clash or impact from above. Gaskets are utilized for the opening and closing parts and cable insertion holes to ensure water protection. In addition, screw holes are provided to fix the closure to the road surface. The size of the fabricated closure is 290 mm wide, 115 mm deep, and 14.5 mm high.

We evaluated the closure to determine whether it satisfies the requirements of fiber storage, clash, impact, and water jets.

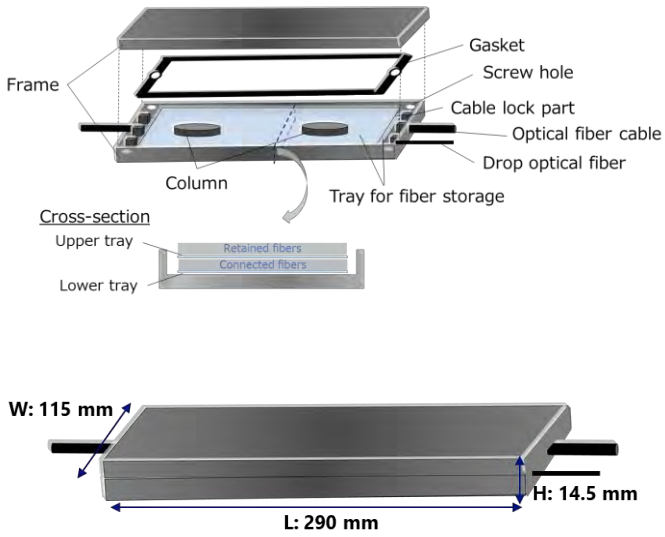


Figure 2. Structure of the planar closure

4. Evaluation

4.1 Fiber storage

As the evaluation model for the fiber storage, a 40 fibers optical fiber cable was inserted through the closure. Four fibers were spliced together with the drop optical fiber and stored in the lower tray, and 36 non-spliced fibers were stored in the upper tray, as shown in Fig. 3. Fiber storage was done using the process shown in Fig. 4. The optical loss change of the 40 stored fibers measured at a wavelength of 1.55 μm before and after the storage procedure was less than 0.1 dB/fiber. The state of the fiber storage after the procedure is shown in Fig. 5. These findings indicate there is no problem with the fiber storage even if the storage density in the closure is increased because the closure is so planar.

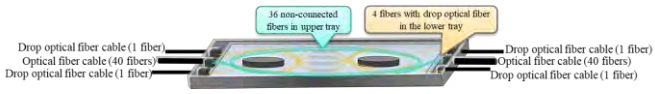


Figure 3. Evaluation model for fiber storage

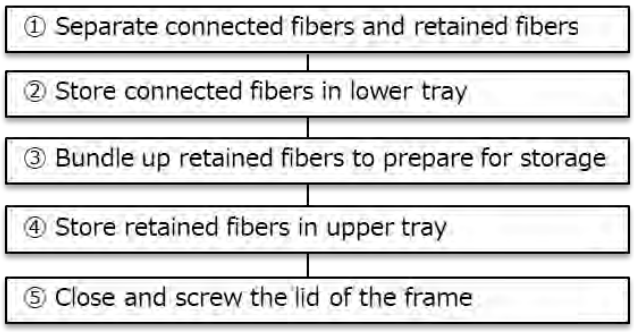
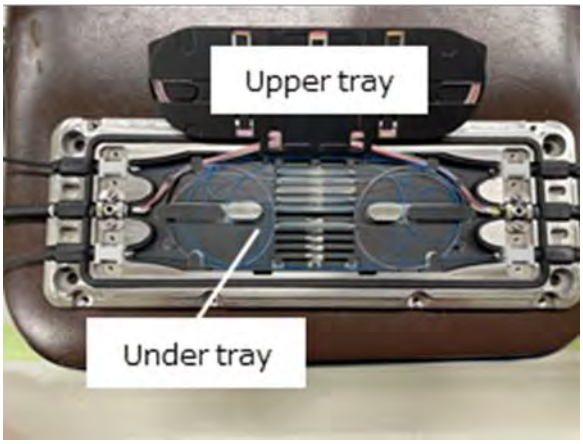


Figure 4. Fiber storage process



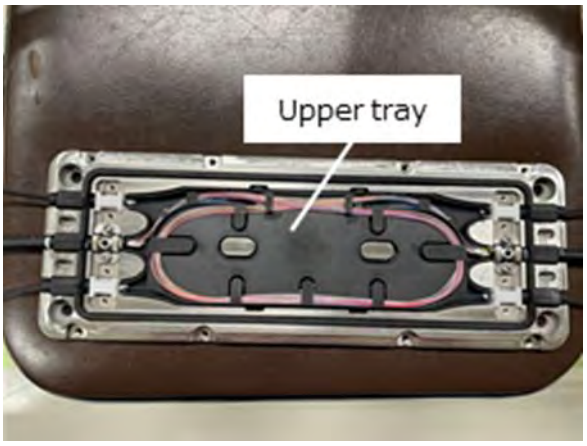


Figure 5. Structure of the two-layer tray

4.2 Clash

For evaluation of the clash characteristics, a load of 1.0 N/mm^2 was applied to the center or 5 cm from the edge (on the column) of the closure (as shown in Fig. 6) to check whether the column structure is effective for strength improvement and the strength of the column itself. The load was applied for 10 min and then we checked for damage and cracks in the frame. Before applying the 1.0 N/mm^2 load, the closure was exposed to temperatures of –30, 20, and 70° C for 1 hour assuming the environment for placing. Table 2 shows the results. As we can see, no damage or cracks are visible in the frame under any condition.

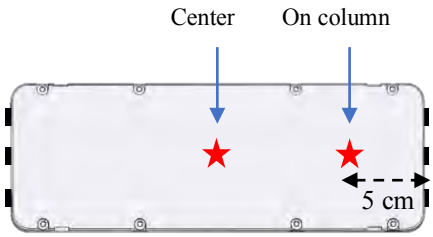


Figure 6. Load application points

Table 2. Results of clash evaluation

Temperature	Load (1.0 N/mm^2)	
	Center	5 cm from the edge
–30 °C	No damage or cracks	No damage or cracks
20 °C	No damage or cracks	No damage or cracks
70°C	No damage or cracks	No damage or cracks

4.3 Impact

For evaluation of the impact, a 15-kg weight was dropped on the center or 5 cm from the edge of the closure (same as in the clash evaluation) from a height of 1 m (15 J). Before applying impact, the closure was exposed to temperatures of –30, 20, and 70° C for 1 hour assuming the environment for placing. Table 3 shows the results. As we can see, no damage or cracks are visible in the frame. These findings demonstrate that there is no problem with the mechanical strength of the closure.

Table 3. Results of impact evaluation

Temperature	Impact (15 J)	
	Center	5 cm from the edge
-30 °C	No damage or cracks	No damage or cracks
20 °C	No damage or cracks	No damage or cracks
70°C	No damage or cracks	No damage or cracks

4.4 Water jets

For evaluation of the water protection, the closure was submerged for 30 min at a depth of 50 cm with and without cables inserted. The detailed conditions of the cable insertion are shown in Fig. 7. In the case of no cable insertion, plugs were placed in the cable insertion holes. After submersion, there was no water penetration inside the closure under any conditions. These findings demonstrate that the closure can withstand water jets during rainfall.

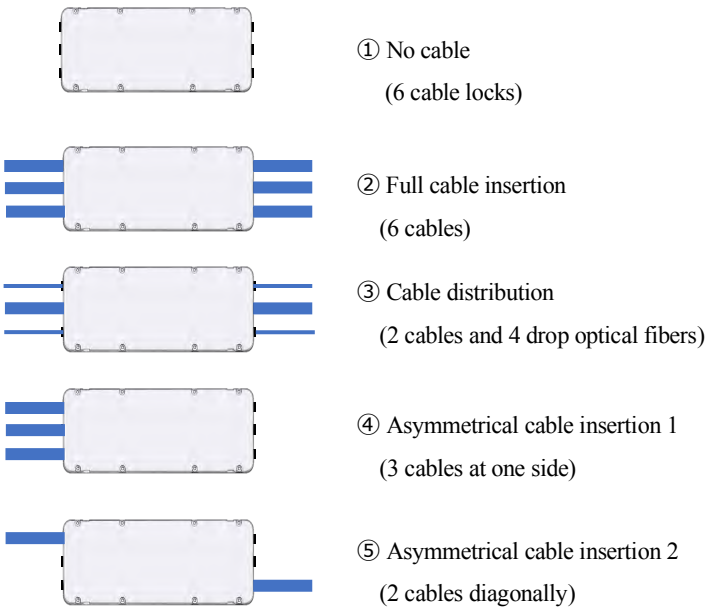


Figure 7. Conditions of cable insertion

5. Conclusion

We developed a planar closure for wiring on-road surfaces used as a cable branch and connection point and then examined its structure to determine whether it satisfies the fiber storage, clash, impact, and water jets requirements. The results using a fabricated closure demonstrated that each requirement was sufficiently met.

6. References

[1] Sakurai et al., IWCS2021 14-1

7. Authors



Shun Kobayashi

In 2014, he joined NTT, where he has been engaged in the development of optical cable. He is currently a Research Engineer at NTT Access Network Service Systems Laboratories.



Takashi Matsuo

In 2006, he joined NTT, where he has been engaged in the development of optical cable. He is currently a Senior Research Engineer at NTT Access Network Service Systems Laboratories.



Yasuhiro Maehara

In 1995, he joined NTT, where he has been engaged in the development of optical cable. He is currently a Senior Research Engineer at NTT Access Network Service Systems Laboratories.



Yusuke Yamada

In 2005, he joined NTT Access Network Service Systems Laboratories, Ibaraki, Japan, where he has been engaged in research on the optical fiber cable. He has been contributing to the activity of IEC SC86B in 2013–2014 and IEC SC86A since 2017. He is currently a senior research engineer, supervisor with NTT Access Network Service Systems Laboratories. He is also a member of the Institute of Electronics, Information, and Communication Engineers (IEICE) of Japan. He received the Best Paper Award at the 12th OptoElectronics and Communications Conference (OECC) / International Conference on Integrated Optics and Optical Fiber Communications (IOOC) in 2007.

Study of easy thin optical fiber cabling method

[1)]*Keitarou Yoshida** , [2)]*Tomoya Shiraishi* , [1)]*Takeshi Sawa* , [1)]*Osamu Sasaki*

[1)]Strategic Network Management Department, NTT East Corporation

[2)]Network Design Department, NTT West Corporation

19-2 Nishi-shinjuku, 3-chome, Shinjuku-ku, Tokyo, 163-8019, Japan

+81 3 5359 4450 keitarou.yoshida@east.ntt.co.jp

*Corresponding Author

Abstract

In this article, we propose a simplified cabling method by utilizing the new suspension hardware designed for thin optical fiber cables. The new suspension hardware for thin optical fiber cables adopts a wedge structure, and it can be optimized for the target cable by adjusting the length of the wedge, inclination taper angle of the wedge, and the shape of the cable gripping part.

As a result, cable laying, sag adjustment, and fixing work can be significantly simplified compared to traditional methods. Furthermore, lowering the ground clearance allows for safer cable laying from the ground level. (In Japan, a ground clearance of 2.5 meters is allowed in areas where vehicle traffic is prohibited, such as private properties.)

Keywords: suspension hardware; safer cable installation; cabling method; thin optical fiber cables; low-cost;

1. Introduction

NTT's FTTH service has been expanding its number of subscribers year by year and covers a large part of Japan's areas. [*1]

[*1] For instance, NTT East's FTTH service had 12 million subscribers and achieved an optical coverage rate of 96.9% as of 2021.

In recent years, the maturity of peripheral technology has resulted in increased demand for agricultural IoT and the construction of mobile networks such as 5G and 6G. As a result, demands have emerged to meet these needs even in areas where FTTH services were previously considered Ill-fated investment recovery. There is an increasing need for low-cost cable laying methods for this reason.

2. Conventional overhead cabling methods and issues

NTT has established standard construction methods for cable construction in order to achieve high-quality communication services. When laying cables in aerial sections, they utilize high-altitude vehicles to pull the cables up to a height of around 5-6 meters, then fix them in place using metal fixtures. The cable installation requires highly skilled personnel due to its complexity and involves multiple work processes, leading to the need for a team of workers and incurring substantial operational costs. Additionally, construction work involves working at heights, which poses risks.

To achieve low-cost cable installation, it is necessary to simplify the required skills for cable laying and reduce the number of work processes. (Figure 1)

3. Efforts on The New suspension hardware for thin optical fiber cables

3.1 Study on achieving simplified laying

In this section, as a low-cost and simple laying method for aerial sections, we propose a new suspending hardware for thin optical fiber cables using a wedge structure that can be fixed by manually pulling the optical fiber cable from the ground and releasing the hand. (Figure 2, Figure 3)

The study of the new hardware focused on thin and lightweight optical fiber cables, and formulated the required specifications. [*2] (Figure 4) [1-2]

[*2] We selected two types of optical fiber cables (A cable and B cable) with different support wire and outer diameter as the target for the new hardware.

- A cable: A structure with a support wire of 1.2 mm in diameter, and the height of the outer diameter is about 6.5 mm.

- B cable: A structure with a support wire of 2.6 mm in diameter, and the height of the outer diameter is about 10.5 mm.

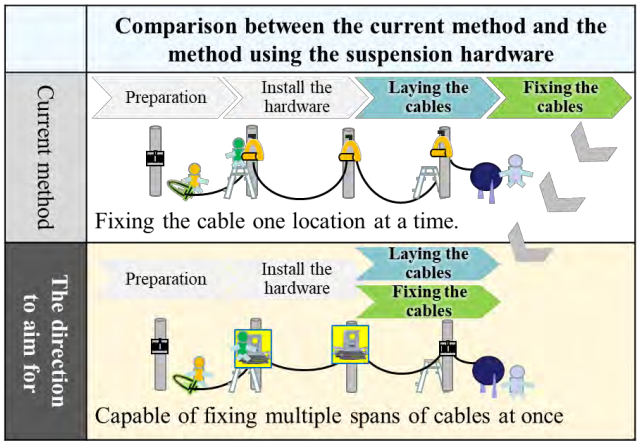


Figure1. The direction to aim for.

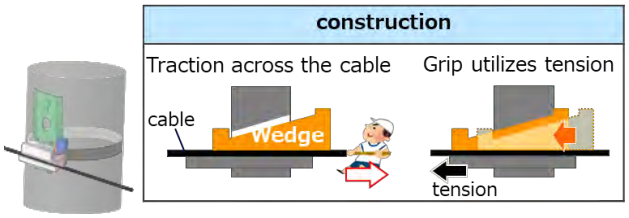


Figure2. The new suspension hardware and wedge structure



Figure3. Construction method



Figure 4. Targeted optical fiber cables

3.2 Requirements Specification for The New suspension hardware

The new suspension hardware specifications include requirements for the gripping force considering wind pressure load and stipulate that there should be no occurrence of microbending loss when gripping the cable. *3

Additionally, the design was studied to ensure smooth sliding of the cable during traction.

*3 The adoption of a structure that directly grips and secures the optical fiber cable using a wedge necessitated the establishment of regulations to ensure communication reliability.

3.2.1 The gripping force requirements

In this section, we will outline the gripping force requirements for the proposed system. The gripping force refers to the ability of the hanger to securely hold and fix the optical fiber cable in place. To ensure the reliability of communication, it is crucial to define specific the gripping force specifications that consider factors such as wind pressure load and potential external forces acting on the cable. These requirements will guarantee a stable and dependable installation of the optical fiber cables using the wedge-based hanger.

The gripping force required for the new hanger will be based on the tension during both calm weather conditions (no wind) and windy conditions. Generally, outdoor installations use the tension during windy conditions as the reference point for determining the gripping force. This approach ensures that the hanger can securely hold and fix the optical fiber cable even under adverse weather conditions, providing a robust and reliable solution for outdoor installations.

Additionally, since the new hanger is expected to secure the cable over multiple spans, it must not only withstand the tension of a single span but also be able to withstand the tension difference that occurs across multiple spans. This requirement ensures that the hanger can effectively handle the varying tension levels and provide reliable support for the optical fiber cable throughout its entire length, guaranteeing a stable and durable installation over the entire span. (Figure5)

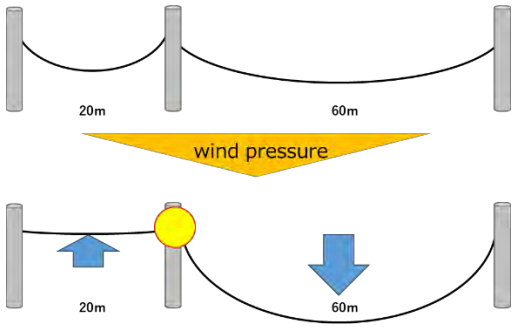


Figure5. The tension difference that occurs across multiple spans

Taking these factors into account, the calculated tension for the targeted optical fiber cable. (Table1,Table2)

Table1. A cable

A cable load difference		distance(m)								
		20	25	30	35	40	45	50	55	60
SAG		0.07	0.11	0.17	0.22	0.29	0.37	0.46	0.56	0.66
vertical load	[N]	210.0	208.8	194.6	204.6	202.8	201.1	199.7	198.5	200.5
Wind load	[N]	640	720	790	860	930	990	1050	1100	1160
load difference	[N]		80	150	220	290	350	410	460	520

first distance \ Second distance	20	25	30	35	40	45	50	55	60
20		80	150	220	290	350	410	460	520
25			70	140	210	270	330	380	440
30				70	140	200	260	310	370
35					70	130	190	240	300
40						60	120	170	230
45							60	170	230
50								50	110
55									60
60									

Table2. B cable

B cable load difference		distance								
		20	25	30	35	40	45	50	55	60
SAG		0.07	0.1	0.15	0.2	0.27	0.34	0.42	0.5	0.6
vertical load	[N]	490.0	535.9	514.5	525.2	508.1	510.7	510.4	518.8	514.5
Wind load	[N]	1570	1760	1910	2060	2190	2330	2460	2590	2710
load difference	[N]		190	340	490	620	760	830	1020	1140

first distance \ Second distance	20	25	30	35	40	45	50	55	60
20		190	340	490	620	760	830	1020	1140
25			150	300	430	570	640	830	950
30				150	280	420	490	680	800
35					130	270	340	530	650
40						140	210	400	520
45							130	260	380
50								130	310
55									120
60									

Based on the calculation results, the criteria for the required the gripping force of the new hanger are as follows.

The gripping force: A cable:520Nm, B cable:1140Nm

3.2.2 The microbending loss requirements

In this section, we will outline the requirements specification for preventing the microbending loss in the new hanger. The microbending loss refers to the phenomenon where optical fibers experience small-scale bending or deformation at the gripping points, potentially leading to signal loss or attenuation.

To ensure optimal performance, the hanger's design must minimize any strain or stress on the optical fiber cable during installation and operation. It is essential to establish specifications that prevent the occurrence of the microbending loss while securely holding and fixing the optical fiber cable.

By meeting these requirements, the new hanger will contribute to maintaining the signal quality and reliability of the optical communication system, ensuring seamless data transmission and communication performance.

The new hanger adopted a direct grip and fixation approach for the targeted optical fiber cable body. Previously, NTT used a method that only fixed the cable's support lines when securing the optical fiber cable, and there was no existing method for directly securing the optical fiber cable body. As a result, the required the microbending loss for the new hanger's fixation was approached from a different perspective, breaking away from the conventional thinking used for the previous hangers. This new approach was necessary to address the unique challenges posed by directly gripping and securing the optical fiber cable body, ensuring minimal the microbending loss and maintaining signal integrity for reliable communication performance.

In NTT's telecommunication equipment, direct grip and fixation of the optical fiber cable are currently limited to aerial optical closures. [3] For these aerial optical closures, the microbending loss of 0.1dB is specified when gripping the optical fiber cable. This specification ensures the provision of high-quality communication services even when multiple optical closures are installed between the exchange equipment and customers' homes.

The new hanger for the targeted optical fiber cable requires significantly higher the gripping force compared to the optical closure's the gripping force. However, to maintain the provision of high-quality communication services, we have decided to adopt the same the microbending loss specification as the aerial optical closure. [*4] Therefore, the criteria for the required the microbending loss for the new hanger are as follows.

The microbending loss: 0.1dB

[*4] The criteria for the required the gripping force of aerial optical closures for the targeted optical fiber cable is set to be approximately 200 Nm.

3.3 Wedge Structure Design for Thin Optical Fiber Cable Hanger

In this section, we will discuss the design of the wedge structure for the thin optical fiber cable hanger. We conducted investigations on the items listed in Table3 and performed multiple trial patterns to determine the final shape.

Table3. The new suspension hardware wedge structure examination items for thin optical fiber cables

No	Items to consider
1	Taper angle of the wedge
2	Length of the wedge
3	Shape of the cable gripping part
4	Wedge optimization

3.3.1 Study of Taper angle of the wedge

In the consideration of the wedge shape,we started by selecting the taper angle of the wedge. For the taper angle selection, we evaluated different angles of the wedge (ranging from 3 degrees to 6 degrees with a 1-degree increment). The evaluation was based on two main criteria Wedge trackability to the targeted optical fiber cable and Ease of installation during construction.

At this stage of the study, the final shape of the hanger was yet to be determined. Therefore, we conducted evaluations based on "trackability" to the cable, which will contribute to improving the gripping force in the future, and "ease of installation" to securely fix the cable without undue complications. The evaluations were not based on the specified criteria, but rather on practical considerations to ensure the hanger's effective performance and ease of use in real-world installations.

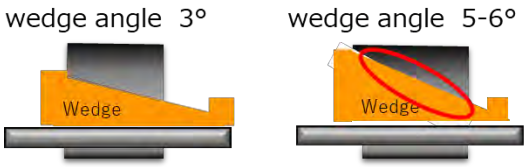


Figure6. Taper angle of the wedge

Table4. The verification results of Taper angle

Taper angle	Wedge trackability	Ease of installation
3°	good	poor[*6]
4°	good	good
5°、6°	poor[*5]	good

[*5] Significantly inferior to the performance of 3°4°

[*6] Optical fiber cable cannot be fixed

The verification results, as shown in Table 4, confirmed that the taper angle of 4 degrees exhibited the best trackability to the targeted optical fiber cable and provided excellent ease of installation during construction.

3.4 Study of Length of the wedge

In the following step, we conducted an investigation regarding the length of the wedge. For this study, we used samples with different lengths to confirm the optimal length.

The investigation of the wedge length began with a length of 52mm. This length corresponds to the minimum unit with sufficient space to secure the thin optical fiber cable, as determined in the previous consideration of the wedge taper angle (3.3.1). From there, we evaluated lengths at 4mm intervals, namely 56mm and 60mm.

During the evaluation, we focused on understanding the relationship between the gripping force of the cable at different wedge lengths, and we carefully examined the results to determine the most suitable length for effectively securing the thin optical fiber cable.

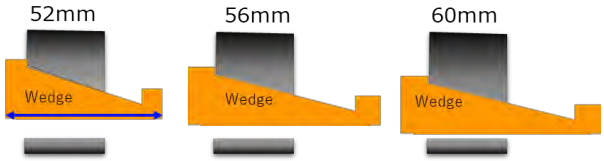


Figure7. Length of the wedge

The verification results, the relationship between the gripping force and the wedge lengths is as follows:

The gripping force Relationship: 52mm < 56mm < 60mm

From the above data, it has been confirmed that as the wedge length increases, the gripping force improves. The longer wedge length provides a more secure grip, ensuring effective fixation of the thin optical fiber cable.

3.5 Study of Shape of the cable gripping part

Next, we conducted an investigation regarding the shape of the gripping portion for directly holding the optical fiber cable. In the study of the gripping portion's shape, we created samples with various surface treatments on the wedge and evaluated the gripping force for each treated sample. By examining the relationship between surface treatments and the gripping force, we aimed to identify the optimal treatment method that would result in higher the gripping force, ensuring effective and secure fixation of the optical fiber cable.

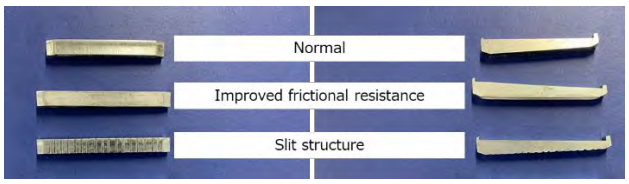


Figure8. The created samples

The created samples were as follows:

A: Untreated(Normal)

B: Samples with improved friction resistance using phosphating or shot blasting

C: Samples with a slit treatment

After testing the gripping force for each sample, it was confirmed that Sample C, the one with the slit treatment, exhibited the highest the gripping force.

The gripping force relationship: A < B < C

Based on these findings, it can be concluded that for the optical fiber cable material commonly used by NTT, such as PE (polyethylene), roughening the contact surface through slit treatment provides higher the gripping force.

However, during the first round of prototyping with the slit treatment, we did not achieve the gripping force specified in the requirements. As a result, we proceeded with a second round of investigation focusing on the shape of the gripping portion for the optical fiber cable.

In the second round of investigation, we utilized samples with even rougher contact surfaces with the optical fiber cable and evaluated the gripping force.

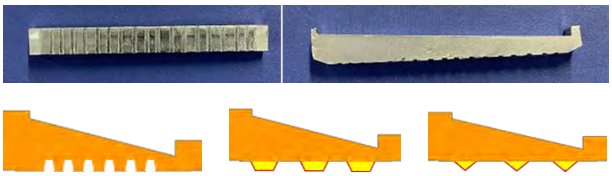


Figure9. second round of investigation

The evaluation results confirmed that, similar to the first round of investigation, the samples with a more roughened contact surface, particularly those with sharp convex shapes, exhibited improved the gripping force. This outcome indicates that the hanger's ability to securely hold and fix the optical fiber cable is further enhanced with the use of samples featuring a more aggressive surface treatment.

Despite the efforts in the second investigation, the gripping force still did not meet the specified requirements. Further exploration of surface treatments was considered; however, increasing the complexity of the surface treatment could lead to higher manufacturing difficulties and potential production errors, resulting in products that fail to meet the required specifications. As an alternative approach, we decided to optimize other factors, such as the length of the wedge and fine adjustments to the surface treatment (e.g., the number and height of the convex portions). By focusing on these aspects, we aim to achieve a balance between stable manufacturing and meeting the required specifications for the hanger, ensuring its reliable performance in securely holding and fixing the optical fiber cable.

3.6 Wedge optimization

To achieve the required specifications for the new hanger (gripping: A cable - 520N, B cable - 1140N, Bending: 0.1db), we will proceed with the following approach:

1.Wedge angle: We will use a wedge angle of 4 degrees.

2.Wedge length: The wedge length will be set at 60mm.

3.Surface treatment of the wedge: We will explore the impact of surface roughness on the gripping force by adjusting the number and height of the convex portions on the wedge surface.

By focusing on these factors, we aim to determine the optimal combination of surface treatment parameters that will meet the required the gripping force and the microbending loss specifications for both A and B cables. This iterative process will enable us to achieve a reliable and stable hanger design that fulfills the specified performance criteria.

The confirmation results. It is confirmed that for A cable, a wedge with 5 convex portions on the surface and a thickness of 0.6mm can meet the required specifications. However, it has been observed that the same shape does not satisfy the required specifications for B cable.

Table5. For the optimization study of A cable

	0.4mm		0.6mm		0.8mm	
number of convexes	Gripping force	Microbending loss	Gripping force	Microbending loss	Gripping force	Microbending loss
3	poor	good	poor	good	poor	good
4	poor	good	good	good	poor	good
5	poor	poor	excellent	good	poor	poor

poor: Does not meet standards for the gripping force or the microbending loss.

Table6. For the optimization study of B cable

	0.4mm		0.6mm		0.8mm	
number of convexes	Gripping force	Microbending loss	Gripping force	Microbending loss	Gripping force	Microbending loss
3	poor	good	poor	poor	poor	good
4	poor	good	poor	poor	poor	good
5	poor	poor	poor	good	poor	good

poor: Does not meet standards for the gripping force or the microbending loss.

Since further adjustments to the surface treatment proved issuing in manufacturing difficulties, you decided to explore other options by modifying the length of the hanger body. In the reevaluation, the length of the hanger was changed from 38mm to 57mm, which is 1.5 times longer. Consequently, the wedge length was adjusted from 60mm to 78mm to align with the new hanger length.

The evaluation results confirmed that by adjusting the length of the hanger body, the wedge length, and the number of convex portions, a significant improvement in the gripping force of B cable was achieved, although it has not yet reached the specified requirements.

Based on the evaluation results, it is expected that further investigation could lead to a further improvement in the gripping force. However, considering the current limitations in the size of the hanger for working in aerial spans, reaching a level where it can be fully utilized is achieved by restricting the applicable span.

Therefore, the shape of the wedge is confirmed to be as depicted in Figure10 and specified in Table7.

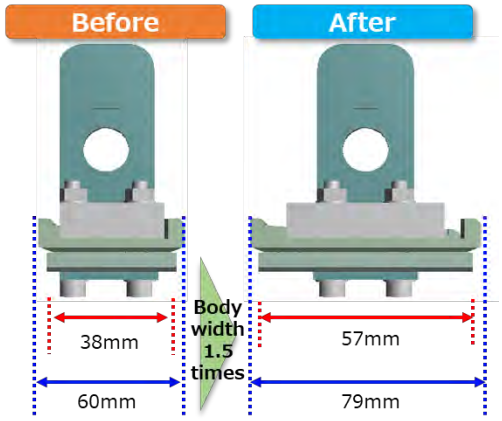


Figure10. The hanger was changed from 38mm to 57mm

Table7. The conditions for the wedge

Taper angle of the wedge	4°
Length of the wedge	79mm
Shape of the cable gripping part	Slit Structure, Convex Structure
Wedge Convex Number	7
Wedge Convex Height	0.6mm

3.7 Wedge Retention Stopper Consideration

When installing the new hangers over multiple spans, an issue arose where the wedge could dislodge if force was applied in the traction direction. To address this, a countermeasure was implemented by using wedge retention stoppers in sections where traction was applied and the sag was determined.

In the consideration of the wedge retention stopper, the shape was examined with the condition of ensuring ease of installation without compromising the existing construction process.

The examined wedge retention stopper is as shown in Figure11. After traction from the ground and determining the sag, the stopper's function is achieved by incorporating a structure that obstructs and secures the movable range between the wedge and the hanger body.



Figure11. Wedge retention stopper

4. Reliability Evaluation of New Hardware

To evaluate the reliability of the newly developed hangers, it is important to consider their performance under harsh environmental conditions. While the gripping force and absence of the microbending loss have been confirmed based on the specified requirements, it is also necessary to assess the potential impact of temperature variations on the cables after installation. Therefore, a heat cycle test will be conducted to examine the cable's performance under such conditions. This test will help ensure that the new hangers can withstand temperature changes without compromising the integrity of the optical fiber cables.

4.1 Heat cycle test

To confirm the impact on the cables when using the new hangers, the following tests were conducted under the following conditions:

◆Target Cables:

A Cable, B Cable (Figure 4)

◆Test Conditions:

The test conditions were set to be equivalent to the standards required for optical fiber cables.

Test condition
Temperature Range: -30℃ to 70℃
Duration: 6 hours or more for each cycle
Number of Cycles: 3 cycles
Measurement Wavelength: 1.55±0.02 μm
Optical Loss Variation: ≤ 0.15 dB/km based on the reference optical loss at 20℃.

The duration of the conducted Heat Cycle Test is as shown in the following Figure 12.

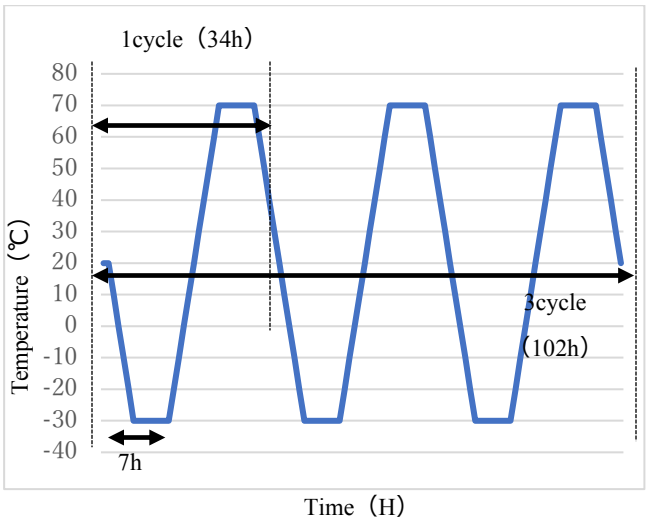


Figure12. The conditions of the Heat Cycle Test

4.2 Heat Cycle Test Results

As a result of the Heat Cycle Test, no excessive losses beyond the standard were observed in both A cable and B cable.

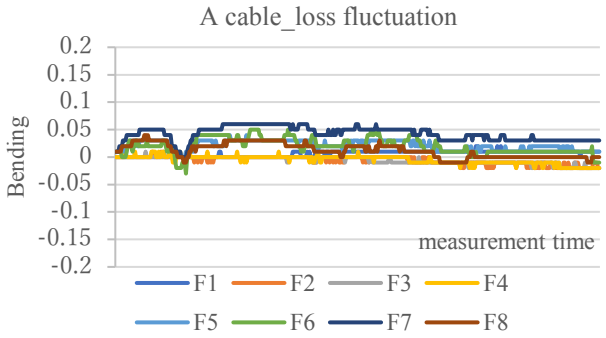


Figure13. Heat Cycle Test Results A Cable

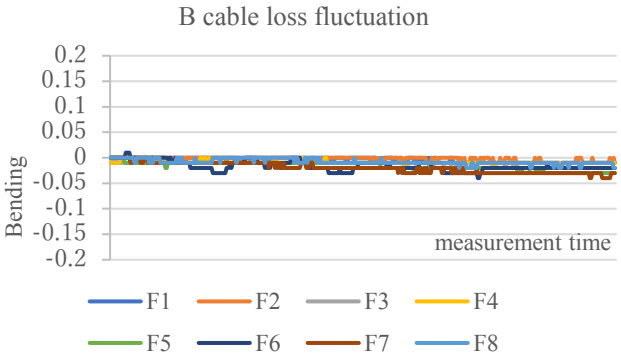


Figure14. Heat Cycle Test Results B Cable

5. Conclusion

We conducted a study on the new suspension hardware with a wedge structure that allows for a low-cost and simple cabling method for thin optical fiber cables in overhead sections. The suspension hardware can be fixed by manually pulling the optical fiber cable and releasing it, making it easy to secure the cable.

During the development of the hardware, we targeted thin optical fiber cables and established the required specifications. These specifications included smooth sliding of the cable, gripping force considering wind pressure, and ensuring no occurrence of microbending losses.

Based on these specifications, we experimented with multiple patterns for the length and taper angle of the wedge and the shape of the cable gripping part in the design of the wedge structure. As a result, we achieved the new suspension hardware optimized for thin optical fiber cables that allows for simultaneous cable laying, sag adjustment, and fixing.

With the newly developed suspension hardware for thin optical fiber cables, we were able to achieve significant reduction in construction personnel and shortened work time compared to conventional construction methods. Additionally, enabling cable pulling from the ground allowed us to achieve safe installation without the need for aerial work vehicles.

6. References

[1] K. Anzai, N. Ogawa, N. Toyota, H. Tanase, M. Awamori, M. Toyonaga and M. Kam,Proc. 56th International Wire & Cable Symposium, IWCS,pp.236-240 (2007)

[2] Y. Yamada, D. Kakuta, S. hamaguchi, H. Nakane, Y. Shinata,S. Kiyosue and K. Shiraki, "Development of Novel OpticalFiber Ribbon Assembled into Extremely High-Density Optical Fiber Cable", Proc. of 61st IWCS, no.2-2, pp.26-30 (2012)

[3] M. Toyonaga, M. Awamori, H. Tanase, M. Kama" New Aerial Optical Closure Technologies" Proc. 65th International Wire & Cable Symposium, IWCS,pp.466-469 (2016)

7. Pictures of Authors



Keitarou Yoshida is an Engineer at NIPPON TELEGRAPH AND TELEPHONE EAST CORPORATION. He joined NTT in 2015 and moved to his current position in 2017. Since then, he has been actively engaged in developmental research on underground and aerial closure technology.



Tomoya Shiraishi is an Engineer at NIPPON TELEGRAPH AND TELEPHONE WEST CORPORATION. He joined NTT in 2020 and moved to his current position in 2022. Since then, he has been actively engaged in developmental research on aerial closure technology.



Takeshi Sawa is a Manager at NIPPON TELEGRAPH AND TELEPHONE EAST CORPORATION. He joined NTT in 2006 and moved to his current position in 2022. Since then, he has been actively engaged in developmental research on underground and aerial closure technology.



Osamu Sasaki is a Senior Manager at NIPPON TELEGRAPH AND TELEPHONE EAST CORPORATION. He joined NTT in 2000 and moved to his current position in 2022. Since then, he has been actively engaged in developmental research on access network systems

Study on Streamlining Cable Removal Process

Keiji Fujihashi ∗, Syunsuke Shibata, Kaoru Kawasaki, Ryo Hasegawa, Takeshi Sawa, Osamu Sasaki

Strategic Network Management Department, NTT East

19-2, Nishi-shinjuku, 3-chome, Shinjuku-ku, Tokyo, 163-8019, Japan

+81 3 5359 4450 ·keiji.fujihashi@east.ntt.co.jp

Abstract

Confronted with the challenges of natural disasters and workforce decline, our study turns its focus to leveraging advanced machinery and robotics engineering to rationalize the telecom cable removal process. Our specific methods include the development of ground-based tools, which combine telescopic poles and versatile cutters, enhancing machinery for underground cables to automate short-length works, and employing Augmented Reality (AR) for accurate target identification. These elements will be integrated in the development of prototype robots. Through these automation approaches, we can effectively streamline the cable removal process. Ultimately, this study offers an efficient risk management solution for telecom infrastructure and addresses the impending workforce decline.

Keywords: Streamlining; Cable Removal Process; Telecom cables; Workforce decline; Robotics; Automation; Natural Disasters; Ground-based works; Safety measures; Augmented Reality (AR).

1. Introduction: Cable Removal Project and Workforce Decline

Cable Removal Project and Workforce Decline: For about 150 years in Japan, there has been an extensive legacy network of telecom cables spanning the entire country, playing a vital role in telecom services. However, these cables are gradually being replaced by more advanced technologies such as fiber optics and wireless communication.

As shown in Figure 01, With natural disasters such as high winds, heavy rain, and earthquakes occurring every year, outdoor telecom facilities are susceptible to damage. The falling of overhead telecom cables can disrupt transportation and safety. Given the high probability of significant earthquakes along the Nankai Trough and the Sagami Trough, the removal of unnecessary overhead telecom cables is essential to mitigate disaster risks. This helps facilitate the movement of emergency vehicles and restoration workers during disasters, assisting in swift repairs.



Figure 01: The Cable may fall due to a typhoon.

As shown in Figure 02, In Japan, due to the aging population and low birth rate, the working-age population has been declining since its peak in 1995 and is projected to decrease by 29.2% from 2021 levels by 2050. This challenge could lead to delays and decreased efficiency in the cable removal process, putting physical strain on the workers.

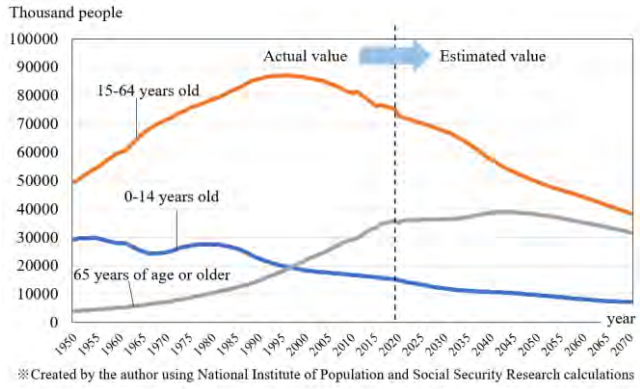


Figure 02: Projected workforce decline in Japan.

This study aims to streamline the cable removal process and pursue the cable removal project in the face of workforce decline. We will explore the development of innovative technologies to ensure the safety of Japan's telecom infrastructure.

2. Details of Telecom Cables removal

2.1 Structure of Telecom Cables

As shown in Figure 03, Telecom cables primarily consist of three layers. The outermost layer is a polyethylene jacket that provides durability and weather resistance. The middle layer houses a conductive shield of varying hardness and thickness depending on its purpose, protecting the signal from electromagnetic interference and external disruptions. At the core, there is a cable core comprised of bundled conductors, which provides communication and transmission services.

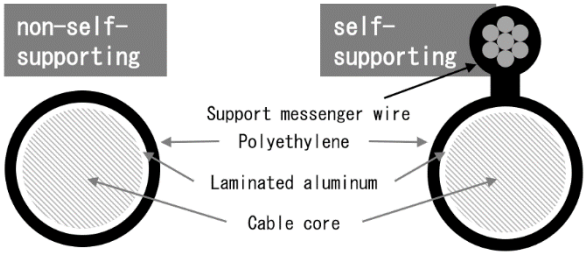


Figure 03: The diagram of telecom cable cross-section.

2.2 Types of Telecom Cables.

As shown in Figure 04, In Japan, two types of telecom cable are used: non-self-supporting and self-supporting cables. When aerial installation of non-self-supporting cables is necessary, additional

items like a support messenger wire and spiral cable hangers are required. On the other hand, self-supporting cables can be installed individually due to the built-in support messenger wire. Additionally, these self-supporting cables serve the function of the support messenger wire. If wrapped with spiral cable hangers, they can also hold other cables in suspension.

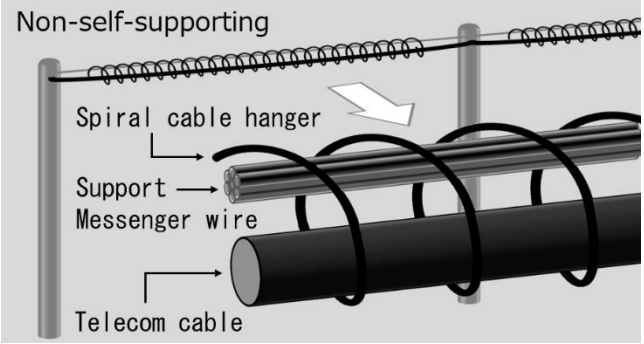


Figure 04: The installation from of the aerial telecom cable.

2.3 Pole Span and Ground Clearance

As shown in Figure 05, Poles are erected at appropriate intervals considering the area characteristics, and wire attachment is installed at a height of 5-6m on the poles. This wire attachment holds and tensions the supporting messenger wires or self-supporting cables, maintaining the legally mandated ground clearance. For the non-self-supporting cable, spiral cable hangers are installed, allowing the telecom cables to pass through and connect to closures.

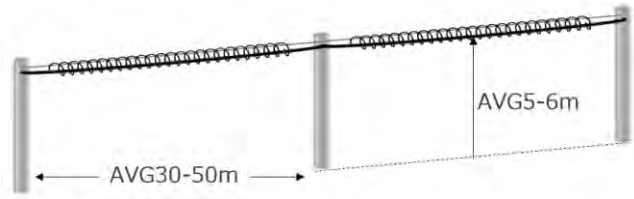


Figure 05: Pole Span and Ground Clearance.

2.4 Overview of the Current Removal Process

The removal of overhead telecom cables typically requires several vehicles and at least three workers. The operation follows the sequence of preparation, aerial work, and ground-based work. All cutting points are marked to avoid accidentally severing the wrong cables. Once the cable cut is confirmed, the cable rope is slowly lowered from the cutting point to the ground, ensuring not to disrupt traffic or cause any injury or property damage. The lowered cables are either cut into lengths suitable for transport, or if to be reused, they are wound onto a cable drum for transportation. Moreover, it's imperative to release the tension before cutting self-supporting cables.

<On-Site Removal Process>

A) Positioning: Setting up aerial work vehicles or heavy machinery at the worksite.

B) Setting: Securing the working area and setting up the tools.

C) Marking: Designating all cutting points.

D) Cutting: The person in charge of the operation performs the cut at the designated points.

E) Pulling out: Removing the cable from the hanger.

F) Lowering: Lowering the cable to the ground.

G) Receiving: Receiving the cut ends on the ground.

H) Shortening: Cutting the cable into shorter lengths on the ground.

I) Loading: Loading the cut cables onto the transport vehicle.

J) Transporting: Carrying away the removed cables.

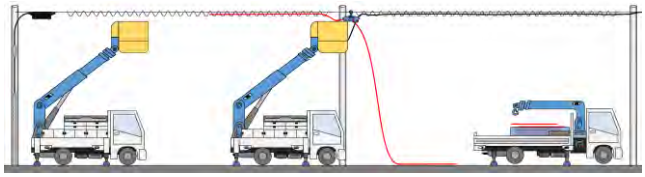


Figure 06: In the current cable removal process.

3. Challenges in Ground-based Works (Pre-validation)

To streamline the cable removal process, it was considered that steps G, H, and I in the current telecom cable removal procedure might be suitable for automation.

As shown in Figure 07, A pre-validation test was conducted to determine if lowering the cut cables using underground-based removal vehicles, directly towing them onto transport vehicles, and enabling their shortening and stowing is possible.



Figure07: On-site Pre-validation of non-self-supporting.

This product is licensed by Kitanihon Electric Cable Co., Ltd.'s patent.

Underground-based removal operations are meant for pulling up non-self-supporting cables from manholes, with the implementation gathering insights on what improvements are needed for the removal of overhead cables.

3.1 Ensuring Telecom Infrastructure Safety

As shown in Figure 08, When the cut cables were allowed to descend using natural gravity, some telecom equipment, such as the connecting parts of spiral cable hangers, were damaged.

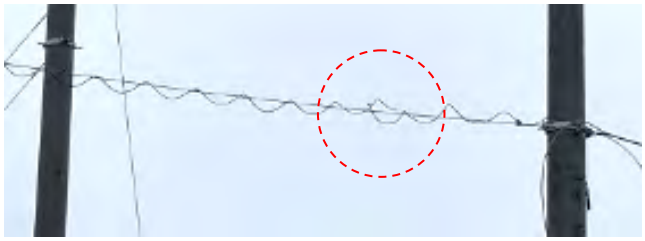


Figure08: The connecting part of the cable spiral hanger is broken.

In existing procedures, cables are placed on a cable car and controlled safely by attaching cable ropes. There is a need to control the cable descent from the ground, and to resolve this, new technologies and devices to absorb and control the descent force are

required, which might involve the development of alternatives to cable ropes. Moreover, there is a risk of cables moving unexpectedly, increasing the danger to workers and surrounding individuals. Therefore, efforts are focused on ensuring safety in emergencies, such as secure cable gripping and immediate machine stoppage, with the aim of improving work efficiency.

3.2 Improving Blade Durability

As shown in Figure 09, During the cutting and shortening of overhead lines, non-self-supporting cables were successfully cut between 10mm and 60mm. However, cutting shielded cables requires a stronger cutting force. Furthermore, problems occur when cutting multiple materials simultaneously, such as support messenger wires embedded in self-supporting cables, resulting in immediate blade chipping.



Figure09: Machine for shortening & after cutting& chipped blade.

This product is licensed by Kitanihon Electric Cable Co., Ltd.'s patent.

To address this, improvements such as the use of high-hardness, durable special steel or super-hard materials, the application of wear-resistant coatings (like diamond-like carbon or titanium nitride), and optimization of blade shape and cutting angles are necessary, and transitioning from single-stage to multi-stage or vibration cutting will also be considered. These enhancements aim to reduce blade replacement frequency, improve force dispersion during cutting, enhance work efficiency and safety. Also, a mechanism to release the blade from the cable in case of a cutting failure, enabling the operation to be restarted, is essential. The feasibility and safety of these improvements will be evaluated through future verification.

3.3 Issues Identified in the Current Removal Process

Upon reviewing the current procedures and discussing with the workers, it was decided to consider rationalization by dividing the process into two major parts.

I. Effort Required to Secure the Work Area (A to F): As ground-based operations progress, the repeated deployment of specialized vehicles such as high-lift trucks and transport carriers is necessary, consuming a large amount of space. Therefore, minimizing the effort spent on equipment setup and relocation is crucial for improving efficiency.

II. Heavy Labor Involved in Telecom Cable Logistics (G to J): Traditional methods place physically demanding tasks on the workforce, including manually cutting the retrieved cables into manageable sizes and loading them onto trucks. Thus, it's important to employ strategies like robotics and automation to alleviate this heavy labor and enhance efficiency.

4. Effort Required to Secure the Work Area (A to F)

The Ground-based Removal Process: Leveraging improvements to existing tools and machines, we will develop new prototype ground-based tools that can cut the telecom cables from the ground without the need for aerial work platforms. The objective is to lighten the workload of the workers, enhance productivity, and minimize manual labor. By taking a ground-based approach, the removal process becomes more efficient, the work scope is compacted, and the strain on the workforce is reduced. The knowledge derived from these prototypes will inform the development of ground-based prototype robots.

4.1 A to B) Efficiency in Preparation

The need for repeated deployments of aerial work platforms and the need to secure a large work area during construction become obsolete, leading to a more efficient and compact work scope for the removal process. Moreover, ground-based work enhances the safety of the workforce and is expected to considerably decrease the time required for setup and removal.

4.2 C) Marking: Cable Marking from the Ground.

As shown in Figure 10, To prevent accidental cutting of telecom cables, we plan to develop a goggle-type device called the "Sky Marker" that uses mapping data and Augmented Reality (AR) technology. This device is a high-precision marker with laser guiding and digital measurement features, capable of overlaying virtual space marking onto the real world.

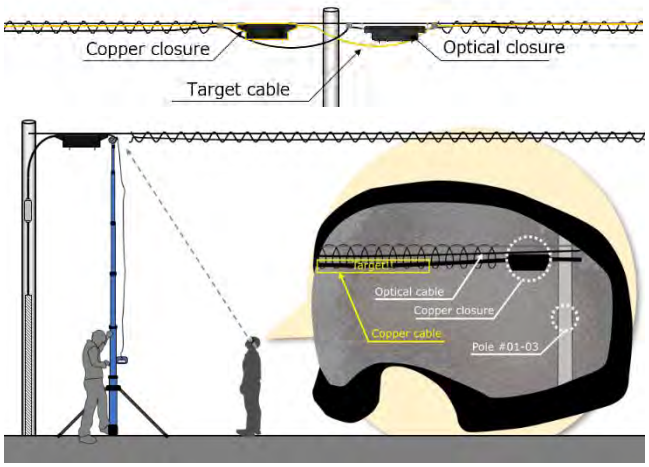


Figure 10: Prevent mis-cutting with AR goggles.

In addition, it implements a feature to accurately identify target cables by comparing local closure and facility information where the cables are connected.

As shown in Figure 11, To do this, it machine-learns parameters like the shape, size, color of closures, and the type, diameter, shape of the connected telecom cables, and uses AR technology to perform real-time image analysis from the ground.

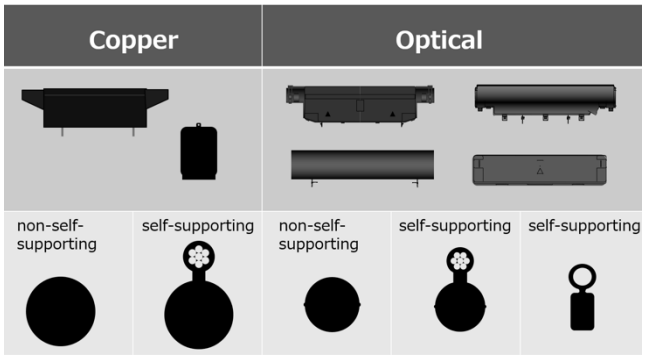


Figure 11: The telecom cables parameters for image analysis.

The method of marking cables depends on the type of utility poles used, whether they are single poles or shared poles. In the case of single poles, only communication cables are present, while shared poles have communication cables at the bottom, cable television in the middle, and power cables at the top.

Special attention is needed to avoid mistakenly cutting other industries' cables. Even with single poles, there may be a combination of metal and optical fiber cables, both enveloped in black PE, making identification from the ground challenging.

As shown in Figure 12, Nonetheless, identification is possible based on physical characteristics (optical fiber cables are thin, while metal cables are thicker) and by correlating them with equipment information using image recognition.



Figure12: Aerial copper and optical cable routing.

Additional research is needed to address challenges related to image recognition accuracy and improvements in machine learning. Through these developments, we aim to safeguard telecom infrastructure and achieve efficient cable management.

4.3 D) Cutting: Sky Cutter

As shown in Figure 13, Consideration is being given to a new type of telescopic pole integrated with a cable cutter at the tip.

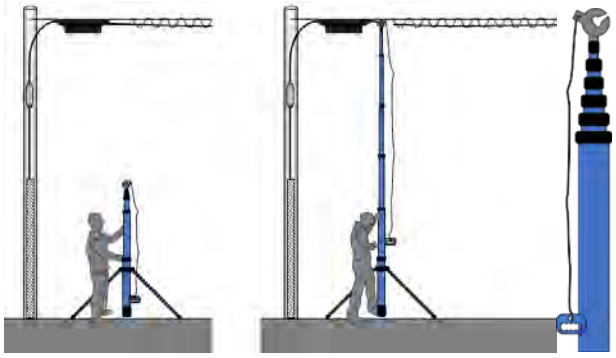


Figure13: Cutting from the ground using a telescopic pole.

This telescopic pole is lightweight and robust, utilizing air pressure for extension. The cutter is engineered to provide ample cutting force and accommodate various cable thicknesses and shapes, with a hydraulic system being considered for its operation. The use of the Sky Cutter eliminates the need for high-altitude operations, making cable cutting from the ground possible.

4.4 E) Pulling out: Sky Balancer

A device called the "Sky Balancer" will be developed, equipped with a cable grip function and tension release wire feature. With the cable grip function, it can securely hold both sides of the cable cut point and extricate the cable from the hanger. To ensure safety, the tension of self-supporting cables is properly released before cutting. The tension release wire gradually mitigates the tension, guaranteeing a safe release. This enhances the safety and efficiency of the operation for the worker.

4.5 F) Lowering: Traction Control Device

As shown in Figure 14, A traction control device is indispensable to ensure the safe descent of telecom cables. This device features a descent speed control function. It also has a feature that can instantly halt the cable in an emergency, ensuring that the cable descends at a safe and controlled speed. The ease of operation and the safety of the worker must be prioritized.

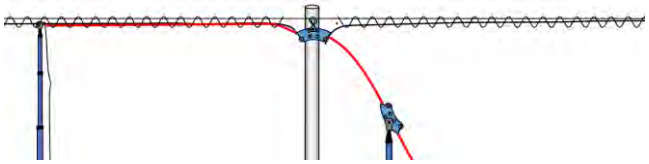


Figure14: Attachable to pully or pole tips.

5. Heavy Labor Involved in Telecom Cable Logistics (G to J)

Automating Logistics: Special work vehicles are proposed to automate the shortening, loading, and transportation of cables. This proposal aims to reduce the physical burden on workers and rationalize these operations.

5.1 G-H) Cable Shortening

To facilitate the handling and storage of cables, it is necessary to cut the cables to an appropriate length.

As shown in Figure 15, Our proposed "shortening device" features automatic cutting at specified lengths and organizes the ends of the shortened cables to prevent twisting and tangling. This allows workers to manage the cable length appropriately, improving handling and storage efficiency.

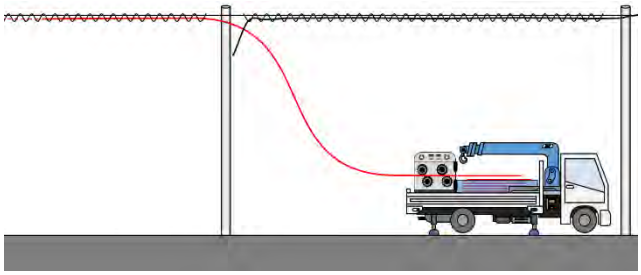


Figure15: Shorten the cable at regular intervals.

By modifying and compacting the machines used for underground cables, we aim to develop a more space-saving and powerful shortening device.

5.2 I-J) Loading & Transporting: Smart Storage

As shown in Table 1, Cable transport requires significant physical labor, causing a heavy burden on workers. To solve this, we plan to develop a "smart storage system".

Table 1. Cable mass difference.

Area	40m of mass	Cutting time	Onto truck time
Urban	4kg(0.1kg/m)	40	20 (pair of 2)
Rural	125kg(3.2kg/m)	40	40

* Rural areas involve heavier labor than urban areas. And due to conductor resistance, power transmission lines to rural areas are thicker and heavier.

This system will store shortened cables from a device built into the truck bed into storage without manual labor and transport them. Furthermore, it can adapt to handle cable sizes according to the situation, rationalizing cable transport regardless of location. With these improvements, manual labor is significantly reduced, the workload is lightened, and work efficiency and safety are enhanced.

5.3 Rationalization of the Removal Process and Safety Improvement

The objective is to rationalize the cable removal process by implementing new devices, machines, and robotic technology. This will result in a reduced need for personnel and vehicles, leading to a more efficient cable removal process.

As shown in Figure 16, Effectively removing a total of 410,000 km of overhead telecom cables that will become unnecessary in the future is crucial for the seamless maintenance of Japan's telecom infrastructure, ensuring its safety, and minimizing damage during disasters.

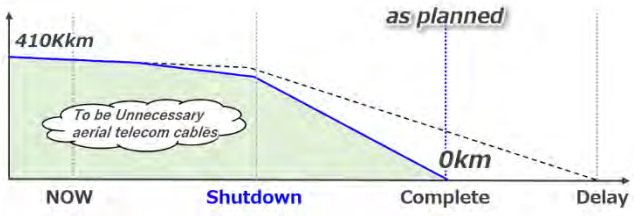


Figure 16: After shutdown [Legacy Telephone Exchange], the mass removal phase begins.

5.4 Safety Measures for Workforce

Cable cutting operations pose specific risks to workers. If cables and tools are not handled properly, there is a risk of worker injuries. Therefore, safety measures for workers are essential. Improvements such as remote operation to avoid direct contact and the installation of sensors at insertion points to enable automatic stops are necessary. These measures will enhance safety and work efficiency.

6. Advancing with Ground-based Tools

By merging the identified challenges and prototypes, we introduce a new "Cable Removal System" designed to foster collaboration between workers and robots, thereby enhancing the efficiency of cable removal processes. The centerpiece of this system is the development of a novel self-propelled robot, the "Cut-Crawler," which is set to optimize cable removal operations. The primary goals of this system are to ensure safety, improve work efficiency, and reduce workforce demands through effective human-robot collaboration.

6.1 Introduction of the Cut-Crawler

As shown in Figure 17, Leveraging insights obtained from refining and enhancing the efficiency of existing tools, we envision the development of a self-propelled robot named the "Cut-Crawler."

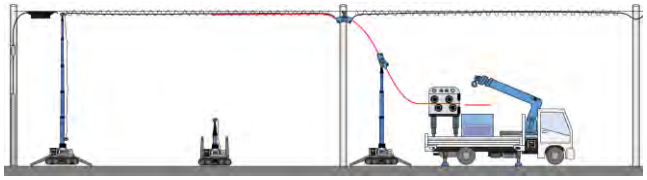


Figure17: An image of self-propelled Cut-Crawler.

It mounts an telescopic pole and a compressor for transmitting pneumatic pressure onto a multipurpose crawler already utilized in construction and agricultural fields. Depending on the tasks at hand, it accommodates interchangeable pole attachments such as the Sky Cutter and Sky Balancer. The ultimate goal is to miniaturize this system and deploy two units on-site.

6.2 System Functions

The Cut-Crawler is capable of extending poles from the ground using pneumatic pressure to access target cables, enabling a seamless sequence of tasks from tension release to gripping and cutting cables. It can also autonomously navigate to the cutting points. The system is engineered to improve the efficiency of the removal process, with the eventual aim of automating all operations within the work area.

6.3 Real-Time Monitoring

The Cut-Crawler is equipped with sensors and cameras, facilitating real-time monitoring of the work environment. The on-site robot can remotely collaborate with the operator stationed in the backyard, significantly reducing the burden on human resources at the work site and maximizing work efficiency.

6.4 Safety Precautions

The three key advantages of this system are safety, efficiency, and workforce reduction. By integrating cable descent control, shortening, and smart storage functions, the overall workflow efficiency is significantly improved.

As shown in Figure 18, Furthermore, the system minimizes the risk of injuries by keeping workers away from direct hazards. Ultimately, the system reduces both physical labor and the number of required workers, leading to enhanced overall efficiency. Through these concerted efforts, the system significantly boosts the overall productivity and safety of cable removal operations.

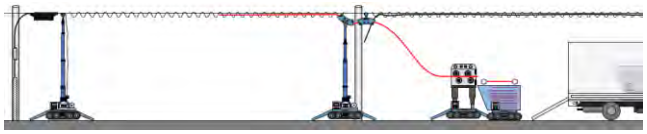


Figure18: An image of human-robot collaboration in the future.

7. Ground-Based Cable Removal Process and its Social Contribution

This study aimed to identify challenges and necessary enhancements in the ground-based process of removing telecom cables, while exploring potential solutions with a particular emphasis on our corporate social responsibility (CSR). Throughout our investigation, we recognized that addressing challenges in cable descent, tension control, cutting, and transportation were crucial

elements for rationalization and efficiency. To tackle these issues, we developed a prototype system called the "Cable Removal System", successfully demonstrating the effectiveness of streamlining the telecom cable removal process.

The utilization of robotics and automation, not only to enhance the efficiency of cable removal but also to uphold our commitment to CSR by improving workforce safety and anticipating a declining workforce in the future. Additionally, we need to consider additional challenges, such as image recognition and measurement technologies, to fully automate the process. Our advancing study on human-robot collaboration could significantly contribute to improving telecom infrastructure safety and building trust within society, further solidifying our commitment to CSR.

8. Acknowledgments

Special thanks to Kitanihon Electric Cable Co., Ltd.

9. References

[1] Ministry of Internal Affairs and Communications, Japan, “WHITE PAPER 2022” https://www.soumu.go.jp/johotsusintokei/whitepaper/eng/WP2022/chapter-2_1.pdf (Last reference2023)

10. Pictures of Authors



Keiji Fujihashi is an Engineer at NIPPON TELEGRAPH AND TELEPHONE EAST CORPORATION. He joined NTT in 2011 and moved to his current position in 2021. Since then, he conducts research on copper cable and pressurized cable maintenance.



Syunsuke Shibata is an Engineer at NIPPON TELEGRAPH AND TELEPHONE WEST CORPORATION. He joined NTT in 2016 and moved to his current position in 2022. Since then, he conducts research on aerial telecom infrastructure.



Kaoru Kawasaki is an Engineer at NIPPON TELEGRAPH AND TELEPHONE EAST CORPORATION. He joined NTT in 2019 and moved to his current position in 2021. Since then, he conducts research on telephone pole and pressurized cable maintenance.



Ryo Hasegawa is an Engineer at NIPPON TELEGRAPH AND TELEPHONE EAST CORPORATION. He joined NTT in 2010 and moved to his current position in 2020. Since then, He organizes the planning of new telecom items and methods.



Takeshi Sawa is a Manager at NIPPON TELEGRAPH AND TELEPHONE EAST CORPORATION. He joined NTT in 2006 and moved to his current position in 2022. Since then, he has been actively engaged in developmental research on underground and aerial closure technology.



Osamu Sasaki is a Senior Manager at NIPPON TELEGRAPH AND TELEPHONE EAST CORPORATION. He joined NTT in 2000 and moved to his current position in 2022. Since then, he has been actively engaged in developmental research on access network systems.

Methodology to Maintain Lower Breaking Load and High Reliability in Optical Fiber Drop Cable

Swarnava Saha, Darshana Bhatt, Sarin Kumar
R&D Cables, Sterlite Technologies Limited
Dadra, DNH, India
+91-0260-6613817. darshana.bhatt@sterlite.com

Abstract
This study focuses on optimizing the design of a last-mile work-safe drop cable for Fiber to the Home (FTTH) networks. By introducing extra fiber module length (EFML), the optical fiber's mechanical reliability and breaking load are optimized. The EFML decouples the fiber module from the composite drop cable, improving strain performance, reducing the requirement of additional strength members which otherwise increases the breaking load of the cable. Experimentally backed data demonstrates the acceptable fiber strain under permanent load after the installation, maintaining the required breaking load. Balancing fiber strain with the breaking load as per the requirement ensures the cable's ability to break in case of accidents, such as vehicle collision that way avoiding human causalities. This optimized design offers a robust solution for high-performance FTTH networks.

Keywords: Drop Cable; Breaking Load; Fiber strain; EFML- Extra Fiber Module Length; Young's modulus; Stress; Strain; Optical Length; Fiber to the home; Safety Hazard; Reliability; ADSS – All Dielectric Self Supporting.

1. Introduction
The introduction of all-dielectric self-supportive (ADSS) cables in the late 1970s and early 1980s marked a significant milestone in the history of optical fiber cable technology. ADSS cables revolutionized the industry by eliminating the need for separate support elements, such as messenger cables or steel wires, which were previously required for installation. This breakthrough made the deployment of optical fiber cables more efficient, cost-effective, and less cumbersome. The self-supporting nature of ADSS cables made them particularly suitable for aerial installations, as they could be attached directly to power transmission lines and utility poles without the need for additional supporting structures.

Simultaneously, the growing demand for high-speed connectivity in the last mile, particularly in fiber-to-the-home (FTTH) and fiber-to-the-premises (FTTP) deployments, led to the development of round drop optical fiber cables. These cables are specifically designed for easy installation in tight spaces, such as residential and commercial buildings. Round drop cables feature small diameters, increased flexibility, and bend-insensitive fibers, allowing for seamless routing around corners, through conduits, and into individual living units. Their compact size and ease of installation have played a pivotal role in expanding the reach of optical fiber networks to the final connection point, facilitating high-speed internet, voice, and video services for end-users.

2. Concept of WorkSafe Cable
The round drop ADSS Cables used in the FTTx networks contains the high-strength modulus elements members which contributes to the higher breaking load of the cable. The breaking load is defined as the maximum external force applied beyond which the cable composite breaks into two separate parts. It is termed Ultimate Tensile Stress (UTS). In the event of a high-speed vehicle collision with the aerial drop cable network, a high breaking load of the cable may prevent it from breaking, leading to potential damage to the support structures and human casualties. This disruption not only affects communication services but also incurs additional expenses for repairs and poses safety hazards. To address this issue, telecom operators and infrastructure providers must carefully evaluate installation locations and heights, adhere to industry standards, and implement protective measures. These measures may include breakaway hardware or sacrificial components that minimize infrastructure damage by detaching or breaking under excessive force. This calls for the high demand of designing a cable which safely breaks under the maximum given load without damaging the pole and the infrastructure or posing any human safety hazard.

3. Designing a WorkSafe Cable for FTTx Network
3.1 Cable Design Requirements
The last mile ADSS low fiber count drop cables are the most sensible design in the optical fiber cables network because of their installation in the outdoor environment and direct engagement of the human enforced installation. The key component of the drop cable is the optical fiber placed in the core of the cable, which needs to be protected from harsh environmental conditions such as storms and ice loads. The cables are also prone to axial pull stress during the installation. The stresses on the cable may get converted into the permanent stress on optical fiber impacting its service lifespan. This stress and relative fiber life expectancy are explained in the technical report of IEC/TR 62048. The fiber reliability can be maintained keeping the

fiber strain lower in any condition. Hence the ADSS drop cables need to be designed in a way such that it can withstand specified maximum external environmental longitudinal stress. The common industrial practice in the optical fiber cable industry is to use strength members inside the cable to provide strength to the cable. The longitudinal stress on to the cable is equally distributed to the strength members so that the stress on the optical fiber element is controlled within the specified limit given in the IEC/TR 60794-1-21 standard. The optical fiber cable operates in the elastic region of the stress-strain curve following the simple non-liner equation:

$$F_C = E_{avg} \times S_C \quad (1)$$

Where, F_c is the longitudinal stress on cable during operational environmental load, E_{avg} is the average young's modulus of the round drop cable composite structure, and S_c is the elongation percentage of the cable structure under the given longitudinal load.

In principle, the cable made up of strength members act as a composite structure and during operational longitudinal stress, the optical fiber inside the cable composite also elongates which is equal to the cable elongation under stress. There are different types of dielectric strength members i.e., aramid fibers (ARY), glass fibers (GRY), aramid reinforced plastic (ARP) and glass fiber reinforced plastic (FRP). Usually, the ARP and FRP are used as strength rods embedded inside the jacket of the cable and ARY and GRY placed as peripheral members in the cable design. The average young modulus of the cable is dependent on the combination of strength members and the thermoplastic material used in the cable design according to the equation as follows.

$$E_{avg} = \frac{\sum(E_{sm} \times A_{sm}) + \sum(E_p \times A_p) + \sum(E_f \times A_f)}{\sum A_{sm} + \sum A_p + \sum A_f} \quad (2)$$

Where, E_{sm} is the young's modulus and A_{sm} is the cross-sectional area of the strength members. E_p is the young's modulus and A_p is the cross-sectional area of the thermoplastic material. E_f the young's modulus and A_f is the cross-sectional area of the optical fibers.

On the other side, the inclusion of strength members adds up the breaking load of the cable which develops unsafe condition causing the damage of network infrastructure architecture as discussed above.

As per the equation (2) the strength members shall be selected in such a way that the E_{avg} is optimized to maintain the desired cable breaking load and acceptable stress on the fiber as per the limit specified in the IEC Standard. The co-relation between cable breaking load and fiber strain as a function of cable's Young's modulus (E_{avg}) is shown in figure (1).

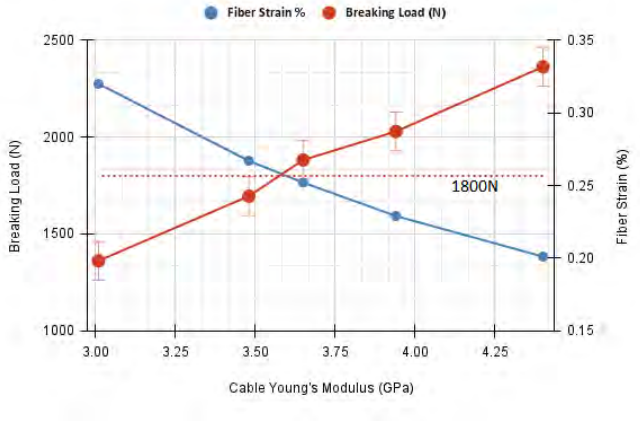


Figure 1. Co-relation between Cable Breaking Load and Fiber Reliability as a function of Cable's Young's Modulus

The strain on fiber (same as the cable elongation in a composite structure) at the permanent installation load is calculated by Equations (1) and (2) for different cable design considering various combination of strength members. The breaking load of the cable is calculated as the sum of all the cable elements' ultimate tensile stress. The calculations are shown in Table 1.

Table 1. Co-relation between Fiber Strain and Breaking load as a function of Cable's Young's Modulus

Design No	E_{avg} (GPa)	Fiber strain @ Cable installation Load (N)	Breaking Load(N)
D-1	4.40	0.201%	2363
D-2	3.94	0.229%	2029
D-3	3.65	0.252%	1882
D-4	3.48	0.267%	1695
D-5	3.01	0.320%	1361

This correlation shown in figure (1) shows an inversely proportional relation between the fiber strain and breaking load which requires the need of the optimization between the two design parameters.

3.2 Understanding of Extra Fiber Module Length

At Sterlite Tech™ a novel round ADSS drop cable design was worked out which finds a good optimization of fiber strain and breaking load requirement. For experimentation purposes the composite cable design D-4 was selected which shows 0.267 % fiber strain. But to achieve the best manufacturing capability including the process tolerances the targeted fiber strain needs to be well within 0.250%. To achieve such low fiber strain without adding any extra strength member in the cable, the excess fiber module length (EFML) to be created inside the composite structure of the drop cable.

The extra fiber module length represents the extra length of the optical fiber module inside the given physical length of the cable. The EFML percentage is calculated as per the equation (3)

$$EFML\ (\%) = \frac{(lenght\ of\ fiber\ module\ inside\ the\ cable\ composite)}{(physical\ length\ of\ the\ cable)} \times 100 \quad (3)$$

The EFML percentage is measured by cutting the samples from the cable produced in the experiments performed mentioned below. The EFML (%) for the selected cable design D-4 helps reduce the fiber strain (%) and provides extra margin as compared to the designed cable elongation.

The EFML (%) represents as,

$$S_f = S_c - EFML \quad (4)$$

where S_f is the fiber strain. The zero EFML represents $S_f = S_c$ in Equation (1).

Certain experiments were carried out with the selected ADSS Drop cable design varying the EFML and then fiber strain and breaking load of those cable samples were measured. Data was collected and analyzed.

4. Experimental Data Analysis

4.1 Experiment Set up.

The cable design under study was tested for Fiber Strain during its tensile test and breaking load at STL Reliability lab. The test method followed for measuring the fiber strain and breaking load is mentioned below.

A 200 m cable was taken out from the reel and wounded on the pulleys (diameter - 50 mm) of the tensile tester. The tensile testing machine is compliant to IEC 60794-1-21 E2 standard. After fastening the cable, the installation load was applied, and the fiber strain was measured. Then the load was increased till its maximum specified load and fiber strain reading was taken. The test set up is shown in Figure 2 and Figure 3

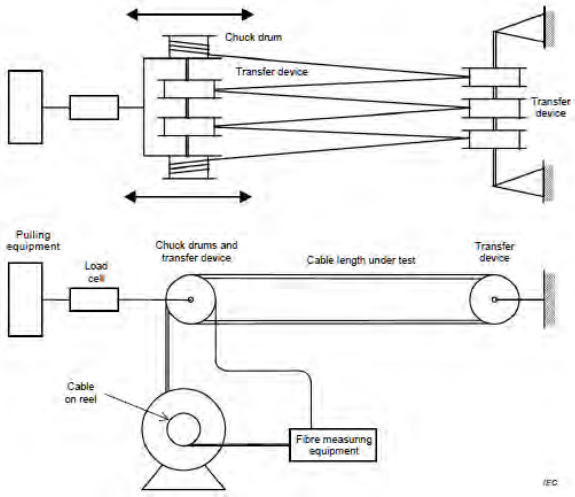


Figure 2. Cable Tensile Test Measurement Setup (Ref. IEC 60794-1-21)

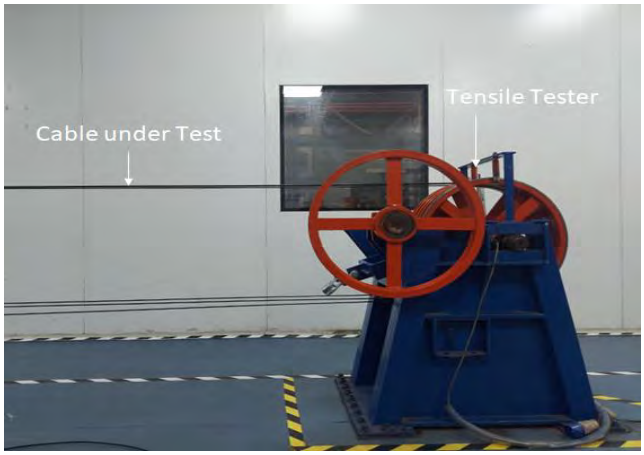


Figure 2. Cable under Tensile Test- Fiber Strain Measurement

After measuring the fiber strain test, an appx 10-meter sample was taken from the same reel segment, and it was again attached to the tensile testing machine but through the helix clamps this time without any turns on the Pulley sets. The tensile load was applied to the cable and increased till the time the cable elements broke. The breaking load reading (in Newton) was recorded as per this test method. The test set up for cable breaking load is shown in Figure 4 and Figure 5.

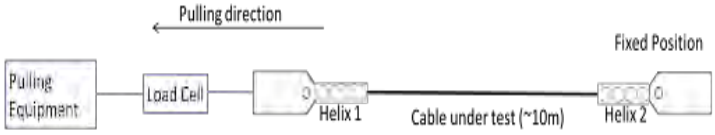


Figure 4. Breaking Load Test Setup Diagram

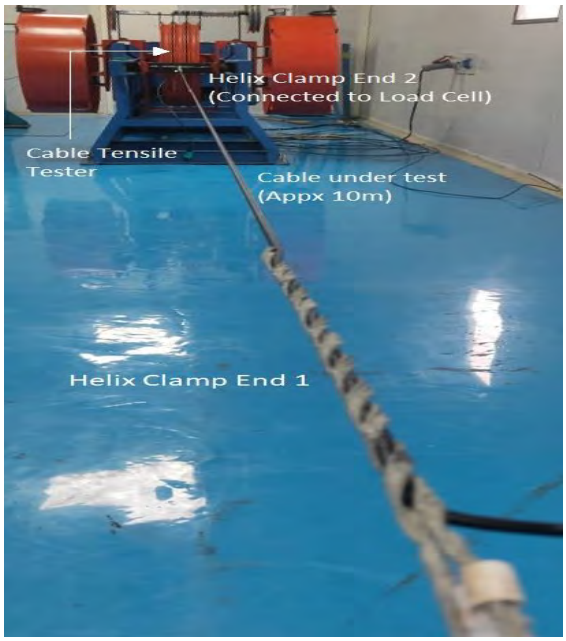


Figure 5. Cable under Breaking Load Test

This study was carried out on around 50 number of cable samples from different reels manufactured at different times. This data was collected to study the co-relation between the breaking load and fiber strain for the given cable design with respect to the EFML. Figure 6 plots the fiber strain reading v/s EFML in the cable.

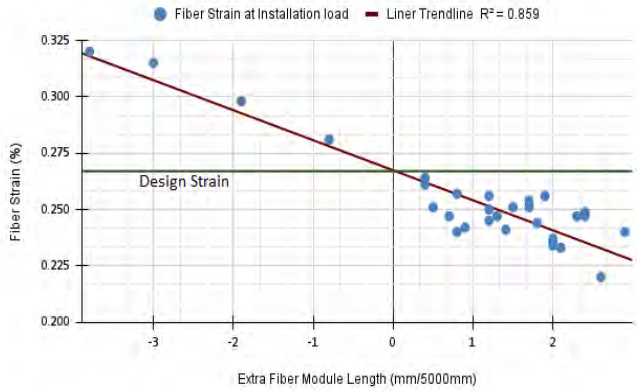


Figure 6. Fiber Strain as a function of EFML

The graph shown in Figure 6 depicts the measured fiber strain as a function of the extra fiber module length. It shows the change in fiber strain at installation load for a fixed design (constant Young's modulus) with respect to the length of the extra fiber module. The cable samples with positive EFML have given the fiber strain less than the targeted 0.25%. On the other hand, the negative EFML gives the fiber strain higher than its calculated or designed strain values.

5. Conclusions

The extra fiber module length helps achieve a balance between the maximum allowable breaking load and fiber strain. It allows the mechanical strength members used in the design to bear the initial operational load on their own without transferring the load to the optical fiber, which significantly reduces the fiber strain of the cable during operation. This reduced fiber strain enables the design of a lightweight work safe cable that ensures the desired lifespan of the optical fiber drop cable.

6. Acknowledgments

Dr. Jitendra Balakrishnan (CTO, Optical Network Business, STL) for his motivation to write this paper, Venkatesh Murthy (COO, Optical Network Business, STL) for resource availability for experiments and STL QA Team for their support during the cable measurements.

7. References

[1] White Paper "Mechanical Reliability of Optical Fibers" by Mr. Ashutosh Goyal, Sterlite Technologies Limited –

[2] IEC 60794-1-21, Optical fiber cables - Part 1-21: Generic specification - Basic optical cable test procedures - Mechanical tests methods

[3] Commission, I.E., Optical Fibers-Reliability-Power law theory, 2011, International Electrotechnical Commission

[4] Griffioen, W., et al., COST 218 evaluation of optical fiber lifetime models, in Optical Materials Reliability and Testing: Benign and Adverse Environments, R.A. Greenwell and D.K. Paul, Editors. 1992, SPIE. p. 190-200

8. Pictures of Authors



Swarnava Saha has been working as a Technology Engineer for New Product Development of Specialty Cables at Sterlite Technologies Ltd for over 2 years. In this role, he is accountable for the new product development of low fiber count Optical fiber cables for Fiber to the Home (FTTH) Networks. Swarnava has done his graduation and post-graduation in Chemical Engineering at the Indian Institute of Technology, Kharagpur. Swarnava has 2 filed/published patent applications, 2 peer-reviewed international journal publications and 2 international conferences presentations under his name.



Darshana Bhatt is the Lead Design and Development and has over 17 years of experience in Design and Development of Power Cable, Jelly Filled Telecommunication cables, Structured Data Cables and Fiber Optic Cables, Hybrid Cables. She is having in-depth understanding of Cable design, testing and its application. From last three years she is working on Product development for Fiber to the Home Networks. She represents STL for various Standard Committees like TIA, BICSI, BIS, SPESA. She has 8 filed/published patent applications, 4 international conferences presentations under her name. She holds a bachelor's degree in electrical.



Dr.Sarin Kumar is the Head: R&D for Cables business at Sterlite Technologies Ltd He is responsible for both Optical fibre cables as well as LAN cables. Sarin has ~22 years of both academic and industrial research experience that includes working at University of Geneva, Norwegian University of Science & Technology, Honeywell, and Eaton. Sarin has served as a member of the Industry Advisory Board at the Dept. of Metallurgy & Materials Science, College of Engineering Pune. He also served as technical program committee member for IEEE International Frequency Control Symposium in 2009, 2010 and 2011. Sarin Kumar has a Ph.D. in Materials Science & Engineering from Tokyo Institute of Technology, Japan.

SESSION 15

Click on a session below to navigate to that section of the Proceedings.

SESSION 15: HIGH DENSITY RIBBON

Chairperson: Bulent Kose, Panduit Corp., USA

15-1 **Development of Low Loss Central Core Rollable Ribbon Cable;** Mr. Tomoaki Gonohe, *Furukawa Electric Co., Ltd., Japan*

15-2 **High-Density Cables with 200-Micron Flexible Ribbons;** Mr. Edward Hudson, *Corning Optical Communications, LLC, USA,*

15-3 **Single Jacket Armored Wrapping Tube Cable with Easy Fiber Access;** Mr. Yusuke Tsujimoto, *Fujikura Limited., Japan*

15-4 **High Fiber Density 3456F Flexible Ribbon Indoor/Outdoor Cable for Indoor Outdoor Data Center Applications;** Eric, Anderson, *Prysmian Group, USA*

15-5 **144F High-Density Ribbon Cable Supporting/Compatible to Legacy Network;** Mr. Kawarpreet Singh, *Sterlite Technologies Limited, India*

15-6 **Optical Fiber Ribbon Cables with Full Color Spectrum;** Mr. Qi Lin, *Yangtze Optical Fibre and Cable Joint Stock Company | State Key Laboratory of Optical Fiber and Cable Manufacture Technology, China*

Click here to return to the **Table of Contents**

Development of Low Loss Central Core Rollable Ribbon Cable

Tomoaki Gonohe, Hirotaka Koriki, Masataka Tabuse and Masaru Nakajima

Optical Fiber & Cable Products Division, Furukawa Electric Co., Ltd.
20-16 Nobono-cho, Kameyama, Mie, Japan
+81-595-85-2444 ·tomoaki.gonohe@furukawaelectric.com

Abstract

The terrestrial central core cables using Rollable Ribbons (RR) with lower transmission loss performances have been successfully developed. It has been achieved by comparing and analyzing different optical fiber types of large core / low transmission loss fiber category compliant with ITU-T G.654.E [1] in optical fiber cable performances, and also by optimizing optical fiber cable design and structure parameters.

The developed optical fiber cables have also achieved necessary mechanical and environmental performances for actual use.

Keywords: G.654.E, Low loss, Central core, Rollable Ribbon, Fiber packing density, Stranding lay length

1. Introduction

The demands of internet transmission capacity have been further increasing due to various application services and those higher resolution videos with more connections and usages of devices to transmission network. To meet those increasing demands, ITU-T G.654 fiber types have been developed and used in submarine optical fiber cables for wider network building and higher transmission capacity.

Recently these increasing demands has been spreading into terrestrial long-haul optical fiber network and ITU-T G.654.E fiber was introduced for this terrestrial use, and developments of terrestrial optical fiber cables with ITU-T G.654.E were needed while maintaining its superior transmission performances and cable mechanical/environmental performances with higher optical fiber packing density in cable cross section area to minimize necessary installation spaces.

This study provides the results of successful development of higher fiber packing density central core cables using ITU-T G.654.E fibers with superior transmission loss and other cable performances.

2. ITU-T G.654.E Fiber

As previously mentioned, it is important to apply suitable fiber type such as ITU-T G.654.E fiber for longer distance transmission with lower transmission loss in long-haul optical fiber network to meet increasing demands.

This ITU-T G.654 recommendation was standardized with A, B, C and D categories mainly for submarine cable applications with lower transmission loss and non-linearity while having larger effective area (A_{eff}) and longer cut-off wavelength in comparison to other fiber type such as ITU-T G.652.D [2].

This larger A_{eff} provides lower optical power density which relieves non-linearity effects, and as a result more higher transmission power and better OSNR (Optical signal-to-noise ratio) are possible [3].

While these superior performances by larger A_{eff} of ITU-T G.654.E, this larger A_{eff} results in larger mode field diameter (MFD) and it could result in inferior bending loss performances.

Since the requirements for terrestrial optical fiber cables are different from those for submarine optical fiber cables because of different cable designs, manufacturing methods, installation conditions and environments when those are in services, it is necessary to study and develop its own design methods for terrestrial cables to manage and control stresses such as macro-bending and micro-bending.

3. Investigated ITU-T G.654.E Fibers

To evaluate those potential risks and concerns of bending loss in terrestrial central core optical fiber cable designs, four different 250 μm diameter ITU-T G.654.E fibers were considered and chosen to be tested in this work as shown in Table 1.

Fiber A has minimum MFD and fiber B has typical MFD specified in ITU-T G.654.E to investigate impacts of different MFD for transmission loss performance to investigate resistance for stresses given. A_{eff}, which is correlated to MFD, is used in Table 1 for descriptive purposes.

Table 1. List of investigated ITU-T G.654.E fibers

Optical fiber	A_{eff} at 1550 nm (μm^2)
A	110
B	125

4. Investigated Cable Designs and Those Design Parameters

4.1 Base cable structure

Figure 1. shows structure and feature of RR adopted in cables in this study. Its structure is achieved by partial bonding of ribbon matrix for ribbon width and longitudinal directions instead of continuous surrounding coating structure of traditional flat ribbon (FR) design.

When being applied in central core cable designs, RR would be rolled because of its flexibility and contributes to A_{eff} use in

limited cable inside area and to achieve higher fiber packing density in cable cross section [4][5].

When being out of cable, RR shapes "flat" as FR design, therefore it keeps some benefits such as mass fusion splice performance and easy handling.

Because of these superior performances, RR has been well known and used in Japanese optical fiber cables and network, and recently it is expanding globally into different area and network all over the world.

In this study, 4F RR and 8F RR were used and those RR were stranded and grouped with bundling tapes into 20F, 40F and 80F RR bundling units for different fiber count cables.

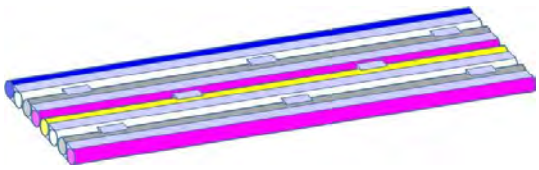


Figure 1. Rollable Ribbon
(Example of 8F Rollable Ribbon)

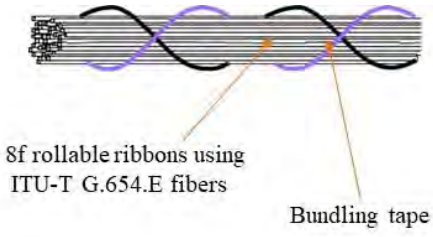


Figure 2. Configuration of RR bunding unit
(Example of 80F Unit)

40 to 1000F cables were investigated in this study, 1000F RR central core cable structure is shown in Figure. 3 as example. All cables have RR bundling units in center of cable cross section, and dielectric strength members are placed one each with opposite 180 degree in its jacket.

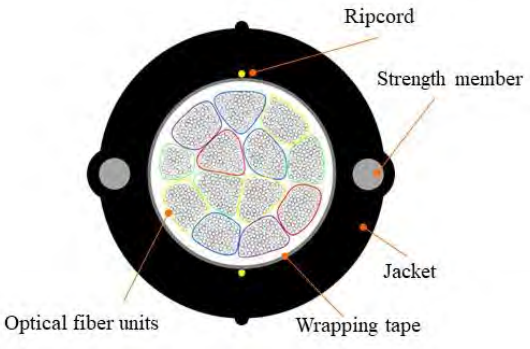


Figure 3. Cable cross sectional view
(Example of 1000F RR central core cable)

Transmission loss performances were studied and investigated with different ITU-T G.654.E fibers listed in Table 1 in RR central core cable designs explained in Figure 2 and 3, by changing major two cable design parameters described in next sections to understand how to secure low transmission performance of ITU-T G.654.E fibers in cables.

4.2 Fiber Packing Density

Fiber packing density, which is provided in ratio of toral RR area divided by cable inside area, was chosen as control parameter to change amount of stresses in cable, and transmission loss performances were measured and compared to optimize within same condition of other strains given on optical fibers by RR unit stranding lay length etc.

4.3 Stranding Lay Length

In general, optical fibers are stranded to use in cable to balance tensile and contraction strains in various different situations. The different stranding lay lengths provide different level of optical fiber bending strains, therefore the impacts of this stranding lay length were also measured and analyzed within same condition of fiber packing density.

5. Transmission Loss Performances

Figure 4 shows transmission loss performances in several central core cables investigated. The results are compared by grouping cable lots within the identical bending strains. The wavelength of transmission loss is measured at 1550 nm by OTDR method. The result found that lower fiber packing density showed lower transmission loss performances and lower A_{eff} (in difference between fiber A and fiber B) showed lower transmission loss performances.

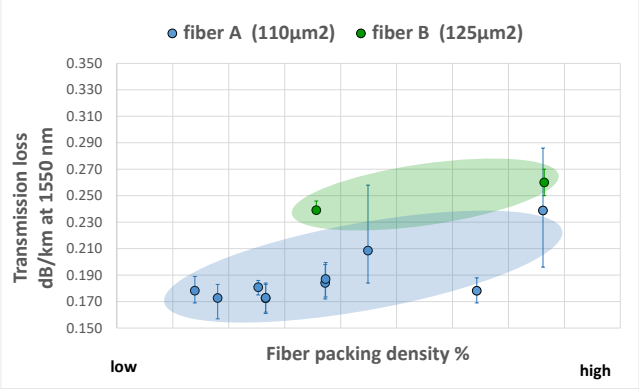


Figure 4. Correlation between transmission loss performances and fiber packing density
(in identical bending strains)

Figure 5 shows correlation between transmission loss performances and stranding lay length. It compares the identical fiber packing density with fiber A. The result found that longer stranding lay length showed lower transmission loss performances.

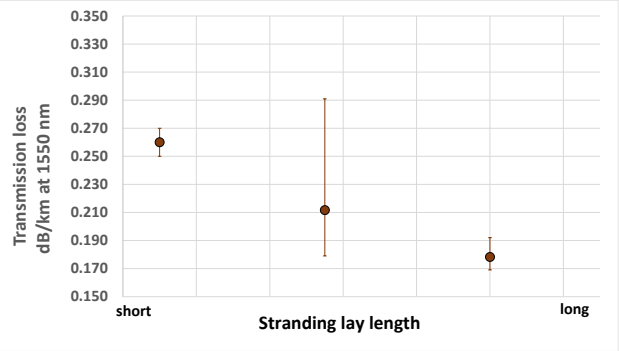


Figure 5. Correlation between transmission loss performances and stranding lay length (in identical fiber packing density)

Table 2 summarizes the contribution parameters for lower transmission loss performances with ITU-T G.654.E fibers for each parameter.

Table 2. Contribution parameters for lower transmission loss performance

A_{eff}	low
Fiber packing density	low
Stranding lay length	long

The 20-32% lower transmission loss was achieved in 40 to 1000F cables.

6. Other cable characteristics

Table 3 shows the mechanical characteristics of 40 to 1000F cables with fiber A tested at 1550 nm wavelength, low fiber packing density and long stranding lay length. The results found to be satisfactory and sufficient to meet the requirements for generic terrestrial and long-haul application.

Table 3. Mechanical characteristics of 40 to 1000F cables with ITU-T G.654.E fibers

Item	Condition	Result
Tensile	IEC 60794-1-21 Tensile load : 1.1×W (W: weight (kg/km))	Strain < 0.05%
Crush	IEC 60794-1-21 Load: 1960 N / 100 mm Holding time: 1 min	< 0.10 dB
Impact	IEC 60794-1-21 1 N × 1 m	< 0.10 dB
Repeated bending	IEC 60794-1-21 Bending Radius: 160 mm (40, 100, 200F cable) 240 mm (400, 1000F cable) Cycle: 10	< 0.10 dB
Torsion	IEC 60794-1-21 +/- 90 deg. / m Cycle: 3	< 0.10 dB
Bending under tension	Tensile load : 1.1×W Bending Radius: 300 mm (40, 100, 200F cable) 600 mm (400, 1000F cable) Test angle: 90 deg Cycle: 4	< 0.10 dB

Table 4 also shows the environmental characteristics of 40 to 1000F cables with fiber A tested at 1550 nm wavelength, low fiber packing density and long stranding lay length. The result found to be also satisfactory and sufficient to meet the requirement.

Table 4. Environmental characteristics of 40 to 1000F cables with ITU-T G.654.E fibers

Item	Condition	Result
Temperature cycling	IEC 60794-1-22 -30°C～70°C Holding time: 6 hours for each temp. Cycle: 3	< 0.15 dB/km

7. Additional investigations

Some compatibilities with accessories are investigated by the optimization of the central core cables with ITU-T G.654.E fibers. One of the accessories is closure for long-haul application. The cables and closure were assembled together and mechanical and vibration tests were conducted. And after temperature aging, watertightness test was conducted. The result found that there were no abnormalities such as flooding or leakage.



Figure 5. Assembly of closure and central core cables

With regard to coating material covering optical fibers, its optimization of Young's modulus is also important parameter for lower transmission loss performances. The investigation of optimal coating material has been conducted and the lower transmission loss performances has been observed by adopting lower Young's modulus for fiber coating materials.

8. Conclusions

The study was investigated by putting the performance of central core cable with ITU-T G.654.E fibers under various conditions to achieve lower transmission loss. Lower A_{eff} of the fiber, lower fiber packing density and longer stranding lay length contributed to lower transmission loss performances. The investigation found to be

effective for suppression of bending stress. Central core cables using RR and ITU-T G.654.E fibers with good transmission loss performances and good mechanical and environmental performances have been successfully developed.

9. References

[1] Recommendation ITU-T G.654, Mar. 2020.

[2] Recommendation ITU-T G.652, Nov. 2016.

[3] T. Gonohe, et al, "Transmission performance of 600 Gbps per Wavelength Signals over Installed Slotted-core cable using G.654.E Optical Fibers", Proceedings of the 68th IWCS Conference, 9-1 (Oct. 2019).

[4] Y. Hoshino, et al, "Development of Rollable Optical Fiber Ribbon and Ultra High Density Cable", Proceedings of the 61st IWCS Conference, 2-3 (Oct. 2012).

[5] M Tsukamoto, et al, "Ultra-High Density Optical Fiber Cable with Rollable Multicore Fiber Ribbon", Proceedings of the 65th IWCS Conference, 14-3 (Sep. 2016).

10. Pictures of Authors



Tomoaki Gonohe received his B. E. degree from Waseda University, Tokyo, Japan, in 2002. In 2002, he joined Furukawa Electric Co., Ltd., where he has been engaged in production engineering of optical fibers cable. He is now the assistant manager of optical cable R&D, Optical Fiber & Cable Products Division.



Hirotaka Koriki received the M.E. degree in Science from Waseda University in 2018. He joined Furukawa Electric Co., Ltd. in 2018. He is now the research engineer of optical cable R&D, Optical Fiber & Cable Products Division.



Masataka Tabuse received his M. E. degree in Physics from Hiroshima University, Hiroshima, Japan, in 2022. In 2022, he joined Furukawa Electric Co., Ltd. He is now the research engineer of optical cable R&D, Optical Fiber & Cable Products Division.



Masaru Nakajima received his M. E. degree in Material Science and Engineering from Waseda University, Tokyo, Japan, in 1999. In 1999, he joined Furukawa Electric Co., Ltd. He is now the manager of optical cable R&D, Optical Fiber & Cable Products Division.

High Density Micro Duct Cables with 200-micron Flexible Ribbons

H. Edward Hudson, William C. Hurley, Chris Kalivoda,

Leigh Josey, Mark H. Bushnell

Corning Optical Communications

Hickory NC, USA

+1-828-901-6082 · ehhudson@corning.com

Abstract

Cables are developed to meet specific user requirements, and each requirement places restrictions on the cable's design. Additionally, the requirements are often opposing to each other which drives the designer to develop new technologies to meet all the requirements simultaneously. For example, customers require high fiber count cables, which drives the designs to large high-density cables, but they need to jet these cables into small ducts. The development of the new high-density cables and flexible ribbons made with 190-micron bend-resilient fibers is described and how these components work together to make globally compliant cables. Herein are presented the results from the development and testing of high-density cables with 200-micron flexible ribbons.

Keywords: High density, 200-micron, flexible, ribbon, micro duct, outside plant (OSP), indoor/outdoor (I/O)

1. Introduction

Industry surveys and discussions with customers indicated the need for high fiber count cables that could be jetted through small ducts. The customers required cables that were easy to splice with low splice loss. Additionally, the end user required outside plant cables (OSP) and indoor cables. The indoor/outdoor (I/O) cables are dual-listed for flame with both OFNR-LS (Riser, Low Smoke) and Euro class (EU Construction Products Regulation) Cca ratings allowing for a single product solution around the globe. This paper describes the development of 288 f micro duct cables for OSP and I/O applications.

2. Fibers

A 190-micron diameter fiber with improved bend resilience was used in the development of the high-density cables with 200-micron flexible ribbons. These 190-micron fibers have 40% less cross-sectional area than fibers with 242-micron diameter. Additionally, the improved bend resilience allows for tighter packing within a high-density cable construction than legacy single mode fibers. Both G.657.A1 and G.657.A2 fibers were explored. It should be noted that the G.657.A1 fibers evaluated have A2-level performance at 7.5 mm and 10 mm bend radii.

In addition to supporting high density applications, these fibers have a nominal 9.2-micron MFD which provides compatibility with the existing installed base in most legacy networks. When an OTDR is used to measure splice loss, a MFD mismatch would cause false gainers and losses in the attenuation signal. Typical mitigation for this measurement error is to perform bidirectional testing, which adds complexity and cost to installation. The MFD compatibility of the fiber selected for development of these high-density cables with flexible ribbon allows the installer to avoid this complexity that would result from use of some alternate bend resilient fibers with a lower MFD. Table 1 shows the ITU-T macro bend attenuation requirements for A1 and A2 fibers.

Table 1. ITU-T Recommendation G.657 Macro bend Requirements

	ITU-T G.657.A1		ITU-T G.657.A2	
Macro bend	**1550 nm**	**1625 nm**	**1550 nm**	**1625 nm**
1 turn at 7.5 mm radius	NA	NA	0.5 dB	1.0 dB
1 turn at 10 mm radius	0.75 dB	1.5 dB	0.1 dB	0.2 dB
10 turns at 15 mm radius	0.25 dB	1.0 dB	0.03 dB	0.1 dB

3. Ribbon Design

Flexible intermittently bonded ribbons are used in this cable design because their ability to deform allows for significantly more efficient packing density in the cable core enabling higher fiber density designs. In addition to enabling higher densities the flexible ribbon also maintains the splicing and organizational benefits of rigid ribbon.

While intermittently bonded ribbon can provide significant benefits to cable designers and end users, they also introduce a few challenges. In particular, the intermittent bonds can introduce microbend losses and can also be a point of failure in downstream processing or in the field, leading to slower termination times.

These challenges were addressed in several ways. Micro bending was primarily managed by optimization of the bonding pattern, the improved bend resilience of the 190-micron fiber, and improvements to the bond material properties.

The flexible ribbon bonding pattern has been designed to prevent bonds from overlapping across the width of the ribbon. This ensures that only one pair of subunits is constrained at any point on the ribbon, allowing for the ribbons to be more tightly packed without inducing attenuation. Figure 1 shows the bonding pattern on the ribbon.

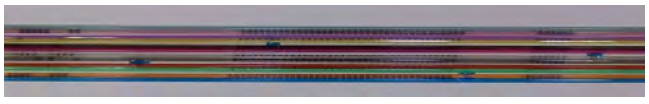


Figure 1. Flexible Ribbon Bonding Pattern

Additionally, the new bend resilient 190-micron diameter fiber has demonstrated significant benefits over standard G.657.A1 190-micron fiber, allowing for higher packing densities while maintaining optical performance. In one cable test, the bend resilient 190-micron fiber had approximately 50 % less delta attenuation at -40 °C than a standard 190-micron fiber in an equivalent packing density, as shown in Figure 2.

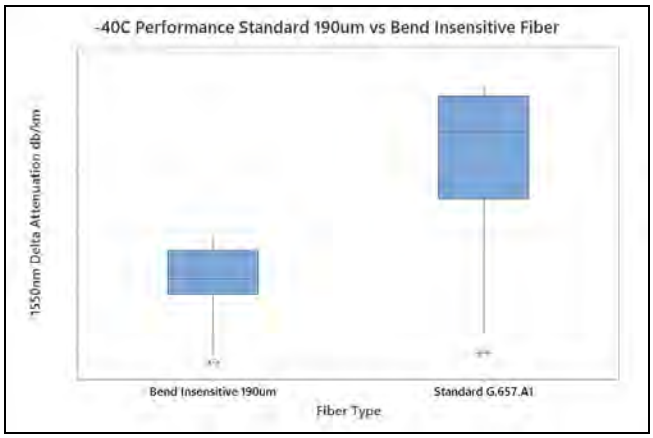


Figure 2. 190-micron Bend Resilient Fiber vs Standard G.657.A1 190um Fiber at -40°C

The final major contributor to microbend performance is the material properties of the bond material. Initial versions of the bond material using off-the-shelf materials were not able to deliver sufficient optical performance and bond strength, so a custom-formulated bond material was produced to ensure good performance. The custom-formulated material ultimately reduced delta attenuation by approximately a factor of 5 relative to the earlier materials.

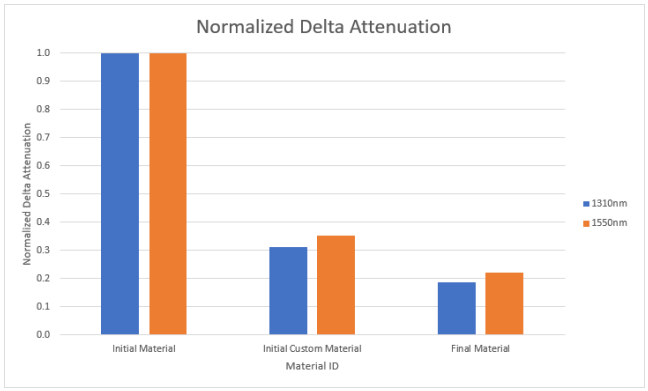


Figure 3. Optical Performance on the Ribbon Reel with Various Bond Materials

Ribbon robustness is primarily managed by ensuring good alignment of the bonding material to the subunit gaps and through bond material properties. Alignment is ensured using a vision system which allows for the alignment quality to be monitored and corrected if needed.

The bond materials properties are the most significant factor to the overall robustness of the ribbon. The current version of the bond material has improved the robustness of the ribbon by approximately a factor of 10 relative to initial prototypes as shown in Figure 4, and by a factor of 2 relative to the earlier viable iterations of the ribbon.

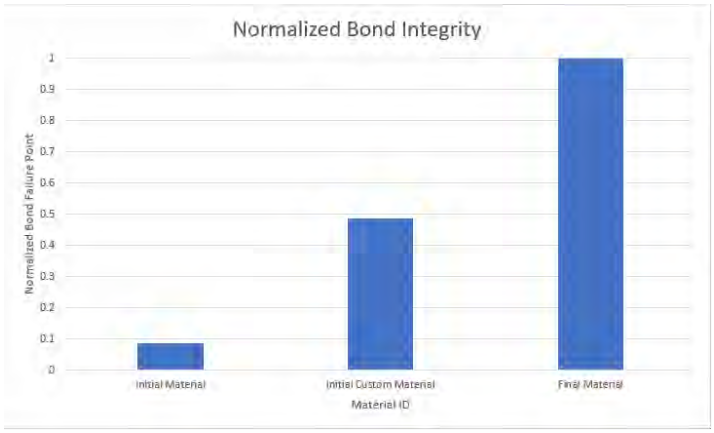


Figure 4. Relative Bond Integrity of Various Bond Materials

4. Ribbon Splicing

The 200-micron flexible ribbons meet applicable portions of GR-20 ribbon testing. The flexible ribbon construction, containing six, two-fiber subunits, intermittently bonded along the length keeps fibers parallel resulting in no fiber crossovers during splicing operations. Furthermore, the ribbons are individually printed for unique identification, and each of the ribbon fibers are color coded for unique fiber identification.

The intermittent bonds allow the ribbon to be separated into two-fiber subgroups (by hand) and the ribbon matrix material is removable. After aging in water, temperature, and humidity, and in water blocking materials, the ribbons are still able to be stripped in preparation for splicing.

Splicing 200-micron flexible ribbon is similar to splicing conventional ribbons in many respects; the process being strip, clean, and cleave. The smaller diameter fibers, coupled with a currently installed base of 250-micron fiber means the 200-micron flexible ribbons must splice to existing, conventional ribbons as well as flexible ribbons.

There are two types of ribbon splicers available in the commercial market: those with 200-micron pitch v-grooves and those with 250-micron pitch v-grooves. If using a 200-micron pitch splicer, the technician can use existing splice handlers.

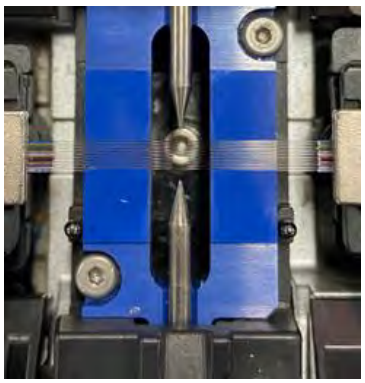


Figure 5. Sumitomo 200-micron Fusion Splicer

However, the splice technician will need to use pitch conversion handlers when splicing flexible ribbon in splice machines with 250-micron pitch v-groove. These handlers separate the fibers

into three groups of 4 fibers (as indicated by arrow in Figure 6). If these three groups are clearly visible after cleaving, the ribbon/fibers easily drop into the v-grooves when the handler is seated into the splice machine.

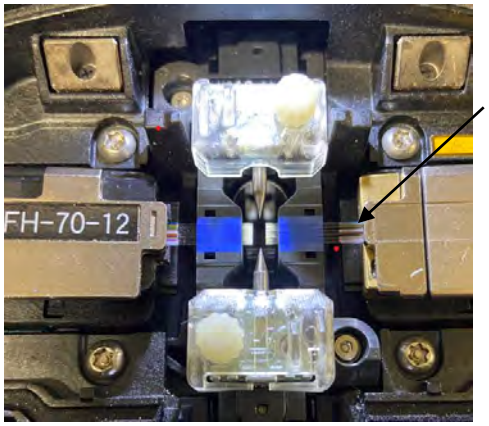


Figure 6. Ribbons in Splicer after Cleaving

It is also possible to splice the rollable ribbon to other 200-micron ribbons in a splice machine with 250-micron pitched v-grooves. The splice technician would need to use two of the pitch conversion handlers as shown below in this instance.



Figure 7. Flexible Ribbon to Flexible Ribbon in 250-micron pitch Splicer

The splice machines produce acceptable splice loss when using flexible ribbon. Figure 8 shows splice loss data using commercially available splice machines with both 200-micron and 250-micron pitch v-grooves. While the industry standard is 0.3dB per splice, splicers target a maximum splice loss of 0.1dB per splice. It should be noted the results were obtained using personnel with little rollable ribbon splice experience.

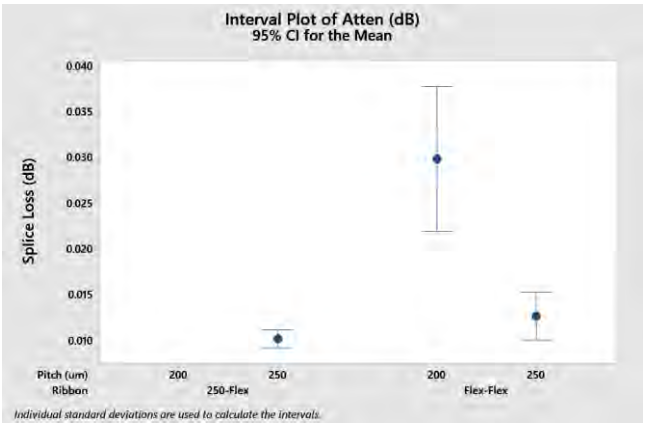


Figure 8. Splice Test Results

Splicing with flexible ribbons is achievable using commercially available splicers.

5. Cable Design

The design and development of outside plant and indoor / outdoor micro duct cables pose several design challenges. First, the end user requires a high fiber density cable design that can be jetted into extremely small micro ducts with a duct fill ratio of greater than 70 percent. Typical duct manufacturers recommend a 65 to 70 percent fill ratio to allow for variation in duct inside diameter and cable outside diameter. Secondly, the micro duct cables must meet existing standards, ANSI/ICEA S-122-744-2016 for outside plant or ANSI/ICEA S-122-696 for indoor / outdoor rated cables. Additionally indoor / outdoor rated cables must meet US burn standards such as UL 1666 and UL 1685 as well as the Construction Products Regulation for European countries if required.

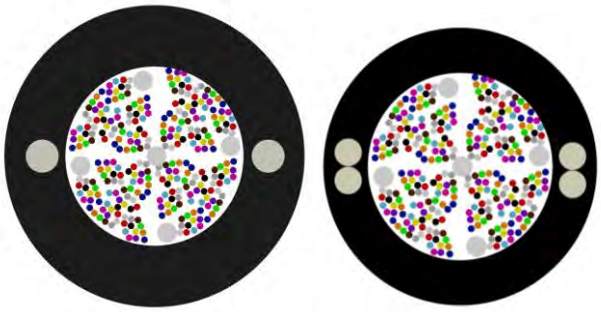


Figure 9. 288 Fiber I/O and Outdoor Cable

5.1 Ribbon Free Space

Extreme high density, small diameter micro duct cables require the use of flexible ribbons to meet outer diameter requirements. Legacy high density ribbon cables with planar rigid ribbons require a minimum diagonal free space which represents the nominal linear distance from the corner of the ribbon stack to the inner diameter of the tube or jacket wall. This minimum diagonal free space results in larger diameter cables which cannot be jetted in required duct spaces. High density micro duct cables with flexible ribbons do not require diagonal free space like legacy ribbon designs. Instead, the optical performance can be obtained by accounting for an area-based free space calculation which compares the cross-sectional area of the air in the inner cavity of the cable to the total cross section of the flexible ribbons in the

cable. The difference in area of the inside-cavity and area of all the materials within that cavity is the area of the air. We define the area of the fibers or ribbons to include the glass, coatings, ink, matrix, and bond dots. The percent free space is the area of the air divided by the sum of the air plus fibers or ribbons times 100 to get percent.

$$\text{Percent FS} = \text{Air} / (\text{Air} + \text{Fibers or ribbons}) * 100 \qquad (1)$$

For example, if the cable has a fiber area of 2 mm^2 and the air area of 3 mm^2, then the free space is

$$\text{Percent FS} = 3/(3+2) * 100 = 60\%$$

The design team used a calculated ribbon free space range of 47 to 55 percent for the specific fibers chosen for development of this cable. It is expected that an acceptable range of free space is dependent on bend resilience of the fiber selected.

5.2 Jacket Wall Thickness and Strength Elements

Small diameter, outside plant micro duct cables require a minimal wall thickness to achieve desired cable diameter and the required ribbon free space to allow for controlled fiber optic ribbon movement, tensile strength, and acceptable cold temperature performance. Because micro cables must be capable of being jetted into the micro ducts, glass reinforced plastic (GRP) rods were embedded into the cable jacket wall. Outside plant cables with wall thicknesses around 1.20 mm would require extremely small GRP rods that could be embedded with adequate wall over and under the GRP. Therefore, a 0.70 mm GRP with EAA coating was selected. Flat or specially shaped strength elements were considered, but these specialty shapes presented additional processing challenges. EAA coating was used to ensure the jacket bonds to strength elements. The outdoor cable was able to achieve 300-pound tensile rating with acceptable levels of fiber strain.

5.3 Crush Performance

Cables with 200-micron flexible ribbons deliver superior crush performance because the ribbons can deform with the jacket sheath during deflection. The OSP micro duct cable was tested to ANSI/ICEA S-122-744 for crush performance. The standard requires one crush test at 500 N load with attenuation measured at load and after load removal. Cables with planar rigid ribbons have good crush performance when the ribbons are aligned parallel to the crush plates and poor performance when the ribbons are on edge between the plates. Repeated crush tests were performed to target both orientations of the ribbons stack. The flexible ribbons do not have the stack structure of the planar ribbons. Repeated crush test showed good performance at all orientations of the flexible ribbons. Additionally, the use of bend insensitive fiber further improves attenuation performance. Figure 10 shows that the attenuation during the crush test is well below the allowed limit.

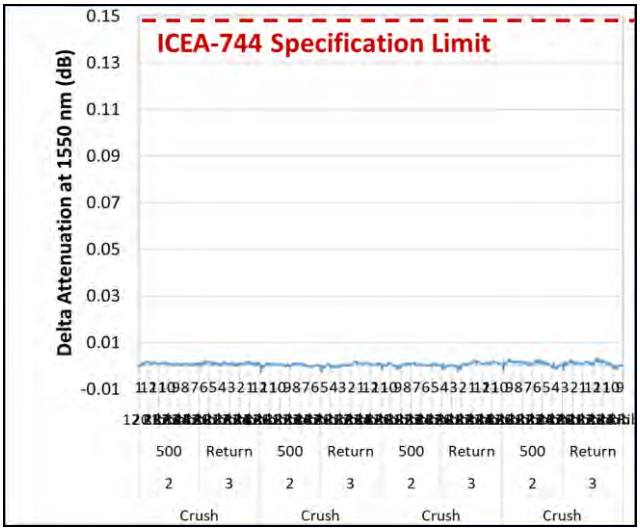


Figure 10. Repeated Crush Test

5.4 Cable Coil Testing

Like in crush and impact testing, flexible ribbon cables have improved bend performance in coil testing versus cables with legacy rigid ribbons. As jacket sheaths become non-round during tight bends, legacy rigid ribbons will experience increased attenuation on edge and corner fibers. Flexible ribbons conform to the inner diameter of the cable during bends and have essentially no increased attenuation when bent around a 100 mm mandrel or eleven times cable diameter.

Table 2. Coil Test Results

Ribbon Type	Mandrel Size mm	Mandrel Size/ Cable OD	Wraps	Attenuation dB
Rigid	600	42	9	0.25
Flexible	250	28	9	0.00
Flexible	100	11	9	0.00

5.5 Cold Temperature Performance

Cold temperature performance must also be considered in the design of a micro duct cable. In the case of outside plant cables, materials such as high-density polyethylene (HDPE) may be used as the outer jacket material. HDPE material typically has a low coefficient of friction and a high modulus that make it ideal for use in jetting cables. In contrast, high modulus materials typically experience high shrinkage during cold temperatures which may cause increased delta attenuation during environmental testing. ICEA 744 allows for two temperature ranges in the standard. A moderate low temperature requirement of -30 degrees Celsius and a standard cold temperature requirement of -40 degrees Celsius. The temperature cycling data of an indoor / outdoor cable is illustrated in Figure 11.

Also, fiber selection has a significant impact on cold temperature performance for micro duct cables, particularly those with the most aggressive free space designs. During low temperature contraction, fibers experience both macro bending and micro bending. In the design of this high-density cable with 200-micron flexible ribbons, selection of a 190-micron fiber with appropriate bend resilience was a key cable design element.

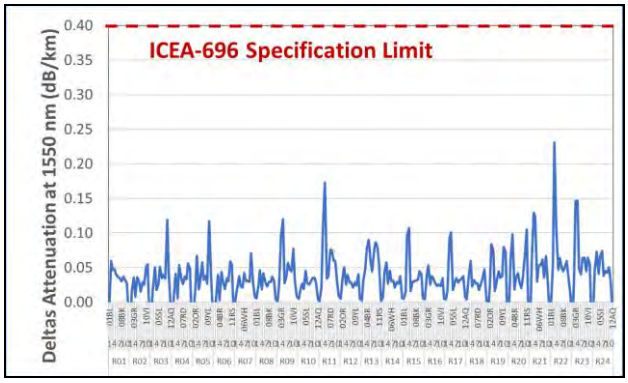


Figure 11. 288 IO Temperature Cycle Data

5.6 Excess Ribbon Length

An additional process and design criteria to consider in micro duct cables is the excess ribbon length of the cable. Excess ribbon length (ERL) is defined as the relative difference in length of the ribbons and the cable jacket. The formula is the length of the ribbons minus the length of the jacket all divided by the length of the jacket. The result is expressed as a percentage. When the cable is placed on a reel, the positive ERL causes the ribbon to move radially outward within the cable jacket. A negative ERL will cause the ribbon to move radially inward within the cable jacket. Figure 12 shows a schematic of the effect of positive and negative ERL. If ERL is high, then the cold temperature performance will be negatively impacted. The cable designer must balance outer cable diameter, jacket material selection, strength member sizing, and excess ribbon length to optimize jetting and cable performance.

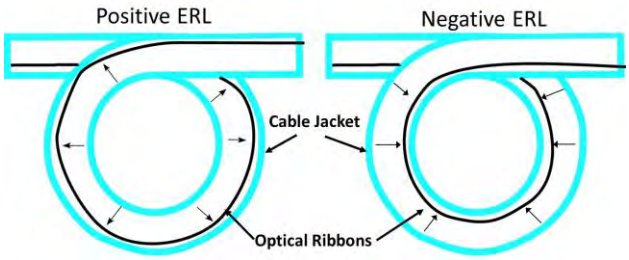


Figure 12. ERL Effect in Cable on a Reel

5.7 Jacket Material Selection

Jacket material selection is even more critical when designing an indoor/outdoor micro cable. The first and primary consideration is selecting a material that meets the required burn performance. For this indoor/outdoor micro duct cable, a global design was preferred. The cable was tested to UL 1666, UL 1685, and Construction Product Regulations (CPR) for Europe. Typical low smoke zero halogen materials with increased burn properties have a high coefficient of friction and a low modulus which are not optimal for jetting designs. The design team recognized these incongruencies and set out to identify and qualify a high modulus, low shrinkage material with excellent burn properties. Typical low smoke zero halogen materials have a flexural modulus of around 300 megapascals. Early jetting trials with this type of material were unsuccessful because the cable was flattened in the capstan belt of the cable jetting equipment causing increased cable ovality and excessive drag on the inside of the duct. A jacket material with an increased modulus of at least 600 megapascals was requested. Unlike the outside plant cable design, the coefficient of thermal expansion (CTE) and shrinkage of the new material was very low. This allowed the design team to achieve a -40 degrees Celsius low temperature rating with only two moderately sized strength elements.

6. Cable Jetting

The project requirements were to jet the 288 f OSP cable through a 10 mm duct and to jet the 288 f I/O cable through a 12 mm duct. The larger duct size for the I/O cable was allowed because the thick FR jacket needed to pass the burn tests resulted in a larger diameter cable. Cable jetting uses a capstan to pull the cable off the reel and push it into the duct. Once the cable is in the duct, air pressure is applied to pull the cable through the duct. Figure 13 shows a schematic of the cable jetting process.

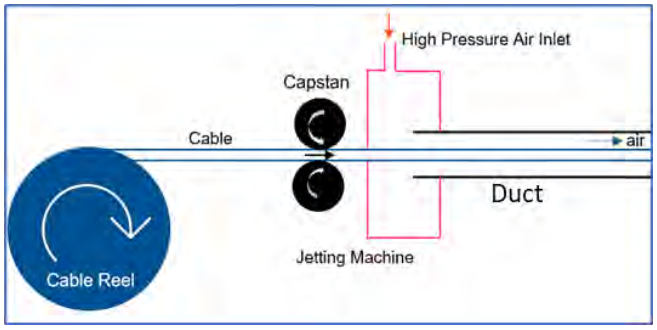


Figure 13. Cable Jetting Process

The fill ratio is an important jetting parameter. A small cable in a large duct allows the air to freely flow over the cable with little drag force on the cable, which results in poor jetting performance. Additionally, a larger compressor might be required to push the larger volume of air through the duct. A large cable in a small duct restricts the air flow and results in poor performance. The restricted air flow causes a rapid pressure drop in the duct that reduces the efficiency of the jetting process. Figure 14 shows a representation of three different fill ratios. The optimum fill ratio for jetting is in the range of 70% to 80% based on cable and duct diameters. The maximum fill ratio of 80% in a 10 mm duct limited the OSP cable diameter to 8.0 mm. Likewise the 80% fill ratio for a 12 mm duct limited the I/O cable diameter to 9.6 mm, which in turn, limited the jacket wall thickness and affected the cable burn performance.

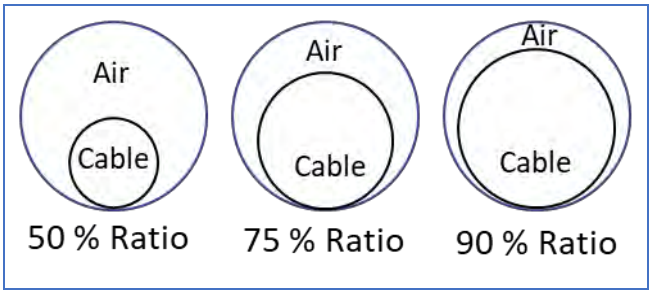


Figure 14. Fill Ratio of Ducts

The cable parameters that have a large impact on jetting performance are the cable weight, cable stiffness, and the

coefficient of friction (CoF) between the cable and the duct. The weight of the cable in the duct times the CoF between the cable and the duct determine the force needed to move the cable through the duct. The cable weight (kg/km) is mostly driven by the cable size. For this project the size of the cable was defined by the required duct size, so there was little opportunity to reduce the weight of the cable. The stiffness of the cable is mostly driven by the size of the jacket and the modulus of the jacket material. However, because the size of this cable is limited by the duct, the stiffness of the cable is essentially driven by the modulus of the jacket material. Outside plant (OSP) cables typically have polyethylene jackets with a modulus of about 800 MPa. In contrast, the LSZH jacket materials for indoor cables are highly filled with fire retardants and generally have a lower modulus and higher friction. Unfortunately, the fire-retardant (FR) jacket materials of indoor/outdoor (I/O) cables are much softer than the polyethylene used in (OSP) cables. Cable jetting requires low friction cable jackets. FR jacket materials tend to have higher friction than OSP jacket materials. These requirements drove the development of a new FR jacket material that was highly fire-retardant with high modulus and low friction.

A jetting model was used to evaluate the effects of cable stiffness and friction. The results are shown in Figure 15. The variables in the model were cable stiffness and friction, with 10 different combinations evaluated. The model indicated that increasing the cable stiffness had a small effect on the jetting distance but decreasing the jacket friction had a large effect on jetting distance.

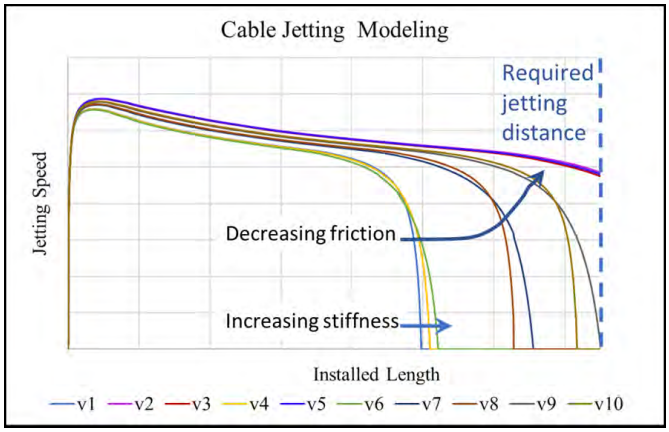


Figure 15. Results of Jetting Model

The model predicted that lubrication would have a major effect on the jetting distance; however, the actual dynamic CoF of the cable in the duct is unknown and difficult to measure. Typically, a lubricant is used in the duct to reduce the CoF. An OSP cable was tested in a 10 mm duct both with and without lubricant. This was accomplished by jetting the cable into a dry duct, removing the cable, lubricating the duct, and jetting the same cable a second time. Figure 16 shows the results of the jetting trials. The cable in the lubricated duct jetted 250% farther than the cable in the dry duct.

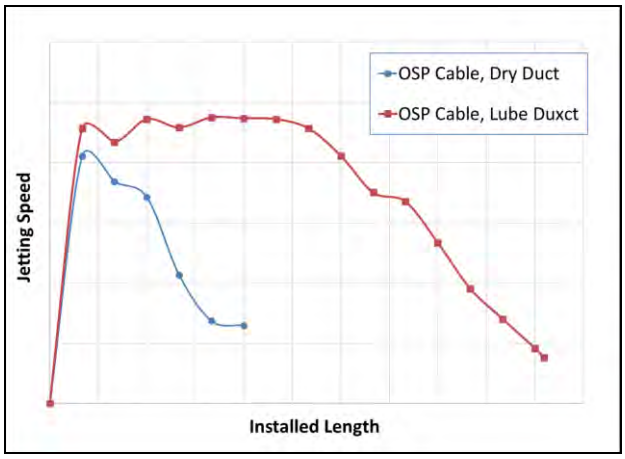


Figure 16. Effect of Lubricant in the Duct

An iterative approach was used in the development of the I/O cable. A cable that passed the burn test was later tested for jetting performance. The cable design and materials were then adjusted to pass the jetting test and meet the required burn performance.

An indoor cable was made with a high grade LSZH jacket material that met the burn requirements and was tested for jetting performance. The cable did not meet the required jetting distance. A new LSZH jacket material was developed that had a higher modulus and a lubricant added to the formulation. The CoF was reduced by both the harder material and the lubricant package. There was concern that the lubricant package in the new jacket material might affect burn perform performance; however, it was found that it performed well in the burn tests as discussed in the next section. Figure 17 shows the jetting results for the I/O cables. Cable A was made initially with a high performance LSZH material. Cable B was made with the new high modulus, low friction jacket material. This combination of cable design and jacket material met both burn test and jetting requirements.

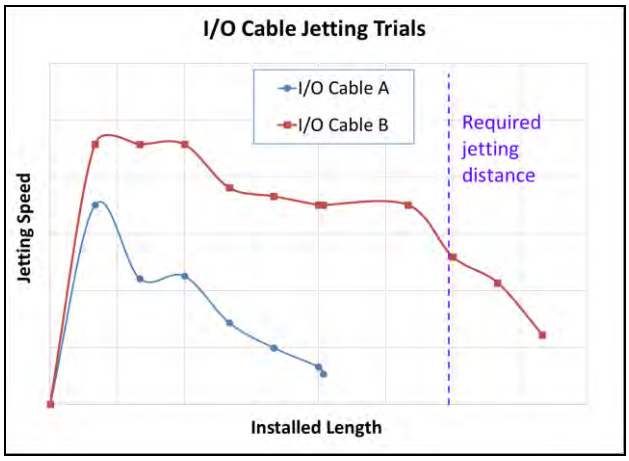


Figure 17. Results of I/O Cable Jetting

7. Burn Testing

Fire safety in building is of international concern, and each country has its own set of fire safety tests for cables. Most cables are designed for regional sales and meet the burn test requirements in the customer's region. However, there are some global customers, such as large data centers, that have facilities

around the world. These customers desire to have universal cables that meet the burn test requirements of all the regions in which they operate. The universal cables simplify the customer's logistics by having one cable to order and stock instead of separate cables for each operating region.

One of the burn tests that is common in North America is UL 1666 for riser rated cables. The UL 1666 test uses a 146-kW burner and requires the flame spread (FS) < 12 feet (3.6 m). Many North America customers want low smoke cables that meet the requirement of UL 1685 that uses a 20-kW burner and requires FS < 5 ft (1.5 m) and total smoke production (TSP) < 95 m^2. One of the primary burn tests in Europe is the Construction Products Regulation (CPR) EN 50399 test that uses a 25-kW burner that measures flame spread (FS), peak heat release rate (PHRR), total heat release (THR) and total smoke production (TSP). The EN 50399 burn performance level required for this project was CPR C_{ca}, which requires FS < 2.0 m, PHRR < 60 kW, THR < 30 MJ, and TSP < 50m^2.

The UL 1666, UL 1685 and EN 50399 burn tests are vertical ladder tests in which the flame is applied at the bottom of the ladder and the fire spreads upward. The major differences in the tests are the sizes of the burners, the allowed limits on the measured response, and the configuration of the test sample on the ladder.

The UL 1666 test uses a more powerful burner and allows more flame spread. In contrast, the UL 1685 and EN 50399 test have less powerful burner but allows less flame spread. The key parameter for the EN 50399 test seems to be the flame spread. The THR is determined by how much of the cable is burned which is driven by the flame spread. The PHRR is determined by maximum amount of the cable that is burning one time, which is also driven by the flame spread. Thus, the flame spread is a critical parameter for both tests.

The placement of the cables in the ladder has a strong effect on the test results, which causes different burning mechanisms in the UL 1666 test and the EN 50399 test. The UL 1666 and UL 1685 tests places one layer of cable in the ladder with each segment touching the adjacent segments. This has the effect that the front of that cable insulates the back of the cable from the flame. Thus, the cable burns from the front to the back. In contrast, the EN 50399 test places the cable segments with a gap between adjacent segments, and the width of the gap is equal to the cable diameter. This arrangement allows the flame to surround the cables, and the cables burn from the outside toward the center. Figure 18 shows the samples from actual burn tests. Figure 19A shows a sample from the UL 1666 test with the cable segments adjacent to each other, and Figure 19B shows a sample from the EN 50399 test with spaces between the cable segments. The difference burning mechanisms explains why some cables do well in the UL 1666 test and poorly in the EN 50399 test and others do well in the EN 50399 test and poorly in the UL 1666 test. The objective of this project was to design a cable that does well in both tests.

The main drivers of the burn test performance are the fuel loading in the cable core and the fire retardancy of the cable jacket. The fire retardance of the jacket is determined by the material selection and the wall thickness of the jacket. There was a constraint on the wall thickness of the cable jacket because the cable had to be jetted into 12 mm ducts. A cable with a high-grade low smoke, halogen free (LSZH) jacket material was tested, and it met the requirements of UL 1666, UL 1685 and EN 50399. Unfortunately, this cable failed in jetting trials. A new material was developed together with our suppliers with a higher modulus and less friction when jetted into a duct. The second cable met the burn test requirements plus the cable jetting requirements. Table 3 show the results of the burn tests



Figure 18. Sample Placement on Ladders

Table 3. Burn Test Results

8		Requirement	Cable A	Cable B
EN 50399	FS	< 2.0 m	Pass	Pass
	PHRR	< 60 kW	Pass	Pass
	THR	< 30 MJ	Pass	Pass
	TSP	< 50 m^2	Pass	Pass
UL 1666 Riser, FS		< 12 ft	Pass	Pass
UL 1658 Low Smoke		< 95 m^2	Pass	Pass

8. Conclusions

A 200-micron flexible ribbon incorporating 190-micron diameter fiber with improved bend resilience was used to achieve high density requirements for the micro duct cable by optimizing cable free space. Splicing the 200-micron flexible ribbon is similar to splicing conventional ribbons in many respects, and the ribbon construction keeps the fibers parallel preventing fiber cross overs. Cable diameter is limited by duct fill ratio for micro duct installation, and specialty jacket materials are required to meet the demanding diameter, burn, and jetting requirements. Initial sales and installations have resulted in very positive feedback for the new micro duct cables.

9. Acknowledgments

Special acknowledgement to Akshay Parmar for modeling cable jetting, Corning Engineering Services for splicing support, and the Corning Organic Materials Group for their bond material formulation.

10. References

[1] Insulated Cable Engineers Association, Inc., "Standard for Optical Fiber Outside Plant Microduct Cables," ANSI/ICEA S-122-744, July 2016

[2] Insulated Cable Engineers Association, Inc., "Standard for Indoor-Outdoor Optical Fiber Cable," ICEA S-104-696, June 2019

[3] "Multicarrier Modulation for Data Transmission: An Idea Whose Time Has Come," *Intell. Commun. Mag.*, 28(5), 5-14 (May 1990).

[4] S. Bonger. and K. D. Loch, eds., *Ethics and Computer Use*, 2nd ed., Elsevier, Amsterdam, p. 105 (1999).

Authors



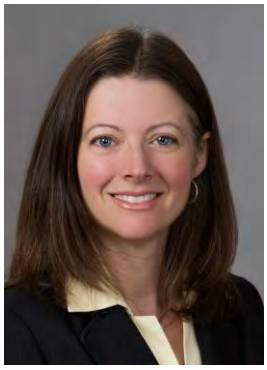
William C. Hurley is a Sr. Development Associate in optical cable design at Corning Optical Communications in Hickory, N.C. His responsibilities include the design, development, and testing of both outside plant and premises cables. He received a B.S. in 1974 and M.S. in 1980 in Chemical Engineering from North Carolina State University. He joined Corning in 1996, after retiring from the United States Air Force as Director of Rocket Systems Engineering at the Air Force Ballistic Missile Office. He holds 71 patents for fiber optic cables and assemblies.



H. Edward Hudson is a Sr. Project Leader in optical cable design at Corning Optical Communications in Hickory, N.C. His responsibilities include the design, development, and testing of both outside plant and premises cables. He received a B.S. from Lenoir Rhyne University. He joined Corning Research and Development in 2000, after working in Siecor plant operations for seven years. He holds 21 patents for fiber optic cables and assemblies



Christopher Kalivoda is a Sr. Product Engineer in optical fiber and cable at Corning Optical Communications in Hickory, N.C. His responsibilities include product specification and qualification of flame retardant and ribbon cables. He received a B.S. in 1987 from the Ohio State University in Engineering Physics and while on active duty in the United States Air Force, he received a Master's Degree in Electro Optics from the University of Dayton. He has been employed with Corning for 17 years.



Leigh Josey is a Product Line Manager for Corning Optical Communications in Charlotte, NC. Her responsibilities fall within Corning's single mode fiber portfolio. She received a B.S in chemical engineering from North Carolina State University in 2001. She joined Corning in cable research and development in 2001 and has held various positions within COC over the course of her career.



Mark Bushnell is a Senior Development Engineer for Corning Optical Communications in Hickory, N.C. His responsibilities include leading the development project for 200-micro flexible ribbon. He joined Coring in cable research and development in 2015 after receiving an M.S. in Chemical Engineering from Cornell University.

Single jacket armored Wrapping Tube Cable® with easy fiber access

Yusuke Tsujimoto[1], Mizuki Isaji[1], Noritaka Ukiya[1] and Akira Kori[1]

1) Optical Cable Research and Development Department, Optical Cable Division, Fujikura Ltd.

1440, Mutsuzaki, Sakura, Chiba, Japan

+81-43-484-3945 · yusuke.tsujimoto@jp.fujikura.com

Abstract

Recently, in regions such as North America, the demand for armored optical fiber cables have been greatly increasing. So far, we have developed double jacket armored cables from 144 to 1728-fiber. These cables have high protection features, but takes additional time for fiber access, since it is necessary to remove two layers of the jacket. In order to provide user-friendly installation, it is also necessary to optimize the armored cable structure.

This paper introduces a new structure of light weight and small diameter armored cables that we have developed, considering the efficiency of cable installation.

Keywords: optical fiber; outside plant; armor; single jacket; wrapping tube cable

1. Introduction

Optical fiber cables are widely used to transmit data in outdoor environments. In outdoor environments where ducts cannot be used, the cables are installed by directly burial methods and it is common for direct buried outdoor cables to have a protective armor layer that provides robust cable design and guards the optical fibers from excessive crush and rodent attacks. The armor layer can be metallic, and is typically covered by a jacket covering that is extruded over the armor.

2. Armored cable design

2.1 Conventional armored Cable

We have developed double jacket armored cables from 144 to 1728-fiber as shown in figure 1. They have a high protection from impact and compression but they become larger in size and heavier in weight. It needs time for access to fibers in the cable compared to standard OSP non armored cables.

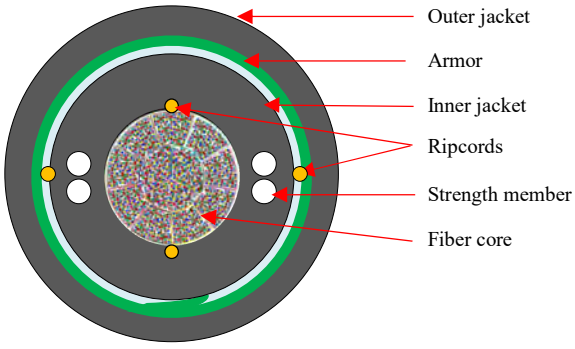


Figure 1. Structure of double jacket armored cable

2.2 Design concept of new armored cable

Increasing demand for armored cables, the development that has a smaller diameter and a light weight with good fiber accessibility armored cables are required. In order to achieve the above, for example, metal strength members are selected in terms of Young's modulus. In the case of that cables with metallic strength members, the strength members themselves can be smaller and there is a possibility of reduction in the thickness of the jacket and cable outer diameter. But when the metallic strength members are used, the outer jacket must be split in half to pick up the ripcord for armor opening in cable end preparation. Such designs have concerns on the fiber access time and workability during termination works when opening the armor and the outer jacket. On the other hand, in case of using the non-metallic strength members, the outer jacket along the armor and non-metallic strength members can be removed by ring cutting with the same method as the standard OSP non armored cables. Therefore, in order to both reduce the cable outer diameter and maintain fiber access workability, non-metallic strength members were appllied and the embedding position of them was changed from the inner layer to the outer layer. By changing the embedding position makes it possible to reduce the thickness of the inner layer and the cable outer diameter as much as possible.

Also in order to make it easier to pick up the target fiber in mid-span access work, new armored cable includes two features as SZ Bunching [1][2] and SZ Stranding.

First, structure of SZ bunching is as shown in figure 2. SZ bunching unit consists of two bundle yarns that are bonded intermittently and winding direction are reversed at the bonded point. This structure is easy to handle as bundle yarns can removed in one operation.

Second, Two types of stranded structures of fiber core are shown in figure 3. In case of helical strand structure, it must be untwisted the fiber core after picking up it. While in case of SZ strand structure in longitudinal direction, it doesn't need to untwisted the fiber core because of its naturally untwist. This facilitates picking up the target unit and contributes to excellent mid-span access workability.

So we have developed small diameter armored cables that have SZ bunching units with an inner buffer tube and have non-metallic strength members embedded in the outer jacket.

Return to Table of Contents

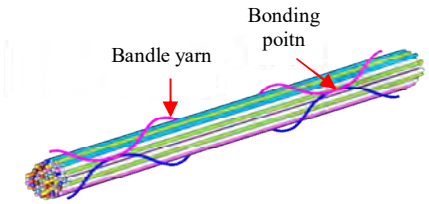


Figure 2. Structure of SZ bunching

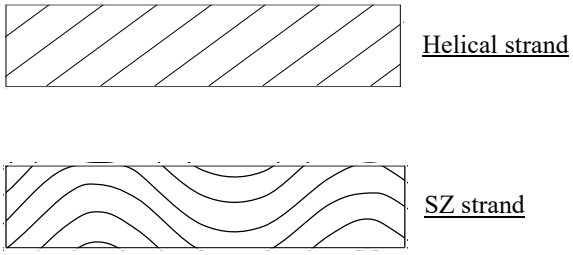
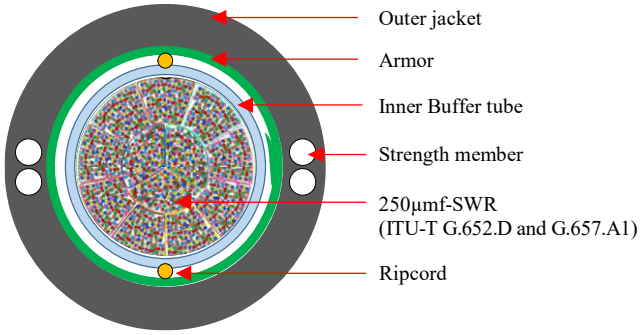


Figure 3. Structures of fiber core stranding

3. Construction of single jacket armored Cable

Figure 4 shows a cross-section of new armored cable that is called single jacket armored (SJA) Wrapping Tube Cable® (WTC®) using 250µm fibers complying with ITU-T G.652.D and G.657.A1 categories. The fiber core is wrapped around by a water blocking tape and covered with a buffer tube. Outer jacket is applied on the outside of the buffer tube in which two pairs of nonmetallic strength members are embedded. Glass-FRP was selected as nonmetallic strength members considering fiber access workability. Application of Glass-FRPs to the outer jacket allows the outer jacket to be ring-cut, which enables the access to the pair of ripcords easily. The above features significantly reduces the time required to slit the outer jacket along the armor.



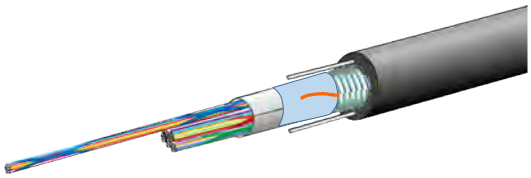
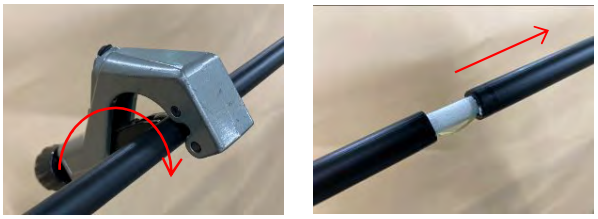


Figure 4. Construction of SJA-WTC

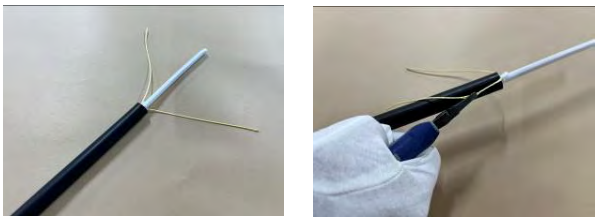
4. Fiber access workability

4.1 Cable end preparation

Cable end preparation process of SJA-WTC is shown in Figure 5. First, perform a ring cut with a tool and pick up a pair of ripcords after removing the outer jacket along the armor. Then, by pulling the ripcords the outer jacket can be split easily. When the operators pull the ripcords, they can use ordinary plier and can easily handle since the position of ripcords can be controlled. After removing the required length of the outer jacket, remove the buffer tube with commercially available general tools.



1. Ring cut and remove the outer jacket



2. Pick up and pull a pair of ripcords



3. Open and Remove the outer jacket

Return to Table of Contents




4. Ring cut and remove the buffer tube

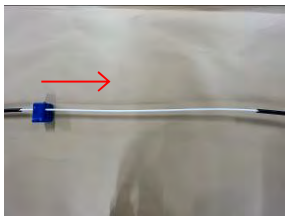



5. Cut the water blocking tape and Fiber removal is complete

Figure 5. Process of cable end preparation

4.2 Mid-span access

If required, the mid-span access can be done as shown in Figure 6. After removing the outer jacket and the armor, pull a tool to make a longitudinal slit in buffer tube. Since SJA-WTC has a SZ strand fiber core, it doesn't need to untwist during mid-span access work. Longitudinal slit or Ring cut can be performed on the buffer tube with the general tools easily.




1. Slit the buffer tube with general tool




2. Cut the buffer tube and fiber removal is complete

Figure 6. Process of Mid-span access

4.3 Result of fiber access working time

Figure 7 shows fiber access working time of SJA-WTC and double jacket armored cable respectively. SJA-WTC realized extremely short time to pick up the fiber.

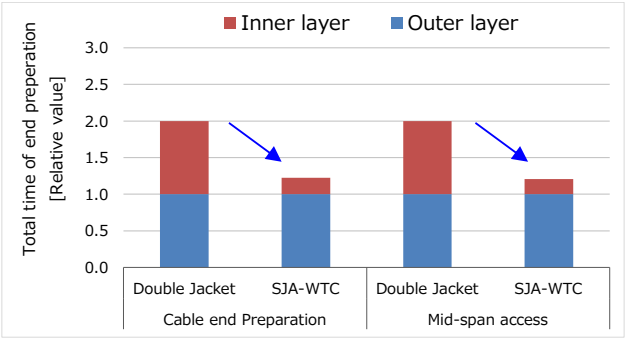


Figure 7. Total time of fiber access workability

5. Cable performance

Table 1 shows the mechanical and environmental characteristics of 144-fiber and 288-fiber SJA-WTC. The test methods were based on Telcordia GR-20-CORE [3] and ANSI/ICEA S-87-640. The wavelength for the tests was 1550nm. Figure 8 shows excellent results of the temperature cycling test under -40/+70°C, 2cycles. Good mechanical and environmental characteristics were obtained.

Table1. Characteristics of 144f and 288f SJA-WTC

Item	Condition	Result	
		144 fiber	288 fiber
Low-and High-Temperature Cable bend	Bending radius: 15D (D: cable diameter) -30/+60 degree C, 2Cycles	Pass	Pass
Impact Resistance	4.4 J	Pass	Pass
Compressive Strength	110 N/cm 10 minutes	Pass	Pass
Tensile strength of Cable	2700 N, 1 hour	Pass	Pass
	810 N, 10 minutes	Pass	Pass
Cable Twist	Sample length: 2 m ±90 degree, 10 Cycles	Pass	Pass
Cable Cyclic Flexing	Bending radius: 10D (D: cable diameter) 25 Cycles	Pass	Pass

Return to Table of Contents

Temperature Cycling	-40/+70 degree C, 2cycles	Pass	Pass
Water Penetration	Height of water: 1 m Sample length: 3 m 24 hours, Tap water	Pass	Pass

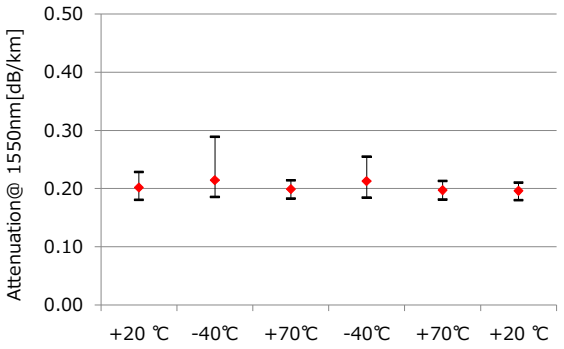


Figure 8. Result of 288f temperature cycling test

6. Design for 144 to 864 fiber SJA-WTC

Table 2 shows the design of 144 to 864-fiber cables using 250µm fiber complied with ITU-T G.652.D and G.657.A1 categories. It indicates that the SJA-WTC has succeeded in maximum 20% cable diameter and maximum 25% weight reduction compared to conventional armored cables as shown in figure 9 and 10. In addition, by reducing a diameter of the cable, the cable winding length on shipping drum becomes longer and it will be possible to offer the winding lengths typically required by customers.

Table2. Design of SJA-WTC

Fiber count		144	288	432	864
SJA-WTC	Cross section				
	Outer diameter [mm]	14.0	14.5	16.0	20.0
	Weight [g/m]	175	190	235	340

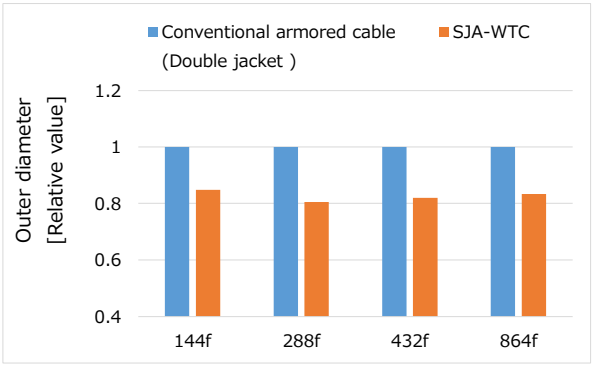


Figure 9. Cable outer diameter

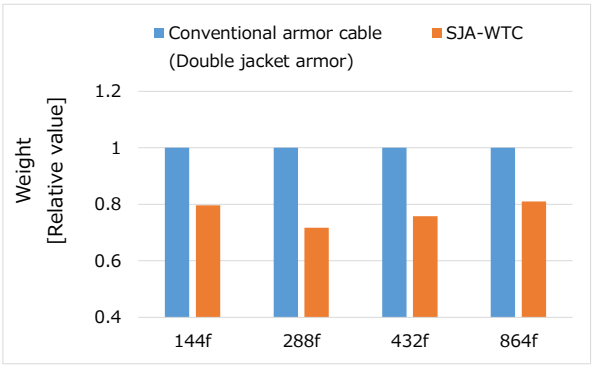


Figure 10. Cable Weight

7. Conclusions

Single jacket armored WTC using 250µm fiber was developed. By innovative structural modification, new cable realizes extremely easy fiber access and the cable outer diameter and weight have been reduced when compared to the conventional double jacket armored cables. This innovative cable will contribute to the economical and effective construction of optical fiber network. Additionally, reducing the plastic materials and the environmental impact from transportation, also contribute to Green Transformation (GX).

Return to Table of Contents

8. References

[1] M. Yamanaka, et al. “Ultra-high density optical fiber cable with Spider Web Ribbon”, Proceedings of 61st IWCS, 2012 pp.37-41 (2012)

[2] M. Isaji, et al., “Ultra-High Density Wrapping Tube Optical Fiber Cable with 12-Fiber Spider Web Ribbon”, Proceedings of 62nd IWCS, 2013 pp.605-609 (2013).

[3] Telcordia Technologies Generic Requirements GR-20-CORE issue4 (2013)

[4] ANSI/ICEA S-87-640, “STANDARD FOR OPTICAL FIBER OUTSIDE PLANT COMMUNICATIONS CABLE,” (2016).

9. Pictures of Authors



Yusuke Tsujimoto
Mr. Yusuke Tsujimoto joined Fujikura Ltd. in 2018 after graduation from Yamagata University with M.E. degree, and has been engaged in research and development of optical fiber cables. He is now an engineer in optical cable R&D Dept.



Mizuki Isaji
Mr. Mizuki Isaji joined Fujikura Ltd. in 2003 after graduation from Tokyo Institute of Technology with M.S degree, and has been engaged in research and development of optical fiber cables. He is now a senior researcher in optical cable R&D Dept.



Noritaka Ukiya
Mr. Noritaka Ukiya joined Fujikura Ltd. in 1994 after graduation from Chiba University with B.E. degree, and has been engaged in design and research and development of optical fiber cables. He is now a group manager in optical cable R&D Dept.



Akira Kori
Mr. Akira Kori joined Fujikura Ltd. in 1989 after graduation from Yamagata University with B.E. degree, and has been engaged in optical fiber cable production engineering. He is now a general manager in optical cable R&D Dept.

Return to Table of Contents

High Fiber Density 3456F Flexible Ribbon Indoor/Outdoor Cable for Data Center Applications

Eric Anderson, Gavin Lin, Jeff Barker, Brian Risch, Ben Wells
Prysmian Cables and Systems
700 Industrial Drive,
Lexington, SC 29072
+1-803-951-4018 · eric.anderson@prysmiangroup.com

Abstract
Recently demand has grown for high fiber count optical cables in places like data centers. Cables utilizing flexible ribbon technology have also proven to be very good options for data center applications because of their lower outer diameters and compatibility with mass fusion splicing. Many customers deploy cables in the European countries, outside the US and Canada. This necessitates the use of high-density fiber optic cables that not only meet the building codes of the US and Canada but also fulfill the fire performance criteria necessary for indoor installation in European regions.

The 3456F flexible ribbon indoor/outdoor cable presented in this paper features a high fiber density compact design combined with UL-1685/FT4 and UL-1666 as well as CPR flame ratings. These features make the cable extremely versatile. The cable is suitable for the indoor and outdoor applications in the U.S., Canada, and the European countries. Beyond its impressive flame rating, the cable also passed various mechanical and environmental testing, per GR-20 and ICEA-696 specifications, all yielding passing results which will be shared in this paper.

Keywords: Fiber Optic Cable; Indoor/Outdoor; UL/cUL; CPR; High Fiber Density; Flame Rating

1. Introduction
Since the Covid-19 pandemic, demand has significantly grown for fiber optic cable. The global market size for fiber optic cable is expected to reach a value of over 20 billion U.S. dollars by 2028 and have a CAGR of over 15%. In addition, the growing 5G network, fiber to the home (FTTH), fiber to the cabinet (FTTC), and fiber to the premises (FTTP) only further the demand for reliable fiber optic cable [1].

Furthermore, there is a strong demand for high fiber density cables that can connect between data centers in an outdoor environment, and also extend into the data center buildings for indoor applications. These cables need to meet specific requirements, beyond what is required for outdoor only applications to be certified for safe use in an indoor application.

The flexible ribbon product line has provided an excellent solution for customers desiring high fiber counts along with smaller outer diameters. The structure of flexible ribbon allows for smaller fiber bundle diameters compared to the flat ribbon product line. In addition to this, mass fusion splicing times have been reduced to make installation times comparable to flat ribbon [2].

As the number of data centers continues to grow in North America, the same is happening in Europe. The demand for high-density fiber optic cables that meet fire safety requirements outlined by the Construction Product Regulation (CPR) is becoming more crucial. These cables are essential for maintaining efficient and reliable communication within data centers while ensuring compliance with safety standards.

The 3456F flexible ribbon indoor/outdoor cable has achieved UL/cUL rating of OFNR/FT4-ST1 and CPR rating of B2ca-s1b, d2, a1. These ratings allow it to be a viable solution for a customer needing the high fiber count of a 3456 flexible ribbon cable as well as meet or exceed building codes and fire performance requirements of the US, Canada, and European countries. In addition, the mechanical and environmental testing on this cable guarantees performance that meets or exceeds industry standards. This paper shows both the UL and CPR flame results and the mechanical/environmental test results conducted per GR-20 and ICEA-696.

2. Cable Structure
Figure 1 shows a cross-sectional view of the 3456F flexible ribbon indoor/outdoor cable. The cable contains twenty-four buffer tubes, each containing twelve 12f flexible ribbons with 200um bend insensitive fiber (144 fibers per buffer tube). Each tube contains water swellable yarns and tape for protection against water intrusion. The first nine buffer tubes are S/Z stranded around an upjacketed GRP member. The remaining fifteen buffer tubes are S/Z stranded around the first nine tubes. Each stranded layer contains water-swellable tape wrapped around the tubes for protection against water intrusion in the cable. The outer stranded layer contains flame resistant tapes. The cable is jacketed with a flame-resistant compound to a specified outer diameter and wall thickness. In addition, twelve water swellable strength yarns are added to enhance cable's stiffness and tensile strength.



Figure 1. Cross-sectional View of the 3456F Flexible Ribbon Indoor/Outdoor Cable

3. Mechanical Test Results

Various mechanical performance tests were conducted on the 3456F flexible ribbon indoor/outdoor cable, per GR-20 and ICEA-696. These tests simulate both external forces that may be present during cable installation or operation and the change in attenuation of the fibers while those forces are present. The following sections show the results of the mechanical testing performed on this cable.

3.1 Low and High Temperature Cable Bend Test

A Low and High Temperature Cable Bend test was conducted on the cable to simulate mechanical bending forces combined with temperature extremes that may be present during installation. The test was performed in accordance with FOTP-37. Figure 2 shows the results of the Low and High Bend Temperature cable test. All fibers were significantly below the ICEA-696 attenuation increase limit of .40 dB. The jacket did not show any signs of physical damage following the test.

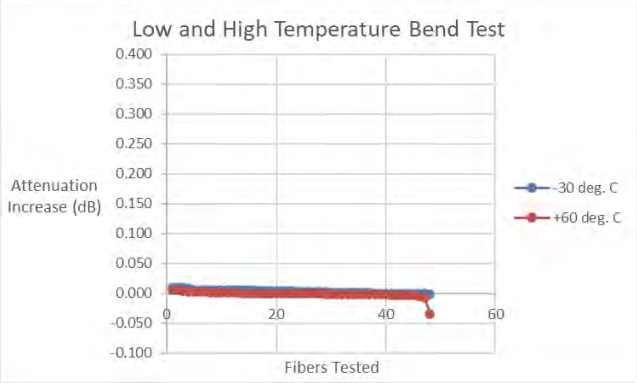


Figure 2. Low and High Temperature Bend Test Results

3.2 Cable Cold Impact Test

Per ICEA-696, the cable was tested to meet the requirements to withstand an impact to the jacket at cold temperature during installation. The cable was conditioned for four hours at -10 deg. C prior to impact. An impact energy of 2.94 N•m was applied to the jacket following temperature conditioning. The cable was tested at three separate locations, each receiving passing results with no physical damage present. Table 1 shows the results.

Table 1. Cable Cold Impact Test Results

Test Data:				
Test Sample:	Site 1	Site 2	Site 3	Pass / Fail
Number Splits	0	0	0	Pass
Length of Splits	NA	NA	NA	

3.3 Cable Tensile Loading and Fiber Strain Test

A Tensile Loading and Fiber Strain test was conducted on the 3456F flexible ribbon indoor/outdoor cable. The purpose of this test is to evaluate the fiber attenuation increases and physical changes that can occur when the cable is exposed to bending combined with tensile loading. A cable sample is wrapped around a machine consisting of multiple pulleys and exposed to the rated load of 600 lbs. for one hour. The load is then reduced to the residual load (200 lbs.) for 10 minutes, and then removed completely for five minutes. The attenuation increase is measured at the residual load and with the load removed. Strain is measured at the rated installation load and residual load. All fibers had significantly less attenuation increase and strain than the maximum stated in ICEA-696. Figures 3 and 4 show the results.

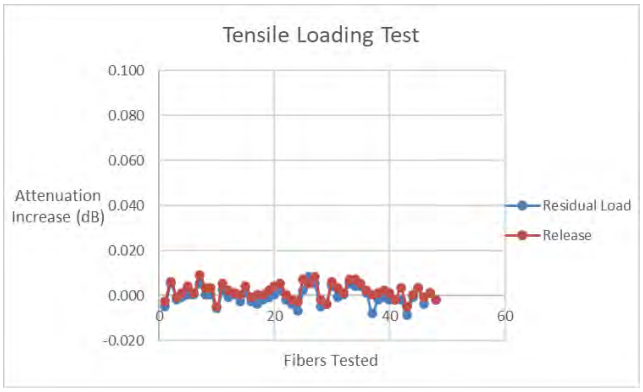


Figure 3. Cable Tensile Loading Test

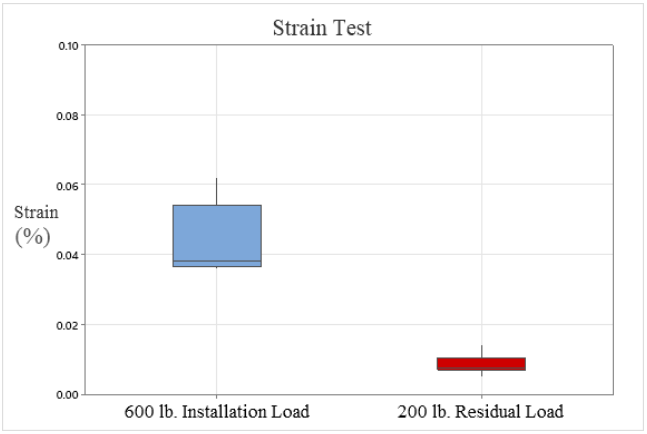


Figure 4. Cable Strain Test

3.4 Cyclic Flex, Cable Impact, Cable Compressive Loading, Cable Twist Tests

The 3456F flexible ribbon indoor/outdoor cable underwent Cyclic Flex, Cable Impact, Cable Compressive Loading, and Cable Twist tests and performance was evaluated with all these external forces that may be seen during installation of the cable. The Cyclic Flex test performs a 180-degree flexure load on the cable. The cable is inserted into a mandrel and bended back and forth for 25 cycles. The cable impact test involves a weight dropping on the cable with a minimum energy of 4.4 N•m. The weight is dropped twice at three separate locations. The Cable Compressive Loading test applies a 220 N/cm incidental load on a cable sample at a rate of 2.5mm/min. That load is held constant for a period of 1 minute. The incidental load is removed and within 5 minutes a 110 N/cm long-term load is applied at a rate of 2.5mm/min and held for 10 minutes. Attenuation is then measured on the fibers being tested. The Cable Twist test applies a twist load to a sample that is connected to a fixture. The sample is twisted 180 degrees for 10 cycles and attenuation is measured after the last cycle. Figure 5 shows the results for these four mechanical tests. The ICEA-696 attenuation increase limit is 0.40 dB. All fibers tested pass with a comfortable margin. In addition, no external jacket damage was observed.

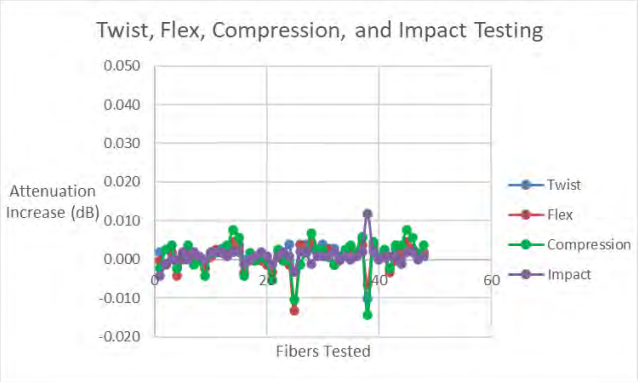


Figure 5. Twist, Flex, Compression, and Impact Test Results

3.5 Cable External Freeze Test

A Cable External Freeze test was conducted to evaluate the capability of the fibers to resist attenuation increase when freezing water develops around the cable. Another purpose of this test is to ensure that cracks do not develop at the extreme cold temperature in moist conditions. To perform this test, a coil sample was wrapped inside a tank filled with water. This tank was placed inside a sealed chamber and brought to cold temperature sufficient for ice formation around the sample. The temperature was then raised to -2 deg. C and held for 1 hour. Attenuation increases were then measured and compared to the ICEA-696 limit of 0.40 dB. Figure 6 shows the attenuation increase at -2 deg. C. The results show the cable passing with a comfortable safety margin. The jacket also did not develop any visible cracks during the test.

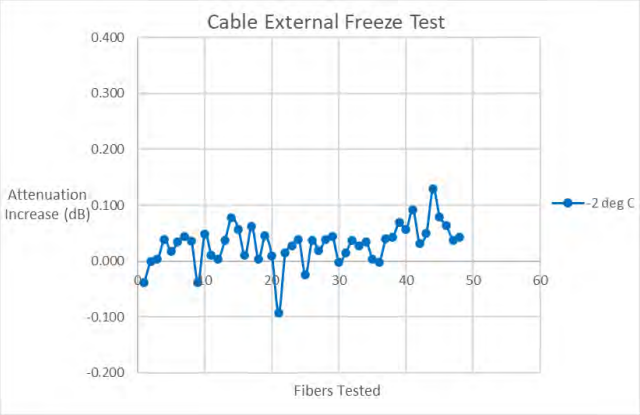


Figure 6. Cable External Freeze Test

3.6 Water Penetration Test

This cable was evaluated for prevention against external water penetration according to GR-20 and ICEA-696. This test involved removing a 3-meter sample and pre-soaking 100mm of one end of the cable with tap water. That same end was inserted into a pipe connected to a tap water reservoir with 1m water head. After 24 hours, there was no water penetration observed at the opposite end. Table 2 shows the results.

Table 2. Water Penetration Results

Sequential No.	Sample Length	Date / Time On	Date / Time Off	Duration	Pass/Fail
2860' - 2868'	3 meters	1/24/22 10:50 AM	1/25/22 10:50 AM	24:00:00	Pass
Inspector:		TJ	TJ		

4. Environmental Testing

This cable underwent temperature cycling to measure attenuation increase against the extreme cold and hot temperatures that might be seen in the field. The cable is placed in a sealed chamber and allowed to reach the extreme hot and cold temperatures for a given amount of time. Attenuations are compared to reference measurements at room temperature. Figures 7 and 8 show the attenuation elevation for A1 and A2 fiber respectively. For A1 fiber, it meets the ICEA-696 specification of ≤.40 dB/km at -30^{0}C and +70^{0}C. As expected, the A2 fiber has a stronger performance at low temperatures as seen from Figure 8, where all fiber attenuation elevations are below .40 dB/km at -40^{0}C.

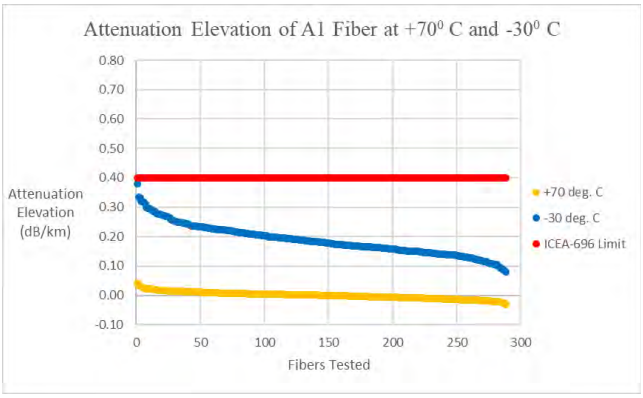


Figure 7. Attenuation Elevation of A1 Fiber at +70^{0}C and -30^{0}C

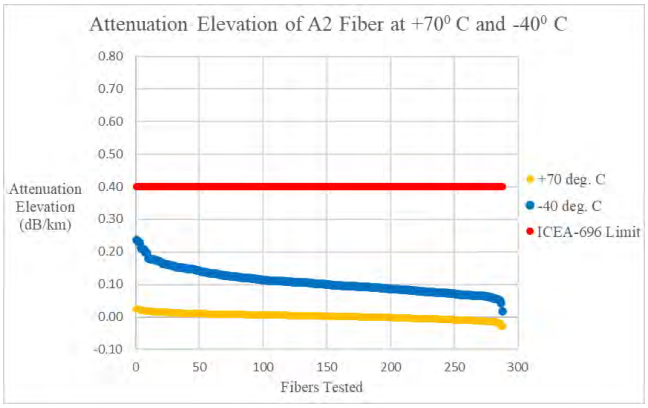


Figure 8. Attenuation Elevation of A2 Fiber at +70^{0}C and -40^{0}C

5. Burn Test Results

This cable was evaluated with UL and CPR requirements in order to be qualified for indoor/outdoor applications in both the US and Canada as well as the European countries. Cable samples were burn tested per UL-1666, UL-1685 type 2 (with smoke measurement) requirements, and EN50399, EN60332-1-2 per CPR regulation. Table 3 shows the performance of the cable against the CPR specifications. Based on the burn test results, this cable achieved a UL/cUL OFNR/FT4-ST1 riser cable rating and a B2ca-s1b,d2,a1 CPR rating.

Table 3. Performance of 3456F Flexible Ribbon Indoor/Outdoor Cable Against CPR Specifications

Euroclass	FS (m)	THR 1200s (MJ)	HRR Max (KW)	FIGRA (W/s)	Smoke	TSP 1200s (m^2)	Peak SPR (m^2/s)	Acidity	Conductivity (µS/mm)	pH	Flaming Droplets	
3456F FlexR I/O Cable Performance												
B2ca	0.8	13.4	20	29	s1	1.1	0.01	a1	0.3	5.3	d2	>10s
CPR Specifications												
B2ca	≤1.5	≤15	≤30	≤150	s1	≤50 m^2	≤0.25	a1	< 2.5	>4.3	d0	No
Cca	≤2.0	≤30	≤60	≤300	s2	≤400 m^2	≤1.5	a2	< 10	>4.3	d1	<10s

6. Conclusion

Demand has grown considerably for fiber optic cable in the US, Canada, and European countries. The 3456F flexible ribbon indoor/outdoor cable provides an excellent solution for applications like data centers and college campuses where high fiber density combined with flame and smoke resistant properties can be desirable. The UL-1685/FT4 and UL-1666 and CPR test results show performance that guarantees compliance with US and Canada building codes and fire-resistant requirements of European countries. In addition, this cable has met or exceeded ICEA-696 industry standards with regards to environmental and mechanical performance. This cable provides an excellent contribution to the growing telecommunications industry.

7. References

[1] IMARC Group, "Fiber Optics Market Outlook 2023: Globally Worth US$ 26.3 Billion Opportunity Till 2028 | Growth Rate (CAGR) of 16.8%". 19, December 2022. Web

[2] *Flexible Ribbons in 144f & 288f RICT OSPs to Reduce Cable Size and Improve Manufacturability*, Prysmian Cables and Systems, 70th IWCS conference

8. Pictures of Authors



Eric Anderson

Prysmian Group

Fiber Optic Cable R&D

700 Industrial Drive,

Lexington, SC 29072

Eric Anderson is a Product Development Engineer for one of Prysmian Group's Telecom manufacturing plants in Lexington, SC. He has four years of experience in the Telecom Industry. Prior to joining the Product Development group, Eric was a Process Engineer for the Lexington Plant Loose Tube Buffering Department. Eric earned his Master's degree in Mechanical Engineering from the University of South Carolina.



Gavin Lin

Prysmian Group

Fiber Optic Cable R&D

700 Industrial Drive,

Lexington, SC 29072

Gavin Lin is the Fiber Telecom OSP Product Development Manager for Prysmian Telecom North America. He holds a master's degree in mechanical engineering from the University of South Carolina. Gavin has been with Prysmian for over 17 years and has more than 19 years of experience in the fiber optic cable manufacturing and development. Gavin has several journal and conference papers.



Jeff Barker

Prysmian Group

Fiber Optic Cable R&D

2512 Penny Rd.

P.O. Box 39

Claremont, NC 28610

Jeff Barker graduated Magna Cum Laude from North Carolina State University with a Bachelor of Science Degree in Mechanical Engineering in 1984. Upon graduation, he went to work for Siecor Corporation in their RD&E department. In 1987, Jeff took a position with Alcatel in their R&D group where he spent the next 16 years in R&D and Engineering positions for Fiber and Fiber Cable before becoming the Global Head of Telecom Cable R&D. In 2004, Alcatel spun off its Telecom Cable business to Draka Comteq and Jeff managed the North American Telecom Cable R&D until Prysmian Group acquired Draka Comteq in 2011. Since 2011, Jeff has been responsible for the Telecom North America R&D for Prysmian Group. He has been active in IWCS for many years and is currently serving as Treasurer and Board member for IWCS. He holds more than 20 US Patents.



Brian G. Risch

Prysmian Group

Fiber Optic Cable R &D

2512 Penny Rd.

P.O. Box 39

Claremont, NC 28610

Brian G. Risch is the Materials Technology Manager for Prysmian Telecom North America. He holds a B.A. degree in physics from Carleton College and a Ph.D. in Materials Science and Engineering from Virginia Polytechnic Institute and State University. Brian has more than 30 years of experience in the study of structure property relationships in polymeric materials and materials reliability. Brian has 20 years of experience in the fiber optic cable business. Prior to working for Prysmian, Brian worked for Alcatel and Draka specializing in cable materials and fundamental material reliability. Brian also has 6 years of experience at Hewlett Packard doing research in electronic materials reliability and failure analysis. Brian also holds more than 40 US and international patents.



Ben Wells

Prysmian Group

Fiber Optic Cable R&D

700 Industrial Drive,

Lexington, SC 29072

Ben H. Wells is Principal Technology Engineer with the Prysmian Group located in Lexington South Carolina, where he is responsible for product design and development. He holds a Bachelor of Science degree in Mechanical Engineering from North Carolina State University. He has worked with Prysmian (previously Pirelli) for more than 30 years in the field of fiber optic cables.

144F high-density ribbon cable supporting/compatible to legacy network

Kawarpreet Singh, Sourabh Singh Panwar, Shubham Sachan, Srinivas Munige
Sterlite Technologies Limited (STL)
Silvassa, Dadra and Nagar Haveli and Daman and Diu
+919079847541
Sourabh.singh@stl.tech

Abstract

Until recently, the optical fiber used in core network complies with ITU-T G.652.D, centered on 9.2 μm Mode Field Diameter (MFD). The use of noval optical fiber which is compatible to legacy network in intelligently bonded ribbon technology has improved the cable design in terms of cable diameter, splicing loss, manufacturability and cost. This paper discuss the design of 144F Celesta cable with intelligently bonded ribbons and ITU-T G.657 complying fiber with MFD centered on 9.1 μm. By using legacy compatible optical fiber in intelligently bonded ribbon technology, the newly designed cables are light weight, smaller, compact, more flexible, and easy to produce and install as compared to the conventional flat ribbon cables.

Keywords: Mode field diameter, Intelligently bonded ribbon, Optical fiber cable, Splice loss

1. Introduction

In the post-covid world, the demand of data has increased exponentially. Owing to the increase in demand, we need faster transmission rates, for example to achieve 5G telecommunication network or over 100G institutional networks. Hence, optical fiber cables (1000× more bandwidth than the copper cables) are entering into the every link of the communication landscape. Most of the core network already utilizes optical fiber for communication. The optical fiber used in core network complies with ITU-T G.652.D, centered on 9.2 μm Mode Field Diameter (MFD). The access or metro network is still in transition phase from copper cables to optical fiber cables. Hence, there is a scope of technological improvement in this link of communication. As the population density of the cities are increasing, due to better opportunities, it is becoming increasingly difficult to lay straight and big ducts into the ground. The optical fibers complying with ITU-T G.657 standards have better macro bending performance as compared to conventional fibers and hence, are suitable for access or metropolitan networks. Most of the commercially available fibers complying with ITU-T G.657 standards have their MFD centered on 8.6 μm, resulting in partial compatibility with backbone network and higher splicing loss.

Considering all the aforementioned shortcomings, we hereby come up with a novel optical fiber ribbon and optical fiber cable to meet the current market requirements. We developed intelligently bonded ribbon, a one of its kind roll-able ribbon, to reduce the diameter of the cable with respect to flat ribbon cables and at the same time match mass fusion splicing property of the flat ribbon. Our in-house developed fiber, which complies with ITU-T G.652.D, G.657.A1 and G.657.A2 standards with MFD centered on 9.1 μm is used to make the optical fiber ribbon, making it fully compatible to all the existing networks.

1.1 Legacy network compatible Optical fiber

Description

STL Stellar 250 fiber is the first to offer ITU-T G.657.A2 bend performance with a 9.1 micron standard mode field diameter, ensuring complete compatibility with existing networks. The induced loss of this fiber at the tightest bends is a factor of two lower than the ITU-T G.657.A2 standard providing installation and operational efficiencies in high density (HD) networks. This low bend loss extends to the longer wavelengths required for future system upgrades. Fibres with low bend loss fibres allow operators to optimize their physical asset utilization and future proof their high-density networks.

Application

The need to improve network installation and operational efficiencies has led to wider application of bend-insensitive fibres. STL Stellar 250 Optical Fibre is suitable for use in any network where full backward compatibility with deployed fibres is required.

Benefits

• Fully compatible with existing networks built with G.652.D and G.657.A1 fibres - due to 9.1 micron standard mode field diameter.
• Provides installation and operational efficiencies in high density networks - due to very low bend loss.
• Future system ready - in that low bend loss extends to longer wavelengths

Stellar fiber has better band performance as compare to ITU-T A1 and ITU-T A2 complied fiber with high MFD. The tabulated data of stellar fiber and ITU-T A1 fiber is mentioned below.

Table-1: Bend performance of Stellar and ITU A1 fiber

Parameter		Units	Stellar	ITU A1
MFD		micron	9.1±0.4	9.1±0.4
Macro bend values	10 Turns R=15mm @1625 nm	dB	≤0.1	≤ 0.3
	10 Turns R=15mm @1550 nm	dB	≤0.03	≤ 0.1
	1 Turn R= 10 mm @1625 nm	dB	≤0.2	≤ 1.5
	1 Turn R= 10 mm @1550 nm	dB	≤0.1	≤ 0.5
	1 Turn R=7.5 mm @1625 nm	dB	≤0.5	
	1 Turn R=7.5 mm @1550 nm	dB	≤0.2	

1.2 Celesta Intelligently bonded ribbon cable

There are various type of ribbon optical fiber cables are available in the market which have stack of ribbons inside the tube and these ribbons are made of no of fibers arranged in array covered with matrix which increases the tube size. Hence, larger cable diameter and bigger ducts are required to install into the grounds.

Unlike flat ribbon, Celesta Intelligently Bonded Ribbons are made of number of fibers arranged in an array and bonded intermittently with matrix such the ribbons could take a size of bundle when put inside a circular cavity.



Figure-1: Pictorial view of rolling of Intelligently Bonded Ribbon

Since the best packing can be achieve with circle in circle rather than rectangle in circle, Celesta IBR results in higher packing density cables.

Table-2: Packing density of 144F flat ribbon and Celesta IBR cable

	Flat Ribbon Cable	Celesta IBR Cable
No of fiber	144	144
Diameter (mm)	14.5	8.5
Fiber density (fibers/mm^2)	0.9	2.5

By using the Celesta IBR the packing density of cables can be improved which helps in reducing the cable diameter of all the outside premises duct cables starting from 96 fibers design.

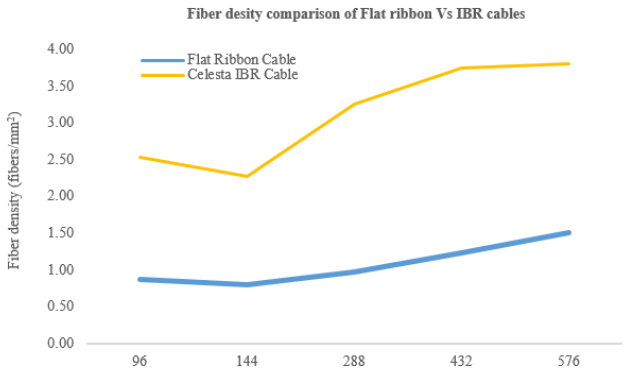


Figure-2: is a comparison between the theoretical fiber density of flat ribbon and Celesta IBR optical fiber ribbon cables across various designs.

2. Cable Design

The development of 144F Celesta IBR cable compatible with legacy network will be discussed in the following sections.

In order to reduce the micro band loss and splicing loss due to mismatch in MFD, Stellar 250 micron fiber complying ITU-T G567 standard was used in this cable design. The cable consist of twelve celesta IBR of 12 fibers along with the water swell able yarns. The complete bunch of 144 fibers are wrapped with water blocking tape.

This core is then covered with polyethylene jacket to provide the mechanical strength to the cable.

To provide the required tensile strength to the cable a number of aramid reinforced plastic rods have been embedded in the outer sheath of the cable which are also less stiff as compared to other strength members available and results in more flexible cable. Putting less diameter strength member to achieve the required tensile strength rather that 2 or 4 bigger one give the advantage of reducing the outer sheath thickness by 42%. Since there is no preferential bending plan exists in the cable, it's easier to install inside the duct.

This cable weighs 68% less compared to conventional optical fiber ribbon cable and for rest of the design there will be 50-80% weight reduction theoretically.

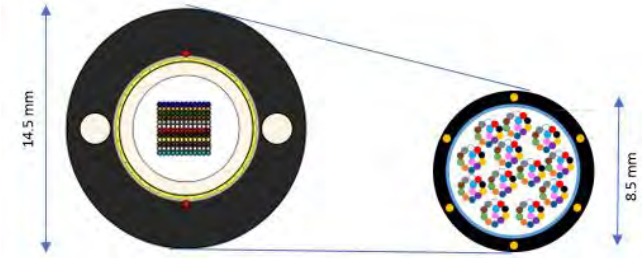


Figure-3 Reduction in cable diameter of 144F duct cable with the introduction of stellar fiber and celesta IBR

The cable diameter have been reduced by 41% from the conventional design.

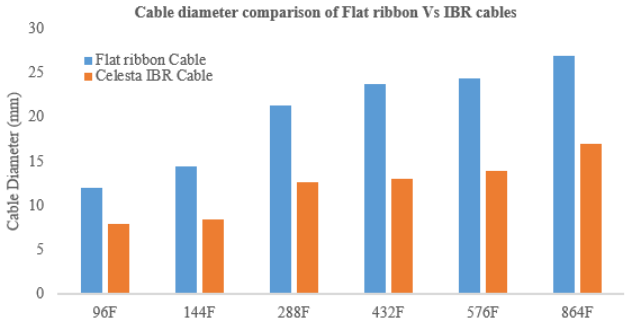


Figure-4 : OD comparison of Flat ribbon Vs Celesta IBR Cables.

3. Cable Performance

The cable has been tested as per the standard of Outside plant cables which Includes Telcordia GR-20 and IEC 60794-5-10 accordance with the relevant FOTP procedures.

3.1 Mechanical Tests

Below table consist of all the mechanical tests that were performed on the cable to evaluate the performance.

Cable has complied all the mechanical tests as per GR-20 and IEC 60794-5-10 mentioned in the table 3.

Table-3: Summary of mechanical tests

Tests Performed	Test Method	Results
Tensile Test	IEC 60794-1-21 E1	Complied
Crush Test	IEC 60794-1-21 E3	Complied
Impact Test	IEC 60794-1-21 E4	Complied
Torsion Test	IEC 60794-1-21 E7	Complied
Cable Kink Test	IEC 60794-1-21 E10	Complied
Cable Bend Test	IEC 60794-1-21 E11	Complied

3.2 Environmental Tests

Below table consist of all the environmental tests that were performed on the cable to evaluate the performance.

Cable has complied all the Environmental tests as per GR-20 and IEC 60794- mentioned in the table 4.

Table-4: Summary of environmental tests

Tests Perfromed	Test Method	Results
Temperature Cycling	GR 20 Clasue No. 6.6.3 FOTP-3	Complied
Cable Aging	GR 20 Clasue No. 6.6.4	Complied

3.3 Blowing Performance

Since the cable dimeter is less as compared to the conventional cable, it can be blown in 10 mm duct which results in the low installation cost.

4. Conclusion

A one of kind 144F high fiber density cable has been developed with our novel Stellar™ fiber and Intelligently Bonded Ribbon™ compatible to legacy network. Owing to the mass fusion splicing of our roll able ribbon, the deployment of the cable becomes fast and easy. The cable design was optimized to have adequate mechanical strength required in installation and at the same time has excellent bending properties for easy blowing of the cable into the duct.

5. Acknowledgements

I would like to the people who have worked on this project directly and indirectly and contributing for the successful development. Mahesh Deshpande, Sarin Kumar, Gahininath Shinde, Kishore Sahoo, Prasanna Pardeshi, Atul Mishra, Viksah Shukla, Jyotiprakash, Sumit Dubey, Abishsekh Saha, Bikram Nayak, Amitesh Dubey, Manoj Garg, Maneesh Kumar, Abasahed Waghmare, Vinayak Pillamari.

6. References

[1] Robust Flexible Ribbon for High Fiber Density Cables Compatible with Mass Fusion Splicing, Proceedings of the 67th IWCS Symposium

[2] Flexible Ribbons in 144f & 288f RICT OSPs to Reduce Cable Size and Improve Manufacturability IWCS Symposium 2021

7. Authors



Kawarpreet Singh

Sterlite Technologies Limited

Survery no 68/1,Rakholi, Silvassa, India 396230

Kawarpreet Singh is the research and development engineer for cables business. He holds master and bachelor degree in mechanical engineering from IIT Kanpur. He has more than 3 years of experience in optical fiber and cable.



Shubham Sachan

Sterlite Technologies Limited

Survery no 68/1,Rakholi, Silvassa, India 396230

Shubham Sachan is the reearch and development engineer for cables business. He holds bachelor degree in mechanical engineering from RKDF university and diploma in polymer science from Central Institute of Plastic Engineering. He has more than 3 years of experience in optical fiber and cable.



Sourabh Singh Panwar

Sterlite Technologies Limited

Survery no 68/1,Rakholi, Silvassa, India 396230

Sourabh Singh Panwar is the research and development engineer for cables business. He holds bachelor degree in mechanical engineering from BITS Pilani. He has more than 5 years of experience in optical fiber and cable. He worked in operations before moving to research and development in 2020. He holds several patents in the optical fiber cables domain.



Dr. Srinivas Munige

Sterlite Technologies Limited

E1, E2, E3, Waluj MIDC, Aurangabad, Maharashtra - 431136, India

Dr.Srinivas Munige is the head of new product development in R&D department for optical fiber business. He has ~12 years of both academic and industrial research experience. He holds doctorate degree from IITB Monash Research Academy and master degree from NIT Warangal in the field of photonics. He also holds several patents in the Optical fiber domai

Optical Fiber Ribbon Cable with Full Color Spectrum

Junwei Xie [1 2], Lei LIU [1 2], Zhuang Xiong [1 2], Aihua Liu [1 2], Feng Chen [1 2], Lin qi [3], Pei Liu [1 2], Yu Zhou [1 2]

[1] Leshan Biological protection optical Cable Engineering technology Research Center, Leshan, 614000, China; [2] Sichuan LEFEI Optoelectric technology Co.,Ltd, Leshan, 614000, China; [3] Yangtze Optical Fiber and Cable Joint Stock Limited Company, Wuhan 430073, China

Author e-mail address: xiejunwei@sclfot.com

Abstract

In order to further improve the intuitiveness of fiber with cable identification, improve the construction efficiency; solve the limitation of fiber ribbon printing on the production speed of fiber ribbon, improve the production efficiency. This paper introduces a new identification method from the preparation of color resin, curing process of color fiber ribbon and cable.

Keywords

Color resin Fiber Ribbon UV curing

1. Introduction

With the optical fiber communication entering the 5G era, the demand for optical fiber and cable continues to increase. Optical fiber ribbon cable is widely used in the core layer and the main section of urban optical cable with its advantages of high connection efficiency and slightly low cost. At present, the optical fiber ribbon cable is printed on the surface of the natural color optical fiber ribbon, the optical fiber ribbon forms a rectangular array is placed in the large loose tube ,the large loose tube is twisted to form the cable core, and the outer sheath is squeezed outside the cable core. This Arabic digital identification of optical fiber optic bands has the following problems:

1) Identification is not intuitive enough. Compared with the full chromatographic identification method, which is widely known by production and construction personnel, it is not intuitive and fast, and the user experience is not good.

2) Identification degree is directly affected by the quality of the inkjet code printing mark(see fig.1). The printing mode mainly uses the lattice mode, in high speed production characters printing mark, incomplete printing mark, leakage phenomenon occurs from time to time, greatly increasing the workload of rework and repair.

3) Low production efficiency. Limited by the printing speed of the inkjet printer, the production speed of the fiber ribbon generally does not exceed 500m / min.

To solve the above problems, a solution of full chromatography color optical fiber ribbon cable is proposed.

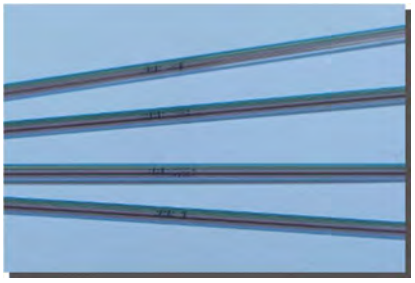


Fig. 1 Fiber ribbon

2. Cable structure design

Take GYDTA-144B1.3 optical cable as an example, the cable core consists of 1 central reinforcement and 4 stranded units, 3 stranded units are three 48-core loose tubes, and the loose tube identification chromatography is blue, orange and green respectively. There are four 12-core optical fiber ribbons in each tube. The identification chromatography of the fiber ribbons are blue, orange, green and brown respectively, and the fiber in the fiber ribbon is the national standard full chromatography.one stranded unit is the filling rope. The cable core adopts SZ stranded production process, the cable core gap is filled with water resistance paste, and the cable core is squeezed into aluminum-polyethylene sheath. The optical cable structure is shown in Figure Fig. 2.

Return to Table of Contents

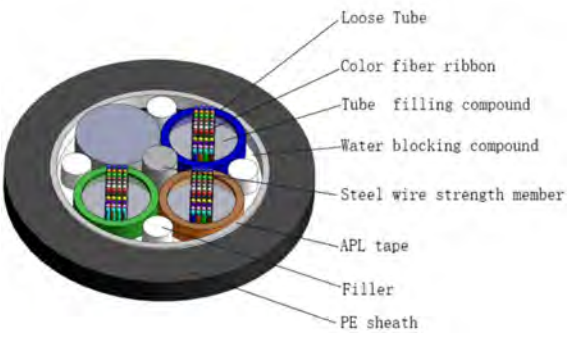


Fig. 2 GYDTA-144B1.3 Full Color Spectrum fiber ribbon cable

3.Process implementation

3.1 Preparation of color resin

Different pigments have different characteristics of light absorption, reflection and scattering, so the degree of obstruction to UV curing is also different. Most pigments have certain transmission zones in the range of some UV light and visible light, which is called the "spectral window" of the pigment, in which the light initiator can fully absorb the UV light radiation energy. The color matching ratio of pigments is particularly important. In the preparation of color resin, we consider the following factors:

1) Do not affect the curing quality of the optical fiber strip. Unlike optical fiber coloring, optical fiber coloring is usually coated with a 5-8um color layer on the surface of the optical fiber, and UV light can easily penetrate into the bottom layer of the color layer to achieve full cure. The thickness of the resin film is usually greater than 20um, which has higher requirements for curing.

2) Does not affect the chromatographic identification of the optical fiber ribbon. Under the premise of ensuring the curing quality of the fiber ribbon, the fiber ribbon chromatography is easy to identify. The color matching ratio is large, the identification is better, and the fiber ribbon cannot be fully cured, which affects the performance of the fiber ribbon; the color matching ratio is small, the fiber ribbon is more fully cured, and the chromatographic identification is difficult.

3) The stirring time and rate of the preparation of color resin. The stirring time and rate directly affect the uniformity of the color material dispersion.

We choose YF-003 natural color with resin, and its performance parameters are as shown in Table 1. The natural color resin is mixed with blue, orange, green and brown pulp in a certain proportion, and the mixing ratio has a direct impact on the curing quality and identification of optical fiber belt. Through a large number of process tests (as shown in Table 2), the optimal ratio of the natural color resin and color slurry mixed ratio (7~9): 1. Mix the mixed resin evenly at 8 rpm for 4 hours, and mix the coloring ink fully with the resin to ensure a uniform color.

Table1

Liquid coating		Unit	Characteristic value
Viscosity，25℃		mPa•s	6000
Density		g•cm-3	1.11
Refractive index		n/a	1.516
Cure coating layer		Unit	Characteristic value
mechanical	Elongation	%	21
	Tensile strength	MPa	24
	Tensile modulus at 2.5% strain	MPa	570
Glass-transition temperature		℃	55.3
Refractive index		n/a	1.536
Degree of cure（Tensile modulus at 2.5% strain）		MPa	0.2
Curing shrinkage rate		%	5.6
Heat weight change（200℃，40minute）		%	4.1

Table2

Colour	Colour schemes		Colour ID	Curing quality	Colour	Colour schemes		Colour ID	Curing quality
	NO.	ratio				NO.	ratio		
blue	1	5:1	√	×	green	1	5:1	√	×
	2	6:1	√	×		2	6:1	√	×
	3	7:1	√	×		3	7:1	√	√
	4	8:1	√	×		4	8:1	×	√
	5	9:1	√	√		5	9:1	×	√

3.2 color optical fiber ribbon

Color resin is used for ribbon production, which increases the process difficulty of ribbon , and the curing power requirement is high. The process test is carried out on MS machine. Through a large number of process tests, the best production process parameters of color optical fiber belt are found: fiber tension 45 cN, wire tension 200 cN, nitrogen flow 22 L/min, power factor 2100m / min, and production speed 600m / min. The performance of full chromatography color fiber band meets the YD / T979-2009 standard. Full chromatographic colored optical fiber bands are shown in Fig. 3

Return to Table of Contents



Fig. 3 Full Color Spectrum fiber ribbon

3.3 large loose tube

The large loose tube is consistent with the conventional cable casing production. Diameter of large loose tube is 5.1±0.1mm, wall thickness is 0.45±0.05mm, and large loose tube more than long is 0.8-1.1 ‰. Each tube 48 core, chromatography blue, orange, green.

3.4 Cable core and sheath

Combine three 5.1mm tubes and one 5.1mm filling rope around 2.25mm metal reinforcement, fill the cable core gap with water resistance ointment, cable joint pitch of 360mm and outer diameter of 12.5mm. The aluminum-polyethylene sheath is squeezed outside the cable core, the aluminum strip is made with tie grain vertical coating, and the extruded mold is made with drawing tube mold. See Fig.4 for the finished optical cable.



Fig. 4 GYDTA-144B1.3 Full Color Spectrum fiber ribbon cable

4.Experimental verification

GYDTA-144B1.3 was tested according to YD / T979-2009 ,YD/T981.3-2009 and IEC60794 standards .

4.1 Transmission performance

Item	Unit	Performance requirement	Result	Conclusion
Attenuation coefficient	dB/km	1310nm，≤0.36	maximal 0.345	qualified
		1550nm，≤0.22	maximal 0.194	qualified
Macro bend attenuation	dB	1550nm，≤0.5	maximal 0.2	qualified
Optical discontinuity	dB	1310nm，≤0.1	maximal 0.03	qualified
		1550nm，≤0.1	maximal 0.02	qualified

4.2 Dimensions of the fiber ribbon

Item	Unit	Performance requirement	Result	Conclusion
Width	μm	≤3400	maximal 3105	qualified
Thickness	μm	≤400	maximal 304	qualified
Adjacent fiber	μm	≤300	maximal 266	qualified
Fiber spacing	μm	≤2980	2782	qualified
Planeness	μm	≤50	29	qualified

4.3 Mechanical performance of the fiber ribbon

Item	Performance requirement	Result	Conclusion
In-band optical fiber separability	The optical fiber is separable, the optical fiber structure should allow the optical fiber to be separated from the band, the color layer without damage.	Easy to separate, optical fiber coloring layer without damage.	qualified
Fiber strip stripping	The single optical fiber coating layer and the optical fiber ribbon bonded material should be easily stripped, the coating layer is stripped without broken fiber, and the optical fiber surface is easy to clean.	No broken fiber, the surface is easy to clean	qualified
Twist ability	After torsion test, none of the fibers separated from the fiber band structure when observed with 5 x magnification.	No fiber separation	qualified
Residual torsion	After the residual torsion test, the residual torsion shall be at least not more than 360° per 0.4m	maximal 90°	qualified

4.4 Mechanical performance of optical cable

Item	Unit	Performance requirement	Result	Conclusion
Tension Strain	%	Long-term tensile = 600N, optical fiber strain ≤ 0.05%	0.008	qualified
	%	Short-term tensile =2600N, optical fiber strain ≤ 0.25%	0.112	qualified
	%	Fiber residual strain ≤ 0.01% (After tension removal)	0.002	qualified
	%	cable residual strain ≤ 0.08%(After the tension removal)	0.03	qualified
Tension Additional attenuation	dB	Long-term tensile = 600N, optical fiber additional attenuation ≤ 0.03dB	0.009	qualified
	dB	Short-term tensile =2600N, Fiber additional attenuation ≤ 0.15dB	0.01	qualified
	dB	Fiber residual additional attenuation ≤ 0.03dB(After the tension removal)	0.012	qualified
	—	After test, the sheath is cracked without visual force	N0 Cracking	qualified
Crush	dB	Long-term pressure 300N, fiber additional attenuation ≤0.03dB	0.003	qualified
	dB	Long-term pressure 1000N, fiber additional attenuation ≤0.1dB	0.003	qualified
	dB	Fiber residual strain ≤ 0.03dB(After pressure removal)	0.003	qualified
	—	After test, the sheath is cracked without visual force	N0 Cracking	qualified

Return to Table of Contents

(continue)

Item	Unit	Performance requirement	Result	Conclusion
Impact	dB	weight 450g, fall 1m, impact sphere radius: 12.5mm, impact 5 times; additional attenuation of optical fiber residual ≤ 0.03dB	0.001	qualified
	–	After test, the sheath is cracked without Visual force	N0 Cracking	qualified
Repeated bend	dB	Bending radius is 20D, load 150N, bending times: 30times, fiber residual additional attenuation ≤ 0.03dB	0.002	qualified
	–	After test, the sheath is cracked without visual force	N0 Cracking	qualified
Torsion	dB	Load: 150N, Length under test: 1m,Turns: ±180°,Cycles:10,fiber additional attenuation ≤0.03dB at the twist limit position	0.012	qualified
	dB	After test, additional attenuation of optical fiber residual ≤ 0.03dB	0.003	qualified
	–	After test, the sheath is cracked without visual force	N0 Cracking	qualified
Winding	dB	Axis diameter: ≤ 20D; tight winding: 10 cycles per cycle; cycle times: ≥ 5 times, no fiber fracture and no visible crack	No broken fiber, no Cracking	qualified

4.5 Optical cable temperature performance

Temperature performance test of GYDTA-144B1.3 optical cable according to YD/T981.3-2009 standard, -40- + 60 ℃ with 2 cycles.1310nm wavelength: additional attenuation maximum 0.007dB / km, 1550nm wavelength: additional attenuation maximum 0.012dB / km, meet the standard requirements.

5. Conclusion

Conclusions As a result ,The successful development of color optical fiber ribbon optical cable provides a new identification method for the chromatographic identification of optical fiber ribbon cable, which makes the identification of optical fiber ribbon cable more easy and intuitive, which is conducive to improving the efficiency of production, detection, construction and maintenance, and has a wide application prospect.

6. Reference

[1]China Communications Standardization Association, optical fiber ribbon optical cable for access network Part 3: Pine sleeve layer twisted YD/T981.3-2009.

[2]China Communication Standardization Association, technical requirements and inspection methods of optical fiber belt YD / T979-2009.

[3]IEC60794-1-21 optical fiber cable-part 1-21:Generic specification-Basic optical fiber cable test procedures-Mechanical test methods

[4]IEC60794-1-22 optical fiber cable-part 1-22:Generic specification-Basic optical fiber cable test procedures-Environmental test methods

7. Authors



Junwei Xie
Sichuan LEFEI Optoelectric technology Co.,Ltd
Jiuli Industrial District
Emeishan P.R.China 614222

Mr. Junwei Xie graduated from Southwest jiaotong University in 1997,majoring in applied electronics and got his bachelor's degree in computer network from University of Electronic Science and Technology of China in 2014.He joined Sichuan LEFEI Optoelectric technology Co.,Ltd in 1998,engaged in optical cable product development and production process control .He is the technical manager of Production Department.



Lei Liu
Sichuan LEFEI Optoelectric technology Co.,Ltd
Jiuli Industrial District
Emeishan P.R.China 614222

Mr. Lei Liu graduated from Southwest University of Science and Technology in 2011..He joined Sichuan LEFEI Optoelectric technology Co.,Ltd in 2011.,engaged in optical cable production and R&D work.He is the executive assistant of Production Department.



Zhuang Xiong
Yangtze Optical Fiber and Cable Joint Stock Limited Company
9 Guanggu Avenue
Wuhan P.R.China 430073

Return to Table of Contents

Dr. Zhuang Xiong got his B.E.degree in Mechanical Engineering from Wuhan Institute of Technology in 1994 and received his Ph.D. in Mechanical Manufacture and its Automation from Huazhong University of Science and Technology in 2000,Since then,he has been working in YOFC ,engaged in the researth and development of optical fiber cables.Now he is the optical cable CTO of Manufacturing centre and Deputy General Manager of R&D Centre.Moreover,He is also a senior member of China Institute of Communications and an expert in Chinese Delegation to ITU-T SG15 and IEC SC86A as well as a member of academic committee of State Key Laboratory of Optical Fiber and Cable Manufacture Technology. Now he is director of]Leshan Biological protection optical Cable Engineering technology Research Center.



Aihua Liu
Yangtze Optical Fibre and Cable Joint Stock Limited Company
9# Guangeu Avenue
Wuhan, P.R.China 430073

Mr. Aihua Liu received his master degree of mechanical manufacturing from Xi'an Jiaotong University in 1986. Now he is Cable Department Manager in YOFC and associate director of]Leshan Biological protection optical Cable Engineering technology Research Center.



Feng Chen
Yangtze Optical Fibre and Cable Joint Stock Limited Company
9# Guangeu Avenue
Wuhan, P.R.China 430073

Mr. Feng Chen graduated from Northeastern University in 1998.He received his master degree of Business Administration from Wuhan University in 2016. More than 25 years of optical fiber and cable manufacturing and management experience.Now he is the general manager of Yangtze(Hubei) Electrical Power Cable Co., LTD and Yangtze Optical Fibre and Cable Hanchuan Co., LTD.



Lin Qi
Yangtze Optical Fibre and Cable Joint Stock Limited Company
9# Guangeu Avenue
Wuhan, P.R.China 430073

Mr. Qi Lin received his master degree of Electro-mechanical engineering from Wuhan University of Technical in 2006. He worked in YOFC science 2009, dedicated in optical cable design and development.



Pei Liu
Sichuan LEFEI Optoelectric technology Co.,Ltd
Jiuli Industrial District
Emeishan P.R.China 614222

Mr.Pei Liu his master degree from Wuhan University of Technology.He worked in YOFC science 2008..He joined Sichuan LEFEI Optoelectric technology Co.,Ltd in 2021.Now he is the General Manager.



Yu Zhou
Sichuan LEFEI Optoelectric technology
Co.,Ltd
Jiuli Industrial District
Emeishan P.R.China 614222

Mr.Yu Zhou graduated from University of Electronic Science and Technology of China .He joined Sichuan LEFEI Optoelectric technology Co.,Ltd in 1997,Now he is the technical director and associate director of]Leshan Biological protection optical Cable Engineering technology Research Center.

Return to Table of Contents

POSTER PAPERS

Click on a session below to navigate to that section of the Proceedings.

POSTER SESSION

Chairperson: Alistair Duffy, Faculty of Computing, De Montfort University, UK

- **Development of 22.9Kv Submarine Horizontal Directional Drilling (HDD) Power Cable; Mr. Sangmin Oh, Gaon Cable Co. Ltd., Republic of Korea**
- **Experimental Study on Measuring Method of Residual Torsion of Fiber Ribbon; Mr. Zhou Yuxuan, Nanjing Wasin Fujikura Optical Communication LTD, China**
- **UV Protection and Lightfastness of Outdoor Cables; Ms. Brita Kunze, Delta Tecnic,**
- **A Method for Estimating the Combustion Performance (Smoke Density) of Optical Cables Based on Material Thermal Analysis Techniques; Mr. Qi Lin, Yangtze Optical Fibre and Cable Joint Stock Company | State Key Laboratory of Optical Fiber and Cable Manufacture Technology, China**
- **Research on Shrinkage Performance of Central Core Tube Optical Cable; Mr. Jianbin Duan, State Key Laboratory of Optical Fiber and Cable Manufacture Technology | Yangtze Optical Fibre and Cable Joint Stock Limited Company, China**
- **Optical Cable Impact on Environmental Performance of Single-Fiber Patchcord; Mr. Jianbin Duan, State Key Laboratory of Optical Fiber and Cable Manufacture Technology | Yangtze Optical Fibre and Cable Joint Stock Limited Company, China**
- **Print Length Verification System; Mr. Patrick Jones, Taymer International Inc., Canada**
- **Temperature Performance Study of Loose Tube Materials; Mr. Qi Lin, Yangtze Optical Fibre and Cable Joint Stock Company | State Key Laboratory of Optical Fiber and Cable Manufacture Technology, China**

Click here to return to the **Table of Contents**

Salt Resistance Performance of Submarine HDD Power Cable

***Sangmin Oh* , *Kiho Lee* , *Bongok Park* ***

R&D Team, Gaon Cable CO., Ltd, South Korea *

Korea Electric Power Corporation (KEPCO), South Korea * *

+82-31-459-6224 · smo@gaoncable.com

Abstract

The Submarine Horizontal Directional Drilling (HDD) power cable is a special type of power cable with a structure that can effectively protect the cable from the ingress of seawater inside the conduit. Recently, there is a trend of applying Horizontal Directional Drilling methods to interconnecting power systems between islands. However, there is a problem of seawater ingress into the conduit due to leakage in the conduit. Three protective measures have been established to protect the cable from seawater ingress: 1) Application of salt resistance jacket, 2) Application of aluminum laminate layer, 3) Application of swellable tape for conductors and concentric wire. In this paper, we conducted comparative tests between the existing cable (TR CNCE-W) and the submarine HDD power cable, citing and adopting various international standards, which have proven that the HDD power cable outperforms TR CNCE-W in terms of performance in seawater.

Keywords: HDD Power cable; Sea water; Salt Resistance; Swellable tape; Aluminum laminated tape; Concentric wire;

1. Introduction

Recently, there has been an increasing number of cases where small diesel generators in islands are removed and power is provided by interconnecting the islands with the power grid. Furthermore, the Horizontal Directional Drilling method has the advantage of not requiring compensation for fishing rights. However, there is a problem of seawater ingress into the conduit due to welding defects or damage during the insertion of the HDD power cable into the steel pipe conduit. When saltwater enters the conduit, a primary barrier is required on the cable jacket, and in the event of damage to the cable jacket, a secondary barrier is required on the aluminum laminate layer. To prevent the spread of faults, the flow of saltwater along the conductor and the concentric wire needs to be blocked in case of saltwater ingress. While conventional power distribution cables possess the aforementioned blocking performance only in freshwater, the submarine HDD power cable satisfies the same blocking requirements even in seawater.

In this paper, we validate the salt resistance performance of the submarine HDD power cable by analyzing its salt resistance feature through testing methods specified in IEEE 1580, AEIC GC13, IEC 60502-2, and ES 6145-0028 for each element.

2. Introduction of the submarine HDD power cable

In this paper the structure and characteristics of the submarine HDD power will be introduced and explained below.

To ensure salt resistance performance, the submarine HDD power cable applies a salt resistant jacket and an aluminum laminate layer was taped longitudinally. Each layer of the conductor is sealed with a swellable tape longitudinally and one layer of swellable tape is applied longitudinally to the lower part of the concentric wire, while two layers of expanding tape are spiral-wrapped with a 5mm gap on the upper part of the neutral wire. The structure is depicted in Figure 1 and Table 1.

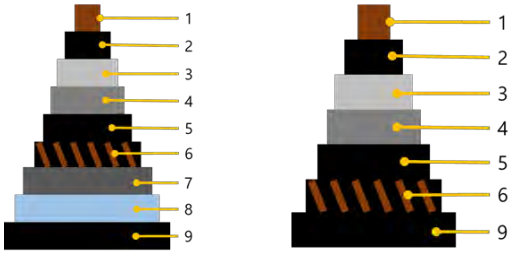


Figure 1. Structure of submarine HDD power cable and TR CNCE-W

Table 1. Structure of submarine HDD power cable and TR CNCE-W

No	items	Material
1	Conductor	Copper (compact round stranded)
2	Conductor screen	Thermosetting compound
3	Insulation	TR XLPE
4	Insulation screen	Thermosetting compound
5	Semi-conducting tape	Swellable tape
6	Concentric wire	Copper
7	Semi-conducting tape	Swellable tape
8	Armour	Al laminated tape
9	Jacket	PE

The jacket number 9 in Figure 1 prevents the ingress of external saltwater. The aluminum laminate layer number 8 also prevents the ingress of saltwater from the outside. The swellable tape numbers 5 and 7 are applied to block the diffusion of saltwater through the concentric wire.

3. Performance Evaluation Test

For the performance evaluation of the submarine HDD power cable, the performance was tested in saltwater using test methods based on IEEE 1580, AEIC GC13, IEC 60502-2, and ES 6145-0028. A 325 mm2 conductor cable was manufactured for the performance evaluation.

3.1 The salt resistance test of the jacket

To verify the salt resistance performance of the jacket, the test method specified in section 5.17.7 of IEEE 1580 was applied. Three completed cable samples with an effective length of 1.1m were

immersed in a 60°C, 20% sodium chloride solution for 240 hours. After the immersion treatment, the samples were subjected to a 46kV withstand voltage test and wrapped around a mandrel with a diameter nine times larger than the cable. Then, the presence of cracks on the cable's exterior was examined.

3.1.1 Salt resistance test results of the jacket. The results of withstand voltage test, bending test, and sequential test for each cable are presented in Table 2**.**

Table 2. Salt Resistance Test Results of the Submarine HDD Power Cable and TR CNCE-W

	Sample	Withstand Voltage Test (46kV)	Bending Test
Submarine HDD Power Cable	#1	NO BD	No Crack
	#2	NO BD	No Crack
	#3	NO BD	No Crack
TR CNCE-W	#1	NO BD	Crack
	#2	NO BD	No Crack
	#3	NO BD	Crack

3.1.2 Test Result Analysis. The test results confirmed that the submarine HDD power cable exhibited superior salt resistance compared to TR CNCE-W. While TR CNCE-W showed no abnormalities in the withstand voltage test, cracks were observed during the bending test. It was confirmed that the salt resistance treatment in the jacket compound of the submarine HDD power cable proved to be effective.

3.2 Aluminum laminate layer salt resistance test

To verify the salt resistance performance of the aluminum laminate layer, sequential testing was conducted following the guidelines of AEIC GC 13. In the first step, the cable assembly was bent completely in the forward direction around a mandrel at room temperature, and after being completely straightened, fully bent in the opposite direction around the mandrel. This bending process was repeated for a total of three cycles. In the second step, the cable was installed in a heating cycle equipment, and a current was passed through to heat it until the conductor temperature reached 90-95°C. This heating and cooling process was repeated for 100 cycles, with 8 hours of heating followed by 16 hours of cooling in each cycle. In the third step, the cable core, bedding, and concentric wire were removed, and the sample is sealed on both ends and installed in a humidity penetration test device. A 3.5% salinity water mixed with dye at room temperature was pressurized inside the cable at 0.5 atmosphere for 72 hours, from the interior to the exterior. After the aforementioned preconditioning, the samples were thoroughly dried in an oven at 50-60°C. Then, they are longitudinally cut along the overlapping part of the aluminum laminate layer as the center of the reference point. After slicing with a width of 4-5cm around the overlapping area as the center, the overlapping portion of the aluminum laminate layer is peeled off to check for dye penetration. Figure 3 shows the configuration of the humidity penetration tester in the third step.

3.2.1 Aluminum Laminate Layer Salt Resistance Test Results and Analysis. The results of checking for dye penetration in the submarine HDD power cable are shown in Figure 4. It was confirmed that there was no ingress of dye into the aluminum laminate layer of the cable. TR CNCE-W does not have an amour, making the corresponding test impossible. The inside of the aluminum laminate layer is composed of aluminum, while the outside is coated with polymer. During the cable manufacturing, heat is applied to the outer polymer layer to bond it together, creating a strong adhesion between layers that effectively prevents the ingress of seawater.



Figure 4. Aluminum Laminate Layer's Salt Resistance Test Results

3.3 Conductor and Concentric Wire's Salt Resistance Test

The conductors and concentric wire were tested following the procedures specified in ES 6145-0028 and IEC 60502-2.

3.3.1 Conductor's salt water penetration test. To verify the salt water penetration performance of the cable conductor, testing was conducted following the procedures specified in ES 6145-0028. After removing the cable's jacket and concentric wire, the insulated sample was installed in the conductor's water penetration tester. A 3.5% salinity artificial salt solution at room temperature is applied at a pressure of 0.5 atmosphere for 24 hours, and leakage is checked from the other end. Figure 5 shows the conductor's water penetration tester.

3.3.1.1 Conductor's salt water penetration test results and analysis. The test results of conductor water leakage in the submarine HDD power cable and TR CNCE-W are shown in Table 3. The test results confirmed that the submarine HDD power cable exhibited conductor's superior salt water penetration performance compared to TR CNCE-W. The swellable tape applied to the TR CNCE-W conductor exhibited suitable performance in freshwater; but, immediate leakage occurred in saltwater. This is due to the difference in the tape's saltwater absorption performance. In addition, when applying a swellable tape with a thickness of 0.45mm to the submarine HDD power cable conductor, a conductor resistance was measured below the threshold due to the weight reduction of the conductor. Hence, the optimal thickness of 0.4mm was selected.

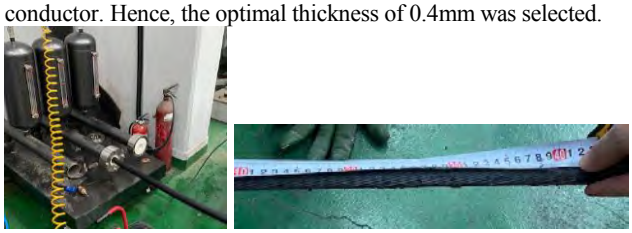


Figure 5 Conductor's salt water penetration tester, sample.

3.3.2 Water penetration test of concentric wire. The test was conducted in accordance with IEC 60502-2 to verify the salt water penetration performance of the cable's concentric wire. At room temperature, 3.5% saltwater is filled into a tube within 5 minutes, adjusting the height of the saltwater inside the tube to rise above 1m from the center of the cable. The samples were left at room temperature for 24 hours, and then subjected to 10 heating cycles with current passing through the conductor until it reached the maximum operating temperature (90℃). Each heating cycle had a minimum duration of 8 hours. The temperature of the conductor

must be maintained within the specified temperature range during each heating cycle of at least 2 hours. After that, it should undergo natural cooling for a minimum of 3 hours. The water level should be maintained at 1m. The depth of moisture penetration in the tested samples is determined. Figure 6 shows the concentric wire's salt water penetration tester.

3.3.2.1 Concentric wire's water penetration test results and analysis. The results of the moisture penetration depth verification for the submarine HDD power cable and TR CNCE-W are shown in Table 3. The test results confirmed that the submarine HDD power cable shows superior salt water penetration performance of the concentric wire compared to TR CNCE-W. The swellable tape applied to the TR CNCE-W concentric exhibited suitable performance in freshwater; however, immediate leakage occurred in salt water. This is due to the difference in the tape's saltwater absorption performance. Furthermore, when applying a 0.45mm thick swellable tape to the concentric wire of the submarine HDD power cable, leakage occurred, and therefore a 0.6mm swellable tape was chosen.



Figure 6. Concentric wire's salt water penetration tester, sample

Table 3. Conductor and concentric wire's salt water penetration test results

Classification		Tape Thickness (mm)	Test Results	Notes
Submarine HDD power cable	Conductor	0.45 (for seawater use)	PASS	excessive resistance
		0.4 (for seawater use)	PASS	
	Concentric Wire	0.45 (for seawater use)	Fail	penetration depth: 190cm
		0.6 (for seawater use)	PASS	penetration depth: 35cm
TR CNCE-W	Conductor	0.2 (for general use)	Fail	immediate leakage
	Concentric Wire	0.4 (for general use)	Fail	immediate leakage

4. Conclusion

In this paper, tests were conducted in line with the testing methods of IEEE 1580, AEIC GC13, IEC 60502-2, and ES 6145-0028 to verify the salt resistance performance of the jacket, aluminum laminate layer, and conductor concentric wire of the submarine HDD power cable. This evaluation has confirmed improved salt resistance performance of the jacket, amour, conductor, and concentric wire compared to existing cables. Furthermore, the structure was designed considering compatibility with existing connectors, and compatibility verification tests with connectors confirmed that there are no issues with the use of existing connectors. It is expected that this will be expanded for application not only in the conduit section but also in salt damaged areas such as reclamation land in the future.

5. Acknowledgments

This research was supported by the Korea Electric Power Corporation (KEPCO) between 2021 and 2022.

6. References

[1] Lindberg, R.E. "Water Blocking and Reterminatng at Sea of Floded High Voltage Cable" *IEEE; Marine Technilogy Society*, Vol.3 (2003).

[2] Guerts W.S.M, eds., "Water diffusion through sheaths and its effects on cable construction" *Jicable*, Vol.6, p.714-718 (1995).

[3] Powers, W. F. "An Overview of Water-Resistant Cable Designs" *IEEE transactions on industry applications*, Vol.29, No.5 p.93-94(1993)

Experimental study on measuring method of residual torsion of fiber ribbon

Xiaoquan Wang [1] **Yicheng Guan**[3] **Cheng Liu** [2] Dongxiang Wang[2] Zhuhai Chen[1] **Yuxuan Zhou**[4]

1: Nanjing Wasin Fujikura Optical Communication LTD,

2: FiberHome Telecommunication Technologies Co., Ltd.

3:Nanjing University

4:Artcenter college of design

Abstract:

The residual torsion stress of optical fiber ribbon has a certain impact on the subsequent production and application of optical fiber ribbon. Therefore, the relevant standards of optical fiber ribbon all have requirements on the test methods and indexes of optical fiber ribbon residual torsion test methods. As the IEC wants to revise the test methods of optical fiber ribbon residual torsion test methods, we have consulted the international standards commonly used and found that the test methods are not the same. In this paper, a more practical test method of residual torsion of optical fiber tape is proposed according to the test data.

Key words: residual torsion stress, aging

1. **Preface**

With the development of the optical communication industry, the demand for bandwidth is becoming more and more intense, and large core number and high-density optical cables are widely used. In the design of large core number optical cables, the cable is the first choice for design, so the demand for optical fiber ribbon is gradually increasing. As shown in Figure 1, the bidding cable quantity of mobile companies from 2019 to now is also increasing year by year in the case of the downturn in the optical communication industry.

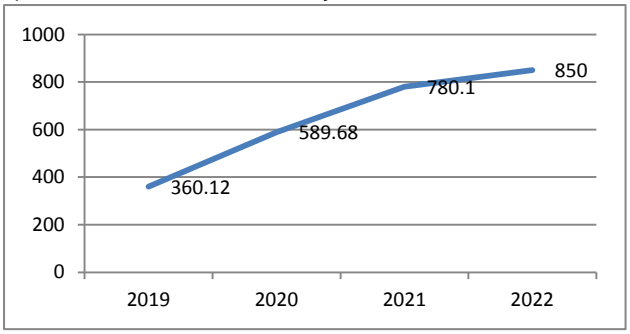


Figure 1 Non-skeleton cable bidding volume of mobile companies in 2019-2022

The fiber ribbon as the optical unit of the cable plays a decisive role in its quality, so the quality requirements of the fiber ribbon are getting higher and higher, the previous IEC test standard on the fiber strip is placed in a general standard file, only a rough description, due to the different understanding of the manufacturers, the actual fiber ribbon test methods are also different. IEC also put forward a detailed standard description of each fiber ribbon test method in this environment, our company undertook the preparation of IEC60794-308 residual torsion test method, so this paper mainly focuses on the experimental method of fiber ribbon residual torsion test, in the process of writing the problems encountered and the differences between various standards did some comparative tests. Some suggestions for the revision of the standard are given based on the experimental results and the current optical fiber ribbon.

2, **Optical fiber ribbon residual torsion test method**

2.1 Causes of residual torsion of the optical fiber ribbon

The generation of residual torsion stress of optical fiber ribbon can be divided into internal causes and external causes. 1) Internal causes: the main optical fiber ribbon itself has stress to produce torsion after it is formed. Among them, the fiber in the fiber ribbon is twisted during the production process, and the uneven stress caused by foreign matter or uneven cooling during the fiber production process causes the fiber ribbon to twist after the formation of the belt. Because the fiber can not be disconnected from beginning to end, and the head and tail are fixed during storage and transportation, the stress is not easy to release, so there will be torsion when the fiber ribbon is made, and the stress is not easy to release after curing into the strip. There is also residual stress in the optical fiber caused by uneven pay-off tension when the optical fiber ribbon is formed, and this residual stress can not be eliminated in the subsequent process. Another is that the degree of solidification of the

Return to Table of Contents

optical fiber r is not uniform, resulting in torsion of the optical fiber ribbon. This residual torsion stress will be eliminated during the aging process. 2) External cause: in the winding process of the fiber ribbon extrusion, there will be a certain twist, this will not be on the whole disk, to avoid the problem of resampling is no problem, this twist will become better if placed for a certain time. There is also the distortion of the fiber ribbon caused by the cable twisting and tying in the cable process, and the fiber strip is fixed after the cable is formed, the deformation cannot be recovered, and the torsion is generally more obvious, and it is not easy to eliminate. Generally speaking, if the band of fiber is seriously deformed, the optical properties of the fiber ----- fiber attenuation performance will also change.

2.2 Influence of residual torsion stress of fiber strip on production

The influence of residual torsion of optical fiber ribbon on production may lead to poor winding of optical fiber ribbon in the production process, and in severe cases may lead to excessive attenuation. In the process of optical cable production, there exists the phenomenon of reverse banding in the process of pay-off, which affects the subsequent detection and connection. In the production process of fiber strip devices, because most of the fiber ribbon is to be wound in the box body, the residual torsion stress of the fiber strip will cause difficult winding, or the winding state is not beautiful, as shown in Figure 2, the application of fiber ribbon in the fiber splitter. General devices have to undergo a 7-day temperature cycle experiment, which is equivalent to an aging test. There are also 2,000 hours of aging tests at 85 degrees temperature and 85 percent humidity.

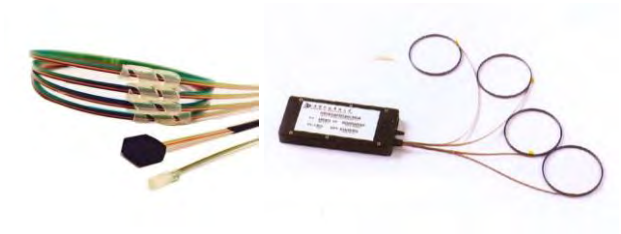


Figure 2 Fiber ribbon structure in fiber device

2.3 The existing standard on the residual torsion test method of optical fiber ribbon

The comparison of IEC, TIA and industry standards used more frequently in existing standards is shown in Table 1.

Table 1 Comparison of test methods for residual torsion of optical fiber ribbon in the standard

Item	IEC60794-308-2012	TIA-455-131-1997	YD/T 979-2009
Test purpose	The ribbon residual twist test, or flatness test, evaluates the degree of permanent twist in a cabled optical fibre ribbon.	Optical fibre ribbon residual twist is a measure of how much a ribbon rotates, or twists, along a given length. Residual twist can result from the ribbon manufacturing process,	To ensure that the fibre ribbon does not produce a twist that affects the connection or the use of the connection protective bushing:
Test sample length	50 cm ± 5 cm	50 cm	It should not be smaller than 50cm
Actual test length	ambiguity	ambiguity	40cm
load	100 g ± 5 g	100 g ± 5 g	1N
Sample pretreatment	Preconditio n the ribbon at 85 °C ± 2 ° C, uncontrolle d relative humidity, for 30 days in its cable, unless otherwise specified in the detail specificatio n.	85 + 2 o C for a period of 30 days / uncontrolled humidity If possible, fibre ribbons should be preconditione d in the cable structure. Cables with filling compounds should be capped to prevent leakage. If ribbon cable is not available, the ribbon samples may be axially twisted the number of times per meter specified in the cable design and submerged uncoiled in a filling compound or commercially available low molecular	The samples were aged at 85℃ for 30 days:

Return to Table of Contents

		weight mineral oil for preconditioning.	
Test standard	ambiguity	ambiguity	Residual torsion should be measured at least every 0.4 torsion is not greater than 360°

Through the comparison of torsion testing in different standards, the substantial difference is that there is a clear difference in sample pretreatment. But what are the effects of different pretreatment methods on the test, why do different experimental methods need to be used, and which method is more reasonable? This requires us to do a research and analysis of the fiber ribbon residual torsion experiment.

2.4 Research and test on residual torsion of optical fiber ribbon

From the above analysis, we can see that the fiber ribbon torsion is mainly due to the different pretreatment methods, so our research direction is the difference of the residual torsion test of the fiber ribbon under different pretreatment.

2.4.1 Test plan:

In order to study the differences between residual torsion experiments of fiber strip under different pretreatments, a set of comparative tests are planned, the specific contents of which are as follows:

1, Taking 6 disks of optical fiber ribbon sample test its residual torsion performance, the testing value of the optical fiber ribbon after unloading. It is also the ratio of the later test values.

2. Other properties should be tested and put into an 85 degree incubator after passing the test, and take it out after 30 days to test its residual torsion;

3. The 6 disks of optical fiber ribbon are sampled and twisted together for many times. After twisting, the optical fiber ribbon is buried in a box of fiber paste and sealed, and then the box is placed in an 85-degree incubator. After 30 days, the residual torsion performance is tested again.

4. The 6 disks of optical fiber ribbon are made into a loose sleeve with fiber paste, and then twisted together with other optical fiber ribbon and sheathed to form a cable. Take 1 meter sample of the cable, put it in the 85 degree incubator, take it out after 30 days, take out the fiber ribbon in the cable, and test its residual torsion performance.

2.4.2 Test results

2.4.2.1 Residual torsion of optical fiber ribbon without pretreatment, test sample length 50cm,2 groups of optical fiber ribbon test results are shown in Table 2:

Table 2 Residual torsion test results of fiber ribbon without pretreatment

list	1 #	2 #	3 #	4 #	5 #	6 #
first	35°	12°	25°	30°	40°	15°
second	32°	15°	30°	30°	35°	10°
average	33.5°	13.5°	27.5°	30°	37.5°	12.5°

The unpretreated fiber ribbon sample is taken as the original(原样), and its average value is taken as the ratio.

2.4.2.2 Aging at 85° for 30 days, put the samples that have not been aging tested into the aging sample 1（老化样 1） and re-sample the aging sample 2(老化样 2). The experimental results are shown in Figure 3

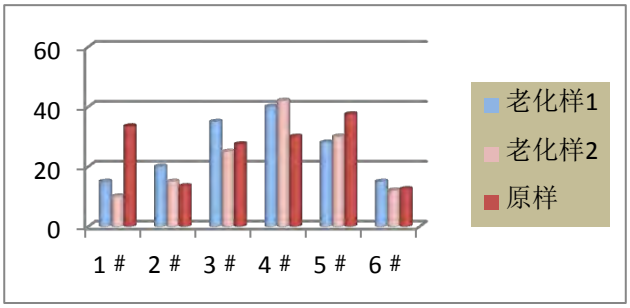


Figure. 3 Comparison between the test data after 30 days of aging at 85° and the original data of the optical fiber ribbon

he residual torsion stress of the 1# and 5# ribbons became smaller after aging, the residual torsion stress of the 2# and 4# ribbons became larger after aging, and the residual torsion stress of the 3# and 6# bands had large and small changes after aging, except for the 1# band, the others did not change much, and the change did not exceed 10° at 50cm.

2.4.2.3 The 6 disks of optical fiber ribbons shall be sampled in one group and twisted together for many times. After twisting, the optical fiber ribbons shall be buried and sealed in a box with fiber paste, and then the box shall be placed in an 85° incubator for sampling after 30 days of aging. The sample shall be called the aging sample with fiber paste (TIA 加纤膏老化样)and taken out to test its residual torsion; The test results are shown in Figure 4 below.

Return to Table of Contents

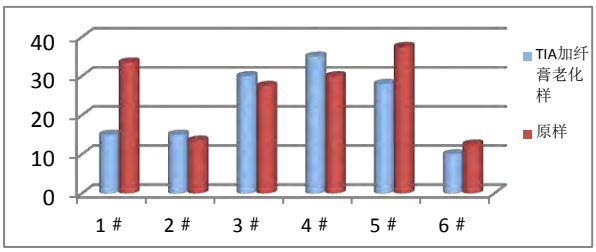


Figure 4 Comparison of residual torsion data between the aged sample and the original one

It can be seen from the figure that the basic law of aging and original of the fiber paste is also that the residual torsion stress of the 1# and 5# ribbons becomes smaller after aging, while the residual torsion stress of the 2#, 3#, 4# and 6# ribbons does not change much after aging. Basically within 5°, it can be said that the change is very small, and the system error may also have such a result.

2.4.2.4 The 6 disks of optical fiber ribbon are made into a loose sleeve with fiber paste, and then twisted together with other optical fiber tapes and sheathed to form a cable. A sample of 1 meter of optical cable was taken, and after 30 days of aging at a temperature of 85°, （IEC 成缆后老化样）the fiber strip inside was removed and its residual torsion was tested.

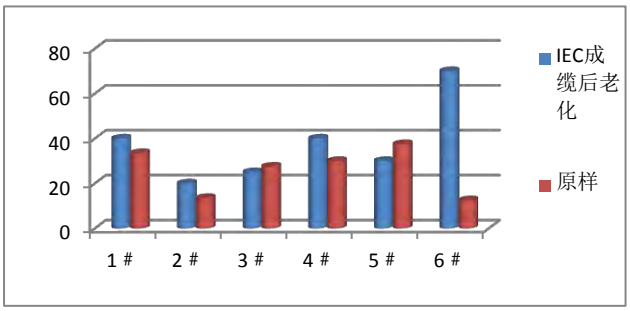


Figure 5 Comparison of residual torsion data between cable aged sample and original sample

From the figure, the change is most obvious in the 6# band, the increase is very obvious, and the residual torsion of the 1# band is also larger than that of other residual torsion test samples after aging.

2.4.3 Comprehensive analysis of test results

2.4.3.1 Comparison of experimental data of residual torsion stress of fiber optic tape after aging. Figure 6

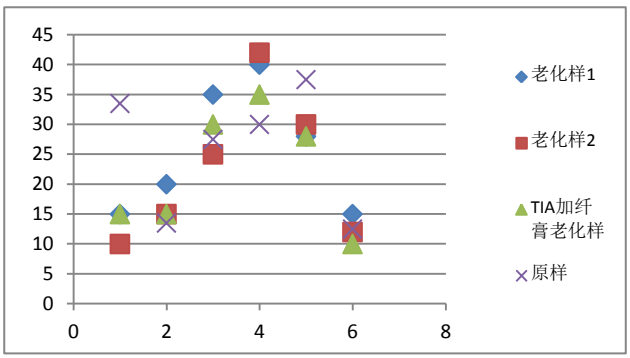


Figure 6 Residual torsion stress test data of fiber ribbon after aging

It can be seen from the figure that the residual torsion stress of the fiber ribbon aged after the cable is relatively large, mainly because the data of the two side fibers are obvious. We carefully observed the test sample and found that there is distortion on the surface of the sample, as shown in Figure 7, without coating damage at the distortion, and the distortion can still exist under the condition of vertical and 1N weight added, indicating that it is generated after a long time after tying the yarn and forming. If the cable is released shortly after completion, there may not be such a situation. The main reason for the distortion of the fiber ribbon is that there are a lot of stranding in the cable forming process, such as the S-Z stranding of the loose sleeve, and the stranding of the yarn in the layer stranding process may cause the fiber ribbon to be stressed and deformed, but the deformation amount does not change the optical performance of the fiber ribbon. In terms of dispersion, the sample data after aging is basically small, and compared with the original fiber ribbon without aging, the dispersion is larger, which also indicates that the residual torsion of the fiber ribbon after aging will have a certain change, the main reason may be related to the cause of the residual torsion of the fiber strip, generally speaking, if it is caused by the fiber (fiber torsion and payout tension). Because the fiber is cured after being banded, it is difficult to eliminate the stress, but if the illumination is uneven during curing, it will be gradually eliminated during the aging process, because the elimination of this stress may cause the residual torsional stress of the fiber ribbon to change.

Return to Table of Contents

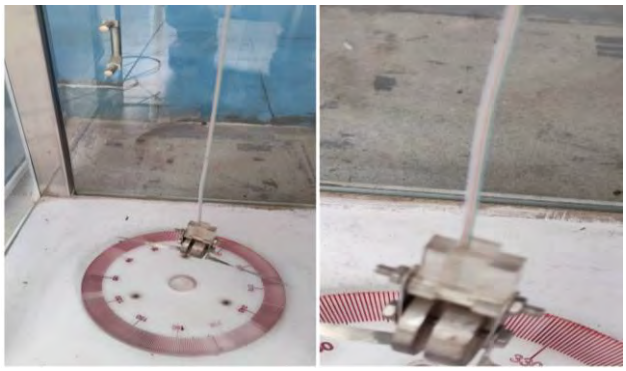


Figure 7: The fiber strip is deformed after aging

2.4.3.2 The above experimental data are based on the non-twist-twisted fiber commonly used in optical fiber belt. Now there are more and more twist-twisted fiber, and many manufacturers also use twist-twisted fiber as optical fiber belt. In the process, we added a set of experimental data before and after the aging of the twisted fiber. The results are as follows:

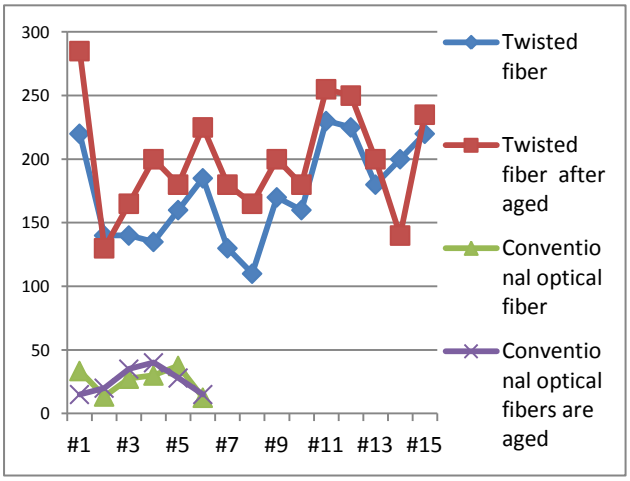


Figure 8 Twisted and untwisted fiber l torsion stress test data of fiber ribbon after aging

2.4.4 Test results

1) The aging of the fiber ribbon will affect its residual torsion stress, and the change is larger and smaller;

2) Aging will also affect the residual torsion stress of the fiber ribbon after cable formation;

3) The situation is the same after the ribbon of the twist-twisted fiber and the non-twist-twisted fiber, and the residual stress changes after aging, and the change is the same

3. How to develop the residual torsion test method of optical fiber tape under existing circumstances

As can be seen from the above test results, it is reasonable for IEC test methods to conduct experiments on fiber ribbons after cable aging, but it is unnecessary from the actual use situation, because the results have been inevitable, and the residual torsion stress of the fiber ribbon is the residual torsion stress of the fiber ribbon itself, which ultimately affects the welding performance. The residual torsion stress is large to a certain extent, resulting in reverse banding, affecting welding or attenuation exceeding the standard, but it is not necessary to test the residual torsion as long as the optical fiber ribbon printing and optical fiber ribbon color sequence can be found. The test requirements of TIA are more narrow, only for outdoor optical cables, and the test results are not different from direct aging. Previously, the optical fiber ribbon is basically only used in optical cables, and now with the development of all-optical network, the use of optical fiber ribbon is more and more extensive, widely used in indoor optical cables, terminal optical components, the use of the environment has also undergone qualitative changes, indoor optical cables do not need fiber paste, the optical fiber ribbon in the terminal optical components is basically also there are no cables. IEC and TIA have some limitations on the test method of residual torsion of optical fiber ribbon.

How to develop a reasonable fiber ribbon residual torsion test method, from the existing standard analysis is mainly a unified pre-treatment problem, whether the fiber ribbon as a product, or as a semi-finished optical cable to become an optical unit, the purpose of testing the residual torsion stress of the fiber ribbon is to make the later production of defective products, the test method needs to have the following principles: 1) simple and easy; 2) It works. According to the actual situation of production combined with our test results, first of all, the fiber ribbon needs to be sampled for residual torsion test after aging, aging will affect the residual torsion stress of the fiber ribbon, which is necessary, but whether it is outdoor fiber cable, indoor fiber cable or terminal component, there are problems of immediate use and long-term use. The terminal optical component not only has the requirement of winding into a circle during the production process, but also the residual torsion stress is required after the double 85 (long-term test at 85° temperature and 85% humidity) of the component.

Therefore, it is suggested that: 1) there should be two situations for the torsion test of optical fiber ribbon, that is, the residual torsion stress is directly tested after the formation of the band and the residual torsion stress is tested after aging. The test result should be the maximum test data as the final test data. 2) As a test method, sometimes not only for product inspection, it may also be bad cause investigation, or arbitration

Return to Table of Contents

between the two parties, is the fiber optic cable caused by the fiber ribbon torsion or the fiber ribbon itself caused by the torsion, the purpose of pre-treatment is to restore the entire production process, IEC and TIA test methods can be used.

About the author
Xiaoquan wang (1973 -), female, graduated from University of Shanghai for Science and Technology, is the deputy chief engineer of Research and Development and technical support Department of Nanjing Wasin Fujicura Optical Communication Co., LTD. She has been engaged in the research of optical fiber and optical fiber belt for a long time.

Return to Table of Contents

TITLE: LIGHTFASTNESS AND UV PROTECTION IN OUTDOOR CABLES.

AUTHORS: Eva Gotor/Brita Kunze-DELTA TECNIC.

PRESENTER: Brita Kunze

Main Subject Matter: The Role of Masterbatches in Polymer Protection and Color Stability.

Presentation Description: Poster Paper.

Primary End Use Area: Outdoor cable applications that require Lightfastness and Weathering.

ABSTRACT:

Outdoor cables are vulnerable to degradation and discoloration due to exposure to environmental elements like light, temperature, and humidity. This abstract presents essential strategies for safeguarding outdoor cables.

Outdoor cable challenges are classified into two categories: lightfastness, associated with light exposure, and weathering, encompassing temperature and humidity fluctuations. Distinguishing between these factors is crucial, as pigments with strong lightfastness may not address weathering issues.

Prevention is paramount, involving accelerated testing of pigment performance under various environmental conditions. This aids in selecting the right pigments and predicting cable lifespan accurately.

Industries reliant on outdoor cables, including medium voltage, photovoltaic, power, and fiber optic cables, aim to combat photodegradation caused by ultraviolet (UV) radiation. UV exposure leads to photooxidative degradation, generating free radicals that degrade cable appearance, shine, surface, and mechanical properties.

Mitigating photodegradation involves three strategies: UV filters, Hindered Amine Light Stabilizers (HALS), and carbon black. UV filters absorb UV light, HALS react to free radicals, and carbon black efficiently absorbs UV radiation.

Preserving cable color necessitates selecting pigments designed for outdoor conditions and understanding pigment behavior in different cable polymers. Collaborative partnerships with experts are essential for maintaining consistent cable color over their outdoor lifespan.

KEY WORDS:

Cables, Lightfastness, Weathering, Color stability, Masterbatches, Color, Polymer degradation, Discoloration, Outdoor cables,

Ultraviolet (UV) radiation, Photodegradation

INTRODUCTION:

This presentation delves into the critical challenges faced by outdoor cables subjected to the rigors of various environmental elements. Many organizations grapple with the perplexing issue of their outdoor cables succumbing to discoloration and the deterioration of polymer materials. These challenges primarily stem from exposure to factors such as light, temperature variations, and humidity fluctuations.

In essence, the presentation explores the paramount importance of ensuring the longevity and reliability of outdoor cables and provides comprehensive insights into effective strategies for achieving this objective. It highlights two fundamental concepts: lightfastness, which pertains to the effects of light exposure, and weathering, encompassing broader environmental influences. Discriminating between these factors is essential, as the solutions to combat them may differ significantly.

The overarching message is one of proactive prevention being preferable to reactive solutions, emphasizing the significance of accelerated testing and the careful selection of pigments and additives to shield outdoor cables from the detrimental effects of photodegradation and other environmental challenges. Industries reliant on outdoor cables, such as energy, telecommunications, and construction, are increasingly recognizing the value of these strategies in maintaining the integrity and longevity of their cable installations.

MAIN BODY OF SUBMISSION:

1. Understanding the Challenges of Outdoor Cables:

Outdoor cables serve critical functions in various industries, from energy distribution to telecommunications and construction. However, they face formidable challenges when exposed to the outdoor environment. The primary culprits behind cable degradation are light exposure, temperature fluctuations, and varying humidity levels.

2. Distinguishing Between Lightfastness and Weathering:

To effectively combat cable degradation, it's essential to differentiate between two key factors: lightfastness and weathering. Lightfastness refers to a cable's ability to withstand the damaging effects of light exposure, particularly ultraviolet (UV) radiation. Weathering encompasses a broader range of environmental factors, including temperature variations and humidity levels.

3. The Role of Photodegradation:

Ultraviolet (UV) radiation is a major contributor to photodegradation. When UV light interacts with cable polymers, it initiates a photooxidative degradation process, generating free radicals. These free radicals trigger a chain reaction that negatively impacts the cable's visual appearance, surface quality, shine, and mechanical properties. Understanding this process is crucial for developing effective mitigation strategies.

4. Strategies to Prevent Photodegradation:

There are three primary strategies for mitigating photodegradation in cable polymers:

a. UV Filters: UV filters are additives designed to absorb and neutralize UV light, preventing it from reaching the polymer. This process is akin to using a parasol to shield the cable.

b. Hindered Amine Light Stabilizers (HALS): HALS additives react with free radicals generated by UV exposure, effectively blocking their damaging effects and preserving the integrity of polymer chains.

c. Carbon Black: Carbon black is used to absorb a significant portion of UV radiation. Fine-particle carbon black, with its increased surface area, is particularly effective at trapping solar radiation and preventing it from reacting with the polymer.

5. Addressing Cable Color Preservation:

While protecting the polymer is essential, maintaining the cable's color is equally crucial. Unfortunately, there are no additives that can safeguard color as effectively as the polymer. To address this, the solution lies in selecting pigments explicitly formulated to withstand outdoor conditions. This entails a thorough study of pigment behavior in various cable polymers used in the industry, including PVC, HFFR, TPU, XLPE, and EPDM.

6. The Importance of Collaboration and Expertise:

Achieving lightfastness and preventing cable degradation demands collaboration with experts in the field. This collaborative approach involves conducting in-depth studies on pigment behavior, accelerated testing under diverse environmental conditions, and the selection of appropriate pigments and additives. Industries dedicated to energy, wireless networks, and telecommunications understand the value of such collaborations in ensuring the long-term stability and reliability of their cable installations.

CONCLUSSIONS:

In the realm of outdoor cables, where exposure to the elements poses significant challenges, the pursuit of lightfastness and the prevention of cable degradation and discoloration are paramount. This presentation has shed light on key insights and strategies to address these critical concerns.

Discriminating Factors: Understanding the distinction between lightfastness, associated with light exposure, and weathering, which encompasses broader environmental influences like temperature and humidity, is crucial. This differentiation allows for targeted solutions.

Photodegradation: A Central Concern: The detrimental effects of photodegradation, initiated by ultraviolet (UV) radiation, have been highlighted. UV radiation triggers a chain reaction that impacts cable appearance, surface quality, shine, and mechanical properties. Addressing this process is fundamental to cable longevity.

Mitigation Strategies: Three primary strategies to combat photodegradation have been outlined. UV filters, Hindered Amine Light Stabilizers (HALS), and carbon black each offer distinct mechanisms to shield cables from UV damage.

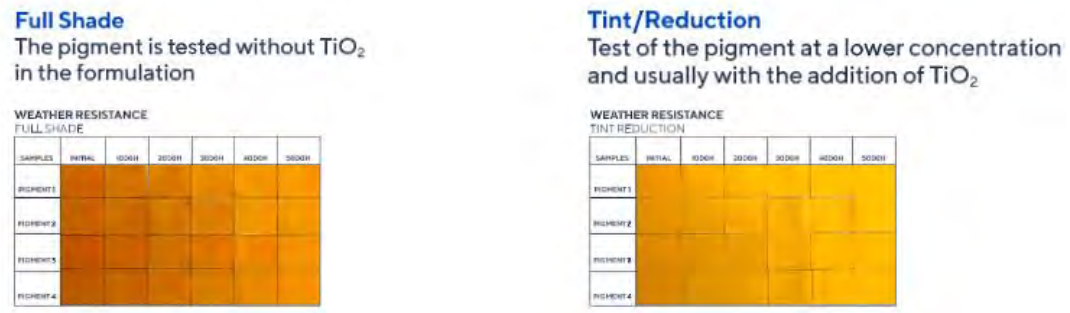
Color Preservation: Preserving cable color presents a unique challenge, necessitating the selection of pigments tailored for outdoor conditions. Comprehensive studies on pigment behavior in various cable polymers are essential to maintain consistent cable color.

Collaboration and Expertise: The importance of collaborative partnerships with experts in the field cannot be overstated. Conducting accelerated tests, studying pigment behavior, and selecting appropriate additives are best achieved through collaboration, ensuring the long-term stability and reliability of outdoor cable installations.

In conclusion, safeguarding outdoor cables is a multifaceted endeavor that requires a holistic approach, involving an understanding of environmental challenges, proactive strategies, and collaboration with experts. By implementing these measures, industries relying on outdoor cables can ensure the sustained performance and durability of their critical infrastructure, ultimately minimizing maintenance costs and maximizing operational efficiency.

TABLES:

Correct selection of pigments to avoid color degradation

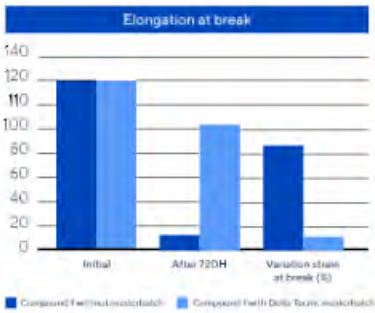


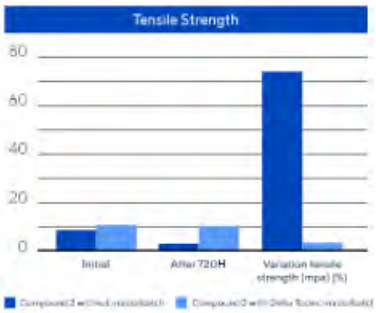
THNN building wire color range



Study of Mechanical Properties according to the industry standards IEC-62930 and EN-50618

	Elongation at break			Tensile Strength		
	Initial	After 720H	Variation strain at break (%)	Initial	After 720H	Variation tensile strength (mpa) (%)
Compound 1 without masterbatch	120	14	88,33	8,88	2,3	74,10
Compound 1 with Delta Tecnic masterbatch	122	106	13,11	13,11	10,21	3,13
Compound 2 without masterbatch	85	32	62,35	15,23	10,23	32,83
Compound 2 with Delta Tecnic masterbatch	97	78	19,59	12,53	12,12	3,27





A Method for Estimating the Combustion Performance (Heat Release) of Optical Cables Based on Material Thermal Analysis Techniques

Jia Wang, Yunfang Ruan, Haifeng Hu, Siyi Tang, Zhuang Xiong

[1]State Key Laboratory of Optical Fiber and Cable Manufacture Technology, Yangtze Optical Fibre and Cable joint stock limited company; [2]Optics Valley Laboratory, Hubei 430073, China

Author e-mail address: wangjia@yofc.com

Abstract

In this study, we use differential scanning calorimetry (DSC) to test low-smoke and halogen-free flame-retardant sheath materials. The heating rate is 10°C/min, and the experimental procedures range from 30°C to 400°C. The test samples are selected to be around 10 mg, and the material's heat of fusion and melting peak are obtained. The limiting oxygen index and heat release value of each component material of the optical cable are measured. Following the EN 13501-6 standard, combustion tests are conducted on the optical cable to obtain the total heat release within 1200 seconds of exposure to flame (THR1200s). The thermal analysis data of the cable sheath, limiting oxygen index, and heat release value are correlated. The theoretical calculation results of heat release value are compared with actual values to assess the feasibility of using material thermal analysis techniques to predict the combustion performance (heat release) of optical cables.

Keywords: thermal analysis, heat release, limiting oxygen index

1. Introduction

Flame-retardant properties are required for optical cables in various applications such as subways and buildings. The total heat release during combustion is an important parameter for evaluating cable burning characteristics. Typically, heat release values are only known after conducting combustion tests on the manufactured cables. To predict the theoretical maximum heat release value during cable combustion in the design phase, it is necessary to calculate the heat release values of combustible components in the cable. This calculation requires knowing the heat release value of combustible material per unit mass. Although cone calorimeters can provide heat release values, they require specialized exhaust systems and are not commonly available in cable or material laboratories. On the other hand, DSC instruments, due to their compactness and convenience, are more commonly found in these laboratories. However, they are mostly used for measuring the oxidative induction time of water-blocking compounds, determining the processing temperature of sheath materials, and are not often associated with measuring heat release values.

In flame-retardant cable design, the types and grades of materials constituting the cable core generally remain relatively stable compared to the sheath materials. In this paper, different grades of low-smoke and halogen-free flame-retardant sheath materials are selected. The relationship between the heat of fusion or melting enthalpy of the sheath material and the limiting oxygen concentration and heat release value is studied. When engineers face difficulties in selecting flame-retardant sheath materials with various grades during the cable design stage, they can use DSC to measure the melting peak or enthalpy, and with the help of relevant functions, estimate the heat release value of new flame-retardant sheath materials introduced, based on the known melting enthalpy and heat release value of a specific flame-retardant material. This approach allows for a relatively accurate calculation of the total heat release value of the entire cable, providing significant convenience for cable design engineers.

2. Experiments

2.1 Material Thermal Analysis Experiment

Differential scanning calorimetry (DSC) is used to perform thermal analysis on three types of low-smoke and halogen-free flame-retardant sheath materials and one type of high-density polyethylene (HDPE) sheath material. The heating rate is 10°C/min, and the experimental procedure ranged from 30°C to 400°C. The test samples are selected to be around 10 mg, and the material's heat of fusion and melting peak are obtained. Figure 1 shows the differential scanning calorimetry (DSC).



Figure 1. Differential scanning calorimetry (DSC)

2.2 Material Combustion Experiment

A cone calorimeter is used to measure the heat release values of combustible materials in the optical cable, including core materials (such as fiber coloring ink, sheath material, fiber filling compound, FRP, water-blocking yarn, cable binder) and different grades of cable sheath materials. The limiting oxygen index of these materials is measured using an oxygen index tester (or obtained from the manufacturer's test report), which is a routine test item for materials.

2.3 Optical Cable Combustion Experiment

Referring to the EN 13501-6 standard, two types of optical cables, a layered twisted flame-retardant optical cable and a central tube flame-retardant optical cable, are subjected to combustion tests. The total heat release within 1200 seconds of exposure to flame (THR1200s) is measured. The structural diagrams of the cables are shown in Figure 2 and Figure 3.

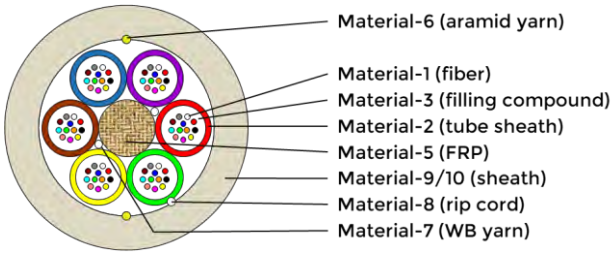


Figure 2. Schematic diagram of layered twisted flame-retardant optical cable

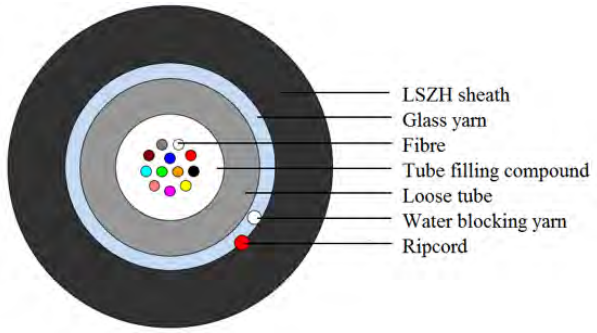


Figure 3. Schematic diagram of central tube flame-retardant optical cable

3. Results

3.1 Clear Correspondence between Sheath Material's Melting Enthalpy or Melting Peak and Limiting Oxygen Index, Heat Release Value

Thermal analysis is conducted on different grades of low-smoke and halogen-free flame-retardant sheath materials (LSZH), and HDPE is used as a control. The original test curve for the LSZH-A sheath material is shown in Figure 4, and the compiled melting enthalpy and melting peak data for different grades of sheath materials are shown in Table 1. A correlation is observed between the melting enthalpy or melting peak of the material and the limiting oxygen index, as shown in Figure 5 and Figure 6. A correlation is also observed between the limiting oxygen index and the heat release data, as shown in Figure 7.

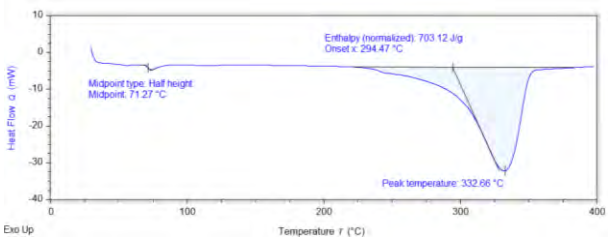


Figure 4. LSZH-A original test curve

Table 1. the compiled melting enthalpy and melting peak data for different grades of sheath materials

Material	Heat enthalpy (J/g)	Peak temperature (℃)	Limiting oxygen index
LSZH-A	703.12	332.66	0.39
LSZH-B	574.08	327.85	0.355
LSZH-C	365.65	323.53	0.35
HDPE	192.21	121.23	0.2

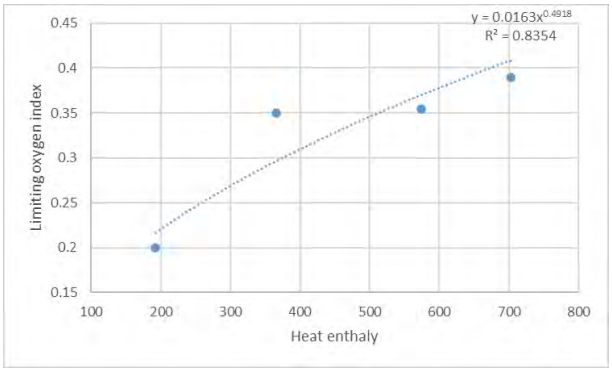


Figure 5. Correlation between the melting enthalpy and the limiting oxygen index

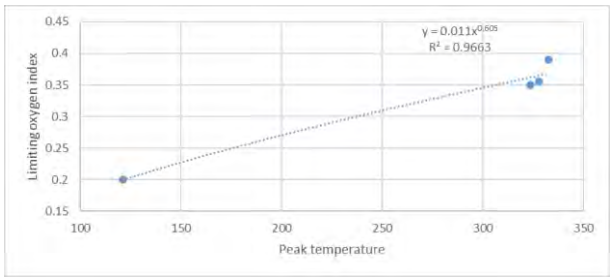


Figure 6. Correlation between the melting peak and the limiting oxygen index

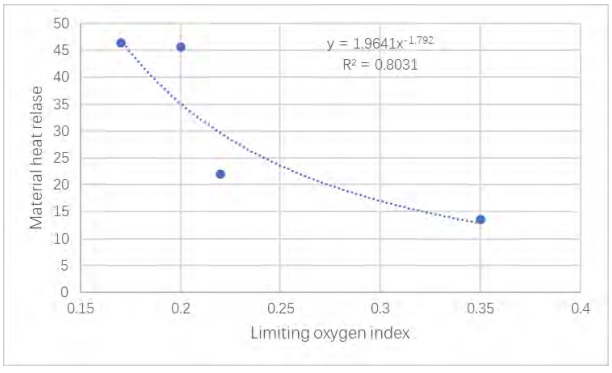


Figure 7. Correlation between the limiting oxygen index and the heat release data

3.2 Feasibility of Estimating Material's Heat Release Value through DSC Thermal Analysis

DSC is used to perform thermal analysis on the newly introduced LSZH-D material, and a melting peak of 430°C is obtained. Using the functions mentioned in the experimental results, the calculated theoretical limiting oxygen index is 0.43, which is very close to the manufacturer's reported limiting oxygen index of 0.44, indicating a good fit. Furthermore, the heat release value (fuel load) of LSZH-D is calculated to be 8.55 MJ/kg. Combining this with the heat release data of each core material, the theoretical total heat release value for 1 meter of cable is calculated. Taking into account the number of cables in the combustion test, the actual burning distance of the cable, and the proportion of the cross-sectional area of the cable that actually burns, the theoretical heat release for the combustion test is determined and compared with the actual heat release during the combustion test (THR1200s). By conducting combustion tests on the layered twisted flame-retardant optical cable and the central tube flame-retardant optical cable, it is found that the theoretical heat release during the combustion test is very close to the actual heat release, demonstrating the accuracy of the heat release values obtained through function fitting.

Table 2 Combustion Heat Release of Layered Twisted Flame-retardant Optical Cable

Material in Cable	Type Estimated Heat Release Value per 1 Meter of Cable (MJ)	Theoretical Total Heat Release Value per 1 Meter of Cable (MJ)	Theoretical Heat Release Value in Combustion Test
Colored Ink	0.0106	1.0923	14.57MJ
PBT	0.0997	Number of fiber cables in the combustion test	
Fiber Filling Compound	0.2920	18	
FRP	0.0081	Actual burning distance of optical cable	Actual Heat Release Value in Combustion Test
Water-Blocking Yarn	0.0092	1.3m	14MJ
Ripcord	0.0053	The proportion of the cross-sectional area of the actual burning part of the optical cable	
LSZH-D Sheath	0.6674	57%	

Table 3 Combustion Heat Release of Central Tube Flame-retardant Optical Cable

Material in Cable	Type Estimated Heat Release Value per 1 Meter of Cable (MJ)	Theoretical Total Heat Release Value per 1 Meter of Cable (MJ)	Theoretical Heat Release Value in Combustion Test
Colored Ink	0.0003	0.7743	17.89MJ
PBT	0.0926	Number of fiber cables in the combustion test	
Fiber Filling Compound	0.1888	21	
/	/	Actual burning distance of optical cable	Actual Heat Release Value in Combustion Test
Water-Blocking Yarn	0.0031	1.1m	18MJ
Ripcord	0.0128	The proportion of the cross-sectional area of the actual burning part of the optical cable	
LSZH-D Sheath	0.4767	100%	

4. Conclusions

There is a clear correspondence between the melting enthalpy or melting peak of flame-retardant sheath materials tested in a nitrogen environment using DSC and the limiting oxygen index and heat release value.

Estimating the heat release value of materials by measuring their melting peak or enthalpy and using function fitting is relatively accurate, providing a close match to actual values of theoretical heat release for optical cables.

This study provides a new approach for the indirect measurement and prediction of material heat release using DSC.

5. Reference

[1] BSI. Fire classification of construction products and building elements—part 6: classification using data from reaction to fire tests on electric cables: BS EN 13501-6: 2014 [S]. British: BSI Standards Publication,2014.

6. Pictures of Authors



Mr. Jia Wang received his M.S degree in Materials Processing from University of Science and Technology of China in 2020. Since then, he has been working in YOFC. Now he is a R&D engineer of R&D Centre of YOFC, engaged in research and development of optical fiber cable.



Mr. Yunfang Ruan received his B.S degree in mechanical and electronic engineering from Hubei Institute of Technology in 1996. He has been working in YOFC since 1997. Now he is R&D engineer, mainly engaged in cable production process control and product development work.



Mrs. Haifeng Hu received her M.S degree from Huazhong University of Science and Technology. Now she is a R&D engineer of R&D Centre of YOFC, engaged in research and development of optical fiber cable.



Miss. Siyi Tang received her M.S degree in Polymer science and engineering from Sichuan University in 2021. Since then, she has been working in YOFC. Now she is a R&D engineer of R&D Centre of YOFC, engaged in research and development of optical fiber cable.



Dr. Zhuang Xiong got his B.E. degree in Mechanical Engineering from Wuhan Institute of Technology in 1994 and received his Ph.D. in Mechanical Manufacture and its Automation from HUST in 2000. Since then, he has been working in YOFC, engaged in the research and development of optical fiber cables. Now he is the chief scientist of optical cable.

Research on Shrinkage Performance of Central Core Tube Optical Cable

Jianbin Duan, Zhuang Xiong, Wei Gao, Xin Mao, Kesen Yang, Kai Qin, Huixia Gao, Chao Sun
State Key Laboratory of Optical Fiber and Cable Manufacture Technology, Wuhan 430073, China
Yangtze Optical Fibre and Cable Joint Stock Limited Company, Wuhan 430073, China
Hubei Optics Valley Laboratory, Wuhan 430074, China
+86-027-68789157 · duanjianbin@yofc.com

Abstract
Shrinkage performance is critical for optical cable termination. In this paper, several environmental tests based on IEC 60794-1-22 method F17 were designed to evaluate the thermal shrinkage performance of central core tube optical cable. Some general conclusions for thermal shrinkage of central core tube optical cable has been summarized from the test results.

Keywords: Cable Shrinkage, Cable Termination, Central Core Tube Optical Cable, Outdoor Cable, Fibre protrusion

1. Introduction
Shrinkage performance of optical cables has been studied for decades. But most researches focus on optical cables to be terminated with connectors. Actually outdoor optical cable, such as loose tube optical cable, has a high cable shrinkage which will seriously affect cable termination performance. In IWCS 2022, we have reported our research on shrinkage performance of stranded loose tube optical cable [1]. In this paper, research on cable shrinkage of central core tube optical cable was presented.

Historical research shows that for loose tube cable, the change of protrusion of the central strength members was moderate and smaller than the fibre protrusion and little or no change of the loose tubes protrusion was induced [2]. So in general, fibre protrusion is the most serious compared with other components. In this paper, we focus on the fibre protrusion in the cable shrinkage of central core tube optical cable.

Two commonly used experimental methods for cable shrinkage test are test method F11 and F17 in IEC 60794-1-22 [3]. Method F11 is suitable for cables where the fibre or buffered fibre and the sheath of the cable are intended to be fully terminated into a connector at cable ends. Method F17 provide a method suitable for long optical cable sample (10 m or longer). So method F17 is available for central core tube optical cable.

In this paper, several environmental tests have been designed to evaluate the thermal shrinkage performance of central core tube optical cable. Based on it, the influence factors of cable shrinkage for central core tube optical cable were studied.

2. Central Core Tube Optical cable
Loose Tube Optical cable is mainly used for outdoor cable. There are two typical types, stranded tube type and center tube type. In this paper, central core tube type was chosen for research.

Figure 1 is a structure diagram of the cable sample used in this paper. This is a typical outdoor optical cable with central core tube. It contain 12 twelve-fiber ribbons with totally 144 fibres inside. It has a PE sheath and all-dry water-blocking component.

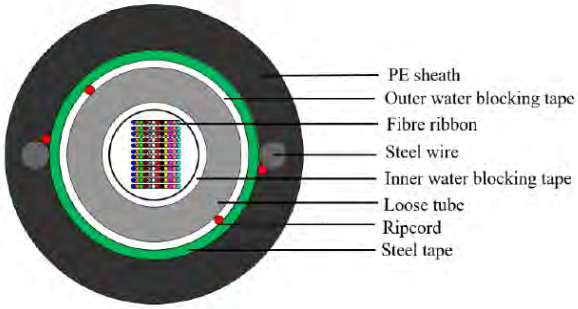


Figure 1. Structure diagram of central core tube optical cable sample

Shrinkage is strongly dependent on the thermal and mechanical history of optical cable. Some shrinkage can occur after cutting the sample from the drum, during storage or transportation. These shrinkage happens before testing will affect the reliability of cable shrinkage test results. The samples used in this paper is a fresh optical cable which was produced within a month before testing and stored in a standard laboratory environment.

3. Experiment
The experiments design and details were listed in table 1.

Table 1. Experiments design and test conditions

Experiments	Sample	Conditions
Low temperature	A	Temp: -20°C, -40°C Test period: 8 days
High temperature	A	Temp: 60°C, 85°C Test period: 8 days
Temperature cycle	A	Low temp: -40°C High temp: 60°C, 70°C, 85°C Cycle number: 12 Heating and cooling rate: 1 °C/min. Hold time at extreme point: 4 hour.
Effect of cable length	A	Temp cycle: -40 °C~ 70 °C, other condition is same with upper temperature cycle test. Cable length: 10m, 20m, 50m
Effect on optical performance	A+B	Temp cycle: -40 °C~ 70 °C, other condition is same with upper temperature cycle test. Loop one fibre in each tube, monitor the attenuation of the loop at 1550nm.
Note: The cable coil diameter in all the test is 80cm; The sample length in tests except comparison of cable length is 10m. Sample A and B have same structure as shown in chapter 2. However, due to different production processes, they have different cable shrinkage performance. A has a high shrinkage and B has a low shrinkage.		

Other test conditions not mentioned in table 1 are according to method F17 of IEC 60794-1-22 except for the preparation of the cable ends and test data processing. In method 17, the tube and fiber should protrude 100mm and 200mm respectively. In our experiments, we only test the protrusion of the fiber relative to the cable sheath. For the convenience of protrusion testing, we carefully cut the fiber optic cable end vertically without blocking the loose tube. So, the initial fibre protrusion is 0mm. For the final data processing, to reduce the impact of accidental factors, we take the average fibre protrusion in two cable ends as the test result. Typical cable end after test is shown in Figure 2.

In Low temperature and High temperature tests, fibre protrusion was tested everyday. In Temperature cycle test, fibre protrusion was measured every two cycles. In the Effects on optical performance test, fibre protrusion was measured every six cycles.

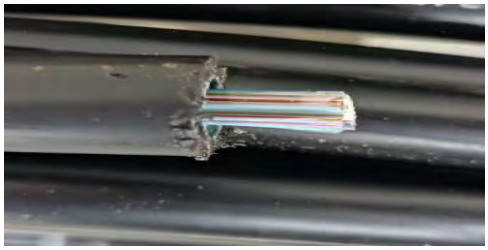


Figure 2. Photo of cable end after cable shrinkage test

4. Low & High temperature effect

The results of continuous low temperature and high temperature test are listed in Figure 3. Similarly to our study on stranded loose tube optical cable [1], fibre protrusion of samples under low temperature or high temperature increase with test period as shown in Figure 3. Most fibre protrusion occurred within the first 4 to 6days.

Fibre protrusion results under high temperature test is significantly bigger than the low temperature test and the higher the high temperature, the greater the fibre protrusion. This may be because the higher the temperature, the greater the thermal shrinkage of the polymer material [4].

But the low temperature test did not exhibit the same trend. The fibre protrusion under -40℃ is bigger than that under -20℃ . The specific reasons for it need further analysis and research.

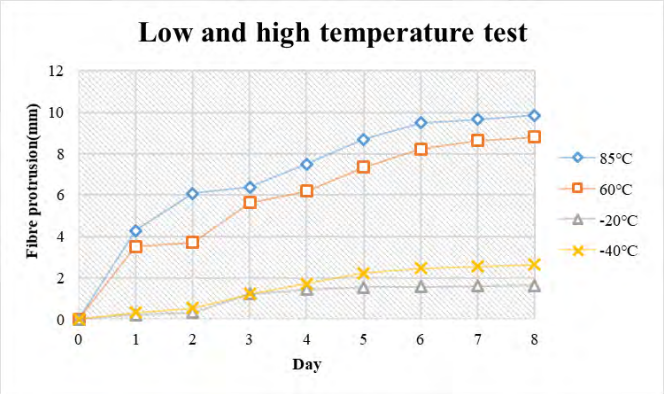


Figure 3. Fibre protrusion measured under low and high temperature test

5. Temperature cycle

The results of temperature cycle test are listed in Figure 4. As shown in Figure 4, under the same low temperature conditions, the higher the upper temperature (60℃, 70℃ and 85℃) in a TCT test, the higher the cable shrinkage. And fibre protrusion is stabilized after 8 to 10 cycles.

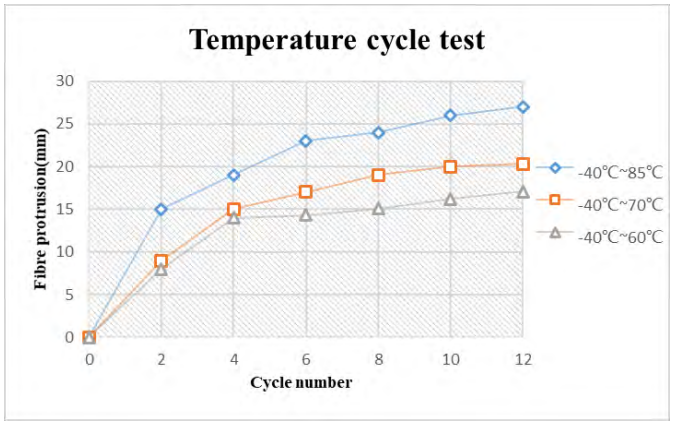


Figure 4. Fibre protrusion measured under temperature cycle test

In addition, we put the TCT and the corresponding low and high temperature test results together for comparison and take time as the abscissa. The result is shown in Figure 5. It is obvious to see that TCT test induced higher fibre protrusion than a continuous high temperature aging or low temperature test using the same high or low temperature.

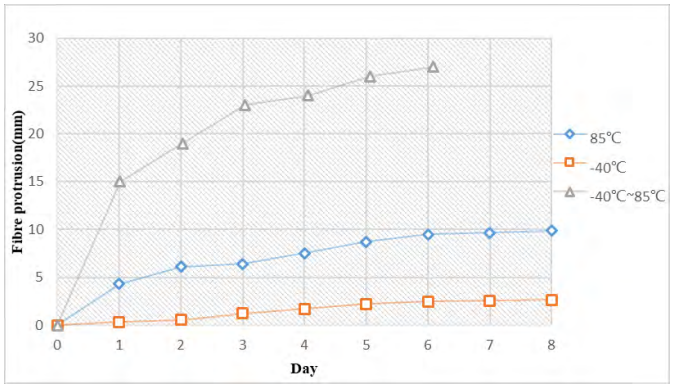


Figure 5. Comparison of TCT test and continuous low temperature or high temperature test

6. Effect of cable length

The results of samples with different length are listed in Figure 6. As shown in Figure 6, fibre protrusion has increased with the length of the cable sample. But this is not a linear change. There is no big difference in the protrusion lengths between the sample lengths of 10 m and 20 m. And fibre protrusion of 50 m sample is not as big as 5 times of the 10m sample.

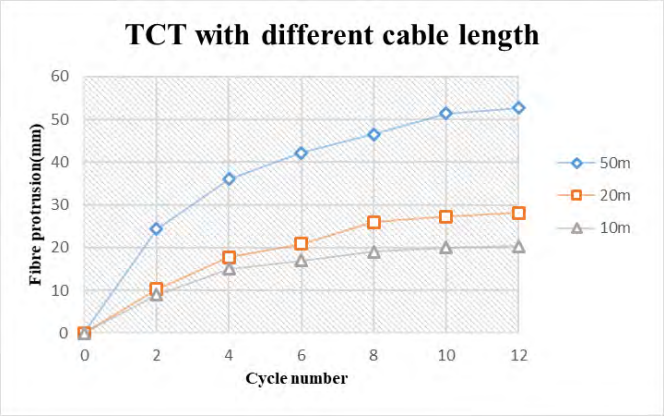


Figure 6 Fibre protrusion measured under different cable length

7. Effect on optical performance

Table 2 shows the results of two samples in effects on optical performance test. Based on the results, the fibre protrusion of sample A is more than four times that of sample B. But their attenuation change in TCT tests show almost no difference. So, a relationship between shrinkage and attenuation change was not obvious.

Table 2. Test results of effects on optical performance test

Sample	A	B
Fibre protrusion at Cycle 6	17mm	4mm
Max attenuation change before Cycle 6	0.03	0.02
Fibre protrusion at Cycle 12	20mm	6mm
Max attenuation change before Cycle 12	0.03	0.03

8. Conclusions

We have studied the shrinkage performance of a central core tube optical cable based on IEC 60794-1-22 method F17. The fiber protrusion is taken as the index parameter in the designed environmental tests.

According to the test results, similar conclusions as stranded loose tube optical cable were obtained [1]. Temperature cycle induced higher shrinkage than a continuous high temperature aging or low temperature test using the same high or low temperature. Most of the shrinkage occurred within 8 to 10 cycles or 4 to 6 days (for continuous high or low temperature test). Under the same low temperature conditions, the higher the high temperature in a TCT test, the higher the cable shrinkage. Longer sample lengths (10 m, 20 m and 50 m) often showed a higher shrinkage. But it was not a linear change. A relationship between shrinkage and attenuation change was not obvious.

There are many factors that affect the shrinkage performance of optical cable, and the change of fibre protrusion values vary significantly between the different cable types and different cable material. In this paper, we have covered only one type cable and several factors. The mechanism of cable shrinkage performance needs further research

9. References

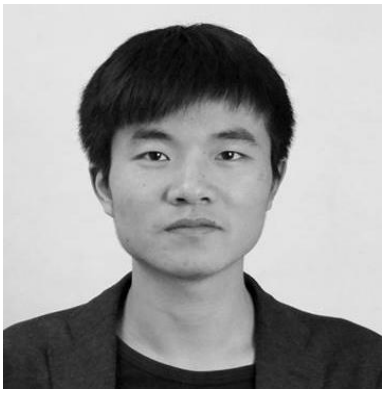
[1] Jianbin Duan, "Research on Shrinkage Performance of Loose Tube Optical Cable." IWCS, Providence RI (October, 2022)

[2] IEC TR 62959: 2021, Optical fibre cables - Shrinkage effects on cable and cable element end termination – Guidance

[3] IEC 60794-1-22: 2017, Optical fibre cables - Part 1-22: Generic specification - Basic optical cable test procedures - Environmental test methods

[4] Li Ranshan et al, “Analysis and prevention of thermal shrinkage of optical fiber tight buffer tube and optical cable sheath” [J]. Modern Transmission, 2013(2):7

10. Authors



Jianbin Duan

Yangtze Optical Fibre and Cable Joint Stock Limited Company

9# Guanggu Road, Wuhan, China，430073

Jianbin Duan is a senior R&D engineer of Test Center in YOFC. He joined YOFC in 2014 and mainly worked on fibre measurement research and cable standardization. He received his BS and MS degree in Material Science from Huazhong University of Science and Technology.

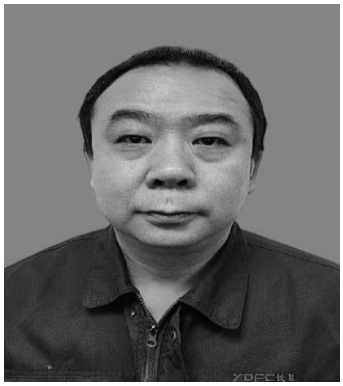


Zhuang Xiong

Yangtze Optical Fibre and Cable Joint Stock Limited Company

9# Guanggu Road, Wuhan, China，430073

Dr. Zhuang Xiong got his B.E. degree in Mechanical Engineering from Wuhan University of Technology in 1994 and received his Ph.D. in Mechanical Manufacture and its Automation from Huazhong University of Science and Technology in 2000. Since then, he has been working in Yangtze Optical Fiber and Cable Joint Stock Co., Ltd., engaged in the research and development of optical fiber cables. Now he is the chief cable scientist in YOFC Group Innovation Center. He has obtained over 100 patents and published more than 90 technical papers. He is IWCS symposium committee member and associate rapporteur of ITU-T SG15 Q7. More over, he is also CIC(China Institute of Communications) fellow and IEC SC86A expert as well as a member of academic committee of State Key Laboratory of Optical Fiber and Cable Manufacture Technology.



Wei Gao

Yangtze Optical Fibre and Cable Joint Stock Limited Company

9# Guanggu Road, Wuhan, China，430073

Wei Gao is a chief technician of Test Center in YOFC. He has more than 20years experience in cable testing and has joined many R&D projects as test team member.



Xin Mao

Yangtze Optical Fibre and Cable Joint Stock Limited Company

9# Guanggu Road, Wuhan, China，430073

Xin Mao is a chief R&D engineer of Test Center at YOFC. He joined YOFC at 2010 and mainly worked on optical fibre and cable measurement research and standardization works. He received his BS and MS degree in Optic Engineering from Huazhong University of Science and Technology.



Kesen Yang
Yangtze Optical Fibre and Cable Joint Stock Limited Company
9# Guanggu Road, Wuhan, China，430073

Kesen Yang is a senior R&D engineer of Test Center in YOFC. He joined YOFC in 2014 and mainly worked on cable and material measurement research. He received his MS degree in Material Science from Huazhong University of Science and Technology.



Kai Qin
Yangtze Optical Fibre and Cable Joint Stock Limited Company
9# Guanggu Road, Wuhan, China，430073

Kai Qin is a chief technician of Test Center in YOFC. He has more than 20years experience in cable testing and has joined many R&D projects as test team member.



Huixia Gao
Yangtze Optical Fibre and Cable Joint Stock Limited Company
9# Guanggu Road, Wuhan, China，430073

Huixia Gao is an assistant engineer of Test Center in YOFC. She joined YOFC in 2004. She has more than 6years experience in cable testing and has joined many R&D projects as test team member.



Chao Sun
Yangtze Optical Fibre and Cable Joint Stock Limited Company
9# Guanggu Road, Wuhan, China，430073

Chao Sun is a senior technician of Test Center in YOFC, joined YOFC in 2001, and mainly engaged in optical cable materials and mechanical properties testing work. He graduated from Jianghan University.

Optical Cable Impact on Environmental Performance of Single-fiber Patchcord

Jianbin Duan, Zhuang Xiong, Huixia Gao, Lu Liu, Kesen Yang, Wei Jiang, Su Wang
State Key Laboratory of Optical Fiber and Cable Manufacture Technology, Wuhan 430073, China
Yangtze Optical Fibre and Cable Joint Stock Limited Company, Wuhan 430073, China
Hubei Optics Valley Laboratory, Wuhan 430074, China
+86-027-68789157 · duanjianbin@yofc.com

Abstract
Optical cable is an important port of single-fiber patchcord. In this paper, the effect of optical cable on single-fiber patchcord's environmental performance was studied. Several environmental tests were designed to evaluate the attenuation change in TCT experiment contributed by the optical cable. Furthermore, the effect of optical fiber type and sheath shrinkage of optical cable was studied.

Keywords: Single-fiber Patchcord, LC connector, FC connector, Simplex optical cable, Temperature Cycling, Sheath Shrinkage

1. Introduction
Optical patchcord have been widely used in the communication industry. It consists of optical cable and optical connectors at both ends. Generally, the cable in patchcord is not very long. The attenuation introduced by optical cable is considered to be small, especially for single-mode patchcord. Users and technical standards mainly focus on the performance of optical connectors. But both components (optical cable and connector) have impact on the performance of patchcord. In this paper, optical cable impact on environmental performance of patchcord was studied.

IEC 60794-1-22 method F12 specify a temperature cycling test for optical cables to be terminated with connectors [1]. In this method, the two ends of optical cable were fixed to simulate the cable ends terminated by connectors. All components of the cable shall be fixed together to avoid any relative movement between the cable elements at the fixing point. The fixing may be by means of clamps, or adhesive injection.

In this paper, several temperature cycling tests were performed on patchcords, optical cable with free ends and optical cable with fixed ends for comparison. Based on it, the effect of optical fiber type and sheath shrinkage on single-fiber patchcord's environmental performance was studied.

2. Sample and test configuration
In order to simplify our research, commonly used single-fiber patchcords were used for samples. The connector types are LC/UPC and SC/UPC. The optical cable of patchcord is 2.0mm simplex cable with 900um tight buffered fiber and reinforced by aramid. Its length is fixed at 10 m. The fiber type is G.652.D and G.657.A2. Besides the single-fiber patchcord samples, simplex optical cable samples were also used in this paper for comparison. All the samples are listed in table 1.

The test configuration of patchcord samples is shown in Figure 1. It was used to evaluate the attenuation change of the whole patchcord sample in environmental tests.

Table 1. Patchcord and cable samples

Sample No.	Description
LC-A	Patchcord sample (10m), LC/UPC, 2.0mm simplex cable, G.652.D
LC-B	Patchcord sample (10m), LC/UPC, 2.0mm simplex cable, G.657.A2
SC	Patchcord sample (10m), SC/UPC, 2.0mm simplex cable, G.652.D
C-A	Cable sample (10m), 2.0mm simplex cable, G.652.D
C-B	Cable sample (10m), 2.0mm simplex cable, G.657.A2
LC-C	Patchcord sample (10m), LC/UPC, 2.0mm simplex cable, G.652.D (with greater sheath shrinkage compared to sample LC-A)

Note:
All the fiber in different samples are from the same supplier and same batch.
The cable with G.652.D fiber in samples (LC-A, SC, C-A) are from the same cable reel.
The cable with G.657.A2 fiber in samples (LC-B, C-B) are from the same cable reel.
The only difference of LC-A and LC-C samples is the cable sheath material. Sample LC-C has a relatively greater sheath shrinkage.

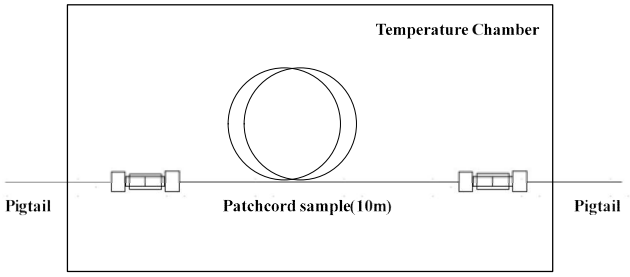


Figure 1. Test configuration of patchcord samples

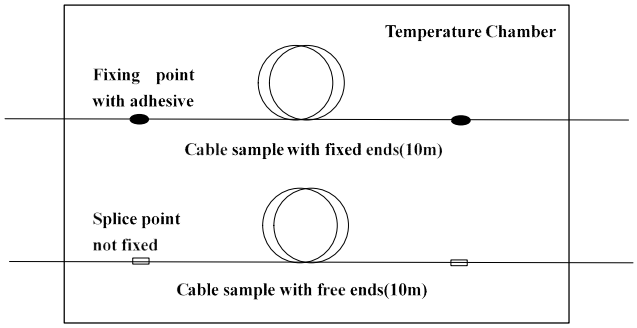


Figure 2. Test configuration of cable samples

Return to Table of Contents

The test configuration of cable samples is shown in Figure 2. There are two types of cable samples. The cable with free ends sample was used to evaluate the attenuation change contributed by the cable itself. The cable with fixed ends (according to IEC 60794-1-22 method F12) sample was used to simulate the cable ends terminated by connectors.

3. Experiment

The experiments design and details were listed in table 2.

Table 2. Experiments design and test conditions

Experiments	Sample	Conditions
Temperature cycling of patchcord	LC-A SC	Low temp: -25°C High temp: 70°C Cycle number: 12 Hold time at extreme point: 1 hour Time of one cycle: 8 hours
Temperature cycling of cable	C-A	Same TCT condition as patchcord
Effect of fiber type	LC-B, C-B	Same TCT condition as patchcord
Effect of sheath shrinkage	LC-A, LC-C	Same TCT condition as patchcord
Note: In all these tests, test 5 specimens for each sample. The cable coil diameter in all the test is about 60cm. All the attenuation was measured @1550nm.		

Other test conditions not mentioned in table 2 are according to IEC 61300-2-22 [2]. The sheath shrinkage of LC-A and LC-C samples were tested according to IEC 60794-1-22 method F11 (1 m sample, TCT conditions same with table 2) and the test results are listed in Chapter 7.

4. Temperature cycling of patchcord

The results of temperature cycling of patchcords are listed in Figure 3 and Figure 4. As shown in the figures, these is no big difference between the two kind single-fiber patchcords. The attenuation of patchcords (both LC and SC type) show periodic changes with temperature and the maximum attenuation change during test is about 0.06 dB and after test is about 0.03 dB.

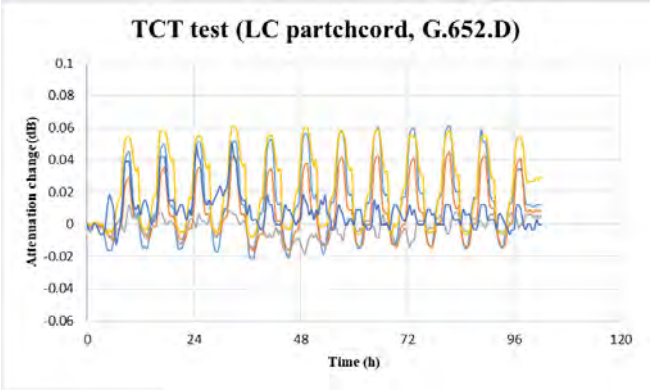


Figure 3. Temperature cycling of LC patchcord (G.652.D)

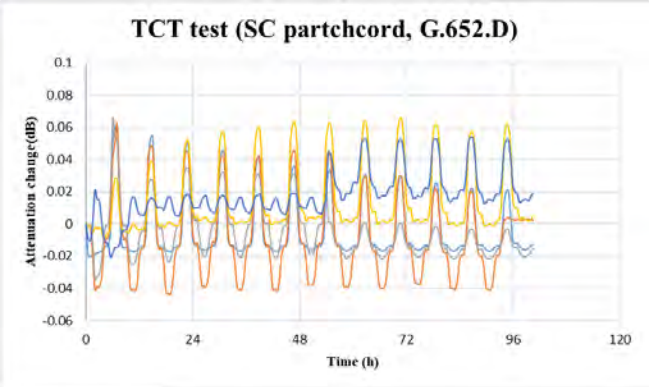


Figure 4. Temperature cycling of SC patchcord (G.652.D)

5. Temperature cycling of cable

The results of temperature cycling of cables are listed in Figure 5 and Figure 6. As shown in Figure 5, there is almost no attenuation change in the TCT test of cable with free ends. So the attenuation change caused by the cable itself in a patchcord is quite small.

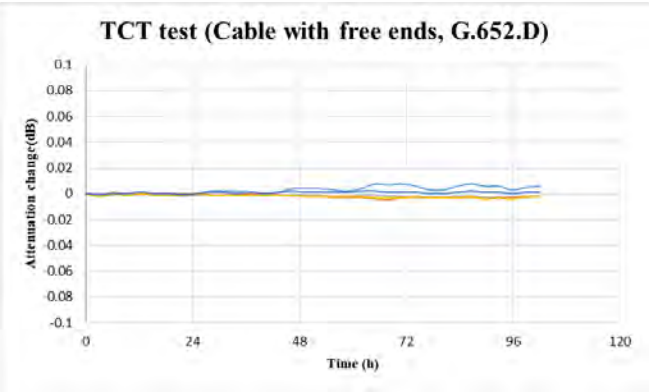


Figure 5. Temperature cycling of cable with free ends (G.652.D)

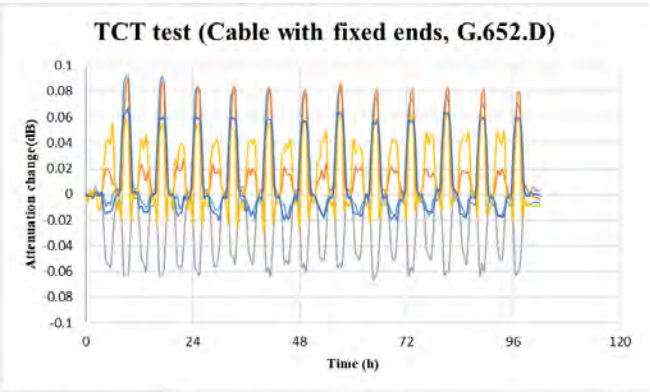


Figure 6. Temperature cycling of cable with fixed ends (G.652.D)

Figure 6 is the results of cable sample with fixed ends. Similar with the patchcord, the attenuation show periodic changes with temperature. If we compare Figure 6 with Figure 3 and 4. The attenuation change of patchcords is smaller than the cable samples with fixed ends. This may because some fiber overlength can be

Return to Table of Contents

absorbed by the bend inside the connector housing, while this is not possible with fixed cable elements samples.

6. Effect of fiber type

According to the test results of chapter 5, the attenuation change of cable itself can be ignored in a patchcord. But fiber buckling in both ends caused by temperature change may be the main reason for attenuation increase.

So if we use bending loss insensitive single-mode fiber like G.657.A2 in a patchcord, the attenuation change caused by fiber buckling in connector may decrease. Table 3 show the attenuation change of samples with two type fibers. After using G.657.A2 fiber instead of G.652.D fiber, the attenuation change for both patchcords or cable with fixed ends decrease a bit.

During the G.657.A2 fiber samples, the attenuation change of the cable with fixed ends is also bigger than the patchcord.

Table 3. Attenuation change of samples with two type fibers

Sample	G.652.D	G.657.A2
LC patchcord (Sample LC-A and LC-B)	Avg: 0.05 dB Max: 0.06 dB	Avg: 0.02 dB Max: 0.03 dB
Cable with fixed ends (Sample C-A and C-B)	Avg: 0.06 dB Max: 0.09 dB	Avg: 0.03 dB Max: 0.05 dB

7. Effect of sheath shrinkage

The results of effect of sheath shrinkage are listed in table 4. Based on the results, when cable has a bigger sheath shrinkage, the attenuation change of patchcord in TCT test seem to be greater.

Table 4. Attenuation change of patchcord samples with different sheath shrinkage

Item	LC-A	LC-C
Sheath shrinkage (IEC 60794-1-22 method F11)	6 mm	11 mm
Average attenuatin change in TCT	0.05 dB	0.07 dB
Max attenuatin change in TCT	0.06 dB	0.10 dB

8. Conclusions

In this paper, several temperature cycling tests were performed on patchcords, optical cable with free ends and optical cable with fixed ends for comparison. Based on it, the effect of optical fiber type and sheath shrinkage on single-fiber patchcord's performance was studied.

According to the test results, the attenuation of patchcords (both LC and SC type) show periodic changes with temperature and the difference is small. There is almost no attenuation change in the TCT test of cable with free ends. While the attenuation change of cable sample with fixed ends is bigger than the patchcord samples. After using G.657.A2 fiber instead of G.652D fiber, the attenuation change for both patchcord or cable with fixed ends decrease a little. And when using cable with a bigger sheath shrinkage, the attenuation change in TCT test seem to be greater.

Based on these, some general conclusions can be summarized. The attenuation change of cable itself can be ignored in a patchcord with short length cable. Fiber buckling in both ends caused by temperature change may be the main reason for attenuation increase of patchcord. The test with patchcords may give a lower attenuation change in TCT test than the test with all cable elements fixed at two ends. This may because some fiber overlength can be absorbed by the bend inside the connector housing, while this is not possible with fixed cable elements samples. So using the method IEC 60796-1-22, method F12 to evaluate temperature cycling performance of cables to be terminated with connectors may provide a more stringent result. In order to reduce the cable impact on patchcord's environmental performance, using bend loss insensitive fiber or small sheath shrinkage material are available choices.

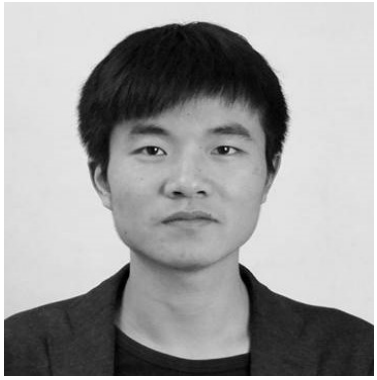
9. References

[1] IEC 60794-1-22: 2017, Optical fibre cables - Part 1-22: Generic specification - Basic optical cable test procedures - Environmental test methods

[2] IEC 61300-2-22: 2007, Fibre optic interconnecting devices and passive components - Basic test and measurement procedures - Part 2-22: Tests - Change of temperature

Return to Table of Contents

10. Authors



Jianbin Duan

Yangtze Optical Fibre and Cable Joint Stock Limited Company

9# Guanggu Road, Wuhan, China，430073

Jianbin Duan is a senior R&D engineer of Test Center in YOFC. He joined YOFC in 2014 and mainly worked on fibre measurement research and cable standardization. He received his BS and MS degree in Material Science from Huazhong University of Science and Technology.



Zhuang Xiong

Yangtze Optical Fibre and Cable Joint Stock Limited Company

9# Guanggu Road, Wuhan, China，430073

Dr. Zhuang Xiong got his B.E. degree in Mechanical Engineering from Wuhan University of Technology in 1994 and received his Ph.D. in Mechanical Manufacture and its Automation from Huazhong University of Science and Technology in 2000. Since then, he has been working in Yangtze Optical Fiber and Cable Joint Stock Co., Ltd., engaged in the research and development of optical fiber cables. Now he is the chief cable scientist in YOFC Group Innovation Center. He has obtained over 100 patents and published more than 90 technical papers. He is IWCS symposium committee member and associate rapporteur of ITU-T SG15 Q7. More over, he is also CIC(China Institute of Communications) fellow and IEC SC86A expert as well as a member of academic committee of State Key Laboratory of Optical Fiber and Cable Manufacture Technology.



Huixia Gao

Yangtze Optical Fibre and Cable Joint Stock Limited Company

9# Guanggu Road, Wuhan, China，430073

Huixia Gao is an assistant engineer of Test Center in YOFC. She joined YOFC in 2004. She has more than 6years experience in cable testing and has joined many R&D projects as test team member.



Lu Liu

Yangtze Optical Fibre and Cable Joint Stock Limited Company

9# Guanggu Road, Wuhan, China，430073

Lu Liu is a chief test engineer of Test Center at YOFC. She joined YOFC at 2010 and mainly worked on optical fibre measurement research. She received her MS degree in Material Science from Hubei University of Technology.

Return to Table of Contents



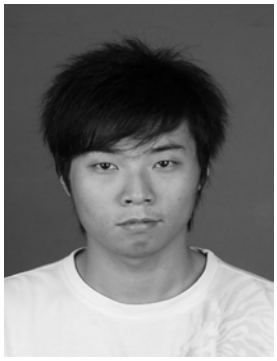
Kesen Yang
Yangtze Optical Fibre and Cable Joint Stock Limited Company
9# Guanggu Road, Wuhan, China，430073

Kesen Yang is a senior R&D engineer of Test Center in YOFC. He joined YOFC in 2014 and mainly worked on cable and material measurement research. He received his MS degree in Material Science from Huazhong University of Science and Technology.



Su Wang
Yangtze Optical Fibre and Cable Joint Stock Limited Company
9# Guanggu Road, Wuhan, China，430073

Su Wang is a senior technician of Test Center in YOFC. He has more than 6years experience in cable testing and has joined many R&D projects as test team member.



Wei Jiang
Yangtze Optical Fibre and Cable Joint Stock Limited Company
9# Guanggu Road, Wuhan, China，430073

Wei Jiang is a technician of Test Center in YOFC. He has more than 6years experience in cable testing and has joined many R&D projects as test team member.

Return to Table of Contents

Print Verification System for Wire and Cable with Optical Character Recognition

Mr. Craig Girdwood, Mr. Benjamin Lively
Taymer International Inc.
Markham, Ontario, Canada
+1-905-479-2614

Abstract

The use of the Print Verification (PV) system in detecting print defects greatly improves quality assurance on wire and cable. Print defects on the jacket are continuously detected by a machine vision system at production line speed. Images of the defects are processed and saved. This technology improves the print quality of the cable produced, thereby preventing defective products from reaching the end customer. Taymer utilizes Optical Character Recognition (OCR) in their print verification application to identify defects that are unidentifiable by print verification alone and to inspect the accuracy of the printing systems.

Keywords: Wire, cable, print defects, print verification, quality assurance, print legend inspection, inkjet printing, ink wheel printing, hot foil printing, laser printing, optical character recognition

1. Introduction

Incorrect messages, print smudging, faded print, and missing print are all print defects that should not be present on good quality products. These types of defects are not only cosmetic problems as they can also lead to misuse of the cable when it reaches the end-user. By being able to detect these defects, corrective actions can be taken at the production level and allow for the reprinting or discarding of defective pieces.

The PV system uses machine vision technology and optical character recognition to analyze, isolate, and identify print defects. The system runs inline and saves all defect image data in a database, including length and defect size. The camera is generally positioned close to the printer to optimize print legend identification and print location on the cable. Images of the print legend are captured and processed through high-speed image processing algorithms and optical character recognition. Any illegible or incorrect print legends are detected by the software, alerting the operator to take corrective action. The defective print images are stored together, allowing for further analysis or report generation.

The alert provides operators with instant feedback on current printing conditions resulting in immediate corrective actions and, more importantly, allowing the operator and process engineers to identify and reduce the root causes of print defects. This helps reduce future print defects before they happen; improving print quality, reducing rework costs, wasted consumables, and defective products.

The PV system can be easily integrated into existing production lines and works well for all types of printed products (twisted pair, jacketed, bare wires, and convoluted profiles). The system can analyze print legends from any type of printing method such as hot foil, inkjet, and laser printing.

Maintenance on the unit involves a quick wipe when the unit is dusty. The lifetime of the lights can be over 50,000 hours of usage and are the only consumable part of the whole system.

2. Current Print Inspection Techniques and Limitations

2.1 Inline Visual Inspection Using Stroboscope

This type of inspection involves using a stroboscope inline. A stroboscope flashes light at the proper period, making the print legend appear slow-moving or stationary. This allows the operator to verify the existence or quality of the print. However, there is often insufficient time to thoroughly inspect length print messages. This method is also sample-based, which means that lengthy sections of the product are not inspected. Additionally, the flashing strobe lights can be a nuisance to the operator.

2.2 Offline Viewing Through Magnifying Lens

Another sample-based technique to detect print defects is having operators inspect the print manually through a

magnifying glass. Although the operator can see the individual print defects and categorize them accordingly, this method is limited to small portions of the total product length. It can also only be used up to a relatively slow speed, so is usually only used for customers who require it. As print legends can be lengthy, there is a high chance of human error during the inspection. The repeatability of this method is also limited as each operator makes a judgment call of what is considered a 'bad' print.

2.3 Image Capture and Sampling

This process involves a camera acquiring an image based on an encoder signal and a set sampling rate. Captured images are then shown on a display for operators to assess if there are any print defects. This method has several of the same limitations as stroboscope and offline inspection. Fatigue, operator's individual judgments, and slower processing speed all reduce the effectiveness of image capture and sampling. The possibility of missing print defects is also fairly high, depending on operator attentiveness and the sampling rate.

3.Machine Vision Inspection System

3.1 Optical Mechanical Design

The Print Verification system (Figure 1) consists of a camera and focused LED lighting to capture images of print legends moving at speeds more than 1400 feet (450 meters) per minute. Multi-camera systems are used for lines where the product has multiple faces with print.

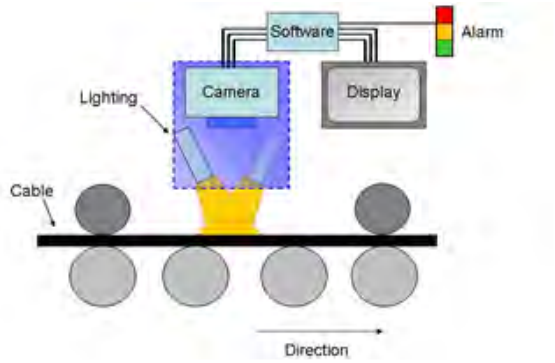
The camera and lens continuously capture images of the entirety of every print legend (Figure 2). Image capture is synchronized with the printer timing and line speed. The captured image is used for further software processing.

Lighting setups can be customized depending on the application. Factors considered include reflectivity of the surface material, surface profile, color, line speed, and lens aperture.

Figure 1. Taymer Print View System



Figure 2. Print View System Overview



3.2 Optical Character Recognition (OCR)

The Print Verification system is enhanced with Optical Character Recognition to inspect printed characters on the cable. The process involves automatic recognition of the printed text that the PV is inspecting. Images of the cable with printed characters are captured. The software analyzes and converts these characters to a machine-readable format and adds it to the captured image in the quality inspection report. This way the text on the cable is processed and understood without needing the help of the operator, and the operator can view it in the defect report.

3.3 Improving Quality Assurance

Suitable for any Type of Product

Using specialized lighting and machine vision, the PV system can inspect print legends on any type of product. With proper set-up the system can be used on wires, cables, pipes, tubes, tapes, flat sheets, and even discrete products.

Suitable for any type of Printer/ Fonts

Taymer's optical character recognition system is trained through a diverse dataset that includes a wide range of fonts and styles that enables it to recognize different character variations and makes it suitable for any type of print and font. Each PV system uses captured images of good print as a reference. This allows the system to be used to inspect print from any type of printer. As long as there is print, the PV can be used for inspection.

Reduce Defects On The Fly

The PV system provides the operator with a view of the current print legend as well as the most recent print defects. The OCR is applied to the captured image and the machine-readable characters are displayed over the print legend on the PV's user interface. This continuous stream of real-time information – especially failure data – allows operators to isolate the causes of print defects while

production lines are still running. If the print quality degrades below the set threshold, the alarm alerts the operators. Operators can use the PV system at the beginning of runs to set up printers to ensure the print legend is correct and of good quality. The real-time nature of the PV system allows changes to be made on the fly, greatly reducing costs from post-production reprinting.

Quality Assurance

The PV system captures images of printed legends at high line speeds, saving all images of print defects for use in quality reports. This combined with OCR allows the PV system to inspect accuracy as well. The display makes it easy for operators, engineering and production supervisors to examine defects alongside the accurate print. Without having to view the defect on the actual product itself – saving significant amounts of time. Defect images are saved together with location information, allowing corrective action to be taken accurately and efficiently.

Figure 3: Optical Character Recognition



3.4 Limitations

There are a few limitations to the print verification system.

- Different types of cable surfaces (round/ twisted profile), or different fonts may cause the same legend to appear different. Therefore, after significant line changes, a new reference should be taken to ensure an accurate assessment of print quality.
- As the camera captures images of the product surface, if water droplets or grease or dust particles are present on top of the print legend the print quality may appear low and trigger an alarm. This can be avoided by proper positioning of the system in line and by maintaining a clean, dry product.

3.5 Test Results

Taymer's Print Verification System has been tested and used extensively on many different types of products, with a wide range of print messages, and inspecting print from various types of printers. In studies performed on real production lines, the implementation of PV systems was found to reduce the occurrence of print defects by over 50%.

The reasons are as follows:

- Minor print quality issues are caught before they become actual defects. These are corrected by the operator adjusting the printer or fixing cable alignment.
- Printer maintenance can be initiated before printers malfunction as operators receive real-time feedback on print quality.
- Incorrect print legends are identified before entire runs are misprinted.

3.6 Sample Images

Below are sample images or screenshots (Figure 4-6) of print defects found by the PV optical system on different products.

Figure 4. Missing Print Detected at 900 ft/min



Figure 5. Poor Print Quality Detection at 200 ft/min



Figure 6. Screenshot of Print Quality Comparison



4. Conclusions

With the Print Verification system, print legends on the wire and cable can be inspected thoroughly for defects. The system provides several benefits.

- Suitable for any type of product – wire/ cable/ hose/ pipes/ bars/ plates/ stranded product
- Suitable for any type of printer – inkjet, ink wheel, hot foil, laser, etc.
- Ensures end customers do not receive defective products, improving customer relationships and confidence
- Reduces reprinting and eliminates consumable waste resulting in material cost and labor cost savings
- Assists in internal process improvements to reduce future defects

5. Pictures of Authors

Craig Girdwood
VP Sales and Marketing
Taymer International Inc.
208 Telson Road, Markham, Ontario L3R 1E6, Canada



Benjamin Lively
Machine Field Engineer
3623 E. US Hwy 70
Claremont , NC 28610



Study on thermal behavior of loose tube materials

Haifeng Hu, Yunfang Ruan, Zhuang Xiong, Jia Wang, Siyi Tang, Lin Qi

State Key Laboratory of Optical Fibre and Cable Manufacture Technology, Wuhan, 430073, China

Yangtze Optical Fibre and Cable Joint Stock Limited Company, Wuhan, 430073, China

+86 27 67887341, huhaifeng@yofc.com

Abstract

Optical fibre cables are very sensitive to thermal conditions, due to the expansion, contraction or shrinkage of the cable elements. Especially in some central loose tube cables, there is no rigid supporting element like FRPs or steel wires in the cable core. The optical fibre may reach out due to loose tube contraction, leading to fibre breakage.

To better understand the thermal performance of loose tubes, we have manufactured loose tubes made of different materials, i.e. polybutylene terephthalate (PBT), polycarbonate (PC) or polycarbonate (PP). We analyzed their dimension change under thermal conditions by Thermal Mechanical Analyzer(TMA). The test is done in the axial direction of the loose tube, the temperature range is -25~+100℃.

It is shown that the PC loose tube dimension is much more stable than the other two polymers. The PP has the biggest shrink back under thermal conditions. When we use PP to manufacture the loose tubes, we should pay more attention to its thermal behavior.

Keywords: Shrinkage, Retraction, Expansion, CLTE, Tg

1. Introduction

At present, optical fibre cables are in various structures and used in different conditions. Loose tube is widely used as secondary coating of optical fibres in optical cables, for its excellent mechanical and temperature performances. Polybutylene terephthalate (PBT) is the most widely used thermal plastic material to manufacture loose tubes. With the development of cabling technology, i.e. polybutylene terephthalate polycarbonate (PC) or polycarbonate (PP). The thermal behavior including expansion, contraction or shrinkage of these materials are different due to their natures.

To ensure the transmission performance of optical cables in different cable structure and under different temperature, we should study the thermal behavior of the cable elements and adjust manufacture processing according to its thermal behavior. In this paper, we manufactured loose tubes with different materials (i.e. PBT, PC and PP) and studied their thermal behaviors by Thermal Mechanical Analyzer(TMA).

2. Samples and experiments

Firstly, loose tubes were extruded with PBT, PC and PP materials respectively. The process was melting, extruding, drawing, cooling by water and finally taking up on drums. The diameter was 2.4mm and thickness was 0.35mm. Then, a 5~10mm sample of each loose tube was cut. The sample was placed on the TMA bench(Fig.1) to test the dimension variation in the axial direction. The test was done by heating up and cooling down the sample in the temperature range of -25~+100℃ at a rate of 10℃/min. The variation of axial dimension vs temperature was recorded.



Fig.1 TMA test bench

3. Results and Analysis

3.1 Expansion when heating up

The average coefficient of linear thermal expansion (CLTE) of different materials in the temperature range -25~100℃ was calculated and shown in table 1. The CLTE of PC was 73 x10^{-6}/℃ and was the smallest. While CLTE of PBT was 133 x10^{-6}/℃ and was the biggest.

Fig.2 showed TMA curves of the three different materials. It was observed that the curve of PC was almost linear, no glass transition behavior was observed since the glass transition temperature (Tg) was above 100℃. The PC was in glassy state and only vibration of molecular bond existed, so the CLTE was quite small. While in the PBT curve, there was a turning point observed at around 40℃ which was the Tg temperature. The PBT was in glassy state under Tg and then transited to elastomeric state when heated up to above Tg. The CLTE of PBT became 159 x10^{-6}/℃ from 99 x10^{-6}/℃ when it transited to elastomeric state. It can be explained as that the molecular of polymers could move in the elastomeric state while only molecular bond could vibration in glassy state. Unlike the other two, the curve of PP was not linear and there was no transition point. Because Tg of PP is below -25℃, PP was in elastomeric state at above -25℃. There was a decrease of CLTE at around 40℃, it was perhaps due to the cold crystallization of PP at the temperature range of 55~80℃. Because the crystallization degree is high, the rapid cooling speed led to incompletely crystallization or thermal stress when manufacturing the loose tube samples.

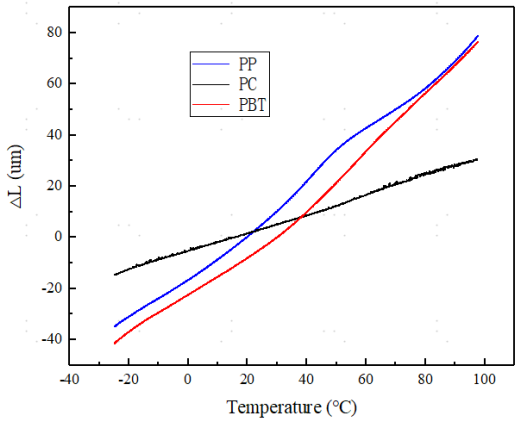


Fig.2 TMA curves of different materials when heating up

Table 1. CLTE of different materials when heating up

Material	Temperature	CLTE
PBT	-25~100°C	133x10^{-6}/°C
PC	-25~100°C	73 x10^{-6}/°C
PP	-25~100°C	107x10^{-6}/°C

3.2 Retraction when cooling down

The average coefficient of linear thermal expansion (CLTE) of different materials in the temperature range 100~-25°C was shown in table 2. Compared to heating up, the CLTE of all three materials increased and the CLTE of PP increased the most. Fig.3 showed TMA curves of the three different materials. As shown in figure, the shapes of PC and PBT curves were the same with heating up curves. While the shape of PP changed, the decrease of CLTE at 60~80°C was not observed. Because the thermal history was eliminated after the first heating up.

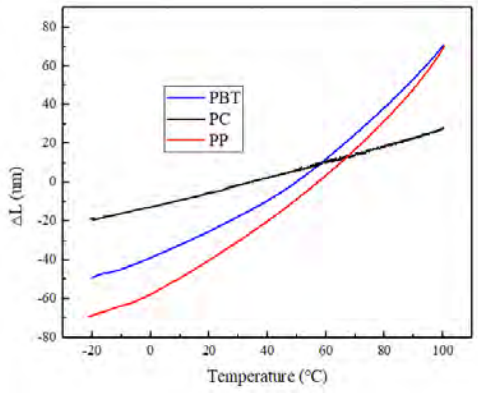


Fig.3 TMA curves of different materials when cooling down

Table 2. CLTE of different materials when cooling down

Material	Temperature	CLTE
PBT	100~-25°C	139x10^{-6}/°C
PC	100~-25°C	77 x10^{-6}/°C
PP	100~-25°C	133x10^{-6}/°C

3.3 The dimension variation after TCT

Fig.4 showed the TMA curves of heating up and cooling down for PBT. Fig.5 showed the TMA curves of heating up and cooling down for PC. Fig.6 showed the TMA curves of heating up and cooling down for PP. It was observed that the curve of heating up did not coincide with the curve of cooling down. There was a gap between the two curves, meaning a permanent shrinkage after temperature cycling test (TCT). The shrinkage of PP was the biggest. Table 3 showed the length variation (ΔL) at room temperature after TCT. It was shown that the PP shrank back 4.73‰, PBT shrank back 2.41‰ and PC shrank back only 1.45‰. So more attention should be paid to shrinkage influence when manufacturing PP loose tubes.

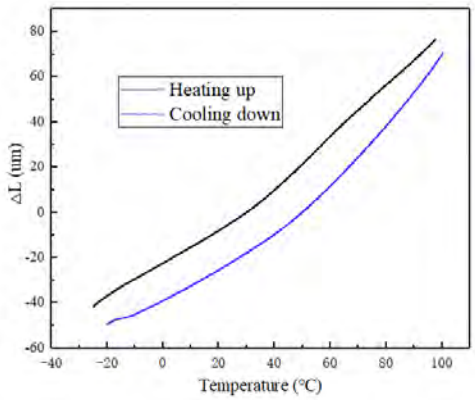


Fig.4 TMA curves of TCT for PBT

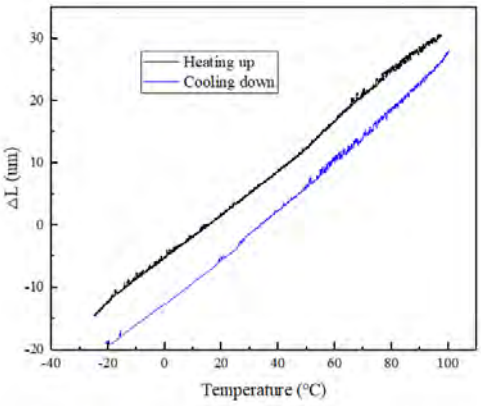


Fig.5 TMA curves of TCT for PC

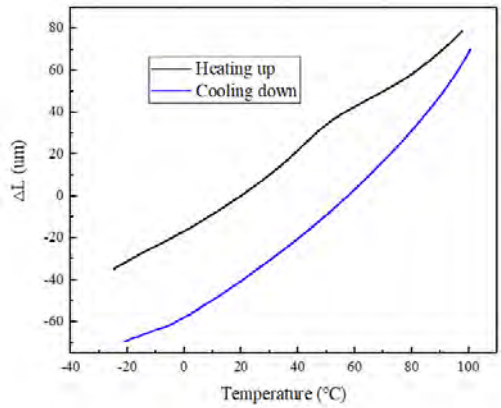


Fig.6 TMA curves of TCT for PP

Table 3. ΔL at room temperature after TCT

Material	Heating up	Cooling down	Variation
PBT	-0.22‰	-2.95‰	-2.41‰
PC	0.70‰	-0.76‰	-1.45‰
PP	0.14‰	-4.09‰	-4.73‰

4. Conclusions

In this paper, we studied thermal behavior of PBT, PC and PP loose tube materials by TMA in the temperature range of -25~100℃. The CLTE was calculated. It was found that the PC was the most stable in the work temperature range. While CLTE of PBT and PP loose tube were much bigger than PC. It is import that the dimension of PP loose tube changed the most after heating up and cooling down for one time. So in the cabling process of PP loose tube cables, we should control EFL as negative in secondary coating process, since the sheathing process will heating up and cooling down the loose tube for one cycle. On the other hand, PP is a high crystallization degree material, more attention should be paid to manufacture process to avoid thermal stress in PP loose tubes.

5. Acknowledgments

The author would like to express gratitude to everyone who cooperated in the completion, manufacture and test of the loose tube samples.

6. Pictures of Authors



Haifeng Hu

Yangtze Optical Fiber and Cable Joint Stock Limited Company

9# Guanggu Avenue

Wuhan P.R.China 430073

Miss Hu got her M.E. degree in Material Science and Engineering from Huazhong University of Science and Technology in 2013. She jointed Yangtze Optical Fibre and Cable Company Ltd in 2017. She is now a research and development engineer of R&D dept.



Yunfang Ruan

Yangtze Optical Fiber and Cable Joint Stock Limited Company

9# Guanggu Avenue

Wuhan P.R.China 430073

Mr. Yunfang Ruan received his B.S degree in mechanical and electronic engineering from Hubei Institute of Technology in 1996. He has been working in YOFC since 1997. Now he is R&D engineer, mainly engaged in cable production process control and product development work.



Zhuang Xiong

Yangtze Optical Fiber and Cable Joint Stock Limited Company

9# Guanggu Avenue

Wuhan P.R.China 430073

Dr. Zhuang Xiong got his B.E. degree in Mechanical Engineering from Wuhan Institute of Technology in 1994 and received his Ph.D.in Mechanical Manufacture and its Automation from Huazhong University of Science and Technology in 2000. Since then he has been working in Yangtze Optical Fiber and Cable Co.



Jia Wang

Yangtze Optical Fiber and Cable Joint Stock Limited Company

9# Guanggu Avenue

Wuhan P.R.China 430073

Mr. Jia Wang received his M.S degree in Materials Processing from University of Science and Technology of China in 2020. Since then, he has been working in YOFC. Now he is a R&D engineer of R&D Centre of YOFC, engaged in research and development of optical fiber cable.



Siyi Tang

Yangtze Optical Fiber and Cable Joint Stock Limited Company

9# Guanggu Avenue

Wuhan P.R.China 430073



Mrs. Siyi Tang received her M.S degree in Polymer science and engineering from Sichuan University in 2021. Since then, she has been working in YOFC. Now she is a R&D engineer of R&D Centre of YOFC, engaged in research and development of optical fiber cable.

Lin Qi

Yangtze Optical Fiber and Cable Joint Stock Limited Company

9# Guanggu Avenue

Wuhan P.R.China 430073

Mr. Qi Lin received his master degree of Electro-mechanical engineering from Wuhan University of Technical in 2006. He worked in YOFC science 2009, dedicated in optical cable design and development.

THANK YOU TO OUR SPONSORS

PARTNER

alphagary
An Orbia business.

CABLE COMPONENTS GROUP

Chemours™

COMMSCOPE®

CORNING

covestro

DOW®

HUBER ADVANCED MATERIALS

LAPP

ofs

Prysmian Group

TA TEKNOR APEX

UL Solutions

PLATINUM

EPIC

Lloyd & Bouvier Inc.

MASTERCHEM SOLUTIONS

THANK YOU TO OUR SPONSORS

GOLD

BASF We create chemistry

CARRISREELS employee-owned • customer driven

COPPERWELD

DAIKIN

fiber optic center

GRAHAM ENGINEERING

INDORE "Strengthening Tomorrow"

MHolland

Nabaltec

PROTON PRODUCTS

REELEX PACKAGING SOLUTIONS INC.

TEIJIN

YOFC Smart Link Better Life.

DONOR

AGC

ARKEMA

Cimteq by UL Solutions

Heraeus Noblelight

kuraray

SICCETUSA Your Special Cables Solutions

WONDERFUL

ASSOCIATION & MEDIA PARTNERS

CCCA Communications Cable & Connectivity Association

Connector Supplier™

CRU World Optical Fibre & Cable 2023 Hosted by YOFC 24-26 October 2023 • Jakarta, Indonesia

euro Wire

submarine telecoms FORUM

INSTITUTE vinyl

VINYL SUSTAINABILITY COUNCIL

WIRE JOURNAL INTERNATIONAL

WCISA Wire and Cable Industry Suppliers Association®

Wire & Cable ASIA

WCMA Wire & Cable Manufacturers Alliance

THE WIRE ASSOCIATION INTERNATIONAL, INC.

wire WORLD

Wire & Cable Technology International

Wire & Cable Technology International (WCTI) is the "Official Magazine of the IWCS", and we publish several IWCS articles throughout the year as well as the annual IWCS preview article and the annual IWCS supplier exhibition directory.

2023 IWCS BOARD & SYMPOSIUM COMMITTEE MEMBERS

IWCS STAFF

DAVID B. KIDDOO (CEO/Director)
IWCS, Inc., USA

MICHELLE MELSOP (Senior Operations Manager)
IWCS, Inc., USA

REBECCA DIPPEL (MarCom Manager)
IWCS, Inc., USA

BOARD OF DIRECTORS

DR. SCOTT H. WASSERMAN (Chair)
Dow, USA

BEN WAITE (Vice-Chair)
Fiber Optic Center, Inc., USA

JEFF S. BARKER (Treasurer)
Prysmian Group, USA

ROBERT A. WESSELS, JR. (Chair Emeritus)
CommScope, Inc., USA

LARRY BLEICH
CommScope, Inc., USA

DAVID BRAUN
Teknor Apex Company, USA

ERIC BULINGTON
UL Solutions, USA

ROBERT M. CANNY
TE Wire & Cable, USA

ALISTAIR DUFFY
Faculty of Computing, De Montfort University, UK

ROBERT B. ELKINS
Corning Optical Communications LLC

DAVE FALLOWFIELD
Canada

STEVEN A. GALAN
USA

CHARLES GLEW
Cable Components Group, USA

TRENT HAYES
CommScope, Inc., USA

BOARD OF DIRECTORS *continued*

KAZUNORI KATAYAMA
NTT Access Network Service Systems Laboratories, Japan

MARKUS F. KEMMLER
Kemmler Consulting GmbH, Germany

MIKE PATEL
Teknor Apex, USA

KERRY SMITH
Nabaltec, USA

JERMAINE TAYLOR
OFS Optics, USA

2023 SYMPOSIUM COMMITTEE OFFICERS

DR. BIANCA HYDUTSKY (Chair)
The Chemours Company, USA

MIKE GURRERI (Vice-Chair)
CommScope, Inc., USA

BULENT KOSE (2nd Vice-Chair)
Panduit Corp., USA

2023 SYMPOSIUM COMMITTEE MEMBERS

YOSHIHIRO ARASHITANI
Furukawa Electric Co., LTD., Japan

DMITRIY BODIK
UL Solutions, USA

PAUL BRIGANDI
Dow, USA

KENNETH CORNELISON
Wire & Cable Technology Resources, USA

JOHN DIMEGLIO
Lapp Inc., USA

HÉLIO J. DURIGAN
Furukawa Electric LatAm S.A., Brazil

MEHDI EMAD
Solvay Specialty Polymers, USA

ED FENTON
Daikin America, USA

2023 SYMPOSIUM COMMITTEE *continued*

EDUARDO GARZA
Hitachi Cable America, Inc., USA

MICHAEL J. GIMBLET
Corning Optical Communications LLC, USA

DR. SVEND HOPLAND
Hopland MarinInstal, Norway

WAYNE KACHMAR
Technical Horsepower Consulting LLC, USA

ROBERT LAROCCA
UL Solutions, USA

ERIC LAWRENCE
Leviton Manufacturing Co., USA

MICHAEL J. MCNULTY
Wire & Cable Technology Int'l, WCISA®, USA
Wire & Cable Industry Suppliers Association®, USA

JON MELLO
Teknor Apex Company, USA

DOUGLAS A. PARKER
FO Connect Consulting, USA

DR. BRIAN RISCH
Prysmian Group, USA

LYNNE RUSSELL
Cable Components Group, USA

THOMAS SCHELLING
J.M. Huber Corporation, USA

MATTEO SOLARI
S.I.C.C.E.T. S.r.l., Italy

MARIE-ANGE VATIN
Covestro, USA

ERIC WHITHAM
OFS, a Furukawa Company, USA

DANIEL WINKLER
E.G.O. North America, Inc., USA

SHARON WROBEL
Wesco Distribution, USA

ZHUANG (FRANK) XIONG
Yangtze Optical Fibre and Cable Joint Stock Ltd. Co., China

Questions?
Please contact Michelle Melsop, *Sr. Operations Manager* E-Mail: mmelsop@iwcs.org

IWCS, Inc.
6920-B Braddock Road, PMB 650
Annandale, VA 22003 USA

IWCS.ORG

#IWCS2023

IWCS, Inc. produces an annual forum for the presentation and discussion of key technology developments for the wire, cable and connectivity industry. In providing such a forum, IWCS neither endorses, sanctions, nor recommends any technical developments described in the presented work. IWCS also neither recommends that parties make development plans nor that they make purchasing decisions based on any work presented in written, live or video formats observed as part of our forum.